Contributions to the Foundations of Multidisciplinary Research in Mechanics

Papers presented during the 24th International Congress of Theoretical and Applied Mechanics ICTAM2016, Montreal 22-26, 2016

Editor: J.M. Floryan

Volume 1

Mechanics — Foundation of Multidisciplinary Research

La méchanique — fondement de la recherche multidisciplinaire

ICTAM 2016
MONTRÉAL

International Union of Theoretical and Applied Mechanics

Foreword

These Proceedings contain all papers presented during the 24th International Congress of Theoretical and Applied Mechanics (ICTAM 2016) held in Montreal, Canada, August 22-26, 2016. Papers have been reviewed by the National Mechanics Committees (where appropriate), chairs of thematic sessions and mini-symposia and the International Papers Committee which made the final determination regarding their suitability.
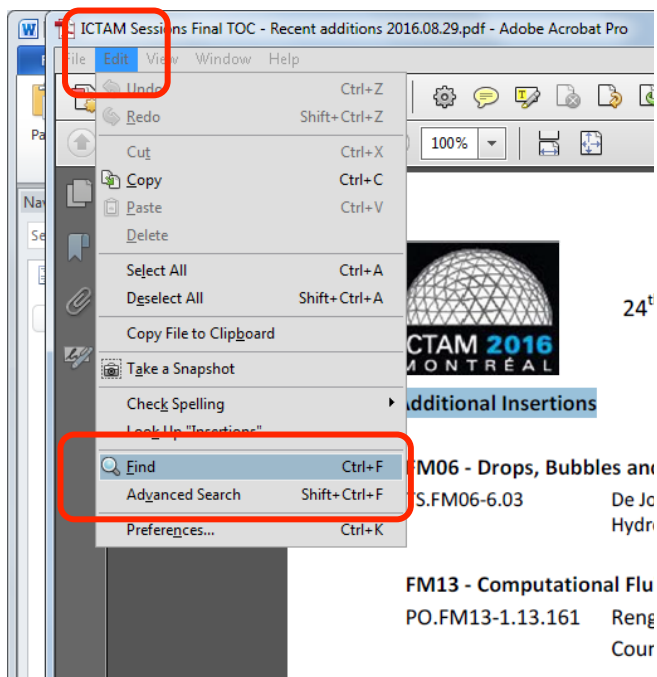
We would like to acknowledge contributions of the International Papers Committee to the development of the scientific program of ICTAM 2016. The editing work has been assisted by the National Research Council of Canada and Legend Conference Planning.

J.M. Floryan
President, ICTAM 2016

Search feature

This ICTAM 2016 Proceedings pdf's search features are enhanced when opened with Adobe Acrobat Reader or Pro. To download the latest version of Adobe Acrobat Reader, visit: https://get.adobe.com/reader/

To search for an author, a keyword or an expression, use the find function under Edit >> Find:

or hit the Ctrl + F keys:

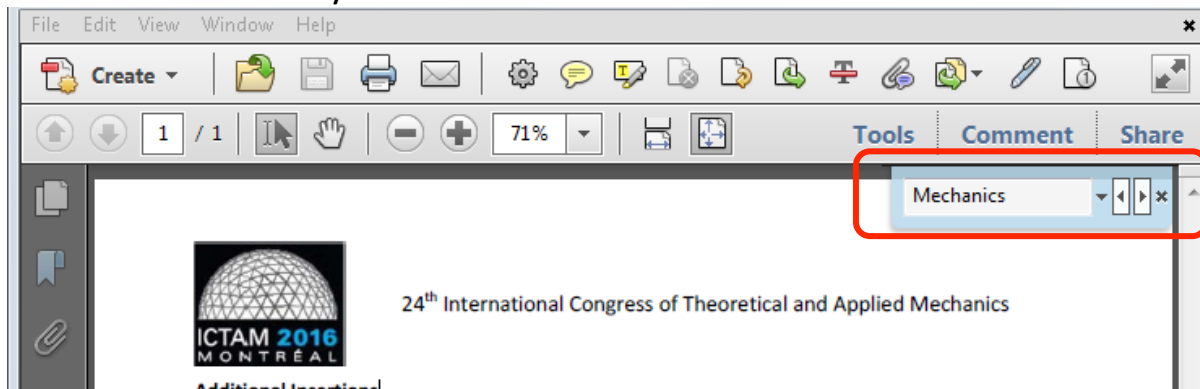# Table of Contents

VOLUME 2

Papers Contributed to Thematic Sessions - Fluid Mechanics

VOLUME 3

Papers Contributed to Thematic Sessions - Solid Mechanics

VOLUME 4

Papers Contributed to Thematic Sessions on Fluid-Solid Interactions and on Education in Mechanics

OCEAN TURBULENCE AND CLIMATE HISTORY

W. Richard Peltier

Department of Physics, University of Toronto, Toronto, Ontario, Canada

Summary The global oceans play a critical role in the climate system, not only in the transport of heat from the equator towards the poles but also in the global carbon cycle. Although the wind driven component of this circulation continues to be of interest, the thermohaline or Meridional Overturning Circulation (MOC) component is of particular importance and interest from a fundamental fluid mechanical perspective. This is because its existence depends upon the continuous generation of small scale turbulence engendered primarily by the breaking of hydrodynamic waves. A primary source of excitation of these waves is the flow of the lunar barotropic tide over ocean bottom topography. The turbulence produced by wave breaking effects a vertical flux of mass that may be characterized by an effective turbulent diffusivity and it is this vertical flux of mass that enables the high density deep water that forms at the poles to return to the surface. Following a review of recent advances in the characterization of this diffusivity, it will be demonstrated that a previously unexplained phenomenon in climate system history, the so-called Dansgaard-Oeschger oscillation (see Figure 1), can be understood in terms of a global-scale relaxation oscillation of the Atlantic MOC. It is furthermore shown that this nonlinear oscillation is highly sensitive to the representation of stratified turbulence. This is an extreme example of a multi-scale dynamical phenomenon in which small scale turbulence controls not only the existence but also the millennium timescale of a truly global scale climate related oscillatory phenomenon.

BREAKING WAVE INDUCED MIXING: MODEL PROBLEMS

Our interest is in the high Reynolds number regime that is appropriate for environmentally relevant circumstances, specifically but not exclusively for the oceans. Since we are interested in phenomenology in which the turbulence of interest develops in a background that is stably stratified in density, appropriate model problems will consist of "parallel" flows in which the background is destabilized by shear, in which case the primary instability leading to transition will be governed by the Miles-Howard Theorem which asserts that a necessary condition for instability is that the gradient Richardson number be less than 0.25 somewhere in the vertical. Although there are several distinct types of instability that may occur in such circumstances, the primary types are those first identified by Kelvin and Helmholtz (hereafter KHI) and by Holmboe (hereafter HI) which differ from one another by the ratio of the depth of the shear zone to that of the coincident density inversion. Both mechanisms generate waves which inevitably break at sufficiently high Re and the turbulence thereby produced may be analysed through DNS analyses to infer the diapycnal diffusivity that is characteristic of the typical life-cycle of such an event [we employ the spectral element software of Fischer et al., 1, to obtain the DNS results to be described]. This requires careful distinction between the irreversible "mixing" associated with the event and the entirely reversible "stirring" that can contribute nothing to diapycal turbulent diffusion. This requires explicit use of the concept of Available Potential Energy (APE) that was originally introduced by Lorenz in the context of his analysis of the atmospheric general circulation [eg. 2]. We employ the results from these model problems to compare the turbulent diffusivities inferred on the basis of analyses of the associated stratified turbulence to reveal explicitly the nature of the errors incurred when these diffusivities are determined on the basis of several commonly employed models including the simplest model based upon the Prandtl mixing length idea as well as more sophisticated but nevertheless inaccurate models such as that due to Osborn [3] which continues to be widely employed in the area of physical oceanography [4].

A critical issue that cannot be avoided in the inference of irreversible mixing is that of mixing "efficiency", an estimate of which Osborn believed to be provided by the "flux" Richardson number and which he imagined could be assumed to be fixed to a constant value of 0.2 for practical oceanographic applications. It is now widely understood, however, that mixing efficiency is a strong function of at least two characteristics of the turbulence, respectively a measure of turbulence intensity as provided by the buoyancy Reynolds number and a parameter dependent upon the shear that is perhaps best represented by "bulk" Richardson number. In the oceans, where density may be strongly controlled by salinity due to the highly nonlinear nature of the equation of state, especially under cold temperature conditions, the Prandtl number may also exert a further impact upon mixing efficiency [5]. Its inference on the basis of the DNS data requires a complete sorting of the individual density elements of which the flow is comprised at each time step in its evolution so as to determine the evolution of the minimum potential energy state that could be reached by adiabatic rearrangement and thereby the extent to which irreversible processes associated with the destruction of small scale density variance have occurred.

DIAPYCNAL TURBULENT DIFFUSIVITY AND MOC TIME DEPENDENCE

Although it is well understood that the existence of the MOC depends entirely upon the action of small scale diapycnal turbulent diffusivity, it is an interesting issue as to what role this physical process might play, if any, in the time dependence of this global scale component of the ocean general circulation and thereby climate. Although such time dependence has often been invoked in the understanding of isolated events in the Climate System, it has only recently proven possible to

---

[a] Corresponding author. Email: peltier@atmosp.physics.utoronto.ca

make a connection between observations of climate variability and MOC time dependence. This has been possible by providing a detailed fluid mechanical understanding of the so-called Dansgaard-Oeschger oscillation phenomenon, an oscillation with a timescale of approximately a millennium in the temperature of the North Atlantic sector of the climate system which has been inferred to have occurred under cold glacial climate conditions. The data, shown on Figure 1, in terms of which the existence of the phenomenon has been inferred, consist of measurements of oxygen isotopes in ice cores extracted by drilling into the Greenland ice sheet, the modern data shown on this figure being derived from holes drilled at the Summit location. Inspection of the figure will show that the individually numbered D-O cycles appear to be triggered by events labelled "H" in the individual time series. These so-called "Heinrich" events correspond to intense inputs of floating ice from the eastern flank of the ice sheet that covered all of Canada at the last maximum of glaciation approximately 21,000 years ago. When measured in an ice-core, the oxygen isotopic signal is a proxy for the temperature of the air from which the precipitation over Greenland derived. It is therefore a climate related signal that requires explanation.

The hydrodynamic explanation of this phenomenon, one that connects it unambiguously to the time dependence of the MOC, proves to be quite sensitive to the representation of turbulent diapycnal diffusivity employed in a global ocean model. In order to establish this fact, a modern coupled climate model that includes a detailed representation of ocean hydrodynamics, the CESM1 model of the US National Center for Atmospheric Research, has been integrated at high spatial resolution over a period of multiple millennia with the surface boundary conditions of ice cover and land-sea distribution appropriate to cold glacial maximum conditions. The results of this analysis have demonstrated that, when the surface ocean under these conditions is struck by a Heinrich event related transient forcing that causes intense cooling of the northern hemisphere, a fibrillation in the strength of the MOC on the observed millennium timescale occurs. The model also explains the temperature signal inferred on the basis of Greenland oxygen isotopic data as well as the related signal derived from ice cores drilled from the Antarctic ice sheet in the opposite hemisphere. I have referred to the D-O phenomenology as involving the action of a "kicked" salt oscillator in the Atlantic [6], the details of which I will explain in the presentation
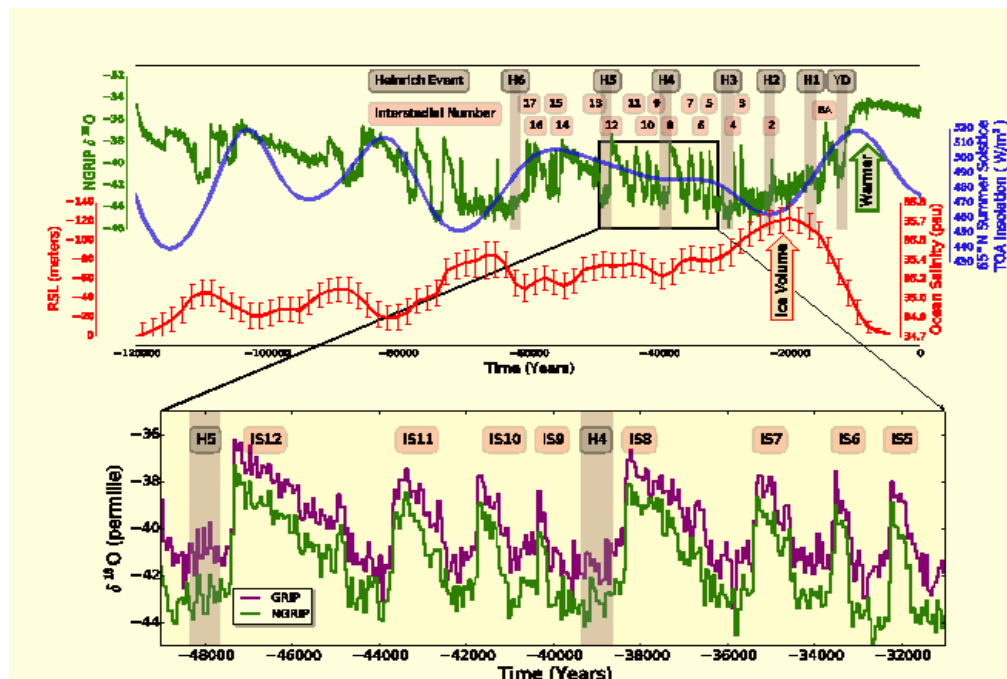
Figure 1. The upper frame illustrates the evolution of a number of climate related variables over the most recent 100,000 years of Earth history including northern hemisphere summer solar insolation at 65 degrees north latitude (in blue), continental ice volume (in red) and the oxygen isotopipc signal from the NGRIP ice core from summit Greenland (in green). The lower frame shows a blow-up of the oxgen isotopic signal from NGRIP compared to that from the GRIP hole which was drilled some km distant, a comparison that demonstrates that the signals are very highly correlated. The numbered shaded regions correspond to Heinrich events while those number IS (for InterStadial) correspond to individual D-O cycles.

References

[1] Fischer, P.F. et al. J. Sci. Comput. 17, (1-4), 2002.

[2] Peltier, W.R. and Caulfield, C.P. Ann. Rev. Fluid Mech.. 35, 135-167, 2003.

[3] Osborn, P.F. J. Phys. Oceanogr. 10, 83-89, 1980.

[4] Salehipour, H. and Peltier, W.R. J. Fluid Mech. 775, 464-500, 2015.

[5] Salehipour, H., Peltier, W.R. and Mashayek, A. J. Fluid mech. 773, 178-223, 2015.

[6] Peltier, W.R. and Vettoretti, G. Geophys. Res. Lett. 41, 7306-7313, 2014.

MICROARCHITECTURED MATERIALS: ARE THEY EFFECTIVE?

Norman Fleck[1a],
[1]Cambridge University Engineering Dept., Trumpington St., Cambridge, CB2 1PZ, UK

Summary An overview is presented of the role of microarchitecture in dictating the properties of engineering materials, ranging from the bulk to coatings and adhesive joints.   Some properties (modulus, strength) are remarkably insensitive to imperfections, whilst others (toughness and ductility) can be severely degraded by imperfections.   There is scope to reinforce by the addition of a second phase, and indeed to prestress, akin pre-stressed concrete.   The presentation considers 3 inter-related topics: the effective properties of bulk lattices, microacrhitectured adhesive joints and the significance of boundary layers in composite coatings.

FROM BRITTLE FOAMS TO TOUGH AND DUCTILE LATTICES

Lattice materials are emerging with a broad range of properties due to their combination of microarchitecture, length scale and composition.   They have impressive properties: as bulk materials, as the cores of sandwich panels and as engineered surfaces.   Toughness knows no bounds, and high toughness can be achieved by the successive renucleation of fracture in the lattice ahead of a macroscopic crack tip.   Likewise, there are no theoretical bounds for tensile ductility.   There is a recent emergence of multi-phase lattice materials due to a combination of two or more constituent lattices.   Extreme properties, such as high strength are evident with a diminishing length scale, but new challenges (such as adhesion of neighbouring cell walls and low toughness) also appear.

The sensitivity of toughness and ductility to microstructure of elasto-plastic lattices are assessed.   A range of imperfections are considered in order to attempt to explain the remarkably low tensile ductility of metallic and polymeric foams;   these include randomly displaced joints, missing cell walls and Plateau borders for the case of foams.   The formation of densification bands in compression is explored, and it is shown that buckling and volumetric lock-up can protect a lattice from failure of the struts.

Reinforcement (and pre-stressing) of foams (and lattices) is possible by the addition of a second phase as an inter-penetrating lattice.   This is explored for the case of a foam-cored sandwich beam with pre-stressed faces.

MICROARCHITECTURED ADHISIVE JOINTS

Adhesive joints are used increasingly structural engineering components. There is a challenge to control the strength and toughness of the joint (under remote tension and under remote shear), by suitable design of the microarchitecture of the joint. A joint of 'square-wave' topology is manufactured using aluminium substrates and a silicone-based elastomeric adhesive layer.   Under remote tensile loading of the joint, the top and bottom faces of the square-wave behave as butt joints, while the side faces behave as lap joints.   The overall tensile strength and work of fracture of the 'square-wave' joint can thereby be predicted, see Fig. 1.   Maps are constructed to show the sensitivity of joint strength, toughness and transition flaw size to joint architecture (amplitude/wavelength of square wave).   Additionally, the crack resistance of the square-wave joint is measured by testing a double cantilever beam specimen.   Accurate macroscopic crack growth predictions are made by taking the tensile response of the square-wave joint to define a cohesive zone law between elastic substrates.

EFFECTIVE PROPERTIES OF COMPOSITE LAYERS – FROM COATINSG TO ADHESIVE LAYERS

Surface coatings and embedded layers are ubiquitous in engineering components, and serve a wide range of functions from environmental protection to low friction and wear resistance.   A related geometry to the surface coating is the embedded layer sandwiched between two substrates.   This geometry is also ubiquitous and is representative of adhesive joints, the mortar between the bricks of a building, and interphases at grain boundaries *inter alia*.

Frequently, a coating comprises a multi-phase composite with, for example, particulate reinforcement in order to increase its stiffness and strength.   *The question arises: what are the effective properties of a composite coating?*   A common assumption is to use the effective properties of the *bulk* composite for that of the *coating*.   Whilst this assumption is accurate when the correlation length of each phase is much less than the coating thickness, it is less accurate when the two length scales are of comparable magnitude.   The presence of the substrate or a free surface perturbs the stress field within the composite coating.   This can be re-phrased in a more mathematical manner, as follows.   The usual Hashin-Shtrikman variational approach for the bulk properties of a composite makes use of the infinite-body Greens function in order to determine the ensemble-averaged strain field in terms of a polarization in stress from one phase to the next.   For the embedded layer, the

---

[a] Corresponding author. Email: naf1@eng.cam.ac.uk

infinite-body Greens function is employed, whereas for a surface coating the half-space Greens function is exploited. The presence of the substrate or free surface perturbs the 'interaction stresses' from phase to phase, and consequently the effective properties of the coating differ from those predicted for the bulk composite of equal thickness. Boundary layers emerge within the coating, adjacent to the substrate and free surface.

The purpose of this study is to make accurate predictions for the effective properties of a *surface composite coating* or an *embedded composite* layer, taking into account the presence of the substrate of differing properties, whether *linear* or *non-linear*. Effective properties and associated bounds are generated for composite coatings and for composite sandwich layers of finite thickness, based on the Hashin-Shtrikman approach, but suitably modified to account for the presence of a free surface in the case of a coating and of substrates in the case of a sandwich layer. First, the linear properties are generated and then the method is modified to generate bounds and estimates for a non-linear composite coating. We limit our scoping study to two-dimensional problems by considering anti-plane shear of an isotropic 2-phase composite on a single-phase substrate, with microstructure prismatic along the direction of anti-plane shear.
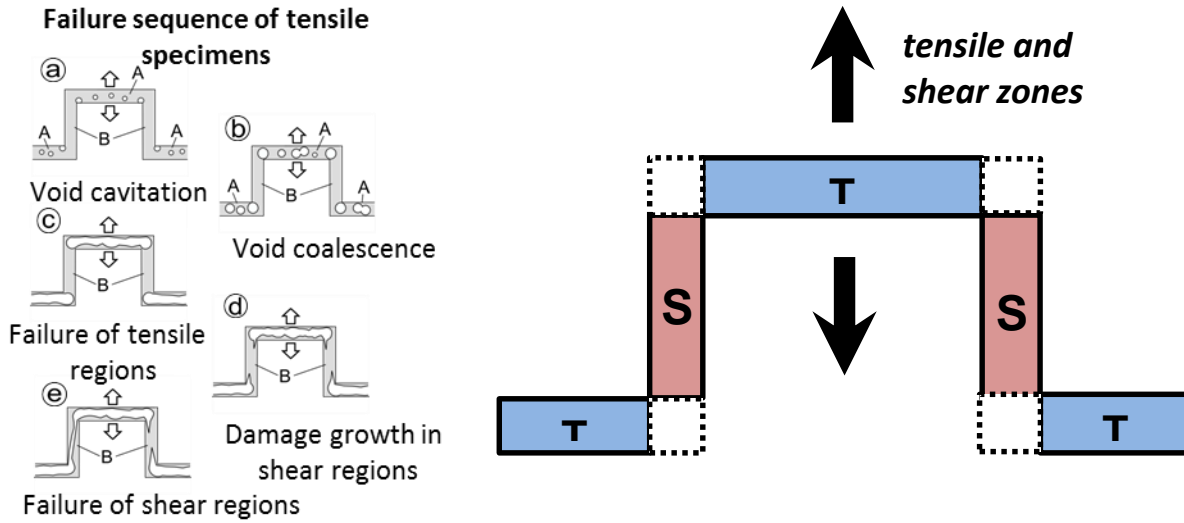
Fig. 1   A microarchitectured adhesive joint

CONCLUSIONS

There is scope to develop microarchitecture lattice materials with a wide range of topologies, and engineering properties. Recent advances in additive manufacture and in nanoscale manufacture have stimulated this activity, due to the ability to co-deposit two or more lattices. The effective properties for a wide range of topologies have been determined, and defect sensitivity assessed. Reinforcement and pre-stressing by a second phase can be used to increase strength and toughness. Finally, the effective properties of composite coatings is explored, and the role of boundary layers emphasised.

APPLICATION OF NONLINEAR ELASTICITY TO SOFT TISSUE BIOMECHANICS

Ray W. Ogden[*1] and Gerhard A. Holzapfel[2]

[1]*School of Mathematics and Statistics, University of Glasgow, Glasgow, UK*
[2]*Institute of Biomechanics, Graz University of Technology, Graz, Austria*

Summary After a short background discussion, this lecture will focus on the application of anisotropic nonlinear elasticity theory to the modelling of the mechanical properties of soft biological tissues, with particular attention paid to the properties of artery walls and their layered fibrous structure. We shall describe how our models have developed in sophistication as more and more experimental data have become available to inform the modelling process, with particular reference to the details of collagen fibre dispersion and the most recent model involving non-symmetric fibre dispersion. We shall also touch on recent work that shows how omitting the contribution of fibres within a dispersion that are compressed during deformation makes a significant difference to the stress response of the material.

BACKGROUND

The theory of nonlinear elasticity was developed largely by Rivlin in the 1940s and 1950s because of the need to describe the properties of rubberlike materials and to predict the behaviour of these materials for different geometries and under various loading regimes. Rivlin's substantial works are contained in the two-volume collection of papers edited by Barenblatt and Joseph [1] and are a continuing source of reference for researchers in the area. In more recent years, while significant interest in the application of the theory of elasticity, and also inelasticity, remains, much attention has turned towards applications in the field of biomechanics, in particular for applications to the mechanics of soft biological tissues such as artery walls and heart tissue, as exemplified in Humphrey's book [2]. Further stimulus for the theory has been found relatively recently in the need to analyze the properties of so-called 'smart materials', which include electro-sensitive and magneto-sensitive elastomers capable of large elastic deformation induced by applied electric or magnetic fields. Such materials have been developed for applications to sensors, actuators and artificial muscles, for example, and to fully understand their behaviour the theories of nonlinear electro-elasticity and magneto-elasticity are required, as summarized in the recent volume [3]. This presentation, however, focuses entirely on the biomechanics applications.

Soft biological tissues have a very complicated structure, only some of which can be seen depicted in this widely used schematic figure from [4]. Within the structure the collagen fibres have a very important role since they are considerably stiffer than the surrounding material in which they are embedded and they endow the material with anisotropic properties. To describe the elastic properties of soft materials with a fibrous structure the theory of nonlinear elasticity that incorporates preferred directions, the local fibre directions, is required. The two main solid mechanically relevant layers of a healthy artery wall, the media and adventitia, typically contain families of collagen fibres that are arranged symmetrically in two helical structures, and this (idealized) structure was the basis for our first contribution to the elasticity of arteries described in [4]. Subsequently it became apparent that a slightly more sophisticated model that accounted for the dispersion in the fibre orientations about the mean helical structure was required, and to accommodate this we introduced the notion of a generalized structure tensor that incorporated a measure of the dispersion, and this was published in [5].

Composite reinforced by collagen fibers arranged in helical structures

Helically arranged fiber-reinforced medial layers

Bundles of collagen fibrils
External elastic lamina
Elastic lamina
Elastic fibrils
Collagen fibrils
Smooth muscle cell
Internal elastic lamina
Endothelial cell

Intima
Media
Adventitia

Both papers have been very successful and the models they contain have been applied to a wide range of soft biological tissues. However, recent very detailed and extensive experimental work [6, 7] highlighting the collagen fibre dispersion in a range of different arteries has shown that a more general model is needed to account for the three-dimensional dispersion. In particular, the rotationally symmetric dispersion model in [5] cannot account for these data. This prompted us to develop a non-symmetric fibre dispersion model to accommodate the new findings, and this was published recently in [8].
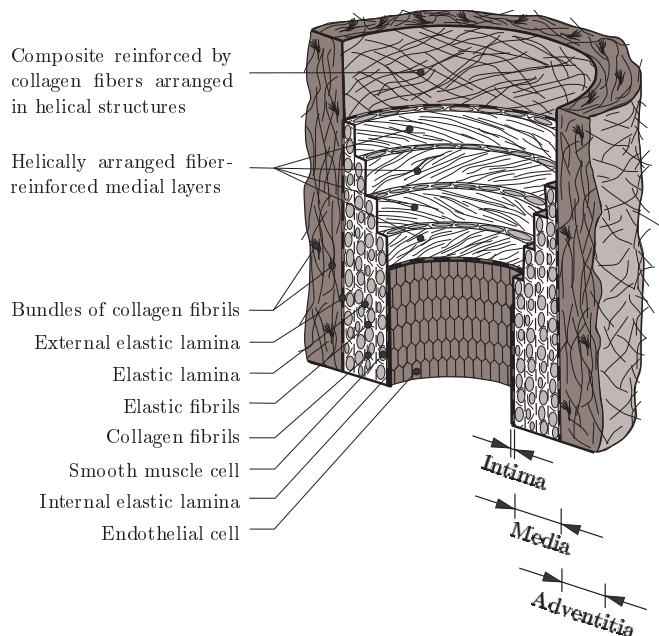
*Corresponding author. Email: raymond.ogden@glasgow.ac.uk

CONTENT OF THE LECTURE

In this lecture we shall describe the development of our constitutive models of arterial elasticity starting from the model with two helically arranged families of fibres in [4] and then going on to the models of fibre dispersion in [5, 8]. The non-symmetric fibre dispersion model in [8] is based on a bi-variate von Mises distribution of fibres and introduces new structure tensors, one for each fibre family, which are incorporated into the constitutive law to model the fibre dispersion. Necessarily we shall cover some background material on nonlinear anisotropic elasticity and constitutive laws that govern the nonlinear elastic response of fibrous solids. Then, with reference to experimental data, models that have a specific structure but are special cases within the general constitutive framework will be described, and their predictions will be examined for particular simple deformations. The non-symmetric fibre dispersion model, in particular, will be described in detail. We shall also make reference to the important effect that residual stresses in unloaded arteries have on their response when loaded.

In the literature it is often considered that collagen fibres do not support significant stress when under compression and so should be excluded from constitutive models when the material is subject to deformations for which they are compressed. It is debatable to what extent this notion should be applied since multiple fibres in the matrix within which they are embedded may well support at least some compressive stress. Nevertheless, in recent (as yet unpublished) work we have explored the effect of omitting compressed fibres within a dispersion from the analysis and we have found that this makes a considerable difference to the stress response of the material when there is significant dispersion. This will be discussed briefly during the lecture.

References

[1] Barenblatt G.I., Joseph D.D.: Collected Papers of R.S. Rivlin. Springer, New York 1997.

[2] Humphrey J.D.: Cardiovascular Solid Mechanics. Springer, New York 2002.

[3] Dorfmann L., Ogden R.W.: Nonlinear Theory of Electroelastic and Magnetoelastic Interactions. Springer, New York 2014.

[4] Holzapfel G.A, Gasser T.C., Ogden R.W.: A new constitutive framework for arterial wall mechanics and a comparative study of material models. J. Elasticity 61:1-48, 2000.

[5] Gasser T.C., Ogden R.W., Holzapfel G.A.: Hyperelastic modelling of arterial layers with distributed collagen fibre orientations. J. R. Soc. Interface 3:15-35, 2006.

[6] Schriefl A.J., Zeindlinger G., Pierce D.M., Regitnig P., Holzapfel G.A.: Determination of the layer-specific distributed collagen fiber orientations in human thoracic and abdominal aortas and common iliac arteries. J. R. Soc. Interface 9:1275-1286.

[7] Schriefl A.J., Reinisch A.J., Sankaran S., Pierce D.M., Holzapfel G.A.: Quantitative assessment of collagen fiber orientations from two-dimensional images of soft biological tissues. J. R. Soc. Interface 9:3081-3093, 2012.

[8] Holzapfel G.A., Niestrawska J., Ogden R.W., Reinisch A.J., Schriefl A.J.: Modelling non-symmetric collagen fibre dispersion in arterial walls. J. R. Soc. Interface 12: 2015.0188, 2015.

FLUID DYNAMICS AT THE SCALE OF THE CELL

Raymond E. Goldstein*

Department of Applied Mathematics and Theoretical Physics, University of Cambridge, United Kingdom

Summary The world of cellular biology provides us with many fascinating fluid dynamical phenomena that lie at the heart of important aspects of physiology, development, and ecology. Advances in imaging, micromanipulation, and microfluidics over the past decade have allowed for high-precision measurements of such flows, providing tests of fundamental theories about microhydrodynamics and also revealing a wealth of new phenomena which call out for explanation. In this lecture I summarize this progress in the context of four issues: cytoplasmic streaming in plant and animal cells, synchronization of eukaryotic flagella, collective behaviour in dense suspensions of microswimmers, and the interaction between swimming cells and surfaces. Throughout, I emphasize the role of fluid dynamics in an interdisciplinary approach to the mysteries of biology.

*Email: R.E.Goldstein@damtp.cam.ac.uk

Sectional Lecture in Fluids

Sectional Lecture in Solids

Sectional Lecture in Fluids-Solids

MODELS OF COHERENT STRUCTURES IN TURBULENT JETS AND THEIR RADIATED SOUND

Tim Colonius[*1], Aaron Towne[1], and Oliver Schmidt[1]

[1]*Department of Mechanical and Civil Engineering, California Institute of Technology, Pasadena, CA USA*

Summary This paper provides an overview of recent research aimed at modeling the coherent structures that comprise the dominant source of mixing noise in high-speed, turbulent jets. A trove of new data from numerical simulations and state-of-the-art measurement techniques are being fruitfully combined with computationally-enabled access to the eigenspace of large, non-normal, linear systems, in order to provide tools whereby turbulent structure and mechanism can be reliably educed, and through which quantitatively accurate models are now emerging. Beyond jet noise, these models have a role to play in controlling turbulence in a variety of free and wall-bounded shear flows.

Background

Enormous progress has been made towards the accurate prediction, via large-eddy simulation (LES), of jet turbulence and its associated radiated sound, a problem of profound and sustained interest in commercial and military aviation. While LES is computationally expensive, motivating the continued pursuit of theory and reduced-order models, the realism of the predictions makes its data a key resource for understanding the physics and modeling the relevant phenomena.

In high Reynolds number turbulent jets, coherent large-scale structures in the form of wavepackets (reminiscent of linear instability waves in transitional flow) have long been observed (see the extensive review in [1]). Their length and time-scales far exceed the integral scale of turbulence, and they propagate with a coherent wavelength and phase speed that is slowly varying with downstream position along the jet potential core and beyond. Their spatiotemporal coherence renders them more acoustically efficient than smaller-scale, more random turbulent fluctuations, especially in high subsonic and supersonic jets. The signatures of these structures can be most clearly identified from modern multi-point measurements such as near-field microphone arrays [2, 3] and time-resolved particle image velocimetry [3]. Within the turbulent jet itself, the envelope, wavelength, and phase speed of these wavepackets have been accurately modeled, compared with these experiments, using a variant of weakly nonparallel spatial linear stability analysis, namely parabolized stability equations (PSE) [2]. A key aspect of the work has been using techniques such as proper orthogonal decomposition, which involve averaging, to extract the coherent wavepacket from more random fluctuations present in the measurements in order to compare to the analytical models; models should therefore be regarded as predicting the *average* wavepackets.

Unfortunately, particularly in subsonic jets, these linear models fail to accurately predict a consistent acoustic signature of wavepackets in the far-field. Random variations in the wavepacket characteristics in different short-duration realizations of the flow lead to preferential amplification to the acoustic field. Simply put, the average wavepacket does not necessarily make the average sound. Thus to predict the acoustic field, it becomes necessary to model the "jitter" [4] of the wavepackets through their stochastic forcing, either at the nozzle exit or in a distributed way throughout the jet.

Input/output models

In our recent work, we consider a more general modeling framework that is based on the full equations of continuity, momentum, and energy, and the Reynolds decomposition separating the flow into mean and fluctuating components. Once spatially discretized and specialized to the case of statistically stationary flow, these equations take the form of a set of large, linear systems (one for each frequency and azimuthal wavenumber) driven by the (generalized) Reynolds stresses representing triadic interactions coupling the frequency/wavenumber components.

In the absence of right-hand-side forcing, the linear system is then identical to that which would be used in modal or transient stability analysis, but linearized about the turbulent mean rather than an equilibrium (laminar) solution. This provides a commonality with previous models built around the weakly parallel flow theory, but allows for the full spectrum of modes associated with the non-parallel flow to also be considered. Further, with nonzero forcing, the input/output (resolvent) behavior of the system can be studied, similar to that being developed for wall-bounded flows [5]. The SVD can be used to extract the highest-gain modes of the multiple-input, multiple-output system, forming a reduced-order (low rank) basis that can be expected to span the energetic, large-scale coherent structures [6].

This approach, while computationally intensive in non-parallel flow, provides new insights into the wavepackets and their associated noise radiation [7]. We note without elaboration that we have recently proposed more computationally efficient solutions to these systems based on the notion of parabolization, or streamwise marching, of the equations [8]. Such methods are in fact necessary if we are to develop "reduced-order" models of turbulence, since the SVD associated with the full complement of frequencies and wavenumbers has a cost approaching LES.

[*]Corresponding author. Email: colonius@caltech.edu

Ramifications for wavepackets and their radiated noise

The present analysis is fueled by an extensive LES database and companion experiment created by our collaborators for a canonical Mach 0.9 jet [9] with Reynolds number 10^6 issuing from a round, converging nozzle. The LES model was carefully developed to replicate, as closely as possible, the turbulent boundary layers emanating from the nozzle exit in the experiment. Within the nozzle, synthetic turbulence injection and wall modeling were found to be of prime importance in accurately predicting the overall jet turbulence and especially the spectrum of radiated sound [9]. Another critical aspect of the LES was to assemble very long-duration records of the entire flow field to allow for adequate convergence of the low-frequency statistics associated with the largest flow structures.

Based on the LES mean flow field, we have computed global and resolvent modes associated with the linear operator, restricting our attention to the jet region downstream of the nozzle exit. Both analyses produce dominant modes in the form of wavepackets over a wide range of frequencies. An interesting twist, however, is that over a range of frequencies, these modes are coupled to what can be understood as trapped acoustic waves within the potential core. These modes appear as discrete lightly damped modes in the global spectra, and their frequencies have also been observed as tones in the near nozzle acoustic field of recent experiments, as will be reported in forthcoming publications.

The extensive LES data allows us to assess the impact of the nonlinear forcing term on wavepacket evolution by directly tabulating, over a range of frequencies, both sides of the forced input/output system described in the previous section. In order to focus the analysis on the dominant coherent structures, we have developed a data decomposition technique that we call *empirical resolvent-mode decomposition* [10]. Given an ensemble of realizations for both the forcing and response, two sets of linked, mutually orthogonal modes can be formed–one for the forcing (inputs) and one for the response (outputs)–that maximize the respective gain between them. For a full-rank dataset these would naturally reproduce the standard resolvent modes associated with the input/output transfer function. For data constrained to lie in the space visited by the LES simulations, the empirical modes are biased towards high-gain "events" that actually occurred, thereby serving as a diagnostic to determine which kind of nonlinear interactions led to the observed coherent structures.

The results of this analysis were striking, in that the forcing modes that produced the highly coherent large-scale wavepackets lacked a coherent wave structure, instead appearing more random and smaller-scale in nature, and particularly concentrated in the near-nozzle thin shear layer region. Whereas a relatively small subset of the response modes were responsible for a large fraction of the flow fluctuations, the forcing modes were essentially no more efficient than white noise in reconstructing their total forcing. These observations support the view that the dominant large-scale structures arise stochastically from uncorrelated forcing from other scales, the structure being associated with the high-gain linear operator itself rather through coherent nonlinear interactions amongst the dominant modes at other frequencies. This provides justifications for the earlier PSE models, which are based on the premise that the waves are initiated stochastically in the near-nozzle region.

By restricting the output of the linear system to be the far-field pressure, acoustically dominant structures and their related forcings can also be characterized. Again it is found that the wavepackets associated with the dominant (low-rank) far-field structures are produced by incoherent, small scale fluctuations, dominant near the nozzle exit but also through the jet shear layers, particularly near the region that would be marked as the critical layer (for a given frequency) in a weakly non-parallel framework. To state the result in cartoon form, both the near-field-dominant wavepackets and far-field-dominant wavepackets are the result of incoherent fluctuations amplified through the low-rank, non-normal operator associated with the mean of the turbulent flow field. This suggests the potential for linear models that capture both the coherent flow and acoustic fields. One approach would be to use RANS to predict the turbulent mean flow field, resolvent analysis (made computationally efficient via the aforementioned spatial marching method), together with parameterizations of the stochastic forcing terms.

References

[1] Jordan P., Colonius T.: Wave packets and turbulent jet noise. Annu. Rev. Fluid Mech. 45:173-195, 2013.
[2] Guðmundsson K., Colonius T.: Instability wave models for the near-field fluctuations of turbulent jets. J. Fluid Mech.
[3] Cavalieri A. V. G. *et al.*: Wavepackets in the Velocity Field of Turbulent Jets. J. Fluid Mech. 730:559-592, 2013
[4] Cavalieri A. V. G., Jordan P., Agarwal A., Gervais Y.: Jittering wave-packet models for subsonic jet noise. J. Sound Vib. 330(18):4474-4492.
[5] McKeon B. J., Sharma A.S.: A critical-layer framework for turbulent pipe flow. J. Fluid Mech. 658:336-382, 2010. 689:97-128, 2011.
[6] Bagheri S: Computational Hydrodynamic Stability... Arch. of Comput. Meth. Engrg. 19(3):341-379, 2012.
[7] Nichols J., Jovanović M.: Input-output analysis of high speed jet noise, Proceedings of the Center for Turbulence Research summer program, 2014.
[8] Towne A., Colonius T: One-way spatial integration of hyperbolic equations. J. Comput. Phys. 300:844-861, 2015.
[9] Brès G. *et al.*: LES for jet noise: the importance of getting the boundary layer right. AIAA 2015-2535, 2015.
[10] Towne A.: Ph.D. Thesis, California Institute of Technology, 2016.

TURBULENT DRAG REDUCTION USING LIQUID-INFUSED SURFACES

<u>Alexander J. Smits</u>*[1,2] and Tyler Van Buren[1]

[1]*Princeton University, Princeton, NJ 08544, U.S.A. and* [2]*Monash University, Melbourne, Australia*

Summary Liquid-infused surfaces are textured surfaces that have a lubricating liquid impregnated in the surface features. When these surfaces are exposed to the flow of an immiscible liquid, it is possible to achieve substantial drag reduction in fully turbulent flow. Liquid-infused surfaces may overcome some of the shortcomings associated with conventional superhydrophobic surfaces, namely failure under turbulent flow fluctuations and conditions of high hydrodynamic pressure. Results are presented for turbulent Taylor-Couette flow with longitudinal grooves. A number of different lubricating liquids are tested, and we find a strong dependence on the ratio between the viscosity of water and that of the lubricating liquid. The drag reduction, remains fairly constant over the Reynolds number range tested ($100 \leq Re_\tau \leq 140$) with a maximum of about 14%, as reported by [6]. The current study extends this previous work to examine the effects of changing the characteristics of the surface features.

INTRODUCTION

It has variously been shown that modifications of the surface can lead to drag reduction for turbulent wall-bounded flows. For example, [1] showed that for V-shaped grooves (riblets) drag was reduced when $h^+ < 25$ and $b^+ < 30$, with the maximum drag reduction of 8% occurring for $h^+ = 10$ and $b^+ = 15$. Here, $h^+ = \rho h u_\tau / \mu$, $b^+ = \rho b u_\tau / \mu$, where h is the riblet height, b is the riblet pitch, $u_\tau = \sqrt{\tau_w / rho}$ is the friction velocity, τ_w is the surface shear stress, and ρ and μ are the fluid density and viscosity, respectively. Shark-skin surfaces, which are broadly similar to riblet surfaces, have been reported to reduce drag by up to 10% [2]. Superhydrophobic surfaces, where water flows over a grooved surface with air infused in the grooves, has shown particular promise for drag reduction, with some researchers reporting up to 75% drag reduction in turbulent flows [3]. However, the air pockets may fail when they are under high pressure and under high shear, and turbulent pressure fluctuations can also cause failure at high Reynolds numbers [4].

Recently, a new technology that uses liquid-infused surfaces has been developed that exhibits negligible contact angle hysteresis when in contact with various polar and non-polar fluids, low sliding angles for drops on the surface, rapid and repeatable self-healing, and extreme pressure stability (at least 675 atm) [5]. These liquid/liquid systems are stable as long as the two liquids are immiscible, the impregnating liquid preferentially wets the substrate compared to the working liquid, and interfacial tension is stronger than destabilizing body and surface forces. Here, we report how this new surface treatment responds to flow, and demonstrate that such liquid-infused surfaces can lead to sustainable drag reduction in turbulent flows. The current study extends the recent work by [6] to examine the effects of changing the characteristics of the surface features on the level of drag reduction that can be achieved. In addition, we discuss related analytical and numerical model development, and preliminary results obtained in large-scale tests.

EXPERIMENTS

A Taylor-Couette flow was used to study the drag reducing characteristics of liquid-infused surfaces. The Taylor-Couette flow was generated using a commercial rheometer (Brabender Rheotron). The inner cylinder was stationary, while the outer cylinder was rotated over a range of angular frequencies ω (rad/s). The radial gap between the outer and inner cylinders, d was $1.982 \pm 0.013\ mm$ and the height of the inner cylinder H was $80.0 \pm 0.1\ mm$. The working fluid, deionized water, was maintained at constant temperature to within $\pm 0.1°C$ for each experiment using a cooling jacket.

In the original experiments reported by [6], the surface of the aluminum inner cylinder was engraved with grooves aligned in the flow direction that had a pitch $b \approx 106\ \mu m$. A confocal microscope (Olympus LEXT OLS4000) was used to measure the surface topography (see figure 1a), and the features had an average height of $h = 75 \pm 3\ \mu m$.

Three configurations of the $h = 75\ \mu m$ surface were tested, as illustrated in figure 1b. These preparations were called "hydrophilic," "superhydrophobic," and "oil-filled," respectively. For the hydrophilic or "control" case, the surface was made wettable so that the water completely filled the texture. For the superhydrophobic case the same cylinder was then placed in an ethanol-based solution containing Masurf FS100 (Mason Chemical Co.), resulting in a strong repellency to water and the entrapment of air in the grooves. For the liquid-infused cases using perfluorinated oils, the oils have a high chemical affinity for the fluorinated aluminum. For the cases using alkanes such as heptane, the surface was made wetting with respect to alkanes by removing the fluorination treatment in the plasma cleaner and then functionalizing the surface with n-Octadecyltrichlorosilane (OTS). The physical and chemical properties of all test surfaces are summarized in table 1.

Figure 1c show the torque measured on the inner cylinder as a function of Reynolds number Re based on the gap size and the outer cylinder speed ($Re = \rho_w d\omega R_o / \mu_w$). The Reynolds number range corresponds to turbulent flow with $100 \leq$
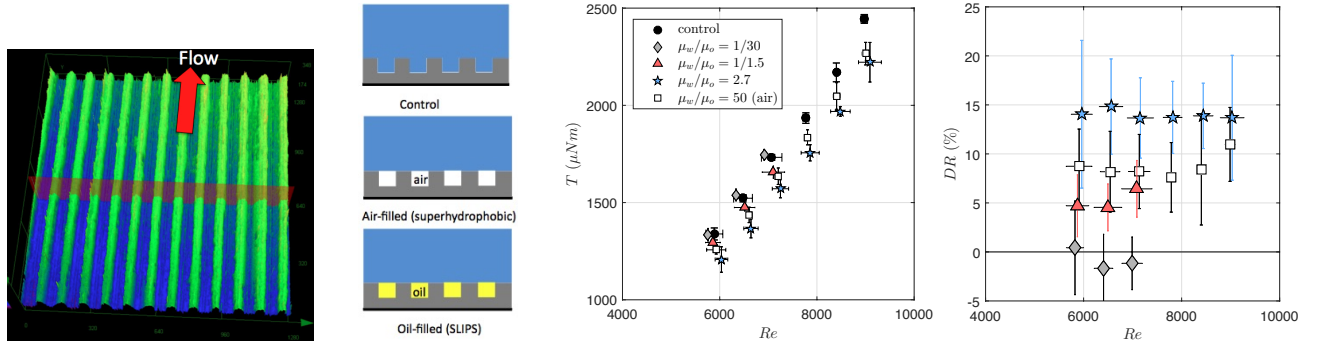

Figure 1: (a) Confocal microscope images of streamwise ridges fabricated by finely threading an aluminum cylinder; (b) Control, superhydrophobic (air-filled), and liquid-infused configurations; (c) Measured torque data for each test surface; (d) Drag reduction over the superhydrophobic and three liquid-infused surfaces. Figures (c) and (d) from [6].

Impregnating fluid	Surface functionalization	μ_w/μ_o	$\rho_o \ (kg/m^3)$	$\gamma_{ow} \ (mN/m)$
Dupont Krytox GPL-101	fluorinated	1/30	1850	$55 - 56$
3M Fluorinert FC-3283	fluorinated	1/1.5	1830	$55 - 56$
Heptane	OTS	2.7 or 1/0.37	684	$51 - 52$
Air	fluorinated	50	1.2	72.8

Table 1: Physical and chemical properties of each air- or liquid-infused surface at $20° \ C$. Data from [6].

$Re_\tau \leq 140$, where $Re_\tau = \rho_w du_\tau/\mu_w$. In figure 1d, we show the percentage drag reduction achieved, where the torque measurements have been corrected for the extraneous drag exerted by the water on the base of the cylinder. Both sets of data indicate that substantial drag reduction is achieved, with the level of drag reduction increasing with decreasing μ_w/μ_o, that is, for less viscous oils. The best performance achieved in these tests were given by the liquid-infused surface using heptane.

In previous work exploring riblet surfaces, the dimensions of the riblets were found to be critical in determining the level of drag reduction, with some surfaces exhibiting drag increases (recall that the maximum drag reduction of 8% occurred for $h^+ = 10$ and $b^+ = 15$) [1]. Similarly, the model developed by [7] for the drag reduction obtained using liquid-infused surfaces indicates that, in addition to the viscosity ratio, the characteristic value of b^+ is a governing parameter. Our current experiments are directed to verifying this model, and are focused on the role of b^+. These results will be reported in the presentation.

References

[1] WALSH, MICHAEL J 1983 Riblets as a viscous drag reduction technique. *AIAA Journal* **21** (4), 485–486.

[2] DEAN, BRIAN & BHUSHAN, BHARAT 2010 Shark-skin surfaces for fluid-drag reduction in turbulent flow: a review. *Philosophical Transactions of the Royal Society of London A: Mathematical, Physical and Engineering Sciences* **368** (1929), 4775–4806.

[3] PARK, HYUNGMIN, SUN, GUANGYI & KIM, CHANG-JIN 2014 Superhydrophobic turbulent drag reduction as a function of surface grating parameters. *Journal of Fluid Mechanics* **747**, 722–734.

[4] ALJALLIS, ELIAS, SARSHAR, MOHAMMAD AMIN, DATLA, RAJU, SIKKA, VINOD, JONES, ANDREW & CHOI, CHANG-HWAN 2013 Experimental study of skin friction drag reduction on superhydrophobic flat plates in high reynolds number boundary layer flow. *Physics of Fluids* **25** (2), 025103.

[5] WONG, TAK-SING, KANG, SUNG HOON, TANG, SINDY K. Y., SMYTHE, ELIZABETH J., HATTON, BENJAMIN D., GRINTHAL, ALISON & AIZENBERG, JOANNA 2011 Bioinspired self-repairing slippery surfaces with pressure-stable omniphobicity. *Nature* **477** (7365), 443–447.

[6] ROSENBERG, B. J., VAN BUREN, T., FU, M. K. & SMITS, A. J. 2016 Turbulent drag reduction over air- and liquid-impregnated surfaces. *Physics of Fluids* in print.

[7] FU, M. K., SAMAHA, M. A., ROSENBERG B. J., HULTMARK, M. 2016 A model for turbulent drag reduction over fluid infused surfaces. Under review.

COHERENT STRUCTURES IN WALL-BOUNDED TURBULENCE

Javier Jiménez*

School of Aeronautics, Universidad Politécnica Madrid, 28040 Madrid, Spain

Summary As a consequence of the recent explosion in the amount and quality of data on turbulent flows, due in large part to direct numerical simulations, the emphasis has moved from what information is available to the choice of how to analyse it. In particular, the deterministic description of turbulence, although still a distant goal, does not appear any longer to be unreachable. We review recent advances in the description of wall-bounded turbulence in terms of identifiable structures that remain coherent for substantial times. We outline their properties and temporal evolution, and trace their connections with other descriptions of turbulence. We enumerate successes and failures, and speculate on the future development of the field.

INTRODUCTION

As far as we know, the flow of Newtonian fluids is well described by the deterministic Navier–Stokes equations. This includes turbulence, and its usual stochastic description can be seen as an admission of our inability to handle complex solutions rather than as an intrinsic property of the flow. Even the usual argument that engineering is primarily interested on mean quantities is disingenuous. While the point-to-point instantaneous description of an industrial flow may never be required, a robust deterministic description would open the door to better prediction and even to control. To give an example, full-scale weather control may always be impractical, but the prevention of individual tornadoes is a simpler proposition that would still be very useful.

Coherent structures have always been part of these descriptive attempts. Ideally, they would be local flow configurations that can be easily recognised and that stay recognisable for a while in a way that can be predicted from the equations. Unfortunately, this is unlikely to be true in general, because pressure in incompressible flows satisfies an elliptic equation that spreads globally the effect of local initial conditions, but it may work locally for strong events. This hope probably stems from the observation of free-shear flows [3] or of eddies in rivers and in the atmosphere, although we now understand that coherence in these systems is linked to fast inviscid instabilities that locally overwhelm the nonlinearity and chaos of the equations.

WALL-BOUNDED FLOWS

Most wall-bounded turbulent flows lack inviscid instabilities in the sense just mentioned, but they don't lack structures that can be 'visually' identified as coherent. That identification can be automated, and most of the results below have good statistical support. Popular examples are streaks [11], hairpins[1], sweeps and ejections [14] and vortex clusters [5]. They differ from the free-shear structures in that we lack a clear theory for their origin, although we believe that we know why they survive once they have been created. For the same reason that there are no strong instabilities to create them, they are only weakly damped once they form.

These structures have often been used as descriptive devices in wall turbulence, and each of them has fierce defenders and, in some cases, detractors. The absence of a fast generation mechanism probably means that no single structure is likely to dominate the flow everywhere. Most reasonable definitions imply a low-dimensional manifold in phase space towards which the flow tends, and in whose neighbourhood it stays for some time, but the intrinsic dimensionality of even very-low-Reynolds number turbulence is high [10]. Moreover, recent results suggest that the inertial range of turbulence is essentially attractor-less, and temporal tracking of the growth and decay of individual structures is more consistent with a memoryless process than with an organised evolution. On the other hand, the visually identified structures are far from being negligible. Streaks carry a large fraction of the fluctuating kinetic energy, and the same is true of the momentum transfer (i.e. drag) by sweeps and ejections.

A wealth of data, and a paucity of models

Some of the ambiguities plaguing coherent structures can be traced to the incomplete information that experiments provide about extended objects. Until the recent appearance of time-resolved PIV, experiments were mostly restricted to time traces at a few points. Even today, experiments rarely extend beyond two-dimensional sections. This left a lot of scope for interpretation and hypothesising, and has been largely superseded by direct simulations that routinely provide three-dimensional time-resolved fields of all flow variables. Numerical Reynolds numbers are also now comparable to experiments, although it is striking that efforts to relate experimental with numerical structural data remain relative rare.

A case that has been studied in some detail are the carriers of intense 'bursts' of momentum transfer, originally defined from point velocity data in terms 'quadrants' in a u–v diagram [14]. They were later generalised to a self-similar hierarchy

*Corresponding author. Email: jimenez@torroja.dmt.upm.es

of irregular three-dimensional objects [12], each of which contains, on average, a short streamwise roller and a side-by-side pair of a sweep and an ejection. They have lifetimes of the order of the local eddy turnover, and owe much of their growth and decay to a series of mergers and splits between objects of comparable size [13]. A sub-family of 'wall-attached' eddies spanning the whole boundary layer carry 60% of the total momentum flux, even if they fill less than 8% of the total volume.

Unfortunately, while data are very useful to determine which hypotheses are untenable, they do not amount to a theory of turbulence. Models incorporating structures are also being developed. For example, we have reasons to believe that the origin of the observed bursts is the quasi-linear transient growth of perturbations to the mean profile [4, 6], and we know that these transient structures exist in all the linearly stable turbulent shear flows in which they have been sought [7]. Linear processes are thus excellent candidates for the driving engine of wall-bounded flows, and they can be easily analysed and predicted. They are also fast and inviscid in the sense of free-shear flows, even if transient. However, it is unclear whether our enthusiasm for these desirable properties simply reflects our inability to deal with fully nonlinear behaviour. A recent analysis in our group reveals that only 10% of the volume and 40% of the drag are represented by 'linear' bursts.

Nonlinear exact solutions of the Navier–Stokes equations, such as permanent waves, cycles [9], and homoclinic and heteroclinic connections [2, 15], are also tantalisingly similar to some of the visual features of low-Reynolds number turbulence, but they are hard to observe at higher Reynolds numbers, and it is even unclear how they could be recognised in a fully chaotic flow if they were present. As long as this continues to be the case, we do not know how significant they are.

A worrying possibility is that we may be looking at the wrong objects. Structures are presently defined in terms of variables, such as the Reynolds stresses, whose main justification is that they can be measured experimentally. But only their divergence enters the equations, and the stresses themselves can be modified by an arbitrary divergence-less 'gauge' [8]. Most present analyses use a particular 'experimental' gauge, but this needs not be the case with numerical data. It is intriguing whether other gauges, or even gauge-invariant quantities, may give results that are easier to interpret.

CONCLUSIONS

The flood of data provided by numerical simulations, and up to a point by experiments, is shifting the focus of turbulence research away from observation and back to theoretical modelling. In particular, coherent structures offer a promising path to the deterministic description of at least the most energetic parts of the flow. This in turn may lead to practical applications in control and modelling. There is by now a virtually unlimited supply of relevant data, including at Reynolds numbers comparable to most experiments in which detailed measurements are possible. On the other hand, theoretical understanding is still limited. In particular, we do not know how to restrict our analysis to a local region. We have argued that part of the problem may be that our methods have inherited the limitations of experiments, and that adapting them to the new numerical capabilities could be a first step in resolving the theoretical impasse.

References

[1] R. J. Adrian: Hairpin vortex organization in wall turbulence. Phys. Fluids, 19:041301, 2007.

[2] N. Aubry, P. Holmes, J. L. Lumley, E. Stone: The dynamics of coherent structures in the wall region of a turbulent boundary layer. J. Fluid Mech., 192:115–173, 1988.

[3] G. L. Brown, A. Roshko: On the density effects and large structure in turbulent mixing layers. J. Fluid Mech., 64:775–816, 1974.

[4] K. M. Butler, B. F. Farrell: Optimal perturbations and streak spacing in wall-bounded shear flow. Phys. Fluids A, 5:774–777, 1993.

[5] J. C. del Álamo, J. Jiménez, P. Zandonade, R. D. Moser: Self-similar vortex clusters in the logarithmic region. J. Fluid Mech., 561:329–358, 2006.

[6] J. Jiménez: How linear is wall-bounded turbulence? Phys. Fluids, 25:110814, 2013.

[7] J. Jiménez: Direct detection of linearized bursts in turbulence. Phys. Fluids, 27:065102, 2015.

[8] J. Jiménez: Optimal fluxes and Reynolds stresses. J. Fluid Mech., submitted.

[9] G. Kawahara, M. Uhlmann, L. van Veen: The significance of simple invariant solutions in turbulent flows. Ann. Rev. Fluid Mech., 44:203–225, 2012.

[10] L. Keefe, P. Moin, J. Kim: The dimension of attractors underlying periodic turbulent Poiseuille flow. J. Fluid Mech., 242:1–29, 1992.

[11] S. J. Kline, W. C. Reynolds, F. A. Schraub, P. W. Runstadler: Structure of turbulent boundary layers. J. Fluid Mech., 30:741–773, 1967.

[12] A. Lozano–Durán, O. Flores, J. Jiménez: The three-dimensional structure of momentum transfer in turbulent channels. J. Fluid Mech., 694:100–130, 2012.

[13] A. Lozano–Durán, J. Jiménez: Time-resolved evolution of coherent structures in turbulent channels: characterization of eddies and cascades. J. Fluid Mech., 759:432–471, 2014.

[14] S. S. Lu, W. W. Willmarth: Measurements of the structure of the Reynolds stress in a turbulent boundary layer. J Fluid Mech, 60:481–511, 1973.

[15] L. Van Veen, G. Kawahara: Homoclinic tangle on the edge of shear turbulence. Phys. Rev. Lett., 107:114501, 2011.

HYDRODYNAMICS AND HAIRY SURFACES

A. E. Hosoi[*1]

[1]*Department of Mechanical Engineering, Massachusetts Institute of Technology, Cambridge, MA*

Summary Flexible slender structures in flow are everywhere. While a great deal is known about individual flexible fibers interacting with fluids, considerably less work has been done on fiber ensembles, such as fur or hair, in flow. These hairy surfaces are abundant in nature and perform multiple functions from thermal regulation to water harvesting to sensing. Motivated by these biological systems, we consider two examples of hairy surfaces interacting with flow: (1) air entrainment in the fur of diving mammals and (2) symmetry breaking in hairy microchannels.

THERMAL REGULATION VIA AIR ENTRAINMENT IN SEMI-AQUATIC MARINE MAMMALS

Arctic mammals are faced with the challenge of maintaining body temperature in extremely cold environments. The task is further complicated by the fact that many of these animals must find solutions that are effective both on land and under water. Unlike fully aquatic mammals which rely on blubber for insulation, semi-aquatic mammals (such as fur seals, otters, and beavers) have specially adapted fur that serves as an effective insulator both above and below water. Many of these animals have evolved pelts that naturally entrap air when they dive. This air: (1) provides additional insulation under water, (2) provides added buoyancy, and (3) facilitates water shedding when the animals resurface. In this study we investigate diving conditions and fur properties which amplify air entrainment in fur.

Our toy model of a furry animal diving into water consists of a textured surface plunged into fluid [1]. Studies of both withdrawal and submersion of rigid surfaces into fluids have a rich history beginning with the pioneering work of Landau-Levich-Derjaguin (LLD) [2]. Here we extend LLD to surfaces with mesoscale textures which are relevant to diving mammals. Hairy surfaces are fabricated using laser cut molds and casting samples with PDMS (Figure 1, Middle). The sample is lowered into a bath of silicone oil at a constant speed, simulating a dive. A representative snapshot of the dive is shown in Figure 1 (Right) in which the dark region indicates a wedge of air entrained by the hairs. The shape of the wedge is set by a dynamic balance between fluid entering from the left between the hairs and air escaping out at the top of the wedge.

To estimate conditions under which we expect air entrainment, we construct a model in which hairs of length L are plunged into liquid at a speed V. The x-direction is defined parallel to the hairs. As the hairs are plunged into the bath, liquid penetrates between the hairs, forming a wetting front. This flow between hairs is analogous to flow in a capillary tube and the balance of pressure at the liquid/air interface is given by

$$\rho g y + \frac{1}{2} \rho \dot{x}^2 = \gamma \kappa + \frac{\mu}{k} \frac{x \dot{x}}{r^2}$$

where γ represents surface tension, κ is the meniscus curvature, μ is the dynamic viscosity, k the effective permeability, r the spacing of the hairs, and ρ is the density of the fluid. In our experiments, bending of the hairs, capillary forces, and inertial
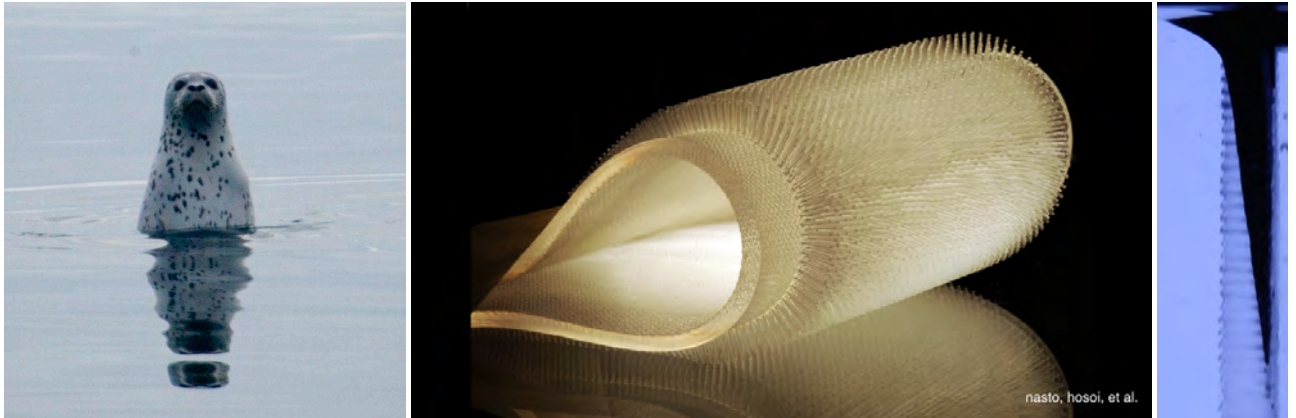

Figure 1: (Left) Spotted seal. Photo credit M. Cameron [3]. (Middle) Fabricated PDMS hair surface. Photo credit Felice Frankel. (Right) PDMS hair surface plunging into a silicon bath. Dark wedge shows a region of entrained air.

*Corresponding author. Email: peko@mit.edu

effects are all negligible. Balancing hydrostatic pressure and viscous resistance we solve for the speed of the advancing front. By comparing this speed with the diving speed, we find a maximum diving depth that can be achieved while maintaining an insulating layer of air given by:

$$\frac{h_{max}}{L} = \left(\frac{V\mu}{k\rho gr^2}\right)^{1/2}.$$

The model is compared with experimental data from our toy system as well as with typical biological data from seals and otters.

LOW REYNOLDS NUMBER SOLID STATE FLOW RECTIFIERS

A fundamental component in hydraulic systems is the flow rectifier in which resistance varies with the direction of the flow. One of the simplest ways to generate such an asymmetry is with a ball valve in which flow is completely obstructed in one direction and free to flow in the other. In this work we seek a variation that: (1) allows the designer to modulate the relative resistances in the rectifier and (2) can be achieved with solid state state components (i.e. no moving parts). Such a device was first proposed by Nikola Tesla who patented the "valvular conduit" in 1920 [4]. Tesla's device relied on fluid inertia to break symmetry in the rectifier. Later Groisman and Quake [5] demonstrated a microfluidic rectifier for viscoelastic fluids in which the non-Newtonian properties of the working fluid break symmetry in the flow via nonlinear effects.

In this project, we design a fluid rectifier for low Reynolds number Newtonian flows [6]. In order to circumvent the time-reversal symmetry inherent in Stokes flow, we again turn to mesoscale elastic hairs that are affixed to the channel walls. Hairs are angled such that flow aligned with the hairs bends them towards the channel walls increasing the effective height of the channel; flow in the other direction bends hairs away from the walls decreasing the effective height.

Consider a channel coated with a bed of elastic fibers, each of radius a and length $L \gg a$. The fibers are anchored to a rigid substrate wall, and tilted at an angle θ_0 to the z-axis. Flow is driven through the channel by an externally imposed pressure differential. The channel, of height $2R$, can be modeled using two zones. The interior zone corresponds to the space in the center of the channel which is free of hairs, hence the flow corresponds to Poiseuille flow. The second zone is comprised of flow through the fiber bed near the wall and is modeled as a porous medium using Darcy flow with a permeability that is dependent on the local orientation of the fibers [7]. Coupling the two zones, we assume that the shear stress is supported by the elastic fibers and that the flow velocity is continuous at the fiber tip. Finally, to close the system we require a model for the deformation of the fibers. We consider two alternate models for fibers: (1) a linear elastic beam and (2) a rigid fiber attached to the substrate via a torsional spring. This system can now be solved to find the equilibrium shape of the fibers which can then be used to find flow rates and resistances.

For the torsional spring model, fiber orientation θ is given by the transcendental equation

$$\cos\theta\left(1 - \frac{\alpha}{2}\cos\theta\right) = \text{Te}(\theta - \theta_0).$$

Hence the system response is characterized by three dimensionless groups: $\text{Te} = (K_s\phi_s)/(\pi a^2 L\mu v)$ which represents the ratio of elastic to viscous stresses, $\alpha = L/R$ the ratio of fiber length to channel height, and θ_0 the undeformed angle of the fiber. Here K_s represents the torsional spring stiffness, ϕ_s is the density of fibers, and v is the average fluid velocity. This equation can be solved numerically to map and optimize impedance asymmetry. Note that in the limit of large Te the fibers are nearly rigid and, owing to the time-reversal symmetry in Stokes flow, there is no impedance asymmetry. At the other extreme, $\text{Te} \to 0$, the fibers are extremely flexible and fold down to the walls regardless of the flow direction, again resulting in no asymmetry. However, there is a region of parameter space in which elastic and viscous forces on the fibers are comparable, maximizing the anisotropic resistive properties of the channel. These predictions are tested by constructing a fiber bed using the fabrication techniques described above and directly measuring resistance asymmetries.

References

[1] Nasto, Regli, Brun, Alvarado, Clanet, Hosoi. PREPRINT, 2015.

[2] Landau, Levich.:Entrainment of fluid by the driven plate, *Acta Phys.-Chim. USSR* **17**: 42, 1942.

[3] Wikimedia Commons, source http://www.ecofoci.noaa.gov/cruiseWeb/ice08/Ice2008_seals.html.

[4] Tesla.: Valvular Conduit, Patent # US 1,329,559 A, 1920.

[5] Groisman, Quake.: A Microfluidic Rectifier: Anisotropic Flow Resistance at Low Reynolds Numbers, *PRL* **92**:094501, 2004.

[6] Alvarado, Comtet, Hosoi. PREPRINT, 2015.

[7] Gopinath, Mahadevan.: Elastohyrodynamics of wet bristles, carpets and brushes, *Proc. Roy. Soc. A* **467**: 1665-1685, 2011.

THE TRANSITION TO THE ULTIMATE STATE IN TURBULEN THERMAL CONVECTION

E. Bodenschatz,[*] G. Ahlers, D. Funfschilling, D. van Gills, X. He, H. Nobach, and S. Weiss
Max Planck Institut für Dynamik und Selbstorganisation, Göttingen, Deutschland

Summary We report measurements on turbulent Rayleigh-Bénard convection using three cylindrical samples with aspect ratios (diameter/height) $\Gamma = 1.00, 0.50$ and 0.33. All samples had the same diameter $D = 1.12$ m, but different heights L. Compressed sulfur hexafluoride gas (SF_6) at pressures up to 19 bar was used as the fluid at the Göttingen Turbulence Facility (see www.EuHIT.org). The measurements were conducted over the Rayleigh-number range $10^{12} \lesssim Ra \lesssim 4 \times 10^{15}$ and for Prandtl numbers Pr near 0.8. In three independent measurements, namely global heat transport, local turbulent Reynolds numbers, and large-scale-circulation dynamics, we observed a transition over a range of Ra from the classical regime to a new regime which has been referred to as "ultimate". We discuss the properties of the classical and the ultimate state, as well as the influence of rotation on this system.

INTRODUCTION

Rayleigh-Bénard convection (RBC), where fluid mass and heat are convected due to a vertical temperature difference ΔT in the presence of gravity, has long been a model system for the study of thermal convection [1]. The fluid is contained between two parallel horizontal plates and heated from below. The dynamics of the system depends on the Rayleigh number $Ra \equiv \alpha g \Delta T L^3/(\kappa \nu)$ and the Prandtl number $Pr \equiv \nu/\kappa$. Here g is the gravitational acceleration, L is the sample height, and α, ν and κ are the thermal expansion coefficient, the kinematic viscosity and the thermal diffusivity respectively. When Ra is moderate, there are two thin laminar boundary layers (BLs), one adjacent to each of the plates. This system is referred to as the "classical state". Each BL emits plumes that rise or fall towards the opposite plate under the influence of buoyancy. The plumes drive, and in turn are carried by, a large-scale circulation (LSC). When L and the diameter D of the sample are not too different, then the LSC consists of a single convection roll occupying the bulk region between the BLs. As Ra increases and exceeds a critical value Ra^*, the LSC mean flow, as well as fluctuations on somewhat smaller scales, will apply shear to the BLs and, at sufficiently large $Ra > Ra^*$, will cause the BLs to become turbulent as well. Since no further structural changes are anticipated as Ra increases beyond Ra^*, the system above Ra^* is referred to as the "ultimate state". The value of Ra^* was predicted to be of the order of 10^{14} for $Pr \simeq 1$ [2], and to increase as Pr increases.

Various properties, such as the Nusselt number Nu (a dimensionless form of the heat transport), the Reynolds numbers Re, and aspects of the the LSC dynamics are expected to have different Ra dependences in the classical and ultimate states. In agreement with the model of Grossmann and Lohse (GL) [2], measurements at the Göttingen Turbulence Facility gave $Nu \propto Ra^{0.32}$ and $Re \propto Ra^{0.43}$ for the classical state. For the ultimate state they yielded $Nu \propto Ra^{0.38}$ and $Re \propto Ra^{0.50}$, as predicted also by GL [3]. Recent measurements of the Reynolds number Re_{θ_m} (which describes the LSC azimuthal diffusivity) revealed a transition from $Re_{\theta_m} \propto Ra^{0.28}$ for the classical state to $Re_{\theta_m} \propto Ra^{0.40}$ for the ultimate state [4].

EXPERIMENTAL FACILITIES AND MEASUREMENTS

The experiments were conducted with three large RBC samples known as the High-Pressure Convection Facilities (HPCFs) which were located in an even larger pressure vessel known as the Uboot of Göttingen at the Göttingen Turbulence Facility. The samples were cylindrical with diameter $D = 1.12$ m and heights $L = 1.12, 2.24$, and 3.40 m, corresponding to aspect ratios $\Gamma \equiv D/L = 1.00, 0.50$, and 0.33. The fluid was gaseous pressurized sulfur hexafluoride (SF_6) at ambient temperatures. For a perfect gas $Ra \propto P^2$ (P is the pressure). Thus, increasing P up to the maximum Uboot design pressure of 19 bar yielded the highest possible Ra values. For $L = 3.40$ m $Ra = 4 \times 10^{15}$ was reached. The value of Pr was close to 0.8. Details about the facilities and experimental procedures were reported elsewhere [5].

EXPERIMENTAL RESULTS

Figure 1(a) shows Nu measurements for the $\Gamma = 1.00$ sample (known as "HPCF-IVb") which cover the range $10^{12} \lesssim Ra \lesssim 1.5 \times 10^{14}$. For $Ra < Ra_1^* \simeq 2 \times 10^{13}$ one sees that $Nu \propto Ra^{0.321}$, consistent with the classical-state prediction [2] and previous measurements. For $Ra > Ra_2^* \simeq 8 \times 10^{13}$ we find $Nu \propto Ra^{0.37}$, consistent with the prediction for the ultimate state [3]. In the range $Ra_1^* < Ra < Ra_2^*$ Nu gently increases from values corresponding to one state to those of the other, indicating the existence of a transition range between the classical and the ultimate state.

Figure 1(b) shows the reduced Reynolds number $Re_V/Ra^{0.5}$ from a different $\Gamma = 1.00$ sample (known as "HPCF-IV") [5]. Here $Re_V \equiv VL/\nu$ where V is the rms velocity fluctuation in the vertical direction. While the data do not give an obvious indication of Ra_1^* (except for a slight increase of the scatter), they clearly show a discontinuity and a change of the Ra

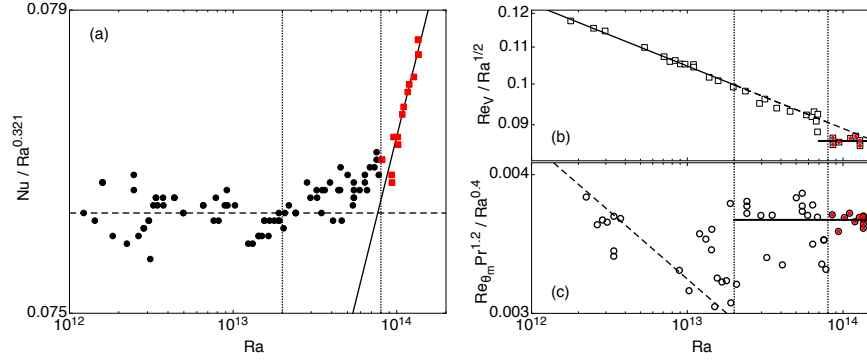[*]Email: Eberhard.Bodenschatz@ds.mpg.de

Figure 1: (a) The reduced Nusselt number $Nu/Ra^{0.321}$ as a function of Ra on logarithmic scales. The solid line is the power-law fit $Nu = 0.0159 Ra^{0.37}$ to the red squares, and the horizontal dashed line is at $Nu/Ra^{0.321} = 0.0763$. (b) The reduced velocity-fluctuation Reynolds number $Re_V/Ra^{0.5}$ as a function of Ra [5]. The solid line is the power-law fit to the data with $Ra \leq Ra_1^* = 2 \times 10^{13}$, which gave an exponent of 0.43. The dashed line is the extrapolation of that fit beyond Ra_1^*. The horizontal solid bar corresponds to 0.0863. (c) The reduced Reynolds number $Re_{\theta_m} Pr^{1.2}/Ra^{0.4}$ as a function of Ra. Dashed line: $Re_{\theta_m} Pr^{1.2} = 0.124 Ra^{0.278}$ as determined using the data from Ref. [6] for $Pr = 4.38$. The horizontal solid bar corresponds to $Re_{\theta_m} Pr^{1.2} = 0.00364 Ra^{0.40}$. In all panels the data are for $\Gamma = 1.00$ and vertical dotted lines represent $Ra_1^* \simeq 2 \times 10^{13}$ and $Ra_2^* \simeq 8 \times 10^{13}$.

dependence at Ra_2^*. Above Ra_2^* the data give $Re_V \propto Ra^{0.50\pm0.02}$, in excellent agreement with the prediction for the mean-flow Reynolds number Re_U in the ultimate state [3] (to our knowledge there is no prediction for Re_V).

The orientation θ_m (measured at the height $z = L/2$) of the LSC plane diffuses in the azimuthal direction because of the stochastic action of the small-scale fluctuations. From the LSC azimuthal diffusivity D_{θ_m} one can construct a Reynolds number $Re_{\theta_m} \equiv L\sqrt{D_{\theta_m}/\nu}$ as a quantitative measure of the stochastic azimuthal dynamics of the LSC. In figure 1(c) we show $Re_{\theta_m} Pr^{1.2}/Ra^{0.4}$ measured with HPCF-IVb. In the classical regime the Ra dependence agrees well with the extrapolation of the result $Re_{\theta_m} \propto Ra^{0.28}$ obtained from a physically smaller $\Gamma = 1.00$ sample for $Ra \lesssim 10^{11}$ and $Pr = 4.38$ [6]. In the ultimate state the data scatter much less than in the transition range, and yield $Re_{\theta_m} Pr^{1.2} = 0.0036 Ra^{0.40\pm0.03}$. While a theoretical explanation of the scaling of $Re_{\theta_m}(Ra, Pr)$ remains a challenge for both the classical and the ultimate state, our measurements of Nu, Re_V and Re_{θ_m} for $\Gamma = 1.00$ clearly reveal the ultimate-state transition and yield consistent values of Ra_1^* and Ra_2^*.

Measurements of Nu and Re for $\Gamma = 0.50$ [7] and $\Gamma = 0.33$ also showed the same ultimate-state transition. As Γ increased, the onset of the transition at $Ra_1^* \simeq 2 \times 10^{13}$ remained almost unchanged, while Ra_2^* decreased. This leads to a shorter transition range at larger Γ. The data suggest that $Ra_1^* = Ra_2^*$ for $\Gamma \gtrsim 1.5$, implying a sharp transition at a unique value Ra^* of Ra.

ACKNOWLEDGEMENTS

References

[1] Ahlers G., Grossmann S., Lohse D.: Heat transfer and large scale dynamics in turbulent Rayleigh-Bénard convection. Rev. Mod. Phys. **81**, 503 (2009).

[2] Stevens J.A.M., van der Poel E.P., Grossmann S. and Lohse D.: The unifying theory of scaling in thermal convection: The updated prefactors. J. Fluid Mech. **730**, 295 (2013); and references therein.

[3] Grossmann S. and Lohse D.: Multiple scaling in the ultimate regime of thermal convection. Phys. Fluids **23**, 045108 (2011).

[4] He X., Bodenschatz E., Ahlers G.: Azimuthal diffusion of the large-scale-circulation plane, and absence of significant non-Boussinesq effects, in turbulent convection near the ultimate-state transition. J. Fluid Mech. **791**, R3 (2016).

[5] He X., van Gils D.P.M., Bodenschatz E., Ahlers G.: Reynolds numbers and the elliptic approximation near the ultimate state of turbulent RayleighBénard convection. New J. Phys. **17**, 063028 (2015).

[6] Brown E., Ahlers G.: Rotations and cessations of the large-scale circulation in turbulent Rayleigh-Bénard convection. J. Fluid Mech. **568**, 351 (2006).

[7] He X., Funfschilling D., Nobach H., Bodenschatz E., Ahlers G.: Transition to the Ultimate State of Turbulent Rayleigh-Bénard Convection. Phys. Rev. Lett. **108**, 024502 (2012).

HYDRODYNAMIC QUANTUM ANALOGS

John W. M. Bush *[1]

[1]*Department of Mathematics, MIT, Cambridge MA, USA*

Summary A decade ago, Yves Couder and Emmanuel Fort discovered that a millimetric droplet may self-propel on the surface of a vibrating bath by virtue of a resonant interaction with its own wave field. This hydrodynamic system is unique in that it exhibits several features, both dynamical and statistical, previously thought to be exclusive to the microscopic, quantum realm. Moreover, its dynamics are reminiscent of an early realist model of quantum dynamics, Louis de Broglie's pilot-wave theory. In my Sectional Lecture, I shall discuss prior and ongoing work in the experimental and theoretical modeling of this rich hydrodynamic pilot-wave system, and its relation to the modern extensions of de Broglie's mechanics.

When a fluid layer is subjected to vertical vibration, its surface goes unstable to a field of Faraday waves when a critical forcing acceleration is exceeded (Figure 1A-B). Below this Faraday threshold, millimetric drops can bounce indefinitely on the surface (Figure 1C). Ten years ago, Yves Couder and Emmanuel Fort discovered that a droplet bouncing in this fashion may destabilize into a dynamic state, interacting with its own wave field in such a way as to walk steadily across the surface [4] (Figure 1D). These walking droplets, or 'walkers', are composed of both the droplet and an extended wave field. The propulsive wave force imparted to the walker during impact is proportional to the local slope of the interface. Since the wave field depends on both the walker's history and environment, the walker dynamics are implicitly non-local in both space and time, said to depend on the system's 'path-memory' [9]. By virtue of this dynamical non-locality, as is most pronounced in the high-memory limit when the waves are most persistent, the walkers exhibit several features previously thought to be peculiar to the microscopic, quantum realm.

The walkers exhibit single-particle diffraction when they pass through a slit, on the basis of which one can infer an uncertainty principle in position and momentum [5]. Single-particle interference has also been reported in the double-slit geometry [5], although these results have recently been contested [1]. The walkers can tunnel across barriers consisting of submerged obstacles, with the tunneling probability decreasing exponentially with barrier width [8]. Walkers in confined geometries follow complex chaotic trajectories, but exhibit coherent statistics reminiscent of electrons in a quantum corral [13]. When the droplets walk in a rotating frame, quantized inertial orbits analogous to Landau levels may emerge owing to the droplet interacting with its own wake [11, 14]. Hydrodynamic spin states and analog Zeeman splitting have also been explored [18]. Walkers in a harmonic potential execute orbits that are quantized in both energy and angular momentum, analogous to the quantum simple harmonic oscillator [20].

When several bouncing or walking droplets interact, they couple through their wave fields to form a variety of static or dynamic bound states. Pairs of identical walkers may either scatter, lock into circular orbits [4, 21] (Figure 1E), walk together with one trailing the other, or walk side by side in the so-called promenade mode [2] (Figure 1F). Atom-like structures can form from small drops near larger ones, with walkers orbiting static bouncers (Figure 1G). Multiple bouncers or walkers may also lock into a stable lattice[7] (Figure 1H). All such multiple droplet arrangements, or 'bound states', are stable below a critical forcing acceleration, beyond which wobbling instabilities set in, followed by the collapse of the compound structure.

Recent experimental studies have been directed towards an improved understanding of walker-boundary interactions. When walkers interact with a planar boundaries, enigmatic reflection laws emerge. Specifically, the reflection angle depends only weakly on the system memory and angle of incidence: for a broad range of incident angles, the angle of reflection is nearly 70°. When a walker scatters off a submerged pillar, it may lock onto a logarithmic spiral. The effective force required to generate such a spiral is found to be proportional to the Coriolis force that would act on the walker if it were in a frame rotating with its instantaneous angular velocity. The equivalent form of the Lorentz force acting on a charge in a uniform magnetic field and the Coriolis force acting on a mass in a rotating frame suggests that the walker is behaving as would a moving charge responding to the magnetic field generated by the current associated with its own motion. These scattering experiments have thus revealed a surprising new behavior analogous to mechanical self-induction.

A hierarchy of theoretical models of increasing sophistication have been developed to describe the walkers [11, 16, 17, 15] Theoretical models now allow for a quantitative description of the walker dynamics, and reveal a strong dependence of the bouncing behavior on drop size and driving acceleration [16]. These models allow for a robust assessment of the stability of a number of dynamical states, including straight line walking and circular orbital motion [17, 18]. The studies of orbital dynamics have provided insight into the origins of quantization and quantum-like statistics in this hydrodynamic pilot-wave system. Quantization arises by virtue of the dynamic constraint imposed on the walker by its monochromatic wave field. When the orbital states destabilize, the chaotic walker drifts between unstable orbital states, the result being multimodal, quantum-like statistics. A similar physical picture provides rationale for the statistical behavior reported for walkers in a circular corral [13], wherein concentric circles may be considered as the quantized orbital states [12]. Current theoretical models are being extended in order to consider walker-boundary interactions and the stability of multiple-walker states.

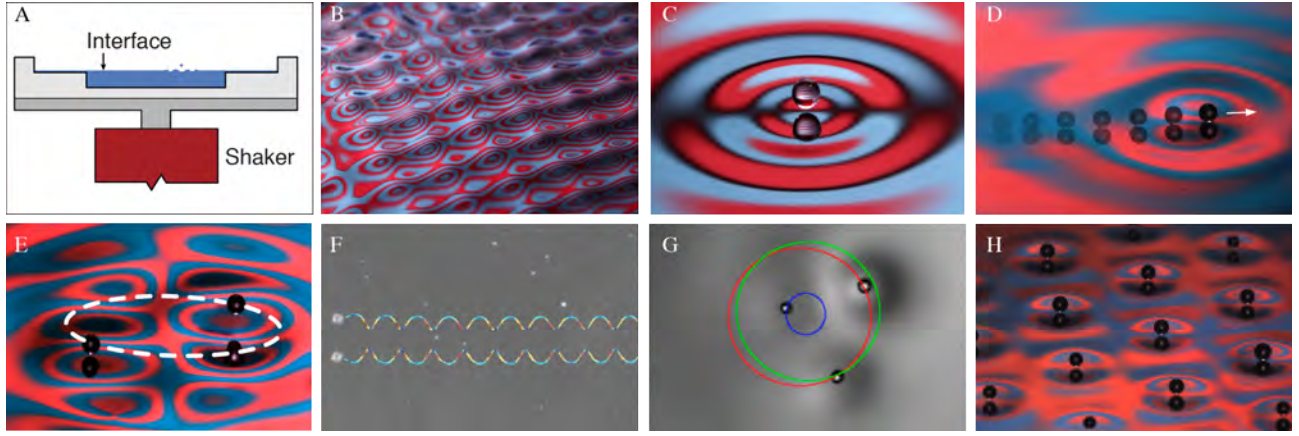*Corresponding author. Email: bush@math.mit.edu

Figure 1: (A) Schematic illustration of the experiment: a drop walks on the surface of a vibrating fluid bath. (B) Faraday waves emerge on the bath when the Faraday threshold is exceeded. (C) A millimetric oil droplet bounces in place on a vertically vibrating fluid bath just below the Faraday threshold. (D) An oil droplet walks due to a resonant interaction with its own wavefield. E) A pair of identical walkers locked in orbit. (F) A pair of identical droplets walk from right to left in the 'promenade mode', their trajectories color coded according to speed. (G) Three drops form a bound state marked by nearly circular orbits for each. (H) A stable lattice of identical bouncing droplets.

In an attempt to reconcile quantum mechanics and relativity, Louis De Broglie proposed that quantum objects such as electrons consist of a localized vibrating particle moving in sync with a spatially extended particle-centered wave field [6]. The particle vibration is characterized by an exchange between rest mass energy and wave energy at the Compton frequency. He proposed that the guiding or 'pilot' wave field consists of a monochromatic wave field with the de Broglie wavelength, and asserted that the resulting pilot-wave dynamics could give rise to a statistical behavior consistent with the predictions of standard quantum theory. While de Broglie did not specify the physical origins of his pilot-wave field, others have sought it in the electromagnetic vacuum field [19]. The walking-droplet system, when considered in light of these modern, vacuum-based pilot-wave theories, would seem to suggest the possibility of an unresolved quantum dynamics on the Compton scale, that a successful non-local hidden-variable theory might be based on the physical picture of particles interacting with the vacuum, and propagating in an equilibrium state of energy exchange within it [3].

References

[1] Andersen A, Madsen J, Reichelt C, Ahl S, Lautrup B, Ellegaard C, Levinsen M, and Bohr T: Double-slit experiment with single wave-driven particles and its relation to quantum mechanics, *Phys. Rev. E* 92, 013006, 2015.

[2] Borghesi C, Moukhtar J, Labousse M, Eddi A, Fort E and Couder Y: Interaction of two walkers: Wave-mediated energy and force. Phys. Rev. E, 90:063017, 2014.

[3] Bush, JWM: Pilot-wave hydrodynamics, *Ann. Rev. Fluid Mech.* 47: 269–292-996, 2015.

[4] Couder Y, Protière S, Fort E, Boudaoud A.: Walking and orbiting droplets. *Nature* 437: 208, 2005.

[5] Couder Y, Fort E.: Single particle diffraction and interference at a macroscopic scale. *Phys. Rev. Lett.* 97: 154101, 2006.

[6] de Broglie L: Interpretation of quantum mechanics by the double solution theory. *Annales de la Fondation Louis de Broglie* 12: 1-23, 1987.

[7] Eddi A, Decelle A. Fort E and Couder Y: Archimedean lattices in the bound states of wave interacting particles, *Europhys. Lett.*, 87: 56002, 2009.

[8] Eddi A, Fort E, Moisy F. Couder Y.: Unpredictable tunneling of a classical wave-particle association. *Phys. Rev. Lett.* 102: 240401, 2009.

[9] Eddi A, Sultan E, Moukhtar J, Fort E, Rossi, M, Couder Y.: Information stored in Faraday waves: the origin of path memory. *J. Fluid Mech.* 674: 433-463., 2011

[10] Eddi A, Moukhtar J, Perrard J, Fort E, Couder Y.: Level splitting at a macroscopic scale. *Phys. Rev. Lett.* 108:264503, 2012.

[11] Fort E, Eddi A, Boudaoud A, Moukhtar J, Couder Y.: Path-memory induced quantization of classical orbits. *PNAS* 107:41: 17515–17520, 2010.

[12] Gilet, T. Dynamics and statistics of wave-particle interactions in a confined geometry. *Phys. Rev. E.* 90: 052917, 2014.

[13] Harris DM, Moukhtar J, Fort E, Couder Y, Bush JWM: Wavelike statistics from pilot-wave dynamics in a circular corral. *Phys. Rev. E* 88, 011001, 2013.

[14] Harris DM, Bush JWM: Droplets walking in a rotating frame: from quantized orbits to multimodal statistics. *J. Fluid Mech.* 739: 444-464, 2014.

[15] Milewski P, Galeano-Rios C, Nachbin A, Bush JWM: Pilot-wave hydrodynamics: modeling and computation. *J. Fluid Mech.*, 778: 361–388, 2015.

[16] Moláček J, Bush JWM: Droplets walking on a vibrating fluid bath: towards a hydrodynamic pilot-wave theory. *J. Fluid Mech.* 727: 612-647, 2013.

[17] Oza A, Rosales RR, Bush JWM. A trajectory equation for walking droplets: hydrodynamic pilot-wave theory. *J. Fluid Mech.* 737: 552-570, 2013.

[18] Oza A, Harris DM, Rosales RR, Bush JWM: Pilot-wave dynamics in a rotating frame: on the emergence of orbital quantization. *J. Fluid Mech.* 744: 404–429, 2014.

[19] de la Pena L, Cetto AM, Valdes Hernandez A: The emerging quantum: The physics behind quantum mechanics, Springer, 2015.

[20] Perrard S, Labousse M, Fort E, Couder Y.: Chaos driven by interfering memory, *Phys. Rev. Lett.* 113:104101, 2014.

[21] Protière S, Bohn S and Couder Y: Exotic orbits of two interacting wave sources. *Phys. Rev. E*, 78:036204, 2008.

THE NON-LINEAR MECHANICS OF SLENDER DEFORMABLE BODIES

Basile Audoly[1]

[1]*Laboratoire de mécanique des solides, École polytechnique and CNRS, Palaiseau, France*

Summary We discuss some challenges arising in the mechanics of slender (quasi-1D) deformable bodies, such as a thin thread of polymer, curly hair, or a carpenter's tape for example. Slender bodies can exhibit a number complex and intriguing behaviors that are accessible through simple experiments. The analysis of slender bodies exposes one to many of the fundamental concepts of 3D non-linear mechanics, albeit in a simpler setting where explicit analytical solutions and fast numerical methods can be proposed. Based on examples, we review some problems arising in the analysis of deformable bodies, including the derivation of accurate 1D mechanical models by dimensional reduction, the solution of non-linear 1D models by analytical or numerical methods, and the analysis of material or geometrical instabilities.

There are many examples of slender (quasi-one dimensional) bodies around us, including computer cables, human hair, sailing and climbing ropes. Being flexible, slender bodies commonly undergo large rotations. As a result, they are prone to instabilities and can display complex behaviors, some of which are illustrated in the figure. In this talk, we will discuss the specific challenges arising in the mechanics of slender deformable bodies. They include the derivation of dimensionally reduced models and their analytical or numerical solution, especially in the non-linear range.
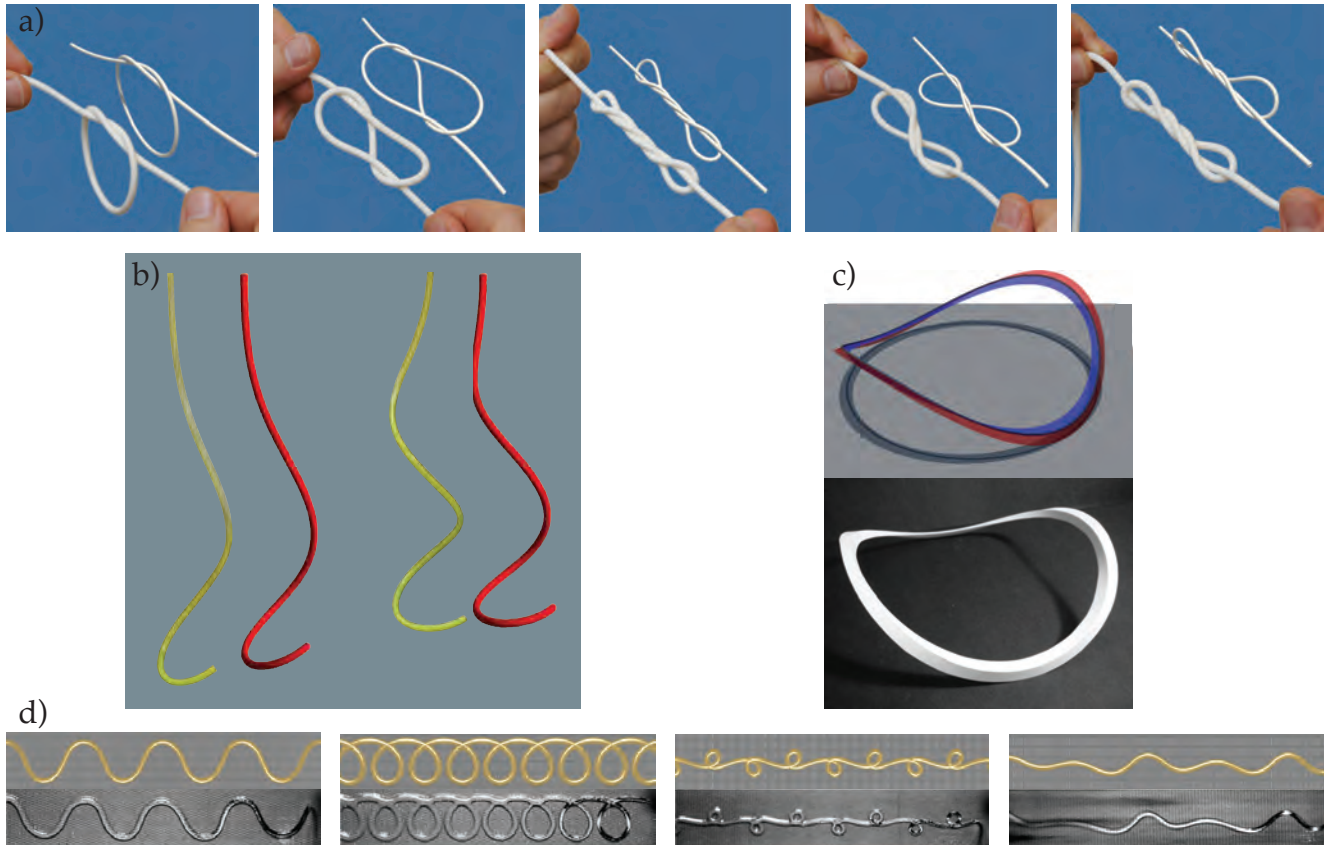
Figure 1: (a) Shapes obtained by twisting a simple knot in both directions: comparison of experiments using a silicone filament and numerical simulations using the Discrete Elastic Rods method [3]. (b) Curly hair: equilibria of a naturally curved rod under its own weight, experiments (green) versus simulation (red) for different values of the natural curvature [8]. (c) 3D origami obtained by pleating a flat annular piece of paper along a central ridge [7, 6]. (d) Patterns produced by a thin jet of viscous fluid stretched by its own weight and impinging on a moving substrate, for different fall heights and substrate velocities: comparison of dynamic simulations based on the theory of viscous rods (yellow) and experiments (black and white) [2, 5, 1, 4].

Even though many aspects of the beam and rod theories are classical and well understood, fundamental (and often simple) problems have been solved recently only, or have remained unsolved to date. This includes for instance the derivation of accurate 1D models for curved strips (*i.e.* narrow shells) such as a carpenter's tape, and for filaments made of non-purely

elastic materials (such as elasto-plastic or visco-plastic materials), the design of robust and efficient simulation methods, and the derivation of explicit solutions to non-linear self-contact problems.

Being effectively one-dimensional, slender bodies are governed by equations that are simpler to write down, more likely to have analytical solutions, and easier to solve numerically than the corresponding equations of 3D continuum mechanics. This allows one to address problems that would be impossible to tackle otherwise. In this talk, we will illustrate the derivation of solutions of this kind.

References

[1] B. Audoly, N. Clauvelin, P.-T. Brun, M. Bergou, E. Grinspun, and M. Wardetzky. A discrete geometric approach for simulating the dynamics of thin viscous threads. *Journal of Computational Physics*, 253:18–49, 2013.

[2] C. Batty, B. Audoly, and E. Grinspun. Discrete viscous sheets. *Transactions on Graphics*, 31(4):113:1–7, 2012.

[3] M. Bergou, M. Wardetzky, S. Robinson, B. Audoly, and E. Grinspun. Discrete elastic rods. *ACM Transactions on Graphics*, 27(3):63:1–63:12, 2008.

[4] P.-T. Brun, B. Audoly, N. Ribe, T. S. Eaves, and J. R. Lister. Liquid ropes: a geometrical model for thin viscous jet instabilities. *Physical Review Letters*, 114(17):174501, 2015.

[5] P.-T. Brun, N. M. Ribe, and B. Audoly. A numerical investigation of the fluid mechanical sewing machine. *Physics of fluids*, 24(4):043102, 2012.

[6] M. A. Dias and B. Audoly. A non-linear rod model for folded elastic strips. *Journal of the Mechanics and Physics of Solids*, 62:57—80, 2014.

[7] M. A. Dias, L. H. Dudte, L. Mahadevan, and C. D. Santangelo. Geometric mechanics of curved crease origami. *Physical Review Letters*, 109(11):114301, 2012.

[8] J. T. Miller, A. Lazarus, B. Audoly, and P. M. Reis. Shapes of a suspended curly hair. *Physical Review Letters*, 112:068103, 2014.

BIOMECHANICS AND THE PHYSIOME PROJECT

Peter Hunter[1]

[1]*Auckland Bioengineering Institute, University of Auckland, New Zealand*

ABSTRACT

Biomechanics underpins many areas of physiology. Anatomically based continuum models of the heart, lungs, skin and musculo-skeletal system have been developed and are essential for a quantitative understanding of the physiological function of these organs and organ systems. Solving the equations of large deformation continuum mechanics and three dimensional viscous fluid mechanics via finite element methods is now a relatively mature discipline. The challenge at the continuum level is to capture the nonlinear, anisotropic and inhomogeneous nature of the biological tissues and to link their constitutive properties to microstructural models. The bigger challenge is to understand the molecular processes that regulate tissue function and the processes of adaptation and growth that characterise all biological tissues. This talk will present work being done for the Physiome Project on these challenges at both the tissue scale and the molecular scale.

THE PHYSIOME PROJECT

The Physiome project was initiated by the International Union of Physiological Sciences (IUPS) in 1997 in order to bring multiscale engineering modelling approaches to the physiological interpretation of the wealth of molecular data becoming available at that time [1]. The interaction between gene expression and the physical environment into which the genes are expressed is key to understanding physiological function. While diseases and drugs operate at the molecular level, the regulation of genetic transcription and hence the assembly of proteins (the building blocks of life) are both highly dependent on environmental factors governed by the physical world in which molecular biology operates. Engineering, and in particular the rapidly growing field of bioengineering, is the discipline that has the integrative skills and tools to put the molecular pieces back together again.

In 2003, six years after the establishment of the Physiome Project by IUPS in 1997, the US 'Interagency Modeling and Analysis Group' (IMAG) began funding physiome project grants. Four years later, in 2007, a consortium of European scientists and engineers published a roadmap 'Seeding the EuroPhysiome: A Roadmap to the Virtual Physiological Human' (VPH) that persuaded the European Commission to call for research proposals under Framework 7 on healthcare related modelling. A VPH Institute (VPH-I) was subsequently established to provide continued global leadership for the VPH/Physiome Project with the goal of '*using computational modelling of biological processes to integrate quantitative biological knowledge from molecular to cell, tissue, organ and whole body scales in order to understand physiological systems in terms of both their molecular components and their interaction with the environment and translate this understanding into clinical practice*' [2].

Mathematics is the language of quantitative science and every scientific discipline should analyse its experimental data in the light of physical laws encapsulated in mathematical equations. The challenge facing the Physiome Project is the enormous complexity, including spatial and temporal scales, of molecular and physiological systems. Mathematical models of these processes quickly become difficult for anyone other than the author of a model to reproduce let alone understand. The engineering solution to this problem is to build models based on 'standards' and 'modularity'. Data and modelling standards, with tools and model repositories based on these standards, ensure reproducibility and testability. And models must be built from modules that define the functional components of a system. To link models of proteins to physiological scale models (i.e. cells, tissues, organs and organ systems) also requires a hierarchy of models that are semantically rich so that an imported component module can be assembled automatically into the right place in the parent model.

A typical multiscale model is shown in Figure 1 [3]. Four spatial scales are shown: the cell (cardiac myocyte), tissue (myocardium), organ (heart) and whole body (torso). The cell model shown here is in fact made up of many individual protein models. Heart disease and heart drugs operate at the protein level, but the diagnosis of disease usually made at the level of the intact organ (e.g., the EKG for electrical function or ultrasound images for mechanical function). The challenge is to link models across these scales.

The talk will describe multiscale modelling work on the heart, lungs and musculo-skeletal system. It will also describe the framework being developed to ensure reproducible modelling using standards and standards-based tools developed for the Physiome Project.

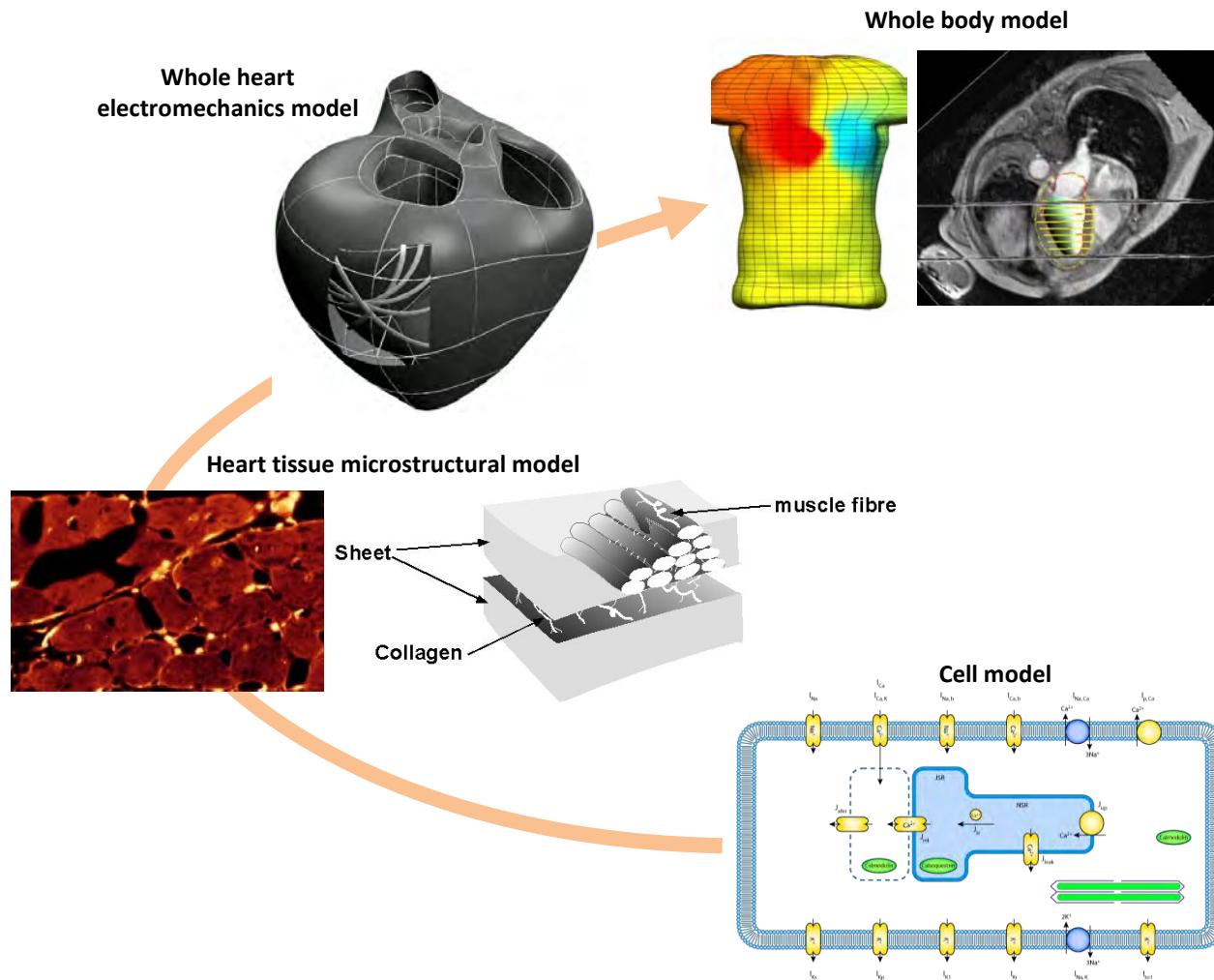a) Corresponding author. Email: **p.hunter@auckland.ac.nz**

FIGURE 1 A multiscale model for electromechanics in the heart. The cell, tissue, organ and torso scales are shown here. The cell model is made up of many imported modules – corresponding, for example, to the individual membrane protein ion channels, pumps and exchangers, and to signalling pathways that control gene expression and growth processes. A microstructural model at the tissue level is used to derive constitutive laws that are used with the field equations of physics at the organ and whole body levels.

The initial focus for the Physiome Project has been on the establishment of standards, based on modular components, that help ensure reproducibility of models [4]. The syntax for the model equations is MathML, the w3c standard for both content and presentation of mathematics. The need for semantically rich metadata is addressed through RDF (Resource Description Framework), another w3c standard, using ontologies such as ChEBI for chemical identifiers, GO for cell components, the CellType ontology, the Foundation Model of Anatomy (FMA), and OPB for biophysical annotation. Based on these, two XML standards have been developed: one called CellML for lumped parameter (not spatially varying) algebraic and ODE models (e.g. the cell model shown in Fig.1) and another called FieldML for spatially varying (typically finite element) models (e.g. the tissue, organ and torso models shown in Figure 1).

References

[1] Hunter P.J., Borg T.K. Integration from proteins to organs: The Physiome Project. *Nature Reviews Molecular and Cell Biology*, 4(3):237-243, 2003.

[2] Hunter P., Chapman T., Coveney P.V., de Bono B., Diaz V., et al. A vision and strategy for the virtual physiological human: 2012 update. *Interface Focus* 3:20130004, 2013.

[3] Hunter P.J., Pullan A.J., Smaill B.H. Modeling total heart function. *Annual Review of Biomedical Engineering*, 5:147-177, 2003.

[4] Cuellar, A.A., Lloyd, C.M., Nielsen, P.F., Halstead, M.D.B., Bullivant, D.P., Nickerson, D.P., Hunter, P.J. An overview of CellML 1.1, a biological model description language. *SIMULATION: Transactions of The Society for Modeling and Simulation International*, 79(12):740-747, 2003.

DEFORMATION AND FRACTURE OF ELECTROMAGNETIC THIN FILMS AND LAMINATES UNDER MULTI-FIELD LOADING

Daining Fang[1a)], Yongmao Pei[2] , Faxin Li[2] & Haosen Chen[1]

[1] *Institutes of Advanced Technology, Beijing Institute of Technology, Beijing, China*
[2]*State Key Laboratory for Turbulence and Complex Systems, College of Engineering, Peking University, Beijing, China*

Abstract

Electromagnetic functional materials, such as ferroelectrics, ferromagnetics and magnetoelectric thin films and laminates, have been widely used in modern industries. Their deformation and fracture behaviors under mechanical loading are affected considerably by an external electric or magnetic field. To provide a deep understanding of the intrinsic coupling properties, a novel electro-magneto-mechanical multi-field nanoindentation apparatus and a novel multi-field bulge-test instrument were designed and constructed. The corresponding characterization method for the thin-film electromagnetic materials was also established. The experimental results reveal the size-dependency of various mechanical properties, ranging from the Young's modulus, to the hardness as well as fracture toughness. Notably, these properties can be well controlled by applying external electric/magnetic fields. Furthermore, a new size-dependent nonlinear constitutive model is developed for the magnetoelectric laminates to account for the coupling mechanisms under multi-field loading. This model is managed to study the dynamic harmonic magnetoelectric response and the microwave magnetoelectric effect.

Main text

With the rapid advances in the materials science and technologies, the characteristic dimensions of electromagnetic functional materials have been pushed down to micro or even nanoscale, creating great challenges in the characterization of their multi-field coupling properties [1,2]. In this work, a novel electro-magneto-mechanical multi-field nanoindenter with powerful functions [Fig. 1(a)] was designed and constructed to study the local mechanical properties of electromagnetic materials [3]. The dependence of Young's modulus and hardness of ferroelectric/ferromagnetic materials on applied electric/magnetic fields were systematically investigated [4]. The field tunable fracture behavior of thin-film structures was studied as well [Fig. 1(b)], which is found to be size-dependent. A new method is proposed to characterize the electro-magneto-mechanical coupled performances resulted from the nanoindentation experiment, based on the field tunable scaling laws. This method can avoid the testing errors encountered in the Oliver-Pharr method for the estimation of contact area [5]. Moreover, a multi-field bulge-test instrument [Fig. 1(c)] was designed and constructed to explore the electro-magneto-mechanical coupling properties of the electromagnetic thin films [6]. The corresponding characterization method for the elastic property and fracture toughness of thin films was also established. A few interesting phenomena were found, including the evident effect of mechanical deformation on the electric/magnetic behaviors (e.g., the ferroelectric hysteresis loops, butterfly curves, magnetization loops and magnetostrictive curves), as well as the underlying dependences of the fracture toughness of the magnetic thin films on both the thickness and the external magnetic field [Fig. 1(d)].
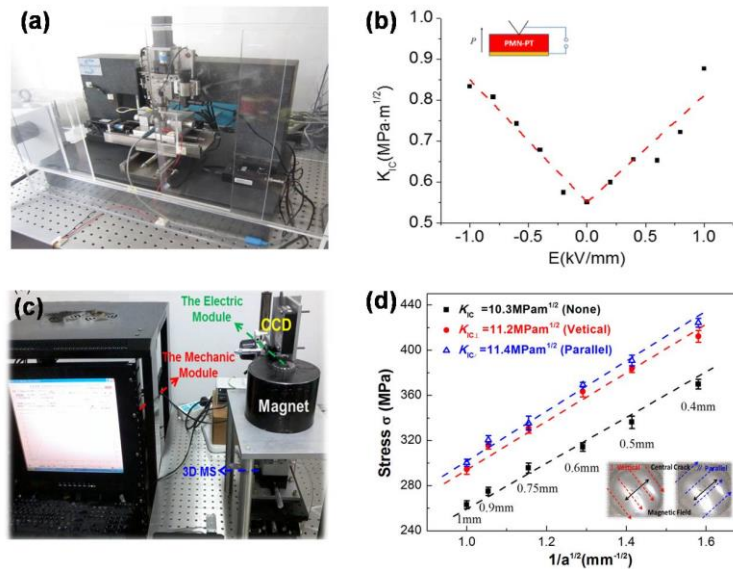
Fig. 1. (a) Photo of the multi-field nanoindenter. (b) Electric-filed dependency of fracture toughness of relaxor ferroelectric Pb(Mn1/3Nb2/3)O3-PbTiO3 crystals measured by nanoindentation. (c) Multi-field bulge-test instrument setup. (d) Fracture toughness of Ni thin films under different magnetic fields.

In order to describe the multi-field coupling deformation behavior of magnetoelectric composites laminates, we develop a nonlinear constitutive model, which can reveal size dependency of coupling behaviors, by use of a probabilistic criterion of domain switching [7]. The various responses (e.g., the polarization, magnetization as well as strain) under combined electro-magneto-mechanical loading were investigated. The results demonstrate quantitatively the electric-field control of magnetization and magnetic-field tuning of polarization, as shown in Fig. 2, which can serve as a guideline for practical device applications. The size effect of the magnetoelectric coupling was also explored, which demonstrates the competition of the strain-mediated and charge-driven effects. Finally, the model is successfully extended to study dynamic harmonic magnetoelectric response and nonlinear microwave magnetoelectric effect.
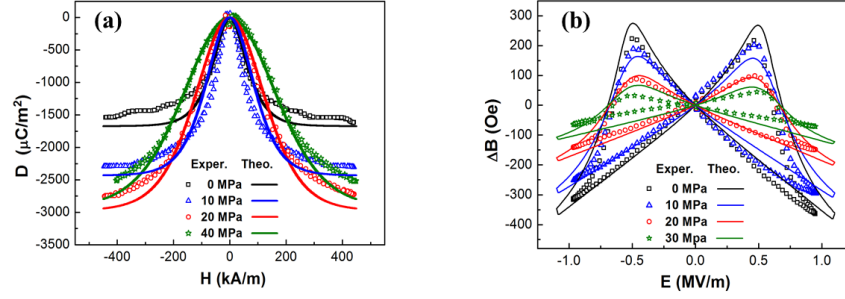

Fig. 2. Comparisons of theoretical results with experimental data: (a) The magnetic-field tuning of polarization. (b) The electric-filed control of magnetization.

References

[1] Bibes M. and Barthelemy A., Multiferroics: Towards a magnetoelectric memory, *Nature Materials*, **7**, 425-426, 2008.

[2] Dagdeviren C., Yang B.D., Su Y., Tran P.L., Joe P., Anderson E., and Rogers J.A.. Conformal piezoelectric energy harvesting and storage from motions of the heart, lung, and diaphragm, *Proceedings of the National Academy of Sciences*, **111**, 1927-1932, 2014.

[3] Zhou H., Pei Y., Huang H., Zhao H., Li F., and Fang D., Multi-field nanoindentation apparatus for measuring local mechanical properties of materials in external magnetic and electric fields. *Review of Scientific Instruments*, **84**, 063906, 2013.

[4] Zhou H., Pei Y., and Fang D., Magnetic field tunable small-scale mechanical properties of nickel single crystals measured by nanoindention technique. *Scientific Reports*, **4**, 4583, 2014.

[5] Zhou H., Zhang H.L., Pei Y., Chen H., Zhao H., and Fang D., Scaling relationship among indention properties of electromagnetic materials at micro- and nanoscale. *Applied Physics Letters*, **106**, 081904, 2015.

[6] Yu, Z.J., Mao, W.G., Li, F.X., Feng, X., Pei, Y.M., and Fang, D.N., Magnetic and electric bulge-test instrument for the determination of coupling mechanical properties of functional free-standing films and flexible electronics, *Review of Scientific Instruments*, **85**, 065117, 2014.

[7] Xu, H., Pei, Y.M., and Fang, D.N. A size-dependent nonlinear constitutive model for the layered piezoelectric-magnetostrictive composites. Unpublished.

CONCEPTS IN MECHANICS FOR 3D, BIO-INTEGRATED ELECTRONICS

John Rogers[1a)]

[1]*Department of Materials Science and Engineering, University of Illinois, Urbana, IL, USA*
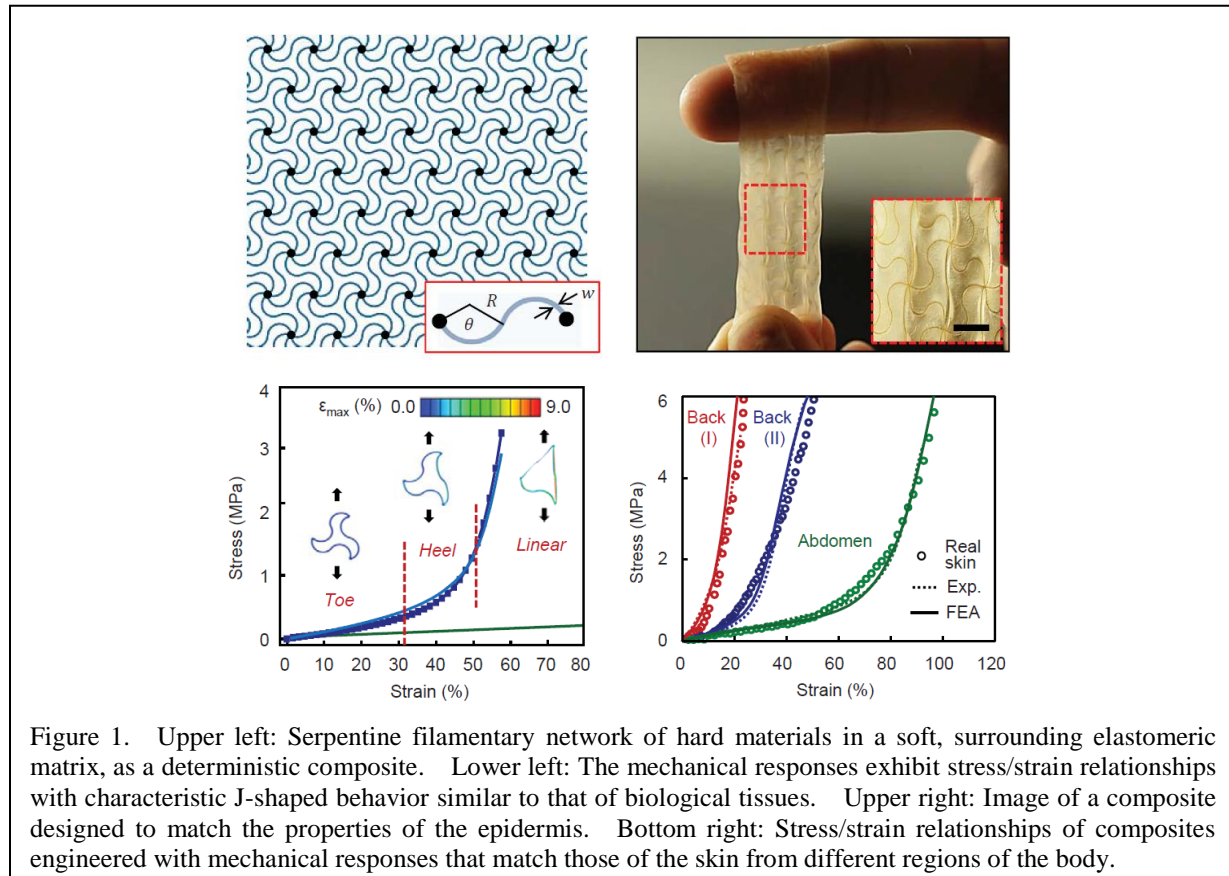
Summary New concepts in mechanics provide routes to high performance electronics with physical characteristics matched to those of vital organs of the human body. The resulting opportunities for integration of sensors, actuators, radios and computing capabilities directly on the surfaces or into the depths of targeted tissues have strong potential to improve current practices in clinical care and physiological monitoring. This paper outlines some of the key ideas, and describes their use in skin-mounted systems and 3D open-mesh networks.

INTRODUCTION

Biology is soft, curvilinear and transient; modern semiconductor technologies are rigid, planar and everlasting. Electronic and optoelectronic systems that eliminate this profound mismatch in properties create opportunities for devices that can intimately integrate with the body, for diagnostic, therapeutic or surgical function with important, unique capabilities in biomedical research and clinical healthcare. A convergence of concepts in mechanics, materials science, electrical engineering and advanced manufacturing has led to the emergence of diverse, novel classes of 'biocompatible' electronic platforms, with capabilities in intimate, persistent physical interfaces with the surfaces of biological tissues, and recent work that foreshadows possibilities in full 3D integration. This paper describes the core ideas, with examples ranging from wireless, skin-like electronic 'tattoos' for continuous monitoring of physiological health to 3D mesoscale electronic networks as active cellular scaffolds.

RESULTS

When mounted on the skin, advanced sensors, circuits, radios and power supply systems have the potential to provide clinical-quality health monitoring capabilities for continuous use, outside of traditional hospital settings or laboratory facilities. The most well-developed component technologies are, however, currently available only in hard, planar

Figure 1. Upper left: Serpentine filamentary network of hard materials in a soft, surrounding elastomeric matrix, as a deterministic composite. Lower left: The mechanical responses exhibit stress/strain relationships with characteristic J-shaped behavior similar to that of biological tissues. Upper right: Image of a composite designed to match the properties of the epidermis. Bottom right: Stress/strain relationships of composites engineered with mechanical responses that match those of the skin from different regions of the body.

[a)] Corresponding author. Email: jrogers@illinois.edu.

formats.   As a result, existing options in system design are unable to effectively accommodate integration with the soft, textured, curvilinear and time-dynamic surfaces of the skin, without irritation or interface failures.   Recent work establishes experimental and theoretical approaches for using soft materials, ultrathin micro/nanostructures, and controlled processes of mechanical buckling to achieve ultralow modulus, thin and highly stretchable, systems of state-of-the-art semiconductor devices, with options in quantitatively matching the effective non-linear stress/strain relationships of the epidermis.   The result is a 'skin-like' technology with measurement fidelity that can match that of large-scale tools currently used in clinical medicine.   Figure 1 shows an example[1].

The essential 3D character of biological systems motivates the development of approaches to 3D electronics that adopt bio-inspired, mesoscale open network designs.   Of the many methods for fabricating such structures, few are compatible with the highest performance classes of electronic materials, such as monocrystalline inorganic semiconductors, and only a subset of these can operate at high speeds, across length scales, from centimeters to nanometers.   New strategies avoid these limitations, via the use of controlled compressive forces imparted by a pres-strained elastomeric substrates with the effect of transforming 2D micro/nanostructures with lithographically defined geometries and points of adhesion into 3D structures, with levels of complexity and control that significantly exceed those that can be achieved with alternative methods[2].   Examples include a diverse set of examples formed using silicon nanomembranes, plates and ribbons and heterogeneous combinations of them with micro/nanopatterned metal films and dielectrics.   Quantitatively accurate theoretical modelling of the solid mechanics of the transformation process provides a design tool to create targeted geometries that offer adaptable shapes and desired modes of operation.
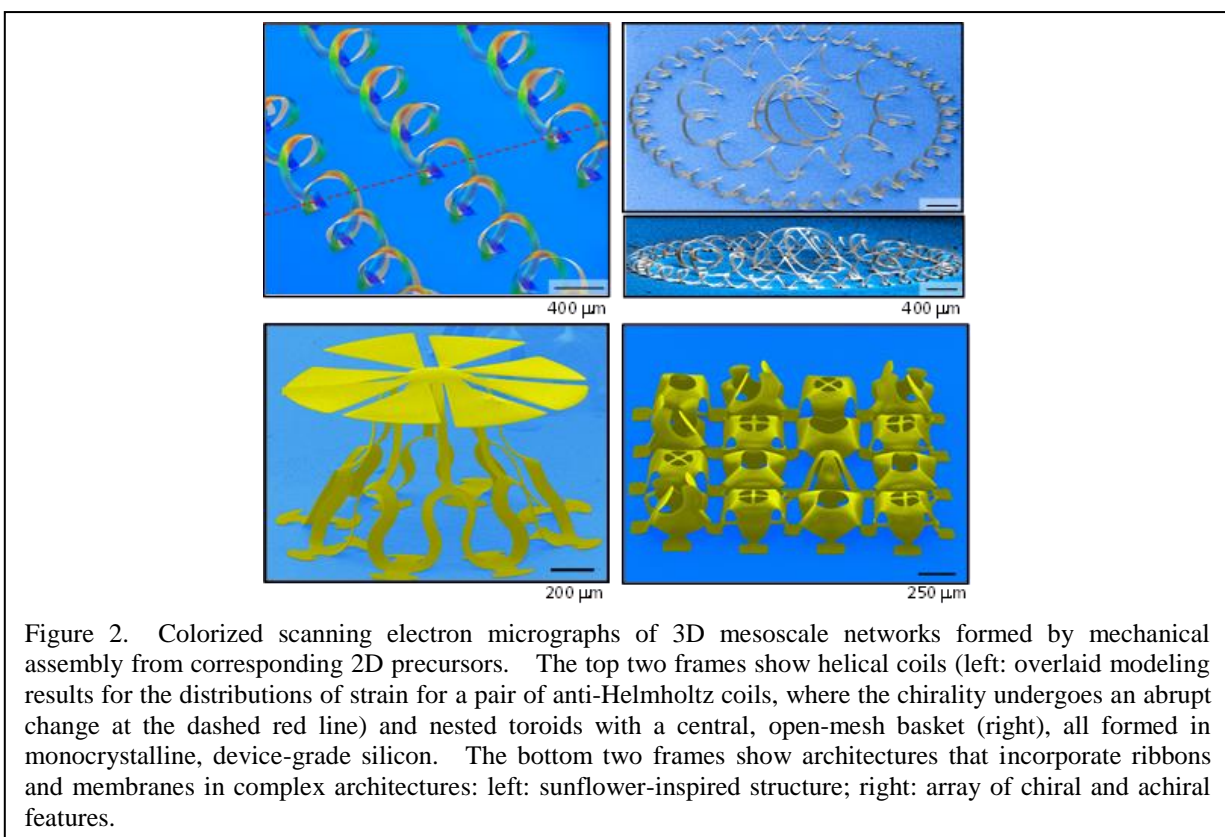

Figure 2.   Colorized scanning electron micrographs of 3D mesoscale networks formed by mechanical assembly from corresponding 2D precursors.   The top two frames show helical coils (left: overlaid modeling results for the distributions of strain for a pair of anti-Helmholtz coils, where the chirality undergoes an abrupt change at the dashed red line) and nested toroids with a central, open-mesh basket (right), all formed in monocrystalline, device-grade silicon.   The bottom two frames show architectures that incorporate ribbons and membranes in complex architectures: left: sunflower-inspired structure; right: array of chiral and achiral features.

CONCLUSIONS

Advanced concepts in mechanics create new opportunities in the construction of 2D and 3D electronic systems with unmatched capabilities in bio-integration.   Research in these areas now ranges from the study of the foundational mechanical science to the development of clinically relevant biomedical devices.

References

[1]   Jang K.I., et al: Soft Network Composite Materials With Deterministic and Bio-inspired Designs. *Nat. Comm.* **6**:6566, 2015.
[2]   Shu, X. et al: Assembly of Micro/nanomaterials into Complex, Three-Dimensional Architectures by Compressive Buckling. *Science* **347**, 154-159, 2015.

SOFT MACHINES

Zhigang Suo [a)]

School of Engineering and Applied Sciences, Kavli Institute for Bionano Science and Technology
Harvard University, Cambridge, MA 02138, USA

Summary Machines in engineering use mostly hard materials, whereas machines in nature are often soft. This difference has been an inspiration for the nascent field of soft machines. What does softness impart to the life of animals and plants? Softness enables deformation, and deformation provides functions. Familiar examples include the beating of the heart, the sound shaped by the vocal folds, and the flapping of the wing. In soft machines, the large deformation enable soft materials to behave as transducers, connecting multiple stimuli to multiple functions. How do molecular processes enable new classes of actuators and sensors? How efficiently can materials convert information from one form to another? These questions are stimulating new and exciting developments at the interface between science and engineering. This talk highlights the behavior of soft materials that enables the creation of soft machines. Examples include highly stretchable and transparent devices that mimic the functions of muscles, skins and axons.

LARGE DEFORMATION ENABLE MANY FUNCTIONS

A conspicuous feature of life is to receive and process information from the environment, and then move. The movements are responsible for diverse functions. Consider the accommodation of the eye, the beating of the heart, the sound shaped by the vocal folds, and the sound in the ear. Abstracting these biological soft machines, we may say that a stimulus causes a material to deform, and the deformation provides a function. Connecting the stimulus and the function is the material capable of large deformation in response to a stimulus.

An exciting field of engineering is emerging that uses soft materials to create soft machines. Soft materials in engineering are indeed apt in mimicking the salient feature of life: movements in response to stimuli. An electric field can cause an elastomer to stretch several times its length. A change in pH can cause a hydrogel to swell many times its volume. These soft active materials are being developed for diverse applications, including soft robots, adaptive optics, self-regulating fluidics, programmable haptic surfaces, and oilfield management [1,2].

TOUGH WATER

What can we do if water is a tough solid? A hydrogel aggregates water and a polymer network. The polymer network makes the hydrogel a stretchable solid, but water retains its exceptional physical and chemical properties. Several recent findings show that hydrogels can achieve properties and applications well beyond previously imagined. Most existing hydrogels, like Jell-O and tofu, are fragile and dry out in open air. We make hydrogels as tough as rubber, and retain water in low-humidity environment [3,4]. We show that hydrogels outperform existing fire-retarding materials [5]. We also demonstrate fiber-reinforced hydrogels [6].

ARTIFICIAL MUSCLES

Existing stretchable, transparent conductors are mostly electronic conductors. They limit the performance of interconnects, sensors and actuators as components of stretchable electronics and soft machines. We describe a class of devices enabled by ionic conductors that are highly stretchable and fully transparent to light of all colors [7], capable of operation at frequencies beyond 10 kHz and voltages above 10 kV. We demonstrate a transparent actuator that can generate large strains, and a transparent loudspeaker that produces sound over the entire audible range. The electromechanical transduction is achieved without electrochemical reaction. The ionic conductors have higher resistivity than many electronic conductors; however, when large stretchability and high transmittance are required, the ionic conductors have lower sheet resistance than all existing electronic conductors.

ARTIFICIAL SKIN

Our skin is a stretchable, large-area sheet of distributed sensors. These properties of skin have inspired the development of mimics, with differing levels of sophistication, to enable wearable or implantable electronics for entertainment and healthcare. We explore the potential of ionic conductors in the development of a new type of sensory sheet, which we call "ionic skin" [8]. The sensory sheet is highly stretchable, transparent, and biocompatible. It readily monitors large deformation, such as that generated by the bending of a finger. It detects stimuli with wide dynamic range

---

[a)] Corresponding author. Email: suo@seas.harvard.edu.

(strains from 1% to 500%). It measures pressure as low as 1 kPa, with small drift over many cycles. A sheet of distributed sensors covering a large area can report the location and pressure of touch. High transparency allows the sensory sheet to transmit electrical signals without impeding optical signals.

ARTIFICIAL AXON

We demonstrate a new type of interconnects to fulfill the primary function of axons: transmitting electrical signals over long distances and at high speeds [9]. The interconnect, which we call "ionic cable", uses ions to transmit signals, and is built entirely with soft, elastic materials—elastomers and gels. The ionic cable is highly transparent, and remains functioning after being stretched nearly eight times its original length. We describe the design, theory and experiment of the ionic cable. We show that the diffusivity of signals in the ionic cable is about 16 orders of magnitude higher than the diffusivity of ions. We demonstrate that the ionic cable transmits signals up to 100 MHz over 10 cm, and transmits music signals over meters. The ionic cable transmits enough power to turn on light-emitting diodes. Our theory shows that the ionic cables scale well, suggesting tremendous opportunities to create miniaturized ionic circuit. Furthermore, we use the ionic conductors to demonstrate electroluminescence of giant stretchability [10].

CONCLUSIONS

A large number of examples in plants and animals demonstrate that deformation of soft materials connect diverse stimuli to many functions essential to the life. An exciting field of engineering is emerging that uses soft materials to create soft machines. To participate in advancing the field of soft active materials and soft machines effectively, mechanicians must retool our laboratories and our software, as well as adapt our theories. This talk highlights this theme using recent advances in materials, devices, and theories.

References

[1] Suo Z.G.: Theory of Dielectric Elastomers. *Acta Mechanica Solida* **23**:549-578, 2010.

[2] Suo Z.G.: Mechanics of Stretchable Electronics and Soft Machines. *MRS Bulletin* **37**, 218-225, 2012.

[3] Sun J.Y., Zhao X.H., Illeperuma W.R.K., Oh K.H., Mooney D.J., Vlassak J.J., Suo Z.G.: Highly Stretchable and Tough Hydrogels. *Nature* **489**, 133-136, 2012.

[4] Bai Y.Y, Chen B.H., Xiang F., Zhou, J.X., Wang H., Suo Z.G: Transparent Hydrogel with Enhanced Water Retention Capacity by Introducing Highly Hydratable Salt. *Applied Physics Letters* **105**, 191903, 2014.

[5] Illeperuma W.R.K., Rothemund P., Suo Z.G., Vlassak J.J.: Fire-Resistant Hydrogel-Fabric Laminates: a Simple Concept That May Save Lives. *ACS Applied Materials and Interfaces*. Accepted manuscript, DOI: 10.1021/acsami.5b10538

[6] Illeperuma W.R.K., Sun J.Y., Suo Z.G., Vlassak J.J.: Fiber-Reinforced Tough Hydrogels. *Extreme Mechanics Letters* **1**, 90-96, 2014.

[7] Keplinger C., Sun J.Y., Foo, C.C., Rothemund P., Whitesides G.M., Suo Z.G.: Stretchable, Transparent, Ionic Conductors. *Science* **341**, 984-987, 2013.

[8] Sun J.Y., Keplinger C., Whitesides G.M., Suo Z.G.: Ionic Skin. *Advanced Materials* **26**, 7608-7614, 2014.

[9] Yang C.H., Chen B.H., Lu J.J., Yang J.H., Zhou J.X., Chen Y.M., Suo Z.G. Ionic Cable. *Extreme Mechanics Letters* **3**, 59-65, 2015.

[10] Yang C.H., Chen B.H., Zhou J.X., Chen Y.M., Suo Z.G. Electroluminescence of giant stretchability. *Advanced Materials*. Accepted manuscript, DOI: 10.1002/adma.201504031

THE MICROMORPHIC APPROACH
TO GRADIENT CRYSTAL PLASTICITY AND DAMAGE

Samuel Forest [*1]

[1]*Mines ParisTech, Centre des Matériaux, CNRS UMR 7633, Evry, France*

Summary The micromorphic method is recalled and applied to continuum crystal plasticity in order to model size effects in the mechanical behavior of single and polycrystals. The constitutive equations are discussed with respect to the prediction of scaling laws. The regularization power of the model is illustrated in the case of crack propagation simulation in single crystals.

INTRODUCTION TO THE MICROMORPHIC APPROACH

The micromorphic approach consists in enhancing the continuum mechanical framework by introducing deformation–like independent degrees of freedom [1]. The set of constitutive variables is then extended to the gradient of these additional degrees of freedom. It originates from Eringen and Mindlin's proposal to endow each material point with a second order generally nonsymmetric microdeformation tensor representing the rotation and stretch of a triad or directors related to the microstructure, in addition to the classical displacement degrees of freedom [2]. A whole hierarchy of generalized continua is built in the micromorphic theory, including the celebrated Cosserat model when the microdeformation reduces to a microrotation [3]. The micromorphic approach was applied to crystal plasticity by [4, 5, 6] using the Cosserat framework and by [7] where a generally nonsymmetric plastic microdeformation tensor is introduced. The latter model reduces to strain gradient plasticity based on the disclocation density tensor when the microdeformation coincides with the plastic deformation itself [8]. These models involve intrinsic characteristic lengths, in contrast to the conventional Cauchy continuum, which makes it possible to describe size effects in the mechanical responses of elastic–plastic polycrystals, including Orowan and Hall–Petch effects associated with the interaction of dislocations with precipitates and grain boundaries. The method can be extended to strain–like scalar degrees of freedom related to elastic or plastic strain or damage [1]. The new scalar degree of freedom must be constitutively related to some strain or internal variable of the original model. In the case of crystal plasticity, a micromorphic variable was associated to an equivalent plastic slip measure by [9] and a microdamage variable was introduced related microcrack opening along cleavage planes in [10]. Close links exist between the micromorphic approach and phase field modeling as discussed by [11], with the difference that the phase field parameter is not necessarily related to a mechanical variable.

SIZE EFFECTS IN THE CYCLIC BEHAVIOUR OF SINGLE CRYSTALS

Strain gradient plasticity theory represents a continuum model of dislocation plasticity. It can be used to represent dislocation pile–up formation at interfaces in single crystals [12]. The *microcurl* model was shown in [7] to predict channel–size effects in the stress–plastic strain response of laminate microstructures made of alternating elastic and plastic layers. The choice of the constitutive functional related to the gradient terms is essential to the quantitative description of such effects. In particular, the quadratic ansatz in the gradient terms, widely used in strain gradient plasticity and phase field models, was shown to predict physically unrealistic scaling laws. Alternative potentials were proposed by [13]. The concept of reversible plasticity is put forward in the latter contribution leading to unusual cyclic stress–strain loops with inflection points. It represents a continuum model of the first–in last–out concept in dislocation pile–ups initially proposed in the seminal paper [14]. A remarkable effect was predicted by the *microcurl* model in the plasticity of polycrystals. Sub–micron grain sizes were shown to promote plastic slip localization in the form of intense slip bands interconnecting grains of the polycrystals whereas more diffuse slip is observed at larger grain sizes. This is due to the high energy cost associated with lattice curvature, as illustrated in Fig. 1.

SIMULATION OF CRACK INITIATION AND PROPAGATION IN SINGLE CRYSTALS

Accumulated plastic slip is known to be responsible for crack initiation, especially under fatigue loading conditions. A coupled plasticity–damage criterion was proposed allowing for damage strain associated with opening of crystallographic planes as the result of a combination of normal stress and accumulated slip [16]. A micromorphic microdamage variable is introduced akin to the cumulated damage variable. The introduction of microdamage gradient into the constitutive model provides a regularization of damage localization into cracks of finite thickness. The regularization properties of the micromorphic approach to damage were used first by [17, 18]. Thermodynamical foundations of this class of regularized models

---

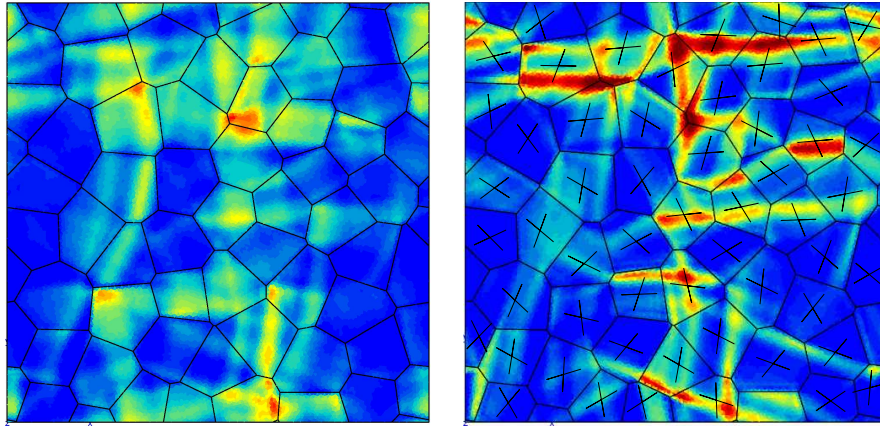[*]Corresponding author. Email: samuel.forest@mines-paristech.fr

Figure 1: Field of accumulated plastic slip in two idealized polycrystals with the same microstructure (grain shape and orientations) but different grain sizes: 100 μm and 4 μm (right). The formation of intense slip bands crossing grain boundaries is observed in the right picture where the traces of the slip planes are represented, after [15].

were provided by [1]. The simulations of crack initiation and propagation in single and polycrystals will be related to recent experiments of 3D observations of short fatigue cracks combining microtomography and diffraction at the ESRF synchrotron in Grenoble [19, 20]. The role of grain boundaries as barriers to short crack growth will be illustrated.

References

[1] S. Forest. The micromorphic approach for gradient elasticity, viscoplasticity and damage. *ASCE Journal of Engineering Mechanics*, 135:117–131, 2009.

[2] A.C. Eringen and E.S. Suhubi. Nonlinear theory of simple microelastic solids. *Int. J. Engng Sci.*, 2:189–203, 389–404, 1964.

[3] S. Forest and R. Sievert. Nonlinear microstrain theories. *International Journal of Solids and Structures*, 43:7224–7245, 2006.

[4] S. Forest, G. Cailletaud, and R. Sievert. A Cosserat theory for elastoviscoplastic single crystals at finite deformation. *Archives of Mechanics*, 49(4):705–736, 1997.

[5] S. Forest, F. Barbe, and G. Cailletaud. Cosserat modelling of size effects in the mechanical behaviour of polycrystals and multiphase materials. *International Journal of Solids and Structures*, 37:7105–7126, 2000.

[6] J.R. Mayeur, D.L. McDowell, and D.J. Bammann. Dislocation–based micropolar single crystal plasticity: Comparison of multi– and single criterion theories. *Journal of the Mechanics and Physics of Solids*, 59:398–422, 2011.

[7] N. M. Cordero, A. Gaubert, S. Forest, E. Busso, F. Gallerneau, and S. Kruch. Size effects in generalised continuum crystal plasticity for two–phase laminates. *Journal of the Mechanics and Physics of Solids*, 58:1963–1994, 2010.

[8] M.E. Gurtin. A gradient theory of single–crystal viscoplasticity that accounts for geometrically necessary dislocations. *Journal of the Mechanics and Physics of Solids*, 50:5–32, 2002.

[9] S. Wulfinghoff and T. Böhlke. Equivalent plastic strain gradient enhancement of single crystal plasticity: theory and numerics. *Proceedings of the Royal Society A*, 468:2682–2703, 2012.

[10] O. Aslan and S. Forest. Crack growth modelling in single crystals based on higher order continua. *Computational Materials Science*, 45:756–761, 2009.

[11] O. Aslan and S. Forest. The micromorphic versus phase field approach to gradient plasticity and damage with application to cracking in metal single crystals. In R. de Borst and E. Ramm, editors, *Multiscale Methods in Computational Mechanics*, pages 135–154. Lecture Notes in Applied and Computational Mechanics 55, Springer, 2011.

[12] S.D. Mesarovic, R. Baskaran, and A. Panchenko. Thermodynamic coarsening of dislocation mechanics and the size-dependent continuum crystal plasticity. *Journal of the Mechanics and Physics of Solids*, 58:311–329, 2010.

[13] S. Wulfinghoff, S. Forest, and T. Böhlke. Strain gradient plasticity modeling of the cyclic behavior of laminate microstructures. *Journal of the Mechanics and Physics of Solids*, 79:1–20, 2015.

[14] R. J. Asaro. Elastic–plastic memory and kinematic hardening. *Acta Metallurgica*, 23:1255–1265, 1975.

[15] N. M. Cordero, S. Forest, E. P. Busso, S. Berbenni, and M. Cherkaoui. Grain size effects on plastic strain and dislocation density tensor fields in metal polycrystals. *Computational Materials Science*, 52:7–13, 2012.

[16] O. Aslan, N. M. Cordero, A. Gaubert, and S. Forest. Micromorphic approach to single crystal plasticity and damage. *International Journal of Engineering Science*, 49:1311–1325, 2011.

[17] R.H.J. Peerlings, W.A.M. Brekelmans, R. de Borst, and J. H. P. de Vree. Gradient–enhanced damage for quasi–brittle materials. *Int. J. for Numerical Methods in Engineering*, 39:3391–3403, 1996.

[18] M.G.D. Geers, R. de Borst, W.A.M. Brekelmans, and R.H.J. Peerling. Strain–based transient–gradient damage model for failure analysis. *Comput. Methods Appl. Mech. Engrg.*, 160:133–153, 1998.

[19] J. Li, H. Proudhon, A. Roos, V. Chiaruttini, and S. Forest. Crystal plasticity finite element simulation of crack growth in single crystals. *Computational Materials Science*, 90:191–197, 2014.

[20] H. Proudhon, J. Li, F. Wang, A. Roos, V. Chiaruttini, and S. Forest. 3d simulation of short fatigue crack propagation by finite element crystal plasticity and remeshing. *International Journal of Fatigue*, 82:238–246, 2016.

PROTEIN MECHANICS: FROM AMINO ACID TO SWIMMING CELLS

Patrick R. Onck

Micromechanics, Zernike Institute for Advanced Materials,
University of Groningen, Groningen, The Netherlands

Summary Proteins are long polypeptide chains of amino acids and their structure and biological function are directly related to their amino acid sequence. In this presentation I will discuss three different biological functions that are dominated by protein mechanics, each at their specific time and length scale. To relate structure to function, multiscale computational models have been developed for (i) the beating of cilia and flagella, (ii) the strain-stiffening of cross-linked cytoskeletal networks and (iii) transport through nuclear pores.

PROTEINS

Proteins are often referred to as the building blocks of life, playing critical roles in almost all structures and activities in biology. At the smallest, atomic length scale, proteins consist of amino acids. There are 20 different amino acids, each with their own atomic structure, chemical and physical properties. The amino acids form peptide bonds that form long polypeptide chains consisting of hundreds and sometimes thousands of amino acids. Depending on the specific amino-acid sequence the polypeptide chains fold into regular structures, such as α-helices and β-sheets (secondary structure). At a larger spatial level of organization, α-helices and β-sheets will fold into three-dimensional (tertiary) structures, i.e., the actual protein molecule. Finally, protein molecules can combine to form large protein complexes (quaternary structures).

In this presentation I will take you on a journey through protein state space, addressing three different
biological functions, each with their own time and length scale.

MULTISCALE MODELLING OF PROTEIN MECHANICS

At the largest length scale I will focus on cilia and flagella, long hair-like projections from the surface of cells that play an important role in cell motility [1]. Cells and micro-organisms use cilia and flagella to propel themselves or to propel the fluid surrounding them. Examples are the beating tails (flagella) of sperm cells (see Fig. 1), or the cilia that line the respiratory tract to propel mucus out of the lungs. The beating of cilia and flagella is enabled by their internal microstrucure, the axoneme, a big protein complex (tens of μm long and 250 nm wide) that is powered by a dense distribution of motor proteins, called dyneins. Motor proteins constitute an important class of proteins that, powered by the hydrolysis of ATP, undergo conformational changes and as such convert chemical energy into mechanical work. We developed a computational model based on a minimal representation of the axoneme. Our results demonstrate that an overall regular beating pattern can emerge with time due to the spatial and temporal coordination of the individual dyneins [2].
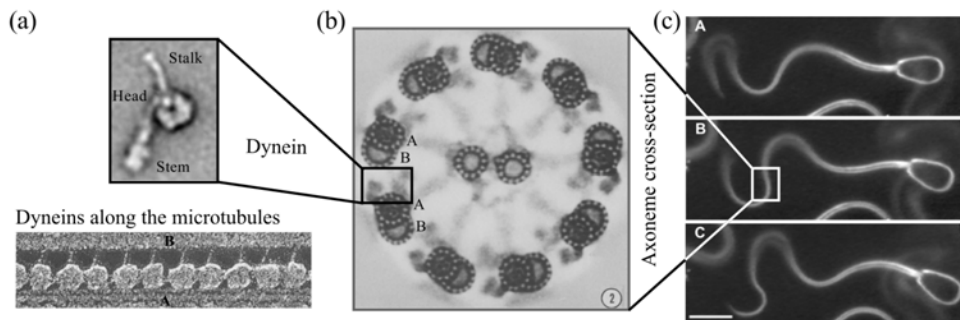

Figure 1: (a) Structure of an axonemal dynein (top). Dyneins at a regular spacing along the microtubules (bottom) [From: Goodenough and Heuser, *J. Cell Biol.* 95, 798–815 (1982)]. (b) An electron micrograph of an axoneme cross-section [From: Afzelius et al., *Tissue and Cell* 27, 241–247 (1995)]. (c) Flagellar beating of a spermatozoon. The three images (A-C) are 200 ms apart. [From: Woolley et al., *J. Exp. Biol.* 212, 18]. Figure is taken from [2].

From a biotechnology point of view, the beating of cilia and flagella are interesting examples for bio-mimicry, utilizing millions of years of biological evolution that led to optimized biological actuators at low Reynolds numbers. Here, artificial, bio-inspired cilia and flagella can be designed using light [3] or magnetic [4-7] actuation to mimic the non-reciprocal motion of their biological counter-part. Artificial cilia can effectively propel fluids in lab-on-chip microfluidic systems, resolving the scale-related problems of downsizing conventional pumping systems [8,9].

Email: P.R.Onck@rug.nl

At a somewhat smaller, subcellular length scale, living cells contain networks of cytoskeletal proteins (Fig. 2). The cytoskeleton is the key cellular component that is responsible for the mechanical behavior of the cell. The major cytoskeletal network is formed by the protein actin, which assembles into a filamentous quaternary structure, and is responsible for maintaining cell shape, stability and for cell motility. Depending on the function and location in the cell, the actin network is cross-linked by different cross-binding proteins, each with their own molecular structure. To capture the constitutive response of actin and other protein networks, we developed a discrete computational network model in two and three dimensions to study the strain stiffening of cross-linked protein networks at large strains [10-12]. Our results show that a wide range of experimental tests on in-vitro reconstituted biopolymer networks can be captured by the competition between two fundamental stiffening mechanisms.
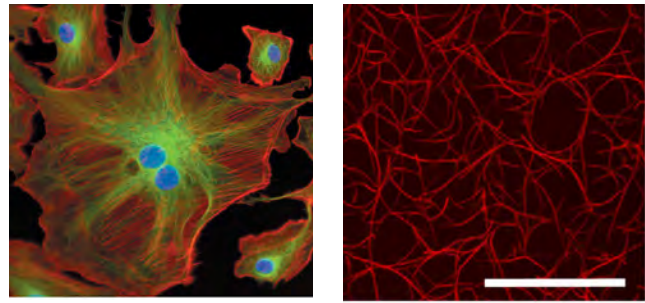

Figure 2: (left) Endothelial cells attached to a substrate, depicting the actin cytoskeleton (red), microtubuli (green) and the nucleus (blue) [from http://probes.invitrogen.com]. (right) Cross-linked actin filament networks [from: Schmoller et al., *Biophys. J.* 97, 83–89 (2009)].

It has long been thought, that proteins need to have a folded structure to perform their function, but more and more evidence is appearing that suggests that also natively unfolded proteins play an important role in many biological functions. One of these roles is in controlling the transport of proteins and nucleic acids in and out of the nucleus of living cells. This transport is mediated by a very large quaternary protein structure, the nuclear po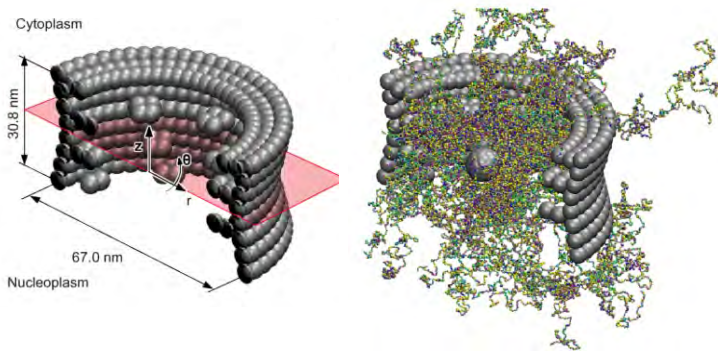re complex (NPC). The NPC is embedded in the membrane of the cell nucleus and features an internal structure that consists of a meshwork of natively unfolded proteins, called nucleoporins (nups), see Fig. 3. These nups are key in controlling transport, but how they exactly do that is unknown. To shed light on this we have developed a one-bead-per-amino-acid (1BPA) molecular dynamics model [13,14]. The 1BPA model distinguishes between all 20 amino acids of the nups and takes into account hydrophobic and electrostatic interactions. Our results show that these nups collectively form a high-density ring, which is encoded in the amino-acid sequence of the nups. The presence of the ring was found to be correlated with cell viability [14] and permeability [15].

Figure 3: Structural model of the NPC featuring a rigid scaffold constructed by 5 nm-sized rigid beads (left). All natively unfolded nups are tethered to the scaffold at their anchor points (right). Figure is taken from: Ghavami et al., (under review).

References

[1]   M.A. Sleigh, *Cilia and flagella*. Academic Press, London, New York, (1974).

[2]   S.N. Namdeo and P.R. Onck, The emergence of flagellar beating from the collective behavior of individual ATP-powered dyneins, *under review*.

[3]   D. Liu, L. Liu, P.R. Onck* and D.J. Broer*, Reverse switching of surface roughness in a self-organized polydomain liquid crystal coating. *P. Natl. Acad. Sci. USA* **112**:3880-3885 (2015). *Shared corresponding authors

[4]   S.N. Khaderi, J.M.J. den Toonder and P.R. Onck, Magnetic artificial cilia for microfluidic propulsion. *Adv. Appl. Mech.* 48, 1-78 (2015).

[5]   S.K. Namdeo, S.N. Khaderi and P.R. Onck, Numerical modeling of chirality-induced bi-directional swimming of artificial flagella *Proc. Royal Soc.* A 470 0130547 (2014)

[6]   S.N. Khaderi and P.R. Onck (2012). Fluid-structure interaction of three-dimensional magnetic artificial cilia, *J. Fluid Mech.* 708, 303-328.

[7]   S. N. Khaderi, C. B. Craus, J. Hussong, N. Schorr, J. Belardi, J. Westerweel, O. Prucker, J. Ruhe, J.M.J. den Toonder and P. R. Onck, Magnetically-actuated artificial cilia for microfluidic propulsion. *Lab Chip* 11, 2002–2010 (2011)

[8]   J.M.J. den Toonder and P.R. Onck, Microfluidic manipulation with artificial/bioinspired cilia, *Trends Biotechnol.* 31, 85−91 (2013).

[9]   J.M.J. den Toonder and P.R. Onck, P.R. (Eds.) *Artificial cilia*. Cambridge, RSC Publishing (2013).

[10] P.R. Onck, T. Koeman, T. van Dillen, E. Van der Giessen, An alternative explanation of stiffening in cross-linked semiflexible networks, *Phys. Rev. Lett.* 95 (17), 178102 (2005).

[11] T. van Dillen, P.R. Onck and E. Van der Giessen, Models for stiffening in cross-linked biopolymer networks: A comparative study, *J. Mech. Phys. Solids* 56 (2008) 2240–2264

[12] G. Zagar, P.R. Onck, E. Van der Giessen, Two fundamental mechanisms govern the stiffening of cross-linked networks. *Biophys. J.* 108, 1470-1479 (2015).

[13] A. Ghavami, E. Van der Giessen and P.R.Onck, Coarse-grained potentials for local interactions in unfolded proteins, *J. Chem. Theory Comp.* 9 432−440 (2013).

[14] A. Ghavami, L.M. Veenhoff, E. Van der Giessen and P.R.Onck, Probing the disordered domain of the nuclear pore complex through coarse-grained molecular dynamics simulations, *Biophys. J.* 107, 1393–1402 (2014).

[15] P. Popken, A. Ghavami, P.R. Onck, B. Poolman and L.M. Veenhoff, Size-dependent leak of soluble and membrane proteins through the yeast nuclear pore complex. *Mol. Biol. Cell*, 26(7), 1386-1394 (2015).

SOFT MACHINES: CHALLENGES TO COMPUTATIONAL DYNAMICS

Haiyan Hu[a)], Qiang Tian & Cheng Liu
School of Aerospace Engineering, Beijing Institute of Technology, Beijing, China

Summary The lecture presents the study on modeling and simulating the dynamics of soft machines from the viewpoint of rigid-soft multibody systems. The study focuses on the description of nonlinear dynamics of coupled overall motion and large deformation of a soft body made of elastic or hyper-elastic material, the modeling of frictional contacts or even entanglements of soft bodies, as well as the efficient dynamic computation algorithm of rigid-soft multibody system governed by a set of differential-algebraic equations of very high dimensions. The lecture illustrates the proposed approach through a number of case studies, including the knotting of two threads, the deployment of a mesh reflector of satellite antenna and the deployment of a spinning solar sails of spacecraft, as well as the corresponding validations via ground experiments.

INTRODUCTION

The concept of soft machine covers a wide range of advanced industrial products, such as a soft robot making surgical operations or handling fragile objects, a snake robot crawling along tunnel corners, a morphing airplane wing and a deployable solar sail. Those soft machines are mainly composed of soft bodies, which are made of soft materials, including polyamide, polyimide, silicon elastomer and electro-active polymer, in order to adapt to very complex environments or missions. Furthermore, the soft bodies are connected via various joints so that they undergo not only large deformations, but also overall motions and frictional contacts with themselves or environments. The dynamic model of a soft machine, hence, is a rigid-soft multibody system, which gives rise to numerous open and tough problems. It is essential to establish proper modeling and efficient simulating approaches for soft machines in the design phase [1,2].

DYNAMIC MODELING AND SIMULATION

Dynamic modelling of absolute nodal coordinate formulation

The finite elements of Absolute Nodal Coordinate Formulation (ANCF) have served as useful tools to describe the coupling of large deformation and overall motion of a flexible body, such as a very slender beam. The fully parameterized beam element of ANCF is able to describe the shear and cross-section deformations of the beam, but suffers from locking problems. On the contrary, the gradient deficient beam element of ANCF is suitable for describing the slender beam and shows good accuracy. Hence, the lecture presents the new spatial curved beam element and shell element of gradient deficient ANCF to model cables and membranes [3], and shows how to deal with possible slacks and wrinkles of a membrane via the integrated stiffness reduction [4].

Numerical simulation of high efficiency

The finite element of ANCF results in a constant mass matrix, and a complex expression of nonlinear restoring force vector, which requires high cost of computation. The lecture presents how to factorize the unknown generalized coordinates from the integration on a finite element level in the case of full parameters and how to reduce the model order on a soft body level so as to greatly speed up the computation. The lecture also shows how to solve the differential-algebraic equations of a soft machine in parallel on OpenMP [5].

The soft bodies in a soft machine may undergo complicated frictional contacts, such as multi-zone contacts between two surgical threads. The lecture presents a detection strategy for multi-zone contacts of two soft bodies, where the mutual penetration is a multi-peak function of the local coordinates of the soft body predicted to have a larger contact zone. It is quite efficient to locate the contact zones of two soft bodies by checking all the local minima of the function. The lecture shows how to compute the normal contact force by using the penalty method and the tangential friction force via the piecewise analytic expression of the LuGre friction model derived within an integration step [6].

CASE STUDIES

Knotting of two threads

To simulate the knotting process of threads of a surgical robot, the lecture presents the knot tightening and knot releasing of two identical threads with circular cross-sections meshed via the gradient deficient beam elements of ANCF. Figure 1a shows the initial configuration of the two straight threads placed crosswise with one end of each thread clamped at the black point. The two threads is deformed to generate three knots progressively by clamping temporarily other two internal nodes marked as smaller black points in Figure 1c and 1d, driving two chosen nodes marked as green points, to move under planning trajectories, and then freeing the temporarily clamped internal nodes. As shown in Figure 1f, at least four contact zones appear in the final configuration of knotting. Actually, the result may contain one or more contact zones separated by non-contact zones of very short lengths [6].

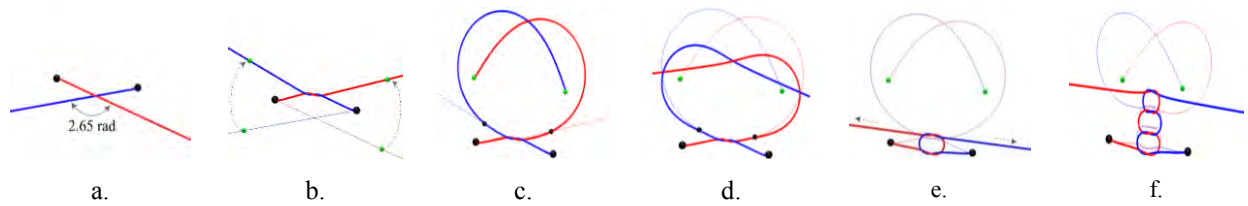[a)] Corresponding author. Email: haiyan_hu@bit.edu.cn

Figure 1 Knotting of two threads

Deployment of a mesh reflector of satellite antenna

To show the feasibility of the above approach to complicated problems, the lecture presents the deployment of a satellite antenna, where the hoop truss and mesh reflector modelled via the gradient deficient beam elements of ANCF have about 200,000 degrees of freedom, as shown in Figure 2.

To speed up the dynamic simulation, the mesh reflector is decomposed into several independent subsystems by cutting its joint. Then, the Schur complement method is used to eliminate the internal generalized coordinates of subsystem and the Lagrange multipliers for joint constraint equations associated with the internal variables. With an increase of the number of subsystems, the dimension of simultaneous linear equations in the numerical solution process will inevitably increase. By using the multilevel decomposition approach, the dimension of the simultaneous linear equations can be further reduced. Figure 2 illustrates the deployment process of the mesh reflector at six specific moments.
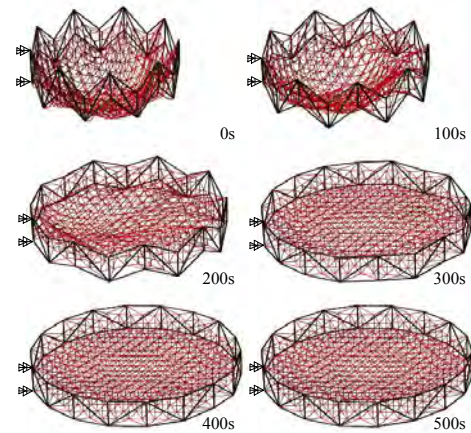

Figure 2 Deployment of a mesh reflector of satellite antenna

Deployment of a spinning solar sail of spacecraft

The spinning deployment of solar sails of spacecraft has called much attention due to their significant advantages since Japan Aerospace Exploration Agency launched IKAROS, the first spacecraft of spinning solar sail. The lecture focuses on a spinning-deployable solar sail shown in Figure 3, where the hexagonal membrane modeled via the shell elements of ANCF is wrapped around the spinning central hub at the initial moment 0s. With the rotation of central hub, the folded membrane is deployed gradually and finally stabilized by the centrifugal forces of the lumped masses at six corners of the solar sail in Figure 3a. The simulation shows the importance of proper description of wrinkle of the membrane. For example, the cyclic "deployment-shrinkage-deployment" shown in Figure 3b appears if the wrinkle is not properly modeled. In fact, the multi-scale coupling effect of small wrinkles and large rotation plays a dominant role in the deployment dynamics [4].
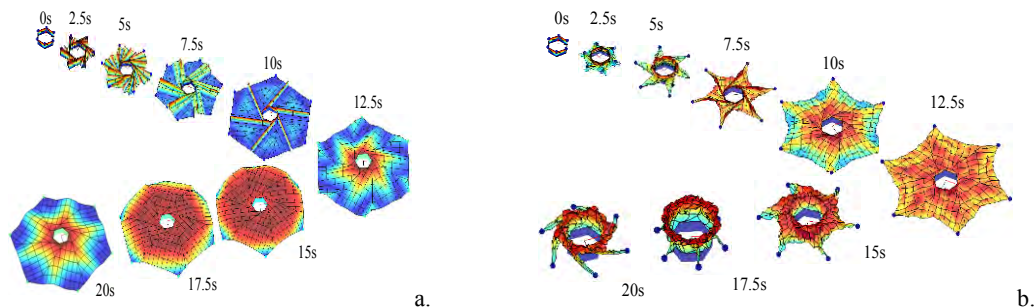

Figure 3 Deployment of a spinning solar sail predicted when membrane wrinkles properly modelled or not.

References

[1]   Iida F., Laschi C.: Soft Robotics: Challenges and Perspectives, *Procedia Computer Science*, **7**: 99-102, 2011
[2]   Nurzaman S. G., Iida F., Margheri L., Laschi C.: Soft Robotics on the Move: Scientific Networks, Activities, and Future Challenges, *Soft Robotics*, **1**: 154-158, 2014.
[3]   Liu C., Tian Q., Hu H. Y.: New Spatial Curved Beam and Shell Elements of Gradient Deficient Absolute Nodal Coordinate Formulation, *Nonlinear Dynamics*, **70**: 1903-1918, 2012.
[4]   Liu C., Tian Q., Yan D., Hu H. Y.: Dynamic Analysis of Membrane Systems Undergoing Overall Motions, Large Deformations and Wrinkles via Thin Shell Elements of ANCF, *Computer Methods in Applied Mechanics and Engineering*, **258**(1): 81-95, 2013.
[5]   Liu C., Tian Q., Hu H. Y.: Dynamics of a Large Scale Rigid-Flexible Multibody System with Composite Laminated Plates, *Multibody System Dynamics*, **26**:283-305, 2011.
[6]   Wang Q. T., Tian Q., Hu H. Y.: Dynamic Simulation of Frictional Multi-Zone Contacts of Thin Beams, *Nonlinear Dynamics*, DOI 10.1007/s11071-015-2456-8 2016.

COMPUTATIONAL FRAMEWORK FOR MULTI-MATERIAL FSI, SHOCKS, TURBULENCE AND FRACTURE

Charbel Farhat [*1], Philip Avery, Arthur Morlot, Dante de Santis[2], and Zhengyu Huan[3]

[1]*Department of Aeronautics and Astronautics, Department of Mechanical Engineering, and Institute for Computational and Mathematical Engineering, Stanford University, Stanford, CA, USA*
[2]*Department of Aeronautics and Astronautics, Stanford University, Stanford, CA, USA*
[3]*Institute for Computational and Mathematical Engineering, Stanford University, Stanford, CA, USA*

Summary The FInite Volume method with Exact two-material Riemann (FIVER) problems is a robust computational framework for the solution of multi-material, Fluid-Structure Interaction (FSI) problems. It was validated for challenging applications characterized by compressible flows, shocks, turbulence, highly nonlinear structures, and dynamic fracture. It couples an Eulerian, finite volume based approach for solving flow problems, with a Lagrangian, finite element approach for solving solid mechanics problems. Most importantly, it enforces the governing fluid-fluid and fluid-structure transmission conditions by solving local, one-dimensional, exact, two-material Riemann problems at evolving interfaces that are embedded in the fluid mesh. First, this framework is reviewed with emphasis on its unique contributions to the field, and the challenging simulations it enabled. Next, recent advances pertaining to the mathematical underpinnings of this framework are presented. Finally, novel capabilities related to viscous flows, porous media, embedded constraints, and sensitivity analysis and optimization are described and demonstrated for realistic applications.

BACKGROUND

FIVER was originally developed in [1], in the context of explicit time-discretizations, for the solution of compressible, inviscid, two-phase flow problems characterized by simple equations of state (EOS) but large contact discontinuities (density jumps). In [2], it evolved into an Eulerian embedded boundary method (EBM) — or immersed boundary method — for the solution of highly nonlinear fluid and FSI problems. These include those FSI problems that cannot be handled by Arbitrary Lagrangian Eulerian (ALE) methods, because of large structural motions, finite deformations, and/or topological changes that challenge the performance of mesh motion schemes. Unlike most other EBMs which operate exclusively on Cartesian grids, FIVER can operate on arbitrary grids. This is noteworthy because even in the pure Eulerian setting, the ability of an EBM to perform on arbitrary, unstructured grids is still particularly advantageous for complex geometries and viscous flows.

For multi-material problems with complex fluid EOSs, the solution of a local, one-dimensional, exact, two-material Riemann problem may be either impossible to obtain analytically, or computationally intensive to evaluate numerically. To address this issue, a computationally efficient sparse grid tabulation technique was developed in [3] for accelerating the numerical solution of arbitrary fluid-fluid and fluid-structure Riemann problems, and thereby enabling the generalization of FIVER to multi-material problems with complex fluid EOS. In [4], the generalized FIVER method was validated for the solution of failure-induced FSI problems. Specifically, it was applied to the simulation of two experiments on the dynamic underwater implosion of cylindrical shells. In both cases, it reproduced with high-fidelity the large deformations of the collapsing structure and the compression waves emanating from it (see Figure 1-left).

FIVER was also extended to implicit time-discretizations in [5], and to viscous, multi-material fluid and FSI problems in [6]. For turbulent viscous flows, Eulerian EBMs typically suffer from the fact that they do not track the boundary layers around dynamic rigid or flexible bodies. Consequently, the application of these methods to such problems requires either high mesh resolutions in a large part of the computational fluid domain, or adaptive mesh refinement. Unfortunately, the first option is computationally inefficient, and the second one is labor intensive to implement. To address these issues, an ALE variant of FIVER that maintains all moving boundary layers resolved during turbulent FSI computations was presented in [7], and validated with the simulation of turbulent flows past a family of highly flexible flapping wings, and the prediction of the vertical tail buffeting of an F/A-18 aircraft configuration at a high angle of attack (see Figure 2).

Most recently, a generic, comprehensive, and yet effective approach for representing a fractured fluid-structure interface was developed in [8] and incorporated in FIVER. Specifically, this approach enables the coupling of FIVER with many finite element based fracture methods for the solution of multi-material FSI problems with dynamic fracture. These methods include, among others, the interelement fracture and remeshing techniques, the extended finite element method (XFEM), and the element deletion method. Equipped with this fractured fluid-structure interface representation, FIVER was further validated for highly nonlinear FSI problems with crack propagation, flow seepage through narrow cracks, and structural fragmentation [8] (see Figure 1-right).

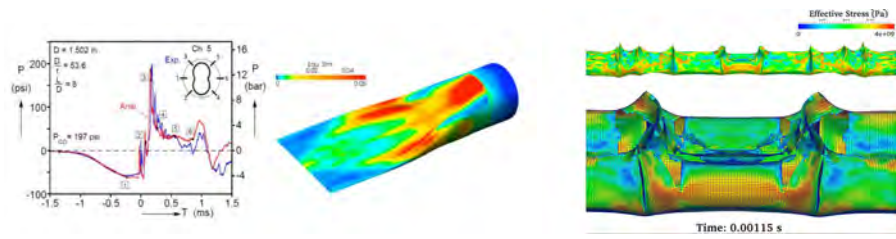*Corresponding author. Email: cfarhat@stanford.edu

Figure 1: Left: Validated simulation of the dynamic implosion of an underwater cylindrical aluminum shell – Right: Simulation of the massive dynamic fracture of an underwater metallic structure induced by an explosive loading.
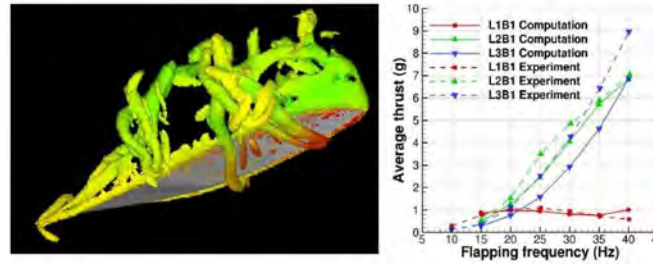

Figure 2: Validated simulation of the thrust generated by a highly flexible flapping wing.

RECENT THEORETICAL RESULTS AND NEW DEVELOPMENTS

In addition to an overview of the computational framework outlined above that emphasizes its physical and mathematical underpinnings, the scope of this "Sectional Lecture in Fluids-Solids" covers recent theoretical advances in FIVER and newly developed extensions and capabilities. Specifically, new results pertaining to numerical stability, energy conservation, and local and global order of spatial and temporal accuracy are discussed with special attention to the behavior of the solution at the material interfaces. In particular, the role of interface limiters in supporting higher-order spatial discretizations for smooth problems and their effects on nonlinear stability is elucidated. The concept of a surrogate material interface, which is ubiquitous in the context of EBMs, is revisited to guarantee the invariance of a predicted turbulent flow with respect to changes in the position of an embedded discrete surface relative to the fluid meshing lines (or simply the fluid mesh). The concept of a local, one-dimensional, exact, two-material Riemann problem is also revisited to incorporate in it a homogenization approach that dramatically enhances computational efficiency in the presence of porous media such as parachutes or porous plug nozzles, to name only a few. A new approach for enforcing *embedded constraints* in a fluid or FSI simulation based on the same concept is also presented and illustrated with several applications ranging from the preservation of symmetry boundary conditions, to the enforcement of non-trivial inlet boundary conditions on embedded discrete surfaces. Finally, an exact sensitivity analysis capability for FIVER is described, and its potential for shape optimization problems with topological changes is demonstrated for complex aeroelastic configurations.

References

[1] C. Farhat, A. Rallu, S. Shankaran, A higher-order generalized ghost fluid method for the poor for the three-dimensional two-phase flow computation of underwater implosions, Journal of Computational Physics 267:7674-7700, 2008.

[2] K. Wang, A. Rallu, J.-F. Gerbeau, C. Farhat, Algorithms for interface treatment and load computation in embedded boundary methods for fluid and fluid-structure interaction problems, International Journal for Numerical Methods in Fluids 67:1175-1206, 2011.

[3] C. Farhat, J.-F. Gerbeau, A. Rallu, FIVER: a finite volume method based on exact two-phase Riemann problems and sparse grids for multi-material flows with large density jumps, Journal of Computational Physics 231:6360-6379, 2012.

[4] C. Farhat, K. Wang, A. Main, J.S. Kyriakides, K. Ravi-Chandar, L.H. Lee, T. Belytschko, Dynamic implosion of underwater cylindrical shells: experiments and computations, International Journal of Solids and Structures 50:2943-2961, 2013.

[5] A. Main, C. Farhat, A second-order time-accurate implicit finite volume method with exact two-phase Riemann problems for compressible multi-phase fluid and fluid-structure problems, Journal of Computational Physics 258:613-633, 2014.

[6] C. Farhat, V. Lakshminarayan, An ALE formulation of embedded boundary methods for tracking boundary layers in turbulent fluid-structure interaction problems, Journal of Computational Physics 263:53-70, 2014.

[7] V. Lakshminarayan, C. Farhat, An embedded boundary framework for compressible turbulent flow and fluid-structure computations on structured and unstructured grids, International Journal for Numerical Methods in Fluids 76:366-395, 2014.

[8] K. Wang, P. Lea, C. Farhat, A computational framework for the simulation of high-speed multi-material fluid-structure interaction problems with dynamic fracture, International Journal for Numerical Methods in Engineering 104:585-623, 2015.

CAN SOLID MECHANICS HELP IN UNDERSTANDING FLUID VORTICES?

George Haller [a)]

Institute of Mechanical Systems, ETH Zürich, Switzerland

<u>*Summary*</u> Coherent vortices are the most important building blocks of complex flows, yet no universally accepted vortex definition has emerged in fluid dynamics yet. A reason is that most vortex definitions depend crucially on the frame of the observer who evaluates them, even though the significance of vortices arises from the frame-invariant material transport they induce. Recently, ideas from nonlinear dynamics and continuum mechanics have lead to new, objective notions of coherence in fluid dynamics. These reveal surprisingly coherent, previously undetected material vortices in turbulent flows. We survey these ideas and illustrate their efficacy on geophysical flow data.

BACKGROUND

Few would disagree about the intuitive statement that vortices are swirling domains of fluid. It has nevertheless proven surprisingly challenging to define coherent vortices unambiguously. Fluid mechanics has a classical focus on features of the velocity field, which indeed reveals all details of material transport in two-dimensional steady flows. Instantaneous velocity features and actual material transport, however, tend to differ vastly in unsteady flows. Still, there is a traditionally broad focus on identifying vortices in fluids from features of the velocity field or its spatial derivatives (see [1-3] for reviews).

Most such velocity features depend on the observer, and hence fail to provide firm conclusions about the material transport induced by vortices. Still, it is precisely this material transport that makes coherent vortices significant in highly incoherent or even turbulent flow fields. Figures 1a-b show examples of mesoscale (100-200km in diameter) vortices in the ocean that owe their significance entirely to the material they carry. The exact perimeter and level of coherence of such vortices, however, cannot be fully ascertained form these sporadic images: a better understanding of what the underlying flow structure is, independent of the nearly passive scalar fields it carries, is highly desirable for environmental forecasting and decision making. Figure 1c shows a smaller-scale example of an unsteady material vortex, highlighted by the volcanic steam it captures and transports. Detection of such three-dimensional structures without reliance on the material they carry, even for steady 3D flows, has long been an outstanding question.
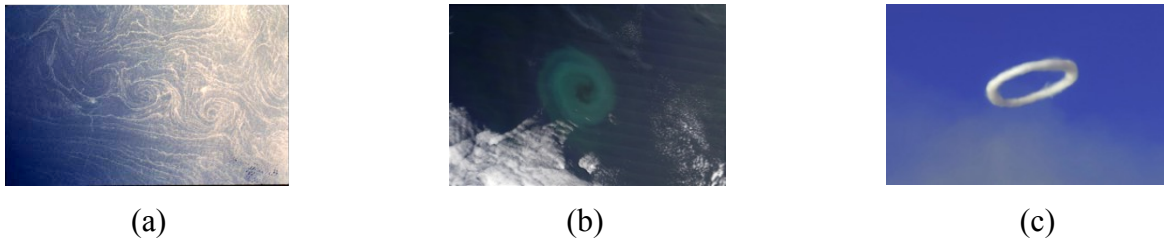

(a)   (b)   (c)

Figure 1. (a) Spiral eddies in the Mediterranean Sea, highlighted by biological surfactants (Paul Scully-Power/NASA) (b) Phytoplankton patch in the Agulhas leakage (Jeff Schmaltz/NASA) (c) Steam ring over Mount Etna (Tom Pfeiffer/ **www.volcanodiscovery.com**).

With its traditional focus on material behavior, as opposed to velocity features, solid mechanics is well-positioned to contribute to the understanding of coherent fluid features in a frame-independent fashion. A new challenge on the solids-side, however, is the development of objective notions of observed material coherence for large deformation fields. Over the past two decades, a number of advances have been made that address this challenge, leading to the emergence of the field of Lagrangian Coherent Structures, or LCSs [4]. Broadly speaking, LCSs are locally the most influential material surfaces in a moving continuum over a finite time interval of interest. Their unique influence is due to a special role they play in the Lagrangian stretching, shearing or rotation field of the continuum.

Specifically, coherent material vortices (elliptic LCSs) can be approached via their distinguished signatures in any of the above fields. Accordingly, material stretching-based and material rotation-based principles have been developed that identify highly coherent flow regions at a previously unseen precision. Some of these approaches are inspired by techniques from nonlinear dynamics, others by continuum mechanics. Here we give a quick overview of both types of approaches, and show their power on real-life unsteady flow data.

STRETCHING-BASED COHERENCE: AN APPROACH FROM NONLINEAR DYNAMICS

There are well-known analogues of vortex boundaries in the phase space of conservative systems of nonlinear rigid bodies. These invariant surfaces are Kolmogorov--Arnold--Moser (KAM) tori filled with quasi-periodic motions [5]. While such idealized objects do not exist in a realistic, finite-time flow of fluid particles, the coherence properties of KAM tori, notably

---

their complete lack of filamentation, can be expressed in a variational principle that applies under arbitrary time dependence as well. Namely, material vortex boundaries in fluids can be sought as outermost, closed stationary curves of the material-surface-averaged relative material stretching functional. The stretching in this variational problem is meant with respect to a finite time interval over which sustained coherence is required. The corresponding Euler-Lagrange equations and boundary conditions can be reformulated into the equivalent problem of finding outermost limit cycles of a two-dimensional steady vector field [6]. These limit cycles are then guaranteed to remain coherent under advection by the original unsteady fluid flow, showing no filamentation over the time interval that was used in defining the underlying stretching functional. An example of the coherent vortices extracted through this dynamical systems approach is shown in the left plot of Figure. 2.
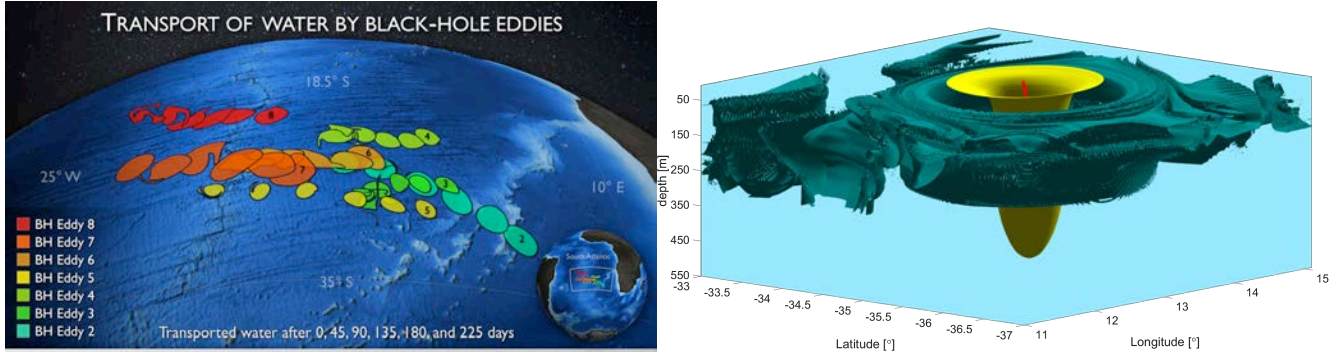

Figure 2. Left: Families of uniformly stretching coherent Lagrangian vortices (black-hole eddies) computed from satellite-detected surface velocities in the Agulhas leakage [6]. **Right:** A rotationally coherent material vortex in the Southern Ocean State Estimate (SOSE) data set [8]. Nearby level surfaces of the LAVD (green) illustrate the complexity in the incoherent water mass surrounding the extracted vortex.

ROTATIONAL COHERENCE: AN APPROACH FROM CONTINUUM MECHANICS

A recent alternative approach targets coherent vortices in terms of the coherent material rotation they exhibit. In continuum mechanics, the rotational component of the deformation is generally inferred from the polar decomposition of the deformation gradient. Rotations inferred from the classic polar decomposition, however, are neither objective nor material. A new dynamic polar decomposition developed in [7] identifies a dynamic rotation tensor that is material, i.e., serves as a self-consistently evolving rigid-body rotation component in the deformation gradient field over any finite time interval. Coherent vortex boundaries can then be identified as outermost convex level surfaces of an intrinsic dynamic rotation angle inferred from the dynamic rotation tensor. This objective material rotation angle turns out to be simply the Lagrangian-averaged deviation (LAVD) of the vorticity field from its spatial mean [8]. An application of this result is shown in Fig. 5.

References

[1] Jeung, J., and Hussein, A.K.M.F.: On the identification of a vortex. *J. Fluid Mech.* **285**:69-94, 1995.

[2] Haller, G.: An objective definition of a vortex. *J. Fluid Mech.* **525**:1-26, 2005.

[3] Chakraborthy, P., Balachandar, S., and Adrian, R.: On the relationships between local vortex identification schemes. *J. Fluid Mech.* **535**:189-214, 2005.

[4] Haller, G.: Lagrangian Coherent Structures. *Ann. Rev. Fluid Mech.* **47**:137-162, 2015.

[5] Arnold, V.I., *Mathematical Methods of Classical Mechanics*. Springer, New York, 1978

[6] Haller, G. and Beron—Vera, F.J.: Coherent Lagrangian vortices: The black holes of turbulence. *J. Fluid Mech.* **731**:R4, 2013.

[7] Haller, G.: Dynamically consistent rotation and stretch tensors from a dynamic polar decomposition. *J. Mech. Phys. Solids.* **80***: 70-93, 2016

[8] Haller, G., Hadjighasem, A., Farazmand, M., and Huhn, F., Defining coherent vortices objectively from the vorticity. *J. Fluid Mech.* submitted, 2015; arXiv:1506.04061 [physics.flu-dyn]

MS01 - Bypass Transition

Directed percolation transition to turbulence

Gregoire Lemoult[1] , Liang Shi[1], Kerstin Avila[1], Shreyas Jalikop[1], Marc Avila [2] & Björn Hof[1]

[1]IST Austria, Klosterneuburg, Austria

[2] Friedrich-Alexander-Universität Erlangen-Nürnberg, 91058 Erlangen, Germany

Summary We report that the transition to turbulence in Couette flow corresponds to a second order phase transition and falls into the directed percolation universality class. The increase of the turbulent fraction above the critical point as well as correlation lengths and times at the transition point are described by three critical exponents, which are in excellent agreement with the exponents of the directed percolation (DP) universality class.

Introduction

The transition to turbulence in wall bounded shear flows (such as pipe, channel or Couette flow) has remained an open problem for over a century [1]. Typically here turbulence arises despite the linear stability of the laminar flow and results from perturbations of finite amplitude. At the lowest Reynolds numbers at which turbulence can be triggered it arises in the form of localised patches (e.g. puffs, spots or stripes) which coexist with laminar flow, resulting in complicated, disordered flow patterns   (spatio-temporal intermittency).   Individual turbulent domains can collapse or they can proliferate and seed other patches of turbulence. Balancing the growth and decay processes allows determining the critical point [2] above which turbulence first becomes sustained (in the thermodynamics limit).

As shown previously [2] the time scales on which flows evolve are extremely large and likewise the relevant length scales (the size of the turbulent domains) is comparatively large (typically 20-30 pipe diameters or wall spacings). In order to fully characterize the transition process the interaction and evolution of many such domains has to be taken into account hence requiring experiments of very large aspect ratios and extremely long observation times.

As first proposed by Pomeau [3] the transition to turbulence may be related to the universality class of directed percolation (DP), one of the simplest universality classes for non-equilibrium phase transitions. One illustration of directed percolation is that of a fluid percolating through a porous medium. Depending on the porosity the fluid will either progress through the medium or it will get stuck at a certain point. For increasing values of the connectivity of the pores (which is expressed by a single parameter, the probability P) a continuous phase transition occurs at a distinct critical point above which there is always a connected path. Figure 1a shows a model of this process (directed bond percolation). Connected bonds (open pores) are marked in blue (closed ones in black).

The transition to turbulence (like DP) is a contact process where turbulence spreads by neighbour interaction, likewise the linear stability of the laminar flow ensures that if at any point in time all turbulent sites decay the flow will afterwards remain laminar for all times. The laminar state hence corresponds to what is called the unique absorbing state in the context of DP. Determining if the transition to turbulence indeed falls into this universality class has posed a major challenge.

Results

We report [4] experiments and direct numerical simulations of Couette flow. Experiments were carried out in a circular Couette set up (a fluid layer sheared between two concentric cylinders). The aspect ratio (gap width to cylinder circumference) was 2750 while the domain height (axial direction) was 8 times the gap size. In addition direct numerical simulations were carried out for Couette flow in a domain of 960 (azimuthally) by 5h (vertically), where h is the gap width between the two cylinders. Figure 1b shows the spatio temporal evolution of turbulent domains (in blue) in the numerical simulations. Notably (like for DP) new turbulent domains branch out from existing stripes (nearest neighbour interaction). A visualisation of turbulent domains/stripes in the experiment is shown in figure 1c. Extensive experiments and simulations covering the Reynolds number regime where turbulence can first be observed, allow us to explicitly measure the critical point at which turbulence becomes sustained in Couette flow. Likewise we determine how the turbulent fraction increases as the critical point is surpassed. Like for DP the transition is continuous and follows a power law with an exponent of ~0.28 which is in excellent agreement with the universal DP value. Furthermore we determine the critical exponents describing the correlation length and correlation time close to the critical point and the respective values are again in excellent agreement with those predicted of the directed percolation universality class.

---

[a] Corresponding author. Email: ictam2016papers@legendconferences.com.
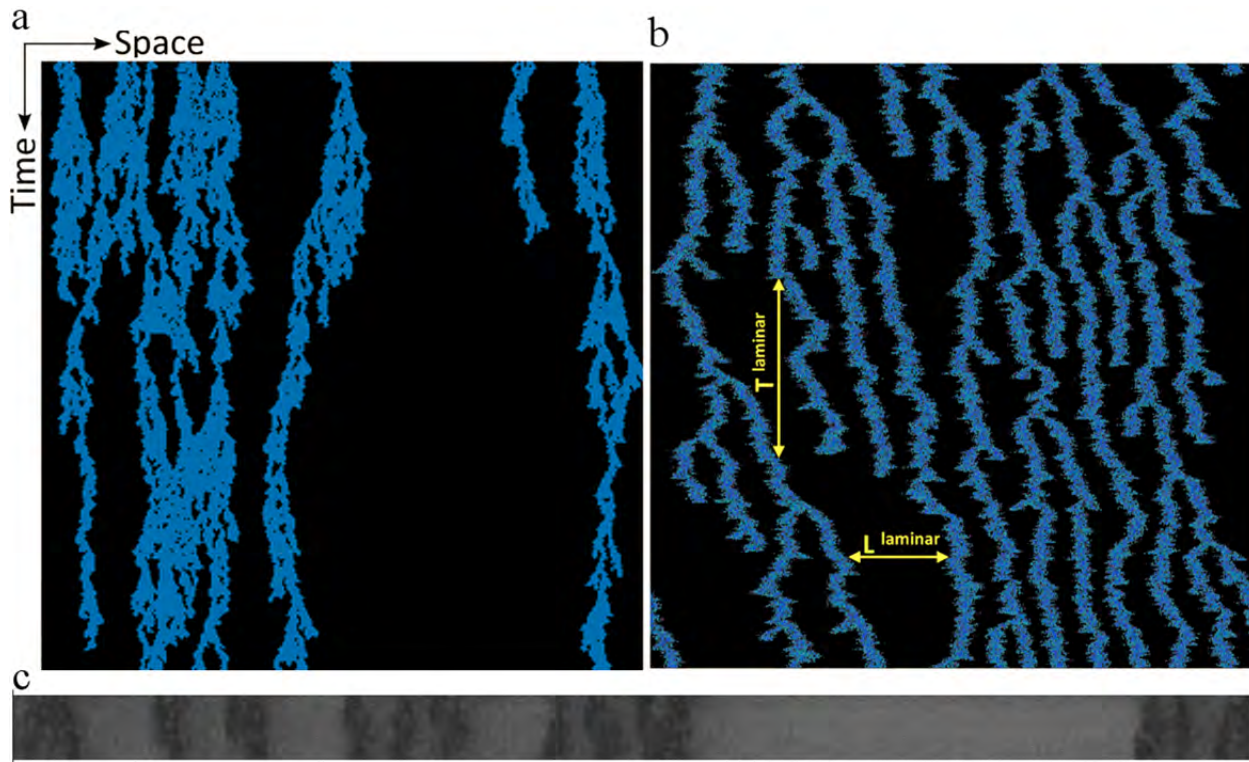
Figure 1: **a** space time plot of directed bond percolation (active sites in blue, absorbing ones in black). **b** Space time plot of turbulence in Couette simulations with turbulent domains in blue and laminar ones in black. **c** Picture of the experimental flow, where turbulent stripes appear in dark whereas the brighter regions correspond to laminar flow.

Summary

We present evidence that the transition to turbulence in Couette flow corresponds to a second order non-equilibrium phase transition and falls into the directed percolation universality class.

References

[1] Reynolds, O.: An Experimental Investigation of the Circumstances Which Determine Whether the Motion of Water Shall Be Direct or Sinuous, and of the Law of Resistance in Parallel Channels. Proc. R. Soc. London. **35**, 84–99 (1883).

[2] Avila, K. et al., The onset of turbulence in pipe flow. Science , **333**, 192–196 (2011).

[3] Pomeau, Y.: Front motion, metastability and subcritical bifurcations in hydrodynamics. Phys. D. **23**, 3–11 (1986).

[4] Shi, L. et al: The universality class of the transition to turbulence. arXiv:1504.03304

EXACT COHERENT STRUCTURES IN TRANSITIONAL FLOWS: DYNAMICS AND LOCALIZATION

John F. Gibson [*][1]

[1]*Department of Mathematics and Statistics, University of New Hampshire, Durham, NH, United States*

Summary Invariant solutions of the Navier-Stokes equations provide a mathematically sound framework for the long-standing idea of coherent structures in turbulence. In recent years, computations of weakly unstable equilibria, traveling waves, and periodic orbits have shed much light on the structure and dynamics of transitional of shear flows. In this talk we present (1) a brief overview of the methodology and goals of invariant solutions or exact coherent structures as framework for analyzing transitional turbulence, and (2) recent results that extend invariant solutions from spatially periodic solutions in minimal flow units to localized solutions in extended flows. The localized solutions provide precise specifications of coherent structures long observed in turbulent shear flows and are potentially a first step towards an understanding of the spatiotemporal dynamics of turbulence as a system of self-organized, interacting coherent structures.

BACKGROUND

In the past twenty years, many equilibrium, traveling waves, and periodic orbits have been calculated for canonical shear flows as invariant solutions of the Naver-Stokes equations with appropriate boundary conditions [1, 2, 3, 4]. These solutions capture commonly observed features associated with coherent structures in transitional shear flows, such as self-sustaining wavey roll-streak structures, and dynamical processes such as bursting [5]. Moreover, numerical linear stability analysis reveals that typical invariant solutions are weakly unstable at transitional Reynolds numbers, i.e. they have only a few unstable eigenmodes, with only weakly unstable eigenvalues. Thus a turbulent trajectory of a transitional shear flow can be understood in dynamical-systems terms as a pseudo-random, chaotic walk between the flow's unstable solutions, along the low-dimensional network of their unstable manifolds. The appearance of an organized coherent structure in a turbulent flow then corresponds to the trajectory making a close pass to a weakly unstable invariant solution. Hence we call such invariant solutions *exact coherent structures*.

DYNAMICS

The dynamical-systems vision described above has been fleshed out explicitly in quantitative detail for transitional shear flows in minimal flow units [6]. For example, figure 1 shows a state-space portrait of plane Couette flow in a minimal flow unit at $Re = 400$. Equilibrium solutions are shown as solid dots and trajectories within their low-dimensional unstable manifold as solid lines. The projection is from the $O(10^5)$-dimensional state space of a DNS to a three-dimensional subspace spanning a few important equilibria, using the standard inner product associated with the L_2 energy norm of the velocity field. The unstable manifolds of the depicted solutions are clearly intertwined; in fact heteroclinic orbits can be found that describe precise dynamic connections between the nearby unstable equilibria. Farther away from laminar solution, the turbulent flow can be analyzed as shadowing a sequence of periodic orbits and transitioning between them along the orbits' low-dimensional unstable manifolds. Animations illustrating the low-dimensional state-space dynamics of heteroclinic connections and periodic orbits are available at `http://www.chaosbook.org/tutorial` and `http://www.channelflow.org/movies`.

LOCALIZATION

More recently spatially localized exact coherent structures have been computed in extended flows [7, 8, 9], with a number of interesting features. Spanwise-localized forms of the Nagata equilibria exhibit *homoclinic snaking*, a process by which additional structure is grown at the fronts of a quasi-periodic pattern through a sequence of saddle-node bifurcations [7]. This behavior in 3D solutions of Navier-Stokes is remarkably similar to that of observed for the one-dimensional Swift-Hohenberg equation, forming an intriguing connection between fluid dynamics and pattern formation theory. Spanwise-localized solutions of plane Poiseuille flow and the asymptotic suction boundary layer bear remarkable resemblance to fundamental staggered and mirror-symmetric roll-streak coherent structures observed in the high-shear region near the walls of boundary layer and channel flows [8]. Doubly-localized solutions of plane Couette flow replicate the elongated turbulent spots from which turbulence is triggered in extended systems [9].

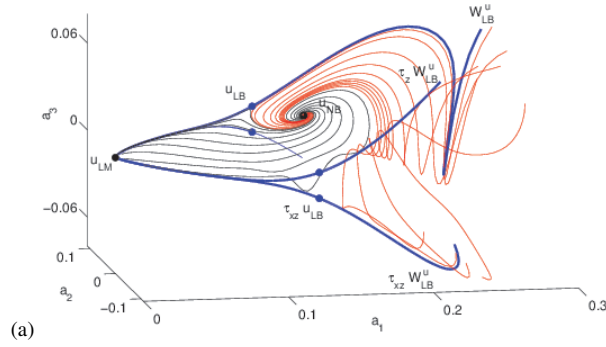[*]Corresponding author. Email: john.gibson@unh.edu

Figure 1: **A state-space portrait of transitionally turbulent plane Couette flow, in the neighborhood of laminar flow.** The origin is placed at near the laminar equilibrium (u_{LM}). Solid dots correspond to unstable equilibrium solutions of the flow; solid lines are trajectories in the low-dimensional unstable manifolds of the equilibria, computed with well-resolved DNS.
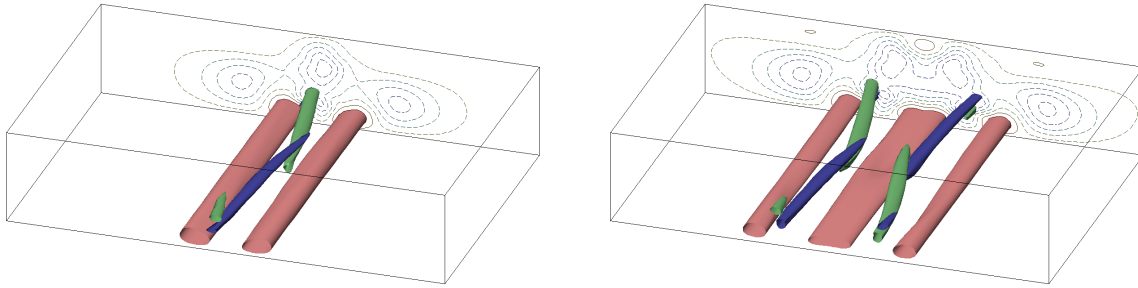
Figure 2: **Exact near-wall traveling waves of plane Poiseuille flow.** Swirling strength in blue (counterclockwise) and green (clockwise), high-speed streaks in red, and isocontours of streamwise velocity perturbation in back plane.

References

[1] NAGATA, M. Three-dimensional finite-amplitude solutions in plane Couette flow: bifurcation from infinity. *J. Fluid Mech.* **217**, 519–527, 1990.

[2] KAWAHARA, G. & KIDA, S. Periodic motion embedded in plane Couette turbulence: regeneration cycle and burst. *J. Fluid Mech.* **449**, 291–300, 2001.

[3] FAISST, H. & ECKHARDT, B. Traveling waves in pipe flow. *Phys. Rev. Lett.* **91**, 224502, 2003.

[4] VISWANATH, D. Recurrent motions within plane Couette turbulence. *J. Fluid Mech.* **580**, 339–358, 2007.

[5] HAMILTON, J.M., KIM, J. & WALEFFE, F. Regeneration mechanisms of near-wall turbulence structures. *J. Fluid Mech.* **287**, 317–348, 1995.

[6] GIBSON, J. F., HALCROW, J. & CVITANOVIĆ, P. Visualizing the geometry of state space in plane Couette flow. *J. Fluid Mech.* **611**, 107–130, 2008.

[7] SCHNEIDER, T. M., GIBSON, J. F. & BURKE, J. Snakes and ladders: Localized solutions of plane Couette flow. *Phys. Rev. Lett.* **104**, 104501, 2010.

[8] GIBSON, J. F. & BRAND, E. 2014 Spatially localized solutions of planar shear flow. *J. Fluid Mech.* **745**, 25–61, 2014.

[9] BRAND, E. & GIBSON, J. F. A doubly-localized equilibrium solution of plane Couette flow. *J. Fluid Mech.* **750** (R3), 1–12, 2014.

RESTRICTED NONLINEAR ROLL/STREAK DYNAMICS IN PLANE COUETTE FLOW

Vaughan Thomas and Dennice F. Gayme*

Department of Mechanical Engineering, Johns Hopkins University, Baltimore, Maryland, USA

Summary The recently developed restricted nonlinear (RNL) modeling framework is used to study a transitioning and turbulent plane Couette flow at moderate Reynolds numbers. The results show that the critical roll and streak structures involved in the self-sustaining process of turbulence are well represented by this model. The transitioning flow shows qualitative similarities in the development and organization of these key flow features when compared to a direct numerical simulation (DNS) of the Navier Stokes (NS) equations. However, there is greater transient energy growth in both the roll and streak structures in the RNL simulations. Further characterization of RNL transitioning flows will determine the merit of studying transition using this type of model, which is an appealing prospect due to its simplified dynamics and the order reduction that leads to significantly reduced computational requirements versus the NS equations.

Studies of disturbance energy growth in wall-bounded shear flows have identified streamwise constant disturbances as preferential in developing the types of large energy amplification associated with bypass transition. This evidence of the important role of streamwise coherent structures in linear energy growth as well as observations of their prevalence in fully developed wall-turbulence motivates the use of a streamwise constant modeling framework to study transition and turbulence in these flows. A streamwise constant projection of the Navier Stokes (NS) equations leads to a two dimensional flow field in three velocity components, a 2D/3C model. Simulations of 2D/3C systems with persistent stochastic forcing have been shown to develop turbulent flow fields that exhibit accurate turbulent velocity profiles and other structural features consistent with turbulent plane Couette flow [1].

A more comprehensive model, which can self-sustain turbulence [2], is obtained by introducing a streamwise varying perturbation field that interacts with a 2D/3C mean flow. The corresponding model is obtained by decomposing the velocity and pressure gradient fields in the NS equations into a streamwise averaged mean and perturbations from this mean, respectively $\mathbf{u_T} = \mathbf{U}(y, z, t) + \mathbf{u}(x, y, z, t) = (U, V, W) + (u, v, w)$ and $\nabla p_T(x, y, z, t) = \nabla P(y, z, t) + \nabla p(x, y, z, t)$. The nonlinear interactions between perturbations ($\mathbf{u}$) are then neglected to obtain

$$\mathbf{U}_t + \mathbf{U} \cdot \nabla \mathbf{U} + \nabla P - \frac{1}{R} \Delta \mathbf{U} = -\langle \mathbf{u} \cdot \nabla \mathbf{u} \rangle, \tag{1a}$$

$$\mathbf{u}_t + \mathbf{U} \cdot \nabla \mathbf{u} + \mathbf{u} \cdot \nabla \mathbf{U} + \nabla p - \frac{1}{R} \Delta \mathbf{u} = \mathbf{f} \tag{1b}$$

$$\nabla \cdot \mathbf{U} = 0, \quad \nabla \cdot \mathbf{u} = 0. \tag{1c}$$

Here $\mathbf{f}$ is a stochastic excitation that is used to initiate turbulence, it is removed once self-sustaining turbulence is achieved.

Previous work shows that simulations of the RNL model in (1) capture salient features of turbulent plane Couette flow at low Reynolds numbers [2]. Two particular features of interest are the roll and streak structures, whose interactions are known to play an important role in both transition and turbulence. In this work we focus on the development of these structures and their characteristics after the transient phase in turbulent flows at two Reynolds numbers, $Re_\tau \approx 65$ and $Re_\tau \approx 196$.

Simulations of the RNL system and the NS equations are out carried using the spectral solver detailed in [2]. Turbulence is initiated through the application of zero-mean delta-correlated (in y, z, and t) forcing in both the RNL simulations, through $\mathbf{f}$ in (1b), and the DNS. We characterize the streak and roll structures based on their respective RMS velocity measurements, which we define as follows.

$$U_{Streak} := \sqrt{\int_0^{L_z} \int_{-\delta}^{\delta} (U - [U])^2 \, dy \, dz}, \quad U_{Roll} := \sqrt{\int_0^{L_z} \int_{-\delta}^{\delta} V^2 + W^2 \, dy \, dz}, \tag{2}$$

where $[\cdot]$ indicates a spanwise average, and the spanwise and wall-normal channel extents are respectively $[0, L_z]$ and $[-\delta, \delta]$.

Figure 1 compares the development of the RMS roll and streak velocities in the RNL simulations and DNS at $Re_\tau \approx 65$ and $Re_\tau \approx 190$. These figures show that the streak and roll energies developed during the transition phase of the RNL simulations are significantly higher than those of the DNS, for an equivalent $\mathbf{f}$. One notable difference is the overshoot in the RMS velocities of the RNL structures that is not present in the DNS. Figure 1 demonstrates how the nature of $\mathbf{f}$ affects the transient behavior of the RNL systems. In particular, reducing the variance of $\mathbf{f}$ by 87.5% and 95% for the RNL simulations with $Re_\tau \approx 190$ lengthens the rise time and increases the magnitude of the overshoot. Although the energy growth of these structures shows the distinct differences discussed above, an interrogation of the instantaneous velocity fields during the transition phase uncovers qualitative similarity in both the development and organization of the roll and streak features. Once the transition phase ends, the RMS velocities of the structures arising from the DNS and RNL simulations are very similar for both Reynolds numbers, which is consistent with previous results [2].

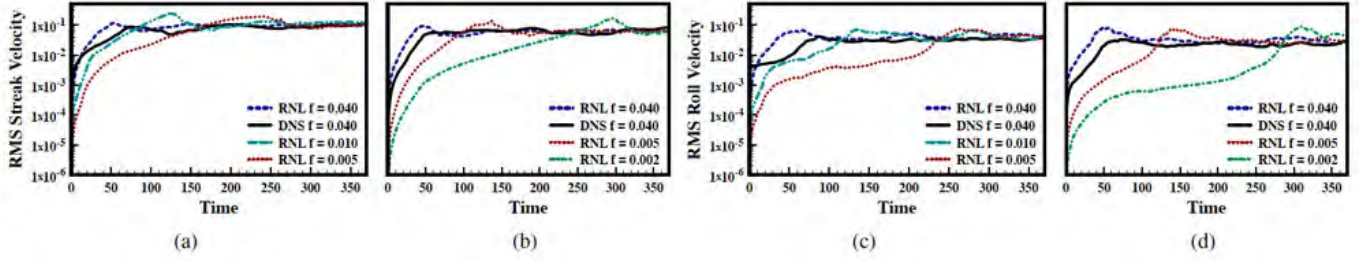*Corresponding author. Email: dennice@jhu.edu

Figure 1: The evolution of the RMS streak velocities for RNL simulations and DNS at (a) $Re_\tau = 66$ and $Re_\tau = 64$ respectively and, (b) $Re_\tau = 196$ and $Re\tau = 186$ respectively. Panels (c) and (d) show the RMS roll velocities for same simulations as in (a) and (b). The variance of the zero-mean stochastic excitation $\mathbf{f}$, in (1b), is given for each simulation.

We further examine the nature of the rolls and streaks in the fully developed (self-sustaining) turbulent regime through instantaneous snapshots of the flow in the cross stream $(y - z)$ plane. Figure 2 shows the $v_T - w_T$ vector field superimposed on contour plots of the streamwise component of velocity field with the laminar solution $U(y) = y$ removed, i.e. $u_T - U(y)$. Figures 2c and 2d demonstrate that the similarity in the structural features previously observed at low Reynolds numbers [2, 3] continues into this modest Reynolds number regime. The feature spacing and intensity of the roll structures also appears to be consistent in the DNS and RNL simulations at $Re_\tau \approx 190$, in accordance with the information provided in Figure 1.
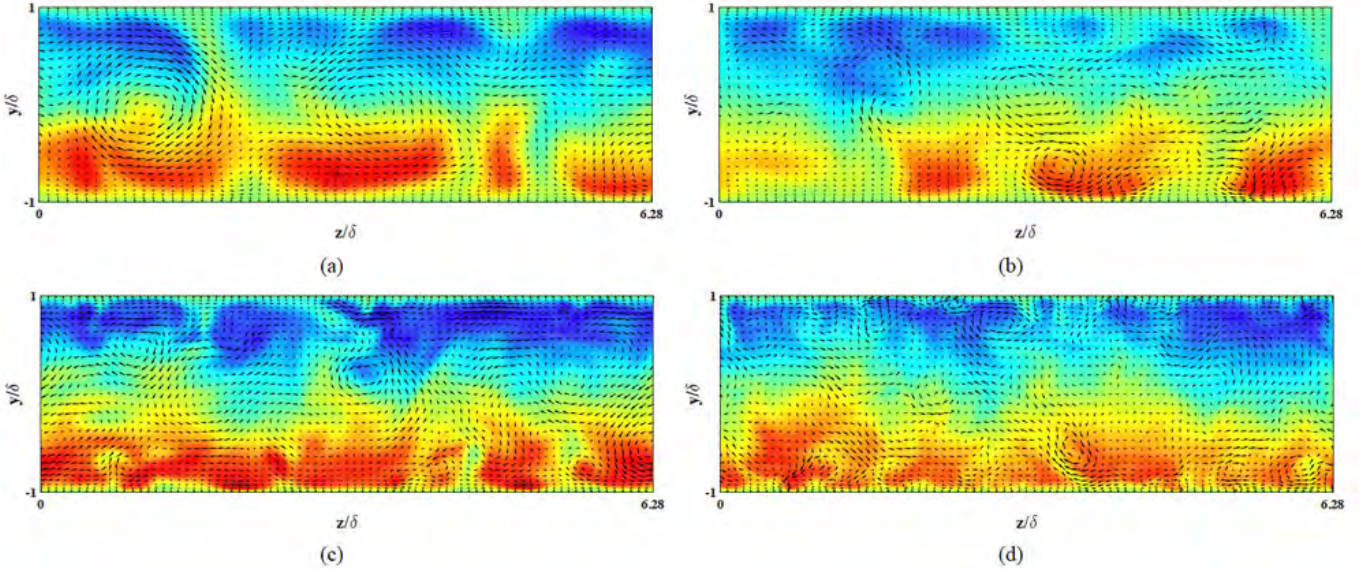

Figure 2: Cross stream ($y - z$ plane) contour plots of the streamwise velocity component with the laminar flow removed, i.e. $u_T - U(y)$ and the $v_T - w_T$ velocity vectors superimposed. (a) A RNL simulation at $Re_\tau = 66$, (b) a DNS at $Re_\tau = 64$, (c) a RNL simulation at $Re_\tau = 196$, and (d) a DNS at $Re_\tau = 186$. The time step shown ($t = 1760$) is long after the initial excitation $\mathbf{f}$ in (1b) is set to zero.

The results presented here demonstrate that the RNL framework shows promise in capturing critical features of turbulent plane Couette flow at modest Reynolds numbers. However, the energetics of the roll and streak structures in a transitioning RNL flow require further examination to better understand how this process compares to current theories regarding turbulent transition. Understanding the extent to which an RNL system can be used to study transition will help determine whether the simplified dynamics that lend to the isolation of critical interactions and the inherent order reduction that makes RNL simulations significantly less costly than DNS can be exploited in this important flow regime.

References

[1] D. F. Gayme, B. J. McKeon, A. Papachristodoulou, B. Bamieh, J. C. Doyle: Streamwise constant model of turbulence in plane Couette flow. J. Fluid Mech., 665:99-119, 2010.

[2] V. Thomas, B. K. Lieu, M. R. Jovanović, B. F. Farrell, P.J. Ioannou, D. F. Gayme: Self-sustaining turbulence in a restricted nonlinear model of plane Couette flow. Phys. of Fluids, 26:105112, 2014.

[3] B. F. Farrell, P. J. Ioannou: Dynamics of streamwise rolls and streaks in turbulent wall-bounded shear flow. J. Fluid Mech., 708:149-196, 2012.

SITTING ON THE EDGE OF TURBULENCE

Philip Hall

School of Mathematical Sciences, Monash University

Summary The properties of vortex-wave interaction states in shear high speed shear flows are investigated. In particular the relevance of these high Reynolds number solutions of the Navier Stokes equations to turbulence is discussed. It is shown that the states usually referred to as lower and upper branch states in the self-sustained process community have quite different stability properties. This explains why lower branch states can act as edge states whilst upper branch states are more closely related to fully turbulent flows. It is shown that there are three naturally occuring instabilities of VWI states and that bifurcation to the slow and fast time-periodic states found numerically by Kawahara and Kida (2001) can be predicted by the theory.

.

VORTEX-WAVE INTERACTION STATES: VWI

In recent years it has been found that exact coherent structures found by numerical or asymptotic reductions of the Navier Stokes equations play key roles in the both the process by which a flow becomes turbulent and the nature of fully developed turbulence. Non-localized structures occurring in both external and internal shear flows naturally fall into two categories at sufficiently high speed. The first kind is described by vortex-wave interaction theory, VWI for short, whilst the second canonical type of structure due to Deguchi and Hall (2014a) is referred to as a free stream coherent structure and sits at the edge of a boundary layer.

In a series of papers Hall & Smith (1989,1990,1991) gave formal asymptotic descriptions of quite general interactions involving waves and stream wise vortices. The analysis described explicitly self-sustaining processes of waves existing as instabilities of streaks and driving a roll flow through their Reynolds stresses. The process was shown to be closed because the roll driven in this way itself drives the streak. The Hall-Smith framework applies to both inviscid and viscous waves though the precise nature of the production of the rolls by the Reynolds stresses depends on the nature of the wave and whether the flow is fully-developed. At about the same time Nagata (1990) discussed numerical results for nonlinear equilibrium states in Couette flow. Subsequently, with the advent of more powerful computers, Waleffe and collaborators, see for example, Waleffe (1997) or Wang et al (2007), found a number of equilibrium states in channel flows. A numerical interrogation of the results showed that the process was a finite Reynolds number version of that described by Hall and Smith (1991). However Waleffe was unaware VWI and so described the interaction as a 'self-sustained' process. More recently such states and the vortex-wave states have been loosely referred to as exact coherent structures.

The VWI approach shows that upper and lower branch states come into existence as a saddle node bifurcation when the streamwise wavenumber of the wave is decreased. The lower branch is approached rapidly by finite Reynolds number computations of the full equations with Reynolds numbers of a few thousand being sufficient for the asymptotic theory of VWI to capture the finite Reynolds number results with remarkable accuracy. On the upper branch the approach is much more slow and significantly higher Reynolds numbers are needed for the asymptotic and finite Reynolds number results to be in excellent agreement.

Hall &Smith (2010) used the vortex-wave framework to describe equilibrium states in Couette flow and found remarkably good agreement with Waleffe et al (2007). More recently Deguchi and Hall (2014b) extended the Hall and Sherwin results to describe both upper and lower branch states. It is well-known in the exact coherent structure community that lower branch states can act as edge states which determine whether disturbances to the unperturbed state ultimately cause the flow to become laminar or turbulent. On the other hand upper branch states cannot act as edge states but are regularly visited by fully turbulent flows. The different properties of the upper and lower branch states arise from their different instability properties with the lower branch state having just a single unstable eigenvalue.

Here we will describe the stability properties of arbitrary VWI states and show how finite amplitude theory can be used to describe the initial evolutions of some neutrally stable modes found. The analysis is based on the linear theory of Deguchi and Hall (2016) who give an asymptotic description of the instabilities of both upper and lower branch states. It is shown that upper and lower branch states are potentially unstable to three types of modes. The first rather ponderous mode corresponds to a gentle oscillation in time of the vortex-wave state on the slow streak diffusion timescale. A second one is a fast Rayleigh instability of the streak. At an intermediate timescale a new mode emerges and Deguchi and Hall (2016) referred to is as the edge mode since it is the only mode of instability of lower branch states. Figure 1 is a schematic of how the instability properties of VWI states vary along the lower and upper branches. On the bulk of the lower branch there is a single unstable edge mode with growth rate $O(R^{-1/2})$ together with stable slow modes of growth rate $O(R^{-1})$. On the upper branch there are unstable fast and slow modes and an unstable edge mode. Note also that neutral periodic forms of the slow and edge
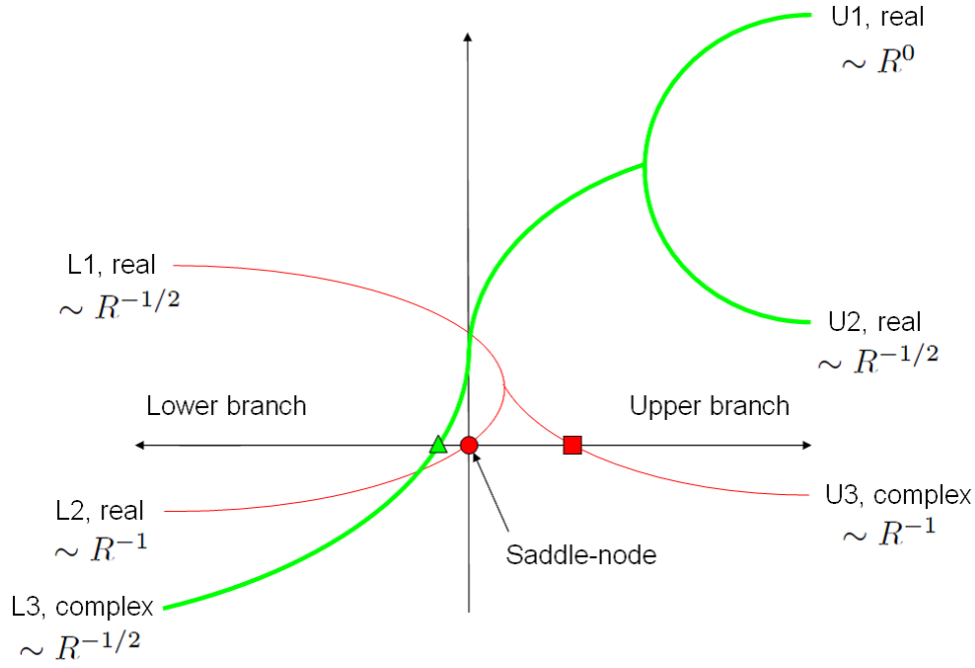
Figure 1: Schematic of the connection of the eigenvalues along the lower and upper branches. The horizontal and vertical axes represents the streamwise wavenumber α and the growth rate σ_r, respectively.

modes occur close to the saddle-node point. The stability classification found explains the results of numerical simulations of shear flows by a number of authors and points to the existence of two time periodic equilibrium states living either on the slow diffusion or edge mode timescales. The predictions of a weakly nonlinear extension of our stability calculation finds solutions closely related to those found by Kalahari and Kida (2001). Since the latter solutions have been found to capture much of the turbulent statistics of Couette flow it appears that the high Reynolds descriptions of time periodic states based on VWI problem might sensibly be used to describe high Reynolds number turbulent flows.

References

[1] DEGUCHI, K. & HALL, P. 2014a The high Reynolds number asymptotic development of nonlinear equilibrium states in plane Couette flow. *J. Fluid Mech.* **750**, 99–112.

[2] DEGUCHI, K. & HALL, P. 2014b Freestream coherent structures in parallel boundary layer flows.*J. Fluid Mech.* **752**, 602–625.

[3] DEGUCHI, K. & HALL, P. 2016 The instability of VWI states. Submitted for publication.

[4] HALL, P. & SHERWIN, S. 2010 Streamwise vortices in shear flows: harbingers of transition and the skeleton of coherent structures. *J. Fluid Mech.* **661**, 178–205.

[5] HALL, P. & SMITH, F. T. 1989 Nonlinear a Tollmien-Schlichting/vortex interaction in boundary layers. *Eur. J. Mech. B/Fluids* **8**(3), 179–205.

[6] HALL, P. & SMITH, F. T. 1990 *Near Planar TS Waves and Longitudinal Vortices in Channel Flow: Nonlinear Interaction and Focussing.* 5–39. Springer.

[7] HALL, P. & SMITH, F. T. 1991 On strongly nonlinear vortex/wave interactions in boundary-layer transition. *J. Fluid Mech.* **227**, 641–666.

[8] KAWAHARA, G. & KIDA, S. 2001 Periodic motion embedded in plane Couette turbulence: regeneration cycle and burst. *J. Fluid Mech.* **449**, 291–300.

[9] NAGATA, M. 1990 Three-dimensional finite-amplitude solutions in plane Couette flow: bifurcation from infinity. *J. Fluid Mech.* **217**, 519–527.

[10] WALEFFE, F. 1997 On a self-sustaining process in shear flows. *Phys. Fluids* **9**, 883–900.

[11] WANG, J., GIBSON, J. F. & WALEFFE, F. 2007 Lower branch coherent states: transition and control. *Phys. Rev. Lett.* **98**, 204501.

UNIVERSAL CRITICAL BEHAVIOR OF THE TRANSITION TO TURBULENCE IN CHANNEL FLOW

Masaki Sano, Keiichi Tamai
Department of Physics, The University of Tokyo, Tokyo, Japan

Summary We identified critical behavior of the transition to turbulence in channel flow. Turbulent domains continuously injected from an inlet ultimately decayed, or in contrast, spread depending on flow rates. Near a transition point, critical behavior was observed. We found that four critical exponents, a universal scaling function and a scaling relation, are all in agreement with the (2+1)-dimensional directed percolation universality class.

INTRODUCTION

Transitions from laminar to turbulent flow have been extensively studied in the past century. Among these studies, the discovery of a well-defined transition to chaos in a fluid heated from below in a small box caused the rewriting of classical textbooks on the onset of turbulence. However, this concerns only temporal disorder. When and how spatio-temporal disorder emerge remains elusive in particular, for flows under shear, such as pipe and channel flows. Is the transition abrupt or continuous? Does it depend on a particular type of perturbation? Are there universal laws in the transition? These fundamental questions have to be revisited. Recently, Hof et al. (1) conducted a series of experiments on a pipe flow and found that the transition can be regarded as a spreading process of a localized turbulent puff created by perturbations that may duplicate or die out indefinitely. Situations are similar for other wall bounded flows. In such flows, the laminar flow becomes turbulent despite its linear stability; laminar states do not break up into turbulent states unless they are invaded by turbulent neighbours due to the stability against infinitesimal perturbations. If the tendency for invasion by a turbulent state increases, the turbulent state will eventually spread over the entire space. It is this behavior that led Pomeau to conjecture that the spatio-temporal intermittency observed at the transition from the laminar flow to turbulence belongs to the directed percolation (DP) universality class (2). DP is a stochastic spreading process of an active (turbulent) state with a single absorbing state, which diverse phenomena such as spreading of epidemics, fires, synchronization, and granular flows potentially belong to. If the transition is continuous and the interaction is short-ranged, universal critical exponents are expected. However, to observe the critical behavior in a pipe flow, if it exists, an extraordinarily long pipe is required. To overcome this difficulty, we chose a quasi-two dimensional channel flow and forced the inlet boundary condition to be active (turbulent) state. It enabled us to study the transition to turbulence as a surface critical phenomena. A clear transition between decay and penetration of the injected turbulent flow was observed. Quantification of the order parameter and the correlation length revealed critical behavior of the transition in channel flow; obtained three independent critical exponents support that the transition to turbulence in channel flow belongs to the DP universality class.

EXPERIMENTAL SETUP

The flow channel has a length of 5880 mm in a streamwise (x) direction, a cross section of 5 mm in depth (the y direction) and 900 mm wide in a spanwise (z) direction. Thus the aspect ratio of the channel was $2352h \times 2h \times 360h$. The flow dynamics in the (x,z) plane were visualized and recorded using a visualization technique and three CCD cameras. Instead of triggering turbulent spots by a local perturbation for each measurement as in the previous experiments, we continuously excited turbulent flow in the buffering box using a grid and injected it at the inlet ($x = 0$).

ORDER PARAMETER

This setup enabled us to attain a steady state measurement of the area fraction of the turbulent region (the turbulent fraction ρ) as a function of x. $\rho(x)$ was estimated by measuring the time fraction occupied by turbulent flow for each of the locations averaged over a long time (about 40 min, 100 times of flow circulation time). $\rho(x)$ seemed to saturate for higher Re and for larger x. Therefore, we measured the turbulent fraction as a function of Re at several distant locations x satisfying $x/h > 1280$. The curves for different positions overlapped, implying that ρ is almost saturated for Re larger than a certain value. Order parameter increased continuously from zero as shown in Fig.1a. Thus we fit by $\rho = \rho_0 \varepsilon^\beta$ in the inset of Fig. 1a, where ε is the reduced Reynolds number, $\varepsilon \equiv (Re - Re^c)/Re^c$. We obtained $\beta = 0.58(3)$ and $Re^c = 830(4)$ as the best fit. Non-vanishing order parameter is due to finite size effect as usual.

---

[a] Corresponding author. Email: sano@phys.s.u-tokyo.ac.jp**.**

DIVERGENCE OF CORRELATION LENGTH

Critical behavior is characterized by a divergence of the correlation length at the critical point. If the transition from the laminar to turbulent state belongs to the DP universality class, the correlation length of the cluster should reflect this critical nature. In order to test this, we measured a distribution of the durations τ of the laminar state (laminar interval distribution) $N(\tau)$ at fixed downstream locations for $Re > Re^c$. For Re sufficiently close to Re^c, $N(\tau) \sim \tau^{-\mu}$ with $\mu = 1.25(5)$ is obtained. This value is close to the universal exponent in DP, $\mu_\perp^{DP} = 1.204(2)$ which characterizes the scale invariance of critical clusters. We defined the correlation length ξ, by fitting the tail of a complementary cumulative probability, $P(\tau) \equiv \int_\tau^\infty N(t)\mathrm{d}t / \int_0^\infty N(t)\mathrm{d}t$ with an exponential function, $P(\tau) \sim \exp(-\tau / \xi)$. As we approached to Re^c, ξ substantially increases. The correlation length as a function of ε showed a divergence with a power law and saturation at the smallest ε (Fig.1b). We fitted by $\xi \sim \varepsilon^{-\nu}$ with an exponent $\nu = 0.71(5)$ which agrees with $\nu_\perp^{DP} = 0.733(3)$. In addition, we obtained $\nu_\parallel$ by looking at a spatial distribution of turbulent fraction $\rho(x)$. The turbulent fraction showed an exponential decay; $\rho(x) \sim \exp(-x / L)$ for $Re < Re^c$. The decay length L increased near the critical point with a power law, $L \sim |\varepsilon|^{-\nu}$. We obtained $\nu = 1.1(3)$. This value is again close to the critical exponent for the divergence of temporal correlation length, $\nu_\parallel^{DP} = 1.295(6)$. Thus we obtained three independent critical exponents β, $\nu_\perp$, and $\nu_\parallel$ for DP together with the exponent for laminar interval distribution, $\mu_\perp$. which satisfies the universal scaling relation, $\mu_\perp = 2 - \beta / \nu_\perp$. Therefore the results strongly support that the transition belongs to (2+1)-dimensional DP universality class.
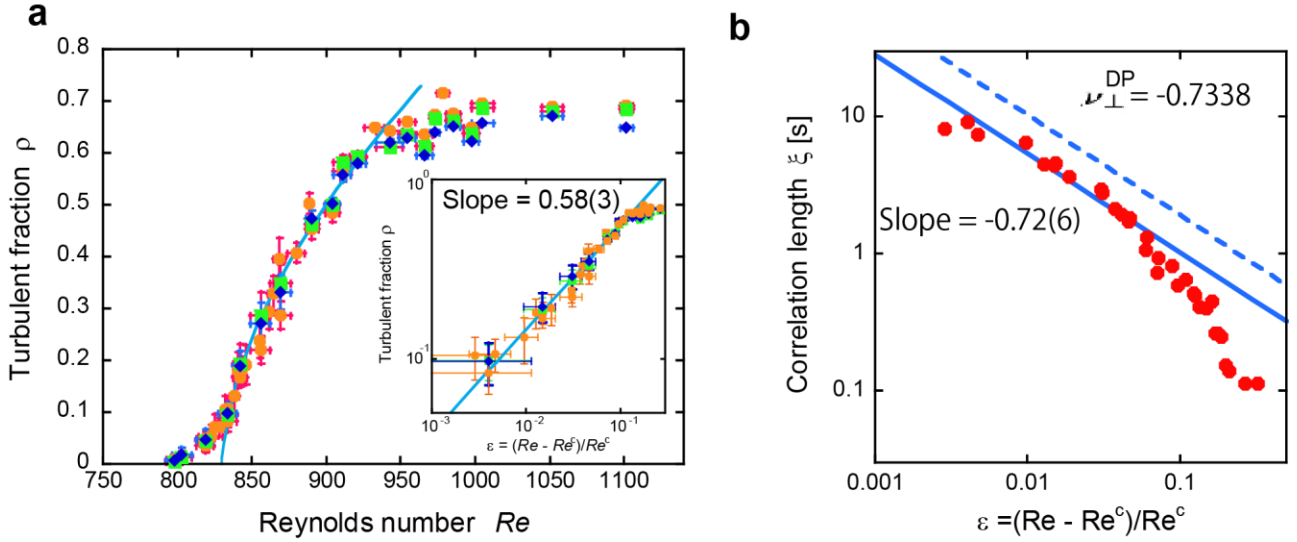
Figure 1, **a**; The turbulent fraction ρ vs. Re is plotted at different downstream locations: $x / h = 1292$ (🟠), $x / h = 1880$ (🔷), and $x / h = 2096$ (🟩). Inset: A log-log plot of ρ as a function of reduced Reynolds number ε. **b**: Correlation length estimated from the tail of laminar length distributions as a function of ε.

CONCLUSIONS

Although larger scale experiments and DNSs are needed in the future, the largest channel flow experiment available at present strongly supports the idea that the transitions to turbulence in shear flows have a universal critical nature of non-equilibrium phase transition, *i.e.*, the transition belongs to the DP universality class.

References

[1] K. Avila, D. Moxey, A. de Lozar, M. Avila, D. Barkley, B. Hof, *Science* **333**, 192 (2011).

[2] Y. Pomeau, *Physica* D **23**, 3 (1986).

[3] K. A. Takeuchi, M. Kuroda, H. Chaté, M. Sano, *Phys. Rev. Lett.* **99**, 234503 (2007), *Phys. Rev*. E **80**, 051116 (2009).

[4] M. Sano, K. Tamai, to appear in *Nature Physics* (2016).

LOCALIZED STRUCTURES ON THE EDGE IN BOUNDARY LAYERS AND THEIR TRACES IN BYPASS TRANSITION

Taras Khapko[1], Tobias Kreilos[2], Philipp Schlatter[1], Yohann Duguet [*3],

Bruno Eckhardt[4,5], and Dan S. Henningson[1]

[1]*Linné FLOW Centre, KTH Mechanics, Royal Institute of Technology, Stockholm, Sweden*
[2]*Emergent Complexity in Physical Systems Laboratory, École Polytechnique Fédérale de Lausanne, Lausanne, Switzerland*
[3]*LIMSI-CNRS, Université Paris-Sud, Orsay, France*
[4]*Fachbereich Physik, Philipps-Universität Marburg, Marburg, Germany*
[5]*J.M. Burgerscentrum, Delft University of Technology, Delft, The Netherlands*

Summary Investigation of the laminar–turbulent separatrix is performed in a boundary-layer flow. Constant homogeneous suction is applied at the wall in order to prevent the spatial growth of the layer, leading to the parallel Asymptotic Suction Boundary Layer (ASBL). Edge tracking is performed in a large computational domain allowing for full spatial localization on the separatrix. The obtained localized structure experiences recurrent dynamics going through calm and bursting phases. During calm phases the structure's active core consists of a single low-speed streak which develops sinuous instabilities leading to a burst in energy. During the burst new streaks are created, with the structure growing in size and its core drifting in both planar directions. The recurrent simple structure observed during calm phases is compared with those seen in the early development of the minimal seed and during bypass transition. The implications on the dynamical systems view of the transition process are discussed.

INTRODUCTION

Lately a stimulating breakthrough occurred in transition to turbulence, when researchers started adopting tools from deterministic chaos theory and dynamical systems, supported by the on-going progress of computer simulations. One of the new concepts arising from these recent developments is the idea of "edge states": nonlinear flow structures living at the dynamical border between laminar and turbulent flow [1]. They are relative attractors within the laminar–turbulent boundary and can be simple objects, like fixed points or periodic orbits, or more complicated chaotic structures. In all cases they serve as an example of simple dynamics in the high-dimensional system. As such they can be used for understanding the mechanisms of the sustained non-trivial flow behavior. In addition, being saddles of the system, they guide the evolution of the flow going towards turbulence.

Recently, this concept was applied to the Blasius boundary-layer flow over a flat plate [2]. However due to the spatial growth of the boundary layer the proper asymptotic dynamics is inaccessible. One way to circumvent this is to apply suction at the plate which counteracts the spatial growth. If the suction is constant and homogeneous the boundary-layer thickness saturates and the associated flow is known as the Asymptotic Suction Boundary Layer (ASBL) [3].

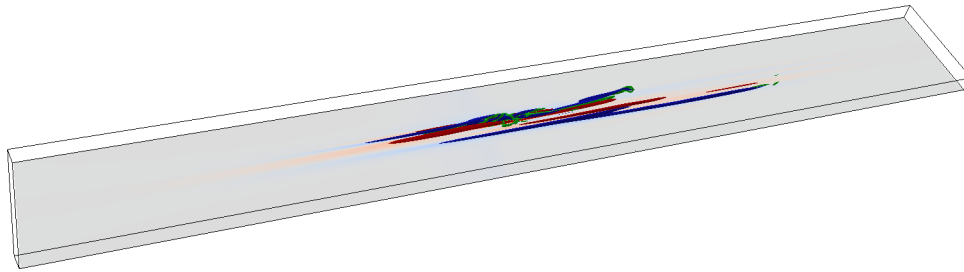Figure 1: Three-dimensional snapshot of the edge state. Low- (blue) and high-speed (red) streaks are shown with the isosurfaces of the streamwise velocity fluctuations $u' = \pm 0.05$. The vortical structures are shown using the $\lambda_2 = -10^{-4}$ isosurfaces (green). Flow from lower left to upper right. The whole computational domain is shown.

*Corresponding author. Email: duguet@limsi.fr

Figure 2: Top views of the edge state showing the typical structure of the active core during the calm phase. Three independent events are displayed. The same color coding is used as in figure 1, however with higher isolevels ($u' = \pm 0.13$ and $\lambda_2 = -4 \times 10^{-4}$) in order to capture the most energetic parts of the structure. Flow from left to right. Only part of the computational domain is shown.

LOCALIZED EDGE STATES IN ASBL

The parameters for the current study were based on the previous results in the numerical domain of limited size [4]. We perform edge tracking in domain of size $[L_x, L_y, L_z] = [800\delta^*, 15\delta^*, 100\delta^*]$ at $Re = 500$ (defined as the ratio of the free-stream velocity U_∞ to the suction velocity V_S) using the fully spectral code with a DECI awarded allocation, as each flow field has 200 million grid points. Here δ^* is the laminar boundary-layer displacement thickness and together with U_∞ they are used for non-dimensionalization.

The obtained structure resembles a turbulent spot at the initial stages of its growth. It consists of low- and high-speed streaks and vortical structures staggered along to the streaks (see figure 1). Both visual inspection and quantitative analysis confirm the fully localized nature of the state. Its energy oscillates erratically showing no signs of regularization. Hence we conclude that the edge state is chaotic in this set-up. Still, calmer and bursting phases alternating with irregular intervals can be identified, indicating pulsating behavior with recurring dynamics.

In the calm phase the active core of the state consists of a single low-speed streak. It develops sinuous instabilities with two counter-rotating vortices flanking the streak and sustaining it through the lift-up effect. The other streaks slowly decay. The vortices above the active streak grow in strength and start leaning over it. When they cross, a region is created where the fluid is pushed down instead of being lifted up. This leads to the breakdown and to a spanwise drift of the whole structure. The vortices generated in the breakdown process create new low- and high-speed streaks and the cycle is closed.

IMPLICATIONS FOR TRANSITION TO TURBULENCE

The performed edge tracking is a way of mapping out parts of the edge manifold, where the edge can be followed for arbitrary large times. Thus it allows to identify recurrent dynamics and the regions of phase space which are repeatedly visited on the edge. The simple structure in the calm phase was identified as this recurrent structure (see figure 2). Surprisingly, very similar structures are also seen as a part of the trajectory of the minimal seed [5]. Similar structures have also been reported in many studies on transitional boundary layers [6] at the verge of the breakdown leading to creation of turbulent spots, the so-called nucleation events. Thus, it is plausible that in bypass transition (*e.g.* induced by free-stream turbulence) the secondary instability of the streaks can be associated with the approach to the stable manifold of the edge state and its linear instability.

Hence we can adopt the following dynamical systems view on the bypass transition process in boundary layers with disturbances of moderate levels. The perturbations are viewed as a cloud of initial conditions of which some are on the turbulent side of *the stable manifold of the edge state*. The corresponding trajectories approach the localized edge state for a finite time. During the approach (the receptivity process) the perturbation evolves into a low-speed streak, the structure repeatedly seen in the edge state computation. Once the sinuous instability builds up and grows, it leads to a burst of the streak. For the trajectory constrained to the edge, the burst would be followed by a decrease of the energy. However being slightly above, the burst leads to the breakdown into a turbulent spot. Thus the nucleation process of turbulent spots in bypass transition is related to appearances of the edge-type structures which can be used in the understanding and modeling of the whole process.

References

[1] Schneider T. M., Eckhardt B. and Yorke J. A.: Turbulence transition and the edge of chaos in pipe flow. Phys. Rev. Lett. 99:034502, 2007.

[2] Duguet Y., Schlatter P., Henningson D. S. and Eckhardt B.: Self-sustained localized structures in a boundary-layer flow. Phys. Rev. Lett. 108:044501, 2012.

[3] Schlichting H.: Boundary-Layer Theory. McGraw-Hill, New York, 7th edn. edition, 1987

[4] Khapko T., Kreilos T., Schlatter P., Duguet Y. , Eckhardt B., and Henningson D. S.: Localised edge states in the asymptotic suction boundary layer. J. Fluid Mech., 717:R6, 2013.

[5] Duguet Y., Monokrousos A., Brandt L. and Henningson D. S.: Minimal transition thresholds in plane Couette flow. Phys. Fluids 25:084103, 2013.

[6] Schlatter P., Brandt L., De Lange H. C. and Henningson D. S.: On streak breakdown in bypass transition. Phys. Fluids 20:101505, 2008.

TEMPORAL AND SPATIAL INTERMITTENCIES WITHIN NEWTONIAN TURBULENCE

Anubhav Kushwaha[1] and Michael D Graham [*][1]

[1]*Department of Chemical and Biological Engineering, University of Wisconsin-Madison, USA*

Summary Direct numerical simulations of a pressure driven turbulent flow are performed in a large rectangular channel. Extreme and moderate drag regimes within turbulence that have earlier been found to exist temporally in minimal channels at low Reynolds numbers have been observed both spatially and temporally in full-size turbulent flows. These intermittent regimes, namely, "hyperactive", "active" and "hibernating" turbulence, display very different structural and statistical features. Using conditional sampling, we identify these intermittent intervals and present the differences between them in terms of simple quantities like mean velocity, wall shear stress and flow structures. By conditionally sampling of the low wall shear stress events in particular, we show that a Newtonian trajectory in large domains occasionally approaches some of the exact coherent states that are characteristic of very low drag in Newtonian flows.

INTRODUCTION

A way of understanding the chaotic dynamics of turbulent flows is to look at the exact coherent states (ECS) of the Navier-Stokes equations. The low-drag events in Newtonian flows resemble a recently-discovered family of ECS [1]. Similar transient behaviour at low Reynolds numbers in minimal channels has also been observed in viscoelastic flows [2]. The objective of this study is to establish whether temporal intermittency in minimal-channel Newtonian flows translates to temporal and spatial intermittencies in large-domain Newtonian flows.

RESULTS AND DISCUSSION

To detect and sample low and high drag events happening locally with time, we measure the instantaneous wall shear stress at a point on a wall. Our criteria for an event is that the wall shear stress (τ_w) at the point must surpass a threshold value and it must stay on the same side of the threshold for a specified minimum time duration. Specifically, for an event to be called hibernation, the wall shear stress must fall below the specified threshold and must last for a duration $t^* > 3$, and for an event to be hyperactive, τ_w must become higher than the corresponding threshold value and, as before, must stay high for $t^* > 3$. Figure 1(a) shows many low wall shear stress events measured at $\mathrm{Re}_\tau = 85$ that satisfy the criteria for hibernation. The beginning of each event shifted to $t^* = 0$. We are calling such low-drag events hibernating turbulence. The ensemble average of all the instantaneous hibernation events is shown as a thick green line. On average the wall shear stress during hibernation falls to a plateau in the time interval $0.7 \leq t^* \leq 2.8$ and is preceded by a sharp peak in the wall shear stress (higher than the mean, $\overline{\tau_w}$) during $-0.8 \leq t^* \leq 0$. Similarly, for hyperactive intervals we select instances when the wall shear stress becomes more than 110% and 120% of the mean and remains higher than the specified threshold for $t^* > 3$ (Figure 1(b)).

(a) Hibernation, $\tau_w \leq 90\%\overline{\tau_w}$ (b) Hyperactivity, $\tau_w \geq 110\%\overline{\tau_w}$
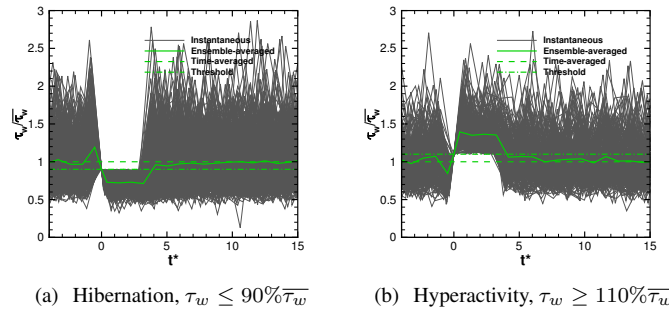
Figure 1: Instantaneous (thin grey lines) and ensemble-averaged (thick green solid line) wall shear stress before, during and after the intervals of hibernation and hyperactivity at $\mathrm{Re}_\tau = 85$. Here, t^* is the time measured in units of eddy turnover times.

To identify low and high drag regions spatially, we choose a detector function, which is a function of flow properties at the wall or in the fluid region. The detector function is lowpass-filtered and thresholded that results in demarcation of weakly and strongly turbulent areas. The sum of the absolute values of the streamwise wall shear stress and the spanwise derivative of the streamwise velocity is chosen as the detector function, *i.e.*, $D \equiv |\partial U/\partial y|_w + |\partial U/\partial z|_{y^+=15}$.

[*]Corresponding author. Email: mdgraham@wisc.edu

The filtered signal is then thresholded using Otsu's method. For a given snapshot, we divide the spatially-varying wall shear stress into three classes – low, intermediate and high – and the range for each class is determined by the thresholds obtained from Otsu's method. Note that no time-criterion has been applied to the spatial sampling technique. The result of the edge-detection algorithm is shown in Figure 2. The contours represent the wall shear stress patterns from an instantaneous flow-field at $Re_\tau = 85$. Solid black line represents the demarcation line between high-drag and intermediate-drag regions and white line separates the intermediate-drag areas from the low-drag areas. A distinct difference between the three regions is observed – areas enclosed by black lines show high wall shear stress and strong fluctuations whereas the areas enclosed by white lines are smooth, local wall shear stress values are low and the variations are small. Regions between red and black lines lie in the intermediate-drag regime.
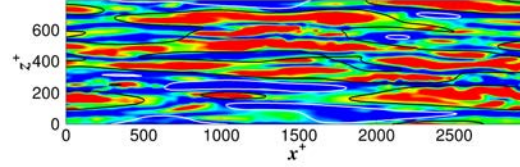

Figure 2: Edges between high- and intermediate-drag regions (black) and between intermediate- and low-drag regions (white). Flow is from left to right.

Conditional mean velocity profiles for hibernating and hyperactive turbulence at $Re_\tau = 85$ occurring both in time and in space are presented in Figure 3(a). It is observed that low-stress conditional averages from edge-detection scheme (spatial) nearly matches pointwise thresholding results (temporal) – both profiles are shifted upward of the unconditional mean profile and lie close to the Virk MDR asymptote. Similarly, the mean velocity profiles during hyperactivity, both temporal and spatial, lie below the unconditional time-averaged profile. The hibernation profiles in a large domain Newtonian flow also lie close to the lower branch ECS profile near the wall (up to $y^+ \approx 25$) observed in a minimal channel (Figure 3(b)).
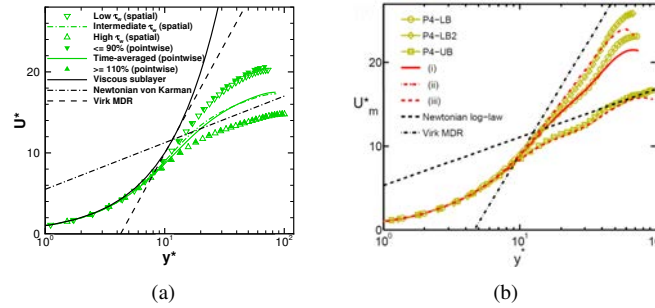

Figure 3: (a) Unconditional (solid lines) and conditional (symbols) streamwise mean-velocity profiles at $Re_\tau = 85$. (b) Mean velocity profiles of lower and upper branches ECS (shown in yellow) in Newtonian flows in a minimal channel [1].

CONCLUSIONS

Intermittent excursions towards low and high drag states, that have earlier been found to exist temporally in minimal channels, have also been observed to occur both temporally and spatially in large-domain Newtonian flows. Using conditional sampling and edge-detection techniques, we identified these transient intervals and it was found that the mean near-wall properties and structures of the low drag events in particular resemble some of the lower branch exact coherent states. These low drag regions in time and space can serve as potential targets for drag reduction schemes to reduce energy consumption in flow processes.

References

[1] Park J S, Graham M D: Exact coherent states and connections to turbulent dynamics in minimal channel flow. J. Fluid Mech 782:430-454, 2015.
[2] Xi L, Graham M D: Intermittent dynamics of turbulence hibernation in Newtonian and viscoelastic minimal channel flows. J. Fluid Mech 693:433-472, 2012.

BIFURCATIONS IN ROTATING PLANE COUETTE FLOW
AT MODERATE REYNOLDS NUMBERS

Masato Nagata [*1]

^{1}*Department of Mechanics, Tianjin University, Tianjin, P. R. China*

Summary Bifurcations in rotating plane Couette flow are investigated when the Reynolds number, R, is relatively small. We clarified the role of the second wavy vortex flow, called Ribbon, in the parameter space. In addition, a new type of tertiary flow with the symmetry classified as $\mathscr{A}_3$ in Nagata (1986) is discovered.

INTRODUCTION

During the past few decades, the problem of plane Couette flow with system rotation has served as a suitable testing ground for comparison between experiments and theories [1,2,3,4,5]. This classical problem is revisited in the current paper in order to gain a new insight into transition to turbulence.

MODEL

We analyze the bifurcation of plane Couette flow subject to a constant spanwise rotation Ω^*, which is governed by the dimensionless Navier-Stokes equations and incompressibility condition,

$$\partial_t \boldsymbol{u} + \boldsymbol{u} \cdot \nabla \boldsymbol{u} + \boldsymbol{\Omega} \times \boldsymbol{u} = -\nabla p + \frac{1}{R}\nabla^2 \boldsymbol{u}, \quad \nabla \cdot \boldsymbol{u} = 0, \tag{1}$$

expressed in the rotating frame of reference, where velocity $\boldsymbol{u}$ has components (u, v, w) in the streamwise (x), spanwise (y) and wall-normal (z) directions, respectively, t denotes time and p is a modified pressure that includes the centrifugal force term. All lengths have been scaled by half the fluid depth, D^*, while velocities have been scaled by the translational wall speed V^*. The Reynolds number, $R = V^*D^*/\nu$, with ν denoting the kinematic viscosity, and the rotation number, $\Omega = 2\Omega^*D^*/V^*$, where $\boldsymbol{\Omega} = [0, \Omega, 0]$, have been introduced. The laminar basic flow satisfying no-slip at the wall, $\boldsymbol{u}(z = \pm 1) = \mp 1$, is given by $\boldsymbol{u} = (u_0(z), 0, 0)$, where $u_0(z) = -z$.

NUMERICAL METHODS

We superimpose disturbances on the laminar basic flow. The development of the disturbances is of our interest. A typical physical disturbance component, q, is expressed in the following form,

$$q(x, y, z, t) = \sum_{l=-L}^{L} \sum_{m=-M}^{M} \sum_{n=-N}^{N} q_{lmn}(t) \exp[im\alpha(x - ct) + in\beta y]T_l(z), \tag{2}$$

where m and n are integers, α and β are the wavenumbers in the streamwise and the spanwise directions, respectively, c is the wavespeed and $T_l(z)$'s denote modified Chebyshev polynomials which satisfy the no-slip condition. Upon using the orthogonality property of the Fourier series, we discretize the equations at a selected wall-normal collocation points. The resulting algebraic equations for the component amplitudes, q_{lmn}'s, and the wave speed, c, are solved by Newton method. It is found c is zero along all the solution branches presented in this paper,

RESULT

It is known that rotating plane Couette flow becomes unstable to streamwise-independent disturbances and, as a result, two streamwise-independent secondary flows, one from the first instability mode [1] and the other from the second instability mode [2], bifurcate. We call these secondary flows TV_1 and TV_2, respectively. Furthermore, it is known that the first and second tertiary flows in the form of three-dimensional wavy vortex bifurcate from TV_1 and TV_2, respectively. We call these tertiary flows WVF and Ribbon. We find that WVF, normally exists along a singly-connected branch, has a window of non-existence for some wavenumber pair (α, β) as the rotation number, Ω, varies and this non-existence window of WVF is filled by Ribbon. In this particular case, three-dimensional Ribbon bifurcates directly from the basic laminar state, as a secondary solution, with its two bifurcation points on the basic state, one at a small Ω end and the other at a larger Ω end (see Figure 1(a) and (b)). It is found that in the limit of small α, Ribbon coincides with WVF, and that, as α is increased, the bifurcation point at the small Ω moves toward a larger Ω value, until it collide with the bifurcation point of TV_2. The bifurcation point of Ribbon, then, *climb up* the TV_2 branch, so that the Ribbon is now recognised as the second tertiary flow (see Figure 1(c)).

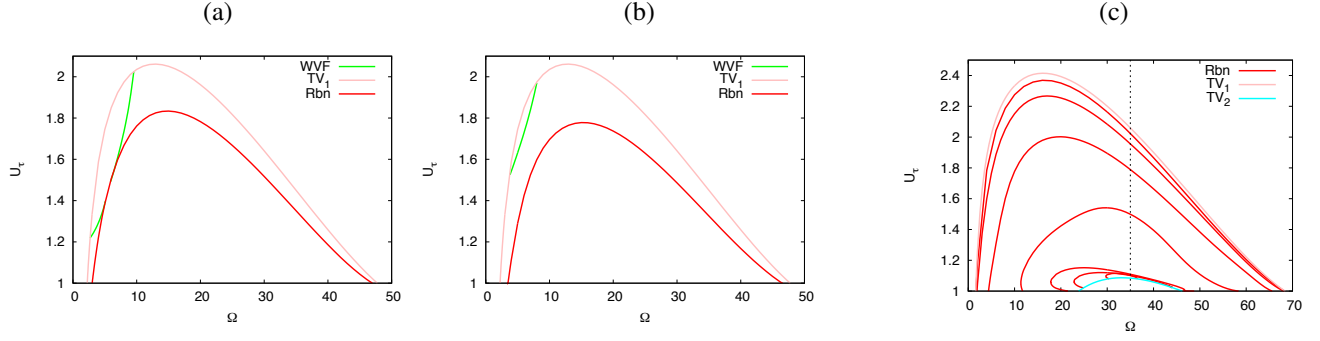*Corresponding author. Email: nagata@kuaero.kyoto-u.ac.jp

Figure 1: (a) and (b): Bifurcation diagram along the Ω-axis for TV_1 (thin pink), WVF (green) and Ribbon (red). The nonlinear measure is represented by U_τ, the momentum transport at the wall. $R = 50$ and $\beta = 1.5$. (a):The non-existence window of WVF at around $\Omega = 5$ filled by Ribbon. $\alpha = 0.20$. (b): Singly-connected WVF. $\alpha = 0.25$. (c): The branches of Ribbon as α varies. $\alpha = 0.04, 0.1, 0.3, 0.5, 0.7$ and 0.9 from outside. $R = 70$. $\beta = 1.34$. TV_2 (cyaan).

Further, we investigate Ribbon for a larger R. Ribbon bifurcates from TV_2 at a smaller Ω-end as before when $R = 160$ (see Figure 2). Regarding its bifurcation point at the larger Ω, although it is hardly seen in the figure, we confirm that it now starts from a new solution branch with the symmetry, $\mathscr{A}_3$, classified in [1]. The new solution branch of $\mathscr{A}_3$ bifurcates from TV2 as a third tertiary flow.
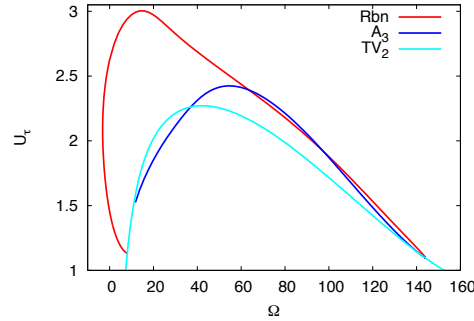

Figure 2: Bifurcation diagram along the Ω-axis for TV_2 (cyaan), $\mathscr{A}_3$ (blue) and Ribbon (red). $R = 160$. $(\alpha, \beta) = (0.8, 1.5)$.

CONCLUSIONS

In addition to the conventional two states, TV_1 and WVF, we are able to identify three flow states, TV_2, Ribbon and $\mathscr{A}_3$, at a high rotation rate. The coexistence of the total five flow states may play an important role to guide the flow into a complicated three-dimensional state, such as called Braided or Spaghetti state, which has not been resolved completely [3,4,5].

References

[1] Nagata M.: Bifurcations in Couette flow between almost corotating cylinders. J. Fluid Mech 169:229-250, 1986.

[2] Nagata M.: A note on the mirror-symmetric coherent structure in plane Couette flow. J. Fluid Mech 727:R1-8, 2013.

[3] Tsukahara T., Tillmark N., Alfredsson P. H.: Flow regimes in plane Couette flow with system rotation. J. Fluid Mech 648:5-33, 2010.

[4] Suryadi A. Tillmark N., Alfredsson P. H.: Velocity measurements of streamwise roll cells in rotating plane Couette flow. Exp. Fluids 15 (11):1617, 2013.

[5] Daly C. A., Schneider T. M., Schlatter P., Peake N.: Secondary instability and tertiary states in rotating plane Couette flow. J. Fluid Mech 781:27-61, 2014.

EFFECTS OF DRAG-REDUCING POLYMERS ON THE TRANSIENT DEVELOPMENT OF TURBULENT COHERENT STRUCTURES

Xue Bai[1] and <u>Li Xi</u> *[1]

[1]*Department of Chemical Engineering, McMaster University, Hamilton, Ontario, Canada*

Summary Drag-reducing polymers have profound impact on the dynamics of turbulence, not only in the statistically-converged stage but also in its transient development. Understanding of the latter is essential for solving all major remaining problems in viscoelastic turbulence. Direct numerical simulation is used to study the transient growth of the laminar-turbulent edge state into full turbulence and comparison is made between Newtonian and viscoelastic fluid flows. Polymers are found to suppress turbulence growth throughout the process. Inspection of flow fields further reveals a different pattern of turbulence development after polymers are introduced.

INTRODUCTION

Flexible long-chain polymer additives are known to cause drastic changes in flow turbulence, including significant reduction in its friction drag [1] and complex behaviors during the laminar-turbulent (L-T) transition [2]. Recent advances indicate that major unsolved problems in viscoelastic turbulence can all be linked to the dynamics in the L-T transition region [3, 4, 5, 6]. Most notably, the edge state – an asymptotic saddle state on the L-T boundary [7, 8] – was found to have invariant flow statistics with increasing polymer elasticity [4, 6], explaining the existence of a universal upper bound for polymer-induced drag reduction (DR) – the well-known puzzle of maximum drag reduction (MDR) [1]. Specific solutions responsible for MDR are yet to be identified, prompting us to shift our attention to the state-space region between the edge state and the turbulent basin. Better knowledge of the dynamics in the region, especially polymer effects thereon, is also the key to solving other important problems such as the transition mechanism of viscoelastic fluids and onset criterion of DR.

Using the edge state (perturbed by numerical errors only) as the initial condition, direct numerical simulation (DNS) is used here to track the growth of a marginal turbulent spot into full turbulence. Newtonian and viscoelastic simulations are compared to study the polymer effects. We focus on a minimal channel flow (720 and 230 wall units in streamwise and spanwise directions, respectively) and a moderate $Re_\tau = 84.85$; viscoelastic simulation was performed with $Wi = 40$ (Wi, Weissenberg number, is the product of polymer relaxation time and wall shear rate; $Wi \gg 1$ indicates strong polymer elasticity). Details of the simulation system and numerical procedures are found in recent publications [9, 6].

RESULTS

State-space trajectories of the process is projected using various quantities of interest and shown in Fig. 1. Fig. 1(a) focuses on global statistics: bulk-average turbulent kinetic energy (TKE) and velocity (U_bulk). Turbulence growth in both Newtonian and viscoelastic systems starts with a spike in TKE, which is followed by a dip then a steady climb toward the magnitude of turbulent basin; U_bulk drastically decreases during the process. In our recent study [6], it became clear that quantities directly measuring near-wall turbulent activities – in particular, the peak value in the Reynolds shear

Figure 1: State-space projections of dynamic trajectories initiated from the edge state: (a) TKE vs. U_bulk; (b) peak value of the RSS profile vs. log-law slope at $y^* = 25$ – A_{25}^* (dashed line marks $A_\text{MDR}^* = 11.7$).

stress (RSS) profile $|\langle v_x^* v_y^* \rangle|_\text{max}$ and log-law slope $A^* \equiv y^*(dU_m^*/dy^*)$ measured at $y^* = 25$, A_{25}^* – more clearly reflects the dynamics of near-walls structures. (Here, superscript "*" indicates quantities in turbulent inner units based on instantaneous wall shear stress [3, 10]; definition of A^* comes from a log-law approximation of mean velocity profiles $U_m^* = A^* \ln y^* + B^*$.) Projections using these variables are shown in Fig. 1(b). For both Newtonian and viscoelastic cases, turbulence growth starts with a massive increase of RSS, which proceeds the growth of TKE: by the time TKE reaches the initial spike (instant B for Newtonian and instant E for viscoelastic), the RSS has already dropped down to magnitudes typical of the turbulent basin.
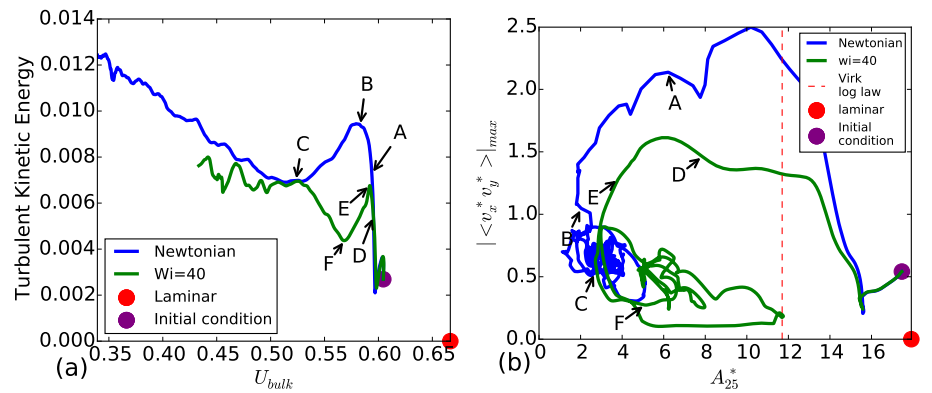

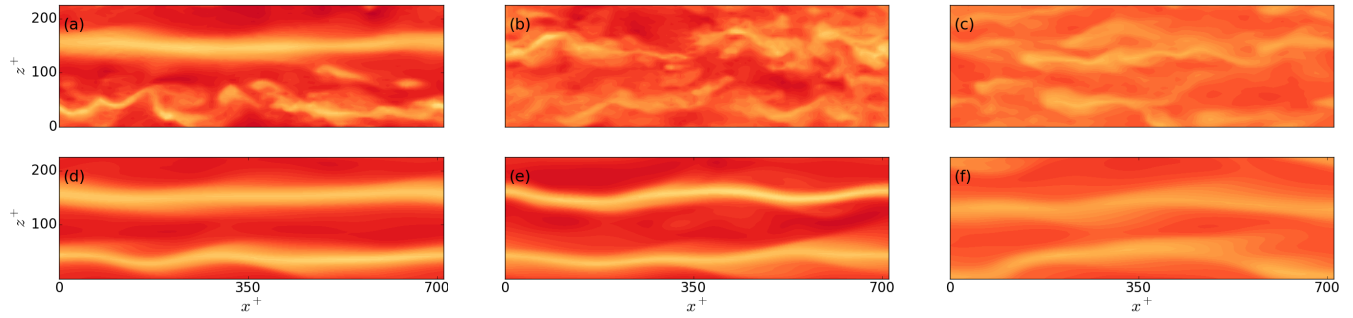*Corresponding author. Email: xili@mcmaster.ca

Figure 2: Distribution of v_x at $y^+ = 25$: (a)-(c) correspond to Newtonian instants A-C, and (d)-(f) correspond to viscoelastic instants D-F (instants defined in Fig 1). The color scale ranges from yellow for 0 to red for 1.

The overall picture arising from Figs 1(a)&(b) is that with a minute perturbation, the edge state, which takes form of a localized turbulent spot [6], quickly grows into a structure with much stronger turbulent activity, whose RSS is even higher than that of the turbulent basin. As RSS of this particular structure decays to typical values of the turbulent basin, its disturbance spreads across the domain, causing the spike in TKE and drop of U_bulk. Growth at the global scale (Fig 1(a)) takes much longer time, which does not converge in the 1500-time-unit (TU) period shown. Meanwhile, during the same time period, the initial structure has already converged to the destination state (Fig 1(b)). Fluctuations afterwards reflect the intermittent dynamics of self-sustaining turbulent cycles. In particular, for the viscoelastic case, these fluctuations lead to recurrent visits toward the direction of the edge state, with A_{25}^* occasionally approaching the magnitude of MDR. This corresponds to the so-called hibernating turbulence, a type of MDR-like states becoming more exposed as Wi increases [3, 10].

Polymer stress acts as a restraining force and inhibits the development of both the initial structure and globle turbulence, with lower TKE and RSS observed during the whole growth stage. Somewhat surprisingly, mean velocity – measured by A_{25}^* in Fig. 1(b) – of the viscoelastic case drops more rapidly despite the lower RSS. This indicates that turbulent fluctuation is no longer the only means through which energy is extracted from the mean flow. Indeed, we found that the conversion rate of mechanical energy to polymer elastic energy is positive throughout the growth stage. This energy is not returned to the flow motion until turbulent basin is reached.

Contour plots of streamwise velocity, of both Newtonian and viscoelastic cases, are shown in Fig. 2 for three representative instants: before, at, and after the TKE peak in Fig. 1. Note that the edge state flow field (not shown here) is dominated by a pair of smooth and elongated low-speed streaks [6]. In the Newtonian case, the initial perturbation first leads to the breakdown of one of the streaks (Fig. 2(a)). When TKE reaches the peak value (Fig. 2(b)), both streaks have disappeared and are replaced by high-density turbulent motions: short irregular streaks with strong streamwise variations. The final instant has similar irregular patterns with lower intensity. By contrast, the viscoelastic case retained the double-streak configuration for the whole period (Figs. 2(d)-(e)). Even at the TKE peak (Fig. 2(e)), the streaks are distorted in shape but do not break into smaller structures. Regulated and elongated coherent structures are now increasingly associated with turbulent states with weak activity and low drag [6]. Our observation here clearly indicates a qualitative change in the turbulent growth mechanism of viscoelastic fluids.

CONCLUSIONS

Starting from a marginal turbulent spot, an infinitesimal perturbation first triggers the growth of its turbulent intensity, which then propagates across the domain toward full-scale turbulence. Polymer additives suppress the growth of turbulent structures throughout the process, during which energy is extracted from the flow to the polymers. Different transition pathways are observed in Newtonian and viscoelastic flows: development of Newtonian turbulence goes through a sharp breakdown of coherent structures whereas for viscoelastic systems the changes are more continuous.

References

[1] Virk, P. S. *AIChE J.* **1975**, *21*, 625–656.

[2] Samanta, D.; Dubief, Y.; Holzner, M.; Schäfer, C.; Morozov, A. N.; Wagner, C.; Hof, B. *Proc. Natl. Acad. Sci. U. S. A.* **2013**, *110*, 10557–100562.

[3] Xi, L.; Graham, M. D. *Phys. Rev. Lett.* **2010**, *104*, 218301.

[4] Xi, L.; Graham, M. D. *Phys. Rev. Lett.* **2012**, *108*, 028301.

[5] Graham, M. D. *Phys. Fluids* **2014**, *26*, 101301.

[6] Xi, L.; Bai, X. **2015**; submitted.

[7] Skufca, J. D.; Yorke, J. A.; Eckhardt, B. *Phys. Rev. Lett.* **2006**, *96*, 174101.

[8] Schneider, T. M.; Eckhardt, B. *Chaos* **2006**, *16*, 041103.

[9] Xi, L.; Graham, M. D. *J. Fluid Mech.* **2010**, *647*, 421–452.

[10] Xi, L.; Graham, M. D. *J. Fluid Mech.* **2012**, *693*, 433–472.

THE ROLE OF ELASTO-INERTIAL TURBULENCE ON CHANNEL FLOW DRAG

Yves Dubief [*][1], Samir Sid[2], and Vincent E. Terrapon[2]

[1]*Department of Mechanical Engineering, University of Vermont, Burlington, Vermont, USA*
[2]*Department of Aerospace and Mechanical Engineering, University of Liege, Liege, Belgium*

Summary The role of Elasto-Inertial Turbulence (EIT) on the bounds of friction drag is investigated in channel flows from subcritical to moderate Reynolds numbers. EIT is a newly discovered state of turbulence emerging from self-sustaining interactions between polymer dynamics and velocity perturbations in parallel shear flows. At low Reynolds numbers, EIT creates an increase in friction drag. Beyond the critical Reynolds number for Newtonian flows, EIT becomes the lower bound of the friction drag of the Maximum Drag Reduction (MDR) state. The drag reduction properties of polymer control the upper bound of MDR.

INTRODUCTION

Elasto-Inertial Turbulence (EIT) [1] is a recently discovered new state of turbulence, where interactions between inertia and elastic effects can sustain a turbulence-like state in channel and pipe flows at Reynolds numbers much lower than the critical Reynolds at which Newtonian flows undergo a transition from laminar to turbulent state. The structure of EIT[2, 3] consists of thin sheets of stretched polymers that are tilted upward by the mean shear and produce spanwise coherent flow structures by opposition to the quasi-longitudinal vortices observed in Newtonian wall turbulence (See Fig. **??**). The proposition investigated here is that EIT is the bounding state preventing a flow with polymer additives from relaminarization.

EQUATIONS

The mathematical nature of the transport equations solved in the present direct numerical simulations is of critical importance for the understanding of EIT. The momentum is transported by the Navier-Stokes equation modified to account for the viscoelastic stress:

$$\partial_t \mathbf{u} + (\mathbf{u} \cdot \boldsymbol{\nabla})\mathbf{u} = -\boldsymbol{\nabla}p + \beta Re^{-1}\nabla^2\mathbf{u} + (1-\beta)Re^{-1}\boldsymbol{\nabla}\cdot\mathbf{T}\,, \tag{1}$$

where β is the ratio of the solvent viscosity to the zero-shear viscosity of the polymer solution and $\mathbf{T}$ is the polymer stress tensor defined as:

$$\mathbf{T} = Wi^{-1}\left(f(trace(\mathbf{C}))\mathbf{C} - \mathbf{I}\right)\,. \tag{2}$$

The non dimensional Weissenberg number Wi is the ratio of the polymer solution time relaxation to a relevant flow time scale. The conformation tensor $\mathbf{C}$ is the tensorial product of the components of the end-to-end vector for a polymer molecule, phased-average over a large ensemble of molecules. The Peterlin function $f(r) = \left(1 - r/L^2\right)^{-1}$ describes the restoring spring force that polymers experience when stretched. L is the normalized polymer length. The transport equation for the conformation tensor,

$$\partial_t\mathbf{C} + (\mathbf{u}\cdot\boldsymbol{\nabla})\mathbf{C} = \mathbf{C}\cdot(\boldsymbol{\nabla}\mathbf{u}) + (\boldsymbol{\nabla}\mathbf{u})\cdot\mathbf{C}^T - \mathbf{T} + (ReSc)^{-1}\nabla^2\mathbf{C} \tag{3}$$

includes on the right hand side, the stretching of polymer molecules by the flow (first two terms), the restoring spring force (third term) and a diffusion term governed by the Schmidt number Sc. This system of equations (supplemented by $\boldsymbol{\nabla}\cdot\mathbf{u} = 0$ constitutes the FENE-P (Finite Elastic Non-linear Extensibility-Peterlin) model commonly used in the direct numerical simulation of polymer flows. Note that the derivation of the FENE-P model requires $Sc \to \infty$.

As explained in [4] (where the numerical method used here is also described), A time scale analysis of the right-hand of Eq. (3), for $Sc \to \infty$ reveals that polymer stretch on the time scale of the flow (first term) and recoil on time scale larger than the Kolmogorov scale, as stipulated by Lumley [5]. Both terms are local, with no diffusion process. On the left hand side, the nonlinear advection term, generates small scales if $Sc \to \infty$. A parallel can be made between Eq. (3) and the small scale dynamics of passive scalar [6, 7]. In the following, a numerical experiment investigates the effect of Sc on the existence of EIT.

OBSERVATION

Using direct numerical simulation in periodic 2D and 3D channel flows, the existence of EIT was established for Reynolds numbers as low as 10, based on the bulk velocity and the channel height. Here EIT was found to arise from a variety of initial perturbations including spatial variation of blowing and suction at the wall over a finite period of time and superimposition of random noise. The increase in the coefficient of drag and deviation from laminar is shown in Fig. 1a for the lowest
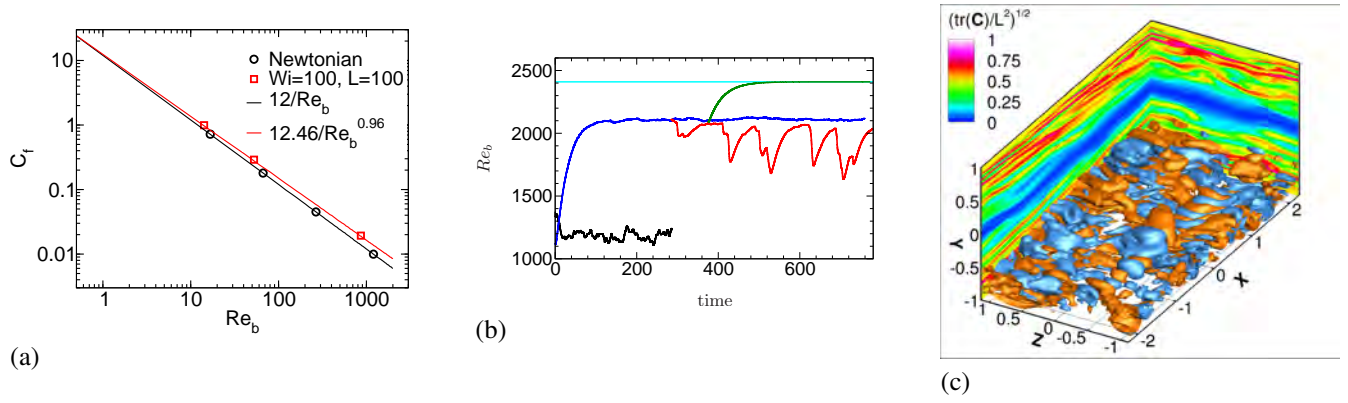
---

[*]Corresponding author. Email: ydubief@uvm.edu

Figure 1: 1a: Coefficient of friction in a 2D channel as a function of the Reynolds number based on the bulk velocity and the full heigh of the channel. (1b) Time history of the bulk Reynolds number for the simulation of [8] constant pressure-gradient minimal flow unit for $Sc \to \infty$ and $Wi_\tau = 400$ (blue), $Sc \to \infty$ and $Wi_\tau = 40$ (red), $Sc = 0.3$ and $Wi_\tau = 40$ (green). The black and cyan lines show the turbulent and laminar bulk Reynolds numbers, respectively. 1c: Flow visualization of EIT at $Wi_\tau = 40$. The orange and blue isosurfaces show positive and negative regions of the second invariant of the velocity gradient tensor Q. The side panels show contours of the polymer extension. The flow is from the left lower corner to the upper right corner.

simulation. EIT was simulated for very long period of times, up to 500 flow-through time, and no decay was observed in the space-averaged turbulent kinetic energy.

In our numerical experiment, we reproduce the minimal flow unit simulation of [8], where $Sc = 0.3$ to 0.5 was used. Fig. 1b shows that small Sc leads to a relaminarization of the flow, as observed by [8] for $Wi_\tau > 31$ (here the Weissenberg number is normalized by the wall shear, equivalent to the Kolmogorov scale). Our simulations at $Sc \to \infty$ for $Wi_\tau = 40$ and 400 demonstrates that the flow does not become laminar, a snapshot of which is depicted in Fig. 1c. The spanwise, cylindrical-looking structures of the regions of positive and negative Q (second invariant of the velocity gradient tensor) are a distinct feature of EIT. As the Weissenberg number increases, the drag becomes quasi steady and the flow structure remains as shown in Fig. 1c. These simulations demonstrate that the addition of a diffusion term with low Sc number filters out the dynamics of EIT. A crucial component of EIT is therefore small scale, since EIT simulation requires $Sc \gg 1$ and numerical resolution much finer than for an equivalent Newtonian flow. Our more recent investigation (not shown here) suggest that EIT is driven by sub-Kolmogorov time scales but not necessarily sub-Kolmogorov length scales. Simulations in larger computational domains and Reynolds numbers, demonstrate that EIT is present at MDR, even in systems that are intermittent, i.e. where the drag oscillates between a low (but not laminar) and a high drag (not fully turbulent) state.

CONCLUSIONS

This abstract shows only a fraction of the body of evidence supporting that EIT is the bound on the friction drag of MDR. For any large Wi, the flow can oscillate between two states: EIT (low drag state) and the state at which the polymer drag reduction mechanism is at its peak efficiency (high drag). Even at the high drag state, we observe the present of EIT structures. In summary, MDR is not a Newtonian state as previously thought.

References

[1] Samanta D., Dubief Y., Holzner M., Schäfer C., Morozov A.N., Wagner C., Hof B.: PNAS 110(26):10557–10562, 2013.

[2] Dubief Y., Terrapon V.E., Soria J.:Phys. Fluids 25(11):110817, 2013.

[3] Terrapon V.E., Dubief Y., Soria J.: J of Turbulence 16(1):26–43,2014.

[4] Dubief Y., Terrapon V.E., White C.M., Shaqfeh E.S.G, Moin, P., Lele S.K.: Flow, Turbulence and Combustion 74(4):311–329, 2005

[5] Lumley J.L.: Ann. Rev. Fluid Mech. 1(1):367–384, 1969.

[6] Batchelor G. K.: J. Fluid Mech. 5(1):113-133, 1959.

[7] Batchelor G. K., Howells,I. D., Townsend,A. A.: J. Fluid Mech. 5(1):134-139, 1959.

[8] Xi L., Graham M.D.: Phys. Rev. Lett. 104(21):301, 2010.

EXACT INVARIANT SOLUTIONS FOR COHERENT TURBULENT MOTIONS IN COUETTE AND POISEUILLE FLOWS

Subhandu Rawat[1], Carlo Cossu [*1], and François Rincon[2]
[1]*Institut de Mécanique des Fluides de Toulouse (IMFT), Toulouse, France*
[2]*Institut de Recherche en Planétologie et Astrophysique (IRAP), Toulouse, France*

Summary The dynamical systems approach recently applied to understand subcritical transitions in wall-bounded shear flows is combined with the use of large-eddy simulations to investigate the nature of large-scale coherent motions in turbulent Couette and Poiseuille flows. Exact invariant solutions of the filtered Navier-Stokes (LES) equations are computed by using the Smagorinsky model to parametrize small-scale motions. These solutions can be continued into exact solutions of the Navier-Stokes equations therefore providing a bridge between coherent large-scale motions in wall-bounded fully developed turbulent flows and invariant solutions appearing in transitional flows.

BACKGROUND

The understanding of subcritical transition in wall-bounded shear flows has been dramatically improved by the computation and the analysis of invariant solutions of the Navier-Stokes equations. These solutions, whose existence is necessary for subcritical transition, are thought to provide the skeleton of turbulent motions, at least up to moderate transitional Reynolds numbers. When the Reynolds number is increased, however, additional invariant solutions appear and their nature can also become increasingly complex both in phase space and in physical space. It is therefore not clear that turbulent motions at high Reynolds numbers could be approximated with a reasonable number of invariant solutions of the Navier-Stokes equations.

In order to keep the number of degrees of freedom reasonable and to simplify the dynamics even at high Reynolds numbers, invariant solutions are computed for the *filtered* Navier-Stokes equations. Subgrid-scale motions are modelled by using the Smagorinsky eddy viscosity $\nu_t = D(C_s \overline{\Delta})^2 \overline{S}$ where C_s is the Smagorinsky constant, $\overline{\Delta}$ is the average mean grid spacing, $\overline{S}$ is the norm of the the rate of strain tensor associated to the filtered velocity and $D(y^+)$ is a standard wall damping function. The reference value $C_s = 0.05$ provides the best *a posteriori* performance. Recent investigations [1, 2, 3] have shown that coherent self-sustained large-scale motions can be isolated by moderately increasing C_s above its reference value in order to artificially quench active processes at smaller scales in fully developed turbulent flows. When computing invariant solutions the Smagorinsky constant is therefore used as a continuation parameter, in addition to the Reynolds number. Furthermore, solutions of the Navier-Stokes equations can be retrieved by setting $C_s = 0$. A modified Newton-Krylov method based on time-marching integrations of the filtered equations (LES) is used to compute steady and travelling wave solutions of the filtered equations.

RESULTS

We first consider plane Couette flow in a horizontally periodic domain having the same size of turbulent large-scale motions $L_x \times L_z = 10.9h \times 5.5h$ (where h is the half-width of the channel). The edge state of coherent large-scale motions is computed, at $Re = 750$ (roughly twice the transitional Reynolds number) and $C_s = 0.14$ (overdamped simulation), by edge-tracking and is found to be a non-trivial lower branch exact steady solution of the filtered equations. By continuation to higher values of C_s it is found that the computed edge state is connected to an upper branch of solutions via a saddle-node bifurcation (see figure 1). Upper branch solutions of the filtered equations are computed up to $Re = 2150$ using specific paths in the $Re - C_s$ parameter plane (see figure 1). These solutions can be connected to Navier-Stokes solutions by continuation to $C_s = 0$, where it is found that they belong to the Nagata-Clever-Busse-Waleffe branch of solutions. We next consider plane Poiseuille flow where a recently computed [4] multi-streaks travelling-wave solution of the Navier-Stokes equations ($C_s = 0$), computed in the periodic domain $L_x \times L_z = 2\pi h \times 5.5h$, is continued from $C_s = 0$ to $C_s = 0.05$ at $Re = 2000$.

The exact solutions consist of a combination of quasi-streamwise vortices and streaks (see figure 2) which, on average, self-sustain via a coherent self-sustained process, as discussed in [1, 2, 3]. The computed 'exact' solutions of the filtered (LES) equations take into account the effect of small scales but only through their averaged effect. This approach makes possible to compute steady coherent solutions despite the fact that motions at smaller scale are unsteady and therefore focus on the relevant dynamics of the large-scale coherent solutions without the complications associated to smaller-scales motions. The spatial and *Re* dependence of the eddy viscosity associated with the averaged (residual) small-scale motions is naturally embedded in the computed solutions (see figure 2).

*Corresponding author. Email: carlo.cossu@imft.fr

References

[1] Hwang Y., Cossu C. : Self-sustained process at large scales in turbulent channel flow. *Phys. Rev. Lett.*, 105:044505, 2010.

[2] Hwang Y., Cossu C. : Self-sustained processes in the logarithmic layer of turbulent channel flows. *Phys. Fluids*, 23:061702, 2011.

[3] Rawat S., Cossu C., Hwang Y., Rincon S. : On the self-sustained nature of large-scale motions in turbulent Couette flow. *J. Fluid Mech.*, 782:515–540, 2015.

[4] Rawat S., Cossu C., Rincon S. : Travelling-wave solutions bifurcating from relative periodic orbits in plane Poiseuille flow. *ArXiv*-1601:01227v1, 2016.
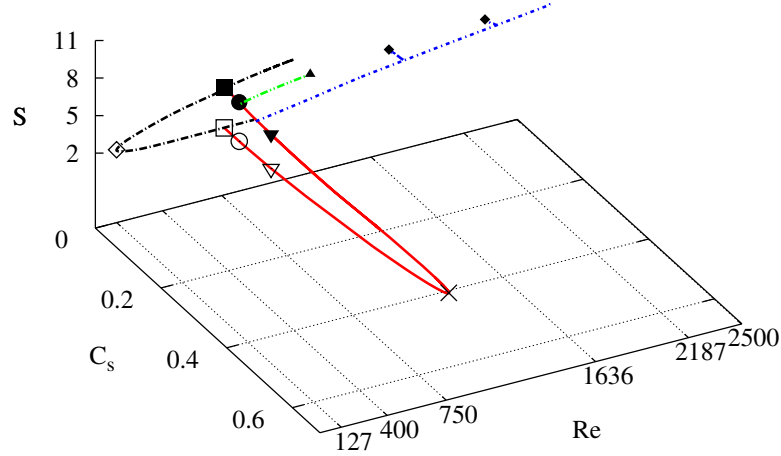
Figure 1: Continuation paths of the steady solutions of the filtered equations (LES) for plane Couette flow. The C_s continuation in C_s at $Re = 750$ (red line) shows how upper-branch solutions can be accessed in this way. Continuation to $C_s = 0$ and then in Re (black line, dashed) show that solutions continued from the turbulent case (square symbols) belong to the Nagata-Busse-Clever-Waleffe branch of Navier-Stokes solutions. Coherent steady solutions at higher Reynolds numbers are found by first continuing the solutions obtained for $C_s = 0.1$ to higher Re (blue line, dashed-dotted) and then reducing C_s.
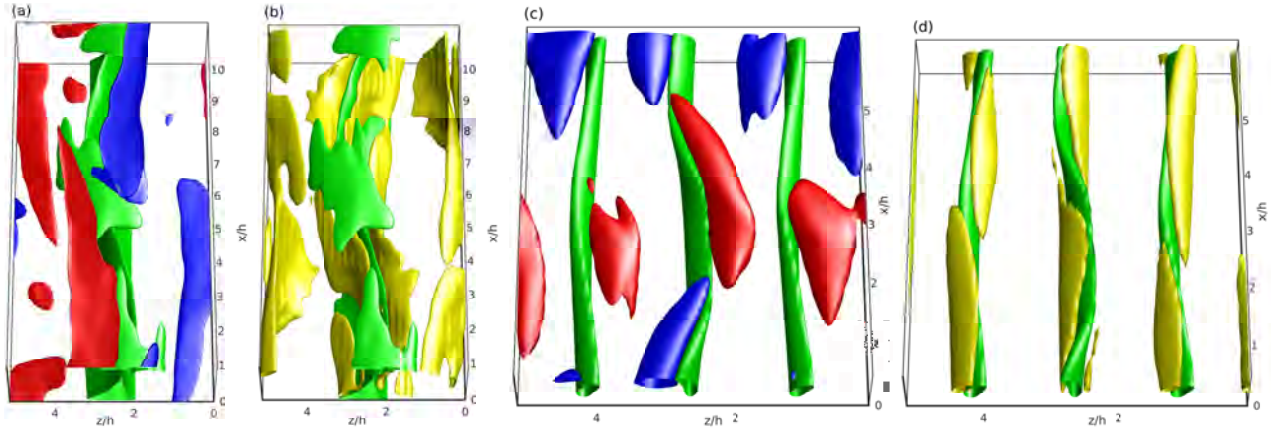

Figure 2: Visualisation of the upper branch solutions of the filtered equations (LES) obtained in plane Couette ($Re = 2150$, $C_s = 0.05$, steady solution, panels a and b) and Poiseuille ($Re = 2000$, $C_s = 0.05$, travelling-wave solution, panels c and d) flow. Panels a and c represent the large-scale coherent (i.e. filtered) streaks (green) and quasi-streamwise vorticity (blue if negative, red if positive) while panels b and d report the relative eddy-viscosity ν_t/ν associated to the residual small-scale motions.

SPATIO-TEMPORAL EVOLUTION OF ISOLATED TURBULENT BANDS IN CHANNEL FLOWS

Jianzhou Lu, Jianjun Tao[a)]

CAPT-HEDPS, SKLTCS, Department of Mechanics and Engineering Science, College of Engineering, Peking University, China

Summary In order to study the natural evolution of a turbulent band without being affected by its nearby disordered patches or domain boundaries in plane-Couette flow, an individual isolated turbulent band in a large computational domain is used as the initial disturbance. It is shown that at Re=340 the turbulent band doesn't grow remarkably in its tangential direction as the oblique extension found in plane-Poiseuille flow, but broadens in its transverse direction. With the increase of the band width, band splitting occurs.

INTRODUCTION

Transition to turbulence in linearly stable flows has remained unsolved over a century. Recent numerical and experimental investigations revealed that the splitting of localized turbulent patches plays an important role during the subcritical transition of Hagen-Poiseuille flow (HPF) [1]. Simulations in a tilted long narrow domain showed that the individual turbulent bands or stripes in plane-Couette flow (PCF) were transient as puffs in HPF, while it was found in simulations with large computational domains that the isolated turbulent band of plane-Poiseuille flow (PPF) could survive and continue to obliquely extend until the boundary influence couldn't be ignored. In simulations of PCF with a large computational domain, initial localized perturbations were found to develop to turbulent bands in a zigzag manner [4]. Due to the interactions among these bands and disturbance residues, it is difficult to examine and distinguish a clear splitting process. Considering that different tilt angles of the narrow domain may lead to different transition scenarios [5] and the artificial periodic boundaries may change the real story of the splitting behaviour, it is necessary to study the spatiotemporal evolution of a single band of PCF in a large domain at moderate Reynolds numbers. This is the motivation of this paper.

SIMULATIONS AND DISCUSSIONS

We conduct numerical simulations of PCF in a large domain of size 800 $h \times 2 h \times 712 h$, where h is the half height of the channel. A spectral code [6] is employed to solve the incompressible Navier–Stokes equations, where the velocity field is expanded in a basis of Fourier modes (in the x- and z-directions) and Chebyshev polynomials (in the wall-normal direction y). The numerical resolution is 2048 spectral modes in x, 33 in y and 2048 in z, which is as fine as the previous study [4]. The boundary conditions are periodic in x and z and no-slip at the walls ($y = \pm h$).

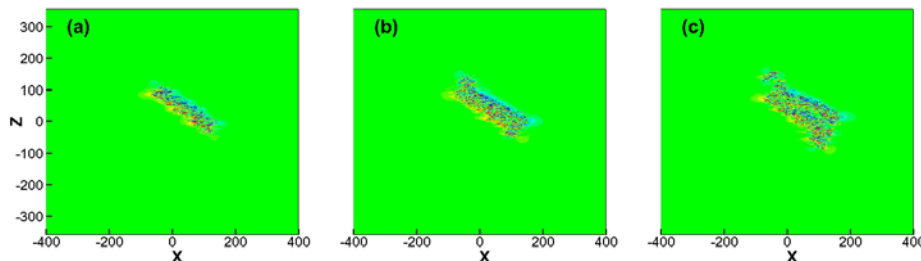Figure 3 Iso-contours of the disturbing streamwise velocity in the mid-plane ($y=0$) of Re=340 at time (a) t=0, (b) t=450 and (c) t=900 (h/U), where U is the amplitude of wall velocity.

Different initial disturbances are tested at moderate Reynolds numbers, and an isolated and straight turbulent band is obtained eventually and is used as the initial perturbation for Re=340 (Fig.1a). It is shown that there are no other perturbations near the band and the domain boundaries are far enough from it. The band doesn't show a fast extension in its oblique tangential direction as what happens in PPF, instead, it grows in its transverse direction and becomes 'fat' as shown in Fig.1(b). Later on, the band splitting occurs (Fig.1c). To our knowledge, it is the first time to show the 'natural' band splitting without being interfered by other bands, disturbances or boundaries. The phenomena illustrated above are similar with the simulation results obtained with a long narrow domain.

References

[1] Avila K, Moxey D, de Lozar A, et al.: The onset of turbulence in pipe flow. Science, **333**: 192–196, 2011
[2] Liang S., Marc A.,Björn H.: Scale invariance at the onset of turbulence in Couette flow, *Phys. Rev. Lett.* **110**:204502, 2013.
[3] Xiong X., Tao J., Chen S.Y., Brandt L.: Turbulent bands in plane-Poiseuille flow at moderate Reynolds numbers, *Phys. Fluids* **27**, 041702, 2015
[4] Duguet Y., Schlatter P., Henningson D.S.: Formation of turbulent patterns near the onset of transition in plane Couette flow. *J. Fluid Mech.* **650**:119-129, 2010.
[5] Tuckerman L.S. and Barkley D.: Patterns and dynamics in transitional plane Couette flow, *Phys. Fluids* **23**, 041301, 2011.
[6] Chevalier M., Schlatter P., Lundbladh A., and Henningson D.S.: SIMSON a pseudo-spectral solver for incompressible boundary layer flows, Technical Report TRITA-MEK 2007:07, 2007.

[a)]Corresponding author. Email: jjtao@pku.edu.cn**.**

TRANSITION TO TURBULENCE IN PLANE COUETTE-POISEUILLE FLOW

Lukasz Klotz[*1], Idalia Frontczak[1,3], Grégoire Lemoult[2], Matthew Chantry[1], and José Eduardo Wesfreid[1]

[1]*Laboratoire de Physique et Mécanique des Milieux Hétérogènes (PMMH), UMR CNRS 7636 ; PSL - ESPCI;*
Sorbonne Université , Univ. Paris 06; Sorbonne Paris Cité - UDD, Univ. Paris 07; Paris, France
[2]*Institute of Science and Technology; Klosterneuburg, Austria*
[3]*Institute of Aeronautics and Applied Mechanics, Warsaw University of Technology; Warsaw, Poland*

<u>Summary</u> We introduce an experimental set-up that enables us to create two dimensional shear flow with zero mean advection velocity. We investigate a plane Couette-Poiseuille configuration, completing the first experimental results for this flow which had only been studied theoretically to-date ([5]). Using flow visualizations we characterize subcritical transition to turbulence and we show the existence of turbulent spots in plane Couette-Poiseuille flow. Due to zero mean advection velocity of the base profile, these turbulent structures are nearly stationary (despite a non-zero pressure gradient in streamwise direction). We ascertain two characteristic wavenumbers correspond to two different inner regions of the base flow. We also determine the evolution of streamwise and spanwise dimensions of turbulent spot as a function of Reynolds number.

EXPERIMENTAL SET-UP

This new experiment is based on the classical plane Couette experimental set-up (see [2], [4]), where the base flow is generated by imposing velocity at test section walls. This is achieved using a single loop of plastic belt which imposes the opposite sign velocity at each wall. The main advantage of such an installation is the zero mean velocity of the profile, as such the generated turbulent structure is not advected ([3]) and an investigation of long time dynamics of turbulent structures is possible.

However, in our case, instead of using a single loop of belt (which can only impose the opposite sign velocity at each wall), we use two loops of belt (one for each wall of the test section). This enables us to control independently the speed at each wall. Let us assume that we set the same speed toward the right at both walls (fig.1, blue), then fluid in the vicinity of plastic belts will be driven in the same direction which in turns will increase the pressure in tank on the right side. This will result in a negative pressure gradient from right to left that will induce a reverse flow in the interior. These two factors (the same positive speed at each wall and the negative induced reverse flow at the center of the gap) will create a parabolic profile with mean advection velocity equal to zero (see the blue profile on right in the inset of fig.1).

Now we present the configuration with a single loop of plastic belt (fig.1, upper loop in red). This consists of upper moving and lower stationary walls respectively. The resulting plane Couette-Poiseuille flow (see the black profile in the inset of fig.1) can be considered as two subregions. The lower one is parabolic (Poiseuille like) and occupies approximately two-thirds of the gap. In the upper region the velocity profile can be approximated by a straight line, like in plane Couette flow. In addition the shear in the Couette region is much higher than that of the Poiseuille region.

RESULTS

We characterise the transition to turbulence with flow visualizations (fig.2). The flow is globally laminar in the test section up to Re=427 (fig.2a), where the Reynolds number is based on the half-distance of gap and the speed of the moving wall. For
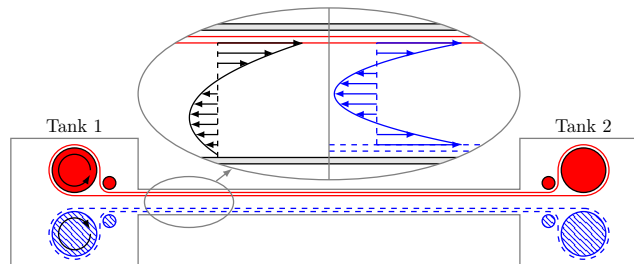

Figure 1: *Schematic of the new experimental set-up, which consists of two independent closed loops of the belt which control the speed at each wall independently. The upper loop (red lines) is used to generate the plane Couette-Poiseuille flow with zero mean advection velocity (black profile in the inset). Plane Poiseuille flow with zero mean advection velocity can be generated (blue profile on right side in the inset, [1]) if the lower loop is added (blue dashed lines).*

*Corresponding authors. Email: lukasz.klotz@espci.fr and wesfreid@pmmh.espci.fr
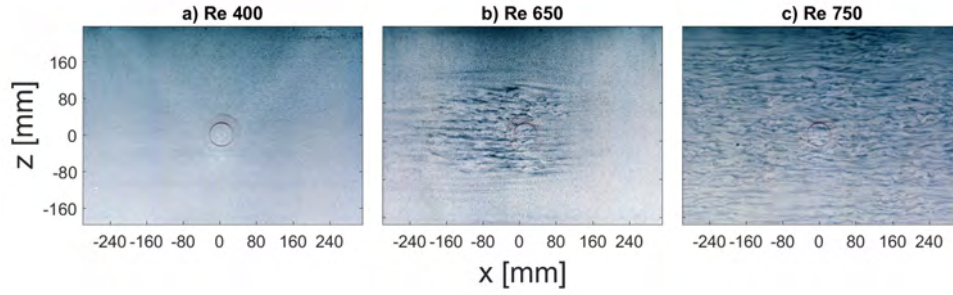
Figure 2: *Visualisations in plane Couette-Poiseuille flow: a) featureless laminar flow for low Reynolds number ($Re = 400$), b) nearly stationary v-shaped turbulent spot in transient regime ($Re = 650$), c) uniform turbulent state ($Re = *750$).*
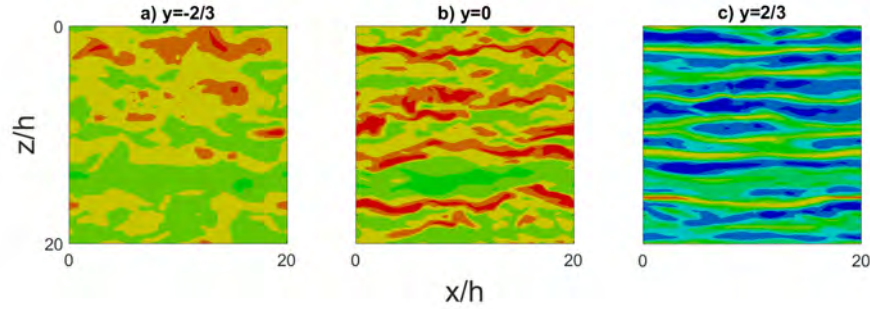

Figure 3: *Streamwise velocity fluctuations in plane Couette-Poiseuille flow in fully turbulent flow: a) near the stationary wall, b) at the center plane (plane Poiseuille region), c) near the moving wall (plane Couette region)*

higher Reynolds numbers we observe a nearly stationary v-shaped turbulent spot which is very slowly advected through the test section (fig.2b). The coexistence of laminar and turbulent phases is observed. Finally for high enough Reynolds numbers the turbulent region occupies most of the test section (fig.2c). To our knowledge this is the first time when turbulent spots in plane Couette-Poiseuille flow are observed and when the advection velocity of turbulent structures in a flow with non-zero pressure gradient is so drastically reduced.

Building on this, we also introduce a finite-size perturbation (localized in space but permanent) to investigate a forced transition to turbulence. We calculate an averaged spectrum k_z using a continuous wavelet transform. The wavenumber k_z is related to the spacing of the streamwise vortices, which dominate the turbulent region (as can be seen in fig.2a,b). We observe two different scales: $k_z = 0.68[cm^{-1}]$ for low Reynolds number ($Re = 200$) and $k_z = 0.54[cm^{-1}]$ for high Reynolds number ($Re = 520$). The former and the latter are associated with the plane Couette and Poiseuille regions respectively.

In addition we show numerical simulations in fully turbulent plane Couette-Poiseuille flow. In fig.3 we present the instantaneous streamwise velocity deviations from the base flow. Indeed the streak spacing near the moving wall (namely in Couette region, fig.3c) is different than near the center plane (Poiseuille region, fig.3b). Near the stationary wall the signature of streaks is less pronounced (fig.3a).

Finally, we determine the evolution of the spanwise and streamwise dimensions of turbulent spots as Reynolds number is varied.

References

[1] Lemoult, G. Étude expérimentale de la transition vers la turbulence dans l'écoulement de Poiseuille plan. (PhD thesis, in french, 2013).

[2] Daviaud, F., Hegseth, J., Bergé, P. Subcritical transition to turbulence in plane Couette flow. *Phys. Rev. Lett.* 69, 2511–2514 (1992).

[3] Dauchot, O. and Daviaud, F. Finite-Amplitude Perturbation in Plane Couette Flow. *EPL* 28, 225 (1994).

[4] Tillmark, N. and Alfredsson, P. H. Experiments on transition in plane Couette flow. *Journal of Fluid Mechanics* 235, 89–102 (1992).

[5] Bergström, L. B. Nonmodal growth of three-dimensional disturbances on plane Couette–Poiseuille flows. *Physics of Fluids* 17, 014105 (2005).

ORIGINATION OF WAVE PACKETS AT LOCALIZED STREAKS

Mikhail Katasonov[1a)], Victor Kozlov[12]

[1] *Khristianovich Institute of Theoretical and applied Mechanics, SB RAS, Novosibirsk, Russia*
[2] *Novosibirsk State University, Novosibirsk, Russia*

<u>*Summary*</u> Turbulence production processes in gradient boundary layer have been studied experimentally. The longitudinal localized disturbances arising in the boundary layer under the action of free-stream turbulence were artificially modeled using a blowing-suction technique. Wave packets, or forerunners, produced in the boundary layer, in the region preceding the abrupt local change of flow velocity near the longitudinal disturbance fronts, were examined. The results of the study make reason to consider the forerunners as wave packets of 3D instability (T-S) waves. It was observed that the forerunners are strongly amplified in the adverse pressure gradient flow. It was found that at downstream development of the forerunners they transform into so - called Lambda-structures.

INTRODUCTION

Researches of a bypass transition problem, whose scenario was proposed by Morkovin in 1984 [1] are still actual. Much attention has been given to the study of longitudinal localized disturbances, or localized streaks, arising in boundary layer under the action of high or enhanced level of free-stream turbulence. Such localized streaks create conditions for the development of high-frequency wave disturbances (secondary instability, wave packets) that can subsequently transform into turbulent spots; as a result, the boundary-layer flow changes its state from laminar to the turbulent [2]. At the same time, the mechanism of formation of secondary unstable oscillations is still far from complete understanding. In this study, it was shown experimentally that the longitudinal localized disturbances can be a source of localized wave packets leading to turbulence.

Experiments under natural conditions fail to give exhaustive answers to posed questions because the emergence of boundary-layer disturbances is a stochastic process, and in most cases it is almost impossible to trace the origin and subsequent evolution of a particular disturbance. For a detailed study, the localized streaks are artificially modeled in boundary layer. In [3] it has been shown that in the boundary layer it is possible to simulate the longitudinal localized disturbances with characteristics close to natural. In [4] it has been shown that the amplitude of the streamwise velocity defect due to the presence of the longitudinal localized streaks can reach about 40 percent of free stream velocity; however, it does not lead to origination of turbulent spots. As it turned out, in these experiments, sufficient conditions for the appearing of instabilities (high-frequency wave packets evolving into the turbulent spots) were not provided. In the present study we show the conditions under which the instability is formed.

WIND TUNNEL EXPERIMENTS

The experiments [5] show that in the vicinity of the leading and rear edges of localized streaks the unstable high-frequency wave packets (denoted below as forerunners) can appear. The forerunners were obtained as a consequence of an impact of a rectangular flow pulse on the boundary layer. In nature, an impact of the local disturbance from free stream on the boundary layer occurs. The rectangular pulse front consists of a continuous disturbance frequency spectrum, of which the most unstable disturbances are enhanced by the boundary layer. In previous experiments the behaviors of the artificial localized streaks and the Tollmien–Shlichting (TS) wave packets in flat plate Blasius boundary layer were studied. The localized streaks were artificially modeled from the incoming flow or wing surface using a blowing-suction technique. It was found that the magnitude of $\partial u/\partial t$ of the localized streaks, which was varied, is a critical factor in generating high-frequency wave packet near the edge of the localized streak. Damping the local streamwise velocity gradient at the edge of the localized streak prevents the formation of the forerunners.

Present investigations were carried out in the subsonic low-turbulent wind tunnels T-324 and MT-324 ITAM SB RAS. Free stream velocity was in the range $4 \leq U_\infty \leq 6$ m/s at the turbulence level at varied from 0.04 to 0.18 %. Test model was s straight wing (see figure 1). The blowing-suction method was used to introduce longitudinal localized structures into the boundary layer through a thin slot arranged in the surface parallel to the leading edge, or from the incoming flow using thin pipe, located at 3 mm upstream of the model nose. Measurements of the flow fields were carried out using a single-wire probe of a constant-temperature hot-wire anemometer.

Typical time traces and flow fields of localized disturbance propagation downstream are presented on figure 2 and figure 3 respectively. Those pictures are demonstrate an appearance and development of the wave packet (forerunner) near the leading and trailing front of artificial localized structure. Forerunner is clearly seen from $X/C_1=0.48$ for the leading front and from $X/C_1=0.83$ for the trailing front at figure 2; at figure 3 for $X/C_1=0.62$ at t=100 ms - leading front and for $X/C_1=0.83$ at 100<t<150 ms - leading front and at 400<t<450 ms - trailing front.

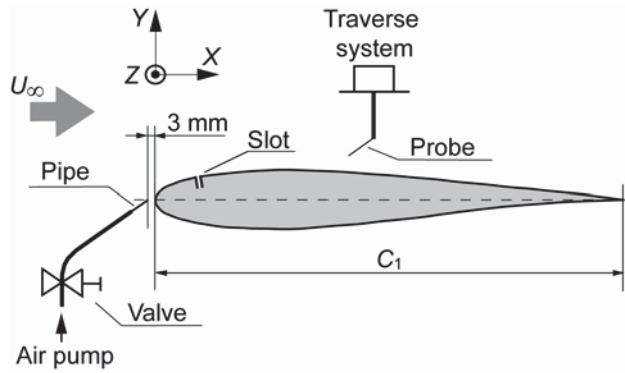[a)] Corresponding author. Email: mikhail@itam.nsc.ru**.**

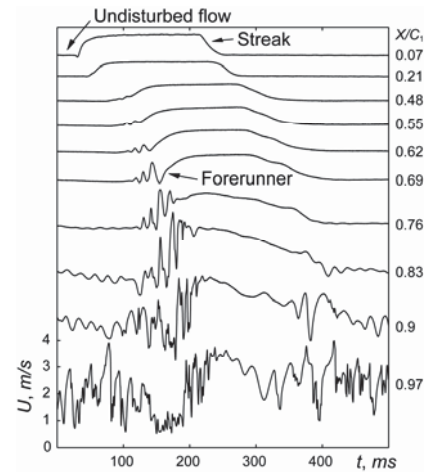Figure 1: Experimental geometry. C_1 = 290 mm. Angle of attack, α = -1.2^0.

Figure 2: Time traces of the hot-wire signal inside the boundary layer at Z=40 mm. Y=Y_{umax}.
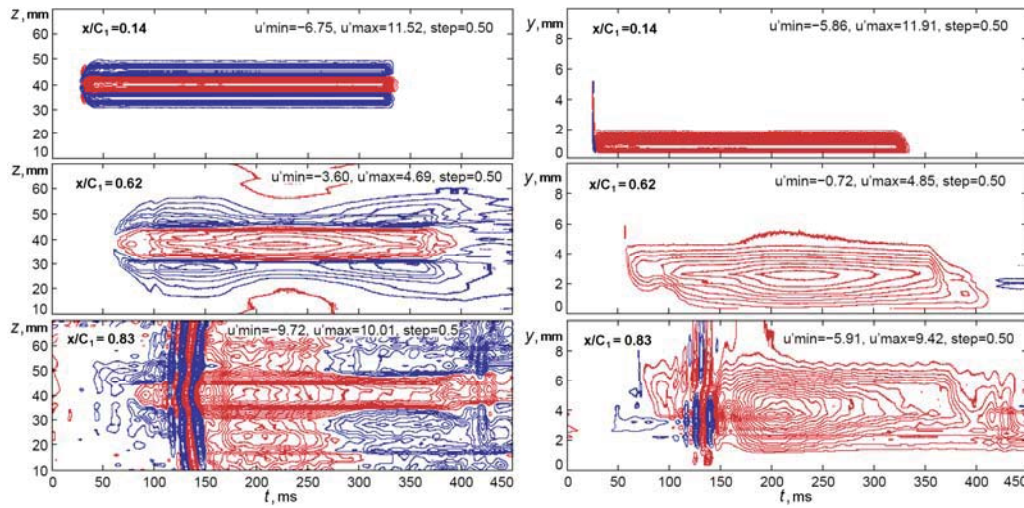

Figure 3: Space evolution of the streak; isolines of longitudinal component of velocity fluctuations. U_∞=3.2 m/s. Z-t plane is plotted at $Y_{(umax)}$ and Y-t plane at Z=40 mm.

CONCLUSIONS

The localization of longitudinal perturbations in space, namely, the presence of a large local velocity gradient near the front/rear front is a necessary condition of the occurrence of wave packets. The results of the study confirm that the forerunners are wave packets of 3D instability (T-S) waves. It was observed that the forerunners are strongly amplified in the adverse pressure gradient flow. It was found that at downstream development of the forerunners they transform into so-called Lambda-structures.

References

[1]   Morkovin M. V. Bypass Transition to Turbulence and Research Desiderata, Transition in Turbines, *NASA-CP-***2386**, 1984
[2]   Katasonov M.M., Park S.-H., Sung H.J., Kozlov V.V. Instability of streaky structures in a Blasius bound. layer *Exper. Fluids*. **V38.3**:363-371, 2005.
[3]   Westin K.J.A., Bakchinov A.A., Kozlov V.V., Alfredsson P.H. Experiments on localized disturbances in a flat plate boundary layer. Pt 1. The receptivity and evolution of a localized free stream disturbances *Eur. J. Mech./Fluids*. **V17**:823-846, 1998.
[4]   Alfredsson P.H., Katasonov M.M. and Kozlov V.V. Generation and development of "passive" disturbances in the Blasius boundary layer.*Thepoph. and Aeromech*. **V8.3**:337-344, 2001
[5]   Katasonov M.M., Kozlov V.V., Nikitin N.V., Sboev D.S. The emergence and development of localized disturbances in a circular pipe and boundary layer. Novosib.State Univ., Novosibirsk, RIC NSU: 222, 2014 (in Russian)

CHARACTERIZATION AND PREDICTION OF STREAK BREAKDOWN USING MACHINE LEARNING

M. J. Philipp Hack[1] and Tamer A. Zaki [*2]

[1]*Center for Turbulence Research, Stanford University, Stanford, United States*
[2]*Department of Mechanical Engineering, Johns Hopkins University, Baltimore, United States*

Summary Characteristics of streaks in DNS flow fields of pre-transitional boundary layers are extracted and compared between streaks that induce the formation of turbulent spots via secondary instability and the remainder of the population. The analysis shows that the two classes of streaks differ in a variety of attributes, including their peak amplitude, distance to the wall and size. The data are used in a machine-learning approach to predict transition to turbulence. An artificial neural network identifies the streaks that will induce the formation of turbulent spots. The method is shown to achieve high prediction accuracy at low computational cost which makes the approach suitable for real-time applications.

INTRODUCTION

In bypass breakdown to turbulence, the pre-transitional boundary layer is characterized by the presence of highly energetic streaks. By introducing inflection points in the instantaneous velocity profile, the streaks promote the amplification of secondary instabilities which ultimately trigger the formation of turbulent spots [1, 2]. Recently, it was demonstrated in Ref. [3] that linear instability analysis applied to cross-flow planes from DNS time series is able to accurately capture the properties of the instabilities such as their growth rate and phase speed. The most unstable eigenfunctions identified the specific streaks that transition to turbulence farther downstream. The work also demonstrated that while the streak amplitude is an important factor, other properties such as their shape and distance to the wall are relevant as well. A visualization of the bypass process in
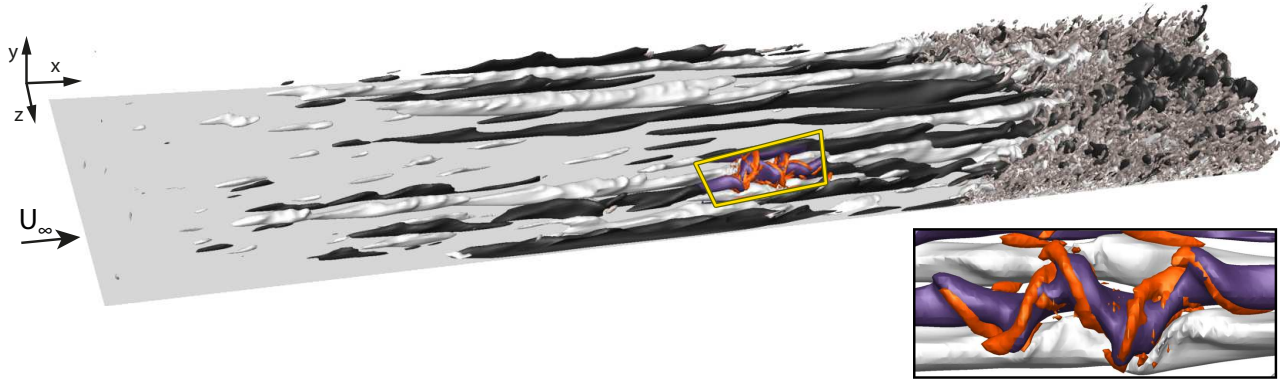

Figure 1: Transitional boundary layer with isosurfaces of low-speed and high-speed streaks and fully turbulent flow downstream with isosurfaces of the λ_2 vortex identification criterion. Enlarged detail: Low-speed streak with sinuous secondary instability.

a boundary layer is presented in figure 1. Only a small fraction of the entire streak population actively promotes the transition process by amplifying secondary instabilities that eventually spawn a turbulent spot. The present work aims to characterize the population of streaks in pre-transitional boundary layers. Streaks that break down into turbulent spots are differentiated from the remainder of the population. This information is used in a machine-learning approach to identify unstable streaks.

ATTRIBUTES OF BOUNDARY-LAYER STREAKS

The properties of the streaks are extracted in cross-planes of the DNS time series (figure 2). Features such as the peak streamwise and wall-normal velocity fluctuations, and the cross-sectional area are considered. Overall, 4,000 DNS snapshots are analyzed and provide about 30,000 data samples of individual streaks, 300 of which are unstable. Discrimination between stable and unstable streaks is achieved by tracking streaks in time and associating them with the formation of turbulent spots. PDFs of attributes of both classes are presented in figure 3. The streamwise and wall-normal velocity fluctuations show the most pronounced difference with an increase in the mean of the distribution by 80 and 155 percent, respectively.

The representation of each streak by a set of features yields a significant compression of the information contained in the DNS fields. By using these low-dimensional data as inputs to an artificial neural network (ANN), an effective and reliable classification scheme for stable and unstable streaks can be devised. In general, artificial neural networks are universal approximators which can represent any continuous, smooth function.

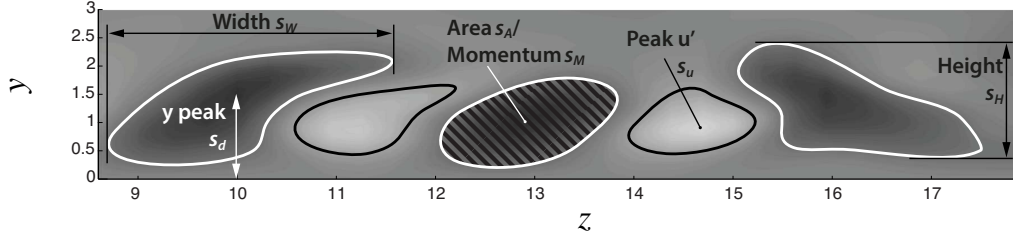[*]Corresponding author. Email: t.zaki@jhu.edu

Figure 2: Streak features in cross-flow plane. Background contours give the streamwise velocity fluctuation, u'. Contour lines indicate $u' = 0.05$ (black) and $u' = -0.05$ (white).
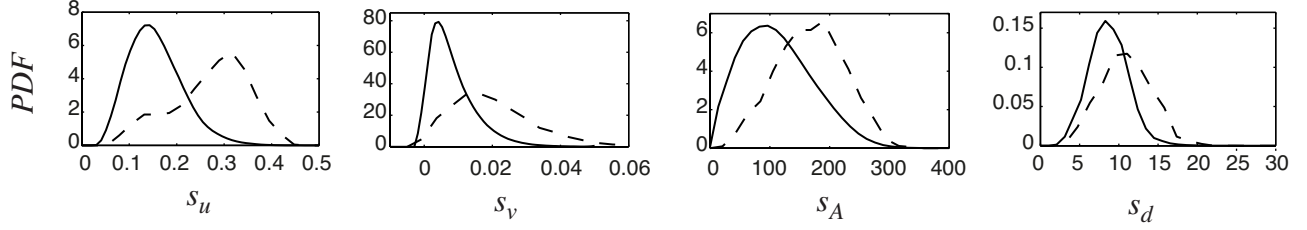

Figure 3: Probability density functions of streak features. Stable streaks (solid) and streaks inducing breakdown (dashed). Left to right: Peak streak amplitude, peak wall-normal fluctuation, cross-sectional area, wall distance of peak streak amplitude.

PREDICTION OF STREAK BREAKDOWN

Features are collected from streaks at 18 equidistant cross planes in the region $200 < Re_\theta < 350$. The performance of the neural network is evaluated using an independent test data set obtained from a second DNS time series of the same duration. The relative prediction accuracy is defined as $\mathcal{A} \equiv \frac{1}{M} \sum_{m=1}^{M} 1 - |\mathcal{P}_m - \mathcal{T}_m|$, where $\mathcal{P}_m$ is the prediction made by the neural network and $\mathcal{T}_m$ is the target value (1 for unstable streaks and 0 otherwise) of the m-th streak. Figure 4(a) shows the accuracy obtained with the ANN when using a single input feature. The peak wall-normal velocity fluctuation is the most significant indicator and leads to an identification accuracy of stable and unstable streaks of approximately 75 percent. The reliability of the approach can be further enhanced by combining inputs (figure 4b). Starting with the peak wall-normal fluctuation, other features are added in the order of their relevance when used as single input feature. The best prediction accuracy, $\mathcal{A} \approx 92\%$, is achieved when all available input features are combined.
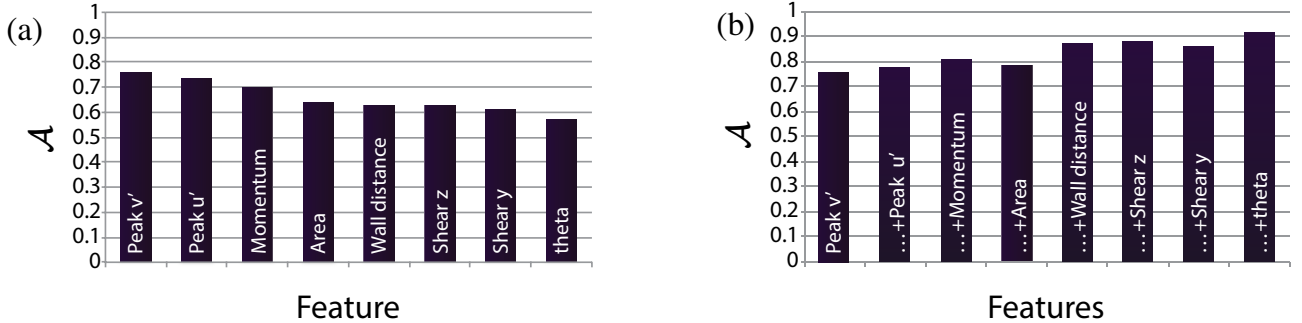

Figure 4: Prediction accuracy $\mathcal{A}$ of the neural network. (a) Single input feature. (b) Accumulated input features.

The computational cost for the classification of a single streak is several orders of magnitude lower than the solution of the eigenvalue problems which arise in classical linear stability theory. In addition to accurately identifying unstable streaks, computational efficiency is thus another significant advantage of the ANN approach. Finally, the network trained with ZPG data can be generalized to make predictions in more complex configurations, e.g. in the presence of pressure gradients.

References

[1] P. Andersson, L. Brandt, A. Bottaro, and D. S. Henningson. On the breakdown of boundary layer streaks. *J. Fluid Mech.*, 428:29–60, 2001.

[2] N. J. Vaughan and T. A. Zaki. Stability of zero-pressure-gradient boundary layer distorted by unsteady Klebanoff streaks. *J. Fluid Mech.*, 681:116–153, 2011.

[3] M. J. P. Hack and T. A. Zaki. Streak instabilities in boundary layers beneath free-stream turbulence. *J. Fluid Mech.*, 741:280–315, 2014.

MS02 - Fluid Active Matter

COLLECTIVE DYNAMICS OF CONFINED BACTERIAL SUSPENSIONS

Raymond E. Goldstein*

Department of Applied Mathematics and Theoretical Physics, University of Cambridge, Cambridge, United Kingdom

Summary It is now well-established that laterally unbounded dense suspensions of motile bacteria can exhibit collective behaviour consisting of transient, recurring vortices and jets on scales large compared to the individual cells. Recently, through a combination of theoretical and experimental work, attention has focused on the effects of confinement on such dynamics, with the discovery that in sufficiently small circular domains there can be spontaneous circulation in the form of a spiral vortex. Subsequently it has been shown that lattices of interconnected domains can exhibit ordered patterns that are, by analogy to magnetic systems, ferro- or antiferromagnetic depending upon details of the coupling between adjacent domains. In this talk I present an overview of these systems and highlight very recent work on the role of 'edge currents' of bacteria in organizing the large-scale patterns.

Since the discovery [1] that concentrated suspensions of the aerobic bacterium *B. subtilis* exhibit collective behaviour characterized by the formation of large, transient vortices and jets, there has been intense interest in the mechanisms that create such flows. Considerable attention has been paid to the possibility that long-range hydrodynamic interactions set up by the stresslet flow fields surrounding individual swimming cells are the ultimate cause of these patterns, which constitute an intriguing form of low Reynolds number turbulence [2]. Motivated by phenomena in cytoplasmic streaming, it was conjectured [3] and then verified experimentally [4] that confining such a system in a sufficiently small, quasi-two-dimensional domain would lead to spontaneous circulation in the form of a spiral vortex. One striking and unexpected result to come from the experimental study was that there is a thin layer of cells at the domain boundary that appear to swim in a direction opposite to the interior bulk flow. A subsequent study [5] using a double-label fluorescence method to visualize separately the cell body and flagella revealed that the cells in the vortex actually swim upstream against the flows set up in the boundary layer, and computational studies of a discrete model of swimming cells revealed the crucial role of long-range hydrodynamic interactions in the phenomenon. These results led to the question of how the cells would organize if confined to two circular domains connected by a narrow neck through which edge currents might pass. Systematic study [6] of lattices of such connected domains revealed that both ferromagnetic and antiferromagnetic order are possible depending upon the lattice structure and the neck width. Returning to the simpler geometry of a channel, it is possible to see in detail [7] how the interplay between edge currents and the tendency toward vortex formation compete to determine the observed flows.

References

[1] "Self-Concentration and Large-Scale Coherence in Bacterial Dynamics", Christopher Dombrowski, Luis Cisneros, Sunita Chatkaew, John O. Kessler, and Raymond E. Goldstein, *Physical Review Letters* **93**, 098103 (2004).

[2] "Fluid Dynamics of Bacterial Turbulence", Jörn Dunkel, Sebastian Heidenreich, Knut Drescher, Henricus H. Wensink, Markus Bär, and Raymond E. Goldstein, *Physical Review Letters* **110**, 228102 (2013).

[3] "Spontaneous Circulation of Confined Active Suspensions", Francis G. Woodhouse and Raymond E. Goldstein, *Physical Review Letters* **109**, 168105 (2012).

[4] "Confinement Stabilizes a Bacterial Suspension into a Spiral Vortex", Hugo Wioland, Francis G. Woodhouse, Jörn Dunkel, John O. Kessler, and Raymond E. Goldstein, *Physical Review Letters* **110**, 268102 (2013).

[5] "Fluid Flows Created by Swimming Bacteria Drive Self-Organization in Confined Suspensions", Enkeleida Lushi, Hugo Wioland, and Raymond E. Goldstein, *Proceedings of the National Academy of Sciences USA* **111**, 9733 (2014).

[6] "Ferromagnetic and Antiferromagnetic Order in Bacterial Vortex Lattices", Hugo Wioland, Francis G. Woodhouse, Jörn Dunkel, and Raymond E. Goldstein, *Nature Physics* **12**, in press (2016).

[7] "Directed Collective Motion of Bacteria Under Channel Confinement", Hugo Wioland, Enkeleida Lush, and Raymond E. Goldstein, submitted (2016).

*Email: R.E.Goldstein@damtp.cam.ac.uk

HYDRODYNAMIC COOPERATIVITY AND SELF-ORGANIZATION IN ACTIVE SUSPENSIONS

Ignacio Pagonabarraga[*1]

[1]*Department of Fundamental Physics, University of Barcelona, Av. Diagonal, 645, 08028 Barcelona (Spain)*

Summary I will discuss the role that hydrodynamic coupling, through self propulsion and active stress generation, has in the collective motion of suspensions of self-propelled particles. I will exploit a powerful mesoscopic computational approach to reach the large length and time scales required to sample the spontaneous structures in which these suspensions self-organize. I will describe the appearance of stable cluster phases sustianed only through hydrodynamics and will describe their main features.

Active systems generate motion due to energy consumption, usually associated to their internal metabolism or to appropriate, localized, interfacial chemical reactivity. As a result, these systems are intrinsically out of equilibrium and their collective properties result as a balance between their direct interactions and the indirect coupling to the medium in which they displace. Therefore, a dynamical approach is required to analyze their evolution and quantify their selfassembly and ability to generate intermediate and large scale stable structures.

There has been significant advances in recent years to understand the basic physical mechanisms that control the collective behavior of self-propelled particles and their connection with effective, equilibrium counterparts. The role of the mobility and its coupling to the preferential direction of motion has emerged as a key player to understand how collections of self-propelled particles move and self-organize. In many circumstances self-propelled particle swim and move inside a fluid environment. The role of the medium in the collective behavior of such systems remains less well understood. In particular, the effect it may have modulating or modifying the understood mechanisms for self-assembly in their absence has not been properly addressed.

The use of computational models that couple individually-resolved self-propelling particles and the continuum solvent in which they move provides a useful means to analyze and quantify the properties of spontaneous emerging structures. I will describe how to take advantage of these coarse grained computational methods that capture the essence of activity generation and the appropriate hydrodynamic coupling when ensembles of active particles move together. I will analyze the relevant physical mechanisms underlying the specific properties of the collective behavior of model active suspensions. By focusing on simplified models, it is possible to identify the relevant parameters which control such behavior. Understanding the mechanical principles which determine the emergence of cooperativity will provide a solid basis to clarify the role of hydrodynamics in active materials and understand how to combine them with biochemical interactions to control their properties and behavior.

[*]Corresponding author. Email: ipagonabarraga@ub.edu

COLLECTIVE BEHAVIOR OF ACTIVE-PARTICLE SUSPENSIONS

Adam Wysocki[1], Masoud Abkenar[1], Thorsten Auth[1], Roland G. Winkler[1], and Gerhard Gompper[*1]

[1]*Theoretical Soft Matter and Biophysics, Institute of Complex Systems, Forschungszentrum Jülich, Germany*

Summary Active, self-propelled particles in suspension generically exhibit motility-induced clustering and phase-separation. A closer look reveals a pronounced dependence on particle shape and alignment interactions, hydrodynamic interactions, and noise strength. Mesoscale simulations of large ensembles of such particles help to unravel the complex dynamical behaviors of such systems. A rich variety of emergent collective behaviors is observed, ranging from motile polar clusters to jets, swirls, and travelling fronts.

ARGGREGATION AND DYNAMICS OF SELF-PROPELLED PARTICLES

Assemblies of intrinsically active objects represent an exceptional class of non-equilibrium systems. A generic phenomenon in such systems is the emergence of self-organized large-scale dynamical patterns like vortices, swarms, waves, or self-sustained turbulence. This intriguing dynamics is a consequence of the complex interplay of self-propulsion, internal or external noise, and steric and hydrodynamic interactions [1].

We have studied the collective behavior self-propelled rods [2, 3], spheres [4, 5], and beating flagella [6] or cilia [7] by mesoscale computer simulations. For rods, we investigate structure formation of bacterial carpets or motility assays, where the agents can repel and align, but also pass across each other. For spheres, we study aggregation of active colloidal particles without alignment interactions. Clustering appears in all of these different systems. However, in many other aspects, structure formation and collective dynamics strongly depend on the shapes and interactions of the active particles.

Self-Propelled Rods

Due to their excluded-volume interactions, rods align during collisions. This leads to the formation of polar motile custers, which are typically elongated in the direction of rod orientation. Depending on concentration and propulsion velocity, a disordered phase, a small-cluster phase, phase separation between a high-density polar cluster and a low-density disordered phase, and a nematic laning phase are found. However, a phase of travelling waves, as observed experimentally in motility assays, has not been found so far in simulations of self-propelled rods.

Self-Propelled Brownian Spheres

For Brownian spheres, orientation is completely decoupled from particle motion and interactions. Thus, active Brownian spheres have no obvious alignment mechanism. Simulations show that a minimal propulsion strength is required for self-propelled spheres to induce phase separation [5]. Interestingly, active Brownian spheres display the formation of large-scale swirls and jets, see Fig. 1, despite of the absence of an alignment interaction. The origin of this dynamical behavior seems to be an interfacial sorting mechanismi [5]. At the interface, particles are oriented preferentially toward the dense phase, so that they are partially blocked. They can only start to move again after orientational diffusion makes them point parallel to the interface. This implies a collection of particles with the same orientation in concave parts of the interface, which then together push in the same direction.

Mixtures of active and passive Brownian particles

Natural extensions of single-component active Brownian particle (ABP) fluids are mixtures of particles with, e.g., different activities, temperatures, or diameters. We consider mixtures of active and passive Brownian spheres. The emergent dynamics in phase-separated mixtures is studied numerically in two dimensions [8]. A novel steady-state of well-defined traveling fronts is observed, where the interface between the dense and the dilute phase propagates and the bulk of both phases is (nearly) at rest. Two kind of interfaces, advancing and receding, are formed by spontaneous symmtry breaking, induced by an instability of a planar interface due to the formation of localized vortices. Above a threshold in the fraction of active particles, necessary to induce phase separation, the interface velocity decreases linearly with increasing fraction of active particles [8].

CONCLUSIONS

Mesoscale simulations of self-propelled particles provide new insights into the emergent non-equilibrium behavior of active-particle suspensions. It becomes increasingly evident that this non-equilibrium behavior is much more complex than previousy anticipated, and many more interesting phenomena can be expected to be discovered in the near future.

---

*Corresponding author. Email: g.gompper@fz-juelich.de
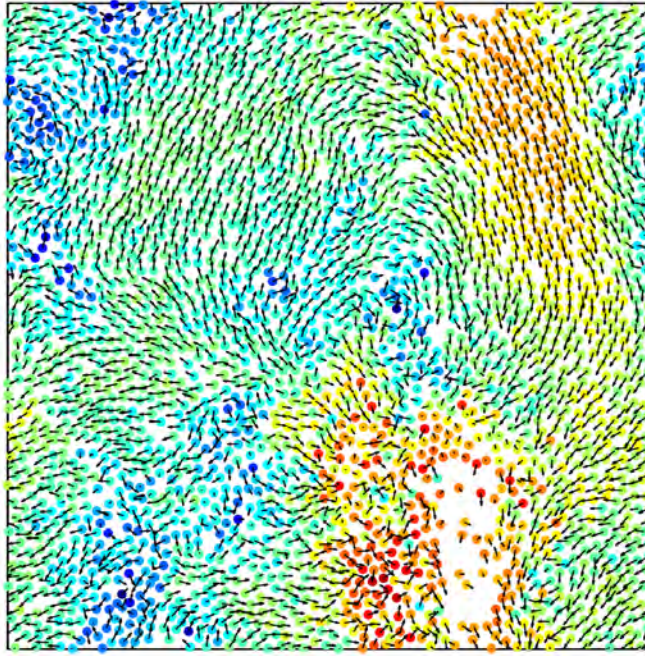
Figure 1: Self-propelled Brownian spheres display phase separation and collective swirl-like motion on large length scales. Particle displacements are shown in a cut through a three-dimensional system with periodic boundary conditions. Red (blue) color indicates large (small) displacements in a fixed time interval.

References

[1] Elgeti J., Winkler R.G., Gompper G.: Physics of Microswimmers – Single Particle Motion and Collective Behavior: a Review. Rep. Prog. Phys. 78:056601, 2015.

[2] Yang Y. , Marceau V., GompperG.: Swarm behavior of self-propelled rods and swimming flagella. Phys. Rev. E 82, 031904, 2010.

[3] Abkenar M., Marx K., Auth T., Gompper G.: Collective behavior of penetrable self-propelled rods in two dimensions. Phys. Rev. E 88:062314, 2013.

[4] Elgeti J., G. Gompper G.: Wall accumulation of self-propelled spheres. EPL 101:48003, 2013.

[5] Wysocki A., Winkler R.G., Gompper G.: Cooperative Motion of Active Brownian Spheres in Three-Dimensional Dense Suspensions. EPL 105:48004, 2014.

[6] Yang Y., Qiu F., Gompper G.: Self-organized vortices of circling self-propelled particles and curved active flagella. Phys. Rev. E 89:012720, 2014.

[7] Elgeti J., Gompper G: Emergence of Metachronal Waves in Cilia Arrays. Proc. Natl. Acad. Sci. USA 110:4470, 2013.

[8] Wysocki A., Winkler R.G., Gompper G.: Travelling fronts in active-passive particle mixtures. arXiv: 1601.00850, 2016.

This paper has been removed from the Congress Proceedings.
Page 1

COPEPOD ESCAPE AND RELOCATION JUMPS IN TURBULENCE

Markus Holzner & François-Gaël Michalec

Institute of Environmental Engineering, ETH Zurich, Zurich, Switzerland

<u>*Summary*</u> We study the swimming behaviour of copepods using three-dimensional particle tracking velocimetry by tracking simultaneously the motion of many organisms and the flow surrounding them. In this work we analyse the jump reaction of the organisms in response to hydrodynamic stress, focusing on the strong escape jumps and the weaker relocation jumps. We find that the two types of jumps are influenced differently by increasing levels of turbulence and hydrodynamic stress. This may be important for their survival and mating performance in dynamic environments

INTRODUCTION

Planktonic copepods live in environments such as oceans and estuaries where they form the largest part of the zooplankton and where flows are typically turbulent. Because of their small size and relatively slow swimming speeds, zooplankton interacts very little with the large features of the flow, but at small scales swimming behaviour can overcome advective transport. Because three-dimensional observations of copepods swimming freely in turbulent flows remain scarce, most of what is known about their behaviour in energetic environments derives from extrapolation of results obtained in still water, where a local disturbance simulating turbulence is introduced [1-3]. Only recently have methods matured to enable the monitoring of many organisms in turbulent flows [4,5] and it has become possible to simultaneously measure the motion of finite sized particles [6] or organisms [7] and the flow surrounding them. In [5], an active response of copepods to background turbulence has been identified that cancels gender specific differences in motion strategy. A modification of escape reactions has been found when organisms were exposed to a contracting flow but no response has been noted in turbulence [7]. Here we focus on the response of copepods to turbulence and analyse relocation and escape jump reactions for varying turbulence intensity.

METHODS

We carried out three-dimensional particle tracking measurements using three synchronized Mikrotron EoSens high speed cameras to track the turbulent flow and one EoSens camera fitted with a four view image splitter to simultaneously track the copepods. The measurements were conducted in a water tank containing a forcing device creating quasi homogeneous and isotropic turbulence [5]. We seeded the flow with neutrally buoyant tracer particles and introduced about 1000 Eurytemora affinis parent individuals obtained from laboratory cultures at Wimereux Marine Station.

RESULTS

The intensities of turbulence produced with our set-up are comparable to characteristic values observed in coastal zones, tidal fronts and estuaries. We observed that copepods do not behave passively even at substantial turbulence intensities. Jumps and swift movements were clearly visible in all our experiments. In particular we observed that both relocation jumps and strong escape jumps are influenced by turbulence intensity.

CONCLUSIONS

This contribution will illustrate the potential of our method to characterize the behavioural response of copepods to local hydrodynamic conditions and to investigate their interactions in complex environments.

References

[1] Kiørboe T., Saiz E., Visser A.: Hydrodynamic signal perception in the copepod Acartia tonsa. *Mar. Ecol. Prog. Ser.* 179, 97–111, 1999.
[2] Fields D.M., Yen J.: The escape behavior of marine copepods in response to a quantifiable fluid mechanical disturbance. *J. Plankton Res.* 19, 1289–1304., 1997
[3] Waggett R.J., Buskey E.J.: Copepod escape behavior in non-turbulent and turbulent hydrodynamic regimes. *Mar. Ecol. Prog. Ser.* 334, 193–198, 2007.
[4] Yen J., Rasberry K.D., Webster D.R.: Quantifying copepod kinematics in a laboratory turbulence apparatus. *J. Mar. Syst.* 69, 283–294, 2008.
[5] Michalec F.G., Souissi S. & Holzner M.: Turbulence triggers vigorous swimming but hinders motion strategy in planktonic copepods. *J. Roy. Soc. Interface*, 12(106), 20150158.
[6] Saha D., Bäbler M.U., Holzner M., Soos M., Lüthi B., Liberzon A. & Kinzelbach W.: Breakup of Finite-Size Colloidal Aggregates in Turbulent Flow Investigated by Three-Dimensional (3D) Particle Tracking Velocimetry. *Langmuir*, 32 (1), 55–65, 2016.
[7] Adhikari D., Gemmell B.J., Hallberg M.P., Longmire E.K. & Buskey E.J.: Simultaneous measurement of 3D zooplankton trajectories and surrounding fluid velocity field in complex flows. J. Exp. Biol., 218(22), 3534-3540, 2015.

TRANSITION TO SPONTANEOUS DIRECTIONAL FLOWS IN CONFINED ACTIVE FLUIDS

Maxime Theillard[1], Barath Ezhilan[1], and <u>David Saintillan</u>[*1]

[1]*Department of Mechanical and Aerospace Engineering, University of California San Diego, 9500 Gilman Drive, La Jolla, CA 92093, USA*

Summary Recent experimental, theoretical and computational studies have shown that confinement can profoundly affect self-organization in concentrated active suspensions leading to striking features such as formation of steady and spontaneous vortices in radial confinement. Motivated by these observations, we study the two-dimensional dynamics in a confined suspension of biologically active particles using a mean-field kinetic theory for which we developed a novel numerical solver. The dynamics in both circular and racetrack geometries are investigated, where we show that the interplay of confinement and activity can stabilize collective motion into spontaneous flowing states, including steady vortices, unidirectional motion, and travelling waves. Our simulation results are also shown to compare favorably with predictions from a linear stability analysis.

INTRODUCTION

Recent years have seen significant developments in the understanding of the emergence of collective motion in biologically active suspensions. There is widespread consensus that self-organization in such suspensions are driven by the stresses exerted by the active particles on the fluid as they propel themselves [1, 2]. Continuum kinetic theories,where a Smoluchowski equation for the probability distribution of the active particle positions and orientations is coupled to the Stokes equation for the flow arising from the active stresses is a powerful approach for understanding active fluids [3], in which the emergent behavior in active systems is viewed as a breakdown of stability of the various equilibrium states. While most of the mean-field based studies have focussed on unconfined systems, the interplay of confinement and activity has excited much interest recently. Experiments have shown that confinement can stabilize the collective motion into defined patterns such as a double vortex [4, 5, 6]. While various phenomenological models for active liquid crystals have focussed on the effect of confinement on collective behavior and have predicted spontaneous flow transitions, such predictions have yet to be confirmed from a hydrodynamics first-principles perspective.

Our primary motivation for this study are recent experiments [4, 5] and simulations [6] of active fluids in circular confinement. These experiments predicted that when the radius of confinement is below a critical value (or is within a critical range of values), the suspension will spontaneously form a steady single vortex encircled by a counter-rotating boundary layer closer to the wall. Their later particle simulations [6] using a simple model accounting for hydrodynamic and steric interactions reproduced these experimental observations and also clarified details about the cell orientation and swimming direction showing that the cells swim upstream against the flow. A unified picture that provides a complete characterization of the stability properties and non-linear chaotic dynamics of circularly confined active suspensions for different degrees of confinement, strength of activity and propulsion is still lacking, however, and we seek to address these questions using a continuum model and numerical simulations. A striking crucial result of our work is that several of the experimental results in the literature including the double vortex [4, 5, 6] can be captured within the mean-field theory in the complete absence of steric interactions. Hence, this double vortex could simply a result of a coupling between circular confinement and self-generated fluid flows.

KINETIC MODEL

Starting from the Smoluchowski equation for the probability density function $\Psi(\mathbf{x}, \mathbf{p}, t)$ of particle positions and orientations, hierarchical evolution equations for the concentration c, polarization $\mathbf{m}$, and nematic order parameter tensor $\mathbf{D}$ can be obtained [2], which are written in conservative form as:

$$\partial_t c = -\nabla \cdot \mathbf{F}_c, \tag{1}$$

$$\partial_t \mathbf{m} = -\nabla \cdot \mathbf{F}_m + \tfrac{3}{5}\beta \mathbf{E} \cdot \mathbf{m} - \mathbf{W} \cdot \mathbf{m} - 2\mathbf{m}, \tag{2}$$

$$\partial_t \mathbf{D} = -\nabla \cdot \mathbf{F}_D + \tfrac{2}{5}\beta c\mathbf{E} + \tfrac{6}{7}\beta \mathbf{E} \cdot \mathbf{D} + \mathbf{W} \cdot \mathbf{D} - \mathbf{D} \cdot \mathbf{W} - 6\mathbf{D}, \tag{3}$$

where the dimensionless parameter β denotes Bretherton's constant, and where the various fluxes are detailed in [2]. The source terms arise from alignment and rotation by the rate-of-strain and vorticity tensors $\mathbf{E}$ and $\mathbf{W}$ of the disturbance velocity field $\mathbf{u}$, which satisfies the incompressible Navier-Stokes equations forced by the divergence of the active stress tensor $\alpha\mathbf{D}$:

$$\nabla \cdot \mathbf{u} = 0, \quad Re\left(\partial_t \mathbf{u} + \mathbf{u} \cdot \nabla\mathbf{u}\right) = -\nabla p + \nabla^2\mathbf{u} + \alpha\nabla \cdot \mathbf{D}. \tag{4}$$

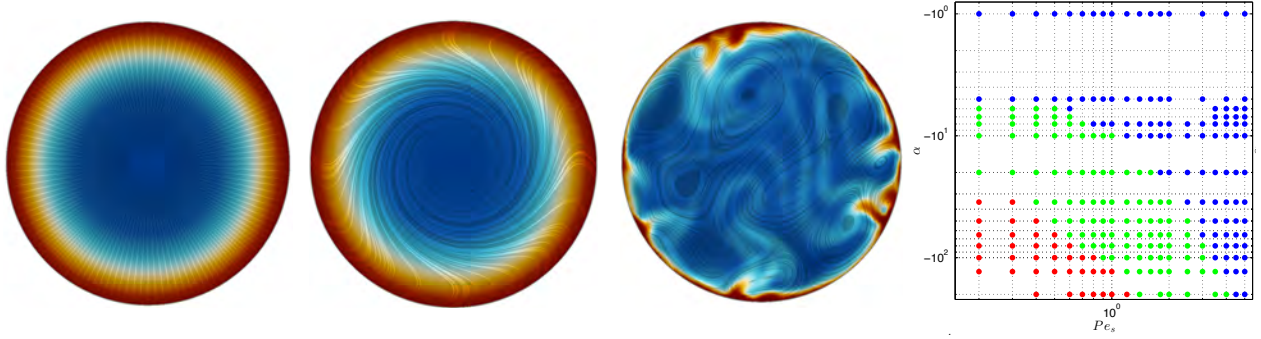[*]Corresponding author. Email: dstn@ucsd.edu

Figure 1: Left: typical simulations in circular geometries, illustrating the three observed phases: quiescent equilibrium distribution with wall accumulation; double vortex flowing state; chaotic motion. Right: phase diagram illustrating the transition between phases (blue: equilibrium; green: vortex; red: chaos).

Upon non-dimensionalization, the equations are governed by four dimensionless parameters:

$$Re = \frac{\rho H^2 d_r}{\mu}, \quad Pe = \frac{V_s}{2 d_r H}, \quad \alpha = \frac{\sigma_0 n}{\mu d_r}, \quad \Lambda = \frac{d_r d_t}{V_s^2}. \tag{5}$$

In particular, the swimming Péclet number Pe denotes the ratio of the persistence length of swimmer trajectories to the size of the domain and is a measure of confinement. The activity parameter α compares the destabilizing effects of active stresses and of concentration to dissipative processes, namely viscosity and orientation decorrelation by rotational diffusion. The equations are solved numerically using an adaptive finite-volume algorithm on quad-tree grids.

RESULTS

Typical simulation results in circular confinement are illustrated in Figure 1 and exhibit the same phenomenology as in experiments [5]. In very strong confinement (or at low activity/concentration), the distribution is axisymmetric and shows wall accumulation with wall-normal polarization and zero flow. As confinement decreases or activity increases, a transition to a double vortex state similar to that reported in experiments is observed. Finally, at very high levels of activity, the steady vortex destabilizes leading to chaotic dynamics akin to those in bulk systems [3]. Figure 1 also shows a phase diagram in terms of Pe and α.

We also simulation dynamics in periodic racetrack geometries, where a transition from equilibrium to spontaneous unidirectional flow with net pumping is observed (not shown). Upon increasing activity, the formation of traveling concentration waves is also reported in agreement with recent experiments on dense sperm suspensions [7] We further elucidate this transition to unidirectional flow by performing a linear stability analysis in a periodic channel geometry, which provides the marginal curve for the transition and compares favorably with our simulations.

References

[1] Marchetti, M. C., Joanny, J.-F., Ramaswamy, S., Liverpool, T. B., Prost, J., Rao, M. & Simha, R. A. Hydrodynamics of soft active matter, *Rev. Mod. Phys.* **85** 1143 (2013).

[2] Saintillan, D. & Shelley, M. J. Active suspensions and their nonlinear models, *C. R. Physique* **14** 497 (2013).

[3] Saintillan, D. & Shelley, M. J. Instabilities, pattern formation, and mixing in active suspensions, *Phys. Fluids* **20** 123304 (2008).

[4] Woodhouse, F. G. & Goldstein, R. E. Spontaneous circulation of confined active suspensions, *Phys. Rev. Lett.* **109** 168105 (2012).

[5] Wioland, H., Woodhouse, F. G., Dunkel, J., Kessler, J. O. & Goldstein, R. E. Confinement stabilizes a bacterial suspension into a spiral vortex, *Phys. Rev. Lett.* **110** 268102 (2013).

[6] Lushi, E., Wioland, H. & Goldstein, R. E. Fluid flows created by swimming bacteria drive self-organization in confined suspensions, *PNAS* **111** 9733 (2014).

[7] Creppy, A., Plouraboue, F., Praud, O, Druart, X. & Cazin, S. Symmetry breaking phase transitions in highly concentrated semen (submitted).

EFFECTIVE INTERACTIONS BETWEEN CHEMICALLY ACTIVE COLLOIDS AND SURFACES

Mihail N. Popescu* [1,2], William Uspal[1,2], Mykola Tasinkevych[1,2], and Siegfried Dietrich[1,2]

[1]*Max Planck Institute for Intelligent Systems, Stuttgart, D-70569, Germany*
[2] *IV. Institut für Theoretische Physik, Universität Stuttgart, Pfaffenwaldring 57, D-70569 Stuttgart, Germany*

Summary Micron-sized particles moving through solution by using self-generated chemical gradients serve as model systems for studying active matter. The self-generated hydrodynamic and chemical fields, which induce particle motion, probe and are modified by the environment, including its boundaries. We show that near a hard planar wall such a particle may exhibit motion with a steady orientation and height above the wall, or motionless, steady "hovering". Furthermore, when also chemi-osmotic hydrodynamic flow at the wall is induced, we predict that the interplay between this and the self-diffusiophoretic one can be "tuned" by chemical patterning of the wall such that one can achieve controlled motion of the active particle, e.g., the particle following a chemical stripe.

MODEL

The model system we consider is shown in Fig. 1 (left panel). A spherical particle of radius R, covered by a catalyst over a spherical cap region parametrized by ψ (black segment in Fig. 1, left panel), is suspended in a Newtonian liquid solution bounded by a planar wall. The catalytic cap releases a solute which diffuses in the solution. The particle and the wall are impenetrable to the solute and solvent. There are additional interactions, of range $\delta \ll R$, between the solute and the particle surface, as well as between the solute and the wall. In the absence of thermal fluctuations, and if the wall is chemically uniform, the particle moves only in the plane containing the wall normal and the particle's symmetry axis. In such case, the cap orientation θ and the height h of the particle's center above the wall (see Fig. 1, left panel) completely specify the particle configuration. (If the wall is chemically patterned, a situation discussed in the second part of **Results**, the position and orientation of the particle in respect to the pattern are added to the variables characterizing the configuration.) The translational and angular velocities are denoted by $\mathbf{U}$ and $\boldsymbol{\Omega}$, respectively. The hydrodynamic flow is assumed to have a very small (vanishing) Reynolds number, and the diffusion of the molecular solute is much faster than the transport by advection (small Péclet number). The motion of the sphere is assumed to be sufficiently slow and the diffusion of the solute to be sufficiently fast such that at each instantaneous (h, θ) a quasi-steady state of the solute number density $c(\mathbf{r})$ and of the hydrodynamic flow $\mathbf{u}(\mathbf{r})$, respectively, is established.
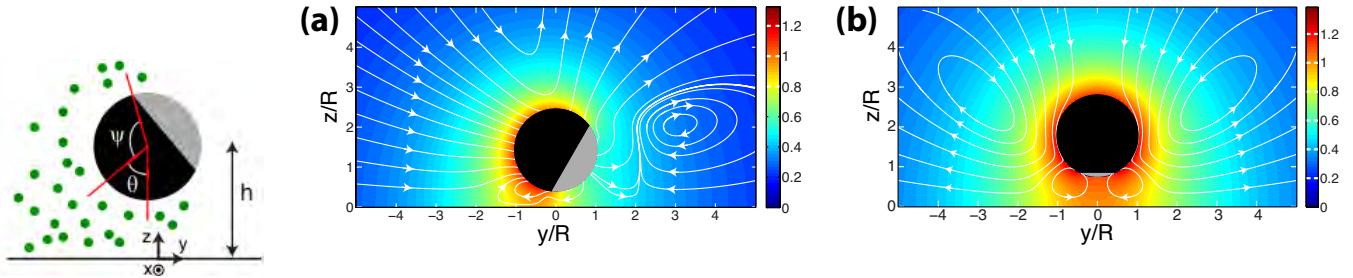

Figure 1: Schematic drawing of a chemically active Janus sphere above a planar wall located at $z = 0$ (left panel). (a) Sliding and (b) hovering steady-states for $b_i = b_w < 0$; the coverage by catalyst is given by $\psi \simeq 114°$ (a) and $\psi \simeq 154°$ (b). Streamlines (white lines) illustrate the flow field in the spatially fixed coordinate system; the color coding represents the solute number density $c(\mathbf{r})$ in units of the characteristic density $c_0 = \mathcal{K}R/D$. (Adapted from Ref. [3].)

$\mathbf{U}$ and $\boldsymbol{\Omega}$ are calculated within the framework of the classical theory of diffusiophoresis [1, 2]. This accounts for the solute-surface interaction via phoretic "mobilities b_k (where $k \in \{i, c, w, s\}$ indicates b can take different values at the "**i**nert" or "**c**ap"regions of the particle, as well as at the **w**all or **s**tripe), which are connecting the surface-gradients of solute density with "phoretic slip" hydrodynamic boundary condition at the corresponding surfaces: $\mathbf{v}_s(\mathbf{r}) = -b_k \nabla_{||} c(\mathbf{r})$. The signs and magnitude of b_i and b_c determine the direction of motion (catalyst- or inert-face forward). The Lorentz theorem is applied in order to reduce the complexity of the hydrodynamic problem [1, 3]. The Laplace equation with uniform particle flux $\mathcal{K}$ over the cap region of the particle (accounting for the activity), which governs the distribution of solute molecules) and the incompressible Stokes equations, governing the hydrodynamics, are solved numerically using the Boundary Element Method (BEM) (see details in Ref. [3]). For both problems (diffusion and hydrodynamics), approximate analytical expressions are obtained by employing the standard point-singularities representation of the solution [3, 4]. The rigid-body overdamped motion of the spherical colloid follows straightforwardly from the translational and angular velocities $\mathbf{U}$ and $\boldsymbol{\Omega}$.

*Corresponding author. Email: popescu@is.mpg.de

RESULTS

The case of a no-slip wall ($b_w \equiv 0$)**.** In this situation, the no-slip hydrodynamic boundary condition applies at the wall. The sole role played by the wall is that of reflecting back the density and hydrodynamic fields. By analyzing the dynamics in the phase-plane (h, θ), we have established that certain steady-states of motion at fixed height h^* above the wall and with fixed orientation θ^* of the symmetry axis of the colloid, and which are stable attractor points for the dynamics in the (h, θ) plane, can emerge. The values h^* and θ^* depend on the coverage parameter ψ as well as on the phoretic mobilities b_i and b_c at the inert and catalytic regions, respectively. Figs. 1(a) and (b) illustrate the distribution of solute and the hydrodynamic flow for two examples of such steady states: (a) "sliding" (fixed height and fixed orientation $\neq$ the direction normal to the wall) and (b) "hoverer" (motionless particle at a fixed height above the wall, steadily pumping the surrounding fluid). Such states stem-out from a complex feeback-loop: the coupling of the wall-induced chemical gradients to changes in the distribution of phoretic slip on the particle surface gives rise to a hydrodynamic flow that does not rotate the particle once in configuration (h^*, θ^*).

The case of osmotic-flow response at the wall ($b_w \neq 0$)**.** Here we focus on a particle with half of the surface catalytically active (i.e., $\psi = \pi/2$), "sliding" above the substrate at a fixed height h and orientation $\theta \simeq \pi/2$; i.e., the particle axis $\hat{\mathbf{d}}$ is parallel to the wall. As an example of chemically patterned wall we choose a chemical stripe (see Fig. 2), i.e., $b = b_s$ on the stripe and $b = b_w \neq b_s$ on the rest of the wall. The linearity of the Stokes equation allows to write the translational and angular velocity of the particle $\mathbf{U}$ and $\mathbf{\Omega}$, respectively, as $\mathbf{U} = \mathbf{U}^{sd} + \mathbf{U}^w$ and $\mathbf{\Omega} = \mathbf{\Omega}^w$, where the superscripts indicate the contributions from *self-d*iffusiophoresis (phoretic slip at the wall set to zero) and from the *w*all (phoretic slip on the particle set to zero), respectively. (the constraints on h and $\mathbf{d}$ imply $\mathbf{\Omega}^{sd} = 0$.) $\mathbf{U}^{sd}$ is treated as a model parameter (since it can be computed separately, following the procedure in the previous Subsection). The wall-slip contributions are calculated using the Lorentz theorem and the BEM method (similar to subsection [4]). Approximate analytical expressions for $\mathbf{U}^w$ and $\mathbf{\Omega}^w$ are obtained by using a reduced set of singularities together with their corresponding images: the monopole and dipole terms for the diffusion equation, the Stokselet or the rotlet for the hydrodynamics (auxiliary problems).
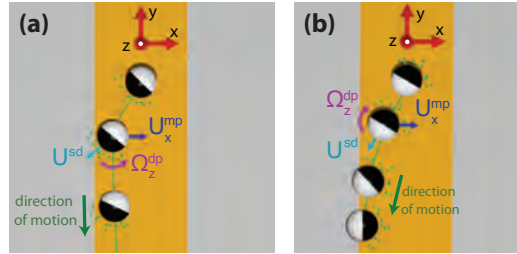

Figure 2: Mechanisms (a) stabilizing and (b) destabilizing, respectively the stripe-bound state of an (a) catalyst-forward and (b) inert-forward particle, respectively [4]. Here $b_w/b_s = 3$. Superscripts mp and dp indicate the monopole and dipole contributions, respectively, to $\mathbf{U}^w$ and $\mathbf{\Omega}^w$.

As shown in Fig. 2, a catalyst-forward moving active particle can follow a stripe: it is attracted to the center and aligns its axis parallel to the edges of the stripe. The attraction to the stripe center is driven by the contribution from the monopolar term U_x^{mp}; at the center, the contributions to U_x^{mp} from the two edges cancel. The alignment of $\mathbf{d}$ with the edges of the stripe is driven by rotations induced by the dipolar contribution U_x^{sd}, which vanish at the aligned state (Fig. 2(a)). In contrast, for an inert-forward particle, edge induced rotations of $\mathbf{d}$ towards a normal-to-the-stripe alignment are enhanced; for sufficiently small U^{sd}, the particle docks (Fig. 2(b)), while for large U^{sd} the particle escapes the stripe region.

CONCLUSIONS

We have shown that by engineering the chemistry of an active particle and that of the near-be wall one can achieve control of the motion of the particle, e.g., constrain the particle to slide along the wall and to follow a chemical stripe.

References

[1] Anderson, J. L.: Colloid Transport by Interfacial Forces. Ann. Rev. Fluid Mech. 21:61-99, 1989.
[2] Golestanian, R., Liverpool, T. B., Ajdari, A.: Designing phoretic micro- and nano-swimmers. New J. Phys. 9:126, 2007.
[3] Uspal, W. E., Popescu, M. N., Dietrich, S., Tasinkevych, M.: Self-propulsion of a catalytically active particle near a planar wall: from reflection to sliding and hovering. Soft Matter 11, 434-438, 2015.
[4] Uspal, W. E., Popescu, M. N., Dietrich, S., Tasinkevych, M.: Guiding catalytically active particles with chemically patterned surfaces. (unpublished)

STOCHASTIC GAIT-SWITCHING IN MOTILE MICROALGAE

Kirsty Y. Wan[1] and Raymond E. Goldstein [*2]

[1]*DAMTP, University of Cambridge, UK*

Summary Self-propulsion by flagella is a significant selective advantage for microorganisms which possess such capabilities. There is great diversity in the number of flagella, their beating modes, and greater still in the ultrastructure of the basal apparatus into which the flagella are inserted. For free-living unicellular eukaryotes with few flagella the question of their coordination has been receiving increasing attention from theorists and experimentalists alike. We propose that this coordination is driven intracellularly, and use select algal species to perform a comparative study of their swimming gaits. Over longer timescales, we can visualize at high spatiotemporal resolution the stochastic transitions between different gaits which produce striking manifestations of a bacteria-like run-and-tumble locomotion.

GAITS OF FREE-LIVING FLAGELLATES

Uniflagellates including many species of plant and animal sperms navigate fluidic environments by undulating a posteriorly-oriented flagellum. This single appendage can be used to effectuate directional changes, such as turning towards a source of chemoattractant. In contrast, ciliated microorganisms including the freshwater protozoan *Paramecium* and the large colonial alga *Volvox* [3] rely on a large-scale coordinated motion of large numbers of surface-attached cilia for swimming and feeding. In this case coordination is thought to be largely due to hydrodynamic interactions between the neighbouring cilia, which tend to drive pairs of cilia into in-phase synchrony, and arrays of cilia into metachrony. The generality of this phenomenon is challenged when one examines the robust in-phase breaststroke swimming of the unicellular alga *Chlamydomonas*, the physical mechanism for synchrony between its two front-mounted flagella is the subject of extensive study and some contention. The current view is that some form of intracellular coupling must be present, most likely through the contractility of connecting fibers between the basal bodies whence emanate the flagella [1].

If this were true, then a correlation must be expected between observed gaits or modes of flagellar actuation and the symmetries of the basal apparatus which not only define the configuration of flagella but also the strength and directionality of the coupling between flagella. Here we explore the morphospace of distinct modes of flagellar synchrony maintained by flagella across species of naturally-occurring quadriflagellate algae (for free-swimming or pipette-held individuals) in the context of their differing basal architectures. Unicellular flagellates possessing more than four flagella are rare, with only a few species that have either eight or sixteen flagella [1]– the selective advantage of having ever greater numbers of flagella must be eventually be outweighed by the energetic and activity costs of flagellar synthesis and coordination. By analogy with well-documented forms of locomotion in quadrupeds, we find that quadriflagellate gaits include the trot, the pronk, the gallop, and even a stand gait in which all flagella are non-moving. Species-specific symmetries existing within the basal apparatus are therefore implicated in constraining the possible phase relations between flagella.

GAIT SYMMETRIES

As in many biological systems exhibiting complex periodic behaviour, it has proved useful to consider a dimension-reduced analysis of oscillations in terms of phase. We were able to measure the phases of individual flagella in several species of quadriflagellates through a combination of micromanipulation, cell tracking, and high-speed imaging. For flagellar phases ψ_j (flagellum index j) we compute the matrix $\Delta_{ij} = \psi_i - \psi_j$ $(i, j = 1, \ldots, 4)$, where $\Delta_{ij} = \Delta_{ji}$, $\Delta_{ii} = 0$, and $\Delta_{ik} = \Delta_{ij} + \Delta_{jk}$. Each gait is then associated with a 3-tuple of phase differences: $[\Delta_{12}\,\Delta_{13}\,\Delta_{14}]$. The primitive Prasinophyte alga
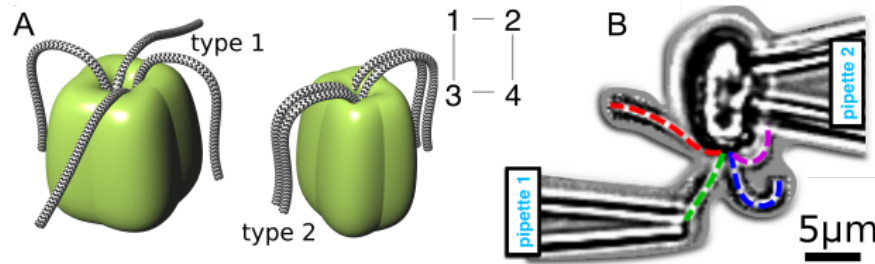
Figure 1: A) In free-living quadriflagellates, two possible configurations are possible (types 1,2). The flagella emerge from basal bodies comprising a species-specific network whose symmetries may constrain observed swimming gaits. B) In *T. suecica* (type 2) the relative phase between the remaining flagella is unchanged when beating is purposefully stalled in one flagellum.

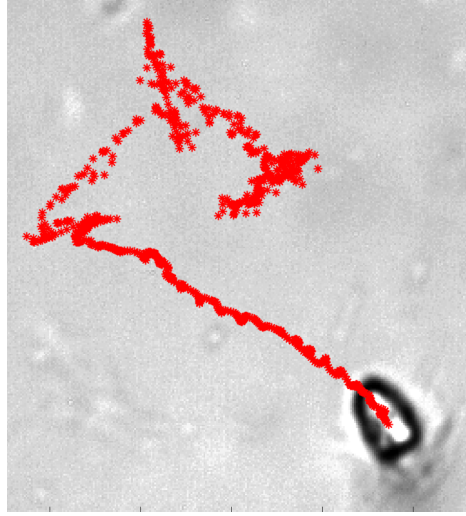[*]Corresponding author. Email: r.e.goldstein@damtp.cam.ac.uk

Figure 2: Flagellated eukaryote performs biased random walk by actively modulating the orientation and coordination of anteriorly-positioned flagellla.

P. parkeae swims with two pairs of precisely alternating breaststrokes akin to the 'trot' of a horse, for which $[\Delta_{12}\,\Delta_{13}\,\Delta_{14}] = [\pi\,0\,\pi]$. On the other hand the advanced green alga *C. crucifera* exhibits a rotary gallop gait ($[\Delta_{12}\,\Delta_{13}\,\Delta_{14}] = [\pi/2\,\pi\,3\pi/2]$). Inspired by studies of central pattern generators (CPGs) in the control of multilegged locomotion in vertebrates, we sought features of the basal apparatus in these species that may correlated with the spatiotemporal symmetries of observed gaits (where a spatiotemporal symmetry comprises a permutation of flagella and a temporal phase shift that fixes the dynamics). For instance the rotary gallop of four oscillators (Figure 1A) is fixed by the identity transformation, but also by interchange of diagonals with a phase shift of π, and can emerge from a square network in which the coupling between all oscillators are identical. This square symmetry is shown in electronmicrographs of sections through *C. crucifera*, in which basal bodies are inserted radially at corners of a square.

GAITS SWITCHING DURING FREE-SWIMMING

The flagellate stand gait has the most symmetries (reflection in the horizontal, in the vertical, interchange of diagonals and arbitrary phase shift) and has the symmetry group $D_2 \times S^1$, where D is a dihedral group and S the circle group. Intriguingly, bifurcation from the stand to an alternate swimming gait is observed in many species. Forward swimming can further bifurcate to a shock response in which the front-mounted flagella change from a puller-type to a pusher-type motility, and the swimming direction is dramatically reversed or altered. Such gait transitions can occur either stochastically or be induced by mechanical perturbations, but the backward-swimming phase is transient and a steady-state beating pattern is re-established within a few beats [2]. Over time (Figure 2), these episodic runs (forward-swimming) and tumbles (gait-switching) allow the cell to navigate a much larger region (effective diffusion constant of $D \propto v^2\tau \approx 10^{-4}$ cm^2/s for an alga swimming at $v = 200$ μm/s and mean run duration τ of 0.5 s, compared to passive Brownian diffusion $D_b = 10^{-9}$ cm^2/s for a 20 μm cell body).

CONCLUSIONS

Somewhat surprisingly, we find that motile algae can i) maintain precise gaits of swimming defined by specific phase relations between flagella, yet ii) also rapidly modify these gaits in response to mechanical or biochemical cues to overcome microscale diffusion barriers. Thus the propensity for a run-and-tumble like dynamics appears to be a general strategy adopted not only by peritrichously flagellated bacteria [4, 5], but many species of eukaryotic flagellates alike. In light of these results the control of flagellar coordination and synchrony must now be re-evaluated in the context of intracellular signalling.

References

[1] Wan K.Y., Goldstein R.E.:"Coordinated beating of algal flagella is mediated by basal coupling", *PNAS* 113, *in press*, 2016.

[2] Wan K.Y., Goldstein R.E.:"Spontaneous and induced gait-switching in motile microalgae", *preprint* 2016.

[3] Brumley D.R., Wan K.Y., Polin M., Goldstein R.E.:"Flagellar synchronization through direct hydrodynamic interactions", *eLife* 3 (e02750), 2014.

[4] Berg H.G.: "Random walks in biology", *Princeton University Press*, 1983.

[5] Xie L., Altindal T., Chattopadhyay S., Wu X-L.: "Bacterial flagellum as a propeller and as a rudder for efficient chemotaxis", *PNAS* 108 (6): 2246–2251, 2011.

METABOLY IN EUGLENIDS: A MODEL AND ITS EXPERIMENTAL VALIDATION

Giovanni Noselli[1], Marino Arroyo[2], Alfred Beran[3] & Antonio DeSimone[1a)]
[1]SISSA – International School for Advanced Studies, Trieste, Italy
[2]UPC – Universitat Politècnica de Catalunya, Barcelona, Spain
[3]OGS – Istituto Nazionale di Oceanografia e di Geofisica Sperimentale, Trieste, Italy

<u>*Summary*</u> Euglenids are unicellular aquatic organisms capable of moving either by beating a flagellum or by executing dramatic shape changes. These are accomplished thanks to a complex structure underlying the plasma membrane, made of interlocking proteinaceous strips, microtubules, and motor proteins. We study the mechanisms by which the sliding of pellicle strips leads to shape control and locomotion, by means of both theory (through the mechanics of active surfaces and its coupling to computational fluid dynamics for the surrounding fluid) and experiments. Moreover, we implement them into a new concept of surfaces with programmable shape, obtained by assembling 3d-printed strips in a construct mimicking the biological template. We show that the subtle balance between constraints and flexibility leads to a wide variety of shapes that can be obtained with relatively simple controls. This suggests that euglenids exploit the passive resistance of body parts to reduce the complexity of controlling their shape.

INTRODUCTION

Euglenids are unicellular organisms (protists) living in a wide range of aquatic environments, which are capable of moving either by beating a flagellum, or by executing dramatic shape changes (metaboly, or euglenoid movement). Beneath the plasma membrane, they exhibit a complex structure made of interlocking proteinaceous pellicle strips, with microtubules aligned with the strips and localized at the strip junctions. It is commonly believed that shape changes associated with metaboly are achieved through the relative sliding of the pellicle strips, which is in turn driven by motor proteins running along the microtubules. While a quantitative check of this hypothesis is not yet available, analyzing the mechanisms of euglenoid movement is interesting from many perspectives. One is to assess whether it provides a viable motility strategy and, if so, when and how the organism switches between flagellar-based and shape-change-driven propulsion. Another one, is that shape control by the relative sliding of pellicle strips provides a new concept to program the shape of surfaces, namely, control by active surface shears, which is unexplored.

SHAPE CONTROL BY ACTIVE SHEARS DUE TO RELATIVE SLIDING OF PELLICLE STRIPS

Pellicle structures are clearly visible in (dead) euglenids by Scanning Electron Microscopy. Fig. 1 (left) shows the correlation between local pellicle orientation and shape, with the organism thinner where the strips are parallel to the body "axis" (the mid curve), and thicker where they are at an angle. The mechanism by which the surface shears associated to relative sliding of pellicle strips determine the shape of the surface is complex. To highlight the main principles, we have implemented this mechanism in prototypes obtained by assembling 3d-printed strips, see Fig. 1 (center). This picture illustrates the mechanism quite vividly in a simple case, where a family of cylinders of increasing radius and decreasing height is obtained from a cylinder in which all the strips are initially aligned with the cylinder axis, and then a uniform relative sliding of the strips (hence a uniform surface shear) is imposed. Note that, in this way, surface area is preserved.

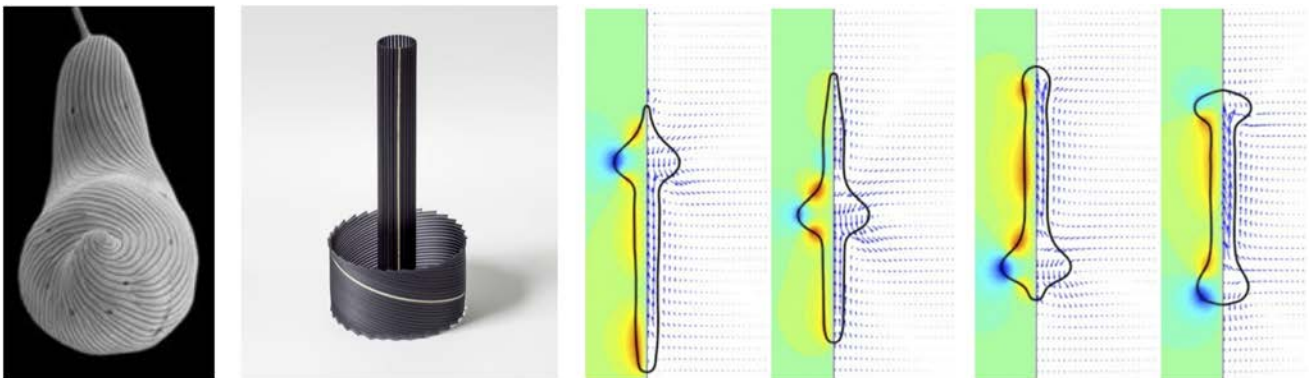

Fig. 1 Left: SEM image of the pellicle structure in Euglena sp.; center: illustration of the mechanism of shape control by relative sliding of interlocking 3d-printed strips; right: snapshots of numerical simulations to calculate displacements induced by propagating a bulge along the body in a model mimicking metaboly in Distigma.

[a)] Corresponding author. Email: desimone@sissa.it**.**

By allowing non-uniform relative sliding of the strips along their contour length (hence spatially variable surface shears), one can cause the propagation of a bulge along the cylinder, hence generating a propulsive force when the cylinder is immersed in a fluid. Building upon our previous work [1], we have explored this idea quantitatively. By solving numerically for the low Reynolds number flow induced by the shape changes observed in a variety of species of Euglena, and simultaneously solving the equation of motion for the swimmer subject to the forces transmitted by the surrounding fluid, we have computed the net displacements in one swimming stroke. We found that in some cases such as the one depicted in Fig.1 (right), displacements of the order of a few tenths of a body length per stroke can be attained. This suggests that metaboly can provide a viable motility strategy.

In order to validate the conclusions of our theoretical approach, we have studied the motion of euglenids executing metaboly by optical microscopy. Our preliminary observations show good agreement with the predictions of our model. In particular, Fig. 2 shows that shape changes are indeed directly correlated with the changes of orientation of the pellicle strips. An extensive campaign aimed at a quantitative comparison of theoretical predictions and experimental observations is the subject of ongoing work [2].
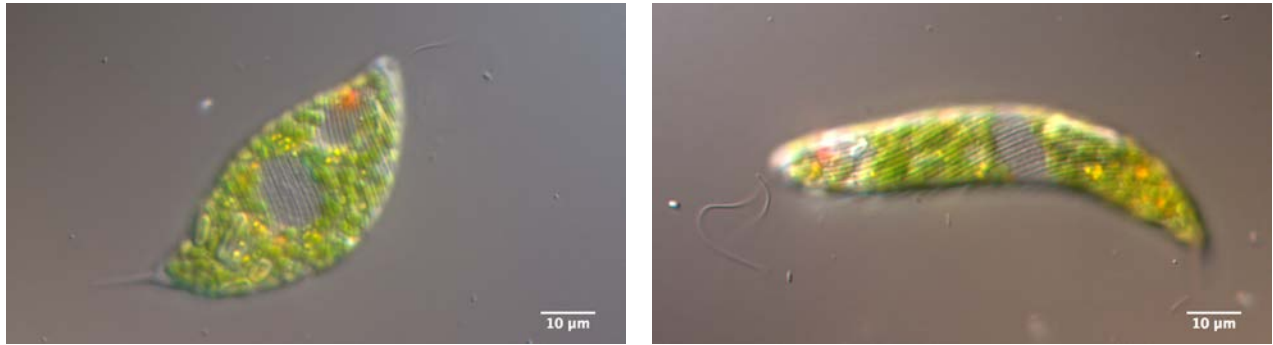

Fig. 2 Two light micrographs of the protist Euglena Ehrenbergii, showing that shape changes are correlated with changes of orientation of the pellicle strips. Images taken with an Olympus BX61 microscope equipped with a 100X/NA1.30 objective.

An interesting question arising naturally from our work is to characterize the shapes that are achievable by actuating a surface through active shears both in general (with an arbitrary continuous distribution of surface shears), and when specific discrete mechanisms (such as the interlocking 3d-printed strips of Fig. 1) are employed. The answer we find is that the range of achievable shapes is very large. For the general case, even restricting oneself to actuation by axisymmetric surface shears, we find that achievable shapes include portions of cones, spheres, pseudoshperes, or spindles [3]. By allowing non-axisymmetric shears, non-axisymmetric bent shapes can be obtained. One implication is that shape control by the relative sliding of pellicle strips provides a subtle balance between constraints and flexibility: a wide variety of shapes can be obtained with relatively simple controls. This suggests that euglenids exploit passive resistance of body parts (the stiffness of the pellicle strips, the constraints due to interlocking) to reduce the complexity of controlling their shape, in agreement with the notion of morphological computation that has been proposed for the control of soft, bio-inspired robots.

CONCLUSIONS

We have developed and validated a model of euglenoid movement based on active surface shears induced by the relative sliding of pellicle strips. Our results suggest that metaboly can provide a viable motility strategy. Moreover, we have implemented the mechanisms underlying shape changes in euglenids into a new concept of a surface with programmable shape, obtained by asssembling 3d-printed strips. We have shown that the subtle balance between constraints and flexibility leads to a wide variety of shapes that can be obtained with relatively simple controls. This suggests that euglenids exploit the passive resistance of body parts to reduce the complexity of the task of contolling their shape.

ACKNOWLEDGEMENTS

References

[1] Arroyo M., Heltai L., Milan D., DeSimone A.: Reverse engineering the euglenoid movement. PNAS **109**:17874–17879, 2012.
[2] Noselli G., Arroyo M., Beran A., DeSimone A.: In preparation.
[3] Arroyo M., DeSimone A.: Shape control of active surfaces inspired by the movement of euglenids. J Mech Phys Solids **62**:99–112, 2014.

EFFECTS OF DISCRETENESS ON POPULATION PERSISTENCE IN AN OASIS

Stefano Berti [*1], Massimo Cencini[2], Davide Vergni[3], and Angelo Vulpiani[4,2]

[1]*Laboratoire de Mécanique de Lille, FRE 3723, Université Lille 1, 59650 Villeneuve d'Ascq, France*
[2]*Istituto dei Sistemi Complessi, CNR, Via dei Taurini 19, 00185, Rome, Italy*
[3]*Istituto per le Applicazioni del Calcolo, CNR, Via dei Taurini 19, 00185, Rome, Italy*
[4]*Dipartimento di Fisica, Università "La Sapienza", Piazzale Aldo Moro 2, 00185 Roma, Italy*

Summary Determining the conditions for persistence of species and populations is a question of paramount importance in population biology. The problem was first theoretically investigated adopting a continuous reaction-diffusion equation for population dynamics in a patch of finite size surrounded by a completely hostile environment, representing an oasis in a desert. The main result of this model, today known as the KiSS model (after Kierstead, Slobodkin and Skellam), is that patches need to be larger than a critical size to let the population survive. To explore the effects of discreteness and demographic stochasticity, here we propose an individual-based formulation of the KiSS model. We investigate population dynamics in our discrete model, focusing on the average time to extinction (above and below the critical patch size of the continuous model) and on the quasi-stationary distribution of the number of individuals for patch sizes larger than the critical value.

INTRODUCTION

Biological and chemical processes often involve the dynamics of discrete entities (e.g., molecules or organisms) that diffuse and interact with each other and/or with an external environment. If the number density of "particles" is very large, a macroscopic description in terms of continuous fields is typically appropriate; a well established approach to model the spatio-temporal evolution of the population density field is in terms of a reaction-diffusion equation. Conversely, if the density of particles is not very large the discrete nature of the population cannot be neglected [1], new effects arise and the continuous description becomes inaccurate. In order to account for such effects, we consider a system of particles diffusing in space and interacting when they get within a given interaction distance [2, 3]. In particular, revisiting the continuous KiSS model [4, 5], we investigate the effects induced by discreteness on the dynamics of a population inhabiting a favorable region ("an oasis") surrounded by a deadly environment ("a desert"). Accounting for such effects is important to assess the role of demographic and environmental stochasticity on extinction dynamics [6]. A peculiarity of our work with respect to previous investigations (see, e.g., [6, 7] and [8, 9] for studies respectively adopting non-spatial and spatial models) is that we fully describe the movement of individuals in space and we do not restrict the attention to steady state properties but we also deal with dynamical features of extinctions.

MODEL

The persistence/extinction problem was first ivestigated by Kierstead, Skellam and Slobodkin [4, 5] who considered a continuous population logistically growing with rate r and diffusing with diffusion coefficient D within a one-dimensional patch of size L surrounded by a deadly environment. For a given growth rate, higher diffusivities imply larger fluxes across the boundaries, so that larger patches are necessary to compensate the population loss in order to allow stable persistence. Standard eigenvalue computation for the linearized system (close to extinction the population density will be very small) gives $L_c = \pi\sqrt{D/r}$ for the minimal (critical) patch size ensuring persistence.

Among the various factors influencing extinction, demographic stochasticity, associated to the unavoidable random occurrence of birth and death events, is one of the most important ones. Here we introduce a discrete version of the KiSS model (see [2, 3] for details) to examine its role. The model is constructed with the essential feature of reproducing the FKPP (Fisher-Kolmogorov-Petrovskii-Piskunov) dynamics $\partial_t \theta = D\partial_x^2 \theta + r\theta(1-\theta)$, where θ is the population density, for large numbers of particles [2]. The FKPP equation can be derived from the two coupled reaction-diffusion equations for the concentrations θ_A and θ_B of the species undergoing an autocatalytic reaction, provided the diffusion coefficients of species A and B are equal and $\theta_A + \theta_B = 1$ (i.e. local mass conservation). To discretize these equations we pass from the concentrations $\theta_{A,B}$ to a particle description in terms of N_A particles of type A and N_B of type B, with $N = N_A + N_B$ fixed. All particles undergo independent diffusive processes with the same diffusion coefficient, D, within the favorable patch $[0, L]$. A simple way to implement the interaction term $r\theta_A\theta_B$ is to impose that an A particle changes into B with a probability rate depending on the intrinsic rate, r, and on the number of B particles within an interaction distance R. Finally to reproduce the boundary conditions of the KiSS model and locally ensure mass conservation, we impose that A particles hitting the boundaries are reflected (nutrients are present only within the patch), and that if a B particle hits the boundary it is absorbed (as it cannot survive outside the favorable patch) and it is replaced in-place by an A-particle.

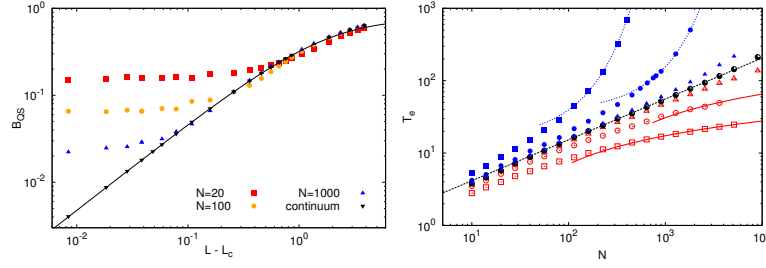*Corresponding author. Email: stefano.berti@polytech-lille.fr

Figure 1: (Left panel) Long-time limiting biomass $\mathcal{B}_C^\infty$ in the continuous case and average biomass in the quasi-stationary state, $\mathcal{B}_{QS}$, as a function of $L - L_c$ for different values of N. The solid curve corresponds to the behavior $\mathcal{B}_C^\infty(L) \approx \lambda_1$ obtained with a mean-field-like argument, where λ_1 is the largest eigenvalue of the linearized KiSS model. (Right panel) Mean extinction time, T_e, vs population size, N, for different patch sizes $L = L_c + \delta L$: from bottom to top $\delta L = -0.3, -0.1, -0.02, 0, 0.02, 0.1, 0.3$, encompassing the extinction (empty red symbols) and persistence (blue filled symbols) regions, as well as the critical point (black half filled symbols) of the continuous model. The continuous red lines display the logarithmic prediction (see text) with b' fitted from data; the dashed blue lines correspond to the exponential behavior (see text) with a fitted. For $L = L_c$ we found a power-law behavior, $T_e \sim N^\gamma$, with best fitting exponent $\gamma = 0.565$.

RESULTS ON BIOMASS AND EXTINCTION TIMES

The main difference between the continuous model and the discrete one is that while the (continuous) stationary state $\theta = 0$ becomes unstable above the critical patch size, the (discrete) absorbing state $N_B = 0$ can always be reached due to demographic stochasticity, even when $L > L_c$. Nevertheless, the time taken by the system to be absorbed can be very long (for N and L large enough) and, in that case, the system reaches a quasi-stationary state. We have investigated the properties of this state at varying the system and population sizes by means of extensive numerical simulations. The results show that above the KiSS critical patch size the biomass in the quasi-stationary state recovers the continuum limit value only if the population is large enough (Fig. 1, left). On the other hand, when the population has a small number of individuals, the link between biomasses, defined in the continuous and particle models, ceases to exist. In particular, when the patch size tends to the critical value the number of individuals required to recover the continuum limit diverges.

We further analysed how the survival/extinction transition of the continuous KiSS model translates in the behavior of the average time to extinction T_e. Different functional dependencies of T_e on the population size N were found in the extinction ($L < L_c$), critical ($L = L_c$) and persistent ($L > L_c$) regions of the continuous model (Fig. 1, right). In the extinction region, the population density exponentially decays to zero with a rate given by the first eigenvalue $\lambda_1 = 1 - (L_c/L)^2$ (in non-dimensional units), which implies the logarithmic dependence $T_e \sim (\log N)/|\lambda_1| + b'$ (where $b' = \text{const}$). On the other hand, for $L > L_c$, T_e exponentially grows as $T_e \sim \sqrt{N}e^{aN}$ (where $a = \text{const}$), similarly to what is observed in non-spatial models. In the present case, such a behavior can be shown to be consistent, at least for L and/or N large enough, with Gaussianity of the quasi-stationary distribution. Finally, at the transition, the logarithmic and exponential behaviors are separated by the power-law $T_e \sim N^\gamma$. The value of the exponent is $\gamma = 0.565$ from a best fit, not far from the analytical prediction ($\gamma = 1/2$) obtained in the non-spatial logistic model. Despite small, the difference is clearly measurable and might be due to the spatial structure of the system under consideration.

We conclude mentioning that it would be interesting in the future to investigate the effects of population discreteness in more complex heterogeneous environments and possibly in the presence of advection.

References

[1] Durret R., Levin S.: The importance of being discrete. Theor. Popul. Biol. 46:363-394, 1994.

[2] Berti S., López C., Vergni D., Vulpiani A.: Discreteness effects in a reacting system of particles with finite interaction radius. Phys. Rev. E 76: 031139, 2007.

[3] Berti S., Cencini M., Vergni D., Vulpiani A.: Extinction dynamics of a discrete population in an oasis. Phys. Rev. E 92:012722, 2015.

[4] Skellam J.G.: Random Dispersal in Theoretical Populations. Biometrika 38:196-218, 1951.

[5] Kierstead H., Slobodkin L.B.: The size of water masses containing plankton blooms. J. Mar. Res. 12:141-147, 1953.

[6] Lande R.: Risks of population extinction from demographic and environmental stochasticity and random catastrophes. Am. Nat. 142:911-927, 1993

[7] Doering C.R., Khachik V.S., Sander L.M.: Extinction times for birth-death processes: exact results, continuum asymptotics, and the failure of the Fokker–Planck approximation. Multiscale Model. Simul. 3:283-299, 2005.

[8] Méndez V., Hortshemke W., Casas-Vázquez J., Zemskov E.: Variational principles and the effect of a cutoff on population pattern size. Eur. Phys. J. (Special Topics) 146:189-197, 2007.

[9] Escudero C., Buceta J., de La Rubia F.J., Lindenberg K.: Extinction in population dynamics. Phys. Rev. E 69:021908, 2004.

MS03 - Multiphase Flow in the Processing Industry

CURRENT CHALLENGES IN UPSCALING MULTIPHASE FLOWS IN POROUS MEDIA USING THE VOLUME AVERAGING METHOD

Krishna M. Pillai[1a]

[1]*Laboratory for Flow and Transport Studies in Porous Media, Department of Mechanical Engineering, University of Wisconsin-Milwaukee, Milwaukee WI, USA*

Summary The talk will start with an introduction of multiphase flows seen in industrial applications. It will be followed by the current state of theoretical development for multiphase flows as proposed using the volume averaging method. The two viscous drag tensors proposed by the theoretical developments will be discussed. Then the results of experiments and simulations done using micromodels will be presented which describe different flow regimes possible in multiphase flows including viscous fingering, capillary fingering and stable displacement. At the end, the need for a new mathematics to explain the contradictions posed by these findings.

Since any typical porous medium consists of numerous smaller particles or fibers separated by interstitial spaces, it is not practical to conduct CFD simulations in the entire domain to predict flow and transport. Hence upscaling is employed to describe the phenomena in terms of averaged quantities so that flow and transport predictions can be undertaken in porous media. The volume averaging method is a well-established method to upscale flow and transport variables in porous media. Compared to other upscaling methods such as the mixture theory or the homogenization method, the volume averaging method establishes a good connection between the larger *macroscopic* domain of volume averaged variables used to describe the porous-continuum space and the smaller *microscopic* domain of point-vise variables used to describe the pore-level (discrete) space. This allows the estimation of macroscopic properties, such as the permeability or thermal diffusivity tensors that are used in the macroscopic or upscaled governing equations, using the closure formulation on pore-level microstructures [1,2].

Displacement of one fluid by another is an example of the multiphase flow in porous media. Such multiphase flows through porous media are quite common in the processing industry where the applications range from reducing void content during processing of composites to tracking the presence of water in gas diffusion layer in fuel cells to optimizing design of person hygiene pads. Using the volume averaging method, Whitaker and co-workers [3,4,5] showed that the upscaled Stoke's equation will have the form:

$$\langle \boldsymbol{v}_\beta \rangle = - \frac{\boldsymbol{K}_\beta}{\mu_\beta} \cdot \left(\nabla \langle p_\beta \rangle^\beta - \rho_\beta \, \boldsymbol{g} \right) + \boldsymbol{K}_{\beta\gamma} \cdot \langle \boldsymbol{v}_\gamma \rangle \qquad (1)$$

$$\langle \boldsymbol{v}_\gamma \rangle = - \frac{\boldsymbol{K}_\gamma}{\mu_\gamma} \cdot \left(\nabla \langle p_\gamma \rangle^\gamma - \rho_\gamma \, \boldsymbol{g} \right) + \boldsymbol{K}_{\gamma\beta} \cdot \langle \boldsymbol{v}_\beta \rangle \qquad (2)$$

where $\boldsymbol{K}_\beta$ and $\boldsymbol{K}_\gamma$ are permeability tensors and $\boldsymbol{K}_{\beta\gamma}$ and $\boldsymbol{K}_{\gamma\beta}$ are viscous drag tensors. The proposed form was different from the usual well-accepted form of the generalized Darcy's law for the two phases, β and γ, that are identical to Eqns. (1) and (2) when the terms containing the viscous drag tensors are removed. Though this proposed form of Darcy's law is novel and based on rigorous derivation, it is yet to find acceptability due to the absence of any experimental verification of the two viscous drag tensors. We explore the possibility of conducting some accurate pore-level simulations using modern methods such as the Lattice-Boltzmann method to simulate two-phase flow in a representative elementary volume and then using the closure formulations for the two phases to upscale and estimate the two viscous-drag tensors.

In the end, the further difficulties on the path of upscaling multiphase flow in porous media will be discussed. In

[a] Corresponding author. Email: krishna@uwm.edu

particular, the three different flow regimes of capillary fingering, stable displacement and viscous fingering, encountered during the flow of two phases through porous medium [6], will be presented. These flow regimes have been shown to be strong functions of two dimensionless groups, the Capillary number and the viscosity ratio [6]. Development of capillary fingers is quite similar to the formation of large clusters (islands of wet phase) witnessed during drying which is simulated quite accurately using the invasion-percolation algorithm in network models [7]. A common feature of these formations is that they are governed entirely by the inhomogeneities seen at the pore level and lead to a rather disconcerting result—the concept of volume averaging becomes inapplicable since the presence of such fingers lead to creation of large structures of the same size as the solution domain. (A condition of volume averaging is that the REV (representative elementary volume) used for averaging the flow and transport variables should be smaller than the solution domain but much bigger than the individual pore-level formations seen in [7].) The challenge of developing a closure formulation, that can represent these three different flow regimes, is the current obstacle facing the volume averaging method as applied to multiphase flows.

References

[1] "Estimation of Tortuosity and Effective Diffusivity Tensors using Closure Formulation in a Sintered Polymer Wick during Transport of a Nondilute, Multicomponent Liquid-Mixture", S. Beyhaghi and K.M. Pillai, *Special Topics & Reviews in Porous Media - An International Journal*, Vol. 2, issue 4, pp. 267-282, 2011.

[2] "Fast 2D Micrograph-Based Method of Permeability Estimation through Micro-Macro Coupling in Porous Media," B. Barari, S. Beyaghi and K.M. Pillai, under review with *Journal of Porous Media*.

[3] "Flow in Porous Media II: The Governing Equations for Immiscible, Two-Phase Flow," S. Whitaker, *Transport in Porous Media*, v 1, pp 105-125, 1986.

[4] "The Closure Problem for Two-Phase Flow in Homogeneous Porous Media," S. Whitaker, *Chemical Engineering Science*, v 49, n 5, pp 765-780, 1994.

[5] "Determination of Permeability Tensors for Two-Phase Flow in Homogeneous Porous Media: Theory," D. Lasseux, M. Quintard and S. Whitaker, *Transport in Porous Media*, n 24, pp 107-137, 1996.

[6] "Numerical Models and Experiments on Immiscible Displacements in Porous Media," R. Lenormand, E. Touboul and C. Zarcone, *Journal of Fluid Mechanics*, v 189, pp 165-187, 1988.

[7] "A Study on Slow Evaporation of Liquids in a Dual-Porosity Porous Medium using Square Network Model", K M. Pillai , M. Prat, M. Marcoux, *International Journal of Heat and Mass Transfer*, v 52, n 7-8, p 1643-1656, March 2009.

THE FLUID MECHANICS OF POLYURETHANE FOAM EXPANSION AND POLYMERIZATION

Rekha R. Rao[1], Lisa A. Mondy[1], Christine C. Roberts[1], Melissa M. Soehnel[1], Kevin Long[1], Victor E. Brunini[2], David Noble[1], Mathew C. Celina[3], James J. Tinsley[4]

[1]*Engineering Sciences Center, Sandia National Laboratories*, MS 0836, Albuquerque, NM USA*
[2]*Systems Engineering Center, Sandia National Laboratories, MS 9957, Livermore, CA USA*
[3]*Materials Science Center, Sandia National Laboratories, MS 01411, Albuquerque, NM USA*
[4]*Honeywell Federal Manufacturing & Technologies, 14520 Botts Road, Kansas City, MO USA*

Summary In this presentation, we discuss our new, experimentally driven, approach to foam expansion and polymerization modeling. We are working to develop high-fidelity computational models to be used to design and troubleshoot mold filling for polyurethane structural foam parts.

INTRODUCTION

We are studying PMDI polyurethane with a fast catalyst, such that filling and polymerization occur simultaneously. The foam is over-packed to twice or more of its free rise density, to reach the density of interest. Developing a relevant model to represent the expansion, filling, curing, and final foam properties is quite challenging. PMDI is chemically blown foam, where carbon dioxide is produced via the reaction of water and isocyanate. The isocyanate also reacts with polyol in a competing reaction, which produces the polymer. A new kinetic model is implemented, which follows a simplified mathematical formalism that decouples these two reactions. The model predicts the polymerization reaction via condensation chemistry, where vitrification and glass transition temperature evolution must be included to correctly predict this quantity. The foam expansion kinetics are determined by tracking the molar concentration of both water and carbon dioxide. The conservation equations, including the equations of motion, an energy balance, and three rate equations are solved via a stabilized finite element method [1]. We assume generalized-Newtonian rheology dependent on the cure, gas fraction, and temperature. The conservation equations are combined with a level set method to determine the location of the free surface over time.

RESULTS

The model is applied to a geometry similar to a flow visualization experiment we conducted of polyurethane foam expansion in a clear mold. Results from the model are compared to the experimental data (Figure 1) and post-test CT data for the density in a simpler bar geometry.
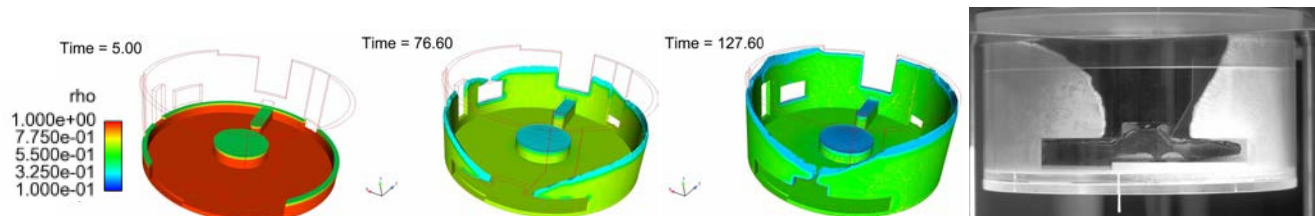

Figure 1. The left three images show the filling profile and density variations of polyurethane foam expansion as predicted by the model. The right-most image shows a flow experiment for validation of the model.

The model calculates the molar volume of carbon dioxide and uses that to predict the final density of the part. These results can be seen in Figure 2. The concentration of carbon dioxide is highest under the large circular feature and lower on the walls. The concentration is very noisy, possibly due to numerical oscillations. The density varies spatially with the lowest density seen at the bottom, including trapped gas below the largest feature.   The density is higher at the walls than in the interior of the mold. The model predicts a thin skin of higher density at the walls, mostly due to temperature gradients and internal exothermic heating.

Density predictions in the bar geometry have been compared to X–Ray CT data [2]. From this comparison, we have seen that the average density was fairly representative, but that the data showed much larger density gradients than the model, even when including an ideal gas law representation of the gas bubbles. It under predicts density gradients, especially in the gravity direction and the skin is much thinner in the computational model than in the CT data. We think that some of these effect are due to bubble-scale phenomena such as foam drainage, bubble migration, and wall shear rate effects. To capture

---

[a] Corresponding author. Email:rrrao@sandia.gov**.**

this phenomenon, we plan to solve a Rayleigh-Plesset equation to determine the local bubble size over time, including both gas and liquid phase concentrations of CO_2.
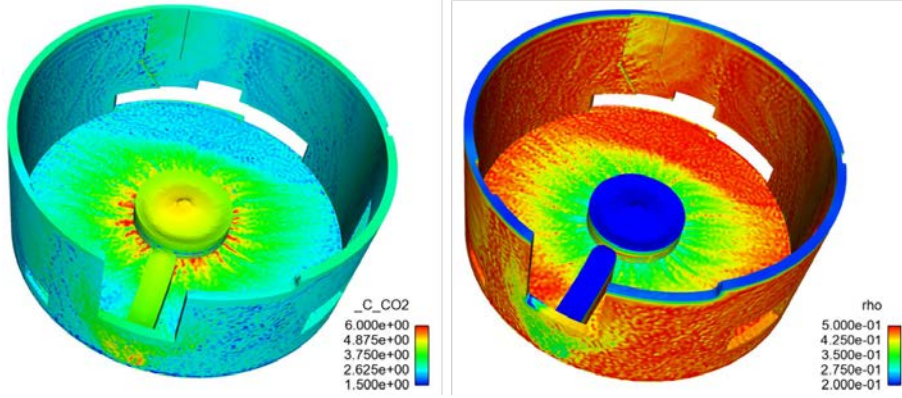

Figure 2. Carbon dioxide concentration (.01 scaling of mmol/ml) and resulting density variations (g/cm3) in pie mold showing voids under large features.

CONCLUSIONS

A numerical model has been developed for foam expansion and polymerization in complex geometries based on the finite element method and a level set method to capture the dynamic filling process. The method has been applied to various geometries and shown to capture average density and filling profiles well, though density gradients are still under predicted.

FUTURE WORK

For the next generation foam model, we will need to have an estimate of bubble size so that we can include bubble-scale effects such as foam drainage, bubble-pressurization, and coarsening. To capture this phenomenon, we need to track the carbon dioxide in both the gas and liquid phases. A Rayleigh-Plesset equation is then used to determine the local bubble size (R) over time, including both gas and liquid phase concentrations of CO_2, where ρ_{liq} is the density, $\eta_{polymer}$ is polymer viscosity, σ is the surface tension, and p is the pressure in either the bubble or the polymer.

$$\rho_{liq}(\frac{3}{2}\dot{R}^2 + R\ddot{R}) = p_{gas} - p_{liq} - 2\frac{\sigma}{R} - 4\eta_{polymer}\frac{\dot{R}}{R} \tag{1}$$

From this equation, we can see that evolving viscosity and surface tension effects will be taken into account explicitly, allowing the bubble growth to halt even if excess carbon dioxide is present. The volume fraction ϕ and the foam density can then be determined from the bubble radius and an experimentally determined bubble number density.

$$\phi(t) = N_{bubbles}\sum_{i=1}^{ng}\frac{4}{3}\pi R_i^3 \tag{2}$$

$$\rho_{foam} = (\rho_{gas} - \rho_{liq})\phi(t) + \rho_{liq}$$

The bubble size and number will then be used to predict the density and density gradients of the macroscopic foam, including a foam drainage model linked to bubble size. We hope this new model will be more predictive of the density gradients seen in the X-ray CT data.

ACKNOWLEDGMENTS

References

[1] R.R. Rao, L.A. Mondy, et al., "A Level Set Method to Study Foam Processing: A Validation Study," *IJNMF*, April 2012.
[2] R.R. Rao, L.A. Mondy, et al., "A Kinetic Approach to Modeling the Manufacture of High Density Polyurethane Structural Foam: Foaming and Polymerization," September 2015, SAND2015-8282.

MODELLING REQUIREMENTS FOR PARTICLE AGGLOMERATION IN FLUID FLOWS

Martin Sommerfeld [a)]

Martin-Luther-Universität Halle-Wittenberg, Zentrum für Ingenieurwissenschaften, D-06099 Halle/Saale, Germany

<u>Summary</u> Particle agglomeration is important for many unit operations in process technology. A numerical calculation of such processes requires appropriate models for describing the agglomeration itself and the behaviour of the agglomerates in the flow. This implies the occurrence of collisions, the sticking probability of particles, the mapping of the agglomerate structure and the fluid dynamic drag of complex agglomerates. Models accounting for these elementary processes were developed, implemented in an in-house numerical code and tested for several flow situations, including a spray dryer.

INTRODUCTION

In the process industries agglomeration of solid particles in gas or liquid flows is relevant for many unit operations. Such an agglomeration may be a desired or undesired phenomenon and results in an effective growth of particles forming more or less complex structures. Examples for eligible particle agglomeration are particle capture in a cyclone whereby the particle size effectively grows and separation efficiency improves as well as powder production in a spray dryer wherein larger particles with desired structures may be produced through on purpose agglomeration.

Nowadays many industrial areas apply multiphase flow CFD (computational fluid dynamics) for process design and optimization. For the considered dispersed particle-laden flows, the well-known hybrid Euler/Lagrange approach is most suitable since the particle size distribution is very important to be resolved. For industrial applications the mostly turbulent fluid flow is calculated by solving the Reynolds-averaged conservation equations (RANS) in connection with an appropriate turbulence model. In the Lagrangian part a large number of particles are tracked in the before-hand calculated flow field in order to eventually obtain reliable averaged dispersed phase properties. So far such calculations consider mostly spherical particles represented as point-masses which however is a bad approximation for agglomerates. Real agglomerates consist of many primary particles which may be organized in a compact way with relatively low porosity or are made up of numerous dendritic branches yielding very high porosities. In each case however, the effective size of agglomerates is much larger than the volume equivalent diameter so that the effective size and particle density need to be accounted for in particle tracking using resistance force coefficients also accounting for porosity.

Essential for the formation of agglomerates is the occurrence of inter-particle collisions which are mainly determined by high particle concentrations and large relative velocities between particles; the latter being induced by inertial effects and/or turbulence. Agglomeration of particles will only occur if interaction forces such as Van der Waals, electrostatic and liquid binding become strong enough. Consequently these three effects, namely particle collisions, agglomerate formation and tracking of agglomerates need to be appropriately modelled in a numerical calculation.

LAGRANGIAN AGGLOMERATION MODEL

In order for appropriately conducting Euler/Lagrange calculations of agglomeration processes, a stochastic inter-particle collision model was developed, which also accounts for the impact efficiency [1, 2], i.e. a small particle might move around a larger particle with the relative flow and hence not collide. Once two particles collide it is necessary to decide whether they rebound or stick together forming an agglomerate. For dry particles, this may be done based on an energy balance, comparing the relative kinetic energy with dissipated and Van der Waals energy [1]. This yields a critical upper velocity for particle adhesion and agglomeration. If high viscous or mushy droplets collide (e.g. in a spray dryer) they may penetrate partially and form also structured agglomerates [3]. The penetration of a high viscous droplet into one with lower viscosity is calculated by considering Stokes drag and shear forces [3, 4].

Agglomeration of solid particles might be modelled in different ways depending on the degree of information expected from the two-phase flow calculations. Different modelling approaches are summarized in Figure 1. The most straight forward approach assumes that the two agglomerating particles form a new volume equivalent sphere with a velocity resulting from a momentum balance. This model does however not provide any information on the realistic structure and size of agglomerates. The second model, called sequential model, assumes that for every two particle agglomeration a new spherical particle is formed with the volume consisting of the volume of the involved two spherical particles plus the void volume resulting from the convex hull wrapped around the two particles (see Fig. 1 middle). The new particle is now tracked with a size being larger than that resulting from the volume of the two primary particles and a porosity resulting from the two particle configuration. This procedure is successively repeated for each agglomeration considering however, that the "spherical" agglomerate has already porosity. This model was applied for calculating particle separation in a gas cyclone [5]. The most sophisticated agglomeration model (Figure 1 right) allows the estimation of the complete structure of agglomerates through statistical approaches. From an initial primary particle location vectors are stored for each new primary particle being collected by the agglomerate. This information is carried throughout the flow field for every

---

Lagrangian agglomerate produced (Figure 1 right). Thereby it is possible to obtain a realistic agglomerate size from the convex hull volume, agglomerate porosity and effective particle density [4]. It should be noted that the agglomerate is yet treated as a point-particle.
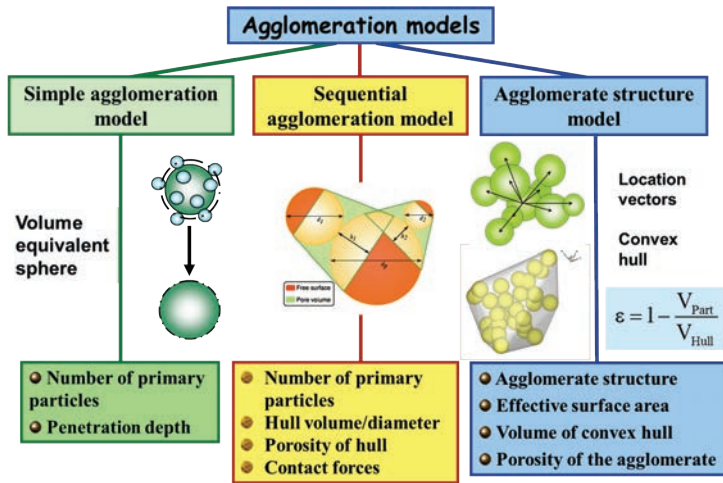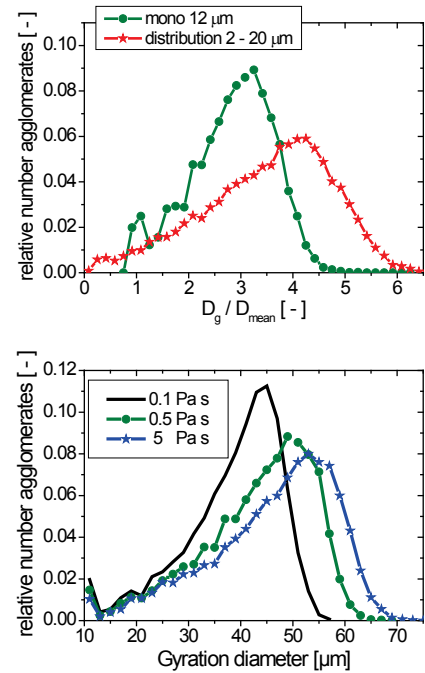

Figure 1: Overview of different approaches for modelling particle agglomeration.

Figure 2: Simulated PDF of agglomerate sizes in homogeneous isotropic turbulence for different particle properties; a) dry particles mono-sized (12 μm) versus size distribution; b) mushy droplets with different viscosity for initially mono-sized particles (12 μm).

Having now a porous particle with an effective size and density the question arises, which drag coefficient should be used for tracking the agglomerate? It is known, that the drag coefficient decreases with increasing porosity since the flow intensity through the agglomerate increases. In order to determine the dependence of drag coefficients on porosity, Lattice-Boltzmann simulations were conducted for different randomly generated agglomerates fixed in a cubic flow domain and exposed to a laminar plug flow [6]. The results showed, that even for a compact agglomerate with a porosity of $\varepsilon = 0.8$ the drag coefficient at low Reynolds number (i.e. 0.3) is about 10 % lower than for a compact sphere.

RESULTS

For demonstrating the performance of the novel agglomerate structure model, first results obtained for particle motion in a homogeneous isotropic turbulence field are presented [4]. The results for example show that for a poly-sized population the agglomerates grow faster, have a higher porosity and become larger than for a comparable mono-sized population with the same mean diameter (Figure 2 a). Considering mushy droplets, like in a spray dryer, an increasing viscosity yields lower penetration and as a result larger Gyration diameters and more porous agglomerates (Figure 2 b).

Finally, numerical simulations for a spray dryer are being performed in order to obtain the properties of the produced agglomerates. In a spray dryer of course particle interaction is even more complex. Initially solution droplets are injected into the dryer, which, upon collision might coalesce. Due to further drying the droplet viscosity increases remarkably and the droplets become mushy yielding a penetration upon collision. The results show that the agglomerate structure obtained from the simulations is in qualitative agreement with experimental observations.

References

[1] Ho, C.A. and Sommerfeld, M.: Modelling of micro-particle agglomeration in turbulent flow. Chem. Eng. Sci. **57**: 3073 – 3084, 2002.

[2] Sommerfeld, M. and Lain, S.: From elementary processes to the numerical prediction of industrial particle-laden flows. Multiphase Science and Technology **21**: 123 – 140, 2009.

[3] Sommerfeld, M., Blei, S., Stübing, S. and Lipowsky, J.: Modelling of agglomerate structure in the Lagrangian point-particle approximation. Transport Phenomena in Multiphase Systems (Eds. Butrymowicz, D. Goscik, J. and Skiepko, T.), Proceedings of the 5th International Conference on Transport Phenomena in Multiphase Systems, June 30. to July 3. 2008, Bialystok, Poland, Vol. 1, 173-188 (2008)

[4] Sommerfeld, M. and Stübing, S.: Lagrangian modeling of agglomeration for applications to spray drying. 9th International ERCOFTAC Symposium on Engineering Turbulence Modeling and Measurements, Thessaloniki, Greece, 6. – 8. June 2012.

[5] Lipowsky, J. and Sommerfeld, M.: Influence of particle agglomeration and agglomerate porosity on the simulation of a gas cyclone. Proceedings 6th Int. Conf. on CFD in Oil & Gas, Metallurgical and Process Industries. Trondheim Norway, Paper No. CFD08-043, June 2008.

[6] Dietzel, M., Ernst, M. and Sommerfeld, M.: Application of the Lattice-Boltzmann Method for Particle-laden Flows: Point-particles and Fully Resolved Particles. Flow Turbulence Combust, DOI: 10.1007/s10494-015-9698-x.

SCALING RELATIONSHIPS DESCRIBING MICROFLUIDIC ACOUSTIC NOZZLES FOR 3D-PRINTING

Rachel Collino[1a], Tyler Ray,[1] Leanne Friedrich, [1] James Cornell [1] & Matthew Begley [1]

[1]*Materials Department, University of California, Santa Barbara, Santa Barbara, California, United States of America*

Summary: Acoustic forces are an attractive pathway to achieve directed assembly for two-phase materials *via* additive processes. On one hand, they can be used to align and consolidate particles in uncured matrices to effectively print composites in three dimensions. On the other hand, they can be used with traditional self-assembly to create hierarchical assembly techniques in which chemically-assembled 'meso-particles' (*e.g.*, each consisting of multiple nanoscale particles) are aggregated at much faster time scales than those associated with diffusion. We present key scaling relationships controlling the time for aggregation and alignment of particles, which can be used to identify acceptable levels of acoustic excitation and the required dimensions for focusing regions. The results are used to predict optimal combinations of these parameters that lead to deposition of highly packed particles without jamming.

The impact of three-dimensional printing will be enhanced considerably by developing techniques to deposit multiphase materials with controlled density and alignment of the constituents. The optical, thermal, and electrical properties of two-phase functional materials can be improved by controlling particle distributions to introduce photonic band-gaps[1], coupled electro-mechanical behaviors[2], coupled thermo-mechanical behaviors[3,4], *etc*. The control of particle aggregation and deposition within a single print stream is thus of interest for reducing the complexity and cost of multiphase printing for materials with advanced functionalities.
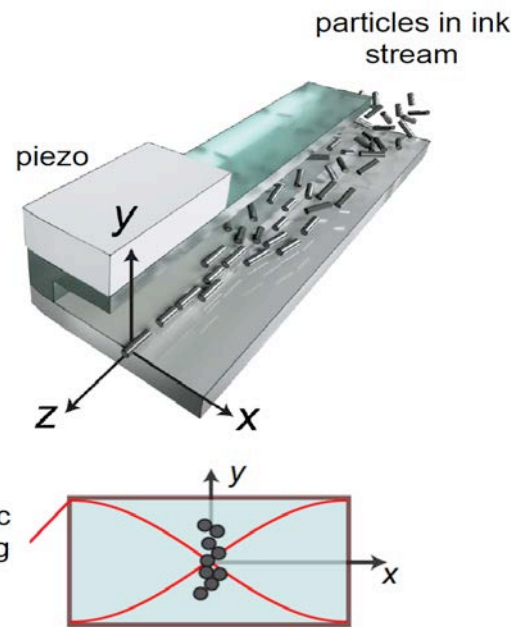

Figure 2: Microchannel print nozzle geometry and coordinate system. The piezo is excited at a frequency corresponding to a standing half-wave in pressure.
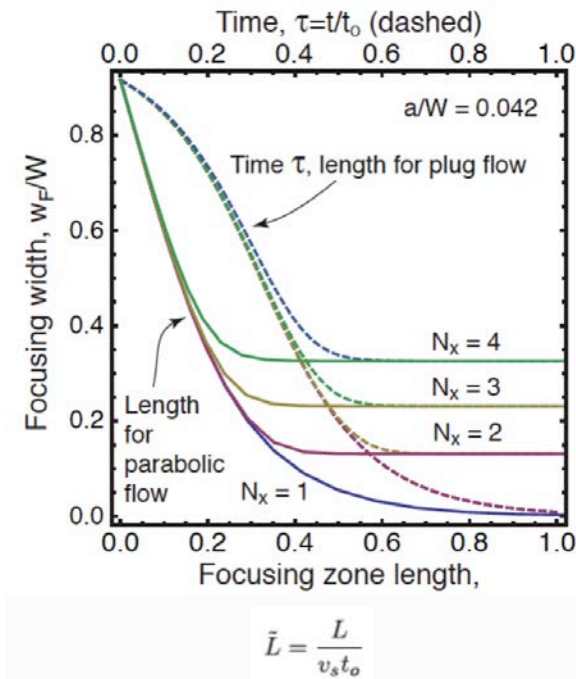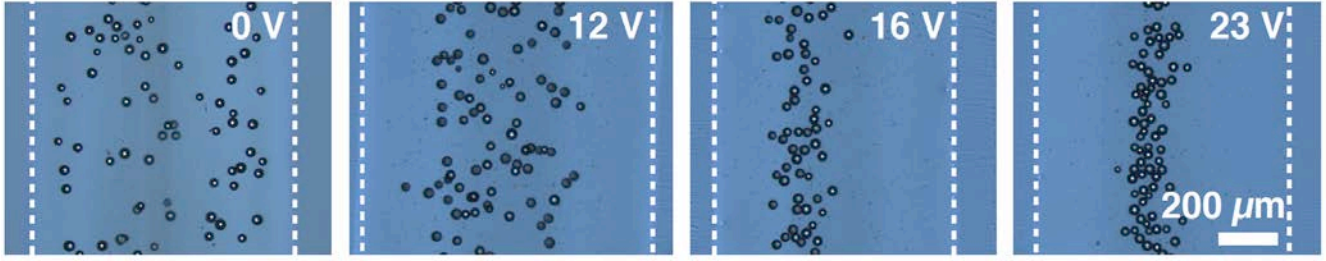

$$\tilde{L} = \frac{L}{v_s t_o}$$

Figure 2: The predicted focusing behavior of particles experiencing primary radiation and secondary scattering forces, in parabolic and plug flows.

Acoustic forces created by standing pressure waves are an attractive pathway to increasing the density and alignment of particles: they are active over large distances and relatively material agnostic (*i.e.*, they do not require specific surface functionalization, solution chemistries, or electromagnetic properties). In many of the above applications, the particles are micron-sized or larger, such that the magnitude of easily achieved acoustic forces is much greater than those associated with fluid drag, implying that particles can be transported and assembled over relatively long distances on the order of seconds or less. These benefits create new opportunities to incorporate acoustic excitation in nozzles used for three-dimensional printing, to dramatically increase the density and alignment of particles relative to that of the 'ink'.

In this work, we use previously developed solutions for acoustic forces generated by standing waves in a channel[5] to identify the

[a] Corresponding author. Email: rcollino@engr.ucsb.edu

Figure 3: Microstructural variation of printed lines (outlined by dashes) of barium titanate spheres in epoxy, illustrating the effect of the excitation voltage of the piezoelectric element on the focusing width of the particles.

scaling relationships that control particle transport and ordering. The goal is to elucidate the connections between channel dimensions, particle dimensions, acoustic pressures, focusing zone size and flow characteristics needed to design effective

nozzles for material deposition. We consider a standing half-wave in pressure and particles (with radius a) that are less compressible than the fluid, which implies that particles are driven to the center of the channel, *i.e.,* there is a single focusing node at the center of the channel of width W and flow at uniform velocity v_S. The coordinate system and device geometry used in this work is shown in Fig. 1, where the direction of the wave is transverse to the channel in the $x-$direction (with $x = 0$ being the center of the channel), while the flow direction is in the positive $z-$direction. Fig. 2. Shows the normalized focusing width, w_F/W, as a function of time and as a function of the distance travelled. The effect of excitation energy of the piezoelectric element is illustrated in Fig. 3, where focusing width of particles is varied according to the applied voltage.

This analysis allows one to identify a dimensionless measure of focusing efficacy for a print nozzle, by balancing time scales for transverse focusing, and aggregation in the flow direction, as shown in Fig. 4. If the time required for axial aggregation is too small, the printed line will be have greater transverse density than axial density. Conversely, if the time for axial aggregation is too large, aggregates may form to that would lead to axial variations in printed microstructures (along the print line), critically, jamming might occur. Contours of the ratio of these time scales are shown in Fig. 4 as a function of the volume fraction of particles and the effective focusing zone length. This key result provides guidance as to the desired length of the nozzle as a function of the acoustic excitation and initial particle density.
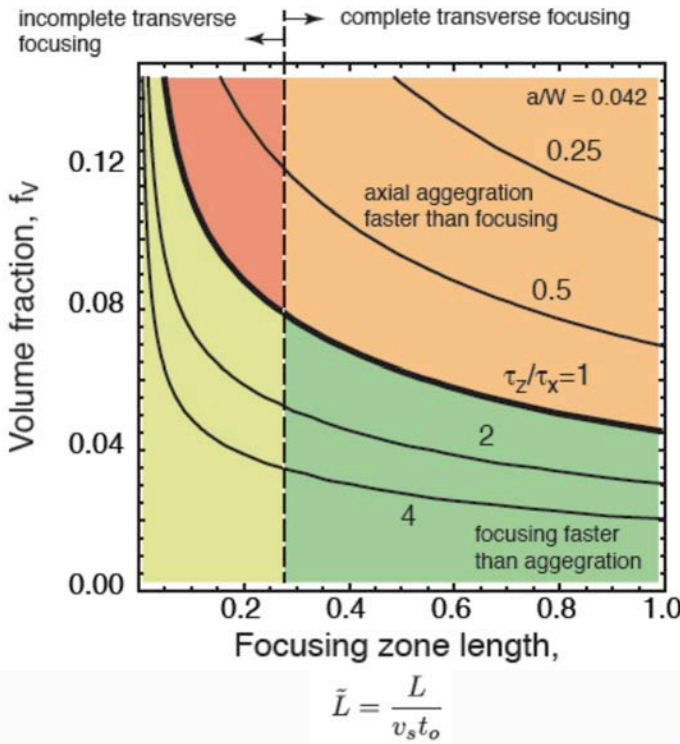

$$\tilde{L} = \frac{L}{v_s t_o}$$

Figure 4: Contours of the aggregation parameter $P_A = \tau_z/\tau_x$, where a value of one represents a balance of transverse focusing and axial aggregation time scales, as a function of the focusing zone length. For $P_A < 1$, axial aggregation occurs faster than focusing; the opposite is true for $P_A > 1$

References

[1] Kim, S.-H., Lee, S. Y., Yang, S.-M., Yi:, G.-R. Self-Assembled Colloidal Structures for Photonics, *NPG Asia Mater.* **3**: 25-33, 2011.

[2] O'Halloran, A., O'Malley, F., McHugh, P. A Review on Dielectric Elastomer Actuators, Technology, Applications, and Challenges. *J. Appl Phys* **104**:071101, 2008.

[3] Ge, Q., Qi, H. J., Dunn, M. L. Active Materials by Four-Dimension Printing, *Appl Phys Lett.* **103**:131901, 2013.

[4] Bakarich, S. E., Gorkin, R. Panhuis, M. i. h., Spinks, G. M. 4D Printing with Mechanically Robust, Thermally Actuating Hydrogels. *Macromol Rapid Comm* **36**:1211-1217, 2015.

[5] Collino, R. R., Ray, T.R., Fleming, R. C., Cornell, J. D., Compton, B. G., Begley, M. R. Deposition of Ordered Two-Phase Materials using Microfluidic Print Nozzles with Acoustic Focusing. *Extreme Mech Lett* **5**: 37-46, 2015.

EXPERIMENTAL STUDY OF FLOW REGIMES AND EMPIRICAL CORRELATIONS OF THE PRESSURE DROP IN A TRICKLE BED REACTOR

Imen Ben Salem[1], Humair Nadeem[1], Amna Al Maqtari[2], Mohamed Sassi[1]
[1]Institute Center for Energy (iEnergy), Department of Mechanical and Materials Engineering, Masdar Institute of Science and Technology, Masdar City, Abu Dhabi, United Arab Emirates
[2]Takreer Research Center (TRC), Abu Dhabi, UAE

<u>*Summary*</u> Trickle bed reactors (TBRs) are an important component in the refining processes. TBRs are widely popular in the hydro-treatment of the "bottom-of-the-barrel" components of medium and heavy oil fractions specifically the hydrocracking of residual oils, hydrogenation of aromatics in gasoil and the hydrocracking of lube-oils (Sie and Krishna, 1998). When such heavy oil suspensions are treated in TBRs, a residual fraction of fine particles may be deposited onto the bed surface. If continued unabated, the deposition even in small concentrations, will overtime cause pore plugging and increases the pressure drop over the TBR. The catalyst operates as a huge filter now capturing the fine particles instead of its primary role to the extent that the chemically active catalyst has to be replaced before the completion of its operating life that incurs economic costs.

METHODOLOGY

In this work, we focus on multi-scale experimental investigations of the inter-play between flow regimes and fines deposition in trickle bed reactors in pursuit of mitigation of the pressure build-up problem. The experimental work includes the visualization and characterization of flow regimes in quasi-two-dimensional porous medium with an average pore diameter close to the values encountered in trickle beds. A parametric study is done for the development of flow regimes and the transition between them when the geometry and arrangement of the particles within the porous medium are varied. Experimental observations are made to investigate the development and transition of these flow regimes over a wide range of liquid and gas velocities. Cylindrical particles are placed between two glass plates that are sealed on the sides and water and air are injected over them using an injection manifold to simulate multiphase flow in a TBR. A diffused LED light table is used to illuminate the experimental window while real time images are obtained using a high-speed camera (figure 1).

A Pilot tubular TBR was used to determine the pressure drop across the Trickle Bed Reactor with and without fine particles brought in by the liquid feed (figure 2). The pilot plant consisted tubular reactor with length 0.79 m and dia. 0.0183. Due to its similarity to the fines found commercial TBRs, kaolin particle of size 50 ☐m were used as fine particles. In order to prevent cake formation, Homogeneous mixing of the suspension was accomplished in the inlet tank which was equipped with a magnetic stirrer and were stirred continuously in different concentrations with LGO in the feed tank. The desired flow of LGO through the feed tank was pumped to the inlet of the reactor where it mixes with the desired flow of incoming gas and enters the Trickle Bed Reactor.

In order to record pressure drop across the reactor, two pressure transducers were installed, each at the inlet and the outlet of the reactor. After passing through the reactor, the LGO-nitrogen mixture enters the separator where gas is separated and liquid goes into the collector tank. The amount of liquid that leaves the feed tank and enters the collector tank is measured by placing the tanks at the weighing scale. The pressure of the transducers can be monitored and recorded by the electronic unit associated with the pressure transducers. The system was single pass and LGO obtained at collector end was not recycled to the feed tank to maintain concentration of fine particles in the feed.
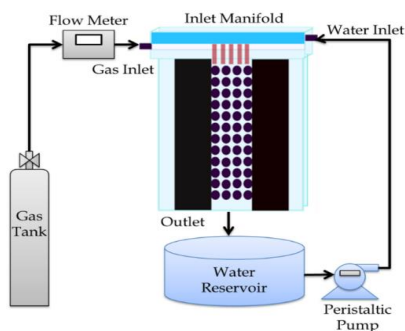

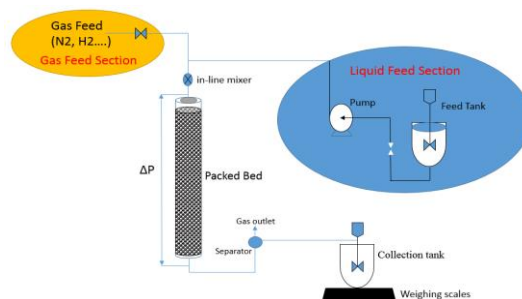Figure 1: Schematic representation of experimental setup to visualize flow regimes in a TBR

Figure 2: The pilot tubular TBR for high pressure and fine deposition study

[a] Corresponding author. Email: msassi@masdar.ac.ae

DISCUSSION

In Figure 3, flow maps are reported depicting all four regimes and the transition regions between them. Transition regions occur where the characteristics of more than one flow regime coexist. The 2D experimental results are then compared with existing literature data of three dimensional results and found to be in good agreement. Emphasis is placed on the transition between the trickle and pulse regimes since that is the most important mode of operation in industrial trickle bed reactors. It is observed that the change in diameters of the cylindrical particles in a two dimensional trickle bed reactor has no significant effect on the transition between the flow regimes when the porosity of the bed is kept constant.

Once the dominant flow regime in the TBR has been identified, the pressure drop was investigated for different fluids with pressure varying between 10-30 bars and varying liquid and gas velocities in the ranges of 0.1-0.5 cm/s and 20-95 cm/s, respectively in a tubular TBR. Glass beads of different diameters were used instead of the catalyst in the tubular pilot reactor. Pressure drop values were plotted against superficial liquid and gas velocities, operating pressures, glass bead diameters and fluid properties. The results thus compiled were used to obtain a correlation for the pressure drop in the pilot plant reactor within a given set of operating conditions. The correlation obtained was compared with data available in literature (Giri and Majumder, 2014) and was found to be in good agreement.

It was mainly found that increases in the superficial fluid velocities, operating pressures, gas density and liquid viscosity caused a rise in the pressure drop whereas an increase in the size of the catalyst particles decreased the pressure drop in the reactor, as shown in Figure 4.
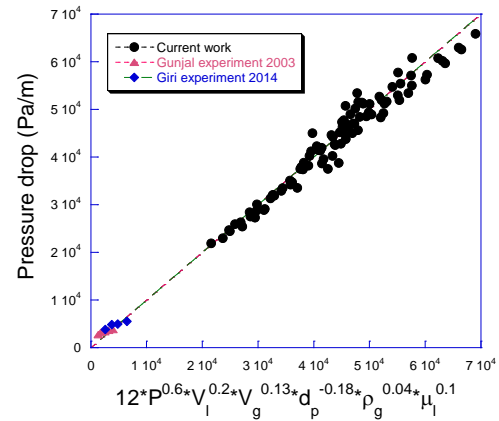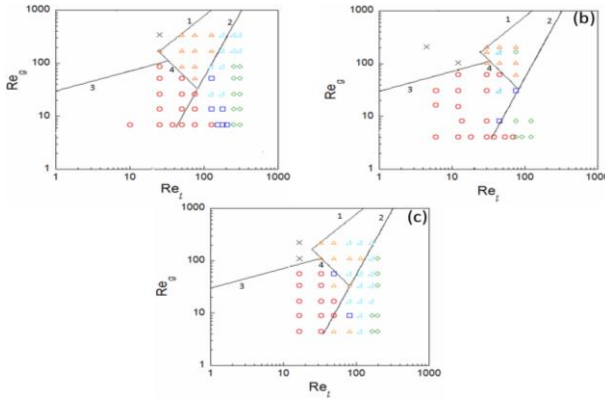
| Figure 3: Boundaries between flow regimes observed for different Reynold's numbers where the lines 1-4 denote literature empirical relations ($\bigcirc$Trickle, $\square$Trickle-Bubble, $\diamondsuit$Bubble, $\blacktriangle$Bubble-Pulse, $\triangle$Pulse and $\times$Spray) | Figure 4: Pressure drop in TBR with respect to different operating and geometrical parameters compared to literature data. |

The effect of fines deposition on the pressure drop is finally examined and compared with two-phase pressure drop in the absence of fine particles. It was found that with the deposition of the fine particles, the pressure drop across the reactor increases dramatically.

ACKNOWLEDGEMENTS

References

[1] Giri, Ajit Kumar, and Subrata Kumar Majumder. 2014. "Pressure Drop and Its Reduction of Gas – Non-Newtonian Liquid Flow in Downflow Trickle Bed Reactor (DTBR)." Chemical Engineering Research and Design 92(1): 34–42.

[2] Sie, S.T., and R. Krishna. 1998. 14 Process Development and Scale Up: Scale up and Scale down of Trickle Bed Processes. TU Delft: Delft University of Technology, Faculty of Chemical Technology and Materials Science.

MS04 - Nonlinear Dynamics of Engineering Systems

SIMULATING NONLINEAR DYNAMICAL TRANSITIONS OF SINGLE MOLECULE DNA

N. C. Perkins[1], A. Hirsh[2] & T. D. Lillian[3]
[1]Mechanical Engineering, University of Michigan, Ann Arbor, Michigan, USA
[2]MathWorks, Novi, Michigan, USA
[3]Mechanical Engineering, Texas Tech University, Lubbock, Texas, USA

<u>*Summary*</u> The dynamics of DNA molecules play essential roles in the life cycle of cells. Large dynamical transitions in the conformations of single DNA molecules are required for many cellular functions including, for example, DNA transcription, replication and repair. This paper summarizes how dynamical transitions of DNA can be simulated using a nonlinear rod theory that captures the nonlinear bending and twisting of the molecule on long length/time scales. The resulting numerical solutions describe conformational changes of DNA in the context of two examples; namely 1) the dynamic relaxation of DNA supercoils induced by enzymes, and 2) the dynamic ejection of DNA from viruses during host infection.

BACKGROUND AND SUMMARY

DNA is a fascinating and enormously long biopolymer molecule that encodes the genetic information to sustain life. While the chemical composition of DNA has been known for over 50 years, many unresolved questions remain regarding how the *structure* of DNA affects its cellular functions [1, 2]. By *structure,* we refer to the shape and stress of the molecule and how these control DNA's primary functions including DNA transcription, replication and repair. For example, the biomolecular motor RNA polymerase, which actively transcribes the genetic code within DNA, also mechanically twists the molecule and to a degree that frequently induces distant DNA supercoils that can hinder transcription. How supercoils and other DNA structures form, and the dynamics and energy required for their formation, are issues examined in this paper. The results contribute to our newly developing knowledge of the genome-scale dynamics of DNA.

The results in this paper follow from a nonlinear rod theory that describes the nonlinear twisting/bending dynamics of DNA on biologically relevant length/time scales [3-6]; refer to Fig. 1. This theory incorporates the physics of large twisting/bending of the DNA helical axis, DNA-protein interactions, electrostatic interactions, and the hydrodynamics of the surrounding fluid [7, 8]. These effects are present in two example systems reviewed in this paper. The first concerns the formation and the dynamical relaxation of DNA supercoils as further detailed in [7]. The second example considers the rapid ejection of DNA from viruses during host infection. In particular, we review salient results from [8] which reveal how the ejection process is initiated by a highly strained DNA supercoil that explosively straightens to prime the ejection process.
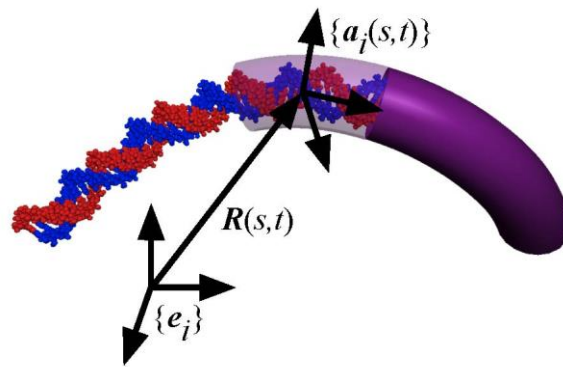
Figure 1: The DNA double-helix is approximated as a nonlinear rod that captures the nonlinear and three-dimensional bending and twisting of the helical axis, and additional forces due to DNA-bound protein/enzymes, electrostatics and hydrodynamics.

RESULTS AND DISCUSSION

Consider first the important example of DNA supercoil formation and relaxation. Note that a single DNA molecule, on the centimetre scale in length, must be compacted by four orders of magnitude to fit within the small confines of the micron-scale cell nucleus. Doing so requires that this exceedingly long but slender molecule bend and twist massively in the form of supercoils. Supercoiling is not static and it changes significantly during cellular processes including DNA transcription, replication and repair. An excellent example of this is the effect induced by the aforementioned

---

biomolecular motor RNA polymerase which, during transcription, locally untwists the double helix to gain access to the genetic code (base-pairs) tucked within. Sustained local untwisting during transcription alters the long-length scale supercoiling of DNA and can build strain energy that ultimately impedes further transcription. Fortunately, nature provides a means to relieve that strain energy by relaxing tight supercoils. That action derives from enzymes known as topoisomerases that chemically cut through one or both helical strands to relieve strain energy. This first example employs the nonlinear rod theory to model the dynamic relaxation of supercoils induced by the action of a particular enzyme known as human Topoisomerase IB (Topo IB) that cuts through a single DNA strand. Figure 2(A) reports the simulated relaxation of a large DNA supercoil which rapidly unwinds on the microsecond time scale. The relaxation manifests in large conformational changes of the molecule and in a cascading decrease in DNA elastic energy as signalled by the step-like decrease in the linking number Lk which describes the topology of the supercoil.

The second example concerns the packing of DNA in viruses during maturation and the subsequent ejection of the viral genome into a host during infection. The example of our study concerns the bacteriophage virus $\phi 29$ which is one of the smallest bacteriophages and it has long served as a model system to study virus structure, assembly, and ejection. Recent cyroelectron micrography [9] revealed a stunning, highly strained DNA toroidal supercoil within the so-called connector domain of the virus that connects the capsid to the tail tube through which DNA passes during infection. While the function of that highly-strained DNA is unknown, it was hypothesized to play a role during DNA ejection. That role is confirmed in the simulated results reported in Figure 2(B) which illustrate a violent straightening of this energetic supercoil at the very start of the ejection process. This large conformation change occurs on a microsecond time scale and prior to initiating the ejection of the remainder of the DNA contained in the capsid (now shown). Thus, the DNA toroid primes the ejection process through a rapid release of stored energy.
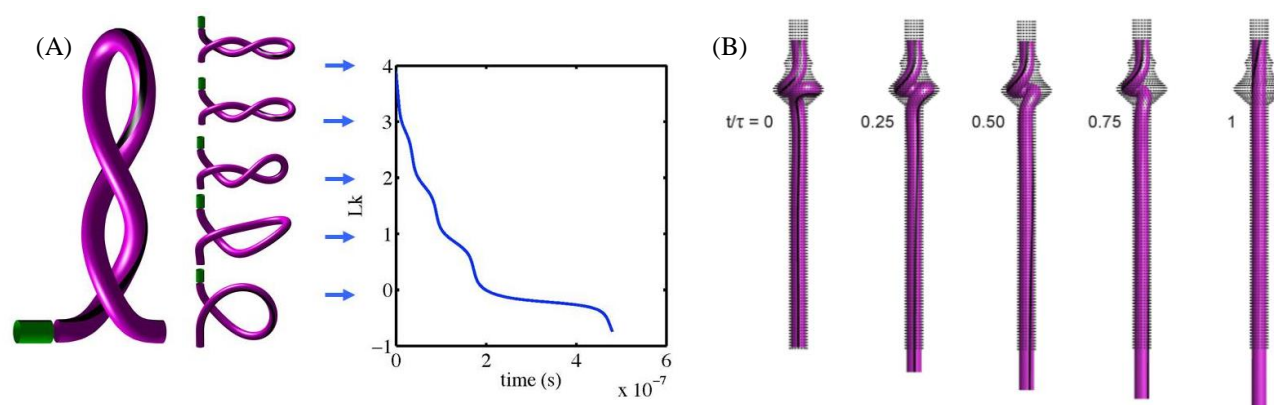
Figure 2: (A) Dynamic relaxation of a large DNA supercoil (far left) through the action of Topo IB which locally relieves strain energy (green site) and induces large and rapid conformational changes of the molecule. The strain energy (related to the linking number Lk) relaxes in a stepwise manner in a fraction of a microsecond. (B) Dynamic relaxation of a highly strained DNA supercoil confined to the connector region of the bacteriophage $\phi 29$. The explosive straightening of this constrained supercoil primes the DNA ejection process during host infection.

References

[1] Alberts B., Johnson A., Lewis J., Raff M., Roberts K., Walter P.: Molecular Biology of the Cell, (5th Ed.), Garland Science 2008.

[2] Lodish H., Berk A., Matsudaira P, Kaiser C.A., Krieger M., Scott M.P., Zipursky L., Darnell J.: Molecular Cell Biology (5th Ed.), W.H. Freeman, New York NY 2004.

[3] Schlick T.: Modeling Superhelical DNA: Recent Analytical and Dynamic Approaches. *Curr. Opinion Structural Biology* **5**:245-262, 1995.

[4] Olson W. K.: Simulating DNA at Low Resolution. *Curr. Opinion Structural Biology* **6**:242-256, 1996.

[5] Tobias I., Swigon D., Coleman B.D.: Elastic Stability of DNA Configurations. I. General Theory. *Phys. Rev. E* **61**:747-758, 2000.

[6] Goyal S., Perkins N.C., Lee C.L.: Nonlinear Dynamics and Loop Formation in Kirchhoff Rods with Implications to the Mechanics of DNA and Cables. *J. Comp. Physics* **209**:371-389, 2005.

[7] Lillian T.D., Taranova M., Wereszczynski J., Andricioaei I., Perkins, N.C.: A Multi-scale Dynamic Model of DNA Supercoil Relaxation by Topoisomerase IB. *Biophysical J.* **100**:2016-2023, 2011.

[8] Hirsh A.D, Taranova M., Lionberger T.A., Lillian T.D., Andricioaei I., Perkins N.C.: Structural Ensemble and Dynamics of Toroidal-like DNA Shapes in Bacteriophage $\phi 29$ Exit Cavity. *Biophysical J.* **104**:2058-2076, 2013.

[9] Tang J., Olson N., Jardine P.J., Girimes S., Anderson D.L., Baker T.S.: DNA Poised for Release in Bacteriophage $\phi 29$. *Structure* **16:**935-943, 2008

ON THE ANALYSIS OF CHATTER IN MECHANICAL SYSTEMS WITH IMPACTS

Harry Dankowicz *[1], Erika Fotsch[2], and Alan Champneys[3]

[1]*Mechanical Science and Engineering, University of Illinois at Urbana-Champaign, Urbana, Illinois, USA*
[2]*Mechanical Science and Engineering, University of Illinois at Urbana-Champaign, Urbana, Illinois, USA*
[3]*Department of Engineering Mathematics, University of Bristol, Bristol, United Kingdom*

Summary In rigid-body mechanics, models that capture collisional contact as an instantaneous exchange of momentum may exhibit dynamics that include infinite sequences of impacts accumulating in finite time to a state of persistent contact. In this paper, we describe recent observations of such chatter-like behavior both in forward and reverse time dynamics in several example systems. We review theoretical tools that enable a successful analysis of transient and steady-state behavior with chatter in such systems by effectively bypassing the tail end of a chatter sequence of impacts. Finally, we show how such theoretical insight informs computational implementations for forward simulation as well as parameter continuation of associated boundary-value problems.

INTRODUCTION

In models of mechanical systems that account for persistent or intermittent contact with hard and rough obstacles, a common approximation considers the limit of time-scale separation in which collisions are described as instantaneous impacts associated with sudden changes to the system velocities, and sustained contact is described in terms of the set-valued Coulomb-Amonton law of dry friction. Time histories of position and velocity coordinates are naturally partitioned into disjoint segments, governed by segment-specific force interactions, and characterized by termination conditions associated with the onset or cessation of contact, or with transitions between relative stick and slip.

Following Goebel, Sanfelice and Teel [1], we characterize a segmented time history in terms of a subset E of $R_{\geq 0} \times \mathbb{N}$ given by a sequential union of sets $([t_j, t_{j+1}], j)$ with $t_j \leq t_{j+1}$, possibly terminated by a set $([t_N, T), N)$ for some integer N and T finite or $T = \infty$. Here, the index j tracks the number of transitions, while $[t_j, t_{j+1}]$ and/or $[t_N, T)$ describe intervals of absolute continuity of the system dynamics. A time history is said to be *Zeno* if E contains an infinite union of sets $([t_j, t_{j+1}], j)$, such that the sequence $\{t_j\}$ is bounded. It follows that a Zeno time history includes infinitely many transitions in finite time and, by compactness, a finite time of accumulation of a subsequence of these transitions. We refer to the time of accumulation as the corresponding *Zeno point*.

A forward-time Zeno point occurs naturally in a mechanical system with impacts governed by a dissipative impact law, e.g., the Newtonian coefficient of restitution model for normal impacts or the Stronge energetic coefficient of restitution model for arbitrary impacts that include frictional interactions. Surprisingly, the analysis in Nordmark, Dankowicz, and Champneys [2] shows the possibility also for a reverse-time Zeno point in the Stronge impact model, even for constant free-flight acceleration. Indeed, as discussed in [2], both forward and reverse chatter is associated with one-parameter families of chatter sequences with a common Zeno point. In the case of reverse-time chatter, such a degeneracy poses a serious challenge to the description of the forward-time dynamics in terms of a unique time history past the corresponding Zeno point.

AN ANALYTICAL TREATMENT

A proper accounting of the exchange of momentum between a mechanical system and a rigid obstacle during a forward-time chatter sequence necessitates an analysis of the asymptotic behavior at the tail end of chatter. In this paper, we review the work of Nordmark & Piiroinen [3], wherein this asymptotic behavior is described in terms of dynamics along the stable manifold of a fixed point corresponding to persistent contact in a suitably defined iterated map. In particular, [3] derives an implicit equation for a *bypass* map that associates an impact late in the chatter sequence to the configuration and velocity state at the corresponding Zeno point. An explicit approximation for the bypass map, including the corresponding jump in time, is further provided in the form of a series expansion in the impact velocity.

A critical border condition occurs along a family of time histories with forward-time chatter under variations in system parameters when the Zeno point is associated with an immediate release (with zero acceleration) into sustained free flight. When the border orbit is a periodic trajectory of the dynamical system, a persistent periodic trajectory in which the chatter sequence is followed by a phase of sustained contact exists only on one side of the critical parameter value. As shown in unpublished work by Nordmark and Kisitu [4], a complex bifurcation scenario is obtained on the opposite side of the critical parameter value, including cascades of smooth saddle-node and period-doubling bifurcations, intervals of robust chaos, and grazing bifurcations. In this paper, we provide a detailed review of the analysis in [4] and illustrate the predictions on example physical applications described in Alzate and Piiroinen [5] and Fotsch [6] (cf. Fig. 1).

---

*Corresponding author. Email: danko@illinois.edu
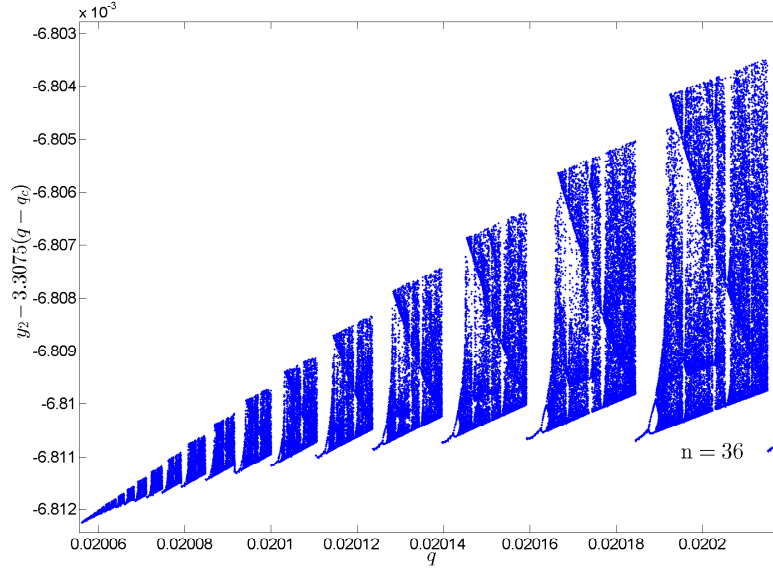
Figure 1: Bifurcation cascade of the steady-state response of a mechanical pressure-relief valve [6] near a critical parameter value q_c corresponding to a periodic orbit with forward-time chatter accumulating at a transition to free flight. Here, y_2 denotes a sampled velocity and q describes a flow rate.

COMPUTATIONAL TOOLS

As discussed in [3], the bypass map associated with chatter may be encoded in computational tools for forward integration and parameter continuation. Here, the tail end of the chatter sequence is replaced by the application of an approximate jump in state space and time in such a way that an appropriate error estimate falls below a given tolerance. Using a shooting-based approach, [3] investigates families of periodic orbits and their bifurcations under variations in problem parameters for a sample two-degree-of-freedom mechanism.

As an alternative implementation, in this paper we briefly describe a collocation implementation of a forward-time truncated chatter sequence in a computational toolbox compatible with the MATLAB-based COCO development platform. We show how the toolbox may be embedded in a periodic orbit continuation problem for a mechanical system with impacts, and how error estimation is used to make adaptive updates to individual segment meshes, as well as to the number of segments.

CONCLUSIONS

In hybrid dynamical systems, e.g., mechanical systems with impacts and friction, degenerate interactions between system time histories and surfaces of discontinuity in the governing dynamics give rise to a unique set of phenomena that call for advances in theoretical and computational tools. For the phenomenology associated with forward-time chatter, a relatively mature theory provides insight and forms the foundation for computational tools for simulation and parameter continuation. Predictions of reverse-time chatter in simple models of rigid-body dynamics add to a library of paradoxes that call attention to the need for a better understanding of the effects of time-scale separation on the predictability of the forward-time dynamics.

References

[1] Goebel R., Sanfelice R.G., Teel A.R.: Hybrid Dynamical Systems: Modeling, Stability, and Robustness. Princeton University Press, 2012.

[2] Nordmark A., Dankowicz H., Champneys A.: Friction-Induced Reverse Chatter in Rigid-Body Mechanisms with Impacts. IMA J. Appl Math 1-35, 2011.

[3] Nordmark A.B., Piiroinen P.T.: Simulation and Stability Analysis of Impacting Systems with Complete Chatter. Nonlinear Dyn 58:85-106, 2009.

[4] Nordmark A.B., Kisitu R.E.M.:. On Chattering Bifurcations in 1 DOF Impact Oscillator Models. Unpublished, 2003.

[5] Alzate R., Piiroinen P.T., di Bernardo M.: From Complete to Incomplete Chattering: A Novel Route to Chaos in Impacting Cam-Follower Systems. Int J Bifur Chaos 22(5):1250102 1-14, 2012.

[6] Fotsch E.L.: Bifurcation Analysis Near the Cessation of Complete Chatter and Shilnikov Homoclinic Trajectories in a Pressure Relief Valve Model. MSc Thesis, University of Illinois at Urbana-Champaign, Department of Mechanical Science and Engineering, Urbana, IL, USA, 2016.

SYNCHRONIZATION-BASED ESTIMATION OF THE MAXIMAL LYAPUNOV EXPONENT OF NONSMOOTH SYSTEMS

Remco I. Leine[*1] and Michael Baumann[2]
[1]*Institute for Nonlinear Mechanics, University of Stuttgart, Germany*
[2]*Institute of Mechanical Systems, ETH Zurich, Switzerland*

Summary Lyapunov exponents of chaotic attractors are hard to estimate, especially for non-smooth systems. One method to estimate the maximal Lyapunov exponent is by using its relationship with the synchronization properties of coupled systems. The maximal Lyapunov exponent is equal to the minimal proportional feedback gain necessary to achieve full state synchronization with a replica system. In this paper, we prove this statement for the general class of nonsmooth systems in the framework of measure differential inclusions. Numerical results of a mechanical impact oscillator illustrate the effectiveness of the method for nonsmooth systems.

LYAPUNOV EXPONENT

The spectrum of Lyapunov exponents is an important characteristic of limit sets. It measures the exponential convergence or divergence of nearby trajectories, thereby capturing the sensitivity of solutions with respect to initial conditions. A chaotic attractor has at least one positive Lyapunov exponent. Estimating the maximal Lyapunov exponent using chaos synchronization has been proposed for mechanical systems with impacts and for discrete maps by the authors of [1]. In this paper, we employ this idea for the class of nonsmooth systems written in framework of measure differential inclusions [2] as

$$\frac{\mathrm{d}\boldsymbol{x}}{\mathrm{d}\mu} \in \boldsymbol{\mathcal{F}}(\boldsymbol{x}, t), \tag{1}$$

where $\frac{\mathrm{d}\boldsymbol{x}}{\mathrm{d}\mu}$ is the density of the measure $\mathrm{d}\boldsymbol{x}$ with respect to a positive Radon measure $\mathrm{d}\mu$.

Consider a reference solution $\boldsymbol{x}(t) = \boldsymbol{\varphi}(t, \boldsymbol{x}_0, t_0)$ and a perturbed solution $(\boldsymbol{x} + \Delta\boldsymbol{x})(t) = \boldsymbol{\varphi}(t, \boldsymbol{x}_0 + \boldsymbol{e}h, t_0)$ for the initial conditions $\boldsymbol{x}(t_0) = \boldsymbol{x}_0$ and $\Delta\boldsymbol{x}(t_0) = \boldsymbol{e}h$. We define the normalized disturbance as

$$\boldsymbol{\xi}(t, \boldsymbol{e}, t_0) := \lim_{h\downarrow 0, h\notin E_h^\xi} \frac{1}{h}(\boldsymbol{\varphi}(t, \boldsymbol{x}_0 + \boldsymbol{e}h, t_0) - \boldsymbol{\varphi}(t, \boldsymbol{x}_0, t_0)). \tag{2}$$

The limit exists almost everywhere, if the following assumption is fulfilled.

Assumption 1. The difference of the solutions of system (1) is in the order of the perturbation, that is, $\boldsymbol{\varphi}(t, \boldsymbol{x}_0 + \boldsymbol{e}h, t_0) - \boldsymbol{\varphi}(t, \boldsymbol{x}_0, t_0) \in \mathcal{O}(h)$ a.e.

Assumption 1 implies continuous dependence on initial conditions and, consequently, uniqueness of solutions in forward time. Uniqueness of solutions implies that the density $\frac{\mathrm{d}\boldsymbol{x}}{\mathrm{d}\mu}$ is unique as well and the dynamics can be written as the measure differential equation

$$\frac{\mathrm{d}\boldsymbol{x}}{\mathrm{d}\mu} = \boldsymbol{f}(\boldsymbol{x}^-, t) \tag{3}$$

with $\boldsymbol{f}(\boldsymbol{x}, t) \in \boldsymbol{\mathcal{F}}(\boldsymbol{x}, t)$. The maximal Lyapunov exponent is defined using the normalized difference as

$$\lambda_{\max} := \max_{\boldsymbol{e}} \lim_{\substack{t\to\infty \\ t\notin E_t^\xi}} \frac{1}{t} \ln \|\boldsymbol{\xi}(t, \boldsymbol{e}, t_0)\|. \tag{4}$$

CRITICAL COUPLING

We consider two coupled non-smooth systems, where (3) is accompanied by a replica extended by a proportional error feedback in the form

$$\frac{\mathrm{d}\boldsymbol{y}}{\mathrm{d}\mu} = \boldsymbol{f}(\boldsymbol{y}^-, t) - k(\boldsymbol{y}^- - \boldsymbol{x}^-)\frac{\mathrm{d}t}{\mathrm{d}\mu}, \tag{5}$$

*Corresponding author. Email: leine@inm.uni-stuttgart.de
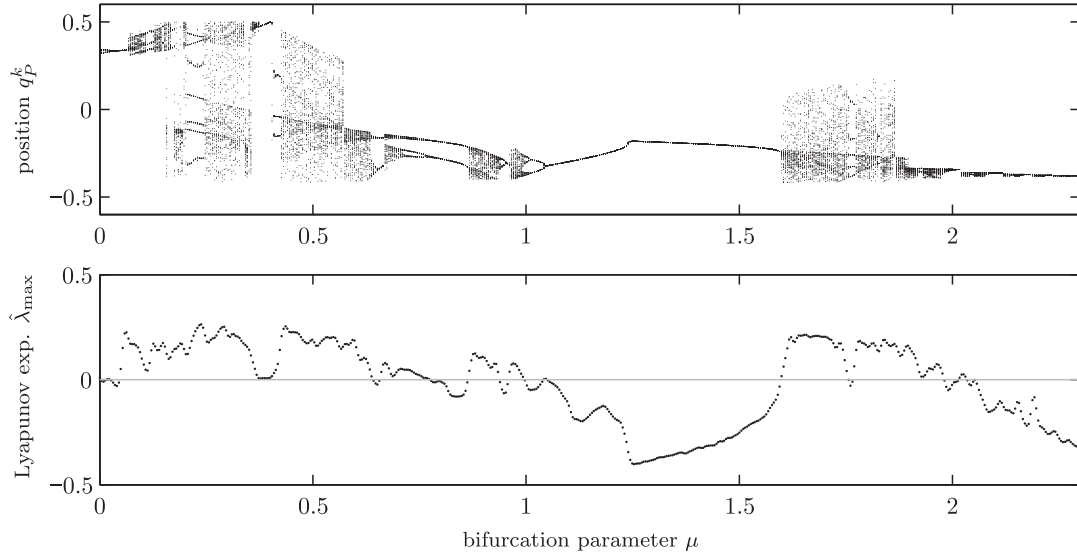
Figure 1: Brute force diagram (top) and estimation of the maximal Lyapunov exponent $\hat{\lambda}_{\text{max}}$ (bottom) with the bifurcation parameter h. The chaotic solutions correspond to $\hat{\lambda}_{\text{max}} > 0$, while the periodic windows correspond to $\hat{\lambda}_{\text{max}} < 0$.

where $k \in \mathbb{R}$ is the proportional feedback gain. Let $\boldsymbol{y}(t) = \boldsymbol{\varphi}_k(t, \boldsymbol{x}_0 + \boldsymbol{e}h, t_0)$ be the solution of (5) for a given k. Therefore, local synchronization is achieved if the normalized synchronization error

$$\boldsymbol{\zeta}(t, \boldsymbol{e}, t_0) := \lim_{h \downarrow 0, h \notin E_h^\zeta} \frac{1}{h}(\boldsymbol{\varphi}_k(t, \boldsymbol{x}_0 + \boldsymbol{e}h, t_0) - \boldsymbol{\varphi}(t, \boldsymbol{x}_0, t_0)) \tag{6}$$

tends to zero. The normalized disturbance $\boldsymbol{\xi}$ in (2) and the normalized synchronization error $\boldsymbol{\zeta}$ in (6) fulfill

$$\boldsymbol{\zeta} = \boldsymbol{\xi}e^{-k(t-t_0)} \quad \text{a.e.} \tag{7}$$

if Assumption 1 is fulfilled. The statement (7) together with (4) imply that local synchronization of systems (3) and (5) is achieved if the coupling gain k is larger than the maximal Lyapunov exponent λ_{max}. Conversely, $k < \lambda_{\text{max}}$ implies that no local synchronization is achieved for some initial conditions. In practice, the perturbation for any initial condition will eventually turn into the direction of maximal expansion. Therefore, the maximal Lyapunov exponent can be estimated using the minimal proportional feedback gain for which synchronization is achieved.

NUMERICAL EXAMPLE

The results are illustrated using the example of a mechanical Duffing-oscillator with two geometric unilateral constraints. The impact oscillator is excited by an external, harmonic forcing and the generalized Newton's impact law is chosen. The viscous damping coefficient is chosen as bifurcation parameter. The brute force diagram in Figure 1 shows the position at the Poincaré sections for a sweep down of the bifurcation parameter. The estimated maximal Lyapunov exponent is positive for the chaotic attractors and negative ($\hat{\lambda}_{\text{max}}$ at zero is not considered) during the periodic windows.

References

[1] A. Stefanski and T. Kapitaniak, "Estimation of the dominant Lyapunov exponent of non-smooth systems on the basis of maps synchronization," *Chaos, Solitons & Fractals*, vol. 15, no. 2, pp. 233–244, 2003.

[2] R. I. Leine and N. van de Wouw, *Stability and Convergence of Mechanical Systems with Unilateral Constraints*, vol. 36 of *Lecture Notes in Applied and Computational Mechanics*. Berlin: Springer-Verlag, 2008.

NONLINEAR COUPLING BETWEEN AXIAL AND TRANSVERSAL OSCILLATIONS OF SHEARABLE BEAMS

Stefano Lenci[1a)], Francesco Clementi[1] & Giuseppe Rega[2]

[1]*Department of Civil and Building Engineering, and Architecture, Polytechnic University of Marche, Ancona, Italy*
[2]*Department of Structural and Geotechnical Engineering, Sapienza University of Rome, Rome, Italy*

<u>*Summary*</u> Nonlinear free oscillations of a straight planar Timoshenko beam are investigated by means of the asymptotic development method. Attention is focused on the nonlinear coupling between axial and transversal oscillations of the beam, that are decoupled in the linear regime. The existence of coupled and uncoupled motion is discussed, and the softening vs hardening behaviour of the beam is investigated in depth.

INTRODUCTION

It is known that the axial boundary conditions affect significantly the oscillation behaviour of beams. In particular, axially restrained beams exhibit hardening behaviour, while axially free beams have softening behaviour. This difference, already reported by Atluri [1], is a peculiarity of the nonlinear regime, since in the linearized framework the natural frequencies (for transverse oscillations) are unaffected by the axial restraint when the beam is initially straight. Luongo et al. [2] addressed the same problem by the Galerkin method, while Lacarbonara and Yabuno [3] applied the multiple scale method directly to the governing PDEs and also provided an experimental verification of the phenomenon.

Previous works considered slender beams, and perfectly restrained vs perfectly unrestrained boundary conditions. These limitations have been removed by the authors [4, 5]. Consistently, the (nonlinear) Timoshenko beam model has been considered, taking into account shear deformation and rotational inertia. In order to comprehensively revisit the problem, axial deformation and axial inertia have been included in the model, too. Moreover, an axial spring has been added at one hand to simulate the effect of an elastic constraint with stiffness κ. The limit cases of axially free and axially constrained boundary conditions have been obtained for $\kappa = 0$ and $\kappa \to \infty$, respectively.

In [4] the governing equations have been obtained, and the asymptotic development method, in the Poincaré-Lindstedt version, has been applied to obtain an analytical approximate solution. The expressions of the nonlinear correction coefficient ω_2 have been obtained. In [5] a detailed investigation of the effects on ω_2 of slenderness, end spring stiffness, axial and rotational inertia, and shear stiffness is reported.

To the first order of the asymptotic development, the linear regime is obtained. Here, the axial and transversal behaviour are decoupled. In [4, 5] it is assumed that to first order the axial oscillation is negligible with respect to the transversal one, which is an hypothesis commonly done in the literature. It is based on the observation that for slender beams axial natural frequencies are meaningfully larger than transversal natural frequencies. For stubby beams, however, the gap between axial and transversal frequencies reduces, and they become comparable.

To overcome the previous limitation, in this work the axial *and* transversal first order oscillations are considered simultaneously, and their (nonlinear) coupling at higher orders of the asymptotic development is investigated in depth.

NONLINEAR TIMOSHENKO BEAM MODEL AND ANALYSIS

The following kinematically exact governing equations have been obtained in [4] for the *free* oscillations of a planar, linearly elastic, initially straight Timoshenko beam:

$$\left\{ EA\left[\sqrt{(1+W')^2 + U'^2} - 1 \right] \frac{1+W'}{\sqrt{(1+W')^2 + U'^2}} + GA\left[\theta - \arctan\left(\frac{U'}{1+W'} \right) \right] \frac{U'}{\sqrt{(1+W')^2 + U'^2}} \right\}' = \rho A \ddot{W},$$

$$\left\{ EA\left[\sqrt{(1+W')^2 + U'^2} - 1 \right] \frac{U'}{\sqrt{(1+W')^2 + U'^2}} - GA\left[\theta - \arctan\left(\frac{U'}{1+W'} \right) \right] \frac{1+W'}{\sqrt{(1+W')^2 + U'^2}} \right\}' = \rho A \ddot{U},$$

$$\left[EJ \frac{\theta'}{\sqrt{(1+W')^2 + U'^2}} \right]' - GA\left[\theta - \arctan\left(\frac{U'}{1+W'} \right) \right] \sqrt{(1+W')^2 + U'^2} = \rho J \ddot{\theta},$$

where $W(Z,T)$, $U(Z,T)$ and $\theta(Z,T)$ are the axial and the transversal displacements of the beam axis and the rotation of the cross-section, respectively. Z is the spatial coordinate in the rest rectilinear configuration, which ranges from 0 to the length L, T is the time, prime means derivative with respect to Z and dot means derivative with respect to T.

The considered boundary conditions are (H_0 is the horizontal internal force and M is the bending moment)

$$W(0,T) = 0, \quad H_0(L,T) + \kappa W(L,T) = 0, \quad U(0,T) = 0, \quad U(L,T) = 0, \quad M(0,T) = 0, \quad M(L,T) = 0.$$

The beam is axially fixed at the left end ($Z=0$), while it has an axial linear spring, of stiffness κ, at the right end ($Z=L$).

[a)] Corresponding author. Email: lenci@univpm.it

The previous equations and boundary conditions have been solved approximately by the Poincaré-Lindstedt method, up to the third order, to obtain the linear frequency ω_0 and the nonlinear correction coefficient ω_2. The details of the computations are reported in [6], where the following dimensionless parameters (z measuring the shear stiffness) are used

$$l = L\sqrt{A/J}, \quad z = 1/[2(1+\nu)\chi] = 0.3205, \quad \kappa_h = \kappa L^3/EJ.$$

COUPLED BEHAVIOR WITHIN A REVISITED OVERALL FRAMEWORK

The main results consist of determining the region of existence of the coupled axial-transversal oscillations, and the dependence of ω_2 on the slenderness l and the end spring stiffness κ_h. The results are summarized in the behaviour chart of Fig. 1, where the meaning of the colours is the following:
1. light red: only uncoupled solutions exist and they are hardening;
2. dark red: only uncoupled solutions exist and they are softening;
3. light green: coupled and uncoupled solutions coexist and they are both hardening;
4. dark green: coupled and uncoupled solutions coexist and they are both softening;
5. light blue: coupled and uncoupled solutions coexist; the coupled is softening and the uncoupled is hardening;
6. dark blue: coupled and uncoupled solutions coexist; the coupled is hardening and the uncoupled is softening.
Light/dark colours correspond to hardening/softening of the uncoupled solutions, that always exist. Apart from the region of low values of l and κ_h, the former behaviour occurs mostly for high κ_h (i.e. toward hinged-hinged) and low slenderness, along with the coexisting, prevailingly softening (light blue), coupled oscillation. In turn, the latter occurs for very low κ_h (i.e. toward hinged-supported) and whatever slenderness, along with the coexisting, prevailingly hardening (dark blue), coupled oscillation; but the uncoupled oscillation is again hardening (light green) for not too low values of κ_h.
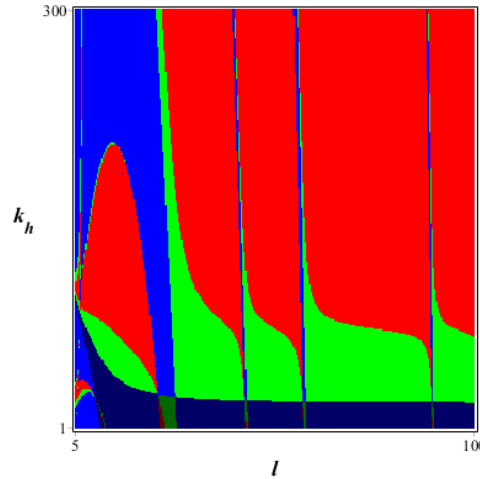
Figure 1. The behaviour chart of ω_2 in the parameters space (l, κ_h) for the first bending mode and the first axial mode.

CONCLUSIONS

An asymptotic solution of the PDEs of a planar beam with whatever slenderness and axial boundary condition has been obtained up to third order, with the aim to study the coupled axial-transversal nonlinear free oscillations. Behaviour charts show the dependence of the nonlinear behaviour upon the problem parameters and the existence of meaningfully coupled oscillations in some relevant regions. The addition of axial oscillations can meaningfully affect the character (hardening to softening or viceversa) of formerly uncoupled transverse oscillations. Numerical validation of asymptotic results is presently going on.

References

[1] Atluri S.: Nonlinear vibrations of hinged beam including nonlinear inertia effects. *ASME J. Appl. Mech.* **40**, 121-126, 1973.
[2] Luongo A., Rega G., Vestroni F.: On nonlinear dynamics of planar shear indeformable beams. *ASME J. Appl. Mech.* **53**, 619-624, 1986.
[3] Lacarbonara W., Yabuno H.: Refined models of elastic beams undergoing large in-plane motions: Theory and experiments. *Int. J. Solids Struct.* **43**, 5066-5084, 2006.
[4] Lenci S., Rega G.: Nonlinear free vibrations of planar elastic beams: A unified treatment of geometrical and mechanical effects. *IUTAM Procedia*, accepted, 2015.
[5] Lenci S., Rega G.: A comprehensive analysis of hardening/softening behaviour of shearable planar beams with whatever axial boundary constraint. *Submitted*, 2015.
[6] Lenci S., Rega G.: Asymptotic analysis of axial-transversal coupling in the free nonlinear vibrations of Timoshenko beams with arbitrary slenderness and axial boundary conditions. *In preparation*, 2016.

OPTIMIZATION OF LOCOMOTION FOR MULTIBODY SYSTEMS MOVING ALONG A PLANE

Felix Chernousko[1] and Tatiana Figurina [*2]

[1,2]*Institute for Problems in Mechanics of Russian Academy of Sciences, Moscow, Russia*

Summary Dynamics and control of multibody systems moving along a horizontal plane are considered. The bodies perform translational motions subject to friction along the plane and control forces due to the interaction between the neighboring bodies. The friction forces obey Coulomb's law. Several types of multibody systems are considered. Optimal motions are obtained that correspond to the maximum average speed or to the shortest way of translation. The obtained results are applicable to mobile robotic systems.

OPTIMIZATION OF RECTILINEAR MOTION OF TWO-BODY SYSTEM

A system consists of two interacting bodies of masses m and M, $m < M$, moving along the horizontal x axis (Fig.1a). The interaction forces acting upon masses m and M are f and $-f$, respectively. They are bounded by the constraint $f \leq f_0$, where f_0 is a given constant, the inequality $f_0 > Mgk$ holds to ensure the translational motion of the system. Hereafter k is the dry friction coefficient and g is the acceleration due to gravity. Denote by x_1 and x_2 the coordinates of the bodies m and M, respectively. We find the control $f(t)$ and the corresponding motion of the system for the given interval $t \in [0, T]$ under condition $f \leq f_0$ and the following assumptions:

$$x_i(0) = 0, \ \dot{x}_i(0) = \dot{x}_i(T) = 0, \ i = 1, 2, \quad x_1(T) = x_2(T), \quad 0 \leq x_2(t) - x_1(t) \leq L, \quad \dot{x}_2(t) \geq 0, \quad t \in [0, T], \quad (1)$$

where L is fixed. Thus, the bigger mass M does not move backwards. Also, we assume that the motion consists of several phases with constant acceleration for both masses.

For several versions of optimal control problems, optimal motions subject to conditions (1) and $f \leq f_0$ are found [1]. For example, the motion having the maximum average speed is described by explicit formulas. We have

$$v = \max\{[x_2(T) - x_2(0)]/T\} = [gkLm(M - m)]^{1/2}(M + m)^{-1} \quad (2)$$

in the case where $f_0 \to \infty$. The optimal ratio m/M that provides the maximum v in the last expression is $1/3$; in this case $v = (gkL)^{1/2}/4$. Similar results are obtained for a more general situation where the coefficients of friction for the bodies m and M are different [1].

If the actuator creating the interaction force rapidly brings the bodies to a state of constant relative velocity, another formulation of the locomotion control problem is reasonable. We can assume that the relative velocity of the bodies is the control bounded by certain constraints. The analysis and optimization of such motions is considered in [2].

OPTIMAL RECTILINEAR MOTION OF A CHAIN OF IDENTICAL BODIES

Let us consider a system consisting of $n \geq 3$ bodies with equal masses $m_i = m$, $i = 1, ..., n$, lying on a horizontal straight line with dry friction acting between the line and the masses (Fig.1b). The interaction forces between the adjacent masses are unbounded so that the velocities of the masses can change instantly. Let x_i and v_i be the coordinate and velocity of the i-th mass, and let F_i be the dry friction force acting on it. Denote by f_i the control force applied by mass i to mass $i + 1$ (we assume $f_0 = f_n = 0$). The motion of the system is governed by equations

$$\dot{x}_i = v_i, \quad m\dot{v}_i = f_{i-1} - f_i + F_i, \qquad F_i = -kmg \, \text{sgn} \, v_i, \qquad i = 1, .., n. \quad (3)$$

Let at the initial and final time instants all masses be at rest and their positions be the same:

$$x_i(0) = 0, \quad v_i(0) = v_i(T) = 0, \quad i = 1, ..., n, \quad x_i(T) = x_1(T), \quad i = 2, ..., n. \quad (4)$$

The problem is to find a motion of the system obeying relations (3) and (4), which maximizes the displacement of the system, $x_1(T) \to \max$.

There exist infinite number of optimal motions with the same maximal terminal displacement [3].

Proposition 1. When optimal motion occurs, for any $t \in [0, \tau]$, $\tau = n(n-1)^{-1}T/2$, one of the masses moves with acceleration $(n-2)kg$, and all other masses are at rest. At the end of its movement, each moving mass stops instantly giving its momentum to another mass. At the time instant τ, all masses have the coordinate $n(n-2)(n-1)^{-2}kgT^2/8$ and acquire the

---

[*]Corresponding author. Email: t_figurina@mail.ru
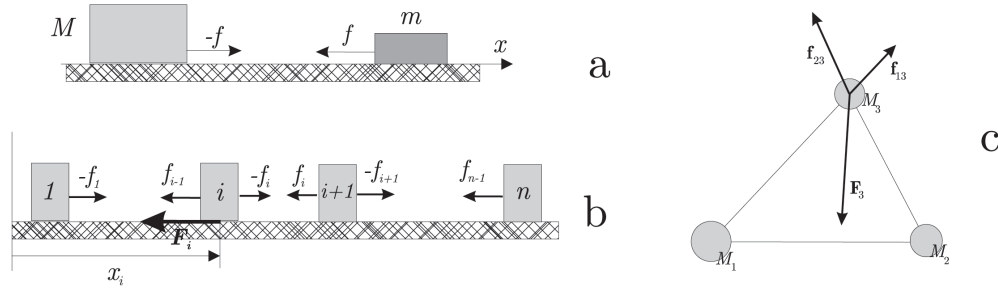
Figure 1: Multibody systems on a plane

velocity equal to $(n-2)(n-1)^{-1}kgT/2$. In the time interval $[\tau, T]$, all masses synchronously decelerate with the acceleration equal to $-kg$ until they stop at the time instant T. The maximum displacement of the system $x(T)$ subject to the optimal control is equal to $(n-2)(n-1)^{-1}kgT^2/4$. One of the possible optimal motions is defined by relations

$$v_i = \begin{cases} (n-2)kgt, & t \in [t_{i-1}, t_i], \\ 0, & t \in [0, t_n] \setminus [t_{i-1}, t_i], \\ kg(T-t), & t \in [\tau, T], \end{cases} \quad t_i = \frac{\sqrt{ni}}{2(n-1)}T, \quad i = 1, ..n, \quad t_n = \tau, \quad t_0 = 0. \tag{5}$$

OPTIMIZATION OF QUASI-STATIC MOTIONS FOR THREE-BODY SYSTEM ON A PLANE

Let us consider the system consisting of three point bodies M_i with masses m_i on a horizontal rough plane (Fig.1c). Between each pair of bodies M_i and M_j, control forces $\mathbf{f}_{ij}$ and $\mathbf{f}_{ji} = -\mathbf{f}_{ij}$ act, changing the distances between the bodies. The system moves along a plane when changing its configuration due to the dry friction forces $\mathbf{F}_i$ between the bodies and the plane. We study possible quasi-static motions of the system, i.e. the motions with infinitesimal velocities and accelerations of the bodies. In such motions, the equilibrium equations hold, $\mathbf{F}_i + \mathbf{f}_{ji} + \mathbf{f}_{ki} = 0$. We suppose that point masses satisfy triangle inequalities $m_i + m_j \geq m_k$, $\{i, j, k\} = \{1, 2, 3\}$, each of the inequalities is a necessary condition for body M_k to move [4].

Proposition 2. Quasi-static motion of body M_3, with bodies M_1 and M_2 fixed, is possible iff the straight line containing point M_3 and parallel to its velocity intersects set D. Here, set D is the intersection of the circles with centers in points M_1 and M_2 and radii $|M_1M_2|m_2/m_3$, $|M_1M_2|m_1/m_3$, respectively.

Let it be required to move quasi-statically body M_3 from point A to point B with minimal work against friction, i.e., to construct the trajectory of quasi-static motion for body M_3 with the minimum length.

Proposition 3. If the straight line AB intersects set D, then the trajectory with the minimum length for body M_3 quasi-statically moving from point A to point B is the segment AB. If the the straight line AB does not intersect set D, then the trajectory with the minimum length is two-link broken line ACB with links AC and BC belonging to the supporting straight lines of set D. Here, point A and set D are located on different sides of straight line BC, and point B and set D are located on different sides of straight line AC.

The following algorithm for the displacement of the three–body system from any initial position to any given terminal one can be used. At any moment, only one body is moving, and each body moves only during one time interval. The bodies M_i, M_j, M_k move one after another, while two other bodies are at rest. During each time interval, the moving body follows along the shortest trajectory which is either a straight line or a two-link broken line, according to Proposition 3. Comparing six ways of displacement, with different sequences of moving body, the sequence corresponding to the minimum work easily can be chosen.

CONCLUSIONS

Optimal motions of multibody systems along a horizontal plane are considered that correspond to the maximum average speed or minimum work against friction. These results are useful for planning possible locomotion of mobile robots.

References

[1] Chernousko F.L.: The optimum rectilinear motion of a two-mass system. J. Appl. Math. Mech. 66(1): 1-7, 2002.
[2] Chernous'ko F.L.: Analysis and optimization of the rectilinear motion of a two-body system. J. Appl. Math. Mech. 75(5):493-500, 2011.
[3] Figurina T.Yu.: Optimal control of system of material points in a straight line with dry friction. J. Comput. Syst. Sci. 54(5): 671-677, 2015
[4] Borisenko I.N., Figurina T. Yu., Chernousko F.L.: The quasistatic motions of a three-body system on a plane. J. Appl. Math. Mech. 78(3):220-227, 2014

ENTRAINMENT AND MULTISCALE DYNAMICS IN VIBRATIONALLY DRIVEN NONHOLONOMIC SYSTEMS

Scott David Kelly[*1]

[1]*Mechanical Engineering and Engineering Science, UNC Charlotte, Charlotte, North Carolina, USA*

Summary Mechanical systems subject to nonholonomic constraints can exhibit surprising dynamics. A well-known system that illustrates this point is the rattleback, which can reverse its direction of spin on a horizontal platform atop which it rolls without slipping, defying the conservation of angular momentum in a dramatic way for a subtle reason. The present paper documents two new instances of unexpected behavior by nonholonomically constrained mechanical systems, one characterized by a phenomenon akin to vibrational synchronization and the other characterized by the emergence of dynamics on two distinct time scales in response to forcing on only one.

Hat trick

The left panel in Figure 1 depicts the *Chaplygin beanie*, so named in [1] because it combines features of two canonical systems in the mechanics literature, the *Chaplygin* (or *Carathéodory*) *sleigh* and *Elroy's beanie*. A balanced rotor (the "beanie") surmounts the center of mass of a cart (the "sleigh") that's supported in the front by casters and in the rear by a wheel that rolls without slipping relative to the ground. The casters and wheel are assumed to have negligible inertia. If the system is initially at rest and the rotor is induced thereafter by internal actuation to rotate relative to the cart, then the cart will translate forward. In particular, if

$$J_{LT} = m\dot{x}\cos\theta + m\dot{y}\sin\theta, \qquad J_{RW} = -m\dot{x}a\sin\theta + m\dot{y}a\cos\theta + (B+C)\dot{\theta} + B\dot{\phi}$$

represent the system's forward translational momentum and its angular momentum relative to a vertical axis passing through the center of the rear wheel, respectively, then the system's dynamics satisfy

$$\dot{J}_{LT} = \frac{ma\left(J_{RW} - B\dot{\phi}\right)^2}{\left(ma^2 + B + C\right)^2}, \qquad \dot{J}_{RW} = \frac{-a\left(J_{RW} - B\dot{\phi}\right)J_{LT}}{ma^2 + B + C}.$$

Here m, B, and C represent the system's total mass and the rotational inertias of the rotor and cart relative to their centers, respectively. The fact that m and a are necessarily positive requires that the forward momentum J_{LT} be nondecreasing. Sinusoidal oscillations of appropriate amplitude in the rotor's orientation relative to the cart will induce the cart to advance in a slaloming motion, speeding up as it goes. A movie of this is visible at `http://tinyurl.com/gm4h2nh`.

Imagine that two such devices, one with an actuator coupling the rotor to the cart and the other with a linear torsional spring in place of the actuator, are placed atop a horizontal platform. If the platform has finite mass and is free to translate in response to forces arising from its interaction with the carts, then an analogy is apparent between this system and that studied by Huygens in the 1660s [2] comprising a pair of pendulum clocks with a shared nonrigid support. In Huygens' case, the oscillations of each clock contributed to small movements of the support and thus exerted influence on the motion of the other clock, inducing the clocks to exhibit an "odd kind of sympathy" by synchronizing their oscillations. The present problem is asymmetric — one rotor will be actuated in a prescribed way while the other responds passively — but the reader familiar with Huygens' study will suppose correctly that if the actuated rotor is driven sinusoidally so that the first cart slaloms forward relative to the platform, then the platform will vibrate, inducing the second cart to pivot back and forth about its rear wheel, and the unactuated rotor will begin to oscillate, inducing the second cart to translate forward relative to the platform as well.

The number of degrees of freedom in the motion of each cart distinguishes the present system from that comprising Huygens' clocks. In principle, energy transferred through the platform from the actuated cart to the passive cart could excite any combination of translational and rotational dynamics, perhaps depending on the initial position or orientation of the one cart relative to the other. The fact that the cart with the passive rotor is biased to translate forward in response to arbitrary platform vibration suggests an analogy to the more recent experiment described in [3], in which the flexible corpse of a fish was observed to swim forward — against a background flow — when excited to undulate by vortices shed from a bluff body.

What's surprising about the present system is the way in which the relative orientation of the carts evolves. The passive cart doesn't merely begin to move forward relative to the platform when the actuated cart does. If the initial orientation of the driven cart differs substantially from that of the passive cart, then the latter will reorient as it translates — in some cases gradually, over many cycles of oscillation — in order to follow the former. This is true even if the carts are initially antiparallel, back to back. Numerical simulation with a variety of initial conditions indicates that the asymptotic average difference between the carts' orientations — "average" because both carts undulate persistently as they translate — is generally not zero, but is consistently small regardless of the initial difference in the carts' orientations. Typical results are shown in the center and right panels of Figure 1.

---

[*]Corresponding author. Email: scott@kellyfish.net
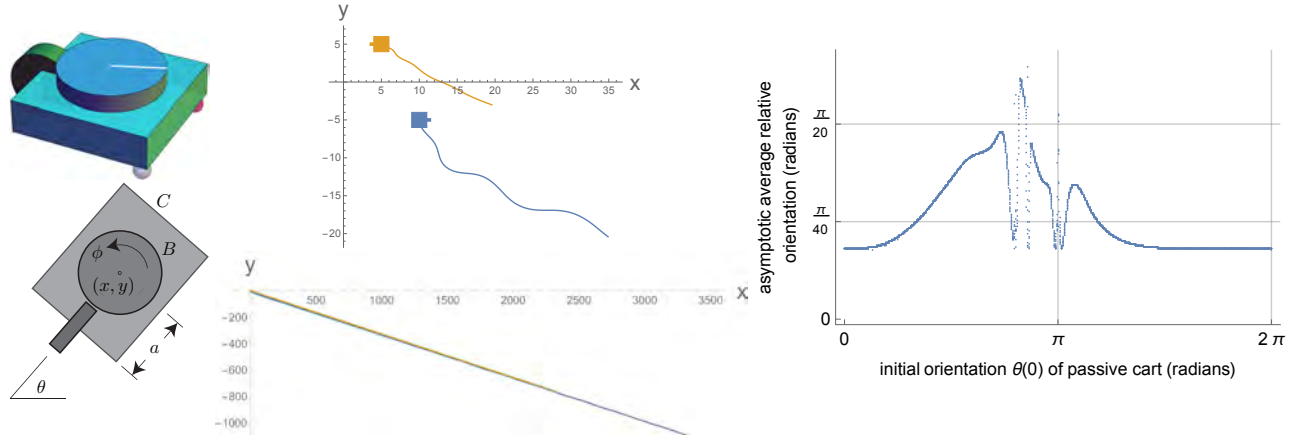
Figure 1: *Left*: Chaplygin beanie. *Center*: Trajectories of two such devices relative to a common planar support with finite mass, when the rotor atop the blue cart is driven such that $\phi = \sin t$ and the rotor atop the orange cart is coupled to the orange cart through a linear torsional spring. The carts are depicted in their initial configurations; their trajectories are shown through $t = 20$ (top) and $t = 400$ (bottom). The parameters m, B, C, and a are set to unity for both carts, as are the mass of the platform and the stiffness of the spring. *Right*: The average long-term difference in the carts' headings as a function of the initial orientation $\theta(0)$ of the passive (orange) cart, with the initial positions of the two carts as depicted in the center panel.
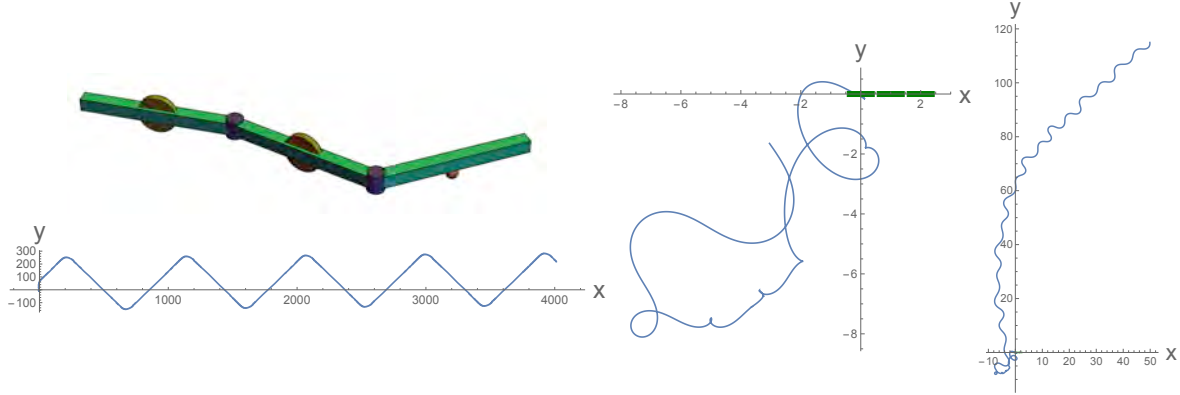
Figure 2: *Top left:* Three-link snake with spring-loaded hinges. *Remainder*: Trajectory relative to a platform induced to vibrate sinusoidally in the y direction with unit amplitude, at $t = 30$ (middle), $t = 80$ (right), and $t = 2000$ (bottom left).

Snake on a plane

The top left panel in Figure 2 depicts a mechanical system comprising three identical coplanar rigid links joined at two hinges. Two links are supported by wheels that roll without slipping, the third by a caster. With a third wheel in place of the caster, this system has been called a *kinematic snake* in the robotics literature [4]. If the hinges are fitted with linear torsional springs and the platform beneath is induced to vibrate, the system will begin to translate relative to the platform. In particular, suppose that the plane of the platform is the (x, y) plane, the three links are initially aligned at rest along the x axis, the masses and rotational inertias of the links are set to unity, and the platform is induced to accelerate perpendicular to the links from rest with $\ddot{y}_{\text{platform}} = \cos t$. If the torsional springs have equal unit stiffness, the system will exhibit long-term dynamics on two distinct time scales, settling into a slaloming trajectory that corresponds in the net to translation along the y axis. If the stiffness of the spring between the center wheel and the caster is reduced to zero, the system will instead be attracted to a slaloming path along the x axis. The latter is depicted in the remaining panels of Figure 2.

References

[1] S. D. Kelly, M. J. Fairchild, P. M. Hassing, and P. Tallapragada. Proportional heading control for planar navigation: The Chaplygin beanie and fishlike robotic swimming. In *Proceedings of the American Control Conference*, pages 4885–4890, 2012.

[2] M. Bennett, M. F. Schatz, H. Rockwood, and K. Wiesenfeld. Huygens's clocks. *Proceedings of the Royal Society of London A*, 458:563–579, 2002.

[3] D. N. Beal, F. S. Hover, M. S. Triantafyllou, J. C. Liao, and G. V. Lauder. Passive propulsion in vortex wakes. *Journal of Fluid Mechanics*, 549:385–402, 2006.

[4] J. P. Ostrowski. *The Mechanics and Control of Undulatory Locomotion*. PhD thesis, California Institute of Technology, 1995.

MBS APPROACH FOR A CHAIN FOUNTAIN

Friedrich Pfeiffer, Johannes Mayet

Applied Mechanics, Mechanical Engineering, TU-Muenchen, Germany

Summary Chain fountains are known since long time, and many efforts have been taken to model and to explain the dynamics of such a chain fountain. A chain consists of many small elements starting from an inertial beaker, moving upwards by forming an arc and coming to an inertial position again after a rather long vertical distance. As the chain elements are all connected by a bearing type structure, they all have to go with the same velocity v. In the following we shall consider the stationary case and assume small chain elements (Fig. 1).

MODELING

The strange behavior of a chain leaving a beaker has interested many scientists, in the nineteenth century for example Routh [5] and Painleve [3], more recently Biggins [1] and internally Mayet [2]. Most of the contributions try a kind of a belt approach with good success. In spite of the not too complicated dynamics there remain open questions, which could not be answered completely. This paper tries a multibody approach (MBS), also with good results. Geometry and forces are depicted in Figure 2, from which we receive the following equations of motion:
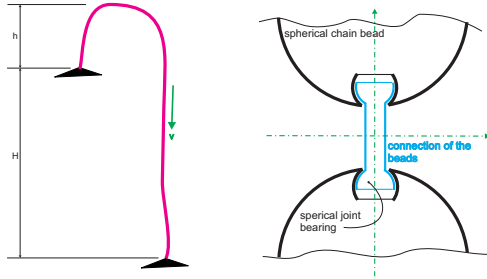
Figure 1: Chain Fountain and Chain Structure

$$\Delta m \ddot{x}_i = F_i cos\beta_i - F_{i-1}cos\beta_{i-1} + F_{Ti}sin\beta_i$$
$$- F_{T,i-1}sin\beta_{i-1}$$
$$\Delta m \ddot{y}_i = F_i sin\beta_i - F_{i-1}sin\beta_{i-1} - F_{Ti}cos\beta_i$$
$$+ F_{T,i-1}cos\beta_{i-1} - \Delta mg. \quad (1)$$

The frictional force writes $F_{Ti} = \mu(sign\dot{\alpha})F_i$, and the centrifugal effects with the force $F_{Ci} = \Delta m \frac{v^2}{R_i}$ and $\kappa_i = \frac{1}{R_i} = (\frac{d\alpha}{ds})_i$, are included in the acceleration terms. The initial conditions are $F_0 = k_0(\lambda v^2)$, $\alpha = \alpha_0, \beta = \beta_0$, The curvature κ_i depends on the change of the angle α with the trajectory coordinate s. The form of the chain fountain requires $\kappa_i < 0$. The factor k_0 takes uncertainties with respect to the force at the start into account. For the very small beads including their connection bars we may discretize with ($ds \approx \Delta s \approx d_i$, $dx \approx d_i cos\beta_i$, $dy \approx d_i sin\beta_i$, $\kappa_i \approx (\frac{\Delta\alpha}{\Delta s})_i \approx (\frac{\Delta\alpha}{d})_i$). Introducing the abbreviations ($f_i = \frac{F_i}{\Delta mg}$, $w_i = \frac{v^2}{gd_i}$), rearranging the eqs (1) and regarding the discretizations we come out with

$$f_i = f_{i-1}[cos(\beta_i - \beta_{i-1}) - \mu(sign(\Delta\alpha))sin(\beta_i - \beta_{i-1})] + sin\beta_i - \kappa_i d_i w_i sin(\alpha_i - \beta_i),$$

$$\kappa_i d_i w_i cos(\alpha_i - \beta_i) + \mu(sign(\Delta\alpha))(f_{i-1} + sin(\beta_i))-$$
$$f_{i-1}[sin(\beta_i - \beta_{i-1}) + \mu(sign(\Delta\alpha))cos(\beta_i - \beta_{i-1})] + cos\beta_i = 0, \quad (2)$$

which within the framework of small magnitude assumptions allows the solution

$$\Delta\alpha_i \approx -\left(\frac{cos\alpha_i + \mu_\alpha sin\alpha_i}{w_i - f_{i-1} - \frac{1}{2}sin\alpha_i + \frac{1}{2}\mu_\alpha cos\alpha_i}\right). \quad (3)$$

Knowing $\Delta\alpha_i$ we find from the first equation (2) also f_i. Moreover, within the framework of these approximations we can write the first of the equations (2) in the reduced form ($f_i \approx f_{i-1} + sin\beta_i$). Summing up this gives the well-known result ($F_N - F_0 \approx \lambda gH$). The difference of the two ground forces F_N and F_0 is the weight of the chain part below the arc.

Considering work and energy according to Figure 2 there are several possibilities to regard the ground forces F_N and F_0. This is one of the open questions. We choose a form, where F_0 "works" along the fountain with length s_E:

$$E = \sum_{i=1}^{N}\{\frac{1}{2}\Delta mv^2 - (\Delta mg)y_i\} - F_0 s_E sin\beta_0 = \frac{1}{2}\lambda s_E v^2 + \frac{1}{2}\lambda gH^2 - \lambda k_0 v^2 s_E sin\beta_0. \quad (4)$$

The centrifugal forces over the complete fountain have to carry the whole chain together with the forces at the ground. With Figure (2) and the results above we get the balance

$$\sum_{i=1}^{N}F_{Ci}cos\alpha_i = \sum_{i=1}^{N}\Delta mg - F_N sin\alpha_E + F_0 sin\alpha_0, \qquad s_E \approx (1 - k_0)(sin\alpha_0 - sin\alpha_E)(\frac{v^2}{g}) + Hsin\alpha_E. \quad (5)$$
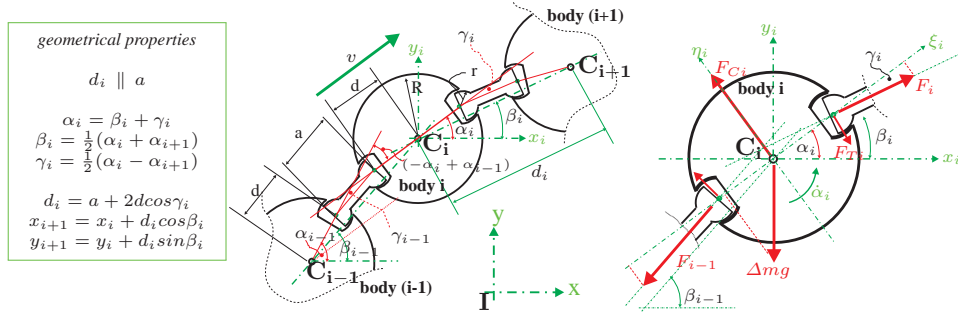
Figure 2: Chain Model - Geometry and Forces

Together with the energy equation (4) and with the property, that the fountain coordinate y can be approximated by two linear functions with respect to s, we thus can evaluate

$$\left(\frac{Hg}{v^2}\right) \approx \frac{1}{2}(1 - 2k_0 sin\beta_0)\left\{1 - \sqrt{1 - 4\frac{(1-k_0)(1+sin\alpha_0)}{(1-2k_0 sin\beta_0)}}\right\}, \qquad \left(\frac{s_E g}{v^2}\right) \approx -\left[\frac{(\frac{Hg}{v^2})^2}{1 - 2k_0 sin\beta_0}\right]. \qquad (6)$$

With the above MBS structure we come out with one iteration, because a good approximation of the two magnitudes H and s_E is known. We have to iterate the empirical magnitude k_0 in dependence of the initial chain angle α_0 for meeting the height ratio $(\frac{h}{H}) \approx 0.14$, which is an experimental finding and something like a general law connected with the chain fountain. It belongs to the open questions. For $(50° \leq \alpha_0 \leq 85°)$ we get $(0.75 \leq (\frac{Hg}{v^2}) \leq 1.07)$ with a k_0 value around $k_0 \approx \frac{5}{6}$.

RESULTS AND CONCLUSIONS

In addition to the calculations some measurements have been performed. Additional calculations have been carried through for a belt approximation, which appears in literature (for example [6]) but has also developed by a co-worker to appear later [2]. The comparisons are good and confirm the model, Figure 3.
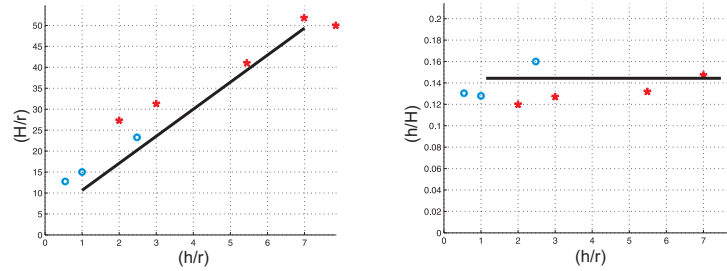
Figure 3: Results for the MBS and belt approximations compared with measurements (scaled with the arc radius r): black lines MBS approximation, blue circles belt approximation, red stars measurements (adaptation of the force F_0 by the starting coefficient k_0 to come out with a $(\frac{h}{H}) \approx 0.14$)

The dynamics of the first and the last bead in the fountain includes still open questions. The equations of motion allow a derivation of the difference of the forces connected with the first and last beads to be proportional to the weight of the chain height H $(F_N - F_0 \approx \lambda g H)$. Many publications connect this result with the initial bead force only, which is not correct. On the other hand the initial force F_0 alone can be evaluated for the starting bead to be $F_0 = \lambda v^2$, which does not fit into real dynamics. Therefore we put $F_0 = k_0(\lambda v^2)$ and adapt k_0 to the ratio $\frac{h}{H} \approx 0.14$. As stated by literature the fountain process is also highly dissipative. But it is not yet clear, where dissipation takes place and if it is necessary to regard that for an analysis. First investigations indicate the ground processes, start and end.

References

[1] J.S. Biggins, M. Warner *Understanding the chain fountain*. Proceedings of the Royal Society A, March 2014

[2] J. Mayet *Chain Fountain*. Internal Communication, AM-TUM 2015

[3] P. Painleve *Cours de Mecanique I*. Ecole Polytechnique, 2eme Division, 1919-1920

[4] F. Pfeiffer, Th. Schindler *Introduction to Dynamics*. Springer Berlin Heidelberg 2015

[5] E.J. Routh *Dynamics of systems of rigid bodies, with numerous examples*. MacMillan, London, UK, 1860

[6] E. Willerding *Dynamik von Weltraumseilen - Space Elevator*. E. Willerding 2014

PRECESSION ON A ROTATING SADDLE: A GYRO FORCE IN AN INERTIAL FRAME

Oleg Kirillov,[1a] Mark Levi[2]

[1]*Russian Academy of Sciences, Steklov Mathematical Institute, 119991 Moscow, Russia*
[2]*Mathematics Department, Pennsylvania State University, University Park, State College, PA 16802*

Summary Particles in rotating saddle potentials exhibit precessional motion which, up to now, has been explained by explicit computation. We show that this precession is due to a hidden gyroscopic force which, unlike the standard Coriolis force, is present in the inertial frame. We do so by finding a hodograph-like "guiding center" transformation using the method of normal form, which yields a simplified equation for the guiding center of the trajectory that coincides with the equation of the Foucault's pendulum. In this sense, a particle trapped in the symmetric rotating saddle trap is, effectively, a Foucault's pendulum, but in the inertial frame.

INTRODUCTION

The existence of Trojan asteroids in a triangular Lagrange libration point on the orbit of Jupiter is a consequence of the basic fact that a particle can be trapped in the rotating saddle potential [4,9]. Stability conditions for a heavy particle sliding without friction on a rotating saddle surface in the presence of gravity (Fig. 1) were obtained by Brouwer as early as 1918 [1,11]. Brouwer explicitly demonstrated that the saddle can be stabilized by rotation of the potential (in two dimensions) in contrast to the Paul trap for suspending charged particles in an oscillating electric field by analogy with the so-called Stephenson-Kapitsa pendulum in which the upside-down equilibrium is stabilized by vibration of the pivot [3]. Stabilization of the unstable saddle equilibrium by both rotation and vibration is well described by the concept of effective potential, which is equal to the kinetic energy of the high frequency motions of the system generated by the imposed oscillating field and affects the energy spectrum of the averaged motion [5-7]. In the case when the saddle potential is symmetric, the trajectory of the particle trapped by the rotating saddle in the non-rotating frame exhibits a slow prograde precession, Fig 1. This somewhat mysterious precession discovered first in the context of accelerator physics [2] and particle traps [8-10] is specific in that the standard averaging methods do not grasp the phenomenon [6].
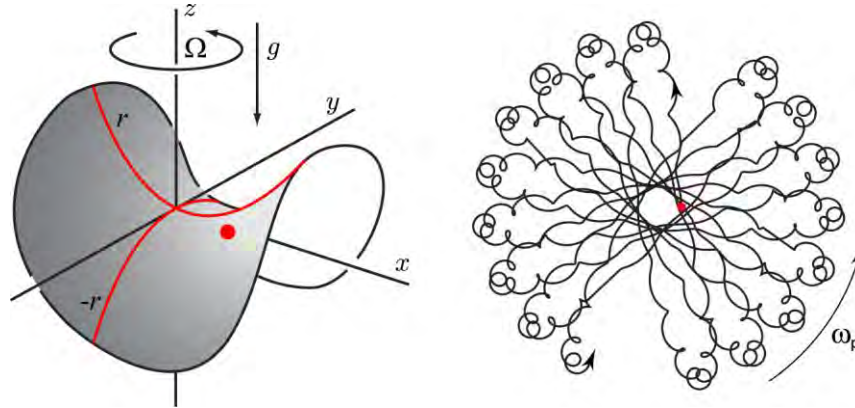
Fig. 1 (Left) A heavy particle on a symmetric rotating saddle surface and (right) prograde precession of its orbit in the non-rotating frame (figure adapted from [12])

HODOGRAPH TRANSFORMATION AND THE GUIDING CENTER EQUATION

We consider a point mass sliding without friction on a saddle surface rotating about a vertical axis with the angular velocity $\omega = \varepsilon^{-1}$, $\varepsilon \ll 1$, Fig 1. Assuming the principal curvatures of the saddle at the equilibrium point to be equal, linearized equations near the equilibrium in the non-rotating frame after appropriate rescaling of time take form

$$\ddot{x} + S(\omega t)x = 0, \ x \in \mathbb{R}^2, \tag{1}$$

where

$$S(\tau) = \begin{pmatrix} \cos 2\tau & \sin 2\tau \\ \sin 2\tau & -\cos 2\tau \end{pmatrix}, \quad \tau = \omega t.$$

[a)] Corresponding author. Email: kirillov@mi.ras.ru
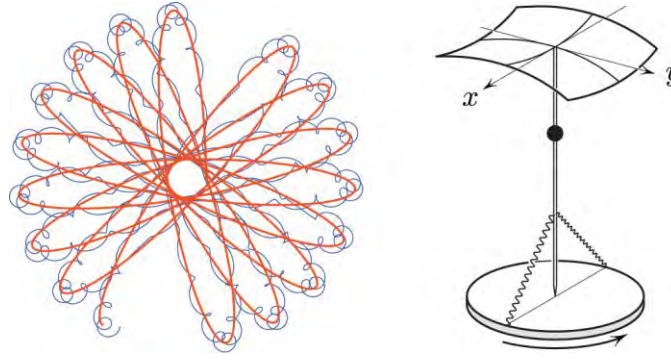
Fig. 2 (Left) Trajectory of the guiding center u (thick curve) tracking the corresponding trajectory x (thin curve). The view is in the inertial frame with $\varepsilon = 0.45$. (Right) A possible mechanical realization of the rotating saddle trap. Here, x and y are the angular variables of the inverted pendulum, and the graph of the potential energy is shown (figure adapted from [12]).

Theorem. Given a vector function $x : \mathbb{R} \to \mathbb{R}^2$, consider its "guiding center", or the "hodograph" image

$$u = x - \tfrac{\varepsilon^2}{4} S(t/\varepsilon)(x - \varepsilon J \dot{x}), \quad J = \begin{pmatrix} 0 & -1 \\ 1 & 0 \end{pmatrix}.$$

If $x(t)$ is a solution of (1), then $u(t)$ satisfies

$$\ddot{u} - \tfrac{\varepsilon^3}{4} J \dot{u} + \tfrac{\varepsilon^2}{4} u = \varepsilon^4 f(u, \dot{u}, \varepsilon),$$

where f is a function linear in u, $\dot{u}$ and analytic in ε, in a fixed neighbourhood of $\varepsilon = 0$. The guiding center therefore behaves, (ignoring the $O(\varepsilon^4)$ - terms) as a point charge of unit mass in the potential $V(u) = \tfrac{\varepsilon^2}{8} u^2$ in the magnetic field of constant magnitude $B = \varepsilon^3/4$ perpendicular to the u-plane.

Fig.2 illustrates a possible mechanical implementation of the rotating saddle trap as a light rod with a massive ball mounted on a turntable via a ball joint. Two springs are attached to the rod, and the height of the ball is adjustable, like in a metronome. If the ball is placed sufficiently low then the springs will stabilize the pendulum in the x-direction while the y-direction remains unstable; thus, the potential acquires a saddle shape.

CONCLUSIONS

We demonstrated that the rapid rotation of the symmetric saddle potential creates a weak Lorentz-like, or a Coriolis-like force, in addition to an effective stabilizing potential - all in the inertial frame. As a result, the particle in the rotating saddle exhibits, in addition to oscillations caused by effective restoring force, a slow prograde precession in the inertial frame caused by this pseudo-Coriolis effect. By finding a hodograph-like "guiding center" transformation using the method of normal form, we found the effective equations of this precession that coincide with the equations of the Foucault's pendulum.

References

[1] Brouwer L.E.J. Beweging van een materieel punt op den bodem eener draaiende vaas onder den invloed der zwaartekracht. *N. Arch. v. Wisk.* **2**: 407–419, 1918.
[2] Pearce R. M. Strong focussing in a magnetic helical quadrupole channel. *Nucl. Instrum. Methods* **83**(1): 101–108, 1970.
[3] Paul W. Electromagnetic traps for charged and neutral particles, *Rev. Mod. Phys.* **62**: 531–540, 1990.
[4] Bialynicki-Birula I., Kalinski M., Eberly J. H. Lagrange equilibrium points in celestial mechanics and nonspreading wave packets for strongly driven Rydberg electrons, *Phys. Rev. Lett.* **73**:1777–1780, 1994.
[5] Veselic K. On the stability of rotating systems, *Z. Angew. Math. Mech.* **75**: 325–328, 1995.
[6] Shapiro V.E. The gyro force of high-frequency fields lost by the concept of effective potential. *Phys. Lett. A* **238**: 147–152, 1998.
[7] Levi M., Geometry of Kapitsa's potentials. *Nonlinearity* **11**: 1365–1368, 1998.
[8] Thompson R. I., Harmon T. J., Ball M. G. The rotating-saddle trap: A mechanical analogy to RF-electric-quadrupole ion trapping? *Can. J. Phys.* **80**: 1433–1448, 2002.
[9] Bialynicki-Birula I., Bialynicka-Birula Z., Chmura B. Trojan states of electrons guided by Bessel beams. *Laser Physics* **15**(10): 1371–1380, 2005.
[10] Hasegawa T., Bollinger J. J. Rotating-radio-frequency ion traps. *Phys. Rev. A* **72**: 043403, 2005.
[11] Kirillov O. N. *Nonconservative Stability Problems of Modern Physics*, De Gruyter, Berlin/Boston, 2013.
[12] Kirillov O. N., Levi M. Rotating saddle trap as Foucault's pendulum. *Am. J. Phys.* **84**(1): 26–31, 2016.

FREAKY MOTION OF A SPINNING SPHEROID INDUCED BY A SLIGHT BREAK OF ITS AXIAL SYMMETRY

Yutaka Shimomura

Department of Physics, Hiyoshi Campus, Keio University, Yokohama, Japan

Summary The Euler equations are derived for spinning spheroids whose mass distribution slightly loses the axial symmetry. Based on the obtained equations, the motion of a spheroid spinning on a flat surface is studied by numerical simulations, and it is found that a significant nutation is induced with a precession and it generates a beat, both by the slight break of its axial symmetry.   As the initial spin rate increases, the period of nutation becomes smaller while its amplitude does larger.

INTRODUCTION

Motions of spinning bodies are so attractive, as represented by spinning tops, that many studies have been carried out up to now.   However, it seems that some curious motions are left mysterious and unexplained.   In fact, it was just the beginning of this century when the rising of a spinning egg was explained [1], its jumping was predicted [2] and observed [3], and the spin reversal of celt stone (or, a rattleback) was clarified [4].   Hard-boiled eggs are basically axisymmetric bodies, but the celt stones slightly lose the axial symmetry, which results in a little misalignment of the celt's principle axes of inertia and its axes of curvature at the point of contact with the table, and leads to the spin reversal.

In 2012, Cross [5] introduced to the author what he called a 'pathological egg', which shows a freaky motion.   He put the "blu-tack" into the bottom of a toy egg for the axial symmetry to be lost, and spun it at a small spin rate to find its axis of geometrical symmetry oscillates between the horizontal and the vertical positions.   He conjectured from his observation that spheroids with the axisymmetric structure never show such a big nutation and that it is caused by a slight break of the structure's axial symmetry.

In the present study, we derive the Euler equation for such quasi-axisymmetric spheroids to verify the Cross's conjecture by numerical simulations and study the feature of the nutation.

THE EULER EQUATIONS FOR QUASI-AXISYMMETRIC SPHEROIDS
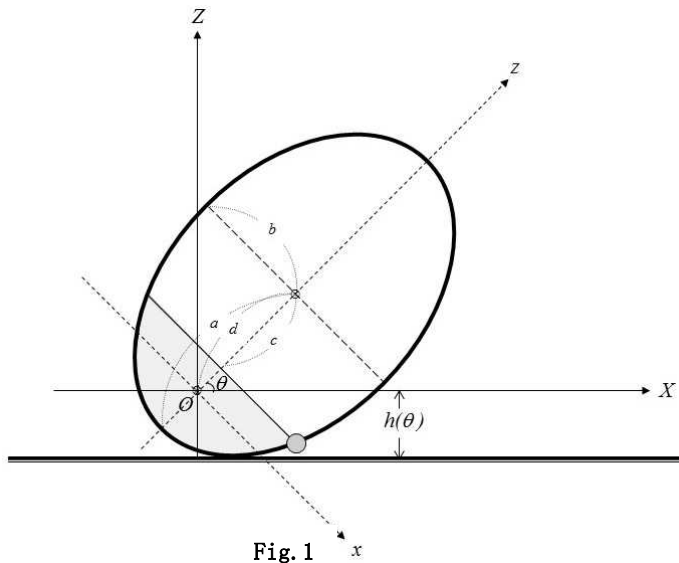
Fig. 1

As a quasi-axisymmetric spheroid, we study the kind as illustrated in Figure 1.   Inside of a spheroid, there is a blunt mass M at its bottom like a weighted toy tumbler. The ellipse has the dimensions a and b, and the parameter c denotes the distance between the centre of shape and the blunt end of the mass distribution on the axis of symmetry.   We add a small mass εM of point to the surface of the blunt end to make it slightly lose the original axial symmetry.

Provided the friction could be neglected, the Euler equations of order up to $O(\varepsilon)$ are derived for such quasi-axisymmetric bodies as in Figure 1, whose centre of mass is displaced a little bit off the axis of geometric symmetry and whose principle axes of inertia and its geometrical axes are misaligned generally.   So, the spin angle itself comes into the Euler equations through sinusoidal functions.

The Euler equations of $O(1)$ predicts, as a result of Moffatt, Shimomura and Branicki [6] and Shimomura [7], the critical angular velocity n along z axis, over which the vertical spin state is stable.   Figure 2 shows the critical angular velocity n as a function of $\gamma = -c/a$ in the case of $a/b = 3/2$.   Here, we should note that the spheroids with $\gamma < -0.3$ is always stable even for zero spin.

RESULTS OF NUMERICAL SIMULATIONS

Simulations for a spheroid with $a = 3cm, b = 2cm, \gamma = -0.5$ spinning on a frictionless flat surface are carried out by numerically solving a full system of five first order ODEs using the fourth-order Runge-Kutta method with the time step about 5µs. The initial conditions for the angle θ are $\theta = 0.01$ for $\varepsilon = 0$ and $\theta = 0.4$ for $\varepsilon = 1.0$, which mean the almost balanced states of rest for the still spheroid not spinning. After the spheroid in this almost balanced state is spun at $t = 0$ with a spin rate n (the angular velocity along the z-axis), the variations of θ in time are obtained.

First, it is confirmed that significant nutations are observed with a precession in the quasi-axisymmetric case of $\varepsilon = 1.0$, but not in the axisymmetric case of $\varepsilon = 0$. Second, as shown in Figure 3, it is also found that the nutations generate a beat, and as the initial spin rate n increases, the period of nutation becomes smaller while its amplitude does larger.

In the lecture, a demonstration will be available to observe the freaky motion of an egg-shaped body with a quasi-axisymmetric structure.
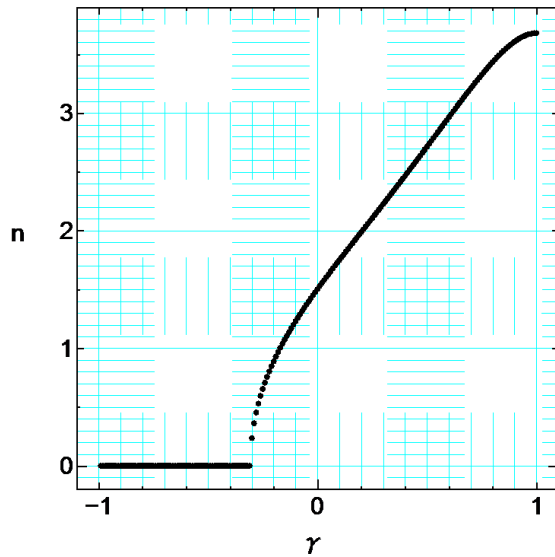
Fig. 2
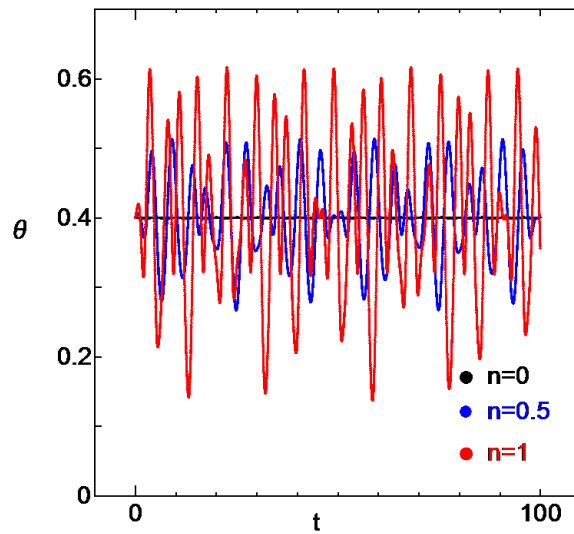
Fig. 3

CONCLUSIONS

The Cross's conjecture [5] is validated by numerical simulations of the Euler equations in the frictionless case: a slight break of the axial symmetry of a spinning spheroid gives rise to a significant nutation, which leads to its freaky motion with a precession. It is found that the nutation generates a beat, and the period of nutation becomes smaller and its amplitude does larger as the initial spin rate increases.

References

[1] Moffatt H. K., Shimomura Y.: Spinning eggs --- a paradox resolved. *Nature* **417**(2002)385 -386.
[2] Shimomura Y., Branicki M., Moffatt H. K.: Dynamics of an axisymmetric body spinning on a horizontal surface. Part II: Self-induced jumping. *Proc. Roy. Soc.* A **461**(2005)1753-1774.
[3] Mitsui T., Aihara K., Terayama C., Kobayashi H., Shimomura Y. : Can a spinning egg really jump? *Proc. Roy. Soc.* A **462**(2006)2897- 2905.
[4] Moffatt H. K., Tokieda T.: Celt reversals: a prototype of chiral dynamics. *Proc. Roy. Soc. Edinburgh* **138A**(2008)361-368.
[5] Cross R.: *Private communication* (2012).
[6] Moffatt H. K., Shimomura Y., Branicki M.: Dynamics of an axisymmetric body spinning on a horizontal surface. Part I: Stability and the gyroscopic approximation. *Proc. Roy. Soc.* A **460**(2004)3643-3672.
[7] Shimomura Y.: Effects of the air chamber and the shape on the rising motion of a spinning egg. Kyoyo－Ronso **123**(2005)39-54.

GIBBS-APPEL FORMULATION OF NON-HOLONOMIC MOTION
OF A BALL ON A SPHERICAL SURFACE

Jiří Náprstek*[1] and Cyril Fischer[1]

[1]*Institute of Theoretical and Applied Mechanics, Prague, Czech Republic*

Summary A new type of a passive vibration absorber is proposed and investigated as a non-linear non-holonomic system. It consists of a semi-spherical horizontal cavity in which a ball of a smaller diameter is rolling. The system of six degrees of freedom with three non-holonomic constraints is investigated. Instead of conventional way via Hamiltonian functional and Lagrangian procedure, the respective differential system is derived using the Gibbs-Appel function and related steps. Comparison of both approaches has been done. The system has an auto-parametric character and hence the semi-trivial solution and dynamic stability is investigated. Some principal post-critical regimes are outlined and qualitatively evaluated in the resonance neighborhood. Numerical experiments are performed and physically interpreted.

INTRODUCTION

Passive vibration absorbers are very widely used in engineering to suppress vibration induced by various environmental resources, e.g. wind, earthquake, technology, etc. Among many commonly used types widely discussed in literature, a non-conventional type being based on a heavy ball rolling inside a spherical cavity appeared recently. It approved many advantages over other systems in certain conditions. Schemes of pendulum and ball absorbers are outlined in Fig. 1. Dynamic character of a ball absorber is much more complicated and unlike conventional types its non-linear space character must be ever respected.

It is basically an auto-parametric system with several bifurcation points of the generalized Hopf type being very prone to achieve a local or global stability limit and to fall into a post-critical state.

Authors tried in the past to formulate this problem by a classical way constructing the Hamiltonian functional with non-holonomic constraints for the planar and space problem. Then the respective Lagrangian governing system has been carried out. The planar configuration leads to the quite transparent system, see [1], which can be treated analytically. However, the full space approach provides the differential system which is too complicated and its physical interpretation can be multivalent, [2]. The system should be treated almost only numerically. Therefore it is not very suitable for further discussion. For easier analysis of a dynamic system is the problem formulated using Appel-Gibbs function. For theoretical background see, e.g., [3] and others. A similar problem related with anti-seismic protection of a building has been discussed for instance in [4]. The main advantage of the Appel-Gibbs function consists in easier problem definition and easier more transparent introduction of non-holonomic constraints.
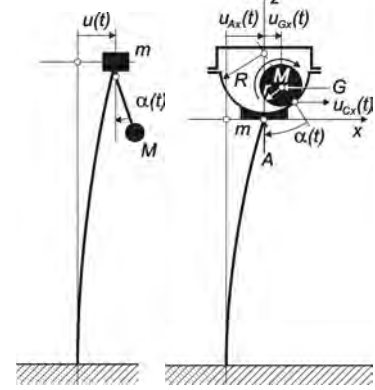
Figure 1: Tuned mass damper: a) pendulum principle; b) rolling ball principle.

GOVERNING DIFFERENTIAL SYSTEM

The Appel-Gibbs approach is used to formulate the governing non-linear differential system. The basis is the Appel function (often referred to as an energy acceleration function) defined as follows, see for instance [3]:

$$S \; = \; \frac{1}{2}M(\ddot{u}_{Gx}^2 + \ddot{u}_{Gy}^2 + \ddot{u}_{Gz}^2) + \frac{1}{2}J(\dot{\omega}_x^2 + \dot{\omega}_y^2 + \dot{\omega}_z^2), \tag{1}$$

where M - mass of the ball, J - central inertia moment of the ball with respect to point G, $\boldsymbol{\omega}$ - angular velocity of the ball with respect to the center G, $\mathbf{u}_G$ - velocity of the ball center, x, y, z - cartesian coordinates with origin in the point A.

The function S allows to write the Appel differential system:

$$\partial S^r / \partial \dot{\omega}_x \; = \; F_x, \quad \partial S^r / \partial \dot{\omega}_y \; = \; F_x, \quad \partial S^r / \partial \dot{\omega}_z \; = \; F_x, \tag{2}$$

where S^r is the reduced Appel function where only terms with 2nd time derivatives ($\ddot{\mathbf{u}}_G, \dot{\boldsymbol{\omega}}$) are kept, $\mathbf{F}_G$ - external force vector acting in G. Vector $\mathbf{F}_G$ can be determined using the virtual displacements principle. The system (2) should be completed by three non-holonomic constraints including a conjecture of non-sliding contact between the ball and cavity:

$$\dot{u}_{Gx} = \dot{u}_{Ax} - \rho(\omega_y(u_{Cx} - R) - \omega_z u_{Cy}), \; \dot{u}_{Gy} = \dot{u}_{Ay} - \rho(\omega_z u_{Cx} - \omega_x(u_{Cz} - R)), \; \dot{u}_{Gz} = -\rho(\omega_x u_{Cy} - \omega_y u_{Cx}) \tag{3}$$

*Corresponding author. Email: naprstek@itam.cas.cz

where $\rho = 1 - r/R$, r - ball radius, R - cavity radius. Final form of the differential system reads:

$$\begin{array}{rcl}
\dot{\omega}_x & = & L\left[\;\ddot{u}_{Ay}(u_{Cz} - R) - gu_{Cy} + (R - r)\omega_n(u_{Cy}\omega_z - (u_{Cz} - R)\omega_y)\right], \\
\dot{\omega}_y & = & L\left[-\ddot{u}_{Ax}(u_{Cz} - R) + gu_{Cx} - (R - r)\omega_n(u_{Cx}\omega_z - (u_{Cz} - R)\omega_z)\right], \\
\dot{\omega}_z & = & L\left[\ddot{u}_{Ax}u_{Cy} - \ddot{u}_{Ay}u_{Cx} + (R - r)\omega_n(u_{Cx}\omega_y - u_{Cy}\omega_x)\right], \\
L & = & \rho/((R - r)^2 + 0.4r^2), \quad \omega_n = [\omega_x, \omega_y, \omega_z] \cdot \mathbf{n},
\end{array} \tag{4}$$

where $\ddot{\mathbf{u}}_A = [\ddot{u}_{Ax}, \ddot{u}_{Ay}, 0]^T$ - vector of external acceleration, $\mathbf{u}_C$ - displacement in the contact of the ball with cavity. The system Eqs (4) should be solved simultaneously together with kinematic constraints following from non-holonomic constraints Eqs (3):

$$\dot{u}_{Cx} = -\rho(\omega_y(u_{Cx} - R) - \omega_z u_{Cy}), \;\; \dot{u}_{Cy} = -\rho(\omega_z u_{Cx} - \omega_x(u_{Cz} - R)), \;\; \dot{u}_{Cz} = -\rho(\omega_x u_{Cy} - \omega_y u_{Cx}) \tag{5}$$

The Eqs (4, 5) make up the system of six differential equations with six unknowns $\boldsymbol{\omega}, \mathbf{u}_C$.

NUMERICAL EXPERIMENTS

A large program of numerical experiments with Eqs (4, 5) has been performed regarding general and special configurations. A sample solution is plotted in Fig. 2. It represents free movement without external excitation and initiated by initial conditions. The ball in $t = 0$ is placed at angle $\alpha = 0.1$ above point A in the vertical plane declined from (xz) plane in $\gamma = 1.0$. Damping ratios $\delta_1 = 0.21, \delta_2 = 0.22$. Plots φ, θ, ψ are respective Euler angles evaluated as quasi-coordinates from parameters of the above solution to enable a comparison with Lagrangian approach. Coincidence was perfect. Nevertheless a number of additional configurations have been examined and compared with results obtained earlier, e.g. [2], using analytical and numerical procedures. For instance: rolling the ball on a horizontal plane $(R \to \infty)$, forced movement of the ball in the cavity in a horizontal plane, spin processes $(\omega_n \neq 0)$ and its independency on other coordinates, limit cycles, etc.
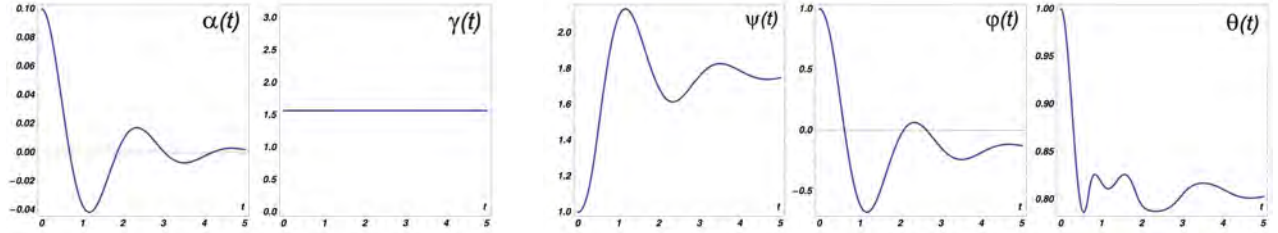
Figure 2: Sample solution of governing system in quasi-coordinates.

CONCLUSIONS

The heavy ball in a spherical cavity used as a TMD has been investigated. Unlike other systems it must be modeled in the non-linear domain. Any attempt for a linear approach failed completely. Appel-Gibbs formulation of a non-holonomic system dynamics approved excellent efficiency in comparison with a conventional way being based on Lagrangian differential system and non-holonomic constraints adjoined via indefinite Lagrange multipliers. Nevertheless, it reveals that the Lagrangian procedure can be defined as a special case of the Appel-Gibs formulation for a certain choice of quasi-coordinates, which, however, are not very convenient for detailed investigation. A simple model of the damping mechanism has been incorporated into the Appel-Gibbs system.

ACKNOWLEDGEMENT

References

[1] Náprstek J., Fischer C., Pirner M., Fischer O.: Non-linear dynamic behaviour of a ball vibration absorber. In: Proc. COMPDYN 2011 (M.Papadrakakis et al. eds). ECCOMAS - NTU Athens, Kerkyra, Corfu, 2011, CD ROM, paper 180, 14 pgs.

[2] Náprstek J., Fischer C.: Dynamic response of a heavy ball rolling inside a spherical dish under external excitation. In: Proc. Engineering Mechanics 2013 (I. Zolotarev edt.). IT ASCR Praha, Svratka, 2013, pgs 96-106, CD #46.

[3] Pars L.A.: A Treatise on Analytical Dynamics (2nd edition). Ox Bow Press, Connecticut, USA, 1972.

[4] Matta E., De Stefano A., Spencer B.F. Jr.: A new passive rolling-pendulum vibration absorber using a non-axial guide to achieve bidirectional tuning. Earthquake Engineering and Structural Dynamics, vo. 38 (2009) 1729-1750.

ESCAPE FROM POTENTIAL WELLS IN MULTI-DIMENSIONAL EXPERIMENTAL SYSTEMS

Shane D. Ross*[1], Amir E. BozorgMagham[2], Shibabrat Naik[1], and Lawrence N. Virgin[3]

[1]*Department of Biomedical Engineering and Mechanics, Virginia Tech, Blacksburg, VA, United States*
[2]*Department of Atmospheric and Oceanic Science, University of Maryland, College Park, MD, United States*
[3]*Department of Mechanical Engineering, Duke University, Durham, NC, United States*

Summary Predicting the escape from a potential energy well is a universal exercise, governing myriad engineering and natural systems, e.g., buckling phenomena, ship capsize, and human balance. Criteria and routes of escape have previously been determined for 1 degree of freedom (DOF) mechanical systems with time-varying forcing, with reasonable agreement with experiments. When there are 2 or more DOF, the situation becomes more complicated, and the theory of tube dynamics provides the criteria for which phase space states will escape. We report the validation of the tube dynamics theory for a 2 DOF experiment of a ball rolling on a surface. This experimental validation establishes a theoretical framework which can be exploited for purposes of control, e.g., avoiding or triggering escape or transition between metastable states in mechanical systems.

INTRODUCTION

Our objective is to study routes of escape from a potential well in an experimental 2 degree of freedom system. For this aim we study the chaotic motion of a rolling ball on a surface ($H(x, y)$) which has 4 potential wells, one in each quadrant of the (x, y) plane, Fig. 1(a)(b) [1]. We adopt a global geometric view of the motion analysis, using techniques which have been fruitful in other areas of mechanics, such as celestial mechanics [2] and physical chemistry [3]. The equations of motion are obtained from the Lagrangian; $\mathcal{L}(x, y, \dot{x}, \dot{y}) = T(x, y, \dot{x}, \dot{y}) - U(x, y)$. The kinetic energy (translational plus rotational for a ball rolling without slipping) is,

$$T(x, y, \dot{x}, \dot{y}) = \frac{1}{2}\frac{7}{5}\left(\dot{x}^2 + \dot{y}^2 + (H_x\dot{x} + H_y\dot{y})^2\right) \tag{1}$$

and the potential energy is $U(x, y) = gH(x, y)$, where,

$$H(x, y) = \alpha(x^2 + y^2) - \beta(\sqrt{x^2 + \gamma} + \sqrt{y^2 + \gamma}) - \xi xy + H_0. \tag{2}$$

We use parameter values $(\alpha, \beta, \gamma, \xi) = (0.07, 1.017, 15.103, 0.00656)$ in the appropriate units, along with $H_0 = 12.065$ cm and $g = 981$ cm/s². The ball's mass factors out and is not included.

Small damping is present, but over short time-scales, the motion approximately conserves energy, and the conservative dynamics are the dominant contributor to transition between wells. Let $\mathcal{M}$ be the *energy manifold* given by setting the energy integral ($\mathcal{E}(x, y, v_x, v_y) = T(x, y, \dot{x}, \dot{y}) + U(x, y)$) equal to a constant, i.e., $\mathcal{M}(E) = \{(x, y, v_x, v_y) \subset \mathcal{R}^4 \mid \mathcal{E}(x, y, v_x, v_y) = E\}$ where E is a constant. The projection of the energy manifold onto configuration space, the (x, y) plane, is the region of
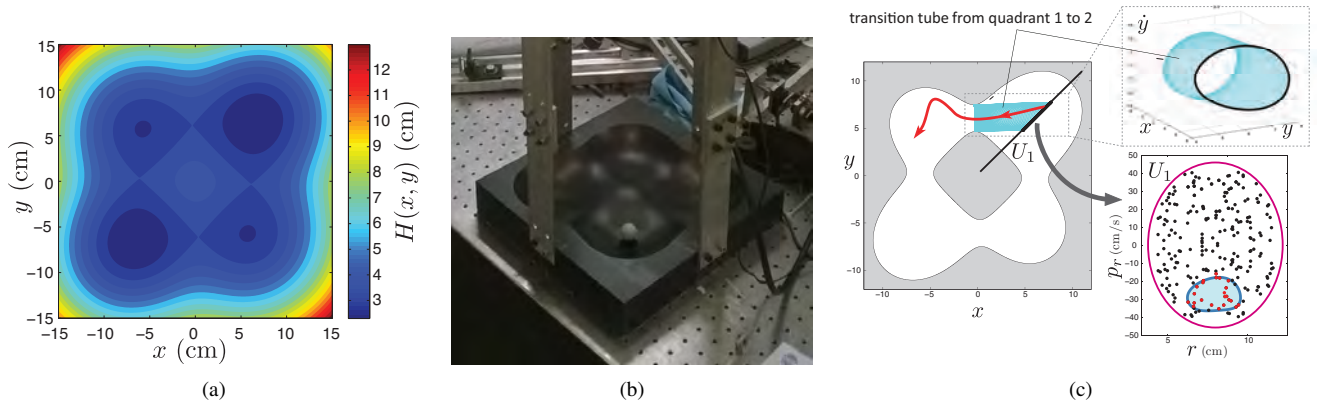
Figure 1: (a) Surface height $H(x, y)$. (b) Experimental apparatus. (c) For a fixed energy, E, above a critical value E_e, the permissible region (in white) has potential wells connected by necks around saddle-type equilibria. All motion from the well in quadrant 1 to quadrant 2 must occur through the interior of a stable manifold tube associated to an unstable periodic orbit in the neck between them. In the schematic of the U_1^+ Poincaré section, we the color intersecting trajectories by their near-future fate; black = no transition, red = imminent transition from quadrant 1 to 2 (an example of such a trajectory is also shown). A schematic tube boundary and interior is also shown for comparison on U_1^+. The large oval is the theoretical boundary of the energy manifold on U_1^+.

*Corresponding author. Email: sdross@vt.edu

energetically possible motion for a ball of energy E, $M(E) = \{(x, y) \mid U(x, y) \leq E\}$. The zero velocity curves are the boundary of $M(E)$ and are the locus of points in the (x, y) plane where the kinetic energy vanishes. The ball's state is only able to move on the side of this curve where the kinetic energy is positive, shown in white in Fig. 1(c). The critical energy of escape, E_e, is the same as the energy of the saddle points in each neck (which are all equal), and divides the global behavior into two cases, according to the sign of $\Delta E = E - E_e$:

Case 1, $\Delta E < 0$: the ball is safe against escape since potential wells are not energetically connected.

Case 2, $\Delta E > 0$: "necks" between all the potential wells open up around the saddle points, permitting the ball to move between the two potential wells (e.g., Fig. 1(c) shows this case).

TUBE DYNAMICS: TUBES LEADING TO ESCAPE

Within a given potential well the set of all states leading to escape to a different potential well (or having just escaped a different potential well) are within a cylindrical manifold or *tube*, as shown in Fig. 1(c). This tube bounds the set of all states for a fixed energy which will soon reach, or have just passed from, a different potential well [2, 3] (nested energy manifolds will have correspondingly nested tubes). For each E, the boundary of the tubes in phase space (or more precisely, within $\mathcal{M}(E)$) are the stable and unstable manifolds of an unstable periodic orbit of the same energy residing in the neck connecting the adjacent wells. The resulting geometric framework for understanding escape and transition we term 'tube dynamics'.

EXPERIMENTAL RESULTS

We use a Poincaré section which is selected based on the symmetry of the surface and the equations of motion, and which are best described in polar coordinates (r, p_r); $U_1^{\pm} = \{(r, p_r) \mid \theta = \frac{\pi}{2}, \text{ sign}(p_\theta) = \pm 1\}$. Taking Poincaré sections of 120 experimental trajectories (e.g., the typical trial shown in Fig. 2(a)) should reveal the tube cross-sections. We first determine the instantaneous ΔE for every point on the Poincaré section U_1, so we can consider only narrow ranges of ΔE, to approximate a single energy manifold. In Fig. 2(b) we see an example of the Poincaré section U_1^+ for all intersections in the energy range $200 < \Delta E < 300$ $(\text{cm/s})^2$. The intersection points which are about to transition from quadrant 1 to 2, determined by following the experimental trajectory forward in time, and are marked with red circles.

| (a) | (b) | (c) |
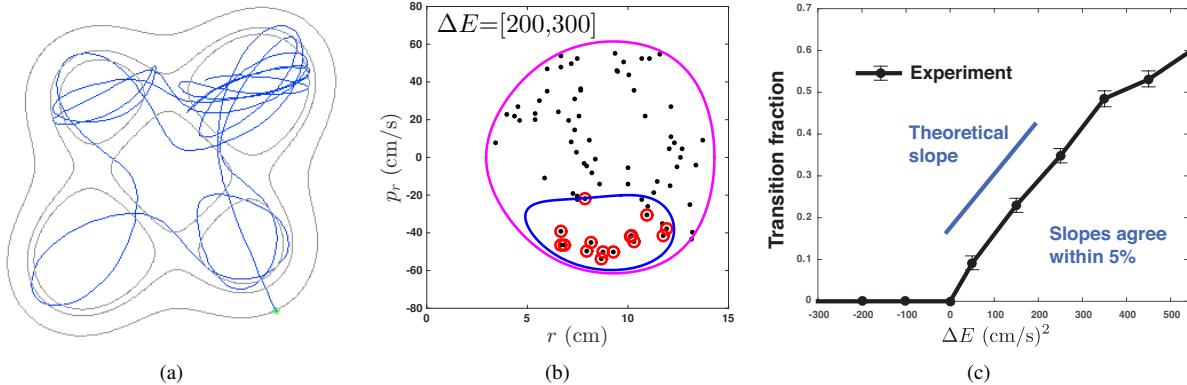
Figure 2: *Experimental results.* (a) A typical experimental trajectory in blue, which is released from rest at the lower right. Notice how it moves seemingly erratically between the 'wells'. Some height iso-contours are also shown, in light gray. (b) Histogram of energy for crossings of the U_1^+ Poincaré section (blue: $\Delta E < 0$, gray: $\Delta E > 0$, red: transitioning). (c) On U_1^+, we consider only a narrow range of energy ($\Delta E \in [0, 100 \, (\text{cm/s})^2]$) and label intersecting trajectories by their recent past or future; black: no transition, red: recent transition to quadrant 1 from quadrant 2 and magenta: imminent transition from quadrant 1 to 4. (d) Fraction of transitioning trajectories as a function of energy above the saddle.

CONCLUSIONS

The transitioning points at each energy are all found to be within the theoretical tube boundary (blue curve); as in, e.g., Fig. 2(b). Furthermore, the fraction of transitioning trajectories increases linearly with ΔE, Fig. 2(c), as expected theoretically from arguments related to the phase space flux over a saddle [4]. This experimental validation of tube dynamics establishes a theoretical framework which can be exploited for purposes of control, e.g., avoiding or triggering escape or transition between metastable states in mechanical systems. SDR thanks the NSF for partially funding this work through grant 1537349.

References

[1] Virgin, L. N., Lyman, T. C., Davis, R. B. Nonlinear dynamics of a ball rolling on a surface. *Am. J. Phys.*, 78(3):250–257, 2010.

[2] Koon, W. S., Lo, M. W., Marsden, J. E., Ross, S. D. Heteroclinic connections between periodic orbits and resonance transitions in celestial mechanics. *Chaos*, 10:427–469, 2000.

[3] Gabern, F., Koon, W. S., Marsden, J. E., Ross, S. D. Yanao, T. Application of tube dynamics to non-statistical reaction processes. *Few-Body Systems*, 38:167–172, 2006.

[4] MacKay, R. S. Flux over a saddle. *Physics Letters A*, 145:425–427, 1990.

PASSIVE LINEARIZATION OF NONLINEAR SYSTEM RESONANCES

Giuseppe Habib[*1], Chiara Grappasonni [1], and Gaetan Kerschen[1]

[1]*Space Structures and Systems Laboratory, University of Liège, Liège, Belgium*

Summary In this work we demonstrate that the addition of properly-tuned nonlinearities to a nonlinear system can increase the range over which a specific resonance responds linearly. Specifically, we seek to enforce two important properties of linear systems, namely the force-displacement proportionality and the invariance of resonance frequencies. Theoretical findings are validated through numerical simulations and experiments.

Devices used for sensing, imaging and detection are usually required to exhibit linear behavior in their dynamic range. However, nonlinearity is a frequent occurrence in physical and engineering applications. Nonlinearity may result in plethora of dynamic phenomena which can drastically limit the performance of the devices [1]. One well-established approach for enforcing linear behavior is feedback linearization, which uses feedback control to cancel the undesired nonlinearities. However, feedback linearization requires an accurate monitoring of the system's states, an actuator and an external source of energy, which complicates its practical realization.

We propose a fully passive, resonance-based approach for dealing with undesired nonlinearities in mechanical systems. Properly-tuned nonlinearities are introduced in the nonlinear system to increase the range over which a specific resonance responds linearly. Specifically, we seek to enforce two important properties of linear systems, namely the force-displacement proportionality and the invariance of resonance frequencies. Our approach relies on a principle of similarity [2] which states that the added nonlinearity should possess the same mathematical form as that of the original nonlinear system. This principle of similarity enables us to extend the linear regime over a larger range of motion amplitudes.

We consider an n-degree-of-freedom (DoF) mechanical system with concentrated nonlinearities subject to harmonic excitation:

$$\tilde{\mathbf{M}}\ddot{\mathbf{x}} + \tilde{\mathbf{C}}\dot{\mathbf{x}} + \tilde{\mathbf{K}}\mathbf{x} + \tilde{\mathbf{b}}_{nl}\left(\mathbf{x}\right) = \sqrt{\varepsilon}\tilde{\mathbf{v}}f\cos\omega t, \tag{1}$$

where ε is a small bookkeeping parameter. The vector $\tilde{\mathbf{b}}_{nl}\left(\mathbf{x}\right)$ contains both the original and additional nonlinearities, which are of polynomial nature. According to the principle of similarity [2], the additional nonlinearities should possess the same exponent as the original nonlinearity. Without loss of generality, cubic nonlinearities are considered herein.

The objective of this study is to linearize one specific resonance of system (1) through the proper design of the additional nonlinearities. To this end, the nonlinear normal mode (NNM) theory is exploited, because nonlinear resonances are known to occur in the neighborhood of NNMs [3]. First, we transform Eq. (1) into modal space through the change of variables $\mathbf{x} = \mathbf{U}\mathbf{y}$ where $\mathbf{U}$ contains the normal modes of the underlying linear system, and we define normalized modal displacements, $\mathbf{q} = \mathbf{y}/\left(\sqrt{\varepsilon}f\right)$, such that

$$\ddot{\mathbf{q}} + \mathbf{C}\dot{\mathbf{q}} + \mathbf{\Omega}\mathbf{q} + \mathbf{b}_{nl}\left(x\right) = \mathbf{v}\cos\omega t, \tag{2}$$

where $\mathbf{\Omega} = \text{diag}\left[\Omega_j^2\right]_{j=\overline{1,n}}$, $\mathbf{C} = [c_{ij}]_{i,j=\overline{1,n}}$ and $\mathbf{b}_{nl}\left(\mathbf{x}\right) = \left[\ \ldots, \quad \varepsilon f^2\sum_{h_1+\ldots+h_n=3}b_{jh_1\ldots h_n}\prod_{i=1}^{n}q_i^{h_i}, \quad \ldots\ \right]^{\mathrm{T}}$. $\mathbf{b}_{nl}\left(\mathbf{x}\right)$ is the projection of $\tilde{\mathbf{b}}_{nl}\left(\mathbf{x}\right)$ in modal space, thus, even if $\tilde{\mathbf{b}}_{nl}\left(\mathbf{x}\right)$ is sparse, $\mathbf{b}_{nl}\left(\mathbf{x}\right)$ can be fully populated. $b_{jh_1\ldots h_n}$ are scalars, where j indicates the mode number and varies according to the rows of $\mathbf{b}_{nl}\left(\mathbf{x}\right)$, while subscripts $h_1\ldots h_n$ are in accordance with the exponents of the modal coordinates of the corresponding terms. We assume that the system features no internal resonances, i.e., natural frequencies Ω_j are incommensurate.

The NNMs are now calculated by removing damping and forcing terms in Eq. (2). Following a standard perturbation technique and limiting the solution to the fundamental harmonic, the approximate solution has the form $\mathbf{q} = \left(\mathbf{q}_0 + \varepsilon\mathbf{q}_1 + O\left(\varepsilon^2\right)\right)\sin\left(\left(\omega_0 + \varepsilon\omega_1 + O\left(\varepsilon^2\right)\right)t\right)$, where $\mathbf{q}_0 = [\cdots, q_{j0}, \cdots]^{\mathrm{T}}$ and $\mathbf{q}_1 = [\cdots, q_{j1}, \cdots]^{\mathrm{T}}$. Imposing resonance condition at order ε^0 and solving terms of order ε^1 yields for the lth NNM

$$q_{j0} = 0,\ q_{j1} = -\frac{3}{4}\frac{b_{j0\ldots3\ldots0}q_{l0}^3}{\Omega_j^2 - \Omega_l^2} \quad \text{for } j = \overline{1,n},\ j\neq l, \quad \omega_0 = \Omega_l,\ \omega_1 = \frac{3}{4}\frac{b_{l0\ldots3\ldots0}q_{l0}^2}{2\Omega_l}. \tag{3}$$

q_{j0} and q_{j1} ($j \neq l$) represent the influence of the nonresonant modes on the lth mode. ω_1 is the variation of the lth natural frequency with respect to the amplitude of oscillation q_{l0}. Thus, if $b_{l0\ldots3\ldots0} > 0\ (<0)$, the resonance is of hardening (softening) type.

In order to relate the undamped, unforced NNM motions to the resonances of the damped, forced system, the energy balance criterion [4] is utilized:

$$\int_0^T \dot{\mathbf{x}}(t)^{\mathrm{T}}\tilde{\mathbf{C}}\dot{\mathbf{x}}(t)\mathrm{d}t = \int_0^T \dot{\mathbf{x}}(t)^{\mathrm{T}}\sqrt{\varepsilon}\tilde{\mathbf{v}}f\cos\omega t\,\mathrm{d}t, \tag{4}$$

*Corresponding author. Email: giuseppe.habib@ulg.ac.be

where T is the period of motion. Eq. (4) indicates that at resonance the energy dissipated by damping over a full period is equal to the input energy. Inserting the approximate solution for **q** in Eq. (4) gives

$$q_{l0} = \frac{v_l}{\Omega_l c_{ll}}, \quad q_{l1} = \frac{\Omega_l q_{l0}\left(\sum_{\substack{j=1\\j\neq l}}^{n} c_{lj}q_{j1} + \sum_{\substack{j=1\\j\neq l}}^{n} c_{jl}q_{j1}\right) - \sum_{\substack{j=1\\j\neq l}}^{n} q_{j1}v_j}{v_l - 2\Omega_l q_{l0}c_{ll}} + \frac{\omega_1 q_{l0}^2 c_{ll}}{v_l - 2\Omega_l q_{l0}c_{ll}} \tag{5}$$

and $x_k = \sqrt{\varepsilon}f\left(u_{kl}q_{l0} + \varepsilon\left(\sum_{j=1}^{n} u_{kj}q_{j1}\right) + O\left(\varepsilon^2\right)\right)$. Eqs. (3) and (5) completely define the lth resonance of system (1) and form the basis of the design procedure developed in this paper. Based on these equations, force-displacement proportionality for coordinate x_k of the lth resonance can simply be enforced through $\sum_{j=1}^{n} u_{kj}q_{j1} = 0$. Similarly, invariance of the lth resonance frequency can be enforced through $\omega_1 = 0$, such that the lth natural frequency $\omega_l \approx \omega_0$. Since these two conditions involve the n coefficients of the nonlinear terms $b_{j0\ldots3\ldots0}$, they can be used to design the additional nonlinearities in function of the original ones.

An experimental set-up is utilized to demonstrate the proposed idea. It comprises a cantilever beam made of steel to which a doubly-clamped beam is connected (Fig. 1a). A thin steel lamina located at the free end of the cantilever and the doubly-clamped beam itself generate two hardening nonlinearities, which can be modeled using cubic springs. A two-DoF reduced model of the system was identified experimentally. From this model, applying the aforementioned procedure, the nonlinearity of the doubly-clamped beam was designed, such that the second resonant peak satisfies force-displacement proportionality. In Fig. 1b, solid and dashed lines depict the envelopes of the normalized amplitude of the second resonant peak, respectively with and without the nonlinearity related to the doubly-clamped beam. The red circles depict the measured resonant peaks. These circles are almost aligned horizontally, which translates the fact that the displacement of the cantilever beam around the second resonance is proportional to the amplitude of the harmonic forcing. This condition is not verified if the additional nonlinearity is not included (dashed line).

Successively, in order to compensate the frequency shift of the first resonance, due to the hardening nonlinearities, a couple of permanent magnets was placed on the doubly-clamped beam and two others were placed symmetrically next to them on a fixed support. The two couples of magnets are mutually attractive in order to generate a softening nonlinearity. The amplitude of this nonlinearity was controllable by varying the distance between the two magnets. Choosing the appropriate distance, according to the analytical procedure proposed, we were able to linearize the frequency backbone of the first resonance, as illustrated in Fig. 1c (solid black lines). Dashed red lines in Fig. 1c show the frequency response of the system if the nonlinear magnetic force is neglected. The blue circles depict the resonance peaks measured experimentally.
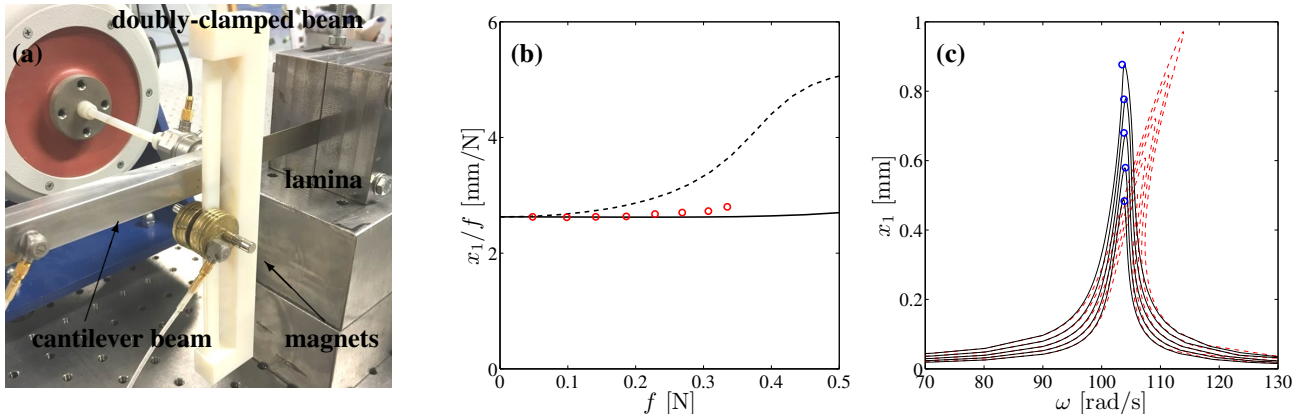
Figure 1: (a) experimental set-up. (b) first part of the experiment, envelops of resonant peak for different forcing amplitude; dashed line: nonlinearity of doubly-clamped beam neglected, solid line: nonlinearity of doubly-clamped beam included, red circles: experimental results. (c): second part of the experiment, frequency response without (dashed red lines) and with (solid black lines) magnetic nonlinear force; blue circles: experimental results.

References

[1] Postma H.C., Kozinsky I., Husain A., Roukes M.: Dynamic range of nanotube-and nanowire-based electromechanical systems. Appl Phy Lett 86:223105, 2005.

[2] Habib G., Kerschen G.: A principle of similarity for nonlinear vibration absorbers. In Proc. ASME 2015 IDETC, 2015.

[3] Vakakis A.F., Manevitch L.I., Mikhlin Y.V., Pilipchuk V.N., Zevin A.A.: Normal modes and localization in nonlinear systems, Springer, 1996.

[4] Hill T., Cammarano A., Neild S., Wagg D.: An analytical method for the optimisation of weakly nonlinear systems. Proc. EURODYN, 1981-1988, 2014.

ON THE STRONGLY NONLINEAR RESONANCE OF A ROTOR WITH A SELF-BALANCING DEVICE

Olga Drozdetskaya [1] & Alexander Fidlin[1a)]
[1]*Institute of Engineering Mechanics, Karlsruhe Institute of Technology, Karlsruhe, Germany*

Summary Passage through and capture into the resonance of a rigid rotor with the attached self-balancing device and driven by an induction engine of limited power is investigated using an averaging procedure for a partially strongly damped system. The approach is closely related to a singular perturbation technique. It is demonstrated that the system's dynamics can be reduced on the slow manifold to three first-order differential equation predicting both stationary and transient solutions of the original system. Solutions captured into the resonance differ strongly from those in the system without self-balancing devices. The velocity of the rotor oscillates slowly around a certain value while the resonant vibrations of the rotor's axis are strongly modulated in the vicinity of the resonance. The approximate results are compared with the direct numerical simulations of the full system and demonstrate very good accuracy everywhere except in the small vicinity of the bifurcation point.

INTRODUCTION

Self-balancing devices providing the perfect balancing of rigid rotors in the overcritical speed range is well known [1, 2]. However in the undercritical domain these devices maximize the overall unbalance which leads to significantly increasing amplitudes of vibrations or even to capture into the resonance while accelerating or decelerating the rotor. The last effect (also known as the Sommerfeld effect) is well analyzed and easy to understand for simple rotors [3]. Many important mathematical results on passage through and capture into the resonance have been achieved for weakly damped systems [4]. The significant complexity of this analysis even in two-frequency systems is connected to the appearance of the so-called semi-slow oscillations [5]. However, a rotor with a self-balancing device has at least four frequencies, which makes the appropriate analysis extremely elaborate [6]. On the other hand, damping in technical systems is usually not too small. The corresponding asymptotic approach suggested in [7] enables efficient analysis of strongly damped systems.

In the present paper the last approach is applied to investigation of the strongly nonlinear interaction between the rotor with self-balancing device mounted on a linear carrier system and the induction motor while passing through the main resonance. Especial attention is payed to the slowly modulated solutions arising in case of capturing resonance.

MINIMAL MODEL OF A ROTOR WITH A SELF-BALANCING DEVICE DRIVEN BY AN INDUCTION MOTOR

The simplest model of the rotor with the attached self-balancing device is shown in figure 1a.
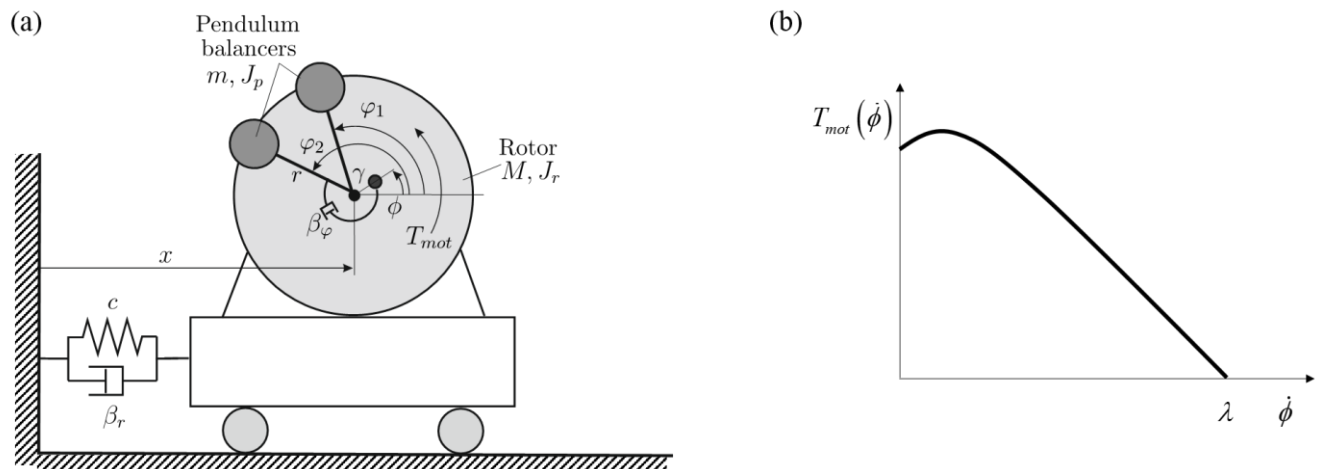
Figure 1. (a) Model of the rotor with self-balancing device; (b) the torque characteristics of the induction motor.

The rotor of mass M and mass moment of inertia J_r is elastically suspended by a spring-damper of a certain stiffness c and damping β_r. Its center of mass has an offset γ relative to the rotation axis. Two pendulum balancers of mass m, mass moment of inertia J_p and length r are placed on the axis of rotation of the rotor. A rotational damping β_φ is applied between the rotor and each of the balancers. The rotor is excited by an induction motor of limited power which static characteristics is displayed in figure 1b.

[a)] Corresponding author. Email: alexander.fidlin@kit.edu.

Equations of motion of the system are as follows:

$$\left(M+2m\right)\ddot{x}+\beta_r\dot{x}+cx=M\gamma\left(\dot{\phi}^2\cos\phi+\ddot{\phi}\sin\varphi\right)+mr\sum_{i=1}^{2}\left(\dot{\varphi_i}^2\cos\varphi_i+\ddot{\varphi_i}\sin\varphi_i\right)$$

$$\left(M\gamma^2+J_r\right)\ddot{\phi}+\beta_\varphi\left(\dot{\phi}-\dot{\varphi}_1-\dot{\varphi}_2\right)=T_{mot}+M\gamma\ddot{x}\sin\phi \tag{1}$$

$$\left(J_p+mr^2\right)\ddot{\varphi}_i+\beta_\varphi\left(\dot{\varphi}_i-\dot{\phi}\right)=mr\ddot{x}\sin\varphi_i;\ \ i=1,2.$$

ASYMPTOTIC ANALYSIS OF THE PASSAGE THROUGH THE RESONANCE AND COMPARISON WITH NUMERIC SIMULATIONS

Approximate asymptotic solutions for these equations have been obtained using averaging technique for strongly damped systems [7] under the assumption that the unbalance of the rotor $M\gamma^2/J_r$ and the mass ratio m/M are small parameters of the same magnitude order. Dimensionless damping coefficients are assumed to be not small. The whole dynamics of the system can be reduced to three first order differential equations for the velocity of the rotor and two phase differences between the pendulum balancers and the rotor. Two examples of the transient solutions obtained by solving the averaged equations are shown in comparison to the numerical simulations of the full system (1) are presented in figure 2.
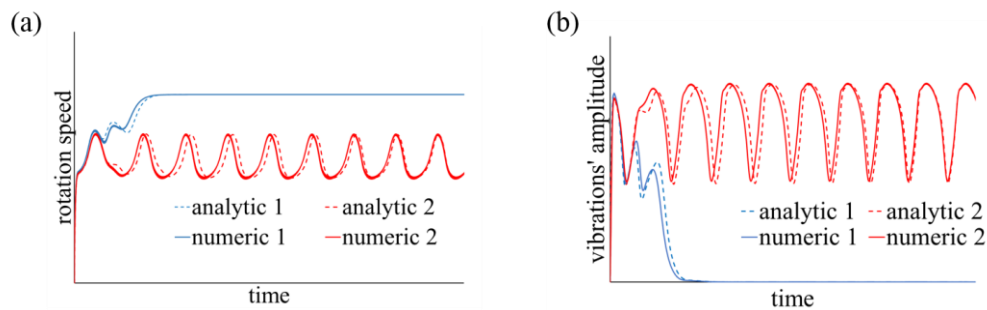
Figure 2. (a) Rotation speed of the rotor while passing through resonance (blue lines) and for capture into the resonance (red lines) (b) amplitude of the vibrations of the rotor's axis; numerical results – solid lines, analytical results – dashed lines.

Stationary capture into the resonance is not possible in a wide range of the system's parameters although the rotor speed does not reach the objected value (figure 1, red curves). Instead of the stationary solutions usual for Sommerfeld effect, periodic oscillations of the rotor speed are taking place accompanied by the slowly modulated resonance vibrations of the rotor axis attached to the carrier system (figure 2, red curves). In case of the successful passage through the resonance (blue curves) vibration of the system can be also slowly modulated. The attraction basin for the captured solutions depends strongly on the initial orientation of the pendulum balancers. The qualitative and quantitative discrepancies between the analytical and the numerical results are quite small.

CONCLUSIONS

Passage through and capture into the resonance are investigated for the unbalanced rotor with the attached self-balancing device. The system is driven by an induction engine and mounted on a linear carrier. Averaging for strongly damped systems appears to be a very efficient analytical method enabling to identify the slow manifold of the system and to obtain accurate analytical approximations. This method can be used for analysing a wide class of strongly nonlinear systems operating close to resonance in presence of significant dissipation.

References

[1] Blekhman I. *Synchronisation in Science and Technology*, ASME Press, New York, 1988.

[2] Sperling L, Ryzhik B, Duckstein H. Single-Plane Auto-Balancing of Rigid Rotors. *Technische Mechanik* **24, 1**: 1 – 24, 2004.

[3] Blekhman I. *Vibrational mechanics*. World Scientific, Singapore, 2000.

[4] Neishtadt A. Capture into resonance and scattering on resonances in two-frequency systems. *Proceedings of the Steklov Institute of Mathematics* **250**: 183 – 203, 2005.

[5] Pechenev A, Fidlin A. Hierarchy of resonant motions excited in a vibroimpact system with contact zones by an inertial source of limited power. *Izw. AN SSSR Mechanika Tverdogo Tela* **27**: 46 – 53, 1992.

[6] Ryzhik B., Amer T., Duckstein H., Sperling L. Zum Sommerfeldeffekt beim selbsttätigen Auswuchten in einer Ebene. *Technische Mechanik* **21, 4:** 297- 312, 2001.

[7] Fidlin A, Thomsen J.J. Non-trivial effects of high-frequency excitation for strongly damped mechanical systems. *Int. J. of Non-Linear Mechanics* **43**: 569 – 578, 2008.

NONLINEAR OSCILLATIONS OF A BELT DRIVE

<u>Alois Steindl</u>*and Yury Vetyukov
Institute for Mechanics and Mechatronics, Vienna University of Technology, Vienna, Austria

Summary The dynamics of a visco-elastic belt drive is investigated after loss of stability of its steady configuration. It is well known, that for sufficiently large drive speeds the steady configuration generically loses stability by either a zero eigenvalue or a pair of purely imaginary eigenvalues. Using bifurcation theory we investigate the branching behaviour and stability of the bifurcating solution. Special attention will be paid to the influence of viscous material damping on the stability boundary and the postcritical branching behaviour.

INTRODUCTION

A stable steady configuration of a belt drive is an important operating requirement in many industrial applications. The stability of the steady state of a stretched cable with bending stiffness and different boundary conditions at the endpoints has already been derived in [1]. It is shown, that after the transport speed exceeds the wave speed, either a zero eigenvalue occurs or two pairs of purely imaginary eigenvalues collide and leave the imaginary axis. This scenario is well known as "Hamiltonian Hopf Bifurcation" or as "Trojan Bifurcation" ([2, 3]). By calculating the Normal Form equations at the bifurcation point, one can determine whether the bifurcating periodic solution branches are stable or unstable.

Since the Hamiltonian Hopf bifurcation applies only to conservative systems, but in real world applications there will always occur non-conservative forces like damping, we either have to include non-conservative perturbation terms in the nonlinear analysis of the double imaginary eigenvalues, or introduce these perturbations already in the initial setup.

Frequently it has been observed, that small viscous damping forces may considerably influence the stability properties of oscillatory systems. Although it leads to a decay of the kinetic energy, it sometimes destabilizes the equilibrium state, especially, if two pairs of eigenvalues close to the imaginary axis approach each other.

Usually the tension forces for belt drives are assumed sufficiently large, such that the belt moves along a straight line during normal operation. If for some reason the tension force is considerably smaller, the belt may display a considerable sag. In this case the oscillations around the steady configuration contain also axial components and it becomes necessary to study two-dimensional motions of the system.

MODELLING AND TREATMENT OF THE BELT DRIVE

We investigate an inextensible, unshearable visco-elastic cable with bending stiffness, which travels with constant speed V between the eyelets. First we present the equations of planar motion in an Eulerian frame using the fundamental equations of Kirchhoff rods. Assuming a constant velocity of the belt, we first calculate the equilibrium configuration.

Stability boundaries of the equilibrium configuration

Starting with the known results for the straight, undamped configuration we study the influence of viscous damping and gravity on the equilibrium state and on the distribution of eigenvalues and stability boundaries. It should be noted, that in this case also the equilibrium configuration depends on the damping, because the belt's particles are not at rest in the equilibrium configuration, but move along the center line with constant speed. Therefore also a steady sagged configuration causes damping forces. Since the damping coefficient is usually very small, the governing equations for the steady state and the eigenmodes are singularly perturbed boundary value problems.

Preliminary results indicate, that already the introduction of a very small viscous damping changes the spectral properties considerably: Without damping most eigenvalues lie on the imaginary axis. Variation of the drive speed into the critical range causes some eigenvalues to move into the right half plane. As soon as some tiny amount of damping is added to the model, almost all eigenvalues reside in the left half plane, far away from the imaginary axis. A few eigenvalues, corresponding to low mode numbers, may still cross the imaginary axis at some critical values of the drive speed.

Bifurcations of the equilibrium configuration

Depending on the critical eigenvalues at the stability boundaries, we investigate 3 different bifurcation problems:

1. For a zero eigenvalue we calculate the bifurcating branch of steady solutions. Since in the undamped problem this zero eigenvalue occurs, when a pair of imaginary eigenvalues approaches the origin, the bifurcation point is actually a Bogdanov-Takes bifurcation with a non-semisimple pair of zero eigenvalues. In the absence of dissipative forces the investigation of that bifurcation reduces to the treatment of the ordinary steady state bifurcation.

---

*Corresponding author. Email: Alois Steindl@tuwien.ac.at

2. For a double pair of purely imaginary eigenvalues a Hamiltonian Hopf bifurcation has to be investigated. Proceeding as in [3], we calculate the Normal Form equation and derive the branching conditions and stability properties of a family of periodic solutions. In the conservative case the bifurcating oscillations are either elliptic or hyperbolic, depending on a certain coefficient, which is calculated in the Normal Form procedure.

At this stage it is also possible to consider a small perturbation by non-conservative forces. This perturbation usually destroys almost all periodic solutions and leaves distinct periodic orbits, which are either stable or unstable. The situation is quite similar to the Van der Pol equation, where for $\epsilon \neq 0$ only the trivial state and the periodic orbit of radius 2 survive.

3. The generic Hopf bifurcations occur at the stability boundary of the damped system. Due to the sag of the equilibrium configuration the periodic oscillations have vertical and horizontal components.

CONCLUSIONS

In this talk we extend the available results about instabilities of a driven belt in two directions: We consider the influence of viscous damping on the equilibrium configuration and its spectral properties. Second we allow a moderate sag of the equilibrium state.

References

[1] Wickert J. A., Mote Jr. C. D.: Classical Vibration Analysis of Axially Moving Continua, J. Appl. Mech., 57(3), 1990.

[2] Van der Meer, J. C.: The Hamiltonian Hopf bifurcation. Lecture Notes in Mathematics 1160, Springer-Verlag, 1986.

[3] Meyer K. R., Hall G. R.: *Introduction to Hamiltonian Dynamical Systems and the N-Body Problem*. Number 90 in Applied Mathematical Sciences. Springer-Verlag, 1992.

[4] Chen Li-Qun: Analysis and Control of Transverse Vibrations of Axially Moving Strings, Appl. Mechanics Reviews, 58, 2005.

[5] Sandilo S.H., van Horssen, W. T.: On a cascade of autoresonances in an elevator cable system. Nonlinear Dynamics, 80(3), 2015.

[6] Eliseev V., Vetyukov Yu.: Effects of deformation in the dynamics of belt drive. Acta Mechanica 223, (2012).

STRANGE ATTRACTORS OBSERVED IN ELECTROSTATIC MEMS ACTUATORS

Sangtak Park[1a)], Mahmoud Khater[2], Ahmed Abdel Aziz[3], Eihab M. Abdel-Rahman[1]

[1] *Systems Design Eng.,* [3] *Electrical and Computer Eng., University of Waterloo, Waterloo, Ontario, Canada*
[2] *Mechanical Engineering, KFUPM, Dhahran, Saudi Arabia*

<u>*Summary*</u>   We present an electrostatic MEMS actuator exhibiting superharmonic resonances as well as chaotic behaviour in soft vacuum, 500 mTorr. The displacement and velocity of the electrostatic actuator are measured with a laser vibrometer. These responses are analysed and presented in the time and frequency domains.

INTRODUCTION

Electrostatic actuator have been reported to exhibits diverse nonlinear behaviors, such as superharmonic resonances [3] and aperiodic motions [1, 2, 4]. In this paper, we demonstrate a strange attractor that is experimentally observed when an electrostatic microplate actuator is excited by a biased harmonic signal in vacuum.

FABRICATION
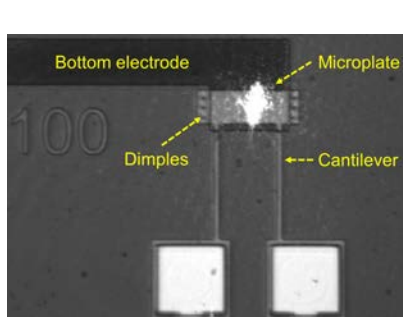
FIG. 1-(a) Top view of the actuator   FIG. 1-(b) Magnified view of the plate   FIG. 1-(c) Cross-sectional view
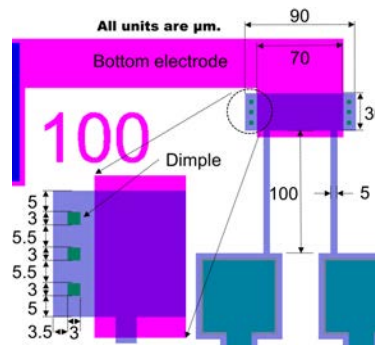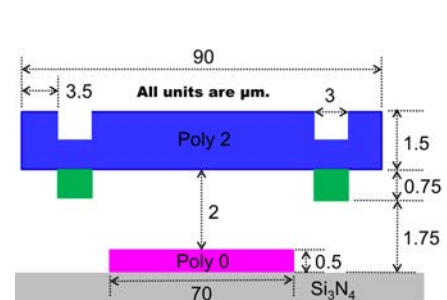
The actuator is fabricated in the PolyMUMPs process, FIG. 1-(a). It consists of two cantilever beams ($100\times5\times1.5$ µm) supporting a microplate ($90\times30\times1.5$ µm) equipped with three dimples ($3\times3\times0.75$ µm), green colored in the top and fronts views of FIG 1-(b) and (c), on each side of the microplate. The bottom electrode, made in the Poly 0 layer, is narrower than the microplate, so that the dimples can land on the insulating Si_3N_4 layer. This design is adopted to prevent dielectric charging and electrical short between the microplate and the bottom electrode when the microplate lands on the substrate.

EXPERIMENT

To reduce squeeze film damping and increase the quality factor of the actuator, we perform all experiment inside a vacuum chamber at soft vacuum, 500 mTorr. The bottom electrode is electrically connected to a function generator, while the microplate is grounded. This test set-up minimizes charge leakage from the microplate to the Si_3N_4 layer during contact. The velocity and displacement of the microplate mid-point are measured using a laser Doppler vibrometer.
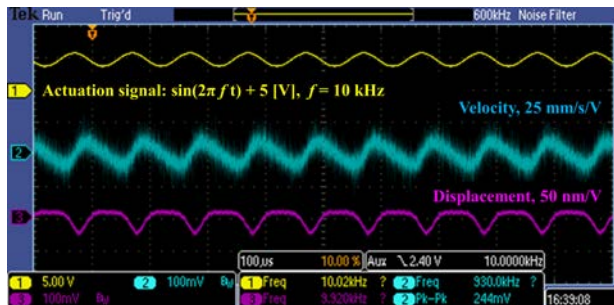
FIG. 2. Forced response of the actuator at 10 kHz   FIG.3. Superharmonic resonance at 33 kHz
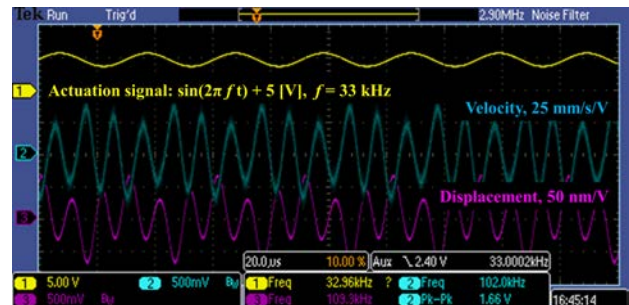
When excited by a harmonic signal, 5 V_{dc}, and 2 V_{pp} (peak-to-peak) at f = 10 kHz, the actuator exhibits a forced harmonic response as seen in FIG. 2. However, when the actuator is excited by the same waveform at f = 33 kHz, superharmonic

---

a) Corresponding author. Email: sangtak@uwaterloo.ca**.**

resonance of order three is observed in FIG. 3. Superharmonic resonances of order four and five were also observed at 25 kHz and 20 kHz as well as the superharmonic resonance of order two at 46 kHz and 50 kHz.

(a)　　　　　　　　　　　　　　　(b)　　　　　　　　　　　　　　　(c)
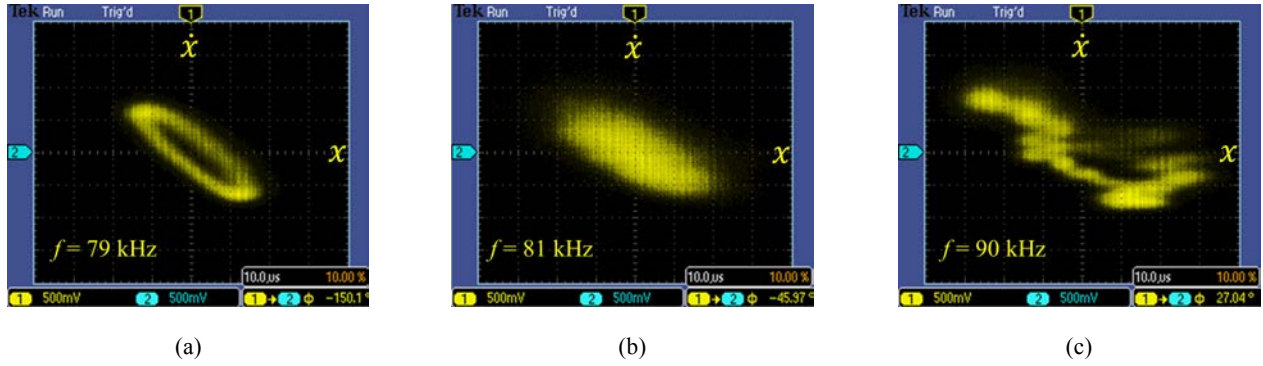
FIG. 4. Phase portraits of the actuator response to the harmonic signal, $\sin(2\pi f t) + 5$ [V], at the frequencies: (a) $f = 79$ kHz, (b) $f = 81$ kHz, and (c) $f = 90$ kHz. The negative slope of the phase portraits is due to phase delay in the vibrometer's velocity decoder with respect to the displacement decoder.

The phase portrait of the actuator excited with the same waveform shows a stable period-one periodic orbit in the vicinity of primary resonance, FIG. 4-(a), at 79 kHz. The phase portraits at 81 kHz and 90 kHz, FIGs. 4-(b) and (c), respectively, show that periodicity is lost to be replaced with an aperiodic chaotic attractor [2, 4]. The resulting strange attractor evolves from filling a limited area in the phase-space to a banded structure, as the excitation frequency increases from 81 kHz to 90 kHz.

The FFTs of the stable periodic orbit at $f = 79$ kHz are, FIG. 5, show a typical electrostatic response with peaks at the excitation frequency, 79 kHz, and its second harmonic, 158 kHz. The FFTs of the attractor at $f = 81$ kHz show elevated noise floors [2, 4] over a wide frequency range (wide-based peaks) as opposed to the flat noise floors of the stable orbit. Phase portraits that fill (wander in) areas of phase-space as well as wide-based peaks are typical characteristics of chaos.
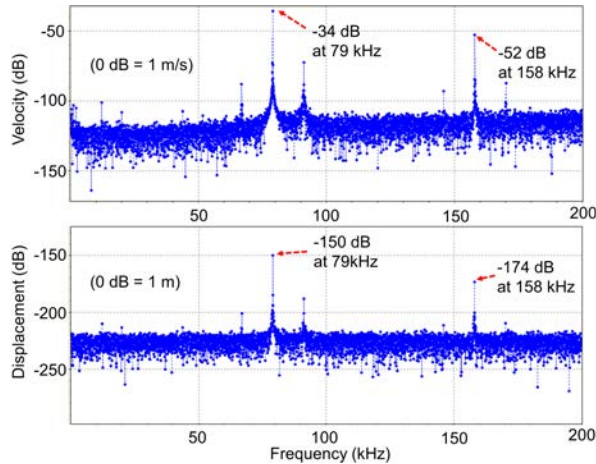
FIG. 5. FFTs of the measured velocity and displacement of the microplate at $f = 79$ kHz show flat noise floors.
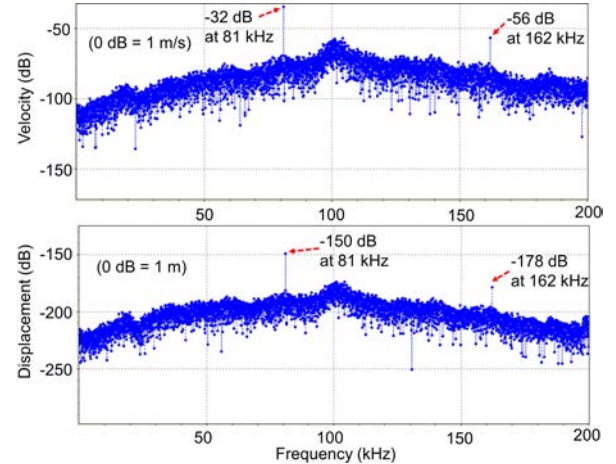
FIG. 6. FFTs of the microplate excited at $f = 81$ kHz show elevated noise floors over a wide frequency range.

CONCLUSIONS

We experimentally observed four superharmonic resonances as well as strange attractors, aperiodic motion confined to closed regions of phase-space, in the response of an electrostatic actuator in soft vacuum. The actuator demonstrates a softening nonlinearity and the attractors appear to belong to its primary resonance. The FFTs corresponding to the aperiodic attractors display wide-based peaks confirming that those attractors are chaotic.

References

[1]　J. Stulemeijer, R.W. Herfst, J.A. Bielen, IEEE 22nd International Conference on MEMS, pp. 920-922, 2009.

[2]　T. Carmon, M.C. Cross, K.J. Vahala, IEEE/LEOS International conference on Optical MEMS and their applications, pp.56-57, 2006.

[3]　S.K. De, N.R. Aluru, Journal of Microelectromechanical Systems, vol.15, no.2, pp.355-369, 2006.

[4]　B.E. DeMartini, H.E. Butterfield, J. Moehlis, K.L. Turner, Journal of Microelectromechanical Systems, vol.16, no.6, pp.1314-1323, 2007.

DIFFERENCE COMBINATIONAL INTERNAL RESONANCE IN NONLINEAR VIBRATIONS OF THIN PLATES

Marina Shitikova[*1], Yury Rossikhin[1], and Jean Claude Ngenzi[2]

[1]*Research Center on Dynamics of Solids and Structures, Voronezh State University of Architecture and Civil Engineering, Voronezh, Russia*
[2]*École Normale Supérieure, ENS Burundi*

Summary In the present paper, the dynamic response of a nonlinear plate embedded into a fractional derivative viscoelastic medium is studied by the method of multiple time scales under the condition of the combinational internal resonances of difference type using a newly developed approach resulting in uncoupling the linear parts of equations of motion of the plate. The influence of viscosity on the energy exchange mechanism between interacting nonlinear modes has been analyzed.

PROBLEM FORMULATION

It is well known that the nonlinear vibrations of plates are an important area of applied mechanics, since plates are used as structural elements in many fields of industry and technology [1]. Moreover, nonlinear vibrations could be accompanied by such a phenomenon as the internal resonance, resulting in multimode response with a strong interaction of the modes involved [2] accompanied by the energy exchange phenomenon.

Nonlinear free vibrations of a thin plate embedded into a fractional derivative viscoelastic medium have been considered recently [3] for the case when the plate motion is described by three coupled nonlinear differential equations. It has been shown that the occurrence of the internal resonance results in the interaction of modes corresponding to the mutually orthogonal displacements. As this takes place, the displacement functions are determined in terms of eigenfunctions of linear vibrations. The procedure resulting in decoupling linear parts of equations has been proposed with the further utilization of the method of multiple scales for solving nonlinear governing equations of motion, in so doing the amplitude functions are expanded into power series in terms of the small parameter and depend on different time scales. It has been shown that the type of the resonance depends on the order of smallness of the fractional derivative entering in the equations of motion of the plate.

In the recent paper [3] it has been shown that the following three combinational resonances could occur during vibrations of a free supported non-linear thin rectangular plate:

$$\omega_1 + \omega_2 = 2\omega_3, \tag{1}$$

$$\omega_1 - \omega_2 = 2\omega_3, \tag{2}$$

$$\omega_2 - \omega_1 = 2\omega_3, \tag{3}$$

where ω_1 and ω_2 are some particular natural frequencies of in-plane vibrations, and ω_3 is one of the natural frequencies of the out-of-plane modes.

Reference to (1)-(3) shows that the combinational resonance (1) is of the additive type, while combinational resonances (2) and (3) are of the difference type. In the present paper, we will focus our attention on the qualitative analysis of the case of the difference $\omega_1 - \omega_2 = 2\omega_3$ combinational internal resonance, when two different modes of in-plane vibrations are coupled with a certain mode of out-of-plane vibrations.

Difference combinational resonance $\omega_1 - \omega_2 = 2\omega_3$

Now let us consider the case of the difference combinational resonance (2), when $\omega_1 - \omega_2 = 2\omega_3$. Then the set of equations describing the modulations of amplitudes a_i and phases φ_i ($i = 1, 2, 3$) has the following form:

$$\left(a_1^2\right)^{\cdot} \quad + \quad s_1 a_1^2 = -2\omega_1^{-1}\zeta_1 k_6 a_1 a_2 a_3^2 \sin\delta, \tag{4}$$

$$\left(a_2^2\right)^{\cdot} \quad + \quad s_2 a_2^2 = 2\omega_2^{-1}\zeta_2 k_7 a_1 a_2 a_3^2 \sin\delta, \tag{5}$$

$$\left(a_3^2\right)^{\cdot} \quad + \quad s_3 a_3^2 = \omega_3^{-1}(\zeta_{13}k_6 + \zeta_{23}k_7)a_1 a_2 a_3^2 \sin\delta, \tag{6}$$

$$\dot{\varphi}_1 \quad = \quad \frac{1}{2}\,\sigma_1 + \omega_1^{-1}\zeta_1 k_5\,a_3^2 + \omega_1^{-1}\zeta_1 k_6 a_1^{-1} a_2 a_3^2 \cos\delta, \tag{7}$$

---

[*]Corresponding author. Email: shitikova@vmail.ru

$$\dot{\varphi}_2 \;\;=\;\; \frac{1}{2}\,\sigma_2 + \omega_2^{-1}\zeta_2 k_6\,a_3^2 + \omega_2^{-1}\zeta_2 k_7 a_1 a_2^{-1} a_3^2 \cos\delta, \tag{8}$$

$$\dot{\varphi}_3 \;\;=\;\; \frac{1}{2}\,\sigma_3 + \frac{1}{2}\,\omega_3^{-1}\zeta_{13} k_7 a_1^2 + \frac{1}{2}\,\omega_3^{-1}\zeta_{23} k_8 a_2^2 + \frac{1}{2}\,\omega_3^{-1}\left(\zeta_{13} k_2 + \zeta_{23} k_4\right) a_3^2$$
$$+\;\; \frac{1}{2}\,\omega_3^{-1}\left(\zeta_{13} k_6 + \zeta_{23} k_7\right) a_1 a_2 \cos\delta, \tag{9}$$

where the phase difference has the form $\delta = 2\varphi_3 + \varphi_2 - \varphi_1$, and

$$s_i = \mu_i \tau_i^\gamma \omega_i^{\gamma-1} \sin\psi, \qquad \sigma_i = \mu_i \tau_i^\gamma \omega_i^{\gamma-1} \cos\psi, \quad \psi = \frac{1}{2}\,\pi\gamma \ \ (i = 1, 2, 3). \tag{10}$$

Reference to (10) shows that damping coefficients s_i depend of natural frequencies of the coupled modes ω_i and the fractional parameter γ, i.e., the order of the fractional derivative.

Thus, during free vibrations of the plate with internal resonances three regimes can be observed: stationary (absence of damping at $\gamma = 0$), quasi-stationary (damping is defined by an ordinary derivative at $\gamma = 1$), and transient (damping is defined by a fractional derivative at $0 < \gamma < 1$).

For a particular case at $\Sigma = 0$ and $s_1 = s_2 = s_3 = s$, introducing a new function representing a relative displacement $\xi(T_2)$, it is possible to obtain two first integrals of nonlinear set of Eqs. (4)-(9), one of which gives the energy distribution, while the other results in the stream function

$$G(\xi, \delta) \;\;=\;\; (c_3 + \xi)\sqrt{(c_1 - \xi)(c_2 + \xi)}\,\cos\delta - \frac{1}{2}\,K_1 b^{-1}(c_1 - \xi)^2 + \frac{1}{2}\,K_2 b^{-1}(c_2 + \xi)^2$$
$$+\;\; \frac{1}{2}\,K_3 b^{-1}(c_3 + \xi)^2 = G_0(\xi_0, \delta_0), \tag{11}$$

where c_1, c_2, and c_3 are constants of integration such that $4c_1 + 2c_2 + 2c_3 = 1$, and K_i are certain coefficients.

The stream-function allows us to construct phase portraits in terms of two functions, ξ and δ. The phenomenological analysis carried out for the combinational internal resonance of the difference type with the help of the phase portraits constructed for different magnitudes of the plate parameters reveals the great variety of vibrational motions: stationary vibrations, two-sided energy exchange between two subsystems under consideration, and onesided energy interchange resulting in the complete one-sided energy transfer. Under the presence of small viscosity all regimes attenuate with time.

CONCLUSIONS

The proposed analytical approach for investigating the damped vibrations of a nonlinear plate in a fractional derivative viscoelastic medium subjected to the combinational internal resonances of the difference type has been possible owing to the new procedure suggested recently in [3], resulting in decoupling linear parts of equations with further utilization of the method of multiple scales for solving nonlinear governing equations of motion.

The phenomenological analysis carried out for the difference combinational internal resonance using the phase portraits constructed for different magnitudes of the plate parameters reveals the great variety of vibrational motions: stationary vibrations, two-sided energy exchange between two subsystems, and complete one-sided energy transfer. The analysis of the phase portraits for various oscillatory regimes shows that they contain closed and non-closed streamlines separated by the rectilinear and curvilinear separatrixes, along which analytic solutions have been found, which define the irreversible energy transfer from one subsystem into another and are inherently soliton-like solutions in the theory of vibrations.

References

[1] Breslavsky I.D., Amabili M., Legrand M.: Physically and geometrically non-linear vibrations of thin rectangular plates. Int. J. Non-Linear Mech. 58:30-40, 2014.

[2] Nayfeh A.H.: Nonlinear Interaction: Analytical, Computational, and Experimental Methods. Wiley, New York, USA 2000.

[3] Rossikhin Yu.A., Shitikova M.V., Ngenzi J. Cl.: A new approach for studying nonlinear dynamic response of a thin plate with internal resonance in a fractional viscoelastic medium. Shock Vibr. 2015, 2015, Article ID 795606, 28 pages, http://dx.doi.org/10.1155/2015/795606.

ON NONLINEAR DIFFERENTIAL EQUATIONS WITH DELAYED SELF-FEEDBACK

Si Mohamed Sah[1] and <u>Richard Rand</u>[*2]

[1]*Nanostructure Physics, KTH Royal Institute of Technology, Stockholm, Sweden.*
[2]*Dept. of Mathematics, Dept. of Mechanical & Aerospace Engineering, Cornell University. Ithaca, NY, USA.*

<u>*Summary*</u> This work concerns the dynamics of nonlinear systems that are subjected to delayed self-feedback. Perturbation methods applied to such systems give rise to slow flows which characteristically contain delayed variables. We consider two approaches to analyzing Hopf bifurcations in such slow flows. In one approach, which we refer to as approach **I**, we follow many researchers in replacing the delayed variables in the slow flow with non-delayed variables, thereby reducing the differential-delay equation (DDE) slow flow to an ordinary differential equation (ODE). In a second approach, which we refer to as approach **II**, we keep the delayed variables in the slow flow. By comparing these two approaches we are able to assess the accuracy of making the simplifying assumption which replaces the DDE slow flow by an ODE.

INTRODUCTION

When investigating a differential-delay equation (DDE) by use of a perturbation method, one is often confronted with a slow flow which contains delay terms. It is usually argued that since the parameter of perturbation, call it ϵ, is small, $\epsilon << 1$, the delay terms which appear in the slow flow may be replaced by the same term without delay, see e.g. [1, 2, 3]. The purpose of the present paper is to analyze the slow flow with the delay terms left in it, and to compare the resulting approximation with the usual one in which the delay terms have been replaced by terms without delay.

EXAMPLE 1: DUFFING EQUATION

For example take the following version of the Duffing equation with delayed self-feedback.

$$\ddot{x} + x = \epsilon \left[-\alpha \dot{x} - \gamma x^3 + k\, x_d \right] \tag{1}$$

where $x_d = x(t - T)$, where T = delay. We treat eq.(1) with the two variable perturbation method, where $x(\xi, \eta)$, where $\xi = t$ and $\eta = \epsilon t$. We expand $x = x_0 + \epsilon x_1 + O(\epsilon^2)$ and obtain the following equation on x_0:

$$Lx_0 \equiv x_{0\xi\xi} + x_0 = 0 \quad \Rightarrow \quad x_0(\xi, \eta) = A(\eta) \cos\xi + B(\eta) \sin\xi \tag{2}$$

Eliminating secular terms in the x_1 equation gives the following slow flow:

$$\frac{dA}{d\eta} = -\alpha\,\frac{A}{2} + \frac{3\,\gamma\,B^3}{8} + \frac{\gamma\,A^2 B}{8} - \frac{k}{2}A_d \sin T - \frac{k}{2}B_d \cos T \tag{3}$$

$$\frac{dB}{d\eta} = -\alpha\,\frac{B}{2} - \frac{3\,\gamma\,A^3}{8} - \frac{\gamma\,AB^2}{8} - \frac{k}{2}B_d \sin T + \frac{k}{2}A_d \cos T \tag{4}$$

where $A_d = A(\eta - \epsilon T)$ and $B_d = B(\eta - \epsilon T)$ are delay terms in the slow flow.

Method I involves replacing the delay terms A_d, B_d in the slow flow (3),(4) respectively by undelayed terms A, B, resulting in a slow flow of ODEs. It is argued that such a step is justified if the product ϵT is small:

$$A_d = A(\eta - \epsilon T) \approx A(\eta) + O(\epsilon), \qquad B_d = B(\eta - \epsilon T) \approx B(\eta) + O(\epsilon). \tag{5}$$

Method II involves studying the slow flow (3),(4) as it is.

Figure 1 (left side) shows a comparison, in the case of the Duffing equation (1), between the analytical Hopf conditions obtained via the two approaches and the numerical Hopf curves. The approach **II** plotted by red/dashed curves gives a better result than the approach **I** (black/dashdot curves). Therefore in the case of Duffing equation, treating the slow flow as a DDE gives better results than approximating the DDE slow flow by an ODE.

---

[*]Corresponding author. Email: `rrand@cornell.edu`
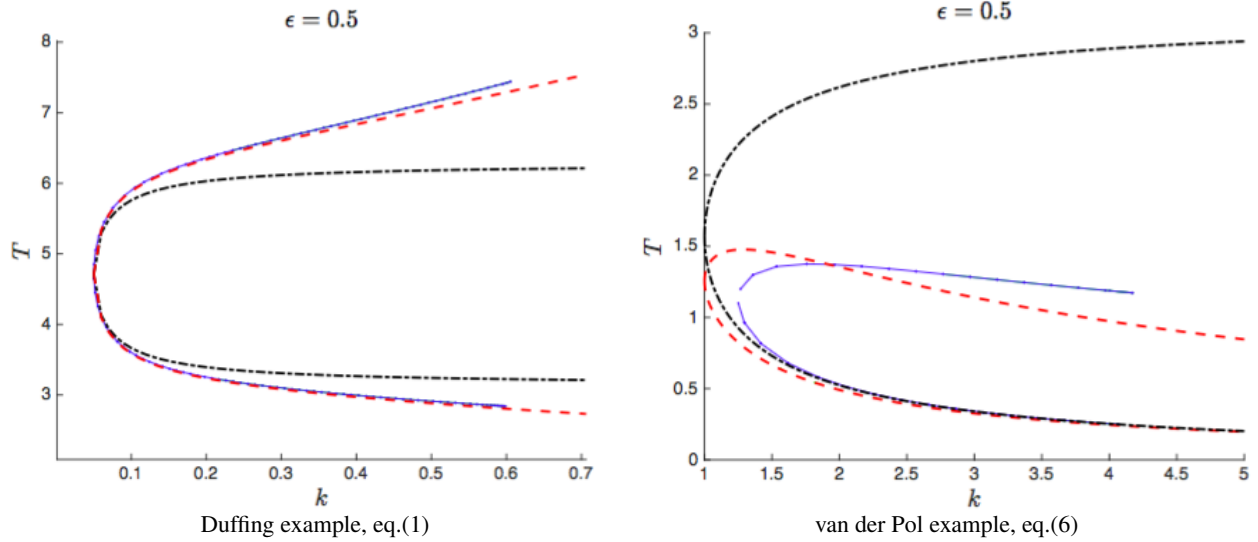
Figure 1: Numerical Hopf bifurcation curves (blue/solid). Also shown are the results of approach **I** (black/dashdot), and the results of approach **II** (red/dashed)

EXAMPLE 2: VAN DER POL EQUATION

As a second example, we consider a version of the van der Pol equation with delayed self-feedback [4]:

$$\ddot{x} + x = \epsilon \left[\dot{x}(1 - x^2) + k\,x_d - k\,x \right] \tag{6}$$

We apply the same procedure here as we did for the Duffing equation (1) and show the results in Figure 1 (right). Figure 1 (right) shows that approach **II** gives better results than approach **I**. However approach **I** still gives a good fit for the lower Hopf curve.

CONCLUSIONS

When a DDE with delayed self-feedack is treated using a perturbation method (such as the two variable expansion method, multiple scales, or averaging), the resulting slow flow typically involves delayed variables. In this work we compared the behavior of the resulting DDE slow flow with a related ODE slow flow obtained by replacing the delayed variables in the slow flow with non-delayed variables. We studied sample systems based on the Duffing equation with delayed self-feedback, eq.(1), and on the van der Pol equation with delayed self-feedback, eq.(6). In both cases we found that replacing the delayed variables in the slow flow by non-delayed variables (approach **I**) gave better results on the lower Hopf curve than on the upper Hopf curve.

Our conclusion is therefore that the researcher is advised to perform the more lengthy approach **II** analysis on the DDE slow flow in situations where values of the product ϵT is relatively large, as in the upper Hopf curves in Figures 1.

References

[1] Atay, F.M., Van der Pol's oscillator under delayed feedback. J. Sound Vib. 218(2), 333-339 (1998)
[2] Wirkus, S., Rand, R.H., The dynamics of two coupled van der Pol oscillators with delay coupling. Nonlinear Dyn. 30, 205-221 (2002)
[3] Morrison, T.M., Rand, R.H., 2:1 Resonance in the delayed nonlinear Mathieu equation. Nonlinear Dyn. 50, 341-352 (2007)
[4] T. Erneux, J. Grasman, Limit-cycle oscillators subject to a delayed feedback, Phys. Rev. E 78 (2) (2008) 026209.

ANALYSIS OF SYSTEMS WITH STATE-DEPENDENT DELAYS AND APPLICATIONS IN METAL CUTTING

Andreas Otto [*1] and <u>Günter Radons</u>[1]
[1]*Institute of Physics, Chemnitz University of Technology, Chemnitz, Germany*

Summary The equivalence between systems with state-dependent delays and systems with constant delays is studied. Systems with state-dependent delays appear when the dynamics of the system does not only depend on the instantaneous configuration but also on a delayed configuration of the system, and the size of the delay depends on the state of the system. It is shown that, indeed, the condition for a transformation to a constant delay is related to the mechanism that generates the state-dependent delay. With an example for the cutting force in turning it is demonstrated that variable and state-dependent delays in metal cutting vibrations can be transformed to constant delays.

INTRODUCTION

Time delay systems can be found in many engineering applications. They range from metal cutting vibrations and laser dynamics to traffic models and teleoperation of mobile robots (see [1] and Refs. therein). In some systems, as for example in laser dynamics, the assumption of time-invariant delays is quite reasonable. However, in many applications, the delays are actually time-varying or state-dependent. For example, in metal cutting the vibrations of the tool directly affect the time delay and lead to a state-dependent delay [2]. Moreover, variable delays are used for a better control of the system. Indeed, metal cutting vibrations can be suppressed by an active variation of the spindle speed, which is equivalent to a time-varying delay [3]. Thus, the analysis of systems with time- or state-dependent delays is relevant in many research areas.

Here, we focus on the analysis of systems with state-dependent delays because time-varying delays can be put in the framework of state-dependent delays. However, in contrast to the well-established theory for systems with constant delays there are many open problems in systems with state-dependent delays [4]. In this contribution we shown how a system with state-dependent delay can be transformed to a system with constant delay. It turns out that, indeed, the mathematical condition for the existence of such a transformation is fulfilled in many real word examples.

TRANSFORMATION FROM STATE-DEPENDENT DELAYS TO CONSTANT DELAYS

In general, a system with state-dependent delay $\tau(\boldsymbol{x}_t)$ can be described by the delay differential equation (DDE)

$$\dot{\boldsymbol{x}}(t) = \boldsymbol{f}\left(\boldsymbol{x}(t), \boldsymbol{x}(t - \tau(\boldsymbol{x}_t))\right), \tag{1}$$

where $\boldsymbol{x}(t)$ is the configuration of the system at time t. The state of the DDE can be specified by the vector function $\boldsymbol{x}_t = \boldsymbol{x}(t - \theta)$, $\theta \in [0, \tau_{\max}]$, where the constant $\tau_{\max}$ is the maximum delay [4]. A nonlinear time scale transformation $\varphi = \Phi(t)$ can be used to change the delayed argument $t - \tau(\boldsymbol{x}_t)$ of the DDE Eq. (1). The function $\Phi(t)$ is assumed to be bijective, which means that there is a one-to-one mapping between the time t and the new independent variable φ. The configuration in terms of the new variable φ is given by $\boldsymbol{y}(\Phi(t)) = \boldsymbol{x}(t)$. We demand for a constant delay δ in the new representation, $\boldsymbol{x}(t - \tau(\boldsymbol{x}_t)) = \boldsymbol{y}(\varphi - \delta)$, which is equivalent to the condition

$$\Phi(t) - \delta = \Phi(t - \tau(\boldsymbol{x}_t)) \quad \leftrightarrow \quad \delta = \int_{t-\tau(\boldsymbol{x}_t)}^{t} \dot{\Phi}(t')dt'. \tag{2}$$

Eq. (2) can be interpreted as follows. The state-dependent delay $\tau(\boldsymbol{x}_t)$ is the traveling time for a transport of a particle over the constant distance δ with the velocity $\dot{\Phi}(t)$. The absolute distance covered by the particle at time t is given by the function $\Phi(t)$. A graphical illustration of the condition is presented in Fig. 1 a). The function $\Phi(t)$ defines a mapping between time t (horizontal) and space φ (vertical). A vertical shift of the function $\Phi(t)$ by the constant distance δ leads to a variable horizontal displacement (red lines), which is equal to the time delay $\tau(\boldsymbol{x}_t)$. In particular, a state-dependent delay occurs if the absolute distance $\Phi(t)$ covered by the particles is a component of the configuration $\boldsymbol{x}(t)$ or affected by the configuration $\boldsymbol{x}(t)$ of the system. In the spatial domain the system can be described by the DDE

$$\boldsymbol{y}'(\phi) = \left(\Phi^{-1}\right)'(\varphi)\boldsymbol{f}\left(\boldsymbol{y}(\varphi), \boldsymbol{y}(\varphi - \delta)\right). \tag{3}$$

Thus, a DDE with state-dependent delay $\tau(\boldsymbol{x}_t)$ Eq. (1), whose time delay is specified by the condition Eq. (2), is equivalent to the DDE Eq. (3) with constant delay δ. In other words, every delay that can be interpreted as a variable transport over a constant distance can be transformed to a constant delay. These delays are sometimes called variable transport delays and occur in many applications [5]. On the other hand, it is also possible that variable delays are generated by a transport over a variable distance. In this case it is not clear a priori if the delay is a variable transport delay or not.

---

*Corresponding author. Email: otto.a@mail.de
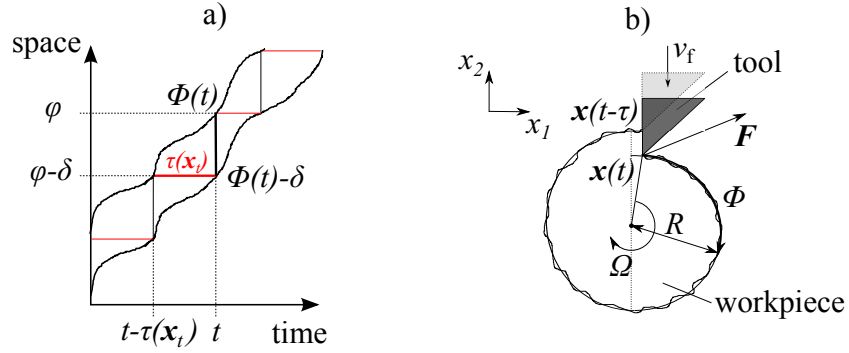
Figure 1: a) Illustration of the condition Eq. (2) between the constant delay δ (vertical shift) and the state-dependent delay $\tau(\boldsymbol{x}_t)$ (red horizontal displacement). b) State-dependent delay in turning (see text for explanations).

STATE-DEPENDENT DELAYS IN METAL CUTTING APPLICATIONS

The occurrence of undesired large vibrations at machine tools is still a significant problem in metal cutting applications. These so-called chatter vibrations are not acceptable in manufacturing industry because they cause noise, bad surface finish and increased tool wear. As a consequence the prediction of machine tool vibrations and the stability of metal cutting processes is an important field in research and industry.

An example of a turning process is shown in Fig. 1 b). Small fluctuations of the cutting force $\boldsymbol{F}(t)$ lead to dynamic displacements $\boldsymbol{x}(t) = \mathrm{col}\,(x_1(t), x_2(t))$ of the turning tool and a wavy surface of the workpiece. The instantaneous and time-delayed vertical displacements $x_2(t)$ and $x_2(t - \tau(\boldsymbol{x}_t))$ determine the inner and the outer surface of the chip, respectively, and lead to dynamic variations of the chip thickness and the cutting force. In particular, the time delay $\tau(\boldsymbol{x}_t)$ between the present and the previous cut at the same location of the workpiece is equivalent to the time for one revolution of the workpiece. Hence, the delay in turning is defined by a variable transport delay similar to Eq. (2) with the constant distance $\delta = 2\pi R$, where R is the radius of the workpiece. In this case, the spatial variable $\Phi(t)$ can be interpreted as the absolute machined distance given by $\Phi(t) = \Omega t R - x_1(t)$, where Ω is the angular velocity of the workpiece and $x_1(t)$ are the horizontal dynamic displacements of the tool. This mechanism of self-excitation of the vibrations in machining is called regenerative effect (see [2], [3]). If the closed-loop of the regeneration is unstable, chatter vibrations occur. In many other cutting processes the time delay is similarly defined by a constant distance between two subsequent cuts.

Since the structural dynamics can be described by ordinary differential equations, metal cutting processes, in general, can be described either in time domain by Eq. (1) with state-dependent delay or by a system similar to Eq. (3) with constant delay. For Eq. (3) the linearization of the system is much simpler, whereas for systems with state-dependent delay similar to Eq. (1) the linearization is not straight forward [2], [3]. In addition, many methods for the stability analysis of linear non-autonomous DDEs can be only applied to systems with constant delay, which follow from the linearization of Eq. (3), whereas the equivalent linear system of Eq. (1) is a DDE with time-varying delay.

CONCLUSIONS

The transformation of a system with state-dependent delay to a system with constant delay is studied, which can be used to simplify the analysis in many applications. It is shown that the transformation is possible if the state-dependent delay is generated by a variable transport over a constant distance. Using the example of a turning process it is demonstrated that the time-varying and state-dependent delays in metal cutting applications belong to the class of variable transport delays and can be transformed to constant delays.

References

[1] Kyrychko Y.N., Hogan S.J.: On the Use of Delay Equations in Engineering Applications. J. Vibr. Control 16:943960, 2010.

[2] Insperger T., Stepan G., Turi J.: State-dependent delay in regenerative turning processes. Nonlin. Dyn. 47:275-283, 2007.

[3] Otto A., Radons G.: Application of spindle speed variation for chatter suppression in turning. CIRP J. Manuf. Sci. Technol. 6:102-109, 2013.

[4] Hartung F., Krisztin T., Walther H.-O., Wu J.: Functional Differential Equations with State-Dependent Delays: Theory and Applications. In: Canada A., Drabek P., Fonda A. (editors): Handbook of Differential Equations: Ordinary Differential Equations 3:435-545, North-Holland, 2006.

[5] Zhang F., Yeddanapudi M.: Modeling and simulation of time-varying delays. Proc. TMS/DEVS 34:1-8, San Diego, CA, USA, 2012.

HIGHER-ORDER ESTIMATION OF LIMIT CYCLE AMPLITUDE IN METAL CUTTING

Tamás G. Molnár [*1], Tamás Insperger[1], and Gábor Stépán[1]

[1]*Department of Applied Mechanics, Budapest University of Technology and Economics, Budapest, Hungary*

Summary Global dynamics of an orthogonal cutting model is discussed, which is governed by a nonsmooth delay differential equation (DDE), namely, the delayed term intermittently disappears if the amplitude of the vibrations exceeds some critical value. Along the linear stability boundaries of the fixed point of the DDE, subcritical Hopf bifurcation occurs and consequently, a parameter domain of bistability can be identified where the stable fixed point, an unstable periodic orbit, and a large-amplitude stable bounded motion (chatter) coexist. The first approximation of the amplitude of the unstable periodic orbit is the standard square-root function of the bifurcation parameter that is the chip width. A non-standard higher-order approximation is proposed that takes into account that the periodic solution disappears as the chip width approaches zero. This allows the construction of a more accurate still simple formula for the size of the bistable region, which is highly important for the real-world application of regenerative cutting theory.

MECHANICAL MODEL

Consider the single-degree-of-freedom mechanical model of orthogonal cutting where the tool's motion is governed by

$$\ddot{x}(t) + 2\zeta\omega_{\mathrm{n}}\dot{x}(t) + \omega_{\mathrm{n}}^2 x(t) = \frac{1}{m}F_x\left(h(t)\right) . \tag{1}$$

Here, ω_{n} is the undamped natural angular frequency, ζ is the damping ratio, and m is the modal mass of the machining system corresponding to vibrations in the feed direction x. The x-component F_x of the cutting force acting on the tool is proportional to the chip width w and can be given as a cubic polynomial of the chip thickness h according to [1]:

$$F_x(h) = w\left(\rho_1 h + \rho_2 h^2 + \rho_3 h^3\right) \quad \text{if } h > 0, \tag{2}$$

where $\rho_1 = 6.1096 \times 10^9 \text{ N/m}^2$, $\rho_2 = -5.41416 \times 10^{13} \text{ N/m}^3$, and $\rho_3 = 2.03769 \times 10^{17} \text{ N/m}^4$ were identified in [1] for a milling tool of four teeth. Note that for non-positive chip thickness ($h \leq 0$), loss of contact takes place between the tool and the workpiece and the cutting force is zero. The instantaneous chip thickness can be calculated from the feed h_0 per revolution according to the theory of regenerative machine tool vibrations:

$$h(t) = h_0 + x(t-\tau) - x(t), \tag{3}$$

where $\tau = 2\pi/\Omega$ is the regenerative delay related to the angular velocity Ω of the workpiece.

Transforming Eq. (1) to shift its equilibrium to zero, scaling the tool position by h_0 and the time by ω_{n}, one obtains the dimensionless equation of motion in the form

$$\xi''(t) + 2\zeta\xi'(t) + \xi(t) = p\Big(\left(\xi(t-\tau) - \xi(t)\right) + \eta_2\left(\xi(t-\tau) - \xi(t)\right)^2 + \eta_3\left(\xi(t-\tau) - \xi(t)\right)^3\Big). \tag{4}$$

Here, p is the dimensionless chip width, η_2 and η_3 denote dimensionless cutting-force coefficients:

$$p = \frac{w\left(\rho_1 + 2\rho_2 h_0 + 3\rho_3 h_0^2\right)}{m\omega_{\mathrm{n}}^2}, \quad \eta_2 = \frac{\rho_2 h_0 + 3\rho_3 h_0^2}{\rho_1 + 2\rho_2 h_0 + 3\rho_3 h_0^2}, \quad \eta_3 = \frac{\rho_3 h_0^2}{\rho_1 + 2\rho_2 h_0 + 3\rho_3 h_0^2} . \tag{5}$$

ANALYSIS OF THE HOPF BIFURCATION AND REGION OF BISTABILITY

Analyzing the stability of Eq. (4) by the D-subdivision method, one obtains the linear stability boundaries in the form

$$p_{\mathrm{st}}(\omega) = \frac{\left(\omega^2 - 1\right)^2 + 4\zeta^2\omega^2}{2\left(\omega^2 - 1\right)}, \quad \tau_{\mathrm{st}}(\omega) = \frac{2}{\omega}\left(j\pi - \arctan\left(\frac{\omega^2 - 1}{2\zeta\omega}\right)\right), \quad \Omega_{\mathrm{st}}(\omega) = \frac{2\pi}{\tau_{\mathrm{st}}(\omega)}, \quad j \in \mathbb{N}^+ . \tag{6}$$

The linear stability boundaries are shown by solid line in the left panels of Fig. 1 for $\zeta = 0.02$. Along these boundaries, a subcritical Hopf bifurcation occurs [2, 3], which gives rise to an unstable limit cycle of approximate angular frequency ω.

The standard approximation [4, 5] of the amplitude $r(\omega, p)$ of the unstable limit cycle is given by a square-root function of the bifurcation parameter p:

$$r(\omega, p) \approx \sqrt{-\frac{\gamma(\omega)}{\Delta_{\mathrm{cr}}(\omega)}\left(p - p_{\mathrm{st}}(\omega)\right)}, \tag{7}$$

---

*Corresponding author. Email: molnar@mm.bme.hu
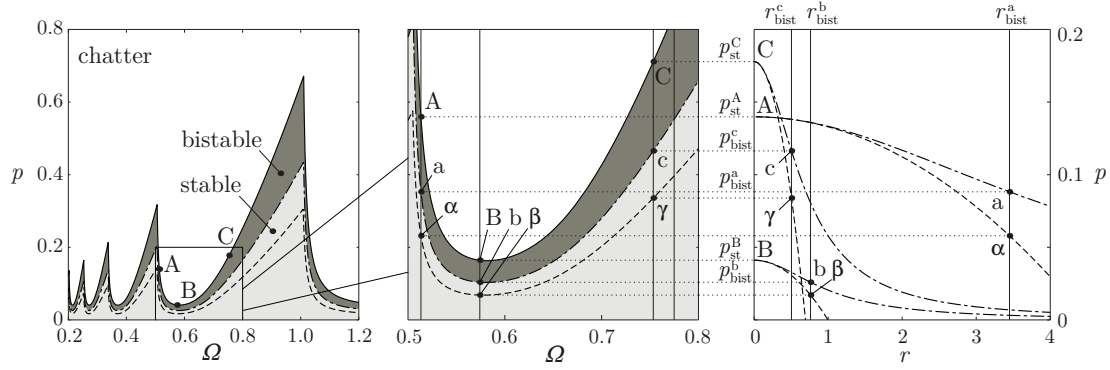
Figure 1: Left and middle panels: stability charts of the cutting process. Right panel: the corresponding bifurcation diagrams.

where $\gamma(\omega)$ is the crossing speed (root tendency) of the critical pair of imaginary eigenvalues and $\Delta_{\mathrm{cr}}(\omega)$ is the Poincaré-Lyapunov constant, which can be obtained by center manifold reduction and normal form calculations [2, 3]. A non-standard higher-order approximation of the amplitude can also be obtained by taking into account that for $p = 0$ the right-hand side of Eq. (4) vanishes and the system reduces to a damped free oscillator with no periodic solution. That is, the unstable limit cycle disappears as the bifurcation parameter p tends to zero, and it happens so that its amplitude tends to infinity: $\lim_{p \to 0} r(\omega, p) = \infty$. Accordingly, the proposed approximation of the amplitude of the unstable limit cycle becomes

$$r(\omega, p) \approx \sqrt{-\frac{\gamma(\omega)}{\Delta_{\mathrm{cr}}(\omega)} \frac{p - p_{\mathrm{st}}(\omega)}{1 + \dfrac{p - p_{\mathrm{st}}(\omega)}{p_{\mathrm{st}}(\omega)}}} \; . \tag{8}$$

The estimations (7) and (8) of the amplitude of periodic solutions bifurcating from points A, B, and C indicated in the left and middle panels of Fig. 1 are shown for $h_0 = 250 \ \mu m$ in the right panel by dashed and dash-dot line, respectively. The results obtained by the proposed approximation (8) overlap with numerical results computed using DDE-BIFTOOL [6].

Due to the existence of an unstable periodic solution, the basin of attraction of the linearly stable equilibrium is bounded. Consequently, a parameter domain of bistability exists where the linearly stable equilibrium associated with stationary cutting coexists with large-amplitude stable solutions (chatter), which involve intermittent loss of contact between the tool and the workpiece [7]. The boundary $p_{\mathrm{bist}}(\omega)$ of the bistable region is located where the amplitude of the unstable limit cycle reaches the critical value $r_{\mathrm{bist}}(\omega)$ for which loss of contact ($h \leq 0$) occurs [7] (see points a,b,c, and α, β, γ in Fig. 1). The boundary of the bistable region computed from Eqs. (7) and (8) is indicated in the left panels of Fig. 1 by dashed and dash-dot lines, respectively. The bistable region obtained from Eq. (8) is shaded with dark grey, the globally stable region is light grey. Using the proposed approximation (8), the relative width of the bistable region can be approximated by a simple formula

$$R_{\mathrm{bist}}(\omega) = \frac{p_{\mathrm{st}}(\omega) - p_{\mathrm{bist}}(\omega)}{p_{\mathrm{st}}(\omega)} \approx \frac{3\rho_3 h_0^2}{4\rho_1 + 8\rho_2 h_0 + 15\rho_3 h_0^2} \, , \tag{9}$$

which allows engineers to select the technological parameters needed for a globally stable chatter-free cutting process.

References

[1] Shi H. M., Tobias S. A.: Theory of finite amplitude machine tool instability, Int J Mach Tool D R 24(1):45-69, 1984.

[2] Stépán G., Kalmár-Nagy T.: Nonlinear regenerative machine tool vibrations. Proc of DETC97, ASME Design and Technical Conferences, Sacramento, CA, USA, 1-11, 1997.

[3] Dombóvári Z., Wilson R. E., Stépán G.: Estimates of the bistable region in metal cutting, P Roy Soc A - Math Phy 464:3255-3271, 2008.

[4] Hassard B. D., Kazarinoff N. D., Wan Y.-H.: Theory and Applications of Hopf Bifurcation, London Mathematical Society Lecture Note Series 41, Cambridge, 1981.

[5] Guckenheimer J., Holmes P.: Nonlinear Oscillations, Dynamical Systems, and Bifurcations of Vector Fields, Springer, New York, 1983.

[6] Engelborghs K., Luzyanina T., Roose D.: Numerical bifurcation analysis of delay differential equations using DDE-BIFTOOL, ACM T Math Software 28(1):1-21, 2002.

[7] Dombóvári Z., Barton D. A., Wilson R. E., Stépán G.: On the global dynamics of chatter in the orthogonal cutting model, Int J Nonlin Mech 46(1):330-338, 2011.

DELAY EFFECT ON MOTION CONTROL OF A TWO-WHEELED INVERTED PENDULUM

Yusheng Zhou[1] and Zaihua Wang [*1]

[1]*State Key Laboratory of Mechanics and Control of Mechanical Structures, Nanjing University of Aeronautics and Astronautics, Nanjing, China*

Summary Two-wheeled inverted pendulum (TWIP, for short) is an open-loop unstable nonlinear system, the delay effect arising in the feedback loop has not been reported in the literature. This paper designs a delayed robust control for controlling the back-and-forth motion of a TWIP against the influence of uncertainties, and shows that the delay effect cannot be neglected in control design.

INTRODUCTION

Two-wheeled inverted pendulum, an inverted pendulum mounted on two parallel wheels, is a common mechanical model of two-wheeled robots. A TWIP is an essential nonlinear and under-actuated system, subjected to nonholonomic constraints. It is a system of open-loop unstable, different control strategies are required for different control tasks under different environment [1]. If the stabilization of the inverted pendulum is addressed only and uncertainty is not considered, a proportional feedback of the acceleration signal can be used to stabilize the inverted pendulum. Analysis shows that the inevitable time delay in the controller has a substantial influence on the stability of the closed-loop [2]. When uncertainties must be considered, more delicate control strategies are usually used, such as H_∞ control, adaptive control, disturbance observer, and especially the sliding mode control that is the mostly used strategy in controlling TWIPs. No results about delay effect on the control of TWIPs with delayed feedback have been reported in the literature [1]. This paper shows that the delay has an important influence on the robust motion control and the delay effect must be taken into account in controlling a TWIP.

DYNAMIC MODEL AND CONTROL DESIGN OF THE TWIP

Let us consider a basic motion of a TWIP, Back-and-Forth motion, for which the TWIP is required to move forward to pass a prefixed point and return back to the starting point, keeping the inverted pendulum stabilized during the whole process. Figure 1(a) shows a 2-DOF model of the TWIP, without considering the turning motion. Let $L = T_w + T_b - P$ be the Lagrangian function, where T_w, T_b are the kinetic energies of the wheels and the intermediate body respectively, and P is the gravitational potential energy of the system. Then the Euler-Lagrange equation gives the dynamic equation of the TWIP

$$\begin{cases} (Ml^2 + I_B)\ddot{\varphi} + Ml\cos\varphi\ddot{x} - Mgl\sin\varphi = -T, \\ Ml\ddot{\varphi}\cos\varphi + (M_w + M + \frac{I_w}{r^2})\ddot{x} - Ml\dot{\varphi}^2\sin\varphi = \frac{T}{r}, \end{cases} \tag{1}$$

where T is the control. With the delay in control taken into consideration, T can be written as $T = u(t - \tau)$, where $\tau > 0$ is the time delay. Let $\mathbf{X} = [x_1, x_2, x_3, x_4]^T = [\varphi, \dot{\varphi}, x, \dot{x}]^T$, let $\boldsymbol{\omega}(t)$ stand for the integrated effect of the linearization error and bounded system uncertainties, then the dynamic equation can be rewritten on the basis of the linearized system $\dot{\mathbf{X}}(t) = \mathbf{AX}(t) + \mathbf{B}u(t - \tau) + \boldsymbol{\omega}(t)$. The control takes place only when $t \geq \tau$. Let $\bar{\mathbf{X}} = [\bar{x}_1, \bar{x}_2, \bar{x}_3, \bar{x}_4]^T = [\bar{\varphi}(t), \dot{\bar{\varphi}}(t), \bar{x}(t), \dot{\bar{x}}(t)]^T$ be the trajectory tracking target vector depending on the control task, and let $\mathbf{Y}(t) := \mathbf{X}(t) - \bar{\mathbf{X}}(t)$, $\boldsymbol{\sigma}(t) := \mathbf{A}\bar{\mathbf{X}} - \dot{\bar{\mathbf{X}}}$, then

$$\dot{\mathbf{Y}}(t) = \mathbf{AY}(t) + \mathbf{B}u(t - \tau) + \boldsymbol{\omega}(t) + \boldsymbol{\sigma}(t). \tag{2}$$

To reduce the linearization error, a quadratic performance criterion with large weight of tilt angle error is introduced

$$J = \frac{1}{2}\mathbf{Y}^T(t_f)\mathbf{MY}(t_f) + \frac{1}{2}\int_0^{t_f} \left[\mathbf{Y}^T(t)\mathbf{QY}(t) + u^T(t - \tau)\mathbf{R}u(t - \tau)\right] dt, \tag{3}$$

where $\mathbf{M}, \mathbf{Q}$ are nonnegative definite symmetric matrices, $\mathbf{R}$ is a positive definite matrix, and $t_f (> 2\tau)$ is the terminal time of the control. With a large weight of the tilt angle error in J, the tilt angle error can be "forced" to be small when an optimal control is applied. Thus, the linearization error is small enough and can be considered as bounded, and thus the integrated disturbance $\boldsymbol{\omega}(t)$ can be assumed bounded. A robust controller can be designed in two parts: $u(t - \tau) = u_0(t - \tau) + u_1(t - \tau)$, $t \in [\tau, t_f]$, where $u_0(t - \tau)$ is an optimal controller for the nominal error system (2) that minimizes the performance criterion J in (3), and $u_1(t - \tau)$ is a switched control based on an integral sliding manifold for compensating the effect of the integrated disturbance significantly. In designing the optimal delayed control $u_0(t - \tau)$, it is usually required to convert (2) into a delay-free one and then to design the controller in terms of the state of the reduced system, while in [3] the optimal controller $u_0(t - \tau)$ can be represented directly in terms of the state $\mathbf{Y}(t)$. In constructing the switch control $u_1(t - \tau)$, the optimal state of the nominal error system can be chosen as the integral sliding mode manifold. In this way, the controller not only works well in implementing the control task, but also has strong robustness against the integrated disturbance.

*Corresponding author. Email: zhwang@nuaa.edu.cn

NUMERICAL SIMULATION ON THE CONTROL PERFORMANCE

For the Back-and-Forth motion, the trajectory tracking target can be chosen in different form, for example, $[\bar{\varphi}(t), \bar{x}(t)]^{\mathrm{T}} = [0, (at - t^2)\mathrm{e}^{-\alpha t}]^{\mathrm{T}}$, where $\bar{\varphi}(t) = 0$ means that the inverted pendulum should be kept stable, the numbers a and α are to be determined by the distance s and the weight matrices in J. The terminal time is $t_f = +\infty$ for simplicity. To addresses the special feature of this paper that uses linear optimal control theory to design a robust controller for systems with strong nonlinearity and an input delay, $\boldsymbol{\omega}(t)$ is assumed for simplicity to be $\boldsymbol{\omega}(t) = [0, \omega_2, 0, \omega_4]^{\mathrm{T}}$, where ω_2, ω_4 are linear combination of φ^2, $\dot{\varphi}^2$ and $\varphi\dot{\varphi}$, with the coefficients assumed in the form of $f_i \sin(\Omega t)$, $(i = 1, 2, 3)$. Case studies are made for a given parameter comination with $\tau = 0.01$ and $\Omega = 200\,\mathrm{Hz}$ or $\Omega = 0.02\,\mathrm{Hz}$ respectively. Figs.(b)-(d) and Figs.(g)-(i) show the time-histories of the inverted pendulum and the TWIP respectively, which imply that the control task has been well implemented; While Figs.(e)(f) and Figs.(j)(k) show the corresponding time histories by neglecting the delay in the controller, and Fig.(l) is the plots of the performance criterion with respect to time, which mean that the time delay, although very small in quantity, has a significant influence on the control performance and cannot be neglected in control design.
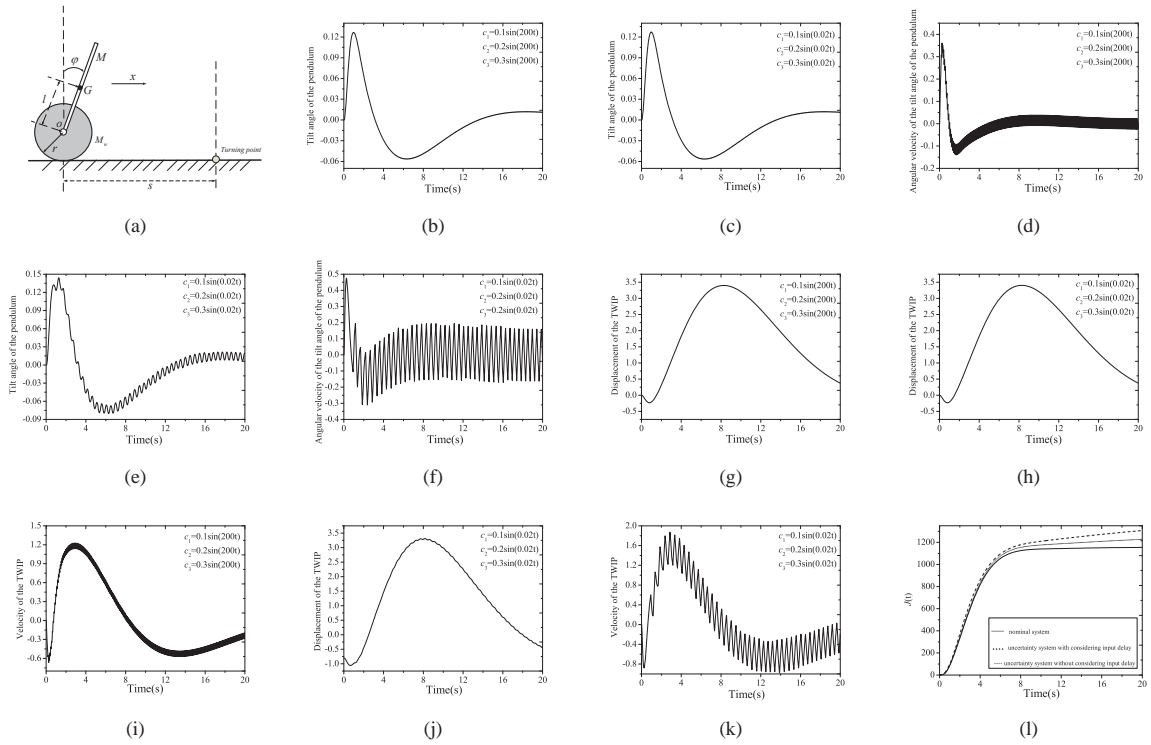
Figure 1: The model of the TWIP and its control performance.

CONCLUSIONS

The designed controller based on the linearized model works well for the TWIP with strong nonlinearity, by introducing a quadratic peformance criterion with large weight to make the linearization error small enough, and by using integral sliding mode control to make the controller very robust against the integrated effect of disturbance. The results show that in the applications of the widely used sliding mode control to TWIPs, the delay effect cannot be neglected in control design.

References

[1] Chan, R.P.M., Stol, K.A., Halkyard, C.R.: Review of modelling and control of two-wheeled robots. *Annual Reviews in Control*, **37**(1): 89-103, 2013.

[2] Xu, Q., Stepan, G., Wang, Z.H.: Balancing a wheeled inverted pendulum with a single accelerometer in the presence of time delay. *Journal of Vibration and Control*, doi:10.1177/1077546315583400, 2015.

[3] Zhou, Y.S., Wang, Z.H.: Motion controller design of wheeled inverted pendulum with an input delay via optimal control theory. *Journal of Optimization Theory and Applications*, 10.1007/s10957-015-0759-z, 2015.

DYNAMICAl BEHAVIOURS OF AN ARCHETYPAL SELF-EXCITED SD OSCILLATOR

Qingjie Cao[*1], Zhixin Li[1], and Marian Wiercigroch[2]

[1]*School of Astronautics, Harbin Institute of Technology, Harbin, 150001, China*
[2]*Centre for Applied Dynamics Research, Department of Engineering, University of Aberdeen, King's College, Aberdeen AB24 3UE, Scotland, UK*

Summary In this paper, we propose an archetypal self-excited smooth and discontinuous oscillator, which is constructed with the smooth and discontinuous (SD) oscillator and the classical moving belt. Phase portraits are depicted to present the hyperbolic structure transition, multiple stick regions and the friction-induced asymmetry phenomena. Chaotic thresholds of the perturbed self-excited SD oscillator are derived by using the Melnikov's method. The numerical simulations are carried out to demonstrate the friction-induced vibration of multiple stick-slip phenomena and the stick-slip chaos for the perturbed self-excited system.

INTRODUCTION

Much attention has been paid on self-excited vibration induced by friction in mechanical engineering system, i.e. brake[1], drill string[2] and others. In this paper, we propose an archetypal self-excited smooth and discontinuous oscillator[3] based upon the SD oscillator[4] and classical moving blet, which comprises a block of mass M, supported by a moving belt, connected to a fixed support by a inclined linear spring of stiffness coefficient K, as shown in Fig. 1. The mass vibrates under the influence of dry friction F_S modeled as Coulomb friction existing in the contact zone created by the mass 's surface and the outer belt's surfaces that moves with a constant velocity V_0.
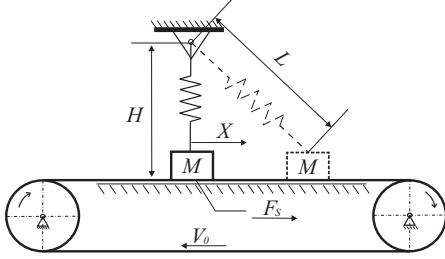
Fig. 1. The dynamical model of a self-excited oscillator.

The dimensionless equation of motion in the sense of differential inclusion of Filippov type is given by

$$\ddot{x}+x\Big(1-\frac{1}{\sqrt{x^2+\alpha^2}}\Big) \in \mu\Big(g_1-\alpha+\frac{\alpha}{\sqrt{x^2+\alpha^2}}\Big)Sign(v_0-\dot{x}), \quad (1)$$

where μ is the friction coefficient of contacting surfaces and assumed to be constant in this friction model and $Sign(\cdot)$ denotes the set-valued sign function $Sign(p)=p|p|^{-1}$ for $p \neq 0$, and $Sign(0) = [-1, 1]$.

EQUILIBRIUM BIFURCATION AND MULTIPLE STICK REGIONS

In this section, we discuss the complex phase portraits by investigating the equilibrium and the bifurcation of this system. The transition set $\mathcal{H}$ of the equilibrium surface in a parameter space (α, μ) can be obtained and plotted in Fig. 2, where

$$\mathcal{H} = \{(\alpha,\mu)|F(x,\alpha,\mu) = F_x(x,\alpha,\mu) = 0, \alpha, \mu > 0\},$$

$$F(x,\alpha,\mu) = x\Big(1 - \frac{1}{\sqrt{x^2 + \alpha^2}}\Big)$$
$$-\mu\Big[g_1 - \alpha\Big(1 - \frac{1}{\sqrt{x^2 + \alpha^2}}\Big)\Big].$$

The bifurcation diagram is constructed and depicted in Fig. 2. In the parameter space (α, μ), the surface M can be divided into two persistence regions by $\mathcal{H}$, marked by I and II, as shown in Fig. 2(M). Suppose that a point $Q(\alpha, \mu)$ in the parameter plane (α, μ) starts from region II into region I, the stationary $(x_1, 0)$ state exhibits the transition from hyperbolic structure to non-hyperbolic at $\mathcal{H}$. All the corresponding phase portraits of system (1) are presented in Figs. 2(a)-2(j).
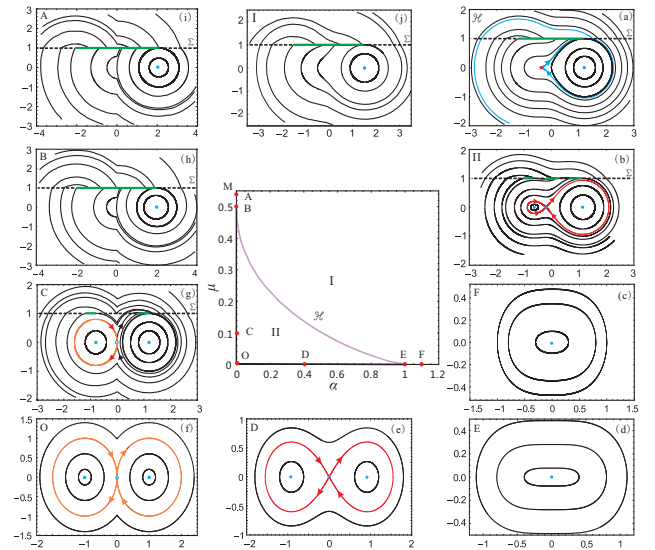
Fig. 2. Bifurcation diagram and corresponding phase portraits.

*Corresponding author. Email: qingjiecao@hotmail.com

The blue dots denote the centers and the saddle points connecting the corresponding homoclinic orbits, marked by red, see Figs. 2(b) and 2(e). While small cycles indicate non-standard or saddle-like equilibria[4] connecting the corresponding homoclinic-like orbits, marked by pink, as shown in Figs. 2(f) and 2(g). Especially, Fig. 2(a) shows a orbit, marked by blue, connecting with a non-hyperbolic equilibrium called the center-saddle point. In all the phase portraits, the symbol Σ denotes the discontinuous boundary $y = v_0$ for this self-excited system, in which, the stick regions marked by green indicate the mass have a same velocity with the belt. Hence, the difference between the SD oscillator and the self-excited SD oscillator can be seen from Fig. 2. For $\mu = 0$, the system (1) becomes the SD oscillator shown in Figs. 2(c)-2(f). For $\mu \neq 0$, Figs. 2(a)-2(b) and 2(g)-2(j) present the phase portraits of the self-excited SD oscillator. Obviously, the moving belt friction destroys the symmetry of the original SD oscillator. In conclusion, the self-excited SD oscillator with dry friction is characterized by friction-induced asymmetry and multiple stick regions in the phase plane.

PERTURBED DYNAMICS

It is assumed that the system (1) is perturbed by a viscous damping of coefficient c and an external harmonic excitation of amplitude f an frequency ω, the equation of motion can be written as

$$\ddot{x} + c\dot{x} + x\left(1 - \frac{1}{\sqrt{x^2 + \alpha^2}}\right) \in f\cos\omega t - \mu\left[g_1 + \alpha\left(1 - \frac{1}{\sqrt{x^2 + \alpha^2}}\right)\right]Sign(v_0 - \dot{x}), \tag{2}$$

The chaotic boundary obtained by using the Melnikov's method for this system is shown in Fig. 3. This criterion predicts that above this curve chaos can appear. In Fig. 4(a)-4(d), the short horizontal parts marked with green lines in phase portraits correspond to the sticking during the motions. A pair of asymmetric stick-slip period 1 solutions coexist $f = 0.2$, as shown in Fig. 4(a), the system dynamic responses are regular motions. With an increase of amplitude f, the regular motion vanishes and the multiple stick-slip chaotic motion follows when $f = 0.474$, as depicted in Fig. 4(b). These results are in good agreement with the Melnikov's criterion. When $f = 0.5125$, a period-3 solution with three stick-slip motions is shown in Fig. 4(c). when f increases to $f = 0.85$, chaotic motion occurs and the chaotic attractor is depicted in Fig. 4(d).
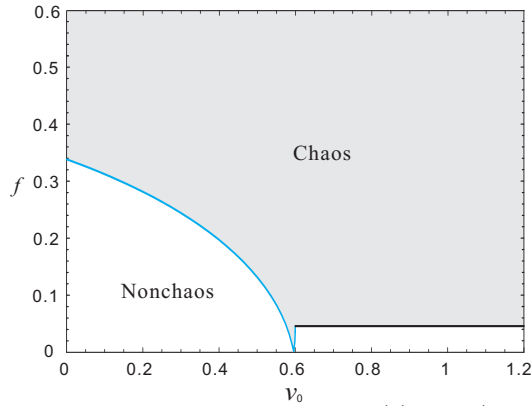
Fig. 3. Chaotic boundaries for system (2) in the (f, v_0) plane for $\alpha = 0.4$.
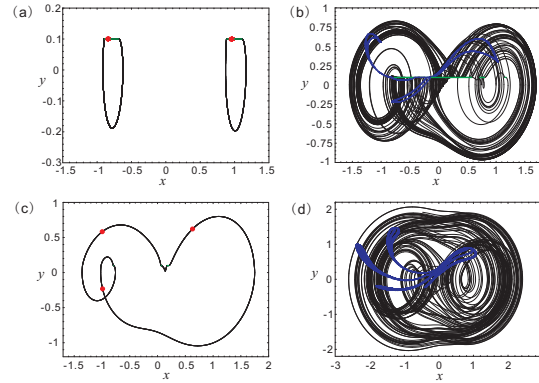
Fig. 4. The periodic motion and chaotic attractors of system (2) for $\alpha = 0.4$. (a) $f = 0.2$, (b)$f = 0.474$, (c) $f = 0.5125$, (d) $f = 0.85$.

CONCLUSIONS

In this paper, we have proposed a novel self-excited SD oscillator driven by moving belt friction. The self-excited system is characterized by the existence of multiple stick regions in the phase portraits which exhibit the hyperbolic structure transition and friction-induced asymmetry phenomena. The obtained results characterized the existence of the multiple stick-slip chaos in a range of the excitation force amplitudes as predicted by the Melnikov's criterion.

References

[1] Rhee S. K., Tsang P. H. S., Wang Y. S.: Wear 133: 39-45, 1989.
[2] Mihajlović N., Van de Wouw N., Hendriks M. P. M., Nijmeijer H.: Non. Dyn. 46: 273-291, 2006.
[3] Li Z. X., Cao, Q. J., Léger, A.: Chin. Phys. B, 2016, 25(1), 010502(1-9).
[4] Cao Q. J., Wiercigroch M., Pavlovskaia E. E., Grebogi C., Thompson J. M. T.: Phys. Rev. E 74: 046218, 2006.

ANALYSIS OF FORWARD AND BACKWARD WHIRLS IN DRILLING

Marcin Kapitaniak[1], Vahid Vaziri Hamaneh[1], Joseph Páez Chávez[2,3], and Marian Wiercigroch [*][1]
[1]*Centre for Applied Dynamics Research, School of Engineering, University of Aberdeen, UK*
[2]*Center for Dynamics, Department of Mathematics, TU Dresden, D-01062 Dresden, Germany*
[3]*Facultad de Ciencias Naturales y Matemáticas, Escuela Superior Politécnica del Litoral, Guayaquil, Ecuador*

<u>*Summary*</u> In this paper we discuss whirling motion of the Bottom Hole Assembly (BHA) that occurs in downhole drilling, with particular attention to the co-existence of forward and backward whirls. First we present experimental results obtained on the unique drilling rig developed in Aberdeen and described in [2, 3], which are then used to calibrate a non-smooth low-dimensional model to investigate complex dynamics of the whirling motion.

INTRODUCTION

During a downhole drilling process, excessive vibrations can occur, which in most cases have a negative effect on the effectiveness of the process and the drilling equipment. Such vibrations may lead to an accelerated wear and a premature damage of the expensive drilling equipment. Often different dynamic effects such as bit-bounce, stick–slip, forward and backward whirl may appear simultaneously. In this work we focus on the whirling of the BHA inside the borehole, which nature is still not well understood and can lead to a catastrophic failure of the the drill-sting. .

EXPERIMENTAL OBSERVATIONS

In this section we present examples of experimental results showing co-existing forward and backward whirls, which have been observed on the unique experimental rig [2, 3]. The most important feature of the experimental apparatus is its versatility, which means that depending on chosen configuration, different type of drilling associated phenomena could be analyzed including stick-slip, bit-bounce and whirling. Here we concentrate on the whirling motion only to get further inside into its dynamics. Therefore, the experimental configuration depicted in Fig. 1(a) is used, where the main part is the loose bearing, that holds the BHA in place. A radial clearance between the BHA and the holding bush is 1 mm, what allows us to observe different types of whirling motion. The BHA is driven from the top using a flexible shaft and at its other end there is a drill-bit, that drills in a sandstone sample.

Interestingly, it has been possible to capture for the first time experimentally co-existence of forward and backward whirling, which can be seen in Figs. 1(c)-(d). Both of these phenomena can be observed for the same set of parameters (WOB=2.59 kN and angular velocity at the top, $\varphi_t = 9.36 \, \text{rad/s}$). Type of whirling motion is determined by comparing the angular displacements at the top, φ_t with the angular displacement of the BHA inside the bearing, θ, which are depicted in panels (e) and (f) for backward and forward whirling motion respectively. When comparing the phase portraits shown in panels (c) and (d), we notice that the qualitative responses are different, but both cases can be characterized as periodic whirling.

The top angular speed φ_t is constant (marked as black curve in panels (g) and (h)), whereas there is a considerable difference in amplitude between the angular velocity of the BHA, $\dot{\varphi}_b$ for the backward and forward whirls. In the case of the forward whirling, the amplitude of the BHA's angular velocity oscillations is considerably smaller than for the backward whirling . This demonstrates the fact that the backward whirling is more dangerous for the drill-string than the forward one due to a higher amplitude of torsional vibrations, which in turn result in higher stresses in the drill-string.

MATHEMATICAL MODELING

In order to understand the physics behind whirling phenomenon we introduce a simplified model of the analyzed experimental setup. Thereby, the model is similar to a Jeffcott rotor with a snubber ring, which has been studied extensively in the literature, e.g. [4]. We introduce a simplified rotor model depicted in Fig. 1(b), which consists of a disc having mass m and radius r, which spins inside the borehole with a constant angular velocity Ω. The position of the disc inside the borehole is described using polar coordinates r and θ, that constitute a two degree-of-freedom model. We assume a small imbalance of the disc. The disc is assumed to be supported by a radial bearing having a stiffness k_1 and a viscous damping c in the radial direction. The model does not include damping due to the rotation of the disc. The radial clearance between the disc and the borehole is γ. Due to the fact that two modes of operation are present, contact and non-contact, there are two sets of equations which need to be switched. We model contact of the BHA with the borehole using a spring of stiffness k_2, and dry friction

---
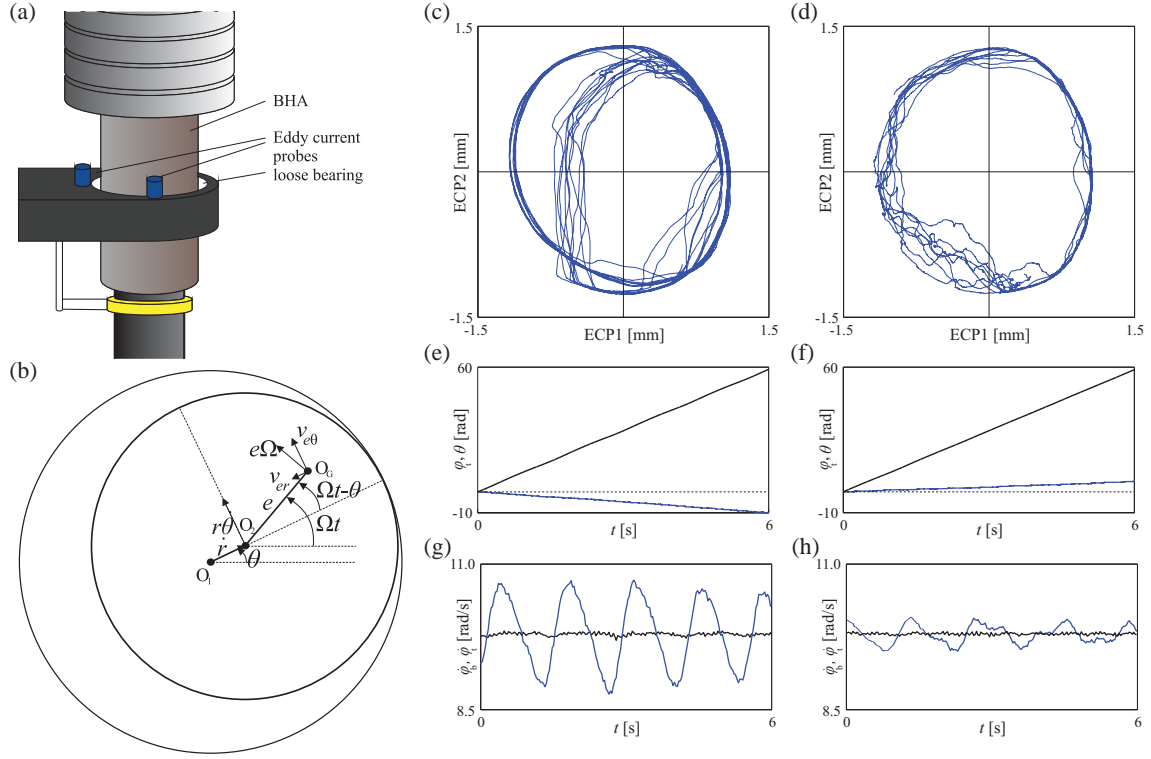
Figure 1: (a) A part of the drilling rig, showing the BHA and the bearing to simulate whirling motion; (b) schematic of the rotor model; (c)-(h) comparisons between co-existing periodic backward and forward whirling observed for WOB = 2.59 kN; panels (c)-(d) show phase portraits, where panels (e)-(f) compare angular displacement of top φ_t vs. angular displacement inside the borehole θ and panels (g)-(h) show the angular velocity of top, $\dot{\varphi}_t$ and bottom, $\dot{\varphi}_b$ for backward and forward whirl respectively.

friction μ between the disc and the borehole in tangential direction. Therefore, the system can be described by following set of equations:

$$\begin{cases} M\ddot{r} - Mr\dot{\theta}^2 + k_1 r + c\dot{r} = M\Omega^2\rho\cos(\Omega t - \theta) - k_2(r - \gamma)H(r - \gamma), \\ Mr\ddot{\theta} + 2M\dot{r}\dot{\theta} + cr\dot{\theta} = M\Omega^2\rho\sin(\Omega t - \theta) - \mu k_2(r - \gamma)H(r - \gamma)sgn(v_c), \end{cases} \quad (1)$$

where $H(\ )$ stands for a Heaviside function switching between contact and non-contact states [1]. In other words this means that the disc can be in contact (C) or noncontact (N) state, depending on the value $r - \gamma$. There are other modes of operation for the model, including the condition when the disc sticks to the wall [3].

CONCLUSIONS

In this paper first we have shown experimentally the co-existence of forward and backward whirling. Then a low dimensional non-smooth model to study the complexity of the whirling behaviour is introduced. After a careful calibration of the proposed model, one is able to analyze conditions that trigger forward and backward whirls [3] and ultimately to control the BHA dynamic behaviour.

References

[1] Páez Chávez J., Vaziri Hamaneh V. and Wiercigroch M.: Modelling and Experimental Verification of an Asymmetric Jeffcott Rotor with Radial Clearance. Journal of Sound and Vibration 334: 86-97, 2014.

[2] Kapitaniak M., Vaziri Hamaneh V., Páez Chávez J., Nandakumar K. and Wiercigroch M.: Unveiling complexity of drillstring vibrations: Experiments and modelling. International Journal of Mechanical Sciences 101-102: 324-337, 2015.

[3] Kapitaniak M.: Nonlinear Dynamics of Drill-Strings. PhD Thesis, University of Aberdeen, UK, 2015.

[4] Karpenko E. V., Wiercigroch M., Pavlovskaia E. E. and Neilson R. D.: Experimental verification of Jeffcott rotor model with preloaded snubber ring. Journal of Sound and Vibration 298: 907-917, 2006.

SELF-EXCITED MICROCANTILEVERS FOR SENSING APPLICATIONS

<u>Hiroshi Yabuno</u>[*1], Daichi ENDO[*1], Ekiichi Higashino[2], Yasuyuki Yamamoto[3], and Sohei Matsumoto[3]

[1]*Graduate School of Systems and Information Engineering, University of Tsukuba, Tsukuba, Ibaraki, Japan*
[2]*Faculty of Science and Technology, Keio University, Yokohama, Japan*
[3]*National Institute of Advanced Industrial Science and Technology (AIST), Tsukuba, Ibaraki, Japan*

<u>*Summary*</u> In the measurement procedure of vibrating-type sensing systems, the frequency response curve under external or forced excitation has been conventionally used. For instance, viscosity measurement and mass sensing are preformed from the estimation of difference in the Q-value related to the resonance amplitude and of shift in the resonance frequency, respectively. However, in the high viscosity range, it is very difficult to accurately measure these values. To overcome such difficulties, we propose the utilization of self-excited oscillation without relying on the frequency response curve; the positive velocity feedback is applied to compensate the damping force and to produce the self-excited oscillation. In the presentation, we introduce some measurement systems using self-excited microcantilevers as ultra-sensitive mass sensor, viscometer for high viscosity sensing, and AFM.

INTRODUCTION

Vibrating-type sensing devices allow for instantaneous and continuous measurements of changes in the viscosity and the mass of the sample occurring with time, i.e., on-line monitoring. In the measurement procedure of vibrating-type viscometers, the frequency response curve under external or forced excitation is employed. The viscosity is estimated by the Q-value related to the resonance amplitude (for example, see Ref. [1]) and in the mass sensing, the shift of the resonance frequency is utilized (for example, Ref. [2]). However, in the high viscosity range, it is very difficult to accurately estimate differences in Q-values and the shifting of the resonance frequency. To overcome such difficulties, we have proposed the utilization of self-excited oscillation without relying on the frequency response curve; the positive velocity feedback is applied to compensate the damping force and to produce the self-excited oscillation. First, merits of the use of self-excited oscillation are indicated using an application to the viscometer for high viscosity sensing. Next, the concept is implemented to micro-cantilevers which is widely used as a resonator for high sensitive measurement. In particular, non-contact AFM using van der Pol-type self-excited microcantilever beams are proposed and the performance of ultra-sensitive mass sensor using self-excited coupled cantilevers are experimentally shown.

SELF-EXCITED OSCILLATION BY POSITIVE VELOCITY FEEDBACK AND HIGH-VISCOSITY SENSING

We consider a resonator expressed as spring-mass-damper system with external force whose equation of motion is

$$m\frac{d^2y}{dt^2} + c\frac{dy}{dt} + ky = f, \tag{1}$$

where m and k are the equivalent mass and stiffness of the resonator, respectively. c expresses the viscous environment for the resonator and the viscosity sensing corresponds to the measurement of c [3]. In conventional viscometers, f is set to be sinusoidal force as $a\cos\nu t$. However, in the case of high viscosity, the frequency response curve has no peak and there is no Q value and the identification of c is impossible from the frequency response curve. To overcome the difficulty, f is set based on the following positive velocity feedback as $f = c_{cont}dx/dt$, where c_{cont} is positive feedback gain. Then, the critical feedback gain to produce the self-excited oscillation $c_{cont-cr}$ is equal to c and c can be estimated from the critical feedback gain which can be experimentally obtained. This method can be applicable regardless of the magnitude of viscosity [4].

AFM USING VAN DER POL-TYPE POL-TYPE SELF-EXCITED MICROCANTILEVER

FM-AFM carries out the imaging of the surface of sample in nano-meter accuracy by detecting the natural frequency shift of the cantilever due to the variation of the atomic force. The compensation of viscosity based on the above positive velocity feedback makes the eigenstate of the resonator emerge. The response frequency of the self-excited oscillation produced under the positive velocity feedback gain near the critical one corresponds to the natural frequency and the detection is easy even in liquid environments. The equation of motion of the cantilever is expressed as follows:

$$\rho A\frac{\partial^2(y+\Delta y)}{\partial t^2} + EI\frac{\partial^4 y}{\partial t^4} = 0, \tag{2}$$

where y is the deflection of the beam and Δy is displacement of the supporting point which is applied to produce the self-excited oscillation in the cantilever. In the actuation accoridng to the feedback as

$$\Delta y = c_{lin}\int y dt + c_{non}\int y^3 dt, \tag{3}$$

---

*Corresponding author. Email: yabuno@esys.tsukuba.ac.jp

the linear term produces the above mentioned self-excited oscillation. Furthermore, the additional nonlinear feedback of the second term can avoid the monotonically increasing response amplitude and realizes the self-excited oscillation with small steady state amplitude under high gain nonlinear feedback. Then, the non-contact imaging in AFM is achieved [5].

MASS SENSING USING SELF-EXCITED COUPLED MICROCANTILEVERS

Mass sensing by a resonator has been also based on the shift of the natural frequency, i.e., eigenvalue of the resonator system, depending on the mass. In contrast with this method, it is clarified that the utilization of the shift of an eigenmode in weakly coupled oscillators realizes more accuracy mass detection [6]. The frequency response curve under the external excitation is used to detect the eignemode. Similar to the above measurement, it is impossible in a viscous environment. Accordingly, we propose the self-excited coupled cantilevers which is modeled to two-degrees-of freedom systems as Fig. 1, where m is equivalent mass of the resonator and Δm is a measured mass. The base excitation of Δy is established by the displacement of one of cantilevers to produce the self-excited oscillation [7]. The detection of the displacements of
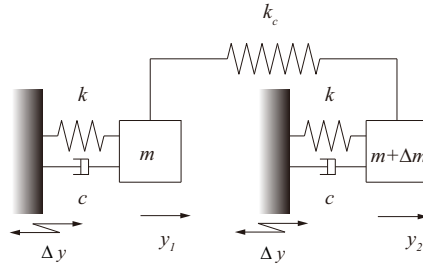
Figure 1: Sprin-mass-damper model for self-excited coupled microcantilevers.

the coupled cantilevers is carried out two laser Dopper vibrometers by the experimental apparatus as shown in Fig. 2. The experiment demonstrated mass sensing of the order of ng [8].
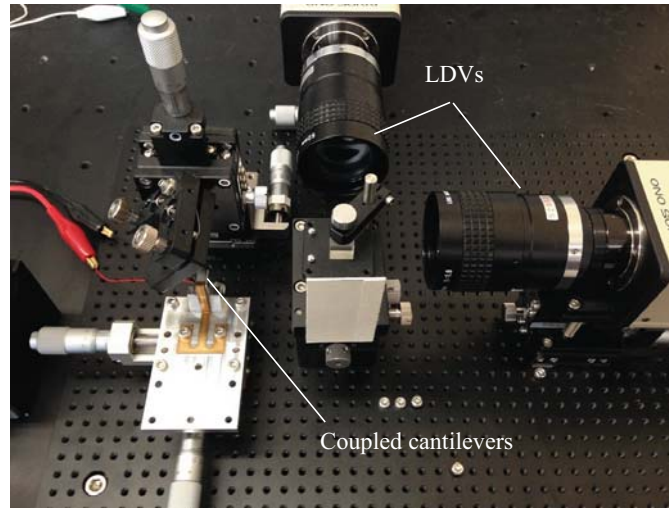
Figure 2: Experimental apparatus of self-excited coupled microcantilevers.

References

[1] Gupta, A., Akin, D., and Bashir, R.: Single virus particle mass detection using microresonators with nanoscale thickness. Physics Letters. Vol 84, pp. 19761978, 2004.

[2] Lee, I., Park, K., and Lee, J.:Precision viscosity measurement using suspended microchannel resonaors. Review of Scientific Instruments, Vol 83, 116106, 2012.

[3] Woodward, J. G., J. Acoust. Soc. Am. Vol 25, pp. 147151, 1953.

[4] Yabuno, H., Higashino, K., Kuroda, M., and Yamamoto, Y.: Self-excited vibrational viscometer for high-viscosity sensing. Journal of Applied Physics. Vol 116, 124305, 2014.

[5] Yabuno, H., Kuroda M., Someya, T., Nishimura, K., Hayashi, K., Ashida, K.: Japanese Journal of Applied Physics. Vol 50, 076601, 2011.

[6] M. Spletzer, A. Raman, A. Q. Wu, X. Xu, and R. Reifenberger, Appl. Phys. Lett., 88: 254102, 2006.

[7] H. Yabuno, Y. Seo, and M. Kuroda, Appl. Phys. Lett., 103: 063104, 2013.

[8] D. Endo, H. Yabuno, K. Higashino, Y. Yamamoto, and S. Matsumoto, Appl. Phys. Lett., 106: 223105, 2015.

TAILORING NONLINEAR DYNAMICS OF MICROBEAM RESONATORS WITH ELECTROSTATIC ACTUATION

Jakob S. Jensen[*1], Suguang Dou[1], and Steven W. Shaw[2,3]

[1]*Dept. of Elec. Eng., Technical University of Denmark, Kgs. Lyngby, Denmark*
[2]*Dept. of Mech. and Aerospace Eng., Florida Institute of Technology, Melbourne, Florida, USA*
[3]*Depts. of Mech. Eng. and Phys. and Astronomy, Michigan State University, East Lansing, Michigan, USA*

<u>*Summary*</u> We have developed an efficient shape optimization procedure for tailoring the nonlinear dynamic performance of microbeam resonators with electrostatic excitation. By relatively simple modifications of the cross-sectional dimensions along the length of the beam we demonstrate a considerable degree of control over the characteristic cubic nonlinear coefficient, allowing e.g. for extending the linear range of operation for resonant MEMS devices, which is important for improving signal-to-noise and other performance metrics.

INTRODUCTION

Recently, we demonstrated in a numerical study [1] the possibility to significantly alter the nonlinear dynamic behavior of beams and frames by employing shape optimization of the cross-sectional beam dimensions based on direct finite element calculations of the cubic nonlinear coefficient. This was later supported by experimental observations for microbeams for MEMS applications [2]. Both an increase of more than a factor 3 and a decrease of almost a factor 3 in the characteristic cubic nonlinear coefficient was demonstrated for beams with optimized height profiles.

In the present paper the design procedure is extended to cover electrostatic excitation which is of major relevance for MEMS applications. Furthermore, it introduces an additional nonlinearity in the problem due to the electrostatic force that depends on the transverse displacements. In addition to the added complexity in modelling, the extra nonlinearity offers increased possibility for tailoring the behavior since two nonlinear effects counteract: the structural hardening nonlinearity (due to midplane stretching) and the electrostatic nonlinearity which is softening. Examples of shape optimization of electrostatically actuated microbeams have recently appeared (eg. [3]), however, with focus on control of pull-in voltage and stability. To the authors' best knowledge we here present the first study on structural optimization with the aim to control the nonlinear dynamics of electrostatically actuated microbeams.

COMPUTATIONAL MODEL

The basis for the optimization procedure is a model of a clamped-clamped beam including nonlinear effects from midplane stretching and from electrostatic actuation caused by a symmetric set of fixed actuators located at distance d from the undeformed beam midplane (Figure 1 left). The basic beam equation with a variable beam height $h = h(x)$ reads:

$$\rho h b \ddot{w} + \frac{Eb}{12}(h^3 w'')'' - \frac{Eb}{2L}w'' \int_0^L h(w')^2 dx = \frac{\varepsilon b V_{\mathrm{DC}}^2}{2}\Big(\frac{1}{(d-w-\frac{h}{2})^2} - \frac{1}{(d+w-\frac{h}{2})^2}\Big) \tag{1}$$

here, w is the transverse beam displacement, ρ is the mass density, E is Young's modulus, b is the out-of-plane thickness, L is the beam length, ε is the permittivity of air and V_{DC} is the constant DC voltage applied to both fixed electrodes (the time-dependent actuation part is here omitted). The r.h.s. represents a simplification of the electrostatic actuation force but has
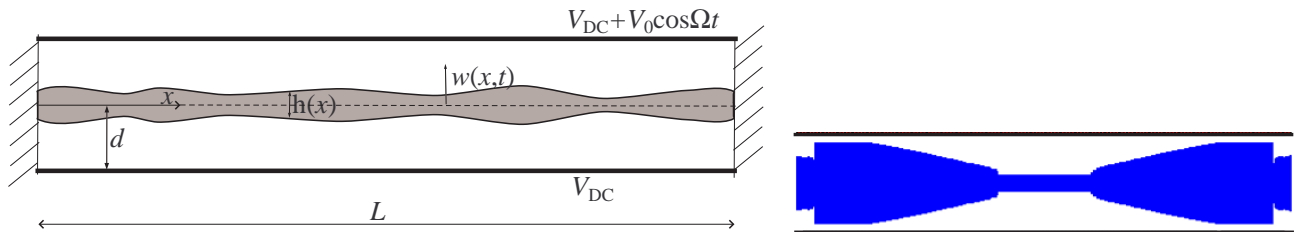
Figure 1: Left: Microbeam with variable height $h(x)$ with two fixed electrodes on each side at the nominal distance of d from the beam centerline. Deflections of the beam are given as $w(x,t)$. Right: Example of optimized beam profile.

*Corresponding author. Email: json@elektro.dtu.dk

recently been experimentally supported for a similar configuration [5]. The model is discretized using Bernoulii-Euler beam finite elements as outlined in [1].

As the first step in the analysis the corresponding linear FE eigenvalue problem is solved and based on the fundamental linear mode $\mathbf{\Phi}_1$ we directly compute the cubic nonlinear coefficient using normal forms [1, 4] as

$$\alpha = \sum_{e=1}^{ne} \frac{Ebh_e}{8l}(\mathbf{\Phi}_1^T\mathbf{K}_g\mathbf{\Phi}_1)^2 - \sum_{e=1}^{ne} \frac{\varepsilon V_{dc}^2 b}{d_e^5} \int_0^l (\mathbf{N}^T\mathbf{\Phi}_1)^4 dx \tag{2}$$

where $\mathbf{N}^T$ is the shape function matrix and $\mathbf{K}_g$ the geometric stiffness matrix.

PARAMETRIZATION AND OPTIMIZATION PROCEDURE

We choose the height of each beam element to be our design variables, i.e. we set

$$h_{\min} < h_e < h_{\min} \tag{3}$$

where the minimum and maximum values of the beam height are chosen from fabrication tolerance (min) and minimum allowable distance to the electrodes (max).

The optimization problem is now defined as a minimization problem wrt. the cubic nonlinear coefficient:

$$\begin{aligned} \min_{\mathbf{h}} : \quad & \alpha(h_e) \\ \text{s.t.} \quad & \omega_1(h_e) \leq \omega^* \\ & f(h_e, \mathbf{\Phi}_1(h_e)) \geq f^* \end{aligned} \tag{4}$$

where we have introduced constraints in form of the maximum value of the first eigenfrequency ω^* and on the minimum value of the modal excitation force f^*. To solve the optimization problem we apply an iterative gradient-based approach with analytically computed sensitivities and use the robust mathematical programming tool MMA [6] to obtain design updates.

RESULTS

A preliminary beam design is shown in Figure 1 (right). The initial configuration has a softening nonlinearity due to the dominating electrostatic effect. However, by modifying the shape of the beam the magnitude of the nonlinear coefficient has been reduced by a factor of approximately 5. At the same time both the fundamental eigenfrequency as well as the modal excitation force is unchanged compared to the initial straight beam.

CONCLUSION

We have demonstrated that it is possible, by simple variations of the beam cross-sectional geometry along the beam, to significantly reduce out the effective nonlinearity while keeping the actuation level and linear dynamic unchanged. The results shows promising perspectives for enhancing the linear operation range for electrostatically actuated microbeams and also more complex microsized structures and devices. Further work include modifying also the shape of the electrostatic actuators as well as experimental validation of the results.

References

[1] Dou S., Strachan B.S., Shaw S.W., Jensen J.S.: Structural Optimization for Nonlinear Dynamic Response. Phil Trans R Soc A 373:20140408, 2015.

[2] Li L.L., Polunin P.M., Dou S., Shoshani O., Strachan B.S., Jensen J.S., Shaw S.W., Turner K.L.: Systematic Design of MEMS Resonators for Optimal Nonlinear Dynamic Response. Abstract for Hilton Head Conference, 2016.

[3] Trivedi R.R., Bhushan A., Joglekar M.M., Pawaskar D.N., Shimpi R.P.: Enhancement of Static and Dynamic Travel Range of Electrostatically Actuated Microbeams using Hybrid Simulated Annealing. Int J Mech Sci 98:93-110, 2015.

[4] Touze C., Vidrascu M., Chapelle D.: Direct finite element computation of non-linear modal coupling coefficients for reduced-order shell models. Comp Mech 54:567-580, 2014.

[5] Hajjaj A.Z., Ramini A., Younis M.I.: Experimental and Analytical Study of Highly Tunable Electrostatically Actuated Resonant Beams. J Micromech Microeng 25:125015, 2015.

[6] Svanberg K.: The method of moving asymptotes a new method for structural. Int J Num Meth Engng 24:359373, 1987.

EVIDENCE OF AN INTERMITTENCY ROUTE TO CHOAS IN ELECTROSTATIC MEMS

Sangtak Park [1a)], Mahmoud Khater [2], Beichen Li [3], Majed Al-Ghamdi [1],
Ahmed Abdel Aziz [4], Eihab M. Abdel-Rahman [1], Ali H. Nayfeh [5], Mustafa Yavuz [3]
[1]Systems Design Engineering, [3]Mechanical and Mechatronics Engineering, [4]Electrical and Computer Engineering,
University of Waterloo, Waterloo, Ontario, Canada
[2]Mechanical Engineering, KFUPM, Dhahran, Saudi Arabia
[5]Engineering Science and Mechanics, Virginia Tech, Blacksburg, VA, USA

Summary We provide experimental evidence for an intermittency route to chaos in an electrostatic MEMS actuator. To our knowledge, this is the first time that an intermittency route to chaos has been observed in an electrostatic MEMS actuator. We present our experiment results obtained by a laser vibrometer that measures the displacement and the velocity of the actuator in both of the time and frequency domains.

INTRODUCTION

Chaos has, thus far, been experimentally observed in the response of three MEMS/NEMS devices: a non-interdigitated comb actuator [1, 2], a nano-resonator [3], and an RF MEMS switch [4]. Chaos occurs along different routes including a homoclinic tangle [1, 2], multi-frequency excitation following the Ruelle-Takens criteria [3], or a cascade of period-doubling bifurcations [4]. Intermittency is another route to chaos, having not been experimentally observed to date in electrostatic MEMS devices.

This article reports on experimental observations for an intermittency-type III route to chaos subsequent to a subcritical period-doubling bifurcation in the motions of an electrostatic MEMS actuator.

EXPERIMENT
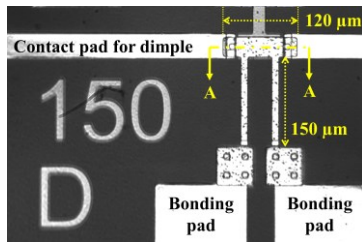
FIG. 1. Top view of the actuator
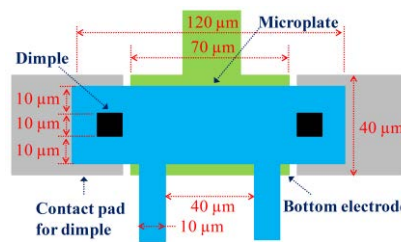
FIG. 2. Top view of the micro-plate
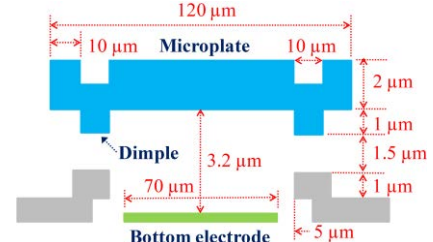
FIG. 3. A cross-sectional view

The electrostatic actuator is made of a micro-plate supported by two micro-cantilever beams presented in Fig. 1, and it is fabricated out of an electroplated gold structural layer in the UW-MEMS process [5]. A bottom electrode below the micro-plate provides the actuation voltage

$$V(t) = V_{dc} + V_{ac} \cos(2\pi f t) \tag{1}$$

Two dimples are fabricated onto both sides of the micro-plate, in Fig. 3, so as to act as stoppers in case of pull-in in conjunction with two contact pads in Fig. 2. The actuator is held close to its pull-in point by applying a DC bias voltage close to but less than the pull-in voltage that is measured to be 12 V. It is actuated by a DC biased AC signal throughout the experiments reported below. A laser vibrometer is used to measure the displacement and velocity of the micro-plate in both of the time and frequency domains. The screenshot in the upper panel of Fig. 4 shows the actuator superimposed with a grid of the measurement points used by the vibrometer.

RESULTS

The lower panel in Fig. 4 shows the frequency spectrum of the micro-plate velocity averaged over of all 85 measurement grid points, when excited by the sinusoidal signal: V_{dc} = 8.0 V, V_{pp} = 1 V at f = 10 kHz. Period-doubling is indicated in Fig. 5-(a) by the peaks appearing at half of the excitation frequency and its integer multiples. However, the measured velocity and displacement signals of the micro-plate centre point in the time domain, Fig. 5-(b), show aperiodic responses characterized by bursts occurring at irregular periods, typical of intermittent behaviours. The bursts occur over long time intervals; for example, three bursts are observed in Fig. 5-(b) within 40 seconds.

[a)] Corresponding author. Email: sangtak@uwaterloo.ca**.**
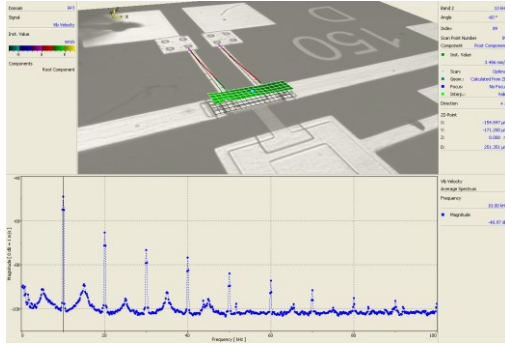
FIG. 4. Screenshot of a vibrometer interface with the actuator post-processed with the measured velocity (top panel) and its FFT (bottom panel), when actuated by the signal, 8 V_{dc} and 1 V_{pp} at 10 kHz. Peaks observed at $\frac{nf}{2}$ indicate a period-doubling bifurcation.
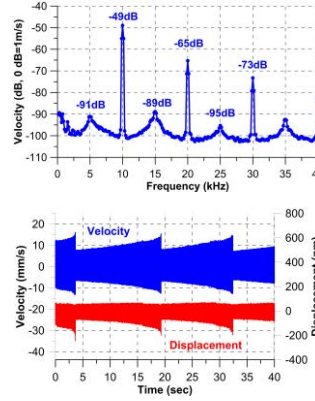
FIG. 5-(a) Measured velocity in the frequency domain indicates a period-doubling (top), (b) Measured velocity and displacement in the time domain show evidence of intermittency.
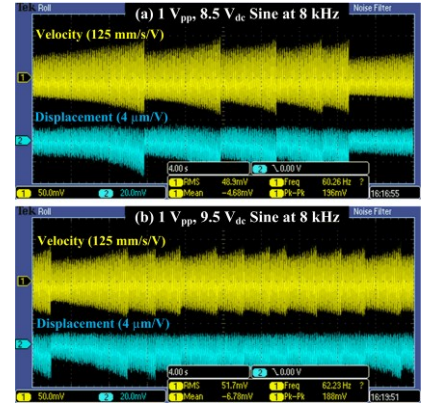
FIG. 6. Bursts occur more frequently as the intermittency approaches towards fully developed chaos with the DC bias voltage increasing from (a) V_{dc} = 8.5V to (b) V_{dc} = 9.5V.

Intermittency was observed over a wide frequency range, f = [8-10] kHz, and for the waveforms characterized by a combination of large DC bias 8 V and small AC 1 V_{pp}. Furthermore, as the DC bias voltage increases from V_{dc} = 8.5 V to V_{dc} = 9.5 V, while the AC excitation amplitude and frequency are held constant at V_{pp} = 1 V and 8 kHz in Fig. 6, we found that the bursts occurred more frequently and took less time to develop. This is also a typical characteristic of intermittent behaviours, as it approaches toward fully developed chaos with bursts interrupting shorter intervals of almost periodic (laminar) response more frequently.
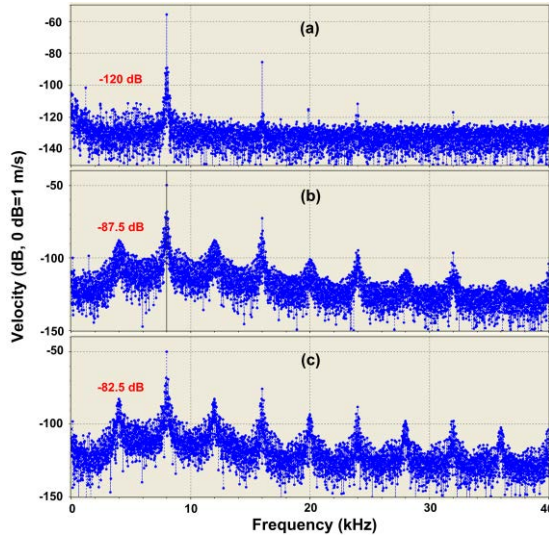
FIG. 7. Peaks in the measured velocity appear at $\frac{nf}{2}$ and grow, as laminar flow develops towards a burst; a sinusoidal waveform is used as an excitation signal, V_{dc} = 8.5 V, V_{pp} = 1 V at f = 8 kHz.

To examine the mechanism driving the intermittency, we present the FFT of the measured velocity in Fig. 7 for three subsequent intervals during a laminar build-up to a burst similar to those shown in Fig. 6. As the laminar interval develops, the power in the peaks at integer multiples $\frac{f}{2}$ increases from -120 dB to -82.5 dB, indicating unstable period-doubled oscillations leading to pull-in (the burst). Upon pull-in, the dimples come into contact and the actuator rebounds back to flight (i.e., it is re-injected into the basin of safe motions) to start another laminar interval.

CONCLUSIONS

In this experiment, we observe the period-doubling and the intermittency route to chaos in electrostatic MEMS actuators for the first time, while exciting the electrostatic actuator with a simple harmonic signal with a DC bias. Due to the aperiodic nature and low frequency components of the intermittency, we observe the intermittency mainly in the time domain at a slow time scale. However, we observe the period-doubling bifurcation mainly in the frequency domain at a fast time scale because the period-doubling bifurcation cannot be distinguished from the measured velocity signal in the time domain.

References

[1] Y. C. Wang, S. G. Adams, J. S. Thorp, N. C. MacDonald, P. Hartwell, and F. Bertsch, IEEE transactions on circuits and systems. 1, Fundamental theory and applications 45, 1013, 1998.

[2] B. E. DeMartini, H. E. Butterfield, J. Moehlis, and K. L. Turner, Journal of Microelectromechanical Systems, 16, 1314, 2007.

[3] D. V. Scheible, A. Erbe, R. H. Blick, and G. Corso, Applied physics letters, 81, 1884, 2002.

[4] J. Stulemeijer, R. Herfst, and J. Bielen, IEEE 22nd International Conference on in Micro Electro Mechanical Systems, pp. 920-922, 2009.

[5] K. Y. Chan, M. Daneshmand, R. R. Mansour, and R. Ramer, IEEE Transactions on Microwave Theory and Techniques, 57, 1612, 2009.

MULTISTABILITY OF A CANTILEVER MEMS/NEMS CAPACITIVE SWITCH MODEL

Devin Kalafut,* Anil Bajaj, and Arvind Raman

School of Mechanical Engineering, Purdue University, West Lafayette, Indiana, USA

Summary   In order to fully understand nonlinear dynamics of cantilever beam micro- and nanoelectromechanical capacitive switches, thorough knowledge of static behavior is vital. Presented herein is the analysis for equilibrium positions of a generalization of such devices. The representative system model employs multiphysics features based on Euler-Bernoulli beam theory, parallel plate capacitance for electrostatics, and a form of surface interaction with both attractive and repulsive regions. The geometry, material properties, and surface features of a device are condensed into just a few dimensionless quantities, creating a parameter space of low enough dimensionality to provide accessible representations of all system equilibria within physically relevant ranges. The results offer insight into the breadth of obtainable multistability as well as sensitivity to parametric uncertainty, which is crucial for informing studies on switching dynamics and various device performance metrics.

INTRODUCTION

Micro- and nanoelectromechanical systems (MEMS/NEMS) based switches are of great interest in low-power, portable electronics and RF telecommunications devices due to their favorable operating voltages, low-insertion loss, switching time, and size [1]. Mathematical models of electrostatically actuated MEMS and NEMS switches have been key to understanding the dynamic behavior of such systems [2]. Toward this end, a first goal is to explore the eventual states of an electrostatically actuated cantilever and understand the connection between the various physical properties and the occurrence of bi- and tristability in these switches.

Many past works have focused on multistability without explicit inclusion of surface forces [3, 4, 5]. Broadly speaking, these tend to be interested in the relationship between the electrostatic forces and equilibrium positions. Conversely, varius studies have analyzed surface forces relevant to MEMS/NEMS switches without directly extending results to the breadth of multistability that may be present [6, 7]. Finally, there are a couple examples of research groups assessing both concepts for specific purposes. Stulemeijer, Bielen, Steeneken, and van den Berg analytically and experimentally identified equilibrium positions of a rectangular plate capacitive MEMS switch suspended by for spring-like supports[8], while Ouakad and Younis looked specifically at the influence of capillary forces on instabilities of a cantilever beam [9]. A void exists in discussing the basic relationship between surface forces and equilibrium positions of a cantilever capacitive switch in its most simple representation.

MODEL FORMULATION

Cantilever MEMS/NEMS capacitive switches are manufactured with a small air gap between the beam and the dielectric-coated substrate, as shown in Fig. 1 (a). Device operation is controlled by the electric potential applied between the metallic beam and underlying electrode beneath the dielectric. When a high enough potential is applied for a given configuration, it is possible for the deflecting beam to come into contact with the dielectric. Thus, surface forces between the two materials play a key role in determining final resting states and shapes of the cantilever, and, in turn, the overall capacitance of the component.

For each contributing multiphysics interaction in the model, a simple formulation is chosen to capture the most basic behavior relevant to the analysis. Bernoulli-Euler beam theory is assumed to be sufficient for deformations, as is parallel plate capacitance for the electrostatic actuation. For surface interactions, a model based on the Lennard-Jones potential is incorporated. This is physically appropriate when assuming flat surfaces approaching contact, but could also be extended as a fit to imperfect scenarios. When combined, nondimensionalized, and assessed at rest, the resulting form studied is shown in Eqn. (1). The left side is the remaining static term from beam theory, and the right side terms are from electrostatics and surface interactions, in order, where all symbols are dimensionless. Here, w is related to the deflection of the beam at a point x along the beam length, as in Fig. 1 (a), while the parameters V, g, H, and z_0 come from applied voltage, dielectric effects, surface force strength, and zero-pressure gap, respectively. It is helpful to note that the nondimensionalization of w, g, and z_0 are all done by simply dividing by the manufactured air gap, but that of V and H are more intricate, involving beam stiffness, geometry, and material properties.

$$\frac{\partial^4 w}{\partial x^4} = \frac{V^2}{(1+g-w)^2} - \frac{H}{(1-w)^3}\left[\left(\frac{z_0}{1-w}\right)^6 - 1\right]$$

(1)

*Corresponding author. Email: kalafut@purdue.edu
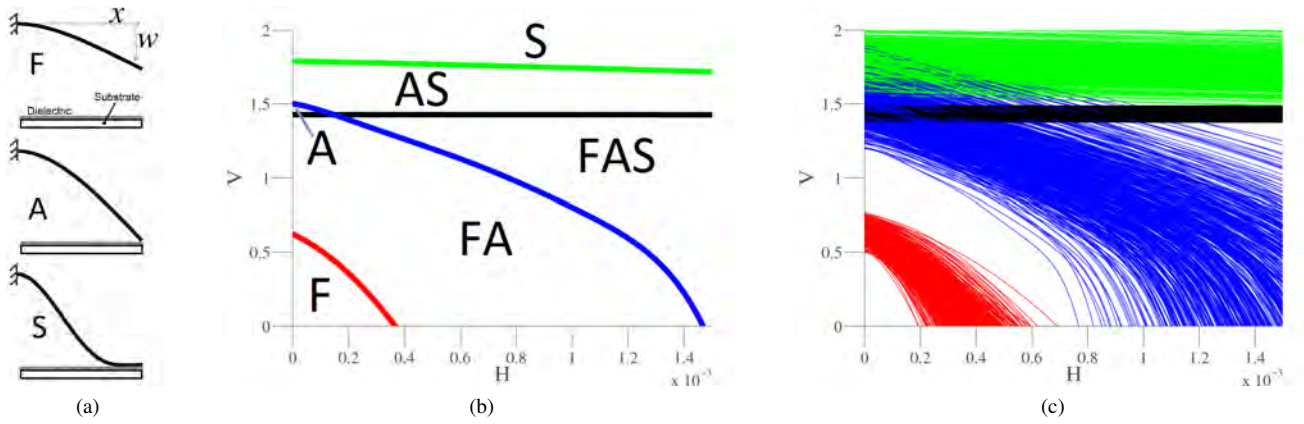
Figure 1: (a) Equilibrium shapes: floating (top), arc-shaped (middle), s-shaped (bottom). (b) Multistability diagram for $g = 0.0.066667$, $z_0 = 0.005$. (c) Parameter uncertainty with nominal values $g = 0.0.066667$, $z_0 = 0.005$.

ANALYSIS

Investigation methodology is composed of 1-parameter continuation in V of nonlinear Eqn. (1), followed by successive distillations of key outcomes toward a final depiction of multistability behavior. Continuation itself is implemented in the AUTO bifurcation software using the boundary value problem structure, while stability is inferred from direct time integration about equilibrium solutions. These solution branches can be identified as three different static equilibrium shapes: floating (freestanding, no contact), arc-shaped (point-contact), and s-shaped (line-contact), as depicted in Fig. 1 (a). Furthermore, they can be collected into various multistability categories by determining locations of turning points, as shown for one set of dimensionless parameters in Fig. 1 (b). While slices in parameter space reveal underlying behavior, the parametric sensitivity of the multistability regions is investigated using a Monte Carlo scheme. Per chosen physically-reasonable parameter distributions, the outcome provides indication of high sensitivity to the given parametric uncertainty, shown in Fig. 1 (c).

Results are relevant to the design and performance of cantilever capacitive switches, as their intended operation between capacitive states depends on what configurations are possible. Knowledge of anticipated mono-, bi-, and tristability is critical to investigations on switching dynamics, while the simplicity of the proposed model serves to inform a basic understanding of the relationship between surface interactions and multistability in the context of an ideal case.

ACKNOWLEDGMENT

References

[1] Gabriel M. Rebeiz, 2003. *RF MEMS : theory, design, and technology*. JWiley, Hoboken, NJ.

[2] Abdel-Rahman, E. M., Younis, M. I., and Nayfeh, A. H., 2002. "Characterization of the mechanical behavior of an electrically actuated microbeam". *Journal of Micromechanics and Microengineering,* *12*(6), Nov., p. 759.

[3] Gorthi, S., Mohanty, A., and Chatterjee, A., 2006. "Cantilever beam electrostatic MEMS actuators beyond pull-in". *Journal of Micromechanics and Microengineering,* *16*(9), Sept., pp. 1800–1810.

[4] Snow, M. G., and Bajaj, A. K., 2010. "Comprehensive Reduced-Order Models of Electrostatically Actuated MEMS Switches and Their Dynamics Including Impact and Bounce". pp. 579–588.

[5] Krylov, S., 2007. "Lyapunov exponents as a criterion for the dynamic pull-in instability of electrostatically actuated microstructures". *International Journal of Non-Linear Mechanics,* *42*(4), May, pp. 626–642.

[6] Kim, H., Shaik, N. H., Xu, X., Raman, A., and Strachan, A., 2013. "Multiscale contact mechanics model for RFMEMS switches with quantified uncertainties". *Modelling and Simulation in Materials Science and Engineering,* *21*(8), Dec., p. 085002.

[7] Knapp, J., and de Boer, M., 2002. "Mechanics of microcantilever beams subject to combined electrostatic and adhesive forces". *Journal of Microelectromechanical Systems,* *11*(6), Dec., pp. 754–764.

[8] Stulemeijer, J., Bielen, J., Steeneken, P., and van den Berg, J., 2009. "Numerical Path Following as an Analysis Method for Electrostatic MEMS". *Journal of Microelectromechanical Systems,* *18*(2), Apr., pp. 488–499.

[9] Ouakad, H. M., and Younis, M. I., 2009. "Modeling and Simulations of Collapse Instabilities of Microbeams due to Capillary Forces". *MATHEMATICAL PROBLEMS IN ENGINEERING.*

NON-LINEAR MODES OF VIBRATION OF CNTs

Pedro Ribeiro[1 a] & Olivier Thomas[2]

[1] *DEMec/INEGI, Faculdade de Engenharia da Universidade do Porto, Porto, Portugal*
[2]*Arts et Métiers Paris Tech, LSIS UMR CNRS 7296, Lille, France*

<u>*Summary*</u> The non-linear modes of vibration of carbon nanotubes are investigated. For that purpose, a *p* version finite element is implemented; it takes into account geometrically non-linear and non-local effects. For the first time in this problem, the free, steady-state, oscillations - which occur when the conservative system is vibrating in one of its modes of vibration – are not enforced to be harmonic by the solution procedure. Furthermore, not only the first, but also higher order modes are analysed. Modal interactions are found and it is shown that they are fundamental in some oscillations. Non-local effects are known to be influential in carbon nanotubes of very small length. However, it is demonstrated here that, because of modal interactions, non-local effects influence the non-linear oscillations of CNTs with longer lengths than what was previously believed.

INTRODUCTION

Vibrating carbon nanotubes (CNT) can be used as sensors, based on changes in the natural frequency or on alterations of the response to excitations [1]. If CNTs experience oscillations with amplitudes above about 10%-20% of their very small diameter, one should take geometrical non-linear effects into account. Furthermore, one can take advantage of geometrical non-linearity to enhance the properties of nanodevices [2, 3]. Studying the non-linear modes of vibration of CNTs is important, because these modes define essential vibratory properties.

This communication is devoted to the study of the modes of vibration of CNTs oscillating in the geometrically non-linear regime. To carry out the study, a beam *p*-version finite element for CNTs is implemented. In order to take the small scale effects into account, the non-local elasticity theory of Eringen is followed [4,5]. The equations of motion are solved by the harmonic balance method (HBM), in conjunction with an arc-length continuation method. For the first time in this problem, several harmonics are considered in the HBM, allowing us to describe modal interactions on CNTs, and to find previously undetected impacts of non-local effects on the non-linear modes of vibration of CNTs.

FORMULATION OUTLINE

In a non-local Euler-Bernoulli beam, the constitutive equation is [5]:

$$\sigma_x(x,y,t) - \mu \frac{\partial^2 \sigma_x(x,y,t)}{\partial x^2} = E \varepsilon_x(x,y,t) \tag{1}$$

where $\sigma_x(x, t)$ and $\varepsilon_x(x, t)$ represent, respectively, the axial stress and the axial strain, E the Young modulus and μ a non-local parameter. The non-local parameter is defined as $\mu=(e_0 a)^2$, with a representing an internal characteristic length and e_0 a constant that depends on the material; it is determined via comparisons with experiments or with molecular mechanics/dynamics simulations [4-6].

The geometrically non-linear relation between the axial strain and the displacement components $u(x,t)$ and $v(x,t)$ is:

$$\varepsilon_x(x,y,t) = \frac{\partial u(x,t)}{\partial x} + \frac{1}{2}\left(\frac{\partial v(x,t)}{\partial x}\right)^2 - y\frac{\partial^2 v(x,t)}{\partial x^2}. \tag{2}$$

In this work, a *p*-version finite element method (*p*FEM) approach is followed; this is characterized by the fact that, when more detailed FE models are required, the number of shape functions and generalized coordinates in the finite elements is increased, but the mesh is not altered. The *p*FEM equations of motion have the following form

$$\left[\mathbf{M}_v + \mathbf{M}_{\mu v}\right]\ddot{\mathbf{q}}_v(t) + \mathbf{K}_v^0 \mathbf{q}_v(t) - \left[2\mathbf{K}_{uv}^{1\ T}\left(\mathbf{q}_v(t)\right) + \mathbf{K}_{\mu uv}^1\left(\mathbf{q}_v(t)\right)\right]\mathbf{K}_u^{0\ -1}\mathbf{K}_{uv}^1\left(\mathbf{q}_v(t)\right)\mathbf{q}_v(t)$$
$$+ \left[\mathbf{K}_v^2\left(\mathbf{q}_v(t)\right) + \mathbf{K}_{\mu v}^2\left(\mathbf{q}_v(t)\right)\right]\mathbf{q}_v(t) = \mathbf{0}. \tag{3}$$

There are two mass matrices in equation (3), $\mathbf{M}_v$ and $\mathbf{M}_{\mu v}$; the former is the local mass matrix, the latter represents the effects of transverse inertia on the non-local part of the bending moment. In the stiffness matrices $\mathbf{K}$, numbers in superscript specify the dependence of the matrices on the transverse generalised displacements $\mathbf{q}_v(t)$ in the following way: number 0 indicates that the matrix is constant; number 1 indicates that the matrix is a linear function of $\mathbf{q}_v(t)$ and number 2 indicates a quadratic dependence. The letters in subscript identify the displacement components or non-local effects that are related with the matrix. The influence of non-local effects on the stiffness of CNTs only transpires when the geometrical non-linearity is taken into account.

We are specifically interested in periodic solutions of equations of motion (3) and, therefore, the generalised displacements $\mathbf{q}_v(t)$ can be written as a Fourier series. Applying the harmonic balance method, a system of non-linear algebraic equations is obtained. This system is solved by an arc-length continuation method.

---

a) Corresponding author. Email: pmleal@fe.up.pt**.**

SAMPLE RESULTS

Several tests were carried out, of which only a small ample is given in this short text. Figure 1(a) shows the variation of the amplitude of the first harmonic with the vibration frequency when CNTs oscillate in their first mode of vibration; Figure 1(b) when CNTs oscillates in the second mode of vibration. The local and one non-local case are compared. The non-dimensional non-local parameter $\zeta = \frac{e_0 a}{L}$, where L represents the length of the CNT, is equal to 0.04. The horizontal axes provides the natural frequency of vibration in the non-linear regime, represented by ω, divided by the natural frequency of vibration in the linear regime, represented by ω_n.

Analysing Figure 1(a), one sees that the influence of non-local effects on the main branch of the backbone curve of the first mode of vibration is not large: it changes slightly the hardening spring effect, showing that non-locality has a stiffening effect at larger displacement amplitudes. Both when $\zeta = 0$ and $\zeta = 0.04$, a 1:5 internal resonance due to an interaction between the first and third modes of vibration is found. But the non-dimensional frequency and vibration amplitude at which this internal resonance occurs is strongly affected by the non-locality. Furthermore, close to $\omega/\omega_{\ell 1} = 1.84$ a second bifurcation occurs if $\zeta = 0.04$. It is due to the excitation of the 4th mode of vibration and higher harmonics, where the fifth harmonic outstands. This bifurcation is not visible if non-local effects are neglected.

Proceeding to the second mode, Figure 1 (b), the backbone curves are initially similar, with non-local effects inducing a small increase in hardening. However, the non-local effects have a major influence on bifurcations. Plots of shapes assumed by the CNTs along a vibration cycle, as well as plots of time histories and projections of trajectories on phase planes – not shown here due to space limitations – complete the demonstration that, due to bifurcations and modal couplings, non-local effects can have an influence on the dynamics of CNTs that is stronger that what has been previously found.

(a) First non-linear mode and bifurcations   (b) Second non-linear mode and bifurcations
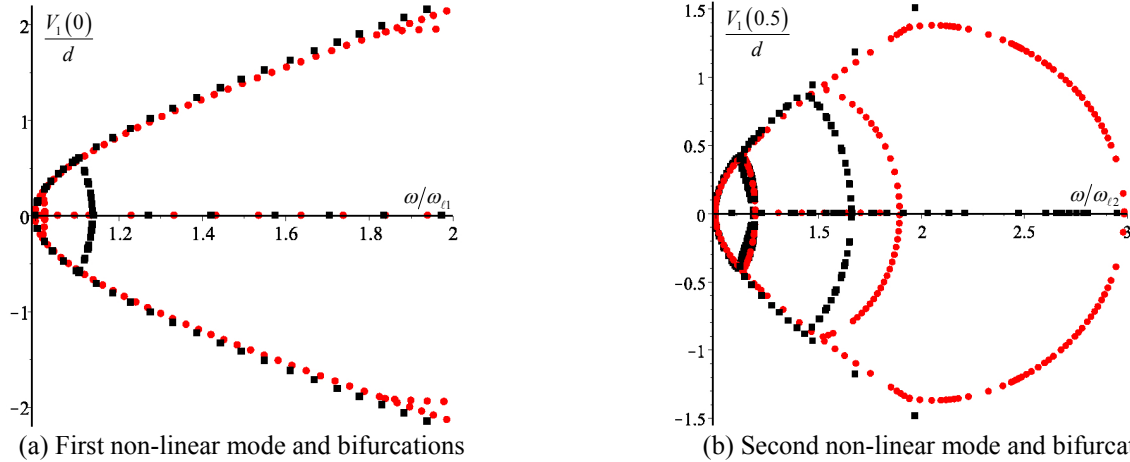
Figure 1. Amplitudes of first harmonic of the transverse vibration displacement of CNT, when $\zeta = 0$ ■ and when $\zeta = 0.04$ ●.

CONCLUDING COMMENTS

A pFEM, non-local, formulation is applied to investigate the modes of vibration of CNTs vibrating in the geometrical non-linear regime. It is shown that the modes of vibration of non-local CNTs can be very different from the modes of local CNTs, chiefly due to the alterations that non-local effects cause on internal resonances promoted by the non-linearity. Internal resonances result in rich vibrations, with contributions of more than one harmonic and with significant variation of the shape assumed along a vibration period. It is also found that, because of internal resonances, the non-local effects are still noticeable at lengths that are longer than what has been previously detected.

References

[1] Li, C., Thostenson, E.T., Chou, T.W.: Sensors and actuators based on carbon nanotubes and their composites: A review. Compos. Sci. Technol. **68**(6): 1227-1249, 2008.
[2] Karabalin, R.B., Masmanidis, S.C., Roukes, M.L.: Efficient parametric amplification in high and very high frequency piezoelectric nanoelectromechanical systems. Appl. Phys. Lett. **97**(18): 183101, 2010.
[3] Lazarus, A., Thomas, O., Deü, J.F.: Finite element reduced order models for nonlinear vibrations of piezoelectric layered beams with applications to NEMS. Finite Elem. Anal. Des. **49**(1): 35-51, 2012.
[4] Eringen, A.: On differential equations of nonlocal elasticity and solutions of screw dislocation and surface waves. J. Appl. Phys. **54**: 8, 1983.
[5] Simsek, M.: Large amplitude free vibration of nanobeams with various boundary conditions based on the nonlocal elasticity theory. Compos: Part B **56** 621–628 (2014).
[6] Arash, B., Wang, Q.: A review on the application of nonlocal elastic models in modeling of carbon nanotubes and graphenes. Comput. Mater. Sci **51**, 303-313 (2012).

SYMMETRY-BREAKING IN A THREE-NANOMECHANICAL-RESONATOR ARRAY FOR MASS DETECTION

C. GRENAT[*1], V-N. NGUYEN[1], S. BAGUET [†1], R. DUFOUR [‡1], and C-H. LAMARQUE [§2]

[1]*Université de Lyon, CNRS, INSA-Lyon, LaMCoS UMR5259, F-69621, Villeurbanne, France*
[2]*Université de Lyon, CNRS, ENTPE, LTDS UMR5513, F-69518, Vaulx-en-Velin, France*

Summary Due to their accuracy and their size, M/NEMS resonant sensors are present in a lot of domain such as automotive, aerospace and biotechnology. They are used as accelerometers, gyroscopes for inertial navigation and also mass detection which is the target application of this investigation. The literature essentially focus on improving the sensitivity of a single resonator. Mass sensors are now able to detect a mass around a few zeptograms. This work presents a three-nanomechanical-resonator array analysis. The original contribution lies in the use of the array symmetry-breaking for mass detection.

ARRAY OF THREE NANOMECHANICAL RESONATORS

An array of three clamped-clamped beams is considered, as sketched in Fig. 1. All beams are assumed to have identical dimensions (length l, width b, height h, moment of inertia I, gap g between two adjacent beams) and identical material properties (Young's modulus E and material density ρ). Each beam is subjected to the electrostatic forces due to its two adjacent beams. The two beams at both ends of the array (beam 0 and $n + 1$) are clamped and non-deformable.
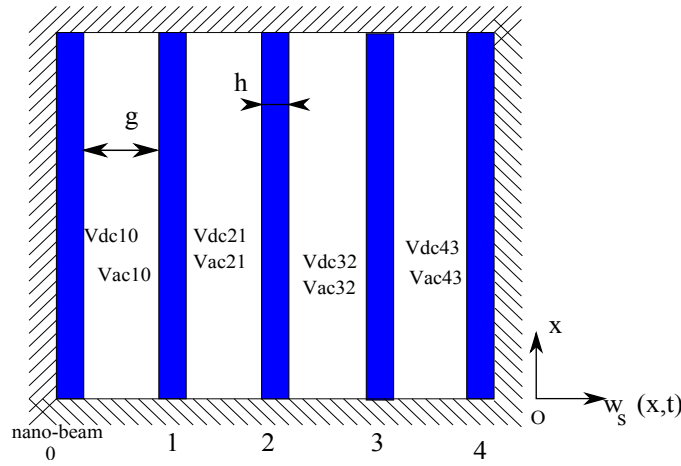
Figure 1: Array of three clamped-clamped M/NEMS beams.

Let $\tilde{w}_s$ be the lateral displacement in the plane $x - z$ along the z-axis of the s-th beam and $V_{s,s+1} = Vdc_{s,s+1} + Vac_{s,s+1}\cos(\Omega t)$ the voltage between s-th and s+1-th beams. The s-th resonator motion equation can be written as [1, 2]:

$$EI\frac{\partial^4 \tilde{w}_s(\tilde{x},\tilde{t})}{\partial \tilde{x}^4} + \rho bh\frac{\partial^2 \tilde{w}_s(\tilde{x},\tilde{t})}{\partial \tilde{t}^2} - \left[\tilde{N} + \frac{Ebh}{2l}\int_0^l \left(\frac{\partial \tilde{w}_s(\tilde{x},\tilde{t})}{\partial \tilde{x}}\right)^2 \mathrm{d}\tilde{x}\right]\frac{\partial^2 \tilde{w}_s(\tilde{x},\tilde{t})}{\partial \tilde{x}^2}$$
$$= \frac{\epsilon_0 bC_n}{2}\left[\frac{V_{s,s+1}^2}{\left(g + \tilde{w}_{s+1} - \tilde{w}_s\right)^2} - \frac{V_{s-1,s}^2}{\left(g + \tilde{w}_s - \tilde{w}_{s-1}\right)^2}\right] \quad (1)$$

where $s = 1,..,3$ and $\tilde{N}_s$ is the axial force acting on the s-th beam and resulting from an externally applied load or from residual manufacturing stress. ϵ_0, C_N are the dielectric constant and fringing field coefficient respectively. First and last resonators are clamped, therefore the following conditions apply:

$$\tilde{w}_0(\tilde{x},\tilde{t}) = \tilde{w}_{N+1}(\tilde{x},\tilde{t}) = 0. \quad (2)$$

[*]Email: clement.grenat@insa-lyon.fr
[†]Email: sebastien.baguet@insa-lyon.fr
[‡]Corresponding author. Email: regis.dufour@insa-lyon.fr
[§]Email: claude.lamarque@entpe.fr

By assumption the three identical beams have the same eigenmodes. First, a Galerkin expansion is used to eliminate the spatial dependence of the lateral displacement. Then the electrostatic forces in Eq. (1) are treated by either multiplying by the denominator or either using Taylor series expansions. Then the Harmonic Balance Method associated with the Asymptotic Numerical Method (HBM+ANM) [3] is used to solve Eq. (1). The ANM is preferred to a more conventional Newton- Raphson method because of the robustness of the ANM-based continuation and its ability to follow very complicated solution branches.

MASS DETECTION USING SYMMETRY-BREAKING OF NANOMECHANICAL RESONATOR ARRAYS

In order to use the symmetry-breaking of the resonator array for mass detection, a symmetric configuration is considered, with symmetric voltages as defined in Table 1. The electrostatic forces acting on both sides of the central beam are therefore compensating each others. Consequently, the central resonator will not vibrate. The symmetry-breaking appears when a mass fall on either the first or the third resonator. The symmetry is then broken and the central resonator starts to vibrate. The presence of a mass is thus detected.

Depending on the value of the added mass, different responses are obtained. The corresponding curves are plotted in Fig. 2. The central figure represents the response of the central beam. Without added mass ($m = 0$) the central beam does not vibrate. As soon as a mass is added on the first or the third beam, the symmetry is broken and the vibration amplitude of the central beam is not null anymore and increases with the value of the added mass.

Vdc_{10}	Vac_{10}	Vdc_{21}	Vac_{21}	Vdc_{32}	Vac_{32}	Vdc_{43}	Vac_{43}
0	0	5.3	1	5.3	1	0	0

Table 1: Voltage configuration of the three array beams.
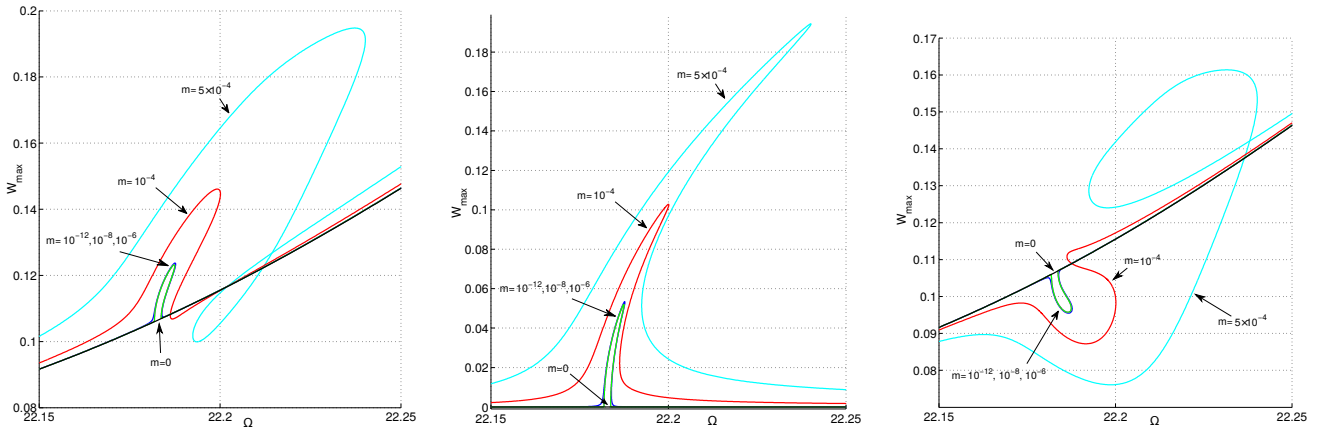
Figure 2: Array of three clamped-clamped M/NEMS beams.

CONCLUSIONS

A new mass detection method using symmetry-breaking of a M/NEMS array has been proposed. This method gives an original way to detect particles and to determine their mass. This work is a first step towards MEMS-based mass spectrometry via the implementation of thousands resonators in parallel.

References

[1] S. Gutschmidt and O. Gottlieb. Nonlinear dynamic behavior of a microbeam array subject to parametric actuation at low, medium and large dc-voltages. Nonlinear Dynamics 67(1):136, 2012.

[2] Van Nghi Nguyen, Sbastien Baguet, Claude-Henri Lamarque, Rgis Dufour: Bifurcation-based micro-/nanoelectromechanical mass detection. Nonlinear Dynamics 79(1):647-662, 2014.

[3] N. Kacem, S. Baguet, S. Hentz, and R. Dufour: Computational and quasi-analytical models for non-linear vibrations of resonant MEMS and NEMS sensors. International Journal of Non-Linear Mechanics 46(3):532-542, 2011.

NONLINEAR IDENTIFICATION OF DAMPING IN LARGE AMPLITUDE VIBRATIONS OF PLATES AND PANELS

Marco Amabili[1,a], Farbod Alijani[2], Giovanni Ferrari[1], Joachim Delannoy[1], Prabakaran Balasubramanian[1]

[1]Department of Mechanical Engineering, McGill University, Montreal, Quebec, Canada
[2]Faculty of Mechanical, Maritime and Materials Engineering, Delft University of Technology, Delft, Netherlands

Summary   A nonlinear identification technique is presented to obtain the damping of isotropic and laminated sandwich rectangular plates and curved panels subjected to harmonic excitation as a function of the vibration amplitude. The response of the structures is approximated by (i) reduced-order models with 10 to 100 degrees of freedom and (ii) a single-degree of freedom Duffing oscillator. The method uses experimental frequency-amplitude data and the least-squares technique to identify parameters and reconstruct frequency-response curves by spanning the excitation frequency in the neighbourhood of the lowest natural frequencies. In order to obtain the experimental data, a sophisticated measuring technique has been used. The results reveal a strongly nonlinear correlation between the damping and the vibration amplitude.

Introduction

A challenging concept in nonlinear system identification is the characterization of damping from experimental data. Dissipation is intrinsically a nonlinear phenomenon. The modal damping assumption is a convenient tool that has been extensively used to model dissipation. However, this model generally does not take into account that damping changes with the vibration amplitude. Different nonlinear damping mechanisms have been proposed, the most common being the quadratic damping [1]. Other forms of nonlinear damping include quadratic and cubic powers of relative velocity [2]. Another damping model that is quite often used is the viscoelastic model [3]. Although there have been numerous studies about nonlinear damping, so far none has discussed the change of damping with the vibration amplitude. Therefore, different from previous studies, we propose a nonlinear identification technique to examine the damping behavior of plates and panels during large amplitude vibrations. In order to perform the identification technique, first nonlinear experiments are conducted on isotropic and laminated sandwich plates and curved panels with (i) free edges and (ii) clamped boundary conditions by using a Laser Doppler Vibrometer and a LMS signal processing system to obtain nonlinear experimental frequency-response curves. Then, the frequency-amplitude data obtained from experiments are used as the inputs for the identification scheme and the least squares method is utilized to minimize the error between the measured response and the identified model. It is observed that damping grows very significantly with the vibration amplitude.

Experimental procedure

The non-linear vibration tests have been performed by increasing and decreasing the excitation frequency in very small steps in the frequency neighbourhood of the fundamental mode by using a stepped-sine testing technique [4]. The excitation has been provided by an electro-dynamic shaker, driven by a power amplifier, via a stinger connecting the shaker to the piezoelectric miniature force transducer (B&K type 8203) attached to the structure. The response is then measured by using a very accurate Polytec single point Laser Doppler Vibrometer (sensor head OFV-505 and controller OFV-5000) in order to have non-contact displacement measurement with no introduction of added mass. The time responses have been measured by using a SCADAS III front-end connected to a workstation and the LMS Test.Lab software has been used for signal processing, data analysis and excitation control. In particular, the MIMO Sweep & Stepped Sine Testing application of the LMS system has been utilized to generate the excitation signal and its closed loop control has been used to keep the force constant while the excitation frequency is varied in the neighbourhood of the fundamental frequency.

Modelling and identification method

In order to identify the damping for the experimental data, two procedures are used and their results are compared. First, a very accurate reduced order model with a number of degrees of freedom of the order of 10 to 100 is built and the equations of motions are integrated numerically by using a pseudo-arclength continuation and collocation scheme and the damping is varied until the experimental results are matched. The details on the reduced-order models are given in [4]. In the second procedure, the response of the tested structures is approximated by a single dimensionless nonlinear oscillator with viscous damping, quadratic and cubic non-linearities as follows:

$$r^2\ddot{x} + \zeta\dot{x} + x + \eta_2 x^2 + \eta_3 x^3 = \lambda\cos(t) , \tag{1}$$

where x and t are made dimensionless with respect to the structure's thickness and the excitation frequency, respectively. Moreover, ζ is the damping ratio, λ is the dimensionless force, r is the frequency ratio (the ratio between the excitation frequency and the fundamental frequency), and η_2 and η_3 are the dimensionless quadratic and cubic non-linear terms, respectively. Next, the harmonic balance method is applied and the solution of equation (1) is approximated by

$$x \approx x_N = x_0 + \sum_{k=1}^{N}\left[x_{2k-1}\sin kt + x_{2k}\cos kt\right] , \tag{2}$$

where N is the chosen order of truncation and x_N is the truncated Fourier series representation of x. A system of algebraic equations is obtained that relates the frequency ratio r to the amplitudes x_N. Next, the identification is conducted by assuming that the vibration amplitude x_N, the frequency ratio r and the harmonic force amplitude are already known for every frequency step from experiments. Therefore, in order to obtain the damping and the non-linear parameters, the

a) Corresponding author: marco.amabili@mcgill.ca**.**

following system should be solved for every j-th frequency step, $r^{(j)}$:

$$\begin{bmatrix} 2r^{(j)}\text{DS}_{x^{(j)}} & \text{P}_{x^{(j)}} & \text{Q}_{x^{(j)}} \end{bmatrix} \cdot \begin{Bmatrix} \zeta \\ \eta_2 \\ \eta_3 \end{Bmatrix} = \begin{bmatrix} -\text{S}_{x^{(j)}} - r^{(j)}\text{D}^2\text{S}_{x^{(j)}} + \text{S}_{f^{(j)}} \end{bmatrix}, \quad \text{D}=\begin{pmatrix} 0 & 0 & \cdots & 0 \\ 0 & \text{D}_1 & \cdots & 0 \\ \vdots & \vdots & \ddots & \vdots \\ 0 & 0 & \cdots & \text{D}_N \end{pmatrix}, \quad \text{D}_k = \begin{pmatrix} 0 & -k \\ k & 0 \end{pmatrix}, \ k=1,...,N \ , \ j=[\![1:m]\!]. \tag{3}$$

where m is the number of excitation frequency steps for which the experimental data was obtained at a specific excitation level. S_x, P_x and Q_x are vectors comprising truncated Fourier coefficients of x, x^2 and x^3, respectively, and S_f is the dimensionless force vector. System (3) is over-constrained, since it contains $(2N+1)\times m$ equations. Therefore, in order to obtain the damping ratio and the non-linear parameters the least squares technique has been applied.

Non-linear identification results

The procedure outlined in the previous section has been applied to (i) AISI 304 stainless steel plate with 0.25×0.24×0.0005m dimensions bolted to a AISI 410 stainless steel rectangular frame exhibiting clamped boundary conditions; (ii) AISI 304 stainless steel circular cylindrical panel (0.199×0.132×0.0003m) inserted in a heavy rectangular steel frame made having V-grooves designed to hold the panel and to avoid displacement of the edges; (iii) a stainless steel rectangular plate (0.3×0.45×0.0008m) with free-edge boundary conditions; (iv) a free-edge sandwich plate (0.46×0.9×0.0033m) with Carbon/Epoxy skins having (0/90) stacking sequence and a DIAB® Divinycell foam core; (v) a second free-edge sandwich plate (0.46×0.9×0.0036m) with Carbon/Epoxy skins having (0/90) lay-up and a PLASCORE® PN2 aramid fiber honeycomb paper core. For the clamped cases the response is measured at the center while for free edges the response is measured at one of the corners. Figures 1(a), 1(b) and 1(c) compare the experimental frequency response curves for different excitation levels and the identified ones for three cases: the free edge rectangular plate, the clamped plate and the curved panel, respectively. It can be observed that the identification (red *) is reasonably accurate and the identified amplitudes are perfectly following the experimental data (blue •) predicting hardening response in case of the flat plates and softening for the curved panel. Figure 1(d) depicts the evolution of damping (normalized with respect to the small-amplitude linear damping) with the normalized peak amplitude for all studied cases (including the two sandwich plates). It is interesting to see that the damping ratio varies nonlinearly with the increase of the peak vibration amplitude. It is evident that for the supported plate and sandwich free-edge plates, the damping could increase more than 250% for vibration amplitudes greater than 1.5 times the thickness. This increase is about 50% for the curved panel and for the same vibration amplitude. However, for the completely free steel plate the increase in damping is around 280% for vibrations greater than 3 times the thickness. This behavior confirms the presence of large dissipation during large-amplitude vibrations.
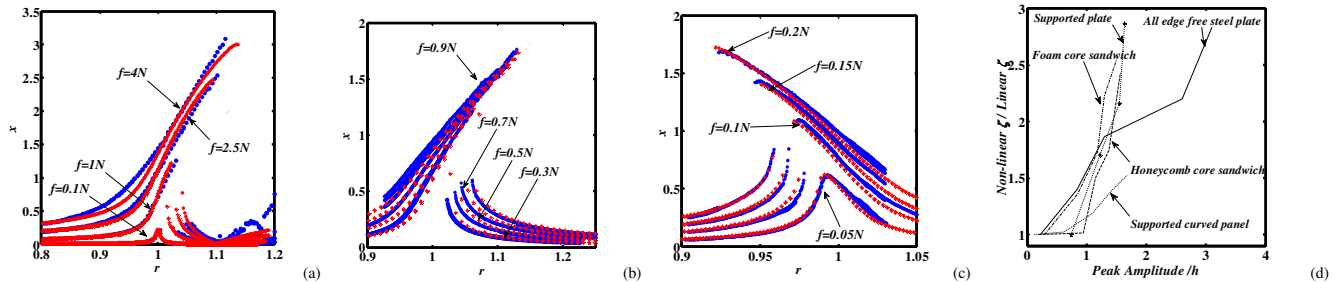
Fig. 1. (a) Comparison between the experimental and identified curves for the tested free-edge isotropic rectangular plate; (b) comparison between the experimental and identified frequency-amplitude curves for the tested clamped rectangular plate; (c) comparison between the experimental and identified curves for the tested clamped curved panel; (d) nonlinear variation of damping (normalized with respect to the linear damping) versus the peak vibration amplitude (normalized with respect to the thickness) for all the studied cases. In (a), (b) and (c) red * denote harmonic balance identification while blue • indicate experimental results.

Conclusions

A nonlinear identification technique is presented to track the evolution of damping during large-amplitude vibrations. The identified damping parameters confirm the presence of a strongly nonlinear correlation between damping and vibration amplitude in plates and curved panels. Particularly, it was found that plates and panels exhibit much larger dissipation during large-amplitude vibrations than in case of small-amplitude vibrations. Specifically, the damping increases with the vibration amplitude well over twice the linear damping ratio for the isotropic and sandwich plates experimentally investigated, and over 50 % for the circular cylindrical panel.

References

[1] Worden K., Tomlinson G.R.: Nonlinearity in structural dynamics: detection, identification and modeling, Institute of Physics Publishing, Bristol, 2001.

[2] Ozcelik O., Attar P.: Effect of non-linear damping on the structural dynamics of flapping beam. *Int. J. Non-linear Mech* **65**:148-163, 2014.

[3] Amabili M.: Nonlinear vibrations of viscoelastic rectangular plates. *J Sound Vib* **362**:142-156, 2016.

[4] Amabili M.: Nonlinear vibrations and stability of shells and plates, Cambridge University Press, New York, 2008.

NONLINEAR SYSTEM IDENTIFICATION OF MECHANICAL INTERFACES BASED ON WAVE PROPAGATION

Keegan J. Moore[1], Mehmet Kurt[2], Melih Eriten[3], D. Michael McFarland[4], Lawrence A. Bergman[4], Alexander F. Vakakis[1]
[1]*Department of Mechanical Science and Engineering, University of Illinois, Urbana, IL, USA*
[2]*Department of Bioengineering, Stanford University, Stanford, CA, USA*
[3]*Department of Mechanical Engineering, University of Wisconsin at Madison, Madison, WI, USA*
[4]*Department of Aerospace Engineering, University of Illinois, Urbana, IL, USA*

Abstract We study stress wave propagation in an impulsively forced split Hopkinson bar system with a frictional interface. By first considering only the primary-wave transmission and reflection, we reduced the problem to a first-order, strongly nonlinear ordinary differential equation. An Iwan element is chosen to model the frictional interface. The primary-wave propagation model is used to identify the Iwan parameters by maximizing the R-squared value between the experiment and simulation results. Using the optimized Iwan parameters, a high-order finite element model is used to simulate multiple transmissions and reflections across the interface. The results demonstrate that the primary-wave propagation model can be used for nonlinear system identification at a lower computational cost compared to higher-order models.

INTRODUCTION

High-order finite element (FE) models are often employed to identify system parameters, leading to high computational costs. As such, it is often desirable to develop low-cost reduced order models (ROMs) that can be used to identify accurately system parameters. One area where this proves difficult is in the prediction of mechanical wave propagation across a nonlinear interface in a waveguide due to an impulsive load. A conventional waveguide is the split Hopkinson pressure bar (SHPB) [1]. Recently, an SHPB system has been used to study the effects of threaded interfaces [2]. This work presents a new nonlinear system identification method based on the primary-wave propagation (PP) model proposed in [3]. We show that the PP model can accurately identify the parameters in an Iwan element used to model the nonlinear interface studied in [2] at a reduced computational cost.

PROBLEM FORMULATION

We consider the system depicted in Figure 1, composed of two linear elastic layers coupled by a nonlinear interface. The equation of motion governing the longitudinal waves in each layer is

$$\partial^2 u_i / \partial t^2 - \partial^2 u_i / \partial x^2 = 0, \quad i = 1, 2, \tag{1}$$

where $u_i = u_i(x,t)$ is the ith longitudinal displacement. Additionally, all variables are normalized such that $0 \le x \le 1$. The layers are assumed to start with zero initial conditions, with $t = 0$ defined as the time when the primary pulse reaches the left boundary $x = 0$ of the layer. The boundary conditions for the layers are

$$\partial u_1 / \partial x \big|_{x=0} = F_{in}(t), \quad \partial u_1 / \partial x \big|_{x=1} = K(z, \dot{z}), \quad \partial u_2 / \partial x \big|_{x=0} = K(z, \dot{z}) = F_2, \quad \partial u_2 / \partial x \big|_{x=1} = 0, \tag{2}$$

where the relative displacement is $z(t) = u_2(t,0) - u_1(t,1)$. With the system defined, we turn to the method developed by Pilipchuk in [3], which reduces the problem to a single first-order, nonlinear, ordinary differential equation (ODE) by considering only the primary transmission and reflection. Pilipchuk provides a full derivation in [3]; here only the resulting equations are presented:

$$(1/2)\dot{z} + K(z, \dot{z}) = F_{in}(t), \quad z\big|_{t=0} = 0, \tag{3}$$

$$F_2(t) = F_{in}(t) - (1/2)\dot{z}, \tag{4}$$

where F_2 is the transmitted force. Additionally, the reflection into the first layer is
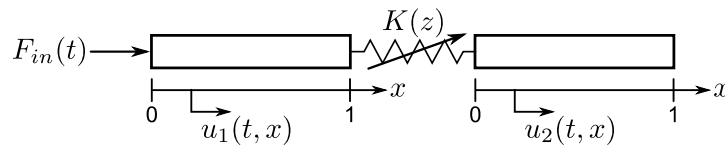
Fig. 1 Impulsively forced dual-layer system with nonlinear interface

---

a) Keegan J. Moore. Email: **kmoore14@illinois.edu.**
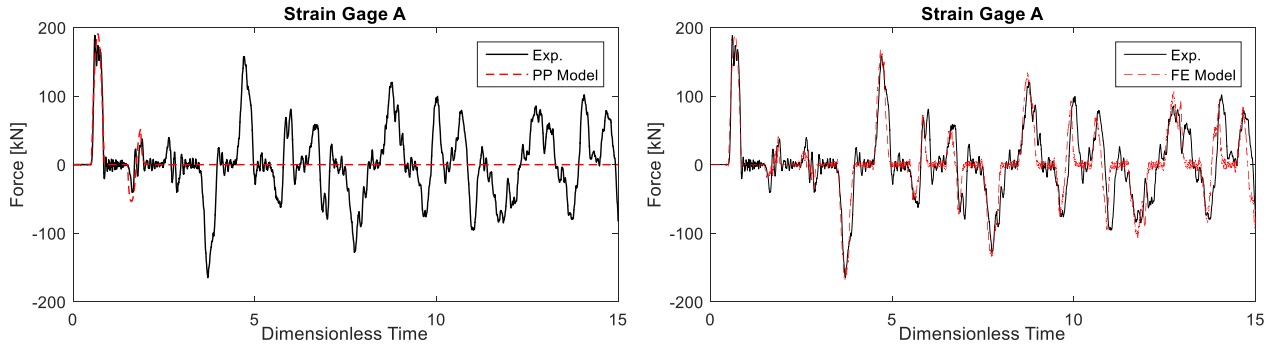
Fig. 2 Resulting waves for a preload of 25 ft-lbf and a striker velocity of 44.3 ft/s predicted using PP model and FE model.

$$\Phi_1(t) = -F_{in}(t-2) + K(t-1), \tag{5}$$

where Φ_1 is the reflection in the first layer based on the D'Alembert representation of the solution. Thus, by solving for $\dot{z}$ in (3), the transmitted and reflected forces are calculated using (5). By matching the predicted forces with the experimentally measured strains (converted into forces), the system parameters can be identified.

NONLINEAR SYSTEM IDENTIFICATION

We study an SHPB system composed of two hardened AISI 1566 steel bars with a threaded interface. Both the incident and transmission bars had a length of 48 in. and a diameter of 1.5 in. The threaded interface was made using 1"-8 UNC threads with male threads on the incident bar and female threads on the transmission bar. An initial static torque preload, applied by hand (near zero torque) or by using a handle-less strap wrench, ranged from 25 ft-lbf to 40 ft-lbf. The incident bar was dynamically excited by a 6 in. long striker, propelled by an air gun, at velocities ranging from 23.0 to 44.9 ft/s. Strains were measured at two locations before and two locations after the interface using uniaxial semiconductor strain gages. The Air Force Research Laboratory at Eglin Air Force Base, FL conducted all experiments and documented them fully in [2].

The frictional interface is modeled using an Iwan element [4], which contains an infinite distribution of Jenkins elements in parallel, where each Jenkins element consists of a linear spring in series with a Coulomb friction slider. All springs are chosen to have equivalent stiffness, but the slip forces vary in the form of a band-limited distribution as used by Iwan in [4]. Due to the lack of striker force measurements, the input force was modeled using a half-sine impulse in the simulations. The Iwan and forcing parameters are identified using MATLAB's *patternsearch* optimization algorithm with the objective of maximizing the R-squared value between the experimental data and the PP model results. The PP model simulations were computed up to a dimensionless time of 2.5 before any secondary transmissions and reflections. Using the optimized Iwan parameters, a high-order FE model was used to predict the secondary transmissions and reflections. Figure 2 presents the results for a static torque of 25 ft-lbf and a velocity of 44.3 ft/s.

CONCLUDING REMARKS

This paper presented a nonlinear system identification method for identifying nonlinear interfaces in waveguides based only on primary transmissions and reflections. In this way, the problem was reduced to a first-order, nonlinear ODE, resulting in a reduced order model, the PP model, without sacrificing the interface nonlinearity. Using the PP model, Iwan parameters were identified to model a threaded interface in an SHPB system. The PP model accurately captured the primary transmission and reflection across the interface, allowing accurate identification of the Iwan parameters. Additionally, multiple transmissions and reflections were computed using a high-order FE model with the Iwan parameters identified from the PP model and the results compared to those from the ROM.

References

[1] Hopkinson, B., "A Method of Measuring the Pressure Produced in the Detonation of High Explosives or by the Impact of Bullets," Philos. Trans. R. Soc. (London) A, 213, pp. 437-456, 1914.
[2] Dodson, J. C., Lowe, R. D., Foley, J. R., Mougeotte, C., Geissler, D., and Cordes, J., "Dynamics of Interfaces with Static Initial Loading", Dynamic Behavior of Materials, vol 1. In: Song B (ed) Conference Proceedings of SEM Series, Springer, New York, pp. 37-50, 2014.
[3] Pilipchuck VN, Azeez, MAF, and Vakakis AF, "Primary-pulse Transmission in Strongly Nonlinear Periodic System." Nonl. Dyn., **11**, pp. 61-81, 1996.
[4] Iwan WD, A Distributed-Element Model for Hysteresis and Its Steady-State Dynamic Response. In: ASME Journal of Applied Mechanics, **33**, pp. 839-900, 1996.

UNCERTAINITY QUANTIFICATION AND ROBUSTNESS ISSUES IN PLANAR NONLINEAR RESONANT STRUCTURES

Astitva Tripathi[1] and Anil K. Bajaj [*1]

[1]*School of Mechanical Engineering, Purdue University, West Lafayette, IN, USA*

Summary Nonlinear resonators employing 1:2 internal resonance have been proposed as sensing elements in some Micro-Electro Mechanical Systems (MEMS). A critical aspect of their performance is their robustness of performance with respect to variations resulting from fabrication uncertainties. In this study, an uncertainty quantification analysis is performed on several candidate designs for 1:2 internal resonances obtained via a computational synthesis method, and the interplay of geometric fabrication errors and robustness is illustrated.

INTRODUCTION

MEMS Devices operating on the principal of resonant behavior under 1:2 internal resonance have been proposed in applications such as mass and chemical sensors [1]. Additionally, new synthesis methods have been developed [2] which can generate several candidate designs for such resonators. Resonators based on 1:2 internal resonances are often designed so as to have their first two natural frequencies in the ratio of 1:2. In the computational synthesis method in [2], structures composed of beams having constant cross section joined orthogonally to each other are linearly designed as candidate structures for 1:2 internal resonance by varying the shape and size of structural elements. The intended properties of 1:2 frequency ratio are achieved by optimizing topology of the linear structure and dimensions of individual beams. As manufacturing processes have some inbuilt variability in the dimensions they can produce, it is critical to analyze the candidate resonators for their ability to provide sufficient performance in the face of dimensions achieved in actual fabrication compared to the nominal structure. While applicable for linear resonators as well, such uncertainty quantification and robustness considerations are especially important for nonlinear systems as the resonators are quite sensitive to variations in the frequency ratio from nominal value. In this work, four resonators synthesized using the method described in [2] are compared for robustness of their nonlinear resonant performance in face of uncertainties induced in dimensions due to manufacturing tolerances.

STRUCTURE SYNTHESIS AND NONLINEAR REDUCED ORDER MODEL

As stated in the introduction, the candidate resonators for 1:2 internal resonances consist of constant cross-section beams joined orthogonally to each other and undergoing planar vibrations. A hierarchical optimization method described in detail in [2] is used to synthesize these structures so that their first and second natural frequencies are in the ratio 1:2. Figure 1 shows four of these candidate structures for 1:2 internal resonance obtained using the hierarchical optimization method. Note that when the structures are fabricated using MEMS fabrication techniques, the structures deviate from nominal designs.

To obtain the nonlinear equations of motion for the candidate structures, Euler-Lagrange conditions coupled with the method of averaging are used. It is assumed that the overall nonlinear structural response of these systems consists predominantly of the lowest two modes. The transverse deflection of the ith beam of the structure can be written as:

$$v_i = \epsilon(A_1\phi_{i1} + A_2\phi_{i2}) , \tag{1}$$

where A_1 and A_2 are the modal amplitudes that are only functions of time, and ϕ_{i1} and ϕ_{i2} are the first and second linear modes of the ith beam, respectively. Following the standard averaged Lagrangian approach [3], the two-mode nonlinear resonant dynamics with quadratic (inertial) nonlinearity is reduced to four first-order equations describing the slow evolution of the amplitudes A_1 and A_2 in Eq. (1) and the frequency response is obtained using these first-order equations. It is well-known [1, 2, 3]that when the second mode is excited near its natural frequency, under the 2:1 internal resonance, the first mode is excited due to its nonlinear modal coupling with the second mode. The strongest coupling is when the two modal frequencies have a ratio of 2. In the presence of frequency mistuning, the response of the first mode goes down significantly.
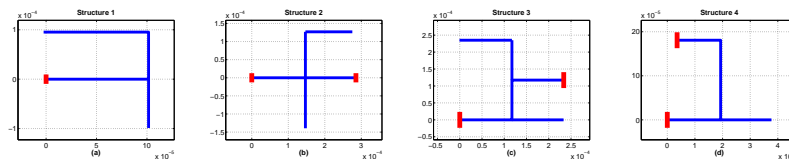
Figure 1: Optimized structures obtained for 1:2 frequency ratio as obtained in [2]. The planar structures are clamped at the red ground. The ratio of the first two natural frequencies for each of the structures is 2.0000.

[*]Corresponding author. Email: bajaj@purdue.edu
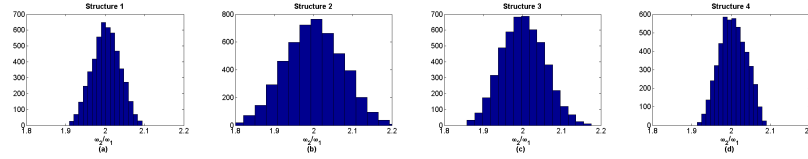
Figure 2: Histograms of the frequency ratio $\frac{\omega_2}{\omega_1}$ of the structures shown in Fig 1.
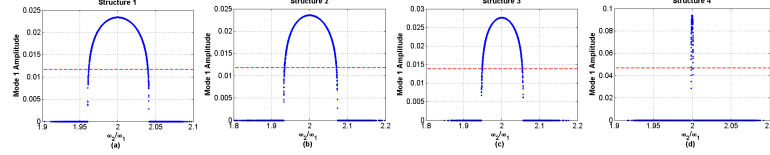
Figure 3: Mode 1 amplitude at zero external mistuning (excitation frequency equal to ω_2) of the structures shown in Fig. 1. The red line indicates the failure criterion amplitude.

UNCERTAINITY QUANTIFICATION

Variations in structural dimensions of the optimized structures result in the natural frequency ratios of the structures to deviate from 2 and thus, a degradation in device performance. To study the effects of variations in the beam lengths on the nonlinear response of the structure, consider the variations in lengths to be governed by a uniform distribution. Thus, beam length variations are assumed to be $\pm 10\%$ from the nominal. Samples generated using the Latin Hypercube Sampling technique are then used to compute the variation in natural frequencies with respect to the beam lengths. This relationship is expressed in the form of a response surface using the Multiadaptive Regression Splines (MARS) [4] which can be sampled to study the effect of dimensional uncertainties on nonlinear response of the first mode, and thus the device performance.

To compare the four candidate structures shown in Fig. 1 from the point of view of robustness of the nonlinear response, a test is defined to quantify each resonator's operational success or failure. This test can be stated as, "If for a given set of parameters along with a fixed value of forcing at the second natural frequency, the amplitude of the first mode response is more than or equal to 50% of the first mode amplitude for the nominal case, the device is said to be successful". This is based on the expectation that when a certain number of devices (or structures) are fabricated using identical manufacturing process, a certain fraction will not exhibit strong internal resonance, and thus the coupled mode nonlinear response. Figure 2 shows the histogram of the frequency ratios for the four structures. Figure 3 shows the mode 1 amplitudes of the four candidate structures at exact external resonance. Mode 1 amplitude is highest when the design is at its nominal point (i.e., the frequency ratio is equal to 2), and deviations from a frequency ratio of 2 cause a gradual drop in efficacy of modal coupling finally leading to the mode 1 amplitude becoming zero. The device failure rates for the respective structures are 28.98%, 34.62%, 35.30% and 97.14%. Thus, it is clear that among the four structures Structure 1 from Fig. 1 is the most robust to fabrication errors.

DISCUSSION AND CONCLUSIONS

Several candidate structures were compared for resonant coupled mode dynamics with regards to their ability to provide functionality in face of dimensional variability. The study brings forth the added aspect of nonlinear resonator design for internal resonances as some optimal designs, such as structure 4, may not be robust enough to handle uncertainties in device fabrication.

References

[1] Vyas A., Bajaj A. K., Raman A., Peroulis D. (2009) A Microresonator Design Based on Nonlinear 1 : 2 Internal Resonance in Flexural Structural Modes. *Journal of Microelectromechanical Systems* **18**:744-762.

[2] Tripathi A., Bajaj A. K. (2013) Computational Synthesis for Nonlinear Dynamics Based Design of Planar Resonant Structures. *Journal of Vibration and Acoustics* **135**: 051031:1-13

[3] Balachandran B., Nayfeh A. H. (1999) Nonlinear Motions of Beam-Mass Structure. *Nonlinear Dynamics* **1**:39-61

[4] Friedman J. H. (1991) Multivariate Adaptive Regression Splines. *Annals of Applied Statistics* **19**:1-67

STUDIES OF ROTOR-STATOR SYSTEM SUBJECTED TO NOISE EXCITATIONS

Vipin Agarwal[*1] and Balakumar Balachandran[1]

[1]*Department of Mechanical Engineering, University of Maryland, College Park, Maryland, 20742, USA*

Summary In this work, the authors present stochastic averaging studies conducted to examine torsional vibrations of a Jeffcott rotor subjected to continuous stator contact. The rotor drive input includes a deterministic input and white noise. The influence of noise on both forward and backward whirling motions is considered. In the experimental arrangement, noise is introduced through the drive motor signal. The experimental results are presented along with the results of the analytical-numerical studies and discussed.

INTRODUCTION

Noise is unavoidable and present is a range of engineering systems, and it can play a significant role in influencing system dynamics. In the current study, a combination of experimental and analytical-numerical studies are undertaken to understand the response of a rotor-stator system subjected to noise. The authors make use of the stochastic averaging method [1] to determine the response of the rotor-stator system. This averaging method has been used quite effectively to study the response of linear and nonlinear systems subjected to a combination of deterministic and noise inputs (e.g., [2, 3]). The physical system of interest here is a drill-string system, a representative illustration of which is provided in Fig. 1. Drill strings are long, tubular structures that are used for boring holes in the ground. These systems can undergo large torsional deformations as well as lateral displacements.. In general, noise is considered undesirable for the performance of an engineering system. However, noise may have beneficial effects on the dynamical behavior of systems and it can have a significant influence on the system dynamics (e.g., [4]). As an extension of their prior study, the authors consider the influence of noise on the dynamics of a flexible rotor with continuous stator contact.

EXPERIMENTAL ARRANGEMENT

The experimental arrangement consists of a rotor disc attached to a rotating rod. The rotating rod is made of aluminium and referred as a string due to its slenderness. In the experiments, this structure has a diameter of 3.2 mm and spans a length of approximately 2.0 m. The rotor is made of aluminium and has a diameter of 15.2 cm, and this rotor is enclosed within a circular stator with an inner diameter of 20.3 cm. A small mass is attached to the rotor in order to create an imbalance and eccentricity in the string-rotor system. The complete assembly is shown in Fig. 2.
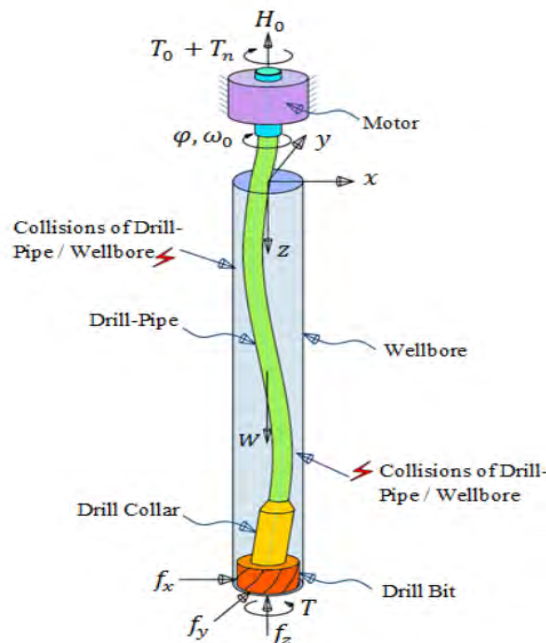
Figure 1: Representative drill-string system [5].

*Corresponding author. Email: vagarwal@umd.edu
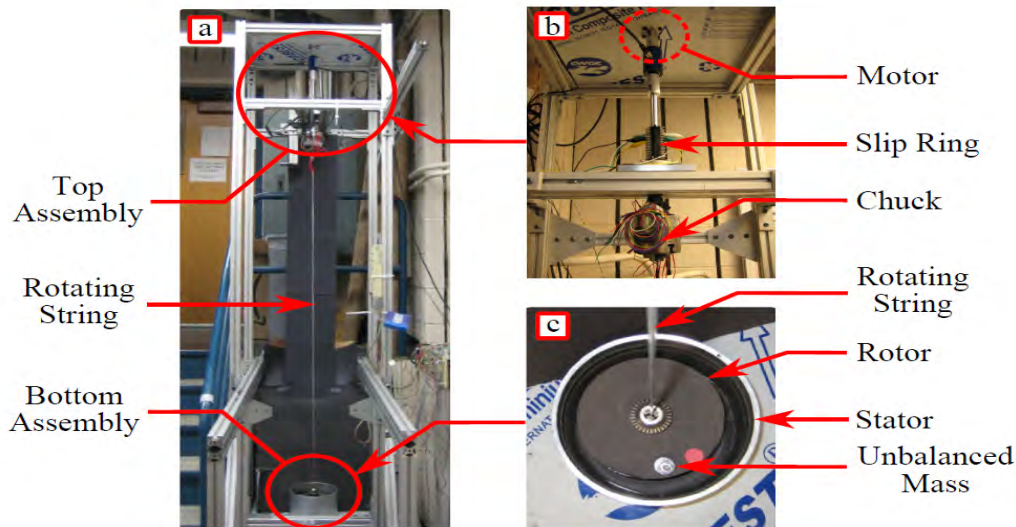
Figure 2: Experimental Arrangement. (a) Complete Experimental Arrangement, (b) Top Assembly, (c) Bottom Assembly

The entire string-rotor assembly is driven by a three-jaw self centering chuck that is connected to a stiff stainless steel driven shaft and motor. Additionally, a slip ring placed along the drive shaft allows for strain gages to be secured to the string. The strain due to bending and torsional vibrations may be measured depending upon the configuration of strain gages. For certain drive speeds, the rotor comes into contact with the stator and is subjected to frictional forces. The rotor may either stay in continuous contact in stator while it experiences different types of whirling motions or return back to the center of the stator. In the present study, the authors consider the constant contact cases in the experiments.

MODELING AND ANALYTICAL-NUMERICAL STUDIES

To complement the experiments, analytical-numerical studies based on the stochastic averaging method is carried out. The rotor-stator system is nonlinear in nature. The torsional and lateral vibrations are coupled by the eccentricity of the unbalanced mass through the inertial terms and rotor is also subjected to discontinuous forces that arise from the contact with the stator. A reduced-order model, in the form of a modified Jeffcott rotor model, is used for the averaging and numerical studies when noise is present in the system input. As part of the studies, the averaged Fokker-Planck-Kolmogrov equation is solved by using the path integration method. Numerical results are obtained for making comparisons with the experimental observations.

CONCLUDING REMARKS

The stochastic averaging method has been used to study the response of a flexible rotor system in continuous stator contact. Experiments are conducted with a laboratory scale arrangement of a portion of a drill-string system. The effectiveness of noise in influencing backward and forward whirling motions is examined through the analytical-numerical and experimental studies and discussed.

ACKNOWLEDGMENT

References

[1] Stratonovich, R. L., 1967. *Topics in the theory of random noise*, Vol. 2. CRC Press.
[2] Huang, Z., Zhu, W., Ni, Y., and Ko, J., 2002. "Stochastic averaging of strongly non-linear oscillators under bounded noise excitation". *Journal of Sound and Vibration,* **254**(2), pp. 245–267.
[3] Chen, L., and Zhu, W., 2009. "Stochastic averaging of strongly nonlinear oscillators with small fractional derivative damping under combined harmonic and white noise excitations". *Nonlinear Dynamics,* **56**(3), pp. 231–241.
[4] Agarwal, V., and Balachandran, B., 2015. "Noise-influenced response of duffing oscillator". In ASME 2015 International Mechanical Engineering Congress and Exposition, American Society of Mechanical Engineers.
[5] Liu, X., Vlajic, N., Long, X., Meng, G., and Balachandran, B., 2013. "Nonlinear motions of a flexible rotor with a drill bit: stick-slip and delay effects". *Nonlinear Dynamics,* **72**(1-2), pp. 61–77.

TRANSIENT RESPONSES OF A FORCED TRIPLE WELL POTENTIAL SYSTEM WITH FUZZY UNCERTAINTY

Ling Hong[1a)], Jun Jiang[1] & Jian-Qiao Sun[2]

[1] *State Key Lab for Strength and Vibration, Xi'an Jiaotong University, Xi'an, 710049, China*
[2] *School of Engineering, University of California at Merced, Merced, CA 95344, USA*

Summary Transient responses of a forced triple-well potential system with fuzzy uncertainty are studied by means of the Fuzzy Generalized Cell Mapping (FGCM) Method. The FGCM method is first introduced. A rigorous mathematical foundation of the FGCM is established as a discrete representation of the fuzzy master equation for the possibility transition of continuous fuzzy processes. The FGCM offers a very effective approach for solutions to the fuzzy master equation based on the min-max operator of fuzzy logic. A fuzzy response is characterized by its topology in the state space and its possibility measure of membership distribution functions (MDFs). This paper focuses on the evolution of transient MDFs of the fuzzy response. It is found that as the time goes on, transient MDFs spread around three potential wells. The evolutionary orientation of transient MDFs aligns with unstable invariant manifolds leading to stable invariant sets.

FUZZY GENERALIZED CELL MAPPING

Consider a dynamical system with fuzzy uncertainty,

$$\dot{\mathbf{x}} = \mathbf{f}(\mathbf{x}, t, S), \quad x \in \mathbf{D} \tag{1}$$

where $\mathbf{x}$ is the state vector, t the time variable, S a fuzzy set with a membership function $\mu_S(s) \in (0,1]$ where $s \in S$, and $\mathbf{f}$ is a vector-valued nonlinear function of its arguments. $\mathbf{D}$ is a bounded domain of interest in the state space. When the system parameter S is a fuzzy number, Equation (1) is a fuzzy differential equation. The equation of the FGCM system is given as follows by discretizing the time t, state variables $\mathbf{x}$ and the fuzzy set S in Equation (1)

$$\mathbf{p}(n+1) = \mathbf{P} \circ \mathbf{p}(n), \quad \mathbf{p}(n) = \mathbf{P}^n \circ \mathbf{p}(0), \quad p_i(n+1) = \max_j \min[p_{ij}, p_j(n)] \tag{2}$$

where $\mathbf{P}^{n+1} = \mathbf{P} \circ \mathbf{P}^n$ and $\mathbf{P}^0 = \mathbf{I}$. $\circ$ denotes the min-max operation. The matrix $\mathbf{P}$ denotes the one-step transition possibility matrix, $\mathbf{P}^n$ denotes the n-step transition possibility matrix. The vector $\mathbf{p}(n)$ is called the n-step membership distribution vector and $\mathbf{p}(0)$ the initial membership distribution vector. The (i, j)th element p_{ij} of the matrix $\mathbf{P}$ is called the one-step transition possibility from cell j to cell i. Equation (2) describes the evolution of a fuzzy response process and its MDFs.

Consider the fuzzy master equation for the possibility transition of continuous fuzzy process [1],

$$p(\mathbf{x}, t) = \sup_{\mathbf{x}_0 \in \mathbf{D}} [\min\{p(\mathbf{x}, t | \mathbf{x}_0, t_0), p(\mathbf{x}_0, t_0)\}], \quad \mathbf{x} \in \mathbf{D}. \tag{3}$$

where $\mathbf{x}$ is a fuzzy process, $p(\mathbf{x}, t)$ is the membership distribution function of $\mathbf{x}$ at t, and $p(\mathbf{x}, t, \mathbf{x}_0, t_0)$ is the transition possibility function. Equation (2) of the FGCM can be viewed as a discrete representation of fuzzy master equation (3). The solution to this equation is in general very difficult to obtain analytically. The FGCM offers a very effective method for solutions to this equation, particularly, for fuzzy nonlinear dynamical systems [2]

TRANSIENT ANALYSIS OF MDFS

Consider a forced Duffing oscillator with a triple-well potential driven by additive fuzzy noise,

$$\begin{cases} \dot{x} = y \\ \dot{y} = -0.35y - x + 0.5x^3 - 0.05x^5 + 0.2\cos t + S \end{cases} \tag{4}$$

where S is a fuzzy parameter with a triangular MDF,

$$\mu_S(s) = \begin{cases} [s - (s_0 - \varepsilon)]/\varepsilon, & s_0 - \varepsilon \leq s < s_0 \\ -[s - (s_0 + \varepsilon)]/\varepsilon, & s_0 \leq s < s_0 + \varepsilon \\ 0, & otherwise \end{cases} \tag{5}$$

where $\varepsilon > 0$ is a parameter characterizing the intensity of fuzziness of S and is called fuzzy noise intensity. s_0 is the nominal value of S with membership grade $\mu_S(s_0) = 1$. We take $s_0 = 0, \varepsilon = 0.4$.

The domain $\mathbf{D} = \{-3.5 \leq x \leq 3.5; -2.0 \leq y \leq 2.0\}$ is discretized into 141×141 cells. The 5×5 sampling points are used within each cell. S is discretized into 401 segments. Hence, out of each cell, there are 10,025 trajectories with varying membership grades. Transient MDFs are shown in Figures 1 and 2. T is one step mapping step.
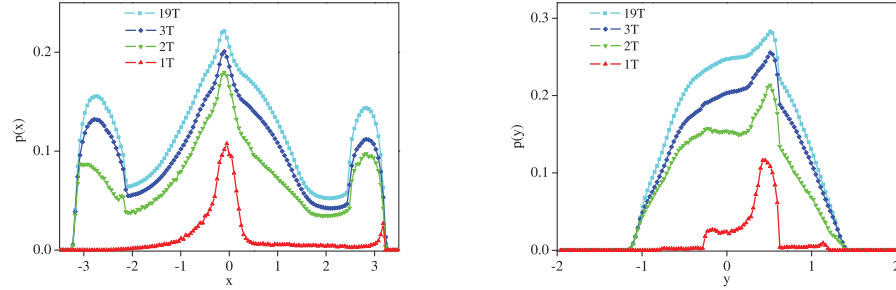
Figure 1. Transient marginal MDFs of displacement x and velocity y for the fuzzy Duffing equation (4) with the intensity of fuzzy noise $\varepsilon = 0.4$ at different times 1T, 2T, 3T and 19T.
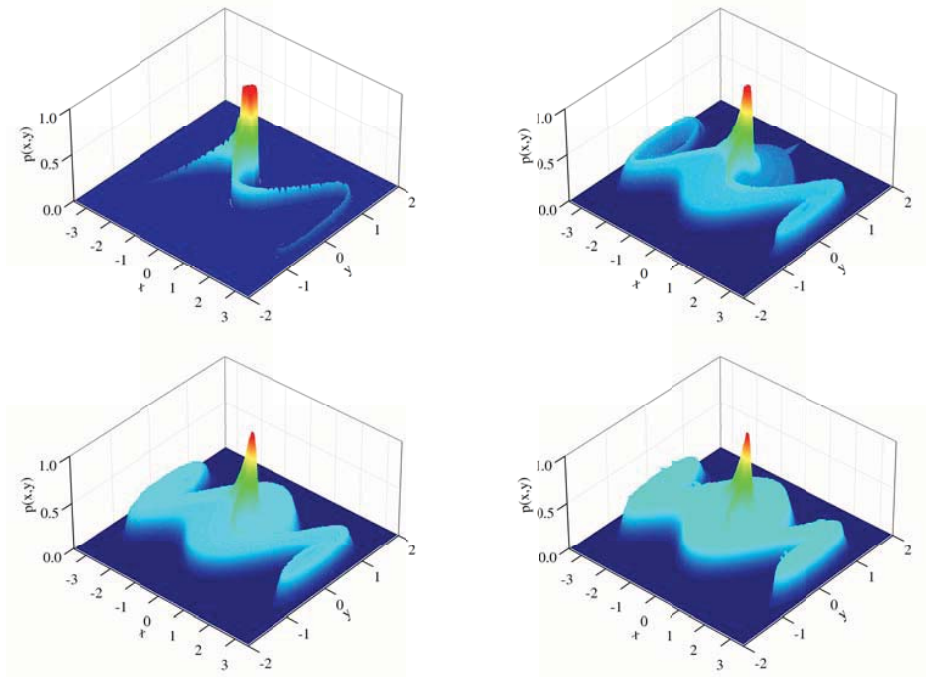
Figure 2. Transient MDFs of displacement x and velocity y for the fuzzy Duffing equation (4) with the intensity of fuzzy noise $\varepsilon = 0.4$ at different times 1T, 2T, 3T and 19T.

CONCLUDING REMARKS

This paper investigates the evolution of transient MDFs of the fuzzy response. It is found that the evolutionary orientation of transient MDFs aligns with unstable invariant manifolds leading to stable invariant sets. As the time goes on, the mean values of transient MDFs increase moving towards to form three possibility peaks around three potential wells. The results obtained herein are of value to real engineering problems. Especially, the evolution of transient state MDFs may be difficult to obtain with other conventional methods.

References
[1] Friedman Y., Sandler U.: Evolution of Systems under Fuzzy Dynamic Laws. *Fuzzy Sets and Systems* **84**:61-74, 1996.
[2] Hong L., Jiang J., Sun J.Q.: Response Analysis of Fuzzy Nonlinear Dynamical Systems. *Nonlinear Dynamics* **78**:1221-1232, 2014.

SYNCHRONIZATION OF SELF-INDUCED FRICTION OSCILLATORS

Michal Marszal & Andrzej Stefański
Division of Dynamics, Lodz University of Technology, Lodz, Poland

Summary In this paper, the synchronization properties of self-induced dry friction oscillators coupled in array are investigated. As a research tool which allows one to predict the synchronization thresholds, the method called master stability function is applied. It is realized in the form of the reference probe of two coupled oscillators. Our results demonstrate that this technique can be successfully applied for such strongly non-smooth systems with discontinuities.

INTRODUCTION

Phenomenon of synchronization can be defined as a correlation (adjustment) in time of two or more different processes. Collective motion of dynamical systems has been known for a long time, i.e., since the second half of 17th century, when Christian Huygens observed that two pendulum clocks hanging at the same beam can synchronize in phase [1]. Next, this phenomenon has been observed and investigated in various types of mechanical or electrical systems [2]. Recently, the idea of synchronization has taken a more interdisciplinary character as a powerful basic concept in nature regulating a large variety of complex processes [3].

A concept called master stability function (MSF) is a useful tool to determine the complete synchronization (CS) thresholds for different coupling configuration of identical oscillators [4]. In general, we can define the MSF as a surface of the largest transversal Lyapunov exponent (TLE) over the complex numbers plane (α, β) representing arbitrary eigenvalue γ of the connectivity matrix $\mathbf{G}_n$ (see Sec. II), where $\alpha = \sigma \mathrm{Re}(\gamma)$ and $\beta = \sigma \mathrm{Im}(\gamma)$. In mechanical oscillators one has mutual and symmetrical interaction yielding to real coupling, i.e. $\beta = 0$. Then the MSF is a function of the real number α, such that

$$\alpha = \sigma\gamma \tag{1}$$

If all the eigenmodes corresponding to discrete spectrum of eigenvalues $\sigma\gamma_i$ ($i = 1, ..., n$) of the can be found in the ranges of negative TLE then the synchronous state is stable. According to the idea of two oscillators probe these synchronous ranges of α are approximated (via relation (1)) by corresponding σ-intervals of zero synchronization error [5]. Concluding, results obtained for a pair of oscillators allow us to approach possible synchronization ranges for any configuration of coupled oscillators.
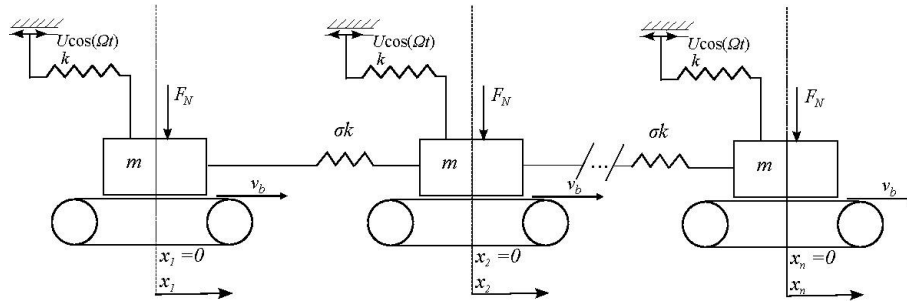
Figure 1. Array of friction oscillators coupled by springs

MODEL

Consider an array composed of forced stick-slip friction oscillators shown in Fig. 1. A single oscillator is described by the following equation

$$m\ddot{x} = -k(x - U\cos\Omega t) + F_N f(v_r), \tag{2}$$

where k is the stiffness constant, U amplitude of kinematic excitation, Ω forcing frequency, F_N normal load force, $v_r = v_b - \dot{x}$ is a relative velocity between the contact surfaces and $f(v_r) = \left(\mu_k + (\mu_s - \mu_k)\exp(-a|\vartheta|)\right)\mathrm{sgn}\,\vartheta$ represent assumed friction characteristic. Introducing $\omega_0 = \sqrt{k/m}$, static deflection $x_0 = g/\omega_0^2$, dimensionless time $\tau = \omega_0 t$ and the following substitutions: $\omega = \Omega/\omega_0$, $u = U/x_0$, $\varepsilon = F_N/mg$, $\vartheta_b = \vartheta_b/x_0\omega_0$, $\vartheta = \vartheta_b - \dot{y}$ we obtain dimensionless equations of friction oscillators array in form

---

$$\begin{Bmatrix} \ddot{y}_1 \\ \vdots \\ \ddot{y}_n \end{Bmatrix} = -\begin{Bmatrix} y_1 \\ \vdots \\ y_n \end{Bmatrix} + \sigma \mathbf{G}_n \begin{Bmatrix} y_1 \\ \vdots \\ y_n \end{Bmatrix} + \begin{Bmatrix} \varepsilon f(\vartheta_1) + u\cos\omega\tau \\ \vdots \\ \varepsilon f(\vartheta_n) + u\cos\omega\tau \end{Bmatrix}, \quad \text{where} \quad \mathbf{G}_n = \begin{pmatrix} -1 & 1 & \dots & 0 \\ 1 & -2 & \dots & 0 \\ \vdots & \vdots & \ddots & \vdots \\ 0 & 0 & \dots & -1 \end{pmatrix} \quad (3)$$

is a the connectivity matrix defining the structure of array connections. Coupling coefficient σ defines the overall strength of the coupling.

RESULTS

Let us consider the array composed of four coupled oscillators. For the assumed driving frequency $\omega = 1.40$ the single oscillator operates in chaotic regime. Other parameters are: $\vartheta = 0.1$, $\mu_s = 0.3$, $\mu_s = 0.15$, $a = 2.5$, $\varepsilon = 2.0$, $u = 0.1$. In Fig. 2 the MSF, represented by synchronization error $e_{II}(\alpha)$ calculated from two oscillators probe, is projected via eigenvalues of connectivity matrix $\mathbf{G}_4$ on the bifurcation diagram of average synchronization error e_{IV} evaluated for four coupled oscillators. Synchronization error $e_{II}(\sigma)$ is scaled according to Eq.(1) by absolute value of non-zero eigenvalue of connectivity matrix $\mathbf{G}_2$ (i.e $|\gamma_1| = 2$) in order to obtain $e_{II}(\alpha)$ function. This function is plotted vertically on top left part of Fig. 2, whereas eigenvalues spectrum $|\sigma\gamma_i|$ on top right. At the bottom, average synchronization error for four coupled oscillators as a function of coupling strength σ is presented. The synchronization occurs if all eigenmodes corresponding to the discrete spectrum of eigenvalues are found in the ranges of zero synchronization error for two oscillators test probe (horizontal grey regions in Fig. 1). As one can see in Fig. 2, synchronization of four oscillators occurs only in very narrow interval of σ, i.e. $0.153 \geq \sigma \geq 0.177$, where all three eigenvalues are located in the α-region of zero error $e_{II}(\alpha)$. Thus, knowing beforehand the synchronization thresholds for two oscillators probe, we are able to predict synchronization thresholds for longed chains of oscillators.
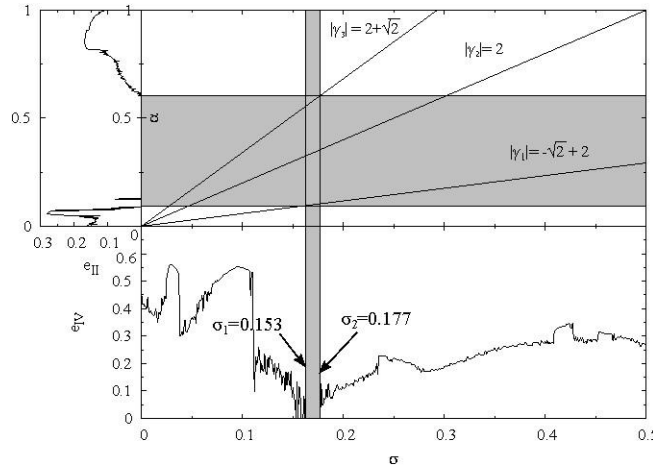
Figure 2. The MSF $e_{II}(\alpha)$ projected onto average synchronization error for three coupled self-induced dry friction oscillators via eigenvalues of connectivity matrix, for excitation angular frequency $\omega = 1.40$. Synchronous regions are depicted with grey.

CONCLUSIONS

We investigated the synchronization properties of coupled self-induced dry friction oscillators. The array of four oscillators coupled by linear springs was analyzed in order to determine the synchronization thresholds using the MSF approach, basing on synchronization error of two oscillators probe. Our results confirmed that this technique can be successfully applied for the networks of strongly non-smooth dynamical systems.

References

[1] C. Huygens, Horologium Oscillatorium (Apud F. Muquet, Parisiis, 1673).
[2] B. van der Pol, Radio Rev. 1, 701 (1920).
[3] A. Pikovsky, M. Rosenblum J. Kurths, Synchronization: a Universal Concept in Nonlinear Science (Cambridge University Press, Cambridge, 2010).
[4] L.M. Pecora, T.L. Carroll, Phys. Rev. Lett. 80, 2109 (1998).
[5] K.S. Fink, G. Johnson, T. Carroll, D. Mar, L. Pecora, Phys. Rev. E 61, 5080 (2000).

NONLINEAR SPATIO-TEMPORAL DYNAMICS OF AN ELASTIC PANEL IN UNIFORM LAMINAR FLOW

Alex Kleiman & <u>Oded Gottlieb</u>[1a)]

[1]*Department of Mechanical Engineering, Technion-Israel Institute of Technology, Haifa, Israel*

<u>*Summary*</u> We formulate an initial-boundary-value problem that consistently couples an elastic field for a panel immersed in a two-dimensional viscous compressible fluid field. A finite-difference numerical solver is formulated to investigate strongly nonlinear spatio-temporal fluid-structure interaction in uniform compressible laminar flow (100<Re<1000). The investigation reveals a complex bifurcation structure that includes quasiperiodic and chaotic-like non-stationary limit-cycles that evolve from stability loss of periodic ultra-sub-harmonic solutions. These bifurcations correspond to transitions in wake formations and transitions between two distinct fluctuation modes.

The field of fluid-structure interaction (FSI) incorporates a wide range of phenomena that are of great scientific and engineering interest in various disciplines, including aerospace and ocean engineering, biology, energy harvesting, heat removal and acoustics. The essence of this interaction is in the information transfer between the structure and the surrounding fluid, where the fluid exerts a load on the structure, which in turn complies and disturbs the flow in its vicinity. One of the highly investigated FSI problems is the complex motion of an elastic rectangular panel immersed in a uniform stream parallel to the longitudinal panel direction [1]. In spite of the comprehensive research done to-date, there are large discrepancies between documented experiments and the outcome of proposed simplistic analytical models [2]. Moreover, the existing numerical analytical and computational studies lack the full insight of the complex physical bifurcation structure which includes non-stationary dynamics and culminating with a possible chaotic spatio-temporal complexity.

We thus consistently formulate an initial-boundary-value problem that incorporates a two-dimensional viscous compressible fluid field described by the Navier-Stokes equations and an extensible Euler-Bernoulli elastic panel truncated to cubic order (Fig.1-left). Following [3] we implement a first-order loose coupling where the structure and fluid are solved alternatively by a fluid and structural solvers respectively. The fluid filed is solved via a Beam-Warming finite-difference scheme whereas the structure is solved using a fourth-order Runge-Kutta method [4]. Validation of the FSI solver is done by comparison to results obtained for an elastic panel both the flutter (Hopf) and a secondary bifurcation thresholds (Fig.1-middle) where periodic limit-cycle solutions become aperiodic, is consistent with the curve-fitting thresholds obtained in [5] as a function of both Reynolds number (100<Re<1000) and mass ratio (0<m*<0.3). A characteristic bifurcation diagram (Fig.1-right) depicts the free-edge amplitude ($A_{w)}$ vs. the mass ratio for Re=750 which includes steady solutions (region I), periodic limit-cycles (region II), quasiperiodic (region III) and non-stationary chaotic-like (region V) solutions that are separated by an ultra-sub-harmonic (m/n=5/3) solution (region IV).
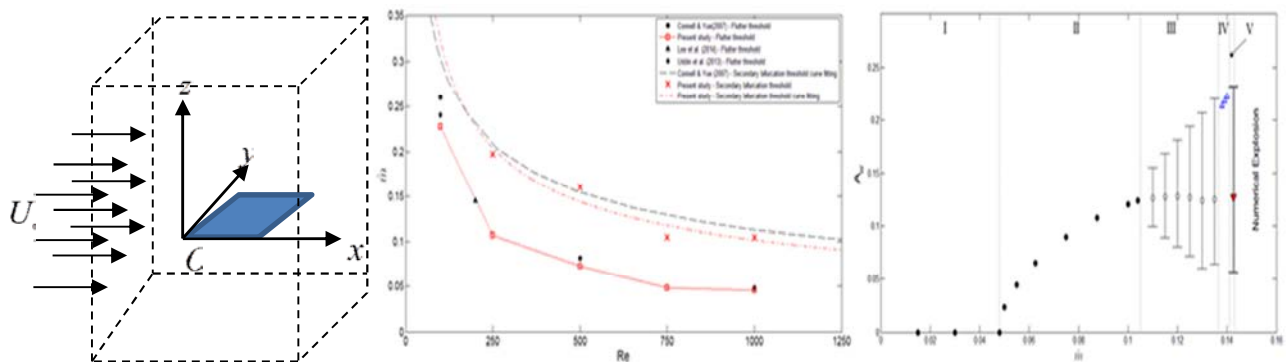
Figure 1: Elastic panel definition sketch (left), stability map (middle), bifurcation diagram (right).

The panel position snapshots for constant time-stepping intervals (Fig.2) reveals for Re=1000 a growing spatio-temporal complexity for increasing mass ratios. The periodic solution (m*=0.1) reveal an organized multi-mode spatial motion (Fig.2-left) whereas the quasiperiodic (m*=0.125) and non-stationary (m*=0.131) solutions reveal an irregularity with alternating spatio-temporal complexity which is more extensive for the chaotic-like oscillations (Fig.2-right).

---

a) Corresponding author. Email: oded@technion.ac.il
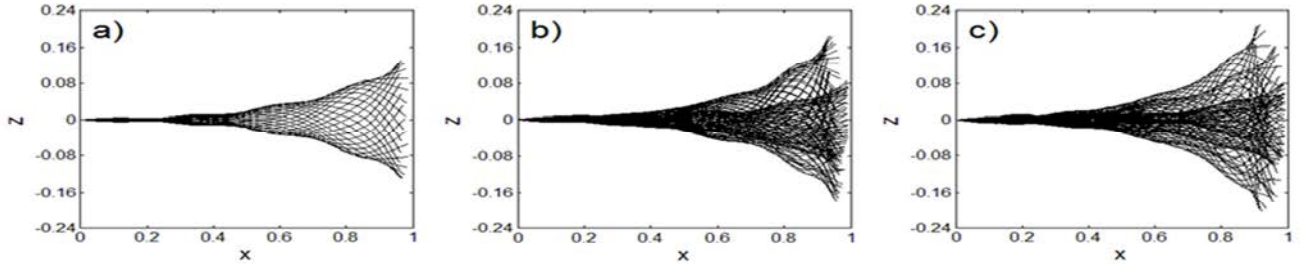
Figure 2: Panel position: periodic (left), quasiperiodic (middle), non-stationary (right).
.

The non-stationary temporal behaviour (Fig.3) is demonstrated for Re=1000 and m*=0.131 via the panel edge time-series (Fig3-left), its wide-banded power spectra (Fig.3-middle) and irregular state-space overlaid with a stroboscopic sampled Poincare' map (Fig.3-right) that is the outcome of torus breakdown.
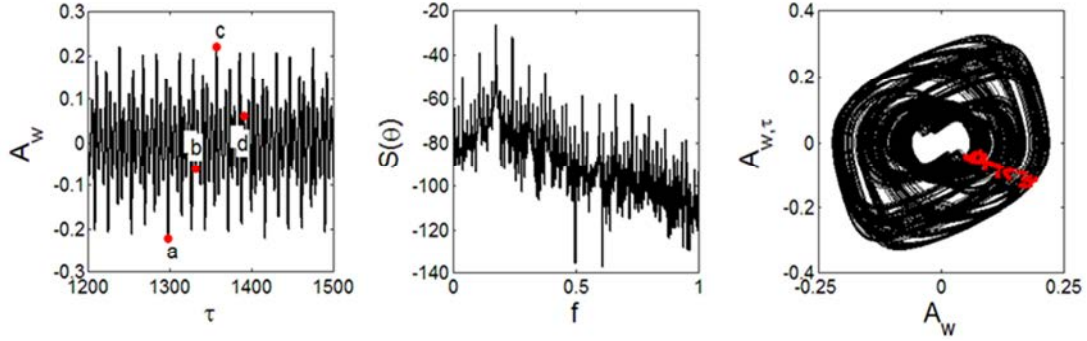
Figure 3: Chaotic time-series (left), power spectra (middle), overlaid state-space and Poincare' map (right).

The vorticity field snapshots (Fig.4) of the non-stationary solution (Re=1000, m*=0.131) reveal that the fluid dynamics is governed by an intermittent "2P" vortex shedding formation. This behaviour includes interplay between primary and secondary vortices which are governed by different distinct frequencies.
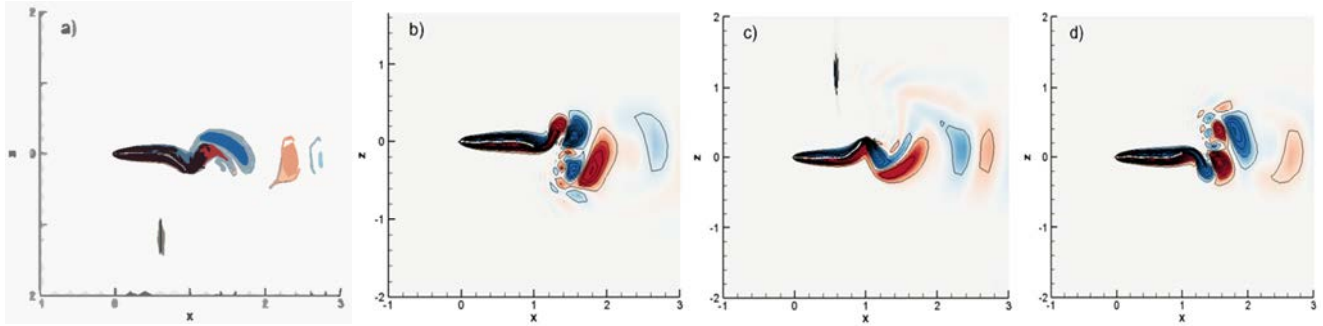
Figure 4: Snapshots of vorticity (corresponding to selected times denoted in Fig.3 left).

The results of this investigation reveal a complex bifurcation structure that includes quasiperiodic and non-stationary chaotic-like limit-cycles that are foliated with periodic ultra-sub-harmonic solutions. These bifurcations correspond to transitions in wake formations, and transitions between two distinct fluctuation modes.

References

[1]   Alben, S.: Physics of Fluids, 27, 033603, 2015.

[2]   Gibs C.S., Wang, I., Dowell, E.H.: Journal of Fluids and Structures, 34, 68-83, 2012.

[3]   Aginsky Z., Gottlieb, O.: Physics of Fluids, 25, 076104, 2013.

[4]   Gendel S., Gottlieb O., Degani D.: AIAA Journal, 53, 5, 1309-1318, 2015.

[5]   Connell B.S.H. , Yue, D.K.P.: Journal of Fluid Mechanics, 581, 33-67, 2007.

NONLINEAR VIBRATIONS OF ELASTICALLY SUPPORTED CYLINDER MOVING IN THE FLUID FLOW

Ekaterina Pavlovskaia [*1], Andrey Postnikov[1], and Marian Wiercigroch[1]

[1]*Centre for Applied Dynamics Research, School of Engineering, Aberdeen University, King's College, Aberdeen, AB24 3UE, Scotland, UK*

Summary In this paper nonlinearities in the fluid-structure interactions of an elastically supported cylinder moving in the uniform fluid flow are discussed. A new two degrees-of-freedom wake oscillator model [1, 2] is utilised to describe vortex-induced vibrations of elastically supported cylinders capable of moving in cross-flow and in-line directions. Total hydrodynamic force acting on the cylinder is obtained here as a sum of lift and drag forces, which are defined as being proportional to the square of the magnitude of the relative flow velocity around the cylinder. The two van der Pol type oscillators are then used to model fluctuating drag and lift coefficients. The resulting equations of motions of the cylinder in cross-flow and in-line directions are coupled through the fluid forces. Experimental data and Computational Fluid Dynamics (CFD) results are used to calibrate the proposed model and to verify the obtained predictions of complex fluid-structure interactions for different mass ratios.

INTRODUCTION

As offshore oil and gas fields are moving into deeper waters, the nonlinearities in the slender marine structures such as risers, mooring cables and umbilicals, and the fluid-structure interaction phenomena such as vortex induced vibrations (VIVs) become more and more important. Many of VIV aspects still require further advanced modelling to investigate the impact of the phenomenon which significantly affects the service life of marine structures. This work is motivated by the need of industry to predict loads and fatigue damage on riser systems, especially most common Top Tensioned Risers (TTRs) and Steel Catenary Risers (SCRs). Accurate prediction of VIVs can help to produce more robust structural design and lead to substantial savings in the offshore applications. Although the problem of vortex-induced vibrations could be addressed by different approaches, which include experimental studies, computational fluid dynamics modelling and analytical models, in present work, we focus on analytical model known as wake oscillator model.
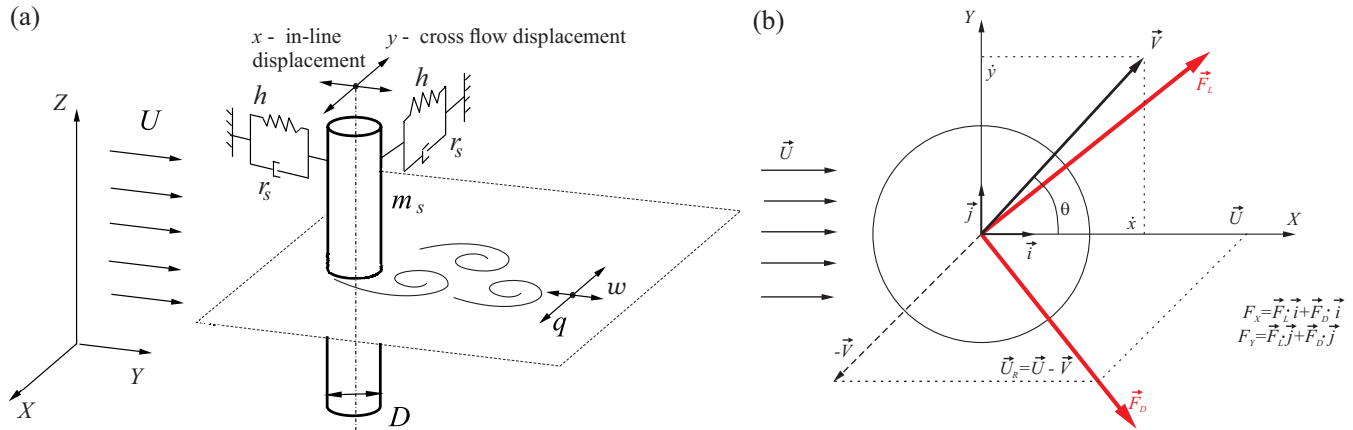
Figure 1: (a) Wake oscillator model for the cylinder moving in transversal and in-line directions; (b) Fluid forces acting on the structure [3]. Drag force $\vec{F}_D$ acts in line with relative stream velocity $\vec{U}_R$ and lift force $\vec{F}_L$ acts in perpendicular direction.

MATHEMATICAL MODELLING

In this work we consider an elastically supported cylinder experiencing VIV shown in figure 1(a), that is free to vibrate in cross-flow and in-line directions. As discussed in [1, 2], for a cylinder capable of oscillating in both directions, the equations of motion on an XY plane in terms of the displacements in in-line and cross-flow directions, x and y, are

$$m^\star \ddot{x} + r_s \dot{x} + hx = F_X, \tag{1}$$

$$m^\star \ddot{y} + r_s \dot{y} + hy = F_Y, \tag{2}$$

where the total hydrodynamic force components in X and Y directions are F_X and F_Y. Here $m^\star$ is mass per unit length including an added mass $m^\star = m_s + \frac{1}{4}\pi C_M \rho_f D^2$, r_s is structural damping, and h is stiffness of the support.

*Corresponding author. Email: e.pavlovskaia@abdn.ac.uk

This total hydrodynamic force, $\vec{F} = F_X\vec{i} + F_Y\vec{j}$, is the result of the actions of the sectional vortex-induced drag $\vec{F}_D$ and lift $\vec{F}_L$ forces which are shown in figure 1(b). As can be seen from this figure, the drag force $\vec{F}_D$ is acting along the velocity, $\vec{U}_R = \vec{U} - \vec{V}$ which is the fluid velocity relative to the cylinder ($\vec{V}$ is velocity of the cylinder and $\vec{U} = U\vec{i}$ is the velocity of the flow). The lift force $\vec{F}_L$ is then acting in the perpendicular directions and the magnitudes of lift and drag forces depends on the magnitude of relative velocity $\vec{U}_R$ $\left(|\vec{U}_R| = \sqrt{(U-\dot{x})^2 + \dot{y}^2}\right)$:

$$\vec{F}_D = \frac{1}{2}\rho_f C_D D |\vec{U}_R|^2 \frac{\vec{U}_R}{|\vec{U}_R|}, \qquad \vec{F}_L = \frac{1}{2}\rho_f C_L D |\vec{U}_R|^2 \frac{\dot{y}\,\vec{i} + (U-\dot{x})\vec{j}}{|\vec{U}_R|}. \tag{3}$$

Here the parameters are ρ_f, the fluid density, C_L, lift coefficient, and $C_D = C_{D_0} + C_D^{fl}$, total drag, which can be represented as a sum of constant mean sectional drag C_{D_0} and fluctuating drag, C_D^{fl}. Following the approach employing nonlinear oscillator equations of the van der Pol type (see for example [4]), the fluctuating lift C_L and drag C_D^{fl} coefficients could be modeled by two wake oscillators using q and w variables ($q = 2C_L/C_{L_0}$ and $w = 2C_D^{fl}/C_{D_0}^{fl}$). Thus the system can be described by the following set of the equations where the acceleration coupling recommended by Facchinetti *et. al* [5] was adopted in the wake oscillator equations:

$$(m_s + \frac{1}{4}\pi C_M \rho_f D^2)\ddot{x} + r_s\dot{x} + hx = \sqrt{(U-\dot{x})^2 + \dot{y}^2}\left(\frac{1}{4}\rho_f C_{L_0} q D\dot{y} + \frac{1}{2}\rho_f(C_{D_0} + \frac{1}{2}C_{D_0}^{fl}w)D(U-\dot{x})\right), \tag{4}$$

$$(m_s + \frac{1}{4}\pi C_M \rho_f D^2)\ddot{y} + r_s\dot{y} + hy = \sqrt{(U-\dot{x})^2 + \dot{y}^2}\left(\frac{1}{4}\rho_f C_{L_0} q D(U-\dot{x}) - \frac{1}{2}\rho_f(C_{D_0} + \frac{1}{2}C_{D_0}^{fl}w)D\dot{y}\right), \tag{5}$$

$$\ddot{w} + 2\Omega_F \varepsilon_x(w^2 - 1)\dot{w} + 4\Omega_F^2 w = (A_x/D)\ddot{x}, \tag{6}$$

$$\ddot{q} + \varepsilon_y \Omega_F(q^2 - 1)\dot{q} + \Omega_F^2 q = (A_y/D)\ddot{y}. \tag{7}$$

The developed equations of motion (4)-(7) describe the vibrations of the cylinder in the fluid flow. However, a careful calibration of the model is required and specifically empirical wake oscillators equations parameters A_x, A_y, ε_x and ε_y need to be found. In case of a single degree-of-freedom system, numerical results by Facchinetti [5] where fitted against experimental data, with A_y and ε_y estimated as 12 and 0.3 respectively. However, further investigation and calibration for 2DOF models are essential. It should be noted that in general these coefficients may be a function of various parameters of the system such as mass ratio, damping ratio, reduced velocity, added mass coefficient, Reynolds number, etc.

In this study, first, the published experimental results were utilised to calibrate the proposed wake oscillator model. Three sets of experimental data [6, 7, 8] were considered, and comparisons are made for different mass-damping ratio parameters. Then, CFD model has been created in ANSYS Fluent 12.0.16 utilizing User Defined Functions (UDFs) in order to compute the displacement of the cylinder on each time step based on the forces obtained from the dynamic pressure. Relatively low Reynolds numbers (600 to 2000) were considered for the sake of simplicity. However, even for these low Reynolds numbers ($Re > 300$) the vortex street is turbulent, and a high quality grid is required for solution to converge. The results of the simulations and comparisons with both experimental data and CFD calculations will be presented in this paper.

CONCLUSIONS

In this paper nonlinearities in the fluid structure-interactions of an elastically supported cylinder moving in the uniform fluid flow are discussed utilising new two degrees-of-freedom wake oscillator model. Equations of motion of the cylinder in cross-flow and in-line directions are coupled through the fluid forces calculated from the instantaneous relative flow velocity around the cylinder. This description of the fluid forces allows one to generalise the problem statement for the flexible structure and conduct the analysis similar to transversal vibration case considered in [3].

References

[1] Postnikov, A.: Wake Oscillator and CFD in Modelling of VIVs. PhD Thesis, School of Engineering, University of Aberdeen, UK, 2015.

[2] Postnikov, A., Pavlovskaia, E., and Wiercigroch, M.: 2DOF CFD Calibrated Wake Oscillator Model to Investigate Vortex-Induced Vibrations, submitted 2015.

[3] Pavlovskaia, E., Keber, M., Postnikov, A., Reddington, K. and Wiercigroch, M.: Multi-Mode Modelling of Vortex-Induced Vibration, International Journal of Nonlinear Mechanics, in press 2015.

[4] Bishop, R.E.D., Hassan, A.Y.: The Lift and Drag Fores on a Circular Cylinder in a Flowing Field, Proc. Roy. Soc. (London) Ser. A 277:51-75, 1964.

[5] Facchinetti M.L., de Langre E., Biolley F.: Coupling of Structure and Wake Oscillators in Vortex-Induced Vibrations, Journal of Fluids and Structures 19:123-140, 2004.

[6] Williamson, C.H.K., Jauvtis, N.: A Hight-Amplitude 2T Mode of Vortex-Induced Vibration for a Light Body in XY Motion, European Journal of Mechanics B/Fluids 23:107-114, 2004.

[7] Stappenbelt, B., Lalji, F., Tan, G.: Low Mass Ratio Vortex-Induced Motion:, The 16th Australian Fluid Mechanics Conference, Gold Coast, Australia, 1491-1497, 2007.

[8] Williamson, C.H.K., Jauvtis, N.: The Effect of Two Degrees of Freedom on Vortex-Induced Vibration at Low Mass and Damping", J. Fluid Mech. 509:23–62, 2004.

NONLINEAR DYNAMICS OF AN ELECTRO-MECHANICAL SYSTEM: NUMERICAL AND EXPERIMENTAL STUDY

Francesco Romeo [*1] and Ioannis Georgiou[2]

[1]*Department of Structural and Geotechnical Engineering, SAPIENZA University of Rome, Rome, Italy*
[2]*Naval Architecture and Marine Engineering School, National Technical University of Athens, Athens, Greece*

Summary The dynamic behavior of an electro-mechanical coupled system excited by harmonic voltage is numerically and experimentally studied. The system governing equations involve coupling quadratic nonlinearity; as a result, the obtained numerical and experimental results show the occurrence of the non-linear resonance related to the current quadratic nonlinearity and a jump, after which the mass of the mechanical oscillator undergoes large amplitude oscillations and coexisting attractors appear.

INTRODUCTION

The dynamic experimental response of a system in which a mechanical linear oscillator is nonlinearly coupled to a linear electric circuit through an electromagnet is studied. Previous analytical and numerical studies were carried out by the authors on this type of multi-physics system [1]. According to these studies, when the mechanical oscillator is excited via harmonic voltage applied to the electric circuit, interesting nonlinear phenomena arise such as the non-linear resonance related to the current quadratic nonlinearity which imposes a natural linear resonance at half the frequency of the linear oscillator, jump phenomena and transitions to complex chaotic interaction dynamics. The experimental investigations here presented aims at validating these theoretical findings.

ELECTRO-MECHANICAL MODEL

The system consists of a linear oscillator coupled nonlinearly through an electromagnet to a linear electric circuit. The motion is governed by the following two coupled differential equations:

$$\ddot{x} + 2\zeta_m\omega_m\dot{x} + \omega_m^2 x = \epsilon\alpha\dot{q}^2 + \hat{f}$$
$$(1 + \alpha x)\ddot{q} + (2\zeta_e\omega_e + \alpha\dot{x})\dot{q} + \omega_e^2 q = \hat{e}, \tag{1}$$

in which m, c, k denote mass, dissipation and stiffness parameters of the linear oscillator and L, C, R denote the inductance, capacitance, and resistance of the electrical circuit. The variables x and q denote the mechanical and electrical displacement (charge), respectively. The velocity of the mass and the electric current are $v \equiv \dot{x}, i \equiv \dot{q}$, respectively; f and e denote external mechanical forcing and voltage excitation. The inductance is approximated by $L(x) = L_0 + L_1 x$. The remaining parameters are defined as: $\omega_m^2 \equiv \frac{k}{m}$, $\omega_e^2 \equiv \frac{1}{L_0 C}$, $\zeta_m \equiv \frac{c}{2\sqrt{km}}$, $\zeta_e \equiv \frac{R\sqrt{C}}{2\sqrt{L_0}}$, $\epsilon \equiv \frac{L_0}{2m}$, $\alpha \equiv \frac{L_1}{L_0}$, $\hat{f} \equiv \frac{f}{m}$, $\hat{e} \equiv \frac{e}{L_0}$, $\mu \equiv \omega_m/\omega_e$. Therefore the considered multi-physics coupled system is a nonlinear dynamical system with its coupling nonlinearity stemming from the dependence of the inductance on the metallic mass displacement. The interest lies in investigating how the mechanical
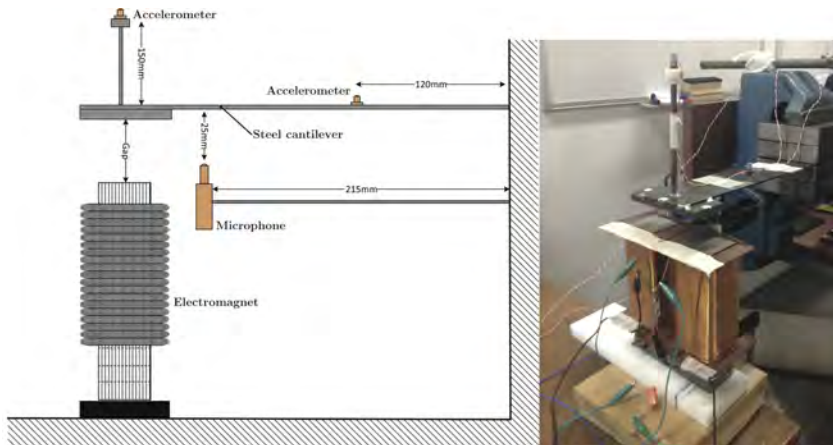
Parameter	Symbol	Num.	Exp.
Singular parameter	μ	0.2	0.021
Mechanical dissipation factor	ζ_m	0.01	0.01
Electrical dissipation factor	ζ_e	0.1	0.0011
Electro-mechanical coupling	ϵ	5.0	0.34
Inductance nonlinearity	α	10.0	-

Figure 1: Experimental setup of the electro-mechanical system and parameters of the numerical and experimental tests.

*Corresponding author. Email: francesco.romeo@uniroma1.it

part will respond when it is actuated by the electrical part. Previous Slow Invariant Manifold analytic approximations and numerical investigations [1] have shown that the system has a slow periodic response over a well-defined region of the forcing parameters. This region starts from low frequencies and includes the frequency at which the linear system undergoes a resonance due to the presence of the quadratic nonlinear dependence on the current. At some critical value depending on μ the amplitude-frequency response loses its smoothness via bifurcation mechanism that creates a finite jump.

NUMERICAL AND EXPERIMENTAL RESULTS

In Figure 1 the experimental realization of the above described coupled dynamical system is shown through a sketch and a picture. The experimental setup located in the Nonlinear Dynamics Lab at N.T.U.A. consists of the following components: electromagnet, steel cantilever beam, two acceleration sensors, sound measurement sensor, electric current recording sensor, frequency generator, power and sensor signal amplifiers. The experimental tests have been carried out by applying a constant voltage amplitude of 25 V and performing quasi-static forward and backward frequency sweeps. Different values of gap between the surface of the electromagnet and the cantilever tip were investigated in order to tune the strength of the nonlinear coupling. In the numerical and experimental investigations the system parameters are set as reported in Figure 1.

Figure 2a shows the numerical frequency-mechanical response amplitude plot. The different branches corresponding to forward and backward sweeps show how the coupling nonlinearity affects the dynamics. As shown in [1], starting from $\Omega = 2.5$, as the frequency decreases the upper branch of the period-1 attractor grows until an instability is reached around $\Omega = 1.55$. At the critical frequency $\Omega = 0.966$ (dashed red line) the period-1 attractor suffers an abrupt downwards finite jump; afterwards, the lower branch shows the resonance around $\Omega = 0.5$ (dashed blue line). The experimental results are
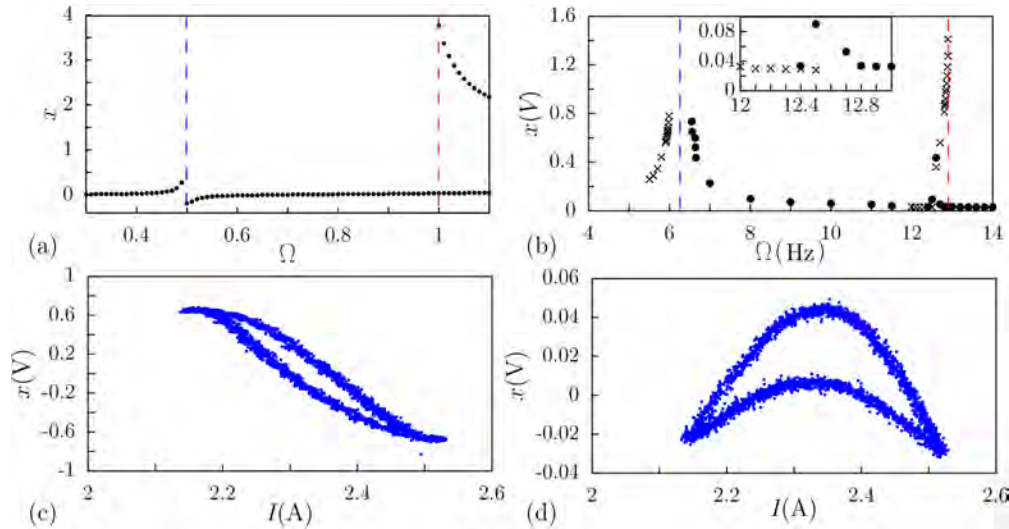
Figure 2: Numerical (a) and experimental (b) oscillator frequency-amplitude plots (forward (x) and backward (●) frequency sweep). (c)-(d) Experimental coexisting attractors on the current-mechanical displacement plane (I-x).

shown in Figure 2b; the qualitative agreement with the numerical results obtained by direct numerical integration of (1) can be seen in terms of both, the non-linear resonance related to the current quadratic nonlinearity, which imposes a natural linear resonance at half the frequency of the linear oscillator given by $\Omega = 6.4$ Hz (dashed blu line) and a jump at the cantilever natural frequency occurring at $\Omega = 12.86$ Hz (dashed red line). The coexistence of (at least) two periodic attractors can be seen by the experimental phase portraits reported in Figures 2c,d for $\Omega = 12.7$ Hz.

CONCLUSIONS

The dynamics of a coupled nonlinear electro-magneto-mechanical system was addressed by means of numerical and experimental approaches. The numerical predictions obtained via Poincaré mappings were qualitatively validated experimentally in a cantilever steel beam coupled to an electromagnet driven by harmonic voltage.

References

[1] Georgiou, I. T., Romeo, F.: Multi-physics Dynamics of a Mechanical Oscillator Coupled to an Electro-magnetic Circuit. Int. J. Nonl. Mech. 70, 153-164, 2015.

INFLUENCE OF TEMPERATURE ON MIDDLE EAR WITH SHAPE MEMORY PROSTHESIS

Rafal Rusinek[1], Jerzy Warminski[1], Marcin Szymanski [2]

[1]*Department of Applied Mechanics, Mechanical Engineering Faculty, Lublin University of Technology,*
Nadbystrzycka 36, 20-618 Lublin, Poland
[2]*Department of Otolaryngology Head and Neck Surgery, Medical University of Lublin*
Jaczewskiego 8, 20-854 Lublin, Poland

<u>*Summary*</u> The paper presents some dynamical aspects of dynamics of a human middle ear reconstructed by means of a prosthesis made of shape memory alloy. A two degrees of freedom nonlinear model is developed. On the base of the model a bifurcation analysis is performed and an influence of external excitation and temperature on system dynamics is presented.

INTRODUCTION

The human middle ear contains three ossicles: malleus, incus and stapes. The ossicles form a sound conduction system which transmits sound from the external ear to the fluids of the inner ear. The ossicles are connected to each other by incudomallear and incudostapedial joint. Such a complex bio-system is modelled in the literature from the last half century. The first study in this field was published in 1961 by Mőller [1] where also the first scheme of middle ear mechanism was proposed. Next, a similar model was investigated by Zwislocki [2]. In both publications, authors used an electrical circuit to analyse middle ear system. In the last decades mechanical models are developed where ossicles are represented by lumped masses, connected with springs and dashpots. In the literature, one can find three or four degrees of freedom (dof) model and sometimes even six dof but always they are linear. Usually these models focus only on kinematics of an intact middle ear however hardly ever, dynamics models are built.

Moreover, in medicine practice middle ear can be damaged e.g. by chronic otitis media. In this case usually middle ear prostheses is applied to reconstruct connection between stapes and malleus or tympanic membrane. Therefore, here a nonlinear model of reconstructed middle ear with shape memory prosthesis is proposed. Next, an influence of temperature on a reconstructed middle ear behaviour is analysed.

MIDDLE EAR MODEL

Adjustment of the prosthesis size and location is one of the main problem occurring during surgery operation. Therefore, a new concept of shape memory prosthesis (AMP) is proposed here to improve a process of implementation in a human body. The SMP can be made of shape memory alloy (SMA) which characteristic is given by the stress (σ) polynomial of the strain (ε) [3]:

$$\sigma = a_1(T - T_M)\varepsilon - a_2\varepsilon^3 + a_5\varepsilon^5 \qquad (1)$$

where, a_1, a_2, a_3 are the material constants, T is temperature and T_M is phase temperature where martensite is stable.

Since, in most cases the incus is damaged and should be removed from ossicluar chain, the proposed model is nonlinear with 2dof presented in Fig.1
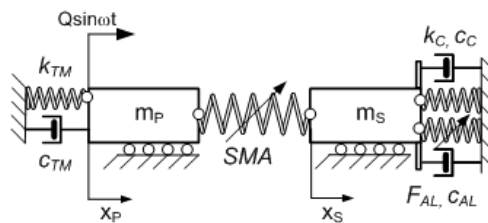
Fig.1: Two degrees of freedom model of middle ear with shape memory prosthesis.

The differential equations of motion, governing the model presented in Fig.1 is presented in the form

---

[a] Corresponding author. Email: r.rusinek@pollub.pl

$$m_P \ddot{x}_P + k_{TM} x_P + c_{TM} \dot{x}_P + F_{SMA} = Q \sin \omega \tau$$
$$m_S \ddot{x}_S + k_C x_S + k_{AL} x_S + k_{2AL} x_S{}^2 + k_{3AL} x_S{}^3 + c_C \dot{x}_S + c_{AL} \dot{x}_S - F_{SMA} = 0 \tag{2}$$

where, the spring force F_{SMA} is given as

$$F_{SMA} = a_1(T - T_M)(x_p - x_s) - a_2(x_p - x_s)^3 + a_3(x_p - x_s)^5 \tag{3}$$

Dynamical behaviour of the stapes tested in the normal temperature of human body (36.6°C) is presented as a bifurcation diagram in Fig.2 showing different kind of possible solutions.
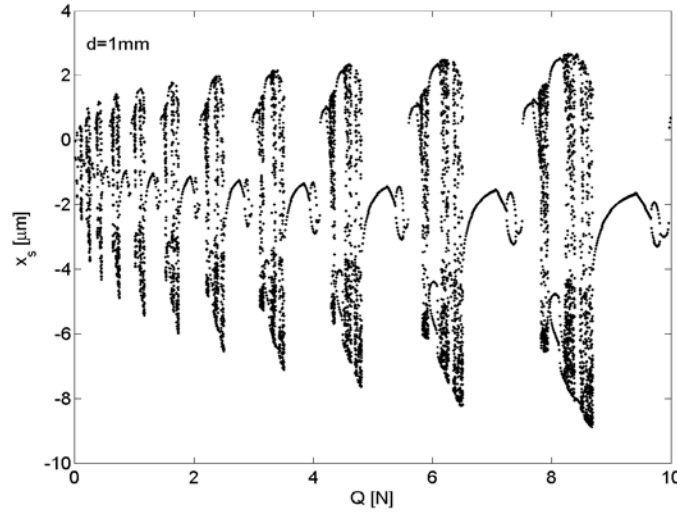
Fig.2: Bifurcation diagram of stapes vibrations versus excitation amplitude

More, examples will be given in a full paper (presentation).

CONCLUSIONS

- Smart prosthesis of human middle ear, made of shape memory alloy is an interesting alternative for classical prosthesis for the sake of possibility of easy adjustment its length and shape to individual medical case.

- Strong external excitation of middle ear system with the smart prosthesis generates irregular vibrations which lead to deterministic chaos.

- Behaviour of the SM prosthesis depends also on temperature and system nonlinearities.

References

[1]   Moller A. R.: Network Model of the Middle Ear. *Journal of the Acoustical Society of America* **33:** 168–76, 1961
[2]   Zwislocki J.: Analysis of the Middle-Ear Function. Part I: Input Impedance. *Journal of the Acoustical Society of America* **34:** 1514–23, 1962
[3]   Paiva A., Savi M. A.: An overview of constitutive models for shape memory alloys. *Mathematical Problems in Engineering* **43:** 1–31, 2006

ASYMPTOTIC APPROACH TO FLUTTER CONTROL VIA HYSTERETIC ABSORBERS

Arnaldo Casalotti, Andrea Arena and Walter Lacarbonara [*]

Department of Structural and Geotechnical Engineering, Sapienza University of Rome, Rome, Italy

Summary The aerodynamic control problem in long-span suspension bridges is discussed. A reduced-order bridge model (see Fig. 1) is augmented by the degree of freedom of a hysteretic mass nonlinearly tuned to control two aeroelastic instabilities: vortex-induced parametric resonances and limit cycle oscillations (LCO) past the flutter speed. The model comprises the plunge (vertical) and pitch (torsional) motions while the aerodynamic lift and moment are governed by a quasi-steady formulation. The restoring force of the absorber is characterized by linear and cubic elastic terms together with a hysteretic part governed by the Bouc-Wen differential model. The method of multiple scales is adopted to obtain an asymptotic approximation of the LCO behavior. An optimization procedure based on the Differential Evolutionary Algorithm is employed to obtain the set of constitutive parameters that lead to an optimal mitigation of the wind-induced oscillations.

INTRODUCTION

Parametric resonances and flutter are aerodynamic instabilities that affect engineering structures such as civil and military aircraft wings or long-span suspension bridges [1]. A study on a lifting airfoil [2] revealed that a vibration absorber characterized by a hysteretic restoring force can enhance the pre- and post-flutter behavior of the structure. In [3] the wind-induced oscillation problem was tackled in the context of long-span suspension bridges showing that the Hopf bifurcation due to the aerodynamic effects can be considerably shifted towards higher wind speeds by the introduction of multiple arrays of hysteretic mass dampers tuned to the lowest two flexural-torsional flutter modes.

Here, an asymptotic approach based on the method of multiple scales is applied to a bridge sectional model [4] comprising a hysteretic vibration absorber to provide proper control force and moment. The absorber hysteresis is described by the Bouc-Wen differential law [5] and an optimization procedure based on the Differential Evolutionary Algorithm [6] is developed to obtain the set of absorber design parameters that lead to optimal control.

EQUATIONS OF MOTION

The equations of motion for the sectional bridge model coupled with the hysteretic absorber in the vicinity of flutter can be expressed in nondimensional form as

$$\dot{\mathbf{q}} - \mathbf{p} = \mathbf{0},$$
$$\mathbf{M}_a\dot{\mathbf{p}} + \mathbf{C}_a\mathbf{p} + \mathbf{K}_a\mathbf{q} + \mathbf{n}_k = -\epsilon^2\sigma_u(\bar{\mathbf{C}}_a\mathbf{p} + \bar{\mathbf{K}}_a\mathbf{q}) \tag{1}$$

where the vector $\mathbf{q} = (h, \alpha, x)$ lists the plunge h, the pitch angle α of the cross section and the absorber displacement x, and $\mathbf{p} = \dot{\mathbf{q}}$ represents the velocities. To study the Hopf bifurcation and the associated LCOs, the wind speed is expressed as a perturbation of the critical speed according to $U = U_c + \epsilon^2\sigma_u$, where U_c is the flutter speed and ϵ is a small nondimensional ordering parameter. The subscript a denotes the fact that the aeroelastic effects were absorbed into $\mathbf{M}_a$, $\mathbf{C}_a$ and $\mathbf{K}_a$ which thus represent the modified mass, damping and stiffness matrices, respectively, whereas $\bar{\mathbf{C}}_a$ and $\bar{\mathbf{K}}_a$ denote the perturbed damping and stiffness aerodynamic matrices. On the other hand, the vector $\mathbf{n}_k$ collects the nonlinear terms due to the bridge structural quadratic and cubic nonlinearities and also to the VA hysteresis. According to [5], the hysteresis evolution law is solved analytically, and a Taylor series expansion yields the hysteretic force as a summation of linear, quadratic and cubic terms. These hysteretic terms are piece-wise continuous along the hysteresis cycle and the subscript k denotes the branch index (see the hysteresis loop in Fig. 1). The other investigated instability is induced by vortex shedding occurring at a frequency Ω nearly twice one of the bridge frequencies with an aerodynamic forcing term expressed by $\epsilon\mathbf{f}(\alpha, \dot{h}, \dot{\alpha})\cos\Omega t$.

ASYMPTOTIC APPROACH AND OPTIMIZATION

The state-space coordinates are expressed according to the method of multiple scales as $\mathbf{q} = \sum_{i=1}^{3}\epsilon^i\mathbf{q}_i(t_0, t_2)$ and $\mathbf{p} = \sum_{i=1}^{3}\epsilon^i\mathbf{p}_i(t_0, t_2)$, where $t_0 = t$ and $t_2 = \epsilon^2 t$ are the fast and slow time scales, respectively. Under these assumptions, by collecting terms of like powers of ϵ, the typical hierarchy of perturbation problems is obtained. The unique aspect of the associated perturbation problems is the piece-wise nature of the inhomogeneous terms.

When dealing with the flutter instability, the linear problem coincides with the eigenvalue problem, which furnishes the critical flutter speed and the associated mode shape. The quadratic problem does not contain resonant terms, but only the

[*]Corresponding author. Email: walter.lacarbonara@uniroma1.it

terms due to structural and hysteretic nonlinearities. The linear and quadratic solutions, substituted into the cubic problem, give rise to the resonant terms which are removed by the solvability conditions. Since the problem is piece-wise across the four branches of the hysteresis loop, the solvability conditions are enforced via the following integrals:

$$\sum_{k=1}^{4} \int_{\tau_k}^{\tau_{k+1}} \bar{\mathbf{w}}^{\top} \mathbf{r}_3^{(k)} dt_0 = 0 \quad \text{and} \quad \sum_{k=1}^{4} \int_{\tau_k}^{\tau_{k+1}} \mathbf{w}^{\top} \mathbf{r}_3^{(k)} dt_0 = 0 \tag{2}$$

where $\mathbf{r}_3^{(k)}$ represents the right-hand-side vector of the cubic problem on the kth branch; $\mathbf{w}$ is the solution of the adjoint problem and $\bar{\mathbf{w}}$ its complex conjugate; τ_k denotes the time instant within the linear oscillation period associated with the characteristic displacements where velocity reversal or full unloading takes place. Equations (2) govern the slow modulation of the amplitude and phase of the critical mode when the wind speed is in the vicinity of the flutter condition. The modulation equations provide the bifurcation diagrams for the LCO.

An optimization procedure, based on the Differential Evolutionary Algorithm [6], is employed to determine the optimal design parameters for the hysteretic absorber that shift the flutter condition to higher speeds and further minimize the LCO amplitude. The results on the flutter response shown in Fig. 1 demonstrate that, besides shifting the flutter bifurcation to higher speeds, the introduction of hysteresis has the ability to reduce the LCO amplitude. In particular, while the linear VA reduces the LCO amplitudes by 33%, the hysteretic VA reduces the LCO amplitudes by 50%.
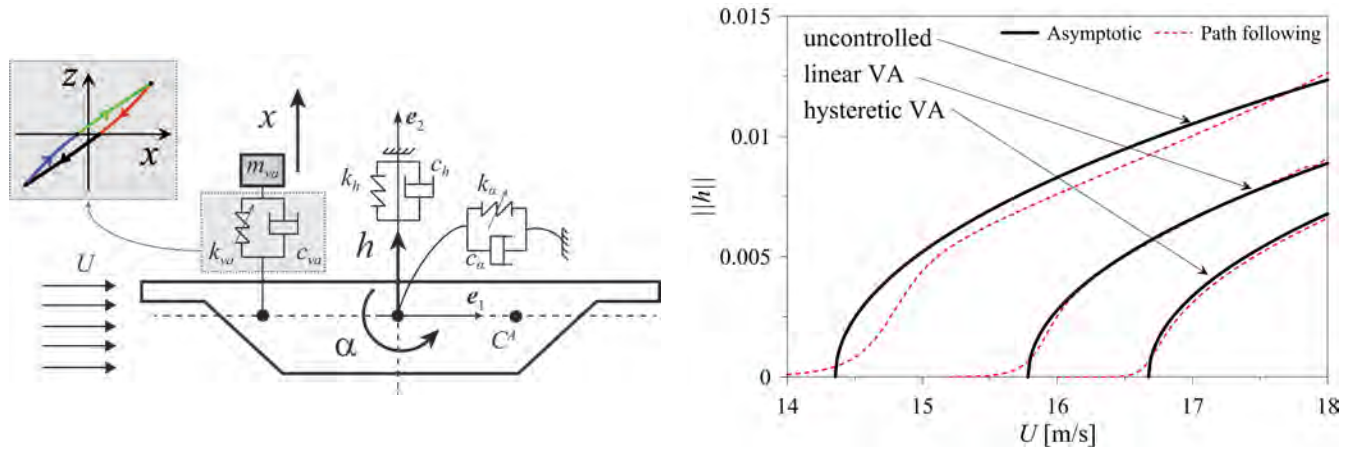
Figure 1: Left part: sectional bridge model endowed with the hysteretic vibration absorber. Inset (top left): hysteretic loop of the absorber where z represents the hysteretic part of the restoring force, the four branches are denoted by the red, black, blue and green lines. Right part: LCO bifurcation diagram of the uncontrolled system, system endowed with the linear VA or with the hysteretic VA. The red dashed lines represent the solution obtained numerically via path following, the black lines indicate the asymptotic solution.

CONCLUSIONS

The asymptotic procedure proposed here in the context of the bridge sectional model is in good agreement with the fully numerical solution. The extreme rapidity and low cost associated with the use of the asymptotic solution in computing the cost function were critical to enhance the multi-parameter optimization procedure. Moreover, the use of nonlinear hysteretic vibration absorbers leads to a considerable enhancement in the flutter oscillation mitigation task compared to linear absorbers. This is true also for vortex-induced parametric resonances.

References

[1] Lacarbonara W.: Nonlinear Structural Mechanics. Theory, Dynamical Phenomena and Modeling. Springer, New York, USA 2013.
[2] Lacarbonara W. and Cetraro M.: Flutter Control of a Lifting Surface via Visco-Hysteretic Vibration Absorbers. Int. J. of Aeronautical & Space Sci. 12:331-345, 2011.
[3] Casalotti A., Arena A., Lacarbonara W.: Mitigation of Post-Flutter Oscillations in Suspension Bridges by Hysteretic Tuned Mass Dampers. Eng. Struct. 69:62-71, 2014.
[4] Abdelkefi A., Vasconcellos R., Nayfeh A.H., Hajj M.R.: An Analytical and Experimental Investigation into Limit-Cycle Oscillations of an Aeroelastic System. Nonlinear Dyn. 71:159-173, 2013.
[5] Casalotti A. and Lacarbonara W.: Nonlinear Vibration Absorber Optimal Design via Asymptotic Approach. Procedia IUTAM 19:65–74, 2016.
[6] Storn R. and Price K.: Differential evolution - A Simple and Efficient Heuristic for Global Optimization over Continuous Spaces. J. Global Optim. 11:341-359.

DYNAMIC BEHAVIOR OF A TUNABLE MAGNETIC VIBRATION ABSORBER

Simon Benacchio[1], Arnaud Malher[1], Stefania Lo Feudo[1], Jean Boisson [*1], and C. Touzé[1]

[1]*IMSIA (Institute of Mechanical Sciences and Industrial Applications), ENSTA ParisTech - CNRS - EDF - CEA, 828 Bd des maréchaux, 91762 Palaiseau Cedex*

Summary A magnetic vibration absorber (MVA), completely relying on magnetic forces, is used to reduce the displacement of a vibrating structure. The distinctive feature of this absorber is the ability of tuning its linear stiffness together with its nonlinear cubic and quintic stiffnesses. Repulsive and corrective magnets are used to finely tune the values of these stiffness coefficients. A modelisation, relying on a multipolar expansion of the magnetic fields of each magnets, is used to predict the values of the stiffnesses from the geometry. Using only three geometrical parameters the MVA can be passively designed either as a nonlinear tuned vibration absorber (NLTVA), a nonlinear energy sink (NES), or a bi-stable absorber with negative linear stiffness.

INTRODUCTION

Due to its passive feature, the vibration mitigation of mechanical structures using vibration absorbers is an important solution for engineering issues. Linear vibration absorbers like the well-known Tuned-Mass Damper (TMD) [1, 2] have been studied for the vibration reduction of both linear undamped [3] and damped [4] primary structures (PS). However, the main drawback of the TMD is related to its narrow bandwidth of optimal control. To overcome this limitation a Nonlinear Energy Sink (NES) with an essentially nonlinear restoring force can be used. Having no natural frequency, the NES can thus adapt itself to the frequency of the PS [5, 6]. Another idea is to use the nonlinearity of the absorber in order to control the nonlinearity of the PS and has led to the concept of the nonlinear tuned vibration absorber (NLTVA). Recently, bi-stable vibration absorber devices have been investigated to make smaller the energy barrier required to activate the energy transfer between the PS and a NES [7]. If numerous experimental devices have been proposed to experiment these absorbers they are often designed for a specific application [8, 9, 10].

The proposed magnetic vibration absorber (MVA) has the ability of properly tuning its linear and nonlinear characteristics. Thus, this flexible device can be used either as an NES, an NLTVA, or a bi-stable vibration absorber, all these tunings being realized passively with a simple change in the geometry of the system. The experimental realisation of the MVA is presented in this paper. Then, preliminary results of the reduction of the PS vibration are presented when the MVA is tuned as an NLTVA, an NES and a bi-stable absorber.

THE MAGNETIC VIBRATION ABSORBER

The magnetic vibration absorber is shown in Fig. 1. It is composed of 7 permanent ring magnets. Their length, internal
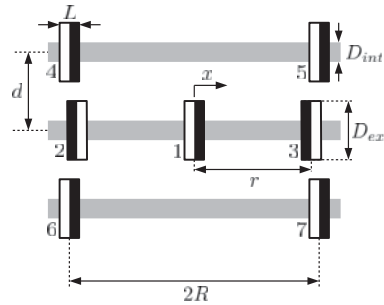
Figure 1: Diagram of the magnetic vibration absorber (MVA).

and external diameters are denoted L, D_{int} and D_{ext} respectively. Oscillating around the central position $x = 0$, the magnet 1 plays the role of the vibrating mass of the absorber. The other magnets (2, 3, 4, 5, 6 and 7) are fixed on plastic rods. The black and white parts of each magnet give the direction of their axial magnetisation. Magnets 2 and 3 are named the repulsive magnets since their magnetisation is the opposite of the magnetisation of the magnet 1. The amplitude of the repulsive force is tuned by modifying the geometric parameter r. Magnets 4, 5, 6 and 7 are named the corrective magnets since their magnetisation is the same that the magnetisation of the magnet 1. The amplitude of the corrective force is tuned by modifying

*Corresponding author. Email: jean.boisson@ensta-paristech.fr

the geometric parameters R and d. Therefore, the total force $\boldsymbol{F}_{\text{Tot}}$ applied on the mass of the MVA is tuned by the independent modifications of the geometric parameters r, R and d. Modeling the MVA using a multipolar expansion, this force can be written as

$$\boldsymbol{F}_{\text{Tot}}(x) \approx -K_1\, x - K_3\, x^3 - K_5\, x^5.$$

Modifying the geometric parameters r, R, and d, the linear, cubic and quintic stiffness terms can be tuned to change the properties of the MVA designing it as an NLTVA, an NES or a bi-stable absorber. More details about the design of the MVA can be found in [11].

VIBRATION MITIGATION

The MVA is then used to reduce the displacement of a plate selected as a PS vibrating with a large amplitude around one of its modal frequencies. Two opposite sides of the rectangular plate are clamped, whereas the other two are free. The device is attached to the PS and tuned successively as an NLTVA, an NES and a bi-stable absorber. Figure 2 shows the measured maximum displacement of the PS in each case and when the MVA is removed from the plate. These results present the effects of the linear stiffness coefficient tuning.
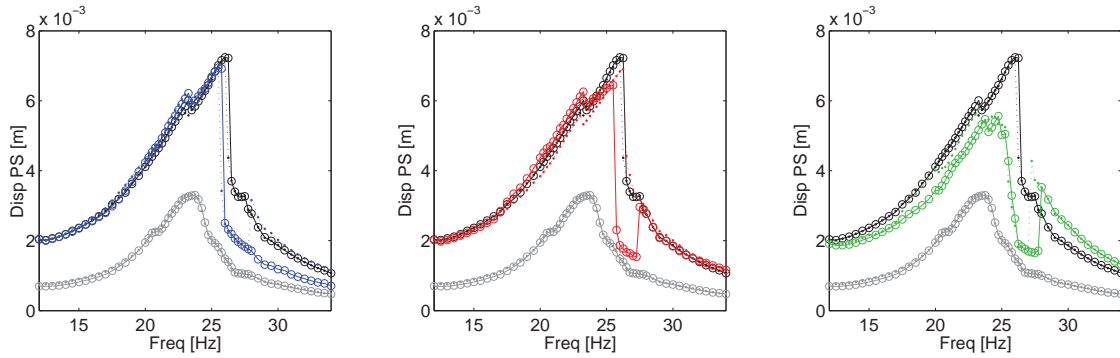
Figure 2: Maximum displacement of the primary structure without the MVA [ooo] and with the MVA tuned as an NLTVA [ooo] ($K_1 > 0$), an NES [ooo] ($K_1 \approx 0$) and a bi-stable absorber [ooo] ($K_1 < 0$). The gray circles [ooo] indicate the linear displacement of the primary structure for a lower excitation force. Circles and dots correspond to forward and backward sweeps respectively.

The measurements first show undoubtedly the effect of the vibration absorber on the nonlinear dynamics of the plate. Depending on the tuning, one can expect to control different parameters area in the frequency response curve. Current measurements are realised in order to analyze more deeply the advantages of each configurations as well as showing the best tuning that can be expected.

References

[1] Frahm H.: Device for Damping Vibrations of Bodies. US No. Patent 989958, 1909.

[2] Den Hartog J.P.: Mechanical Vibrations. McGraw-Hill, New-York, 1934.

[3] Ormondroyd J., Den Hartog J.P.: The Theory of the Dynamic Vibration Absorber. Transactions of ASME, 50:9-22, 1928.

[4] Asami T., Nishihara O., Baz A.M.: Analytical solutions to H∞ and H$_2$ optimization of dynamic vibration absorbers attached to damped linear systems. Journal of Vibration and Acoustics, 124:284-295, 2002.

[5] Gendelman o., Manevitch L.I., Vakakis A.F., Closkey R.M.: Energy pumping in nonlinear mechanical oscillators, I: dynamics of the underlying Hamiltonian systems, Journal of Applied Mechanics, 68(1):34-41, 2001.

[6] Vakakis A.F., Gendelman O.: Energy pumping in nonlinear mechanical oscillators, II: resonance capture, Journal of Applied Mechanics, 68(1):42-48, 2001.

[7] Manevitch L.I., Sigalov G., Romeo F., Bergman L.A., Vakakis A.F.: Dynamics of a Linear Oscillator Coupled to a Bistable Light Attachment: Analytical Study, J. Appl. Mech., 81(4):041011, 2013.

[8] AL-Shudeifat M.A., Wierschem N., Dane Quinn D., Vakakis A.F., Bergman L.A., Spencer Jr. B.F.: Numerical and experimental investigation of a highly effective single-sided vibro-impact non-linear energy sink for shock mitigation, International Journal of Non-Linear Mechanics, 52:96-109, 2013.

[9] Grappasonni C., Habib G., Detroux T., FengWen W., Kerschen G., Jensen J.S.: Practical design of a nonlinear tuned vibration absorber, Proceedings of the ISMA 2014 conference, 2014.

[10] Yamakawa I., Takeda S., Kojima H.: Behavior of a new type dynamic vibration absorber, Bulletin of the JSME, 20(146):947-954:, 1977.

[11] Benacchio S., Malher A., Boisson J., Touzé C.: Design of a Magnetic Vibration Absorber with Tunable Stiffnesses, Submitted to Nonlinear Dynamics.

NON-SYNCHRONOUS FREE OSCILLATIONS OF ZIEGLER'S COLUMN

Carlos Eduardo Nigro Mazzilli[1] & Stefano Lenci[2]
[1]Escola Politécnica, University of São Paulo, São Paulo, Brazil
[2]Università Politecnica delle Marche, Ancona, Italy

Summary A condition for non-synchronous free oscillations is addressed, which can be satisfied by systems with non-symmetric stiffness matrix. The dynamical response of a previously buckled Ziegler's column subjected to a follower force is looked at, leading to a high-frequency motion of the tip mass and a low-frequency motion of the mid span mass. Localization phenomenon can also take place, depending on the system initial conditions.

PROBLEM STATEMENT

In structural dynamics, the linear normal modes play a fundamental role. For such motions, all physical coordinates oscillate with the same frequency and phase, so that they simultaneously attain their maximum (minimum) values. Hence, by definition, they are synchronous modes and, for undamped systems, they are periodic too. This concept has been extended by Rosenberg [1] to nonlinear systems, through the definition of the "nonlinear normal modes" as vibrations in "unison". Shaw and Pierre [2] enlarged the meaning of nonlinear modes, defining them as motions restricted to an invariant manifold of the phase space tangent to the respective eigenplanes and containing an equilibrium point. In the general case, Shaw and Pierre's nonlinear modes are potentially non-synchronous, since they are influenced by both the displacements and the velocities, and phase differences between these two fields can happen. The consequence is that the vibration modes are not necessarily a standing wave. By the way, even linear systems with non-proportional damping can behave like that.

Yet, it is neither necessary, nor essential, to evoke the nonlinear modes to address non-synchronicity at this very moment. Indeed, it suffices focusing the linearized undamped free-vibration equation of a discrete system about an equilibrium configuration (which may, of course, require nonlinear analysis to be assessed)

$$\mathbf{M\ddot{u}} + \mathbf{Ku} = \mathbf{0} .$$ (1)

In (1), both $\mathbf{M}$ (mass matrix) and $\mathbf{K}$ (stiffness matrix) are typically symmetric and positive definite. Yet, at times, this latter can be non-symmetric (for circulatory systems, such as those with follower forces, caused by internal/external fluid flow or friction) and even non-positive definite (static instability caused by conservative non-gyroscopic or centrifugal forces, for example). Of course, $\mathbf{u}$ and $\mathbf{\ddot{u}}$ stand for the displacement and acceleration vectors with respect to the equilibrium configuration. For undamped 2DOF systems, the so-called isolated non-synchronous vibration modes are connected to its possible non-conservativity, although this is not mandatory. A necessary condition for non-synchronous harmonic response $u_i = u_i^0 \sin \omega_i t$ of a system described by (1) states that there should co-exist at least two generalized coordinates u_j and u_k, oscillating with distinct frequencies ω_j and ω_k [3]. Suppose that these frequencies are non-null

$$\omega_j^2 = \frac{K_{1j}}{M_{1j}} = ... = \frac{K_{jj}}{M_{jj}} = ... = \frac{K_{kj}}{M_{kj}} = ... = \frac{K_{Nj}}{M_{Nj}} \text{ and } \omega_k^2 = \frac{K_{1k}}{M_{1k}} = ... = \frac{K_{jk}}{M_{jk}} = ... = \frac{K_{kk}}{M_{kk}} = ... = \frac{K_{Nk}}{M_{Nk}} .$$ (2)

Hence, the condition $\omega_j \neq \omega_k$ implies that the stiffness matrix cannot be symmetric ($K_{jk} \neq K_{kj}$), assuming that the mass matrix is symmetric.

The study of Ziegler's column under follower force loading is an iconic problem to start with, since it is a simple model, yet displaying a rich dynamical behaviour. Moreover, it is a natural introduction to vibration problems in pipes carrying fluid flows. Other than flutter instability, it is seen that it can also display non-synchronous free oscillations, with characteristics of the localization phenomenon which may eventually be explored in energy harvesting applications or vibration control.

BUCKLED ZIEGLER'S COLUMN ACTED UPON BY A FOLLOWER FORCE

It is considered the Ziegler's column of Figure 1, subjected to both a conservative loading (weights mg and αmg plus the compressive vertical force F applied at the middle hinge) and a non-conservative loading (follower compressive force P applied at the free end) that supposedly causes it to buckle and a stable post-critical equilibrium configuration $(\hat{\theta}_1, \hat{\theta}_2)$ is then attained. Forces F and P are calibrated so that the system oscillates synchronously/non-synchronously about the post-critical equilibrium configuration. The post-critical equilibrium configuration must comply with

$$\hat{\theta}_1 - \delta[\Lambda_F - 1 - \alpha]\sin\hat{\theta}_1 - \frac{1}{\beta}\hat{\theta}_2 = -\Lambda_P\sin\hat{\theta}_2 \quad \text{and} \quad \hat{\theta}_2 = -\delta\alpha\beta\sin(\hat{\theta}_1 + \hat{\theta}_2)$$ (3)

---

[a] Corresponding author. Email: cenmazzi@usp.br**.**

where $\delta = \dfrac{mg\ell}{\beta k}$ and $\Lambda_F = \dfrac{F}{mg}$. The necessary condition for non-synchronicity (2) requires that:

$$\left(1 + cos\hat{\theta}_2\right)\left[1 - \delta(\Lambda_F - 1 - \alpha)cos\hat{\theta}_1 + \alpha\delta cos\left(\hat{\theta}_1 + \hat{\theta}_2\right)\right] - \delta cos\left(\hat{\theta}_1 + \hat{\theta}_2\right)\left[1 + 2\alpha\left(1 + cos\hat{\theta}_2\right)\right] = 0 \tag{4}$$

$$\Lambda_P = \frac{\left(1 + cos\hat{\theta}_2\right)}{cos\hat{\theta}_2}\left[\frac{1}{\beta} + \alpha\delta cos\left(\hat{\theta}_1 + \hat{\theta}_2\right)\right] - \alpha\delta\frac{cos\left(\hat{\theta}_1 + \hat{\theta}_2\right)}{cos\hat{\theta}_2}$$
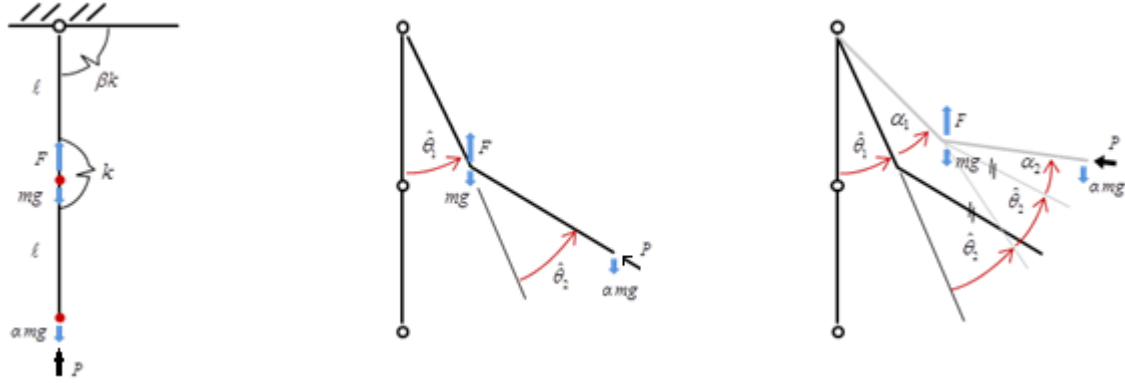
Figure 1: Buckled Ziegler's column acted upon by a follower force

For a convenient choice of parameters, such as: $m = 5kg$, $k = 100 Nm\,rad^{-1}$, $\ell = 1m$, $\alpha = 1$, $\beta = 1$, $\delta = 0.5$, $\Lambda_F = 3.26615$ and $\Lambda_P = 2.450234$, the post-critical equilibrium solution is $\hat{\theta}_1 = -0.91431$, $\hat{\theta}_2 = 0.291614$, fulfilling simultaneously conditions (3) and (4). Figure 2 displays a typical dynamical response for the system with such parameters, for a particular choice of initial conditions.
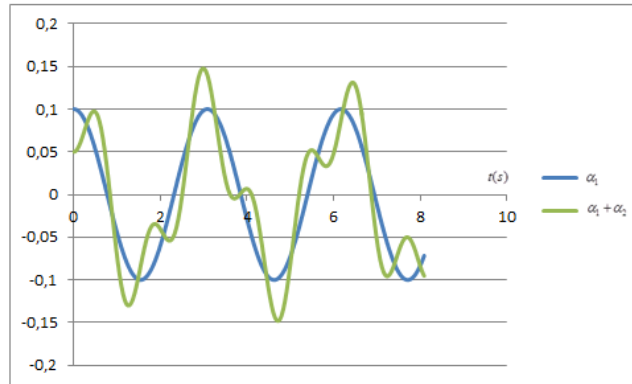
Figure 2: Example of non-synchronous motion of the masses at mid span and column tip (see Fig. 1 for the definition of α_i)

CONCLUSIONS

The tip mass can be excited by both the first ($\omega_1 = 2.03694 rads^{-1}$) and the second ($\omega_2 = 5.30312 rads^{-1}$) modes, whereas the one at mid span will not be excited by the second mode. Hence, depending on the initial conditions, the motion can be practically localized and the system energy would be concentrated in just a part of the system (possibly with large amplitude and high frequency). Both conditions can be of interest in the design of energy harvesting and vibration control systems.

References

[1] Rosenberg R. M.: The normal modes of nonlinear n-degree-of freedom systems, *J. Appl Mech* 29:7-14, 1962.
[2] Shaw S.W., Pierre C.: Non-linear normal modes and invariant manifolds, *J. Sound Vibr*, 150 (1):170-173, 1991.
[3] Lenci S., Mazzilli C.E.N.: On non-synchronous oscillations (*in preparation*), 2015.

NONLINEAR OSCILLATION OF A CIRCULAR PLATE ENERGY HARVESTER

Li-Qun Chen[1,2 a)] & Tianchen Yuan[2]

[1]*Department of Mechanics, Shanghai University, Shanghai 200444, China*
[2] *Shanghai Institute of Applied Mathematics and Mechanics, Shanghai University, Shanghai 200072, China*

Summary Nonlinear oscillation is treated for a piezoelectric vibratory energy harvester. The harvester consists of a circular composite plate with the clamped boundary, a proof mass and two steel rings. The harvesting system is analytically modeled, numerically simulated, and experimentally tested. A lumped parameter model of the harvester is established with its parameters identified from the experimental data. The equivalent capacitance and the electromechanical coupling coefficient are analytically determined. A technique is proposed to identify the electrical parameter. A fifth polynomial is employed to approximate the nonlinear restoring force. The measured response can be approximately described by the nonlinear lumped model. Both the experimental and the numerical results demonstrate that the circular plate harvester has soft characteristics under low excitation and both hard characteristics and soft characteristics under high excitation. The characteristics can be used to broaden the working bandwidth of the harvester and thus to enhance the energy harvesting.

INTRODUCTION

Vibratory energy harvesting from the environment is now an active and promising research field. Nonlinearities can be employed to broaden working frequency bandwidth of harvesters [1,2]. The circular plate structure has an axial symmetric structure which is easy to be processed and thus attracts more and more attentions.

MODELING AND PARAMETER IDENTIFICATION

As shown in Fig.1, the piezoelectric composite plate is fabricated from a brass plate (R_b=25 mm and h_b=0.2 mm) and two piezoelectric plates (R_p=25 mm and h_p=0.2 mm). The brass plate (2.5 mm) is clamped by 2 steel rings (R_s=22.5).
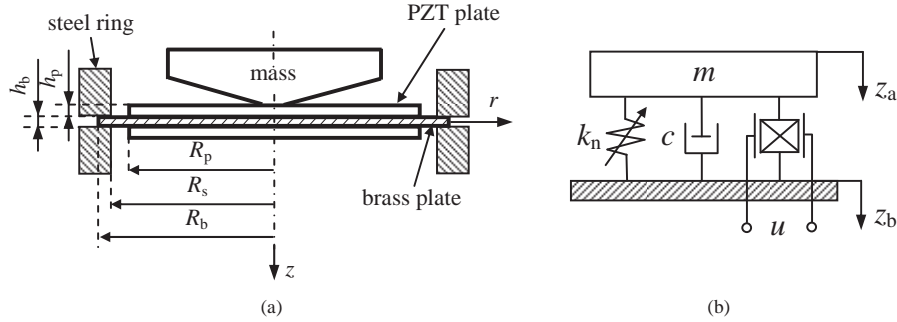
Figure 1 (a) Cutaway view of the circular plate harvester. (b) Lumped-parameter model.

The lumped-parameter model is governed by a set of equation with respect to $z(t)=z_a(t)-z_b(t)$ and u as

$$m\ddot{z} + c\dot{z} + \left(k_1 z + k_2 z^2 + k_3 z^3 + k_4 z^4 + k_5 z^5\right) + \eta u = -m\ddot{z}_b, \quad -\eta R_L \dot{z} + C_p R_L \dot{u} + u = 0 \tag{1}$$

where, R_L is the load resistance, and the fifth polynomial approximates the restoring force. Damping coefficient c and k_i (i=1,…,5) can be identified from measured accelerations and its integration filtered by the empirical mode decomposition. The electromechanical coupling coefficient and the equivalent capacitance can be derived from the elasticity solution as

$$\eta = \frac{4\pi R_p^2 d_{zr}\left(h_p + h_b\right)\gamma^2 \left(\ln R_p - \ln R_s\right)}{R_s^2 s_{rr}^E \left(1-\mu\right)}, \quad C_p = \pi R_p^2 \frac{\varepsilon_{zz}^T s_{rr}^E\left(1-\mu\right) - 2d_{zr}^2}{s_{rr}^E\left(1-\mu\right)h_p} \tag{2}$$

where μ is PZT Poisson's ratio, ε_{zz}^T is the permittivity, ε_{zz}^T is the elastic compliances constant, and d_{zr} is the piezoelectric constant. Based on the jth experiment with excitation frequency ω_j, load resistance R_{Lj}, mass acceleration amplitude A_j, and output voltage amplitude U_{ej}, N times of experiments yield the parameter identification via the least square method

$$\min \sum_{j=1}^{N} \left[U_j - U_{ej}\right]^2, U_j = \frac{\eta R_{Lj} A_j}{\omega_j \sqrt{\left(C_p R_{Lj}\omega_j\right)^2 + 1}} \tag{3}$$

The theoretical and the identification results as well as the theoretical results of a beam [18] are listed in table 1.

Table 1. Electromechanical coupling coefficient and equivalent capacitance

parameter	unit	experimental results	theoretical results	cantilevered beam [3]
η	N/V	0.0108	0.0115	0.0037
C_p	nF	65.5	62.98	58.14

---

a) Corresponding author. Email: lqchen@staff.shu.edu.cn.

The beam is with larger area of piezoelectric bimorph and thicker piezoelectric layers than the plate, where the electromechanical coupling coefficient of the beam is much smaller than that of the plate. Thus a circular plate has the much high electromechanical coupling coefficient than a beam in similar sizes, which is beneficial to energy harvesting.

AMPLITUDE-FREQUENCY RESPONSE

The amplitude-frequency responses are determined by the experiment and the simulations. Figures 2 and 3 show the voltage response under 1.5 g and 2 g excitation, respectively. The results show softening characteristic in Fig. 2 and both softening and hardening nonlinearities in Fig. 3. In Fig. 3 the curve bends to the right with the jumping both in the experiment and the simulation, and at the left side of the resonance peak, a slight jump resulted from the softening can be found. The possible reason for coexistence of the soft and the hard characteristics lies in the expression of the restoring force, in which the coefficient of the quintic term is positive, and that of the cubic term is negative.
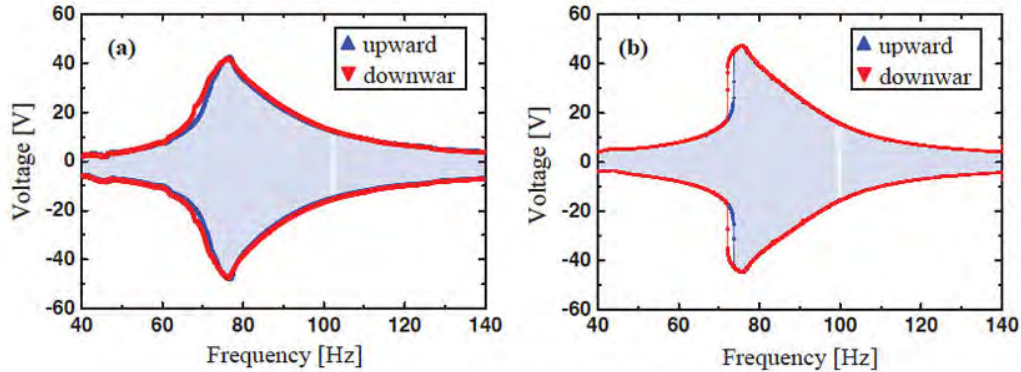
Figure 2 Voltage responses under 1.5g excitation: (a) Experiment and (b) Simulation.
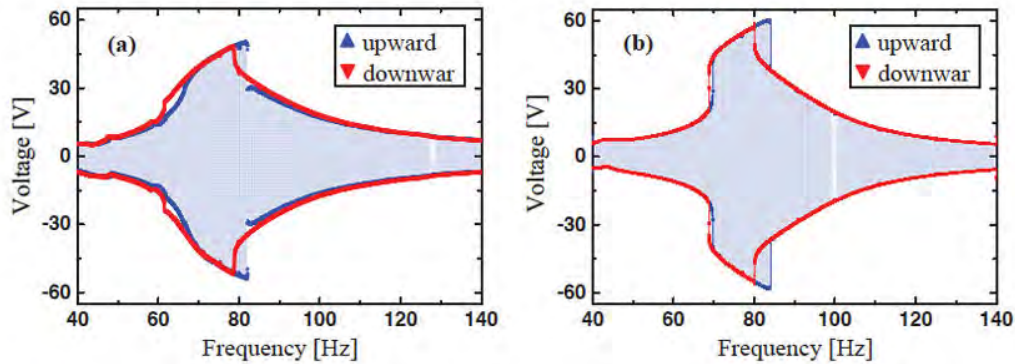
CONCLUSIONS

The experimental and the numerical investigations yield the following conclusions: (1) the circular plate harvester has a higher electromechanical coupling coefficient than the cantilevered beam system, which is beneficial to energy harvesting; (2) the proposed technique to identify the electrical parameter is effective; (3) the experiment and the simulation show that the harvester has softening nonlinearity under small excitation, which may be caused by the negative cubic term in the nonlinear restoring force function; (4) both hardening nonlinearity and softening nonlinearity are discovered when the harvester is subjected to sufficient large excitation, which can be used to broaden the bandwidth of the harvester.

References

[1] Daqaq M. F., Masana R., Erturk A., Quinn D. D.: On the Role of Nonlinearities in Vibratory Energy Harvesting. *Appl. Mech. Rev.* **66**: 040801, 2014.
[2] Chen L. Q., Jiang W. A.: Internal Resonance Energy Harvesting. *J. Appl. Mech.* **82**: 031004, 2015.
[3] Erturk G., Inman D. J.: A Distributed Parameter Electromechanical Model for Cantilevered Piezoelectric Energy Harvesters. *J. Vib. Acoust.* **130**: 041002, 2008.

NON-LINEAR DYNAMICS OF A PENDULUM VIBRATION ABSORBER WITH A MAGLEV HARVESTER

Krzysztof Kecik [*1], Andrzej Mitura[1], Jerzy Warminski[1], and Stefano Lenci[2]

[1]*Department of Applied Mechanics , Lublin University of Technology, Lublin, Poland*
[2]*Department of Civil and Building Engineering and Architecture , Polytechnic University of Marche, Ancona, Italy*

Summary This paper describes and analyse a novel harvester-absorber device that uses magnetic levitation (maglev) in order to recover energy. The energy harvester is mounted in a pendulum which plays a dynamic absorber role. The non-linearity of the magnetic field suspension exhibits a hardening Duffing's characteristics. We propose a new model of an electromechanical coupling which depends on a magnet position in a coil. Theoretical investigations are followed by a series of experimental tests that validate the theoretical predictions and allow us to obtain a final model of optimized harvester.

INTRODUCTION

Energy harvesting is promising research area as demands for renewable energy sources increase. Electromagnetic energy harvesters (EEH) are based on Faradays law of induction - the property that a change in the magnetic flux of a circuit will result in the induction of an electromotive force. Maglev systems are electromechanical devices that suspend ferromagnetic materials using electromagnetism, and are characterized by non-linear dynamics, instability and are described by highly non-linear differential equations.

HARVESTER-ABSORBER MODEL

Energy harvesting under investigation is based on motion of the autoparametric vibration absorber. The model of a harvester-absorber system (HAS) consists of the main mass (oscillator) with the attached the pendulum vibration absorber. The pendulum is made of nonmagnetic tube with two magnets fixed on the ends, which ensure the levitation of a third moving magnet (Fig.1c). A coil of wire is wrapped around the outside of the pendulum tube (Fig.1d). While, the moving magnet oscillate it induces the electromotive force. The view of the laboratory rig is presented in Fig.1b. The system works as the dynamical vibration absorber with the energy recovery at the same time.
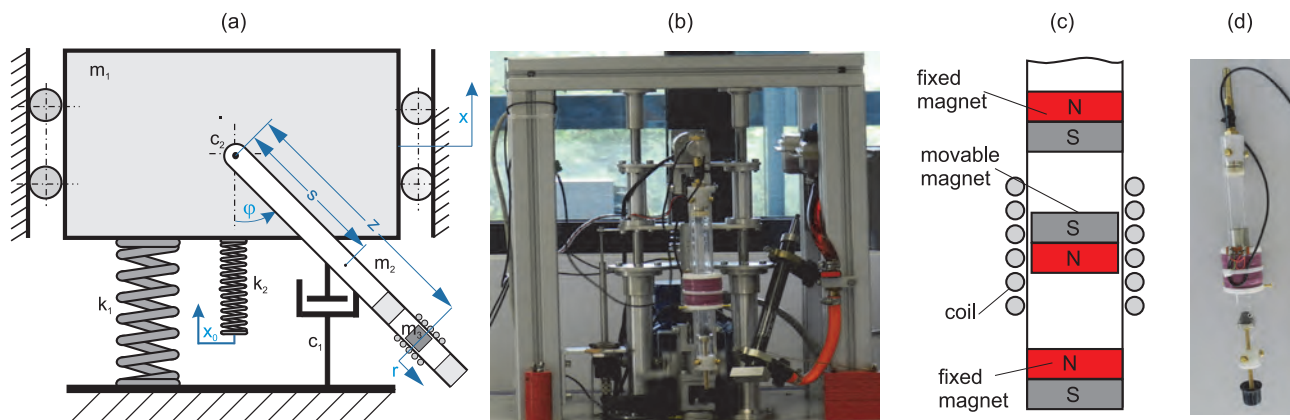
Figure 1: Model of harvester absorption system: a physical model (a), laboratory rig (b), scheme (c) and experimental device of the maglev system (d)

A schematic diagram of the proposed model is shown in Fig.1a. This is a coupled three mechanical and one electrical degrees of freedom system. The mass m_1, spring k_1 and damping component c_1, are connected to the base. The pendulum m_2 with magnet m_3 creates the vibration absorber engaged with oscillator motion, which is kinematically excited by the spring k_2 in the vertical direction. If the pendulum swings, then amplitude of the oscillator can be reduced.

---

*Corresponding author. Email: k.kecik@pollub.pl

EQUATION OF MOTION AND MAGLEV CHARACTERISTICS

The governing equations of the non-linear harvester-absorber system derived from the Lagrange's equations of the second kind have the form

$$(m_1 + m_2 + m_3)\ddot{x} + (m_2 s + m_3(z+r))[\ddot{\varphi}sin(\varphi) + \dot{\varphi}^2 cos(\varphi)] + m_3(2\dot{r}\dot{\varphi}sin(\varphi) - \ddot{r}cos(\varphi)) + c_1\dot{x} + k_1 x = k_2 x_0, \quad (1)$$

$$(I_0 + m_3(z+r)^2)\ddot{\varphi} + (\ddot{x}+g)[m_2 s + m_3(z+r)]sin(\varphi) + 2m_3\dot{\varphi}\dot{r}(z+r) + c_2\dot{\varphi} = 0, \quad (2)$$

$$m_3\ddot{r} - m_3[\ddot{x}cos(\varphi) + \dot{\varphi}^2(z+r)] - m_3 g cos(\varphi) + F(r) + \alpha(r)i = 0, \quad (3)$$

$$L\dot{i} + R_T i - \alpha(r)\dot{r} = 0. \quad (4)$$

The first three equation (1)-(3) describe motion of mechanical parts (i.e. oscillator, pendulum and magnet), while the last equation (4) characterizes electrical circuit obtained by applying Kirchoffs law. The i is the electrical current, R_T is the total resistance (internal coil and external load resistances), and $\alpha(r)$ means the electromechanical coupling coefficient.

The magnetic restoring levitation force $F(r)$, given by the sum of the repulsive forces acting on the top and bottom magnets, leads to the the form of hardening Duffing's characteristic $F(r) = k_3 r + k_4 r^3$, where k_3 and k_4 are estimated experimentally (see Fig.2a). The changes in the magnets separation cause alter stiffness leading to resonance [1]. For small values of relative displacements r of the moving magnet, the levitation suspension can be reduced to a linear problem.
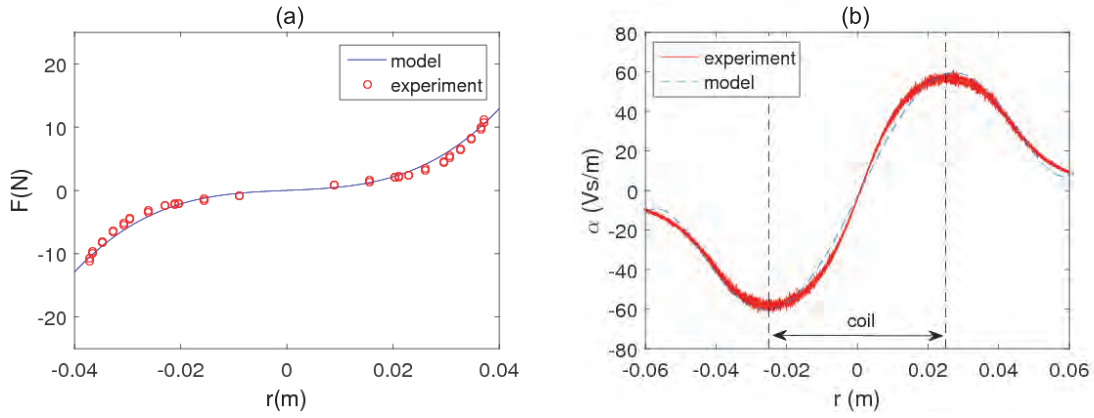
Figure 2: The force displacement characteristic (a), and electromechanical coupling coefficient vs. magnet's position for the magnet velocity $v = 0.7 m/min$ (b).

Usually, in literature, the coupling coefficient (α) is constant [1, 2], assuming the magnetic flux density as uniform. The experimental investigations show that α strongly depends on the magnet position in the coil (Fig.2b). This is due to the fact, that magnetic flux density depends on the separation distance between the magnet and the coil. We propose a five-degree polynomial function to describe coupling coefficient $\alpha(r) = \sum_{n=0}^{5} \alpha_n r^n$, where α_n are coefficients computed in order to fit the experimentally determined characteristic.

CONCLUSIONS

The design and analysis of a novel energy harvesting device that uses maglev to produce energy is presented in the paper. The magnetic suspension leads to the Duffing's type equation. The coupling coefficient strongly depends on the magnet's position (but does depend on velocity) and has sinusoidal form. The highest values of α occurs at the coil ends. The system is strongly non-linear producing several interesting phenomena, including regions of multiple solutions and chaotic behavior.

References

[1] Mann B. P., Sims N. D.: Energy harvesting from the nonlinear oscillations of magnetic levitation. J. Sound Vib 319:515530, 2009.
[2] Olaru R., Gherca R., Petrescu C.: Analysis and design of a vibration energy Harvester using permanent magnet. Rev. Roum. Sci. Techn. Electrotechn. et Energ.:59(2):131140, 2014.

POSSIBILITY OF ENERGY EXTRACTION FROM NOISE
UNDER STOCHASTIC RESONANCE

Madoka Kubota, Ryo Takahashi,* and Takashi Hikihara

Department of Electrical Engineering, Kyoto University, Katsura, Nishikyo, Kyoto 615-8510, Japan

Summary Noise must be restrained at sensing and data processing. However, in nature, noise inevitably appears through energy spread surrounding us. From a viewpoint of energy harvesting, it has been shown that resonators can absorb energy from the excitation around each resonant frequency. In the sinusoidal vibration, the energy exchange depends on the on-site resonance and inter-cite phase between resonators and exciters. The simple noise with finite number of frequencies causes the difficulty of energy extraction. This paper discusses the stochastic resonance, when unidirectional energy flow works for energy harvesting.

STOCHASTIC RESONANCE AND EFFECT OF NOISE

Stochastic Resonance (SR) is known as a phenomenon in which a signal is enhanced by noise of moderate strength. As an example, here consider the following system,

$$m\ddot{x} = -m\gamma\dot{x} - \frac{\mathrm{d}U}{\mathrm{d}x} + h\cos\Omega t + R(t), \quad U(x) = \frac{1}{4}x^4 - \frac{1}{2}x^2. \tag{1}$$

Where m denotes mass of a particle, x displacement of the free particle, γ damping constant, $h\cos\Omega t$ sinusoidal external force, and $U(x)$ bistable potential. ($\dot{}$) is time differential $\mathrm{d}/\mathrm{d}t$. Assuming the sinusoidal external force $h\cos\Omega t$ changes relatively slow to noise $R(t)$, which is the zero-mean white Gaussian noise of auto-correlation function:

$$\langle R(t)R(t+\Delta t)\rangle = 2\gamma mkT\delta(\Delta t). \tag{2}$$

Where k denotes Boltzmann constant and T noise temperature. $\langle\ \rangle$ shows the operation of ensemble average. The effect of noise with sinusoidal external forcing is given by the following potential:

$$V(x) = \frac{1}{4}x^4 - \frac{1}{2}x^2 - xh\cos\Omega t. \tag{3}$$

Depending on the frequency of sinusoidal excitation, the noise response shows various features. The faster frequency than a certain frequency Ω_0, the lower probability of the stochastic switching. (see Fig.1). Ω_0 is obtained by Kramers rate [1]:

$$\Omega_0/\pi = W/2. \tag{4}$$
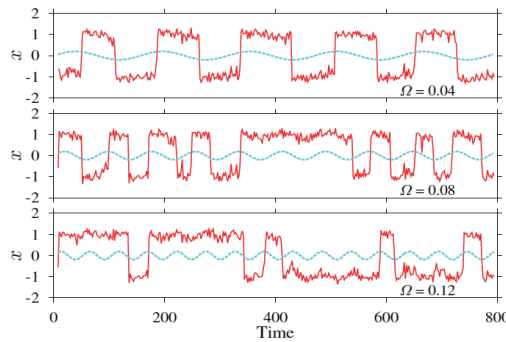
Figure 1: Response depending on Ω with $kT = 0.07$ and $h = 0.20$ kept constant; 0.04 (upper), 0.08 (middle), and 0.12 (bottom). Blue broken curve draws the sinusoidal force $h\cos\Omega t$.

The rate implies the duration required for transition from one state to the other in the bistable potential wells. The rate increases with the noise intensity kT and decreases with the potential barrier U [1]. It corresponds to the mechanical transition probability depending on kT [2].

*Corresponding author. Email: takahashi.ryo.2n@kyoto-u.ac.jp

EXTRACTION OF ENERGY FROM NOISE

The amplitude of displacement x, the velocity of displacement $\dot{x}$ and their power spectrum are direct input to the transducer from mechanical energy to electrical energy at harvesting. Electrically potential will not generate the energy flow between resonators, so that the velocity is focused. In the sinusoidal vibrations, the velocity keeps the phase shift at $\pi/2$ to the displacement. Figure 2 is the displacement of resonator and the power spectrum. It shows the clear enhancement of power from input because of stochastic resonance. However, under the long-term free vibration with noise, the power will finally converge one of balanced states between resonators. Therefore it is inevitable to push the range of power spectrum narrower for producing the energy flow from the displacement [3]. This requests the resonator and the attached transducer to match the mechanical to electrical impedances and vice versa.

The energy exchange between resonators is
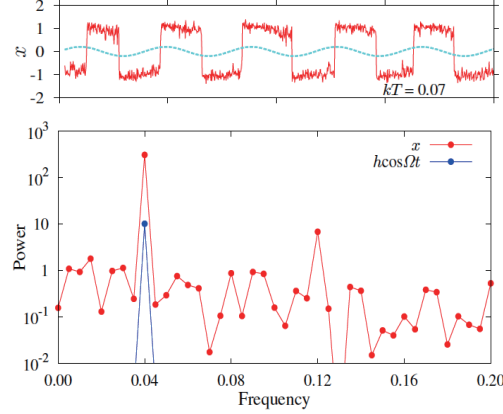
Figure 2: Displacement x and the power spectrum with sinusoidal force $h\cos\Omega t$ (blue broken line) under the noise intensity $kT = 0.07$, $h = 0.20$, and $\Omega = 0.04$.

CONCLUSIONS

This paper began to discuss the possibility of energy extraction from noise through stochastic resonance. The concept is not established but includes the general directions of research including power exchange between harmonic generators like a synchronous generator. The research on energy extractions form noise will be a rich research seed not only in nonlinear dynamics but also in applications of nonlinear characteristics [4].

References

[1] P. Hänggi, P. Talkner, and M. Borkovec, Reaction-rate theory: fifty years after Kramers, Reviews of Modern Physics, 62 (2), 251 (1990).

[2] M. Kubota, R. Takahashi, and T. Hikihara, Active and Reactive Power in Stochastic Resonance for Energy Harvesting. IEICE Transactions 98-A(7): 1537-1539 (2015).

[3] Madoka Kubota, Energy Harvesting Characteristics of Nonlinear Oscillators under Excitation, PhD dissertation, Kyoto University (2015).

[4] B. Kim, V. Putkaradze, and T. Hikihara, Manipulation of single atoms by atomic force microscope as a resonance effect, Phys. Rev. Lett. 102, 215502 (2009).

HARDENING SOFTENING BEHAVIOR OF ANTIRESONANCE FOR NON LINEAR TORSIONAL VIBRATION ABSORBERS

Alexandre Renault[1,2], Olivier Thomas [*1], Hervé Mahé[2], and Yannick Lefebvre[2]

[1]*Arts et Métiers ParisTech, LSIS UMR CNRS 7296, 8 bd. Louis XIV 59046 Lille, France*
[2] *Valeo Transmissions, Centre d'Étude des Produits Nouveaux Espace Industriel Nord, Route de Poulainville, 80009 Amiens Cedex 1, France*

Summary We address non linear torsional vibration absorbers (TVA), used in rotating machinery to counteract irregularities of rotation at a some order of the engine speed of rotation. The TVA is analogous to a tuned mass damper (TMD), tuned on the desired order. It exhibits non-linearities of various natures which affect resonance and antiresonance frequencies at large amplitude of motion, which consequently causes the detuning of the system from the targetted order. This study focuses on some non linear systems (several TVA designs and a more general Duffing like system) to study the impact of non-linearities on the hardening / softening behavior of antiresonances. Non linear solutions are obtained by a numerical continuation procedure coupled with the harmonic balance method to follow periodic solutions in forced steady-state. Moreover, we propose an original direct antiresonance continuation method for undamped systems.

INTRODUCTION
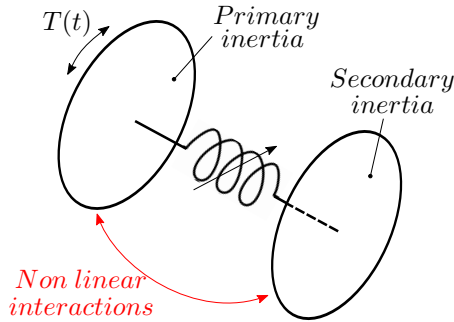
Figure 1: TVA scheme

Non linear torsional vibration absorber (TVA) is used in rotating machinery to counteract irregularities of rotation, called "acyclisms", at a some order of the engine speed of rotation. It is compose of a primary and secondary inertia and acts as the classical tuned mass damper (TMD). It is tuned on the desired engine order. In practice, the secondary inertia represents a mass subjected to move in a particular path on the primary inertia which is linked to the rotating assembly. However the TVA includes strong non-linearities. Geometric non-linearities and those due to Coriolis effect, intrinsic to rotating articulated systems. They cause the detuning of the TVA and the shifting of the operating order of TVA (an antiresonance of the whole system) from the targeted engine order. Knowledge of operating point behavior of the device is therefore essential to ensure optimal acyclisms filtering. This study focuses on tow points. First, several non linear systems, including torsional and translational systems, are studied to highlight how the hardening / softening behavior is modified by non-linearities. Non linear frequency responses in steady state are obtained by numerical continuation procedure, the harmonic balance method (HBM) [3] coupled with the asymptotic numerical method (ANM) [1], which leads to a fast and robust algorithm. Secondly, we propose an original direct antiresonance continuation method for undamped systems.

MODELLING

The equations of motion of the TVA can be written in general following form :

$$\boldsymbol{M}(\boldsymbol{x})\ddot{\boldsymbol{x}} + \boldsymbol{f_{in}}(\boldsymbol{x}, \dot{\boldsymbol{x}}) + \boldsymbol{C}\dot{\boldsymbol{x}} + \boldsymbol{f_{int}}(\boldsymbol{x}) = \boldsymbol{F}\cos(\omega t), \tag{1}$$

where $\boldsymbol{x}$ is the vector of unknowns. $\boldsymbol{M}(\boldsymbol{x})$ is the mass matrix and depends on $\boldsymbol{x}$. $\boldsymbol{C}$ is the damping matrix. $\boldsymbol{f_{in}}(\boldsymbol{x}, \dot{\boldsymbol{x}})$ is the inertial forces vector, including Coriolis terms, and depends on $\boldsymbol{x}$ and $\dot{\boldsymbol{x}}$. $\boldsymbol{f_{int}}(\boldsymbol{x})$ is the internal forces vector and depends on $\boldsymbol{x}$. Here, because only one oscillator is forced, the external forces vector is $\boldsymbol{F} = [0 \; \cdots \; f \; \cdots \; 0]$ where f is the amplitude of excitation of the forced oscillator. Assuming a periodic solution of (1), the vector of unknowns is expanded in truncated Fourier series :

$$\boldsymbol{x}(t) = \boldsymbol{x_0} + \sum_{i=0}^{H} \boldsymbol{x_{ci}}\cos(i\omega t) + \boldsymbol{x_{si}}\sin(i\omega t). \tag{2}$$

Then substituting (2) into (1) and applying HBM, we obtain a system of algebraic equations relating $\boldsymbol{x_0}$, $\boldsymbol{x_{ci}}$, $\boldsymbol{x_{si}}$, ω and f. The accuracy of the periodic solution depends on H, the number of harmonics retains on (2). The final system to solve can be written :

$$\boldsymbol{R}(\boldsymbol{U}, w, f) = 0. \tag{3}$$

*Corresponding author. Email: olivier.thomas@ensam.eu

Where $U = [x_0\ x_{ci}\ x_{si}\ ...\ x_{cH}\ x_{sH}]$. Finally, (3) is solved by an asymptotic numerical method, for which a quadratic recast of $R(U, \omega, f)$ is convenient [2]. In practice, the software Manlab 2.0 is used [4]. Unlike to predictor-corrector algorithms, where the solution is computed point by point, ANM adopts a piecewise continuous representation of the solution using a power series expansion of the pseudo arc length along the branch of solution.

ANTIRESONANCE CONTINUATION

Standard continuation procedure consist in considering ω and f as continuation parameters and compute the solutions with respect to one of them in forced vibration [2]. In free vibration ($f = 0$), the oscillation frequency can also be computed as a function of the amplitude, obtaining so-called backbone curves. In this case, the system has to be conservative so that periodic solutions are obtained and damping must be cancelled ($C = 0$)[5]. Here, we propose an original method to perform non linear antiresonance continuation, i.e. the computation of the antiresonance frequency as a function of the amplitude of forcing. Unlike free oscillations continuation, the system has to be forced. For a linear system, an antiresonance occurs only for undamped systems, for which the response of one of the unknowns is strictly zero, $x_i(t) = 0\ \forall t$ at a given frequency, x_i being the i-th component of x. If the system shows non-linearities, the antiresonance is not strict and only some harmonics of $x_i(t)$ can be set to zero, whereas the others are non zero. The antiresonance continuation is obtained by solving (3) with ω and f left free and by adding an additional condition: here the first harmonic of a given unknown is set to zero.

RESULTS
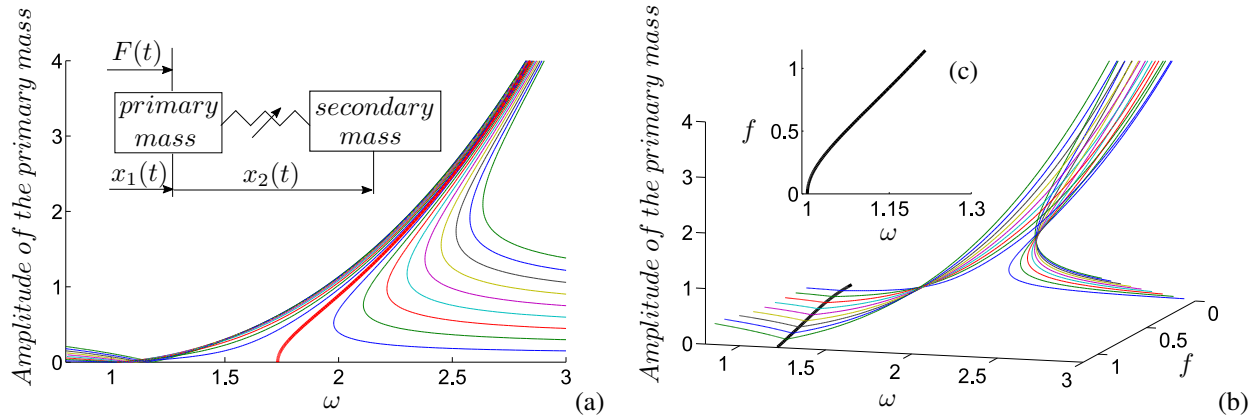
Figure 2: Frequency responses of the non linear TMD for several amplitudes of excitation (a) and antiresonance continuation (black bold line) (b)

Here, we consider a free-free non linear TMD. The equations of motion can be written :

$$\begin{cases} \ddot{x}_1 (m_1 + m_2) + \ddot{x}_2 m_2 = f \cos(\omega t), & \text{(4a)} \\ \ddot{x}_1 m_2 + \ddot{x}_2 m_2 + k x_2 + \gamma x_2^3 = 0, & \text{(4b)} \end{cases}$$

where γ and k are the non linear and linear stiffness constants, respectively. Figure 2(a) shows the frequency responses of the first harmonic of the primary mass, subjected to an harmonic forcing, for several amplitudes of excitation f. The system exhibits a hardening behavior due to the positive non linear stiffness constant. The backbone curve (red bold line), represents the oscillation frequency in free vibration. The antiresonance continuation can be viewed on the three dimensions representation, on the figure 2(b), and also on the plane (ω,f), on the figure 2(c). This procedure is very useful to accurately predict the detuning with respect to the amplitude of excitation. Moreover, it avoids redundant frequency responses simulations.

References

[1] Cochelin B. A path-following technique via an asymptotic-numerical method. *Computers & Structures*, 53(5):1181 – 1192, 1994.
[2] Cochelin B. and Vergez C. A high order purely frequency-based harmonic balance formulation for continuation of periodic solutions. *Journal of Sound and Vibration*, 324(12):243 – 262, 2009.
[3] Ali H Nayfeh and Dean T Mook. *Nonlinear oscillations*. John Wiley & Sons, 1979.
[4] Arquier R., Karkar S., Lazarus A., Thomas O., Vergez C., and Cochelin B. Manlab2.0 : an interactive path-following and bifurcation analysis software. *Tech. rep., Laboratoire de Mécanique et d'Acoustique, CNRS*.
[5] Karkar S., Cochelin B., and Vergez C. A comparative study of the harmonic balance method and the orthogonal collocation method on stiff nonlinear systems. *Journal of Sound and Vibration*, 333(12):2554 – 2567, 2014.

STRONGLY NONLINEAR RESONANCE DYNAMICS OF QUASI-ONE-DIMENSIONAL FINITE OSCILLATORY CHAINS

Leonid Manevitch[1a)], Irina Koroleva (Kikot')[1], Valeri Smirnov[1]

[1]*Semenov Institute of Chemical Physics of Russian Academy of Sciences, Moscow, Russia*

Summary We present an extension of recently developed approach to stationary and non-stationary resonance dynamics of strongly nonlinear two degree of freedom (2DoF) systems to finite strongly nonlinear oscillatory chains (strong nonlinearity implies impossibility to use the linearized equations of motion even as a starting point of dynamic analysis). The proposed extension allows revealing new nonlinear effects in series of widely used mechanical and physical systems. There are in particular: i) breaking the symmetry caused by instability of almost all nonlinear normal modes (NNMs) and appearance of stable elliptic modes (EMs) in the initially un-stretched strings and membranes carrying discrete masses; ii) mobile breathers excitation by localized initial pulse in the un-stretched membrane; iii) efficient inter-cluster energy exchange and transition to energy localization in the un-stretched membrane and in the finite system of weakly coupled pendulums. The applications of revealed strongly nonlinear effects to solution of significant mechanical and physical problems are discussed.

NONLINEAR EFFECTS

The resonance processes are responsible for energy exchange, localization and transfer in many significant mechanical and physical systems. Among them, there are un-stretched strings and membranes carrying discrete masses; arrays of Josephson junctions, ferromagnetic chains and oligomer crystals (all three latter ones can be modelled by the finite system of weakly coupled pendulums). We consider the case of strong nonlinearity when the equations of motion may not be linearized even as a starting point of dynamic analysis. Our new approach which was examined in the case of 2DoF models implies a closeness of the system to 1:1 internal resonance only. We describe briefly the revealed strongly nonlinear effects which include such phenomena as symmetry breaking because of instability and bifurcation of almost all NNMs, formation of mobile transversal breathers, transition from intense energy exchange to energy localization, and appearance of a chaos accompanying such transition.

The symmetry breaking caused by instability of NNMs in un-stretched string and membrane. The simplest model of such system is presented in Fig.1.
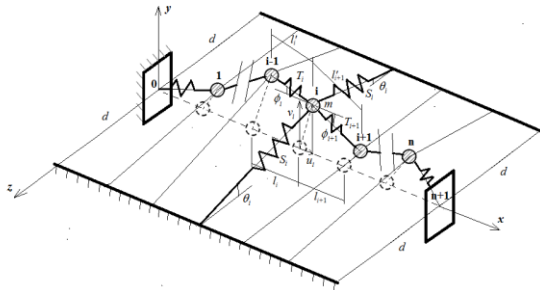
Fig. 1. The model of grounded unstretched string (symplest model of unstretched membrane) carrying n particles and possessing linear interchain and lateral stiffneseses (for the sake of clarity only the lateral spring supporting the $i-th$ particle is depicted). If the lateral springs are absent one deals with un-stretched string.

As it is shown by us recently ([1],[2],[4]) the asymptotic equations of motion in the case of dominating transversal motion can be written as

$$\frac{d^2 v_j}{d\tau^2} + \frac{1}{\mu}v_j^3 + \frac{1}{2(N+1)}\left(2v_j - v_{j-1} - v_{j+1}\right)\sum_{s=0}^{N}(v_{s+1} - v_s)^2 = 0, j = 1, N, v_0 = v_{N+1} = 0,$$

where v_j is normalized transversal displacement of j-th oscillator, N is a number of the oscillators. These equations admit N exact solutions for NNMs: $v_j(t) = A_k(t)\sin\frac{\pi k j}{N+1}$ for k-th NNM, $k=1,...,N$. The direct analytical study reveals instability of all NNMs except the mode with highest wave number. The result of this instability can be identified as uni-directional energy flow from given NNM to those with larger wave numbers (an inverse energy flow is not observed) (fig. 2). This strongly nonlinear effect is illustrated below on the example of non-grounded un-stretched string carrying 10 particles.

The highly non-stationary dynamics of the system can be adequately described in terms of Limiting Phase Trajectories (LPTs) corresponding to maximum possible energy exchange between different parts (clusters) of the string. This process is shown in Fig.3 for the same system. For grounded string (membrane) a threshold from complete inter-cluster energy exchange to energy localization on the initially excited cluster is (Fig.4) revealed.

[a)]Corresponding author. Email: manevitchleonid3@gmail.com
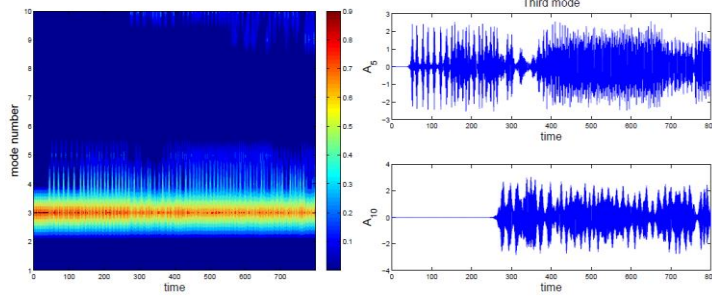
Fig. 2. Instability of third NNMs and uni-directional energy flow to fifth and tenth NNMs.
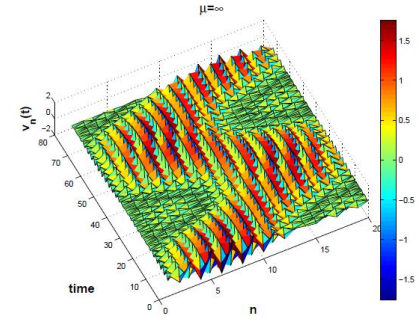
Fig. 3. Energy exchange between two parts of oscillatory chain.

System of weakly coupled pendulums

Similar transition can be observed in other significant strongly nonlinear model which is a finite system of N weakly coupled pendulums (without any restrictions on the amplitudes of oscillation). Behavior of this system in the vicinity of internal 1:1 resonance in terms of cluster variables $\{\chi_1, \chi_2\}$ can be described by complex equations (derived for parricular case of 2DoF model in [3]):

$$i\partial_{\tau_1}\chi_j - \mu\frac{\omega}{2}\chi_j + \frac{\beta}{\omega}\sin^2\kappa\left(\chi_j - \chi_{3-j}\right) + \mu\Sigma\left(\frac{\psi_k f_{j,k}}{\sqrt{2\omega}|\psi_k|}J_1\left[\sqrt{\frac{2}{\omega}}|\psi_k|\right]\right) = 0, j = 1,2$$

where ω is a resonant frequency, β is a coupling parameter, $k=\pi/N$, J_1 – modified Bessel function of 1st kind, $\psi_k = \chi_1 f_{1,k} + \chi_2 f_{2,k};\ f_{j,k} = 1 + (-1)^{3-j}(\sin\kappa k + \cos\kappa k)$. The inter-cluster energy exchange is similar to that presented in Fig.3. The transition to energy localization is illustrated in Fig.5.
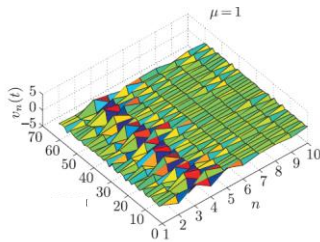
Fig. 4. Localization of the displacement (leading to energy localization) on the initially excited part of the grounded string in the presence of grounding supports.
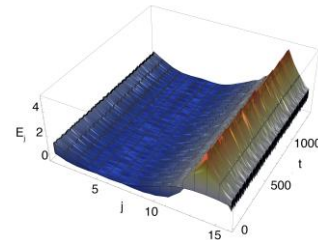
Fig. 5. Energy distribution along the chain of pendulums after transition to energy localization. Amplitude of the pendula oscillation $Q=\pi/2$.

CONCLUDING NOTES

The analysis of considered strongly nonlinear systems reveals instability of NNMs and abrupt transition from intensive inter-cluster energy exchange to energy localization on the initially excited cluster. The analytical prediction of this transition is confirmed by the results of computer simulation. The analytical results for grounded string as well as for weakly coupled pendulums were obtained in the framework of resonance asymptotics.

The above described strongly nonlinear effects can be directly applied for solution of targeted energy transfer problem and the series of physical problems mentioned in Introduction.

References

[1] Manevitch L.I., Vakakis A.F.:Nonlinear Oscillatory Acoustic Vacuum. *SIAM Journal of Applied Mathematics* **74**(6): 1742-1762, 2014.

[2] Koroleva (Kikot) I.P., Manevitch L.I., Vakais A.F.: Non-stationary resonance dynamics of a nonlinear sonic vacuum with grounding supports. *Journal of Sound and Vibration* **357**:349-364, 2015.

[3] Manevitch L.I., Romeo F.: Non-stationary resonance dynamics of weakly coupled pendula. *EPL,* **112**(3): 30005, 2014.

[4] Koroleva (Kikot) I.P., Manevitch L.I.: Oscillatory chain with grounding support in conditions of acoustic vacuum. *Rus. J. Nonlin. Dyn.,* **11**(3): 487–502 (Russian), 2015.

ACCELERATING OSCILLATORY FRONTS IN A SONIC VACUUM WITH NON-LOCAL INTERACTIONS

Oleg Gendelman[1a)], Vadim Zolotarevskiy [1)], Alexander V. Savin[2)], Lawrence Bergman[3)] & Alexander F. Vakakis [4)]

[1]*Faculty of Mechanical Engineering, Technion -- Israel Institute of Technology, Haifa 32000, Israel*
[2]*Semenov Institute of Chemical Physics, Russian Academy of Sciences, Moscow 119991, Russia*
[3]*Department of Aerospace Engineering, University of Illinois in Urbana-Champaign, USA*
[4]*Department of Mechanical Science and Engineering, University of Illinois in Urbana-Champaign, USA*

<u>*Summary*</u> We describe a novel class of dynamical excitations -- accelerating oscillatory fronts in nonlinear sonic vacua with strongly non-local effects. Such models naturally arise in dynamics of common and popular lattices. In this study, we consider a chain of particles oscillating in the plane and coupled by linear springs, with fixed ends. When one end of this system is harmonically excited in the transverse direction, one observes accelerated propagation of the excitation front, accompanied by an almost monochromatic oscillatory tail. The front propagation obeys the scaling law $l \sim t^{4/3}$. This scaling law results from the nonlocal effects; we derive it analytically (including the scaling coefficients) from a continuum approximation. Moreover, a certain threshold excitation amplitude is required in order to initiate the front propagation. The initiation threshold is explained on the basis of a simplified discrete model, further reduced to a new completely integrable nonlinear system.

We start with simple numeric experiment: a fragment of common straight linear mass-and-spring chain without pre-tension is allowed to move in plane. One end of the chain is fixed, and the other is forced to move in the direction transversal to the chain axis, in accordance with harmonic law: $y_1 = A \sin \omega t$. Energy distribution in the chain is presented in Figure 1.
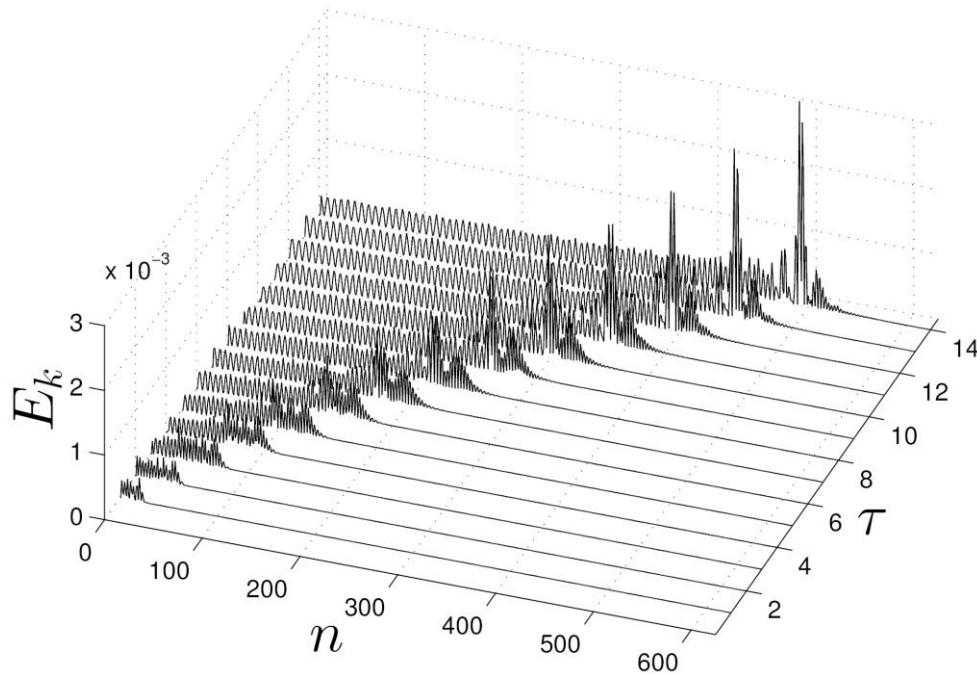
Figure 1. Propagation of the oscillatory front.

One can observe the propagation of the excitation front, accompanied by an apparently monochromatic oscillatory tail. Propagating fronts with oscillatory tails are well-known in models of phase transitions in solid state and similar problems. However, the solution presented here has very interesting new feature, not known in the settings mentioned above. It follows from Figure 1 that this front accelerates in the course of propagation.

In order to explain this finding analytically, we use continuum approximation of the transversal dynamics of the chain. It is described by the following well-known equation [1,2]:

$$y_{tt} - \frac{y_{xx}}{2L} \int_0^L y'^2 dx = 0 \tag{1}$$

Here $y(x,t)$ is continuous field of transversal displacements of the chain. Density and stiffness characteristics of the chain are set to unity without effecting the generality, *L* is the chain length. Equation (1) exemplifies the concept of the sonic vacuum, since it has no linear sound velocity. Moreover, due to integral term the nonlinear interactions turn out to be

---

non-local. Besides modal characteristics, the nonlinear dynamics and wave propagation in such systems were almost not addressed in previous studies.

We then consider a simplified model of the oscillatory region in the chain and suppose a monochromatic wave in the oscillatory tail after the front:

$$y(x,t) = \begin{cases} A\sin(\omega t - kx), 0 \le x \le l(t) \\ 0, x \ge l(t) \end{cases}$$
(2)

Here $l(t)$ is the instantaneous coordinate of the front, and k is the wavenumber. It is also assumed at this stage that the front propagation is slow enough compared to the frequency of transverse oscillations of the particles. An additional condition can be obtained from the assumed stationary character of the front propagation. To this end, the phase velocity of the oscillatory tail should be equal to the front velocity. Substituting (1) into (2), keeping principal terms and applying the condition of the phase velocity, one obtains the following explicit expression for the front propagation dynamics:

$$l(t) = Kt^{4/3}, K = \left(\frac{81A^2\omega^2}{1024L}\right)^{1/3}$$
(3)

Quality of approximation (3) is illustrated in Figure 2 for three different sets of parameters, with the curves depicting the front position versus time (shifted by ln K). One can observe that the curves perfectly collapse, proving the self-similar nature of the observed regime.
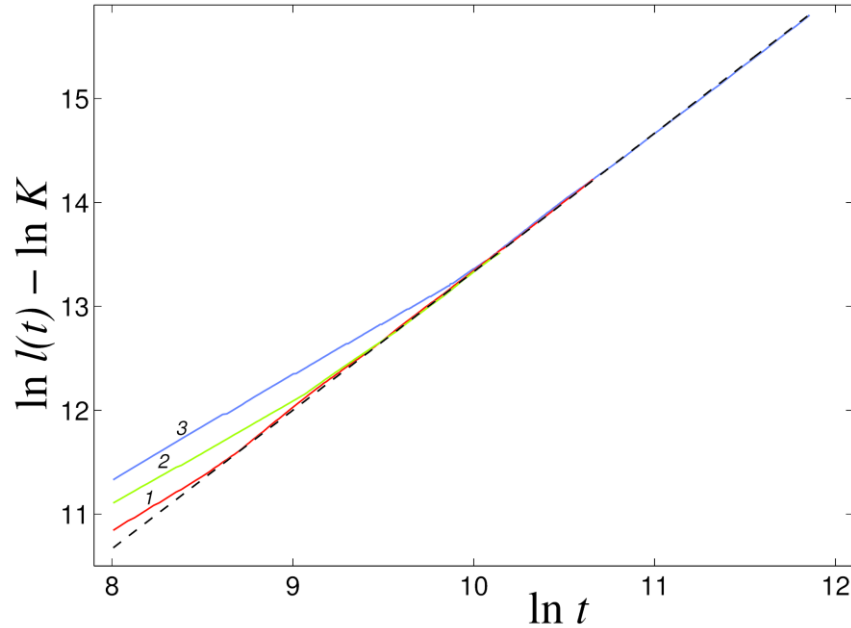
Figure 2. Numeric simulation: position of the oscillatory front versus time for different parameter values (double logarithmic scale). Line slope is 4/3.

The front formation and propagation is observed for given excitation frequency, if the amplitude overcomes certain threshold value. This value can be evaluated from discrete counterpart of Equation (1), derived recently in paper [3]. This estimation yields:

$$A_{cr} = a\omega\sqrt{2L}$$
(4)

Numeric simulations completely confirm scaling predictions for critical excitation amplitude (4). Numeric value of coefficient a is also predicted with accuracy of about 15%.

To conclude, we revealed a new type of excitations in a lattice representing a nonlinear sonic vacuum with strong nonlocal dynamical interactions (despite only next-neighbour physical coupling). Such fronts reveal themselves in most well-known and popular models, such as the suspended string without pre-tension and the chain of linear springs and masses with fixed ends. Simple analytic considerations allow derivation of all main parameters of the front, including the scaling characteristics and the excitation threshold.

References

[1]   L. D. Landau and E. M. Lifshitz , Theory of Elasticity, Pergamon Press, 1970

[2]   A. H. Nayfeh, Nonlinear Interactions, Wiley, 2000

[3]   L. I. Manevitch and A. F. Vakakis, Nonlinear Oscillatory Acoustic Vacuum, *SIAM Journal of Applied Mathematics*, **74**, 1742-1762, 2014.

NONLINEAR INTERACTIONS BETWEEN COUPLED NONLINEAR OSCILLATORS AT DIFFERENT LAYERS OF TIME

Claude-Henri Lamarque[1], <u>Simon Charlemagne</u>[1], and Alireza Ture Savadkoohi [*1]

[1]*Univ Lyon, ENTPE, LTDS UMR CNRS 5513, Vaulx en Velin, France*

Summary The energy exchanges between two coupled systems during extreme nonlinear interactions between them around a $1:1$ resonance is studied. The auxiliary nonlinear oscillator, named as nonlinear energy sink (NES) [1, 2, 3, 4, 5], which is used for controlling the main one and/or to harvest its energy, possesses both global and local potentials and can be under external forcing terms. Slow invariant of the system and detected equilibrium and singular points provide design tools for tuning parameters of the NES for the aim of its usage.

MATHEMATICAL MODEL OF THE SYSTEM

The main forced oscillator with scaled displacement, damping and natural frequency as y, a and ω_0 is coupled to a forced NES with scaled displacement and local potential x and $\tilde{g}(x)$, respectively. Its global potential is split in linear (ω_c^2) and nonlinear (W) parts. The two nonlinear potentials W and $\tilde{g}$ are supposed to be odd functions. We can summarize governing equations of the system as it follows:

$$\begin{cases} \ddot{y} + a\dot{y} + \omega_0^2 y + c(\dot{y} - \dot{x}) + \omega_c^2(y - x) + W(y - x) = \epsilon f^0 \sin(\omega t) \\ \\ \epsilon \ddot{x} - c(\dot{y} - \dot{x}) - \omega_c^2(y - x) - W(y - x) + \tilde{g}(x) = \epsilon f_{NES}^0 \sin(\omega_N t) \end{cases} \tag{1}$$

The ϵ parameter is the mass ratio of the NES and the main oscillator. We assume that $1 < \epsilon \ll 1$.

TREATMENTS OF THE SYSTEM AND ITS BEHAVIORS AT DIFFERENT TIME SCALES

- The system is shifted to the center of masses ($v = \dfrac{y + \epsilon x}{1 + \epsilon}$) and relative displacement ($w = x - y$). Then complex variables of Manevitch [6] as $\psi e^{i\omega t} = \dot{v} + i\omega v$ and $\varphi e^{i\omega t} = \dot{w} + i\omega w$ are introduced to the system ($i^2 = -1$).

- A Galerkin technique is endowed: first harmonics are kept and higher ones are truncated. This technique for an arbitrary function Γ reads:

$$S = \frac{\omega}{2\pi} \int_0^{\frac{2\pi}{\omega}} \Gamma(t) e^{-i\omega t} dt \tag{2}$$

  We assume that ψ, φ are independent of fast $\tau_0 = t$ time scale, but could depend on slow $\tau_1 = \epsilon\tau_0$, $\tau_2 = \epsilon^2\tau_0$,... scales.

- System equations at fast time scale provide its slow invariant while at slow time scale around its invariant we can detect its equilibrium and singular points. These points correspond to potential periodic and strongly modulated responses.

Moreover, following assumptions are made:

- We investigate 1:1:1 resonance of the main system: $\omega = \omega_0(1 + \sigma\epsilon)$ and $\omega_N = \omega_0(1 + \sigma_N\epsilon)$.

- Damping coefficients are at ϵ^1 order: $c = \epsilon d$ and $a = \epsilon a_0$.

- Linear part of the global potential is at the order of ϵ^1: $\omega_c^2 = \epsilon\Omega^2$. Nonlinear part of global potential and local potential are assumed to be at the ϵ^1 order: $\tilde{g}(z) = \epsilon\mathcal{A}^0 z^3$ and $W(z) = \epsilon\mathcal{B}^0 z^3$.

- We introduce polar coordinates $\psi = N_1 e^{\delta_1}$ and $\varphi = N_2 e^{\delta_2}$.

In following sections we present two examples corresponding to two cases: the NES without external excitation and forced NES. All analytical predictions are compared with results obtained from direct numerical integration of equation (1).

The NES without external excitation: $f_{NES}^0 = 0$
Slow invariant of the system possesses three branches namely, branch l, $l = 1, 2, 3$. At slow time scale we can trace two levels of N_2 which prepare the system for bifurcations. We name them as N_{21} and N_{22} which are called as fold lines. Meanwhile, for each branch l two functions $Hjl = 0$, $j = 1, 2$ are defined. Intersections of Hjl out of fold lines are equilibrium points of the system while their intersections on fold lines are singular points of the system. Figure 1 illustrates prediction of all possible regimes (periodic and strongly modulated regimes) of the system for given parameters. It can been seen that due to the existence of singular point no. 2 (see Figure 1(a)), the system presents strongly modulated response (see Figures 1(d) and 1(e)).

---

*Corresponding author. Email: alireza.turesavadkoohi@entpe.fr
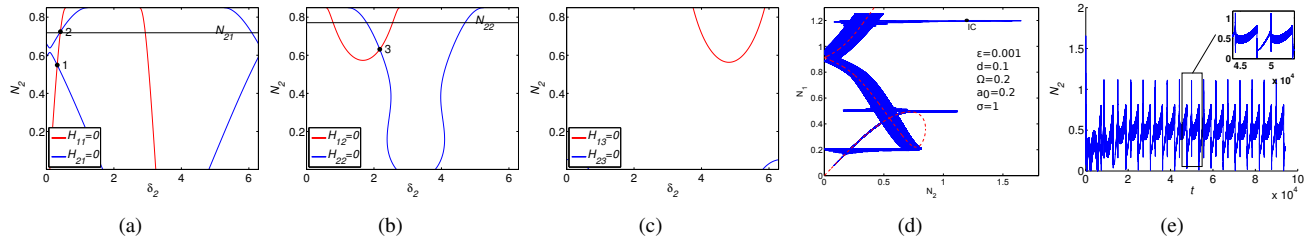
Figure 1: $\mathcal{A} = 0.25$, $\mathcal{B} = 0.6$, $\omega_0 = 1$ and $f^0 = 0.81$: (a), (b), (c) Positions of equilibrium points and fold singularities on branch 1, 2 and 3 of the slow invariant, respectively. The system has two equilibrium points (no. 1 and no. 3) and one fold singularity on fold line N_{21} (no. 2)- (d) Slow invariant (in red, dashed line) and corresponding numerical results (in blue, solid line) - (e) Numerical results of the evolution of the energy of the NES N_2 - IC stands for "Initial Conditions"

The NES with external excitation: $f^0_{NES} \neq 0$

Here, we consider the system with forced NES. Analytically predicted results and corresponding numerical ones are depicted in Figure 2. The system finally is attracted by an equilibrium point (see green line in Figure 2(b)) which is predicted by analytical techniques that has not been presented in this paper.
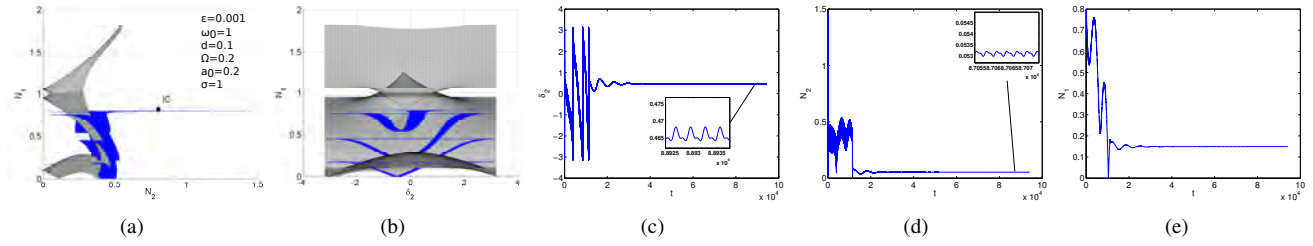
Figure 2: Slow invariant of the system and corresponding numerical results in blue - $\mathcal{A} = 2$, $\mathcal{B} = 0.5$, $f^0_{NES} = 0.1$ and $f^0 = 0.3$ - (a) N_1 vs N_2; (b) N_1 vs δ_2 - "IC" stands for initial conditions - Behavior of the system around the equilibrium point predicted via analytic technique at slow time scale is plotted in green. (c) δ_2 vs t; (d) N_2 vs t; (e) N_1 vs t.

CONCLUSIONS

Time multi-level energy exchanges and nonlinear interactions between a main forced oscillator and an auxiliary forced nonlinear system with local and global potentials are studied. Detected slow invariant and equilibrium and singular points at slow time scale provide design tools for tuning parameters of the auxiliary system for the goal of its implementations which can be passive control and/or energy harvesting of the main oscillator. Same method will be applied for an oscillator coupled to a chain of light nonlinear oscillators for localization of its vibratory energy.

References

[1] Gendelman O., Manevitch L. I., Vakakis A. F., MCloskey R.: Energy pumping in nonlinear mechanical oscillators: part i - dynamics of the underlying hamiltonian systems. J. Appl. Mech. 68: 34–41, 2001.

[2] Vakakis A. F.: Inducing passive nonlinear energy sinks in vibrating systems. J. Vib. Acoust 123: 324–332, 2001.

[3] Lamarque C.-H., Ture Savadkoohi A.: Dynamical behavior of a Bouc-Wen type oscillator coupled to a nonlinear energy sink. Meccanica 49: 1917–1928, 2014.

[4] Lamarque C.-H., Thouverez F., Rozier B., Dimitrijevic Z.: Targeted energy transfer in a 2-DOF mechanical system coupled to a non-linear energy sink with varying stiffness. J. Vib. Control, doi: 10.1177/1077546315618540, 2016.

[5] Ture Savadkoohi A., Lamarque C.-H., Contessa M. V.: Trapping vibratory energy of main linear structures by coupling light systems with geometrical and material non-linearities.Int. J. Nonlinear Mech., doi:10.1016/j.ijnonlinmec.2015.11.011, 2016.

[6] Manevitch L. I.: The description of localized normal modes in a chain of nonlinear coupled oscillators using complex variables. Nonlinear Dyn. 25: 95–109, 2001.

SYNCHRONIZED FREQUENCY CONVERSION IN NONLINEAR LATTICES

Miguel Molerón[1], Marc Serra-Garcia[1], André Foehr[1], Joseph Lydon[1], Christopher Chong[2] & Chiara Daraio [1,3a]

[1]*Department of Mechanical and Process Engineering, Swiss Federal Institute of Technology, ETH Zurich CH-8092, Zurich, Switzerland*

[2]*Department of Mathematics, Bowdoin College, Brunswick, ME 04011, United States*

[3]*Division of Engineering and Applied Science, California Institute of Technology, Pasadena, CA, 91125, United States*

Summary We investigate energy transfer between frequencies in lattices of interacting magnets with defects. The nonlinear coupling between localized and extended lattice modes enables to convert energy between arbitrary frequencies (i.e., non related by integer ratios). In addition, in systems with multiple defects, this frequency conversion mechanism allows harvesting energy from several input frequencies in a synchronized manner. These results may inform the design of new vibration energy harvesting systems.

Vibration energy harvesting systems are able to convert ambient vibrations into electric power and are receiving a lot of interest in recent years [1]. Regardless of the transduction mechanism (e.g., piezoelectric, electromechanic), these systems operate optimally at or close to resonance. However, ambient vibrations are in general broadband or composed of multiple frequencies, which render these devices unsuited in most practical situations. A possible way to solve this issue is to introduce a frequency conversion mechanism in the system in order to match the spectrum of the excitation with the resonance frequency of the transducer. Typical uses of nonlinearity for frequency conversion are based on the phenomena of harmonic generation [2] and parametric down conversion [3]. In these mechanisms, the energy transfer occurs at a frequency that is an integer multiple or submultiple of the excitation frequency, limiting the applicability of these techniques. In this work, we demonstrate a frequency conversion mechanism in lattices of interacting magnets with mass defects that transfers energy between arbitrary frequencies, i.e., without being necessarily related by integer ratios.

To illustrate this behavior we consider two cases: a lattice with a single defect [Fig. 1(a)] and a lattice containing two defects [Fig. 1(b)]. The linear spectrum of these lattices is composed of two types of modes: extended modes, which are responsible for the propagation of energy in the lattice; and defect modes, which are localized around the defect. Localized and extended modes represent respectively the inputs and outputs of our system. Due to the hardening nonlinearity of the magnetic potential [5], when the defect mode is excited harmonically at a frequency close to its resonance frequency, the mode undergoes hysteretic cycles in which the mode pumps the input energy to the chain [5]. This results in a modulation of the localized mode amplitude that creates an energy transfer from the localized modes to the extended modes.
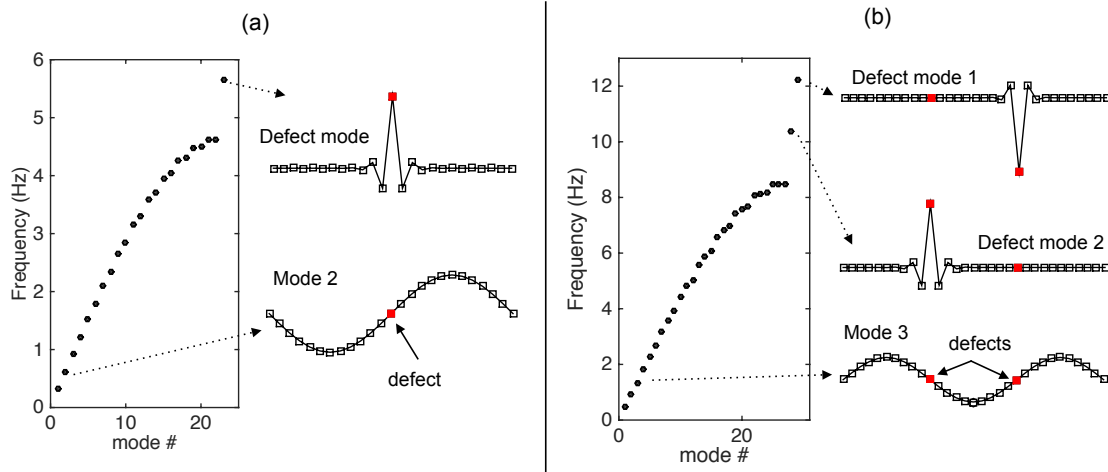
Figure 1. (a) *Linear spectrum of the single-defect lattice. (b) Linear spectrum of the double-defect lattice.*

We first illustrate this frequency conversion mechanism in the single defect lattice. The defect is excited harmonically at frequency $f_{in} = f_d + f_2$ where f_2 and f_d are, respectively, the resonance frequencies of the second extended mode and the defect mode, see Fig. 1(a). The left panel in Fig. 2(a) shows the amplitudes of mode 2 (A_2, black line) and the defect mode (A_d, red line) as a function of time. After the transient regime ($t \approx 15s$) we observe that the amplitude A_d becomes modulated by A_2, which indicates a transfer of energy from the input frequency f_{in} to the frequency of the extended mode

---

[a] Corresponding author. Email: daraio@ethz.ch**.**

f_2. This modulation can be clearly observed in the right panels of Fig. 2(a), which zooms in the modal amplitudes A_2 and A_d in the time window $[32 - 40]$s.
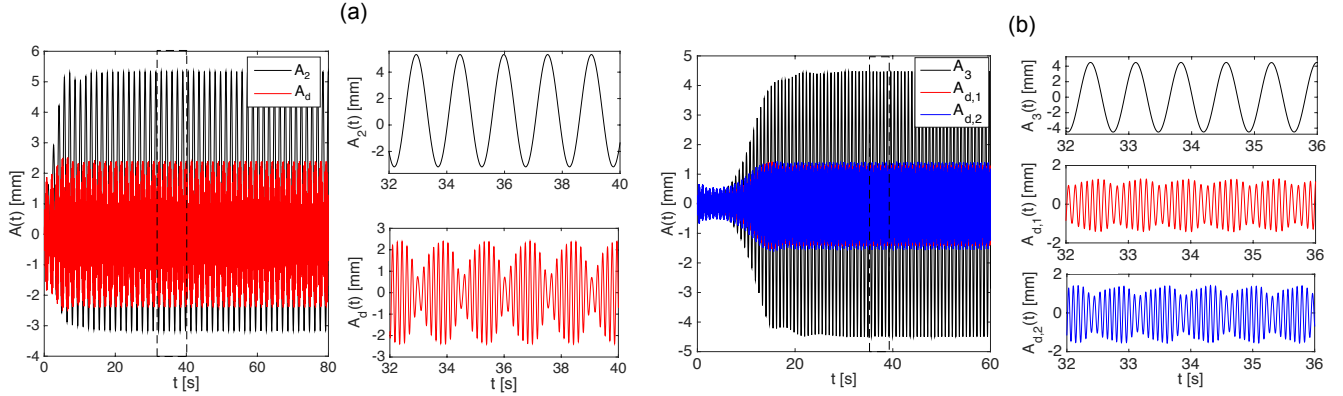
Figure 2. (a) Left panel, A_2 (black line) and A_d (red line) as a function of time for the single defect lattice. Right panels, zoom in on the region 32-40 s. (b) Right panel, A_3 (black line), $A_{d,1}$ (red line) $A_{d,2}$ (blue line) and as a function of time for the lattice with two defects. Right panels, zoom in on the region 32-36 s.

An interesting aspect of this frequency conversion mechanism is that in systems with multiple inputs (defects) the energy extracted from each input is added up in phase to the output signal. This is because the amplitude of the extended mode synchronizes the modulation of each defect mode. To illustrate this phenomenon, we show in Fig. (b) the modal amplitude of the two defect modes and the third extended mode in the double defect lattice [see Fig. 1(b)], respectively denoted respectively by $A_{d,1}$, $A_{d,2}$, A_3. In this case, the input frequencies are $f_{in,1} = f_{d,1} + f_3$ and $f_{in,2} = f_{d,2} + f_3$, where $f_{d,1}$, $f_{d,2}$, and f_3 are the resonance frequencies of the two defect modes and the third extended mode. Again, passing the transient regime the amplitude of the defect modes $A_{d,1}$ and $A_{d,2}$ become modulated by the amplitude of the extended mode A_3, showing a synchronized energy transfer from the two input frequencies $f_{in,1}$ and $f_{in,2}$ to the output frequency f_2.

The results shown in this work were obtained integrating numerically the equations of motion of the system. We are currently developing an analytical model containing a reduced number of modes in order to gain physical insight on the underlying phenomena. In addition, an experimental validation of this frequency conversion mechanism is in progress. Additional results coming out from this ongoing work will be presented.

References

[1]   R. L. Harne and K W Wang, *Smart Materials and Structures*, **22**, 023001, 2014
[2]   M. M. Fejer, G. A. Magel, D. H. Jundt, and R. L. Byer, *IEEE Journal of Quantum Electronics* **28**, 2631, 1904 (2010)
[3]   N. C. Wong, *Opt. Lett*, **15**, 1129, (1990)
[4]   M. Molerón, A. Leonard and C. Daraio, *J. Appl. Phys*, **115**, 184901, (2014)
[5]   M. Serra-Garcia, J. Lydon and C. Daraio, Phys. Rev. E, **93**, 010901, (2016)

CHIMERA STATES FOR COUPLED PENDULA

Tomasz Kapitaniak[a]

Division of Dynamics, Lodz University of Technology, Lodz, Poland

Summary The phenomenon of chimera states in the systems of coupled, identical oscillators has attracted a great deal of recent theoretical and experimental interest. In such a state, different groups of oscillators can exhibit coexisting synchronous and incoherent behaviors despite homogeneous coupling. Here, considering the coupled pendula, we find another pattern, the so-called imperfect chimera state, which is characterized by a certain number of oscillators which escape from the synchronized chimera's cluster or behave differently than most of uncorrelated pendula. The escaped elements oscillate with different average frequencies (Poincare rotation number). We show that imperfect chimera can be realized in simple experiments with mechanical oscillators, namely metronomes. The mathematical model of our experiment shows that the observed chimera states are controlled by elementary dynamical equations derived from Newton's laws that are ubiquitous in many physical and engineering systems.

MODEL OF COUPLED PENDULA

Chimera states correspond to the spatiotemporal patterns in which synchronized and phase locked oscillators coexist with desynchronized and incoherent ones[1-2]. Dynamically, it represents a sort of spatially extended symmetry breaking which develops in networks of identical oscillators, surprisingly without any evidence of asymmetry or external perturbation. Furthermore, this surprising hybrid behavior obeys a substantial reserve of robustness surviving at different kind of perturbations. The experimental proof of chimeras' existence has only recently been provided for optical, chemical, mechanical and electronic systems.

Here, we show that other pattern, the so-called *imperfect chimera state*, which is characterized by a certain, small number of oscillators (solitary states) which escape from the synchronized chimera's cluster or behave differently than the most of uncorrelated pendula can be observed in the networks of identical oscillators. As a proof of concept we use the network of coupled metronomess, i.e., the system of coupled pendula which are excited by the escapement clock's mechanism.
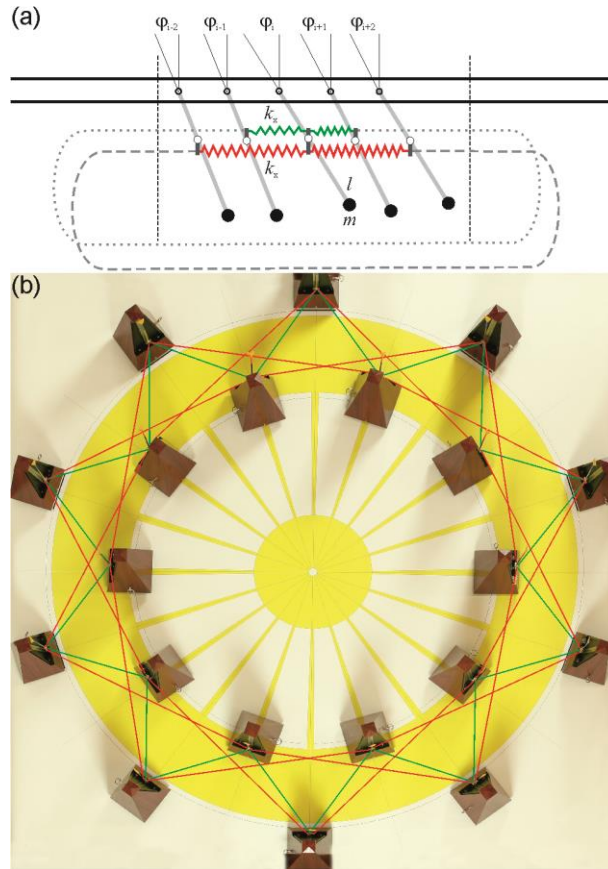
Figure 1:(a). *n* pendula coupled on the ring through springs and dampers, (b) Experimental implementation of the system of Figure 1(a) with *n*=20 metronomes which pendula are coupled by spring elements

[a] Corresponding author. Email: tomaszka@p.lodz.pl**.**

We consider the system of n pendula which hung from the unmovable disc as shown in Figure 1(a). Pendula of length l and mass m are coupled through the linear spring with stiffness coefficient k_x and linear dampers with damping coefficient c_x. Pendula's displacements are given by the angles φ_k. Springs and dampers are connected to each pendulum at distance l_s from the pivot. Each pendulum is connected with the nearest neighbor (green spring) and the second nearest neighbor (red springs). Additionally, the motion of each pendulum is damped by the linear damper characterized by damping coefficient c_φ. The pendula are excited by the escapement mechanism which for $\varphi_l < \gamma_N$ generate excitation torque M_N. This system can be implemented experimentally using the metronomes with the pendula connected by the spring elements as shown in Figure 1(b).

The dynamics of the system of Figure 1(a) can be analyzed using the equations of motion which are derived from Newton's laws of dynamics. We present the results for two different coupling schemes, (i) each pendulum is coupled with the nearest neighbor (local coupling), (ii) each pendulum is coupled with two nearest neighbors (nonlocal coupling).

RESULTS

Numerical simulations show that the state of complete synchronization of all pendula co-exists with the state of phase synchronization in which there exists the constant phase shift between neighboring pendula and various chimera states (including imperfect chimeras). These results have been confirmed experimentally.
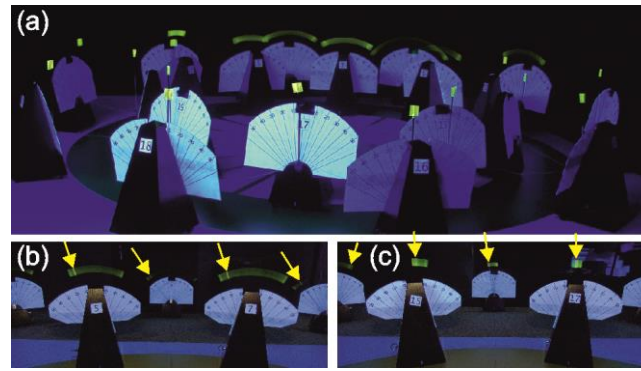
Figure 2: Experimentally observed imperfect chimera state.

The example of experimentally observed imperfect chimera is shown in Figure 2(a-c). The group of metronomes at the background of Figure 2(a) is synchronized. Their escapement mechanisms are switched on and they oscillate with the frequency equal to the nominal frequency of 200 tics per minute . The metronomes on the first plane of Figure 2(a) are either at rest or oscillate with smaller amplitudes. The escapement mechanisms of most of them are permanently switched off but metronome 15 (see Figure 2(c)) oscillates with larger amplitude and different frequency (approximately 23 tics per minute). Its escapement mechanism is intermittently switched on. The yellow arrows in Figure 2(b,c) indicate the actual positions of the pendula (snapshot). The imperfect chimera states coexist with the state of complete and phase synchronization and perfect chimeras. Imperfect chimera states are easily observed for both local and nonlocal coupling and the wide range of initial conditions (moreover, in our experiment it is easier to observe imperfect chimera states than the perfect ones).

CONCLUSIONS

We have constructed the simple experimental setup to explore the spatio-temporal dynamics of the network of the coupled pendula. The nodes in the network are locally and nonlocally coupled pendula (Huygens' clocks realized by metronomes). We observe the formation of coexisting coherent and incoherent domains in which the newly discovered patterns of imperfect chimera or multi-headed chimera are the most typical one. This behavior is observed experimentally and confirmed in numerical simulations.

References
[1] Kuramoto, Y.: Chemical Oscillations, Waves and Turbulence, Springer, New York, 1984.
[2] Kuramoto, Y. & Battogtokh, D.: Coexistence of coherence and incoherence in nonlocally coupled phase oscillators, *Nonlinear Phen. Complex Syst.* **5**, 380-385, 2002.
[3] Kapitaniak, T., Kuzma, P., Wojewoda, J., Czolczynski, K., & Maistrenko, Yu.: Imperfect chimeras for coupled pendula, Scientific Reports, **4**, 6379, 2014.
[4] Jaros, P., Borkowski, L., Witkowski, B., Czolczynski, K., & Kapitaniak, T.: Multi-headed chimera states in coupled pendula, EPJ ST, **224**, 1605, 2015.

ANALYSIS OF SYMMETRY-BREAKING AND MULTI-BIFURCATION FOR MULTI-FOLDING STRUCTURES

Ichiro Ario[1 a]

[1]*Department of Civil Engineering, Hiroshima University, Higashi-Hiroshima, Japan*

<u>*Summary*</u> Recently, it is well-known as the symmetry-breaking phenomena in the field of physics, the block-diagonalization method (BDM) based on *representation theory of group* with the utilization of symmetry has come to be utilized to exploit structural analysis of the symmetric structure. According to the fact that topological factor is unclear in the homogeneous structures, in this paper, we present the mechanism of the breaking-down from high-symmetry of the stratified symmetry which is developed by the translation law of group theory. We propose that there is the finite element mesh issue of numeric error of computing analysis which it is confirmed *hidden symmetry* and its *symmetry-breaking* on the dynamic simulation problem by using group representation. It is possible to trace the dynamic nonlinear process from symmetric structures with strange behavior. It is found that there are different solution on dynamic process without the issue of the numeric method, it depends on the number of divided elements on symmetric structure.

THEORY OF MFM FOR A DESCRETE CYLINDRICAL STRUCTURES

We review the interesting eigenvalues problem of a folding truss allowing for the deformation using both analytical and numerical approaches. An experimental approach by Holnicki [1] showed an active shock-absorber based on the truss system. From these approaches the authors developed the concept of a pantograph truss to model the multi-folding of microstructures [2]. The paper [2] presents the theoretical basis for both static and dynamic numerical approaches to the elastic stability of a folding multi-layered truss. Both analyses are based on bifurcation theory and include geometrical nonlinearity. Comparisons are made between published experimental folding patterns and the patterns obtained from both numerical methods in which bifurcations are demonstrated as having elastic unstable snap-through behaviour. The authors suggest that understanding this behaviour will be very useful for the development of lightweight structures subject to dynamic loading based on the bifurcation static analysis and dynamic analysis.

In this paper, we investigate the mechanism of several folding patterns for the numerical work to trace the folding patterns of the system shown in Fig.1. This structure is similar to the carbon nano-tube, and inside this cage sets up the membrain structure. We consider the folding mechanisms for the cylindrical (pantographic) truss structure subject to a vertical load at the top node of the system. The system is a pin-jointed elastic truss and all nodes of the system displace vertically only. No allowance is made for friction or gravity for this geometrically nonlinear problem.

THEORETICAL APPROACH FOR A FOLDING DIAMOND TRUSS [2]

We focus a diamond truss with right-left symmetry in MFM system. Hence in this paper the theoretical bifurcation analysis, is limited to considering a collapse with symmetric deformation.

Now let's consider a theoretical estimation for a folding diamond truss model. We assume a periodic height for each layer of $h_j = \gamma_j L$ where the width L of the truss is fixed. Therefore, the initial length for each bar in geometry of the figure is expressed as

$$\ell_{ij} = \sqrt{L^2 + h_j^2} = L\sqrt{1 + r_j^2}, \quad i,j = 1,2 \tag{1}$$

The deformed length of each bar denoted as $\hat{\ell}_{ij}$, is a function of the height and the nodal displacement variables

$$\hat{\ell}_{ij} = L\sqrt{1 + (\gamma_j - q_{ij}(\bar{v}_{ij}, \bar{v}_{i2}))^2}, \tag{2}$$

where $\gamma_j = h_j/L > 0$, $q_{i1}(\bar{v}_{11}, \bar{v}_{i2}) = \bar{v}_{11} - \bar{v}_{i2}, q_{i2}(\bar{v}_{i2}, 0) = \bar{v}_{i2}, \bar{v}_{ij} = v_{ij}/L, \quad (i,j = 1,2)$.

Using Green's expression for strain, the total energy of half of the system is given by

HILL-TOP BIFURCATION EQUILIBRIUM PATHS [3]

By allowing for symmetric model, we can therefore consider nonlinear equilibrium equations based on the total strain energy theoretically.

For the 1st and 2nd equilibrium equations chained

a) Corresponding author. Email: mario@hiroshima-u.ac.jp
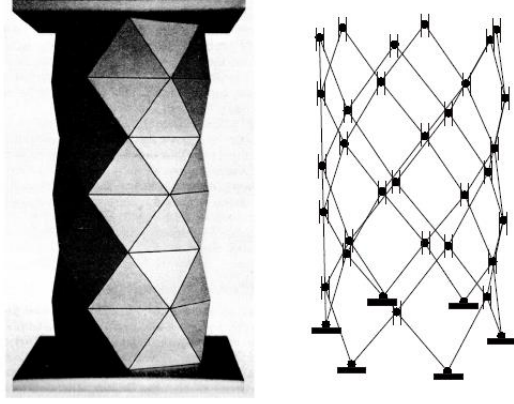
Figure 3: D_6-invariant axes-symmetric structure with MFM

$$F_{11} = \frac{\partial V}{\partial v_{11}} = \sum_{i=1}^{2} \frac{\partial V}{\partial q_{i1}} \frac{\partial q_{i1}}{\partial \bar{v}_{11}} \frac{1}{L} = \frac{\beta}{2} \sum_{i=1}^{2} \prod_{k=0}^{2} (\bar{v}_{11} - \bar{v}_{i2} - k\gamma) - f = 0, \tag{3}$$

$$F_{i2} = \frac{\partial V}{\partial v_{i2}} = \sum_{j=1}^{2} \frac{\partial V}{\partial q_{ij}} \frac{\partial q_{ij}}{\partial \bar{v}_{i2}} \frac{1}{L} = \beta \left\{ \prod_{k=0}^{2} (\bar{v}_{11} - \bar{v}_{i2} - k\gamma) + \prod_{k=0}^{2} (\bar{v}_{i2} - k\gamma) \right\} = 0,$$

These equations equal 0 in the limit value problem of total potential energy. It is possible to solve all variables $\bar{v}_{ij}$ by substituting the obtained solutions into the next limited condition using the theorem of implicit function.

$$F_{i2}(\bar{v}_{11}, \bar{v}_{i2}) = 0 \rightarrow \bar{v}_{i2} = \mathcal{F}_{i2}(\bar{v}_{11}) \tag{4}$$
$$F_{11}(\bar{v}_{11}, \bar{v}_{i2}) = F_{11}(\bar{v}_{11}, \mathcal{F}_{i2}(\bar{v}_{11})) = 0, \tag{5}$$

where $F(\, . \,)$ denotes a function of the nonlinear solutions. Finally, we obtain all solutions completely as equilibrium paths and it is shown the nonlinear kinetic equation in the following;

$$M\ddot{\bar{v}}_{11}(t) + C\dot{\bar{v}}_{11}(t) + K(\bar{v}_{11}(t)) = 0. \tag{6}$$

We can consider this differential equation with nonlinear stiffness for dynamic problem. Here, *M* is mass, *C* is damping and *K* is nonlinear stiffness matrices.

References

[1]   I. Ario and A. Watson: Structural Stability of Multi-Folding Structures with Contact Problem: Int. J. Non-Linear Mechanics, Vol.324 (1-2), pp.263-282.

[2]   I. Ario and M. Nakazawa: Nonlinear Dynamics behavior of Multi-Folding Microstructure Systems based on Origami Skill: Int. J. Non-Linear Mechanics, Vol. 45(4), pp. 337-347, 2010.

[3]   I. Ario: Structure with the expanding and folding equipment as a patent (No.2006-037668), 2006.

A NEW VERSATILE TWO-STATE FIVE-PARAMETER HYSTERESIS MODEL

Saurabh Biswas[a) & Anindya Chatterjee

Mechanical Engineering, IIT Kanpur, Kanpur, Uttar Pradesh, India

Summary: We present a new five-parameter two-state hysteresis model, derived from a high dimensional frictional system. The model captures a useful range of hysteretic behaviours, including minor loops. Several examples are presented to show the versatility of the model.

INTRODUCTION

Hysteresis is a rate-independent, irreversible phenomenon observed in material stress-strain relations, damping, magnetism, and other areas. For mechanical systems with elasticity and friction, a model due to Iwan [1] seems promising, but is high dimensional. In contrast, the Bouc-Wen model [2,3] is one-dimensional, but is unrealistic under small reversals within larger load paths (minor loops are not captured, leading to unrealistic dissipation estimates). With this motivation, we have recently studied [4] a high dimensional frictional hysteretic system given by

$$\mu \, \text{sgn}(\dot{x}) + Kx = bf(t), \tag{1}$$

where μ is diagonal, K is symmetric and positive definite, b is a column matrix, and $f(t)$ is scalar and differentiable. From Eq. 1, in [4] we developed a reduced order model with 6 states based on a new simple approximation for the frictional dissipation. However, some shortcomings remained in [4]. The choice of basis vectors was non-intuitive; order reductions below 6 gave poor results; and there were too many free parameters for practical use. Here, we report further on subsequent developments reported by us in [5]. A new high-dimensional model has now been studied, motivated by the Iwan model. The basis vectors are intuitively more pleasing. A model with just 2 states shows usefully rich behavior. The number of fitted parameters is 5, which is usefully small. Numerical solution is simplified, requiring solution of a 4×4 eigenvalue at each step. Use of the model by many analysts is now practical.

HIGH DIMENSIONAL FRICTIONAL SYSTEM

Figure 1(a) shows the underlying high dimensional frictional system [5]. In this system, each spring has stiffness $1/n$, and frictional coefficients are linearly varying $\mu_1 = \mu_0/n$, $\mu_2 = 2\mu_0/n$,..., $\mu_2 = n\mu_0/n$. As indicated in the figure, $u(t)$ is a displacement input, for which a force $f(t)$ is needed. Friction forces at the slip sites are $F_1 = -\mu_1 \text{sgn}(\dot{\xi}_1)$, $F_2 = -\mu_2 \text{sgn}(\dot{\xi}_2)$,..., $F_n = -\mu_n \text{sgn}(\dot{\xi}_n)$.
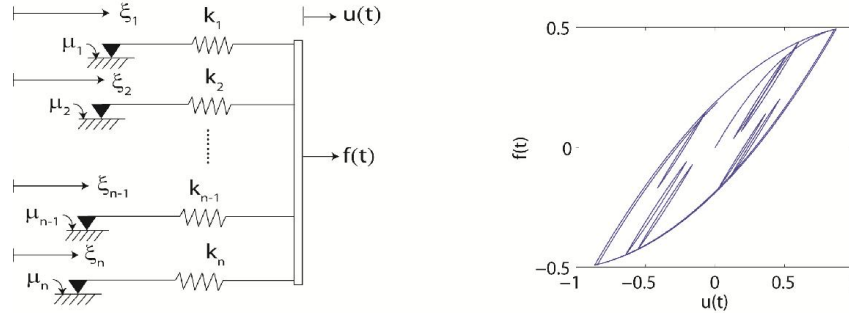
Figure 1. (a) A high dimensional frictional system. (b) Hysteresis curve obtained for the 500 dimensional system.

The governing equation of the system is

$$\mu \, \text{sgn}(\dot{\xi}) + K\xi = bu(t), \tag{2}$$

Equation (2) resembles Eq. (1) but is in fact has simpler structure. Equation (2) is first incrementally solved *via* an LCP [6]. For our numerical simulation, we use $n = 500$, $\mu_0 = 0.002$, $u(t) = 0.554 \sin(t) + 0.317 \sin(4.858 t)$. The solution shows hysteresis with minor loops (see Figure 1(b)). Such minor loops are not predicted by the Bouc-Wen model.

REDUCED-ORDER MODEL

Singular value decomposition of high dimensional data from the solution suggests that a two-state reduced order model is feasible (details omitted). From graphical inspection of the singular vectors, we chose basis vectors $\phi_k = \exp(-\alpha x^{15})$ $(x^{15})^{k-1}$, where $k = 1, 2$ and the power of 1.5 is based on heuristic observations (omitted). The free parameter α gives some flexibility. We orthonormalize the ϕ_k's for analytical convenience. We then derive a reduced order model based on a

---

[a)Corresponding author. Email:**s.biswas90@gmail.com.**

slip-and-work criterion. Slip cannot occur if the associated frictional dissipation exceeds the external work input minus the internal increase in potential energy. Let $\xi = \Phi q$, and $\dot{\xi} = \Phi \eta$. The criterion yields

$$\eta^T \Phi^T \mu \operatorname{sgn}(\Phi \eta) + \eta^T (\Phi^T K \Phi) q - \eta^T (\Phi^T b) u \leq 0. \tag{3}$$

Thus, if the minimum value of the above is positive, then slip cannot occur; and the minimizing η gives the direction of potential slip. We minimize the left hand side of Eq. (3) at each time step to find η. Here, though the first term of Eq. (3) is complicated, we have found a useful approximation [4]

$$\eta^T \Phi^T \mu \operatorname{sgn}(\Phi \eta) \approx \frac{(\eta^T A \eta)^\beta}{(\eta^T \eta)^{\beta - 05}} \tag{4}$$

where $\beta = 05$ gives convenient yet near-optimal results, and the fitted A is symmetric and positive definite. Let $\Phi^T K \Phi = \overline{K}$, $\Phi^T b = \overline{b}$, $\sqrt{\eta^T A \eta} + \eta^T (\overline{K} q - \overline{b}) = y$. Based on Eqs. (3) and (4), we develop the following reduced order model

$$\dot{s} = \left[\frac{\eta^T \overline{b}}{\eta^T \overline{K} \eta} \dot{u} - My|\dot{u}| \right] \{y \leq 0\},$$

$$\dot{q} = \eta \dot{s} \{\dot{s} > 0\},$$

where $\dot{s}$ is the slip rate, and M is a user-defined positive number (like unity), and η can be found by solving a 4×4 eigenvalue problem (details in [5]).

FITTING PARAMETERS TO GIVEN DATA

Our reduced order model has three system matrices, namely A, $\overline{K}$, and $\overline{b}$. The model has $2 + 1 + 2 = 5$ parameters. Figure 2 shows several loop shapes that can be captured by changing the five fitted parameters.
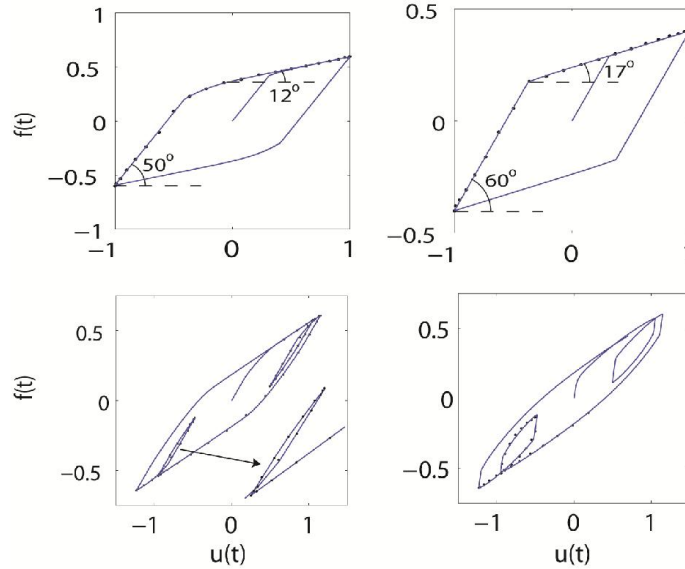
Figure 2. Various behaviours and loop shapes, to match application requirements, can be captured by the model.

CONCLUSIONS

The two-state hysteresis model has several advantages over many hysteresis models in the literature. These advantages include a minimal number of states for capturing minor loops (see [4]), a small number of fitted parameters, and the ability to match a reasonable range of hysteretic behaviors. It can now be easily used for modelling various phenomena.

References

[1] Iwan, W. D: A distributed-element model for hysteresis and its steady-state dynamic response. *J. Appl. Mech.*, **33**:4, 893-900. 1966.
[2] Bouc R: Forced vibrations of mechanical systems with hysteresis. *Proc. the Fourth Conf. on Nonlinear Oscillation*, Prague. p. 315. 1967.
[3] Wen Y. K: Method for random vibration of hysteretic systems. *J. Eng. Mech. Div.,* ASCE, **102**:2, 249-263. 1976.
[4] Biswas S. & Chatterjee A: A reduced-order model from high-dimensional frictional hysteresis. *Proc. R. Soc. A.* **470**: 20130817. 2014.
[5] Biswas S. & Chatterjee A: A two-state hysteresis model from high-dimensional friction. *R. Soc. Open Sci.* **2**: 150188. 2015.
[6] Cottle R. W., Pang, J. S. & Stone, R. E.: *The Linear Complementarity Problem*. New York, NY: Academic Press. 1992.

HARMONIC DIFFERENTIAL QUADRATURE METHOD FOR NONLINEAR VIBRATIONS OF TRANSMISSION BELTS

Jieyu Ding[1,2a)], Wei Zhang[3,2]

[1]*College of Computer Science & Technology, Qingdao University, Qingdao, China*
[2] *Beijing Center for Scientific and Engineering Computing, Beijing University of Technology, Beijing, China*
[3]*College of Mechanical Engineering, Beijing University of Technology, Beijing, China*

Summary Harmonic differential quadrature method (HDQ) is developed for the nonlinear vibration of axially moving viscoelastic belts. Different types of quadrature nodes such as Chebyshev-Gauss-Lobatto, Gauss-Legendre points, and triangle basis functions are used to discrete the partial differential vibration equations to ordinary differential equations with respect to the time. Hadamard product and SJT product are used to improve the computational efficiency of the discretized nonlinear equations. Numerical results show that the HDQ method has advantages both in efficiency and stability.

INTRODUCTION

Differential quadrature method (DQ) is a popular approach used in the area of engineering and mechanics because of its advantages of less computation, simple form and convenience. The DQ method was firstly introduced by Bellman and Casti[1], in which the partial derivatives of a function in one direction is expressed as a linear combination of the function values at all mesh points along that direction. The following studies of the DQ method were focused on the choice of mesh points, the treatment of boundary conditions, the choice of basis function, the property of weight coefficients and the convergence of solution. In the Harmonic differential quadrature (HDQ) method, the researchers chose the trigonometric functions to determine the weight coefficients, which is appropriate to the periodic solutions and is applied to structural and vibration area [2,3].

In this paper, the HDQ method is applied to the analysis on the nonlinear vibrations of two-pulley belt-drive system which is obtained in paper [4]. The different types of the quadrature nodes, such as Chebyshev-Gauss-Lobatto, Gauss-Legendre points, Hadamard product and SJT product [5], are used to discuss the nonlinear vibrations of two-pulley belt-drive system, the efficiency and stability of the algorithm.

HARMONIC DIFFERENTIAL QUADRATURE METHOD

The basis function in the DQ method can be chosen as Legendre polynomial, Lagrange interpolation polynomial, spline function, radial basis function, etc. Striz et al. developed the DQ method by using the following trigonometric functions to determine the weight coefficients, which is called harmonic differential quadrature method (HDQ). In the recent study, the basis function of the HDQ method can be chosen as

$$l_j(x) = \frac{\sin\frac{\pi}{4}(x-x_1)\cdots\sin\frac{\pi}{4}(x-x_{j-1})\sin\frac{\pi}{4}(x-x_{j+1})\cdots\sin\frac{\pi}{4}(x-x_N)}{\sin\frac{\pi}{4}(x_j-x_1)\cdots\sin\frac{\pi}{4}(x_j-x_{j-1})\sin\frac{\pi}{4}(x_j-x_{j+1})\cdots\sin\frac{\pi}{4}(x_j-x_N)}, \tag{1}$$

where $j = 1,\cdots, N$, and N is the number of grid points which is normally an odd number, and $0 \le x \le 1$. The corresponding explicit forms of weight coefficients for each order derivatives can be calculated by equation (1) and easy programed.

The grid points can be chosen as Chebyshev-Gauss-Lobatto, Gauss-Legendre points etc. The different types of quadrature nodes have different influences on the solutions.

NONLINEAR VIBRATIONS OF AXIALLY MOVING VISCOELASTIC BELTS

The two-pulley belt-drive system, in which the accessory shaft and the driven pulley are coupled by a wrap spring with stiffness K_d as illustrated schematically in Figure 1, where c and P_0, respectively, are the axial speed and the initial axial static tension of the translating belt and are assumed to be constant and uniform, l is the length of the belt spans, x_1, x_2 are the neutral axis coordinates of the belt span, $\omega_1(x_1,t)$, $\omega_2(x_2,t)$ are the transverse vibration displacements of the belt span at x and time t, $\theta_1(t)$ and $\theta_2(t)$, respectively, are the angular vibration displacements of the driven pulley and the driving pulley, M_1 is the preload between the accessory shaft and the driven pulley, J_a and $\theta_a(t)$ are the rotational inertia and the angular displacements of the accessory, respectively.

[a)] Corresponding author. Email: qdudjy@126.com**.**
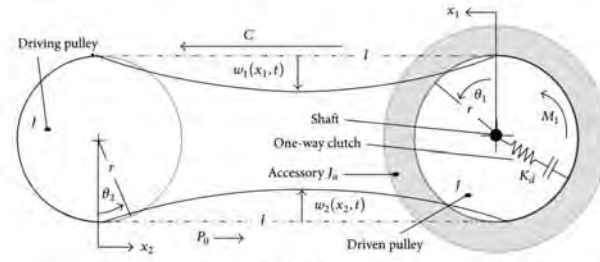
FIGURE 1: Schematic representation of a two-pulley belt-drive dynamical system coupled with a one-way clutch.

Considering the bending stiffness of the belt, the two spans of the translating belt are both modelled as Euler Bernoulli beams. The equation of transverse motion of the belt spans is nondimensionalized as

$$w_i,_{tt} + 2c\, w_i,_{x_i t} + \left(c^2 - 1\right) w_i,_{x_i x_i} + k_f^2 w_i,_{x_i x_i x_i x_i} + \alpha w_i,_{x_i x_i x_i x_i t} = T_i w_i,_{x_i x_i},$$

$$J\ddot{\theta}_2 = -c_b \dot{\theta}_2 + T_2 - T_1,$$

$$J\ddot{\theta}_1 = -c_b \dot{\theta}_1 + T_1 - T_2 + M_1 - \frac{r_a}{r_1} f\left(\theta_1 - \theta_a\right)\left[k_d\left(\theta_1 - \theta_a\right) + \mu_c\left(\dot{\theta}_1 - \dot{\theta}_a\right)\right],$$

$$J_a \ddot{\theta}_a = -c_a \dot{\theta}_a - \frac{r M_1}{r_a} + f\left(\theta_1 - \theta_a\right)\left[k_d\left(\theta_1 - \theta_a\right) + \mu_d\left(\dot{\theta}_1 - \dot{\theta}_a\right)\right]$$

(3)

The boundary conditions are $w_i\left(0,t\right) = 0, w_i\left(1,t\right) = 0, w_i,_{x_i x_i}\left(0,t\right) = w_i,_{x_i x_i}\left(1,t\right) = l/r$.

Using the HDQ method, we discrete the equation (3) to an ordinary differential equation set with respect to the time. Hadamard product and SJT product are used to reduce the computational complexity of the nonlinear equations. The results of different types of quadrature nodes are compared to show the influences of the grid points on the solutions.
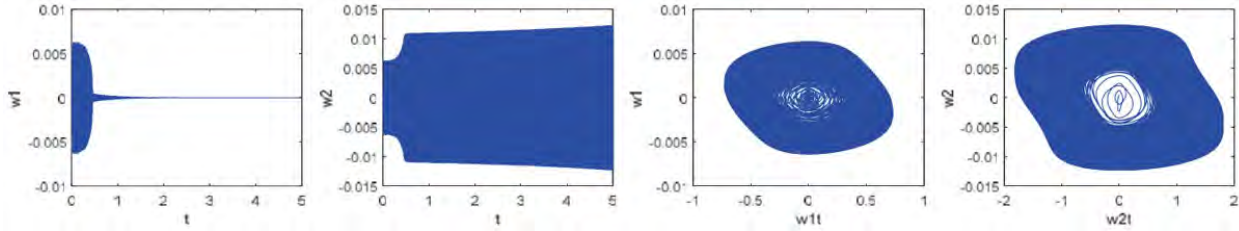
FIGURE 2: The time history and phase portrait of belt span 1 and belt span 2

CONCLUSIONS

The HDQ method is an efficient approach which can be used to solve the equations on the nonlinear vibrations of the axially moving viscoelastic belts. The HDQ method with Guass quadrature nodes illustrates the better convergence. Using Hadamard product and SJT product can reduce the computational complexity of the nonlinear equations. For the further study, localized harmonic differential quadrature method can be developed to avoid the illness of the coefficient matrices when the number of grid points reaches a certain value.

ACKNOWLEDGEMENTS

References

[1] Bellman R., Casti J.: Differential Quadrature and Long-Term Integration. Journal of Mechanical Analysis and Applications 34:235-238, 1971.

[2] Striz A. G., Wang X., Bert C. W.: Harmonic Differential Quadrature Method and Applications to Analysis of Structural Components. Acta Mechanica 111:85-94, 1995.

[3] Lal R., Rani R.: On the Radially Symmetric Vibrations of Circular Sandwich Plates with Polar Orthotropic Facings and Isotropic Core of Quadratically Varying Thickness by Harmonic Differential Quadrature Method. Meccanica 2015:1-24, 2015.

[4] Ding H., Zu J.: Effect of One-way Clutch on the Nonlinear Vibration of Belt-drive Systems with a Continuous Belt Model. *J. Sound Vib* **332**:6472–6487, 2013.

[5] Chen W.: Differential Quadrature Method and its Applications in Engineering − Applying Special Matrix Product to Nonlinear Computations and Analysis. *PhD Thesis*, Shanghai Jiao Tong University, Department of Mechanical Engineering, Shanghai, 1996.

NON-LINEAR DYNAMIC ANALYSIS OF A STEERING GEAR SYSTEM WITH BACKLASHES

Qian Ding [a), Yuxin Fang &Wei Zhang
Department of Mechanics, Tianjin University, Tianjin, China
Tianjin Key Laboratory of Nonlinear Dynamics and Chaos Control, Tianjin, China

Summary Steering Gear transmission plays an important role in various transmission systems. This paper investigates the dynamic behaviour of a steering system with several backlashes. First, the motion equations of a 3-DOF system about relative movements were established. Then the modal analysis was used to analyse the natural frequencies and amplitude-frequency curves of the system using the harmonic balance method. Second. the system was numerically simulated by Runge-Kutta method. Bifurcation, chaos and other complex dynamic phenomena were presented. Finally, influences of rotational speed ratio, gear backlashes, load force and damping coefficients on dynamics of the system were analysed. The result of the paper indicates that both the operating conditions and the structural parameters of the steering gear system can be designed properly to avoid undesirable dynamic motion and realize better mechanical properties.

INTRODUCTION

Transmission systems are widely used in automotive, aerospace and other industrial machinery. Based on dynamic analysis of the steering gear parts, a transmission system can be designed with high stability, durability and efficiency. Ozguven and Hourser [1] presented a review on gear dynamics with 188 references, which also gives a summary of the mathematical models. Another review by Wang [2] presents the gear dynamic behaviours under the influence of nonlinear factors. Basic concepts, mathematical models and the solving methods were also summarized. Backlashes between the meshed gears can influence heavily on the system vibration behaviour, as described in more theoretical researches recently [3-5]. Though the electric steering gear system is an important type of transmission system, which often contains several gears and a feed screw-nut structure, the dynamics of this type of gear system has been seldom investigated. Therefore, the dynamics of a 3 degree-of-freedom steering gear system with backlashes is analysed in this paper by using of the harmonic balance method. Influences of the operating conditions and structural parameters on the system dynamics are also presented.

EQUATION OF MOTION AND MODAL ANALYSIS

The steering gear system considered is shown in Fig.1. Three gear wheels and one feed screw-nut structure, acted by the external torque T_1 on gear 1 and concentrating force T_4 on the feed screw-nut structure respectively. The displacement excitations $e(t)$, acting on each gear, are resulted from the relative gear errors of the meshing teeth. Due to the backlashes, the restoring force generated during gears meshing can be modeled by piecewise linear function in Fig 2. Considering the relative movement of the meshed gears and screw-nut, the steering gear system can be reduced as a 3 degree-of-freedom system without rigid displacements. Then dynamic equations can be established and non-dimensionalized by introducing b_0 and $\bar{t}$ as the nominal size and nominal time. The harmonic balance method based on discrete Fourier transform is adopted to modal analysis of the transmission system with backlashes. Natural frequencies and amplitude-frequency curves are presented, as an example shown in Fig 3. They indicate that the resonances occur at the nondimensional frequencies 0.67, 1.01 and 1.85 respectively. All relative vibrations are intense at the first natural frequency. Whereas at the second and third natural frequencies, only one or two relative vibrations are quite intense.
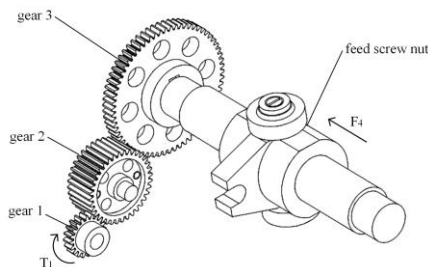
Fig. 1 The structure of a steering gear system   Fig. 2 Piecewise linear function of backlash   Fig. 3 A /F diagrams (b=1.2e^{-4} m)
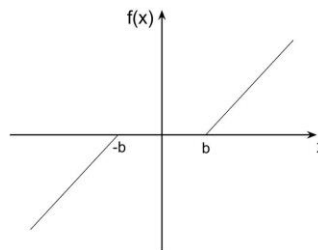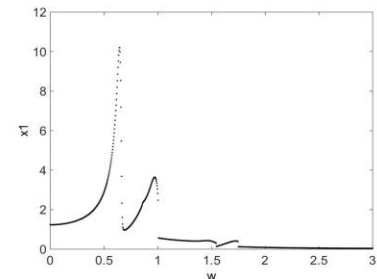
DYNAMIC TRANSMISSION ERROR AND COMPLEX DYNAMIC PHENOMENA

The dynamical behaviors of the steering gear system are numerically solved and illustrated by bifurcation diagrams, mean value, mesh state ratio, root-mean-square (RMS) of dynamic transmission error (DTE), and so on. Results of one gear

---

pair are shown in Fig 4-6 over the dimensionless rotating frequency Ω range of 0 to 4. In the range of 0-0.4, the mean value of DTE changes slightly and the RMS value is small, which means that the gears engage with each other only in one side and there is no collision between them at all. That is the gear engagement state is steady. In the Ω range of 0.4-0.6, the RMS value rises significantly while the mean value jumps down, and mesh state ratio of the front side is reduced by about 50%, which reflect the occurrence of double sides' collisions between the gears under the resonant conditions. As Ω increases and the mean value, RMS value and mesh state ratio value fluctuate extensively, which reflect intense gear collisions. Further increase of Ω brings the system returns back to steady movement.
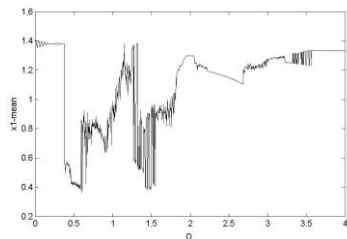
Fig 4. Mean value of DTE   Fig 5. RMS value of DTE   Fig 6. Mesh state ratio
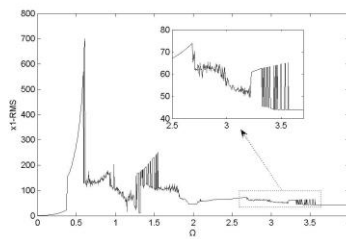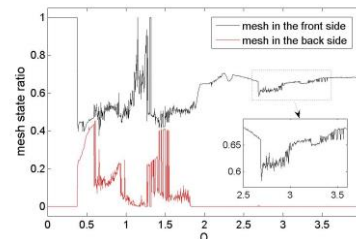
INFLUENCES OF THE PARAMETERS

In general, the gear backlash is the cause of nonlinearity and has a significant effect upon the system dynamics. The research shows that every single backlash in the system can cause complex motion and the sensitive frequency areas of each backlash are different. Fig 7-9 presents the bifurcation diagrams of the system using gear backlash, dimensionless load force and damping coefficient as the bifurcation parameter, respectively. The results demonstrate the reinforce power of the complex motions when backlashes increase and the effectiveness of the higher load force and damping coefficient in suppressing non-periodic motions of the spur gear system. What is more realistic is that the parameters could be used as control parameter to avoid chaotic responses.
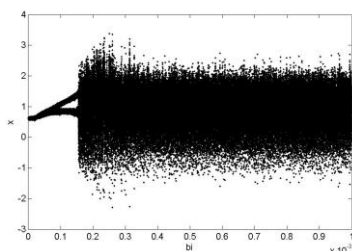
Fig 7. Bifurcation with increase of backlashes   Fig 8. Bifurcation with increase of load force   Fig 9. Bifurcation with increase of damping
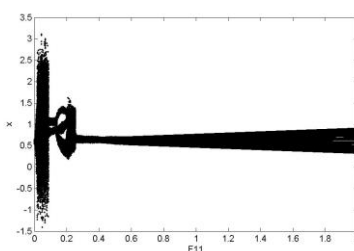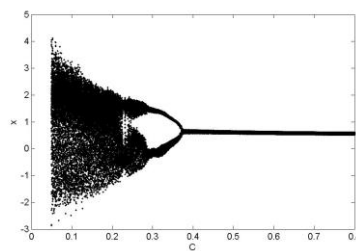
CONCLUSIONS

Dynamics of a steering gear system with gear backlash nonlinearities and transmission error excitation are investigated by harmonic balance method and numerical simulations in this paper. The result shows that gear backlash is a significant factor to the bifurcations and chaos phenomenon in the steering gear system which cannot be ignored. According to the diagrams of mean value of dynamic transmission error, mesh state ratio and RMS value, bifurcations and chaos can cause gear collisions and unstable transmission to the system. Variations of the rotational speed ratio, gear backlash, dimensionless load force and damping coefficients can influence the state of the system response. The unexpected chaotic behavior, collisions within parts of the system as a result, can be avoided by designing the parameters with suitable values.

References

[1]   H. Ozguven, D. Houser: Mathematical models used in gear dynamics—a review. *Journal of Sound and Vibration* **121**:383-411, 1988.

[2]   Wang Jianjun, Li Runfang: A survey to nonlinear vibration of gear transmission system. *Applied Mechanics Reviews* **56**:309-329, 2003.

[3]   Al-shyyab A, Kahraman A: Non-linear dynamic analysis of a multi-mesh gear train using multi-term harmonic balance method: period-one motions. *Journal of Sound and Vibration* **284**:151-172, 2005.

[4]   Cai Wan, Chang Jian: Bifurcation and chaos analysis of spur gear pair with and without nonlinear suspension. *Nonlinear Analysis: Real World Applications* **12**:979–989, 2011.

[5]   Chen, G. Y., Chen, G. D: Dynamic analysis of a face gear drive with spur involute pinion with backlash considered. *Mechanical Science and Technology for Aerospace Engineering* **28**:1244–1251, 2009.

NONLINER DYNAMICS OF GEARBOXES WITH FLEXIBLE FRICTION CLUTCH

Georg Jehle[1], Olga Drozdetskaya[1a] & Alexander Fidlin[1]
[1]Institute of Engineering Mechanics, Karlsruhe Institute of Technology, Karlsruhe, Germany

<u>*Summary*</u> Two dynamic phenomena in automotive transmissions are investigated, which both arise while shifting. The first one is the radial displacement between the rotation axes of the clutch's discs. The second one is friction induced flutter provoking vibrations, noise and sometimes significant durability problems. The interaction between the sliding clutch and the helical gearing in the transmission is of crucial importance for both phenomena. A minimal model of a gearbox incorporating a flexible clutch disc is presented and the relevant instability mechanisms are discussed. The stability analysis based on linearization is compared to transient simulations of the complete nonlinear system, which enable to identify the main mechanisms limiting the vibration amplitude: stick-slip transitions within the clutch due to strong rotational vibrations, contact losses between the clutch discs and between the gears due to axial vibrations. It is shown that complex sequences of these events can take place within one limit cycle.

INTRODUCTION

Shifting gearboxes are common elements of mechanical transmissions, which are used both in industrial and automotive drivetrains. Combined with friction clutches they enable to operate the motor under optimal conditions and cover a wide range of operation speeds and torques. A great variety of gearboxes established itself especially in the automotive area. Manual and automatic transmissions combined with dry or wet operated clutch systems have to be mentioned here alongside with double clutch systems, which became very popular because of its fast and comfortable shifting without interruption of drive power. Friction induced phenomena are of principal importance for all these systems, because sliding within friction clutches is an inevitable part of each gear shifting. Two of the phenomena have attracted high interest of the research in the last years. The first one is the radial displacement between the engine side (primary side) disc and the gearbox side (secondary side) disc of the clutch [1, 2]. The second one is eek-noise (also called squeal) accompanied by strong vibrations of the transmission components. Different models describing particular mechanisms of the eek-noise' excitation have been suggested in the literature [3 − 5]. However, they were mainly concentrated on the modelling of the friction clutch itself (except [5]) and primarily limited to the linear stability analysis.

In the present paper, the depth of detail of the gearbox model is significantly increased concerning clutch and gears. Besides the identification of new instability mechanisms and the recognition of the governing parameters, the full nonlinear dynamics is simulated in order to distinguish between effects of different nonlinearities limiting the amplitudes of vibrations.

MINIMAL MODEL OF A HELICAL GEARBOX WITH ELASTIC LAMELLA

In the studied model, the complex structure of a real gearbox is reduced to its main components. The clutch primary side is taken to be a flexible lamella (L, cf. Figure 1), which is attached to the flywheel, mounted on the crankshaft and rotating with the constant rotational velocity Ω. The lamella is modelled using Kirchhoff's plate theory in a rotating frame.
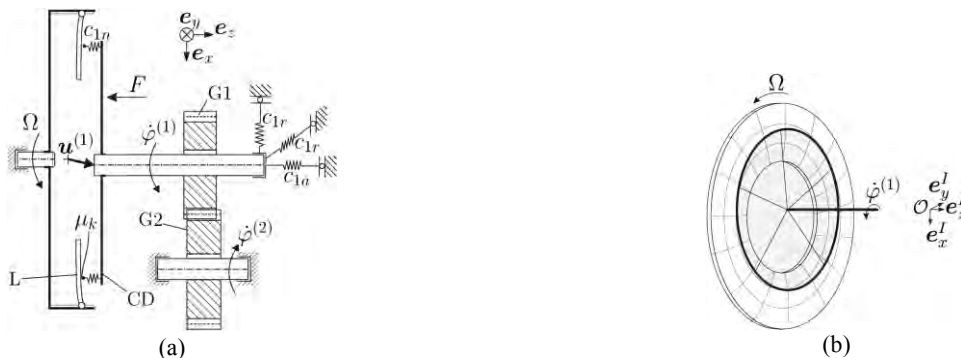
Figure 1. (*a*) Model of the shifting gearbox with a flexible lamella L; (*b*) contact between the lamella and the eccentric friction disc.

The clutch disc CD is attached to the gearbox' input shaft G1. It has four degrees of freedom $\boldsymbol{u}^{(1)} = \left[u_x^{(1)}, u_y^{(1)}, u_z^{(1)}\right]$ and $\boldsymbol{\omega}^{(1)} = \left[0, 0, \dot{\varphi}^{(1)}\right]$. The compound is elastically supported by springs representing the rolling bearings. Bending or tilting of the input shaft is not taken into account, because the corresponding effects have been elaborately discussed in [3, 4]. The teeth on the input shaft contact with those placed on the secondary shaft G2. In the stationary case, this contact can be modelled as a non-holonomic constraint. For transient simulations, the unilateral tooth contact is not necessarily closed. An alternative tooth force model is needed here which is obtained through regularization of the line tension at both front and rear of the

---

flanks. The contact between the elastic lamella and the clutch disc occurs along the contact circle (cf. Figure 1b). The gear normal force shifts the input shaft away from the engine's axis, leading to a radial displacement which depends strongly on the transmitted torque. In this context, non-symmetrical deformation of the lamella arises which requires taking the corresponding elastic modes into account.

FRICTION INDUCED FUTTER AND NONLINEARITIES LIMITING VIBRATION AMPLITUDES

Depending on design parameters and operating conditions, different instability mechanisms can occur in the described system, which are all of the type friction induced flutter due to mode coupling. However, depending on the dominant oscillation modes, the instabilities can be split into several groups:

- radial-torsional instability of the input shaft
- wobbling instability of the lamella alongside with torsional vibrations of the input shaft
- combination of both
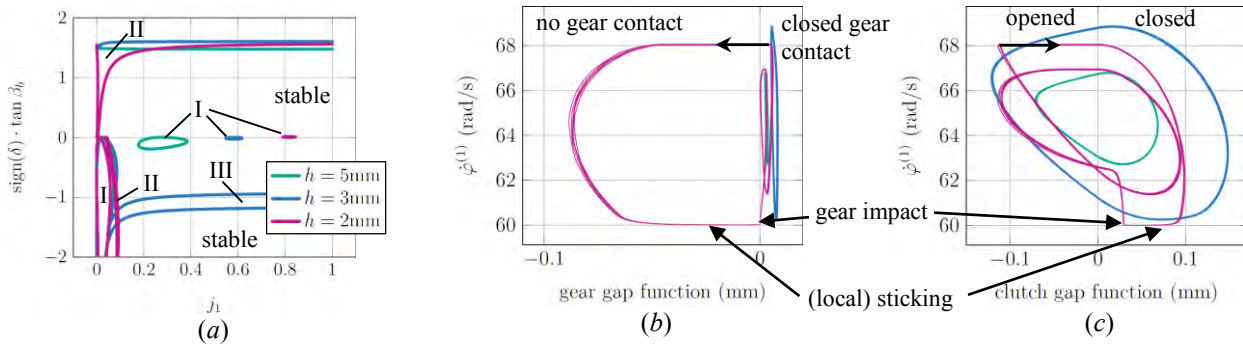
Figure 2. (*a*) Instability domains in the parameter space for different values of the lamella's thickness h: I –radial-torsional flutter, II – wobbling instability of the lamella, III – combination of I and II; (*b*) and (*c*) steady state oscillation: green – opening in the clutch, blue – opening and partial sticking in the clutch, magenta – opening and sticking in the clutch, impacts between the gears.

The existence domains for each type of instability are calculated in the parameter space (cf. Figure 2*a*). Here $j_1 = \frac{J_1}{m_1 R^2}$ is the ratio between the gear unit input shaft's rotational inertia and its mass times square of the friction radius, β_b is the gear helical angle and sign(δ) is the slip direction within the clutch.

The amplitudes of the self-excited vibrations can be limited by different nonlinearities. Contact losses between the lamella and the clutch disc (gap function < 0) alongside with the impacts within the gears are of main importance at low clamping force in the clutch which results in the low transmitted torque. At a high level of the clamping force, temporal (local) sticking along the friction circle becomes the most important nonlinearity. Complex behaviour can be observed in the intermediate range of the clamping forces, where all these mechanisms can contribute to the occurrence of the limit cycle (cf. Figure 2 (*b*) and (*c*)).

CONCLUSIONS

A wide variety of friction induced effects exists in a gearbox with attached dry friction clutch, such as radial displacement and several types of instabilities. The suggested minimal model enables the parameter value- and operation dependant description of both effects. The influence of different nonlinearities on the amplitude of the transient oscillation demonstrates the principally non-smooth character of the system, making the numerical analysis extremely difficult. Nevertheless, some approaches could be identified, which enable to capture the principal behaviour of a gearbox with a more complex structure.

References

[1] Fidlin A., Stamm W.: On the radial dynamics of friction discs. *Eur. J. Mech. – A/Solids* **28**:526-534, 2009.
[2] Weiss C., Morlock M.M., Hoffmann N.P.: Friciton induced dynamics of ball joints: Instability and post bifurcation behavior. *Eur. J. Mech. – A/Solids* **45**:161-173, 2014.
[3] Herve B., Sinou J.-J., Mahe H., Jezequel L.: Analysis of squeal noise and mode coupling instabilities including damping and gyroscopic effects. *Eur. J. Mech. – A/Solids* **27**:141-160, 2008.
[4] Fidlin A., Drozdetskaya O., Waltersberger B.: On the minimal model for the low frequency wobbling instability of friction discs. *Eur. J. Mech. – A/Solids* **30**:665-672, 2011.
[5] Jehle G., Fidlin A.: Friction induced vibrations in shift gearboxes. *ZAMM, Z. Angew. Math. Mech.* **94:** 911- 916, 2014.

VIBRO-IMPACT DYNAMICS IN SYSTEMS WITH TRIGGER OF COUPED THREE SINGULAR POINTS: COLLISION OF TWO ROLLING BODIES

Katica R. (Stevanović) Hedrih[1,2]

[1]*Department of Mechanics, Mathematical Institute Serbian Academy of Sciences and Arts, Belgrade, Serbia*
[2]*Faculty of Mechanical Engineering, University of Niš, Serbia*

Summary Under the author's use Petrovič's elements of mathematical phenomenology, especially mathematical analogy, new expressions of post-collision outgoing angular velocities of two rolling rigid bodies are determined. Advances to theory of collision between two bodies are generalized to collision of two rolling rigid bodies. Using these results, nonlinear dynamics in the vbro-impact system with trigger of coupled singular points and homoclinic trajectory in phase trajectory portraits is study. Use phase portraits of two nonlinear dynamical systems in which appear central collision of thin rolling different size disks are studied. In first vibro-impact system disks is in rolling along straight line and coupled by springs, and in second rolling disks are moving along a circle line rotate with constant angular velocity around vertical central axis. In both considers system dynamics exist a trigger of coupled singular points.

ADWANCES TO THEORY OF COLLISION OF TWO RIGID ROLLING BODIES

Advances to theory of collision between two bodies are generalized to collision of two rolling rigid bodies. Under the authors' use Petrovič's elements of mathematical phenomenology [1,2,3,4], especially mathematical analogy, new expressions of post-collision outgoing angular velocities of two rolling rigid bodies are determined in following forms (see Figure 1.a*):.
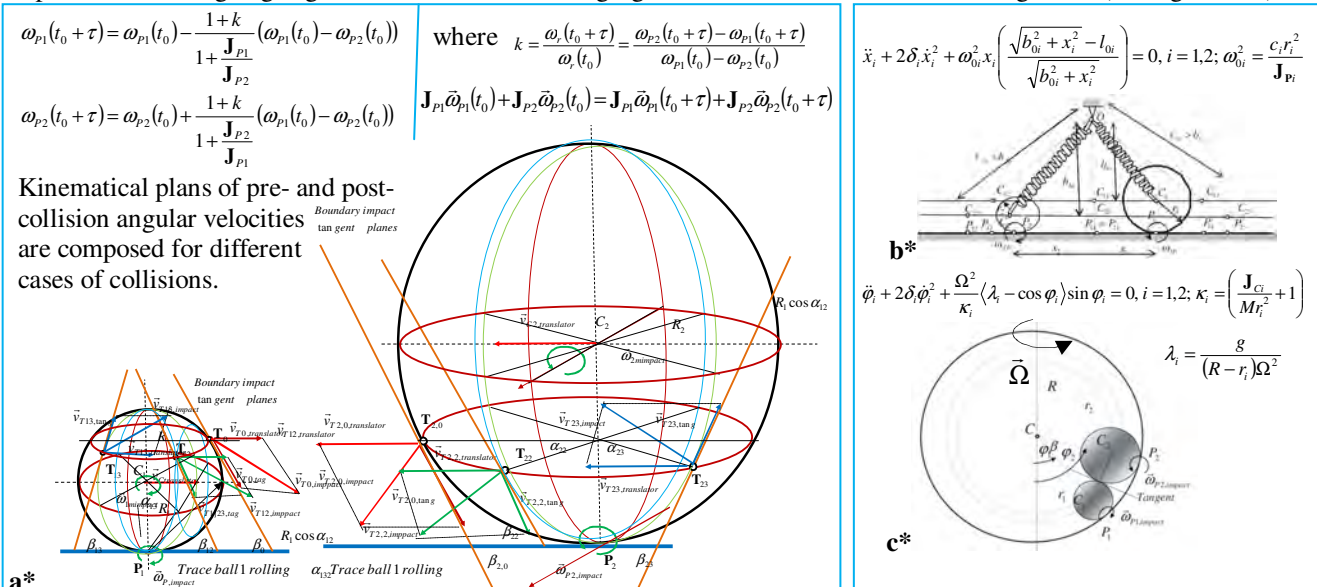
Figure 1. a* Plans of the impact velocities of possible points at corresponding circles at same height of balls in central and skew collisions of two rolling heavy balls different radiuses: left for first smaller ball and right for second bigger ball. b* and c* Two vibro-impact systems each containing two rolling thin different radiuses disks in central successive collisions.

NON-LINEAR DYNAMICS OF TJE VIBROIMPACT SYSTEMS WITH TRIGGESR OF COUPLED SINGULAR POINTS AND HOMOCLINIC ORBITS IN FORM NUMBER EIGHTIN PHASE PORTRAITS

In Figure 1.b* and c* two mechanical vibro-impact systems containing two rolling thin different size disks are presented. Each disks, in both considered systems dynamics, a corresponding trigger [5,6] of coupled three singular points and homocclinic orbit in the form of number "eight" posses in corresponding phase portraits for corresponding relation of parameters of system, In both system exists a bifurcation parameter and with its variation in the phase portraits layering of phase trajectories appear, as well as appearance and disappearance of trigger of coupled singular points. Kinetic parameters and phase portraits of each vibro-impact system (in Figure 1. b* and c*) in ideal constraints as conservative and, also, in the field of turbulent damping as no conservative, and of each of the rolling disks are determined and graphically presented. in Figure 2 a* and b* phase trajectory branches in phase portraits of two rolling disks for motion in interval between configurations of the initial condition configurations and configurations of pre-first-collision and post-first-collision between two rolling disks for corresponding conservative systems are presented. On the phase portraits alternations of the pre-collision impact velocities of the disks into post-collision corresponding translator or angular velocities are visible.

---

[a] Corresponding author. Email: khedrih@sbb.rs,khedrih@eunet.rs**.**
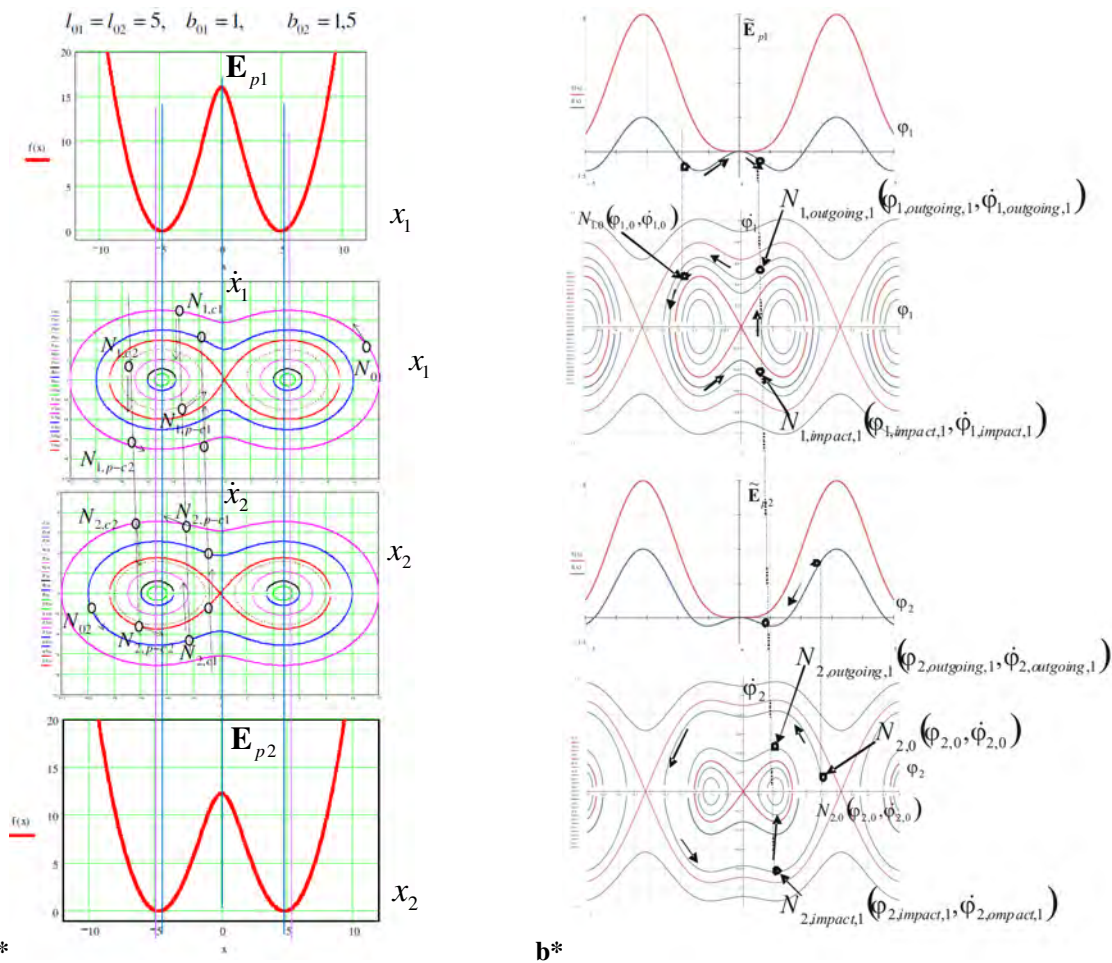
Figure 2. Phase trajectory branches in phase portraits and total mechanical energy branches of two rolling disks for motion in interval between initial condition configuration and configurations of pre-first-collision and post-first-collision between two rolling disks with vibro-impact dynamics (a*) along a line and (b*) on rotate circle trace with constant angular velocity around vertical central axis for the conservative systems presented in Figure 1,b* and 1.c*.

CONCLUDING REMARKS

Advances to theory of collision of two rolling rigid bodies open new possibilities for progress in knowledge of vibroimpact system dynamics. Obtained results are related to different ceases of conservative as well as no conservative vibro-impact dynamics. Emery analysis for turbulent damping with generalized function of energy dissipation $\Phi = b\dot{x}^3/3$ gives rate of total mechanical energy degradation in the form: $d(E_k + E_p)/dt = -3\Phi$.

References

[1] Petrović M., Elementi matematičke fenomenologije (Elements of mathematical phenomenology), Srpska kraljevska akademija, Beograd, 1911. str. 389.. http://elibrary.matf.bg.ac.rs/handle/123456789/476?locale-attribute=sr

[2] Petrović M., Mecanismes communs aux phenomenes disparates, Paris 1921.

[3] Preface:Elements of mathematical phenomenology and phenomenological mapping in non-linear dynamics, Edited by Katica R. (Stevanovic) Hedrih, Ivan Kosenko, Pavel Krasilnikov and Pol D. Spanos, Special Issue of International Journal of Non-Linear Mechanics, Volume 73, Pages 1-128 (July 2015)

[4] Hedrih (Stevanović) K.R. , (2015), Elements of mathematical phenomenology: I. Mathematical and qualitative analogies,. Труды МАИ Выпуск №84, pp. 42 (1-42); II. Phenomenological approximate mappings, №84, pp. 29 (1- 29) www.mai.ru/science/trudy/ , http://www.mai.ru/upload/iblock/5f6/hedrih_eng_1.pdf, Эл № ФС77-58560, ISSN: 1727-6942

[5] Hedrih (Stevanović) R. K., (2004), A Trigger of Coupled Singularities, MECCANICA, Vol.39, No. 3, 2004., pp. 295-314. , DOI: 10.1023/B:MECC.0000022994.81090.5f,

[6] Andronov A. A., Vitt A. A., Haykin S., (1981), Teoriya kolebaniy, Nauka, Moskva., pp. 568.

SWITCHING SENSITIVE AND INSENSITIVE RESPONSES IN A PIECEWISE SMOOTH RUBBING ROTOR SYSTEM

Jun Jiang[a], Ling Hong

State Key Laboratory for Strength and Vibration, Xi'an Jiaotong University, Xi'an 710049, China

Summary In this work the response characteristics of a two-degree-of-freedom piecewise smooth nonlinear isotropic rubbing rotor system, which consists of a linear subsystem and a nonlinear subsystem controlled by a switching surface that gives the rubbing condition, are investigated. It is found that the parameters of the piecewise smooth system can be classified into the switching sensitive and insensitive regions. We show that the responses of the full non-smooth system *in the switching insensitive regions* can be well determined through the analysis of the responses both the linear and the nonlinear subsystems by the theory of nonlinear dynamics. *In the switching sensitive regions*, some responses of the full non-smooth system, although unpredictable theoretically, can still be explained from the response characteristics of the subsystems, and some other responses cannot be well understood from our current knowledge.

PIECEWISE SMOOTH MODEL FOR A RUBBING ROTOR

Rotor/stator rubbing is a malfunction in rotating machinery that degrades the machine performance and may lead to the catastrophic failure of a whole machine through dry whip in the worst case [1]. A rubbing rotor system (see Fig.1) can be modeled by a piecewise smooth system [2]:

$$m\ddot{x} + c\dot{x} + k_s x + \Theta k_b \left(1 - \frac{r_0}{r}\right)(x - \mu y) = me\omega^2 \cos\omega t$$

$$\text{deflection magnitude} \quad r = \sqrt{x^2 + y^2} \tag{1}$$

$$m\ddot{y} + c\dot{y} + k_s y + \Theta k_b \left(1 - \frac{r_0}{r}\right)(\mu x + y) = me\omega^2 \sin\omega t$$

where x, y are the deflections of the rotor in the horizontal and vertical directions, and m, c, k_s are mass, damping and stiffness of the rotor. e is mass eccentricity and ω the rotating speed of the rotor. k_b is the stiffness of the stator. r_0 and μ are clearance and friction coefficient between the rotor and the stator.

Θ is Heaveside function with $\Theta=0$ when the deflection amplitude $r < r_0$, that is, there is no rubbing in the rotor and the system is govern by linear equations. $\Theta=1$ when $r \geq r_0$ is the rubbing case whereby the system is governed by the nonlinear equations. Therefore, the rubbing condition is governed by the switching surface by

$$\sigma = \{(x, \dot{x}, y, \dot{y}) \mid \sqrt{x^2 + y^2} - r_0 = 0\} \tag{2}$$

The piecewise smooth system possesses some specific features: (1) the switching surface is defined as a deflection magnitude of two displacement coordinates of the system; (2) when a periodic trajectory of the system begins to touch the switching surface, it touches switching surface at all points to make it different from gazing in the usual non-smooth systems; (3) there is no periodic motion formed by crossing the switching surface between the two subsystems.

DYNAMICS OF LINEAR AND NONLINEAR SUBSYSTEMS

By solving the equations of the linear subsystem of (1) when $\Theta=0$, the existence boundaries of the periodic solution of linear subsystem are obtained by considering the switching condition (2), which are shown by the red dashed lines marked respectively by Ω_L and Ω_U in Fig.1(left). Here Ω is the non-dimensional rotating speed defined by ω over the natural frequency of the coupled rotor/stator system. These two lines also give the rotating speeds at which the piecewise smooth system (1) is in the grazing state.

The periodic solutions of the nonlinear subsystem of (1) when $\Theta=1$ can be also solved analytically. There are two branches periodic solutions of the nonlinear subsystem, one is stable and the other is unstable. The existence ranges of the periodic solutions are decided by three saddle-node bifurcation points denoted by the black solid curves in Fig.1(left). However, when the switching condition (2) is taken into account, the periodic solutions are meaningless in the ranges between SN_1 and Ω_L as well as in right side of SN_3 because the amplitudes of the periodic solutions are smaller than the clearance r_0. The boundaries of Hopf bifurcation for each of the two periodic solutions are also derived analytically and shown by the green solid curves in Fig.1(left). It is found that the meaningful stable periodic solution of the nonlinear subsystem exists only in the range between Ω_L and SN_2 and under the green curve (+). So a meaningful quasi-periodic solution with amplitude fluctuating around r_0 exists after Hopf bifurcation in the corresponding region but above the green curve (+). Through numerical simulations, the nonlinear subsystem possesses only a pair of meaningless periodic solutions in the range between SN_1 and Ω_L, but there are meaningful chaotic and quasi-periodic responses in the ranges between SN_2 and SN_3, or in the region in the right side of SN_3, where another pair of meaningless periodic solutions exist. The dynamical characteristics of subsystems have significant influence on the behavior of the full piecewise smooth system.

---

[a] Corresponding author. Email: jun.jiang@mail.xjtu.edu.cn.

SWITCHING INSENSITIVE AND SENSITIVE RESPONSE REGIONS

It is found that the response characteristics of the full piecewise smooth in the region corresponding to the regions I, II and III in Fig.1(left) can be well determine by using the dynamic information derived from the linear and the nonlinear subsystems, as shown in Fig.1(right) as given by [2]. These regions are thus defined as *switching insensitive regions* of the full piecewise smooth system (1). The features of these regions are quite different. In region I, the only meaningful solution is the periodic solution of the linear subsystem. In region II, the only meaningful response is the periodic or the quasi-periodic response of the nonlinear subsystem. In region III below green curve (+), periodic solutions of both linear and nonlinear subsystems are meaningful but they do not interference each other and can coexist. In region III above green curve (+), the meaningful quasiperiodic response loses stability due to the response at the nonlinear normal mode [3].

However, the response characteristics of the full piecewise smooth system (1) in the region in the right side of SN_2, marked by IV and V in Fig.1(left), cannot be well predicted or even understood from the responses of the linear and nonlinear subsystems. These regions are thus defined as *switching sensitive regions* of the full piecewise smooth system (1). The features of these two regions are as follows: the linear subsystem has a periodic solution with amplitude almost touch the switching surface, and on the other hand, the nonlinear subsystem has a meaningful chaotic or quasi-periodic response with the amplitude fluctuating around the switching surface and the meaningless periodic solutions with amplitudes less than the clearance r_0.

CONCLUSIONS

The responses of piecewise smooth rotor system are investigated from the point view to find the relationship between the response characteristics of the subsystems and those of the whole system. It is demonstrated that the responses of the whole system can be well predicted from those of subsystems in the switching insensitive regions. On the other hand, it is still a challenge to understand and predict the responses in the switching sensitive regions.
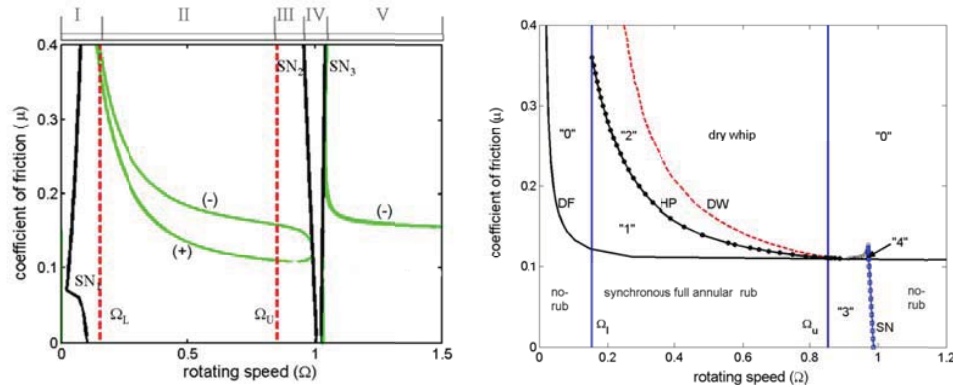
Fig.1 (Left)The existence and bifurcation boundaries of periodic solutions of the linear and nonlinear sub-systems.(Right) Response characteristics of system (1) with the boundaries of no-rub are denoted by Ω_l and Ω_u, synchronous full annular rub by curves of Ω_l, SN and HP, partial rub by HP and DW, and dry whip marked by DF. The multi-stable sub-regions are denoted by "0", "1", "2"and "3".

References

[1]   Yu J. J., Goldman P., Bently D.E., Muszynska A.: Rotor/seal experimental and analytical study on full annular rub. *ASME Journal of Engineering for Gas Turbines and Power* **124**: 340–350, 2002.

[2]   Jiang J.: Determination of the Global Responses Characteristics of A Piecewise Smooth Dynamical System with Contact. *Nonlinear Dynamics* **57**: 351-361, 2009.

[3]   Chen Y. H., Jiang J.: Determination of nonlinear normal modes of a planar nonlinear system with a constraint condition. *Journal of Sound and Vibration* **332**: 5151–5161, 2013.

MIXED-MODE OSCILLATIONS IN A SLOW-FAST FLEXIBLE JOINT SYSTEM WITH TIME DELAY

Shanying Jiang[1a)], Jian Xu[2]

[1]*School of Mechanical Engineering, Shanghai Institute of Technology, Shanghai, China*
[2]*School of Aerospace Engineering and Applied Mechanics, Tongji University, Shanghai, China*

Summary Mixed-mode oscillations (MMOs) are observed in a delay-coupled flexible joint system with multiple time scales, which behaves as a complex oscillatory pattern consisting of small amplitude oscillations followed by large excursions of relaxation type in a period. The existence of homoclinic orbits induced by Bogdanov-Takens bifurcation of the fast subsystem is proposed to explain the mechanisms of the occurrence of MMOs. It is numerically proved that the small parameter in a slow-fast system influences the convergence rate of oscillatory trajectories and thus leads to the transitions of mixed-mode oscillations.

THE SLOW-FAST FLEXIBLE JOINT SYSTEM

A delay-coupled flexible joint robot manipulator is remodelled and transformed into a typical slow-fast system in [1] as

$$\begin{cases} \varepsilon\dot{\theta}_1(t) = p_1(t), \\ \varepsilon\dot{p}_1(t) = \bar{\alpha}_1\left(\varepsilon p_2(t) - p_1(t-\tau)\right) + \left(\theta_2(t) - \theta_1(t-\tau)\right) - \beta\sin\theta_1(t), \\ \dot{\theta}_2(t) = p_2(t), \\ \dot{p}_2(t) = -\bar{\alpha}_1\left(\varepsilon p_2(t) - p_1(t-\tau)\right) - \left(\theta_2(t) - \theta_1(t-\tau)\right) - \alpha_2 p_2(t) + u(t), \end{cases} \tag{1}$$

where θ_1 and p_1 are defined as fast variables, θ_2 and p_2 are fast variables and the parameter ε is usually called as the small parameter. It is obtained that the small parameter multiplies the highest derivative of the state variables in Eq. (1), which leads to the fact that the order of the system for $\varepsilon = 0$ becomes lower than that for $\varepsilon \neq 0$. This is just why the singularity comes up in a slow-fast problem. According to geometric singular perturbation theory [2], the limit of the original full system as $\varepsilon \to 0$ is defined as the reduced slow subsystem while the limit of the rescaled full system with $t = \varepsilon\bar{t}$ and $\varepsilon \to 0$ is the reduced fast subsystem.

EXISTENCE OF HOMOCLINIC ORBITS

Projecting the 4-dimensional fast subsystem onto the 2-dimensional plane p_1-θ_1 and regarding the state variable $\theta_2(t)$ as a constant, the fast subsystem on the p_1-θ_1 plane is obtained as

$$\begin{cases} \theta_1'(t) = p_1(t), \\ p_1'(t) = -\bar{\alpha}_1 p_1(t-\tau) + \left(\theta_{20} - \theta_1(t-\tau)\right) - \beta\sin\theta_1(t). \end{cases} \tag{2}$$

After a translation of the equilibrium to the origin, the corresponding characteristic equation is derived as

$$F(\lambda) = \lambda^2 + e^{-\lambda\tau}\bar{\alpha}_1\lambda + e^{-\lambda\tau} + \beta\cos(\theta_{10}) = 0. \tag{3}$$

It tells that $\lambda = 0$ is a double zero root of the characteristic equation $F(\lambda) = 0$ when the condition $\bar{\alpha}_1 - \tau = 0$ holds. Namely, the characteristic equation (3) has a zero eigenvalue with multiplicity two. Bifurcation theory in dynamical system [3] says that when the characteristic equation of a linearized system has a zero eigenvalue with multiplicity two, a BT bifurcation may occur in the original nonlinear system. Fig. 1 illustrates a series of boundary curves dividing the parameter plane τ-θ_1 into nine areas, where the boundary curves H_i and S_i correspond to the pure imaginary eigenvalues
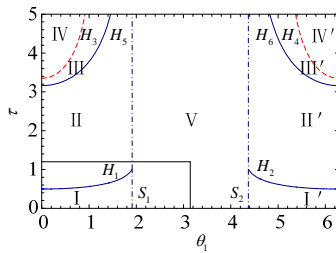
Fig. 1 The stability boundaries near the BT point.   Fig. 2 The critical boundary of homoclinic bifurcation.   Fig. 3 The BT bifurcation diagram on the parameter plane τ-θ_1.
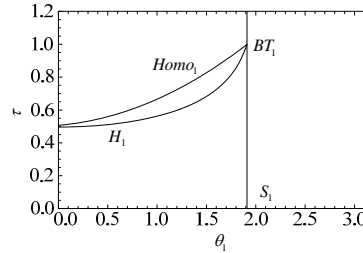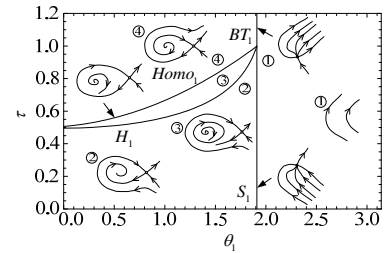
[a)]Corresponding author. Email:jiangshanying@sit.edu.cn
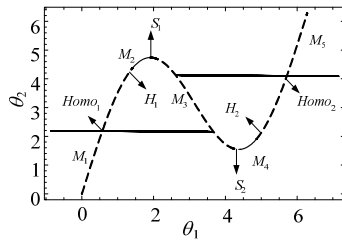
Fig. 4 Structure and stability of the slow manifold with $\tau = 0.653$.
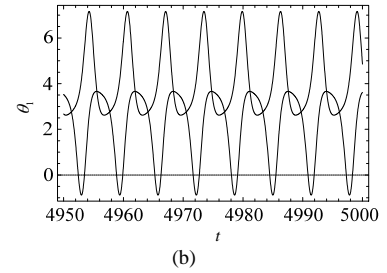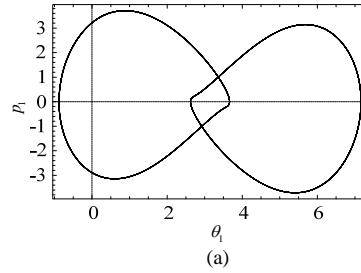
Fig. 5 Limit cycles and corresponding time-history plots, (a) limit cycles, (b) time-history plots.

and the zero eigenvalue respectively. Fig. 3 illustrates the corresponding phase diagrams in each region separated by critical bifurcation curves shown in Fig. 2. Fig. 4 explains the structure of the slow manifold with two limit cycles near the homoclinic points $Homo_1$ and $Homo_2$. The corresponding phase portraits and time histories of two limit cycles starting from different initial points are presented in Fig. 5. Numerical results show that with the variation of time delay, these two limit cycles could be infinitely close to the homoclinic orbits. So far, the existence of homoclinic orbits is identified.

OSCILLATION ANALYSIS AND EFFECTS OF SMALL PARAMETER

Once the fast manifold fails to intersect with the stable segments or the stable limit cycles bifurcated from unstable segments of the slow manifold, the flows in the phase space would not be attracted to any of the stable attractors and they would have to wander in the space. In fact, it is just these wandering flows that result in the mixed-mode oscillations. The phase portraits and the time-history plots corresponding to $\varepsilon=0.05$ and $\varepsilon=0.01$ are displayed in Fig. 6. From the comparison of Fig. 6(a) to (d), one may easily figure out that with the reduction of the small parameter ε, the convergence rate of flows being attracted to the stable segment M_4 is slowed down. Based on the results obtained above, it can be seen that with the same time delay, the mixed-mode oscillations can be transferred via adjusting the small parameter ε. Besides, the scales of the small parameter influence the attraction rate of flows to the stable segments.
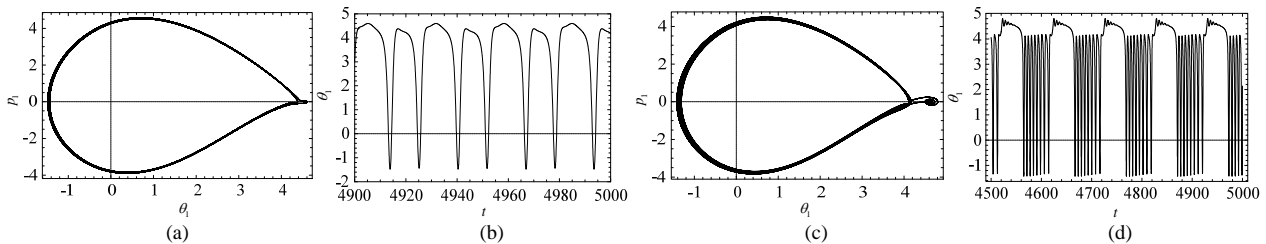
Fig. 6 Mixed-mode oscillations, (a) phase portraits with $\varepsilon=0.05$, (b) time series with $\varepsilon=0.05$, (c) phase portraits with $\varepsilon=0.01$, (d) time series with $\varepsilon=0.01$.

CONCLUSIONS

A slow-fast flexible joint system is investigated in this paper to explain the mechanism of mixed-mode oscillations. The eigenvalue analysis of the fast subsystem achieved the condition of BT bifurcation and then confirmed the existence of homoclinic orbits around the slow manifold. Numerical results reveal that the mixed-mode oscillations can be transferred from one to another through the scale variation of the small parameter. The smaller the parameter is, the slower the convergence rate of the flows to the stable homoclinic orbit and the stable segment of the slow manifold are.

Acknowledgments

References

[1] Jiang, S., Xu, J. & Yan, Y.: Stability and oscillations in a slow-fast flexible joint system with transformation delay. *Acta Mech. Sinica,* **30**: 727-738, 2014.

[2] Jones, C.: Geometric singular perturbation theory. *Lect. Notes Math,* **1609**: 45-118, 1994.

[3] Wiggins, S.: Introduction to applied nonlinear dynamical systems and chaos, 2nd Ed. Springer-Verlag, New York, 2003.

DYNAMIC RESPONSE OF ACOUSTICALLY EXCITED PANELS
RESTING ON ELASTIC FOUNDATIONS IN THERMAL ENVIRONMENTS

Liu Liu[1], Bingyang Lv[1] &Tiren He[1]
[1]School of Aerospace Engineering, Department of Mechanics
Beijing Institute of Technology, Beijing, China

<u>*Summary*</u> In order to ensure integrity of thermal protection system for hypersonic vehicles, the stochastic dynamic response induced by the combination of thermal and acoustic loadings has been investigated for a thin panel resting on a two-parameter elastic foundation. A theoretical model is developed based on the Kirchhoff thin-plate assumptions and general von Kármán-type equation through Galerkin method. A dynamic response evolution parameter deduced from the primary-mode modal equation and the Fokker-Planck distribution function is proposed to characterize a transition from linear vibration to fully nonlinear dynamic snap-through for a thermally-buckled panel. The study demonstrates the combination of acoustic excitation, thermal effect and structural stiffness including elastic foundation stiffness governs the dynamic response evolution. As the elastic foundation stiffness increases, the buckling temperature increases and the postbuckling deflection decreases, which promote the nonlinear dynamic snap-through response remarkably for the postbuckled panel with reducing snap-through amplitude.

INTRODUCTION

In order to protect the substructure of a hypersonic flight vehicle, a multi-layered structure with a plain-woven C/SiC composite thin skin panel adhesively bonded to a very thick and light Si-C-O aerogel thermal insulator is used as a typical thermal protection system (TPS) structure. However the ceramic based composite thin skin panel is structurally weak and can fail easily. Under the overall sound pressure level (OASPL) of 140-170 dB, an erratic fully nonlinear large amplitude snap-through behavior has been observed experimentally for the thin panel at elevated temperature, which might lead to the so-called thermal–acoustic fatigue damage. In order to ensure structural integrity, it is desired to have a computationally efficient methodology to predict the dynamic response of the thin skin panel subjected to a combined loading. Few investigations have been conducted to characterize the dynamic response of the top facesheet panel for the multi-layer TPS. Current methods can neither characterize and predict occurrence of the snap-through response for the examined structure under a certain combination of thermal and acoustic loadings, nor provide an efficient way to understand the effects of the model parameters, such as elastic foundation stiffness, loadings, boundary conditions, and material properties on the stochastic dynamic response due to high computational expenses.

THEORETICAL MODEL

The top facesheet panel of the multi-layer TPS can be modeled as a thin composite plate resting on a Pasternak-type elastic foundation, where the thick thermal insulator has been considered as an elastic foundation. The theoretical model is developed based on the Kirchhoff thin-plate assumptions and general von Kármán-type equation that includes the plate-foundation interaction and the contribution of the membrane load on the transverse deflection. The governing equation has been derived using the first four symmetric modes through Galerkin method and a set of higher order coupled nonlinear ordinary differential modal equations (ODEs) have been given. It is noteworthy that three contributions to the linear stiffness term include the usual structural linear stiffness, the elastic foundation stiffness and the temperature variation, which are not related to the nonlinear stiffness terms. The modal equations can be expressed with the primary mode only and the stationary density function of the oscillator is given by the Fokker-Planck distribution:

$$f(q) = N_0 \, exp\left\{-(2\xi\omega/D_0)[\tfrac{1}{2}k_o(1-s)q^2 + \tfrac{1}{4}\alpha q^4]\right\} \tag{1}$$

Hamiltonian of the oscillator is:

$$H = \tfrac{1}{2}\dot{q}^2 + \tfrac{1}{2}k_o(1-s)q^2 + \tfrac{1}{4}\alpha q^4 \tag{2}$$

and the depth of the potential energy well h can be determined by substituting the static postbuckling displacement amplitude into the Hamiltonian. The parameter Δ is proposed to characterize the gradual evolution from no snap-through to persistent snap-through by the ratio between the density of zero-crossing and the density of reaching the static postbuckling equilibrium positions.

$$\Delta = \frac{f(q)_{q=0}}{f(q)_{q=Q}} = e^{\left[-\left(\frac{\xi\sqrt{k_o}}{D_0}\frac{k_o^2(s-1)^2}{2\alpha}\right)\right]} \tag{3}$$

where the combination effect of the acoustic sound pressure level, the strength of the thermal effect and the structural stiffness including the elastic foundation stiffness on the dynamic response evolution have been taken into account in one parameter. Three distinct cases can be identified. As $\Delta \to 0$, it represents the motion characteristic of the oscillator with high potential energy well depth or low energy input level. The oscillator is confined entirely in one of the double potential

---

[a]Corresponding author. Email:liuliu@bit.edu.cn.

energy wells and no snap-through occurs; As $\Delta \to 1$, it represents the motion characteristic of the oscillator with low potential energy well depth or high energy input level. The oscillator is driven out the potential energy well constantly and the persistent dynamic snap-through appears. As $0 < \Delta < 1$, it represents the intermittent snap-through and can be expected that the snap-through motion is more frequent with higher value of Δ. The parameter clarifies the competition mechanism among the excitation energy, the strength of the thermal effect, the structural stiffness including the foundation stiffness and the nonlinear cubic stiffness, and can predict the characteristic of the dynamic response of the postbuckled panel with system parameters.

RESULTS AND DISCUSSIONS
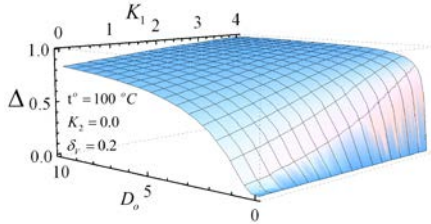
Figure 1. The surface plot of Δ for $K_1 = (0, 5)$ and $D_0 = (0.1, 10)$
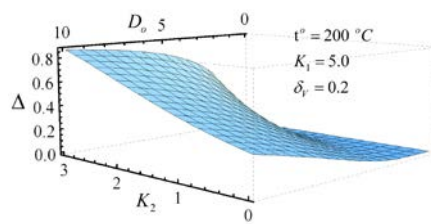
Figure 2. The surface plot of Δ for $K_2 = (0, 3)$ and $D_0 = (0.1, 10)$
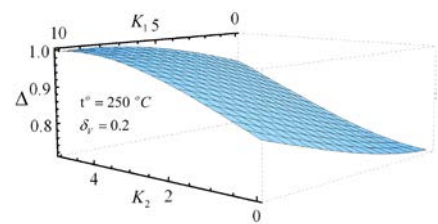
Figure 3. The surface plot of Δ for for $K_1 = (0, 10)$ and $K_2 = (0.0, 5.0)$.

The variations of the parameter Δ with the excitation energy level and the foundation stiffness for the post-buckled panel have been given in Fig. 1 - 3. The results demonstrate some significant finds the first of which is the contribution of the stiffness to the dynamic response for the panel. Higher elastic foundation stiffness can promote the nonlinear snap-through response significantly. As the excitation energy level decreases, the dynamic response evolution parameter Δ is more sensitive to the elastic foundation stiffness. The evolution parameter is more sensitive to the shear layer stiffness compared with the Winkler foundation stiffness.

The remarkable contribution of the foundation stiffness to the dynamic response evolution can be explained through its effects to the buckling and post-buckling behavior of the panel. The thermal buckling temperature increases and the postbuckling deflection decreases significantly for the panel resting on the two-parameter elastic foundation. Hence the depth of the potential energy well reduces by increasing the elastic foundation stiffness, which can promote the nonlinear snap-through response with reducing the snap-through amplitude. However, from the point of view of acoustic fatigue damage to the panel, although the dynamic snap-through motion between two symmetric post-buckling equilibrium positions with zero mean is activated more easily by increasing the elastic foundation stiffness, the amplitude of the dynamic snap-through vibration decreases significantly with increasing the foundation stiffness. For the panel without the elastic foundation subjected to the same combination of loadings, it might exhibit small-amplitude linear vibration around large static postbuckling deflection. Thus the comparison of acoustic fatigue damage induced by a persistent nonlinear dynamic response around zero mean and a linear dynamic vibration around large thermal induced static postbuckling deformation needs to be investigated further.

CONCLUDING REMARKS

The stochastic nonlinear dynamic response of a thermally buckled composite panel resting on a two-parameter elastic foundation, where the uniform temperature rising with in-plane thermal gradient has been considered has been studied using based on Galerkin procedure. The transverse displacement w time history, the histogram and the accompanying pseudo-phase plane have been provided to demonstrate the global dynamic behavior. A dynamic response evolution parameter deduced from the primary-mode modal equation and Fokker-Planck distribution function can be used to characterize the transition from a persistent snap-through to no snap-through for the postbuckled panel. The contribution of the foundation stiffness to the nonlinear dynamic snap-through response has been clarified by the depth of the potential energy well, which decreases by increasing the elastic foundation stiffness and can lead to a transition from no snap-through to persistent snap-through.

References

[1] Liu L, Bing Y. L., Ti R. H.: The stochastic dynamic snap-through response of thermally buckled composite panels. *Compos Struct* 131:344-355, 2015.

[2] Jon L.: Large amplitude plate vibration in an elevated thermal environment. *Applied Mechanics Reviews* 46(2): 242-254, 1993.

[3] Jon L.: Topology of the four-mode strain energy of thermally buckling plates. *J. of Thermal Stresses* 25:813-857. 2002.

[4] Adam P., Stephen R.: Nonlinear reduced-order analysis with time-varying spatial loading distributions. *J. of Aircraft* 46(4): 1395-1402, 2009.

PARTIAL CONTROL AND AVOIDANCE OF ESCAPE FROM A POTENTIAL WELL

Shibabrat Naik[*1] and Shane D. Ross[2]

[1,2]*Engineering Science and Mechanics program, Dept. of Biomedical Engineering and Mechanics, Virginia Tech, Blacksburg, VA-24061, USA*

Summary In this work, we present application of geometric and topological approaches of phase space transport to dynamical systems which exhibit transition out of a potential well or escape from the realm of bounded motion. This phenomena is observed in problems of celestial mechanics, chemical kinetics and ship dynamics where by transition and escape may be beneficial or detrimental. We present results in the context of mechanical systems that can be geometrically reduced to two-dimensional maps using invariant manifolds of unstable periodic orbits and suitable Poincaré surfaces-of-section. We apply a recently developed notion of controlling a dynamical system, in the presence of a random bounded disturbance while applying a smaller control, to avoid transition and escape into an undesirable realm of phase space.

PROBLEM DESCRIPTION

In a myriad of natural and engineering systems, there are instants of critical motion when the trajectory *escapes* from a (or *transitions* into another) metastable state, often characterized by a potential well. This phenomenon may be undesirable if it implies a catastrophic event or could be desirable from a control and design perspective. In any case, it is of paramount interest to understand the mechanisms underlying such critical motion, providing in essence a reduced order model of transitions. The discovery of such mechanisms will also lead us to propose strategies to avoid or trigger escape/transition and make better predictions.

We will illustrate our results in the context of a ship dynamics problem. Consider a model of ship dynamics that has nonlinear coupling of roll and pitch degrees of freedom (DOF) and is of interest in naval engineering for ship safety against capsize in the presence of wave forcing. The dynamical system of interest can be expressed by the Lagrangian $\mathcal{L}(x, y, \mathring{x}, \mathring{y})$ given by

$$\mathcal{L}(x, y, \mathring{x}, \mathring{y}) = T(\mathring{x}, \mathring{y}) - V(x, y)$$
$$= \frac{1}{2}\mathring{x}^2 + \frac{1}{2}\left(\frac{2}{R^2}\right)\mathring{y}^2 - \left(\frac{1}{2}x^2 + y^2 - x^2 y\right)$$

$$\left.\begin{aligned}
\mathring{x} &= v_x \\
\mathring{y} &= v_y \\
\mathring{v}_x &= -x + 2xy + f_x(t) \\
\mathring{v}_y &= -R^2 y + \frac{1}{2}R^2 x^2 + f_y(t)
\end{aligned}\right\} \tag{1}$$

with $V(x, y) = \frac{1}{2}x^2 + y^2 - x^2 y$ as the corresponding effective potential energy, x, y denotes the roll and pitch degrees of freedom which is non-dimensionalized using the roll and pitch angle of vanishing stability, $R = \omega_\theta/\omega_\phi$, ratio of the pitch to roll natural frequencies. In what follows, $R = 1.6$ is chosen so as to lessen the effects of parametric resonance. The equations of motion can be expressed in first order ODE form given by (1), where time is non-dimensionalized using the natural roll frequency and the non-conservative time-varying generalized forces, $f_x(t), f_y(t)$, which denote rescaled angular accelerations due to wave moments. Our objective is to apply a geometrically motivated approach of identifying trajectories that lead to capsize and find if a control smaller than a disturbance can be used to avoid such event.

TUBE DYNAMICS AND PARTIAL CONTROL

When the system is autonomous i.e., $(f_x(t) = f_y(t) = 0)$, Eqn. (1) conserves the energy, $E(x, y, v_x, v_y) = \frac{1}{2}v_x^2 + \frac{1}{2}\left(\frac{2}{R^2}\right)v_y^2 + \frac{1}{2}x^2 + y^2 - x^2 y$ since damping isn't considered and which represents a hypersurface in $\mathbb{R}^4$. However, by using a suitable geometric reduction technique we can classify orbits with varied fates for a given instantaneous energy, e. This is typically done by using a Poincaré surface-of-section (S-O-S), in this case a plane $\mathbb{R}^2$, that captures motion leading to escape from the potential well i.e., capsize. We consider a Poincaré S-O-S that is intersected by trajectories with motion to the right and given by $\Sigma_{U_1} = \{(y, v_y)|x = 0; v_x > 0\}$ (where $v_x > 0$ captures motion to the right) and shown in Fig. 1(a) and Fig. 1(b). Furthermore, the regions of energetically accessible motion for a ship of given energy, e, is defined by considering the projection of energy surface onto the configuration space, (x, y) plane, given by $\mathcal{M}(e) = \{(x, y)|V(x, y) \leqslant e\}$ which is historically known as *Hill's Region* (see [1]). Using basic dynamical systems theory, we obtain the critical points for the conservative system at $(\pm 1, 0.5, 0, 0)$ which is a rank-1 saddle (with eigenvalues $\pm\lambda, \pm i\omega$). The energy of saddle equilibrium points is defined as *critical energy* given by $E(\pm 1, 0.5, 0, 0) = E_{critical} = 0.25$ and all motions leading to escape from the potential well occur above this value i.e., a ship rolling and pitching with instantaneous energy e will capsize when $e > E_{critical}$.

This can be systematically explained by considering the invariant manifolds of the rank-1 saddles (this theory goes by the name of *tube dynamics* and is applied to celestial mechanics in [1]) to organize trajectories exhibiting ship's safe and capsize configuration. For a 2-DOF system (phase space is $\mathbb{R}^4$) the globalized manifolds are topologically a cylinder or *tubes* (hypersurface in $\mathbb{R}^4$ and co-dimension 1) and forms a boundary between capsize and non-capsize trajectories i.e., escape

*Corresponding author. Email:shiba@vt.edu

(a)   (b)
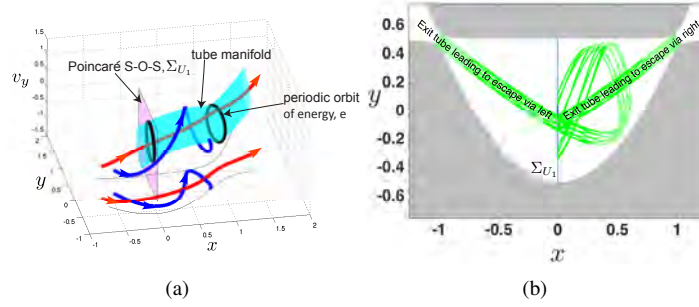
Figure 1: Fig. 1(a) shows a schematic of escape (red) and non-escape (blue) trajectory, while tubes form the boundary for such critical motion and Poincaré S-O-S reduces the analysis to a study of map on $\mathbb{R}^2$. The boundary of Hills region i.e., zero velocity curve (kinetic energy vanishes) is shown in the (x, y) plane. Fig. 1(b) shows the Hill's region as shaded (where kinetic energy is negative) and the white regions are energetically accessible for $e > E_{critical}$. The stable tubes of the rank-1 saddle equilibrium points are shown in green which act as the boundary for escape and non-escape trajectories.

beyond the saddles of potential well as shown schematically in Fig. 1(a). Therefore dimension of *tubes* for a 2 DOF system is given by $\mathbb{S}^1 \times \mathbb{R}^1$ and thus its intersection with a Poincaré S-O-S, Σ_{U_1}, is $\mathbb{S}^1$ or 1-sphere in $\mathbb{R}^2$. On the plane, Σ_{U_1} the closed curves represent *forbibben* region (shown as white inside the blue in Fig. 2(a)) and trajectory entering this region will lead to imminent escape from the potential well. When the systems is non-autonomous, this geometric picture still forms the skeleton on which the escape manifests itself.

In presence of any disturbance, e.g., wave forcing or unmodeled fluid-vessel interaction, escape from the potential well becomes more prominent and our objective is to ask if it is possible to avoid escaping i.e., not entering the forbidden regions by exploiting the topology of *tubes* of the rank-1 saddles. This can be answered using a recently developed approach of *partial control* which is based on the notion of a safe set (see [2]). A safe set, say S, is a subset of the set we want to stay in, say Q, such that for every point $\mathbf{q} \in S$, we have $\max_{\mathbf{q} \in S, ||\boldsymbol{\xi}|| \leqslant \boldsymbol{\xi}_0} dist(f(\mathbf{q}) + \boldsymbol{\xi}, S) = \boldsymbol{u}_0 < \boldsymbol{\xi}_0$. When the safe set exists, we can find

(a)   (b)   (c)   (d)
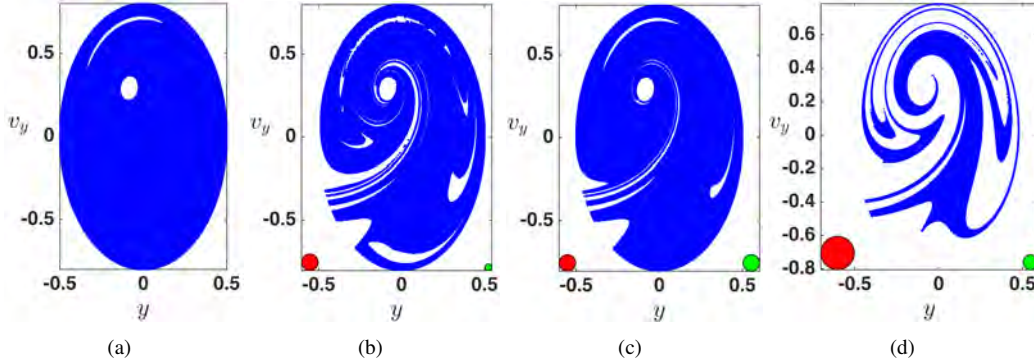
Figure 2: Fig. 2(a) shows the initial set in blue on the Poincaré S-O-S, Σ_{U_1} with white regions inside the blue denoting intersection of tube manifolds. Fig. 2(b), 2(c) and 2(d) show the safe sets in blue for $\xi_0 = 0.05, 0.05, 0.1$ for $u_0 = 0.405\xi_0, \xi_0, 0.445\xi_0$ respectively. The red and green disks denote the disturbance and control magnitudes that are applied on the map.

safety by using a control that is smaller than the disturbance. This is illustrated for an arbitrary disturbance, ξ_0, acting on the return map $\Sigma_{U_1} \to \Sigma_{U_1}$ in Fig. 2 and computed using the sculpting algorithm in [3].

CONCLUSION

We considered two arbitrary disturbance magnitudes, for illustration here, $\xi_0 = 0.05, 0.1$ and show that the safe sets exist for a minimum control magnitudes of $u_0 = 0.405\xi_0, 0.445\xi_0$ for an instantaneous energy, $e = 0.25307$. Thus, a ship's safety can be ensured by controlling the trajectories from entering the stable tubes that lead to imminent escape from the potential well. However, from a ship's motion stand point, the magnitude of a disturbance needs to be related to the wave forcing that acts in a rough/regular sea environment while interpreting the applied control magnitude in the form of a algorithmic control law.

References

[1] Koon W. S., Lo M. W., Marsden J. E., Ross S.D.: Dynamical Systems, the Three-Body Problem and Space Mission Design. Book, 2011.

[2] Sabuco J., Zambrano S., Sanjuán M. A. F., Yorke J.A.: Dynamics of partial control. Chaos (Woodbury, N.Y.) 22:4 047507, 2012.

[3] Sabuco J., Zambrano S., Sanjuán M. A. F., Yorke J.A.: Finding safety in partially controllable chaotic systems. Communications in Nonlinear Science and Numerical Simulation (Elsevier B.V.) 11:17, 4274–4280, 2012.

SYMMETRY-INDUCED DYNAMIC LOCALIZATION IN LATTICE STRUCTURES

Nathan Perchikov *and O.V. Gendelman

Faculty of Mechanical Engineering, Technion, Haifa 32000, Israel

Summary The existence of internal symmetry in lattice structures may give rise to stationary compact solutions, even in the absence of disorder or nonlinearity. These compact solutions are related to the existence of flat dispersion curves (bands). Nonlinearity can be a destabilizing factor for such compactons. This can be illustrated by a simple one-site model, in which the compacton corresponds to a single hidden antisymmetric mode. This antisymmetric mode can lose its stability through parametric resonance, when accounting for nonlinear interactions.

SETTING AND LINEAR ANALYSIS

A chain of linearly coupled elements with symmetric internal structure is considered, as presented in Figure 1.
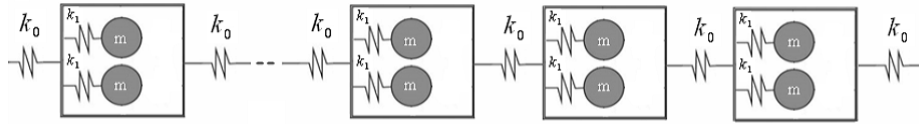
Figure 1: Schematic plot of the basic setting.

The boxes are considered to be massless. Evidently, due to internal symmetry, the antisymmetric mode in each box will not interact with the other modes in the system. Thus in the considered case, one obtains a completely localized solution (compacton). This localized solution emerges already in a linear homogeneous system. Therefore, in addition to two well-known origins of localization in lattices − disorder [1] and nonlinearity [2] − there appears to be a third possible source of localization: internal symmetry. Due to lack of direct interaction with external excitation, the aforementioned compactons may also be referred to as "hidden modes". The dispersion curves for the system depicted in Figure 1 are presented in Figure 2.
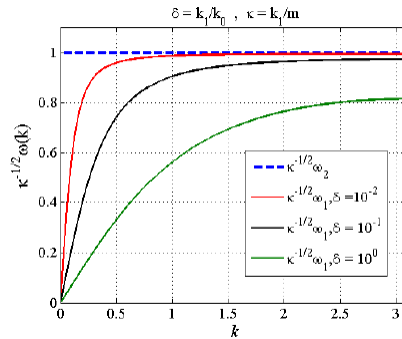
Figure 2: Oscillatory spectra for the system described in Figure 1.

One of the dispersion curves (bands) is flat, i.e. independent of the wavenumber, k. Its frequency corresponds to the frequency of compactons. In the specific system depicted in Figure 1, this flat band always lies above "regular" dispersion bands. However, for more complicated structures (for instance, for the case when internal transverse motion of particles is permitted), the emerging flat bands may also intersect other dispersion bands. In such cases, the regular "intersection avoidance" of dispersion curves is absent (due to lack of linear coupling between the modes). The existence of compactons in the model system described above depends only on the symmetry in the considered system. For a single site of such lattice, we demonstrate that slight perturbation to the symmetry can reveal the "hidden mode" under external excitation, with an additional, thin, resonance peak emerging. However, small damping (proportional to the asymmetry) can efficiently destroy this additional resonance peak, restoring the mode "hiding" effect.

---

*Corresponding author. Email: perchico@gmail.com

NONLINEAR DYNAMICS

The inclusion of (symmetric) nonlinearities does not affect the existence of compacton solutions. In the same time, in the nonlinear case, the compacton mode becomes coupled to the other modes of the system. Such nonlinear coupling can be destructive for compacton existence − stability can be lost through the mechanism of parametric resonance. To explore this scenario, we consider the same single-site (sub)system, only with the addition of internal cubic nonlinearity. The emerging system can represented by the following equations:

$$m\ddot{x}_1 + k_1(x_1 - x_0) + p(x_1 - x_0)^3 = 0$$
$$m\ddot{x}_2 + k_1(x_2 - x_0) + p(x_2 - x_0)^3 = 0 \tag{1}$$
$$k_0 x_0 - k_1(x_1 - x_0) - p(x_1 - x_0)^3 - k_1(x_2 - x_0) - p(x_2 - x_0)^3 = 0$$

In Eqs. (1), x_1 and x_2 denote the displacements of the masses, and x_0 − the displacement of the external box. The last equation in the system is algebraic, as arising due to the zero box mass assumption. Evidently, system (1) admits symmetric and antisymmetric nonlinear normal mode (NNM) solutions. The antisymmetric mode is "hidden" and corresponds to the compacton solution. Partial results of numerical Floquet analysis for the NNMs of Eqs. (1) are presented in Figure 3.
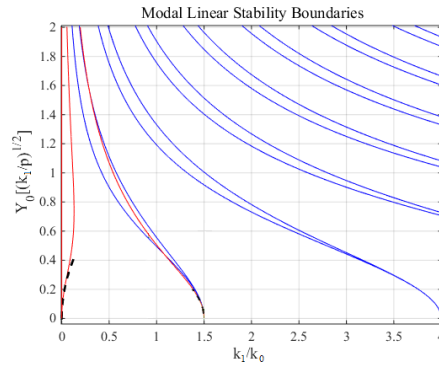
Figure 3: 1st (finite-width) and 2nd (degenerate) instability tongues of the purely antisymmetric mode (in solid red) with asymptotic expansions for tongue boundaries (dashed black), and multiple (finite-width) instability tongues of the symmetric mode (in solid blue). Y_0 denotes the (normalized) amplitude of $(x_1 + x_2)/2 - x_0$.

In addition to a finite-width instability tongue for small k_1/k_0 ratios, there exists a 2nd narrow region of instability, characterized by emerging resonance-related KAM islands, around the rightmost red curve in Figure 3, as shown in Figure 4.
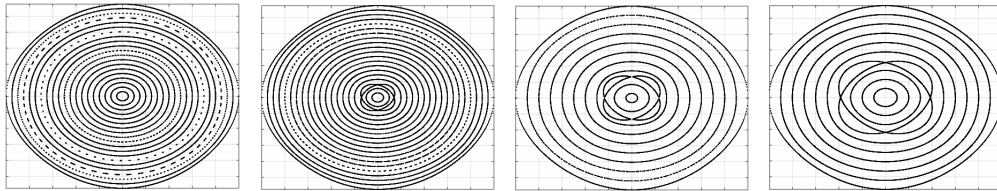
Figure 4: Poincaré sections at $x_1 = x_2$ for $k_1/k_0 = 1.25$ for (rightwards) increasing amplitudes $Y_0 = 0.31, 0.313, 0.316, 0.325$

CONCLUSIONS

In view of the above, one finds that in the presence of internal symmetry, a localized solution (a "hidden" mode, or, a compacton) exists even with no nonlinearity or disorder, and can either remain stable, when accounting for nonlinear interactions, or be destroyed by them, depending on the parameters.

References

[1] Ludlam J. J., Taraskin S.N., Elliott S.R.: Phys. Rev. B 67(13), 2003.
[2] Perchikov N., Gendelman O.V.: *Physica* D 292-293:8-28, 2015.

DATA-BASED METHOD FOR EXTRACTING NAVIGATIONAL LEADERSHIP BETWEEN TWO BATS

Subhradeep Roy and Nicole Abaid *

Department of Biomedical Engineering and Mechanics, Virginia Tech, USA

Summary We study the navigational leadership roles in bats by implementing a recently developed dynamical systems tool, convergent cross mapping, to detect the information transfer between two bats. Small groups of bat paths are continuously tracked, from which 3D path points are extracted and converted to 1D curvature-based time series data to perform convergent cross mapping analysis. This work seeks to answer the question of whether individuals fly independently of each other or interact to plan flight paths.

NAVIGATIONAL INFORMATION TRANSFER BETWEEN A PAIR OF BATS

Collective behavior in groups of social animals is the interaction and negotiation of individuals to reach an agreement, examples of which are coordinated motion and synchronous migration. Bats are unique among such social animals in that they use active sensory echolocation or "bio-sonar", wherein they emit ultrasonic waves and sense echoes to detect and navigate surroundings. Jamming occurs when multiple bats are using echolocation and each individual's calls become difficult to distinguish, which may lead to misinterpretation of echoes and thus their environment. In the biological literature, there is evidence of such jamming happening in bats and of their different strategies to avoid misinterpretation, like frequency modulation or vocalization cessation. Also, there are instances where bats purposefully jam conspecifics during competition for food. Hence, it is clear that bats act differently in groups than alone and, in many situations, this can benefit their survival.

In real bat swarms, understanding the navigational leadership roles is a challenge and quantitative assessment of leadership appears to be an entirely untouched area of study. Given the broadcast nature of bio-sonar, the active sensing of one individual can directly influence the motion of others, making the directionality of leadership unclear. Here, we seek to understand navigational leadership in bats from direct observation of bat swarms in flight. The exploration of this area is refined by focusing efforts on pairs of bats and pursuing a method of analysis involving the evaluation of directional information transfer.

Real-world leader-follower interactions can be studied as information transfer by the use of the concepts of Granger causality (GC) [1], transfer entropy (TE) [2], and convergent cross mapping (CCM) [3]. These different tools measure the directional information transfer between two random processes. We focus on CCM which is a recently developed method for determining causality between two time series [3]. We choose this method because of the following reasons. First, it can be extended to nonlinear, non-separable dynamical systems, involving weakly coupled variables and in the presence of a third driving variable, in each of which GC does not apply [3]. Secondly, the principal difficulty to calculate TE from experimental data is in estimating probability distributions which are computed using binning methods such as histograms [4]; such challenges can be overcome with CCM.

We seek to understand the navigational leadership in a pair of bats, for which we perform CCM analysis to detect the information transfer which is assumed to flow from leader to follower. For each bat in the pair, we compute a curvature-based time series from 3D trajectories that are captured in a field experiment in a mountain cave in Jinan, China.

Convergent cross mapping (CCM)

CCM was first introduced in [3], in which it has been reported as a necessary condition for causation. This method is based on an algorithm that compares the ability of lagged components of one process to estimate the dynamics of another.

Given two time series, $X(t)$ and $Y(t)$ are causally linked if they share a common attractor manifold, M, where t denotes time index. From Taken's theorem, generically a shadow version of the original manifold M can be reconstructed from the projection of any of this time series. The time series data $X(t)$ and its delayed components, $X(t - \tau)$ and $X(t - 2\tau)$, where τ is the time delay, can be used as variables to construct the shadow version of the original manifold called M_X. The reconstructed manifold preserves the properties of the original system, such as the topology and the Lyapunov exponents. This method represents a one-to-one mapping of the original manifold M and the reconstructed manifold, M_X, and similarly maps one-to-one to the reconstructed manifold, M_Y, built from the time series Y. The next step is to find the nearest neighbors in M_Y, and use the time indices to find the corresponding points in M_X. If these points are also nearest neighbors in M_X, then X and Y are causally related. This allows the historical records in Y to estimate states in X, and vice-versa. This method is used to find an estimate of Y, labeled as $\widehat{Y}(t)|M_X$. Finally, a correlation coefficient is calculated between the original time series and an estimate of Y. For a pair of time series, we will have two correlation coefficients corresponding to considering each bat as a leader in turn; these are then compared to determine the CCM causality and its directionality. A more detailed description of the algorithm can be found in the supplementary materials of [3].

---

*Corresponding author. Email: nabaid@vt.edu
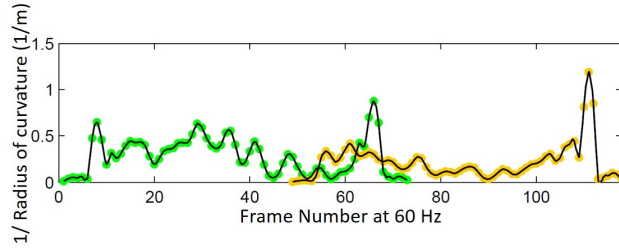
Figure 1: Inverse radius of curvature plotted for a pair of bats. Green and yellow represent front and rear bat, respectively [8].

The CCM technique requires the knowledge of the two parameters, namely embedding dimension and the time delay. To determine the minimum embedding dimension, we use the method as described in [5] because of the following advantages. First, it depends on time delay only, and does not depend on any other system parameters, unlike the method of false neighbors [6]. Second, this method is computationally very efficient.

Time delay is a required parameter for both the methods to calculate embedding dimension and CCM. If the time delay, τ is chosen to be very small, for a two dimensional construction of the state-space, $X(t)$ and $X(t+\tau)$ will be indistinguishable and all the trajectories will appear to lie on the line, $X(t) = X(t+\tau)$. This can be avoided by the choice of τ that makes $X(t)$ and $X(t + \tau)$ independent. Linear independence can be achieved by choosing the corresponding τ for which the autocorrelation function first passes through zero. However, we choose mutual information since it measures the general dependence of two variables.

CURVATURE TIME SERIES

The 3D path points of each bat were extracted from the video data collected in a mountain cave in Jinan, China, where small groups of bat paths were continuously tracked. In order to perform CCM analysis of pairs of bats, it is necessary to generate 1D time series from 3D path data. We choose an inverse radius of curvature metric for representing 1D time series for the following reasons. First, a curvature-based time series is a reflective of a bat's steering and hence provides a good depiction of the 3D navigation of the bat pairs. Secondly, an absolute inverse radius of curvature formulation ensures the data remains positive and close to zero, resulting a logarithmic binning strategy possible to calculate the minimum embedding dimension. Finally, curvature-based metrics are frequently used to assess the motion of interacting agents, such as in the study of laboratory insects [7]. Figure 1 presents an exemplary 1D time series plot for a pair of bats. In a previous study, we have seen that information flows from bats which are positionally in front to those behind as measured using TE [8]. These results are compared to the analogous analysis with CCM in this work.

CONCLUSIONS

Here we study the navigational leadership roles in bats who use active sensing making it a challenge to understand the directionality of leadership. We implement the above mentioned tools to detect the navigational information transfer between a pair of the bats, in terms of a curvature-based time series that are captured in a field experiment in a mountain cave in Jinan, China. We observe that the front bat in particular plays a leadership role for the pair and the rear bat displays path coupling behavior with the leading bat using TE, and we compare these results to those measured with CCM.

References

[1] C.W.J. Granger. Investigating causal relations by econometric models and cross-spectral methods. *Econometrica: Journal of the Econometric Society*, pages 424–438, 1969.

[2] T. Schreiber. Measuring information transfer. *Physical Review Letters*, 85(2):461, 2000.

[3] G. Sugihara, R. May, H. Ye, C. Hsieh, E. Deyle, M. Fogarty, and S. Munch. Detecting causality in complex ecosystems. *Science*, 338(6106):496–500, 2012.

[4] M. Vejmelka and M. Palus. Inferring the directionality of coupling with conditional mutual information. *Physical Review E*, 77(2):026214, 2008.

[5] L. Cao. Practical method for determining the minimum embedding dimension of a scalar time series. *Physica D: Nonlinear Phenomena*, 110(1):43–50, 1997.

[6] M. B. Kennel, R. Brown, and H. Abarbanel. Determining embedding dimension for phase-space reconstruction using a geometrical construction. *Physical Review A*, 45(6):3403, 1992.

[7] J. G. Puckett, D. H. Kelley, and N. T. Ouellette. Searching for effective forces in laboratory insect swarms. *Scientific Reports*, 4, 2014.

[8] N. Orange and N. Abaid. A transfer entropy analysis of leader-follower interactions in flying bats. *European Physical Journal: Special Topics*, 224(17):3279–3293, 2015.

MODELLING NON-PLANAR VIBRATIONS OF A STRING IN THE PRESENCE OF A DOUBLY CURVED OBSTACLE

Harkirat Singh[1] and Pankaj Wahi [*2]

[1,2]*Department of Mechanical Engineering, Indian Institute of Technology Kanpur, Kanpur, India*

Summary The present paper investigates the characteristics of a string vibrating against a smooth unilateral obstacle pertaining to the Indian stringed musical instruments. In particular, we have studied the effect of coupling due to the variable tension and the geometry of the obstacle. The mathematical model has been developed using Hamilton's principle followed by system discretization using the Galerkin approach and numerical investigations using runge-kutta algorithm. Numerical simulations have divulged the transition in characteristics of a string beyond a certain amplitude.

BRIEF BACKGROUND

Theoretically, the problem of a string vibrations against a parabolic obstacle, considering the inelastic impacts, was first studied by the Burridge et al[1]. Subsequently equations of motions were derived, assuming smooth wrapping and unwrapping and a conservative model, in the literature [2, 3, 4]. However, all these analysis were carried out for planar motions of a string. In the present paper, we have developed a mathematical model, assuming the conservative system, for non-planar vibrations of a string vibrating against a obstacle with known geometry. The model is relevant to the Indian musical stringed instruments, since the motion of a string in such case is non-planar and quite complicated.

FORMULATION

The schematic representation of the physical system under consideration is shown in figure 1. It consists of a ideal string(no bending stiffness) vibrating against a smooth unilateral obstacle which is assumed to be fixed and rigid in our model. The tension in the string is assumed to be variable, giving rise to stretching non-linearity(σ in our case) which introduces coupling between the mutually perpendicular modes. We further assume that the string remains tangent to the bridge surface
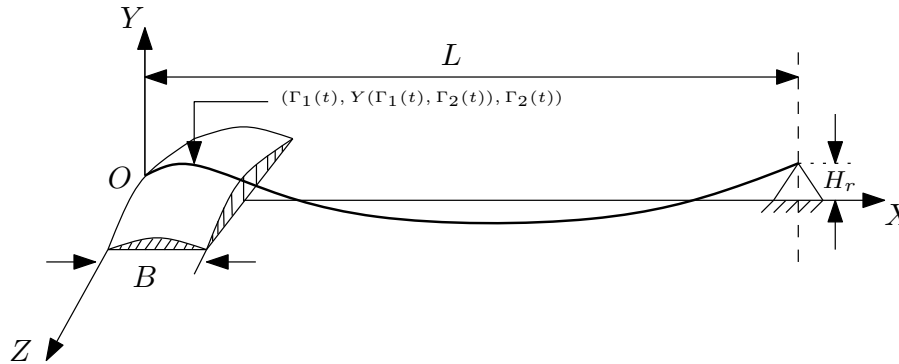
Figure 1: Simplified model for the string vibrations in musical instruments like tanpura and sitar.

at the point of separation ($X = \Gamma_1(t)$ and $Z = \Gamma_2(t)$) in figure 1. The continuity of string along with slope continuity implies zero velocity at the point of separation and thus a conservative system. The geometry of the obstacle is defined, in non-dimensionalized form, by the following surface

$$Y_B(x, z) = ax(b - x) + c\left(\frac{d}{2} - z\right)\left(\frac{d}{2} + z\right). \tag{1}$$

Using Hamilton's principle and calculus of variation, the governing equations for the wrapped portion comes out to be

$$2cz\frac{\partial^2 z}{\partial \tau^2} + 2c\left(\frac{\partial z}{\partial \tau}\right)^2 - 2cz\frac{\partial^2 z}{\partial x^2} - 2c\left(\frac{\partial z}{\partial x}\right)$$
$$+\sigma\frac{\partial}{\partial x}\left((ab - 2ax - 2czz_x)\left((ab - 2ax - 2czz_x)^2 + z_x^2\right)\right) - 2a + \lambda = 0, \tag{2}$$

$$-\frac{\partial^2 z}{\partial \tau^2} + \frac{\partial^2 z}{\partial x^2} + \sigma\frac{\partial}{\partial x}\left(z_x\left((ab - 2ax - 2czz_x)^2 + z_x^2\right)\right) + \lambda(2cz) = 0. \tag{3}$$

[*]Corresponding author. Email: harkiratb104@gmail.com

Here, $\lambda(x, z)$ represents the constraint force between the string and the obstacle. For the free portion of a string the governing equations(non-dimensional form) are

$$-y_{tt} + y_{xx} + \sigma \frac{\partial}{\partial x}\left(y_x\left(y_x^2 + z_x^2\right)\right) = 0, \qquad \gamma_1^+ \le x \le 1 \tag{4}$$

$$-z_{tt} + z_{xx} + \sigma \frac{\partial}{\partial x}\left(z_x\left(y_x^2 + z_x^2\right)\right) = 0. \qquad \gamma_1^+ \le x \le 1. \tag{5}$$

Discretization

We discretize the system using Galerkin projection approach. The functional form of the modes are assumed as

$$z = \alpha(t)\sin(\pi x), \qquad 0 \le x \le 1 \tag{6}$$

$$y = a\gamma_1(b - \gamma_1) + c\left(\frac{d}{2} - \alpha(t)\sin(\pi x)\right)\left(\frac{d}{2} + \alpha(t)\sin(\pi x)\right), \qquad 0 \le x \le \gamma_1^- \tag{7}$$

$$y = \frac{a\gamma_1(b - \gamma_1) + c\left(\frac{d}{2} - \gamma_2\right)\left(\frac{d}{2} + \gamma_2\right)}{1 - \gamma_1}(1 - x) + \beta(t)\sin\left(\frac{\pi(x - \gamma_1)}{1 - \gamma_1}\right), \qquad \gamma_1^+ \le x \le 1. \tag{8}$$

Here, γ_1 and γ_2 are the non-dimensional forms of $\Gamma_1(t)$ and $\Gamma_2(t)$. For clarity, γ_1^- and γ_1^+ are the positions just before and after the separation point respectively. To begin with, the above representation is restricted to unimodal analysis, since that alone can capture the underlying fascinating characteristics. Besides this, unit tangent vector continuity engenders the following condition

$$a\gamma_1^2 - 2a\gamma_1 + ab + \frac{cd^2}{4} - c\gamma_2^2 - 2c\pi\gamma_2\alpha(t)\cos(\pi\gamma_1) + 2c\pi\gamma_2\gamma_1\alpha(t)\cos(\pi\gamma_1) - \pi\beta(t) = 0. \tag{9}$$

KEY RESULTS

The resultant ODEs are numerically investigated using runge-kutta algorithm. Numerical simulations unearth the peculiar features of string dynamics, i.e, the behavior of a string changes qualitatively beyond the certain amplitude of vibrations. The results in figure 2 are reported for chosen obstacle parameters, i.e, $b = 0.05$, $a = 1440$, $c = 0.1$, $d = 2$ and $\sigma = 0.001$. The
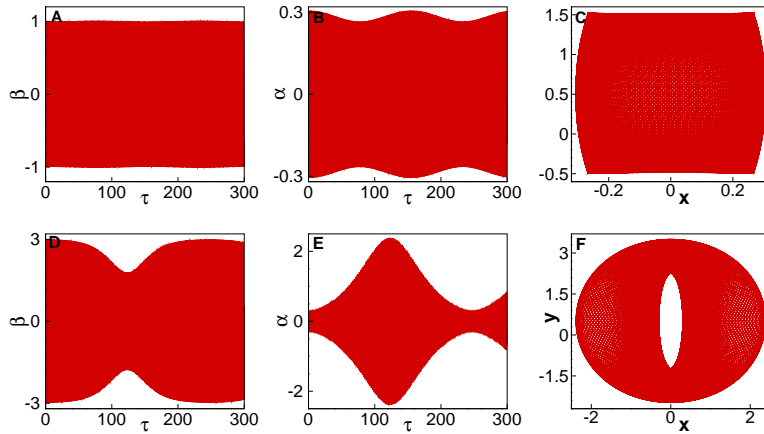
Figure 2: Fig (A),(B) and (C) correspond to the initial condition $\beta(0) = 1$ and $\dot{\alpha}(0) = 1$, and fig (D),(E) and (F) correspond to $\beta(0) = 3$ and $\dot{\alpha}(0) = 1$. Fig (A) and fig (D) represent the variation of β with non-dimensional time, and fig (D) and fig (E) represent the variation of α with non-dimensional time. Fig (C) and fig (F) represent the trajectories of the mid point of a string for corresponding initial conditions.

transition in the characteristics of the string beyond a certain amplitude indicates onset of unstable solutions, which can be checked using Floquet theory. Numerical study also suggests that number of planar motions reduced to one unlike infinitely many in the absence of obstacle.

References

[1] Burridge R., Kappraff J., and Morshedi C.: The sitar string, a vibrating string with a one-sided inelastic constraint. J. Applied Mathematics,42(6):1231-1251, 1982.

[2] Vyasarayani C.P.,Birkett S., and McPhee J. :Modeling the dynamics of a vibrating string with a finite distributed unilateral constraint. JASA, 125(6):3673-3682, 2009.

[3] Mandal A.K., Wahi P. :Natural frequencies, modeshapes and modal interactions for strings vibrating against an obstacle. JSV, 338:42-59, 2015.

[4] Singh H., Wahi P. :Non-planar vibrations of a string in the presence of a boundary obstacle. Submitted to JSV.

NONLINEAR VIBRATIONS OF A CIRCULAR PLATE INDUCED BY MECHANICAL AND THERMAL LOADINGS

Anna Warminska[*1], Emil Manoach[2], and Jerzy Warminski[3]

[1]*Department of Thermodynamics, Fluid Mechanics and Aviation Propulsion Systems, Lublin University of Technology, Lublin, Poland*
[2]*Institute of Mechanics, Bulgarian Academy of Sciences, Sofia, Bulgaria*
[3]*Department of Applied Mechanics, Lublin University of Technology, Lublin, Poland*

Summary An effect of thermal loading on vibration of a nonlinear circular plate considered as extended Mindlin model with nonlinear terms due to large deflections is analysed in the paper. The coupled thermal and mechanical model is derived first in the form of nonlinear partial differential equations and then the problem is reduced by modal projection. The importance of the elevated temperature around the main resonance for varied temperature is shown and the nonlinear characteristics with bifurcation points have been computed for selected thermal and mechanical loadings.

INTRODUCTION AND A NONLINEAR THERMO-ELASTIC MODEL OF A CIRCULAR PLATE

The structural elements like beams, shells or plates which are used in many branches of engineering often are subjected to mechanical and thermal loadings leading to large amplitude vibrations [1]. The temperature may change transient dynamics of the structure or even may shift the response to a new dynamic state [2]. In many cases, especially when structures are not very thin and they are subjected to an intensive and short heat flux or even convective heating, the consideration of the propagation of the temperature along the structure is important and then the coupled thermoelastic problem should be considered [3, 4]. These problems are quite complicated from a computational point of view, therefore, simplified techniques which allow reducing the governing partial differential equations into a reduced number of modal coordinates are applied. Such an approach is very effective for nonlinear models due to the fact that it enables the advanced bifurcation analysis as well as a detection of chaotic oscillations [5, 6].

The considered in this paper thermo-elastic model of a circular plate of radius R and thickness h is based on Midlin model. It takes into account large deflections, linear curvatures, shear deformation and rotary inertia. The derived PDEs subjected to mechanical and thermal loadings take the form:

$$Ah\left[\frac{\partial^2 u}{\partial r^2} + \frac{\partial w}{\partial r}\frac{\partial^2 w}{\partial r^2} + \frac{1}{r}\frac{\partial u}{\partial r} - \frac{u}{r^2} + \frac{1}{2r}(1-\nu)\left(\frac{\partial w}{\partial r}\right)^2\right] = A(1+\nu)\alpha_T\frac{\partial\gamma_T}{\partial r},$$

$$D\left[\frac{\partial^2\psi}{\partial r^2} + \frac{1}{r}\frac{\partial\psi}{\partial r} - \frac{\psi}{r^2}\right] - k^2 Gh\left(\frac{\partial w}{\partial r} + \psi\right) - c_2\frac{\partial\psi}{\partial t} - \frac{\rho h^3}{12}\frac{\partial^2\psi}{\partial t^2} = A(1+\nu)\alpha_T\frac{\partial\kappa^T}{\partial r},$$

$$k^2 Gh\left(\frac{\partial^2 w}{\partial r^2} + \frac{1}{r}\frac{\partial w}{\partial r} + \frac{\partial\psi}{\partial r} + \frac{\psi}{r}\right) + Ah\left[\frac{\partial u}{\partial r} + \frac{1}{2}\left(\frac{\partial w}{\partial r}\right)^2 + \frac{\nu}{r}u - \frac{1+\nu}{h}\alpha_T\gamma_T\right]\left(\frac{\partial^2 w}{\partial r^2} + \frac{1}{r}\frac{\partial w}{\partial r}\right)$$

$$+Ah\left(\frac{\partial^2 u}{\partial r^2} + \frac{\nu}{r}\frac{\partial u}{\partial r} - \frac{\nu}{r^2}u + \frac{\partial w}{\partial r}\frac{\partial^2 w}{\partial r^2} - \frac{1+\nu}{h}\alpha_T\frac{\partial\gamma_T}{\partial r}\right)\frac{\partial w}{\partial r} + c_1\frac{\partial w}{\partial t} - \rho h\frac{\partial^2 w}{\partial t^2} = -p(r,t) \quad (1)$$

where $u(r,t)$ is the in-plane displacement, $w(r,t)$ is the transverse displacement, r and ψ are polar coordinates and E is the Young modulus, G is the shear modulus, ν is Poison's ratio, α_T is the coefficient of thermal expansion, c_1 and c_2 denote the damping coefficients and mechanical load intensity is $p(r,t)$. The heat flow acting on the plate is included in functions γ_T and κ_T and is not reported here. The model has been studied for a particular case for fixed elevated temperature uniformly distributed through the plate span. The PDEs have been reduced to ODEs by modal projection for a clamped plate, taking just one mode projection, defined by Bessel functions obtained from the eigenvalue problem. After the reduction the nonlinear ODE take the dimensionless form

$$\ddot{q}_1(t) + 2\xi_1\omega_1\dot{q}_1 + \omega_1^2 q_1 + C_L q_1^3 + C_T\Delta T q_1 = p_1\sin(\Omega t) \quad (2)$$

where ω_1 is the first natural frequency, ξ_1 a modal damping coefficient, p_1 and Ω are the amplitude and frequency of mechanical excitation, C_T and C_L are constant coefficients, and ΔT is the temperature difference.

PLATE DYNAMICS AT ELEVATED TEMPERATURE

The numerical example aims to illustrate the impact of the thermal and mechanical loadings on the structure's response. The results are obtained for the clamped circular plate and uniformly distributed elevated temperature. The plate of radius $R = 0.1$ m, thickness $h = 0.0025$ m is assumed to have the material parameters: $\rho = 2778 kg/m^3$, $E = 0.7 \times 10^{11}\ N/m^2$, $G = 2.612 \times 10^{10} N/m^2$, $\nu = 0.34$, $\alpha_T = 2.39 \times 10^{-5} K^{-1}$. For the assumed structural parameters

---

*Corresponding author. Email: a.warminska@pollub.pl
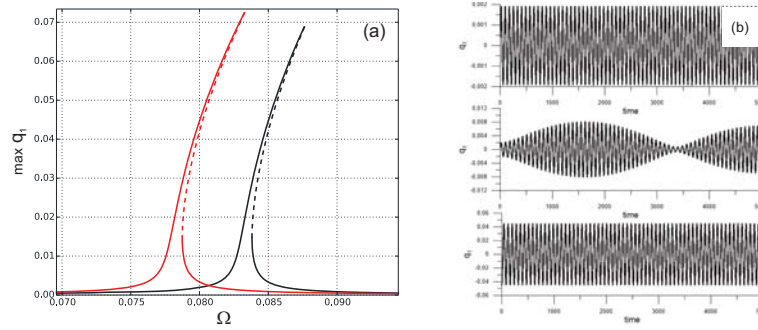
Figure 1: Resonance curves (a) for $\Delta T = 0$ (black) and $\Delta T = 0.5$ (red) and time histories (b) for $\Omega = 0.08$: $\Delta T = 0$ – steady state (upper plot), $\Delta T = 0.5$ – transient state (middle plot), $\Delta T = 0.5$ – new steady state (lower plot).
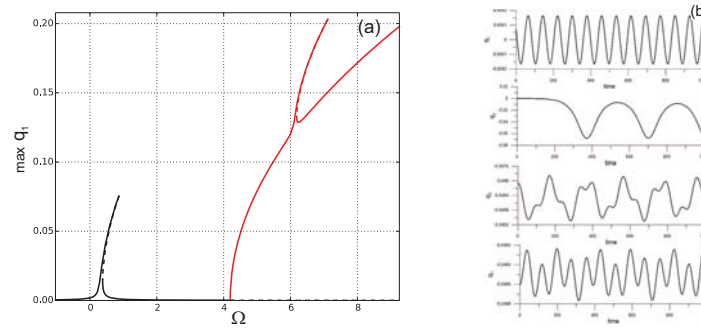
Figure 2: Bifurcation diagram (a) amplitude versus ΔT and fixed mechanical loading $p_1 = 1 \times 10^{-6}$, $\Omega = 0.08$, and time histories (b) for $\Delta T = 4.0$ (upper plot) and below for $\Delta T = 4.5$ – transient states.

the coefficients of Eq.(2) take values: $\omega_1 = 0.08321077$, $C_L = 0.21319$, $C_T = -0.0016501$. The resonance curves presented in Fig.1(a) exhibit nonlinear stiffening effect. The small increase of temperature $\Delta T = 0.5$ makes an essential shift of the resonance zone (red curve). The sensitivity of the system to the temperature is demonstrated on time histories in Fig.1(b); the first plot corresponds to a steady state for $\Omega = 0.08$ and $\Delta T = 0$. Below, due to the change of the temperature to $\Delta T = 0.5$ transient beating phenomena is observed, which finally goes to a new steady state (lower plot). The influence of the elevated temperature for fixed mechanical loading is presented in Fig.2. There are two possible situations. For ΔT up to 4.2 (black line) we observe one region of vibrations increase reminding rezonanse zone. But above the critical point $\Delta T = 4.2$ (red line) the plate loses stability and after buckling, new post-buckling oscillations around shifted vibration centre take place. The steady state for $\Delta T = 4.0$ and then transient states for $\Delta T = 4.5$ are presented in Fig.2(b).

CONCLUSIONS

The nonlinear resonance curves with hardening characteristic of Duffing type have been obtained for the extended nonlinear Mindlin plate model. The elevated temperature influenced the resonance zone and an occurrence of the bifurcation points and new solutions with different amplitudes and periods have been observed. The small temperature difference resulted in large shift of resonance curves and above a certain threshold new post-buckling dynamics has been observed. The transition between states is followed by complex transient dynamics.

References

[1] Dhainaut J.M., Duan B., Mei C., Spottswood C.S.M , Wolfe H.: Non-linear Response of Composite Panels to Random Excitations at Elevated Temperatures. Proc. of 7th Int. Conf. Recent Advances in Str. Dynamics, Vol.2, 769–784, Southampton 2000.

[2] Amabili M., Carra S.: Thermal Effects on Geometrically Nonlinear Vibrations of Rectangular Plates with Fixed Edges. J. of Sound Vib: 321, 936-954, 2009.

[3] Manoach E., Ribeiro P.: Coupled, Thermoelastic, Large Amplitude Vibrations of Timoshenko Beams. Int. J. Mech. Sci: 46,1589–1606, 2004.

[4] Ribeiro P., Manoach E.: The Effect of Temperature on the Large Amplitude Vibrations of Curved Beams. J. Sound Vibr 285: 1093–1107, 2005.

[5] Warminska A., Manoach E., Warminski J.: Nonlinear Dynamics of a Reduced Multimodal Timoshenko Beam Subjected to Thermal and Mechanical Loadings. Meccanica 49: 1775–1793, 2014.

[6] Warminska A., Manoach E., Warminski J., Samborski S.: Regular and Chaotic Oscillations of a Timoshenko Beam Subjected to Mechanical and Thermal Loadings. Continuum Mech. Thermodyn 27:719-737, 2014.

STATIONARY CONTROL OF A FLOATING AIRPORT IN WAVES

Shuyan Xia[1], Daolin Xu[1a)] & Haicheng Zhang[1]

[1]*State Key Laboratory of Advanced Design and Manufacturing for Vehicle Body, Hunan University, Changsha, 410082, P.R. China*

Summary This paper presents a nonlinear feedback control to suppress the surge motion of a serially connected multi-module floating airport in order to improve its operating condition in rough sea environment. An auxiliary system for dealing with the output saturation of actuators is introduced to design a series of the control laws based on Lyapunov stability. Numerical simulations indicate the effectiveness of the control method.

CONTROL MODEL FOR FLOATING AIRPORT

The concept of floating airports has been proposed [1] for land reclamation from sea and to avoid noise contamination on crowded cities. A floating structure with multi-modules may swing badly in wave, sensitive to the wave height and frequency. Since the operation condition of the floating airport requires for stringent tolerances on instability, it therefore seems natural to consider a control method to keep the floating structure stable [2]. This paper will use the backstepping approach [3] with considering the output saturation of actuators.

The floating airport with multi-modules is illustrated in Fig. 1 where adjacent modules are connected by elastic connectors in addition with actuators for control. The two ends of the floating airport are constrained by anchor chains to resist drift. Since each module acts as an oscillator, the connected modules can be viewed as a network where the network theory [4] can be applied.
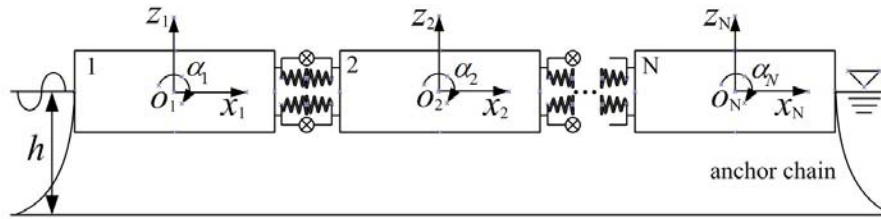
Fig. 1. Sketch for a floating airport with multi-modules connected by connectors and actuators

The network model of the floating airport [5] together with control can be in general written as

$$(\mathbf{M}_i + \boldsymbol{\mu}_i)\ddot{\mathbf{X}}_i + \boldsymbol{\lambda}_i\dot{\mathbf{X}}_i + (\mathbf{S}_i + \mathbf{K}_i)\mathbf{X}_i = \bar{\mathbf{f}}_i \exp[-(\omega t + \theta_i)] + \sum_{j=1}^{N}\left(\varepsilon\Phi_{ij}G(\mathbf{X}_i, \mathbf{X}_j) + u_j(v_j)\Gamma_{ij}\Psi_i(\mathbf{X}_i, \mathbf{X}_j)\right), \quad i = 1, 2, \cdots N \quad (1)$$

By considering a two-dimensional problem, the vector $\mathbf{X}_i = [x_i, z_i, \alpha_i]^T$ denotes the surge, heave and pitch motions of the ith floating module respectively. Symbols $\mathbf{M}_i$, $\boldsymbol{\mu}_i$, $\boldsymbol{\lambda}_i$ denote the matrices of the mass, additional mass and damping, $\mathbf{S}_i$ and $\mathbf{K}_i$ the matrices of buoyancy and mooring, $\bar{\mathbf{f}}_i$, ω, θ_i are the force, frequency and phase angle of regular wave, ε, Φ_{ij}, $\mathbf{G}(\mathbf{X}_i, \mathbf{X}_j)$ are the stiffness of connector, topology matrix and coupling function [5]. Symbol Γ_{ij} denotes the topological matrix of actuators and $\Psi_i(\mathbf{X}_i, \mathbf{X}_j)$ is the control gain matrix, $u_j(v_j)$ the output force of the jth actuator where v_j is the control law to be designed. Without control, the floating airport excited by waves may encounter large oscillations induced by resonances and strong nonlinearity.

CONTROL LAW WITH OUTPUT SATURATION

Since the surge motion is most significant, the aim here is to suppress the surge motions, which may reduce the other motions as well due to the synergetic effect of the network [5]. To halt the surge motions of N number of modules, N actuators are required. A propeller-type actuator is mounted at the first module, and the rest actuators are installed at the same positions of connectors between adjoining modules. The actuator force of $u_i(v_i(t))$ is bounded by a maximum actuation force u_{iM}. Thus the output of an actuator is defined by

$$u_i(v_i(t)) = \text{sat}(v_i(t)) = \begin{cases} \text{sign}(v_i(t))u_{iM}, & |v_i(t)| \geq u_{iM} \\ v_i(t), & |v_i(t)| < u_{iM} \end{cases} \quad i = 1, 2, \cdots, N \quad (2)$$

a) Corresponding author. Email: dlxu@hnu.edu.cn.

where $v_i(t)$ is the ith control law. For the ith module, the coordination is converted by backstepping approach, let error variables $z_{1i} = x_i$, $z_{2i} = \dot{x}_i - \kappa_{1i}$ where κ_{1i} is a virtual control. Taking κ_{1i} in the form of $\kappa_{1i} = -k_{1i}z_{1i}$ where k_{1i} is a positive design parameter. Differentiate z_{2i} with respect to time and get

$$\dot{z}_{2i} = \ddot{x}_i - \dot{\kappa}_{1i}, \quad i = 1, 2, \cdots N \tag{3}$$

where $\ddot{x}_i$ is defined by Eq.(1). Because the outputs of actuators are in saturation, to keep the control system globally stable, an auxiliary system is introduced for the ith module, defined by

$$\dot{\chi}_i = -c_i\chi_i - \frac{1}{\chi_i}\left(|z_{2i}\Theta_1| + \frac{1}{2}\sum_{j=1}^{N}\left(\left(u_j(v_j) - v_j\right)^2\Gamma_{ij}\right)\right) + \sum_{j=1}^{N}\left(\left(u_j(v_j) - v_j\right)\Gamma_{ij}\right) \quad i = 1, 2, \cdots N \tag{4}$$

where $\mathbf{\Theta} = (\mathbf{M}_i + \boldsymbol{\mu}_i)^{-1}\sum_{j=1}^{N}\left(\left(u_j(v_j) - v_j\right)\Gamma_{ij}\Psi_i(\mathbf{X}_i, \mathbf{X}_j)\right)$ and Θ_i represents the ith element of the vector $\mathbf{\Theta}$. By solving the simultaneous equations (1) (2), (3),and (4), leads to $\dot{z}_{2i} = -z_{1i} - k_{2i}(z_{2i} - \chi_i)$ and the design criterion of the control law $c_i - 0.5\sum_{j=1}^{N}(\Gamma_{ij}) - 0.5k_{2i} \geq 0$, where symbols k_{2i} and c_i are positive parameters to be designed in order to satisfy Lyapunov stability. By choosing proper design parameters, the outputs of actuators can be determined.

NUMERICAL SIMULATIONS

The data of the floating airport [2] is used for this numerical simulation. Fig.2(a) shows the significant suppression of the surge motion of the third floating module under control. The heave and pitch motions also appear relatively regular and mild. Owing to the coupling effect among the modules, the controlled motions of the rest modules are similar not presented here. Fig1(b) shows the variation of the control forces actuated on the third module. It can be seen from the first few truncated peaks that the output forces of the actuators are bounded by an assigned limitation of -200kN.
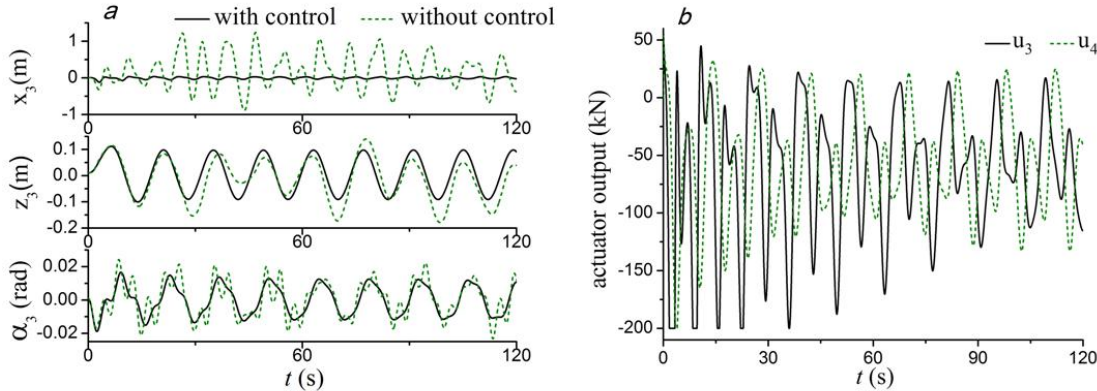
Fig.2 a) the responses of the floating airport with/without control, b) the actuator forces acted on the third floating module.

CONCLUSIONS

A nonlinear control strategy is proposed for suppressing the surge motion of a floating airport excited by waves. An auxiliary system is devised to deal with the output saturation of actuators. The numerical simulation illustrates that the stability of the floating airport is greatly improved, and the control method is effective. Thanks for the support of National Natural Science Foundation of China (11472100), the 973 research grant (2013CB036104).

References

[1] S. Ohmatsu, "Overview: Research on wave loading and responses of VLFS," *Mar. Struct.*, vol. 18, no. 2, pp. 149–168, 2005.Icer D.F., Adams J.A.: Mathematical Elements for Computer Simulation. Montreal, Canada 1977.

[2] S.Y. Xia;D.L. Xu, "On Retaining a Multi-Module Floating Structure in an Amplitude Death State," *Ocean Eng.*, 2015. (in review process)

[3] A. Boucheta, I. K. Bousserhane, a. Hazzab, B. Mazari, and M. K. Fellah, "Adaptive backstepping controller for linear induction motor position control," *COMPEL - Int. J. Comput. Math. Electr. Electron. Eng.*, vol. 29, no. 3, pp. 789–810, May 2010.

[4] D. L. Xu, H. C. Zhang, C. Lu, E. R. Qi, C. Tian, and Y. S. Wu, "Analytical criterion for amplitude death in nonautonomous systems with piecewise nonlinear coupling," *Phys. Rev. E*, vol. 89, no. 4, p. 042906, Apr. 2014.

[5] H. C. Zhang, D. L. Xu, C. Lu, S. Y. Xia, E. R. Qi, J. J. Hu, and Y. S. Wu, "Network dynamic stability of floating airport based on amplitude death," Ocean Eng., vol. 104, pp. 129–139, Aug. 2015.

SELF-INTERRUPTED CHATTER IN CYLINDRICAL GRINDING

Yao Yan*[1] and Jian Xu[2]

[1]*School of Astronautics and Aeronautics, University of Electronic Science and Technology of China, Chengdu, Sichuan, China*
[2]*School of Aerospace Engineering and Applied Mechanics, Tongji University, Shanghai, China*

Summary As a self-excited vibration, chatter in cylindrical grinding is mainly incurred by subcritical Hopf bifurcation and is of large amplitude, which forces grinding wheel to leave workpiece and interrupts the grinding. Normally, interactive wheel-workpiece force is described by regenerative theory and fixed time delays. However, for the self-interrupted, the theory requires modification as the regeneration can be absent. Therefore, instead of using delayed differential equations (DDEs), a model with partial differential equations (PDEs) is proposed for monitoring the regeneration. Results of the PDEs illustrate a smaller amplitude of the chatter compared with the DDEs.

CYLINDRICAL GRINDING

Cylindrical grinding uses a rotating wheel to rub a rotating workpiece, removing workpiece material and regenerating its surface. Besides, as seen in Figure 1(a), the wheel also has a translational motion for feed, which is plunge[1, 2] for wheel moving toward the workpiece and transverse[3] for that along the workpiece. When only the first mode of the workpiece is considered, the continuous model is discretized, which yields the equivalent model in Figure 1(b). Moreover, the interactive grinding force between the wheel and the workpiece is proportional to the instantaneous grinding depth determined by the doubly regenerative effect depicted in Figure 1(c), introducing time delays into the governing equation of the grinding. The grinding force repels the wheel and the workpiece, exciting the system to vibrate when system damping is insufficient.

LARGE-AMPLITUDE GRINDING CHATTER OBTAINED BY DDE

Regarding the dynamical model in Figure 1, the grinding dynamics is governed by

$$\frac{d\mathbf{y}(\tau)}{d\tau} = \mathbf{A}\mathbf{y}(\tau) + \mathbf{F}_{\mathbf{dde}} = (\mathbf{A} + \mathbf{D})\mathbf{y}(\tau) + \mathbf{D}_{\mathbf{W}}\mathbf{y}(\tau - \tau_{\mathbf{W}}) + \mathbf{D}_{\mathbf{g}}\mathbf{y}(\tau - \tau_{\mathbf{g}}) + \mathbf{f}, \tag{1}$$

where $\mathbf{y}(\tau)$ is the state vector of the grinding, $\mathbf{A}$ is the coefficient matrix of the system, $\mathbf{D}$, $\mathbf{D}_{\mathbf{W}}$ and $\mathbf{D}_{\mathbf{g}}$ are coefficient matrices from the grinding force, and $\mathbf{f}$ includes all the nonlinear terms. Using Eq. 1 and eigenvalue analysis, the stability boundary for the grinding is obtained, which is also a critical value for the Hopf bifurcation. Near the boundary, performing bifurcation analysis yields the subcritical Hopf bifurcation illustrated in Figure 2(a). As seen, the branch of periodic motions folds and introduces large-amplitude chatter coexisting with the stable grinding in the linearly chatter-free region. To illustrate, Points I and II have the same parameter value, but presents different time series in Figures 2(b) and (c). Specially, Figure 2(b) shows the grinding chatter accompanied by loss-of-contact effect, and thus the grinding is self-interrupted.

In the transverse grinding, as seen in Figure 2(d), the wheel is slowly moving along the workpiece, introducing a time-varying parameter into the system, and thus the grinding process is quasi-static. Thus, for each fixed wheel position P, the grinding dynamics is investigated by bifurcation analysis. Then, letting P varies between 0 and L and borrowing the idea of fast-slow system, one can construct the chatter of the transverse. Two typical cases are displayed in Figures 2(e) and (f), which are intermittent and of losing contact ($d_{\mathbf{g}} < 0$) as well.
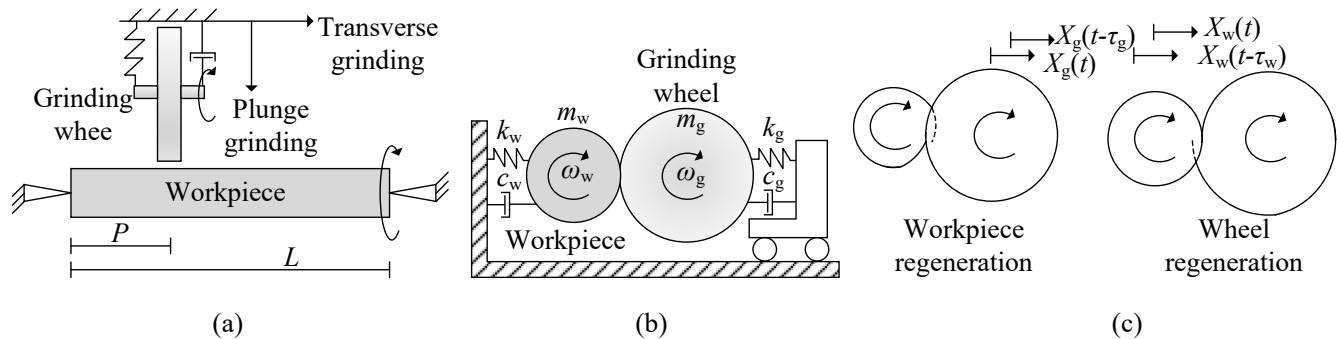
Figure 1: Schematics of the (a) plunge and transverse grinding process, (b) equivalent discrete model of the grinding with respect to the first workpiece mode, and (c) doubly regenerative effect in the wheel and workpiece surfaces.

*Corresponding author. Email: y.yan@uestc.edu.cn
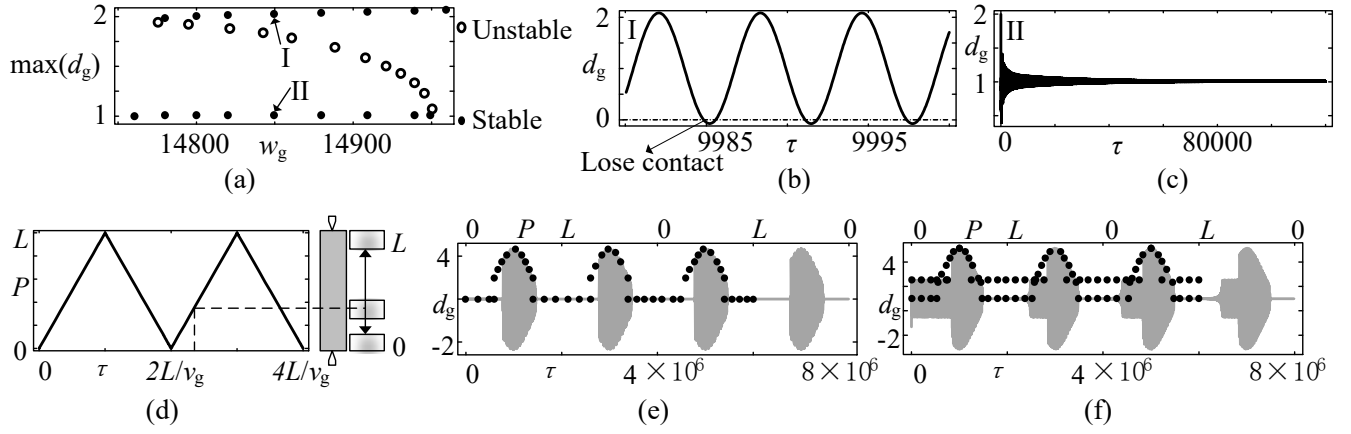
Figure 2: (a) Bifurcation diagram, (b) large-amplitude chatter, and (c) stable grinding in the plunge. (d) Wheel motion, (e) intermittent chatter, and (f) another typical chatter in the transverse.
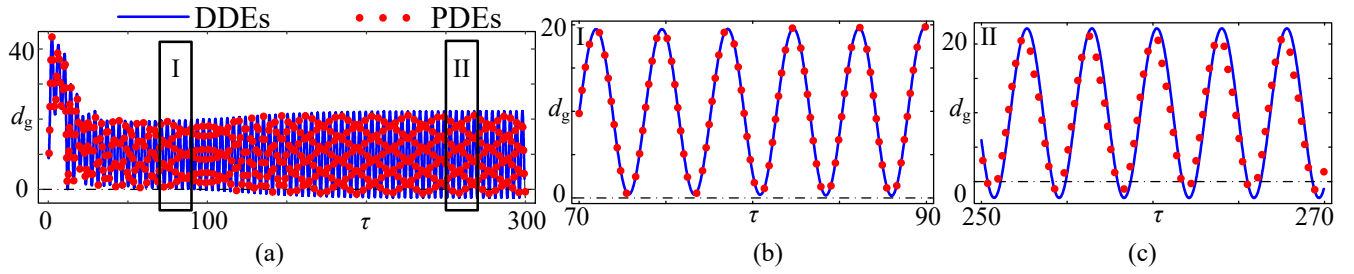
Figure 3: (a) Grinding chatter obtained by PDEs, with Regions I and II blown up and replotted in panels (b) and (c).

LARGE-AMPLITUDE GRINDING CHATTER OBTAINED BY PDE

Instead of the DDEs, PDEs can also be used to monitor the regeneration of workpiece surface by using [4]

$$\frac{d\mathbf{y}(\tau)}{d\tau} = \mathbf{A}\mathbf{y}(\tau) + \mathbf{F}_{\text{pde}} \quad \text{and} \quad \frac{\partial \tilde{r}(\tau,\theta)}{\partial \tau} + \frac{2\pi}{\tau_{\text{w}}} \frac{\partial \tilde{r}(\tau,\theta)}{\partial \theta} = 0, \tag{2}$$

where $\tilde{r}$ is the workpiece radius. Employing Galerkin Projection transforms Eq. (2) into ODEs, and solving it directory yields the grinding dynamics, which is illustrated in Figure 3. As seen in Figure 3(b), the solutions obtained from the DDEs and the PDEs are the same when the wheel keeps grinding the workpiece ($d_{\text{g}} > 0$). By contrast, the time series plotted in Figure 3(c) are different, where the result of the PDEs presents a smaller chatter amplitude when multiple-delay effect shows up.

CONCLUSIONS

Grinding chatter is of large amplitude and accompanied by loss-of-contact effect, making the grinding self-interrupted and introduce multi-regeneration. In this situation, the DDEs cannot describe the multi-delay effect with fixed delays. Therefore, PDEs is employed to record the workpiece profile, obtaining chatter with smaller amplitude.

References

[1] Yan Y., Xu J., Wang W.: Nonlinear Chatter With Large Amplitude in a Cylindrical Plunge Grinding Process. NONLINEAR DYNAM 69(4):1781-1793, 2012.

[2] Yan Y., Xu J.: Suppression of Regenerative Chatter in a Plunge-Grinding Process by Spindle Speed. J MANUF SCI E-T ASME 135:041019, 2013.

[3] Yan Y., Xu J., Wiercigroch M.: Chatter in a Transverse Grinding Process. J SOUND VIB 333:937-953, 2014.

[4] Wahi P., Chatterjee A.: Self-interrupted regenerative metal cutting in turning. INT J NONLINEAR MECH 43:111-123, 2008.

A STUDY ON VARIABLE FOR ESTIMATING MAXIMUM POWER CONVERSION OF PARAMETRIC PENDULUMS

Yuichi Yokoi[*1] and Tsuyoshi Higuchi[1]

[1]*Division of Electrical Engineering and Computer Science, Nagasaki University, Nagasaki, Japan*

Summary The rotational motion of the parametric pendulum can be applied to energy harvesting from vibrations and movements of nature. In the pendulum system for the power conversion, the output power depends on the load resistance. For this reason, the output power can be controlled by regulating the load through a power converter on the basis of the Maximum Power Point Tracking (MPPT). The characteristic power curve implies that the maximum power point cannot be directly tracked by measured power. This paper finds out another variable to estimate the maximum power point for a MPPT method of the converting pendulum system.

INTRODUCTION

The parametrically excited pendulum inherently exhibits a conversion from a vertical vibration into its rotational motion. The converting motion, which can directly drive a rotational generator, is associated with energy harvesting from vibrations and movements of nature such as sea wave. The concept of the power conversion through the parametric pendulum is originated from a series of studies [1, 2, 3]. Among a variety of motions of the pendulum, the periodic rotation is suited for the application with respect to the amount of converted power. The system considered for the power conversion consists of a mechanical pendulum excited vertically or a so-called parametric pendulum, and a DC generator connected with the rotational shaft of the pendulum, and an electrical resistance as the load of the generator, as shown in Figure 1. For a vertical vibration, the output power depends on the load resistance. For this reason, the output power can be controlled by regulating the load through a power converter. The technique to maximize output power is used for wind turbines and photovoltaic systems as Maximum Power Point Tracking (MPPT) [4, 5]. A variety of control methods have been proposed for the MPPT of the systems [4, 5]. However, these methods cannot be applied to the MPPT of the converting pendulum system because the characteristic power curve of this system is different from the conventional ones. The power characteristic is described by a hysteresis curve including a jump phenomenon at the maximum point. This implies that the maximum power point cannot be directly tracked by measured power. This paper finds out another variable to estimate the maximum power point for a MPPT method of the converting pendulum system.

MATHEMATICAL MODEL

For the converting pendulum system as shown in Figure 1, a non-dimensional mathematical model is derived as

$$\frac{\mathrm{d}^2\theta}{\mathrm{d}t^2} + \gamma\frac{\mathrm{d}\theta}{\mathrm{d}t} + (1 + p\cos\omega t)\sin\theta = 0, \tag{1}$$

where θ denotes the angular displacement of the pendulum from the downward position, γ is a non-dimensional parameter governed by the load resistance, and $p\cos\omega t$ corresponds to the vertical excitation with amplitude of p and angular frequency of ω. The parameter γ is called the load coefficient. Without any losses, the input power P_{in} and the output power P_{out} are respectively expressed as follows:

$$P_{\text{in}} = -\frac{1}{2}\left(\frac{\mathrm{d}\theta}{\mathrm{d}t}\right)\omega\cos\omega t\sin\theta \qquad \text{and} \qquad P_{\text{out}} = \gamma\left(\frac{\mathrm{d}\theta}{\mathrm{d}t}\right)^2. \tag{2}$$

(a) Parametric pendulum. (b) Electrical circuit.
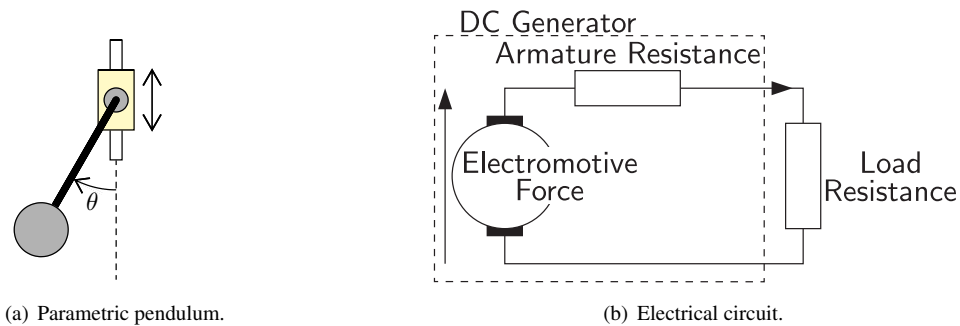
Figure 1: System for the power conversion through a pendulum.

*Corresponding author. Email: yyokoi@nagasaki-u.ac.jp

| (a) Angular displacement θ. | (b) Output power P_{out}. | (c) Phase ϕ. |
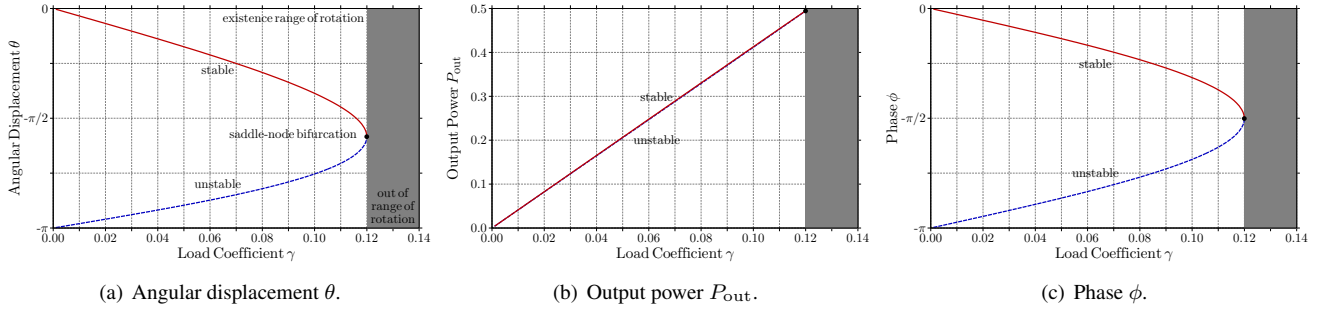
Figure 2: Bifurcation diagram of periodic rotation with respect to the load coefficient γ.

MAXIMUM POWER CONVERSION

The load coefficient γ is regulated to control the amount of the output power P_{out}. Figure 2 shows the bifurcation diagrams of periodic rotation with respect to γ at $p = 0.5$ and $\omega = 2$. These diagrams indicate the existence range of periodic rotation in the load coefficient γ. This implies that the load coefficient γ has to be regulated with the pendulum rotating for the power conversion. The output power P_{out} increases in almost proportion to γ, as shown in Figure 2(b). The power P_{out} is maximized at the maximum limit of γ in the range. Therefore, the load coefficient γ should be carefully regulated to establish the maximum power conversion because the coefficient γ beyond the limit prevents the periodic rotation for the power conversion. For this reason, this control previously requires the information of the maximum limit of γ. The maximum limit of γ is estimated with a variable that is less influenced by the parameters because it is difficult to directly predict the limit that severely depends on the system parameters,

A variable is found to estimate the maximum limit of γ or the maximum value of P_{out} from an analytical approach. The solution for periodic rotation can be written as $\theta = \omega t + \phi + \alpha(t)$, where ϕ corresponds to the phase and $\alpha(t)$ is a periodic function with period $2\pi/\omega$. In the analysis, it is assumed that the function $\alpha(t)$ is negligibly small. The averaging with the solution transforms the input power P_{in} into the averaged input power $\langle P_{\text{in}} \rangle = -(\omega p/2) \sin \phi$. This expression indicates that the input power, which is equal to the output power, is maximized at $\phi = -\pi/2$. The phase ϕ is not dependent on the system parameters on the assumption. Thus, the output power is maximized at $\phi = -\pi/2$ regardless of the system parameters. From the stability analysis of the solution, it is found that the phase ϕ within $-\pi/2$ and 0 corresponds to stable periodic rotations. The phase ϕ is employed as the variable to estimate the maximum limit of the load coefficient γ. The efficacy of the phase ϕ is confirmed numerically, as shown in Figure 2(c). The phase ϕ converges from 0 to the vicinity of $-\pi/2$ as the increased load coefficient γ. On a control method for the MPPT, the load coefficient γ is regulated on the basis of the feedback variable ϕ to control the output power P_{out}.

CONCLUDING REMARKS

This paper finds out a variable to estimate the maximum output power for a MPPT method of the converting pendulum system. The analytical and numerical studies verify that the phase component of periodic rotation performs as the feedback variable. In the presentation, we will show experimental evidences for the estimation through the phase and a feedback control for the MPPT.

ACKNOWLEDGMENTS

References

[1] Xu X. and Wiercigroch M.: Approximate Analytical Solutions for Oscillatory and Rotational Motion of a Parametric Pendulum. Nonliear Dyn 47:311–320, 2007.

[2] Lenci S., et al.: Rotating Solutions and Stability of Parametric Pendulum by Perturbation Method. J Sound Vib 310:243–259, 2008.

[3] Horton B., et al.: Transient Tumbling Chaos and Damping Identification for Parametric Pendulum. Phil Trans R Soc A 366:767–784, 2008.

[4] Baroudi J. A., Dinavahi V., Knight A. M.: A Review of Power Converter Topologies for Wind Generators. Renew Energ 32:2369–2385, 2007.

[5] Esram T., Chapman P. L.: Comparison of Photovoltaic Array Maximum Power Point Tracking Techniques. IEEE T Energy Conver 22:439–449, 2008.

NONLINEAR WAVE TRANSMISSION IN DISORDERED PERIODIC STRUCTURES

Behrooz Yousefzadeh[*1] and A. Srikantha Phani[2]

[1,2]*Department of Mechanical Engineering, University of British Columbia, Vancouver, BC, Canada*

Summary We study wave transmission through a damped nonlinear periodic structure of finite length, subjected to continuous harmonic excitation at one end. Nonlinearity leads to supratransmission phenomenon by which enhanced wave transmission occurs within the stop band of the periodic structure when forced at an amplitude exceeding a threshold. Here, we study supratransmission in the presence of deviations from periodicity (disorder), introduced as small variations in stiffness parameters throughout the structure. We find that disorder does not influence the supratransmission force threshold in the ensemble-average sense, but it reduces the average transmitted wave energy.

INTRODUCTION

A linear periodic structure exhibits filtering characteristics, whereby wave transmission is prohibited within certain frequency intervals known as stop bands. The presence of nonlinear forces provides a route to achieve enhanced transmission within a stop band, known as *supratransmission* [1]. This phenomenon occurs when the periodic structure is harmonically driven with a frequency within its linear stop band. In this case, energy transmission may become possible if the driving amplitude is larger than a certain threshold. The frequency components of the nonlinearly transmitted waves lie within the linear pass band of the structure. This has significant consequences for the transmitted energies if the periodic structure is disordered. The reason is that disorder results in localization of energy near the source of excitation (Anderson localization), particularly for frequencies within the linear pass band [2]. Thus, it is natural to expect a competition between nonlinearity and disorder with regards to transmitted energies above the supratransmission threshold. Our goal is to study this interaction.

MAIN RESULTS

We use a macro-mechanical nonlinear periodic structure that consists of coupled suspended cantilevers beams, shown in Fig. 1. See [3] for the corresponding mathematical models. The supratransmission phenomenon is explained in Fig. 2 for a periodic structure with $N = 10$ units. A key feature for supratransmission is that the motion is no longer periodic beyond the onset of transmission. As a result, the average transmitted energy (E_N) increases by orders of magnitude, where we define

$$E_N \equiv \frac{1}{(m_2 - m_1)T} \int_{m_1 T}^{m_2 T} \left(\frac{u_N(t)}{F} \right)^2 dt \quad \text{where} \quad T = 2\pi/\Omega, m_1 = 500, m_2 = 2500. \tag{1}$$

We introduce disorder throughout the structure by small variations in the stiffness parameter of each unit, drawn from a uniform statistical distribution. The strength of disorder is characterized by the ratio D/C, where D is a relative measure of the deviations in stiffness parameters and C is a measure of the strength of coupling between units [2].

We found that supratransmission persists in the presence of disorder. The change in threshold force amplitude, and whether it occurs or not, depends on the particular realization that is being considered. Nevertheless, when averaged over an ensemble of different realizations of disorder at a fixed D/C, the average onset of supratransmission remains unchanged; see Fig. 2(b).

When excitation is within the linear stop band, increasing the strength of disorder has negligible influence on transmitted energies below the onset of supratransmission, Fig. 3(a). In contrast, the average transmitted energies decrease with disorder above the transmission threshold, Fig. 3(b). This happens because the average frequency spectrum of transmitted waves lies within the linear pass band of the structure, where disorder localizes the response to the driven unit (Anderson localization).

CONCLUSIONS

Disorder does not influence the supratransmission force threshold in the ensemble-average sense, but it reduces the average transmitted wave energy. Generally, the influence of disorder decreases as forcing frequency moves away from the pass band edge, reminiscent of dispersion effects subsuming disorder effects in linear periodic structures. These results are generic to nonlinear disordered periodic structures and may be exploited for design of phononic crystals and acoustic metamaterials[4, 5].

References

[1] Geniet F., Leon J.: Energy transmission in the forbidden band gap of a nonlinear chain. Phys. Rev. Lett. 89:134102, 2002.
[2] Hodges C.: Confinement of vibration by structural irregularities. J. Sound Vib. 82:411-424, 1982.
[3] Yousefzadeh B., Phani A.S.: Energy transmission in finite nonlinear periodic structures from excitations within the stop band. J. Sound Vib. 354, 2015.
[4] Fleck N.A., Deshpande V.S., Ashby M.F.: Micro-architectured materials: Past, present and future. Proc. R. Soc. A 466:2495-2516, 2010.
[5] Liu Z., et al.:Locally resonant sonic materials. Science 289:1734-1736, 2000.

*a) Corresponding author. Email: behroozy@alumni.ubc.ca
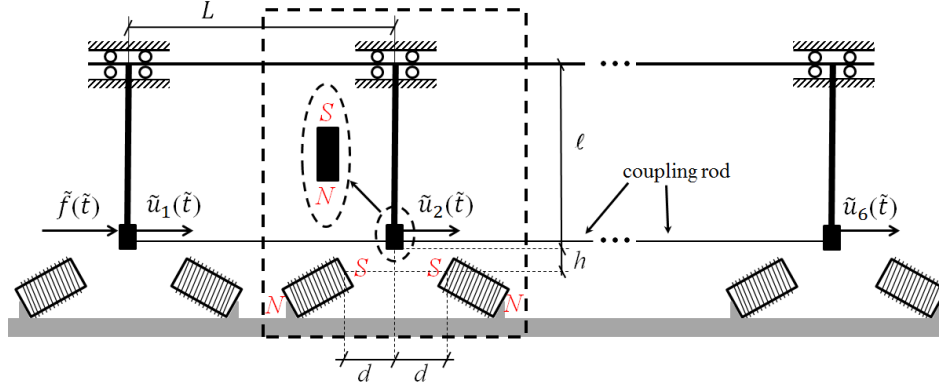
Figure 1: The schematic of the periodic structure made of N repeating units. The unit cell is indicated by the dashed box. An external harmonic force, $f(t) = F\cos(\Omega t)$, is applied to the first unit only. Two electromagnets, operated by direct currents, are fixed under the beam in each unit, such that the electromagnets have the same polarity facing the beam. Thus, the linear restoring force of each beam is combined with a strong nonlinear magnetic force to produce on-site nonlinearity. The magnetic force can be tuned, providing control over the strength of nonlinearity, as well as its type (softening or hardening).
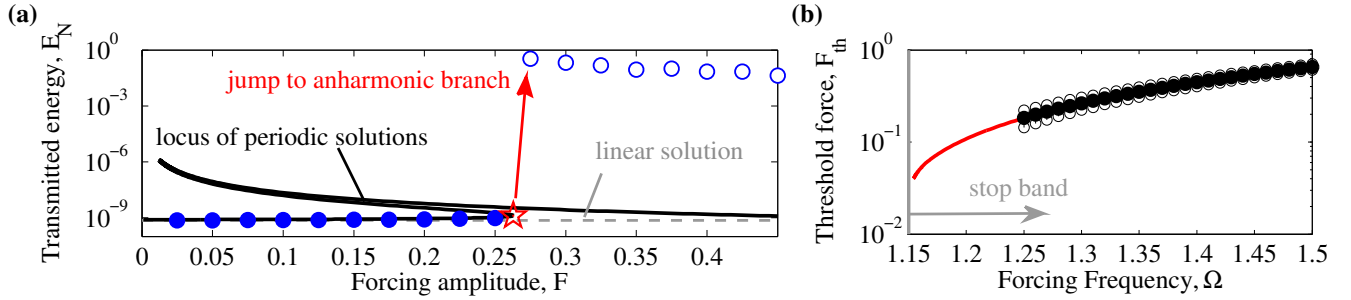
Figure 2: (a) Energy transmitted to the end of the exactly periodic structure (E_N) as a function of driving amplitude (F) at a forcing frequency above the linear pass band ($\Omega = 1.30$). The dashed grey line corresponds to the linear response of the system. The black curve indicates the evolution of periodic solutions. Circle markers indicates results from direct numerical integration of the governing equations, with filled markers indicating harmonic response and empty markers indicating non-periodic response. The periodic solutions lose their linear stability through a saddle-node bifurcation, which is depicted by the red star. (b) The red solid curve depicts the threshold curve for a periodic structure: locus of supratransmission force threshold (F_{th}) as a function of Ω. The filled circles indicate the average value of F_{th} for a disordered structure with $D/C = 2$. The corresponding standard deviations are shown using the empty circles. An ensemble of 1500 realizations is used here.
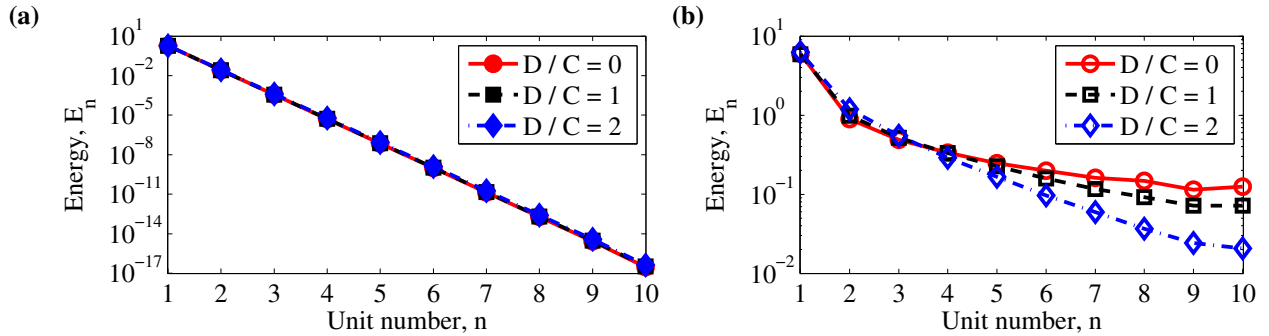
Figure 3: Average energy profiles for (a) the linear system, (b) the nonlinear system above the onset of transmission. Note the difference between the scales for the vertical axes in (a) & (b). Above the threshold, disorder results in localization of energy to the driven unit. An ensemble of 1500 realizations is used for each disordered system.

ON THE LOCOMOTION OF SELF-PROPELLING SYSTEMS IN A LINEAR RESISTIVE ENVIRONMENT

Nikolai Bolotnik[1], Igor Zeidis[2a] & Klaus Zimmermann[2]
[1]Institute for Problems in Mechanics of the Russian Academy of Sciences, Moscow, Russia
[2]Department of Technical Mechanics, Technische Univesitaet Ilmenau, Germany

<u>*Summary*</u> The motion of self-propelling limbless locomotion systems in a linear viscous environment is considered. The resistance force acting on an element of the systems is assumed to be proportional to the velocity of this element relative to the environment. Two models of interaction of the locomotor with the environment are distinguished. In the first model, the coefficient of friction is constant for a mass element, whereas in the second model, this coefficient is constant for a length element. It is shown that progressive locomotion is impossible for the first model and is possible for the second model. This is explained by the fact that in the second model, the coefficient of friction for a mass element is in fact controlled by changing the length of this element due to deformation of the locomotor's body.

INTRODUCTION

This paper relates to mechanics of limbless locomotion. The limbless locomotion systems move without special propelling devices, such as wheels, legs, fins, or caterpillars, due to change in their shape and interaction with the environment. In a number of studies [1-2], the motion of particular systems of lumped masses (particles) along a straight line in a resistive environment was investigated. The motion of the systems was excited by a periodic change in the distances between the adjacent particles. The authors of the cited papers were interested mostly in the steady-state motion, in which the entire system moves with a periodically changing velocity. It was shown that if the resistance forces applied to each of the lumped masses are linear functions of the velocities of these masses relative to the environment, then progressive steady-state motion is impossible for the respective system. In [3], for a particular model, it was shown that a one-dimensional worm-like distributed-mass locomotor can move progressively in a viscous medium with linear rheology in a quasi-static approximation.

We investigate the specific features of the interaction of limbless locomotion systems with the environments possessing a linear rheology that allow or prevent self-propulsion of such systems in these environments. We consider both lumped-mass and distributed-mass systems. We assume that the resistance (friction) force applied by the environment to each element is a linear function of the velocity of the respective element relative to the environment with constant coefficient of friction. Unlike [3], we do not confine ourselves to a quasi-static approximation and proceed from the full dynamic equation of motion.

LUMPED MASS LOCOMOTION SYSTEMS

Consider a set of n particles (point masses) that can move along a horizontal straight line (Figure l).
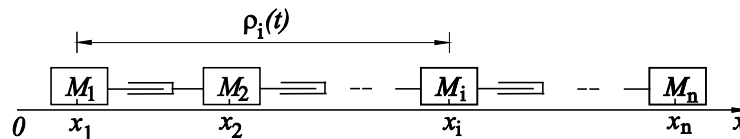
Figure 1. A one-dimensional lumped mass locomotion system.

Let x_i denote the coordinate of the ith particle measured along the line of the motion from a point O fixed in an unmovable (inertial) reference frame; M_i the mass of the ith particle; $m_i = M_i/M$, $M = \sum_{i=1}^{n} M_i$; the coordinate of the ith particle measured relative to point 1 is $\rho_i = x_i - x_1$. Each particle interacts with the other particles of the system and with the environment. We assume that the environmental forces are linear functions of the velocity: $F_i(\dot{x}_i) = -\mu_i \dot{x}_i$, where μ_i is the coefficient of friction. The motion of the center of mass X of the system is governed by the equation

$$\dot{V} = -kV - \dot{\xi}, \quad \dot{X} = V, \quad X(0) = X_0, \quad V(0) = V_0, \quad \xi = \sum_{j=1}^{n}(km_j - k_j)\rho_j, \quad k_i = \mu_i/M, \quad k = \sum_{j=1}^{n} k_j, \quad i = 1,\ldots,n. \quad (1)$$

[a] Corresponding author. Email: igor.zeidis@tu-ilmenau.de**.**

If the function $\xi(t)$ is bounded, i.e., $|\xi(t)| \leq C$, where C is a constant, then the solution $X(t)$ of system (1) is estimated by $|X(t) - X_0| < (|V_0| + |\xi(0)| + C)/k$. Hence, the center of mass of a lumped mass locomotion system on a straight line cannot move by an arbitrary prescribed distance in a linear resistive environment, irrespective of the control law, provided that the change in the distances between the system's particles is constrained. Assume that (i) the system starts moving from a state of rest and, hence, $V_0 = 0$, (ii) the relative position of the system's particles changes during a finite time T, i.e., $\dot{\xi}(t) \equiv 0$ and $\xi(t) \equiv \xi(T)$ for $t > T$ and, in addition, (iii) $\xi(0) = \xi(T)$. Then $\lim_{t \to \infty} X(t) = X_0$. Therefore, if the system starts moving from a state of rest, and the configuration of the system at the terminal instant of the excitation coincides with the initial configuration, then the system eventually returns to its initial position after the excitation has been terminated.

DISTRIBUTED MASS LOCOMOTION SYSTEM

Consider a worm-like locomotion system the body of which has a shape of a thin circular cylinder (Figure 2). The system moves along the axis of the cylinder. The locomotion occurs due to the longitudinal deformation of the cylinder and its interaction with the environment. The motion of the system is excited and controlled by internal forces that act between the parts of the worm's body. We assume that in the reference (undeformed) configuration, the cylinder has length L and mass density per unit length $\rho(x)$; the total mass of the system is M. Introduce the notation: x_0 is the coordinate of the left edge of the cylinder measured from a point O fixed in the inertial reference frame; x, $0 \leq x \leq L$, is the coordinate of a current section of the cylinder measured for the undeformed configuration from the left edge; $u(x,t)$ is the displacement of the section identified by the coordinate x at the time t from its position in the reference configuration.
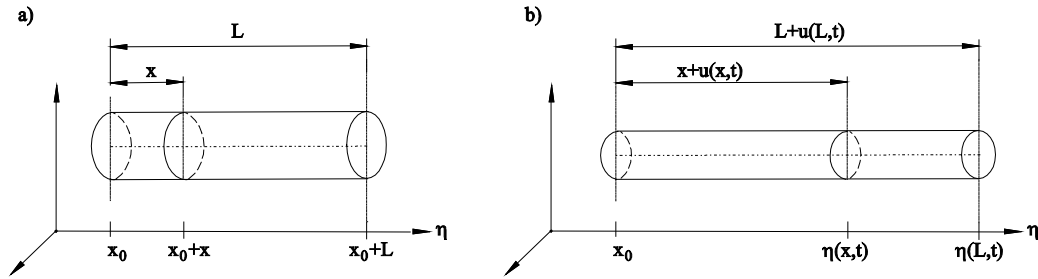
Figure 2. A distributed mass worm-like system: a) undeformed, b) deformed.

The position η of section x of the deformed cylinder with respect to point O is defined by $\eta(x,t) = x_0 + x + u(x,t)$, $u(0,t) = 0$. We assume that the resistance (friction) force acting on an element of the system is proportional to the velocity $\dot{\eta}(x,t)$ of this element relative to the environment, with the coefficient of proportionality (coefficient of friction) being constant. Two models of the interaction between the system and the environment are considered; the coefficient of friction is constant per unit mass for the first model and per unit length for the second model. The motion of the center of mass of the system to an arbitrary position is proved to be impossible for the first model and possible for the second model. It is explained by the fact that for the second model, the coefficient of friction related to a mass element changes, since the length of this element changes due to deformation of the system. The locomotion of the distributed mass system is studied in detail for the case where a periodic deformation wave runs with a constant velocity along the system. It is shown that if the length of the undeformed system is a multiple of the deformation wave length, then for the steady-state mode of motion, at which the system arrives from any initial state, the system's center of mass moves at a constant velocity in the direction of the propagation of the wave, irrespective of the wave shape. For a sinusoidal wave the length of which is incommensurable with the length of the undeformed system, the center of mass of the system moves on the average in the direction of the propagation of the wave with a velocity periodically changing in time.

References

[1]   Chernousko F.L: Analysis and optimization of the motion of a body controlled by means of a movable mass. *J. Appl Math Mech* **70**:819–842, 2006
[2]   Bolotnik N., Pivovarov M., Zeidis I., Zimmermann K.: The undulatory motion of a chain of particles in a resistive medium. *ZAMM* **91**:259–275, 2011
[3]   DeSimone A., Tatone A.: Crawling mobility through the analysis of model locomotors: Two case studies. *Eur J. Phys* E **35**: 2–8, 2012

MODE LOCALIZATION IN CYCLIC SELF-EXCITED STRUCTURE WITH SYMMETRIC DELAYED FEEDBACK

Shu Zhang[1], Jian Xu[1a) & Kwok-wai Chung[2]

[1]*School of Aerospace Engineering and Applied Mechanics, Tongji University, Shanghai, P.R.C.*
[2]*Department of Mathematics, City University of Hongkong, Hongkong, P.R.C.*

Summary We employ the theory of equivariant bifurcation to investigate the mode localization in a cyclic self-excited structure with symmetric delayed feedback. The method of multiple scales is applied to obtain the equation of amplitude based on which the condition for the existence mode localization is given. Our result shows that in the presence of time delays, strong nonlinearity may induce mode localization in the cyclic self-excited structure without imperfections in parameters.

INTRODUCTION

Mode localization is commonly interpreted as a dynamic phenomenon induced by mistuned parameters of a symmetric structure. Namely, the irregularities of the structure will trap the energy in a substructure while it is believed that in the absence of imperfections the energy will be uniformly distributed. The theory of equivariant bifurcation [1] provides another perspective to study this problem, i.e., the symmetry is the reason that induces non-symmetric (asynchronous) oscillation, including localization. This group-theoretic based method has been employed to investigate mode bifurcations [2] and localization of some forced vibration system [3]. However, from the view point of nonlinear dynamics, the mechanism of localization is still not quite clear especially for the self-excited structure which can be found in dry-friction-induced oscillation, the interaction between fluid and structure and so on. Van der Pol-Duffing system is one of the standard models of self-excited structures and will be used in the present paper to investigate the mode localization. The equilibrium of such system is unstable and thus people usually introduce feedback control which brings the time delay. With the aid of equivariant bifurcation theory, we show that in the presence of time delay, the symmetry of the structure can induce mode localization and the nonlinear stiffness has a strong impact on it.

MODEL SETUP AND STABILITY SWITCH BOUNDARIES

In this paper, we consider the following self-excited system of Van der Pol-Duffing type to study the mode localization phenomenon induced by the nonlinearity and delays [4]:

$$\ddot{x}_j + \mu(x_j^2 - 1)\dot{x}_j + x_j + \kappa x_j^3$$
$$= \alpha(x_{j-1}(t-\tau_2) + x_{j+1}(t-\tau_2) - 2x_j(t-\tau_1)) + \beta(\dot{x}_{j-1}(t-\tau_2) + \dot{x}_{j+1}(t-\tau_2) - 2\dot{x}_j(t-\tau_1)), \tag{1}$$

where $x_0 \equiv x_3$, $x_4 \equiv x_1$, μ is the damping coefficient, κ the nonlinear stiffness, α, β are the gain parameters for position and velocity feedback, respectively, τ_1, τ_2 the time lag of self-connection and mutual-connection, respectively. From the point of view of nonlinear dynamics, oscillations can be thought of as bifurcated from the equilibrium. In order to investigate the localization phenomenon, we need to analyze the stability of the equilibrium first. The characteristic equation of the linearized system of (1) around the trivial equilibrium is

$$\left(\lambda^2 - \mu\lambda + 1 + 2(\alpha+\beta\lambda)(e^{-\lambda\tau_1} - e^{-\lambda\tau_2})\right)\left(\lambda^2 - \mu\lambda + 1 + (\alpha+\beta\lambda)(2e^{-\lambda\tau_1} + e^{-\lambda\tau_2})\right)^2 = 0 \tag{2}$$

where λ is the eigenvalue. The curves representing roots of (2) in the plane consisting of τ_1 and τ_2 are plotted in Fig. 1. The expression in the first pair of parentheses is the condition for switching to synchronous oscillation (red curve) while the one in the second pair (blue curve) is the condition for switching to asynchronous state, which may correspond to the localization. In region III, there exists the asynchronous oscillation induced by equivariant Hopf bifurcation. The asynchronous oscillation and its stability will be studied by means of the method of multiple scales, as shown in next section.

MODE LOCALIZATION ANALYSIS

In order to investigate the oscillator behaviour of (1), the method of multiple scales is employed to obtain the equation that the amplitudes of x_1, x_2 and x_3 have to satisfy. It follows from the standard procedure of equivariant Hopf bifurcation analysis that the solution can be assumed as

$$x_j = i\,\omega\chi_1^{j-1}A(T_1,T_2)e^{i\omega T_0} + i\,\omega\chi_2^{j-1}B(T_1,T_2)e^{i\omega T_0} + cc. + o(\varepsilon), \quad j = 1,2,3,$$

where $\chi_1 = e^{2\pi i/3}$, $\chi_2 = e^{2\pi i/3}$, $T_0 = t$, $T_1 = \varepsilon t$, $T_2 = \varepsilon^2 t$. Up to $o(\varepsilon)$, the equation of amplitude is obtained as

---

a) Corresponding author. Email: xujian@tongji.edu.cn.
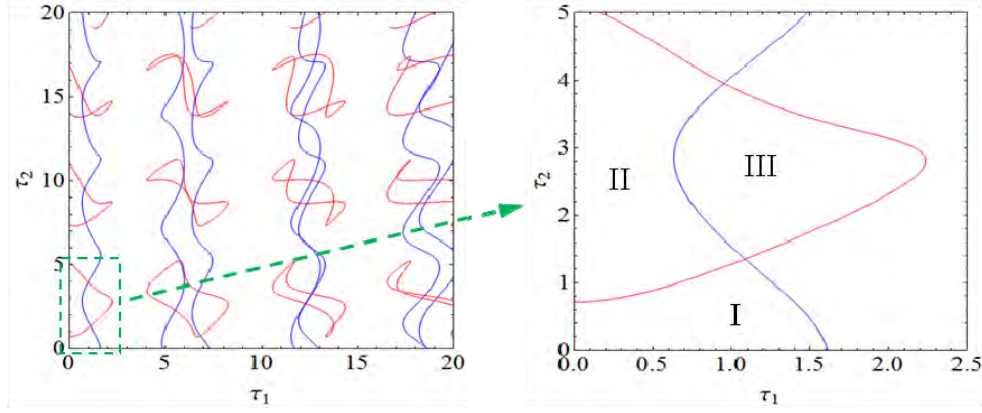
Figure 1: Stability switch boundaries for $\mu = 0.05, \alpha = 0.005, \beta = 0.1, \kappa = 1$, where the equilibrium is stable in Region I.

$$A^{(1,0)} = A\left(p_0 + p_1(A\bar{A} + 2B\bar{B})\right), B^{(1,0)} = B\left(p_0 + p_1(2A\bar{A} + B\bar{B})\right),$$

where p_0 and p_1 are (complex) functions of the parameters. $A^{(0,1)}$ and $B^{(0,1)}$ can be obtained in the similar way and then the final equation of amplitude follows by combining $A^{(1,0)}$, $B^{(1,0)}$, $A^{(0,1)}$ and $B^{(0,1)}$. To provide an example, for $\mu = 0.05$, $\alpha = 0.005$, $\beta = 0.1$, $\tau_1 = 0.7$, $\tau_2 = 3$ (Region III in Fig. 1), we find that $p_0 = 0.004 + 0.0045\mathrm{i}$, $p_1 = (-0.027 + 0.037\kappa) + (0.007 + 1.526\kappa)\mathrm{i}$. Based on the results of [1] (Theorem 3.1, pp. 382), we claim that when $\kappa < 0.73$, the travelling wave (non-localization) is stable, as shown in Fig. 2(a); when $\kappa > 0.73$ the standing wave (mode localization) is stable and thus the mode localization can be observed, as shown in Fig. 2(b).
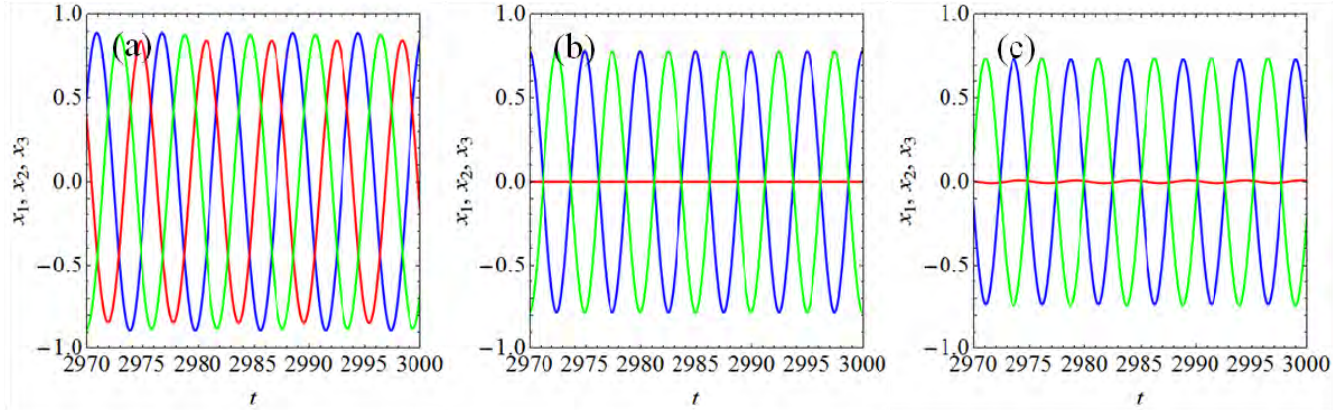
Figure 2: Numerical simulations for (1): (a) $\kappa = 0$; (b)(c) $\kappa = 1$, all integrated from $(x_1, x_2, x_3) = (1.1, -0.08, -0.97)$.

DISCUSSIONS

It should be noticed that the mode localization studied in the present paper persists when the structure symmetry breaks, as shown in Fig.2(c) where the damping coefficients are 0.045, 0.052, 0.05, respectively. This implies that the present result provides another possible explanation for mode localization in self-excited cyclic structure.

References

[1] Golubitsky, M., et al: Singularities and Groups in Bifurcation Theory II. Springer-Verlag, New York 1988.

[2] Vakakis, A. F., et al: Normal Modes and Localization in Nonlinear Systems. Wiley Interscience, New York 1996.

[3] Folley C. N..: Bifurcation and Symmetry in Cyclic Structures *PhD Thesis*, Purdue University School of Mechanical Engineering, Lagos, 1999.

[4] Song Y. L., et al.: Bifurcation, Amplitude Death and Oscillation Patterns in A System of Three Coupled Van der Pol Oscillators with Diffusively Delayed Velocity Coupling. Chaos 21: 023111, 2011.

MS05 - Soft Solid Active Matter

MECHANICALLY GUIDED, DETERMINISTIC THREE-DIMENSIONAL ASSEMBLY

Yonggang Huang[1], Yihui Zhang[2] & John A. Rogers[3]

[1]*Department of Civil and Environmental Engineering, Department of Mechanical Engineering, Department of Materials Science and Engineering, and Skin Disease Research Center, Northwestern University, Evanston, IL, USA*
[2]*Center for Mechanics and Materials, and Applied Mechanics Laboratory, Tsinghua University, Beijing, P.R. China*
[3]*Department of Materials Science and Engineering and Frederick Seitz Materials Research Laboratory, University of Illinois at Urbana-Champaign, Urbana, IL, USA*

<u>*Summary:*</u> *Complex three-dimensional (3D) structures in biology (e.g., cytoskeletal webs, neural circuits, and vasculature networks) form naturally to provide essential functions in even the most basic forms of life. Compelling opportunities exist for analogous 3D architectures in human-made devices, but design options are constrained by existing capabilities in materials growth and assembly. We report routes to previously inaccessible classes of 3D constructs in advanced materials, including device-grade silicon. The schemes involve geometric transformation of 2D micro/nanostructures into extended 3D layouts by compressive buckling. Demonstrations include experimental and theoretical studies of more than 40 representative geometries, from single and multiple helices, toroids, and conical spirals to structures that resemble spherical baskets, cuboid cages, starbursts, flowers, scaffolds, fences, and frameworks, each with single- and/or multiple-level configurations.*

Controlled formation of 3D functional mesostructures is a topic of broad and increasing interest, particularly in the last decade, due to important envisioned uses in nearly every type of micro/nanosystem technology, from biomedical devices to microelectromechanical components, photonics and optoelectronics, metamaterials, electronics, energy storage and others. Although volumetric optical exposures, fluidic self-assembly, residual stress-induced bending and bio-templated/guided growth can be used to realize certain classes of structures in certain types of materials, techniques that rely on rastering of fluid nozzles or focused beams of light provide the greatest versatility in design. Applicability of these latter methods, however, only extends directly to materials that can be formulated as inks or patterned by exposure to light/energetic particles, and indirectly to those that can be deposited onto or into sacrificial 3D structures formed with these materials. Integration of more than one type of any material into a single structure can be challenging. Furthermore, the serial nature of these processes sets practical constraints on operating speeds and overall addressable areas. These and other limitations stand in stark contrast with the exceptional fabrication capabilities that exist for the types of planar micro/nanodevices that are ubiquitous in state-of-the-art semiconductor technologies. Routes to 3D mesostructures that exploit this existing base of competencies can naturally provide options in high performance function that would otherwise be unobtainable. Methods based on residual stress induced bending are naturally compatible with modern planar technologies and they offer yields and throughputs necessary for practical applications. Such schemes provide access to only certain classes of geometries, through either rotations of rigid plates to yield tilted panels, rectangular cuboids, pyramids or other hollow polyhedra, or rolling motions of flexible films to form tubes, scrolls or related shapes with cylindrical symmetry. Here, we present a different set of concepts in which strain relaxation in an elastomeric substrate simultaneously imparts forces at a collection of lithographically controlled locations on the surfaces of planar precursor structures (1). The resulting processes of controlled, compressive buckling induce rapid, large area geometric extension into the third dimension, capable of transforming the most advanced functional materials and planar microsystems into mechanically tunable, 3D forms with broad geometric diversity.

We also introduce ideas for a form of Kirigami that allows precise, mechanically driven assembly of 3D mesostructures of diverse materials from 2D micro/nanomembranes with strategically designed geometries and patterns of cuts (2). Theoretical and experimental studies demonstrate applicability of the methods across length scales from macro to nano, in materials ranging from monocrystalline silicon to plastic, with levels of topographical complexity that significantly exceed those that can be achieved in any other way. A broad set of examples includes 3D silicon mesostructures and hybrid nanomembrane-nanoribbon systems, including heterogeneous combinations with polymers and metals, with critical dimensions that range from 100 nm to 30 mm. A 3D mechanically tunable optical transmission window provides an application example of this Kirigami process, enabled by theoretically guided design.

Finally, Origami is a topic of rapidly growing interest in both the scientific and engineering research communities due to its promising potential in a broad range of applications. Previous assembly approaches of origami structures at the micro/nanoscale are constrained by the applicable classes of materials, topologies and/or capability of control over the transformation. Here, we introduce an approach that exploits controlled mechanical buckling for autonomic origami

---

[a] Corresponding author. Email: y-huang@northwestern.edu

assembly of 3D structures across material classes from soft polymers to brittle inorganic semiconductors, and length scales from nanometers to centimeters (3). This approach relies on a spatial variation of thickness in the initial 2D structures as an effective strategy to produce engineered folding creases during the compressive buckling process. The elastic nature of the assembly scheme enables active, deterministic control over intermediate states in the 2D to 3D transformation in a continuous and reversible manner. Demonstrations include a broad set of 3D structures formed through unidirectional, bidirectional, and even hierarchical folding, with examples ranging from half cylindrical columns and fish scales, to cubic boxes, pyramids, starfish, paper fans, skew tooth structures, and to amusing system-level examples of soccer balls, model houses, cars, and multi-floor textured buildings.

References

[1] Xu S, Yan Z, Jang K I, et al. Assembly of micro/nanomaterials into complex, three-dimensional architectures by compressive buckling[J]. Science, 2015, 347(6218): 154-159.

[2] Zhang Y, Yan Z, Nan K, et al. A mechanically driven form of Kirigami as a route to 3D mesostructures in micro/nanomembranes[J]. Proceedings of the National Academy of Sciences, 2015, 112(38): 11757-11764.

[3] Yan Z, Zhang F, Wang JC, Liu F, Guo XL, Nan KW, Lin Q, Gao MY, Xiao DQ, Shi Y, Qiu YT, Luan HW, Kim JH, Wang YQ, Luo HY, Han MD, Huang Y, Zhang YH, and Rogers JA, "Controlled mechanical buckling for origami-inspired construction of 3D microstructures in advanced materials," Advanced Functional Materials (in press).

THE INTRIGUING DEFORMATION BEHAVIOR OF SOFT BIOMEMBRANES

Edoardo Mazza[1, 2,a], Alexander E. Ehret[1, 2] & Kevin Bircher[1]

[1]*Departement of Mechanical and Process Engineering, ETH Zurich, Switzerland*
[2]*Empa Materials Science and Technology, Dübendorf, Switzerland*

Summary Extensive experimental investigations revealed unexpected features of the mechanical behaviour of soft biomembranes. A comprehensive protocol including mechanical measurements in different stress states and history of loading was applied to human amnion and Glisson's capsule. Highly repeatable mechanical parameters were determined and mechanisms of deformation were identified based on in situ experiments in a multiphoton microscope. This allowed formulating simple model equations able to represent the main features of the observed mechanical response. Liquid phase influx and efflux from the collagenous membrane were shown to play an important role during deformation, and this points at osmotic processes as a mechanism for active control of stress state and membranes deformation.

INTRODUCTION

Examples of highly deformable biological membranes are leaflets of aortic valves, tympanic membrane, connective tissues layers forming skin or arteries, or the capsules covering internal organs. The mechanical behavior of these layers is important for fulfilling their function. We have recently organized a Euromech Colloquium on this topic and part of the contributions were presented in a special issue of the Journal of the Mechanical Behavior of Biomedical Materials [1]. Characterizing and modelling the deformation behaviour of soft biomembranes is relevant for medical applications, such as tissue engineering, surgery planning, car accident simulation, or elastography.

Our interest for soft biomembranes began with the investigation of fetal membranes (FM), i.e. the compliant membranes surrounding the developing fetus inside the uterus. In normal pregnancy FM are progressively deformed due to the increased intrauterine pressure and are further stretched when the fetus moves and pushes against the uterine wall. Thus, the life of the fetus depends on the integrity of a thin biological layer (few hundred µm thick) exposed to severe mechanical loads. Premature rupture of FM represents a devastating complication of pregnancy that accounts for 30 to 40% of preterm deliveries and is associated with a high risk of fetal morbidity and mortality. In order to understand conditions favouring premature rupture of FM, we have developed a comprehensive protocol for characterization of their deformation behaviour. On samples from the same human FM (in particular on the amnion layer) we performed mechanical measurements in different stress states (uniaxial, strip biaxial, equibiaxial), and history of loading (slow and fast monotonic loading, relaxation, creep, low and high number of loading cycles). We also performed the mechanical measurements in situ in a microscope for multiphoton non-linear laser scanning imaging, and thereby could visualize FM tissue through its full thickness, in quasi-physiologic conditions [2]. We thus measured local in-plane stretches based on the relative position of epithelial cell nuclei, local thickness changes during loading, and quantified the orientation and alignment of collagen fibre bundles when stretched. We recently applied the same experimental protocol to other collagenous membranes: bovine Glisson's capsule (GC, the connective tissue layer covering the liver), skin and pericardium. In particular, for GC we applied the whole set of experimental configurations that were used for the characterization of FM. The experimental findings and corresponding model predictions will be presented, illustrating unexpected features and striking similarities in the mechanical behaviour of soft collagenous membranes.

EXPERIMENTS

Details of the loading protocols for investigation of the monotonic, time and history dependence of the mechanical response in different stress states were described in [2-5] and reference therein. Local deformations were quantified using image analysis and correlation algorithms. Biomembrane samples were tested within few hours after extraction from the body and most experiments were performed with test pieces submerged in physiological saline solution. Figure 1 illustrates the set-up used for in situ measurements in the multiphoton microscope, with examples of collagen fiber orientation analysis, full-thickness visualization and cell nuclei staining for local strain measurements [2,4]. Common to all biomembranes is the fact that the uniaxial compliance is much larger than the biaxial one. The analysis of the in-plane behavior in uniaxial tension tests showed that the kinematic response is highly reproducible and that the incremental in-plane and out-of plane Poisson's ratios are very large (of up to 8). Elongation was associated with substantial volume reduction (water efflux), down to about 30% of the initial value for 20% elongation. This behavior was rationalized by mechanisms of rotation, stretching and buckling of the thin fibers which constitute the collagen network of the biomembranes. FM (amnion) and GC showed a large tension reduction during relaxation and a small inelastic strain accumulation in creep. Data indicated that the dissipative behavior is related to two mechanisms: (i) short term volume reduction due to water outflow and (ii) long-term relaxation of collagen fibers without macroscopic deformation and no global reorientation. Recoverable water efflux and influx was evident from the stabilized response in cyclic experiments. The importance of liquid motion was demonstrated also through comparison of experiments using liquids of different osmolarity.

---

a) Corresponding author. Email: emazza@ethz.ch.
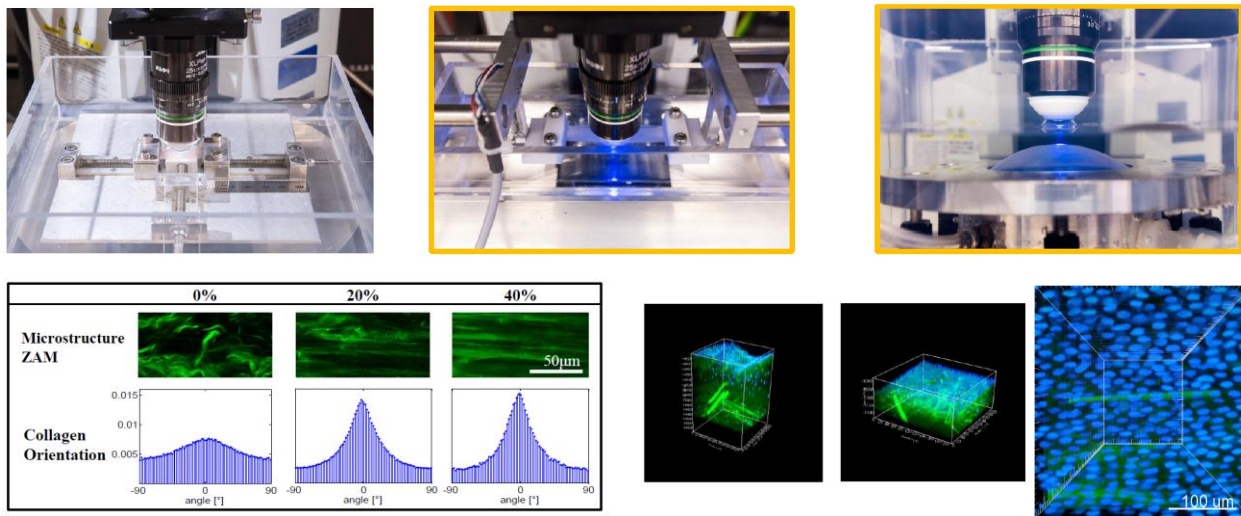
Figure 1 (from [2-6]): top row: in situ tensile devices, two axis, uniaxial and inflation. Bottom row: extraction of collagen fibers' orientation and 3D stack for measurement of thickness changes during loading (showing very large thickness reduction upon in-plane stretching). Right: images of the nuclei of epithelial cells are used to determine in-plane deformation during loading.

MODELING

A large strain viscoelastic continuum model was formulated able to represent the observed deformation mechanisms. The collagen network is phenomenologically represented by *N* representative and mechanically equivalent fiber families that are uniformly distributed in the membrane plane (quasi-isotropic) but slightly inclined out of plane, and embedded in a compressible matrix. The dissipative behavior is represented through the evolution of internal variables, in a way equivalent to a time dependent bulk modulus of the ground matrix (water efflux and influx) and to a viscoelastic deformation of the fibers. The model accurately captures the uniaxial and biaxial monotonic response, as well as the time history of tension in relaxation and strain in creep experiments, and the same formulation can be successfully applied to both, FM and GC [4,5]. While the model include a large number of parameters associated with the different terms in the strain energy function and the evolution equations of the internal variables, it was possible to fix the values of all but 1 of these parameters (for GC and FM respectively) out of one single experimental configuration and predict the response in all other tests by changing one single parameter (addressing sample to sample variability). Next to this continuum model, we developed a discrete fiber network model able to represent the main features of the multiaxial deformation behavior of the biomembranes [6]. Importantly, the discrete model represents non-affine deformations of collagen fibers and this allowed rationalizing differences in the mechanical response of GC and FM based on characteristics of their microstructure.

CONCLUSIONS

The wide range of experimental data provided evidence of unique features of the deformation behavior of these biomembranes. Correspondingly, several biomechanical parameters were highly repeatable among different samples. Based on a simple interpretation of the microstructural observations, it was possible to rationalize the complex mechanical behavior of FM and GC using continuum equations as well as a discrete fibre network model. Application of the experimental protocol to other biomembranes will allow "*comparative biomechanics*", i.e. identifying commonalities and differences in the deformation mechanisms and their relation to the function of each membrane. In particular, our current investigations focus on osmotic mechanisms for active control of stress state and membranes deformation .

References

[1] Mazza E., Ganghoffer J-F., Ehret A.E: Mechanics of biological membranes. J. Mech. Beh. Biomed. Mat., 2016

[2] Mauri A., Perrini M., Mateos J. M., Maake C., Ochsenbein-Koelble N., Zimmermann R., Ehrbar M., Mazza E.: Second Harmonic Generation Microscopy of Fetal Membranes under Deformation: Normal and Altered Morphology, Placenta, 34, 1020-1026, 2013

[3] Mauri, A., Perrini, M.; Ehret, A.E.; de Focatiis, D.; Mazza, E.: Time-dependent mechanical behavior of human amnion. Macroscopic and microscopic characterization. Acta biomaterialia, 11, 314-323, 2015.

[4] Mauri, A., Ehret, A.E.; de Focatiis, D.; Mazza, E.: A model for the compressible, viscoelastic behavior of human amnion addressing tissue variability through a single parameter.   Biomechanics and Modeling in Mechanobiology, in press.

[5] Bircher K., Ehret, A.E.; Mazza, E.: Mechanical characteristics of bovine Glisson's capsule as a model tissue for soft collagenous membranes, submitted.

[6] Mauri, A., Hopf, R.; Ehret, A.E.; Picu, C.; Mazza, E.: A discrete network model to represent the deformation behavior of human amnion. J. Mech. Beh. Biomed. Mat., 2016

SOFT NEURONS ACTIVELY MAINTAIN STRONG TENSION FOR SYNAPTIC FUNCTIONS

M. Taher A. Saif [1)]

[1]*Mechanical Science and Engineering Department, University of Illinois Urbana-Champaign, Illinois, USA*

Summary In-vitro studies over the last three decades revealed that neurons generate tension on culture dishes. But the physiological significance of this tension remained unclear. Here we show, using embryonic fruit flies (*Drosophila*), that (1) *in vivo* neurons actively maintain a rest tension, (2) neurons employ actomyosin machinery to maintain and regulate the tension, (3) this tension is critical for accumulation of neurotransmitor vesicles at the synaptic terminals (junction with muscle or another neuron), i.e., without tension the accumulation disappears, but reappears with the supply of tension, (4) this tension regulates transport of vesicles along the axon of the neurons. Neurotransmission is the single most function of neurons, and it mediates memory and learning in animals. Since neuronal force regulates transport and accumulation of neurotransmitter vesicles, it follows that the neuronal forces are fundamentally linked with memory and learning, and they offer a new and untapped paradigm in understanding neurological diseases. **(150 words)**

BACKGROUND

Most neurons have a long axon that innervates muscles or other neurons to form neuro-muscular or neuron-neuron junctions. Neurotransmitters are packed in small vesicles and are clustered at the presynaptic terminal of the junction. Upon arrival of an action potential or a voltage spike at the presynaptic terminal travelling through the axon, synaptic vesicles exocytose releasing the neurotransmitters, which activate the post synaptic terminal. Thus the signal is transmitted from one neuron to the next, or the muscle is stimulated. The more a synapse is used, the higher is the transmission efficiency, i.e., higher is the post synaptic current due to the same action potential. This usage dependence of efficiency, known as plasticity, forms the basis of memory and learning. Vesicle clustering had long been believed to result from biochemical signaling processes that require the connectivity of the presynaptic terminal with the cell body, the central nervous system, and the postsynaptic cell. Mechanics had no role to play. During late last century, it was realized that neurons cultured on perti dishes adhere to the substrate and apply contractile traction [1]. It was hypothesized that in vivo neurons generate tension as well, which results in folding in the epical cortex of the brains. However, the evidence of tension in *in vivo* neurons was missing, and the role of tension in neuronal function remained elusive.

FRUITFLY (DOSOPHILA) EMBRYO AND NEUROMUSCULAR JUNCTIONS AS MODEL TEST BEDS

Figure 1. Embryonic fruit fly. Neurons glow green when blue light is shined on the embryo. The axons of motor neurons emanate laterally from the central nervous system (CNS). They are about 100 µm long and 500 nm in diameter. Each forms a neuromuscular junction at the end (muscle not shown).

Embryonic fruit flies have extensively been used in Neuroscience for decades to develop fundamental insights on neuronal functions. We chose to study embryonic motor neurons of transgenic flies in which all neurons emit green light when shined with blue light (Fig. 1, [2]). This allows us to visualize the neurons. The cell body of the motor neurons reside at the central nervous system (CNS), but the axons, about 100 µm long and 500 nm in diameter, emanate from the CNS and innervate the muscles at the end forming neuro-muscular junctions. We asked the following questions: (1) are the axons are in tension, and if so (2) what is the origin of tension, (3) does this tension influence neurotransmitter vesicle accumulation at the junction, and their transport through the axon [3]. The significance of these questions is that if indeed tension is found to be related to vesicle accumulation at the junction, then neuro-mechanics becomes a critical component in understanding neuroscience.

EXPERIMENTAL RESULTS

In vivo axons are under tension: We measure tension in the axons of the motor neurons by dissecting live embryos and pulling single axons holding at the middle using a nano scale force sensor (Fig. 2). From the force-deformation relation of the axons we quantify that the axons are at a rest tension of about 2 nN [2]. If the stretch of the axons is held fixed, they relax with time reaching a steady tension with a value higher than the unperturbed tension. If the stretched axons are released, the slackned axons shorten to regain the rest tension. If the axons are slackened significantly by bringing the neuro-muscular junction close to the CNS, the axons shorten, by as high as 40%, to regain the tension (Fig. 3). Thus, axons actively maintain a steady rest tension. (2) Actomyosin machinery maintains the tension: We apply a series of drugs to the embryo independently. These drugs selectively inactivate specific cytoskeletal components. We find, slackned axons fail to

Strain (%) vs Force (nN) plot, Rest tension = 2 nN
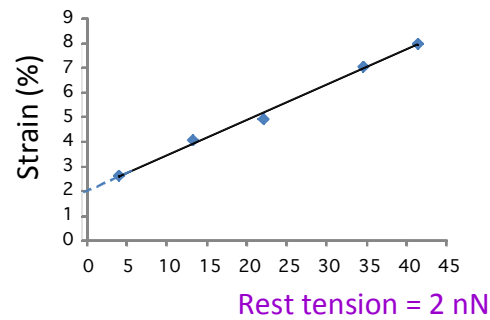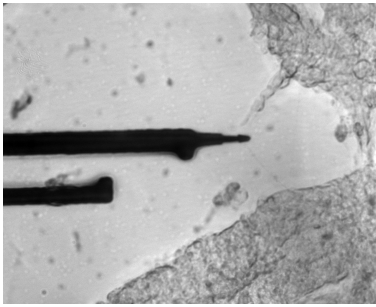
shorten if myosin II is inactivated, or cortical actin is disrupted, but the axons shorten faster if microtubules are depolymerized. (3) Axonal tension regulates neurotransmitter vesicle accumulation at NMJ and transport [3] through axons: We dissected an axon using a laser beam at mid length. This relieves the axon from its tension. We find, vesicle accumulation at the NMJ disappears. However, when the cut end of the axon is pulled by a micropipette, vesicle accumulation reappears (Fig 4), implying that tension alone is sufficient for vesicle clustering. A 10% mechanical stretch on the axon results in 200% increase in vesicle accumulation at the NMJ. We present a simple mechanistic model to explain the above observations. In this model, actin
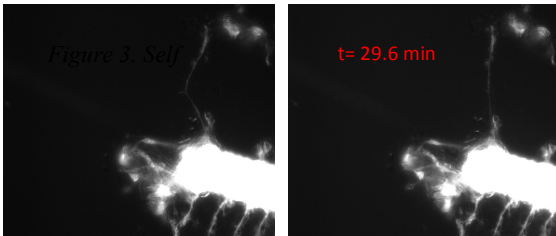
Figure 2. Measurement of axonal tension using a nano mechanical force sensor.
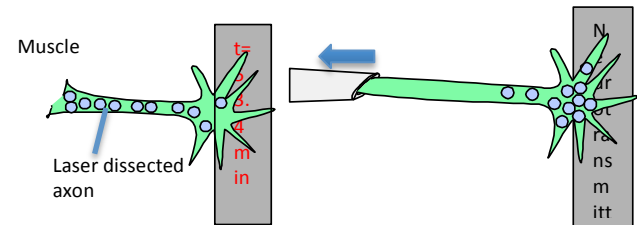
Figure 5. Schematic of the model of axon and the neuro-muscular junction.

network at the NMJ serves as a scaffold for neurotransmitter vesicles allowing them to accumulate. This actin network is mechanically linked with the cortical actin and the rest of the cytoskeleton. Its stability of maintained by the tension it is subjected to due to the acto-myosin activity of the cortical actin. If tension is disrupted, the actin scaffold disappears, and hence the vesicle accumulation (Fig 5).
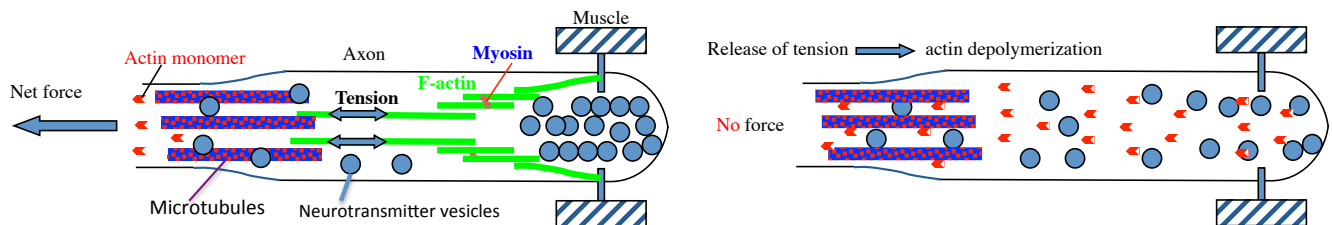
References

[1] Bray, D. Mechanical Tension Produced By Nerve Cells In Tissue Culture. *J. Cell Sci*. 37, 391-410 (1979).
[2] Siechen, S., S. Yang, A. Chiba, and T. Saif, "Mechanical Tension Contributes to Clustering of Neurotransmitter Vesicles at Presynaptic Terminals," Proceedings of the National Academy of Science, 106:31, 12611-12616, August 4, 2009.
[3] Ahmed, W. and T. A. Saif. Active transport of vesicles in neurons is modulated by mechanical tension. Scientific Reports 4, Article number: 4481 doi:10.1038/srep04481, 27 March 2014.

MECHANOCHEMICALLY RESPONSIVE ELASTOMERS: FUNDAMENTAL AND APPLICATIONS

Xuanhe Zhao[1,2 a)]

[1]Department of Mechanical Engineering, MIT, Cambridge, MA, US
[2]Department of Civil and Environmental Engineering, MIT, Cambridge, MA, US

Summary Mechanochemically responsive (MCR) elastomers have been synthesized by incorporating mechanophores – molecules whose chemical reactions are triggered by mechanical force – into conventional polymer networks. Deformation of the MCR elastomers applies force on the mechanophores and triggers their reactions, which manifest as phenomena such as changing colors, varying fluorescence and releasing molecules. In this talk, we first present a microphysical model of MCR elastomers, which quantitatively captures the interplay between the macroscopic viscoelastic deformation of the MCR elastomers and the reversible activation of mechanophores on polymer chains. Our model consistently predicts both the time-dependent stress-strain behaviours and the color or fluorescence variation of the MCR elastomers under large deformations. We then discuss model-guided design of structures and devices with extraordinary functions and applications enabled by MCR elastomers such as synthetic squid skin capable of dynamically varying colours and surface textures on demand.

Introduction

A novel strategy for fabricating mechanochemically responsive (MCR) polymers has been developed by covalently incorporating molecules capable of force-triggered chemical reactions, or so-called mechanophores, into polymer networks[2-5]. Deformation of MCR polymers stretches polymer chains which apply forces on the mechanophores and triggers their reactions, leading to phenomena such as changing colors, varying fluorescence and releasing molecules of the MCR polymers. During the design of MCR devices, it is highly desirable that the MCR polymers can be reversibly and repeatedly activated and deactivated. However, most existing MCR polymers are in glassy or semicrystalline states, whose activation requires irreversible plastic deformation or fracture of the polymers. As a result, these MCR polymers cannot fully recover their initial shapes after the first activation, and therefore cannot be activated reversibly or repeatedly [6-13]. While mechanophores have been incorporated into thermoplastic elastomers[7, 11, 12, 14-16], little success has yet been achieved to activate the MCR polymer repeatedly to fully recover its initial shape at the room temperature.

Recently, we developed new MCR elastomers by covalently coupling spiropyrans [7] – mechanophores that can change color and emit florescence under sufficiently high forces – into the backbone chains of a highly stretchable elastomer network, polydimethylsiloxane (PDMS) Sylgard 184 [17, 18]. The MCR elastomers can recover their initial shapes under multiple cycles of large deformation, allowing for reversible and repeated variations of the color and fluorescence of the elastomers on demand. The MCR elastomers can also be assembled into devices such as a display that is remotely controlled by external physical stimuli (e.g., electric fields) to generate on-demand fluorescent and color patterns (**Fig. 1A**). These MCR elastomer systems open promising venues for creating flexible MCR devices with diverse applications in flexible displays, optoelectronics, biomedical luminescent devices and dynamics camouflage skins [17]. Despite the potential, the microscopic mechanical details underlying the performance of the MCR elastomers have yet to be investigated, and those mechanistic insights might enable the optimization of MCR elastomer response. For example, the relationship between the macroscopic viscoelastic deformation of the MCR elastomers and the extent of activation of mechanophores embedded along those polymer chains is not understood. This understanding, if achieved, can help guide the development of MCR elastomers, and improve the design of various MCR-elastomer devices.
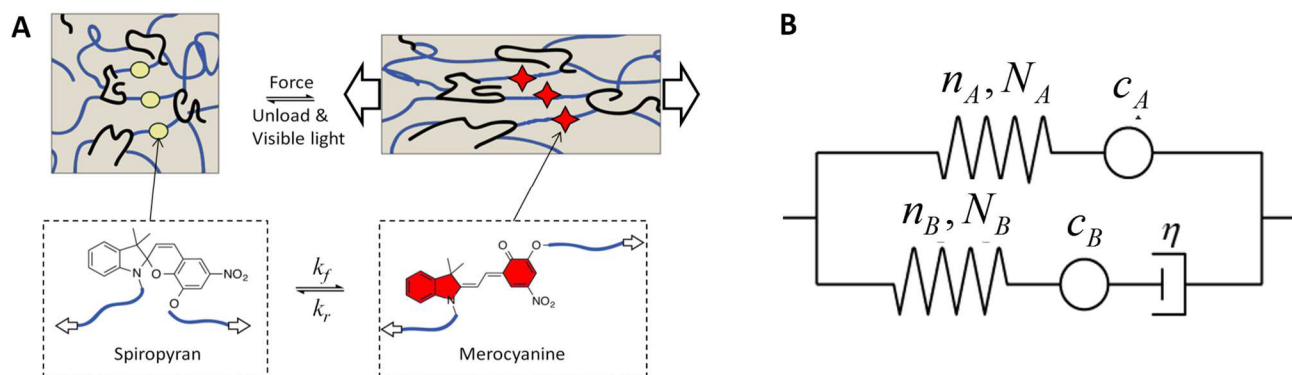
Figure 1. Schematics of the mechanochemically responsive elastomer with mechanophores spiropyran/merocyanine covalently coupled on the network (**A**), and the double-network model to account for the coupling of viscoelastic deformation and mechanochemical reactions in the elastomer (**B**).

a) Corresponding author. Email: zhaox@mit.edu

2．Model formulation

We aim to develop a simple thermodynamic-based model for mechanochemically responsive viscoelastic elastomers to account for the interactions between viscoelasticity and mechanochemical reactions in the elastomers. Adopting the generalized Maxwell model, we assume the viscoelastic behaviour of the elastomer can be attributed to two polymer networks acting in parallel as illustrated in **Fig 1B**. The first network (i.e., network A) characterizes the time-independent mechanical behavior of the elastomer using a non-linear spring, and the second network (i.e., network B) accounts for the time-dependent mechanical behavior of the elastomer using a non-linear spring and a dashpot in series. To account the mechanochemical reactions in the elastomers, we further couple modules of mechanophores in series with the non-linear springs in both networks (**Fig. 1B**).

Assuming Langevin chains in both networks that undergoes affine deformation, the chain forces can be calculated

$$f_A = \frac{k_B T}{l} L^{-1}\left(\frac{\Lambda}{\sqrt{n_A}}\right), \quad f_B = \frac{k_B T}{l} L^{-1}\left(\frac{\Lambda/\Lambda^v}{\sqrt{n_B}}\right) \tag{1}$$

where k_B is the Boltzman constant, T is the absolute temperature, l is the length of a Kuhn monomer; Λ is the stretch in polymer chains of both networks; Λ^v the viscous component of the stretch in network B; and Λ/Λ^v the elastic component of the stretch in network B. The chemical kinetics between spiropyrans and merocyanines on both networks of the MCR elastomer can be expressed as (Hänggi et al., 1990)

$$\frac{dc_A^M}{dt} = k_A^f c_A^S - k_A^r c_A^M, \quad \frac{dc_B^M}{dt} = k_B^f c_B^S - k_B^r c_B^M \tag{2}$$

where c^M and c^S are the concentrations of merocyanin and spiropiran in either network, and k^f and k^r are the forward and reverse reaction rates in either network, as indicated by the subscripts. The reaction rates can be further expressed as

$$k_A^f = k^{f0}\exp\left(\frac{f_A \Delta x}{k_B T}\right), \quad k_A^r = k^{r0}\exp\left(-\frac{f_A \Delta x}{k_B T}\right), \quad k_B^f = k^{f0}\exp\left(\frac{f_B \Delta x}{k_B T}\right), \quad k_B^r = k^{r0}\exp\left(-\frac{f_B \Delta x}{k_B T}\right) \tag{3}$$

where k^{f0} and k^{r0} are forward and reverse reaction rates of the mechanophore under no force, and Δx is a length scale the applied chain forces that affect the reaction rates.

Further adopting the standard nonlinear viscoelastic model, the chain forces in the elastomer can be quantitatively related to the viscoelastic deformation of the elastomer, which therefore affects the chemical reaction of the elastomer through Eqs. (1)-(3).

3．Summary and applications

In summary, we present a theoretical model for mechanochemically responsive elastomers to quantitatively reveal how the macroscopic viscoelastic deformation of the elastomer translates to the molecular forces in polymer networks, and how the chain forces subsequently affect chemical reactions of mechanophores coupled to the networks. We further program the constitutive model into finite-element models, through which we demonstrate the MCR elastomers' potential applications for strain imaging and color/fluorescence displays. These models can further facilitate the design of MCR polymers in the macro/micro structure level to create MCR devices for diverse applications, such as sensors, memories, flexible displays, optoelectronics, biomedical luminescent devices and dynamics camouflage skins.

References

[1]   Y. Sagara, T. Kato, Nature Chemistry 2009, 1, 605.
[2]   M. K. Beyer, H. Clausen-Schaumann, Chemical reviews 2005, 105, 2921.
[3]   M. M. Caruso, D. A. Davis, Q. Shen, S. A. Odom, N. R. Sottos, S. R. White, J. S. Moore, Chemical reviews 2009, 109, 5755.
[4]   A. L. Black, J. M. Lenhardt, S. L. Craig, Journal of Materials Chemistry 2011, 21, 1655.
[5]   Z. S. Kean, S. L. Craig, Polymer 2012, 53, 1035.
[6]   C. K. Lee, B. A. Beiermann, M. N. Silberstein, J. Wang, J. S. Moore, N. R. Sottos, P. V. Braun, Macromolecules 2013, 46, 3746.
[7]   D. A. Davis et al , Nature 2009, 459, 68.
[8]   A. L. Black, J. A. Orlicki, S. L. Craig, Journal of Materials Chemistry 2011, 21, 8460.
[9]   J. M. Lenhardt et al, Journal of Materials Chemistry 2011, 21, 8454.
[10]   G. O'Bryan, B. M. Wong, J. R. McElhanon, ACS applied materials & interfaces 2010, 2, 1594.
[11]   C. K. Lee, D. A. Davis, S. R. White, J. S. Moore, N. R. Sottos, P. V. Braun, Journal of the American Chemical Society 2010, 132, 16107.
[12]   Y. Chen, H. Zhang, X. Fang, Y. Lin, Y. Xu, W. Weng, ACS Macro Letters 2014, 3, 141.
[13]   E. Ducrot, Y. Chen, M. Bulters, R. P. Sijbesma, C. Creton, Science 2014, 344, 186.
[14]   M. B. Larsen, A. J. Boydston, Journal of the American Chemical Society 2014, 136, 1276.
[15]   B. A. Beiermann, S. L. B. Kramer, P. A. May, J. S. Moore, S. R. White, N. R. Sottos, Advanced Functional Materials 2014, 24, 1529.
[16]   H. Zhang, Y. Chen, Y. Lin, X. Fang, Y. Xu, Y. Ruan, W. Weng, Macromolecules 2014, 47, 6783.
[17]   Q. Wang, G. R. Gossweiler, S. L. Craig, X. Zhao, Nature Communications 2014, 5, 4899.
[18]   G. R. Gossweiler, G. B. Hewage, G. Soriano, Q. Wang, G. W. Welshofer, X. Zhao, S. L. Craig, ACS Macro Letters 2014, 3, 216.

MECHANICAL SYNCHRONIZATION OF ACTIVE BEATING WITHIN AND BETWEEN CARDIOMYOCYTES

Ohad Cohen, Kinjal Dasbiswas and Samuel Safran [a]
Department of Materials and Interfaces, Weizmann Institute of Science, Rehovot, Israel

<u>Summary</u> We present theoretical models and predictions of how mechanics due to elastic interactions in actively beating heart cells can lead to synchronization of beating both within single cells and between nearby cells. Our research is motivated by recent experiments that show a correlation between the registry of adjacent muscle fibers and the beating strain of a single, embryonic cardiomyocyte and others that show how a mechanical probe can "pace" the phase and frequency of a nearby heart cell. The theory is generic and analytical in nature and focuses on the role of elastically mediated interactions of oscillating, active force dipoles in these cells. For the single cell, the theory successfully maps the registry data to the strain data. Similar ideas are used to predict the conditions under which an oscillating mechanical probe will or will not "pace" the beating of a nearby heart cell.

Experiments on single, embryonic cardiomyocytes [1] show that both striation, an indication of the structural registry in muscle fibers, as well as the contractile strains produced by beating cardiac muscle cells, can be optimized by substrate stiffness. We show theoretically how the substrate rigidity dependence of the registry data can be mapped onto that of the strain measurements. The elasticity-mediated structural registry is determined [2] including both the elastic interactions of neighboring, actively contractile acto-myosin units as well as the noise inherent in biological systems. By assuming that structurally registered myofibrils also tend to beat in phase, we explain the observed dependence of both structural striation and beating strain measurements of embryonic heart muscle cells on substrate stiffness in a unified manner. The agreement of our ideas with experiment suggests that the correlated beating of heart cells may be limited by the structural registry of the myofibrils which in turn is regulated by their elastic environment.
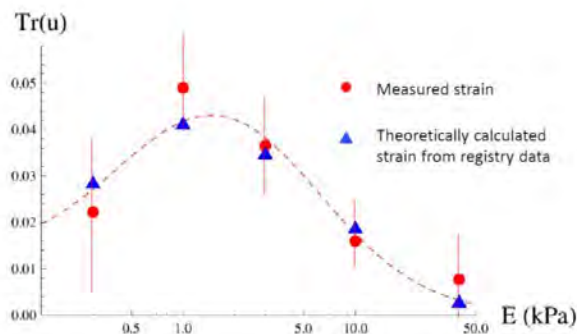
The structural registry data is mapped to strain values using our theoretically derived expressions. The measured strain is shown as solid, red dots together with the experimental error bars. The dashed red line is an interpolated guide to the eye that joins the measured strain data points within their error bars. The blue triangles represent the strain values obtained by the theoretical mapping from the corresponding registry measurements (for the same values of substrate elasticity) and show a close match with the experimentally measured strain values within the error bars. [From Ref. 2.]

Very recent experiments [3] on the synchronization of beating of two nearby neonatal cardiomyocytes has shown that a mechanical probe can "pace" a beating cell to within about twice or a quarter of its natural beating frequency. This is expected to be indicative of how nearby cardiomyocytes embedded in the extracellular matrix or on an elastic substrate can regulate their mutual beating. We predict theoretically [4] the synchronization of the beating phase and frequency of two nearby cardiomyocyte cells or a cell and a mechanical probe. Each cell is represented as an oscillating force dipole in an infinite viscoelastic medium that allows us to predict the propagation of the elastic signal within the medium. We then show that based on elastic interactions alone, two nearby cells can synchronize their phase and frequency in a manner that depends on their mutual orientation. The theory predicts both in-phase and anti-phase synchronization depending on the relative cell orientations and also shows how mechanics can predict the conditions for frequency synchronization of nearby cells. These results may be relevant for the design of cardiomyocyte-based micro devices and other biomedical applications.

[a] Corresponding author. Email: sam.safran@weizmann.ac.il
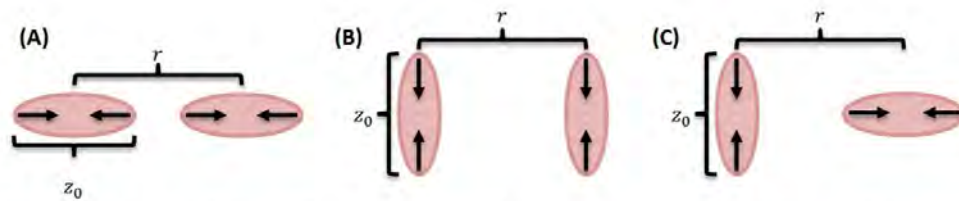
(A) Dipoles are aligned along their axis of contraction. (B) Dipoles are aligned perpendicular to their axis of contraction. (C) Dipoles are aligned to beat in perpendicular directions. Theory predicts that the dipoles in (A) and (B) beat in-phase which those in (C) beat out of phase. [O. Cohen and S. Safran, unpublished].

References

[1]   S. Majkut *et al.*, Current Biology, **23**, 2323 (2013).
[2]   K. Dasbiswas, S. Majkut, D. Discher and S. A. Safran, Nature Comm., **6**, 7085 (2015).
[3]   I. Nitsan, S. Drori, Y. Lewis, S. Cohen and S. Tzlil, Nature Physics, in press.
[4]   O. Cohen and S. A. Safran, unpublished.

ON THE THE FREE ENERGY OF CELLS SPREAD ON MICROPATTERNED SUBSTRATES

Patrick McGarry[1], Eoin McEvoy[1], Tommaso Ristori[2], Sandra Loerakker[2], Vikram S. Deshpande[3]
[1]National University of Ireland Galway, Galway, Ireland
[2]Eindhoven University of Technology, Eindhoven, The Netherlands
[3]University of Cambridge, Cambridge, United Kingdom

Summary A new approach to the analysis of the spreading of cells on micro-patterned substrates is presented. A thermodynamically consistent active cell model with non-local conservation of the total number of cell cytoskeletal proteins is used to simulate a range of spread states. The minimum free energy of the system is identified and corresponding stress fibre distributions are found to match experimental observations.

INTRODUCTION

Several experimental studies demonstrate that control of cell spreading using substrate micro-patterning has a significant impact on cell behaviour. A study by McBeath et al. [1] reveals that stem cell differentiation can be controlled by limiting cell spread area. It has also been shown that the contractility of smooth muscle cells increases with increasing cell area (Tan et al. [2]). Lamers et al. [3] show the spread geometry and stress-fibre (SF) distribution of osteoblasts on grooved surfaces is highly dependent on groove spacing. Wide grooves result in polarized cells with SFs aligned along the grooves. Narrow groove spacing leads to randomly oriented cells and SFs. Finally, a study by Théry et al. [4] has shown that cells spread on V-shaped fibronectin patches exhibit SFs align along the free edge of the cell.

The bio-mechanisms underlying such experimental observations are not fully understood. In the current study we propose a new approach to the analysis of the spreading of cells on micro-patterned substrates. We demonstrate that a non-local thermodynamically consistent active cell model explains several of the key phenomena observed experimentally.

MODEL DEVELOPMENT

The thermodynamically consistent kinetic equation for SF formation/dissociation proposed by Vigliotti *et al.* (2015) [5] reduces to

$$\hat{\eta} = (\hat{N}_u/\pi\hat{n})exp[\hat{n}(\mu_u - \mu_b)/kT] \tag{1}$$

under steady state conditions in a representative volume element (RVE) within a cell. $\hat{\eta}$ is the SF concentration per unit surface area of the RVE, $\hat{n}$ is the number of actin-myosin contractile units along the length of the RVE, μ_b is the free energy of the bound contractile units in a stress fibre, μ_u is the free energy of unbound SF proteins, while k and T are the Boltzmann constant and absolute temperature. $\hat{N}_u$ is the number of unbound SF proteins. Here we implement non-local conservation of the total number of SF proteins within the cell, $\hat{N}_T$, under the assumption that the diffusion of unbound proteins through the cytoplasm is infinitely fast relative to the timescale of SF remodeling. The number of unbound proteins in the whole cell is therefore given as

$$\hat{N}_u = \hat{N}_T - \int_{V_c} \int_{-\pi/2}^{+\pi/2} \hat{\eta}\,\hat{n}d\phi dV \tag{2}$$

where the inner integral computes the number of bound proteins in a RVE, and the outer integral provides a summation over all the RVEs in the entire cell volume V_c. At steady state, $\hat{n}$ in a SF at orientation ϕ is given as

$$\hat{n} = (1 + \varepsilon_n(\phi))/(1 + \tilde{\varepsilon}_{ss}) \tag{3}$$

where ε_n is the SF nominal axial strain. When a SF is extended, contractile units are added, with the effect that the internal strain in the SF is reduced until a steady state value $\tilde{\varepsilon}_{ss}$ is achieved. Conversely, when a SF shortens, functional units are removed. In both cases, the internal fibre steady state strain is different from the axial material strain in the direction of the fibre, $\varepsilon_n(\phi)$. The formulation is completed by the addition of a non-linear hyperelastic formulation (Ogden, N=8) in parallel with the SF model in order to represent the passive components of the cell.

SIMULATIONS AND RESULTS

The model described above is used to simulate two separate cell spreading experiments:

Experiment 1: As shown in Fig. 1, cells spreading across a series of parallel grooves and fibronectin adhesion patches, both of width L_r, is simulated. In order to spread on N grooves the cell must deform from its reference configuration in the x-direction by a stretch λ_x, after which it may spread along the groves by deforming in the y-direction by a stretch λ_y. A parametric study is conducted for a range of spread states (λ_x and λ_y). For each spread state the free energy of the system $\bar{G}$ is computed from

$$\bar{G} = W_{elas} + (\rho kT)ln(\hat{N}_u) \tag{4}$$

where W_{elas} is the elastic free energy due to deformation of the passive components of the cytoplasm during cell spreading. The second term is the cytoskeleton free energy, where ρ is the density of cytoskeletal proteins. Eqn.(4) can be interpreted as a competition between the elastic free energy, which increases with cell spreading, and the cytoskeleton free energy, which decreases with cell spreading (in accordance with eqns.(1-3)).

As shown in Fig. 2(a), results reveal that when the groove spacing is wide (L_c/L_r=3) $\bar{G}$ is minimized when the cell extends along the grooves in the y-direction ($\lambda_y = 1.5$) while spanning only one grove (N=2 and $\lambda_x = 0$). Such spreading in the y-direction, coupled with the global conservation of cytoskeletal proteins, dictates that SFs align primarily in the direction of the grooves. Spreading in the x-direction is discouraged by the high elastic penalty, as shown for the case of N=4. Fig.2(b) considers the case of a small groove spacing (L_c/L_r=12). Here $\bar{G}$ is minimized when $\lambda_x \approx \lambda_y \approx 1.55$ and an isotropic distribution of stress fibres is obtained. Notably, global conservation of cytoskeletal proteins dictates that the SF concentration in any given direction, $\eta(\phi)$, in Fig.2(b) is lower than the concentration of SFs along the grooves in Fig.2(a).
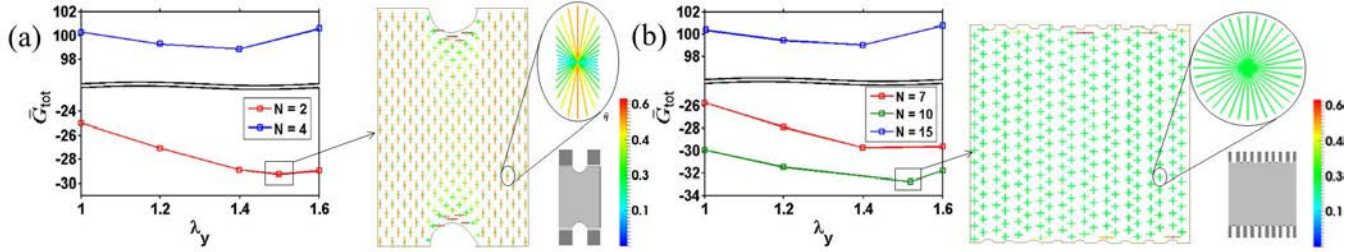
Figure 2: Free energy of the system ($\bar{G}$) and vector plot of SF concentration ($\hat{\eta}$) for: (a) Cell is spread on wide (L_c/L_r=3) grooves; (b) Cell spread on narrow (L_c/L_r=12) grooves.

Experiment 2: In a second series of simulations, a circular unadhered cell spreads on a V-shaped adhesion patch of length L_a, as shown in Fig. 3. For a cell of radius r_c, the spreading process is parameterized in terms of the proportion of the cell perimeter ωr_c that adheres to the patch. The stretch along the patch is therefore given as $\lambda_p = L_a/\omega r_c$. The influence of the ratio of initial cell size to groove length is also considered.

For the longest adhesion patch ($r_c/L_a = 0.38$) $\bar{G}$ is high due to high levels of elastic deformation required for spreading. For the shortest adhesion patch ($r_c/L_a = 0.44$), $\bar{G}$ is high due to the low levels of SF formation associated with limited cell spreading. The minimum free energy spread state, characterized by λ_p, is dependent on the length of the adhesion patch. The lowest value of $\bar{G}$ is computed for $r_c/L_a = 0.40$, with $\lambda_p = 1.24$. In this configuration highest strains occur in the region of the free unadhered edge of the cell. Global conservation of cytoskeletal proteins therefore dictates that the SFs form predominantly parallel to the free edge.

DISCUSSION

The modelling framework presented here captures the key trends reported in the studies by Lamers *et al.* [3] and Théry *et al.*[4], suggesting that cells tend to assume a minimum free energy ($\bar{G}$) spread state. This minimum free energy state is determined by competition between the elastic free energy due to deformation of the passive cytoplasm and the cytoskeleton free energy, subject to a non-local conservation of cytoskeletal proteins throughout the cell. Simulations suggest that the evolving strain distribution during spreading is a critical determinant of the SF distribution. This model represents a significant advance on recent phenomenological approaches to the analysis of cell spreading and SF remodeling [6, 7].

Figure 3: Free energy of the system ($\bar{G}$) and vector plot of SF concentration ($\hat{\eta}$) for cell spreading over V-shaped adhesion patch.

REFERENCES [1] McBeath, R *et al. Developmental Cell*, 6:483-95, 2004; [2] Tan, J *et al. PNAS*, 100(4):1484-89, 2003; [3] Lamers, E *et al.*, *Biomaterials*, 31(12):3307-16, 2010; [4] Théry, M et al., *Cell Motil Cytoskeleton,* 63(6):341-55, 2006; [5] Vigliotti, A *et al.*, *Biomech Model Mechanobiol*, [Epub ahead print], 2015; [6] Ronan, W *et al., J Mech Behav Biomed Mater,* 14:143-57, 2012; [7]. Reynolds, N *et al.*, *Biomaterials,* 35(13):4015-25, 2014.

CATCH BONDS AND MECHANO-SENSITIVITY OF ACTO-MYOSIN FILAMENT NETWORKS

Franck Vernerey [*1] and Umut Akalp[1]
[1]*Mechanical Engineering, University of Colorado, Boulder, USA*

Summary A number of biological filament network are able to generate contratile forces and deformation over large regions with the help of motor proteins, allowing filament to slide along one-another. A particularity of such networks, such as the acto-myosin network in adherent cells, is that the assembly display a mechano-sensitive behavior, that is, contraction can be tuned by the effect of external forces and stiffness. This paper presents a mechanistic model, based on the concept of catch bond, that explains how such responses can be observed at fairly large scales. Particular examples pertaining to the contractile mechanics of adherent cells are presented.

INTRODUCTION

The contraction of adherent cells is a phenomenon that plays a large role in many biological events such as morphogenesis, wound contraction, stem cell differentiation and cell migration. These phenomena particularly rely on contractile filaments, or stress fibers, that anchor to the cell substrate and are capable of sustaining appreciable levels of contraction thanks to their underlying acto-myosin machinery powered by ATP. In the past decade, numbers of studies have shown that the architecture and contraction of the stress fiber cytoskeleton are highly responsive to the cells mechanical environment; the origin of which remains poorly understood. This paper discusses how this mechano-sensitive response can be explained by invoking an ubiquitous element used by biological systems known as the catch bond. We here investigate its role by deriving a model based on an energetic approach and complemented by numerical simulations. The latter show that the catch-bond hypothesis can explain the dependency of cell contraction on substrate stiffness, adhesion or the application of external forces on the cell boundary. The agreements between model predictions and experimental observations not only confirm that catch bonds may play a significant role in the mechano-sensitivity of adherent cells but also pinpoint the importance of the hierarchical structure of acto-myosin filaments across the scales.
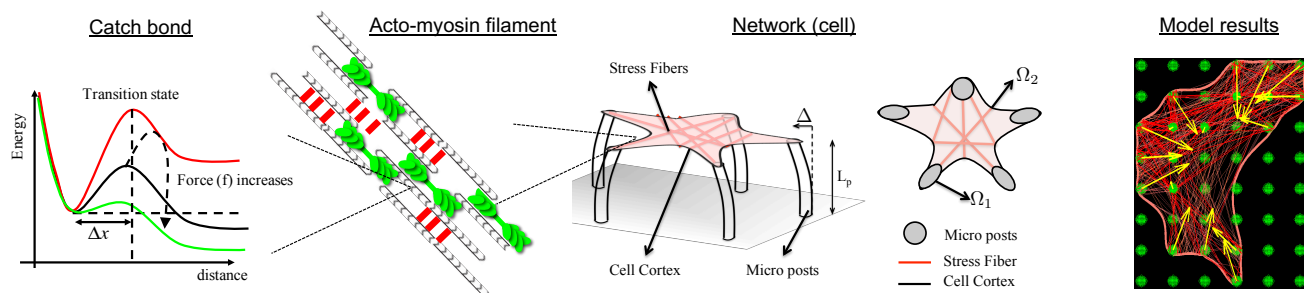
Figure 1: *Summary of the approach depicting, from left to right, the energy landscape of a catch bond, the simplified structure of an acto-myosin filament and the cytoskeleton of a cell lying on a bed of micro-pillars and finally, simulation results of the acto-myosin network and contractility of an adherent cell.*

MODEL

In this paper, we investigate the mechanical response of an acto-myosin segment segment by considering its internal structure made of a mixture of actin and myosin filaments that can slide on one-another thanks to the energy provided by ATP hydrolysis (Fig. 1). Because actin filaments are polarized, these sliding motions generate an overall shortening of the unit, and depending on the mechanical environment, the application of a more or less pronounced contractile force. The mechanics of this assembly was captured by considering an energetic approach for an acto-myosin segment that comprises: (a) the entropic contribution of the large number of acto-myosin bonds within the unit, (b) the stored elastic energy arising from the deformation of acto-myosin bonds, (c) the potential energy E_b stored in the acto-myosin bonds, (d) the work done by external forces F applied on the extremities of the filament, (e) the active power generated by ATP hydrolysis and finally (f) the energy dissipation associated with the sliding motion of myosin on actin. Using energetic principles, this approach allowed

---

us to obtain three Euler-Lagrange equations that govern the ratio η of activated acto-myosin bonds, the sliding velocity v_s of myosin on actin and the elastic deformation d_e of acto-myosin bonds:

$$\eta N k \Delta d_e = F \; ; \qquad E_b + k_B T \ln\left(\eta/(1-\eta)\right) = 0 \; ; \qquad v_s = v_s^0 \left(1 - f/\zeta\right) \tag{1}$$

where v_s^0 is the sliding velocity in the stress-free state, ζ is the active force generated by myosin on actin and N is the total number of available acto-myosin bond in the segment. The first equation is interpreted as the mechanical equilibrium of the control segment, while the second denotes its chemical equilibrium (equality of the chemical potentials) of bonds in attached and detached states. The last equation describes how the cross-bridge velocity is affected by the balance between the active force ζ and passive force $f = k \Delta d_e$. In the range $0 < f < \zeta$, this relation may be thought of as a simplified (bi-linear) form of the velocity-tension relationship that describes how the sliding velocity decreases if an opposing force f is applied to the acto-myosin unit. To complete the model, we then expressed the fact that the actin-myosin complex displays a catch-bond behavior by considering the energy landscape of a single bond shown in Fig. 1 (in which ΔE is the energy barrier separating the bound and unbound states). Typically, the larger the energy barrier, the longer a bond can live under thermal fluctuations. When subjected to a tensile force f, the energy barrier of a conventional "slip bond" typically decreases according to Bell's law as $E_b(f) = E_b^0 - f \Delta x$ where E_b^0 is the reference energy of the bond and $\Delta x \approx 3nm$ is the width of the barrier. Since acto-myosin complexes are known to be temporarily stabilized when moderate pulling forces are applied, a response that can be interpreted as an temporary increase in the energy barrier ΔE_d with forces. This response is well captured by the following two-parameter function:

$$E_b(f) = E_b^0 + \alpha \left[1 - e^{-f/f_0}\right] - f \Delta x \tag{2}$$

where α measures the catchiness of the bond and f_0 is used to scale the force at which the bond stabilizes. We note that when $\alpha = 0$, the above expression degenerates to that of a slip bond following Bell's law. Based on this model, we then constructed a simplified model of the stress fiber cytoskeleton of adherent cells, made of a random assembly of force-sensitive acto-myosin filaments (Fig. 1). This computational procedure was then used to investigate the contractile behavior and cytoskeleton architecture of adherent cells laying on beds of micro-posts, for which a variety of experimental data have been documented.

RESULTS AND SUMMARY

We investigated how the mechano-sensitive response of a stress fiber segment as described by the above equations can give rise to a complex architecture of the actin cytoskeleton observed in most adherent cells. In this context, we simulate the contraction of an adherent cell on soft circular pillars (Fig. 1, right) as presented in various experimental studies. Numerical simulations allow us to predict the evolution of the stress fiber activation, cortex deformation and the corresponding overall force per pillar for different values of the bond catchiness α. Overall results show that at stady state, the cytoskeleton is able to better activate and generate stronger contractile forces as the external environment becomes stiffer. Temporally, we observe a sharp increase in stress fiber density and micropost forces and a steady increase of the average pillar force in time. From a local viewpoint, we note that the unbalanced forces on the cell boundaries are responsible for the cortex deformation into curved arches and the large micropost deflection on the edge of the cell. In contrast, interior pillars, being subjected to more isotropic forces, tend to marginally deform. This restricted deformation in turn, makes interior posts effectively stiffer and prone to adhere to a higher number of stress fibers. Eventually, the final cytoskeleton organization is strongly dependent on the adhesion pattern, micropost stiffness as well as the overall morphology of the cell. The effect of bond catchiness is significant is these processes; a strong catch bond leads to a fairly high level of stress fiber activation and force generation while a slip bond only yields a marginal contraction and a quasi-nonexistent stress fiber cytoskeleton.

In summary, we presented a model of acto-myosin interactions within filament structures that shows that the presence of a catch-bond behavior can explain the activation of the cytoskeleton of adherent cells in response to force and stiffness. The model importantly shows that the consideration of catch bond iss enough to explain a number of experimental measurements of cell contractility with stiffness and size, in both the static and dynamic regimes. These results may therefore enable a better understanding of important biological processes and the development of active and mechano-sensitive polymeric materials.

References

[1] Vernerey F.J, Akalp, U.: The role of catch-bonds in acto-myosin mechanics and cell mechano-sensitivity. Under review
[2] Vernerey F.J, Farsad, M.: A constrained mixture approach to mechano-sensing and force generation in contractile cells. J. Mech. Behav. Biomed 4(8): 1683-1699, 2011
[3] Vernerey F.J, Farsad, M.: A mathematical model of the coupled mechanisms of cell adhesion, contraction and spreading. J. Math. Biol. 68(4): 989-1022, 2014
[4] Foucard L, Vernerey, F.J.: A thermodynamical model for stress-fiber organization in contractile cells, Appl. Phys. Let., 100, 013702 (2012)

BIOCHEMOMECHANICAL POROELASTIC THEORY OF TUMOR GROWTH

Xi-Qiao Feng[a], Shi-Lei Xue & Bo Li

Institute of Biomechanics and Medical Engineering, Department of Engineering Mechanics,
Tsinghua University, Beijing 100084, P. R. China

Summary Tumor growth is a complicated process involving genetic mutation, biochemical regulation, and mechanical deformation. In this paper, a thermodynamics-based nonlinear poroelastic model is established to interrogate the coupling among the mechanical, chemical, and biological mechanisms underpinning the growth of avascular tumors. A volumetric growth law accounting for mechano-chemo-biological coupling is proposed to describe the development of solid tumors. The regulating roles of stresses and nutrient transport in the growth of tumor spheroids are revealed under different surrounding environments. We show that the mechano-chemo-biological coupling triggers anisotropic and heterogeneous growth, responsible for the formation of layered structures in growing tumors. There exists a steady state, in which tumor growth is balanced by resorption. A phase diagram is constructed to illustrate how the elastic modulus and thickness of the confinements jointly dictate the volume of tumors at the steady state. The results are in consistency with relevant experimental results.

INTRODUCTION

Solid tumors account for more than 85% of cancer mortality [1]. Examples of solid tumors are sarcomas, carcinomas, and lymphomas, which often originate from the transformation of small nodes of normal cells into tumor cells that either lose or cease to respond to the normal physiological regulations. The development of solid tumors is a biological process involving multifactorial determinants, e.g. cell molecular and genetic abnormalities, cell–cell and cell–extracellular matrix interactions, and the supply of oxygen and nutrients.

It has been recognized that, besides genetic alterations and biochemical factors, mechanical cues sensed by or transduced to tumor cells also play a vital role in the expansion, invasion, and metastasis of tumors [2]. The mechanical stresses in solid tumors mainly arise from two ways: the heterogeneous growth of tumor itself and the confinement of host tissues. Experiments evidence that tumors respond to stresses through actively altering biochemical pathways and through passively impeding fluid transport. Therefore, the coupling among the mechanical stresses, biological factors, and the reaction–diffusion of chemical species is of paramount importance in tumor pathology [3]. In the present paper, we establish a biochemomechanical theory incorporating the mechano-chemo-biological coupling mechanisms to investigate avascular tumor growth. The tumor tissue is treated as a poroelastic material, which is capable of mass addition and resorption regulated by mechanical, chemical, and biological factors. The system is open and thermodynamic continuous, permitting the transport of mass, momentum, and energy across its boundaries. A growth law that accounts for the interplay among mechanical stresses, biochemical homeostasis, and nutrient transport within tumors is proposed. Furthermore, we also examine the regulatory role which the stiffness of the surrounding host tissues plays in tumor growth.

THEORETICAL MODEL

An avascular tumor is a mixture of cellular elements, ECM constituents, and interstitial space. It corresponds to the primary stage of tumors development before angiogenesis. The cells and ECM in a tumor provide the structural and mechanical integrity and can be considered as a solid skeleton, while the interstitial space is filled with fluid consisting of solvent, generally, water, and solutes such as nutrient, oxygen, and waste. Therefore, a solid avascular tumor is here modelled as a porous medium at the tissue level, and the theory of poroelasticity is applied to characterize its mechanical behavior. To incorporate its volumetric growth, we decompose the geometric deformation gradient tensor $\mathbf{F}$ as $\mathbf{F} = \mathbf{A} \cdot \mathbf{G}$, where $\mathbf{A}$ denotes the elastic deformation tensor and $\mathbf{G}$ is the growth tensor describing the change in mass. On the basis of thermodynamics, we establish the growth evolution law of a tumor

$$\dot{\mathbf{G}} = \sum_{\alpha} f_{\alpha}\left(c_{\alpha}^{\mathrm{g}}\right)\left[\mathbf{A}^{\mathrm{T}} \cdot \frac{\partial W}{\partial \mathbf{A}} - \left(W - W_{\mathrm{h}}\right)\mathbf{I} + \mathbf{b}_{\mathrm{H}}\right] \cdot \mathbf{G}$$

where c_{α}^{g} denotes the concentration of the α-th constituent. $f_{\alpha}\left(c_{\alpha}^{\mathrm{g}}\right)$ is a positive definite scalar function describing chemical kinetics of the α-th constituent. Furthermore, it satisfies $f_{\alpha}\left(c_{\alpha}^{\mathrm{g}}\right) \to 0$ when c_{α}^{g} approaches the threshold for cell survival. W and W_{h} are the Helmholtz free energy of the solid skeleton and the incoming mass per unit volume in the intermediate configuration, respectively. $\mathbf{I}$ is a unit tensor. $\mathbf{b}_{\mathrm{H}}$ stands for the homeostatic stress tensor, that is, the mechanical representation of the biochemical and cellular activity in the steady state of tissues.

NUMERICAL RESULTS

---

[a] Corresponding author. Email: fengxq@tsinghua.edu.cn.

The proposed theory is validated by experimental data in the literature [4]. Recently, microfluidic experiments were performed to examine the morphogenesis of multicellular spheroid in response to external forces or confinements [4]. In the experiments, the spheroid of CT26 mouse colon carcinoma cells underwent free growth (Case I) or confined growth within alginate microcapsules of different radii and thicknesses (Cases II-IV), as shown in Fig. 1(a). The microcapsules were permeable and, hence, enabled outer nutrient and oxygen to flow into interior freely, providing a standard environment for cell proliferation. The following four typical cases were studied: (i) in Case I, the freely growing spheroid exhibited an initial exponential expansion followed by a power-law volume increase, and further growth led to the formation of a necrotic core (the dark region in the image) and a rim occupied by the proliferative cells. (ii) in Case II, the microcapsule was large and thick and, thus, the spheroid initially underwent a free growth. After the spheroid reached the microcapsule, its growth was almost leveled off. (iii) in Case III, the microcapsule was small and thick. The expansion of the spheroid was completely inhibited by the confinement of the microcapsule. (iv) in Case IV, the microcapsule was small and thin. The expansion of the spheroid drove the deformation of the microcapsule until the latter burst. After microcapsule ruptured, the spheroid can resumed the exponential growth observed in the free spheroid (Case I). To simulate the transition from confined growth to free growth in Case IV, we remove the boundary constraint applied on the tumor when the microcapsule bursts. The numerical results show that the proposed theoretical model can well reproduce the experimental observations at different situations, confirming the efficacy and robustness of our theory (Fig. 1(b)).
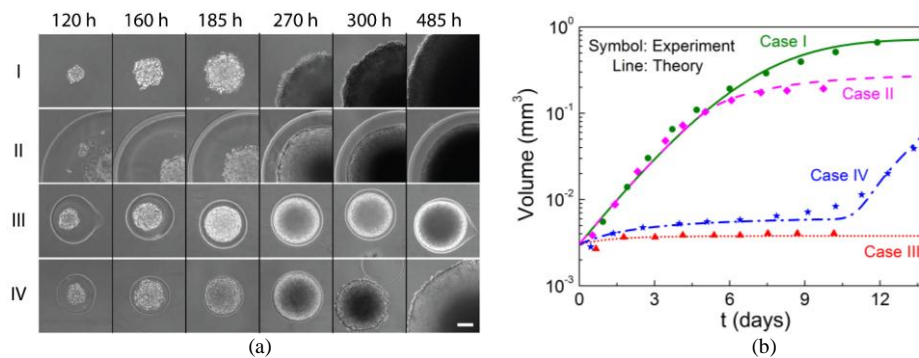
Fig. 1 (a) Microfluidic experiment of in vitro tumor growth under four typical environments [4]; (b) Comparison between theoretical predictions and experimental data.

CONCLUSIONS

Based on thermodynamical compatibility, we develop a nonlinear elastic theory to investigate the interplay among stresses, nutrients, and growth in a solid tumor. The tumor is treated as a porous growing medium allowing for nutrient transport modulated by stresses. As an example, the proposed theory is applied to decipher the MCB coupling in a spheroid avascular tumor under various growing environments such as free growth, compressed growth, confined growth, and the transitions between them. Our model can predict typical features of tumor growth, in agreement with a number of pervious experiments. Although we focus on growth of an avascular tumor, the theory and the results may provide important information for understanding development of a vascular one. The method of present study can also be extended to examine embryogenesis and the development of normal tissues, e.g. hearts, brains, lungs, and blood vessels.

References

[1] Jain R. K.: Normalization of Tumor Vasculature: An Emerging Concept in Antiangiogenic Therapy. *Science* **307**: 58–62, 2005.

[2] Ambrosi, D., Ateshian, G. A., Arruda, E. M., Cowin, S. C., Dumais, J., et al.: Perspectives on Biological Growth and Remodeling. *J. Mech. Phys. Solids* **59**: 863–883, 2011.

[3] Tracqui, P.: Biophysical Models of Tumour Growth. *Rep. Prog. Phys.* **72**: 056701, 2009.

[4] Alessandri, K., Sarangi, B. R., Gurchenkov, V. V., Sinha, B., Kießling, T. R., et al.: Cellular Capsules as a Tool for Multicellular Spheroid Production and for Investigating the Mechanics of Tumor Progression in Vitro. *Proc. Natl. Acad. Sci. USA* **110**: 14843–14848, 2013.

HYDRAULIC FRACTURE AND TOUGHENING OF EPITHELIAL CELL MONOLAYERS

Giovanni Noselli[1a)], Alessandro Lucantonio[1], Xavier Trepat[2], Antonio DeSimone[1] & Marino Arroyo[3]
[1]SISSA – International School for Advanced Studies, Trieste, Italy
[2]IBEC – Institute for Bioengineering of Catalonia, Barcelona, Spain
[3]UPC – Universitat Politècnica de Catalunya, Barcelona, Spain

<u>*Summary*</u> Brittle materials propagate cracks under tensile or shear stresses. When these increase beyond a critical magnitude, then quasi-static crack propagation becomes unstable. In the presence of several pre-cracks, a brittle material always propagates only the weakest crack, leading to catastrophic failure. We show that all these features of brittle fracture are modified when the material susceptible to cracking is bonded to a hydrogel, a common situation in biological tissues. In the presence of the hydrogel, the brittle material can fracture in compression and can hydraulically resist cracking in tension. Furthermore, the poroelastic coupling regularizes crack tip dynamics and enhances material toughness by promoting multiple-cracking.

INTRODUCTION

Epithelial cell layers are two-dimensional, active materials capable of performing a variety of functions (e.g., morphogenesis, wound healing, protection against environmental pathogens) and routinely operating in the presence of significant levels of stretch, such as those arising from breathing manoeuvres or peristaltic contractions. Failure to withstand stretch causes epithelial fracture, leading to developmental defects and severe clinical conditions.

In vitro experiments that resemble the natural environment of epithelial layers have been recently performed [1] on cell clusters adhered to a hydrogel substrate, showing that i) failure of the monolayer can take place under compression, and that ii) this is typically accompanied by the simultaneous growth of multiple, intercellular cracks. The interest for this phenomenology stems from the fact that brittle materials typically fracture under tensile stresses. When these attain a critical magnitude, then quasi-static crack growth becomes unstable and, in the presence of several pre-cracks, catastrophic failure occurs by the propagation of the weakest crack only [2].

In this study, fracture of epithelial layers adhered to a hydrogel substrate is extensively explored by means of a mathematical model [3]. The hydraulic coupling between the fractures and the gel substrate is accounted for, revealing its key role in regularizing crack tip dynamics and in promoting material toughening by multiple-cracking.

SINGLE CRACK DYNAMICS WITH HYDRAULIC COUPLING

We first develop a simplified model [3] to examine the problem of a pre-cracked, elastic solid adhered to a hydrogel substrate, see Fig. 1(a) for a sketch of the geometry. Solutions from Linear Elastic Fracture Mechanics are employed to set the model, while accounting for the hydraulic coupling between the fracture and the gel substrate. Specifically, this requires the time rate of crack area $\dot{A}$ to equal the solvent flux q from the hydrogel into the edge crack. The flux q is approximated by means of Darcy's law, whereas the solvent pressure p acts on the crack faces. Additionally, the geometry is subject to a uniform, remote strain ε that can be either positive (tensile) or negative (compressive).
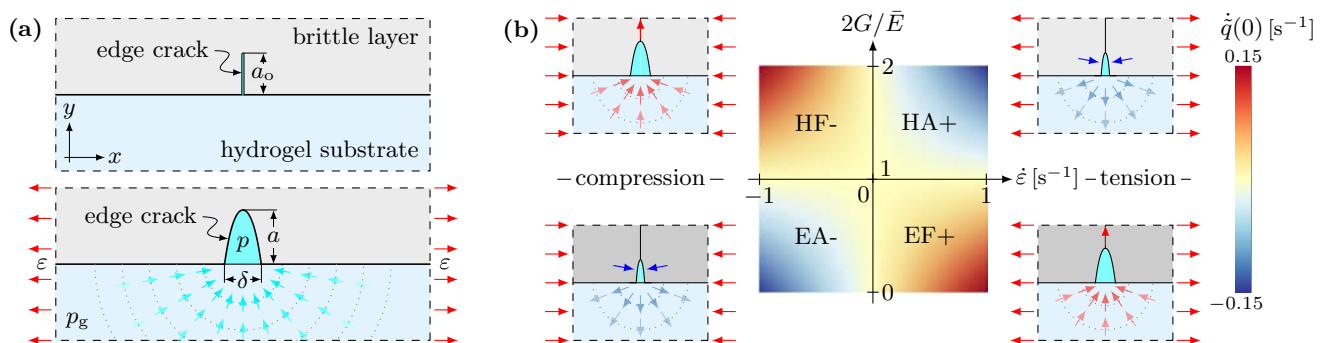
Fig. 1 Sketch of the model system at rest and under stretch (a). Distinct crack opening or closing scenarios (b), depending on the strain rate $\dot{\varepsilon}$ and on the ratio of the shear modulus G of the hydrogel to the effective Young's modulus $\bar{E}$ of the brittle material. The color map represents the time rate of the solvent flux towards the crack cavity immediately after strain application. The labels in (b) describe the dominant driving force at the crack, hydraulic (H) or elastic (E); the phenomenology, fracture (F) or crack arrest (A); and the nature of the imposed deformation, tensile (+) or compressive (−). For instance, HA+ stands for hydraulic (H) arrest (A) under tension (+). (figure adapted from [3])

[a)] Corresponding author. Email: giovanni.noselli@sissa.it.

It is found that, thanks to the hydraulic coupling, distinct fracture scenarios become possible depending upon the material parameters (specifically, the ratio of the shear modulus G of the hydrogel to the effective Young's modulus $\bar{E}$ of the brittle layer) and the loading sign, such that, for instance, the brittle material can fracture in compression (HF-) and can hydraulically resist cracking in tension (HA+), see the representation in Fig. 1(b). Remarkably, it is also shown that the hydraulic coupling regularizes crack tip dynamics allowing for quasi-static crack growth: Irrespective of the failure mode (tensile or compressive), crack tip velocity is dictated by the solvent diffusivity k and the loading rate $\dot{\varepsilon}$.

TOUGHENING BY MULTIPLE CRACKING

We now extend our study to the problem of multiple, competing edge cracks. To this purpose, we consider a detailed nonlinear Finite Element model, coupling large deformations of a neo-Hookean elastic solid with cohesive surfaces along predefined vertical paths, a finite deformation model for the mechanics and fluid transport in the hydrogel [4], and a one-dimensional hydrodynamic model for flow within the crack invoking lubrication theory. For the sake of simplicity, we restrict our computations to the ideal case of two edge cracks, see Fig. 2(b)-(d), and explore the role of solvent diffusivity.
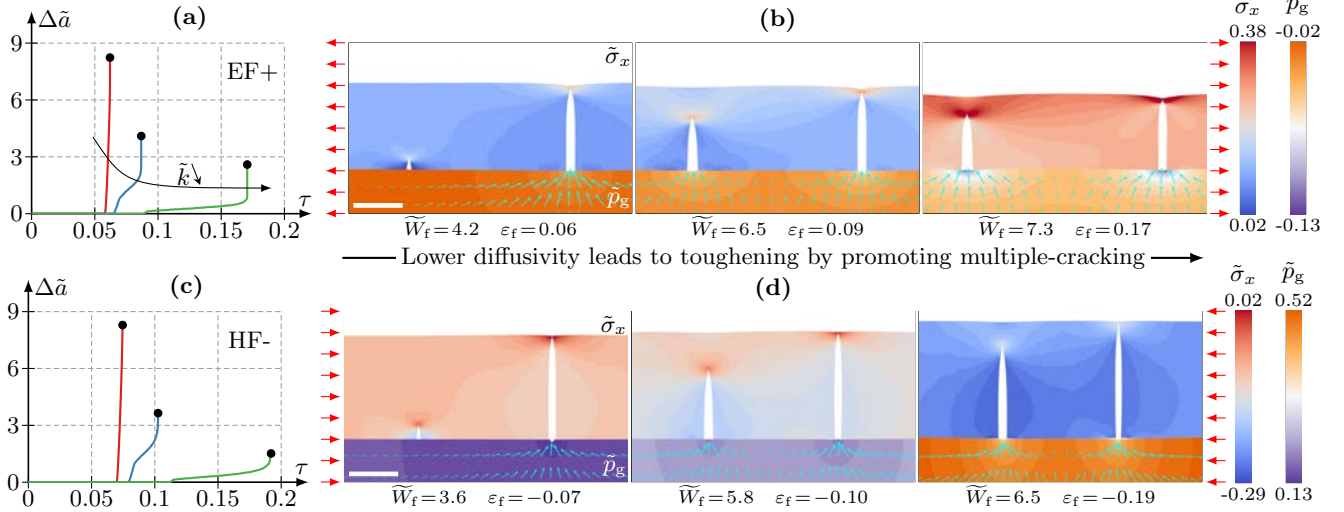
Fig. 2 Dynamics of two competing cracks at different solvent diffusivities k, in tension (a)-(b) and in compression (c)-(d). The plots in (a) and (c) show the relative crack length difference Δa for decreasing values of k. The contour plots in (b) and (d) show the longitudinal stress in the brittle layer and the solvent pressure in the hydrogel immediately prior to failure. The solvent flux in the hydrogel is depicted by means of arrows. (figure adapted from [3])

It turns out that, at high diffusivities, the cracks elastically compete in such a way that localized fracture prevails. This behaviour is similar to that exhibited by a brittle solid in the absence of the poroelastic coupling [2]. In sharp contrast, decreased diffusivity conveys material toughening by promoting multiple-cracking.

CONCLUSIONS

We have shown that the hydraulic coupling between a brittle solid and a poroelastic medium significantly modifies fracture physics. Depending on the sign of strain and the relative stiffness of the two materials, the system can exhibit unexpected fracture modes. We have also shown that, at low diffusivities, the bilayer system develops a toughening mechanism by promoting the simultaneous growth of multiple cracks. We believe that our results may contribute to the understanding of fracture in biological tissues and provide inspiration for the design of tough, biomimetic materials.

ACKNOWLEDGEMENTS

References

[1] Casares L., Vincent R., Zalvidea D. *et al.*: Hydraulic fracture during epithelial stretching. Nat Mater **14**:343–351, 2015.

[2] Noselli G., Deshpande V.S., Fleck N.A.: An analysis of competing toughening mechanisms in layered and particulate solids. Int J Fract **183**:241–258, 2013.

[3] Lucantonio A., Noselli G., Trepat X. *et al.*: Hydraulic fracture and toughening of a brittle layer bonded to a hydrogel. Phys Rev Lett **115**:188105-1–5, 2015.

[4] Lucantonio A., Nardinocchi P., Teresi, L.: Transient analysis of swelling-induced large deformations in polymer gels. J Mech Phys Solids **61**:205–218, 2013.

GEOMETRY AND MECHANICS OF SHELL GROWTH

Douglas P. Holmes[*1], Matteo Pezzulla[1], and Paola Nardinocchi[2]

[1]*Department of Mechanical Engineering, Boston University, Boston, MA, USA*
[2]*Sapienza Università di Roma, via Eudossiana 18, I-00184 Roma, Italy*

Summary Understanding and controlling the shape of thin, soft objects has been the focus of significant research efforts among physicists, biologists, and mechanicians over the last decade. These studies aim to utilize advanced materials in novel, adaptive ways to fabricate smart actuators or mimic living tissues. Our recent work investigates how the underlying geometry of thin sheets will morph into shells when exposed to a local isotropic expansion, which may represent several stimuli such as nonuniform heating, local swelling, and differential growth. We present an analytical model built on a framework of differential geometry and mechanics to predict the mean and Gaussian curvatures of the growing shells. We confirm our results through both numerical analysis, and an experimental technique that relies on the residual swelling of soft, geometric composites.

GROWING SHEETS AND SHELLS

The continuous shape change during the growth and decay of biological structures is a constant presence within the natural world. Structures morph to accommodate an in flux of new material, either growing from an external nutrient source, or swelling from the absorption of water. Often, these morphological changes result in shapes that enhance the biological structure's functionality, for instance the Venus flytrap's leaves snap closed after osmotically swelling – a structural reconfiguration that is essential for its nutrition. Some of the most dramatic growth–induced deformations occur with slender structures, such as growing leaves, wrinkling skin, and the writhing of tendril–bearing climbers. Thin structures like these significantly deform to adopt nontrivial three dimensional shapes because they must bend to release their stretching energy. The coupling between growth and large deformations presents an interesting opportunity for the morphing of synthetic structures, whereby if specific regions within a thin material can be prescribed to stretch the overall structure will adopt a new shape.

In this work, we considered the programmatic shaping of 3D structures by residual swelling. The general concept is straightforward: we prepared a thin structure (beam, plate, shell) with a local excess of free monomer chains, and as this residual solvent diffused it induced a strain in the plate, causing it to morph into a 3D shape. Since the free chains equilibrate within the entire structure, the final shape is permanent. To accomplish this controlled morphing, we prepared geometric composites – structures whose geometries would be incompatible following this material diffusion – and placed the excess
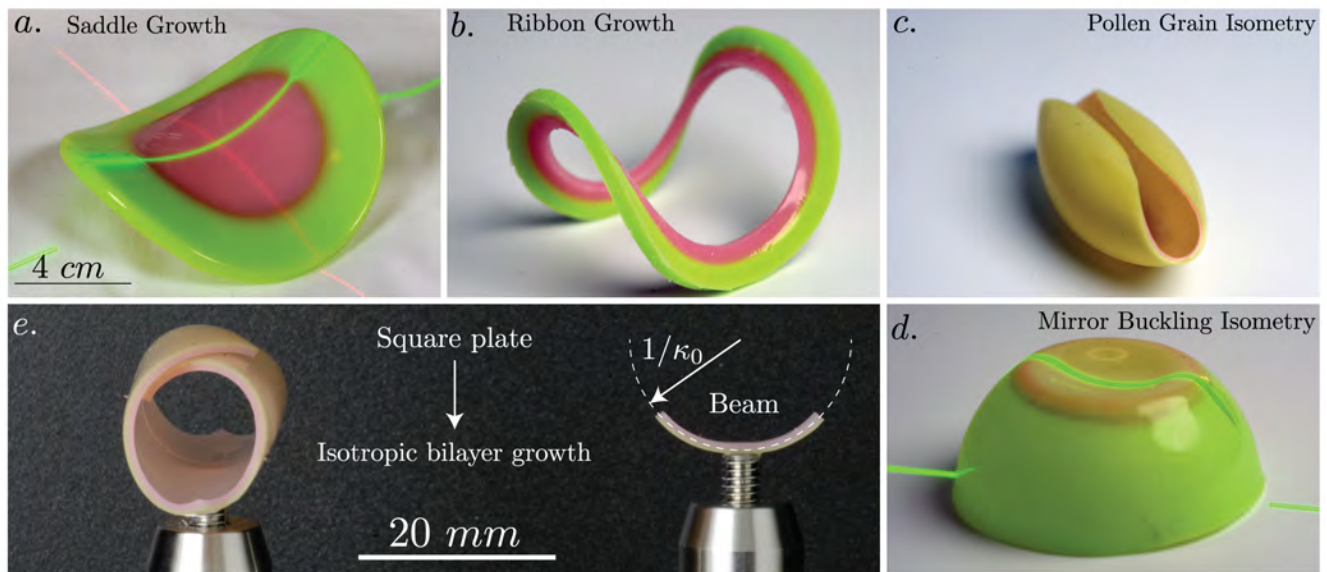
Figure 1: *a*. Flat sheet grows into a saddle as the green annular gets larger while the pink disk gets smaller due to residual swelling. *b*. Buckling of a flat ribbon due to residual swelling. *c*. Growth of a bilayer spherical cap mimicking the pollen grain isometry. *d*. Partial bilayer shell exhibiting a mirror buckling isometry. *e*. The cylindrical isometry of growing thin plates. The mean curvature of this shell can be predicted analytically from the curvature of a similar growing bilayer beam.

*Corresponding author. Email: dpholmes@bu.edu

monomer in one region. A diffusive–like "growth" of the thin shell followed, forming shapes that can be predicted by minimizing the structure's energy. A comparison of the energies for stretching and bending suggests that, if possible, a thin sheet exposed to such stimuli should adopt an isometric deformation in the limit of large stretch. We analytically describe the realization of this asymptotic isometry, corresponding to a zero Gaussian curvature K and a nearly stretch-free sheet. However, when an isometry cannot be realized, a structure will bend as much possible to avoid stretching. An example of this can be seen in Fig. 1a. & 1b., where an initially flat disk and ribbon grew into a saddle as material migrated from the inner disk (pink) to the outer annular ring (green) [1].

When an isometric, or nearly isometric, deformation is available to the growing structure, its morphing becomes quite straightforward as stretching will be avoided entirely, and the structure's shape will be determined by a minimization of its bending energy. This presents a direct approach to identify and exploit near isometries for growing plates and shells with or without topological constraints, *i.e.* a plate versus a cylinder. One such example is the "pollen grain" isometry of a spherical cap [2], where a growing bilayer shell breaks symmetry and adopts a folded structure which conserves the original shell's Gaussian curvature (Fig. 1c.). Growth of a partial bilayer shell accesses a more subtle isometry – the mirror buckling of a cap wherein the apex of the shell everts to a curvature with an opposite sign (Fig. 1d.). By recognizing the structures search for isometric deformations, it is evident that these shells morph in predictable ways in response to residual swelling. This controlled morphing provides a direct way to use the governing underlying geometry as a means for inducing minimally energetic shape changes.

Finally, to fully characterize this class of near–isometries, we investigate the simplest shell growth – growth of a flat sheet into a cylindrical shell. Cylindrically curved thin structures result from the nano-scale fabrication of semiconductor nanotubes, and the nonuniform heating, local swelling, and differential growth of thin sheets. For laminated composites, electrolytic thin film deposition, and concrete slabs, this cylindrical curling presents an engineering challenge, while recent work has utilized it as a mechanism for stimuli responsive self-assembly. The length scales of these examples range from the nanometer to the meter, suggesting that geometry dominates the deformation processes. Mechanically, these structures are bilayer disks in which one layer isotropically expands relative to the other. By coupling geometry and mechanics, we show that in the asymptotic limit of large bilayer growth, any arbitrarily shaped disk will adopt a cylindrical shape whose mean curvature is three-fourth's the natural curvature (Fig. 1e.). We developed an analytical model that captures both the bifurcation from spherical to cylindrical curvature and the isometric limit, verified by numerics and experiments [3]. To predict and explain the transition that turns a spherical growth into a flat state, we compare the energies of the spherical and isometric states, without any *a priori* assumptions of a stress state or displacement. These assumptions usually rely on the consideration of an Airy stress function, which is known only for a very small number of sheet's shapes, and on the account of a linearized version of the Gauss's theorem. Away from large stretches, the two principal curvatures are equal to each other and homogeneous throughout the sheet. However, the morphing into a spherical cap becomes too costly for the sheet when the stretch, or the natural curvature, reaches a critical value. While for small amounts of growth, it is convenient for the sheet to stretch and increase its Gaussian curvature, above a critical threshold it is cheaper to morph isometrically. Thus, we fully characterize the growth of a bilayer with any arbitrary shape from its flat state, through a spherical shell, and finally into a cylindrical isometry by use of an analytical, geometric model.

CONCLUSIONS

We present a novel means to grow thin sheets into shells while analytically predicting their resulting shape. In plane growth, as demonstrated through residual swelling, presents a way to take flat sheets and prescribe a non–zero Gaussian curvature. These results generalize Timoshenko's formula for beams into 2D by expressing how the dimensionless Gaussian curvature varies with material and geometric ratios. We have demonstrated how bilayer disks subjected to dome-like natural curvatures, regardless of their shape, will morph into cylindrical shells with a predictable mean curvature and orientation. We also showed how this simple experimental framework can identify near–isometries in thin shells containing arbitrary topological constraints. The capability to morph 2D shapes into 3D shells by in-plane and transverse residual swelling opens intriguing avenues towards the precise design of soft structures.

References

[1] M. Pezzulla, S. Shillig, P. Nardinocchi, and D.P. Holmes, "Morphing of Geometric Composites via Residual Swelling." Soft Matter, 11, (2015): 5812–5820.

[2] E. Katifori, S. Alben, E. Cerda, D. R. Nelson, and J. Dumais. "Foldable structures and the natural design of pollen grains." Proceedings of the National Academy of Sciences, 107(17), (2010): 7635–7639.

[3] M. Pezzulla, P. Nardinocchi, and D.P. Holmes, "Geometry and Mechanics of Thin Growing Bilayers," arXiv 1509.05259, (2015).

MICROSPHERE MODELING WITH FULL RELAXATION AND INTERNAL EVOLUTIONARY MECHANISMS

Sanjay Govindjee[*1], Miklos J. Zoller[1], and Klaus Hackl[2]

[1]*Structural Engineering, Mechanics, and Materials; Department of Civil and Environmental Engineering; University of California, Berkeley; Berkeley CA, USA*
[2]*Lehrstuhl für Mechanik – Materialtheorie; Ruhr-Universität Bochum; Bochum, Germany*

<u>*Summary*</u> The popular microsphere model, used for creating fully three-dimensional constitutive equations from single polymer chain models, relies upon an energetic relaxation argument. This formulation presents an improvement to the earlier microplane model that is predicated upon an affine, Taylor-like, assumption. While the microsphere framework has been previously applied to a wide variety of phenomena, its application has always involved relaxation only as it relates to quasi-incompressible mechanical motions *but* affine with respect to all other phenomena. In this presentation, we show how to lift these restrictions, thereby permitting the development of fully relaxed constitutive equations based on well characterized one-dimensional micromechanical models even in the presence of other evolutionary microstructural phenomena – such as strain induced crystallization, viscous flow, and other active phenomena.

OVERVIEW

A great deal of experimental and theoretical effort has been expended upon carefully characterizing the behavior of polymeric materials at the chain level. Crowning achievements in this realm include the Gaussian chain model, suitable for long chain polymers stretched to moderate degrees relative to their end-to-end length, and the Langevin chain model for large deformations of chains. These models have been successfully validated experimentally and are thus ubiquitously present in many theories of polymer-system mechanics. Despite these major achievements, among others in polymer chain mechanics, it is still quite challenging to develop mechanical models for networks of polymer chains, say, continuum level constitutive laws, even though good models are available at the chain level. The two primary hinderances that give arise to this situation are: (1) chain-chain interactions are difficult to model and (2) these networks are topologically complex and insufficiently characterized. Despite these complexities, the need for a scheme to transition from one-dimensional mechanical response to three-dimensional behavior is still present.

The original network models for achieving this are the well-known 3-, 4-, and 8-chain models; see e.g. Treloar (1958), Flory (1977), and Arruda and Boyce (1993) or the more general Wu and van der Giessen (1993) and Puso (1994) frameworks. These models are fully affine in nature or quasi-affine. More recently Miehe et al. (2004) proposed an improvement in the mathematical framework that encompasses all of these models by formulating the development of a macroscopic free energy for a network as a constrained relaxation problem – akin to a classical homogenization problem. This further permitted the incorporation of constraint effects as well as internal evolutionary processes, albeit affinely (see e.g. Miehe and Göktepe (2005) or Mistry and Govindjee (2014)). Separately, the line of papers that developed the microplane model (Bazant and Gambarova, 1984) should be noted as intermediate to the earlier cited works and Miehe et al. (2004). The microplane model is in the spirit of the microsphere model, excepting that it is fully affine. Notwithstanding, the developments under this line of thinking provide important discoveries that relevant to a properly formulated relaxed model; see e.g. Carol et al. (2004).

In our proposal, we postulate at the microstructural level that the chain stretch is described by a *tensor $U_m = \lambda n \otimes n + \nu(1 - n \otimes n)$*, where λ is the chain stretch, n is the unit chain orientation vector, and ν is the transverse constraint stretch. The connection to the macroscopic right-stretch tensor is given in terms of Hencky measures by

$$\ln U = \frac{1}{S} \int_S \ln U_m \, dS \,, \tag{1}$$

where S is the microsphere. Following the microplane developments as outlined in Carol et al. (2004), we advocate that in the finite deformation case that the microscopic motion be described by a microstructural Jacobian $j = \lambda \nu^2$ and a microstructural deviatoric stretch $\xi = (\lambda/\nu)^{1/3}$. This permits us to postulate a relaxed macroscopic free-energy

$$\Psi(\ln U) = \inf_{\ln j, \ln \xi} \frac{1}{S} \int_S \psi_{mv}(\ln j) + \psi_{md}(\ln \xi) \, dS \quad \text{subject to (1)} \tag{2}$$

where ψ_{mv} and ψ_{md} are chain level energy functions emanating from microstructural polymer mechanics. The macroscopic constitutive relation follows as the gradient of the free energy, $\tau = \partial_{\ln U} \Psi$.

[*]Corresponding author. Email: s_g@berkeley.edu

The extension to the case of evolutionary processes leverages the evolutionary formulation of Biot (1955). This framework formulates inelastic evolutionary equations utilizing a dissipation potential, a concept valid for a wide variety of internal evolutionary processes. The primary postulate is that the evolution of any internal material parameters z is given by the variational problem:

$$\inf_{\dot{z}} \left\{ \dot{\Psi} + \Delta \right\},$$ (3)

where Δ is the dissipation potential for the phenomena characterized by z and Ψ now additionally depends upon z. In the present context, the macroscopic dissipation potential Δ is constructed from an additional relaxation process on the microscopic dissipation potential Δ_m:

$$\Delta(z, \dot{z}) = \inf_{z_m, \dot{z}_m} \frac{1}{S} \int_S \Delta_m(z_m, \dot{z}_m)\, dS$$ (4)

subject to the constraint $z = (1/S) \int_S z_m\, dS$. Additionally, the free energy relaxation must now include a relaxation with respect to z_m the microscopic internal variables as ψ_{mv} and ψ_{md} will necessarily depend on the new microscopic internal variables.

Combined together, this formulation permits the modeling of a wide variety of phenomena encountered in polymer systems where single (non-interacting) chain mechanics dominates. The elemental ingredients are chain energy relations and micro-state dissipation potentials. The mathematical framework produces sensible macroscopic constitutive laws that are computable and energetically fully relaxed with respect to stretching, transverse constraints, and internal evolutionary processes. Examples will be shown for a variety of systems and compared to prior non-fully relaxed proposals.

REFERENCES

References

Arruda, E. M., Boyce, M. C., 1993. A three-dimensional constitutive model for the large stretch behavior of rubber elastic materials. Journal of the Mechanics and Physics of Solids 41, 389–412.

Bazant, Z., Gambarova, P., 1984. Crack shear in concrete: Crack band microplane model. ASCE Journal of Structural Engineering 100, 2015–2035.

Biot, M., 1955. Variational principles in irreversible thermodynamics with application to viscoelasticity. The Physical Review, 1463–1469.

Carol, I., Jirásek, M., Bažant, Z., 2004. A framework for microplane models at large strain, with application to hyperelasticity. International Journal of Solids and Structures 41, 511–557.

Flory, P. J., 1977. Theory of elasticity of polymer networks. the effect of local constraints on junctions. Journal of Chemical Physics 66, 5720–5729.

Miehe, C., Göktepe, S., 2005. A micromacro approach to rubber-like materials. Part II: The micro-sphere model of finite rubber viscoelasticity. Journal of the Mechanics and Physics of Solids 53, 2231 – 2258.

Miehe, C., Göktepe, S., Lulei, F., 2004. A micro-macro approach to rubber-like materials – Part I: the non-affine micro-sphere model of rubber elasticity. Journal of the Mechanics and Physics of Solids, 2617–2660.

Mistry, S., Govindjee, S., 2014. A micro-mechanically based continuum model for strain-induced crystallization in natural rubber. International Journal of Solids and Structures 51, 530–539.

Puso, M. A., 1994. Mechanistic constitutive models for rubber elasticity and viscoelasticity. Dissertation, University of California, Davis.

Treloar, L. R. G., 1958. The Physics of Rubber Elasticiy. Oxford University Press.

Wu, P. D., van der Giessen, E., 1993. On improved network models for rubber elasticity and their applications to orientationing hardening in glassy polymers. Journal of the Mechanics and Physics of Solids 41, 427–456.

MEMBRANE TENSION CONTROLS KINETICS OF NEURON GROWTH

Prashant K. Purohit[*1] and Douglas H. Smith[2]

[1]*Department of Mechanical Engineering and Applied Mechnaics, University of Pennsylvania, Philadelphia, Pennsylvania, USA*
[2]*Department of Bioengineering, University of Pennsylvania, Philadelphia, Pennsylvania, USA*

Summary In the first phase of axon growth, axons sprout from neuron bodies and are extended by the pull of the migrating growth cones towards their targets. Thereafter, a second phase of axon growth, called stretch growth, ensues as the mechanical forces from the growth of the animal induce rapid extension of the nerves. Here we propose a mathematical model for stretch growth of axon tracts in which the rate of production of proteins required for growth is dependent on the membrane tension. We show that there is a length dependent maximum stretching rate that an axon can sustain without disconnection, and that axon length is increased near the cell body. Our model also predicts that the diameter of an axon subjected to stretch growth must increase. Our results could inform better design of stretch growth protocols to create transplantable axon tracts to repair the nervous system.

INTRODUCTION

Smith and colleagues [1] have previously developed tissue-engineering techniques that exploit a natural "second phase" of axon growth creating long tracts of axons spanning two populations of neurons. In the well known "first phase" of axon growth, axons sprout from neurons guided by chemotactic and haptotactic factors and typically extend only up to a few millimeters to reach their targets. Thereafter, the second phase of purely mechanically stimulated, "stretch growth of integrated axon tracts," begins as the animal's body grows. Here, integrated axons spanning body regions that progressively move further apart undergo continuous mechanical tension. These forces appear to trigger growth somewhere along the center lengths of the axons, otherwise they would be stretched to the point of disconnection. To explore the cellular dynamics and boundaries of axon extension during the first phase of axon growth, several groups have developed computational models, with a focus on polymerization of microtubules as axon cytoskeleton building blocks. In most of these models, as the growth cone is guided forward, tensile forces are induced at the axon terminal or tip, just behind the growth cone. In turn, it is assumed that these forces trigger building of the microtubule selectively in this region. However, once the target is reached typically not more than a few millimeters away, integration and synapse formation essentially abolish the growth cone. Therefore, current mathematical models do not appear to account for mechanical influences during the extreme second phase of axon growth and expansion of tracts over tens of centimeters for humans and even many meters for very large animals. Furthermore, the specific role of membrane tension and stretch activated ion channels in axon stretch growth have not been explored. Here, we propose a model for stretch growth of integrated axon tracts based on overall mechanical stimulation resulting in very regional microtubule polymerization and relative contribution of stretch activated channels in the process.

Growth modeled as a polymerization process

A summary of the equations describing stretch-growth, assuming polymerization occurs at the soma (see figure 1(a)), is [2, 3]:

$$\frac{dL}{dt} = \alpha Q_s - \beta, \qquad \frac{dQ_t}{dt} = \frac{DA}{V_t L}(Q_s - Q_t), \qquad \frac{dQ_s}{dt} = \frac{I}{V_s} - \frac{DA}{V_s L}(Q_s - Q_t) + \frac{G}{V_s}\frac{dL}{dt}, \qquad (1)$$

where L is the length of the axon, $\alpha = ek_{on}$ is related to the on-rate k_{on} for polymerization with e the monomer size, $\beta = ek_{off}$ is related to the off-rate k_{off} for polymerization, Q_s is the concentraton of monomers in the soma, Q_t is the concentration of monomers at the tip of the axon, D is a diffusion constant, A is the axon cross-sectional area, V_t is a small volume at the tip of the axon, I is the rate (in units of number of monomers per unit time) of production of tubulin monomers in the soma, V_s is a small volume in the soma where the polymerization reaction occurs and G is a constant. The steady state solution to these equations is:

$$L = L_0 + Ut, \qquad Q_s = Q_t = Q = \frac{\beta}{\alpha} + \frac{U}{\alpha}, \qquad (2)$$

where $U = I/G$ is the speed of growth. We believe that the rate of monomer production I depends on the membrane tension τ. As a cell is stretched it must 'sense' the increasing membrane tension and increase the rate of production so that growth keeps up with the stretching. A potential source of this cell signaling during stretch growth is likely mechanosensitive channels in cell membranes that have been shown to open in other circumstances when the tension increases. Opening of these channels can cause an influx of ions such as Na^+ and Ca^{2+} that can influence monomer production in the soma by various means. While the exact mechanism may not be known it is reasonable to assume that I depends linearly on the probability p_{open}

---

of the mechanosensitive channels being open, which in turn depends on τ in a known way [4]. Using those expressions we assume that the monomer production rate I is a monotonic function of the tension τ and is given by:

$$I(\tau) = C\left[\frac{1}{1+\exp(-\frac{\Delta G+\tau\Delta A}{k_B T})} - \frac{1}{1+\exp(-\frac{\Delta G+\tau_0\Delta A}{k_B T})}\right], \tag{3}$$

where C is a constant, $k_B T$ is the thermal energy scale, $\Delta G = G_{closed} - G_{open} < 0$, the free energy difference between the closed and open states of the channel is several $k_B T$, $\Delta A = A_{open} - A_{closed} > 0$, the cross-sectional area difference between the open and closed states is on the order of tens of square nanometers, and τ_0 is the rest tension of the axonal membrane. When $\tau = \tau_L$, the lytic tension of the membrane, $I(\tau_L)$ is at its maximum and this corresponds to $U \approx 30\mu$m/hour.

RESULT
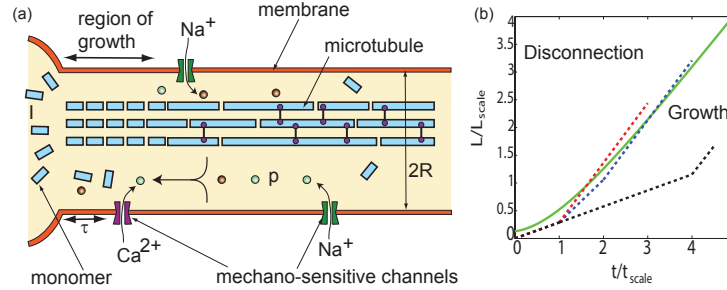
Figure 1: (a) Schematic of the axon with microtubules polymerizing at the junction between the axon and the soma. Mechanosensitive channels in the axonal membrane open in response to increased tension due to stretching causing an influx of ions. This sends a signal to the soma to increase the rate of production of monomers. (b) A limiting $L(t)$ curve is shown as the green line. Growth programs (blue and red dashed lines) that cross this line from below cause disconnection of the neurons.

The major result of the model above is a limiting growth trajectory which when crossed from below will cause the axons to disconnect. Suppose during initial stretching of a neuron the lytic tension is reached, and the cell responds by increasing the monomer production to its maximum value $I(\tau_L)$. As a result the axon grows by the addition of new material and eventually settles into a steady state with $\tau < \tau_L$, and constant growth rate U. Hence, the limit on the growth program is set by the requirement that $\tau = \tau_L$ at all times. Since, I and A are functions of τ only, they remain fixed for this $L(t)$. With these assumptions we can integrate eqns. (1) to find the limiting growth trajectory $L(t)$. This limiting growth trajectory is plotted as the green curve in figure 1(b) in terms of non-dimensional length and time variables. A comparison of the x- and y-axis of this figure to figure 4A of Smith [1](who arrived at the limiting trajectory through experiment) suggests that t_{scale} is about 1 day and L_{scale} is about 0.2mm for axons in stretch growth. In contrast, Wisnner-Gross *et al.* [5] fitted the ODE model of Samuels *et al.* [2] to their experiments on growth of neurons without stretch and concluded that t_{scale} was about 6.4 hours and L_{scale} was about 51 microns. The reason for a lower k_{on} in stretch growth can be that polymerization occurs against a compressive load that the microtubules are experiencing due to increased tension in the membrane caused by stretching.

CONCLUSIONS

We have presented a microscopically based model in which membrane tension modulates the production rate of materials required for neuron growth. We obtain a limiting growth trajectory that is similar to one obtained from experimentss [1].

References

[1] Smith, D. H., "Stretch growth of integrated axon tracts: Extremes and exploitations", *Progress in Neurobiology* **89**, 231-239, 2009.

[2] Samuels, D. C., Hentschel, H. G. E. and Fine, A., "The origin of neuronal polarization: a model of axon formation", *Phil. Trans. Roy. Soc. Series B* **351**, 1147-1156, 1996.

[3] Nguyen, T. D., Hogue, I. B., Cung, K., Purohit, P. K. and McAlpine, M. C., "Tension induced neurite growth in microfluidic channels", *Lab on Chip* **13**(18), 3735-3740, (2013).

[4] Haselwandter, C. A. and Phillips, R., "Connection between oliomeric state and gating characteristics of mechanosensitive channels", *PLoS Computational Biology* **9**(5), e1003055, 2013.

[5] Wissner-Gross, Z. D., Scott, M. A., Ku, D., Ramaswamy, P. and Yanik, M. F., "Large scale analysis of neurite growth dynamics on micropatterned substrates", *Integrative Biology*, (2010).

SOFT NETWORK MATERIALS WITH DETERMINISTIC AND BIO-INSPIRED DESIGNS

Yihui Zhang[1a)], Qiang Ma[1], Yonggang Huang[2], John A. Rogers[3]

[1]*Department of Engineering Mechanics, AML, Tsinghua University, Beijing, China*
[2]*Department of Civil and Environmental Engineering and Mechanical Engineering, Northwestern University, Evanston, IL, USA*
[3]*Department of Materials Science and Engineering, University of Illinois at Urbana-Champaign, Urbana, IL, USA*

ABSTRACT

Hard and soft structural composites found in biology provide inspiration for the design of advanced synthetic materials. Many examples of bio-inspired hard materials can be found in the literature; far less attention has been devoted to soft systems. Here we introduce deterministic routes to low-modulus thin film materials with stress/strain responses that can be tailored precisely to match the non-linear properties of biological tissues, with application opportunities that range from constructs for tissue engineering to stretchable biomedical electronics. The approach combines a low-modulus matrix with an open, stretchable network as a structural reinforcement that can yield classes of composites with a wide range of desired mechanical responses, including anisotropic, spatially heterogeneous, hierarchical and self-similar designs. A finite-deformation model of such network materials is developed, enabling accurate predictions of stress-strain curves and Poisson ratios. Demonstrative application examples include thin, skin-mounted electrophysiological sensors with mechanics precisely matched to the human epidermis.

MAIN TEXT

Concepts in materials science that draw inspiration from the natural world have yielded an impressive collection of important advances in recent years. Structural materials are of particular interest, due to their essential roles in nearly every engineered system. Biology provides examples of two general classes of such materials: (1) mineralized hard (~ GPa) materials, mainly in the form of hierarchically assembled composites that combine minerals with organic polymer additives; and 2) non-mineralized soft (~ MPa) materials, typically constructed with wavy, fibrous constituents that are embedded in extracellular matrices. Although the non-mineralized, soft biological structures offer great potential in areas ranging from artificial tissue constructs to bio-integrated devices, they have received far less attention compared to the mineralized counterparts.
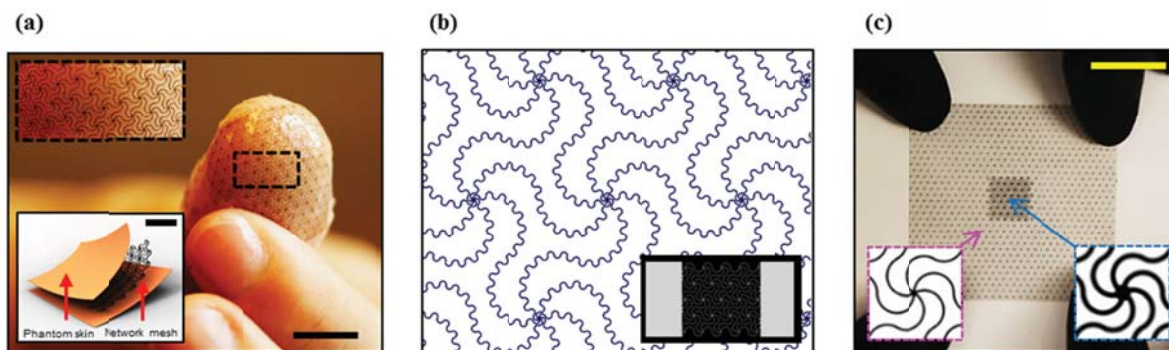
Fig. 1. (a) Optical images and an exploded view schematic illustration (lower left inset) of a skin-like composite with bio-inspired soft network. The scale bar is 1 cm. (b) Schematic illustration of a wavy network with a 2nd order self-similar architecture consisting of horseshoe building blocks. (c) An image of spatially heterogeneous designed soft composite. The scale bar is 2 cm.

Here we introduce deterministic routes to a class of soft, bio-inspired network materials with precisely tailored stress/strain responses to match the non-linear properties of biological tissues, with broad application opportunities that range from constructs for tissue engineering to stretchable biomedical electronics [1]. The concepts combine planar networks of different two-dimensional (2D) lattice topologies, with horseshoe microstructures originally developed for interconnects in stretchable electronics. A low-modulus elastomer or hydrogel serves as a supporting matrix. Such network materials exhibit 'J-shaped' stress/strain curves that offer large levels of stretchability, as well as a huge modulus

[a)] Corresponding author. Email: yihuizhang@tsinghua.edu.cn.

enhancement at large strain to yield a relatively high mechanical strength.   With a computational mechanics model to serve as the design tool, the mechanical responses of the network materials can be precisely tailored by optimizing their key parameters, including the material type, the network topology, the filament dimensions and the microstructure geometry, to meet requirements of interest.   Fig. 1(a) presents a schematic illustration of the strategy in the context of an artificial skin construct, as an application example of the soft network materials.   Hierarchical, self-similar designs of the interconnects and spatially heterogeneous designs, as shown in Fig. 1(b) and (c), can further expand their range of mechanical properties, such as stress/strain responses with multiple hardening and gradient mechanical properties.   The proposed network materials also offer a new insight into the structural design of stretchable electronics that focused more on the design of hard functional devices and/or interconnects previously [2-5].   Successful experimental demonstrations of these soft network materials integrated with electrophysiological sensors and drug release vehicles indicate their potential for practical applications in biomedical devices.

To provide theoretical guidelines for designs of such soft network materials, a nonlinear mechanics model is developed by combining a finite-deformation constitutive relation of the building block (i.e., horseshoe microstructures), with the analyses of equilibrium and deformation compatibility in the periodical lattices [6].   This model, as validated by FEA and experimental results, can predict precisely the nonlinear stress-strain curves and Poisson ratios, as well as the deformed configurations under uniaxial stretching.   Analytic solutions of their key mechanical properties, including elastic modulus, critical strain, peak modulus and the associated strain, were obtained, which can characterize well their dependences on the microstructure geometry.   Moreover, a demonstrative example shows that the developed model can be employed to enable rapid optimization of microstructure geometry for matching precisely the stress-strain curves of human skins, as shown in Fig. 2.
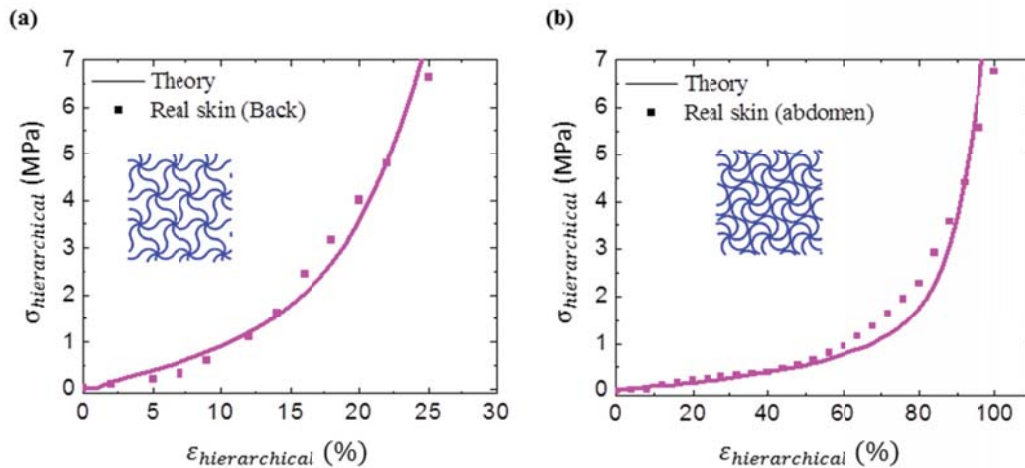
Fig. 2. Stress-strain curves of human skin for two different locations ((a) for back area and (b) for abdomen area) on different individuals and optimized skin-like network materials with triangular lattices.

References

[1] Jang K.-I., Chung H.U., Xu S., Lee C.H., Luan H., Jeong J., Cheng H., Kim G.-T., Han S.Y., Lee J.W., Kim J., Cho M., Miao F., Yang Y., Jung H.N., Flavin M., Liu H., Kong G.W., Yu K.J., Rhee S.I., Chung J., Kim B., Kwak J.W., Yun M.H., Kim J.Y., Song Y.M., Paik U., Zhang Y., Huang Y., Rogers J.A.,: Soft network composite materials with deterministic and bio-inspired designs. *Nature communications* 6, 6566 (2015).
[2] Rogers J.A., Someya T., Huang Y.G.: Materials and Mechanics for Stretchable Electronics, *Science* 327, 1603-1607 (2010).
[3] Xu S., Zhang Y.H., Cho J., Lee J., Huang X., Jia L., Fan J.A., Su Y.W., Su J., Zhang H.G., Cheng H.Y., Lu B.W., Yu C.J., Chuang C., Kim T.-I., Song T., Shigeta K., Kang S., Dagdeviren C., Petrov I., Braun P.V., Huang Y.G., Paik U., Rogers J.A.: Stretchable Batteries with Self-Similar Serpentine Interconnects and Integrated Wireless Recharging Systems. *Nature Communications* 4: 1543 (2013)
[4] Zhang Y.H., Wang S.D., Li X.T., Fan J.A., Xu S., Song Y.M., Choi K.J., Yeo W.H., Lee W., Nazaar S.N., Lu B.W., Yin L., Hwang K.C., Rogers J.A., Huang Y.G.: Experimental and Theoretical Studies of Serpentine Microstructures Bonded To Prestrained Elastomers for Stretchable Electronics. *Advanced Functional Materials* 24: 2028-2037 (2014)
[5] Zhang Y.H., Fu H.R., Xu S., Fan J.A., Hwang K.C., Jiang J.Q., Rogers J.A., Huang Y.G.: A hierarchical computational model for stretchable interconnects with fractal-inspired designs. *Journal of the Mechanics and Physics of Solids* 72: 115-130 (2014)
[6] Ma Q., Cheng H., Jang K.-I., Luan H., Hwang K.C., Rogers J.A., Huang Y.G., Zhang Y.H.: A nonlinear mechanics model of bio-inspired hierarchical lattice materials consisting of horseshoe microstructures. *Journal of the Mechanics and Physics of Solids*. (Submitted)

DYNAMIC INDENTATION: A SIMPLE METHOD TO CHARACTERIZE POROELASTICITY OF GELS IN MICRON SCALE

Yang Lai[1], <u>Yuhang Hu</u>[1a)]

[1]*Department of Mechanical Science and Engineering, University of Illinois Urbana Champaign, Urbana, Illinois, US*

<u>*Summary*</u> In this study, we use the characteristic phase lag between the applied oscillation indentation displacement and the force on the indenter due to the energy dissipation from solvent flow in the gel to characterize the poroelasticity of gels. We will show that the phase lag degree is a function of two parameters, Poisson's ratio and normalized angular frequency. The solutions are derived for several shapes of indenters. The maximum value of the phase lag over a spectrum of actuation frequencies can be used to characterize the Poisson's ratio of the gel, and the characteristic frequency corresponding to the maximum phase lag can be used to characterize its diffusivity.

INTRODUCTION

Gels composed of crosslinked polymeric network and solvent molecules, can swell or contract in response to external stimuli, such as relative humidity, temperature, pH, electric field and light. Gels are almost everywhere in nature, from cells, tissues, to organs. Gels are also important engineering materials, which have been widely used as cell culture scaffold, drug carrier, microfluidic device, sensors, actuators, soft robots, fuel cell membrane, transparent loudspeaker, swellable packers for sealing oil well, etc. Most gels are soft, with a typical modulus of $1 \sim 10^2$ kPa. Some gels are also saggy, brittle, and slippery. Most bio-gels are often inhomogeneous, degradable as time and of gradient properties. These characters of gels raise many practical difficulties in mechanical testing. Traditional techniques such as tension, compression, bending, torsion and shearing are very difficult to apply. Recently there is a growing interest in indentation on soft materials, but most previous works focus on characterizing the elastic modulus of gels. In the PI's pervious work, a poroelastic relaxation indentation method has been developed allowing the poroelastic properties of gels including shear modulus, drained Poisson's ratio and diffusivity to be measured all from one test.[1] While this method is applicable in large scales (mm), it remains challenging to be applied in small scale (1~10 μm), when inhomogeneous and local properties are of interests. In the relaxation indentation technique, identifying the contact point on soft materials and accurately measuring the initial force right after a rapid ramping of displacement are very difficult to realize in small scale. Alternatively, most commercial instruments for small scale testing, such as Atomic Force Microscope and Instrumented Nanoindenter, can perform accurate dynamic measurement with high resolution. Motivated by this fact, we develop a dynamic indentation method to characterize poroelasticity of gels for micro-scale measurement.

METHODOLOGY AND RESULTS

To define quantities of interest, we use the theory of poroelasticity to describe the diffusion-coupled-deformation of gels.[2] The initial gel is taken to be in a homogeneous state, subject to no mechanical load, with C_0 being the number of solvent molecules per unit volume of the gel, and μ0 being the chemical potential of solvent in the gel. When the gel deforms, the displacement is a time-dependent field, $u_i(x_1,x_2,x_3,t)$, and the strain is $\varepsilon_{ij} = (\partial u_i/\partial x_j + \partial u_j/\partial x_i)/2$. The conservation of solvent molecules requires that $\partial C/\partial t = -\partial J_k/\partial x_k$, where C is the concentration of the solvent in the gel, and J_k the flux which is driven by chemical potential gradient $J_k = -(k/\eta\Omega^2)\partial\mu/\partial x_k$, where k is the permeability, η the viscosity of the solvent, and Ω the volume per solvent molecule. The stress in the gel is given by $\sigma_{ij} = 2G[\varepsilon_{ij} + \varepsilon_{kk}\delta_{ij}\nu/(1-2\nu)] - \delta_{ij}(\mu - \mu_0)/\Omega$, where G is the shear modulus, ν Poisson's ratio. The gel is in mechanical equilibrium, so that the field of stress satisfies $\partial\sigma_{ij}/\partial x_j = 0$. A combination of the above equations leads to a familiar diffusion equation $\partial C/\partial t = D\nabla^2 C$, with the diffusivity being $D = [2(1-\nu)/(1-2\nu)]Gk/\eta$. Summarily, the material is fully described by three parameters G, ν and D.

To characterize these three parameters, we develop a dynamic indentation method. As shown in Figure 1, a depth of indentation h_o is applied on a swollen gel with a constant velocity, and then is held
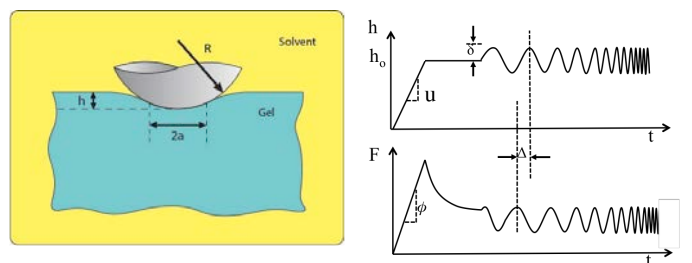
Fig.1: Schemetic of the dynamic indentation method. A depth of indentation h0 is pressed into the swollen gel and held for a period of time. After this period of holding, an oscillation displacement is applied with different frequencies. Meanwhile, the force is measured as a function of time, and the phase lag between force spectrum and displacement spectrum is recorded as actuation frequency.

---

a) Corresponding author. Email: yuhanghu@illinois.edu

for a period of time. Following this period of stress relaxation, an oscillatory displacement $\delta e^{-i\omega t}$ ($\delta \ll h_o$) is applied. Meanwhile the force on the indenter is measured as a function of time. The poroelastic gel is characterized by three parameters: shear modulus G, drained Poison's ratio v, and diffusivity D. During the loading period, solvent molecules in the gel do not have time to migrate, so the gel is incompressible, and the slope of the measured force ϕ can be used to obtain shear modulus G through elastic solutions,

$$G = 3\phi/16R^{1/2}u^{3/2}. \tag{1}$$

The real difficulty lies in how to get v and D. The phase lag between the displacement and force spectrum characterizes the time-dependent behavior of gels. As the oscillatory displacement sweeps through a spectrum of frequencies, a peak value of the phase lag Δ_c between oscillatory displacement and the force measurement is obtained. The angular frequency ω_c corresponding to the peak is a

Fig.2: Phase lag is plotted as a function of normalized angular frequency for materials of different Poisson's ratio.

characteristic value with respect to diffusion that scales with D/a^2 with a being the contact radius. The oscillation indentation problem is solved and the characteristic curve $\Delta = f(D\omega/a^2, v)$ is obtained (Fig. 2). The solution derived here is for spherical indenter.

As is shown in Figure 2, the phase lag is plotted as a function of normalized angular frequency. It reaches a peak at a particular value of the actuation frequency. The value of the peak highly depends on the Poisson's ratio of the material. When Poisson's ratio is small, the amount of liquid that can be squeezed out of the gel is larger. Consequently, more energy is dissipated due to flow of solvent, which corresponds to a larger value of the phase lag. When Poisson's ratio is close to 0.5, liquid does not diffuse in or out of the material, no energy is dissipated, and the phase lag is zero. For ease for extraction of material properties from experimental data, the relation between peak phase lag Δ_c and Poisson's ratio v is fitted with a continuous function as

$$v = 0.5 - 0.02\Delta_c, \tag{2}$$

and the relation between the normalized critical angular frequency and Poisson's ration v is also fitted with a function as

$$D = a^2\omega_c/(0.72 + 0.29v + 0.48v^2) \tag{3}$$

Therefore, equations (1)-(3) can be used to extract the three material parameters from dynamic indentation measurement.

CONCLUSIONS

A dynamic indentation method has been developed that is suitable for characterizing the mechanical and transport properteis of polymer gels. In this technique, a spherical indenter is used to probe the response of gels under oscillatory loading conditions. Solvent transport within the gel is driven by chemical potential gradient. The flow of solvent defines the time-dependent behavior of gels and energy dissipation due to flowof solvent through the network. In dynamic response, a lag of phase appears between the spectrum of responsive force and actuation displacement. Theoretical caculation shows that the peak value of the phase lag can be used to extract Poisson's ratio of the material, and the corresponding critical angular frequency can be used to extract the diffusivity of solvent in polymeric network of gels.

References

[1]. Hu Y., Zhao X., Vlassak J.J., Suo Z.: Using indentation to characterize the poroelasticity of gels. Appl. Phys. Lett. 96: 121904, 2010.
[2]. Biot M.A.: General theory of three-dimensional consolidation. J. Appl. Phys. 12:155-164, 1941.
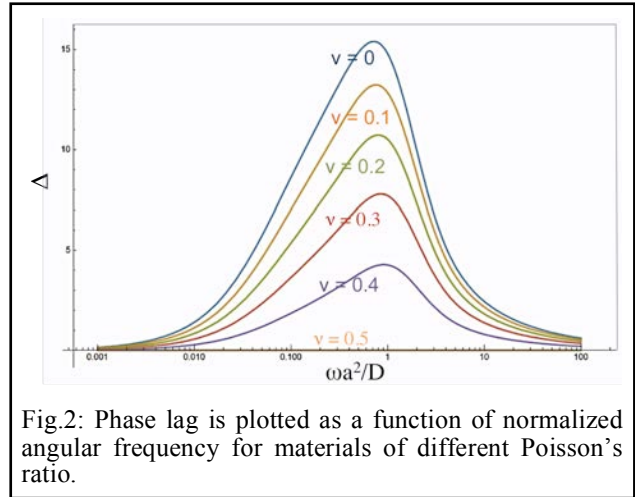
CELL ALIGNMENT FABRICATION USING STRETCHABLE HYDROGELS WITH PROGRAMMABLE STRAIN GRADIENTS

Yuhui Li[1,2], Lin Wang[1,2] , Moxiao Li[2], Tian Jian Lu[2] & Feng Xu [1,2]

[1] *MOE Key Laboratory of Biomedical Information Engineering, School of Life Science and Technology, Xi'an Jiaotong University, China*

[2] *Bioinspired Engineering and Biomechanics Center (BEBC), Xi'an Jiaotong University, China*

Abstract: The mechanical gradients (e.g., stiffness and stress/strain gradients) of extracellular matrix play an important role in guiding cellular alignment, especially in tendons and muscles. Though various methods have been developed to engineer graded mechanical environment to study its effect on cellular behaviours, most of them failed to distinguish stiffness effect from stress/strain effect during mechanical loading. Here, we construct a mechanical environment with strain gradients by using a hydrogel of a linear elastic property. We demonstrate that the pattern of cellular alignment can be rather precisely tailored by substrate strains. The experiment is in consistency with a theoretical prediction when assuming that focal adhesions would drive cell to reorient to the directions where they are most stable. This work not only provides important insights into the cellular response to local mechanical microenvironment, but can also be utilized to engineer patterned cellular alignment that can be critical in tissue remodelling applications.

MAIN TEXT

Mechanical gradient microenvironment has been found to widely exist in native tissues and play an important role in regulating cell behaviors including alignment, migration, proliferation and differentiation in vitro for tissue remolding and regenerative medicine applications[1-2]. Up to now, a variety of methods based on hydrogels have been developed to engineer mechanical gradient microenvironment of cells in vitro[3-4]. However, mostly of these studies were focused on stiffness gradient construction and with less effort for engineering stress/strain gradient microenvironment, which are also associated with normal physiologic processes such as gut peristalsis and heart contraction. Recently, several approaches have been developed to simulate in vitro 3D cell environment with mechanical loading and investigated cell response to varying stress/strain conditions, which are discontinuous and lack of controllability to form gradient environment. Besides, the effects of stiffness and stress/strain are intertwined. Therefore, there is still an unmet need for a simple and controllable method to engineer hydrogels with stress/strain gradients for cells. Here, we developed a simple and facile method based on molding and photolithography approaches to fabricate methacrylate gelatin (GelMA) hydrogels with strain gradients ranging from 0~20%, which covers the muscle and heart contraction in vivo (**Figure 1**). The separation of the effects of stiffness and stress/strain has been achieved through the hydrogels with linear elastic properties in the testing strain range. Hydrogels with programmable strain gradients were formed by UV crosslinking reaction with designed shapes and then applied by static stretch loading. (**Figure 2**) The orientation of C2C12 cells seeded on gradient hydrogels was assessed under static stretch loading conditions (**Figure 3**). The analysis results of cellular stress fiber orientation have shown that cell alignment gradients will formed under strain gradients on hydrogels. For large strain region ($17.0 \pm 0.5\% \sim 19.7 \pm 1.0\%$) on gradient hydrogels, cells aligned predominantly perpendicular to stretching direction whereas cells randomly oriented in control group (non-strech loading). With decreasing strain from $15.4 \pm 0.4\%$ to $13.5 \pm 0.7\%$, stress fibers gradually oriented towards the stretching direction. Stress gradient generated on hydrogels also ranged from 1.9 ± 0.3 kPa to 3.2 ± 0.1 kPa. These results indicated that cellular response to gradient hydrogels supports the principle that cells orient in the direction of minimal substrate deformation, known as strain-avoidance or stretch-avoidance, and is in agreement with the existing findings from corresponding model systems. The gradient hydrogel fabrication approach we developed here holds great potential to impact a wide range of fields, such as cell mechanics, tissue engineering and regenerative medicine.
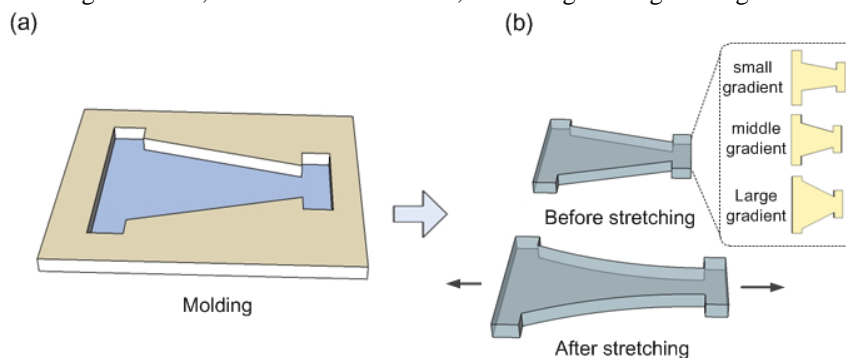
Figure 1. Schematics of fabrication method for hydrogels with stress/strain gradients. (a) Hydrogels with designed trapezoidal shape are fabricated with PMMA mold through an UV crosslinking reaction; (b) Hydrogels with programmable gradients including three levels of strain gradients under stretching.

---

[a] Corresponding author. Email: fengxu@mail.xjtu.edu.cn**.**
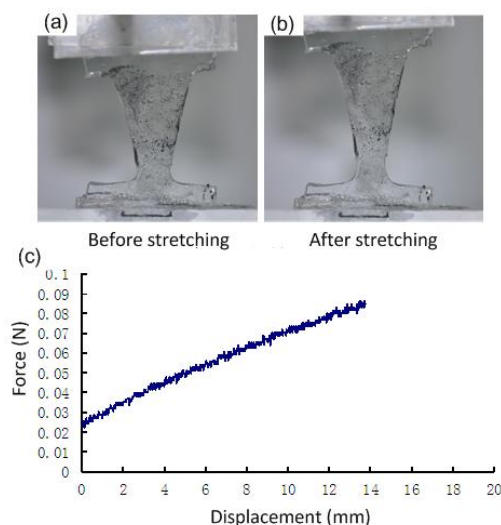
Figure 2. Characterization of strain/stress of different hydrogels. (a) Representative images depict the microbeads used in the texture correlation algorithm before (left) and after (right) stretch to determine strain distribution. (b) Stress/strain curve of hydrogels.
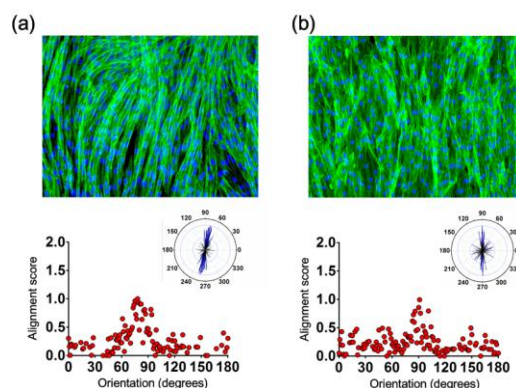
Figure 3. Analysis of cellular alignment generated on gradient hydrogels. (a-b) florescent images and quantification of cell orientation on gradient hydrogels with stretch loading after 3 days culture (cellular F-actin fibers were stained by phalloidin (green) and nuclei by DAPI (blue)).

In conclusion, we here developed a simple and feasible method to engineer patterned cellular alignment in vitro. Programmable stress/strain gradients on GelMA hydrogels are realized by stretching hydrogels with linear elastic property. When seeding cells on such hydrogels subjected to static stretches, we find that cells on hydrogels align almost perpendicularly to stretch direction in regions of large strains, and gradually align towards to stretch direction in regions of relatively small strains, whereas cells orient randomly in control group. The effect of substrate strains on cellular alignment is explained with the theory by assuming that focal adhesions would drive cell to reorient to the directions where they are most stable. The current work not only provides important insights into the cellular response to local mechanical microenvironment for understanding cellular mechanosensitivity, but can also be utilized to engineer patterned cellular alignments that can be critical in tissue remodelling and regeneration.

References

[1] Li, Y., Huang, G., Zhang, X., Wang, L., Du, Y., Lu, T. J., Xu, F. *Biotechnol Adv,* 347−365, 2014.
[2] Etemad-Moghadam, B., Guo, S., Kemphues, K. J. *Cell,* 743−752, 1995.
[3] Berthier, E., Beebe, D. J. *Lab Chip*, 3241− 3247, 2014.
[4] Du, Y., Hancock, M. J., He, J., Villa-Uribe, J. L., Wang, B.; Cropek, D. M., Khademhosseini. *Biomaterials*, 2686−2694, 2010.

MECHANICAL INSTABILITIES AND MULTI-FUNCTIONS OF SOFT ACTIVE STRUCTURES IN SOFT ROBOTS

Tiefeng Li[1,2,3a)], Yiming Liang [1], Yongbin Jin[1], Yuhan Xie [1], Tingyu Cheng[1] & Xuxu Yang [1]

[1]*Institute of Applied Mechanics, Zhejiang University, 38 Zheda Road, Hangzhou, Zhejiang 310027, China*
[2]*Soft Matter Research Center (SMRC), Zhejiang University, Hangzhou 310027, China*
[3]*Key Laboratory of Soft Machines and Smart Devices of Zhejiang Province, Hangzhou 310027, China*

<u>*Summary*</u> The natural animals and insects integrate muscles and skins providing excellent actuating and sensing functions. Inspired by the natural structure, we present various structures of dielectric elastomer (DE) elastomer with various characteristics such as integrated actuating and sensing, bi-stable actuation, and anisotropic actuation. The structure can deform when subjected to high voltage loading and generate corresponding output signal in return. We investigate the mechanical instabilities of the soft active structure of dielectric elastomer both theoretically and experimentally. It is noted that when applying high voltage, the actuating dielectric elastomer membrane deforms and the sensing dielectric elastomer membrane changes the capacitance in return. Based on the concept, finite element method (FEM) simulation has been conducted to further investigate the electromechanical behaviours and guide the structural design of the soft robot.

INTRODUCTION

Electro-active polymer (EAP) actuators have recently attracted increasing research interests due to their various performances. As a typical EAP, dielectric elastomer (DE) is one of the most promising electro-active polymer actuators because of its large deformation, light weight, high energy density, and rust free. When an electric field is applied through the thickness direction, a DE membrane expands its area and reduces its thickness. This electromechanical behaviour of DE material has been widely studied into various application including actuators, sensors and generators [1-5]. Specially, basing on the fact that electric properties such as resistance, capacitance change in accordance with the external forces, the ability to sense its position, deformation or force of dielectric elastomer has also been investigated [6-9]. Recently, numerous works have been done, including the dynamic response of the dielectric elastomer for capacitive sensing [6], a method to monitor capacitance change of the dielectric elastomer actuator during its operation [7], the resistance of electrode changes when actuating [8] and a dielectric elastomer actuator with self-sensing capability [9]. Various methods to actuate and sense the deformation or the displacement of the dielectric elastomer actuator can be applied into the smart structures. Mechanical investigations may further guide the design and optimization of the soft active material and structures [10-13].

SENSING AND ACTUATING

This paper presents a dielectric elastomer structure with integrated function of actuating and sensing Fig.1. Working principal is established to explain the experimental results. And the numerical simulation is also conducted, which corresponds well with the experimental results. This work provides a new method to design and fabricate the dielectric elastomer structure with both actuating and sensing performances, which has a variety of potential applications such as prosthetic sensing and physical monitoring. There are 10 layers of dielectric elastomer in the structure. The layers which are black, blue, yellow represent electrode, VHB4905 membrane, VHB9473 membrane respectively. VHB4905 membrane is worked as driven muscles, whereas VHB9473 membrane is employed to protect electrode and to avoid direct contact with high voltage. Fibers which are tightly sandwiched between elastomer membrane and electrode are shown as the white circles in the schematic. The right part that contains fibers is the actuating module of the structure, and the left part is sensing module correspondingly. Since VHB membrane is extremely sticky, actuating module and sensing module can tightly laminated.
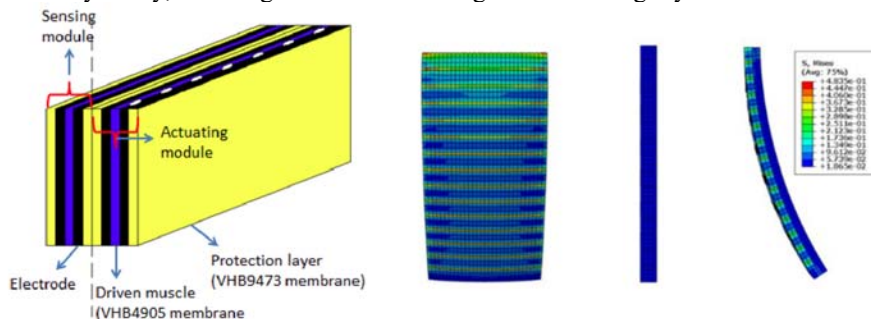
Figure 1. Images of the snap-through deformation process of the hydrogel structure

---

[a)] Corresponding author.   Email: litiefeng@zju.edu.cn

ELECTRO-MECHANICAL INSTABILITY

The DE active structures such as inflated elastomeric balloon and bi-stable beam are quite promising in the application of soft robot as elastomeric actuators and artificial muscles. We carry out both experiment and modelling, focusing on the pre-stretch effect on non-linear behaviours of inflated elastomeric balloons. In the experiment, the pre-stretched elastomeric balloon is subjected to air pressure while the ends are fixed with rigid ring. The shape evolutions of the telastomeric balloons are illustrated. An analytical model based on continuum mechanics is developed to investigate the inflation behaviour of the tubular balloons, and the analytical results agree well with the experimental observation. Analysis shows that snap-through instabilities may happen during the inflation of t. Pre-stretch along the axis of the balloon can suppress instability during inflation and regulate the reaction force along the axial direction. In the buckled structure of DE membrane integrated with rigid frame, fibers can be embedded into the DE membrane and integrate together with the soft active structure to enhance the performances of the soft active device. We demonstrate the effects of fibers in the planar actuator. The long fibers are parallel distributed with fixed spacing in the perpendicular direction. We use nylon fishing lines as the fibers with 80 mm in length and 0.3 mm in diameter. We attach several fibers on one side of the pre-stretched membrane and then put another pre-stretched membrane on the fiber and make the fiber sandwiched between two membranes, and then exclude the air between the two membranes. The DE structure with multi-functions and electromechanical instabilities can be applied in the soft robot..

CONCLUSIONS

We have investigated soft active structures driven by dielectric elastomer possessing characteristics of snap-through actuation, integrated actuating and sensing. The performances of the smart structures are explored with both experiments and FEM simulations. Pre-stretch and structural stiffness play important role before the smart structure is applied with voltage. The buckling curvature will increase while the pre-stretch increases or the structural stiffness decreases. Fiber-reinforced dielectric elastomer structure with integrated function of actuating and sensing can also be combined in to the soft active structure as a functional device.The sensing module deforms by the bending of the DE structure and changes its capacitance. By measuring capacitance variation, we can monitor the deformation of the DE laminates in return. Experiments and FEM simulation have been conducted to investigate the electro-mechanical behaviours of the structure.

ACKNOWLEDGMENTS

References

[1] Yoseph Bar-Cohen, "Electroactive Polymer (EAP) Actuators as Artificial Muscle: Reality, Potential and Challenges", *SPIE Press monograph*, 482, 2001.

[2] R. Pelrine, R. Kornbluh, Q. B. Pei, and J. Joseph, "High-speed electrically actuated elastomers with strain greater than 100%", *Science*, 287, 836, 2000.

[3] F. Carpi and D. De Rossi, "Contractile dielectric elastomer actuator with folded shape", *IEEE Trans. Dielectr. Electr. Insul.* 12, 835, 2005.

[4] G. Kofod, M. Paajanen, and S. Bauer, "Self-organized minimum-energy structures for dielectric elastomer actuators", *Applied Physics A: Materials Science & Processing*, 85,141, 2006.

[5] F. Carpi, G. Gallone, F. Galantini, and D. Rossi, "Silicone–poly(hexylthiophene) blends as elastomers with enhanced electromechanical transduction properties", *Adv. Funct. Mater.*, 18, 235–241, 2008.

[6] P. Sommer–larsen, J. Hooker, G. Kofod, K. West, M. Benslimane, P. Gravesen, "Response of dielectric elastomer actuators", *Proc. Smart Structures and Materials 2001: Electroactive Polymer Actuators and Devices(EAPAD)*, Vol. 4329, pp.157-163, 2001.

[7] K. M. Jung, K. J. Kim, H. R. Choi, "A Self-sensing Dielectric Elastomer Actuator", *Sensor and Actuator A*, published in electronic version, 2007.

[8] B. O'Brien, J. Thode, I.A. Anderson, E.P. Calius, E. Haemmerle and S. Xie, "Integrated extension sensor based on resistance and voltage measurement for a dielectric elastomer", *Proc. Smart Structures and Materials 2007: Electroactive Polymer Actuators and Devices(EAPAD)*, Vol. 6524, pp.6524-1–6524-15, 2007.

[9] Nguyen Huu Chuc, Doan Vu Thuy, Jonggil Park, Duksang Kim, Jachoon Koo, Youngkwan Lee, Jae-Do Namc and Hyouk Ryeol Choi, "A dielectric elastomer actuator with self-sensing capability ", *Proc. SPIE* Vol. 6927, 69270V, 2008.

[10] Xuanhe Zhao, Zhigang Suo, Method to analyze programmable deformation of dielectric elastomer layers. *Applied Physics Letters*, 93, 251902, 2008.

[11] T. Li, C. Keplinger, R. Baumgartner, S. Bauer, W. Yang, and Z. Suo, Giant voltage-induced deformation in dielectric elastomers near the verge of snap-through instability, J. *Mech. Phys. Solids* 61 2013, pp. 611–628.

[12] T. Li, Z. Zou, G. Mao, S. Qu, and M. Shi, Electromechanical bistable behavior of a novel dielectric elastomer actuator, *J. Appl. Mech.* 81 2014, 0410191.

[13] T. Li, W. Li, Z. Zou, Z. Hong, and S. Qu, Effects of stretching rate and size on the rupture of acrylic dielectric elastomer, *Int. J. Appl. Mech.* 2014.

ION-INDUCED SWELLING AND VOLUME PHASE TRANSITION OF POLYELECTROLYTE GELS

Yalin Yu, Chad M. Landis & Rui Huang[a]

Department of Aerospace Engineering & Engineering Mechanics, University of Texas, Austin, TX 78712, USA

<u>Summary</u> This paper presents a theoretical model for equilibrium swelling of polyelectrolyte gels immersed in ionic solutions. By varying the ion concentrations in the external solution, the polyelectrolyte gel may undergo a smooth transition in the swelling ratio or a discontinuous volume phase transition. The theoretical model is further extended for the cases with mixed solvents and compared closely with experiments.

INTRODUCTION

Polyelectrolytes are polymers that contain ionizable groups on the polymer chains. Immersed in an aqueous solution (e.g., water), the polymer network imbibes a significant amount of solvent and those ionizable groups dissociate into mobile charges (counter-ions) in the solvent and fixed charges on the polymer chains. As a result, a polyelectrolyte gel forms. Polyelectrolyte gels are sensitive to many stimuli, such as pH, temperature, ionic strength, electric field, and light. One of the most interesting phenomena is the volume phase transition of polyelectrolyte gels induced by various external stimuli. Instead of a smooth, continuous change of volume in response to a varying stimulus, a discontinuous, abrupt change of volume may occur at a critical condition, similar to the first-order phase transition. While the volume phase transition due to temperature change has been studied extensively, fewer studies have considered volume phase transition induced by the effect of salinity or ion concentration in the external solutions. Ohmine and Tanaka [1] observed in experiments that an ionized acrylamide gel underwent a discrete phase transition in equilibrium volume upon varying the salt concentration in an external solution. In this paper, we present a theoretical model that is capable of predicting equilibrium swelling of polyelectrolyte gels with both smooth and discrete transitions upon changing the ion concentration in external solutions.

THEORETICAL MODEL

Following Hong et al. [2], we write the free energy density of a polyelectrolyte gel as a function of the deformation gradient, the nominal electric displacement, and the nominal concentrations of the solvent and ions, including four parts due to stretching of the polymer network, mixing of the polymer and the solvent, mixing of the solvent and ions, and polarizing of the gel, respectively. It is assumed that the polymer network and the mobile particles (solvent molecules and ions) are incompressible at the molecular level, which is imposed as a kinematic constraint by using a Lagrange multiplier. The nominal electric field and the electrochemical potentials are then obtained from the free energy density function. To simplify calculations, we assume relatively low ion concentrations in the gel so that $J \approx 1 + vC^s$. The nominal concentrations of the ions in the gel can then be obtained explicitly as a function of the electrochemical potential and the volume swelling ratio J.

Next, by a Legendre transform, the free energy density of the gel is rewritten as a function of the deformation gradient, the nominal electric field, and the electrochemical potentials. The nominal stress in the gel is then obtained as the derivative of the free energy density function with respect to the deformation gradient, which includes an elastic part, an electrical part (Maxwell stress), and osmotic pressures of the solvent and ions. For homogeneous free swelling, the stress vanishes and the volume swelling ratio can be solved as a function of the chemical and electrochemical potentials.

When the gel reaches equilibrium with the external solution, the chemical potential of the solvent and electrochemical potentials of the ions in the gel equal to those in the external solution. We treat the external solution as an ionic liquid with a mixture of neutral solvent molecules (e.g., water) and positive/negative ions. The treatment is similar to that for polyelectrolyte gels, but the free energy density function contains only two parts, due to ion/solvent mixing and polarization. Assume an infinitely large reservoir such that the concentrations of the ions are fixed deep in the external solution (far away from the gel), where the electric potential is set to be zero and the solution is assumed to be electrically neutral and stress free. Under these conditions, the electrochemical potential for the ions is obtained as: $\mu^b = v\Pi_0 + kT \ln(vc_0^b)$, where c_0^b is the ion concentration in the external solution and $\Pi_0 = -kT \sum_b c_0^b$ is the osmotic pressure. Correspondingly, the chemical potential of the solvent is: $\mu^s = v\Pi_0$. Therefore, by changing the ion concentrations in the external solution, the chemical potential of solvent and the electrochemical potential of the ions change simultaneously, which leads to change of the equilibrium swelling of the gel.

RESULTS AND DISCUSSION

First consider a simple polyelectrolyte gel with two monovalent ions of opposite charges. The valence of the fixed charge is set to be -1. Let c_0 be the true concentration of the ions deep in the external solution. In this case, the electrical potential of

---

[a] Corresponding author. Email: ruihuang@mail.utexas.edu.

the gel (far away from the interface) can be obtained explicitly as a function of the volume swelling ratio (J) and the ion concentration. The equilibrium swelling ratio can then be solved by setting the stress to zero for free swelling. The result depends on two key parameters: the Flory-Huggins parameter χ and the nominal concentration of the fixed charge C_{fix}. Figure 1a shows the effect of χ for gels with $vC_{fix} = 0.02$ and $Nv = 0.001$. As the ion concentration changes in the external solution, three distinctive swelling behaviours of the polyelectrolyte gels can be identified: (i) a smooth transition when $\chi = 0.5$ or smaller (good solvents); (ii) a discontinuous volume phase transition when $\chi = 0.7$; and (iii) nearly no transition when $\chi = 0.9$ or larger (poor solvents). A phase diagram is constructed in Fig. 1b, showing that the discontinuous volume phase transition from the highly swollen phase to the collapsed phase occurs only within a narrow range of χ (around 0.7). This range depends on the fixed charge as shown in Fig. 1c. Interestingly, a minimum value of vC_{fix} is required for the discontinuous volume phase transition.
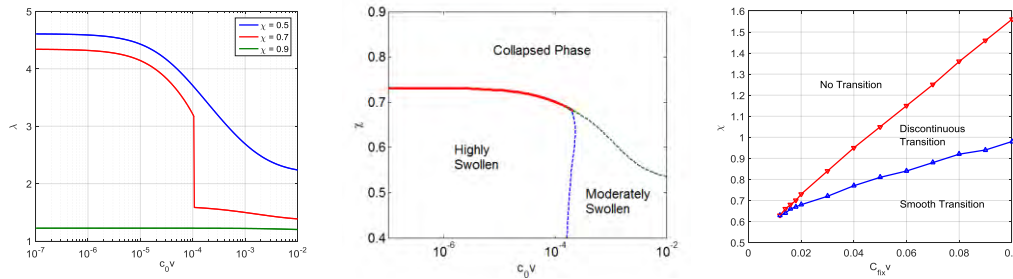
Figure 1. (a) Equilibrium swelling ratio as a function of ion concentration in the external solution; (b) A phase diagram; (c) Different transition behaviours in the two-parameter panel.

Next we take into account the effect of composition on the parameter χ by assuming $\chi = \chi_0 + \chi_1/J$. By varying the two parameters, χ_0 and χ_1, the equilibrium swelling of the gel may undergo a smooth or a discontinuous transition. In the experiments by Ohmine and Tanaka [1], partially ionized acrylamide gels with acrylic acid groups (–COOH) were immersed in a mixed solution of water, acetone, and salt with varying compositions. To compare with the experiments, we extend the model for a mixed solvent with two components (water and acetone) by using an effective interaction parameter that depends on the acetone concentration as: $\chi = \chi^a \varphi^a + \chi^b \varphi^b$. For the polyelectrolyte gel immersed in the mixed solution with NaCl, there are four types of mobile ions: H^+, OH^-, Na^+ and Cl^-. Deep in the external solution, the concentrations of Na^+ and Cl^- are identical and set by the salt concentration c_0. The concentrations of H^+ and OH^- are determined by pH, which is set to be 7. Under these conditions, the chemical and electrochemical potentials are all determined as a function of the salt concentration. Figure 2a shows the equilibrium swelling ratio of the gel as a function of NaCl concentration in the mixed solutions with different acetone concentrations. When the acetone concentration is low (0-40%), the equilibrium swelling ratio undergoes a smooth transition as the salt concentration changes. With relatively high acetone concentration (50-60%), a discontinuous volume phase transition occurs, whereas no swelling transition is observable for 70% acetone concentration. These results agree remarkably well with the experiments. To further test the model, we consider mixed solutions with $MgCl_2$ where the positive Mg^{2+} ions are not monovalent. In this case, the condition of electroneutrality leads to a more complicated relation between the ion concentrations in the gel and the electrical potential. Nevertheless, the equilibrium swelling ratio can be determined numerically by solving two coupled nonlinear algebraic equations. As shown in Fig. 2b, the result is qualitatively similar to Fig. 2a, but the discontinuous transition occurs at lower acetone concentrations (40-50%). In particular, for 50% acetone concentration, the critical salt concentration for the volume phase transition is about three orders of magnitude lower than that for the monovalent salt NaCl. This again agrees with the experiments.
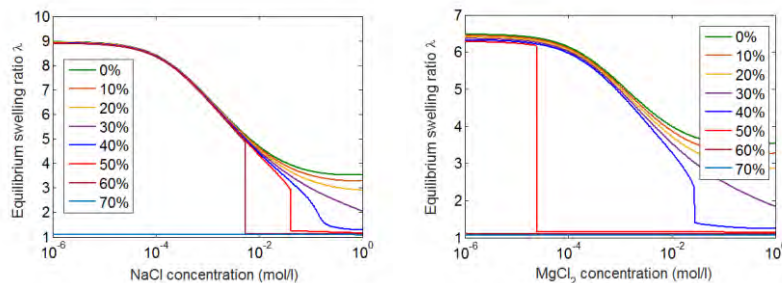
Figure 2. Equilibrium swelling ratio as a function of salt concentration in a mixed solution with (a) NaCl and (b) $MgCl_2$.

References
[1] Ohmine, I., Tanaka, T. , J. Chem. Phys. **77**, 5725-5729 (1982).
[2] Hong, W., Zhao, X., Suo, Z., Journal of the Mechanics and Physics of Solids **58**, 558-577 (2010).

COMBINED MODELING AND EXPERIMENTS OF POLYMERIC GELS

Claudio V. Di Leo[1] and <u>Shawn A. Chester</u>[*2]

[1]*School of Aerospace Engineering, Georgia Institute of Technology, Atlanta, Georgia, USA*
[2]*Mechanical Engineering, New Jersey Institute of Technology, Newark, New Jersey, USA*

<u>Summary</u> The literature on polymeric gels is burgeoning at a remarkable pace. However, the majority of the mechanics work has been directed toward modeling and computational aspects, and not nearly as much on validation. This work overviews recent research on a combined experimental and modeling effort on polymeric gels, from a mechanics based framework. This integrated approach leads to a data set useful to mechanicians to further refine those models found in the literature. Most importantly, it shows some serious faults in current modeling efforts.

INTRODUCTION

An elastomeric gel is no more than a polymer network swollen with a suitable solvent. Many gels can absorb large quantities of solvent, leading to a volumetric swelling far beyond its initial volume. This swelling allows for gels to be exploited in a variety of applications, including actuation and sensing in microfluidics, drug delivery and tissue engineering, and packers for sealing in oilfields. Correspondingly the literature has seen an explosion of interest in recent years for this class of materials (for brevity, see [2] and references therein). However, recent evidence indicates that current constitutive models may not be adequate in describing the real coupled deformation-diffusion behavior of gels [4].

The purpose of this work is to develop an integrated research approach that includes combined modeling and experiments of polymeric gels. This combined approach is used in order to fully characterize the coupled deformation-diffusion behavior of polymeric gels and understand the mechanisms that drive the material behavior.

MODELING AND EXPERIMENTS

For the modeling portion we closely follow our recently published work [1, 2] which is summarized here. We denote the solvent concentration per unit reference volume by c_R, and per unit current volume by c. We employ the decomposition

$$\mathbf{F} = \mathbf{F}^e \mathbf{F}^s, \tag{1}$$

of the deformation gradient into elastic and swelling parts, where $\mathbf{F}^s = (J^s)^{1/3} \mathbf{1}$, with $J^s = 1 + \Omega c_R$, is the swelling distortion, and Ω the molar volume of the solvent. Further, we define the polymer volume fraction $\phi = (1 + \Omega c_R)^{-1}$, such that $\phi = 1$ is a fully dry polymer, and $\phi < 1$ is a swollen gel. We note that due to the decomposition (1), we have $\mathbf{B} = \phi^{-2/3} \mathbf{B}^e$ so that the state of stretch is composed of both swelling and elastic deformation. The final form of the Cauchy stress is given by

$$\mathbf{T} = J^{-1} \left[G\mathbf{B} - P\mathbf{1} \right], \tag{2}$$

where the shear modulus G is stretch dependent and of the form $G = G_0 \zeta$. With $\zeta = \left(\frac{\lambda_L}{3\bar{\lambda}} \right) \mathcal{L}^{-1} \left(\frac{\bar{\lambda}}{\lambda_L} \right)$, and $\bar{\lambda} = \sqrt{\operatorname{Tr} \mathbf{B}/3}$, a scalar measure of the three-dimensional state of stretch, which includes both swelling and elastic stretching. Here $\mathcal{L}^{-1}$ is the inverse of the Langevin function given by $\mathcal{L}(\bullet) = \coth(\bullet) - 1/(\bullet)$. Also, G_0 is the initial shear modulus, and λ_L is the locking stretch. These two parameters are the only parameters required to fully characterize the "dry" mechanical response of the material.

Turning attention to the diffusion, the fluid flux is assumed isotropic and proportional to the gradient in chemical potential,

$$\mathbf{j} = -m \operatorname{grad}\mu, \quad \text{with} \quad m = \frac{Dc}{R\theta}, \quad \text{and} \quad \mu = \mu^0 + R\theta \left(\ln(1 - \phi) + \phi + \chi\phi^2 \right) - \Omega G_0 \phi + \Omega P \phi. \tag{3}$$

Here, R is the gas constant, θ the absolute temperature, D the diffusivity which may be constitutively prescribed, and μ is the chemical potential. The key parameter in the chemical potential is χ, the interaction parameter (sometimes called the Flory parameter), which represents the dis-affinity between the solvent and the polymer network. The final form of diffusion of the fluid flux takes the form $\dot{\phi} = J\Omega\phi^2 \operatorname{div}\mathbf{j}$.

To verify the constitutive forms, and obtain the material parameters appearing in the theory an experimental program was undertaken. Summarizing, the set of material properties to be determined are $\{G_0, \lambda_L, D, \chi\}$.

Dry tension
Dry tension tests, including loading and unloading, were carried out to determine the baseline "dry" material behavior. The tests were carried out quasi-statically at room temperature on flat dog-bone samples with a gauge section 0.25 in wide and 0.22 in thick. The axial deformation was measured using a non-contact digital image correlation system.

*Corresponding author. Email: `shawn.a.chester@njit.edu`

Figure 1a shows a few snapshots of the specimen in the virgin state, as well as the fully stretched ($\lambda = l/l_0 \approx 2.4$) state. Also, Figure 1b shows the measured behavior. Clearly from Figure 1b we can see that this material is essentially hyperelastic with very little hysteresis or time dependence (not all results are shown here). Using the model described above, with $G_0 = 0.056\,\mathrm{MPa}$ and $\lambda_L = 3.9$, the corresponding fit shown Figure 1b.

a)   b)
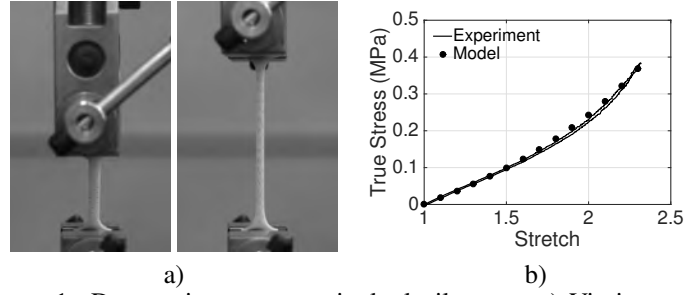
Figure 1: Dry tension tests on vinylpolysiloxane. a) Virgin state and $\lambda = 2.4$. b) Measured true stress stretch response.

Free swelling

Free swelling experiments were performed to obtain the parameters associated with the equilibrium chemistry. Specifically, with the elastic parameters known, after equilibrium stress free swelling, we have $\mu = \mu^0$ everywhere in the body, which we may exploit to find χ. Assuming equilibrium conditions, we have $0 = \ln(1-\phi_e) + \phi_e + \chi\phi_e^2 + \frac{\Omega G_0}{R\theta}\left(\zeta\phi_e^{1/3} - \phi_e\right)$. Then, upon measuring the initial and swollen shapes, we may determine ϕ_e in this freely swollen equilibrium state. Figure 2a,b show the initial and swollen specimen, respectivly. Based on the change in geometry we find the dry volume is $7912.2\,\mathrm{mm}^3$, the swollen volume $34050\,\mathrm{mm}^3$, so that $J_e = 4.3035$, and $\phi_e = 1/J_e = 0.2324$, and correspondingly compute $\chi = 0.5682$ using $\Omega = 1.3162 \times 10^{-4}\,\mathrm{mol/m}^3$ for hexane.

Further experiments were performed on various compositions of PDMS swollen in Pentane. Fig. 2c shows the mechanical locking stretch λ_L, determined through dry tension tests, as well as the steady-state swelling stretch λ_{ss} determined from free swelling experiments as a function of PDSM composition. It is clear that a major discrepancy exists in these results as the measured swelling stretch is larger than the measured locking stretch, an unphysical condition.

a)   b)   c)
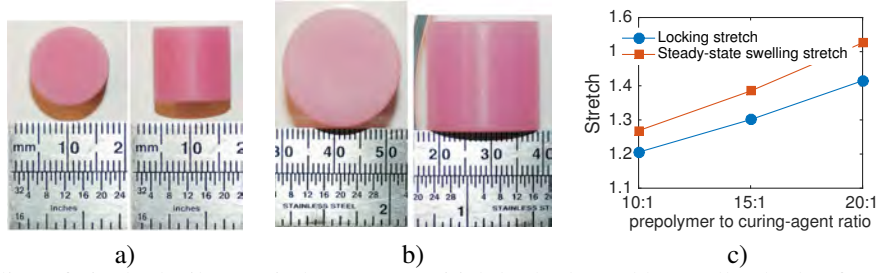
Figure 2: Free-swelling of vinylpolysiloxane in hexane: a) Initial dry body, and b) swollen body after 48 hours in hexane. c) Locking and swelling stretches for PDMS in pentane vs. gel composition.

Constrained Swelling

Obtaining repeatable data to measure the diffusivity is difficult, and still an open area of research. One method of obtaining data regarding the transient behavior of the polymer consists of swelling a gel against a platen and measuring the resulting force as a function of time. Results from such experiments are shown in Fig. 3 for PDMS of various compositions swollen in Pentane along with finite-element simulation results replicating the experiments. Clearly the currently used functional form for the diffusivity is incapable of capturing the correct, experimentally measured, transient and furthter consideration needs to be given to the constitutive form of the diffusivity D.
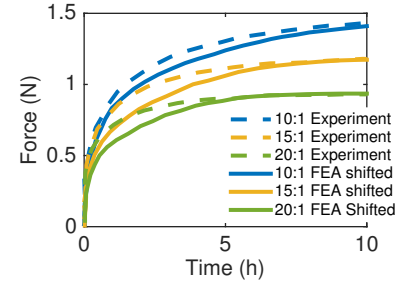
Figure 3: Constrained swelling force vs. time for PDMS swollen in pentane at various compositions.

CONCLUSIONS

We have initiated a combined experimental and modeling effort toward better understanding the behavior of polymer gels. Our results to date show that current constitutive models are in need of improvement. Work is underway to resolve the discrepancies between the experiments and models, and also examine other polymer/solvent systems.

References

[1] Chester, S. A., and Anand, L.: A coupled theory of fluid permeation and large deformations for elastomeric materials. Journal of the Mechanics and Physics of Solids 58:1879-1906, 2010.

[2] Chester, S. A., Di Leo, C. V., and Anand, L.: A finite element implementation of a coupled diffusion-deformation theory for elastomeric gels. International Journal of Solids and Structures 52:1-18, 2015.

[3] Doi, M. Introduction to Polymer Physics. Clarendon Press, 1996.

[4] Lou, Y., Robisson, A., Cai, S., and Suo, Z.: Swellable elastomers under constraint. Journal of Applied Physics 112:034906, 2012.

On the effects of cavitation in hydrogel–based structures

Paola Nardinocchi[*1] and Luciano Teresi[2]

[1]*Dipartimento di Ingegneria Strutturale e Geotecnica, Sapienza Università di Roma, 00184 Roma, ITALY*
[2]*Dipartimento di Matematica e Fisica, Università Roma Tre, 00146, Roma, ITALY*

Summary Cavitation is often observed in soft materials. Many studies focused on cavitation in elastomers, and more recently also in hydrogels, where drying–induced cavitation can determine fractures. In this paper, we investigate cavitation in hydrogel–based structures with the aim to highlight the physical principles which drive a few unique mechanisms in Nature world, which view cavitation as a tool to generate fast movements.

INTRODUCTION

Soft active materials are largely employed in Nature to realise mechanisms whose specific function is triggered by specific stimuli [1, 2]; they are also used to realize man–made devices (*actuators*), where deformations and displacements are triggered by a wide range of external stimuli such as electric field, pH, temperature, and solvent absorption [3, 4, 5, 6]. The effectiveness of these actuators critically depends on the capability of achieving prescribed changes in their shape and size and on the rate of changes. In particular, in gel–based actuators, the shape of the structures can be related to the spatial distribution of the solvent inside the gel, to the magnitude of the solvent uptake (refusal), and to the rate of solvent uptake (refusal) rate. Currently, several approaches to the shape control of swellable materials are being pursued, which involve materials in the form of thin non–homogeneous sheets realized through a controlled assembly of different gels which may be isotropic or anisotropic [10, 11, 12, 13].

The present study focus on cavitation in hydrogels as a tool to generate fast movements in hydrogel–based structures. The starting point is the observation of the cavitation–triggered catapult of fern sporangia, whose function is the realisation of a perfect dispersal mechanism. Therein, the key structural element is the *annulus*, which can be viewed as a curved beam composed by soft material organized in cells separated by stiffer walls. We start by modelling and implementing via a finite element code the mechano–chemical processes occurring in a mechanical analog of a single cell of the anulus: swelling, de–hydration, and building up of water tension up to a critical value corresponding to cavitation; and illustrates in the following the key idea behind our modelling through a simple toy problem.

A MECHANICAL ANALOG

The first step of our work, illustrated in the present abstract, refers to a mechano–chemical toy problem which can be easily solved, and is useful to illustrate the key idea behind our model. Our starting point is the multiphysics model presented and discussed in [14], where three different states of a gel body were introduced: the dry state $\mathcal{B}_d$, a swollen and stress–free state $\mathcal{B}_o$, and the actual state $\mathcal{B}_e$. Within a classical Flory–Rehner thermodynamic contex, the constitutive equation for the stress $\mathbf{S}_d$ at the dry configuration $\mathcal{B}_d$, from now on denoted as dry–reference stress, and the chemical potential μ are:

$$\mathbf{S}_d = G\mathbf{F}_d - p\mathbf{F}_d^\star \quad \text{and} \quad \mu = \mu(J_d) + \Omega p, \text{ with } \mu(J_d) = RT\Big(\log\frac{J_d - 1}{J_d} + \frac{1}{J_d} + \frac{\chi}{J_d^2}\Big), \tag{.1}$$

being $\mathbf{F}_d$ the deformation gradient from $\mathcal{B}_d$ to $\mathcal{B}_e$ and $J_d = \det\mathbf{F}_d$; moreover, G ([G] =J/m^3), Ω ([Ω] =mol/m^3), R ([R] =J/Kmol), T ([T] = K), and χ are the shear modulus of the gel, the solvent molar volume, the universal gas constant, the temperature, and the Flory parameter, respectively. The swollen and stress–free state $\mathcal{B}_o$ is attained from $\mathcal{B}_d$ for $\mathbf{F}_d = \lambda_o\mathbf{I}$; in this case, it holds $G\mathbf{F}_o - p\mathbf{F}_o^\star = \mathbf{0}$ and $\mu = \mu(J_o) + \Omega p = \mu_o$, with μ_o the value of the bath's chemical potential which completely determines the corresponding swelling ratio λ_o.

We consider a cubic gel whose freely swollen state $\mathcal{B}_o$ is a cube with sides of length L_o and faces anchored through linear elastic springs at a solid and permeable container (see figure 1 (left panel)); at $\mathcal{B}_o$ springs are relaxed. Due to a change in the chemical potential of the bath, from μ_o to μ_e, a further deformation process arises; the corresponding deformation gradient $\mathbf{F}$ from $\mathcal{B}_o$ to the actual state $\mathcal{B}_e$ is determined by $\mathbf{F} = \mathbf{F}_d\mathbf{F}_o^{-1}$. Depending on the boundary constraints, the latter deformation process can have different characteristics. In our toy problem, due to the uniformity of the elastic springs over the boundary, we assume that $\mathbf{F}$ can be represented as an isotropic deformation process of homogeneous intensity λ: $\mathbf{F} = \lambda\mathbf{I}$; we also assume that it is controlled by the chemical potential μ_e of the solvent's bath and by the stiffness κ_o of the boundary springs. The swollen–reference stress $\mathbf{S}$ corresponding to $\mathbf{F}$, the *push–forward* of the dry–reference stress $\mathbf{S}_d$,

$$\mathbf{S} = \frac{G}{J_o}\mathbf{F}\mathbf{F}_o\mathbf{F}_o^T - p\mathbf{F}^\star, \tag{.2}$$

*Corresponding author. Email: paola.nardinocchi@uniroma1.it

is homogeneous and the corresponding balance equations of forces prescribe that $\mathbf{S} = \sigma_e \mathbf{F}^\star$. The corresponding equation of chemical equilibrium prescribes that

$$\mu(\lambda_o^3 \lambda^3) + \Omega p = \mu_e \,. \tag{.3}$$

When the chemical potential is reduced, that is $\mu_e < \mu_o$, the gel expels solvent and shrinks, so reducing its volume (see figure 1 (left panel)); springs elongate, thus generating an uniform tension $\sigma_e = -k_o \varepsilon$ on the faces, being $= \varepsilon = \lambda - 1$.

With this, the hydrogel goes from a stress–free swollen state $\mathcal{B}_o$ (blue dot in figure 1 (right panel)) to a shrunken and under tension state $\mathcal{B}_e$, determined by the intersection between the coloured iso–chemical potential lines and the black straight line in figure 1 (right panel). The final state and the uniform tension'value depend on the new value μ_e of the chemical potential through the equations (.2)–(.3) which involve λ, and on the stiffness κ_o of the springs. When $\sigma = \sigma_{cr}$ (red dot on the critical iso–chemical potential line) the solvent inside the gel begins cavitation, hydrogel volume increases, and the spring shorten releasing the elastic energy previously stored.
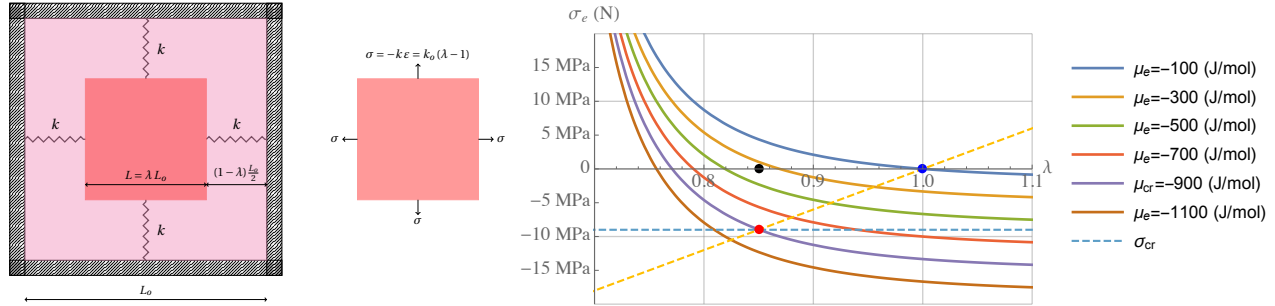
Figure 1: Left: We consider a cubic gel in a free swollen state (light red) whose faces are anchored through linear springs at a solid container (shaded frame). When the chemical potential is reduced, the gel expels solvent, reduces its volume (red square), and the springs elongate, thus generating a tension on the faces. Center: The de-swollen cube is under uniform tension whose value depends on the new value of the chemical potential through λ, and the stiffness of the spring. Right: Pressure-strain curves for different values of the external chemical potential μ_e. We consider a case for which the free-swollen reference (blue point) is realized with $\mu_e = -100$ (J/mol). By decreasing μ_e, the cube shrinks following the line $p = -k_o \varepsilon = k_o(\lambda - 1)$. When $\sigma = \sigma_{cr}$ (red point) the solvent inside the gel begins cavitation.

CONCLUSIONS

The toy problem illustrated above contains the key idea which is behind our investigation about the effects of cavitation on hydrogel–based systems. More complex deformation processes may occur when a series of units as the one shown in figure 1 is shown, and the contribution of the elastic walls surrounding the gel is not uniform.

References

[1] Burgert I., Fratzl P.: Actuation systems in plants as prototypes for bioinspired devices. Philos. Trans. R. Soc. A, 367:1541–1557, 2009.

[2] Noblin X., Rojas N.O., Westbrook J., Llorens C., Argentina M., Dumais J.: The Fern Sporangium: A Unique Catapult. Science 335, 1322, 2012.

[3] Dai S., Ravi P., Tam K.C.: Thermo– and photo–responsive polymeric systems. Soft Matter 5:2513–2533, 2009.

[4] Wallmersperger T., Keller K., Krplin B., Guenther M., Gerlach G.: Modeling and simulation of pH–sensitive hydrogels. Colloid Polym. Sci. 289:535–544, 2011.

[5] Kim J., Hanna J.A., Hayward R.C., Santangelo C.D.: Designing Responsive Buckled Surfaces by Halftone Gel Lithography. Soft Matter 8:2375–2381, 2012.

[6] Nardinocchi P., Pezzulla M.: Curled actuated shapes of ionic polymer metal composites strips. J. Appl. Phys. 113:22906, 2013.

[7] Wheeler T.D. and Stroock A.D.: Stability Limit of Liquid Water in Metastable Equilibrium with Subsaturated Vapors. Langmuir 25(13):7609–7622, 2009.

[8] Wang H., Cai S.: Drying-induced cavitation in a constrained hydrogel. Soft Matter 11(6):1058–1061, 2015.

[9] Wang H., Cai S.: Cavitation in a swollen elastomer constrained by a non–swellable shell. Journal of Applied Physics 117, 154901, 2015.

[10] Lucantonio A., Nardinocchi P., Pezzulla M.: Swelling-induced and controlled curving in layered gel beams. Proc. R. Soc. A 470:20140467, 2014.

[11] Nardinocchi P., Pezzulla M., Teresi L.: Anisotropic swelling of thin gel sheets. Soft Matter 11:1492, 2015.

[12] Nardinocchi P., Pezzulla M., Teresi L.: Steady and transient analysis of anisotropic swelling in fibered gels. Journal of Applied Physics 118:244904, 2015.

[13] Pezzulla M., Shillig S.A., Nardinocchi P., Holmes D.P.: Morphing of geometric composites via residual swelling. Soft Matter 11:5812, 2015.

[14] Lucantonio A., Nardinocchi P., Teresi L.: Transient analysis of swelling-induced large deformations in polymer gels. Journal of the Mechanics and Physics of Solids 61:205–218, 2013.

ON PRESSURE-DRIVEN FLOW THROUGH A GEL-FILLED CHANNEL

Fernando P. Duda [*1], Angela C. Souza[2], and <u>Eliot Fried</u>[3]

[1]*Programa de Engenharia Mecanica - COPPE, Universidade Federal do Rio de Janeiro, Rio de Janeiro, Brasil*
[2]*Programa de Engenharia Mecanica - TEM, Universidade Federal Fluminense, Niteroi, Brasil*
[3]*Mathematical Soft Matter Unit, Okinawa Institute of Science and Technology Graduate University, Okinawa, Japan*

Summary In this paper, we consider the problem of pressure-driven fluid flow through a gel-filled channel. This subject, which is relevant to many areas, has been addressed by several authors. Our interest here is to investigate how the network elastic response affects the solvent flow profile under steady-state conditions. We show that there is a class of elastic materials for which the flow profile is not affected by the applied pressure gradient. This class includes both neo-Hookean and Mooney materials but excludes Gent materials.

INTRODUCTION

A polymer gel is a two-component material composed of a cross-linked polymer network, which is usually described as an elastic, isotropic and incompressible solid, and an incompressible fluid, solvent for short, that permeates the interstices of the network. Such materials exhibit unusual and complex phenomena as a result of the coupling between large deformation and fluid permeation. In this paper, we study the problem of pressure-driven fluid flow through a gel-filled channel. This problem has been investigated by several authors to investigate, for instance, the phenomenon of pressure-induced channel formation (Cogan & Keener (2005)) . This work builds upon Duda, Souza & Fried (2010). Due to lack of space, details will be omitted.

PRELIMINARIES

Solvent permeation in polymer gels is governed by a set of equations comprised by the constraint of local volume preservation, which represents the conventional assumption that the solid and solvent are both incompressible, and a pair of field equations that describe the mechanical force and solvent content balances. These equations are conveniently organized as follows:

$$\det \mathbf{F} = \phi_0/\phi, \quad \operatorname{div} \mathbf{T} = \mathbf{0}, \quad \operatorname{div}(\upsilon \boldsymbol{\jmath} + \mathbf{v}) = 0. \tag{1}$$

Here and henceforth, $\mathbf{F}$ is the deformation gradient, ϕ_0 and ϕ are the polymer volume fractions in the reference and actual configurations, υ is the volume occupied by an individual solvent molecule, $\mathbf{T}$ is the Cauchy stress tensor, $\boldsymbol{\jmath}$ is the solvent flux per unit spatial area, and $\mathbf{v}$ is the network velocity field. External body forces, inertial effects, and solvent supply are neglected here.

From the constitutive point of view, the theory is fully specified by the response functions $\hat{\psi}$ and $\hat{\mathbf{M}}_s$ determining the free energy density ψ and the mobility tensor $\mathbf{M}_s$. Hereafter we suppose that $\hat{\psi}$ incorporates three contributions: the energy of the "unmixed" pure solvent; the isotropic elastic energy due to network deformation; and the energy of mixing. Invoking the Frenkel–Flory–Rehner hypothesis, we assume that the latter two contributions are additive and separable. As for the mobility, we assume a concentration-depedent isotropic response. It then follows that

$$\hat{\psi}(\mathbf{F}, c) = \mu_0 c + \hat{\psi}_e(I_1, I_2) + \hat{\psi}_m(c), \quad \mathbf{M}_s = \hat{m}(c)\mathbf{I}, \quad \hat{m}(c) > 0, \tag{2}$$

where μ_0 is a reference chemical potential, $c = (\det \mathbf{F} - \phi_0)/\upsilon$ is the number of solvent molecules per unit reference volume, and $I_1 = \operatorname{tr} \mathbf{B}$ and $I_2 = (I_1^2 - \operatorname{tr} \mathbf{B}^2)/2$ are the first and second principal invariants of the left Cauchy-Green tensor $\mathbf{B} = \mathbf{F}\mathbf{F}^\top$. Notice that both $\hat{\psi}_m$ and $\hat{m}$ can be viewed as a function of ϕ or $I_3 = \det \mathbf{B}$, the third invariant of $\mathbf{B}$. With these constitutive choices, it can be shown that $\mathbf{T}$ and $\boldsymbol{\jmath}$ can be written as

$$\mathbf{T} = \mathbf{T}_{\mathrm{n}} - p\mathbf{I}, \quad \boldsymbol{\jmath} = -\upsilon\hat{m}(c)\operatorname{grad}p \tag{3}$$

where

$$\mathbf{T}_{\mathrm{n}} = \beta_0\mathbf{I} + \beta_1\mathbf{B} + \beta_{-1}\mathbf{B}^{-1} - \pi\mathbf{I}, \quad \pi = -(\partial\hat{\psi}_m/\partial c)/\upsilon, \tag{4}$$

and

$$\beta_0 = 2I_2\alpha_2/\sqrt{I_3}, \quad \beta_1 = 2\alpha_1/\sqrt{I_3}, \quad \beta_{-1} = -2\sqrt{I_3}\alpha_2, \tag{5}$$

with $\alpha_1 = \partial\hat{\psi}_e/\partial I_1$ and $\alpha_2 = \partial\hat{\psi}_e/\partial I_2$. The quantities p and π are often called the fluid and osmotic pressures (e.g. Doi (2013)). Thus, the total Cauchy stress $\mathbf{T}$ results from two contributions, one due to the network, $\mathbf{T}_{\mathrm{n}}$, and other due to the solvent, $-p\mathbf{I}$. By its turn, the network stress arises from network elasticity and the osmotic pressure.

---

*Corresponding author. Email: duda@mecanica.coppe.ufrj.br

PRESSURE-DRIVEN FLOW THROUGH A GEL-FILLED CHANNEL

Consider the space between two infinitely long parallel plates separated by a gap $2d$ and completely filled by a gel which is fixed to and impermeable at the plates. We introduce a Cartesian coordinate system with the x-axis chosen parallel to the flow, the y-axis orthogonal to the plates, and z-axis orthogonal to the (x, y)-plane. We take the plates to be located at $y = 0$ and $y = 2d$. Suppose that the gel is in a stress-free state with polymer volume fraction constant and equal to ϕ_0. Then, a pressure gradient a is applied causing the solvent to flow through the gel. Our interest here is to investigate the influence of the gel properties on the characteristics this flow under steady-state conditions.

Specifically, we suppose that the pressure p is given up to an arbitrary and constant pressure p_0, that is,

$$p(x, y) = -ax + p_0, \tag{6}$$

with the constant a given. Taking $(1)_3$ into account, this implies that the x-component of the solvent flux $\jmath$ is given by $j_x = \hat{m}(\phi)a$, whereas the remaining components vanish. Since the the solvent flux is fully characterized by j_x, its characteristics depend on the material function $\hat{m}$ and the polymer fraction distribution ϕ, which needs to be determined by invoking the interaction between mechanics and permeation. This issue is discussed in what follows.

We begin by assuming the gel undergoes a special time-independent deformation in which the spatial (x, y, z) and referential (X, Y, Z) coordinates of a gel particle are related by $X = x + f(y)$, with f symmetric with respect to the central line between the two plates, $Y = g(y)$, and $Z = z$. Since the gel is fixed to the plates, the functions f and g must obey the boundary conditions $f(0) = f(2d) = 0$, $g(0) = 0$, and $g(2d) = 2d$. A simple calculation shows that the deformation gradient $\mathbf{F}$ can be viewed as the result of the superimposition of an uniaxial extension with stretch $\eta = 1/g'$ on a simple shear with amount $\gamma := -f'/g'$. In this case, the incompressibility constraint imposes that $\phi = \phi_0/\eta$ which in turn yields that ϕ can depend on y only. This implies, along with the fact that $\mathbf{v} = \mathbf{0}$ and that j_x is the only non-null component of $\jmath$, that the solvent content balance $(1)_3$ is trivially satisfied in the case under consideration. Further, as a consequence of the boundary condition on g, it is easy to see that η must satisfy the condition

$$2d = \int_0^{2d} (1/\eta(y)) \, \mathrm{d}y. \tag{7}$$

We now observe that the mechanical force balance $(1)_2$ can be written as $\operatorname{div} \mathbf{T}_\mathrm{n} = \operatorname{grad} p$ which, under the conditions discussed in this section, implies the following equations for the network shear and normal stresses τ_{xy}^n and σ_y^n:

$$\tau_{xy}^\mathrm{n}(\gamma(y), \eta(y)) = -a(y - d), \quad \sigma_y^\mathrm{n}(\gamma(y), \eta(y)) = k, \tag{8}$$

where k is constant,

$$\tau_{xy}^\mathrm{n}(\gamma, \eta) = 2\gamma(\alpha_1(I_1, I_2) + \alpha_2(I_1, I_2)), \quad \sigma_y^\mathrm{n}(\gamma, \eta) = 2\eta(\alpha_1(I_1, I_2) + 2\alpha_2(I_1, I_2)) - \pi(\eta), \tag{9}$$

$I_1 = 2 + \gamma^2 + \eta^2$, and $I_2 = 1 + \gamma^2 + 2\eta^2$.

The problem under investigation here consists in solving (7) and (8) for $\gamma(y)$, $\eta(y)$ and k. Once this problem is solved, ϕ is obtained via the relation $\phi = \phi_0/\eta$ and the solvent flow via $j_x = \hat{m}(\phi)a$. The main results are as follows. When a pressure gradient is applied, the shear stress τ_{xy}^n is developed in the network to ensure mechanical equilibrium. This stress is accompanied by the amount of shear γ, the determination of which requires the knowledge of the "shear modulus" $2(\alpha_1 + \alpha_2)$. This in turn is a function of γ and η through I_1 and I_2. On the other hand, the polymer volume fraction ϕ is obtained by using $\phi = \phi_0/\eta$, with η being obtained by solving $(8)_2$. This equation does not involve γ wherever $\alpha_1 + 2\alpha_2$ is constant. For this class of materials, it is immediate to see that the polymer volume fraction ϕ, and hence the flow profile, is not affected by the pressure gradient a. A simple calculation shows that both neo-Hookean and Mooney elastic materials belong to this class of materials, whereas Gent elastic materials do not.

CONCLUSIONS

We have shown that the shear stress τ_{xy}^n is a function of the pressure gradient a. Whether the same conclusion applies or not to the normal stress σ_y^n depends on the elastic response. When it does not apply, the polymer volume fraction, and hence the flow profile, is not affected by the pressure gradient. This is the case for both neo-Hookean and Mooney elastic materials.

References

[1] Duda F.P., Souza A.C., Fried E.: A theory for species migration in a finitely strained solid with application to polymer network swelling. J. Mech Phy Sol 58:515-529, 2010.

[2] Cogan N.G., Keener J.P.: Channel formation in gels. SIAM J.Appl Math 65:1839-1854, 2005.

[3] Doi M.: Soft Matter Physics. Oxford University Press, 2013.

ELASTOCAPILLARY SWELLING: WHEN COALESCED STRUCTURES CURL APART

P.-T. Brun[*1], Douglas P. Homes [2], Anupam Pandey[3], and Suzie Protière[4]

[1]*Department of Mathematics, Massachusetts Institute of Technology, Cambridge, Massachusetts, USA*
[2]*Department of Mechanical Engineering, Boston University, Massachusetts, USA*
[3]*Physics of Fluids Group, University of Twente, Enschede, NL*
[4]*IJLRA-CNRS, Université Pierre et Marie Curie, Paris, FR*

Summary We consider the elastocapillary rise between swellable structures using a favorable solvent. We study the elastocapillary rise and subsequent swelling–induced bending, and characterize the dynamic deformations and resulting equilibrium configurations for various beam geometries. Our analysis highlights the importance of two characteristic length scales, and uses these lengths to predict both the elastocapillary rise and the critical curvature for peeling. We predict the transition between coalescence dominated beams and bending dominated beams using a balance of bending, stretching, and surface energies, and use a relaxed constraint on Euler's elastica to describe the fluid ratcheting.

INTRODUCTION

Fluid-structure interactions occur across many length scales within synthetic and biological systems. At large scales, inertial flows and fluid weight can cause substantial structural deformations, while at small length scales, surface forces may dominate a material's deformation. In addition to the forces that a fluid exerts externally onto a flexible structure, the diffusion of a favorable solvent into the material's elastic network can cause substantial swelling-induced deformations. Balancing the relevant energies in each problem leads to an elastocapillary length scale [1, 2], beyond which the fluid's surface tension will dramatically deform it, and an elastoswelling length scale, beyond which swelling by the fluid will cause significant bending. Capillary rise is a classical problem dating back to Leonardo da Vinci, and the description of the diffusive dynamics of the wetting front is attributed to Bell & Cameron, Lucas, and Washburn. The coupled problem of capillary rise between flexible sheets has received attention rather recently [1], with consideration given to the static equilibrium shapes [3] and dynamic imbibition [4, 5, 6] from a fluid bath and fluid droplets. Study of the equilibrium swelling of rubber has classical ties to polymer physics, and its theoretical and experimental origins begin with Flory & Rehner and Treloar. Recent work has focused on the dynamic, swelling-induced deformations that occur when a fluid swells a structure in a non-uniform manner, causing bending [7]. The coupled problem of capillary rise between swellable, flexible structures is new to our knowledge, yet is relevant due to the flexibility and porosity of biological tissues, microfabricated structures, and permeable membranes. In this work, we will study the elastocapillary rise between flexible, swellable sheets to study the dynamic deformations that result from these competing phenomena.
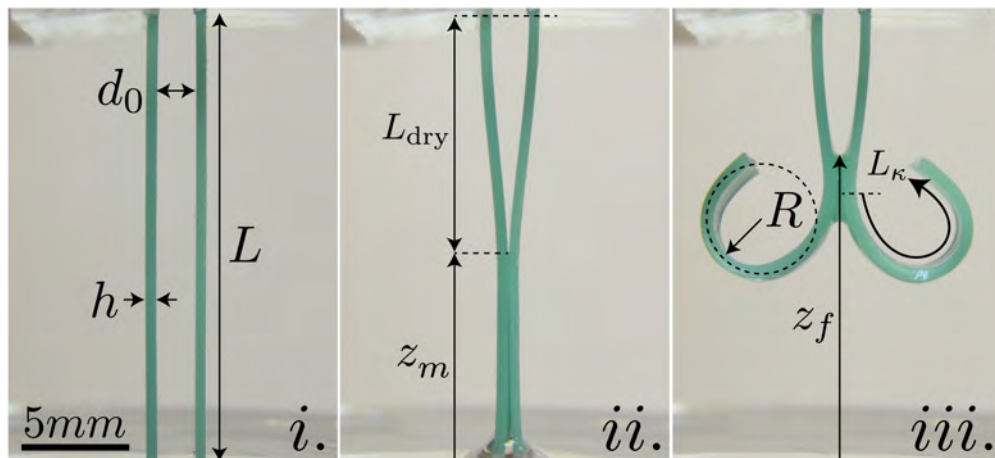
Figure 1: Images of two flexible beams deforming initially due to capillary rise (ii), and then subsequently due to swelling–induced bending (iii).

*Corresponding author. Email: ptbrun@mit.edu

EXPERIMENTS

Two polyvinylsiloxane (PVS, Zhermack Elite Double 22) elastic beams with a Young's modulus E=0.884 MPa, and rectangular cross sections of length L, width b, and thickness h are separated by a distance d_0, clamped at the top, and hung vertically in a gravitational field. We varied the length L from 15mm-24 mm, the initial gap d_0 from 1.2mm-4.9 mm, kept the width constant at b=3.5 mm for all experiments, and studied two thicknesses h=0.5 mm and h=0.8 mm. The beams are then lowered until the tips contact a bath of silicone oil (ν =5 cSt, Sigma Aldrich). Capillary action causes the fluid to rise between the two beams, and the flexibility of the elastic beams enable the capillary pressure from the silicone oil to bend the structures until they coalesce. Silicone oil is a favorable solvent for these silicone rubber beams, so the fluid diffuses through the beam's thickness and swells the elastic network in a nonhomogenous manner. This nonhomogenous swelling causes the beams to bend away from each other [7]. Once the beam's curvature increases beyond some critical point, the deformation is enough to cause separation with the fluid bath, and the swelling-induced bending continues until fluid has permeated through half the beam's thickness. Over the course of this process a volume of fluid is transporting upwards in a ratcheting fashion (Fig1-iii). At long times the beams relax back to their initially straight configuration, and this process repeats itself.

DISCUSSION

In our experiments, E, ν and the surface tension γ are constant, leaving the geometric parameters L, h, and d_0 as our independent variables. By rescaling some of our experimental results by the characteristic length scales in this problem, we gain some insight into the underlying mechanics. First, we can split the elastocapillary rise between swellable beams into two parts by recognizing that the predominant forces act in opposing ways to deform the beam - elastocapillarity bends the beams together, and swelling curls the beams away from each other. The elastocapillary deformation is dominant until the beams peel from the surface of the fluid.

Capillary rise between flexible beams comes from a competition between the force per unit area required to bend the structure and the capillary pressure exerted by the wetting fluid. In this context, minimizing the total energy of this system with respect to the dry length gives [1]: $L_{dry} = \left(\frac{9}{2}\right)^{1/4}\sqrt{d_0 \ell_{ec}}$, where a characteristic elastocapillary length scale $\ell_{ec} = \sqrt{B/\gamma}$ is introduced. The elastocapillary characteristic length scale also arises in the case of a naturally flat flexible sheet in contact with a wetted cylinder [2]. Here, the situation is reversed as the fluid's surface tension exerts a force that tries to flatten a beam with a swelling-induced natural curvature $\kappa_b = R^{-1}$. The result is the same – the coalesced beams will curl apart when the natural curvature reaches a critical value $R_c \propto \ell_{ec}$.

The short time dynamics of our experiments are dominated by capillary rise. At longer times, the swelling-induced bending becomes the main form of deformation. If capillary rise occurs, two general modes of deformation are observed: 1.) elastocapillary coalescence is dominant, and bending is localized near the bottom of beams, or 2.) swelling-induced bending is dominant, and the beams peel apart. We measured the maximum radius of curvature R_c that the beams reached while completely in contact the fluid bath, and observed that above a critical curvature the beams spontaneously peeled away from the fluid surface. The corresponding critical radius of curvature is on the order of ℓ_{ec}. Finally, we rationalize the ratcheting of the fluid integrating using Euler's Elastica equations with the appropriate set of boundary conditions, thereby revealing the energy landscape underpinning the fluid's motion.

In conclusion, we note that the deformations are dramatically different from those observed during traditional elastocapillary rise, and present a rich framework for studying coupled problems with multiple characteristic length and time scales. Our scaling analysis appears to capture some of the underlying mechanics, but we expect that a more robust theoretical approach will be necessary to capture the interplay between wetting, adhesion, and swelling. There is much to be done experimentally as well – in this work the silicone oil swells at a fairly slow rate, and both the solvent and elastomer can be changed to see enhancements in the swelling dynamics and the magnitude of deformation. Preliminary results on increasing the beam's width indicate that out–of–plane twisting can occur, in addition to the in–plane deformations discussed here. It is likely that swelling occurs in various elastocapillary environments, and while similar deformations may not be observed, confinement could lead to unexpected residual stresses, and localized deformations.

References

[1] J. Bico, B. Roman, L Moulin, and A Boudaoud. Elastocapillary coalescence in wet hair. *Nature*, page 690, 2004.

[2] B. Roman and J. Bico. Elasto-capillarity: deforming an elastic structure with a liquid droplet. *Journal of Physics: Condensed Matter*, 22(49):493101, 2010.

[3] H.-Y. Kim and L. Mahadevan. Capillary rise between elastic sheets. *Journal of Fluid Mechanics*, 548:141–150, February 2006.

[4] C. Duprat, J M Aristoff, and H.A. Stone. Dynamics of elastocapillary rise. *Journal of Fluid Mechanics*, 679:641–654, 2011.

[5] J. M. Aristoff, Camille Duprat, and H. A. Stone. Elastocapillary Imbibition. *International Journal of Non-Linear Mechanics*, 46(4):648–656, May 2011.

[6] C. Duprat, S. Protière, A. Y. Beebe, and H.A. Stone. Wetting of flexible fibre arrays. *Nature*, 482(7386):510–513, 2012.

[7] D. P. Holmes, M. Roché, T. Sinha, and H.A. Stone. Bending and twisting of soft materials by non-homogenous swelling. *Soft Matter*, 7(11):5188, 2011.

HIGHLY STRETCHABLE DOUBLE-NETWORK COMPOSITE

Xiangchao Feng, Zhuo Ma, Jonathan V. MacArthur & Wei Hong [a]
Department of Aerospace Engineering, Iowa State University, Ames, Iowa

<u>*Summary*</u> This paper presents the manufacturing and testing results of a soft composite film, consisting of stacked layers of fabric mesh and 3M VHB tapes. The mechanical testing results show that the strength and toughness of the composite is highly dependent on the composition, and in certain range, the composite exhibits much higher mechanical strength and toughness compared with the base materials. The toughening mechanism of the composite is believed to be similar to that in the well-known double-network hydrogels [1]. A 1D shear-lag model is developed to illustrate the damage-distribution toughening mechanism of the composite. The prediction of the model agrees well with the measured properties of the composite in different compositions.

INTRODUCTION

Double-network (DN) hydrogels have drawn much attention as a soft material having both high mechanical strength and toughness, while containing up to 90% of water [1]. It consists of two interpenetrating polymer networks: one consisting of relatively short and stiff chains (the 1st network) and the other with much longer and initially coiled chains (the 2nd network). The origin of strength and toughness has been attributed to the energy dissipation in the irreversible structural change during deformation, induced by the partial damage of the 1st network [2, 3]. Inspired by the structure and working mechanism of DN gels, a highly stretchable soft composite was designed and fabricated. The experimental samples were made by stacking VHB acrylic tapes and layers of fabric mesh. The two constituents serve the same purpose as the two networks in a DN gel: the stiff but brittle mesh provides the high strength as the 1st network of a DN gel, and the soft but stretchable VHB tape serves as the ductile substrate, just like the 2nd network. The two materials were well-bonded initially, but exhibit significant sliding after the fracture and fragmentation of the mesh, which enables distributed partial damage in the mesh. After optimization, the DN composite is as strong as the mesh, and at the same time as stretchable as the VHB tape. With the energy dissipation mechanism similar to that in the DN gels, the DN composite has a toughness at least one order of magnitude higher than either of the base materials.

EXPERIMENTATION

The samples were prepared by stacking nylon fabric mesh with hexagonal grids alternatingly with VHB acrylic tape 4910 (3M Co.). The interlayer bonding is due entirely to the adhesion of the VHB tape. Unless otherwise stated, each sample was cut into rectangular shapes of width 25mm and height 30mm (gauge length between grips). As the mesh has negligible thickness compared to the tapes (~1mm thick), the sample thickness is approximately the total thickness of the VHB tapes. The mechanical tests were carried out over an Instron 5960 dual column testing system. The nominal stress was calculated by dividing the force data by the original cross-sectional area of the sample (i.e. that of the VHB tapes).

RESULTS AND DISCUSSION

As shown by the snapshots C-F in Fig.1a, the DN composite exhibits stable necking during uniaxial tension, just as DN hydrogels [1]. The necking zone corresponds to the area of partially damaged fabric mesh, as shown by the enlarged picture in Fig.1b. After partial damage in the mesh, the load is carried locally by the much softer tape with large deformation. Due to the ductility of the tape, the subsequent step is the fracture of the mesh in other areas, instead of the rupture of the tape. Similar as in a DN gel [3], the propagation of the partial damage zone (necking) corresponds to the stress plateau on the loading curve, as shown by Fig.1a. It is believed that such a damage-distribution mechanism is the key to the toughness of the DN composite as well as the DN gels [2]. This toughening mechanism and the stress-strain behavior are rationalized by the following 1D model.

Experimental observations suggested significant sliding between the mesh and the VHB tape in the partially damaged area, as shown by Fig. 1b. Due to the sliding, a shear stress is present between the mesh and the tape, which transfers the axial load gradually between the two layers. For simplicity, we approximate this interaction by a shear-lag model with constant shear stress τ. Using the shear lag model, the effective stress-stretch curve of the composite is reconstructed theoretically, as in Fig. 2b, with the material parameters extracted from independent experiments on the base materials. The deformation and damage process of the DN composite can be divided into three stages. In stage I, prior to any damage, the behavior of the composite is close to linear elastic, with the stiffness mainly given by the mesh. At a critical stretch, the damage in the mesh initiates, and the stress plateaus at the value

$$s \approx \frac{f^*}{H}\left(1+\frac{3\mu H}{k}\right),\qquad(1)$$

---

[a] Corresponding author. Email: whong@iastate.edu

where k is the effective tensile stiffness of the mesh, H the original thickness of the tape, μ the initial shear modulus of the VHB tape, and f^* the tensile strength of the mesh layer. The monotonic increasing curve in stage III is governed by the behavior of the tape layer, and the stress is bounded by a value set by the strength of the tape.
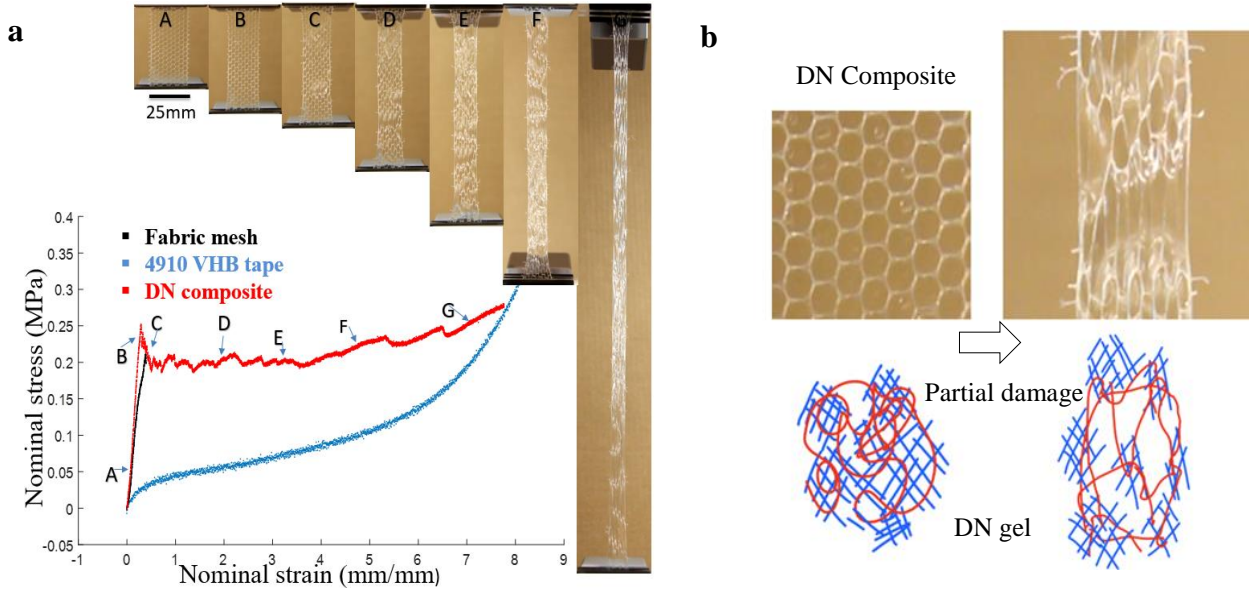
Fig 1. (a) Stress-strain curves of a VHB tape, a fabric mesh, and the DN composite with 1 layer of mesh and 2 layers of tape. For comparison, the nominal stress of the mesh is normalized by the same cross-sectional area as the DN composite. The insets (A-F) are snapshots of the sample correspond to the specific points along the loading curves. (b) Comparison between the undamaged and partially damage zones in the DN composite, and a similar mechanism in DN gels, after Ref. [2].

Comparing to the experiment results in Fig. 2a, the agreement between the shear lag model and experiments is reasonably well.
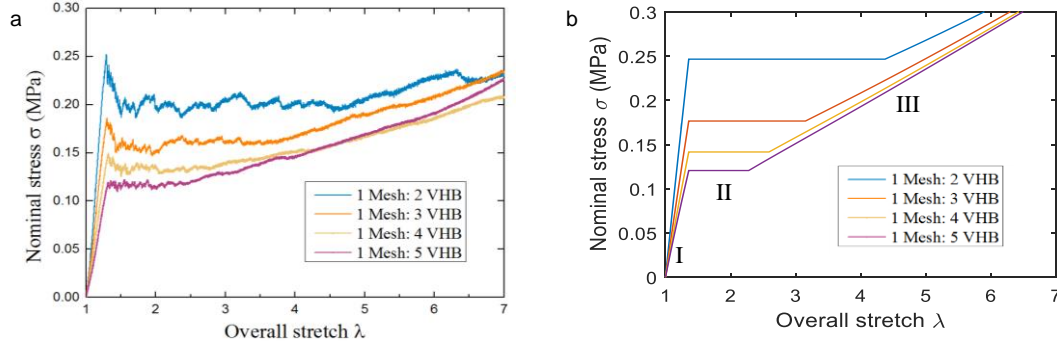
Fig 2. (a) Nominal stress-stretch curve of the DN composite at various compositions. (b) Theoretical prediction by considering the interaction in the sliding zone with a shear-lag model. The four curves have the same composition as the corresponding ones on (a). Material parameters are extracted from independent experiments on base materials.

CONCLUSIONS

Using a fabric mesh and a VHB acrylic tape, a soft but highly stretchable DN composite is manufactured. The DN composite follows the same damage-distribution and toughening mechanisms as in the well-known DN hydrogels. The DN composite is as strong as the mesh, as stretchable as the tape, and much tougher than both materials. The DN composite exhibit stable necking as the DN gels. By using a simple shear lag model to capture the finite interlayer sliding, a theory is developed and its prediction in the stress-strain behaviour agrees well with the experiments. On the other hand, the DN composite itself may be regarded as a macroscopic model for the study of DN hydrogels.

References

[1] Gong, J.P., Katsuyama, Y., Kurokawa, T. and Osada, Y., 2003. Double-network hydrogels with extremely high mechanical strength. *Advanced Materials*, *15*(14), pp.1155-1158.

[2] Gong, J.P., 2010. Why are double network hydrogels so tough? *Soft Matter*, *6*(12), pp.2583-2590.

[3] Wang, X. and Hong, W., 2011. Pseudo-elasticity of a double network gel. *Soft Matter*, *7*(18), pp.8576-8581.

COMPUTATIONAL MODELLING OF LIGHT-SWITCHABLE SURFACE TOPOGRAHIES USING LIQUID CRYSTAL POLYMERS

Ling Liu & Patrick R. Onck[*]
Zernike Institute for Advanced Materials, University of Groningen, Groningen, The Netherlands

Summary Liquid crystal (LC) glassy polymers co-polymerized with azobenzenes respond to ultra-violet (UV) light by undergoing anisotropic dimensional changes. Such a light-induced mechanical response can be used to generate topographical deformations when LC films are fixed to rigid substrates. Various topographical changes, dynamically controlled by light, can be produced by controlling the internal distribution of the average orientation of the liquid crystal molecules. In this presentation, we review our recent simulation results of light responsive topographical transformations of LC polydomain coatings [1].

LIGHT RESPONSIVE SURFACES

Switchable surface topographies enable many potential applications in manipulating friction and adhesion in the design of robotics and human-interactive haptics. In addition, the control of small-scale surface roughness can alter the effective hydrophobicity and thus the wetting properties. Light-driven actuations are preferable over thermal and electrically stimulations, because there is no need to build surrounding heating devices or electrodes. Photo-responsive systems are particularly advantageous in cases where remote control and localized actuation are desired.
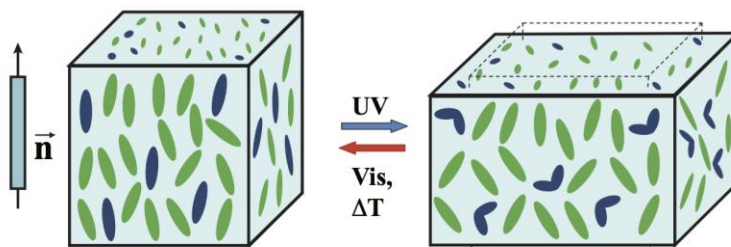
Figure 1: A 3D schematic representing the photo-physics and opto-mechanical response of azo-LC polymers under UV illumination. UV-triggered isomerizations of the embedded azobenzene molecules (blue) decrease the orientational order of the neighboring LC molecules (green) and results in a contraction along the director ($\vec{n}$) and expansions along the two perpendicular directions. Isomerization from trans (straight) to cis (bent) is driven by UV-light and the back-isomerization is driven by visible light and temperature.

Liquid crystal (LC) polymers can respond to ultra-violet (UV) light in the presence of co-polymerized azobenzene molecules [2]. As schematically shown in Fig. 1, triggered by UV-light, conformational changes from the natural trans state azobenzene (rod-like) to the bent-like metastable cis state decreases the orientational order of the liquid crystal network. These changes lead to a density decrease and a spontaneous contraction along the common direction of the LC moieties, i.e., the director, and expansions along the two perpendicular directions [3]. If LC films are fixed to rigid substrates they are able to produce surface topographical changes because their in-plane deformations are suppressed and the density changes manifest themselves as height variations. LC coatings with a spatially pre-designed patterning of the director distribution were recently constructed, which generates reversible protrusions and corrugations under UV illumination [4]. This switchable surface topography can be utilized to dynamically control the coating's friction properties [5].

CMPUTATIONAL MODEL AND RESULTS

In order to understand the underlying actuation mechanisms and to build a tool for design and optimization, a numerical model has been developed to simulate the light-induced surface topography changes of various LC coatings. Using the model, we study the dependencies of the generated surface roughness on the material properties and geometric features. A nonlinear light absorption model was developed to calculate the UV light attenuation through the thickness of the coating. With the absorption model, the corresponding isomerization process of the embedded azobenzenes can be described as a function of the director distribution and the type of the incoming light, i.e., diffuse light or polarized light. The light-triggered spontaneous deformation of the azo-LC polymer was incorporated through an anisotropic eigenstrain which is directly proportional to the relative fraction of azobenzene molecules in the cis state. An anisotropic linear-elastic constitutive relationship was adopted since the glassy LC polymers remain in the elastic regimes under UV illumination.

---

[*] Corresponding author. Email: P.R.Onck@rug.nl.

The key to generate a surface transformation from a flat to a corrugated coating is to create a non-uniform director distribution. For regions where the directors are parallel to the electric field of the incoming light, the azobenzenes inside have maximal absorbance and thus a higher trans-to-cis conversion level is triggered, leading to a large opto-mechanical response. In regions where the directors are perpendicular to the electric field, a much lower deformation is expected due to the low cis fraction. Creating a non-uniform director distribution thus produces switchable corrugations. Various types of liquid crystalline structures were tested. One of the tested cases is a polydomain film (see Fig. 2), in which the director distribution is randomly distributed over different domains and the corresponding photo-induced topographical textures feature domain-wise corrugations. The resulting topographical changes of this type of LC glassy films lead to surface profiles that are found to be in close agreement with the experimental measurements [1]. Roughness parameters were used to quantify the generated surface corrugations. The dependencies of these parameters on the structure's dimensions, illumination conditions and opto-mechanical properties of the LC polymer were studied.
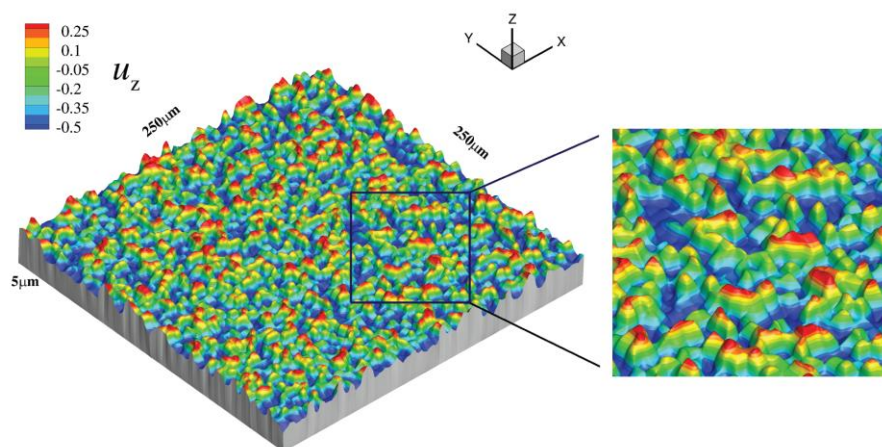
Figure 2: Simulation results of the light-triggered topographical transformation of a liquid crystal polydomain coating and a detailed texture for the boxed region. The polydomain film features domain-wise corrugations [1].

CONCLUSIONS

A computational tool was developed to simulate UV-triggered surface transformations based on azobenzene-modified liquid crystal glassy coatings. Combined with experiments, we show three-dimensional surface topographical changes that can be switched by light. Various optimized topographical textures can be produced depending on the specific director distribution.

ACKNOWLEDGMENT

References

[1] Liu*, D., Liu*, L., Onck, P. R., and Broer, D. J.: Reverse switching of surface roughness in a self-organized polydomain liquid crystal coating. *P. Natl. Acad. Sci. USA* **112**:3880-3885, 2015. *Shared first authorship

[2] Yu, Y., Nakano, M., and Ikeda, T.: Photomechanics: directed bending of a polymer film by light. *Nature* **425**:145, 2003.

[3] Warner, M., and Terentjev, E.M.: Liquid crystal elastomers. Oxford University Press, Oxford, 2003.

[4] Liu, D., Bastiaansen, C.W.M., Den Toonder, J.M.J. and Broer, D.J.: Light-Induced Formation of Dynamic and Permanent Surface Topologies in Chiral–Nematic Polymer Networks. *Macromolecules* **45**:8005-8012, 2013.

[5] Liu, D. and Broer, D.J.: Self-assembled Dynamic 3D Fingerprints in Liquid-Crystal Coatings Towards Controllable Friction and Adhesion. *Angew. Chem. Int. Edit.* **53**:4542-4546, 2014.

COILING A FIBER INSIDE A DROP PROVIDES A HIGHLY STRETCHABLE DEVICE

Sébastien Neukirch *[1], Arnaud Antkowiak[1], Hervé Elettro[1], and Paul Grandgeorge[1]

[1]*Sorbonne Universités, UPMC Univ Paris 06, CNRS, UMR 7190, Institut Jean Le Rond d'Alembert*

Summary Capillary forces acting at the surface of a liquid drop can be strong enough to deform small objects and recent studies have provided several examples of elastic instabilities induced by surface tension. We present such an example where a liquid drop sits on a straight fiber and we show that the liquid attracts the fiber which thereby coils inside the drop. We model the system behavior as a phase transition between a stretched phase, where the drop sits on a straight fiber, and a condensed phase, where the fiber is coiled inside the drop. The force-plateau regime during the transition between the two phases is seen as a Maxwell line, reminiscent of the Martensite-Austenite transition in Shape Memory Alloys.

PACKING OF ELASTIC WIRES

A large variety of physical phenomena can be modeled with elastic filaments packaged in cavities [10], see for example the ejection of DNA from viral capsids [6, 5], or the windlass mechanism in spider capture threads [12]. In the case of a mechanical wire spooled in a sphere, or DNA in a capsid, the presence of a motor is necessary for the packing process, the energy to bend the filament being provided by this external actuator. In the case the cavity is a liquid drop (or a bubble in a liquid medium) surface tension may provide the actuation energy: if the affinity of the filament for the liquid is stronger than that of the filament for the surrounding gas, then the bending energy required for packing could be provided by the difference of surface energies. As always, surface energy prevails at small scale and for millimeter-sized drop-on-fiber systems [7],
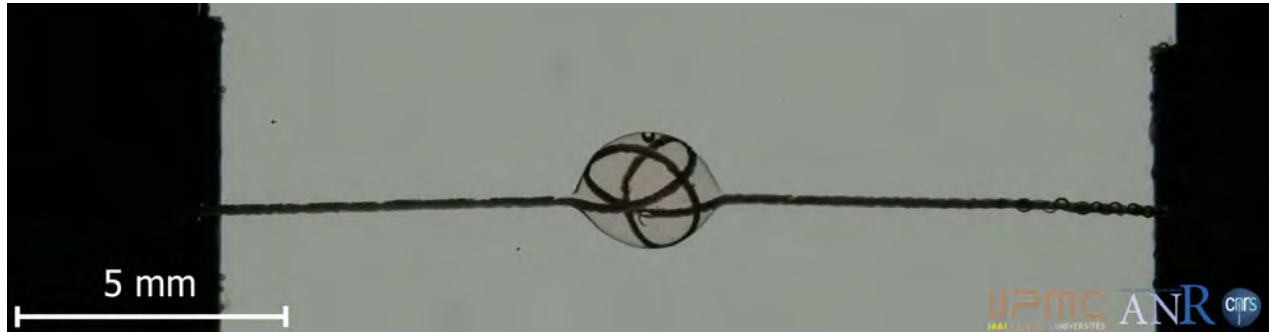
Figure 1: Elastomer beam of 140 μm section bent in a silicone oil drop (diameter $\sim$ 2.7 mm). The system is immersed in a water tank to provide buoyancy.

the competition between capillary and elastic forces is not automatically won by the former: a threshold length emerges and separates systems in which packaging is possible from those in which the fiber remains straight. This threshold length, called elastocapillary length [9], plays a central role in problems in which surface tension bends or buckles slender rods or thin elastic sheets [8]. Computations of configurations of a filament packaged in spherical cavities have been performed using finite elements [11], molecular mechanics [3], or statistical physics [1] approaches. Here we study the buckling and coiling of an elastic rod in a sphere. The rod is held in tension at its extremities and we record this tension as a function of the length of the rod packed in the sphere, while monitoring the different configurations the systems adopts.

RESULTS

We model the system of Figure 1 as an elastic rod in interaction with a rigid sphere. The rod is flexible but inextensible and unshearable, yielding a deformation energy of the form

$$E_{\text{strain}} = \int_0^L (1/2) \left[K_1 U_1^2(S) + K_2 U_2^2(S) + K_3 U_3^2(S) \right] \mathrm{d}S \tag{1}$$

where K_1 and K_2 are the bending rigidities, K_3 is the twist rigidity, U_1 and U_2 are the curvature strains, and U_3 is the twist strain [2, 4]. A liquid spherical drop of radius R is attached to the rod. The rod enters (exits) the drop at meniscus point A (B). The rod is then divided in three regions: (I) where $S \in (0; S_A)$, (II) where $S \in (S_A; S_B)$, and (III) where $S \in (S_B; L)$,

*Corresponding author. Email: sebastien.neukirch@upmc.fr

with region (II) lying inside the liquid drop. In regions (I) and (III) the solid-vapor interface has an energy γ_{SV} per unit area. In region (II) the solid-liquid interface has energy γ_{SL} per unit area. The total surface energy then scales linearly with the contour length:

$$E_{\mathrm{surface}} = P\left[\gamma_{\mathrm{SV}}S_A + \gamma_{\mathrm{SL}}(S_B - S_A) + \gamma_{\mathrm{SV}}(L - S_B)\right] \tag{2}$$

where P is the perimeter of the cross-section of the rod. We minimize this energy under geometrical constraints (encapsulation in the drop, fixed end-to-end distance, etc) and find the different equilibrium configurations of the system as more and more fiber length is spooled inside the drop, see Figure 2.
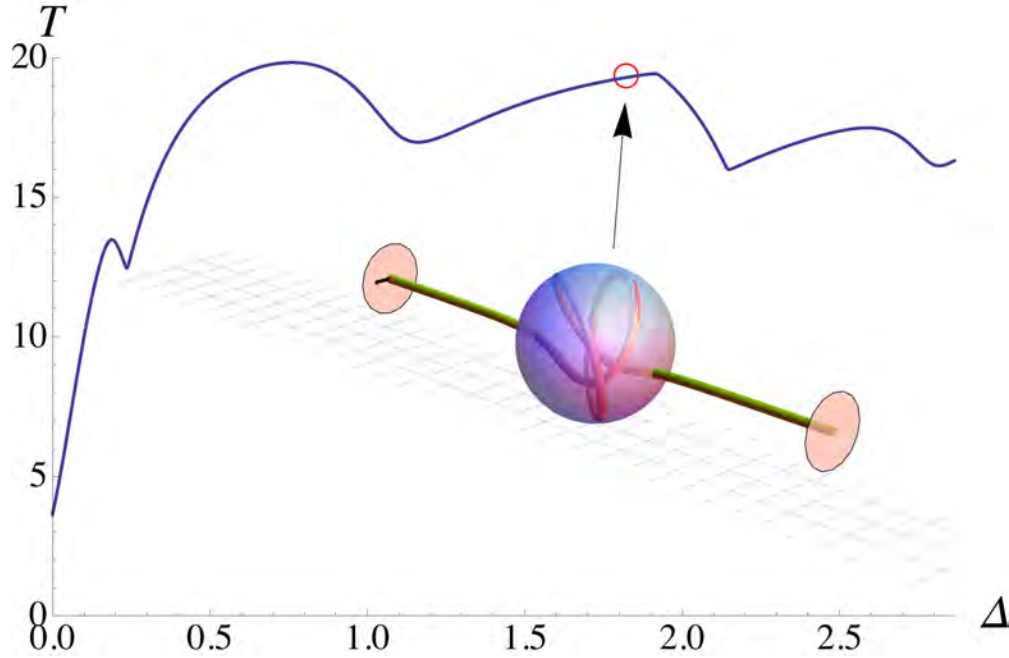
Figure 2: Bifurcation curve showing the end tension T as function of the end-shortening Δ.

ACKNOWLEDGEMENTS

References

[1] Adda-Bedia, M., Boudaoud, A., Boué, L., Debœuf, S.: Statistical distributions in the folding of elastic structures. Journal of Statistical Mechanics: Theory and Experiment **2010**(11), P11 027 (2010)

[2] Antman, S.S.: Nonlinear problems of elasticity, 2nd edn. Springer-Verlag, New York (2004)

[3] Arsuaga, J., Tan, R.K.Z., Vazquez, M., Sumners, D.W., Harvey, S.C.: Investigation of viral DNA packaging using molecular mechanics models. Biophysical Chemistry **101-102**, 475–484 (2002)

[4] Audoly, B., Pomeau, Y.: Elasticity and Geometry: From hair curls to the non-linear response of shells. Oxford University Press (2010)

[5] LaMarque, J.C., vy L. Le, T., Harvey, S.C.: Packaging double-helical DNA into viral capsids. Biopolymers **73**(3), 348–355 (2004)

[6] Leforestier, A., Livolant, F.: Structure of toroidal DNA collapsed inside the phage capsid. Proceedings of the National Academy of Sciences of the USA **106**(23), 9157–9162 (2009)

[7] Lorenceau, É., Clanet, C., Quéré, D.: Capturing drops with a thin fiber. Journal of Colloid and Interface Science **279**(1), 192 – 197 (2004)

[8] Py, C., Reverdy, P., Doppler, L., Bico, J., Roman, B., Baroud, C.N.: Capillary origami: Spontaneous wrapping of a droplet with an elastic sheet. Physical Review Letters **98**(15), 156 103 (2007)

[9] Roman, B., Bico, J.: Elasto-capillarity: deforming an elastic structure with a liquid droplet. Journal of Physics: Condensed Matter **22**(49), 493 101 (2010)

[10] Stoop, N., Najafi, J., Wittel, F.K., Habibi, M., Herrmann, H.J.: Packing of elastic wires in spherical cavities. Phys. Rev. Lett. **106**, 214 102 (2011)

[11] Vetter, R., Wittel, F., Stoop, N., Herrmann, H.: Finite element simulation of dense wire packings. European Journal of Mechanics - A/Solids **37**, 160–171 (2013)

[12] Vollrath, F., Edmonds, D.T.: Modulation of the mechanical properties of spider silk by coating with water. Nature **340**, 305–307 (1989)

NONLINEAR CHARACTERISTICS OF DIELECTIC ELASTOMERS UNDER ELECTROMECHANICAL COUPLING LOADING

Tongqing Lu[1], Le An[1], Jianguo Li[1] & Tiejun Wang[1a)]

[1]*State Key Laboratory for Strength and Vibration of Mechanical Structures, Xi'an Jiaotong University, China*

Summary A membrane of a dielectric elastomer deforms subject to a voltage through the thickness. The voltage induced deformation is highly nonlinear and even non-monotonic, inducing the pull-in instability. A cylindrical elastomeric tube subject to an internal pressure exhibits quite similar instability behavior. We study the deformation behavior a dielectric elastomer tube subject to electromechanical coupling loading. Explicit expressions for the critical conditions of electromechanical bifurcation are derived. The post-bifurcation path and the steady state propagation is comprehensively investigated.

A BRIEF INTRODUCTION TO PULL-IN INSTABILITY

From our common experience, when a rubber balloon is inflated to a certain size it will cost less strength to blow it larger. The characteristic of transition from a stiffer balloon to a softer balloon defines a peak pressure on the pressure-stretch curve. The presence of the peak pressure is due to the strong coupling of the true stress with deformation and high nonlinearity of the material. A pressure inflates the balloon and in turn the true stresses increases such that a mechanism of positive feedback exists, inducing the so-called pull-in instability. Another characteristic of inflating a rubber balloon is the stiffening effect at large stretch due to the limiting length of polymer chains. These two characteristics give the well known N-shaped pressure-stretch curve. A membrane of a dielectric elastomer sandwiched between two compliant electrodes undergoes large deformation subject to a voltage across the thickness. The voltage induced deformation is due to Columbic force and thus the electric field determines the intensity. Like the coupling between the true stress and stretch in inflating a rubber balloon, the electric field couples strongly with deformation. The Columbic force squeezes the membrane and the decreased thickness amplifies the electric field. The positive feedback competes with the elasticity of membrane, inducing the electrical instability. Similarly, the electrical instability defines a peak voltage on the voltage-stretch curve. The curve eventually becomes N-shaped due to strain stiffening.

INSTABILITY OF A DIELECTRIC ELASTOMER TUBE UNDER ELECTROMECHANICAL LOADING

When inflating an initially flat membrane clamped at the boundary from one side, the snap-through behaviour at the peak pressure is usually observed. And the snap-back occurs in deflation. On inflating a purely spherical membrane, refined stability analysis and experiments show that the spherical configuration in inflation is unstable. The spherical membrane may bifurcate into a pear-shaped configuration through a localized thinning near one of the poles. When inflating a tubular balloon, the localized bulging instability is usually observed at a critical pressure. As more fluid is pumped into the tube, the localized aneurysm develops until its radius reaches a critical value. With continuous pumping, the pressure stays unchanged and the aneurysm shifts along the tube with more and more sections bulging up at the expense of unbulged sections. Consider an infinitely long cylindrical DE tube subjected to an internal pressure p, an axial load F at two ends and a voltage Φ through the thickness. We first establish the governing equations of the tube as

$$\frac{d}{dZ}\left(Hs_2 \sin\theta \right) = \lambda_1 \lambda_2 p \cos\theta,$$

$$\frac{H}{R}s_1 - \frac{d}{dZ}\left(Hs_2 \cos\theta \right) = \lambda_1 \lambda_2 p \sin\theta,$$

$$\frac{\partial W\left(\lambda_1, \lambda_2, D \right)}{\partial D} = E,$$

The first two equations represent the force balance along longitudinal and hoop directions respectively, while the last equation represents the electric balance. By using a simplified mathematical approach, we can analytically obtain the critical conditions for bifurcation.

[a)]Corresponding author. Email: wangtj@mail.xjtu.edu.cn**.**

POST BIFURCATION PATH AND STEADY PROPAGATION

In the bifurcation diagram, a 45 degree straight line represents the homogenous deformation while coloured curves show the bifurcated solutions. The dashed lines represent solutions which are either periodic or unbounded. The blue and red lines represent the solutions at different levels of constant voltage or pressure. A pre-stretched membrane by pressure becomes stiffer while a pre-stretched membrane by voltage becomes more compliant. We can also analyze the bifurcation behavior from the loading-state diagram. The black curve represents the homogeneous deformation while coloured curves represent the inhomogeneous bifurcated deformation. Consider the pressure induced bifurcation under a constant voltage. The bifurcation path can be clearly traced from the bifurcation diagram. The original state is marked as O, which derivates from the undeformed state a little due to the presence of a constant voltage. Upon inflation, the deformation follows a homogenous path until the bifurcation point A. After bifurcation, the bulging solution becomes larger, following the red curve. Meanwhile, the solution at infinity becomes smaller, going back from A to O, which means that the infinite parts undergo unloading and remain uniform. Correspondingly, as shown in loading-state diagram, the black curve represents homogeneous deformation. The bifurcation point coincides with the peak of curve. When reaching the bifurcation condition, the peak of the curve, the homogenous deformation becomes unstable and bulging occurs. After bifurcation the pressure drops down and stretches bifurcate into two paths at point A, one to the right as indicated by the red curve representing the bulging section and the other to the left as indicated by the blue curve representing the unbulged section. When the pressure drops to the coexistent pressure (the dashed line), corresponding to the turning point B. Subsequently the steady propagation starts. The unbulged part gradually bulges up and the inhomogeneous transition zone shifts with its shape unchanged. The propagation continues from B to B until the whole tube bulges up. For an infinitely long tube the propagation will not terminate by itself as long as the gas continues to be pumped in. In the steady propagation the stretches remain unchanged so that points B and C coincide. After the whole tube bulges up, if we continue to pump in gas the pressure and homogeneous stretches will increase again following C to D. If we deflate the tube, necking occurs following D to E and then to F.
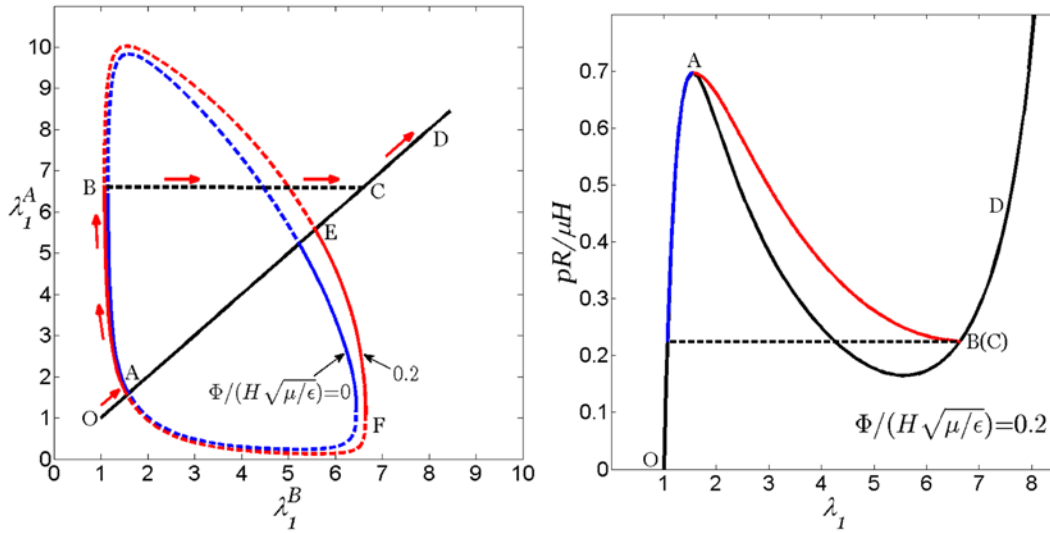
CONCLUSIONS

A cylindrical dielectric elastomer tube under an internal pressure, an axial force, and a voltage across the thickness is considered. The bifurcation condition is analytically established. The post bifurcation path and the steady propagation are analyzed in details. This work characterizes the bifurcation mechanism of rubber-like materials under complex coupling loading. The analogy between charging a dielectric elastomer and inflating a rubber balloon helps to better understand the inherent mechanisms.

References

[1] Lu T.Q., An L., Li J.G., Yuan C., Wang T.J.: Electromechanical coupling bifurcation and bulging propagation in a cylindrical dielectic elastomer tube. *J. Mech. Phys. Solids* **85**:160-175, 2015.

[2] Fu Y.B., Xie Y.X.: Stability of pear shaped configurations bifurcated from a pressurized spherical balloon. *J. Mech. Phys. Solids* **68**: 33-44, 2014

[3] Li T.F., Keplinger C., Baumgartner R., Bauer S., Yang W., Suo Z. : Giant voltage induced deformation in dielectric elastomers near the verge of snap through instability. *J. Mech. Phys. Solids* **61**: 611-628, 2013

VOLTAGE-INDUCED BUCKLING AND WRINKLING IN A DIELECTRIC ELASTOMER

Hareesh Godaba, Ujjaval Gupta, _Jian Zhu_[a]

Department of Mechanical Engineering, National University of Singapore

9 Engineering Drive 1, Singapore, 117575

Summary This paper investigates instability and phase transition in a membrane of a dielectric elastomer. It is found that prestretches play a significant role in determining its instability modes. In the absence of prestretches, the membrane buckles without forming local wrinkles. When the applied prestretches are intermediate, the membrane exhibits discontinuous phase transition from the flat to wrinkled states. The flat and wrinkled regions not only coexist, but also keep moving with the respective areas changing (depending on the variation of the charges). When the prestretches are large, the membrane exhibits continuous phase transition, and the membrane forms wrinkles simultaneously throughout the surface.

INTRODUCTION

A dielectric elastomer actuator, one class of soft actuators, consists of a thin layer of elastomer sandwiched between two compliant electrodes. This soft actuator can deform in response to voltage and can exhibit interesting attributes including large deformation, high energy density and fast response [1]. The dielectric elastomer actuators are being extensively explored as artificial muscles for soft robots [2].

The dielectric elastomer may suffer loss of tension and form wrinkles when the applied voltage reaches a critical value. Plante and Dubowsky observed the coexistence of the flat and wrinkled regions in a circular membrane (Fig. 1), when the membrane suffers electromechanical instability [3]. Zhou et al. simulated the propagation of the instability, using a meshfree method [4]. Huang and Suo theoretically analyzed the phase transition from the flat to wrinkled states in a dielectric elastomer subject to an uniaxial load [5]. Kollosche et al. studied a membrane which is subject to a deadload vertically but is clamped horizontally. The experiments showed three types of phase transitions, including the discontinuous transition from the flat to wrinkled states, continuous transition from the flat to wrinkled states, and discontinuous transition from the wrinkled to wrinkled states [6].

This paper investigates instability and phase transition in a circular membrane of a dielectric elastomer, which is subject to equal-axial prestretches (Fig. 1). It is found that the membrane may buckle or wrinkle, dependent on the applied prestretches (λ_{pre}, Fig. 1b).

EXPERIMENTS

Figure 1 shows the schematic of the experimental setup. At the reference state (Fig. 1a), a circular membrane is subject to no mechanical and electrical loads, and has a radius B and a thickness H (= 1mm). The active part (which will be smeared with the electrodes later) has a radius A. At the prestretched state (Fig. 1b), the membrane is subject to a radial prestretch λ_{pre} and has a radius $B\lambda_{pre}$ (= 6cm), and its boundary is fixed to a rigid circular frame. The active part is brushed with the compliant electrodes and has a

Fig. 1 A schematic of a circular membrane of a dielectric elasotmer

radius $A\lambda_{pre}$ (= 3cm). At the current state (Fig. 1c), the membrane is subject to voltage, the active part expands its area and reduces its thickness, and the point R at the reference state moves to a position with a radius r at the current state.

We employ VHB 4910 (3M) as the elastomer, and carbon grease as the compliant electrodes. Voltage is programmed through Labview (BNC-2120, NI) and is amplifed by a high voltage amplifier (FR30P10, Glassman). We then investigate the electromechanical behaviour of the membranes with different prestretches.

Buckling

In the absence of prestretches (λ_{pre} = 1), the experiments show that the actuator buckles without forming any wrinkles on the surface, when voltage reaches a critical value (Φ = 6kV). Figure 2a shows the state at Φ = 0, and Figure 2b show the buckling of the membrane when the voltage is larger than the critical

(a) Voltage off   (b) When Φ = 21kV

Fig. 2 Buckling of the membrane with λ_{pre} = 1

value. This experimental observation can be interpreted as follows. The active part of the membrane expands when subject to voltage, which will compress the passive part. Consequently, the passive part also applies a compressive force to the active one. In the absence of any prestretches, the thickness of the membrane is large. Meanwhile, at λ_{pre} = 1 (or when the

---

stretch is close to the stretch limit), the stiffness of the membrane is generally large. As a result, the membrane is too stiff to form local wrinkles. However, the compressive stress may make the membrane buckle globally without forming local wrinkles, as shown in Fig. 2b.

Discontinuous transition from the flat to wrinkled states

When the membrane is subject to intermediate prestretches (λ_{pre} = 3), the membrane exhibits a discontinuous phase transition from the flat to wrinkled states. When the voltage is small, the active part expands. When the voltage reaches a critical value (Φ = 7.38kV), the flat and wrinkled regions coexist. Different from [6], in the current experiments we fix the voltage at the critical value (i.e. 7.38kV). It is observed that both the flat and wrinkled regions keep moving with the flat and wrinkled areas changing. Finally the membrane fails by electrical breakdown. Figure 3 show a sequence of still images of the membrane at the fixed voltage. Theoretical analysis shows that the voltage-stretch curve may have a shape of going up, down and up again. When the voltage reaches a critical value, the flat and wrinkled states have the same free energy densities. As a result, the flat and wrinkled states coexist. Since we do not control the charges on the electrodes, the flat and wrinkled regions may move as the charges vary.

Fig. 3 The membrane of a dielectric elastomer exhibits discontinuous phase transition from the flat to wrinkled states, when voltage reaches a critical value. (a) – (j), the state of the membrane at the fixed voltage (Φ = 7.38kV).

Continuous transition from the flat to wrinkled states

When the membrane is subject to larger prestretches (λ_{pre} = 4.5), the membrane may form wrinkles simultaneously throughout the surface, when the voltage reaches a critical value (Φ = 6.4kV). Theoretical analysis shows that the voltage increases monotonically with the stretch. When the voltage reaches the critical value, the active part of the membrane suffers loss of tension, and the membrane forms wrinkles. After loss of tension, the voltage still increases with the stretch.

When the membrane is subject to intermediate or even larger prestretches (but not close to the stretch limit), say λ_{pre} = 3 or 4.5, both its thickness and stiffness are small. Consequently, the membrane may form wrinkles locally, but may not buckle globally.

CONCLUSIONS

This paper investigates instability and phase transition in a circular membrane of a dielectric elastomer. Prestretches are found to play a significant role in determining instability modes of the membrane. In the absence of prestretches (λ_{pre} = 1), the membrane buckles without forming local wrinkles. When the prestretches are intermediate (λ_{pre} = 3), the membrane exhibits discontinuous phase transition from the flat the wrinkled states. The flat and wrinkled regions not only coexist but also move on the surface of the membrane. When the prestretches are large (λ_{pre} = 4.5), the membrane exhibits continuous phase transition, and the membrane form wrinkles simultaneously throughout the surface.

References

[1] Pelrine R., Kornbluh R., Pei Q.B., and Joseph J.: High-speed electrically actuated elastomers with strain greater than 100%. *Science* **287**: 836–839, 2000.
[2] Wang Y.Z., Zhu J.: Artificial muscles for jaw movements. *Extreme Mech. Lett.* **6**: 88-95, 2016.
[3] Plante J.S., Dubowsky S.: Large-scale failure modes of dielectric elastomer actuators. *Int. J. Solids Struct.* **43**: 7727-7751, 2006.
[4] Zhou J.X., Hong W., Zhao X.H., Zhang Z.Q., and Suo Z.G.: Propagation of instability in dielectric elastomers. *Int. J. Solids Struct.* **45**: 3739–3750, 2008.
[5] Huang R., Suo Z.G.: Electromechanical phase transition in dielectric elastomers. *Proc. R. Soc. A* **468**: 1014–1040, 2012.
[6] Kollosche M., Kofod G., Suo Z.G., Zhu J.: Temporal evolution and instability in a viscoelastic dielectric elastomer, *J. Mech. Phys. Solids* **76**: 47-64, 2015.

EXPLORING BAND GAP TUNABILITY IN PHONONIC CRYSTALS USING DIELECTRIC ELASTOMERS

Michael Jandron[*1,2] and David Henann[2]
1Naval Undersea Warfare Center Division Newport, Newport, RI
2School of Engineering, Brown University, Providence, RI

Summary Phononic crystals are periodic, composite materials that exhibit phononic band gaps – frequency ranges in which elastic waves are prohibited. When the periodic structure is deformed, these frequency ranges may be manipulated. Hence, frequency band gaps in phononic crystals made from elastomers may be reversibly tuned through large deformation. Furthermore, dielectric elastomers – materials in which deformation is induced through the application of an electric field – may be used in phononic crystals, opening the door for electrically actuated tunability. In order to realize this exciting capability, robust simulation and design tools are needed. We have developed finite-element technology to address this problem and have applied these tools to designing phononic crystals with band gaps tuned through electrical actuation. We present an application of our simulation capability to the design of a phononic crystal consisting of a square array of circular-cross-section threads embedded in a dielectric elastomeric matrix.

BACKGROUND

A solid phononic crystal utilizes constructive interference through Bragg scattering (see e.g., [1]) to create phononic band gaps – frequency ranges in which elastic waves cannot propagate. These materials have attracted a good deal of research attention in recent years and small-strain (e.g., metallic) phononic crystals have been extensively studied. Tunability of small-strain phononic crystals has been explored using piezoelectrics [2] and magneto-elastics [3,4], but because of the high wave speeds in stiff materials, the physical dimension of the required unit cells tend to be large. Soft materials offer the advantage of slower shear wave speeds which do not require very large unit cell dimensions. Since elasticity of elastomers is nonlinear, it is straightforward to change the stiffness properties of the unit cell through large deformation – thereby changing the speed of wave propagation. Achieving tunability through soft materials is just beginning to be explored. For instance, Bertoldi and Boyce [5] demonstrated significant tunability of band gaps through finite pre-deformations in soft elastomeric phononic crystals containing voids. Moreover, they showed that pre-deformation was not only capable of shifting band gaps but also that new band gaps could be created.

Dielectric elastomers (DEs) offer a unique way to achieve the large reversible deformations required for tunability through an externally applied electric field. These materials – which began appearing in the literature in the late 1990s [6,7] – are characterized by the ability to deform significantly when an electric field is applied. DEs are distinct from piezoelectric materials in that DEs are capable of large, reversible deformations, possess a quadratic relation between electric field and stress, and are non-polar, amorphous materials, while – on the other hand – piezoelectric materials typically only undergo small deformations, possess a linear relation of electric field to stress, and are polar, crystalline materials. The use of DEs in phononic crystals was first discussed by Shmuel [8] who developed analytical solutions for elastic wave propagation in a one-dimensional periodic laminate undergoing large homogeneous deformations in response to an electric field. Shmuel [9] expanded on this work by deriving analytical solutions for a DE phononic crystal composite made up of an array of cylindrical fibers in a matrix, but this was again limited to homogeneous deformations.

Numerical simulation is certainly required in order to study tunability induced by inhomogeneous deformations, but these simulation techniques are largely new to DEs [10,11]. Here, we utilize the finite-element approach of Henann et al. [11] through an Abaqus user-element (UEL) subroutine. This – in conjunction with a Representative Volume Element (RVE) and Bloch-Floquet boundary conditions (see e.g [5]) – allows us to explore band-gap dependence on electric field magnitude and direction without restriction.

RESULTS

Our simulation approach – consisting of the finite-element implementation [11], the RVE (shown in Fig. 1), and Bloch-Floquet boundary conditions [5] – has been verified by reproducing the analytical work of Shmuel [9] for homogenous deformation of a phononic crystal consisting of cylindrical inclusions arranged in a square matrix. However, for brevity, we do not show that result here, instead focusing on the more interesting case of inhomogeneous, electrically-actuated pre-deformation. Representative simulation results for one set of material properties and volume fraction (50/50) is shown in Fig. 1. An electric field is applied along the diagonal of the unit cell with increasing magnitude, as shown in Figs. 1 (a)-(c). The frequency as a function of wave vector for several electric field magnitudes is shown along the top of the figure, demonstrating that phononic band gaps (depicted as blue bars) can be manipulated.
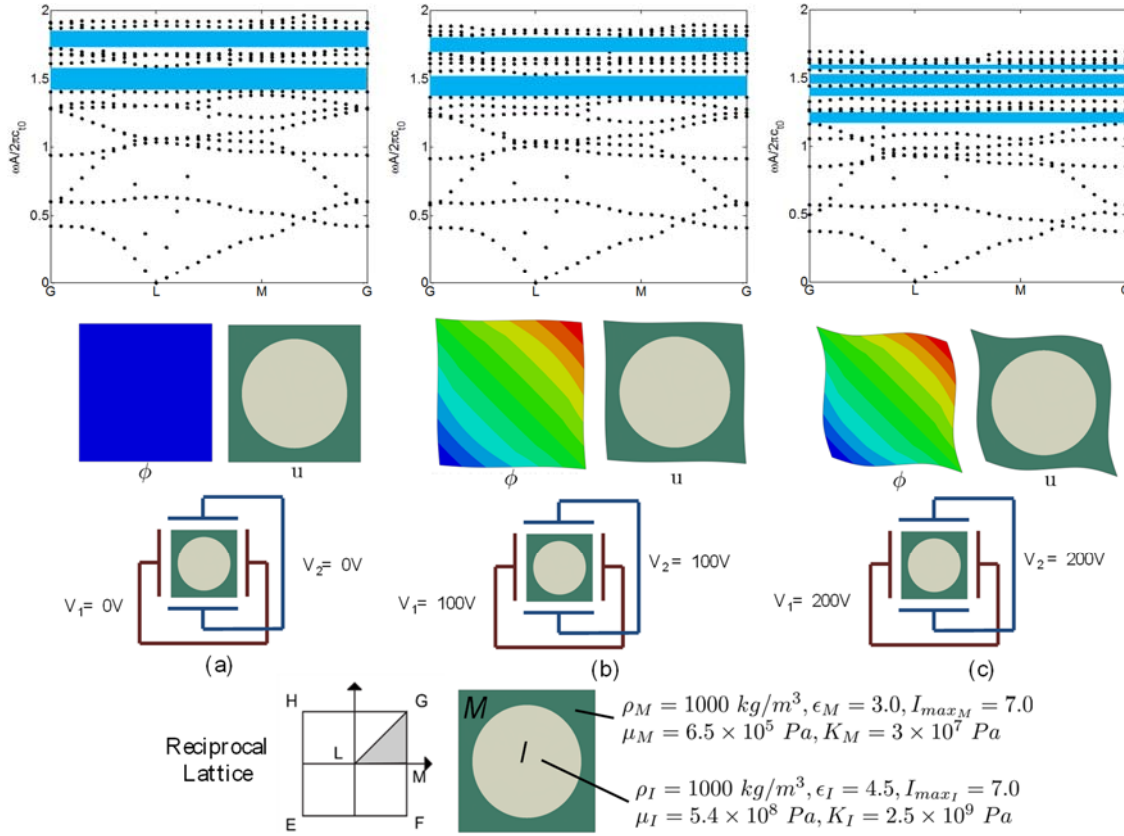
Figure 1. Effect of an external electric field on deformation and phononic band gaps in the composite DE. From left, (a) no electric field, (b) an electric field of 100V/unit cell in both the horizontal and vertical directions lowers the band gaps, and (c) an electric field of 200V/unit cell in each direction lowers the band gaps further and also opens new ones. Note that the voltage is per unit cell, and hence, in a phononic crystal of 20x20 unit cells, the actual applied voltage will be 2kV and 4kV for (b) and (c) respectively. In the figure, φ represents the voltage field, u represents the deformed shape of the unit cell, and the blue bars represent the band gaps. The band gap angular frequencies, ω, are normalized by the unit cell dimension, A, and the composite unit cell shear wave speed, $c_{t0} = c_{tM}c_{tI}/(0.5c_{tM} + 0.5c_{tI})$. The unit cell is composed of a matrix M and an inclusion, I, both modelled using the Gent hyperelasticity model. For material properties: ρ is the mass density, ε is the dielectric permittivity, I_{max} is a material parameter for the Gent hyperelasticity model, μ is the ground-state elastic shear modulus, and K is the elastic bulk modulus – taken to approximately enforce incompressibility. The properties used are representative of 3M VHB 4910 DE for the matrix and nylon for the inclusion material.

In this talk, we will further demonstrate the dependence of phononic band gaps on the direction of the applied electric field, shear modulus contrast, density contrast, electric permittivity contrast, volume fraction, as well as unit cell geometry (i.e., hexagonal instead of square lattice). In summary, phononic crystals made from dielectric elastomers provide an attractive strategy for achieving electrically tunable band gaps, and our work demonstrates a robust numerical simulation capability for the design of these electrically tunable phononic crystals.

References

[1] Lai, Y., Zhang, X., Zhang, Z-Q, Appl. Phys. Lett. 79, Number 20 (2011).
[2] Oh, Lee, Ma and Kim., Appl. Phys. Lett. 99, 083505 (2011)
[3] Vasseur, Matar, Robillard, Hladky-Hennion, Deymier, AIP Advances 1, 041904 (2011)
[4] Matar, Robillard, Vasseur, Jladky-Hennion, Deymier, Pernod, Preobrazhensky, Appl. Phys. 111, 054901 (2012)
[5] Bertoldi, K., Boyce, M., Physical Review B 77 (5), 052105, 2008
[6] Pelrine, R., Kornbluh, R., and Joseph, J., Sens. Act. A 64, 77-85, 1998.
[7] Pelrine, R., Kornbluh, R., Pei, Q., and Joseph J., Science 287, 836-839, 2000.
[8] Shmuel, G., deBotton, G., JMPS, 2012.
[9] Shmuel, G., Int. J. Solids Struct., 50:680-686, 2013
[10] Vu, D., Steinmann, P., Possart, G., Int. J. Numer. Meth. Engng 2007; 70:685–704
[11] Henann, D., Chester, S., Bertoldi, K., JMPS 61, 2013.

RESEARCH ON THE MICROSTRUCTURE AND THE PROPERTY OF MAGNETORHEOLOGICAL ELASTOMER

Taixiang Liu[1], Yangguang Xu[2], Ke Yang[1], Hongwei Yan[1], Xinglong Gong[3] & Xiaodong Yuan[1a]

[1]*Research Center of Laser Fusion, China Academy of Engineering Physics, Mianyang, P. R. China*
[2]*Institute of Systems Engineering, China Academy of Engineering Physics, Mianyang, P. R. China*
[3]*Department of Modern Mechanics, University of Science and Technology of China, Hefei, P. R. China*

<u>*Summary*</u> Magnetorheological elastomer (MRE) is a kind of soft solid magnetic field-responsive material composing of micron-sized magneto-sensitive particles and non-magnetic hyper-elastic matrix. The mechanical or physical behaviour of MRE can be adjusted by using external magnetic field, and the behaviour is strongly correlated with the underlying particle-aggregated microstructures of MRE. This work aimed to find the relation between the microstructure and the property of MRE, and studied the particle aggregation of MRE in curing process and predicted the microstructure-dependent property of cured MRE using particle-level dynamics simulation and finite element analysis, respectively. It is suggested that combining particle-level dynamics with finite element analysis is a preferred way to reveal the dominating mechanism giving rise to the macroscopic performance of MRE.

INTRODUCTION

Magnetorheological elastomer (MRE) is a kind of smart magnetic field-responsive composite material. Usually, MRE is prepared by embedding micron-sized magneto-sensitive particle into magnetically insensitive polymer or rubber matrix. Attractively, the mechanical or physical property of MRE can be altered by using external magnetic field, making MRE be widely developed in vibration absorbers, vibration isolators, sensing devices, etc.[1] When preparing MRE, the composite material behaves as a high-viscosity fluid-like mixture in the curing process. Thus, an external magnetic field is usually applied to control the particle-aggregate microstructure and go further the post-curing property of MRE. Though it is clear that the macroscopic property of MRE is strongly correlated with its underlying microstructures, the microstructure-based dominating mechanism giving rise to the macroscopic property has never been identified clearly [2]. Therefore, it is imperative to reveal the dominating mechanism. As for an analogue to the high-viscosity fluid-like mixture (i.e. MRE in curing process), the microstructure-based mechanism of the performance of magnetorheological plastomer has been well studied by using particle-level dynamics simulation [3,4]. Given this, in this work, particle-level dynamics combining with finite element analysis is developed to study the particle-aggregating mechanism in the curing process and the effect of particle-aggregated microstructure on the post-curing property of MRE.
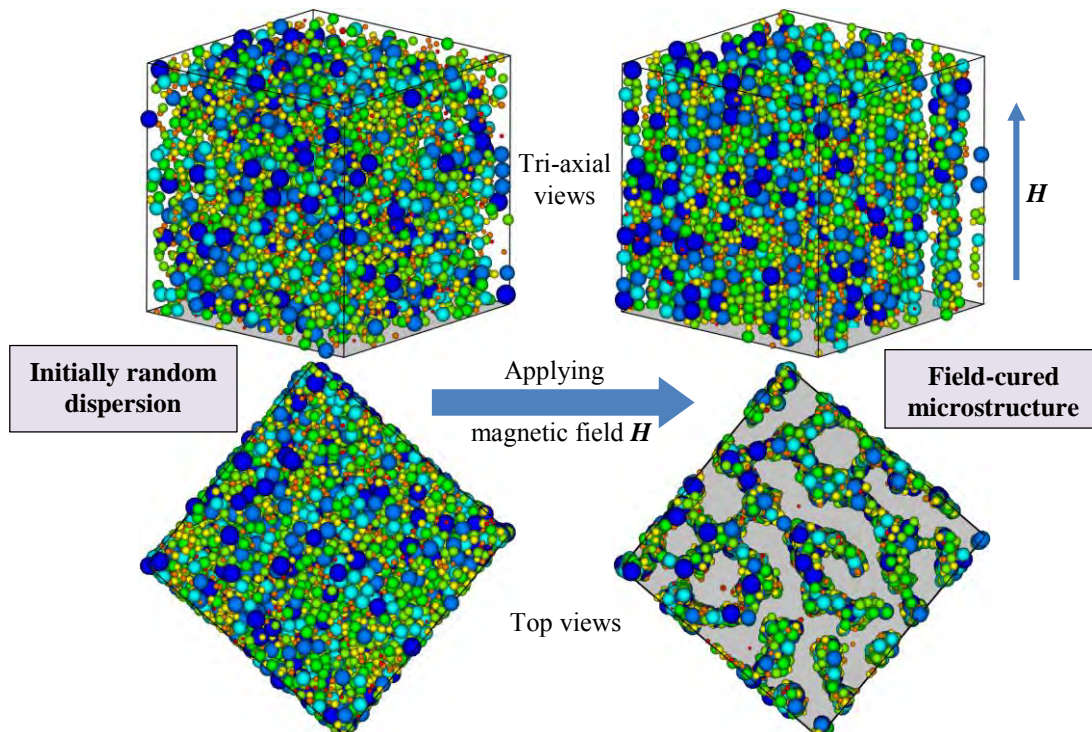
Fig. 1 Magnetic field-induced change of particle-aggregated microstructure in MRE's curing process.

a) Corresponding author. Email: yxd66my@163.com**.**

MODELING AND SIMULATION

MRE composes of magneto-sensitive particles and non-magnetic matrix with a small quantity of dispersing agent, surfactant, vulcanizing agent, etc. The particle and the matrix are the dominating components of MRE and thus the primary factors considered to model MRE. To the particle, it is vital to take its magnetic property and size distribution into consideration. The particle used here is a soft magnetic material and has a log-normal size distribution. To the matrix, its pre-curing, in-curing and post-curing states, as well as their mechanically analytical models, need to be identified clearly. The pre-curing or post-curing matrix affects little on the particle-aggregating structure comparing to the in-curing state. The matrix in curing process behaves as a high-viscosity fluid-like medium, while behaves as an elastic material after curing process. After the models of particle and matrix are identified, the particle-particle interaction and particle-matrix interaction can be constructed accordingly. In this work, a cubic cell with the edge length of 200 μm and the particle volume fraction of 20% is considered for modelling MRE. Then particle-level dynamics simulation is implemented to study the particle aggregation in curing process, and finite element analysis is applied to predict the performance of cured MRE.

RESULTS AND DISCUSSION

Fig. 1 gives the magnetic field-induced microstructural evolution of MRE in curing process. As the top-left subfigure and the bottom-left subfigure show, the particles initially and randomly disperse in the cubic cell before magnetically curing process proceeding. After applying an external magnetic field, the particles gradually aggregate to form chain-like and go further column-like microstructures, as the right subfigures show. In addition, the porous microstructure is formed by magnetic particles from the view of a top point. With the change of particle-aggregated microstructure, the microstructure-based macroscopic properties of MRE, such as storage modulus, damping, thermal conductivity, permeability, electricity, etc., will change a lot. As an example of microstructure-dependent properties in two-dimensional case, **Fig. 2** shows that the thermal conductivity of MRE is strongly microstructure dependent. That is to say, the isotropic particle dispersion leads to isotropic thermal conductivity, while the anisotropic conductivity results from anisotropic particle-aggregation, as a result of that the thermal conductivities of particle and matrix are not the same and they differ much to each other.
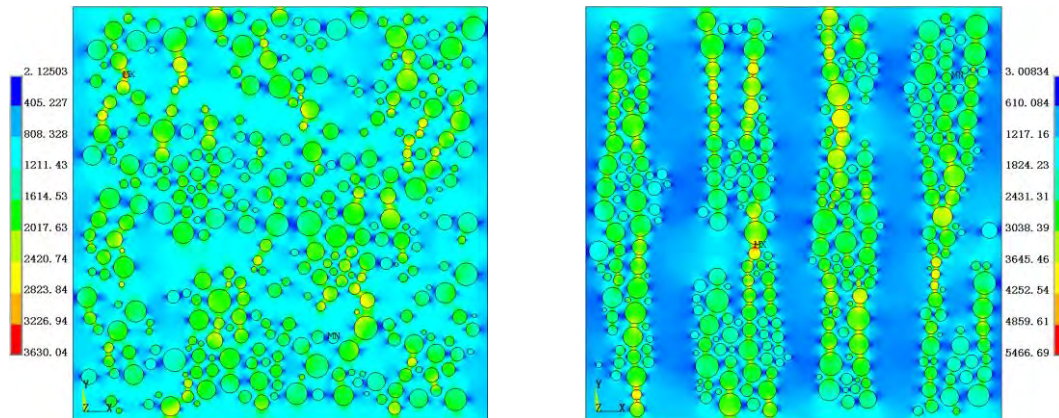
Fig. 2 The microstructure-based isotropic (left) and anisotropic (right) thermal conductivity of cured MRE.

CONCLUSIONS

1) Particle-level dynamics simulation can be developed to study the magnetic field-induced particle aggregation of MRE in curing process. Finite element method can be utilized for analysing the microstructure-based property of cured MRE.

2) Combining particle dynamics with finite element analysis is a suggested way to reveal the microstructure-based dominating mechanism giving rise to the macroscopic property of MRE.

References

[1]   Li Y. C., Li J. C., Li W. H., Du H. P.: A State-of-the-art Review on Magnetorheological Elastomer Devices. *Smart Mater. Struct.* **23**: 123001, 2014.

[2]   Han Y., Hong W., Faidley L. E.: Field-stiffening Effect of Magneto-rheological Elastomers. *Int. J. Solids Struct.* **50**: 2281-2288, 2013.

[3]   Xu Y. G., Gong X. L., Xuan S. H., Zhang W., Fan Y. C.: A High-performance Magnetorheological Material: Preparation, Characterization and Magnetic-mechanic Coupling Properties, *Soft Matter* **7**: 5246-5254, 2011.

[4]   Liu T. X., Gong X. L., Xu Y. G., Xuan S. H., Jiang W. Q.: Simulation of Magneto-induced Rearrrangeable Microstructures of Magnetorheological Plastomers. *Soft Matter* **9**: 10069-10081, 2013.

THICKNESS AND D33 EFFECTS ON THE ENERGY CONVERSION AND ACTUATION OF PIEZOELECTRIC UNIMORPHS

Nanshu Lu[1], Taewoo Ha[1]

[1]*Center for Mechanics of Solids, Structures, and Materials, Department of Aerospace Engineering and Engineering Mechanics, Department of Biomedical Engineering, Texas Materials Institute, The University of Texas at Austin, Austin, TX 78712, United States*

Summary Piezoelectric unimorph is composed of a piezo-layer (with top and bottom electrodes) uniformly laminated on an inactive flexible substrate. Because of their simple construction and flexibility, unimorphs are widely used as flexible sensors and actuators. Here we report a comprehensive theoretical framework to investigate the effects of the film-to-substrate thickness ratio on voltage, charge, and energy outputs when the unimorph is subjected to eight different boundary/loading conditions. For not so thin unimorphs, there is non-zero normal stress in the thickness direction (σ_3), in which case d_{33} can play a significant role. Non-monotonic voltage and energy generation versus thickness ratio relations have been found in some cases and optimum thickness ratio for unimorph generator can be predicted. When the unimorph is actuated by voltage applied across the piezo-layer, non-monotonic actuated deflection versus thickness ratio relation is also found.

INTRODUCTION

Piezoelectric materials have found wide applications in energy harvesting as well as actuation because of their unique combination of mechanical form factors and energy transduction capabilities. Existing unimorph models [1-3] are mostly limited to cantilever configurations and the d_{33} contribution has been neglected because σ_3 is always assumed to be zero. However, unimorphs can also operate under the boundary conditions of pure bending or simple-simple support and can be subjected to variety types of load or displacement excitations. Moreover, σ_3 is non-zero for thick unimorphs and may have significant contributions to the outputs. To find a remedy for aforementioned deficiencies, we derive closed-form solutions for unimorphs subjected to eight different boundary/loading conditions [4]. To validate our theory, finite element modeling (FEM) was performed using COMSOL Multiphysics. Non-monotonic electrical outputs versus thickness ratio curves are found for several boundary value problems (BVP). To resolve the discrepancy between theoretical and FEM results for some scenarios, the d_{33} effect had to be taken into consideration. Simple models to determine average σ_3 along beam length has been proposed and turn out to be very effective in accounting for the d_{33} contribution.

METHOD AND RESULTS

Suppose the piezoelectric layer and the substrate have thicknesses of h_1 and h_2 and Young's moduli of Y_1 and Y_2, as labeled in Fig. 1(a), calculating the voltage, charge, and power output of such a unimorph first requires the determination of the neutral axis and the effective second moment of inertia of the bilayer. The distance from the neutral axis to the bottom surface of the substrate is represented by Δh_1, as labeled in Fig. 1(a), where Δ has been given by [5]

$$\Delta = \frac{1 + 2\Sigma\eta + \Sigma\eta^2}{2\eta(1 + \Sigma\eta)} \tag{1}$$

where $\Sigma = \bar{Y}_1/\bar{Y}_2$ is the film-to-substrate modulus ratio with $\bar{Y} = Y/(1 - \nu^2)$ being the plane strain modulus, Y being the Young's modulus, ν being the Poisson's ratio, and $\eta = h_1/h_2$ is the film-to-substrate thickness ratio.

The effective second moment of inertia of the bilayer is given by [4]

$$I = h_2^3\left\{\Sigma\left[\eta(\Delta\eta - 1)^2 - \eta^2(\Delta\eta - 1) + \frac{\eta^3}{3}\right] + \Delta\eta(\Delta\eta - 1) + \frac{1}{3}\right\} = h_2^3\bar{I} \tag{2}$$

where $\bar{I}$ represents the non-dimensional second moment of inertia and hence the bending stiffness of the unimorph can be written as $\bar{Y}_2 I$. For given piezoelectric and substrate materials (i.e., Σ fixed), the only dimensionless variable in the problem is the thickness ratio η, whose effect is the focus of this study.

Based on Euler- Bernoulli beam theory, the bending induced normal stress in x direction and its vertical distribution of the unimorph is given by $\sigma_1 = (z - \Delta h_1)\Sigma M/I$. When the beam is thick, non-zero σ_3 may also exist. By the linear piezoelectric effect [6], deformation induced polarization density is proportional to stress through the piezoelectric coefficient, i.e. $P_i = d_{ij}\sigma_j$ ($i = 1,2,3$, $j = 1,2,...,6$), therefore z direction polarization is given by

$$P_3 = d_{31}\sigma_1 + d_{33}\sigma_3 \tag{3}$$

Since charges are only collected from the top and bottom surface electrodes of the piezo-layer, only top ($z = h_1 + h_2$) and bottom ($z = h_2$) surface polarization density will be considered to calculate the total amount of charges. Therefore surface charge density can be calculated as the total charge from the surface polarization density divided by the surface area:

$$\rho = \frac{Q}{S} = \frac{-\int_S a_n \cdot P_3 \, dS}{S}. \tag{4}$$

where a_n stands for the surface normal vector and S stands for the overall surface area. Subsequently, the voltage derived through the definition of capacitance, $V=Q/C$, where $C = \varepsilon_p' L/h_1$, with ε_p' being the effective permittivity of the piezoelectric material [2]. Lastly, the generated energy density can also be calculated by $U=\rho V/2$. Following this procedure, the unimorph electric outputs versus thickness ratio has been analysed for different boundary/loading conditions. As an example, Figs. 1(b)-(e) offers the results of simply supported unimorph subjected to central point load. The analytical results (curves) show excellent agreement with finite element modelling (FEM) results (markers) if the effect of d_{33} (or σ_3) is considered. Non-monotonic outputs also suggest that optimal thickness ratio exists.

Thickness ratio also affects the actuated displacement of a unimorph subjected to applied electric field $E = V_0/h_1$ across the thickness of the piezo-layer [7]. As a result, a uniform stress $\sigma_1 = d_{31}\overline{Y_1}V_0/h_1$ is generated in the piezo-layer, while stress in the substrate remains zero. The resultant moment will therefore bend the unimorph and the actuated displacement is again found to be non-monotonic with respect to the thickness ratio, as displayed in Figs. 1(f) & (g).
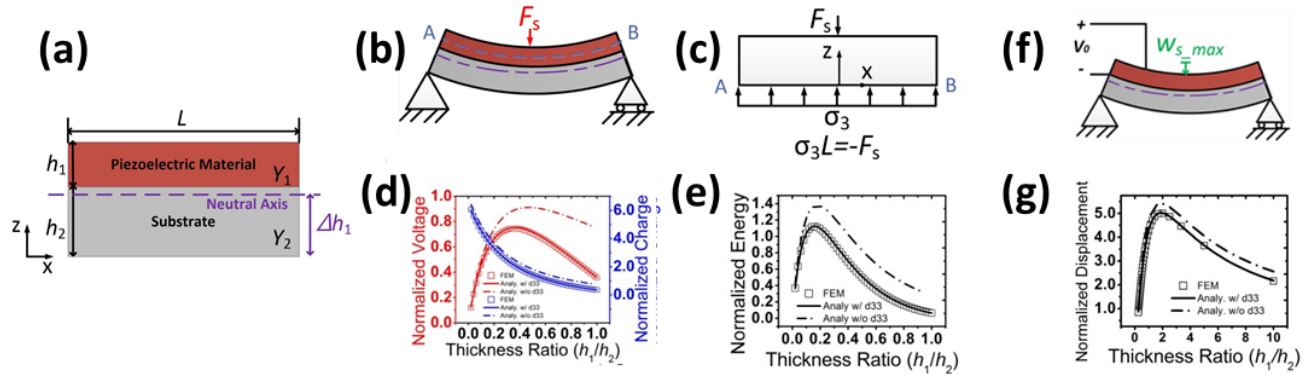
Fig. 1 (a) Illustration of basic variables of the unimorph. (b) A schematic for the simply supported unimorph subjected to central point load. (c) Free body diagram used to calculate average σ_3. (d, e) The analytical and FEM results of normalized voltage, charge density, and energy density as functions of the thickness ratio. (f) A schematic of a simply supported unimorph actuator subjected to constant electric potential. (g) The analytical and FEM results of normalized actuated displacement of the unimorph as a function of the thickness ratio.

CONCLUSIONS

We investigate the electromechanical behaviors of flexible unimorph power generators and actuators. Analytical and numerical models are built to unveil the effects of piezo-layer-to-substrate thickness ratio and piezoelectric material constants on energy conversion under eight different boundary/loading conditions. Our theory reveals that when the unimorph is subjected to displacement-controlled loading conditions, the charge, voltage, and energy outputs are monotonic functions of the thickness ratio whereas when the unimorph is subjected to load-controlled conditions, optimal thickness ratios for maximum voltage and energy outputs exist. Our linear piezoelectric theory has been fully validated by FEM. We have also found that except pure bending conditions, all cantilever and simply supported unimorphs should care about the d_{33} (i.e. σ_3) contribution when the unimorph length is not much larger than the thickness. A simplified average stress model is proven effective in accounting for the d_{33} effect. d_{33} effect may also change the outputs of displacement controlled problems from monotonic to non-monotonic. The effects of elastic mismatch and thickness-to-length ratio have been discussed and analytical solutions for unimorph based actuators are also offered. This work provides a comprehensive and accurate solution for the design and optimization of unimorph based power generators and actuators.

References

[1] Wang Q. M., Du X. H., Xu B. M., Cross L. E.: Theoretical analysis of the sensor effect of cantilever piezoelectric benders. *J Appl Phys* 85:1702-12, 1999.
[2] Smits J. G., Choi W. S.: The constituent equations of piezoelectric heterogeneous bimorphs. *IEEE Trans Ultrason Ferroelectr Freq Control* 38:256-70, 1991.
[3] Park J. K., Moon W. K.: Constitutive relations for piezoelectric benders under various boundary conditions. *Sensor Actuat a-Phys* 117:159-67, 2005.
[4] Ha T. W., Zhang J., Lu N.: Thickness ratio and d33 effects on flexible piezoelectric unimorph energy conversion. *Smart Materials and Structures*, accepted, 2016.
[5] Hutchinson J. W., Suo Z.: Mixed-mode cracking in layered materials. *Adv Appl Mech* 29:63-191, 1992.
[6] Rogacheva N. N.: The theory of piezoelectric shells and plates. Boca Raton: CRC Press; 1994.
[7] Li X. P., Shih W. Y., Aksay I. A., Shih W. H.: Electromechanical behavior of PZT-brass unimorphs. *J Am Ceram Soc* 82:1733-40, 1999.

POROELASTIC TOUGHENING IN POLYMER GELS:
A THEORETICAL AND NUMERICAL STUDY

<u>Alessandro Lucantonio</u>*[1], Giovanni Noselli[1], Robert M. McMeeking[2,3], and Antonio DeSimone[1]

[1]*SISSA - International School for Advanced Studies, Trieste, Italy.*
[2]*Department of Mechanical Engineering and Materials Department, UCSB, Santa Barbara, USA.*
[3]*School of Engineering, University of Aberdeen - King's College, Aberdeen, UK.*

<u>*Summary*</u> We explore the fracture toughness of a polymer gel containing a Mode I growing crack. First, an expression is derived for the energy release rate within the linearized, small-strain setting. This expression reveals a velocity independent toughening that stems from the poroelastic nature of polymer gels. Then, we establish a poroelastic cohesive zone model that allows us to describe the micromechanics of fracture in gels by identifying the role of solvent pressure in promoting poroelastic toughening. We confirm our theoretical findings by means of numerical simulations.

INTRODUCTION

Soft biological tissues, such as cartilage, epithelium and muscles, can withstand relatively high levels of strain without fracturing. Since hydrogels are commonly considered as proxies for soft biological tissues, their fracture behavior is the subject of intense theoretical and experimental investigations.

In general, toughening of hydrogels relies on the energy dissipation that takes place in the process zone around the crack tip [1]. Building upon such a principle, much research currently focuses on the development of experimental techniques for the synthesis of high-toughness hydrogels, where dissipation mechanisms [2, 3] are introduced at the material scale. At the same time, a theoretical effort is needed in modeling diverse fracture modes and sources of toughening in soft materials, starting with the basic, classical fracture mechanics problems.

In this spirit, here [4] we study the propagation of a semi-infinite crack in an infinite polymer gel that is loaded in Mode I conditions and immersed in a solvent. We present a detailed energy analysis that evidences the existence of a velocity-independent toughening, which is innate in the poroelastic nature of polymer gels. Further, we establish a poroelastic cohesive zone model that provides a framework to describe the micromechanics of fracture processes in polymer gels.

ENERGY ANALYSIS FOR A PROPAGATING CRACK IN A POLYMER GEL

We consider a gel consisting of an infinite polymer network immersed in a solvent. The gel contains a semi-infinite crack propagating with velocity v along the $\mathbf{e}_1$ direction. The crack faces are traction-free and in chemical equilibrium with the surrounding solvent. At infinity, the Mode I stress field is applied with intensity factor K_v^∞, and the material responds as an incompressible elastic solid, under the assumption that fluid flow is confined to a small process zone surrounding the crack tip. We develop our theory in the linearized, plane-strain setting.

Manipulations of the energy balance statement appropriate for gels [6] lead to the following definition of the energy release rate $\mathcal{G}$, in a coordinate system $(\hat{x}_1, \hat{x}_2)$ centered at crack tip [4, 5]:

$$\mathcal{G} = \int_{\mathcal{C}} \left(\psi \mathbf{n} \cdot \mathbf{e}_1 - \mathbf{Tn} \cdot \frac{\partial \mathbf{u}}{\partial \hat{x}_1} \right) \mathrm{d}S - \int_{\mathcal{R}} p \frac{\partial \varepsilon}{\partial \hat{x}_1} \, \mathrm{d}A, \quad \psi(\mathbf{E}) = G\mathbf{E} \cdot \mathbf{E} + \frac{1}{2} \left(\kappa - \frac{2}{3} G \right) \varepsilon^2, \tag{1}$$

where ψ is the free energy of the gel in the linearized poroelasticity framework [7], $\mathbf{T}$ is the Cauchy stress, $\mathbf{n}$ is the outer normal to the (arbitrary) contour $\mathcal{C}$ encircling the domain $\mathcal{R}$ and containing the crack tip, $\mathbf{u}$ is the displacement field, p is the solvent pressure within the gel, G and κ are the poroelastic moduli of the gel, and ε is the trace of the small-strain tensor $\mathbf{E}$. The first integral on the right hand side evaluated on a contour $\mathcal{C}^\infty$ far away from the tip provides the far-field energy release rate $\mathcal{G}_v^\infty = (K_v^\infty)^2 / \bar{E}_u$, where $\bar{E}_u = 4G$ is the undrained plane strain modulus. Then, we rewrite eq. (1) as

$$\mathcal{G}_v^\infty = \Gamma + \int_{\mathcal{R}^\infty} p \frac{\partial \varepsilon}{\partial \hat{x}_1} \, \mathrm{d}A, \tag{2}$$

where we have enforced the criterion $\mathcal{G} = \Gamma$ for crack propagation. The area integral may be estimated using the near-tip fields obtained through an asymptotic analysis of the governing equations for crack propagation, thus providing an analytical estimate for the degree of toughening, which is reported in Fig. 1(*Left*) and is confirmed by numerical simulations [4]. This result shows that the applied stress intensity factor needed for crack propagation at a certain velocity $v \neq 0$, which represents

*Corresponding author. Email: alucanto@sissa.it
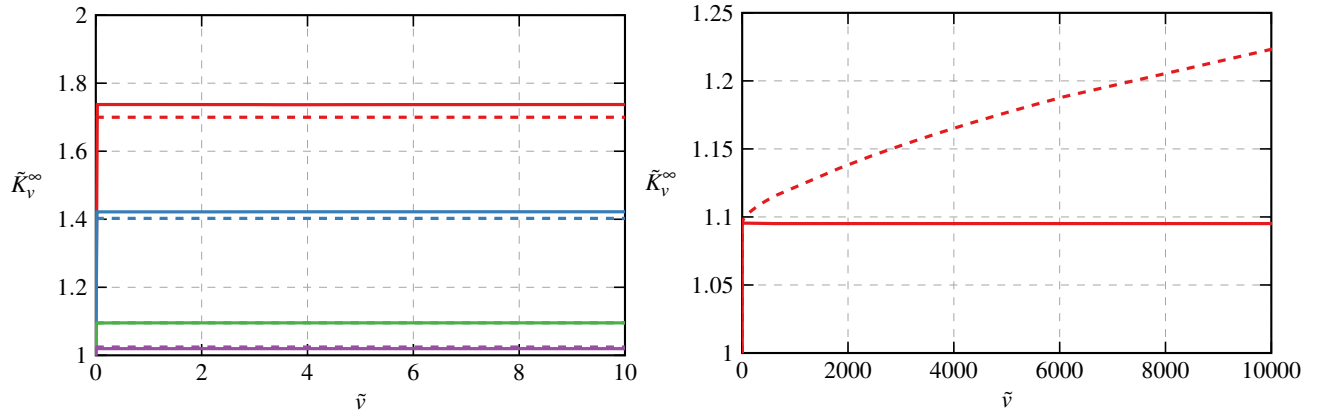
Figure 1: (*Left*) Degree of toughening $\tilde{K}_v^\infty = K_v^\infty/K_o^\infty$ as a function of the dimensionless crack tip velocity $\tilde{v} = v\Gamma/D_cG$, for a Mode I crack, with D_c the effective diffusivity [4] of the solvent. Numerical results (solid lines) and analytical estimates (dashed lines) obtained from eq. (3) using the asymptotic crack tip fields. Blue line corresponds to $\kappa/G = 1$, cyan line to $\kappa/G = 2$, red line to $\kappa/G = 10$ and green line to $\kappa/G = 50$. (*Right*) Degree of toughening as a function of the dimensionless crack tip velocity, for a Mode I crack. The dashed line is the numerical result for the cohesive zone model, with $\kappa/G = 10$. The continuous line is the result obtained computing eq. $(1)_1$ from the numerical solution, without the cohesive zone model (see Fig. 1-*Left*).

the effective toughness of the system, is greater than the critical stress intensity factor needed to initiate propagation of a stationary crack in a purely elastic material, *i.e.* the intrinsic fracture toughness $K_o^\infty = \sqrt{\bar{E}\Gamma}$ of the polymer network. Here, $\bar{E} = E/(1 - \nu^2)$ is the effective plane-strain modulus, where E and ν are computed from G and κ through standard relations of isotropic linear elasticity. Physically, this toughening effect may be explained as follows. The stress concentration in front of the crack tip causes the material to expand. Since expansion requires an increase in solvent volume fraction, a reduction of solvent pressure develops in the process zone to draw solvent towards the crack tip. This solvent flow implies viscous dissipation that is quantified by the area integral in eq. (2). We note that toughening depends on the ratio κ/G (Fig. 1-*Left*).

Next we introduce a poroelastic cohesive zone model [4]. In this case, energy balance arguments similar to those leading to the previous equation provide the following expression for the remotely applied energy release rate

$$\mathcal{G}_v^\infty = \Gamma - \int_{\delta_f}^0 p_c \, \mathrm{d}\delta + \int_{\mathcal{R}^\infty} p \frac{\partial \varepsilon}{\partial \hat{x}_1} \, \mathrm{d}A \,, \tag{3}$$

where p_c is the solvent pressure within the cohesive zone and δ_f is the crack opening at failure. We observe that p_c will be negative in the cohesive zone due to the pressure gradient required to draw solvent into it. Therefore, we conclude that the second term on the right hand side of eq. (3) contributes a positive increment to the toughness of the gel (Fig. 1-*Right*), in addition to toughening contribution provided by the third term on the right hand side.

CONCLUSIONS

We have demonstrated the existence of a velocity-independent toughening in a Mode I-loaded polymer gel specimen containing a semi-infinite, propagating crack. Physically, this toughening derives from the work performed by the solvent pressure against volume expansion within the process zone. For the cohesive zone case, we have shown that the applied stress intensity factor needed for propagation increases with crack tip velocity, thanks to the resistance to crack opening offered by the negative solvent pressure within the cohesive zone. Our results highlight the importance of poroelasticity to reveal and quantify possible toughening mechanisms.

References

[1] Zhao X.: Multi-scale multi-mechanism design of tough hydrogels: building dissipation into stretchy networks. Soft Matter, 10:672-687, 2014.

[2] Gong J. et al.:Double-Network Hydrogels with Extremely High Mechanical Strength, Adv. Mater., 15:1155-1158, 2003.

[3] Sun J.-Y. et al.: Highly stretchable and tough hydrogels. Nature, 489:133-136, 2012.

[4] Noselli G. et al.: Poroelastic toughening in polymer gels: A theoretical and numerical study. Submitted, 2016.

[5] Bouklas N. et al.: Effect of Solvent Diffusion on Crack-Tip Fields and Driving Force for Fracture of Hydrogels. J Appl Mech, 82:081007-081007, 2015.

[6] Lucantonio A. et al.: Transient analysis of swelling-induced large deformations in polymer gels. J. Mech. Phys. Solids, 61:205-218, 2013.

[7] Lucantonio A. et al.: Reduced models of swelling-induced bending of gel bars. Int. J. Solids Struct., 49:1399-1405, 2012.

FRACTURE OF SOFT ELASTIC FOAM

Zhuo Ma, Xiangchao Feng & Wei Hong[a)]

Department of Aerospace Engineering, Iowa State University, Ames, Iowa, USA

Summary Soft elastic foams, which consist of flexible and stretchable ligaments, exhibit extremely high fracture toughness. Comparing the cellular structure of elastic foams with the network structure of rubbery polymers, this paper proposes a scaling law for the fracture energy of soft elastic foam. A phase-field model for the fracture processes in soft elastic structures is developed to verify the scaling law. The numerical simulations in 2D foam structures of different unit-cell geometries agree with the scaling law very well. In addition, the dependences of the macroscopic fracture energy on geometric parameters such as the network connectivity and spatial orientation have also been revealed by the numerical results. To further enhance the fracture toughness, a type of soft foam structures with folded ligaments has been proposed and its effective fracture energy is one order of magnitude higher than the base material can be reached by using the soft foam structure.

INTRODUCTION

Solid foam, a state of highly porous cellular structure, is commonly found in nature and in daily life. Scaling laws between fracture properties and porosity have been proposed and widely accepted [1]. However, most existing theories are based on linear elastic fracture mechanics, their applicability becomes questionable to those consisting of soft and highly stretchable materials, such as elastomers. The major difference between stiff brittle foam and soft elastic foam lies in the slenderness of ligaments. In contrast to the cell walls of rigid foam which partially shares the load after rupture, a fractured cell wall of soft foam merely dangles over the rest of the structure.

Let us start from the fracture process of a rubber, in which the crosslinked network of long polymer chains could be regarded as an extreme case of soft foam when each slender ligament shrinks down to a molecular size. The classic Lake-Thomas model suggests that the fracture energy of a rubber scales with the number of chains per unit cross-sectional area [2]. Analogously, we deduce that the scaling relation for the fracture energy of a soft foam is

$$\Gamma \approx \alpha W_c \psi l \ . \tag{1}$$

Here, we use W_c to represent the critical energy density of cell wall at rupture, ψ for the volume fraction of the solid phase, and l for the characteristic size of the foam. Even though the scaling law (1) seems natural and plausible, it could be hard to verify directly through experiments. Alternatively, we seeks to verify the scaling law numerically through the following phase-field model.

PHASE FIELD MODEL OF FRACTURE

The phase-field model for fracture, which is capable of calculating the crack growth according to the energy criterion without a predetermined crack path, is very suitable for structures with complex geometries such as soft elastic foams. To describe the state of material damage and to avoid tracking the crack front and faces, a phase field $\phi(\mathbf{X}, t)$ varying continuously between the intact region ($\phi = 1$) and a fully damaged region ($\phi = 0$) is introduced. Following Karma et al. [3], we write the free energy density function as:

$$W(\phi, \nabla \phi, \mathbf{F}) = g(\phi) W_s^0(\mathbf{F}) + [1 - g(\phi)] W_c + \frac{\kappa}{2} |\nabla \phi|^2 , \tag{2}$$

where W_s^0 is the strain-energy density of undamaged material, $g(\phi)$ an interpolation function between $g(0) = 0$ and $g(1) = 1$, and κ the coefficient of the gradient energy term. W_c is the critical strain-energy density beyond which the material will degrade spontaneously to lower the total free energy. For the evolution of the phase field variable ϕ, we assume a linear kinetic law with isotropic mobility, so that the rate of change in ϕ is proportional to the variation of the system free energy with respect to ϕ.

The system has an intrinsic length scale $r = \sqrt{\kappa/W_c}$, which represents the characteristic length of the fracture process zone. The intrinsic fracture energy of the solid described by this model is approximately $2rW_c$.

RESULTS AND DISCUSSION

The scaling relation (1) is verified through the simulation on the fracture processes of hexagonal soft foams. A set of 2D hexagonal foams of the same volume fraction but different ligament lengths are modelled first. For the hexagonal foams in both orientations, the dimensionless fracture energy Γ/rW_c is approximately linear in the ligament length l/r, as shown by Fig. 1c. Similarly, we fix the ligament length and vary the solid volume fraction ψ. The results are plotted in Fig. 1d. At relatively small volume fraction, the fracture energy is approximately proportional to the volume fraction just as predicted by (1).

[a)] Corresponding author. Email: whong@iastate.edu.
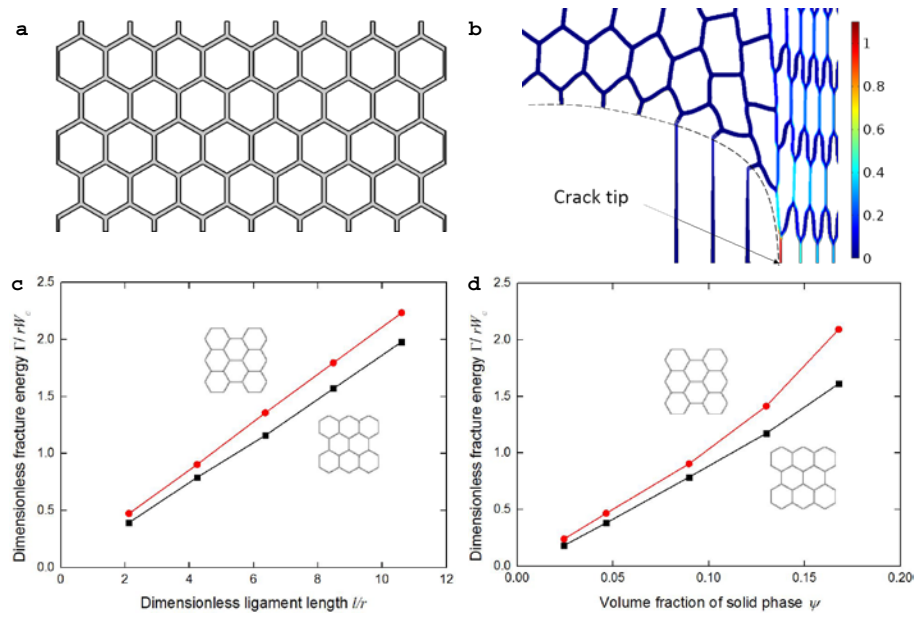
Fig 1. (a) Part of a 2D hexagonal foam structure. (b) Strain energy density of a hexagonal foam near a propagating crack tip. (c) Fracture energy as a function of the ligament length. (d) Fracture energy as a function of the volume fraction of the solid phase.

To further enhance the fracture toughness, a new kind of soft elastic foams with non-straight ligaments is proposed. As an example, the numerical model is constructed by repeating the unit cell sketched in Fig. 2a. By varying the width of the serpentine ligaments, we evaluate the fracture energy of several structures with different solid volume fraction. As plotted in Fig. 2c, the scaling law (1) still holds for the foam structures with serpentine ligaments. However, the dimensionless fracture energy has been significantly improved to $\Gamma/rW_c \approx 25$, more than one order of magnitude higher than the foam structures with straight ligaments or the same bulk material.
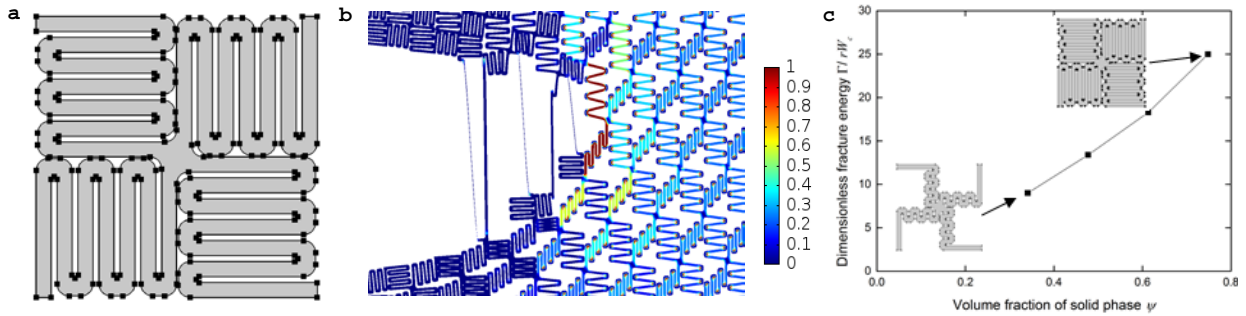
Fig 2. (a) Unit cell of a soft elastic foam containing serpentine ligaments. (b) Calculated dimensionless strain energy density of the soft elastic foam. (c) Calculated fracture energy of soft foam structures with serpentine ligaments, as a function of the solid volume fraction ψ.

CONCLUSIONS

The scaling relation between fracture energy and structural properties of soft foam structures is proposed by making an analogy between compliant ligaments in a soft elastic foam and the polymer chains in an elastomer. Through a phase-field model developed specifically for the fracture of elastomers, the scaling law is verified on soft foam structures of various geometries. Finally, a type of soft foam structures with serpentine ligaments is introduced and numerical study shows such structures may achieve an effective fracture energy much higher than that of the corresponding base material.

References

[1] Gibson L. J., Ashby M. F.: Cellular solids: structure and properties. Cambridge university press, Cambridge, UK 1999.
[2] Lake G. J., Thomas A. G.: The strength of highly elastic materials. Proceedings of the Royal Society of London, Series A, Mathematical and Physical Sciences 300(1460): 108-119, 1967.
[3] Karma A., Kessler D. A., Levine H.: Phase-field model of mode III dynamic fracture. Physical Review Letters 87(4): 045501, 2001.

REVERSIBLE SHAPE CHANGING COMPONENTS BY 3D PRINTING

Yiqi Mao[1], Zhen Ding[2], Martin L. Dunn[2 a], H. Jerry Qi[1 a]

[1]The School of Mechanical Engineering, Georgia Institute of Technology, Atlanta, GA 30332, USA
[2]Singapore University of Technology and Design, Singapore 138682, Singapore

Summary The availability of reversible components that can alter their shapes in response to environmental changes is crucial for active materials. The rapid development of 3D/4D printing technologies also enables the fast implementation of sophisticated designs for sensors and actuators. This paper demonstrates a new reversible component that is 3D printed to combine shape memory polymers and hydrogels. This new method uses the swelling of hydrogel as the driving force for the shape alternation and the change of the modulus of shape memory polymers as a function of temperature to regulate the time of such shape alternation. The component can be activated by changing temperature and aqueous environment, without any other further mechanical loading and unloading. The obtained structure is stiff in two different configurations. Several 2D and 3D shape changing actuators are demonstrated to illustrate the broad application potentials of the proposed design.

INTRODUCTION

Structures and devices that can change its shape in response to environmental stimuli are highly desirable in a wide range of applications [1]. Shape memory materials, such as shape memory alloys (SMAs) and shape memory polymers (SMPs), are candidates that have been widely explored. However, both materials have limitations: SMAs exhibit reversible actuations with sufficient stiffness, but the amount of actuation is low[2]; SMPs have been studied as an alternative with large shape change, but most SMPs can only achieve one-way actuation[3]. Although some new developments in SMPs can achieve reversible actuation, but they either involve complicated fabrication[4] or sophisticated chemistry[5]. One exception is environmentally responsive hydrogels[6], whose capability to hold aqueous solution can be tuned by temperature and thus to generate a large volume change. However, hydrogels have low stiffness, with the typical Young's modulus in the range of a few tens to hundreds of kPas.

3D printing allows materials to be deposited in a layer-by-layer manner to form a 3D component. In addition, the recent development of multi-material 3D printing enables digital materials, whose properties can vary almost continuously. Such capabilities, i.e. printing complicated geometries and digital materials, empower 3D printing to create components with unprecedented properties [7-10]. More interestingly, 4D printing concept was developed where active materials are used to create shape changing components[11-13], which added the 4th dimension (or time) to the 3D printing process.

In this work we achieve reversible actuations through a composite where SMPs and hydrogels are spatially distributed through a careful design, which can be easily implemented by a multi-material 3D printer[14]. We use mechanical constrains to transform an isotropic hydraulic pressure from equiaxial swelling to a uniaxial driving force that powers the shape change of the component; we also utilize the shape memory effect in the SMP to regulate the time of such shape changes. In addition, the SMP provides the stiffness to the component that is much higher than one would achieve in purely hydrogel-based component. Finally, by applying the basic design concept, we demonstrate a folding origami structure.

METHODS AND RESULTS

Design concepts

The two key concepts to our design are to convert the hydrogel swelling force from equiaxial to a linear force that can drive the shape change in one particular direction or in one particular plane, and to use the sensitivity of the SMP properties to temperature to regulate the time for actuation. To achieve this, the hydrogels and the elastomer columns are sandwiched between a layer of the SMP (top) and a layer of the elastomer (bottom). Small holes are placed in the elastomer layer to allow water flowing in and out. During a reversible actuation cycle, the printed component is straight after printing. It is then immersed into water at a temperature ~0°C for a certain amount of time to allow the hydrogel to absorb water; in addition, due to the low temperature, the stiffness of the SMP is high; therefore the volume swelling of hydrogel is highly constrained and the strip does not show significant shape change. Next, the strip is brought into a high temperature environment (such as water bath) where the SMP softens significantly, which allows the hydrogel swelling to induce large shape change. In addition, the elastomer columns that connect the top and bottom layers impose constraints on hydrogel swelling in the z-direction, thus converting the swelling force into the x-y plane, which drives the strip bending. After actuation at high temperature, we cool the strip to a temperature below the T_g of the SMP; due to the increase of the SMP stiffness, the strip is stiff. In the ambient environment, the hydrogel will lose water and dry. After the hydrogel is fully dry, immersing the strip into a high temperature environment will recover the straight shape of the strip. At low temperature, the strip becomes stiff again. This finishes one cycle of reversible actuation, which can be repeated multiple times.

---

[a] Corresponding authors. Email: martin_dunn@sutd.edu.sg; qih@me.gatech.edu.

Design Demonstration

This design concept is demonstrated in Fig.1 The printed strip is shown in Fig.1a. It was firstly immersed in cold water (3°C) for 12hrs and showed a small amount of bending (Fig 1b). The strip was then immersed in water (temperature of 75°C) and bent into the shape showing in Fig. 1c in ~10 sec. The strip was then removed from the water and is cooled down to the RT (Fig. 1d). The strip maintained the bending shape (Fig. 1e). At the low temperature, the strip was stiff. Fig. 1f also shows the bent strip can support the deadweight of 25g. After drying at low temperature, the strip was immersed in high temperature water again and it recovered to the flat shape.

3D Reversible Structure

As an example for 3D structure, we demonstrate a flower that is capable for reversible folding and unfolding. First, we designed and printed a flower-shaped 3D structure composed of three groups of petals, which had different thickness ratios of layers of the elastomer, the hydrogel, and the SMP to allow different folding speeds. The printed structure is shown in Fig. 2a. After being put in low temperature water for 12hrs, then being immersed in high temperature water, all the layers bent immediately, forming a flower-like shape (Fig. 2b). Taking the structure out and let it dry, the structure maintained the flower shape and was stiff. As shown in Fig. 2d, it can carry a load of 25g. The flower-like structure was then put into hot water and the structure became flat again (Fig. 2c). This process could be repeated many times.

CONCLUSIONS

Components with large reversible shape change are highly desirable for many engineering and biomedical applications. However, the materials available for large and reversible shape change are rare. In this paper, by combining shape memory polymers with hydrogels, we demonstrated components with reversible shape changes by using 3D printing. The concept in this paper can be applied to design actuators with faster response and with other actuation method, such as electromagnetic field.

Figure 1. The bending angle of two activated shape memory strip in the desired shape memory cycle. a) The printed strip is straight; b) it bends slightly after immersing in cold water for 12hrs; c) it bends quickly when immersing in hot water; d) it is then taken out of water to the room temperature air; e) it is then air dried; f) the strip is stiff and can carry a load of 25g. If it is heated, it returns to the straight shape.

Figure 2. A self-folding/unfolding flower. a) The printed structure; b) After immersing in water then being transferred to hot water, the structure folds; c) After dry, it becomes flat again when being put into hot water. g) The structure in b) is stiff after it is dried. It can carry a load of 25g.

References

[1] Gandhi, M.V. and B.S. Thompson, *Smart materials and structures*. 1st ed. 1992, London ; New York: Chapman & Hall. xii, 309 p.
[2] Lexcellent, C., *Shape-memory alloys handbook*. Materials science series. 2013, London, UK; Hoboken, NJ: ISTE; Wiley.
[3] Liu, C., H. Qin, and P.T. Mather, *Review of progress in shape-memory polymers*. Journal of Materials Chemistry, 2007. **17**(16): p. 1543-1558.
[4] Westbrook, K.K., et al., *Two-way reversible shape memory effects in a free-standing polymer composite*. Smart Materials & Structures, 2011. **20**(6).
[5] Yakacki, C.M., et al., *Tailorable and programmable liquid-crystalline elastomers using a two-stage thiol-acrylate reaction*. Rsc Advances, 2015. **5**(25): p. 18997-19001.
[6] White, E.M., et al., *Advances in smart materials: Stimuli-responsive hydrogel thin films*. Journal of Polymer Science Part B-Polymer Physics, 2013. **51**(14): p. 1084-1099.
[7] Babaee, S., et al., *3D Soft Metamaterials with Negative Poisson's Ratio*. Adv Mater, 2013. **25**(36): p. 5044-9.
[8] Zheng, X.Y., et al., *Ultralight, Ultrastiff Mechanical Metamaterials*. Science, 2014. **344**(6190): p. 1373-1377.
[9] Pandey, S., B. Gupta, and A. Nahata, *Terahertz plasmonic waveguides created via 3D printing*. Optics Express, 2013. **21**(21): p. 24422-24430.
[10] Sanchis, L., et al., *Three-Dimensional Axisymmetric Cloak Based on the Cancellation of Acoustic Scattering from a Sphere*. Physical Review Letters, 2013. **110**(12): p. 124301.
[11] Ge, Q., H.J. Qi, and M.L. Dunn, *Active materials by four-dimension printing*. Applied Physics Letters, 2013. **103**(13).
[12] Ge, Q., et al., *Active Origami by 4D Printing*. Smart Materials & Structures, 2014. **23**: p. 094007-15.
[13] Raviv, D., et al., *Active Printed Materials for Complex Self- Evolving Deformations*. Scientific Reports, 2014. **4**.
[14] Mao, Y., et al., *3D Printed Reversible Shape Changing Component with Stimuli Responsive Materials*. submitted, 2015.

CONSTITUTIVE THEORY FOR MECHANOCHEMICALLY-BASED ENERGY DISSIPATING ELASTOMER

Meredith N. Silberstein[*1]

[1]*Sibley School of Mechanical and Aerospace Engineering Engineering, Cornell University, Ithaca, NY, USE*

Summary Mechanochemically responsive polymers can be designed through the incorporation of mechanophores, molecular groups with a tailored productive response to applied force. Here we present the design and corresponding constitutive theory for an elastomer that dissipates mechanical energy through the incorporation of length unveiling mechanophores. These mechanophores activate as the elastomer approaches its finite extensibility, but prior to chain scission. The reversible release of contour length temporarily increases the failure strain of the polymer chains subjected to the largest local force. The behavior of the model will be presented for monotonic, cyclic, and stress relaxation loading. Required mechanophore energetics and characteristic recovery times will be discussed.

INTRODUCTION

Mechanochemically responsive (MCR) polymers can be realized through the covalent incorporation of mechanophores chemical units that undergo a specific chemical transformation in response to applied force. While most of the demonstrated MCR to date have shown optical responses to mechanical loading, these systems have potential to adapt mechanical properties in response to mechanical load. Here we propose a synthetic analog to an approach often utilized in biological systems - length release at a critical force. Stress relief by mechanophore-based length extension has been experimentally demonstrated in single polymer chains, but not in polymer networks[1]. Here, we present a constitutive theory for an elastomer with length extending mechanophores.

THEORY

The constitutive theory for the MCR elastomer combines transition state theory for force-biased chemical reactions with polymer mechanics and builds on our prior work for an optically responsive elastomer based on covalently linked mechanophores[2]. Polymer chain segments between cross-links are assumed to follow the freely jointed chain model. The parameters governing the highly non-linear response of a single chain segment are the Kuhn segment length that sets the initial chain stiffness and the number of segments between crosslinks that sets the locking stretch. The mechanophore state is determined using transition state theory. The energy barrier between the closed (initial length) and open (extra length) states is assumed to depend linearly on force (Figure 1). When the mechanophore opens the number of segments between crosslinks increases thereby decreasing the force on the polymer chain segment. In addition to mechanophore opening, mechanochemically-driven polymer chain scission is also included. These equations are analogous to those governing the mechanophore state except that the reverse reaction (healing of the chain) is prohibited. A chain that is broken supports no force. A single polymer chain segment can occupy any one of four states: closed and intact, closed and broken, extended and intact, extended and broken. The polymer chain segments then act in concert to form the polymer network with the same force that drives the mechanophore transition and chain scission summing to give the overall network stress.
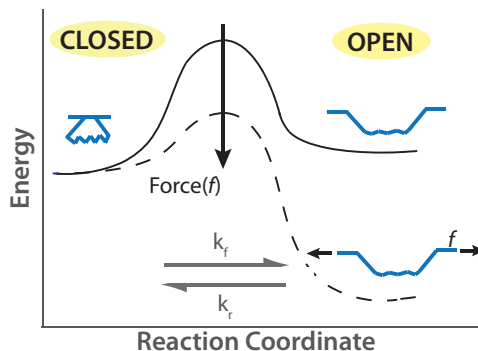
Figure 1: The application of force across a mechanophore reduces the barrier for mechanophore opening.

*Corresponding author. Email: ms2682@cornell.edu

RESULTS AND DISCUSSION

The average force-stretch behavior of an ensemble of aligned polymer chains stretched at a strain rate of $0.01s^{-}1$ is shown in Figure 2a. The polymer chain with no mechanophore behaves hyperelastically breaking at a stretch of 1.77, which corresponds to the the prescribed number of Kuhn segments along the length of the chain $N = 3$. The ensemble of polymer chains with the mechanophores incorporated initially behaves identically to those without, however at a force of 0.55 nN per chain the mechanophores start to activate, N increases to 3.6, and the force drops rapidly. Because of the highly nonlinear force response, all the chains in the ensemble have their mechanophores open over a relatively narrow stretch range. The chains are extended further the force again increases until it reaches a value that causes chain scission. This force is the same as that which causes scission in the chains without mechanophores, however the stretch is significantly larger (1.94 vs 1.77 for these particular chain and mechanophore parameters).

The polymer behavior is qualitatively quite similar to that of the ensemble of aligned chains. The polymer is initially compliant and hardens nonlinearly as the most oriented chains approach the single chain locking stretch. Under monotonic loading the work to when the first damage occurs is nearly twice as large with the mechanophore than without. Further, this model assumes that all mechanophores in a given chain segment activate at once. The energy dissipation performance could be significantly improved by a more gradual length extension that would maintain the chain closer to its present locking stretch. Under cyclic loading (Figure 2b) the difference between the elastomer with and without mechanophores is most apparent in the reloading behavior. The polymer without mechanophores reloads along the unloading curve representing the damaged polymer; the polymer with mechanophores reloads nearly along the initial loading curve since most of the open mechanophores closed during unloading.
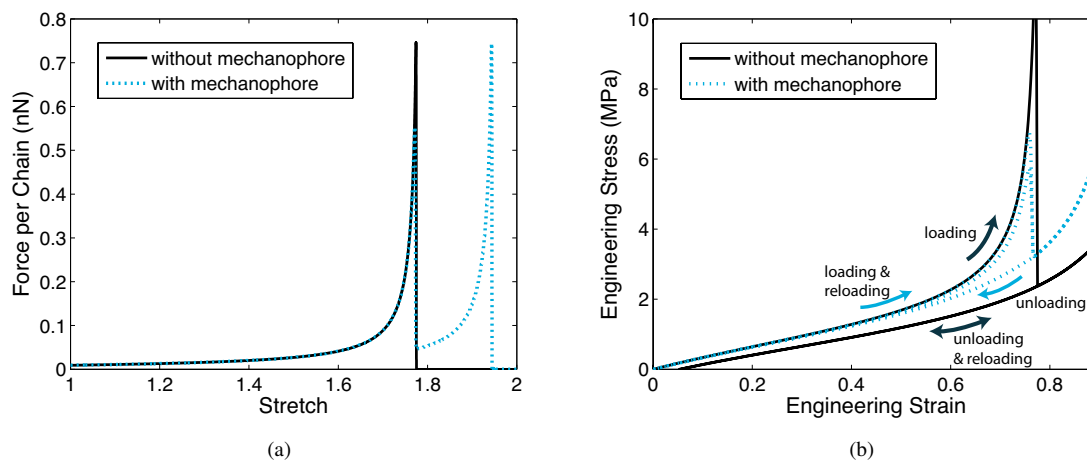
Figure 2: Simulation results for numerically implemented length-extending mechanophore constitutive theory compared to behavior without mechanophores. (a) Force-stretch response of an ensemble of single chains undergoing monotonic extension at a constant strain rate (b) Stress-strain response of a polymer subjected to load-unload-reload to a strain of 0.75 at a constant strain rate magnitude.

CONCLUSIONS

A constitutive model has been presented for an MCR elastomer with repeat energy dissipation capabilities. This model will guide the design and testing of such a material in subsequent work. *Acknowledgements: This work was funded in part by the National Science Foundation under Grant DMR-1307354.*

References

[1] Wu, D., Lenhardt, J. M., Black, A. L., Akhremitchev, B. B., Craig, S. L. : Molecular stress relief through a force-induced irreversible extension in polymer contour length. JACS 132:15936-15938, 2010.

[2] Silberstein, M. N., Cremar, L. D., Beiermann, B. A., Kramer, S. B., Martinez, T. J., White, S. R., Sottos, N. R. : Modeling mechanophore activation within a viscous rubbery network. JMPS 63:141-153.

MODELING THE EFFECT OF INELASTICITY ON INSTABILITIES IN SOFT DIELECTRICS

Shuolun Wang[1], David L. Henann[2], and <u>Shawn A. Chester</u>[*1]

[1]*Mechanical Engineering, New Jersey Institute of Technology, Newark, New Jersey, USA*
[2]*School of Engineering, Brown University, Providence, Rhode Island, USA*

<u>*Summary*</u> Soft dielectrics undergo large deformations in response to an electric field and consequently have attracted a lot of interest as smart active materials with a wide range of applications. The literature on this topic has historically been split between either theoretical studies or device level experiments, with limited communication. In this paper we report on our modeling capability calibrated to VHB 4910, a widely studied soft dielectric material in the literature, which exhibits a significant level of dissipation. We use specially developed finite elements to study the role of visco-elasticity on instabilities in soft dielectrics. Our results show that viscoelastic effects tend to suppress instabilities under cyclic loading.

INTRODUCTION

As soft dielectrics deform under the action of an applied electric field, it is not uncommon to encounter various instabilities. Instabilities of soft dielectrics – a heavily studied topic in the recent literature – are well known under idealized conditions, however work still remains for non-ideal conditions. Using the terminology in [6], instabilities in soft dielectrics may be categorized into three generic modes: i) pull-in, ii) electro-creasing, and iii) electro-cavitation, with the incurred instability based on the boundary conditions. Realizing that such instabilities may be harmful, the mechanics for suppressing an instability and enhancing the performance of soft dielectrics has also been investigated. Some of the proposed methods include applying a mechanical pre-stretch, using materials with "stiffening" properties, and constructing soft dielectric composites to suppress instabilities ([6, 2, 1]).

Motivated by experimental data, and the trend of the literature, the objective of this work is to produce a numerical simulation capability for the broader community that takes the real material behavior into account for more realistic simulation, including the working limits of devices that are susceptible to instability.

CONSTITUTIVE EQUATIONS

Guided by the experimental data for VHB shown in Figure 1, we assume the deformation is accommodated by a combination of one equilibrium mechanism, and N non-equilibrium mechanisms denoted by $\alpha = 1, 2, \ldots, N$. The equilibrium mechanism provides the "long-time" response of the material using the total deformation gradient, whereas the remaining N mechanisms capture the inelastic response of the material using internal variables. Based on the work of [5], we introduce a set of symmetric stretch-like tensorial internal variables $\mathbf{A}^{(\alpha)}$ for the N viscoelastic mechanisms. Although not discussed directly in this paper, thermodynamics and any restrictions required to satisfy the second law are discussed in both [3] and [5] for this class of materials and for brevity are not repeated here. In this work, the Cauchy stress is given by

$$\mathbf{T} = J^{-1}G(\mathbf{B}_{\mathrm{dis}})_0 + K(J-1)\mathbf{1} + \epsilon\left[\mathbf{E}\otimes\mathbf{E} - \frac{1}{2}\left(\mathbf{E}\cdot\mathbf{E}\right)\mathbf{1}\right] + \sum_{\alpha}\left\{J^{-1}G_{\mathrm{neq}}^{(\alpha)}\mathbf{F}\left(J^{-2/3}\mathbb{P} : \mathbf{A}^{(\alpha)}\right)\mathbf{F}^T\right\}, \quad (1)$$
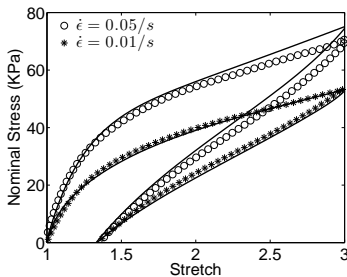
Figure 1: Comparison of the experimental data (shown as points) to our model (shown as lines) in simple tension. The experimental data is taken from [4].

where we have used the notation $G = G_{\mathrm{eq}}\left(\dfrac{\lambda_L}{\bar{\lambda}}\right)\mathcal{L}^{-1}\left(\dfrac{\bar{\lambda}}{\lambda_L}\right)$ for a stretch dependent shear modulus. Also, $\mathbb{P}$ is a fourth order projection tensor $\mathbb{P} = \mathbb{I} - \frac{1}{3}\mathbf{C}^{-1}\otimes\mathbf{C}$ such that the viscous mechanisms have no volumetric contribution. Furthermore, the referential and spatial electric displacements, respectively, are given by

$$\mathbf{D}_R = \epsilon J\mathbf{C}^{-1}\mathbf{E}_R, \qquad \mathbf{D} = \epsilon\mathbf{E}, \quad (2)$$

where ϵ is the permittivity, and we denote the electric potential by φ, such that the spatial electric field $\mathbf{E} = -\mathrm{grad}\,\varphi$.

The calibration of material parameters is straightforward process. First, we calibrate the pure mechanical parameters appearing in our model by fitting to the experimental stress-stretch data found in the literature. Then the electrical parameters are estimated based on values appearing in the literature. Our model fit to the experimental data of [4] is shown in Figure 1.

*Corresponding author. Email: shawn.a.chester@njit.edu

NUMERICAL SIMULATIONS

Now that the material parameters of our theory are calibrated for VHB, in this section we demonstrate our numerical simulation capability in a variety of interesting applications where instabilities in soft dielectrics are prone to arise. We hope to simulate such electro-mechanical instabilities in order to gain deeper understanding of the mechanisms and conditions for the onset of instability. Following the recent work of [6], we consider the following list of simulations; pull in and thinning, and creasing.
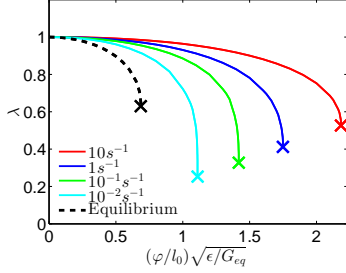
Figure 2: Simulation results for pull-in, the instability is indicated by the × symbols.

The deformation of an unconstrained soft dielectric film coated with compliant electrodes on both surfaces is prone to pull in and thinning under electro-mechanical loading. As the film thickness reduces, a constant applied voltage will induce a higher true electric field, resulting in a higher stress that further deforms the film. At a critical point, the positive feedback may cause the elastomer to thin down abruptly, resulting in the pull-in instability. Figure 2 shows the stretch (λ) corresponding to monotonic loading for multiple rates, for both equilibrium and visco-elastic material responses. It is clear that the addition of visco-elasticity acts to stabilize the instability, delaying the onset of instability with increased loading rates. Also, as reported in [6], in the equilibrium case, the onset of pull-in would occur at a critical stretch of $\lambda_{cr} = 0.63$, which agrees well with our finite element simulations.

Also, in many situations one surface of a soft dielectric is attached to a rigid electrode and another surface free from constraint. In such cases lateral motion is constrained by the rigid electrode, a condition very prone to creasing, and experimental evidence has shown this to be the case [6]. Creasing generally occurs during the application of an applied electric potential, as the soft dielectric begins to attempt to thin down, the potential eventually reaches a critical value where regions of surface on the unconstrained face will form a creasing pattern. Figure 3 shows a few snapshots of a typical plane-strain creasing simulation for cyclic loading as well as a summary of the results for this suite of simulations. Also, as reported in the literature [6], in the equilibrium case, the onset of creasing occurs at a critical electric field of $E_c \approx 1.03\sqrt{G_{eq}/\epsilon}$, which agrees well with our finite element simulations at the slowest loading rate.
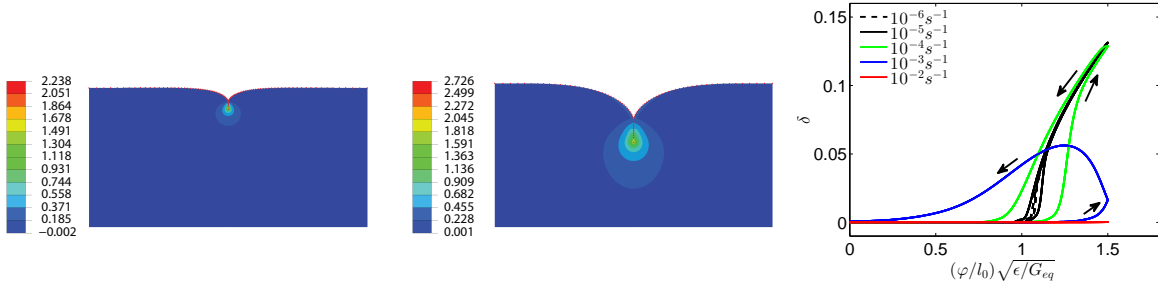
Figure 3: (Left and center) Simulation of a two-dimensional plane-strain crease at a single loading rate showing the maximum log strain. (Right) The relative normalized displacement $\delta = (u_{\text{tip}} - u_{\text{edge}})/l_0$ as a function of the applied potential for a cyclic load and unload at a constant rate. Here the arrows indicate the direction of loading and unloading.

CONCLUSIONS

Using our finite element capability we are able to show how viscoelasticity provides stabilization that may fully suppress instabilities under certain conditions, specifically under cyclic electrical loadings, which may be desirable for many applications. However, much research work yet remains, from both numerical and experimental points of view.

References

[1] Bertoldi, K., Gei, M., 2011. Instabilities in multilayered soft dielectrics. Journal of the Mechanics and Physics of Solids 59, 18–42.

[2] Dorfmann, A., and Ogden, R.W., 2014. Instabilities of an electroelastic plate. International Journal of Engineering Science 77, 79–101.

[3] Henann, D.L., Chester, S.A., Bertoldi, K., 2013. Modeling ofdielectric elastomers:Design of actuators and energy harvesting devices. Journal of the Mechanics and Physics of Solids 61, 2047-2066.

[4] Hossain, M., Vu, D.K., Steinmann, P., 2012. Experimental study and numerical modelling of VHB 4910 polymer. Computational Materials Science 59, 65–74.

[5] Linder, C., Mykola, T., Miehe, C., 2011. A micro mechanically motivated diffusion-based transient network model and its incorporation into finite rubber viscoelasticity. Journal of the Mechanics and Physics of Solids 59, 2134–2156.

[6] Zhao, X., Wang, Q., 2014. Harnessing large deformation and instabilities of soft dielectrics: Theory, experiment, and application. Applied Physics Reviews 1, 021304.

ACTIVE MOTION AND DEFORMATION OF LIQUID CRYSTAL ELASTOMERS

Shengqiang Cai[a], Chihyung Ahn

Department of Mechanical and Aerospace Engineering, University of California, San Diego,
La Jolla, CA 92093, USA

Summary In the talk, I will present our recent research progress on the optically/ thermally actuated motion and deformation in liquid crystal elastomer structures.

INTRODUCTION

A combination of liquid crystal and polymer network can form a new material—liquid crystal elastomer (LCE). The special molecular combination endows LCE with many unique properties such as soft or semi-soft elasticity and multi-responsiveness, which have led to myriad applications ranging from artificial muscle to stretchable optical devices. Recently, several biological materials such as actin filament network and fibrillar collagens have also been found to have similar molecular structure and behaviors as man-made LCEs. In this talk, I will discuss some recent progresses made in our group for the active motion and deformation of LCE structures driven by light or heat.

Experiments

- Material synthesis

We adopt the chemical reaction recently developed by Yakacki et al [1] to synthesize LCEs. The synthetic process is briefly summarized as follows. First, RM257 (liquid crystal monomer), PETMP (crosslinker) and EDDET (spacer) and multiwall carbon nanotubes   are dissolved in toluene by heating and vigorous mixing. The molar functionality composition of thiol monomers from PETMP and EDDET is fixed as 20:80 while that between thiol monomers and acrylate monomer from RM 257 is fixed as 1:1.15 so that there is 15% excess molar functional group of RM257 to that of PETMP and EDDET. A value of 0.5 wt% of HHMP to total monomers and 1.1 wt% of DPA to thiol monomers are added in the solution. After the solution is homogeneously mixed, it is placed in the vacuum chamber to remove bubbles trapped inside the solution. The solution is then transferred to the mold and left overnight at room temperature for the first step reaction. During the first-step reaction, RM257 reacts with PETMP and EDDET through thiol-acrylate Michael addition to form a lightly-crosslinked polydomain LCE film which are ready for applying mechanical stress and second-step reaction after the complete evaporation of toluene at 80℃. In the second-step reaction, LCE film can be completely cured by the photo-polymerization of unreacted LC monomers under the UV light exposure.

- Different active motion and deformation modes in LCE structures induced by light and heat

1. Omnidirectional bending of a LCE cylinder induced by light

As shown in Figure 1, a LCE cylinder is fabricated. With the illumination of light from one side, the LCE cylinder can quickly bend toward the light. The bending is caused by the inhomogeneous contraction of the LCE cylinder induced by the light. There is an optimized diameter of the LCE cylinder which can have the largest light-induced bending curvature.

2. Light-driven rolling of a LCE cylindrical tube

As shown in Figure 2, a LCE cylindrical tube can roll in a flat surface with the light illumination from on direction. When the tube is exposed to light from one side, the tube deforms inhomogenously which will shift the gravity center of the tube. Therefore the gravity of the tube can generate a moment to roll the cylindrical tube forward.

Fig. 1   A LCE cylinder bends toward a light source
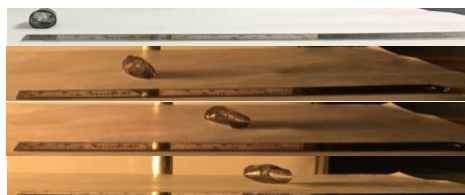
Fig. 2 Rolling of a LCE tube driven by light illumination.

Fig. 3 Rolling of a LCE tube driven by heating.

a) Corresponding author. Email: shqcai@ucsd.edu

3. Heat-driven rolling of a LCE cylindrical tube

As shown in Figure 3, the same LCE tube can also roll in a fat surface when it is heated from the bottom. The mechanism is still under investigation.

CONCLUSIONS

The active motion and deformation mode discussed in the presentation can be potentially useful for designing and fabricating various soft structures and devices.

References

[1]   C. M. Yakacki, M. Saed, D. P. Nair, T. Gong, S. M. Reed, and C. N. Bowman: Tailorable and programmable liquid-crystalline elastomers using a two-stage thiol-acrylate reaction. *Rsc Advances*, **5**:18997-19001, 2015.

OPTIMIZING THE ENERGY HARVESTING PERFORMANCE OF VISCOELASTIC DIELECTRIC ELASTOMER GENERATORS

Jianyou Zhou, <u>Liying Jiang</u>[a) & Roger E. Khayat

Department of Mechanical and Materials Engineering, The University of Western Ontario,
London, Ontario, Canada

<u>*Summary*</u> As a promising technology for renewable energy harvesting, dielectric elastomer generators (DEGs) have drawn much attention from the research community due to their flexibility, light weigh, low cost, large deformation capacity, and most importantly, high energy density. However, their energy harvesting schemes are relatively complex and can be affected by various material properties and failure modes. Based on a particular harvesting scheme, this work presents a theoretical study on the performance of DEGs under equi-biaxial loading. From the simulation results, it is found that the material viscoelasticity exerts a strong effect on the harvested energy. The general framework developed in this paper is expected to provide guidance for the optimal design of DEGs.

INTRODUCTION

Dielectric elastomers (DEs), as a category of soft electroactive materials, can convert energy from one form to another. Due to their large deformation capability and high energy density, DEs are desirable materials for power generators that transduce mechanical energy to electrical energy. In fact, much effort has been devoted to studying the energy harvesting performance of dielectric elastomer generators (DEGs). At the early stage, Pelrine *et al.* proposed a "rectangular" electromechanical harvesting scheme for DEGs, which is relatively easy to manage [1]. Later, various prototypes of DEG have been developed based on this "rectangular" energy harvesting scheme [2-5]. According to these studies, the achieved energy density of DEGs is already more than one order of magnitude higher than that of the piezoelectric and electromagnetic generators, while it is still far less than the predicted maximum energy density [6].

As discussed in the earlier studies, the performance of DEGs can be affected by various factors such as electrical breakdown (EB), loss-of-tension, current leakage, loading configurations and material viscoelasticity. Particularly, it is reported that the efficiency of DEGs is strongly affected by the material viscoelasticity that may lead to high energy dissipation and loss-of-tension [5, 7]. Moreover, to gain a better understanding on the influence of the material viscoelasticity, it is essential to investigate the finite-deformation viscoelastic behavior of DEs since they commonly undergo large deformation during the operation of DEGs. Based on the finite-deformation viscoelasticity model by Hong [8], this work investigates the influence of the material viscoelasticity on a "triangular" harvesting scheme and the harvested energy, aiming to provide an increased understanding on the harvesting mechanisms of DEGs

THE ENERGY HAVESTING MECHANISM AND SCHEME OF DEGS

Regardless of the electromechanical energy harvesting scheme, the energy harvesting principle of a DEG always lies in the cyclic change of the capacitance of the embedded DE, which is realized by its electromechanical deformation. In addition, the electromechanical deformation of a DE is limited by the electrical breakdown (EB) failure and its material extensibility. Figure 1(a) illustrates the electrical breakdown curve on the dimensionless voltage-charge (Φ-Q) plane of a DE. The operation of the DEG is safe when voltage level of the DE is below the EB curve, otherwise it fails by electrical breakdown. Also, the deformation of the DE is commonly restricted within a prescribed range from λ_{min} to λ_{max}, where λ_{min} and λ_{max} are the minimum stretch ratio and the maximum stretch ratio, respectively. Therefore, the maximum achievable energy for such a DEG can be indicated by the area enclosed by the λ_{min}, λ_{max} and EB curves in figure 1(a).

According to this enclosed area, a desirable scheme to maximize the harvested energy should be a triangle as denoted by A-B-C in figure 1(a), which was recently proposed by Shian *et al* [9]. Figure 1(b) shows the energy harvesting circuit of this "triangular" harvesting scheme. At state A, a DE coated with compliant electrodes on both surfaces is stretch to λ_{max} by an equi-biaxial force P (figure 1(c)). Then switch 1 is closed, which connects the DE and the transfer capacitor to the power supply. Thus, charges flow from the power supply to the DE and the transfer capacitor until the voltage of the DE (Φ) increases to the level of the power supply (Φ_L) at state B. The diode between the DE and the transfer capacitor only allow charges flow from the DE to the transfer capacitor when $\Phi > \Phi_C$ (Φ_C is the voltage of the transfer capacitor). After state B is reached, switch 1 is opened and force P is gradually decreased, which allows the DE to shrink back. When the DE shrinks back, its capacitance C decreases ($C = C_0 \lambda^4$, where C_0 the capacitance of the undeformed DE and λ is the stretch ratio) and voltage increases, which forces some charges to flow to the transfer capacitor and increases its voltage. The slope of B-C line is proportional to $-1/C_p$, where C_p is the capacitance of the transfer capacitor. At state C, the DE shrinks back to λ_{min} and most of the charges on the DE have been transferred to the transfer capacitor. After state C is reached, switch 2 is closed and the charges from both the DE and the transfer capacitor flow to the harvesting circuit since they are at the highest level of voltage. After switch 2 is closed, the DE membrane is stretched again, which causes its capacitance to increase and its

voltage to further decrease (the decrease of its voltage is partly due to the discharging). When the deformation of the DE is back to λ_{max} (at state A), switch 2 is opened and the harvesting cycle is finished.

Figure 1. Schematics of a dielectric elastomer generator: (a) energy harvesting scheme and simulation results; (b) energy harvesting circuit diagram; (c) a dielectric elastomer under equi-biaxial loading.

Simulation results and discussion

Based on the finite-deformation viscoelasticity model [8], figure 1(a) shows the simulation result of the energy harvesting cycle of the DEG denoted by A_1-B_1-C_1-D_1-A_1. Due to the material viscoelasticity, loss-of tension occurs before the DE can reach state C in our simulation. This phenomenon is also in agreement with the experimental results by Shian *et al* [9]. Therefore, another state (state C_1 in the simulation) has to be prescribed to determine the time for closing switch 2. In addition, from state B_1 to state C_1 (the DE shrinks back), only a small amount of charges on the DE have been transferred to the transfer capacitor. After state C_1 is reached, switch 2 is closed and the DE continues to shrink back until it reaches a loss-of-tension condition at state D_1, during which time the charges on both the DE and the transfer capacitor flow to the harvesting circuit. After state D_1 is reached, DE is stretched again. When the DE is stretched back to λ_{max} (at state A_1), switch 2 is reopened and the harvesting cycle is complete. Although the area enclosed by A_1-B_1-C_1-D_1 is much smaller than that enclosed by A-B-C, a DEG adopting this harvesting scheme has experimentally demonstrated the highest energy density so far [9].

Since the harvested energy is still significantly less than the maximum achievable value, there is much room for the improvement of the performance of DEGS. Based on the "triangular" harvesting scheme, our simulation results suggest that the harvested energy of DEGs could be improved by some approaches such as increasing the rate of the deformation of the DE (which weakens the viscoelastic effect of the material), optimizing the position of state B_1 and C_1 (the position of state B_1 is determined by the voltage level of the power supply), and choosing an appropriate transfer capacitor (the slope of line B_1-C_1 is determined by the capacitance of the transfer capacitor).

ACKNOWLEDGEMENTS

References

[1] Pelrine R., Kornbluh R. D., Eckerle J., Jeuck P., Oh S., Pei Q., Stanford S.: Dielectric Elastomers: Generator Mode Fundamentals and Applications. *Proc. SPIE* **4329**. 148-156, 2001.

[2] McKay T. G., O'Brien B. M., Calius E. P., Anderson I. A.: Soft Generators Using Dielectric Elastomers. *Appl. Phys. Lett.* **98**. 142903, 2011.

[3] Kornbluh R. D., Pelrine R., Prahlad H., Wong-Foy A., McCoy B., Kim S., Eckerle J., Low T.: Dielectric Elastomers: Stretching the Capabilities of Energy Harvesting. *MRS Bull.* **37**. 246-253, 2012.

[4] Kaltseis R., Keplinger C., Baumgartner R., Kaltenbrunner M., Li T., Machler P., Schwodiauer R., Suo Z., Bauer S.: Method for Measuring Energy Generation and Efficiency of Dielectric Elastomer Generators. *Appl. Phys. Lett.* **99**. 162904, 2011.

[5] Huang J., Shian S., Suo Z., Clarke R.: Maximizing the Energy Density of Dielectric Elastomer Generators Using Equi-Biaxial Loading. *Adv. Funct. Mater.* **19**. 5056-5061, 2013.

[6] Koh S. J. A., Keplinger C., Li T., Bauer S., Suo Z.: Dielectric Elastomer Generators: How Much Energy Can Be Converted? *IEEE/ASME Trans. Mechatron.* **16**. 33-41, 2011.

[7] Zhou J., Jiang L., Khayat R. E.: Investigation on the performance of a viscoelastic dielectric elastomer membrane generator. *Soft Matter* **11**. 2983-2992, 2015.

[8] Hong W.: Modeling Viscoelastic Dielectrics. *J. Mech. Phys. Solids* **59**. 637-650, 2011.

[9] Shian S., Huang J., Zhu S., Clarke D. R.: Optimizing the Electrical Energy Conversion Cycle of Dielectric Elastomer Generators. *Adv. Mater.* **26**. 6617-6621, 2014.

MULTISCALE CONSTITUTIVE MODELING ON FINITE STRAIN VISCOELASTICITY OF ELASTOMERS

Ying Li [*1], Shan Tang[2], Martin Kröger[3], and Wing Kam Liu[4]

[1]*Department of Mechanical Engineering, University of Connecticut, Storrs, CT 06269, USA.*
[2]*Department of Engineering Mechanics, Chongqing University, Shapingba, Chongqing, 400017, China*
[3]*Department of Materials, Polymer Physics, ETH Zurich, CH-8093 Zurich, Switzerland*
[4]*Department of Mechanical Engineering, Northwestern University, Evanston, IL 60208, USA.*

Summary In this work, we present a mechanistic and physics-based constitutive model to describe and design the finite strain viscoelastic behavior of elastomers. Mathematically, the viscoelasticity of elastomers has been decomposed into hyperelastic and viscous parts, which are attributed to the nonlinear deformation of the cross-linked polymer network and the diffusion of free chains, respectively. Combing the non-affine network model for hyperelasticity and modified tube model for viscosity, both understood by molecular simulations, we develop a mechanism-based constitutive model for finite strain viscoelasticity of elastomers. All the parameters in the proposed constitutive model have physical meanings, which are signatures of polymer chemistry, physics or dynamics. The finite strain viscoelasticity obtained from our simulations agrees qualitatively with experimental data on both un-vulcanized and vulcanized rubbers, which captures the effects of cross-linking density, the molecular weight of the polymer chain and the strain rate.

INTRODUCTION

Elastomers consist of long polymer chains joined together by chemical bonds through cross-linkers. They are usually capable of recovering their original shapes after finite deformation due to covalent cross-linkages. Under equilibrium conditions, long polymer chains making up an elastomer are irregularly coiled together. However, when the elastomer is under tension, polymer chains tend to stretch out and straighten along the pulling direction. Upon unloading, the chains return to their original compact and random arrangement. During such a loading-unloading process, energy dissipates due to friction between polymer chains and the elastomer exhibits viscoelastic behavior (cf. Fig. 1). Examples of elastomers include polyisoprene (natural rubber), polybutadiene (butadiene rubber), polychloroprene (chloropene rubber) and the copolymer comprised of butadiene and acrylonitrile (nitrile rubber). These materials have a broad range of applications in engineering and industry.
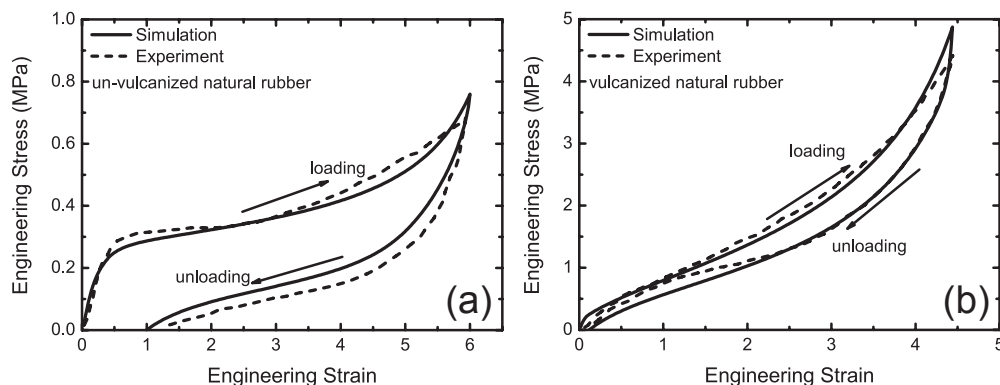
Figure 1: Experimental and computational results on uniaxial stress-strain curves during loading and subsequent un-loading of (a) un-vulcanized and (b) vulcanized natural rubber (NR) with strain rate 0.003 s^{-1} at room temperature. Experimental results are taken from [1].

Due to differences in the degree of cross-linking, the viscoelastic behavior of un-vulcanized natural rubber (NR) can be very distinct from that of vulcanized NR. For un-vulcanized NR under uniaxial tension, the stress initially increases linearly with strain during the elastic deformation stage, followed by a strain-softening stage with a stress plateau, depicted in Fig. 1(a). Upon increasing the strain further, the stress starts to increase rapidly, reminiscent of strain-hardening behavior. When the applied tension is released, the stress drops rather quickly and the polymer chains tend to return to a coiled equilibrium state that might be very different from the initial state. Therefore, the stress-strain curve of un-vulcanized NR exhibits pronounced hysteretic behavior, representing large energy dissipation. Contrary to the behavior of un-vulcanized NR, the vulcanized NR

---

[*]Corresponding author. Email: yingli@engr.uconn.edu

exhibits only the strain-hardening behavior without showing strain-softening, as given in Fig. 1(b). During the unloading stage, the stress slowly reduces with decreasing strain, signaling a much smaller hysteresis with less energy dissipation, because of the constraints applied through the cross-linkages. Moreover, the elastic modulus of vulcanized NR is about 20-30 times larger than that of un-vulcanized NR due to large differences in cross-linking densities. The above stress-strain curves for un-vulcanized and vulcanized NRs characterize the most important mechanical behavior of elastomers, which can greatly affect their performance in applications. However, a reliable constitutive model that is able to capture these qualitative differences in mechanical behavior for un-vulcanized and vulcanized NRs simultaneously does not presently exist.

DEVELOPMENT OF CONSTITUTIVE MODEL

To better understand the viscoelastic behaviors of elastomers, they have been decomposed into a cross-linked network with superimposed free chains. Mathematically, the viscoelasticity of elastomers has been decomposed into hyperelastic and viscous parts, which are attributed to the nonlinear deformation of the cross-linked polymer network and the diffusion of free chains, respectively. The hyperelastic deformation of a cross-linked polymer network is governed by the cross-linking density, the molecular weight of the polymer strands between cross-linkages, and the amount of entanglements between different chains, which we observe through large scale molecular dynamics (MD) simulations. Moreover, a recently developed non-affine network model [2] is confirmed in the current work to be able to capture these key physical mechanisms using MD simulation. The energy dissipation during a loading and unloading process of elastomers is governed by the diffusion of free chains, which can be understood through their reptation dynamics. The viscous stress can be formulated using the classical tube model [3]; however, it cannot be used to capture the energy dissipation during finite deformation. By considering the tube deformation during this process, as observed from the MD simulations, we propose a modified tube model to account for the finite deformation behavior of free chains. Combing the non-affine network model for hyperelasticity and modified tube model for viscosity, both understood by molecular simulations, we develop a mechanism-based constitutive model for finite strain viscoelasticity of elastomers. All the parameters in the proposed constitutive model have physical meanings, which are signatures of polymer chemistry, physics or dynamics. More importantly, the finite strain viscoelasticity obtained from our simulations agrees qualitatively with experimental data on both un-vulcanized and vulcanized rubbers (see Fig.1), which captures the effects of cross-linking density, the molecular weight of the polymer chain and the strain rate.

CONCLUSIONS

The hyperelastic and viscous behaviors of elastomers are attributed to the nonlinear deformation of a cross-linked network and diffusion of free chains, respectively. Large scale molecular simulations were performed to reveal the detailed physical mechanisms of the cross-linked network and free chains under uniaxial tension, simple shear and equal-biaxial tension. For the cross-linked network, its stress response is attributed to the cross-linking and entanglement. Therefore, the classical Arruda-Boyce model [4] is not applicable as it does not include the effect of entanglements. The recently developed non-affine network model [2], simultaneously considering the contributions of cross-linking and entanglement, is identified as the most proper continuum model to describe the hyperelastic behaviors of elastomers. For the free chains, the primitive chain length and tube diameter are found to be dependent on the applied deformations in the molecular simulations [5, 6], which can be captured by our theoretical formulations based on an affine deformation assumption. Based on these observations, the viscous contribution of free chains can be reformulated according to the classical tube model proposed by Doi and Edwards [3], which is named as the updated tube model. Combining the non-affine network model with the updated tube model, a new constitutive model has been proposed for studying the finite strain viscoelastic behavior of elastomers. This new model is found to be able to capture the mechanical responses of un-vulcanized and vulcanized rubber under uniaxial loading and unloading with different strain rates. Moreover, parametric studies have been performed based on the proposed constitutive model, which demonstrate that different viscoelastic behaviors can be achieved through tuning these physical parameters.

References

[1] Amnuaypornsri S., Toki S., Hsiao B.S., Sakdapipanich J.: The effects of endlinking network and entanglement to stressstrain relation and strain-induced crystallization of un-vulcanized and vulcanized natural rubber. Polymer 53: 3325-3330, 2012.

[2] Davidson J.D., Goulbourne N.: A nonaffine network model for elastomers undergoing finite deformations. J. Mech. Phys. Solids. 61: 1784-1797, 2013.

[3] Doi M., Edwards S.F.: The Theory of Polymer Dynamics. Clarendon Press, Oxford 1986.

[4] Arruda E.M., Boyce M.C.: A three-dimensional constitutive model for the large stretch behavior of rubber elastic materials. J. Mech. Phys. Solids, 41:389-412, 1993.

[5] Li Y., Abberton B.C., Kröger M., Liu W.K.: Challenges in multiscale modeling of polymer dynamics. Polymers, 5: 751-832, 2013.

[6] Li Y., Tang S., Kröger M., Liu W.K.: Molecular simulation guided constitutive modeling on finite strain viscoelasticity of elastomers. J. Mech. Phys. Solids. 2015, DOI:10.1016/j.jmps.2015.12.007.

THERMODYNAMICS AND INSTABILITY OF DIELECTRIC ELASTOMERS

Liwu Liu[1a)], Yanju[1] and Jinsong Leng[2]

[1]*Department of Astronautical Science and Mechanics, Harbin Institute of Technology, Harbin, Heilongjiang, China*
[2]*Centre for Composite Materials, Harbin Institute of Technology, Harbin, Heilongjiang, China*

Summary Dielectric elastomer is a kind of typical soft active material. It can deform obviously when subjected to an external voltage. Here, we develop a thermodynamic constitutive model of dielectric elastomers undergoing polarization saturation and strain-stiffening, and then investigate the stability (electromechanical stability, snap-through stability) and voltage induced deformation of dielectric elastomers. Analytical solution has been obtained and it reveals the marked influence of the extension limit and polarization saturation limit on its instability. The developed thermodynamic constitutive model and simulation results would be helpful in future to the research of dielectric elastomer based high-performance transducers.

INTRODUCTION

Dielectric elastomer is a kind of typical soft active material. It can deform obviously when subjected to an external voltage. When a dielectric elastomer with randomly oriented dipoles is subject to an electric field, the dipoles will rotate to and align with the electric field. The polarization of the dielectric elastomer may be saturated when the voltage is high enough. When subjected to a mechanical force, the end-to-end distance of each polymer chain, which has a finite contour length, will approach the finite value, reaching a limiting stretch. On approaching the limiting stretch, the elastomer stiffens steeply. The schematic diagram of voltage-driven dielectric elastomers can be depicted as Fig.1 [1]:
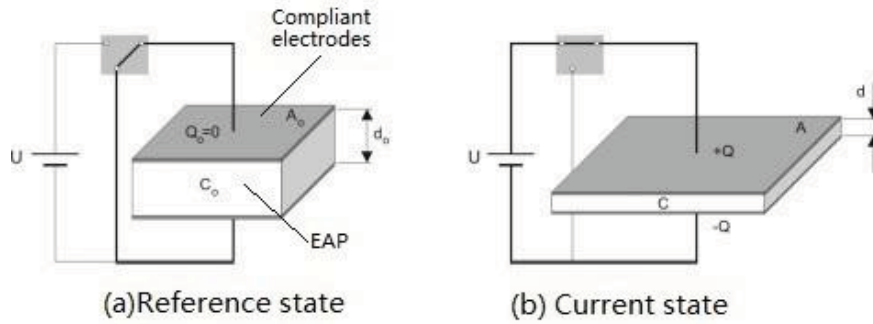
Fig.1 Schematic diagram of voltage-driven dielectric elastomers [1]

THERMODYNAMIC CONSTITUTIVE MODEL OF DIELECTRIC ELASTOMERS

In the paper, a thermodynamic constitutive model of dielectric elastomers undergoing polarization saturation and strain-stiffening is investigated. The constitutive relation of dielectric elastomer undergoing large deformation can be described as the following equations:

$$\sigma_1 = \lambda_2^{-1}\lambda_3^{-1}\frac{\partial U(\lambda_1,\lambda_2,\lambda_3)}{\partial \lambda_1} - \frac{\varepsilon}{2}E^2 - \frac{1}{2}\frac{\partial \varepsilon}{\partial \lambda_1}\lambda_1 E^2 \tag{1-a}$$

$$\sigma_2 = \lambda_1^{-1}\lambda_3^{-1}\frac{\partial U(\lambda_1,\lambda_2,\lambda_3)}{\partial \lambda_2} - \frac{\varepsilon}{2}E^2 - \frac{1}{2}\frac{\partial \varepsilon}{\partial \lambda_2}\lambda_2 E^2 \tag{1-b}$$

$$\sigma_3 = \lambda_1^{-1}\lambda_2^{-1}\frac{\partial U(\lambda_1,\lambda_2,\lambda_3)}{\partial \lambda_3} + \frac{\varepsilon}{2}E^2 - \frac{1}{2}\frac{\partial \varepsilon}{\partial \lambda_3}\lambda_3 E^2 \tag{1-c}$$

where the first parts of the equations represent elastic forces, the second parts mean Maxwell stress, and the third parts are depended on dielectric constant.

STABILITY OF POLARIZATION SATURATION DIELECTRIC ELASTOMERS

The real dielectric elastomer always undergoes a polarization saturation progress. The paper studied the stability of dielectric elastomer considering polarization saturation. An expression is utilized describing the polarization saturation.

$$E = \frac{D_s}{2\varepsilon}\log(\frac{1+D/D_s}{1-D/D_s}) \tag{2}$$

[a)] Corresponding author. Email: liuliwu_006@163.com.

For the uncompressible dielectric elastomer, the true stress and electric field are as follows:

$$\sigma_1 - \sigma_3 = \lambda_1 \frac{\partial U\left(\lambda_1, \lambda_2, \lambda_1^{-1}\lambda_2^{-1}\right)}{\partial \lambda_1} - \frac{D_s D^{\sim} \lambda_1^{-1}\lambda_2^{-1}}{2\varepsilon} \log\left(\frac{1 + D^{\sim}\lambda_1^{-1}\lambda_2^{-1}/D_s}{1 - D^{\sim}\lambda_1^{-1}\lambda_2^{-1}/D_s}\right) \tag{3}$$

$$\sigma_2 - \sigma_3 = \lambda_2 \frac{\partial U\left(\lambda_1, \lambda_2, \lambda_1^{-1}\lambda_2^{-1}\right)}{\partial \lambda_2} - \frac{D_s D^{\sim} \lambda_1^{-1}\lambda_2^{-1}}{2\varepsilon} \log\left(\frac{1 + D^{\sim}\lambda_1^{-1}\lambda_2^{-1}/D_s}{1 - D^{\sim}\lambda_1^{-1}\lambda_2^{-1}/D_s}\right) \tag{4}$$

ELECTROMECHANICAL AND SNAP-THROUGH STABILITY

The electromechanical and snap-through stability of dielectric elastomer undergoing polarization saturation are investigated. When subjected biaxial stretch ($F_1 = F_2 = F$), the dielectric elastomer film will obtain a deformation along two directions equally ($\lambda_1 = \lambda_2 = \lambda$). The free energy can be described as the following equation:

$$W\left(\lambda, D^{\sim}\right) = \frac{C_1}{2}\left(2\lambda^2 + \lambda^{-4} - 3\right) + \frac{kC_1}{2}\left(2\lambda^{-2} + \lambda^4 - 3\right) + \frac{D_s D^{\sim}\lambda^{-2}}{2\varepsilon} \log\left(\frac{1 + D^{\sim}\lambda^{-2}/D_s}{1 - D^{\sim}\lambda^{-2}/D_s}\right) + \frac{D_s^2}{2\varepsilon} \log\left(1 - \frac{D^{\sim 2}\lambda^{-4}}{D_s^2}\right) \tag{5}$$

For convenience, the relation between the dimensionless nominal stress and the dimensionless nominal electric field can be expressed as the following equation:

$$\frac{s}{C_1} = 2\left(\lambda - \lambda^{-5}\right) + 2k\left(\lambda^3 - \lambda^{-3}\right) - 2\frac{D_s}{\sqrt{C_1\varepsilon}} \left[\frac{\exp(2\frac{E^{\sim}}{\sqrt{C_1/\varepsilon}}\lambda^2 \Big/ \frac{D_s}{\sqrt{C_1\varepsilon}}) - 1}{\exp(2\frac{E^{\sim}}{\sqrt{C_1/\varepsilon}}\lambda^2 \Big/ \frac{D_s}{\sqrt{C_1\varepsilon}}) + 1}\right] \frac{E^{\sim}}{\sqrt{C_1/\varepsilon}}\lambda \tag{6}$$

The calculation results are shown as Fig. 2.

(a) Nominal electric field and stretch of dielectric elastomer undergoing polarization saturation

(b) Nominal electric field and nominal electric displacement of dielectric elastomer undergoing polarization saturation
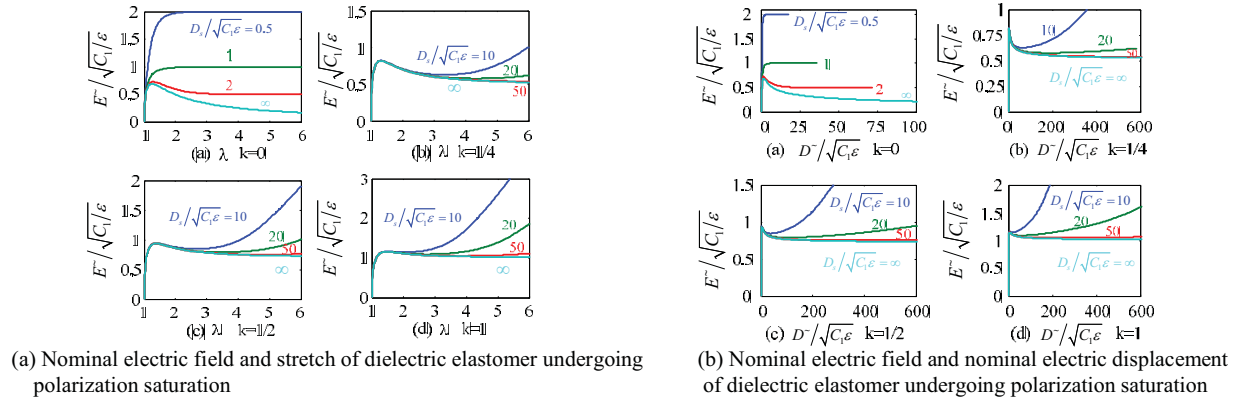
Fig.2 Calculation results of dielectric elastomer undergoing polarization saturation under the loading condition $\lambda_1 = \lambda_2 = \lambda$

CONCLUSIONS

The paper presents the constitutive theory, stability, electromechanical and snap-through stability as well as the simulation results. It would be helpful in future to the research of dielectric elastomer based high-performance transducers.

References

[1] R. Pelrine, R. Kornbluh, Q. Pei: High-speed electrically actuated elastomers with strain greater than 100%. *Science* **287(28):** 836~839, 2000.

A NEW VISCOELASTIC CONSTITUTIVE MODEL OF SHAPE MEMORY POLYMERS

Yunxin Li[1] & <u>Zishun Liu</u> [a1]

[1]International Center for Applied Mechanics, State Key Laboratory for Strength and Vibration of Mechanical Structures, Xi'an Jiaotong University, Xi'an, China

<u>*Summary*</u> In this work, we propose a new viscoelastic model for shape memory polymers (SMPs) based on phase transition, which has clear physical significance and includes the time history. To describe the phase transition phenomenon of SMPs, our new model has different constitutive structures above and below transformation temperature. As the proposed viscoelastic model is based on phase transition, it can be used both for different types of SMP materials and to treat large strain problems. To validate the model accuracy and show the model's capability in reproducing the shape memory effect, two test examples are predicted using the new constitutive model. The simulated and predicted results are compared with available experimental results and good agreement can be observed.

INTRODUCTION

Shape memory polymers (SMPs), a kind of soft and smart material, have been widely used in aerospace structures, biomedical devices, functional textiles and other soft machines/devices. Increasing usefulness of SMPs motivates us to further understand its thermomechanical properties and deformation behavior. With that in mind, the development of more suitable constitutive models for SMPs is imperative. To develop new macro constitutive models for SMPs, two general approaches have been adopted: viscoelastic modeling and phenomenological modeling. The existing viscoelastic models may be able to describe the behavior of SMPs, but they lack a clear physical meaning. The phenomenological models based on phase transition have a clear physical meaning, but do not include the time factor and cannot describe the creep and stress relaxation of rubber. In order to overcome the shortcomings of these two types of models, we propose a new viscoelastic model based on phase transition, which has physical significance and includes the time factor. In previous research work, there is still a lack of unified constitutive model with shape memory effect. At the same time, most studies of SMPs are only based on a specific material. These factors narrow the application of models. Many models are limited to small strain (within 10%). The proposed new viscoelastic model not only can be used for different materials, but can also be used to treat large strain problems. In order to validate the model, simulated and predicted results are compared with the available experimental results. Good agreement between predict values and experimental data can be observed.

CONSTITUTIVE MODEL

With the phenomenological approach, the shape memory effect of SMPs is described by a phase transition at transformation temperature. Normally, SMPs have different microstructures at different temperature ranges. To depict the phase transition phenomenon, we propose a new viscoelastic model for SMPs. The biggest difference between the ordinary viscoelastic model and the proposed model is that the proposed model has different constitutive structures (as shown in Fig. 1) above and below transformation temperature. When the temperature is higher than the transition temperature T_r, the SMPs are in the rubbery state. Rubber is often treated as isotropic incompressible hyperelastic materials in a short time period of loading, but from the point of view of a long time period of loading, the materials in the rubbery state still exhibit stress relaxation and creep viscosity effect. Thus a simple model for SMPs at rubbery state is proposed, as shown in Fig. 1(a). This model is composed of two incompressible hyperelastic element and a viscous damping element. It represents the rubber phase which is responsible for the permanent shape at a temperature higher than transition temperature. It can be called the rubber phase element. As the temperature decreases below T_r, the material enters the glass state. In the glass state, a kind of reversible phase, the second crosslinking chain may be formed in the local area of reticular structure of SMPs, which act as small locks. The second crosslinking chain lock the material's reticular structure to fix the temporal shape at a temperature lower than transition temperature. When the temperature increases above T_r, the second crosslinking chain disappear and permanent shape is recovered. The second crosslinking chain can be considered as small springs with viscous effects. As such, two spring elements and a viscous damping element are introduced to the model to simulate the reversible phase − the second crosslinking chain (as shown in reversible phase of Fig. 1(b)). It can be called the reversible phase element. The constitutive model for SMPs consists of a rubber phase element and a reversible phase element placed in parallel at $T \leq T_r$, as shown in Fig. 1(b). In the model, the effect of thermal expansion, which is assumed to be independent of the mechanical behavior, is also considered (as depicted in Fig. 1(a) and Fig. 1(b)).

The advantages of the new viscoelastic model are that it has good physical significance and includes the time factor essential to describe the creep and stress relaxation of rubber. From the corresponding experimental results, the parameters of the model can be determined for different SMP materials.

---

[a] Corresponding author. Email: zishunliu@mail.xjtu.edu.cn

(a)   (b)
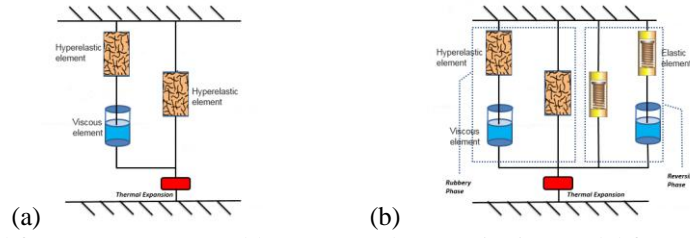
Fig. 1. (a) Constitutive model for SMPs at $T>T_r$ (rubbery state); (b) Constitutive model for SMPs at $T \leq T_r$ (glass state).

VERIFICATION OF THE CONSTITUTIVE MODEL

In order to validate the acuracy of our proposed new model, two examples of uniaxial tests with two different types of SMP materials are simulated. The constitutive model is implemented and the simulated results are compared with available experimental results.

Example one considers the unconstrained free strain recovery experimental test that had been performed by Tobushi et al [1, 2]. First, Tobushi et al [1] had developed a linear viscoelastic model and performed a series of experiments on polyurethane-SMP. Then, Tobushi et al [2] further modified the linear model to a nonlinear model which can treat the behavior of larger strains. Their work can describe the shape memory behavior qualitatively, but it does not have a clear physical meaning. We use the newly proposed constitutive model and corresponding material parameters extracted from experiment results [1, 2] to simulate the uniaxial tests. The stress-strain relationship, the stress-temperature relationship and strain-temperature relationship in an unconstrained free strain recovery cycle are shown in Fig. 2. From Fig. 2, it can be observed that the proposed new constitutive model can successfully predict the shape memory behavior of SMPs. In order to compare model predictions, Tobushi's predicted results are also illustrated in   Fig. 2. Better agreement can be observed between the new model and experimental data.

The second example is to predict experimental test done by McClung et al [3] for large strain recovery test. To verify the ability of the new model in large strain and show the validity for different materials, the experiments of the Veriflex E epoxy-SMP reported by McClung et al [3] are simulated. As shown in Fig. 3, the simulation results match quite well with the experimental data in describing the loading procedure as well as the following strain recovery process.
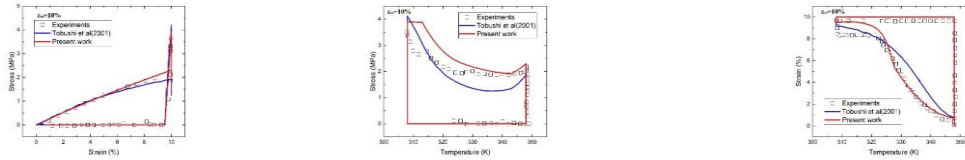
(a) Stress-strain curves   (b) Stress-temperature curves   (c) Strain-temperature curves

Fig. 2. Predicting the shape memory behavior of polyurethane-SMP. Experiments reported by Tobushi et al [2, 3].
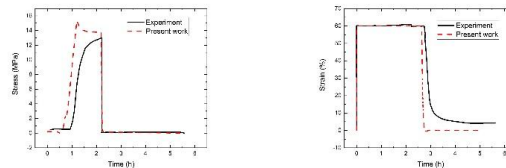
(a) Stress-time curves   (b) Strain-time curves

Fig. 3. Predicting the shape memory behavior of Veriflex E epoxy-SMP, Experiments reported by McClung et al [4].

CONCLUSIONS

Proposed constitutive model of SMPs combines the advantages of phase transition constitutive and viscoelastic constitutive. It has a good physical meaning and also includes the influence of loading time. As we did not make more special assumptions for different materials and the viscoelastic model is based on phase transition, the new model can be used for modeling different materials and large strain problems.

References

[1]   Tobushi, H., Hashimoto, T., Hayashi, S. and Yamada, E. *Mater. Syst. Struct.* 8, 711–718, 1977.
[2]   Tobushi, H., Okumura, K., Hayashi, S. and Ito, N., *Mech. Mater.* 33, 545–554, 2001.
[3]   McClung, A., Tandon, G., Baur, J.W. Mech. *Time-Depend. Mater.* 17(1), 39–52, 2013.

MECHANICS OF THERMORESPONSIVE POLYMER BRUSH BASED SOFT MATERIALS: THEORY AND EXPERIMENTS

<u>Manav</u>*[1], M. P. Bajgai[2], A. S. Phani[1], and J. N. Kizhakkedathu[2]
[1]*Mechanical Engineering, University of British Columbia, Vancouver, BC, Canada*
[2]*Centre for Blood Research, University of British Columbia, Vancouver, BC, Canada*

<u>*Summary*</u> Stimuli responsive soft nanomaterials are of growing scientific and technological interest. Polymer brushes are densely packed, surface tethered polymer chains. A brush behaves like an elastic surface layer with residual surface stress which produces deformation of the substrate. In a thermoresponsive brush, temperature reversibly changes the residual surface stress as well as the elastic modulus of the surface layer due to coil-globule phase transition in the brush. A mechanics model incorporating Young-Laplace effect is developed for high grafting density brush (graft density $>$ 0.2) which produces large surface stress. The model is then applied to experiments on a poly(N-isopropylacrylamide)-co-Poly(N,N-Dimethylacrylamide) (PNIPAm-co-PDMA) polymer brush grafted on a plasticized poly(vinyl chloride) (pPVC) film using surface-initiated atom transfer radical polymerization (SI-ATRP). The model estimates effective surface stress due to the brush to be ~ -10 N/m which can be halved by applying temperature.

THERMORESPONSIVE POLYMER BRUSH

Long polymer chains grafted to a surface arrange themselves into a brush like structure when the grafting density exceeds a threshold value [1] (see Fig. 1(*a*)). This structure arises due to the competition between entropic spring force associated with each polymer chain and inter chain repulsive forces. The entropic spring force tries to keep the two ends of a polymer chain together. Repulsive force between monomers, arising due to steric effects, is relieved by chain extension, resulting in brush like shape. Significantly, these interactions make a brush behave like an elastic surface layer with reversible residual surface stress which may cause deformation in the substrate [2, 3]. Establishing relationship between the molecular scale parameters of the brush with its continuum level properties is an ongoing work [2, 4]. Furthermore, polymer brush made of thermoresponsive polymers show conformation change when temperature is applied to it. This conformation change leads to a change in the residual surface stress as well as the elastic modulus of the surface layer [2]. This behaviour can be utilized in sensing and actuation applications [5].

MECHANICS MODEL OF A POLYMER COATED BEAM

We have developed a mechanics model for a thin flexible beam coated with a polymer brush layer on its top surface (see Fig. 1(*c*))). The polymer brush has been treated as an elastic surface layer with a residual stress, causing deflection in the beam. Mechanical equilibrium for the surface layer introduces correction in stress in the substrate through Young-Laplace relation. For a rectangular cross section of a substrate with thickness t, the correction is considerable if $t \sim \frac{\nu \sigma_s}{E}$, where E and ν are the Young's modulus and the Poisson's ratio of the substrate, and σ_s is surface stress in the surface layer. For a pPVC substrate $E \sim 10^7$ Pa and $\nu \sim 10^{-1}$. For surface stress, $\sigma_s \sim -10$ N/m, correction due to Young-Laplace relation is considerable if $t \sim 10^{-7}$ m. The mechanics model incorporates this effect. Assuming small strain in the beam, the following relation between the surface stress due to polymer brush and the curvature of the beam is derived:

$$\sigma_s = \sigma_s^0 + \epsilon_s E_s = \frac{E}{1-\nu^2}\left(\frac{t^2\kappa}{6 + \frac{\nu}{1-\nu}t\kappa}\right), \tag{1}$$

where σ_s^0 is the residual surface stress in the undeformed substrate, and ϵ_s and E_s are strain and elastic modulus of the surface layer. (1) is akin to Stoney's equation with a correction term in the denominator $(\nu(1-\nu)^{-1}t\kappa)$ arising due to Young-Laplace effect. Surface stress due to polymer brush can be estimated by measuring curvature of a polymer coated beam experimentally, and applying the above formula.

EXPERIMENTAL ESTIMATION OF SURFACE STRESS

To estimate surface stress due to polymer brush, Poly(N- isopropylacrylamide)-co-Poly(N,N-Dimethylacrylamide) (PNIPAm-co-PDMA) polymer brush was grafted on one side of a part of a plasticized poly(vinyl chloride) (pPVC) film using surface-initiated atom transfer radical polymerization (SI-ATRP). Note that by varying polymerization time, molecular level properties of the brush can be varied. For this experiment, it was fixed to six hours. The grafting procedure ensures very high graft densities (number of polymer chains attached to unit area of the substrate) and ultrahigh molecular weight of the polymer chains

---

*Corresponding author. (graduate student, UBC) Email: manav@alumni.ubc.ca
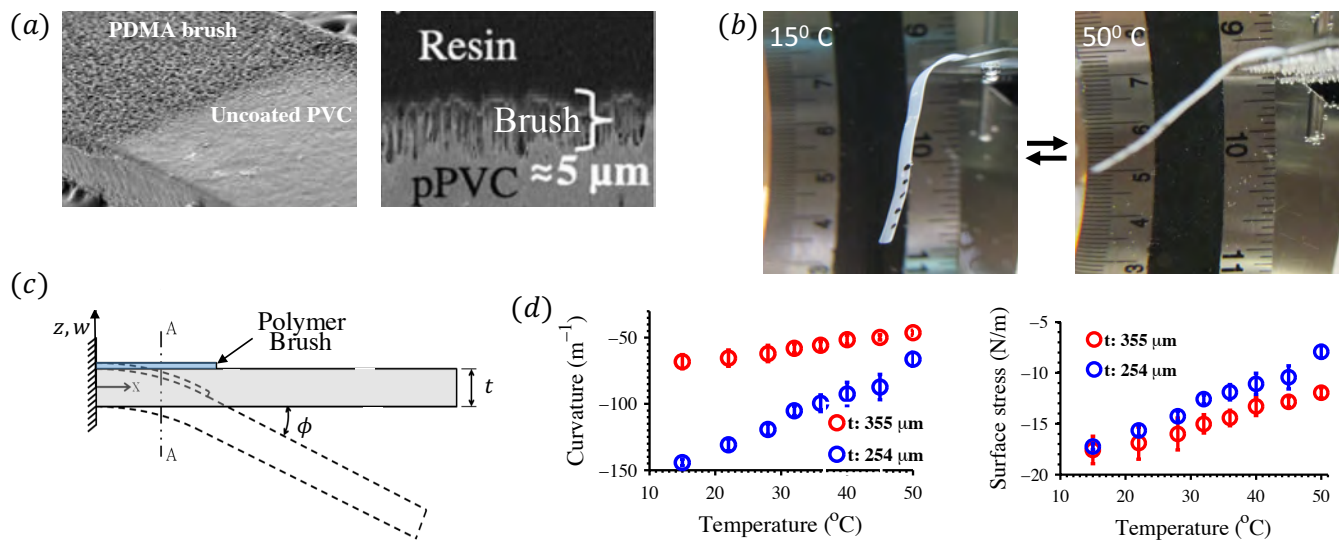
Figure 1: (*a*) SEM images of pPVC substrate partially coated with polymer brush [5]. (*b*) Partially coated pPVC beam in a water bath. Rise in temperature leads to decrease in curvature of the coated part of the beam and it is reversible. (*c*) Schematic of a partially coated beam. 1 cm of the 3 cm long beam is coated with polymer brush. (*d*) Variation of curvature and surface stress with temperature for polymer brush coated beams of thicknesses (*t*) 355 μm and 254 μm.

($\sim 10^6$ g/mol) leading to high surface stresses. The pPVC beams used in the experiment are 3 cm long, 5 mm wide, and 254 μm and 355 μm thick. Only 1 cm of the beam near its fixed edge is coated with polymer brush. Young's modulus and Poisson's ratio for the pPVC film are 12 MPa and 0.3 respectively. Bending rigidities of the beams are 8.19×10^{-8} N $-$ m^2 and 2.24×10^{-7} N $-$ m^2 respectively.

PNIPAm-co-PDMA is a temperature sensitive polymer. To measure curvature of a beam coated with the temperature sensitive polymer brush, the beam was placed in a water bath with temperature control. After reaching the desired temperature, we waited for a minute for the brush to reach steady state before proceeding with measurement at the temperature. At different temperatures of the bath, curvature of the beam changes (see Fig. 1(*b*)) due to change in effective surface stress. The beam was photographed at different temperatures by a fixed camera. Using image processing in MATLAB, the shape of the cantilever beam was traced. Using circle fitting on the part of the traced curve where brush is present, curvature of the coated part is determined, which is in turn used to find effective surface stress in the beam (Fig. 1(*d*)). It can be observed from Fig. 1(*d*) that surface stress is of the order of -10 N/m and it can be halved by increasing temperature. The change in temperature produces change in surface stress through conformation change in the brush. However, the transition is not sharp and happens over a range of temperature near lower critical solution temperature (LCST) ($\sim 32^0$ C) for the polymer. Furthermore, small difference between surface stresses for the two thicknesses, even though curvatures (and hence ϵ_s) at a particular temperature are widely different, suggests that the elastic modulus of the surface layer is very small.

CONCLUSIONS

Equation governing finite deformation of a beam with a coating of a polymer brush on its top surface has been derived including the Young-Laplace term needed to satisfy surface equilibrium. The modified stress-curvature relation was then used to extract surface stress due to polymer brush grafted on a pPVC substrate. The surface stress is found to be on the order of -10 N/m and it can be halved by applying temperature. The ability to control surface stress by varying temperature permits the design and development of soft actuators based on polymer brush material system.

References

[1] Milner S.: Polymer brushes. Science 251 (4996):905–914, 1991.

[2] Utz M. and Begley M. R.: Scaling theory of adsorption-induced stresses in polymer brushes grafted onto compliant structures. J. Mech. Phys. Solids 56:801–814, 2008.

[3] Begley M. R., Utz M. and Komaragiri U.: Chemo-mechanical interactions between adsorbed molecules and thin elastic films. J. Mech. Phys. Solids 53:2119–2140, 2005.

[4] Lei Z., Yang S. and Chen E. Q.: Membrane rigidity induced by grafted polymer brush. Soft matter 11:1376–1385, 2015.

[5] Zou Y., Lam A., Brooks D. E., Phani A. S. and Kizhakkedathu J. N.: Bending and Stretching Actuation of Soft Materials through Surface-Initiated Polymerization. Angewandte Chemie International Edition 50:5116–5119, 2011.

CURVATURE OF THE TRANSVERSE ARCH
GOVERNS STIFFNESS OF THE HUMAN FOOT

Madhusudhan Venkadesan[*1], Marcelo Dias[2], Dhiraj Singh[3], Mahesh M. Bandi[†3], and Shreyas Mandre[‡4]

[1]*Department of Mechanical Engineering & Materials Science, Yale University, New Haven, Connecticut, USA*
[2]*School of Science, Aalto University, Espoo, Finland*
[3]*Collective Interactions Unit, OIST Graduate University, Okinawa, Japan*
[4]*School of Engineering, Brown University, Providence, Rhode Island, USA*

Summary Humans are unique among primates in having arched feet that provide a stiff propulsive lever for locomotion. Using mathematical and physical models of the foot as a curved elastic shell, we show that the transverse curvature is the primary determinant of foot stiffness. The stiffness of shallow thin shells has two asymptotic regimes, one that resembles a soft thin plate, and the other that shows a power-law dependence of stiffness with an exponent of $3/2$. Curvature induced coupling between bending and in-plane stretching underlies the power-law dependence. Analysis of discrete realizations of a shell also show a similar transition, but with an exponent of 2. We present implications of our work to understanding the mechanical origins of stiff human feet, and to the evolution of human feet through an analysis of extant and fossil feet.

Figure 1: Observations on the effect of curvature on stiffness. **A**. The human foot has two distinct arches in the longitudinal and transverse directions. **B**. Common experience and simple experiments show that curvature in the transverse direction significantly increases the longitudinal bending stiffness of thin continuum shells. **C**. Discrete realizations of a shell, namely, rigid bars connected by soft elastic "ligaments" also shows a similar large increase in stiffness upon increasing curvature in the transverse direction.
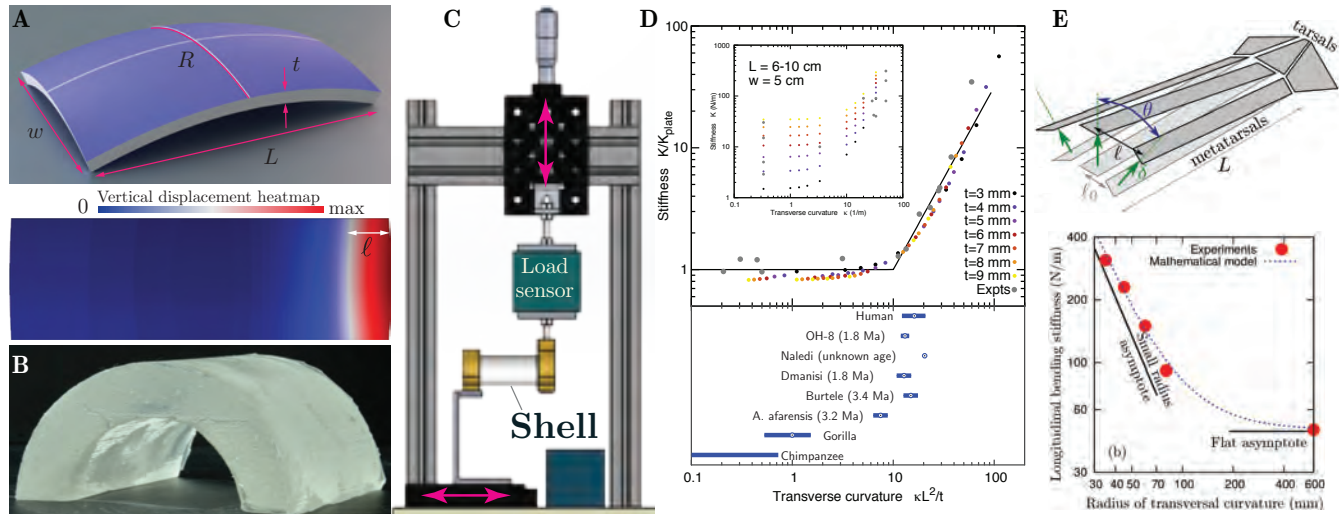
Figure 2: Mathematical and physical analyses of shells, and their implications to human evolution. **A**. Numerical model of curved elastic shells. **B,C**. Experimental fabrication and measurement of stiffness of transversally curved shells. **D**. The inset shows dimensional data, that collapse according to the asymptotic predictions. Comparing the dimensionless curvature of various biological feet, relative to the crossover point of the asymptotes, predicts that a human-like stiff foot might have emerged at least 3.4 million years ago. **E**. Ongoing work to address the mechanics of discrete mimics of the foot, with stiff "bones" and softer interconnecting "ligaments".

Just as a drooping dollar bill stiffens upon curling it in the transverse direction (figure 1B), we hypothesize that the transverse arch of the foot plays a central role in longitudinal bending stiffness. We observe a similar increase in stiffness for physical mimics of the foot, which resemble a discrete realization of the dollar bill (figure 1C).

[*]m.venkadesan@yale.edu
[†]bandi@oist.jp
[‡]shreyas_mandre@brown.edu

MODELS OF THE FOOT

Mathematical models: We modeled the foot computationally (using COMSOL) and experimentally (static loading experiments) as a continuum elastic shell of length L, width w, and thickness t. The shell has radii of curvature R_L and R_T in the longitudinal and transverse directions respectively (figure 2A,B). To isolate the dependence of the stiffness K of the shell on the geometrical parameters L, w, t, R_L, and R_T, but eliminate material nonlinearities, the shell is assumed to be made of a uniform linear elastic solid with Young's modulus E and Poisson ratio ν.

For flat thin plates, it is well known that stretching can be neglected and is decoupled from bending if the deflection of the end is much smaller than the thickness [Landau and Lifshitz(1959)]. For curved shells, however, stretching with bending could be a dominant effect even for small out-of-plane deflections. For a radial displacement by an amount w, the strain scales as $\sim w/R$, where R is the typical radius of curvature. The elastic stretching energy therefore scales as $\mathcal{E}_s \sim EtA(w/R)^2$. When deformations are uniform, pure bending energy scales as $\mathcal{E}_b \sim Et^3A(w/R^2)^2$, always resulting in a large stretching-to-bending ratio, $r = \mathcal{E}_s/\mathcal{E}_b \sim (R/t)^2 \gg 1$.

When the deformation is caused by an external normal force applied to the shell and the characteristic length scale of the range of this deformation is ℓ, bending energy will scale as $\mathcal{E}_b \sim Et^3 lW(w/\ell^2)^2$, where W is the projected width of the shell. Numerical experiments indeed show the localization of the deformation for curved shells (figure 2A). Hence, by balancing the stretching and bending energies (equivalent to minimizing the total elastic energy), we derive a scaling law for the deformation depth, namely $\ell \sim \sqrt{Rt}$. Therefore, for some function f depending on the precise loading of the shell, dimensional analysis implies $\frac{K}{Bw/L^3} = f(R_T t/L^2, R_L t/L^2)$, where the bending rigidity of the cross section of the shell is $B = Et^3/(12(1-\nu^2))$.
Physical models: Experimental realization of this shell was made using the soft elastomer polydimethylsiloxane (PDMS) (figure 2B). The shell was clamped at one edge, and an external force was exerted on the other, to mimic the loading experienced by the foot during toe-off (figure 2C). The ratio of the applied force to the relative displacement between the edges of the shell in the limit of small displacements gives stiffness K.

RESULTS

The inset of figure 2D shows the calculated and measured stiffness K of the foot for shells with different geometries. Using the dimensionless forms of stiffness and curvature cause these data to collapse, in agreement with the asymptotic predictions. There was no such effect on longitudinal bending stiffness because of longitudinal curvature. We also plot the curvature of human, gorilla, chimpanzee and several fossil feet [Harcourt-Smith and Aiello(2004), Pontzer et al.(2010)], shown in the lower half of figure 2D. Among living primates, humans are the only feet that belong to the 3/2 power-law regime, i.e. correctly predicted to exhibit a stiff shell-like behavior [Ker et al.(1987)]. On the other hand, the gorilla and chimpanzee are flat, and correctly predicted to be soft like a thin plate [Bennett et al.(1989)]. The fossil feet show a clear increase in curvature at least 1 million years (Ma) before the emergence of the genus *Homo*. The ~ 3.4 Ma foot (Burtele, Ethiopia), which was previously thought to resemble the gorilla, has a human-like arch even if we assume its proportions to be that of a gorilla.

CONCLUSION

The curvature of the transverse arch in humans is expected to contribute to a 200% increase in stiffness, all else held the same. Human feet are approximately 220% stiffer than chimpanzee feet [Bennett et al.(1989)], after adjusting for size differences and assuming equal Young's modulus (using our dimensionless stiffness). In contrast, the elastic tissue that constitute the longitudinal arch account for less than 30% of the human foot stiffness [Ker et al.(1987)].

Measurements of stiffness as a function of curvature using the discrete foot shown in figure 1C are in agreement with theoretical predictions (with two fitting parameters). However, the power-law now exhibits an exponent of 2, different from the continuum model. We are continuing to investigate the origins of this difference in the exponent.

Our results aid in the study of fossil feet, to infer function from form. There are also implications for flatfoot disorders, and for the the design of lightweight, yet stiff, robotic or prosthetic feet. Finally, we propose that control of the transverse curvature is an attractive method to modulate foot stiffness because of the strong dependence of stiffness on curvature.

References

[Bennett et al.(1989)] M. B. Bennett, R. F. Ker, and R. M. Alexander. *J. Zool*, 217:469–475, 1989.

[Harcourt-Smith and Aiello(2004)] W. E. H. Harcourt-Smith and L. C. Aiello. *J. Anat*, 204(5):403–416, 2004.

[Ker et al.(1987)] R. F. Ker, M. B. Bennett, S. R. Bibby, R. C. Kester, and R. M. Alexander. *Nature*, 325(7000):147–9, 1987.

[Landau and Lifshitz(1959)] L. D. Landau and E. M. Lifshitz. Pergamon Press, 1959.

[Pontzer et al.(2010)] H. Pontzer, C. Rolian, G. P. Rightmire, T. Jashashvili, M. S. Ponce de León, D. Lordkipanidze, and C. P. E. Zollikofer. *J. Hum Evol*, 58(6):492–504, 2010.

COUPLING KINETICS OF REACTIVELY IONIC GELS

Pengfei Wang[1a)], Yingze Cao[1] , Yan Zhang[1] & Fangming Cui[1]

[1]*Qian Xuesen Laboratory of Space Technology, China Academy of Space Technology, Beijing, China*

Summary As typical smart soft materials, ionic gels can present a large deformation induced by environmental temperature, electric field and chemicals, which maintain great potentials in soft actuator, environmental sensor, drug delivery, etc. In this paper, the coupling mechanism of reaction kinetics, deformation of polymer network, mass diffusion and polyelectrolyte effect in the gels will be uncovered, and a general dynamic electro-chemo-mechanical model will be proposed for common ionic gels. Further investigations showed that the dynamic deformation and response time of an ionic gel are dependent on the concentration of reactive and non-reactive ions, the time of exposure to external stimuli, the initial state and the density of ionizable groups on the polymer chains. At the end, a brief introduction will be additionally given on the application of smart soft materials, especially for the space technology.

INTRODUCTION

Ionic gels consist of ionic polymers and a solution. These gels exhibit large amounts of deformation in response to mechanical forces, temperature, pH, light and electrical fields. Natural ionic gels in the periphery of plant and animal cells have important roles in the regulation of water and in stabilizing the shape of cells. Synthetic ionic gels have been widely used in engineering as environmental sensors, biomimetic actuators, autonomous flow controller and drug delivery systems. In these applications, the dynamic characteristics of ionic gels are important in device performance and improvements in the response time of devices based on ionic gels has become a critical parameter in their design. However, ionic gels usually undergo large dynamic deformations accompanied by the migration of ions in and out of the gel as a result of a nonequilibrium ionic chemical reaction. There is therefore a need to develop theoretical models for the design and optimization of devices based on ionic gels. The exploration of the dynamic behavior of ionic gels in response to chemical stimuli is of particular interest.

We consider here the system of a block ionic gel immersed in a dilute solution of reactive and non-reactive ions. The gel has a dynamic behavior (swelling or shrinking) as the result of a nonequilibrium chemical reaction within the gel. By coupling the theories of large deformation, the Donnan effect and the nonequilibrium kinetics of chemical reactions, a chemomechanical theory has been developed to describe the dynamic behavior of the gel. We validated the predictions from the proposed theory using existing experimental and theoretical results. As examples, we report here the oscillation deformation of an actuator changing with the period of externally applied chemical stimuli and the response time of a sensor affected by the initial state, the density of ionizable groups on the polymer and the measured concentration.

When immersed in a solution containing several reactive ions, a polymer network with fixed ionizable groups begins to swell or shrink as a result of the ionic reactions between the fixed and mobile species. This results in a non-equilibrium ionic gel. We focused on a specific system, but without a loss of generality, *i.e.*, a non-equilibrium process for the dissociation and association of ionizable groups

$$AB \underset{k_2}{\overset{k_1}{\longleftrightarrow}} A^- + B^+$$
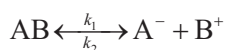
where k_1 and k_2 represent the rate constants of the forward and reverse processes, respectively. When the network imbibes a number of solvent molecules, the ionisable groups AB, chemically bonded on the polymer chains, dissociate into mobile ions B^+ in the solvent and conjugate bases A^- fixed on the polymer chains. During the reversible reaction, the network of polymer chains charges and discharges. For example, the increasing number of conjugate bases A^- gives rise to the fixed electrical charges of the polymer chains and consequently induces the deformation of the reactive ionic gels (forward reaction). The opposite process occurs during the backward reaction. In addition to the mobile ions B^+ and the water molecules, the solution also contains non-reactive counter ions (+) and co-ions (–). This reaction-deformation system represents the basic working mechanism of a broad range of applications, such as hydrogel-based testing devices and drug-delivery systems.

RESULTS AND DISCUSSIONS

We validated the theoretical model by comparing the steady solutions of a previously reported pH-sensitive gel (a familiar ionic gel: A^- are carboxylic acids groups, B^+ is H^+) with the long time-limited solutions of our model (approximating to a steady-state). The solutions of our theoretical model at longer dimensionless times agreed well with the steady-state solutions[1] (Fig. 1a and 1b). We then compared the swelling ratio of our theoretical predictions at longer dimensionless times ($\tau = 100$) with previously reported steady-state experimental results with different concentrations of B^+ ($\bar{c}^{B^+}/N_A$). Here A^- is the methacrylic acid-co-acrylic acid group and B^+ is H^+. The solutions of our theoretical model at longer dimensionless times agreed well with the previous experimental results[2] (Fig. 1c).

[a)] Corresponding author. Email: wangpengfei@qxslab.cn
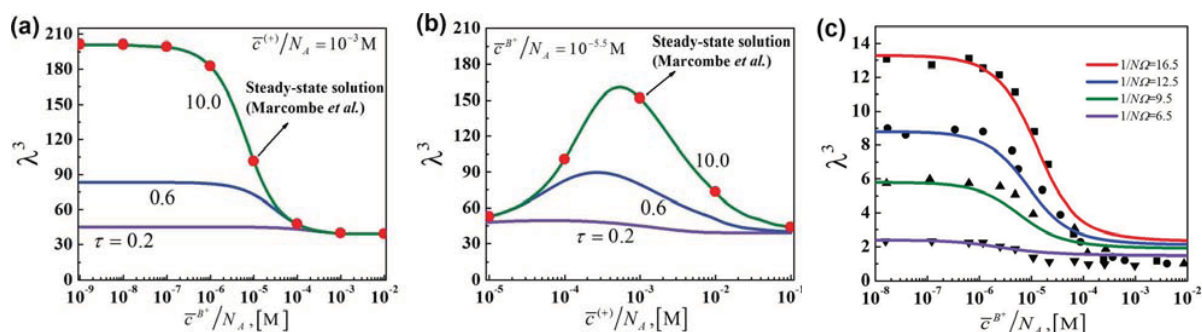
Fig. 1 The swelling ratio of a pH-sensitive gel changes (a) as a function of the concentration of B^+ ($\overline{c}^{B^+}/N_A$) and (b) as a function of salt concentration ($\overline{c}^{(+)}/N_A$) at different dimensionless time points. The red dots are the steady solution from Marcombe et al.[1] The molar fraction of the ionizable group $f = 0.05$ and the dissociation constant $k_1/N_A k_2 = 10^{-4.3}$. (c) Comparison between the swelling ratio of our theoretical predictions at a longer dimensionless time ($\tau = 100$) and the experimental results at steady-state with different concentration of B^+. The scattered dots are experimental data from Eichenbaum et al.[2] and the solid lines are the simulated results from our theoretical model.

CONCLUSIONS

A chemomechanical theory has been proposed to describe the dynamic behavior of ionic gels under non-equilibrium processes. We found that the dynamic behavior of an ionic gel depends not only on the dissociation constant of the ionisable groups on the polymer chains, but also on the concentration of the reactive and non-reactive ions in the external solution. When the ionic gel undergoes alternating stimuli from reactive ions in the external solution, the corresponding behavior is significantly affected by the frequency of the stimulus. The response time of an ionic gel for different measured concentrations of reactive ions is correlated with the initial state and the density of the ionizable groups on the polymer chains.

References

[1] Marcombe, R., et al: A Theory of Constrained Swelling of a pH-Sensitive Hydrogel. *Soft Matter* **6**: 784-793, 2010.

[2] Eichenbaum, G. M., et al: Investigation of The Swelling Response and Loading of Ionic Microgels with Drugs and Proteins: The Dependence on Cross-Link Density. *Macromolecules* **32**: 4867-4878, 1999.

[3] Liu, S. B., et al: Reaction-Induced Swelling of Ionic Gels. *Soft Matter* **11**: 449-455, 2015.

[4] Wang, P.F., et al: Reactive Swelling of Elastomeric Gels. Unpublished.

FAST ACTUATION ACHIEVED BY HYDROGEL STRUCTURES WITH BUILT-IN MECHANICAL INSTABILITY

Xuxu Yang [1], Guorui Li[1], Tingyu Cheng [1], Yongbing Jin[1], Tiefeng Li[1,2,3a] & Wei Yang[1a]

[1]*Institute of Applied Mechanics, Zhejiang University, 38 Zheda Road, Hangzhou, Zhejiang 310027, China*
[2]*Soft Matter Research Center (SMRC), Zhejiang University, Hangzhou 310027, China*
[3]*Key Laboratory of Soft Machines and Smart Devices of Zhejiang Province, Hangzhou 310027, China*

Abstract Stimuli-Responding structures can be actuated by the swelling/shrinking of hydrogels. The response process is slow, due to its strong dependence on the diffusion rate of the inward/outward creeps of solvent within the polymer networks of hydrogel. Inspired by plants like Venus flytrap, which enables "snapping" action with prompt actuation, mechanical instability may be built in a multilayer hydrogel structure. Tough thermo-responsive hydrogel is used to assemble the structure. The shape changing behaviour of the structures can be significantly increased by building blocks with a thermo-responsive layer. At a critical point, a small actuation may tip the structure to undergo a large deformation by fast snap-through mechanism. Finite element simulation is performed to guide the design and to illustrate the versatile responses of the hydrogel structures.

INTRODUCTION

Stimuli-responding hydrogels, with characteristics such as adaptability, biocompatibility, tuneable mechanical properties, and low cost, have broad applications in fields such as actuators, tissue engineering, drug delivery, soft biomimetic robotics and microfluidic control systems [1,2]. Similar to the movements in plants, hydrogels are driven mainly by swelling and shrinking of water. Mechanical motion with large deformations was achieved in those hydrogels by stimuli under pH, light, temperature, magnetic and/or electric fields [3,4]. Conventional structures made of stimuli-responsive hydrogels are actuated directly by the volume change of hydrogels. The size reduction of specimen may speed up the actuation of hydrogel structures. The response time, nevertheless, strongly depends on the diffusion rate of the inward/outward creeps of solvent within the polymer networks of the hydrogel. Attributed to the snap-buckling instability of the structure, plants like Venus flytrap and bladderwort exhibit "snapping" action with ultrashort response time (<1ms) [5-7]. Recent experiments demonstrate bio-inspired structures made of soft materials with various geometry and material properties for the fast, stimuli-responding motion assisted by a snap-through instability [8-10]. However, developing stimuli-responsive hydrogel structure with rapid response remains a challenge.

In this work, we synthesise thermo-responding and non-responding hydrogels with reasonable toughness, by the method of double-network hydrogel [11]. The two hydrogels are assembled into a multilayer structure to harness mechanical instabilities with rapid actuation. The hydrogel structure operates in two steps. In the first step, a temperature raise changes the hydrophilicity of the material, resulting in slow shrinking of the thermo-responding hydrogel. This step is relatively slow due to the limited diffusion rate. As the hydrogel keeps shrinking, the elastic energy of the hydrogel structure accumulates. When the structure deformation reaches the critical condition to trigger a snap-through action, the second step intervenes. The structure snaps from one state to another with fast actuation, while the stored mechanical energy in the first step is quickly released into kinetic energy.

A HYDROGEL STRUCUTRE ENABLING FAST ACTUATION

Built-in mechanical instability

By triggering snap-buckling instability, the Venus flytrap undergoes ultra-fast movement. To design a structure with built-in mechanical instability, one starts with a thin hydrogel plate under circumferential stress. The circumferential stress drives the thin plate to bend upward or downward and to transform into a spherical shell. When the buckled thin plate to deform and to snap from one stable state to another stable state, the sudden fast actuation is manifested. The structure may be accomplished by a tri-layer hydrogel. The first layer is composed of thermo-responding hydrogel, which provides the driven force for the structure deformation. The second layer is a pre-stretched non-responding hydrogel ring, which provides a constant circumferential stress on the structure. The third layer is a balancing layer of non-responding hydrogel, which also maintains the structure symmetry.

Actuated motion of the structure

Experiments are carried out in 0.0025wt% $CaCl_2$ solution. The solution is initially transparent and maintained at 22℃. We put the structure into the solution as the initial state, shown as in Fig. 1(a). The temperature of the solution is then raised to trigger the snap-through action of the structure. As the solution warms up, the thermo-responding hydrogel undergoes phase transition and turns write. The solution turns milk-like simultaneously by the spread of polymers squeezed from the

---

hydrogel. The transparency of the solution could indicate the degree of phase transition of the thermo-responding hydrogel. During the test, the thermo-responding hydrogel in the structure slowly pumps water out and shrinks. The volume change of the thermo-responding hydrogel induces an inverse bending moment on the structure, flattening the structure curvature. It takes 350 seconds for the structure to be flattened counting from the moment of the temperature raise (Fig. 1(a-c)). At the critical point of the structure inversion, the structure instability is triggered. The structure suddenly snaps-through into another stable state with the inversely buckled shape. It only takes less than one second for the structure to snap. Furthermore, the impact force of this snap-through process drives the structure to jump up from the vessel base (Fig. 1(d-f)).
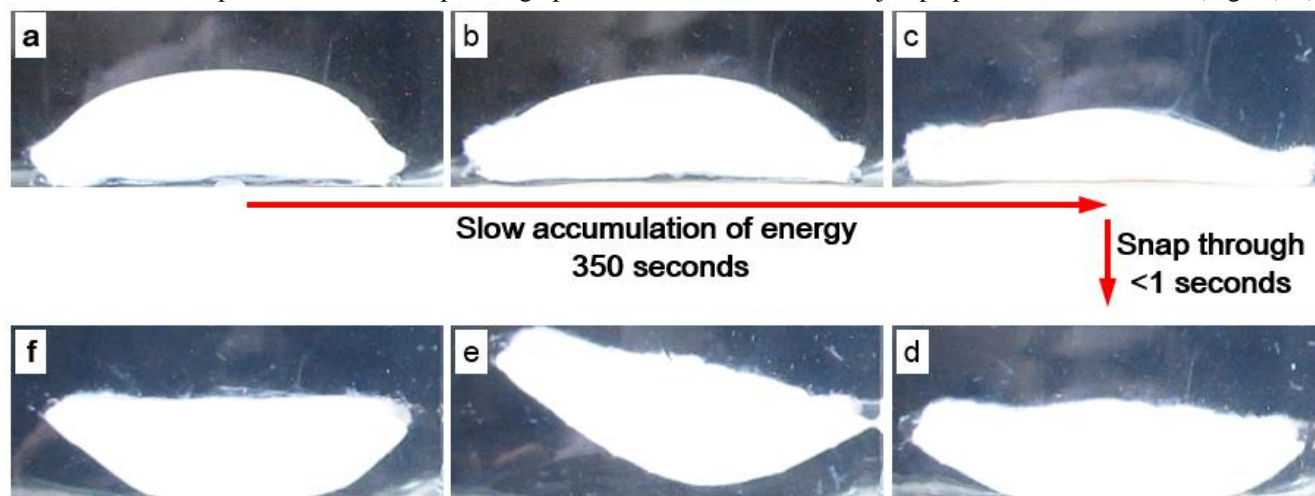
Figure 1. Images of the snap-through deformation of the hydrogel structure.

CONCLUDING REMARKS

In summary, the mechanical instability is induced by a multi-layer hydrogel structure, and fast actuation speed is achieved. A variety of snapping behaviours may be presented when pursued along this avenue. Further mechanics analyses for the snapping procedure are desirable. In addition, the mechanical principle of built-in mechanical instability in stimuli-responding hydrogel may open a door for enabling snapping behaviour of other stimuli-responding materials such as liquid crystal elastomers and shape memory polymers.

References

[1] Ionov L.: Biomimetic Hydrogel-Based Actuating Systems. *Adv. Funct. Mater.* **23**: 4555–4570, 2013.
[2] Kempaiah R., Nie Z.: From nature to synthetic systems: shape transformation in soft materials. *J. Mater. Chem. B* **2**: 2357–2368, 2014.
[3] Stuart M. A. C.: Emerging applications of stimuli-responsive polymer materials. *Nat. Mater.* **9**:101-103, 2010.
[4] Zhang J.: Multi-stimuli responsive macromolecules and their assemblies. *Chem. Soc. Rev.* **42**: 7421--7435, 2013.
[5] Hodick D., Sievers A.: On the mechanism of trap closure of Venus flytrap. *Planta* **179**:32-42, 1989.
[6] Forterre Y.: How the Venus flytrap snaps. *Nature* **433**:421-425, 2005.
[7] Vincent O.: Ultra-fast underwater suction traps. *Proc. R. Soc. B* **278**:2909-2914, 2011.
[8] Xia C.: Solvent-driven polymeric micro beam. *J. Micromech. Microeng.* **20**:085030, 2010
[9] Lee H.: First jump of microgel: actuation speed enhancement by elastic instability. *Soft Matter* **6**:4342-4345, 2010.
[10] Holmes D. P., Crosby A. J.: Snapping Sufaces. *Adv. Mater.* **19**:3589-3593, 2007.
[11] Sun J.: Highly stretchable and tough hydrogels. *Nature* **489**:133-136, 2012.

TOUGH ADHESION OF HYDROGELS

Teng Zhang[1a)], Hyunwoo Yuk[2] & Xuanhe Zhao[2]

[1]*Department of Mechanical and Aerospace Engineering, Syracuse University, Syracuse, New York, United States*

[2]*Department of Mechanical Engineering, Massachusetts Institute of Technology, Cambridge, Massachusetts, United States*

Summary Tough adhesion for synthetic hydrogels is challenging and only achieved very recently by chemically anchoring long-chain polymer networks of tough hydrogels on solid surfaces. Here we provide a quantitative understanding of the mechanism for the tough adhesion of hydrogels on solid materials by using a coupled cohesive-zone and Mullins-effect model. Numerical simulations reveal the toughening mechanism of the energy dissipation and the importance of the high intrinsic work of adhesion as well as the interfacial strength. These findings shed light on the reported strong bonding of tough hydrogels that the chemical anchoring gives high interfacial strength and large intrinsic work of adhesion to trigger significant energy dissipation and further enhance the interfacial toughness.

INTRODUCTION

Adhesion plays an essential role in applying hydrogels to biological load-bearing materials and structures; for example, tough bonding of tendons and cartilages on bones in animals and tough adhesion of mussel's plaque on rocks. Furthermore, tough interfaces between hydrogels and various solids, such as metal, ceramic, silicon and polymers, have been the foundations of the well integration and function in devices and systems in the engineering applications of hydrogels as diverse as biomedicine, biocompatible stretchable electronics, actuators for optics and fluidics, soft robotics and machines. Although the tough hydrogel adhesion is extremely important in both biological and engineering application, it is very challenging to achieve strong adhesion between hydrogels and non-porous solids, as the presence of water complicates the interfaces interaction. Most of reported hydrogel adhesions are not very strong.

Great progress was recently made by Hyunwoo and colleagues [1], who developed a strategy for designing tough hydrogel bonding on various nonporous solid surfaces via chemically anchoring the stretchy polymer networks of tough hydrogels to the solid surface. Through the standard 90-degree-peeling test, the bonding was found to be very strong with an interfacial toughness over 1,500 J/m2 and robust in the wet environment, i.e., stable during constrained swelling under water. Although the real detachment process was complicated and involved finger instabilities, viscoelasticity and possible cavitation, it has been experimentally and numerically demonstrated the strong chemical anchors and energy dissipation were the key factors to achieve the tough bonding of hydrogels. The design methodology is expected to benefit the adhesion of various tough hydrogels for diverse engineering applications and thus calls for more in-depth theoretical understanding of the mechanisms of tough interfaces to guide the rational design of tough bonding and hydrogels. Furthermore, the fundamental toughening mechanisms of the synthetic tough hydrogel interfaces can also shed light on the orders magnitude difference between the work of adhesion of the DOPA molecular interfaces and macroscale mussel's plagues [2].

Here we systemically examine the fundamental mechanisms of strong adhesion of the tough hydrogels due to chemical anchors and energy dissipations e.g., Mullins effect, with the coupled cohesive zone and Mullins effect model. We will present the validation of the simulation model and comparison between simulations and previous experiments and conducts parameter studies of the adhesion enhancement by varying the key materials parameters, such as interfacial strength and maximum energy dissipation ratio.

THEORETICAL MODEL

We developed a 2D finite-element model to simulate the 90-degree-peeling test of soft materials bonded on solid substrates. A stiff backing film (i.e., Young's modulus on the order of GPa) was attached on the top of the soft material film to reduce the elastic energy stored in the detached part so that the work of adhesion can be directly converted from the measured peeling force. The deformation of the system was assumed to be under plane-strain condition. The thickness of the soft material film and stiff backing are denoted as t and b, respectively.

To describe the intrinsic failure of the interface, we adopt the cohesive zone model. The specific model used in the current study is characterized by a triangular cohesive law with interface strength $S_{interface}$ and maximum separation distance δ_{max}. The damage of the cohesive interface follows the quadratic nominal stress criterion,

---

[a)] Corresponding author. Email: **tzhang48@syr.edu.**

$$\left\{\frac{t_n}{S_{\text{interface}}}\right\}^2 + \left\{\frac{t_s}{S_{\text{interface}}}\right\}^2 = 1 \tag{1}$$

where $t_{(\bullet)}$ represents the nominal surface tractions on the crack surface, and the subscripts n and s indicate normal and tangential directions, respectively. The elastic properties and energy dissipation of the soft materials are modeled as the Ogden hyperelastic material [3] and Mullins effect [4], respectively.

CONCLUSIONS

We conduct extensive numerical simulations of tough hydrogel adhesion and show that the total work of adhesion linearly scales with the intrinsic work of adhesion of the interface and the contribution form the energy dissipation to the work of adhesion can be much larger than the intrinsic value. In addition, the simulations can capture the nontrivial thickness dependent work of adhesion observed in the experiments. We then explored the fundamental principles to design tough and adhesive soft materials by systematically varying the key bulk and interface material properties. For a material with given shear modulus and intrinsic work of adhesion, it is found that high interfacial strength and large energy dissipation (high value of $h_{\max}$ and small value of m) are the key of the strong bonding.

References

[1] Hyunwoo, Y., et al.: *Nat. Mater.*, 2015.
[2] Desmond, K.W., et al.: Soft matter **11**: 6832-6839, 2015.
[3] Ogden, R.W., Non-linear elastic deformations. Courier Corporation 1997.
[4] Ogden, R., D. Roxburgh.: Proc. R. Soc. A**. 455** 2861-2877 1999.

[a] Corresponding author. Email: **tzhang48@syr.edu.**

CONTRIBUTIONS OF ECM CONSTITUENTS TO ARTERIAL WALL MECHANICS

Yunjie Wang[1], Shahrokh Zeinali-Davarani[1] & <u>Yanhang Zhang</u> [1,2,a)]
[1]*Department of Mechanical Engineering, Boston University, Boston, MA, USA*
[2]*Department of Biomedical Engineering, Boston University, Boston, MA, USA*

<u>*Summary*</u> Considering the organization and engagement behavior of extracellular matrix (ECM) constituents in the arterial wall, here we proposed a new constitutive model of ECM mechanics that consists of medial elastin, medial collagen, and adventitial collagen, to incorporate the layer-specific distribution of elastin and collagen fiber orientations and the sequential fiber engagement in arterial mechanics. Planar biaxial tensile testing method was used to characterize the orthotropic and hyperelastic behavior of porcine thoracic aorta. Fiber distribution functions obtained previously [1] were incorporated into the constitutive model. Considering the sequential engagement of ECM constituents in arterial mechanics, a collagen recruitment function was incorporated into the model to capture the delayed engagement of adventitial collagen. A freely jointed chain model was used to capture the mechanical behavior of elastin and collagen at the fiber level. The tissue-level ECM mechanics was obtained by incorporating fiber distribution, engagement, and elastin and collagen content.

INTRODUCTION

With a goal to understand how elastin and collagen fibers interrelate and modify the dynamic behavior of the arterial wall, we previously studied the ECM fiber organization, realignment, and recruitment by coupling mechanical loading and multi-photon imaging [1]. Our study provides quantitative evidence on the sequential engagement of ECM constituents in response to mechanical loading. We found that the adventitial collagen exists as large wavy bundles of fibers that exhibit delayed fiber engagement after about 1.15-1.2 tissue stretch. The medial collagen is engaged throughout the stretching process, and prominent elastin fiber engagement is observed up to 1.2 tissue stretch after which the engagement plateaus. These findings suggest that there are intrinsic interrelations between the major ECM constituents, medial elastin, medial collagen, and adventitial collagen fibers, which determines the mechanics of arteries and may carry important implications to vascular homeostasis and mechanobiology. In this study, a new constitutive model is proposed that considers the structural and mechanical interrelations of the three major ECM constituents. The medial elastin, medial collagen, and adventitial collagen each play unique structural and mechanical roles, and their distinct contributions to arterial mechanics are considered. Material parameters in the constitutive model resemble key structural and biological information in the arterial ECM. The layer-specific structural and biological information from quantitative multi-photon imaging and analysis, and biochemical assay is incorporated into the model to study the fitting and predicting capability of the model.

MATERIALS AND METHODS

Biaxial tensile testing

Porcine thoracic aortas from 12-24 month-old pigs were harvested from a local slaughter house and cleaned of adherent tissues. Square aortic samples of about 20 mm × 20 mm were prepared for biaxial tensile testing (n=7). Equi- and nonequi-biaxial tensile tests were performed to characterize the mechanical behavior of the aortic tissue. Following the preconditioning cycles, a preload of 2 ± 0.050 N/m was applied in order to ensure tautness of the sutures. Equi-biaxial and two nonequi-biaxial tensions were applied to each aortic sample according to the following protocols: $f_l{:}f_c$ = 2:3, 1:1, 3:2. Where $f_l{:}f_c$ is the ratio of tension applied in the longitudinal and circumferential directions, respectively.

Constitutive Modeling

A constitutive model of ECM mechanics is developed that considers the contribution from medial elastin ($i = E$), medial collagen ($i = M$), and adventitial collagen ($i = A$) constituents, to incorporate their layer-specific distribution orientations $R_i(\theta)$ and the sequential fiber engagement in the hyperplastic and anisotropic arterial behavior. The total strain energy function of the arterial wall is the sum of the constituent strain energy, W_i, and can be represented as $W = \sum_{i=E,M,A} W_i$. A fiber distribution network model is used to incorporate the experimentally measured fiber distribution function $R_i(\theta)$, and the elastin and collagen content n_i. The ECM constituent strain energy function, W_i, is assumed to be the sum of the individual fiber strain energies and can be expressed as: $W_i = n_i \int_{-\pi/2}^{\pi/2} w_i(\rho_i) R_i(\theta) \mathrm{d}\theta$, where $w_i(\rho_i)$ is the strain energy function at the fiber level and is characterized by a freely-jointed chain model [2].

Considering the sequential recruitment of ECM constituents in response to mechanical loading, a normal recruitment function [3] is included to capture the delayed adventitial collagen engagement. The fiber orientation distribution of the ECM constituents, $R_i(\theta)$, were incorporated in two ways: A) the distributions of fiber orientation of each constituent are incorporated directly based on the analysis of multi-photon images [1]; and B) the measured distribution functions of each constituent were fitted with a three-term von Mises distribution (Figure 1). Parameter n_i is related to the content of ECM constituents. These parameters were allowed to vary within a physiological meaningful range considering the elastin and

a) Corresponding author. Email: yanhang@bu.edu**.**

collagen content in the arterial tissue [4]. The material parameters were determined by minimizing the objective function using the Nelder-Mead direct search method implemented in the *fminsearch* subroutine in Matlab.

RESULTS AND DISCUSSION

The fiber orientation distribution function (Figure 1a) shows remarkably different structural characteristics in ECM constituents. The elastic fibers are relatively more uniformly distributed compared to collagen. The medial collagen shows a preferred circumferential distribution, however the multi-fiber family distribution is evident in adventitial collagen. For all three ECM constituents, the three-term von Mises fittings were able to capture the fiber distributions in the arterial wall. The collagen recruitment function was determined based on the straightness parameter analysis of adventitial collagen fibers from our previous study by Chow et al. [1]. Adventitial collagen was shown to exist as large wavy bundles of fibers that exhibit delayed fiber engagement. The values of the mean and standard deviation of the normal distribution were fixed as 1.25 and 0.05, respectively, which captures a peak recruitment at about 1.25 stretch and an overall collagen engagement between 1.15-1.35 stretch (Figure 1b). Considering the structural characteristics and contributions of elastin, medial collagen, and adventitial collagen, the measured fiber orientation distributions were directly incorporated into the structurally motivated constitutive models and, hence, reduce the number of estimated parameters to only intrinsic fiber properties and fiber content. The model predicts the biaxial mechanical behavior of arteries reasonably well, while requiring less mechanical datasets for reliable estimation. With this constitutive model, we can study the mechanical contributions from the major load-bearding ECM constituents in the arterial wall (Figure 1c). Understanding the mechanical contributions of ECM constituents in the arterial wall may shed light on the underlying mechanisms of vascular remodeling and disease progressions. The small load bearing of adventitial collagen at lower stretches is consistent with its role in preventing the artery from overstretch and rupture. However contributions from the ECM constituents to the mechanical behavior of the arterial wall are highly dependent on the mechanical loading conditions. It is important to understand the interactions between elastin and collagen in arterial wall, which are currently unclear. The coexistence of multiple ECM constituents and their interrelations may be important in maintaining the fiber distributions in the arterial wall and contributing to the anisotropic tissue behavior.
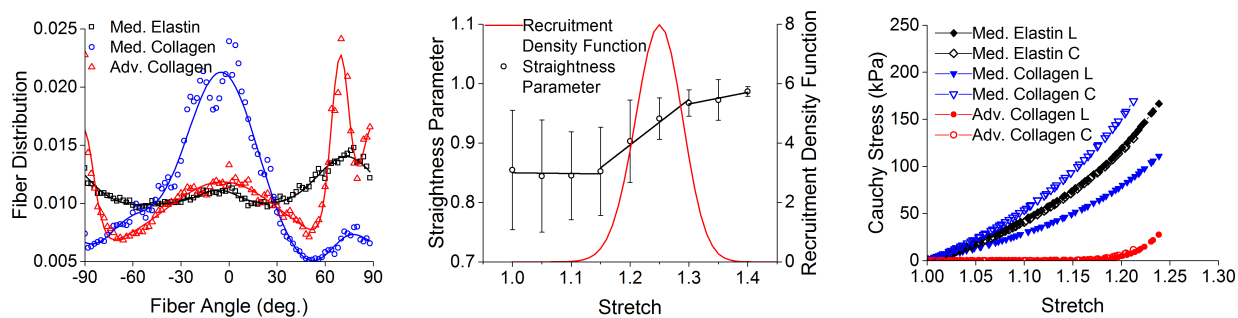
Figure 1: (a) Fiber orientation distributions of medial elastin, medial collagen, and adventitial collagen under 140% equi-biaxial tissue stretch. Symbols represent measured distribution [1] and lines represent the corresponding three-term von Mises distribution function fitting; (b) Straightness parameter of adventitial collagen fibers [1], and the recruitment distribution density function that captures the delayed adventitial collagen engagement in response to mechanical loading; and (c) stress-stretch relationship of the ECM constituents, medial elastin, medial collagen, and adventitial collagen, when the arterial tissue is under equibiaxial tension.

CONCLUSIONS

In this study, we developed a new multi-scale structure-based model of ECM mechanics from a fundamental mechanics perspective coupled with critical biophysical input. The model uniquely integrates the ECM microstructural information, such as fiber distribution, recruitment, elastin and collagen content, and fiber properties, for tissue-level biomechanical function. Contributions from layer-specific ECM structural constituents, medial elastin, medial collagen, and adventitial collagen were considered in the model to reflect the different mechanical and structural role of each individual ECM component. Moreover, the integrated model shows promises in fitting and predicting with a small set of material parameters, which has physical meanings and can be related to the structure and properties of the ECM constituents.

ACKNOWLEDGEMENT

References
[1]   Chow, M.J., Turcotte, R., Lin, C.P., Zhang, Y. *Biophys. J.* 106(12):2684-2692, 2014.
[2]   Kuhn, W., Grün, F. *Kolloid-Zeitschrift* 101(3):248–271, 1942.
[3]   Lanir, Y. *J. Biomech.* 12(6):423–436, 1979.
[4]   Chow, M.J., Mondonedo, J.R., Johnson, V.M., Zhang, Y. *Biomech. Model. Mechanobiol.* 12(2):361–372, 2013.

MS06 - Topology Optimization

DETERMINISTIC APPROACHES FOR SHAPE OPTIMIZATION UNDER RANDOM UNCERTAINTIES

Grégoire Allaire*[1] and Charles Dapogny[2]

[1]*Centre de Mathématiques Appliquées (UMR 7641), Ecole Polytechnique 91128 Palaiseau, France*
[2]*Laboratoire Jean Kuntzmann, CNRS, Université Joseph Fourier, Grenoble INP, Université Pierre Mendès France, BP 53, 38041 Grenoble Cedex 9, France*

Summary We consider shape and topology optimization problems with uncertainties in the loadings, the material properties or the geometry. In view of minimizing the CPU cost of solving such problems, we propose two deterministic approximation methods, based on the assumption of small uncertainties. The first one solves the so-called worst-case design scenario for a linearized approximation. The computational cost is at most twice that of the unperturbed case since it involves three adjoint equations on top of the state equation. The second one minimizes averaged objective functions (mean value, variance) of second-order Taylor expansions of standard cost functions, under the additional assumption that the (small) uncertainties are generated by a finite number N of random variables. The computational cost is now similar to that of a multiple load problems where the number of loads is N. We demonstrate the effectiveness of our approach on various geometric optimization problems in 2-d linearized elasticity. We rely on a gradient algorithm with shape derivatives in a level set framework.

GEOMETRIC OPTIMIZATION SETTING

We consider geometric optimization in the context of linear elastic structures. A shape is a bounded, Lipschitz domain $\Omega \subset \mathbb{R}^d$ ($d = 2, 3$), filled with a linear isotropic elastic material with Hooke's law A. Every such shape is clamped on a part Γ_D of its boundary, submitted to given body forces f and surface loads g, applied on a subset $\Gamma_N \subset \partial\Omega$ disjoint from Γ_D, and only its free boundary $\Gamma := \partial\Omega \setminus (\Gamma_D \cup \Gamma_N)$ is subject to optimization. The displacement u_Ω of a shape Ω is the unique solution of the linear elasticity system:

$$\begin{cases} -\text{div}(Ae(u)) = f & \text{in } \Omega \\ \quad\quad u = 0 & \text{on } \Gamma_D \\ \quad Ae(u)n = g & \text{on } \Gamma_N \\ \quad Ae(u)n = 0 & \text{on } \Gamma \end{cases}. \tag{1}$$

For some integrand functions $j(u)$ and $k(u)$, we consider the optimization problem

$$\inf_{\Omega \in \mathcal{U}_{ad}} \left\{ J(\Omega) = \int_\Omega j(u)\, dx + \int_{\Gamma_N} k(u)\, ds \right\}, \tag{2}$$

with the set of admissible shapes $\mathcal{U}_{ad} := \left\{ \Omega \subset \mathbb{R}^d \text{ is open, bounded and Lipschitz, } \Gamma_D \cup \Gamma_N \subset \partial\Omega \right\}$. When it comes to evaluating the sensitivity of such functionals, we rely on Hadamard's boundary variation method. Namely, variations of a shape Ω are of the form

$$\Omega_\theta := (I + \theta)(\Omega), \ \ \theta \in C^1(\mathbb{R}^d, \mathbb{R}^d), \ \ \|\theta\|_{C^1(\mathbb{R}^d, \mathbb{R}^d)} < 1$$

and shape derivatives are just usual functional derivatives with respect to the vector field θ.
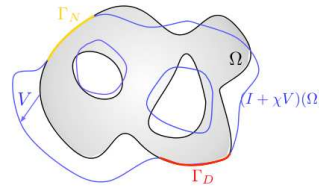
Figure 1: *Uncertainty, parametrized by a vector field V, of the geometry of the shape Ω.*

The same Hadamard setting is useful to define uncertainties with respect to the geometry. Denoting now by V a vector field, a perturbation of a given shape is defined as Ω_V (see Figure 1). It is assumed to be small in the continuous norm, $\|V\|_{C^0(\mathbb{R}^d, \mathbb{R}^d)} \ll 1$. Uncertainties or perturbations of the forces or material properties are defined in a standard way [1], [2] (many more references can be found in the bibliography of these papers).

---

*Corresponding author. Email: gregoire.allaire@polytechnique.fr

A LINEARIZED APPROACH TO WORST-CASE DESIGN

For a given level of uncertainty $m > 0$, we choose to optimize the worst-case scenario, namely

$$\inf_{\Omega \in \mathcal{U}_{ad}} \left\{ \mathcal{J}(\Omega) = \sup_{V \in C^1(\mathbf{R}^d, \mathbf{R}^d), \|V\|_{C^0(\mathbf{R}^d, \mathbf{R}^d)} < m} J(\Omega_V) \right\}.$$

In order to simplify the inner maximization, assuming that m is small, we linearize the objective function $J(\Omega_V)$ with respect to V. Linearizing the state equation (1) requires a standard ajoint state p. Then, the linearized worst-case design problem can be written as

$$\inf_{\Omega \in \mathcal{U}_{ad}} \left\{ \mathcal{J}^{\text{lin}}(\Omega) = J(\Omega) + m \int_\Gamma h(u, p) \, ds \right\}, \tag{3}$$

where the integrand h depends on both u and p and is integrated on the free boundary Γ only (like a shape derivative). Then, it is a standard matter to compute the shape derivative of (3) and to implement a gradient descent algorithm. Note that this shape derivative requires two additional adjoint (see [1] for details). A similar (albeit simpler) method applies to other types of uncertainties in the forces or material properties. In Figure 2, one can see the effect of geometry uncertainties for a gripping mechanism: the small joints are thickened by considering the linearized worst-case approach.

Figure 2: *Gripping mechanism: loadings (left), unperturbed optimal design (middle), linearized worst-case design (right).*

A SECOND-ORDER APPROACH TO AVERAGED OPTIMIZATION

We now switch to the optimization of an average of the objective function, with respect to to the probability distribution of the uncertainties. Still for small uncertainties, we further assume that they are generated by N uncorrelated and normalized random variables. We now perform a second-order Taylor expansion of the cost function (2) with respect to these small uncertainties and we optimize its mean (or combination of mean and variance). It turns out that, for compliance minimization, this expansion is exact and leads to a problem equivalent to N multiple loads optimization [2]. In any case, the only used informations on the random distribution are its mean and variance. In Figure 3 one can see the effect of (vertical) force uncertainties generated by two random variables in the blue region). The optimal design for the mean is clearly more robust than the unperturbed one. This approach extends to other type of uncertainties, including geometrical ones.
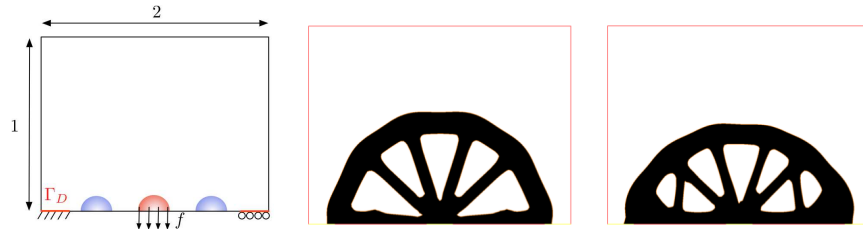
Figure 3: *Minimal compliance bridge: loadings (left), unperturbed optimal design (middle), second-order averaged optimal design (right).*

References

[1] Allaire G., Dapogny C.: A linearized approach to worst-case design in parametric and geometric shape optimization, M3AS Vol. 24, No. 11 (2014) 2199-2257.
[2] Allaire G., Dapogny C.: A deterministic approximation method in shape optimization under random uncertainties, to appear in SMAI J. Comput. Math. HAL preprint: hal-01160256v1 (June 2015).

PROJECTION-BASED TOPOLOGY OPTIMIZATION ALGORITHMS FOR ADVANCED MANUFACTURING

Andrew T. Gaynor[1] & <u>James K. Guest</u>[1a]

[1]*Department of Civil Engineering, Johns Hopkins University, Baltimore, Maryland, USA*

<u>*Summary*</u> The recent and rapid advancement of additive manufacturing technologies has provided engineers the capability to fabricate tailored structures with significant complexity at unprecedented length scales. In order to fully leverage these technologies, the associated new capabilities and limitations must be integrated into the design process. Herein, we extend projection-based topology optimization algorithms to address a number of advanced manufacturing methods including both polymer and metal additive manufacturing, and three-dimensional weaving. Fundamentally, all algorithms draw upon and extend the Heaviside Projection Method in order to impose manufacturing constraints, essentially utilizing tailored geometric and functional relationships between the independent design variables and the physical (and analysis) space. Specifically, we present new topology optimization algorithms for designing with multiple materials, considering support anchors for overhang regions, and respecting various geometric restrictions associated with 3D weaving. Through this, the end goal is to eliminate solution post-processing such that the optimized topologies are directly manufacturable.

DESIGN FOR ADDITIVE MANUFACTURING

With the surge of industry interest in additive manufacturing (AM) comes the increasingy need to properly design components for this truly game-changing manufacturing technology. Topology optimization and AM are a natural design-manufacture pair, with both being capable of addressing and leveraging complexity when such complexity leads to enhanced performance. While manufacturing constraints may be considered reduced for AM as compared to traditional manufacturing technologies, they are of course still present and must be considered in the design process. In this paper, several projection-based topology optimization algorithms are highlighted, which design for a number of advanced manufacturing methods including direct metal laser sintering (DMLS), material jetting, and 3D weaving. All algorithms are derived from the Heaviside Projection Method (HPM) to topology optimization [1].

MAXIMUM OVERHANG ANGLES AND APPLICATION TO DIRECT METAL LASER SINTERING (DMLS)

Direct Metal Laser Sintering (DMLS) is a powder bed additive manufacturing technology in which metal powder is selectively sintered or melted in a layer-wise fashion. After one layer is selectively sintered/melted, the machine sweeps another thin layer of powder across the build plate. While possessing the capability of making truly novel metal parts, this energy-intense process is susceptible to processing errors including curling and shrinkage due to development of large residual stresses. These stresses develop when the heat of the weld-like process cannot dissipate from the point of melting.

To mitigate this deleterious effect, designers often introduce support structures to help anchor the part to the build plate. Not only is the curling from residual stresses counteracted, but these stresses are reduced as the heat can more effectively dissipate from the point of melting. That said, there are signficant advantages to eliminating these material using, sacrificial support materials during the additive manufacturing build process. As such, by stipulating that the built part not possess an overhang angle greater than the maximum observed printable overhang, the need for support material is completely eliminated, thus ensuring that all material used is for an efficient, structural purpose. Here are shown some solutions designing for various overhang angles and printing directions.
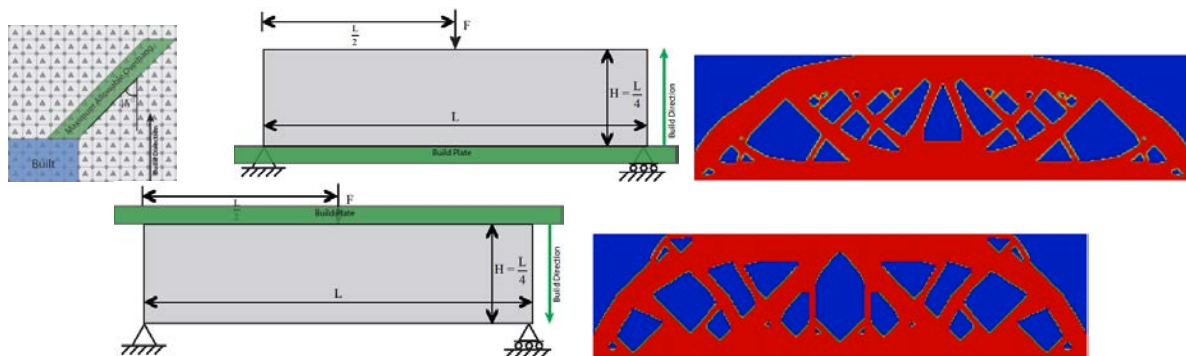
Figure 1: Topology optimization under a 45° overhang angle constraint building from bottom-up and top-down.

---

[a] Corresponding author. Email: jkguest@jhu.edu

As expected, the build directly significantly influences the optimized topology. Building in the bottom-up direction, the topology optimization algorithm designs up to the 45° overhang, creating 45° peaks in the design. Conversely, in the top-to-bottom build, the algorithm creates 45° "wells".

As in the case of imposing the minimum length scale constraint [1], the maximum overhang constraint is imposed through a projection of independent design variables onto the finite element space. The key difference here is the introduction of an additional projection operation from the support material zone onto an element [2]. This leads to a series of two projections, one from the support material region and one from the local region, leading to overhang angle and minimum length scale constraints being observed.

MULTI-MATERIAL TOPOLOGY OPTIMIZATION AND APPLICATION TO MATERIAL JETTING

Multi-material additive manufacturing processes, such as Stratasys PolyJet [3] and 3D Systems MultiJet [4] technologies possess the ability to print multiple materials during the same build. In this material jetting process, the printer extrudes liquid photopolymeric material in a drop-by-drop manner, which is "instantaneously" solidified by ultraviolet light. This technology is clearly unique in its ability to place up to 10+ materials on a pixel-by-pixel basis. To design for this capability, a new projection based topology optimization algorithm is introduced in which a single design variable is capable of not only determining topology, but critically, the material selection.

Recently the authors demonstrated the use of topology optimization to design compliant mechanisms with multiple materials [5]. The algorithm chose to place stiff material where load transfer was critical and compliant material in hinge-like regions to maximize motion (Figure 2).   In this approach, the overall Young's modulus E of a particular finite element in the design domain was expressed as a summation of the Young's modulus contribution ΔE of the material placement variable, ϕ, as follows:

$$E^e = \sum_i^n \rho_i^e(\phi_i)\, \Delta E_i$$

Herein, we introduce a thresholding Heaviside function to allow the independent design variables to specify whether a particular material phase is actively projecting material. Just as in the overhang algorithm, there are two levels of projection. The first level determines which material phase contributions are active, while the next level projection imposes typical minimum length scale control.
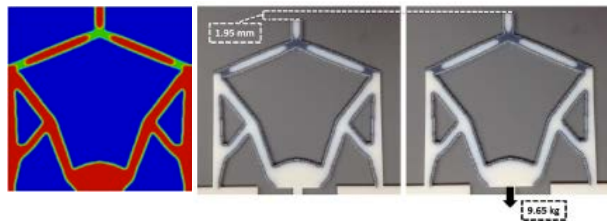
Figure 2: Compliant mechanism designed for E=0,1,2. Mechanical testing seen on right [5]

CONCLUSIONS

In order to fully leverage the capabilities of advanced manufacturing processes, design engineers and optimization algorithms must properly account for the process capabilities and limitations, even if such limitations are significantly reduced over traditional manufacturing processes. This paper presents advancements in projection-based topology optimization algorithms towards this goal, including addressing overhang angles and multiple materials in AM, with extensions to lattice-like materials manufactured through 3D weaving [6] also being achievable.

References

[1] Guest JK, Prévost JH, Belytschko T. Achieving minimum length scale in topology optimization using nodal design variables and projection functions. *International Journal for Numerical Methods in Engineering* 61(2):238–254, 2004.
[2] Gaynor AT, Guest JK. (2014). Topology Optimization for Additive Manufacturing Considering Maximum Overhang Constraint. *Proceedings of the 15th AIAA/ISSMO Multidisciplinary Analysis and Optimization Conference*, Atlanta, GA, p. 1-8, 2014.
[3] "PolyJet Technology." Stratasys. Web. 15 Jan. 2016. <http://www.stratasys.com/3d-printers/technologies/polyjet-technology>.
[4] "MultiJet Printing." 3D Systems. Web. 15 Jan. 2016. <http://www.3dsystems.com/quickparts/prototyping-pre-production/multijet-printing-mjp>.
[5] Gaynor AT, Meisel NA, Williams CB, Guest JK. Multiple-Material Topology Optimization of Compliant Mechanisms Created Via PolyJet Three-Dimensional Printing. *ASME Journal Manufacturing Science and Engineering* 136(6):061015-061015-10, 2014.
[6] Zhao L, Ha S, Sharp KW, Geltmacher AB, Fonda RW, Kinsey AH, Zhang Y, Ryan SM, Erdeniz D, Dunand DC, Hemker KJ, Guest JK, Weihs TP. Permeability measurements and modeling of topology-optimized metallic 3-D woven lattices, *Acta Materialia*, 81: 326-336, 2014.

ON CONVERGENCE SPEEDUP IN TOPOLOGY OPTIMIZATION

Ole Sigmund*

Department of Mechanical Engineering, Solid Mechanics, Technical University of Denmark

Summary This paper introduces a simple-to-implement, multiscale-inspired approach to improve convergence speed in topology optimization. To ensure convergence toward globally optimal Michell-like structures, topology optimization approaches often apply continuation schemes where e.g. the penalization exponent is increased gradually. In this way, one nudges the process by going from an initially convex problem (variable thickness sheet) to a penalized, black and white solution. Iteration counts for such continuation approaches are usually counted in many hundreds or up to thousands. By introducing an extra constraint that limits the p-norm of the difference between the local density field and a smoothed (homogenized) one, the continuation scheme can be eliminated. It is demonstrated that this approach systematically creates extremely detailed and highly optimized Michell-like structures within at most 200 iterations.

THEORY AND METHOD

The standard density-based minimum compliance topology optimization problem reads

$$
\begin{aligned}
\min_{\boldsymbol{\rho}} \quad &: \quad C(\boldsymbol{\rho}) \\
\text{s.t.} \quad &: \quad \mathbf{K}(\hat{\boldsymbol{\rho}}(\boldsymbol{\rho}))\mathbf{D} = \mathbf{F} \\
&: \quad V(\hat{\boldsymbol{\rho}}(\boldsymbol{\rho})) \leq V^* \\
&: \quad \mathbf{0} \leq \boldsymbol{\rho} \leq \mathbf{1}
\end{aligned}
\tag{1}
$$

where $\boldsymbol{\rho}$ is the vector of element-based design variables, $\hat{\boldsymbol{\rho}}(\boldsymbol{\rho})$ are the (density) filtered, physical design variables using a filter size r_{min}, $C(\boldsymbol{\rho})$ is compliance, $\mathbf{K}$, $\mathbf{F}$ and $\mathbf{D}$ are global stiffness matrix, load and displacement vectors, respectively, and V and V^* are volume and volume bound, respectively. The optimization problem (1) is set up for a density filtering approach, however, it can easily be simplified to a sensitivity filtering approach by substituting $\hat{\boldsymbol{\rho}}(\boldsymbol{\rho})$ with $\boldsymbol{\rho}$ or applied with PDE-based filtering [1]. The relation between density design variables and local (isotropic) stiffness is modelled by the SIMP interpolation scheme

$$
E(\rho) = E_{min} + \hat{\rho}^q(E_0 - E_{min}), \quad E_{min} \ll E_0
\tag{2}
$$

where E_0 and E_{min} are Young's modulus of solid and void material, respectively, and q is the penalization factor.

In its standard form, the optimization problem (1) is solved by selecting appropriate penalization factors (c.f. $q = 3$) and filter radii and is then run until convergence. However, this usually results in convergence towards suboptimal topologies, where design features tend to agglomerate, resulting in suboptimal objective values and feature sizes much bigger than those allowed by the filter size. In order to circumvent this, researchers often use continuation approaches where e.g. the (SIMP) filter factor is increased from 1 to 3 in steps of 0.2, c.f. [2]. The increase in penalization factor is performed upon convergence or every say 100 iterations. Although this scheme probably can be tuned, e.g. by a recent constrained approach [3], total iteration counts are often reported to exceed a thousand.

To reduce the iteration count, the original optimization formulation (1) is appended with an extra constraint

$$
\begin{aligned}
\min_{\boldsymbol{\rho}} \quad &: \quad C(\boldsymbol{\rho}) \\
\text{s.t.} \quad &: \quad \mathbf{K}(\hat{\boldsymbol{\rho}}(\boldsymbol{\rho}))\mathbf{D} = \mathbf{F} \\
&: \quad V(\hat{\boldsymbol{\rho}}(\boldsymbol{\rho})) \leq V^* \\
&: \quad \frac{||\bar{\boldsymbol{\rho}}(\hat{\boldsymbol{\rho}}(\boldsymbol{\rho})) - \boldsymbol{\rho}_c||_p}{||\boldsymbol{\rho}_c||_p} \leq \epsilon, \qquad (V(\boldsymbol{\rho}_c) = V^*) \\
&: \quad \mathbf{0} \leq \boldsymbol{\rho} \leq \mathbf{1}
\end{aligned}
\tag{3}
$$

where $|| \cdot ||_p$ indicates p-norm, ϵ is a small number that sets the allowed error, $\bar{\boldsymbol{\rho}}$ is a smoothed version of the physical density field using a large filter radius R_{min} and $\boldsymbol{\rho}_c$ is an auxiliary smoothed density field with subscript c for "coarse" to make the association to multiscale approaches, although its meaning and function can be seen in several different perspectives. The basic requirement to the coarse field $\boldsymbol{\rho}_c$ is that it satisfies the volume constraint. If this is fulfilled and ϵ is small enough, this implies that the volume constraint on the physical density field (third line of (3)) is automatically satisfied. However, the volume constraint is maintained in the optimization problem since it tends to stabilize convergence and allows some freedom

---

*Email: sigmund@mek.dtu.dk
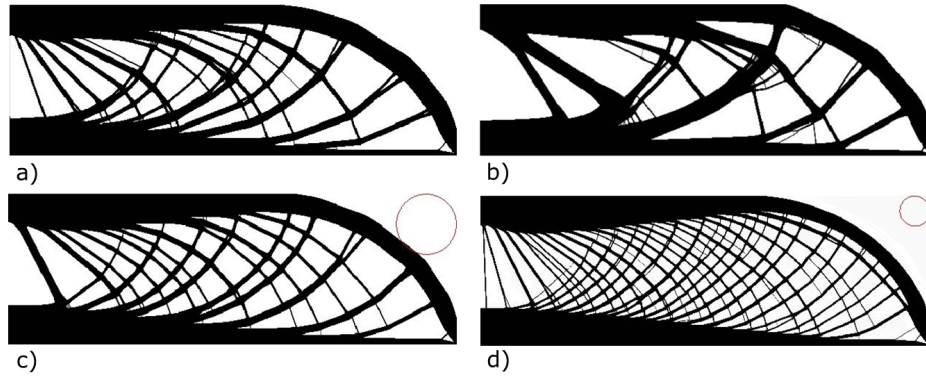
Figure 1: a) Optimized Michell-like half-cantilever structure based on continuation approach. b) Result without continuation. c) Result with proposed scheme and large coarse scale filter radius (radius indicated with circle). d) Result with proposed scheme and small coarse scale filter radius (radius indicated with circle) and finer mesh.

in selecting ϵ. The choice of coarse scale filter radius R_{min} for the $\bar{\boldsymbol{\rho}}$ constraint influences the distance between local features, i.e. it introduces a weakly enforced maximum length scale both on solid and on void regions of the optimized designs.

The added p-norm constraint in (3) effectively introduces a local smoothed density constraint everywhere in the design domain. Hence, choosing different properties of the coarse field $\boldsymbol{\rho}_c$ allows a range of interesting features and effects to be controlled. Here we discuss and apply a concept where $\boldsymbol{\rho}_c$ is obtained as the optimized solution from the variable thickness sheet problem. Here one first solves the convex $q = 1$ SIMP problem (i.e. the variable thickness sheet problem in 2d), possibly on a coarse mesh which afterwards can be smoothed and projected to the fine mesh. This added local density constraint hinders design features in agglomerating and hence ensures convergence to very detailed and highly optimal Michell-like solutions.

RESULTS

Preliminary results are presented in Fig. 1. Subfigure a) shows an optimized half beam obtained through the continuation approach using 1472 iterations. Subfigure b) shows the optimized half beam obtained without continuation approach after 273 iterations. Neither the visual resemblance to an analytical Michell structure nor a quantitative comparison to subfigure a) in terms of objective function speak in favour of subfigure b). Subfigures c) and d) are obtained using the following strategy: A) $\boldsymbol{\rho}_c$ is obtained from running (1) on a coarse mesh. B) Based on A), (3) is run with $q = 2$ and a minimum filter size of $r_{min} = 1.2$ times the element size, either up to 100 iterations or a certain measure of non-discreteness, whichever comes first. Then the added constraint is turned off. After 150 iterations the local filter is switched off and the optimization is continued up to a maximum of 200 iterations. This makes for a fair comparison of approaches and settings if the goal is to provide an efficient algorithm that can converge to excellent designs in less than 200 iterations. Clearly there may be settings that can speed up convergence even further. Usually, one would not remove the local filter entirely, however, it is necessary here in order not to penalize fine detail structures in terms of optimized compliance values. Fine featured structures have large perimeters and hence have more intermediate density elements than coarse scaled structures. The resulting designs in subfigures c) and d) are obtained using two different coarse scale filter sizes R_{min} as indicated with circles. Both visual comparison to the analytical Michell solution as well as objective function values compare favourably to those of subfigure a) that were obtained with the inefficient standard continuation approach.

References

[1] B. Lazarov and O. Sigmund. Filters in topology optimization as a solution to Helmholtz type differential equation. *International Journal for Numerical Methods in Engineering*, 86(6):765–781, 2011.

[2] O. Sigmund, N. Aage, and E. Andreassen. On the (non-)optimality of Michell structures. *Submitted*, 2016.

[3] S. Rojas-Labanda and M. Stolpe. Automatic penalty continuation in structural topology optimization. *Structural and Multidisciplinary Optimization*, 52(6):1205–1221, 2015.

TOPOLOGY OPTIMIZATION UNDER UNCERTAINTY VIA NON-INTRUSIVE POLYNOMIAL CHAOS EXPANSIONS

Daniel A. Tortorelli[*1] and Vahid Keshavarzzadeh[1]

[1]*Department of Mechanical Science and Engineering, University of Illinois at Urbana-Champaign, Urbana, Illinois, USA*

Summary This paper presents a systematic approach for topology optimization under uncertainty. The approach integrates an efficient non-intrusive polynomial chaos expansion with design sensitivities for reliability-based and robust topology optimization. Uncertainty is introduced in the loading and elemental densities to address the manufacturing variability. The manufacturing variability is represented via a random process with a Karhunen Loeve expansion on underlying uncertain parameters. To demonstrate the effect of uncertainty, the results of the optimization under uncertainty are compared with deterministic optimization results.

TOPOLOGY OPTIMIZATION UNDER UNCERTAINTY

The subject of topology optimization has received considerable attention in the past two decades [1]. A majority of these works assume deterministic material distribution parameters and boundary and load conditions in the optimization process. However, the performance of a structure varies due to the inherent uncertainty in these quantities. More recently researchers have developed robust and reliable designs by incorporating the effects of uncertainty into their optimization studies.

In robust design optimization (RDO) researchers minimize the effect of variations on their designs by including higher-order statistics such as variance in the cost and constraint functions. Typically, the statistical moments are obtained via a Monte Carlo approach which requires numerous realizations or a perturbation technique that uses Taylor expansions which requires the computation of higher-order sensitivities with respect to the random variables [2, 3]. Alternatively, in reliability based design optimization (RBDO) researchers constrain the probability of failure. The probability of failure is often approximated via First-Order Reliability Methods (FORM) or Second-Order Reliability Methods (SORM) [4, 5]. The FORM and SORM require the solution of a constrained optimization problem, and hence the RBDO requires the solution of a nested, i.e. two-level, optimization problem. It is evident that the Monte Carlo approach is computationally intractable particularly in conjunction with an optimization process for large scale problems. Moreover, while numerical techniques based on Taylor expansions are efficient, they may not yield enough accuracy when there is a significant variation in uncertain parameters.

POLYNOMIAL CHAOS BASED DESIGN OPTIMIZATION UNDER UNCERTAINTY

In the present study, we adopt a different perspective and pursue a methodology based on polynomial chaos expansion (PCE) for uncertainty propagation[6, 7]. PCE provides a systematic approach to characterize the random response and is an attractive approach due to its fast convergence property and its ability to provide a mapping between the random response and random model parameters.

The PCE greatly facilitates the calculation of statistical moments and their design sensitivities. And for this reason the majority of existing design optimization efforts that utilize PCE concentrate on RDO [8, 9]. Insofar as RBDO is concerned, the PCE can be used to evaluate the probability of failure by integrating the probability of the random variables over the failure region. Indeed, this integral is easily evaluated via Monte Carlo, but bear in mind that the realizations in this Monte Carlo computation are based on the PCE, and thus the computational burden is minimal. The probability of failure design sensitivity computation is another story however. It requires knowledge on the failure region's boundary, and more importantly, how the boundary varies as the design parameters vary. This information is not explicitly available and thus RBDO is problematic, even with PCE.

We provide a systematic framework for design optimization under uncertainty that addresses both RDO and RBDO via the PCE. Uncertainty is introduced in the loading and geometry to address the load and manufacturing variability. The geometry variability is represented via a random process with a truncated Karhunen Loeve expansion that maps the assumed low dimensional underlying uncertainty to correlated random variables in the random field. Accordingly, the PCE of quantities of interest such as volume and compliance are developed on the basis of the low dimensional underlying uncertainty.

We demonstrate the easily implemented non-intrusive PCE in the topology optimization of benchmark problems such as Messerschmitt-Blkow-Blohm (MBB) beam and cantilever beam. To show the significance of uncertainty, the response of designs which considered uncertainty are compared to those that do not, i.e. deterministic designs. Not surprisingly deterministic designs do not necessarily satisfy the probabilistic RDO and RBDO constraints.

---

*Corresponding author. Email: dtortore@illinois.edu

References

[1] Bendsoe MP, Sigmund O. Topology Optimization: Theory, Methods, and Applications Springer-Verlag Berlin Heidelberg. 2004;.

[2] Fu M. Optimization for Simulation: Theory vs. Practice. Informs Journal on Computing. 2002;14(3):192–215.

[3] Sundaresan S, Ishii K, Houser D. A Robust Optimization Procedure with Variations on Design Variables and Constraints. Engineering Optimization. 1995;24(2):101–117.

[4] Haldar A, Mahadevan S. Probability, Reliability, and Statistical Methods in Engineering Design. Wiley, New York. 2000;.

[5] Rackwitz R. Reliability analysisa review and some perspectives. Structural Safety. 2001;23(4):365–395.

[6] Ghanem R, Spanos P. Stochastic Finite Elements: A Spectral Approach. Dover publications. 2002;.

[7] Xiu D, Karniadakis GE. The Wiener–Askey Polynomial Chaos for Stochastic Differential Equations. SIAM Journal on Scientific Computing. 2002;24(2):619–644.

[8] Maute K, Weickum G, Eldred M. A reduced-order stochastic finite element approach for design optimization under uncertainty. Structural Safety. 2009;31(6):450 – 459.

[9] Tootkaboni M, Asadpoure A, Guest JK. Topology optimization of continuum structures under uncertainty A Polynomial Chaos approach. Computer Methods in Applied Mechanics and Engineering. 2012;201204(0):263 – 275.

TWO-SCALE TOPOLOGY OPTIMIZATION BASED ON MOVING MORPHABLE COMPONENTS (MMC)

Gengdong Cheng[1], Liang Xu[2a)]

[1]*State Key Laboratory of Structural Analysis for Industrial Equipment, Dalian University of Technology, Dalian, Liaoning, China*
[2]*Department of Engineering Mechanics, Dalian University of Technology, Dalian, Liaoning, China*

<u>*Summary*</u> This paper studies concurrent topology optimization with multi micro material design. Unlike traditional concurrent topology optimization presented by Liu et al. [1], where a uniform micro material is used, the macro structure in this research is composed of sub domains, each with a different micro material design. This gives more flexibility to industrial use and is more reasonable as materials in different domains may experience different stress states. In micro material design, in order to overcome the zig-zag boundaries and grey elements in SIMP interpolation scheme, the Moving Morphable Component (MMC) approach is used to get a clear and smooth topology in favour of manufacturing applications, like the 3-D printing techniques. A numerical example is given to show the validity of this method. Issues of manufacturability related to 3-D printing techniques are discussed.

INTRODUCTION

Structures with periodic porous material are widely used in engineering applications due to their high specific stiffness, strength and other good performances. In the design of this kind of structures, two-scale concurrent topology optimization is an effective approach. However, there are still some disadvantages of this approach. First, the macro structure is assumed to be composed of a uniform micro material, whereas, in practical applications, micro materials in different areas of the structure may be subject to different stress states, which makes a uniform micro material design not efficient. The second disadvantage is due to the limitation of SIMP interpolation scheme in the micro material design. With the development of 3-D printing technique, porous material with complex geometric micro-structures could be made in industrial applications. However, optimal micro materials with SIMP method may suffer from zig-zag boundaries and grey elements, which make 3-D printing of these materials difficult to implement. In order to overcome this problem, we try the Moving Morphable Component approach, the distinctive feature of which is that a set of morphable components are used as building blocks of topology optimization and the optimal topology is found by optimizing sizes and layout of these components, to obtain a smooth and clear boundary of micro materials in favour of manufacturing perspectives.

In this paper, we consider plane stress continuum with a number of sub domains and each domain is assigned a micro material. The MMC approach is used in the micro scale design to get a clear topology of the micro material.

PROBLEM FORMUILATION AND A NUMERICAL EXAMPLE

Consider a periodic porous structure subject to plane stress in Figure 1(a), where the design domain Ω of the porous structure is divided into s sub domains, denoted as Ω_1, Ω_2 ,……, Ω_S respectively. Each sub domain composed of porous material with different micro structure is homogenized as an equivalent anisotropic continuum in the macro scale. The effective modulus matrix of the equivalent anisotropic continuum is assumed as $\mathbf{D}^{H1}$, $\mathbf{D}^{H2}$,……,$\mathbf{D}^{HS}$ for sub domains Ω_1, Ω_2 ,……, Ω_s respectively.

For topology optimization of macro structure, the design domain Ω is meshed into *N* finite elements. An artificial density is assigned to each element P_i, which is the design variable in macro-scale structural topology optimization. The modulus matrix of *i*th macro element with density P_i is expressed in the PAMP approach, which is the abbreviation for Porous Anisotropic Material with Penalty [1]:

$$P_i^{MA} = P_i^3 \mathbf{D}^H \ \left(i = 1, 2, \cdots, N \right) \tag{1}$$

Where $\mathbf{D}^H$ could be $\mathbf{D}^{H1}$, $\mathbf{D}^{H2}$,……,$\mathbf{D}^{HS}$ depending on which sub domain *i*th element belongs to.
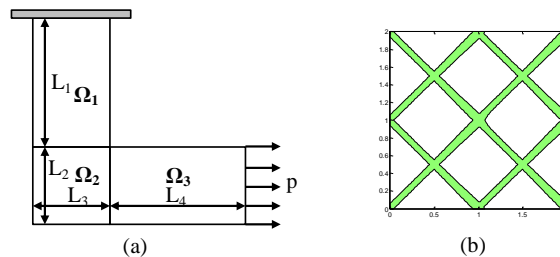
Figure1. (a). A periodic porous structure subject to plane stress; (b). Initial micro design

[a)] Corresponding author. Email: xuliangdagong@163.com.

With MMC approach, the unit cell of micro material is composed of n components and each component has a number of design parameters. The effective property $\mathbf{D}^H$ is calculated by the asymptotic homogenization through MMC approach and the ersatz material model. Thus, $\mathbf{D}^H$ is a function of parameters of components in the unit cell of the micro material, denoted as $\omega_1, \omega_2, \ldots, \omega_S$ respectively. For the example shown in Fig.1, sub domain Ω_1 has components 1 to n, sub domain Ω_2 $n+1$ to $2n$ and sub domain Ω_3 $2n+1$ to $3n$. The design variable of jth component is written as

$$\mathbf{D}^j = \begin{bmatrix} x_0 & y_0 & L & t_1 & t_2 & t_3 & \sin\theta \end{bmatrix}^T \ (j = 1, 2, \cdots, 3n) \tag{2}$$

The design variables of the two scale optimization problem should be

$$\mathbf{d} = \left\{ P_1, P_2, \cdots, P_N, \left(\mathbf{D}^1 \right)^T, \left(\mathbf{D}^2 \right)^T, \cdots, \left(\mathbf{D}^{3n} \right)^T \right\}^T \tag{3}$$

The optimization problem is to minimize the compliance subject to volume constraints on both the macro beam and micro material. The optimization problem can be written as

$$\begin{aligned}
&\text{find} \quad \mathbf{d} \\
&\text{minimize} \quad C = \mathbf{F}^T \mathbf{U} \\
&s.t. \quad \mathbf{K}(\mathbf{d}) = \mathbf{F} \\
&\frac{\sum_{i=1}^{N} P_i V_i}{\sum_{i=1}^{N} V_i} \le \bar{V}, \frac{\int_{\omega_1} H\left(\phi^s(\mathbf{D})\right)dV}{\int_{\omega_1} dV} \le \bar{v}_1, \frac{\int_{\omega_2} H\left(\phi^s(\mathbf{D})\right)dV}{\int_{\omega_2} dV} \le \bar{v}_1, \frac{\int_{\omega_3} H\left(\phi^s(\mathbf{D})\right)dV}{\int_{\omega_3} dV} \le \bar{v}_3
\end{aligned} \tag{4}$$

Where $\bar{V}, \bar{v}_1, \bar{v}_2, \bar{v}_3$ denote prescribed volume fraction for macro beam, micro material ω_1, ω_2 and ω_3 respectively.

For the example structure in Fig.1, the size parameters of the L-shaped beam are $L_1=2$, $L_2=1$, $L_3=1$ and $L_4=2$. The beam is discretized with 4-node plane stress element of size 0.1×0.1 and into $N=500$ elements. The distributed force of the macro beam is p=1. The three units in micro materials scale are of size 2×2 and discretized into 400 elements. The properties of the base material are E=10, ν=0.3.

The prescribed volume fractions for both macro beam and micro materials are 50%. The initial design of the macro plate is uniform and the initial design of the micro material is $n=8$ components for each sub domain, as plotted in Figure 1(b). During optimization, the calculation of effective property $\mathbf{D}^H$, the macro beam analysis, and sensitivities is done in Matlab through proper modification of 188-line MMC Matlab code in Zhang et al. 2016 [2]. The MMA optimizer is used.

The optimal topologies are plotted in Figure 2 with minimum compliance C=4.19.

| macro beam | micro material in Ω_1 | micro material in Ω_2 | micro material in Ω_3 |
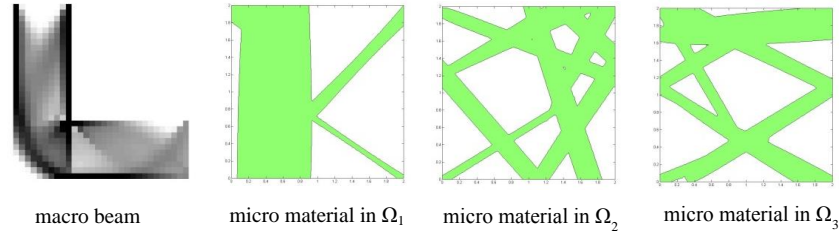
Figure 2. Optimal topologies

CONCLUSIONS

In this paper, a two-scale concurrent optimization is carried out. The macro design domain is divided into three sub domains where micro materials differ from each other. This gives more design flexibility than the traditional concurrent optimization procedure as different parts of the macro structure are subject to different stress state. A trial application of the MMC approach to the micro scale design is given, which achieves smooth boundaries of micro materials, and is more appealing to manufacturing applications. There are also some minor problems with this method. For example, some oscillation may occur during optimization process and the iteration number needed to converge is comparatively large, which will be amended in our future work.

References

[1] Liu L, Yan J, Cheng GD. Optimum Strucutre with Homogeneous Optimum Truss-like Material. Comput Struct 86(13-14): 1417-1425,2008.

[2] Zhang WS, Yuan J, Zhang J, Guo X. A New Topology Optimization Approach Based On Moving Morphable Components (MMC) and the Ersatz Material Model. Struct Multidisc Optim 2016(accepted).

TOPOLOGY OPTIMIZATION AND DESIGN OF SOLID PARTICLES IN SUSPENSION

André Bénard[1], Tong Gao[1,2], & Alejandro R. Dìaz[1]
[1]Department of Mechanical Engineering, East Lansing, Michigan, USA
[2]Department of Computational Mathematics, Science, and Engineering, East Lansing, MI, USA

Summary A methodology for the design of solid particles in suspension is presented as an extension of the material design problem in topology optimization. The tensor describing the interactions of the particles with the surrounding fluid is provided as a target and shapes of particles matching this mobility tensor are identified. The theoretical framework describing the motion of single and ensemble of particles is introduced and discussed in the context of its application to topology optimization.

INTRODUCTION

Nanoparticles and colloids with exotic shapes and functionality are engineered today at the nanometer and micrometer scales and can exhibit interesting flow-induced patterns and result in unusual assembled systems [1,2]. Novel synthesis and fabrication techniques allow the production of particles with various degrees of asymmetry, and a wide range of shapes (fibers, rings, cubes, prisms), and anisotropic interactions. Such shapes include "nano-acorns", "nano-centipedes", "nano-guitars", "nano-squids" and "nano-whiskers" [1]. It is now clear that the shape of particles plays a crucial role, especially at the small scale, in determining many of the interesting physical properties observed. In this work a framework for the design of particles based on topology optimization is presented to identify possible particle shapes allowing the realization of desired orientation states. The design problem is posed as a material distribution problem as in [3,4,5] in which the goal is to find an actual distribution of a material in the fluid that matches the prescribed mobility or fluid interaction tensor for a desired orientation state. The proposed approach is outlined below, beginning with an overview of suspension hydrodynamics.

SINGLE PARTICLE DYNAMICS

The dynamics of neutrally buoyant, rigid ellipsoidal particles in Newtonian fluid flow was first studied theoretically by Jeffrey [6] and he showed that the time-rate-change of the unit vector $\mathbf{p}$ parallel to particle' symmetry-axis can be expressed as $\dot{\mathbf{p}} = \mathbf{W} \cdot \mathbf{p} + \left(\lambda_e^2 - 1\right) / \left(\lambda_e^2 + 1\right)\left(\mathbf{E} \cdot \mathbf{p} - \mathbf{E} : \mathbf{ppp}\right)$. $\mathbf{E}$ and $\mathbf{W}$ are the symmetric and asymmetric components of the velocity gradient. The scalar parameter λ_e represents the fiber-fluid coupling coefficient for particles with certain axisymmetric shapes. This theory has been generalized by Bretherton [7] where a third rank tensor $\mathbf{B}$ is employed to describe the coupling between the shape of a particle and its rate of rotation. For a single particle of arbitrary shape, a formulation based on a "grand resistance matrix" is sometimes employed, which relates exerted force ($\mathbf{F}$), torque ($\mathbf{L}$) and stresslet ($\mathbf{S}$) to particle motion and which can be expressed as

$$\begin{pmatrix} \mathbf{F} \\ \mathbf{L} \\ \mathbf{S} \end{pmatrix} = \begin{pmatrix} \mathbf{X} & \mathbf{P} & \mathbb{Q} \\ \mathbf{P}' & \mathbf{Y} & \mathbb{R} \\ \mathbb{Q}' & \mathbb{R}' & \mathbb{Z} \end{pmatrix} \begin{pmatrix} \mathbf{u} \text{-} \mathbf{U} \\ \boldsymbol{\omega} \text{-} \boldsymbol{\Omega} \\ \mathbf{E} \end{pmatrix} \tag{1}$$

where $\mathbf{X}, \mathbf{Y}, \mathbf{P}$ are second order tensors while $\mathbb{Q}, \mathbb{R}, \mathbb{Z}$ are third order tensors. $\mathbf{B}$ can be solved for a force-free particle as $\mathbb{B} = -2\left(\mathbf{Y} - \mathbf{P}' \cdot \mathbf{X}^{-1} \cdot \mathbf{P}\right)^{-1} \cdot \left(\mathbb{R} - \mathbf{P}' \cdot \mathbf{X}^{-1} \cdot \mathbb{Q}\right)$. Simple cases for which all entries of the tensors are known include ellipsoids and various special cases e.g. the sphere. Such cases can be used for validation purposes. In addition, Bretherton [7] proposed a configuration of arrays of ellipsoids connected with a sphere, which won't tumble but only migrate in the shear flow. Figure 1 below shows a possible candidate of a complex particle. This particle design greatly reduces the particle-particle interaction and facilitates particle aggregation and alignment. If such shapes could be produced and aerosolized, they could deliver, for example, a much larger amount of drugs deep in the lungs when compared to a spherical particle with similar frontal area (a fibrous particles would rotate, thus increasing its propensity at being captured by a sticky surface).

---

a) Corresponding author. Email: diaz@egr.msu.edu
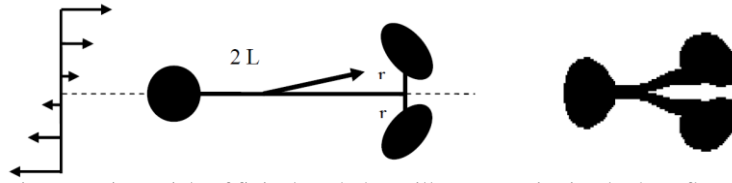
Figure 1. Illustration of a non-axisymmetric particle of finite length that will not rotate in simple shear flow but will migrate laterally toward a center of a channel (adapted from [4]).

ENSEMBLE OF PARTICLES

The flow-induced alignment of ensemble of particles can be described by an orientation distribution function. For rod-like particles it satisfies the following continuity equation in orientation space [8]:

$$\frac{D\Psi}{Dt} = -\nabla_{\mathbf{p}} \cdot \left(\dot{\mathbf{p}} \Psi \right) \tag{2}$$

In the above, $\dot{\mathbf{p}}$ represents the angular velocity of a particle. $D\Psi / Dt$ is the material derivative of the orientation distribution function. The differential operator $\nabla_{\mathbf{p}}$ is defined as $(\mathbf{I} - \mathbf{pp}) \cdot \nabla$ on a surface of a unit sphere. The microstructure of spheroidal suspension is characterized by the second and fourth moments of Ψ :

$$< \mathbf{pp} > = \int_0^{2\pi} \int_0^{\pi} \mathbf{pp} \Psi \sin\theta d\theta d\varphi, \quad < \mathbf{pppp} > = \int_0^{2\pi} \int_0^{\pi} \mathbf{pppp} \Psi \sin\theta d\theta d\varphi , \tag{3}$$

where $\Psi(\mathbf{x}, \mathbf{p}, t) \sin\theta d\theta d\varphi$ represents the fraction of particles with orientation vectors between $\mathbf{p}$ and $\mathbf{p} + \delta\mathbf{p}$. The well-known evolution equation for the second moment $< \mathbf{pp} >$ must be solved to identify the orientation states for a given flow field [8]. The theory has been extend by our group based on a formulation introduced by Rallison [9] involving a rotation tensor $\mathbf{R}$ which include all three Euler angles.

PARTICLE DESIGN PROBLEM

In the material design problem as described in [3,4,5], a target tensor is given and the goal is to find the vector of design variables that result in an effective tensor that matches the target as closely as possible. The problem can be cast as an optimization problem where a prescribed amount of material is provided and the weighted mean square deviation from the target tensor is minimized. The same approach is employed here. We first estimate the shape tensor $\mathbb{B}$ that characterizes the hydrodynamic interactions. The problem is formulated as in [10] for estimating the relevant entries of the mobility tensor of a specific realization. For simple cases where the steady-state solutions of the orientation tensor can be achieved, it is straightforward to solve $\mathbb{B}$ directly by setting the equations to a steady state. For simplicity the rotational diffusion is assumed small, i.e., $D_R \approx 0$, and the concentration of particles Φ are approximately uniform.

SUMMARY AND CONCLUSION

Preliminary work on a methodology for the design of particles is introduced in the work that allows to identify shapes of particles with desired motion. The problem can be cast as a material design problem. Extension of this work is possible for large ensemble of interacting particles in which the target would be specific rheological properties.

References
[1] Glotzer, S.C. and Solomon, M.J., "Anisotropy of building blocks and their assembly into complex structures", Nature Materials, 6 (8), 557-562, 2007.
[2] Bricard, A., Caussin, J.B., Desreumaux, N., Dauchot, O., Bartolo,D. "Emergence of macroscopic directed motion in populations of motile colloids". Nature **503**, 95–98, 2013.
[3] Bendsøe, M.P. and Sigmund, O. *Topology Optimization-Theory, Methods and Applications*. Berlin: Springer, 2003.
[4] Sigmund, O. "Tailoring materials with prescribed constitutive parameters." Mechanics of Materials, 20: 351-368, 1995.
[5] Diaz, A.R. and Benard, A., "Designing materials with prescribed elastic properties using polygonal cells," Int. J. Numer. Meth. in Engng, 57: 301-314, 2003.
[6] Jeffrey, G.B., "The Motion of Ellipsoidal Particles Immersed in Viscous Fluid", *Proc. R. Soc. Lond. A*, **102**, 161-179, 1922.
[7] Bretherton, F. P., "The Motion of Rigid Particles in a Shear Flow at Low Reynolds Number", *J. Fluid Mech.*, **14**,284-304, 1962.
[8] Doi, M. and Edwards, S.F. *Theory of Polymer Dynamics*, Oxford University Press, 1986.
[9] Rallison, J.M., "The Effects of Brownian Rotations in Dilute Suspension of Rigid Particles of Arbitrary Shape", J. of Fluid Mechanics, V. 84, pp. 237-263, 1978.
[10] Borrvall, T. and Petersson, J. (2003 January). Topology optimization of fluids in stokes flow, *International Journal for Numerical Methods in Fluids*: 41,77-107.

OPTIMAL MULTIMATERIAL COMPOSITE STRUCTURES AND OPTIMAL DESIGNS

Andrej Cherkaev [*1] and Gzegorz Dzierżanowski[2]

[1]*Department of Mathematics, University of Utah, Salt Lake City, Utah, U.S.A.*
[2]*Department of Structural Mechanics and Computer Aided Engineering, Politechnika Warszawska, Warsaw, Poland*

Summary Technological capabilities, such are 3d printing and microfabrication, allow a huge variety of structures to be manufactured for roughly the same price, and one wants to know "the best" structure, or how composite microstructures can be optimized. There is no gap between optimal designs and the optimal composites that are structures at at the micro level. So far, the vast majority of related results deals with two-material composites because of theoretical limitations. Meanwhile, numerous applications call for the optimal design of multimaterial composites, or of porous composites made of two materials and void. The paper describes various structures of optimal multi-material composites, the bounds of their effective properties that are achievable by these structures, and optimal designs from several materials. We show designs from two elastic materials and void.

BOUNDS AND OPTIMAL MULTIMATERIAL STRUCTURES

The bounds show the range of improvement that can be achieved for overall composite properties by varying the structure. In particular, we study the bounds of the stored energy, find the exact bounds and the set of matching structures, and use these structures to compose an optimal design. In the past few years (2009-2012), [2, 3, 4, 5] a new approach for optimal bounds of multimaterial mixtures was suggested and tested on several examples. Calculating the lower bound, we also determine sufficient conditions on the fields in materials (wells) in an optimal structure [1, 8, 2]. The bound also provides a hint for optimal structures such as high-rank laminates [1, 8], wheel-type structures [4], or other structures.

Optimal microstructures of multimaterial composites differ drastically from two-material ones. The latter have a steady and intuitively expected topology: a strong material always surrounds weak inclusions, as in Hashin-Shtrikman coated circles and second-rank laminates. In contrast, optimal three-material structures [3, 5, 4], see Figure 1 show a large variety of patterns and the optimal topology depends on the volume fractions.

Optimal structures are diverse; they may or may not contain a strong envelope, and they may contain "hubs" of intermediate material connected by anisotropic "pathways" - laminates from the strong and weak materials, envelopes, and other configurations that reveal a geometrical essence of optimality. The parameters of the A-E of the optimal structures (Figure 1) depend on the volume fractions and the ratio of eigenvalues of the applied external stress σ_0. It is observed that the strongest material is always placed in the most stressed parts, the field in the intermediate material stays isotropic if passible and in the strongest material it is anisotropic.

Testing optimal structures, we stay in the class of structures with explicitly computable effective properties. These structures are obtained by hierarchical modeling, and they are interesting objects for study. These structures may or may not be optimal, but they all provide convenient and realistic models for the various sophisticated geometries; acting like LEGO pieces that are used in the process of modeling to create metamaterial hybrids between composites and machanisms.
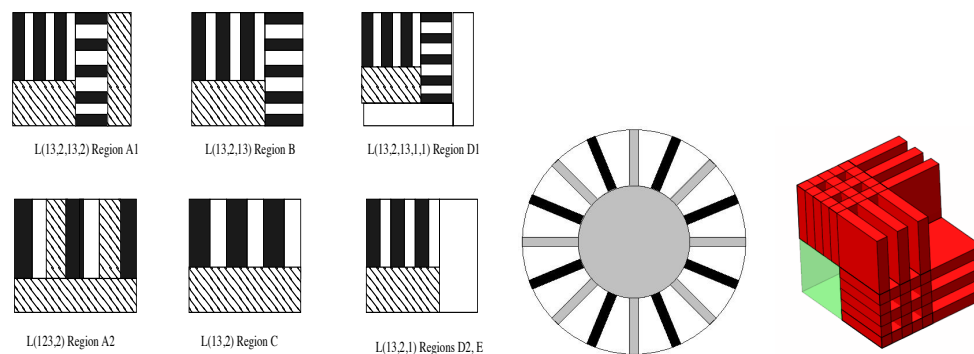
Figure 1: *Left*: Cartoon of optimal multi-rank laminates that minimize elastic energy (compliance) of a three-material composite [3, 5]. Black fields denote void (an infinite compliance), striped fields denote a material of intermediate compliance and white fields denote the stiffest material. *Center*: The wheel assemblage resembles the Hashin?Sthrikman coated spheres. *Right*: The cuboudal structure in a 3d development of Gibiansky-Sigmund 2d structure [7].

*Corresponding author. Email: cherk@math.utah.edu

OPTIMAL DESIGN

The most popular problem in structural optimization today, called "topology optimization", is a problem of optimal layout of a material and void. The optimal structural designs are commonly known as "black-and-white" or "grey" designs. Optimal multilateral composites allow us to instead deal with with "multi-colored" designs, see Figure .
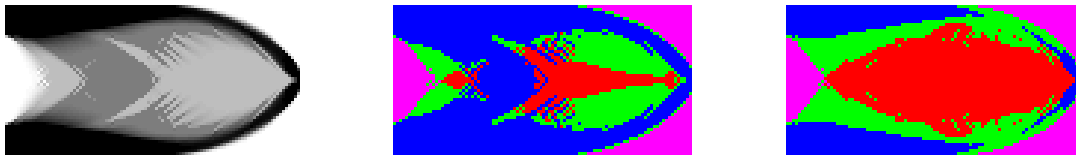
The first obtained optimal designs from three materials are shown in Figure The designs are made from an expensive strong material, a cheap weak material, and void. This design shows that the strong material tends to form elongated beam-like ligaments at the contour of the design, the weaker material is concentrated in the areas where the stress is moderate and close to isotropy.

CONCLUSIONS

1. Investigation of the range of fields in optimal multimaterial structures will allow for prediction of their microstructues and for for computing of optimal design from several materials. The presented examples prove that the problem can be solved.

2. The optimal structures are in fact fractal minimizing sequences of alternating materials. To make the theory usable for practitioners, these structures need to be transformed to a coarse scale designs for suboptimal projects.

References

[1] A. Cherkaev. Variational methods for structural optimization. Springer Verlag NY 2000.

[2] A. Cherkaev. 2009. . Mechanics of Materials 41, 411-433.

[3] A. Cherkaev and Y. Zhang. 2011. . Int. J, of Solids and Structures 48 (20), pp. 2800-2813.

[4] A. Cherkaev. 2012. Int. J. of Eng. Science, 59, 27-39.

[5] A. Cherkaev and G. Dzierżanowski 2013. Int. J. of Solids and Structures, 50, pp. 4145-4160.

[6] A. Cherkaev. 2014. Int. J of Eng. Sc., 83, 162-173.

[7] L. V. Gibiansky, O. Sigmund 2000. JMPS, 48, 3, 461-498.

[8] G. W. Milton 2001. The Theory of Composites. Cambridge University Press.

TOPOLOGY OPTIMIZATION IN NANO-SCALE
FOR GENERATION OF NEW GRAPHENE-LIKE MATERIALS

Tadeusz Burczyński[1a], Wacław Kuś[2] and Adam Mrozek[3]

[1]Institute of Fundamental Technological Research, Polish Academy of Sciences, Warsaw, Poland
[2]Institute of Computational Mechanics and Engineering, University of Technology, Gliwice, Poland
[3]AGH University of Science and Technology, Cracow, Poland

Summary. The paper describes an application of a hybrid algorithm to optimal searching for new, stable atomic arrangements of two-dimensional graphene-like carbon lattices. The proposed approach combines the parallel evolutionary algorithm and the conjugated-gradient optimization technique. The main goal of the topology optimization is to find stable arrangements of carbon atoms under certain imposed conditions such as density, shape and size of the unit cell. The objective function is formulated as the total potential energy of an atomic carbon system. The optimized structure is considered as a discrete atomic model and interactions between atoms are modeled using the AIREBO potential, especially developed for carbon and hydrocarbon materials. The parallel approach used in computations allows significant reduction of computation time. Validation of the obtained results and examples of the models of the new grapheme-like materials are presented.

INTRODUCTION

Carbon atoms form various types of bondings and spatial configurations. This ability is determined by the atoms' hybridization states, which depend on their particular electronic configuration. This phenomenon is responsible for the existence of many different allotropes of the carbon. This is due to unique electronic, thermal and mechanical properties of such structures. Additionally, 2D graphene-like materials can be used to create another, more complex class of nanostructures, such as nanotubes. Graphene-like materials can be classified as periodic, flat atomic networks, made of stable configurations of carbon atoms in certain hybridization states. Since the stable configurations of atoms correspond to the global minima on the Potential Energy Surface (PES), such a task can be considered as a special topology optimization problem in which optimal material layout is searched on the nano-scale. However, the number of local minima increases almost exponentially with the number of atoms in the considered structure, thus searching for the global minimum on a PES became a non-trivial, NP-hard problem.

HYBRID EVOLUTIONARY-GRADIENT OPTIMIZATION METHOD

The hybrid algorithm, proposed and presented in this work, combines the parallel **E**volutionary **A**lgorithm (EA) prepared by the authors, and the classical **C**onjugated-**G**radient (CG) minimization of the total potential energy of the optimized atomic system. Since the processed structure is considered as a discrete atomic model, the behavior and the potential energy of carbon atoms are determined using the **A**daptive **I**ntermolecular **R**eactive **E**mpirical **B**ond **O**rder (AIREBO) potential developed for molecular dynamics simulations of hydrocarbons [2].
Chromosomes represent design variables in the form of real-valued Cartesian coordinates of each atom in the considered unit cell of the newly created atomic lattice. Each chromosome represents a certain spatial arrangement of atoms. In the initial population, atoms have randomly generated coordinates and are placed in the area of the unit cell with periodic boundaries. Dimensions, the rectangular or triclinic type of the unit cell, as well as the number of atoms, are part of a set of parameters of the simulation. Such an approach allows to control the value of atomic density of the newly-created structure. The periodicity of the atomic structure significantly reduces the number of design variables.
The fitness function is formulated as the total potential energy of the considered atomic system, i.e., the total sum of all potential energies of particular atomic interactions. The AIREBO potential in the following form is used in computation:

$$FF = \sum_{i} \sum_{j \neq i} \left(E_{ij}^{REBO} + E_{ij}^{LJ} + \sum_{k \neq i,j} \sum_{l \neq i,j,k} E_{kijl}^{TORSION} \right) \tag{1}$$

where: E^{REBO} corresponds to the short range interactions between covalently bonded pair of atoms, E^{LJ} is responsible for the long range interactions and is computed in a simplified way, using the Lennard-Jones-like function with additional distance-dependent switching functions and $E^{TORSIONAL}$ is torsional potential which depends on the neighboring atom's dihedral angles.
In order to avoid the situation when distances between atoms are very small, the initial and offspring populations have to be equilibrated, i.e., the potential energy has to be minimized by correction of the positions of atoms. The CG algorithm is used for this purpose. This routine is invoked in each iteration of EA for all individuals in the processed population and

---

[a] Corresponding author. Email: tburczynski@ippt.pan.pl
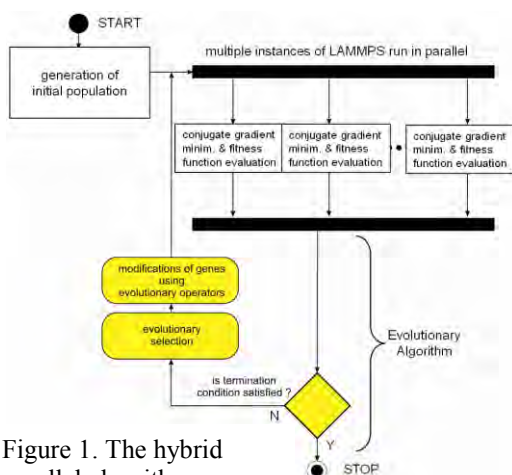
Figure 1. The hybrid parallel algorithm

temporarily pushes solutions into the local minima. Such an approach assists in forming of the new, real carbon-based molecular structure, i.e., during the CG minimization, each individual – a certain spatial configuration of atoms, starts to form a unique, hybridization-dependent, geometry of flat carbon networks. This step ensures that EA does not process the sets of randomly placed atoms, but operates on fragments of properly bonded carbon structures. Additionally, this method ensures that the optimized structure of atoms is properly equilibrated. The coordinates of atoms are exchanged between EA and the LAMMPS software and the equilibration process is performed using the minimization method based on the Polak-Ribiere algorithm. The periodicity of the newly-created structure is also achieved in this step by proper boundary conditions, imposed on the unit cell. After the CG minimization of the potential energy, the objective function is computed for each individual in the population. The CG optimization is the most time-consuming part of the algorithm. To overcome this problem, the authors decided to parallelize the proposed algorithm and make it suitable for running on multiprocessor computers. Thus, the population is scattered into certain number of parts using the MPI library. In the next step, each part is further processed in the parallel way using the dedicated instance of LAMMPS running on a separate core or node of the computer (Figure 1).

VALIDATION AND RESULTS FOR KNOWN GRAPHENE-LIKE MATERIALS

In order to validate the accuracy of the results, certain arrangements of carbon atoms already known from literature have been examined, e.g. the supergraphene (triclinic unit cell containing 8 carbon atoms) and the graphyne (triclinic unit cell containing 12 carbon atoms). Since all the tests yield promising results, the proposed optimization algorithm has been applied to search for new stable configurations of a given number of carbon atoms in a unit cell of given size and periodic boundaries [1]. For eight carbon atoms placed in the 4 Å ×7 Å rectangular unit cell obtained a stable   flat network named X (Figure 2A) and for the same number of carbon atoms placed in the rectangular unit cell 4 Å ×6 Å obtained a stable flat network named Y (Figure 2B).

A)

B)
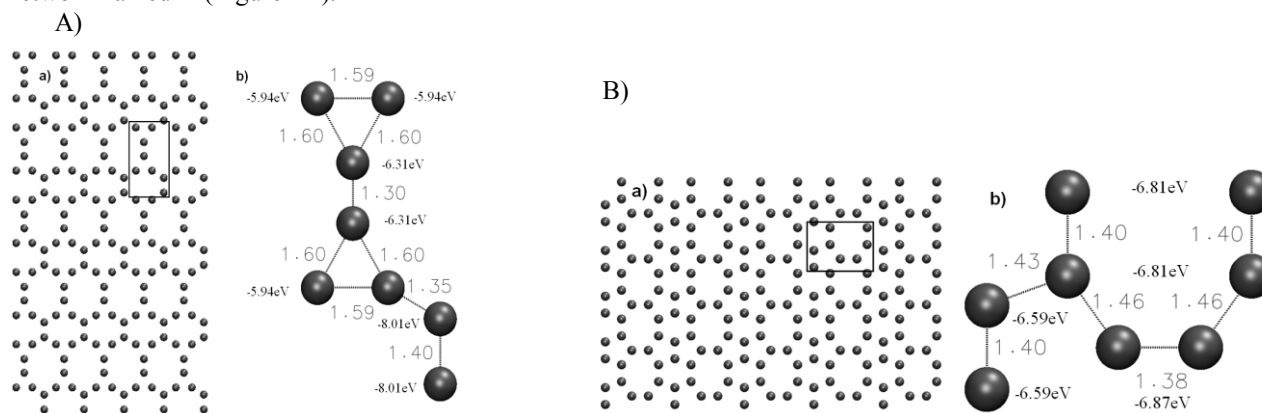
Figure 2. Layout of new stable carbon networks X (A) and Y (B) found by the hybrid algorithm

CONCLUSIONS

The main purpose of this paper was to present the hybrid parallel algorithm, applied to searching for new 2D graphene-like materials. The proposed method is able to find already-known structures like supergraphene and graphyne as well as new stable ones, named X and Y. Examples performed for new carbon networks clearly show that the final form and properties of optimized structures depend on the assumed size, type and atomic density of the unit cell. Thus, the considered topology optimization problem can be reformulated and applied to searching for a molecular structure with predefined material properties, not only in the case of carbon-based structures.

References

[1] Mrozek A., Kuś W., Burczyński T.: Nano level optimization of graphene allotropes by means of hybrid parallel evolutionary algorithm, *Computer Material Science* **106**: 161-1, 2015.

[2] Stuart S.J., Tutein J.A., Harsison A.: A reactive potential for hydracarbons with intermolecular interactions. *J. Chemical Physics* **112**: 6472-6486, 2000.

ON TOPOLOGY OPTIMIZATION OF INERTIA DRIVEN DOSING UNITS

Casper Schousboe Andreasen[1]

[1]*Department of Mechanical Engineering, Section for Solid Mechanics, Technical University of Denmark*

Summary This paper describes how topology optimization can be used to design inertia driven dosing units for the continuous dosage of one fluid into another. These components often referred to as eductors, utilize the low static pressure in a venturi-type nozzle to drive the dosing flow. The fluids are modeled using the steady state incompressible Navier-Stokes equations and the two fluids are considered having the same properties. A Brinkman penalization term is added to the governing equations such that a control problem of the flow topology is obtained. Optimized component geometries for a range of flow conditions are obtained efficiently by using a gradient based numerical optimization scheme in order to investigate the performance limit.

INTRODUCTION

The engineering problem of continuous dosage of one fluid into another has multiple solutions. One easy, but also expensive solution is to use a pump for each fluid and by means of adjusting the flow rate ensure a proper dosage. A more elegant solution is one where a single pump is driving the primary fluid and the secondary fluid is dosed by elaborating on the *venturi principle*. Figure 1 show a sketch of such a unit where the primary inflow is the one driven by the pump. Assuming that the fluid is inviscid and following the Bernoulli principle the dynamic pressure is increasing as the valve contracts and the static pressure is therefore decreasing. The low static pressure at the throat (minimum cross sectional area of the nozzle) will allow fluid to enter through the secondary inlet and mix with the primary fluid and eventually leave at the outlet. The principle is well known and has been used for e.g. ground water pumps, spray paint guns and firefighting foam proportioners.
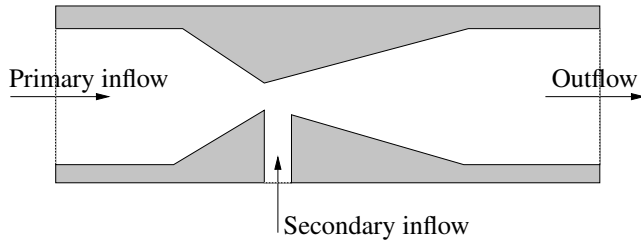
Figure 1: Sketch of an eductor, an inertia driven dosing unit. Left boundary is primary inflow. Right boundary is outlet. The secondary dosed fluid enters from the lower port and is driven by the lower static pressure right after nozzle.
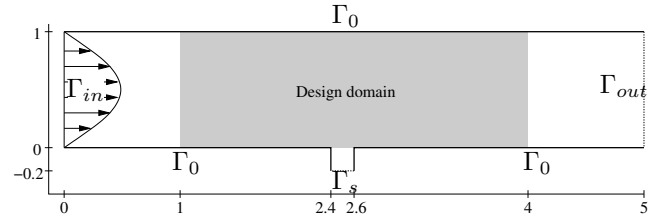
Figure 2: Physical conditions for the optimization problem. Left boundary (Γ_{in}) is a fully developed laminar profile with mean flow rate U. Right boundary (Γ_{out}) is modeled as stress free outlet with $p = 0$. Secondary flow port (Γ_s) has a stress free condition. The remaining thick solid line boundaries (Γ_0) have no-slip condition.

The optimization of such devices, primarily operating at high speed conditions, has previously been studied in the context of shape optimization c.f. [1]. This paper investigates the performance limit at low to moderate flow speeds for such devices by applying topology optimization to the design of the nozzle geometry. The method used in this paper relies on the work published in the seminal paper on topology optimization in Stokes flow[2] and the extension to Navier-Stokes flow[3]. The design problem is shown in Figure 2 where the gray design domain is subject to change controlled by the gradient based optimization algorithm MMA[4]. The objective of the optimization is to maximize the amount of incoming secondary fluid in order to investigate the upper limit for such devices.

Modeling

The flow is modeled by the steady-state incompressible Navier-Stokes equations with an additional Brinkman penalization term yielding

$$-\nabla \cdot (\mu(\nabla \mathbf{u} + (\nabla \mathbf{u})^T) - \mathbf{I}p) + \mathbf{u} \cdot \rho \nabla \mathbf{u} + \alpha(\xi)\mathbf{u} = 0 \tag{1}$$

$$\nabla \cdot \mathbf{u} = 0 \tag{2}$$

where $\mathbf{u}$ is the velocity, p the pressure, μ the dynamic viscosity and ρ the mass density. The α parameter (inverse permeability) is interpolated using the scheme from [2]

$$\alpha(\xi_i) = \overline{\alpha} + (\underline{\alpha} - \overline{\alpha})\xi_i \frac{1+q}{\xi_i + q} \tag{3}$$
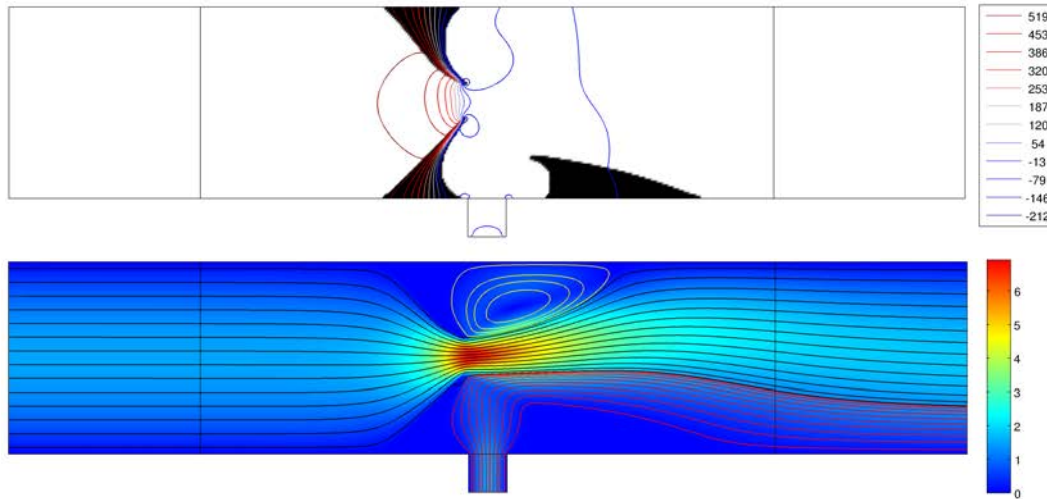
Figure 3: Optimized flow geometry for $Re = 20$ and $\gamma = 10$. Upper: Component design with pressure contours (outlet is $p = 0$). Lower: Flow speed, inflow has mean speed 1, and streamlines seeded at the inlet port (black), secondary port (red) and the recirculation opposite the secondary port (yellow). Mesh has a uniform element size with 100×300 elements in the design domain.

which is dependent on the spatial design field $\xi \in [0; 1]$ where 0 represents solid material (black) and 1 represents fluid (white). The inverse permeability is limited by $(\underline{\alpha}, \overline{\alpha}) = (0, 10^6)$ and the parameter q determines the non-linearity of the interpolation.

The gradients needed for the optimization procedure is obtained using the adjoint method that for this problem is a linear problem of the same size as the original, thus much less computationally demanding. The numerical solution is obtained by discretizing the problem using stabilized finite elements. The implementation is done in a framework of Comsol Mutiphysics used for the modeling and Matlab for the optimization.

RESULTS

The optimized designs depend on the operating conditions. In order to compare the results the Reynolds number is introduced as $Re = \frac{\rho U H}{\mu}$, where U mean flow rate and H is the channel height. The design also depends on the allowed pressure drop over the component why this is unified in terms of relative pressure drop over the component (primary inlet to outlet) in comparison to an empty channel i.e. $\gamma = \Delta p / \Delta p_{empty}$. The study investigates the performance limit and resulting component designs for flow conditions with low to moderate Reynolds numbers. Here only a single design case is presented.

Figure 3 shows the result of an optimization for $Re = 20$ and $\gamma = 10$. From the upper figure it is clear that the design consists of a contracting nozzle that speeds up the fluid flow thus lowers the static pressure right after the nozzle throat. This is also evident from the printed pressure contours that are relative to the condition $p = 0$ at the outlet. After the throat the flow area is suddenly expanded however, at the lower boundary a structure is formed that could be seen as half a diverging nozzle. This structure creates a semi open cavity near the secondary inlet port.

The color surface of the lower figure shows that fluid speed at the throat is increased with almost a factor 7 in comparison to the incoming mean flow rate. After the throat the flow expands and the interface between the diverging fast flow from the nozzle and the surrounding fluid creates a vortex at the upper boundary while fluid is dragged into the component at the lower boundary. This is also illustrated by the colored streamlines that are black if the fluid is entering through the primary inlet and red if it enters from the secondary inlet. The streamlines that illustrates the recirculating vortex opposite the secondary inlet are colored yellow.

References

[1] Dvořák V.: Shape optimization of axisymmetric ejector. In *ECCOMAS CFD 2006: Proceedings of the European Conference on Computational Fluid Dynamics*, Delft University of Technology; European Community on Computational Methods in Applied Sciences (ECCOMAS), 2006.

[2] Borrvall T., Petersson J.:Topology optimization of fluids in Stokes flow. International Journal for Numerical Methods in Fluids, 41(1):77–107, 2003.

[3] Gersborg-Hansen A., Sigmund O., Haber R.B.: Topology optimization of channel flow problems. Structural and Multidisciplinary Optimization, 30(3):181–192, 2005.

[4] Svanberg K.: The method of moving asymptotes - a new method for structural optimization. International Journal for Numerical Methods in Engineering, 24(2):359–373, 1987.

GENERALIZED SFP PARAMETERIZATION FOR TOPOLOGY OPTIMIZATION INCLUDING LATTICE STRUCTURES

Pierre Duysinx[1], Maxime Collet[1], Simon Bauduin[1], Emmanuel Tromme[2] & Michael Bruyneel [1,3]

[1]*Department of Aerospace and Mechanical Engineering, University of Liege, Liege, Belgium*
[2]*Department of Civil Engineering, The Johns Hopkins University, Baltimore, Maryland, USA*
[3]*GDTECH SA, Liege, Belgium*

Summary Laminate selection in composite structure optimization can be formulated as a topology optimization problem with N materials. To interpolate the material properties of the candidate materials, we extend the Shape Function with Penalization (SFP) parameterization introduced by Bruyneel (2011). With the SFP parameterization and Lagrange shape functions, the number of possible materials is limited to the number of nodes found in classical finite elements (N=3, 4, 8…). We show here that is possible to consider any number of materials by resorting to Wachspress functions, which have been used to define finite elements with an arbitrary number of nodes. The generalized parametrization is presented before being validated by solving academic test problems. Then the new parametrization scheme is illustrated in solving composite structures and topology optimization of structures fabricated by additive manufacturing making use of lattice structures subdomains.

INTRODUCTION

High performance structures take advantage of composite materials or cellular materials with superior physical properties per unit of mass. The component layout can be optimized to take benefit of the full capabilities of the porous composite materials to sustain efficiently the applied loads. To this end, topology optimization [1] is an efficient design tool to suggest the best material distribution to maximize the component performance. While black and white designs have been searched for a long while, now availability of additive manufacturing techniques makes possible to fabricate structures including regions of intermediate density made of porous cellular materials. In particular the lattice microstructures have received quite a long of attention in the literature (e.g. Ref [2]). However other microstructural configurations of porous microstructures should be investigated in order to have better material usage under given loading conditions. Some recent pieces of work have focused in optimizing simultaneously the macrostructural material distribution and the local microstructural layouts in all points of the design domain (see Ref [3, 4]).

In this work we adopt a rather practical approach based on the selection of porous cellular materials out of a given catalogue. To this end, we follow along the idea inspired by Stegmann and Lund [5] with the so-called Discrete Material Optimization (DMO). The fundamental items of the approach are 1/ to formulate the design optimization problem as an optimal material selection problem in which the different kinds of cellular porous solids as well as their orientations if orthotropic are considered as different materials, 2/ to solve the selection problem using the topology optimization with multiple materials, 3/ to solve efficiently the optimization problem using continuous existence variables. To transform the discrete problem into a continuous one, one introduces a suitable parametrization identifying each material by a unique set of continuous design variables while the material properties are expressed as a weighted sum of all candidate materials.

The first contribution of this work consists in proposing a novel efficient formulation of the parameterization scheme. For composite structures, Bruyneel [6] has proposed an efficient interpolation scheme based for the Finite Element functions namely the Shape Function Parameterization (SFP), but the extension to any number of plies is still difficult. To this end, the Binary Coded Parametrization (BCP) was proposed by Gao et al. [7]. However the procedure can deal with a catalogue of 2^N materials. Here we show that it is possible to build shape function for an arbitrary number of materials by resorting to the Wachpress rationale functions [8,9] used in polygonal finite elements [10]. The interpolation schemes are compared with the particular perspective of solving large-scale applications. The influences of the penalization factor and initial design variables are studied and discussed.

As a second contribution, we also apply the generalized SFP approach to design components made of void / solid but also different patterns of porous microstructures including lattice microstructures. In order to evaluate the advantages of including subdomains made of porous microstructures, we revisit some of the classical examples of topology optimization. The influence of the types of the porous pattern is investigated for single and multiple load cases applications.

The developments are illustrated by several numerical applications including academic examples and benchmarks inspired by industrial applications.

INTERPOLATION SCHEME OF MATERIAL PROPERTIES USING WACHPRESS FUNCTIONS

The discrete optimal orientation design of the laminate can be treated as an optimization material selection problem with multiple materials. Following the idea by Stegmann and Lund [5], the material stiffness of the local material is a linear

---

[a] Corresponding author. Email: p.duysinx@ulg.ac.be

anisotropic material stiffness matrix C_i of a composite ply/ material noted 'i' as a weighted sum over the stiffness of some candidate materials {j}:

$$\mathbf{C}_i = \sum_{j=1}^{m} w_{ij} \mathbf{C}_i^{(j)} \qquad \text{with} \qquad 0 \le w_{ij} \le 1 \qquad \sum_{j=1}^{m} w_{ij} \le 1 \qquad w_{ik} = 0 \left(k \ne j \right) \text{ when } w_{ij} = 1 \qquad (1)$$

The weighting function w_{ij} are associated with the jth material phase. From the last conditions of (1), it comes that one ends up with a 0/1 design satisfying the constraints. This is achieved by using a penalization of the intermediate densities.

When dealing with the classical balanced composite aerospace structures based on laminates made of plies of the four discrete orientations 0°/90°/45°/-45°, Bruyneel [6] proposed a parameterization model named SFP (Shape Function with Penalization) based on the four node finite element shape functions that, obviously, satisfies the conditions (2):

$$w_{i1,2,3,4} = \left[\frac{1}{4} \left(1 \pm x_{i1}\right)\left(1 \pm x_{i2}\right) \right]^p \qquad -1 \le x_{ij} \le 1, \quad j = 1, 2, 3, 4 \qquad (2)$$

As in the SIMP method, the penalization factor p is applied to push the design variables to their extreme values +/-1. SFP introduces only two variables for four materials, which is an advantage to reduce the size of the optimization problem. The presence of one material phase is characterized by a specific combination of design variables taking values of +1 and/or -1.

Extending the SFP scheme to more than four materials by building complex shape functions related to 'N' node finite elements satisfying the conditions (1) is not straight forward using Lagrange interpolation functions. To account for a variable number of material candidates in the catalogue, the original idea is to use the Wachspress rationale functions [8,9] used in a N-node polygonal reference finite element [10]. As depicted in Figure 1, the shape functions of a regular N-node finite element are used as interpolation schemes between the mechanical properties of the candidate materials.
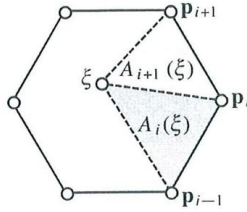
Figure 1: N-Polygonal reference element
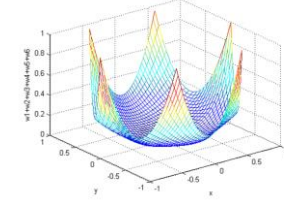
Figure 2: 6-Polygonal interpolation functions

Ref [11] provides a simple expression for Wachpress basis functions:

$$w_i^{PSF} = \frac{\alpha_i(\xi)}{\sum_{j=1}^{n} \alpha_j(\xi)} \quad where \quad \alpha_i(\xi) = \frac{A(p_{i-1}, p_i, p_{i+1})}{A(p_{i-1}, p_i, \xi) \, A(p_i, \xi, p_{i-1})} \qquad (4)$$

Where $A(p_{i-1}, p_i, p_{i+1})$ denotes the area of the triangle with the three vertices p_{i-1}, p_i, p_{i+1}. This expression can be further simplified since the reference element is a regular polygon so that $A(p_{i-1}, p_i, p_{i+1})$ is the same for all i. Figure 2 shows the interpolation function after applying a power law penalization with p=3

Acknowledgment

References

[1] Bendsøe M.P. & Sigmund O. Topology Optimization - Theory, Methods and Applications. Springer Verlag.

[2] Chua C., Grafa G. & Rosen D. W. Design for Additive Manufacturing of Cellular Structures. Computer-Aided Design and Applications. 5 (5), 686-696, 2008

[3] Rodrigues H.C., Guedes J. & Bendsøe M.P. Hierarchical optimization of material and structure. Struct. Multidisc. Optim. 24: 1-10, 2002.

[4] Xia L. Towards Optimal Design of Multiscale Nonlinear Structures. PhD Thesis, Université de Technologie de Campiègne. Novembre 2015.

[5] Stegmann J. & E. Lund. Discrete material optimization of general composite shell structures. IJNME, 62: 2009-2027, 2005

[6] Bruyneel, M. SFP - a new parameterization based on shape functions for optimal material selection: application to conventional composite plies. Structural and Multidisciplinary Optimization 43 (1), 17-27, 2011.

[7] Gao T., W. Zhang & P. Duysinx. A bi-value coding parameterization scheme for the discrete optimal orientation design of the composite laminate. IJNME, 91 (1), 98-114, 2012

[8] Wachspress E.L. A Rational Finite Element Basis. New York: Academic Press, 1975.

[9] Dasgupta G. Interpolants within convex polygons: Wachspress' shape functions. Journal of Aerospace Engineering, 16, 1, pp. 1-8, 2003.

[10] Talischi C., G.H. Paulino, A. Pereira & I.F.M. Menezes. Polygonal finite elements for topology optimization: a unifying paradigm. International Journal for Numerical Methods in Engineering, 82, 6, pp. 671-698, 2010.

[11] Meyer M., Lee H., Barr A.-H., and Desburn M. Generalized barycentric coordinates for irregular n-gons. Journal of Graphic Tools. 1 (1), 13-22. 2002.

TOPOLOGY OPTIMIZATION FOR TRANSIENT THERMO-MECHANICAL PROBLEMS

Evert Hooijkamp[1] and <u>Fred van Keulen</u> [*1]

[1]*Department for Precision and Microsystems Engineering, Mekelweg 2, 2628CD Delft, The Netherlands*

<u>Summary</u> Thermo-mechanical transient problems impose major design challenges for a wide range of applications. This paper focuses on topology optimization for transient thermo-mechanical problems with extreme precision requirements. The transient nature causes standard adjoint sensitivity formulations to suffer from backward time integrations, leading to computational inefficiency. To overcome this obstacle, reduced-order models are used to evaluate the transient thermo-mechanical responses and the associated adjoint sensitivities. Aspects of investigation include the construction of reduced-order models, application of mode acceleration, accuracy of the transient response and associated adjoint sensitivities and their use in topology optimization. It is shown, that good topological designs are obtained, whereas costly adjoint sensitivities are replaced by relatively inexpensive counterparts involving simple backward convolutions.

INTRODUCTION

Transient thermo-mechanical problems emerge in a wide range of applications, for example, energy conversion, combustion processes, but also instrumentation and tooling. The present paper aims at problems with relatively small temperature fluctuations, but with major impact on ultimate performance. Examples are instruments operating at the nanometer scale and precision (manufacturing) tools. For these applications, transient thermal effects cause thermal drift of instruments or thermally induced errors in manufacturing processes [1].

Designing advanced thermo-mechanical systems is very challenging as multiple physics domains are interacting, the transient nature of the problems at hand, complex layouts are required and active thermal management systems might be integrated. Given this complexity, application of topology optimization is an obvious choice. Topology optimization relies on adjoint sensitivities to deal with a large number of design variables. The transient nature however, is severely hindering adjoint sensitivity analysis, as it requires a backward time integration for transient problems.

In the present paper, reduced-order models are investigated to overcome the difficulties caused by the backward time integration. Reduced-order models are based upon so-called thermal modes. Herewith, the tedious backward time integrations can be replaced by simple backward time convolutions. The latter rigorously eliminates the need for huge memory storage and associated computational costs. Different schemes for model reduction are investigated and their effects on sensitivities and application in topology optimization is investigated.

THERMAL MODES

A discretized linear thermal problem can be described by

$$\mathbf{C}_{\mathrm{T}}\dot{\boldsymbol{\theta}}(t) + \mathbf{K}_{\mathrm{T}}\boldsymbol{\theta}(t) = \mathbf{q}(t), \tag{1}$$

here $\boldsymbol{\theta}(t)$ denotes the temperature difference with respect to a reference temperature, $\mathbf{C}_{\mathrm{T}}$ denotes the heat capacity matrix, $\mathbf{K}_{\mathrm{T}}$ the heat conductivity matrix and $\mathbf{q}$ the thermal load. The thermal modes $(\boldsymbol{\phi}_k)$, see [2], and associated thermal time constants (τ_k) follow from the eigenvalue problem defined by setting the thermal load to zero and substituting $\boldsymbol{\theta}(t) = e^{-t/\tau_k}\boldsymbol{\phi}_k$ into (1). Like in structural dynamics, the thermal problem can be represented on the modal basis.

Reduced models may be formulated by selecting only the most relevant modes. Effective mode selection is however paramount and should account for (i) thermal excitation, (ii) observability and (iii) time relevance. Thus, the thermal problem is modeled using a limited number of carefully selected modes. The efficiency and accuracy of these reduced-order models can be improved significantly if a static correction is added, a so-called mode acceleration technique [3]. It is important to emphasize, that the transient behavior is now determined by simple time convolutions which provide the modal coordinates as functions of time.

For the applications mentioned in the Introduction, the relevant thermal time constants are orders of magnitude larger than their mechanical counterparts. This allows for a one-way coupling between the thermal and mechanical domain. Hence, the thermo-mechanical effects are modeled using equivalent loads which enter the equations of motions. If inertia and damping effects can be neglected, then the transient thermo-mechanical solution is determined by

$$\mathbf{K}_{\mathrm{u}}\mathbf{u}(t) = \mathbf{f}(t) + \mathbf{f}_{\theta}(t), \tag{2}$$

here $\mathbf{u}$ denotes the nodal degrees of freedom and $\mathbf{K}_{\mathrm{u}}$ the constant mechanical stiffness matrix. The load is divided into a mechanical load $(\mathbf{f})$ and an equivalent thermal load $(\mathbf{f}_{\theta})$. The latter is evaluated via a reduced-order transient model as summarized above.

[*]Corresponding author. Email: A.vanKeulen@tudelft.nl
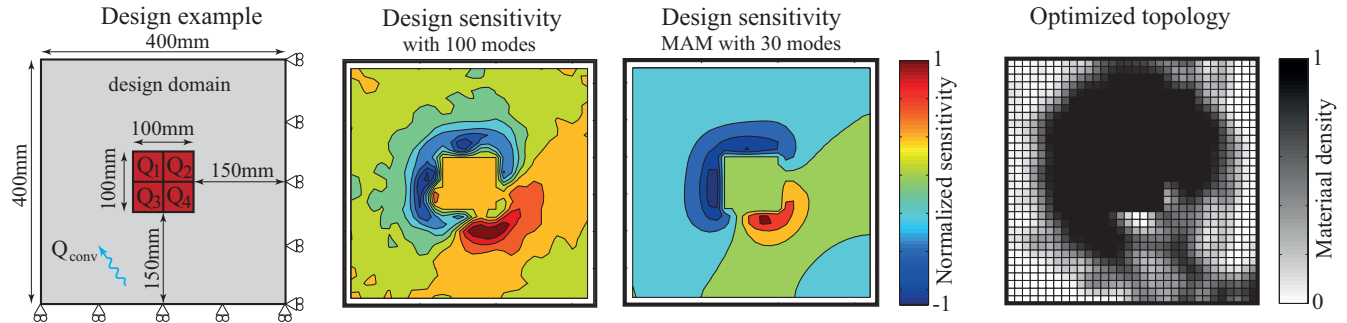
Figure 1: Left, thermo-mechanica topology optimization problem. Heat sources Q1–Q4 switch on alternatingly, whereas the center of the heat exposed area should exhibit minimal displacement once the heat load is activated. Sensitivities obtained with a reduced-order model without and with mode acceleration (MAM) are depicted. Right, the resulting topology.

ADJOINT SENSITIVITIES

For transient problems, adjoint sensitivities require backward time integrations. The latter implies that many intermediate results obtained during the forward response evaluations must be kept, thus, severely hindering topology optimization of transient problems [4].

The adopted reduced modal basis is used as a staring point for the adjoint sensitivity analysis as well. Since for the reduced modal basis the transient thermal behavior is described by decoupled ordinary differential equations, the adjoint sensitvity formulation can be formulated in such a manner that exhaustive memory requirements are avoided and ultimately results in simple backward convolutions. This adjoint sensitivity formulation can be easily adapted to also accommodate a static correction as used in the mode acceleration method.

APPLICATION TO TOPOLOGY OPTIMIZATION

Figure 1 shows a typical test case of a system subjected to convection and alternating heat loads (Q1–Q4). The objective is to obtain minimal center displacement of the area which is exposed to an active heat load. The figure provides results for the sensitivities based on 100 modes and 30 modes but with mode acceleration. It is clearly seen, that the sensitivities with fewer modes, but with mode acceleration are significantly more accurate. The resulting topology design is also provided.

CONCLUSIONS

The proposed topology optimization scheme for transient thermo-mechanical problems makes efficient use of a reduced modal basis. The fact that the transient thermal analysis reduces to a set of ordinary differential equations provides an excellent starting point for an efficient adjoint sensitivity analysis. The best efficiency and accuracy of both response evaluations and adjoint sensitivities are obtained if the modal reduction is combined with a mode acceleration scheme. The advocated method turns out to be effective for topology optimization problems with transient thermo-mechanical responses.

References

[1] Mayr J. *et al.*: Thermal issues in machine tools, CIRP Ann.-Manuf. Techn. 61, 771 (2012).

[2] Biot M.A.: New methods in heat flow analysis with application to flight structures, J. Aeronautical Sciences 24, 857 (1957).

[3] Besselink B. *et al.*: A comparison of model reduction techniques from structural dynamics, numerical mathematics and systems and control, J. Sound Vibration 332, 4403 (2013).

[4] Choi K.K. and Kim N.H.: Structural Sensitivity Analysis and Optimization, Springer (2005).

MULTI-MATERIAL TOPOLOGY OPTIMIZATION OF VISCOELASTICALLY DAMPED STRUCTURES

Max van der Kolk [*1,2], Gijs J van der Veen[1], Jan de Vreugd[2], and Matthijs Langelaar[1]

[1]*Department of Precision and Microsystems Engineering, Delft University of Technology, Delft, The Netherlands*
[2]*Optomechatronics, Netherlands Organisation for Applied Scientific Research, Delft, The Netherlands*

<u>*Summary*</u> *The design of high performance instruments often involves the attenuation of poorly damped resonant modes. Current design methods typically rely on informed trial and error based modifications to improve dynamic performance. In this contribution, we present a multi-material topology optimization as an alternative, systematic methodology to design structures with optimized damping characteristics. A parametric, level set-based topology optimization is employed to simultaneously distribute structural and viscoelastic material to optimize the structure's damping characteristics. To model the viscoelastic behavior a complex-valued material modulus is applied. The structural loss factor is determined from the complex-valued eigensolutions and its value is maximized during the optimization. We demonstrate the performance of the optimization by maximizing the damping of a cantilever beam.*

INTRODUCTION

In this contribution we address the optimization of components containing both viscoelastic and structural material to achieve optimized damping characteristics. The design of high-performance instruments often involves the attenuation of poorly damped resonant modes, as has been encountered in the design of optomechatronic instruments at the Netherlands Organisation for Applied Scientific Research (TNO) [1]. Current design methods typically start from a baseline design and introduce stiffening or damping reinforcements to modify these modes. Difficulties in predicting the influence of these reinforcements leads to a time-consuming, trial and error based design proces. To overcome this, we propose a multi-material topology optimization routine as a systematic method for the design of these structures.

Multi-material designs containing viscoelastic material are known to provide high structural damping [2]. These type of materials dissipate energy during deformation. To increase the structural damping, we can therefore introduce viscoelastic materials at locations that undergo deformation. Moreover, the geometrical design could be modified to promote deformations in the regions of viscoelastic material. This provides a challenging optimization problem, where to goal is to achieve optimal structural damping: both the location and the geometry of the viscoelastic regions are determined during the optimization. In previous works these two aspects have been investigated separately: by shape optimization of (un)constrained layer damping [3] and by topology optimization of the material distribution within predefined damping configurations [4, 5]. These methods are limited by the initial design configuration of the viscoelastic material.

To overcome these restrictions, we present a multi-material topology optimization routine to simultaneously distribute the viscoelastic and structural material throughout the design to optimize the damping characteristics. The proposed method is able to achieve freeform material distributions, resulting in higher structural damping. Moreover, the method does not require the designer to specify any initial (un)constrained layer configuration for the viscoelastic material.

TOPOLOGY OPTIMIZATION OF VISCOELASTIC AND STRUCTURAL MATERIAL

In this work we aim to optimize the damping characteristics for structures subjected to harmonic excitations. This allows to represent the viscoelastic material behavior using a complex-valued material modulus [6]. Either a complex-valued shear, bulk or Young's modulus can be applied. In the remainder of this work, it is assumed that only shear deformation dissipates energy and therefore a complex-valued shear modulus is implemented. The structural loss factor is applied to quantify the damping of these designs [7]. However, compared to the referred implementation the complete complex-valued eigensolutions are used for the formulation of the structural loss factor to achieve better prediction of the structure's Q-factor.

A multi-material, parametric level set method allows to describe multiple material regions within the design domain [8]. We have opted for a level set-based approach, in order to obtain clearly distinct material regions. Trials using density-based multi-material topology optimization often resulted in designs containing mixture of materials that are difficult to interpret. For each material a level set function is defined, which are parameterized using radial basis functions [9]. The numerical implementation applies four-node square quadrilateral (Q4), plane stress elements to discretize the domain. The material properties of any elements near the boundaries of the level set functions are scaled by the ersatz material model. Also, the discrete Heaviside and its derivative are implemented with continuous approximations. Finally, the Method of Moving Asymptotes (MMA) solves the gradient-based optimization problem [10].

The optimization aims to maximize the structural loss factor corresponding to the specified number of eigenmodes. Constraints are applied to limit the volume of viscoelastic material and enforce a minimum eigenfrequency. An exact formulation

---

*Corresponding author. Email: M.vanderKolk@tudelft.nl

of the structural loss factor are found by an adjoint sensitivity analysis. The complex-valued eigenvalue problem encountered in the adjoint sensitivity analysis is dealt with similarly as presented in [11].

To illustrate the performance of the optimization routine the maximization of the damping of a cantilever beam is presented. Figure 1a shows the initial design domain with L = 70 and H = 20 elements.. The average damping of the first and second resonant modes is maximized during the optimization. The volume of viscoelastic material is constrained to 40% of the domain volume and a minimum eigenfrequency for the first resonant mode is imposed. The materials have the following properties: structural $E = 200\,\text{GPa}, \nu = 0.3, \rho = 7.85 \times 10^3\,\text{kg/m}^3$ and viscoelastic: $E = 1\,\text{GPa}, \nu = 0.3, \rho = 1 \times 10^3\,\text{kg/m}^3$ and a material loss factor equal to 1. Figure 1b shows the final converged design after 35 iterations. All constraints are satisfied and an objective value of 0.5057 is obtained. The design shows a freeform distribution of viscoelastic material and achieves higher structural loss factors compared to conventional CLD configurations which vary between 0.26 and 0.39 for the analyzed domain. Since a complex-valued shear modulus was assumed, the dissipated energy is directly related to the shear strains during resonance. Figure 1c and 1d present the shear strain distribution and illustrate that almost all viscoelastic material contributes to the total energy dissipation for the optimized modeshapes.

CONCLUSIONS

A well-performing topology optimization approach has been presented which is able to generate multi-material designs with optimized damping properties. The level-set based formulation provides a clear separation between the different material phases compared with previous investigations using density-based approaches. With the presented example, we have demonstrated that the optimized designs achieve significantly higher structural loss factors compared to conventional constrained layer damping configurations by applying a freeform distributions of the viscoelastic and structural material. This offers new potential for applications where high structural damping is an important design aspect, e.g. high precision equipment and satellite instruments.

(a) Initial design domain

(b) Final design at iteration 35.

(c) Shear strain for eigenmode 1.

(d) Shear strain for eigenmode 2.
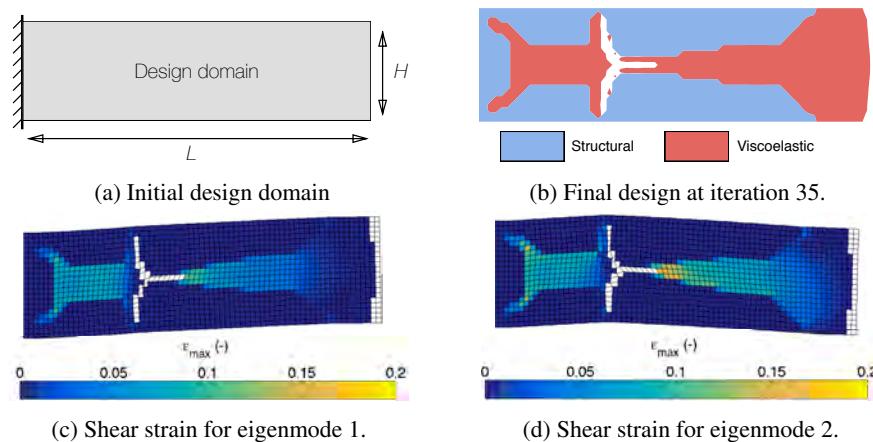
Figure 1: Example of loss factor maximization of a cantilever beam. (a) design domain, (b) obtained distribution of viscoelastic and structural material after 35 iterations, (c) shear strain in first resonant mode and (d) shear strain in second resonant mode.

References

[1] de Vreugd J., de Lange D., Winters J., et al.: Damping in space constructions, Proceedings of ECSSMET, 2014.

[2] Johnson C.D.: Design of passive damping systems. Journal of Vibration and Acoustics, 117:171, 1995.

[3] Plunkett R., Lee C.: Length optimization for constrained viscoelastic layer damping. J. Acoustic Society of America, 48:150-161, 1970.

[4] El-Sabbagh A., Baz A.: Topology optimization of unconstrained damping treatments for plates. Engineering Optimization, 49:1153-1168, 2013.

[5] Zheng W., Lei Y., Li S., et al.: Topology optimization of passive constrained layer damping with partial coverage on plate. J. Shock and Vibration 20:199-211, 2013.

[6] Tschoegl N.W.: The phenomenological theory of linear viscoelastic behavior. Springer-Verlag, Berlin, 1989.

[7] Johnson C.D., Kienholz D.A.: Finite element prediction of damping in structures with constrained viscoelastic layers. J. AIAA, 20:1284:1290, 1982.

[8] Wang Y., Luo Z., Kang Z., et al.: A multi-material level set-based topology and shape optimization method. J. CMAME, 283:1570-1586, 2015.

[9] Wendland H.: Piecewise polynomial, positive definite and compactly supported radial basis functions of minimal degree. Advances in Computational Mathematics 4:389-396, 1995.

[10] Svanberg K.: The method of moving asymptotes - A new method for structural optimization. Numerical Methods in Engineering, 24:359-373, 1987.

[11] van der Veen. G., Langelaar M., van Keulen, F.: Integrated topology and controller optimization of motion systems in the frequency domain. Structural and Multidisciplinary Optimization, 51:673-685, 2014.

DESIGN OF BEAM CROSS SECTIONS WITH EXTREME STRUCTURAL PROPERTIES USING TOPOLOGY OPTIMIZATION

José Pedro Blasques[1] and Miguel Fernandez-Perez[2]

[1]*Department of Wind Energy, Technical University of Denmark, jpbl@dtu.dl*
[2]*Vestas Wind Systems A/S, Hedeager 42, 8200 Aarhus, Denmark, mifpe@vestas.com*

Summary Optimal topologies and material distributions are presented which minimize the individual components of the beam cross section compliance matrix (e.g., transverse shear stiffness, shear-torsion coupling, among other). The entries of the compliance matrix are determined using a finite element based cross section analysis tool. A multimaterial topology optimization framework is employed which accommodates any number of isotropic and anisotropic materials. Results are presented for minimization of the individual entries of the cross section compliance matrix subjected to a volume constraint. Some non-intuitive cross section designs are obtained which help shed light on the role of different topological features and material combinations for design of beam structures with non-trivial static and dynamic behaviour. This approach will be used in the future for large scale structural topology optimization of wind turbine blades with nonlinear aeroelastic constraints.

INTRODUCTION

A beam is a type of structure whose length dimension is much larger than its cross section width and height. Beam type structures include wind turbine, helicopter, and airplane rotor blades, among other. The structural response of beam structures can be correctly analysed using beam finite elements. The analysis of the beam response is split in two steps. Firstly the stiffness properties of the beam cross section are analysed. Secondly, these properties are integrated along the length to build the beam finite element stiffness matrix. The author has previously presented results in which structural topology optimization techniques are used to design beam cross sections to control the static and dynamic properties of beam structures ([1, 2]). This paper follows the same approach to focus on the identification of cross section designs - topology and material distribution - which minimize the entries of the cross section compliance matrix (e.g., transverse shear stiffness, shear-torsion coupling, etc.). The work is analogous to design of microstructures to tailor the material properties whereas here the cross section is designed to tailor the beam properties.

METHODOLOGY

For a linear elastic beam there exists a linear relation between the cross section generalized forces T and moments M in $\boldsymbol{\theta} = \begin{bmatrix} \boldsymbol{T}^T \boldsymbol{M}^T \end{bmatrix}^T$, and the resulting strains $\boldsymbol{\tau}$ and curvatures $\boldsymbol{\kappa}$ in $\boldsymbol{\psi} = \begin{bmatrix} \boldsymbol{\tau}^T \boldsymbol{\kappa}^T \end{bmatrix}^T$ (see Figure 1). This relation is given in its compliance form as $\boldsymbol{F}_s \boldsymbol{\theta} = \boldsymbol{\psi}$, where $\boldsymbol{F}_s$ is the 6×6 cross section compliance matrix. In the most general case, considering material anisotropy and inhomogeneity, all the 21 compliance parameters in $\boldsymbol{F}_s$ may be required to describe the deformation of the cross section. The entries of $\boldsymbol{F}_{s,ij}$ are determined here following the description and nomenclature in [1] of the theory in [3]. The formulation relies on a finite element discretization of the cross section to approximate the three-dimensional cross section deformation or warping. The cross section compliance matrix $\boldsymbol{F}_s$ is obtained as

$$\boldsymbol{F}_s = \boldsymbol{W}^T \boldsymbol{G} \boldsymbol{W}, \text{ where } \boldsymbol{W} \text{ is the solution to } \boldsymbol{K} \boldsymbol{W} = \boldsymbol{F} \tag{1}$$

where the coefficient matrix $\boldsymbol{K}$ and $\boldsymbol{G}$ are associated with the stiffness of the cross section. Furthermore, the solution matrix $\boldsymbol{W}$ contains the cross section rigid body motions $\boldsymbol{\psi}$ and the three dimensional warping displacements $\boldsymbol{u}$. Finally, the load array $\boldsymbol{F}$ is associated with a series of unit load vectors $\boldsymbol{\theta}$.

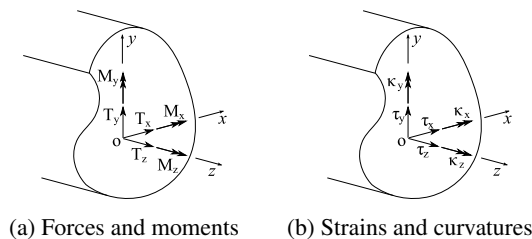(a) Forces and moments   (b) Strains and curvatures

Figure 1: Cross section coordinate system, foces and moments (a), and corresponding strains and curvatures (b).

The optimal design problem is formulated within a multi-material topology optimization context as

$$\underset{\boldsymbol{\rho}\in\mathbb{R}^{n_e \times n_c}}{\text{minimize}} \quad \boldsymbol{F}_{s,ij}(\boldsymbol{\rho})$$

$$\text{subject to} \quad V(\boldsymbol{\rho}) \leq \overline{V} \qquad\qquad\qquad\qquad\qquad (\text{P1})$$

$$\sum_{m=1}^{n_c} \rho_{em}(\boldsymbol{\rho}) < 1 \ , \ \forall e = 1, ..., n_e$$

$$0 \leq \rho_{em} \leq 1, \ \forall e = 1, ..., n_e \ , \ \forall m = 1, ..., n_c$$

where $V(\boldsymbol{\rho})$ is the total volume of the beam occupied with material. The design variable ρ_{em} represent the volume fraction of candidate material m at element e of the cross section finite element mesh, where n_c and n_e are the number of candidate materials and finite elements, respectively. The sensitivities of the cross section compliance matrix $\boldsymbol{F}_s(\boldsymbol{\rho})$ are analytically determined as described in [1]

NUMERICAL RESULTS

A few illustrative results are presented in Figure 2. The design domain defining the beam cross section is 1×1 m and is meshed using 120×120 elements with three degrees of freedom per node. In view of future plans to manufacture and test the resulting beam designs, results are obtained using Polylactic Acid (PLA), an isotropic material typically used in additive manufacturing. The designs presented in Figure 2 refer to the cross sections of the beam. A three-dimensional beam structure with constant cross section can be obtained by simply extruding these cross sections.

(a) min $F_{s,11}$ (b) min $F_{s,22}$ (c) min $F_{s,12}$ (d) min $F_{s,16}$ (e) min $F_{s,44}$ (f) min $F_{s,55}$ (g) min $F_{s,45}$ (h) min $F_{s,66}$
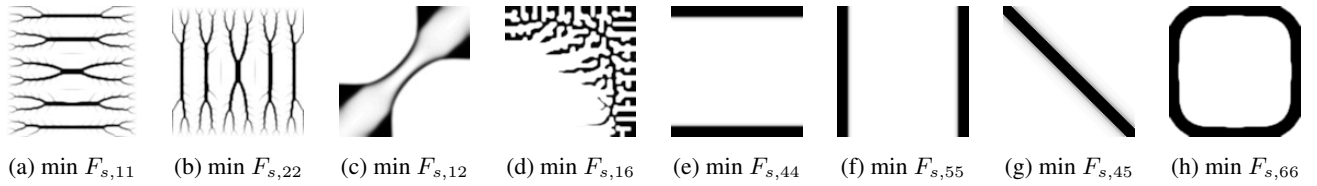
Figure 2: Optimized beam cross section topologies (a) minimizing $F_{s,11}$ (transverse shear compliance in x direction); (b) minimizing $F_{s,11}$ (transverse shear compliance in x direction); (c) minimizing $F_{s,12}$ (transverse shear-shear coupling); (d) minimizing $F_{s,16}$ (transverse shear-twist coupling); (e) minimizing $F_{s,44}$ (bending compliance around x); (f) minimizing $F_{s,55}$ (bending compliance around y); (g) minimizing $F_{s,45}$ (bending-bending coupling); (h) minimizing $F_{s,66}$ (torsion compliance). The topology minimizing $F_{s,26}$ is the same as in (c) rotated 90 degrees with respect to the z axis. The remaining coupling terms (e.g., $F_{s,46}$) cannot be activated using isotropic materials.

CONCLUSION

Initial results are presented for the optimal design of beam cross sections with extreme stiffness properties using isotropic materials. Further results show that including material anisotropy it is possible to activate the remaining coupling terms which were not active using a single isotropic material. Future work will utilize the solutions presented here to establish the bounds on the entries of the cross section compliance matrix to formulate a new class of Free Beam Section Optimization (FBSO) problems, an approach identical to Free Material Optimization applicable to beam structures. The aim is to use this approach to develop a computationally very efficient framework for large scale structural topology optimization of wind turbine blades with nonlinear aeroelastic constraints.

References

[1] Blasques, J. P., Stolpe, M.: Multi-material topology optimization of laminated composite beam cross sections. Composite Structures, 94(11), 32783289, 2012.

[2] Blasques, J. P.: Multi-material topology optimization of laminated composite beams with eigenfrequency constraints. Composite Structures, 111, 4555, 2014.

[3] Giavotto, V., Borri, M., Mantegazza, P., Ghiringhelli, G., Carmaschi, V., Maffioli, G., Mussi, F.: Anisotropic beam theory and applications. Computers & Structures, 16(1-4), 403413, 1983.

ON BIFURCATION SENSITIVITIES AND STABILITY OPTIMIZATION
BASED ON LOCAL SUB-DOMAIN EIGENVALUES

<u>Niels L. Pedersen</u> and Pauli Pedersen

Department of Mechanical Engineering, Solid Mechanics, Technical University of Denmark,
Nils Koppels Allé, Building 404, DK-2800 Kgs. Lyngby, Denmark

<u>*Summary*</u> The engineering approach of fully stressed design is a practical tool with a theoretical foundation. The analog approach to structural bifurcation instability optimization is presented with its theoretical foundation. A numerical redesign procedure is proposed and illustrated with examples. For the ideal case, an optimality criterion is fulfilled if the design have the same sub-domain "critical load" (local Rayleigh quotient). Sensitivity analysis results in a simple relation between system critical load and local "critical load" for a given bifurcation mode.

For a general continuum subjected to loads and boundary conditions, the stability analysis is rather complicated and is normally based on non-linear finite element (FE) analysis. In the present work focus is on bifurcation instability that after non-linear displacement analysis involve an eigenvalue problem to determine a critical load factor at which bifurcation take place. The design problem of maximizing such a load factor by optimized distribution of a given amount of material within a specified design space is the the subject of our work. With analysis being complicated, this synthesis problem seems to relay on pure numerical procedures, but theoretical results are obtained. Due to recent experience on optimal design of eigenfrequencies in [1], simplified results are expected also for the bifurcation eigenvalue problem. This holds for the sensitivity analysis that is necessary for optimizing a design. A simple optimality criterion is derived from the obtained sensitivities..

DIFFERENT STIFFNESS MATRICES FOR ANALYSIS

The static equations of equilibrium for an elastic problem, including reversible non-linear elastic problems, is for a model with a finite number of degrees of freedom written as $[S_s]\{D\} = \{A\}$ where the stiffness matrix $[S_s]$ is the system secant stiffness matrix that directly relate the resulting displacement vector $\{D\}$ and the corresponding force vector $\{A\}$ and may express equilibrium for a total model (system) or for a single element. For the differential of the displacement vector $\{dD\}$ and the differential of the corresponding force vector $\{dA\}$ the relation is described by the tangent stiffness matrix $[S_t]$ by $[S_t]\{dD\} = \{dA\}$

System stiffness matrices may be obtained by accumulating (FE assembled) over all the element stiffness matrices $[S_s] = \sum_e [S_s]_e$ and $[S_t] = \sum_e [S_t]_e$. For non-linear models different stiffness matrices are involved

- $[S_0]$, symmetric stiffness matrix for a non-displaced model,

- $[S_s]$, non-symmetric secant stiffness matrix for a displaced model,

- $[S_\gamma]$, symmetric displacement gradient stiffness matrix for a displaced model,

- $[S_\sigma]$, symmetric stress stiffness matrix for a displaced model and

- $[S_t] = [S_\gamma] + [S_\sigma]$, symmetric tangent stiffness matrix for a displaced model.

For a simple triangular 2D plane element analytical expressions for all these different stiffness matrices are available. These results are derived in [2] and important information follows from these analytical results.

Analysis for bifurcation buckling

With the tangential stiffness matrix available for a FE model, buckling may be determined as described in [3], Chapter 18. In bifurcation buckling two close equilibrium states are possible for the same load. The procedure is here based on an already solved non-linear elastic equilibrium. A such solution is given the index n to indicate a step of a possible incremental load $\{A\}_n = \sum_{\tilde{n}=1}^{\tilde{n}=n} \{\Delta A\}_{\tilde{n}}$. The determined solution gives a determined stress stiffness matrix $[S_\sigma]$ by

$$[S_s]_n\{D\}_n = \{A\}_n \;\Rightarrow\; \{D\}_n \;\Rightarrow\; [S_\gamma]_n \text{ and } \sigma_n \;\Rightarrow\; [S_\sigma]_n \tag{1}$$

with assumed linearity between $\lambda\{\Delta A\}_{n+1}$ and $\lambda[S_\sigma]_n$ giving

$$([S_\gamma]_n + \lambda[S_\sigma]_n)\{\Delta D\}_{n+1} = \lambda\{\Delta A\}_{n+1}$$
$$([S_\gamma]_n + \lambda[S_\sigma]_n)(\{\Delta D\}_{n+1} + \{\Delta\}) = \lambda\{\Delta A\}_{n+1} \tag{2}$$

where $\{\Delta\}$ is the bifurcation mode from $\{\Delta D\}_{n+1}$. The difference of these two equations give an eigenvalue problem

$$([S_\gamma]_n + \lambda_C [S_\sigma]_n) \{\Delta\} = \{0\} \quad \Rightarrow \quad \text{the eigen pair } \lambda_C, \{\Delta\} \tag{3}$$

The critical load $\{A\}_C$ corresponding to the bifurcation displacement $\{\Delta\}$ is

$$\{A\}_C = \{A\}_n + \lambda_C \{\Delta A\}_{n+1} \tag{4}$$

BIFURCATION LOAD SENSITIVITIES

The eigenvalue problem (3) presented without index n and C is

$$([S_\gamma] + \lambda[S_\sigma]) \{\Delta\} = \{0\} \tag{5}$$

This is pre multiplied by the transposed bifurcation eigenmode $\{\Delta\}^T$ to

$$U_\gamma + \lambda U_\sigma = 0 \ \text{ with } \ U_\gamma := \{\Delta\}^T [S_\gamma] \{\Delta\} \ \text{ and } \ U_\sigma := \{\Delta\}^T [S_\sigma] \{\Delta\} \tag{6}$$

with the Rayleigh quotient $\lambda = -\frac{U_\gamma}{U_\sigma}$.

The sensitivity of the bifurcation eigenvalue with respect to the density ρ_e is

$$\frac{\partial \lambda}{\partial \rho_e} = -\frac{\partial \widehat{\frac{U_\gamma}{U_\sigma}}}{\partial \rho_e} - \frac{\partial \frac{U_\gamma}{U_\sigma}}{\partial \Delta} \frac{\partial \Delta}{\partial \rho_e} = -\frac{\partial \widehat{\frac{U_\gamma}{U_\sigma}}}{\partial \rho_e} \tag{7}$$

simplified by the stationarity of the Rayleigh quotient with respect to change of eigenmode and applying a hat notation for gradients with unchanged eigenmode, see [4]. Expanding the final term in (7) give

$$\frac{\partial \lambda}{\partial \rho_e} = -\frac{\partial \widehat{U}_\gamma}{\partial \rho_e} \frac{1}{U_\sigma} + \frac{\partial \widehat{U}_\sigma}{\partial \rho_e} \frac{U_\gamma}{U_\sigma^2} = -\frac{1}{U_\sigma} \left(\frac{\partial \widehat{U}_\gamma}{\partial \rho_e} + \lambda \frac{\partial \widehat{U}_\sigma}{\partial \rho_e} \right) \tag{8}$$

where the energies are accumulated from element energies

$$U_\gamma = \sum_e (U_\gamma)_e \ \text{ and } \ U_\sigma = \sum_e (U_\sigma)_e \tag{9}$$

The stiffness matrices are here assumed to depend explicitly only on the local element density ρ_e and this dependence is assumed to be linear proportionality, that give

$$\frac{\partial \lambda}{\partial \rho_e} = -\frac{1}{U_\sigma} \left(\frac{\partial (\widehat{U}_\gamma)_e}{\partial \rho_e} + \lambda \frac{\partial (\widehat{U}_\sigma)_e}{\partial \rho_e} \right) = -\frac{1}{U_\sigma \rho_e} ((U_\gamma)_e + \lambda (U_\sigma)_e) = \frac{(U_\sigma)_e}{U_\sigma} \frac{1}{\rho_e} (\lambda_e - \lambda) \tag{10}$$

Optimality criterion

With the objective of maximizing the bifurcation load $\{A\}_n + \lambda\{\Delta A\}_n$, i.e., of maximizing λ subject to a constant of unchanged total mass/volume

$$\text{Maximize } \lambda \ \text{ for } \ g = \sum_e \rho_e V_e - V = 0 \tag{11}$$

the necessary optimization criterion with a constant C is

$$\frac{\partial \lambda}{\partial \rho_e} = C \frac{\partial g}{\partial \rho_e} = C V_e \ \Rightarrow \ \frac{\partial \lambda}{\partial \rho_e} \frac{1}{V_e} = -\frac{1}{U_\sigma} \frac{1}{\rho_e V_e} ((U_\gamma)_e + \lambda (U_\sigma)_e)) = \frac{(U_\sigma)_e}{U_\sigma} \frac{1}{\rho_e V_e} (\lambda_e - \lambda) = C \tag{12}$$

where U_σ may be normalized to 1 by normalizing the bifurcation mode $\{\Delta\}$.

References

[1] P. Pedersen and N. L. Pedersen. A note on eigenfrequency sensitivities and structural eigenfrequency optimization based on local sub-domain frequencies. *Struct. Multidisc. Optim.*, 49(4):559–568, 2014.

[2] P. Pedersen. Analytical stiffness matrices with Green-Lagrange strain measure. *Int. J. Numer. Meth. Engng.*, 62:334–352, 2005.

[3] R. D. Cook, D. S. Malkus, M. E. Plesha, and R. J. Witt. *Concepts and Applications of Finite Element Analysis*. Wiley, New York, USA, fourth edition, 2002. 719 pages.

[4] P. Pedersen and N. L. Pedersen. Eigenfrequency optimized 3D continua, with possibility for cavities. *Journal of Sound and Vibration*, 341:100–115, 2015.

EFFICIENT TRANSIENT TOPOLOGY OPTIMIZATION THROUGH DYNAMIC SUBSTRUCTURING

Niels Aage[*1]

[1]*Technical University of Denmark, Department of Mechanical Engineering, Centre for acoustic-mechanical micro systems, Denmark*

Summary This paper presents an efficient topology optimization methodology for dynamic structural design problems. The key to the method is to utilize dynamic substructering, or component mode synthesis, i.e. the Craig-Bampton reduction method to speed up the transient analysis. The dynamic substructuring concept is used for both the forward (the state equation) and the backward (adjoint equation). The developed optimization scheme is demonstrated on design problems for linear elastic Mindlin plates subject to impact loads, where the goal is to minimize the deflection in a specified region.

INTRODUCTION AND MOTIVATION

Structural shape and topology optimization for transient problem is known to be computionally expensive and thus less attractive than its steady state counterparts. This is partly due to the fact that a transient analysis is more expensive than a static analysis - especially for implicit time integration schemes - and partly because the sensitivity analysis requires the solution to a terminal value problem. To illustrate the extra computional efforst required one may use an example from non-linear static optimization. Here one have to solve a non-linear problem for the state equation, bu the adjoint problem turns out to be linear and thus much cheaper than the state problem [1]. Despite this obvious drawback several works on transient structural topology optimization have been presented and studied in the past decade. The approach has, among others, been used for 1D pulse modulators and filter design in [2], material microstructure design in [3] and design of composites in [4].

The focus of this work is to develop a methodology which is capable of speeding up the computations by orders of magnitude. To realize this goal the dynamic substructering method, namely the Craig-Bampton method, is applied [5], [6]. The main idea of dynamic substructuring, or component mode synthesis, is to partition the computational domain into a set of smaller substructures. The finite element equations on each substructure is then reduced in size by its normal modes while retaining the interface, or boundary degrees of freedom, by so-called constraint modes. The reduced substructure stiffness, mass and damping matrices (also known as super elements) are then assemblied into a reduced global system which can be orders of magnitude smaller than the original, full finite element system. Based on the reduced system, it is now possible to perform the transient analysis very fast which paves the way for a fast transient topology optimization methodology.

THEORY

The mechanical problem considered in this work is based on Mindlin plate theory for which the unknowns are the out of plane displacement w and the two rotations $\boldsymbol{\theta} = \{\theta_x, \theta_y\}$. The governing equations can be stated compactly as follows

$$\nabla^T \boldsymbol{G} \left(\nabla w - \boldsymbol{\theta} \right) = \rho h \frac{\partial^2 w}{\partial t^2} \tag{1}$$

$$\left(\boldsymbol{\alpha}_1 \frac{\partial}{\partial x} + \boldsymbol{\alpha}_2 \frac{\partial}{\partial y} \right)^T \boldsymbol{D} \left(\boldsymbol{\alpha}_1 \frac{\partial}{\partial x} + \boldsymbol{\alpha}_2 \frac{\partial}{\partial y} \right) + \boldsymbol{G} \left(\nabla w - \boldsymbol{\theta} \right) = \frac{\rho h^3}{12} \frac{\partial^2 \boldsymbol{\theta}}{\partial t^2} \tag{2}$$

where h is the thickness, $\boldsymbol{G}$ and $\boldsymbol{D}$ are constitutive matrices and $\boldsymbol{\alpha}_1$ and $\boldsymbol{\alpha}_2$ are appropriate 3×2 matrices.

When discretized by the standard Galerkin finite element method and including proportional damping, i.e. $\boldsymbol{C} = \alpha \boldsymbol{M} + \beta \boldsymbol{K}$ the matrix equations becomes as follows

$$\boldsymbol{M}\ddot{\boldsymbol{u}} + \boldsymbol{C}\dot{\boldsymbol{u}} + \boldsymbol{K}\boldsymbol{u} = \boldsymbol{F}(t), \quad t \in [0; T] \tag{3}$$

where $\boldsymbol{u} \equiv \boldsymbol{u}(t)$ is a vector collecting both displacement and rotational degrees of freedom and $\boldsymbol{M}$, $\boldsymbol{C}$, $\boldsymbol{K}$ and $\boldsymbol{F}(t)$ are the mass-, damping-, stiffness-matrices and load vector, respectively. The system, together with appropriate boundary and initial conditions, can now be solved by a time integration scheme from 0 to time T. In this work the unconditionally stable Newmark algorithm is used [5].

*Corresponding author. Email: naage@mek.dtu.dk

Solving Eq. (3) will lead to the aforementioned issues with computional time and we will therefore study a reduced system obtained by the Craig-Bampton method first. For each substructure i in the domain the following reduction is performed

$$\boldsymbol{R}_j = \begin{bmatrix} \boldsymbol{\Phi}_j & \boldsymbol{\Psi}_j \\ \boldsymbol{0} & \boldsymbol{I} \end{bmatrix} \tag{4}$$

where $\boldsymbol{I}$ is the identity matrix, $\boldsymbol{\Phi}_j$ is the matrix with n normal modes computed on the interior i of substructure j, i.e. the solution to the eigenvalue problem $(\boldsymbol{K}_j^{ii} - \omega^2 \boldsymbol{M}_j^{ii})\boldsymbol{\Phi}_j = \boldsymbol{0}$ and $\boldsymbol{\Psi}_j$ is the static correction matrix for the interface b degrees of freedom , i.e. $\boldsymbol{\Psi}_j = -\left(\boldsymbol{K}_j^{ii}\right)^{-1} \boldsymbol{K}_j^{ib}$. The super elements are then obtained by

$$\boldsymbol{M}_j^r = \boldsymbol{R}_j^T \boldsymbol{M}_j \boldsymbol{R}_j, \quad \boldsymbol{C}_j^r = \boldsymbol{R}_j^T \boldsymbol{C}_j \boldsymbol{R}_j, \quad \boldsymbol{K}_j^r = \boldsymbol{R}_j^T \boldsymbol{K}_j \boldsymbol{R}_j \ \boldsymbol{F}_j^r \text{and } \boldsymbol{R}_j^T \boldsymbol{F}_j \tag{5}$$

Once assemblied into a system equivalent to Eq. (3), the time response is obtained effeciently by the Newmark algorithm.

The optimization problem investigated in this work can be posed in discrete form as a standard mathematical programme.

$$\begin{aligned} \min_{x \in \mathbb{R}^n} \quad & \phi = \int_{t_1}^{t_2} \boldsymbol{w}(t)^T \boldsymbol{w}(t) \, \mathrm{d}t \\ \text{s.t.} \quad & \boldsymbol{M}\ddot{\boldsymbol{u}} + \boldsymbol{C}\dot{\boldsymbol{u}} + \boldsymbol{K}\boldsymbol{u} = \boldsymbol{F}(t) \\ & V(\boldsymbol{x})/V^* - 1 \le 0 \\ & 0 \le x_i \le 1, \ \ i = 1, n \end{aligned} \tag{6}$$

where the objective function is the out of plane displacement evaluated in a specified region from time t_1 to t_2. The first constraint refers to the state equation, the second to a volume constraint and the last to a box constraint on the design variables denoted by $\boldsymbol{x}$. The optimization problem is solved using the Method of Moving Asymptotes [7] and the sensitivities are determined using the adjoint method obtained purely from the discretized state equation and objective. This leads to the solution of a terminal value problem for the Lagrange multiplier $\boldsymbol{\lambda}$.

$$\boldsymbol{M}\ddot{\hat{\boldsymbol{\lambda}}} + \boldsymbol{C}\dot{\hat{\boldsymbol{\lambda}}} + \boldsymbol{K}\hat{\boldsymbol{\lambda}} = \left.\frac{\partial \phi}{\partial \boldsymbol{u}}^T\right|_{T-\tau}, \quad \hat{\boldsymbol{\lambda}} = \boldsymbol{\lambda}(T-\tau) \tag{7}$$

here formulated as an initial value problem by a change in variables. The sensitivity can then be obtained from the following

$$\frac{\partial \phi}{\partial x_e} = \int_0^T \frac{\partial(\boldsymbol{w}^T\boldsymbol{w})}{\partial x_e} + \boldsymbol{\lambda}^T \left(-\frac{\partial \boldsymbol{M}}{\partial x_e}\ddot{\boldsymbol{u}} - \frac{\partial \boldsymbol{C}}{\partial x_e}\dot{\boldsymbol{u}} - \frac{\partial \boldsymbol{K}}{\partial x_e}\boldsymbol{u}\right) \, \mathrm{d}t \tag{8}$$

To reduce memory requirements, the developed implementation uses a check pointing scheme to avoid storing all displacements, velocities and acceleration from the forward problem.

DISCUSSION

The presented study shows that it is possible to reduce the computational effort of transient topology optimization by order(s) of magnitude by use of dynamic substructering. As expected, the price for the obtained speed up is the more involved sensitivity analysis and the bookkeeping associated with the substructuring (i.e. a domain decomposition). The findings presented here can, with some modifications, be applied to e.g. acoustic-structural interaction problems and thus pave the way for new, interesting multi-physical transient topology optimization problems.

References

[1] Bendsøe, M. P. and O. Sigmund (2003). *Topology Optimization: Theory, Methods and Applications*. Engineering online library. Springer.

[2] Dahl, J., J. S. Jensen, and O. Sigmund (2008). Topology optimization for transient wave propagation problems in one dimension : Design of filters and pulse modulators. *Structural and Multidisciplinary Optimization 36*, 585–595.

[3] Le, C., T. E. Bruns, and D. a. Tortorelli (2012). Material microstructure optimization for linear elastodynamic energy wave management. *Journal of the Mechanics and Physics of Solids 60*(2), 351–378.

[4] Tavakoli, R. (2016). Optimal design of multiphase composites under elastodynamic loading. *Computer Methods in Applied Mechanics and Engineering 300*, 265–293.

[5] Cook, R. D., D. S. Malkus, M. E. Plesha, and R. J. W. Witt (2002). Concept and Applications of Finite Element Analysis.

[6] Craig, R.R. and Bampton, M.C.C. (1968), Coupling of substructures for dynamic analysis. *AIAA Journal*, Vol. 6 No. 7, pp. 1313-19.

[7] Svanberg, K. (1987). The method of moving asymptotes - a new method for structural optimization. *International Journal for Numerical Methods in Engineering 24*(June 1986), 359–373.

TOPOLOGY OPTIMIZATION FOR FINITE STRAIN PLASTICITY

Mathias Wallin[1]*, Viktor Jönsson[1] and Eric Wingren[1]

[1]*Division of Solid Mechanics, Lund University, Sweden*

Summary In this work finite strain rate-independent plasticity is combined with topology optimization. The employed constitutive model is based on rate-independent isotropic hardening plasticity and to separate the elastic deformation from the plastic deformation, use is made of the multiplicative split of the deformation gradient. The mechanical balance laws are solved using the finite element method and the optimization problem is solved using the method of moving asymptotes. The sensitivity is derived using a coupled transient adjoint strategy. A boundary value problem where the plastic work is maximized is used to demonstrate the capability of the presented model.

INTRODUCTION

Most research related to topology optimization has been concerned with linear problems and only a small fraction of the published research has been concerned with non-linear elasticity. Although topology optimization formulations combined with plasticity are rare they do exist and an early example of topology optimization combined with a path-dependent material is provided by [1]. So far, topology optimization combined with plasticity has, however, been restricted to the assumption of small strains.

One application of topology optimization of path-dependent materials is design of energy absorbing structures and materials where finite strain plasticity evidently is highly relevant. In the present work an isotropic finite strain elasto-plastic model is implemented in a finite element environment and combined with topology optimization.

For path-dependent problems the sensitivity is also path-dependent and as a consequence the sensitivity will be obtained by the solution to a terminal value problem. In the present paper the adjoint procedure for calculating the sensitivity for transient coupled problems proposed in [3] will be utilized. The resulting optimization problem is solved using the method of moving asymptotes (MMA), cf. [4]. The presented formulation will be used to find topologies that generates maximum plastic work when subject to a prescribed displacement.

ELASTO-PLASTIC BOUNDARY VALUE PROBLEM

The employed constitutive model is an isothermal version of the model presented in [2] and it is based on the multiplicative split of the deformation gradient. The strain energy governing the elastic response is a Neo-hookean potential function defined in terms of the elastic Finger tensor. The non-dimensional density, c, reduces the strain energy, or stiffness, using the canonical scaling c^p where the penalty exponent is chosen as $p = 3$.

To distinguish plastic response from elastic response, use is made of the von-Mises yield function formulated in terms of the Kirchhoff stress tensor. Similar to elasticity, the initial threshold to plasticity is scaled with the non-dimensional density, however, for the yield stress the penaly exponent $q = 2$ is employed. The plastic evolution laws are based on the postulate of maximum dissipation, i.e. associated plasticity is utilized. In each integration point throughout the structure, the evolution laws for the plastic deformation and the internal variables are integrated using the implicit backward Euler scheme.

The mechanical balance laws are formulated in the reference configuration and discretized using a total Lagrangian finite element formulation. The set of non-linear equations govering the equilibrium is solved using the Newton-Raphson scheme. Since the problem is path-dependent, the load is applied in a number of load steps and for each step the non-linear mechanical balance laws are solved together with the non-liner constitutive equations.

OPTIMIZATION

The objective of the optimization is to maximize the total plastic work for given prescribed displacements. Based on the spatial and temporal discretization, the plastic work can be expressed as a function of the internal variables in all gauss points and all time steps. The optimization problem will be solved by using the method of moving asymptotes (MMA), cf. [4] and consequently the gradients of the constraints and the objective function with respect to the design variables are required. In contrast to elasticity, plasticity is path-dependent which requires that the entire load path needs to be included in the sensitivity analysis. In this work, the adjoint method for coupled transient problems presented in [3] will be exploited. In this approach the discrete constitutive equations and mechanical balance laws are enforced via Lagrangian multipliers in each load step. The Lagrangian multipliers are then obtained from the solution to a sequence of adjoint problems. To avoid mesh sensitivity, use is made of a PDE based filter strategy.

---

*Corresponding author. Email: Mathias.Wallin@solid.lth.se

NUMERICAL RESULTS

The finite strain plasticity model has been used to simulate the response of the simple boundary value problem depicted
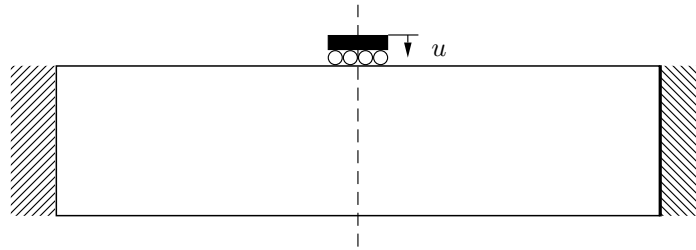

Figure 1: Illustration of geometry of the design domain and boundary conditions used in the numerical example. Due to symmetry only the right hand side of the structure is included in the numerical model.

in Fig. 1. Initially, the design domain is filled with 50% material and after the optimization procedure the optimal design is shown in Fig. 2.
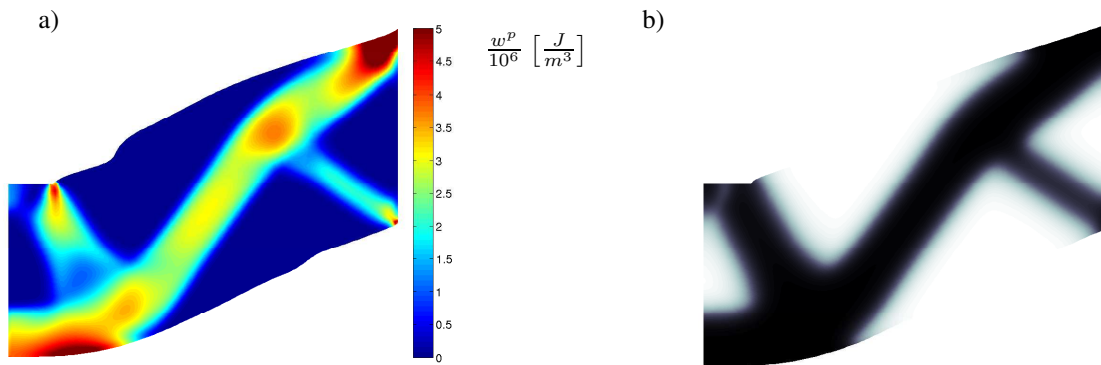
Figure 2: a) Distribution of plastic work, w^p, throughout the design in the deformed state. b) Optimal design.

From Fig. 2a it can be concluded that the plastic work is at maximum where the load is applied and where the structure is attached to the wall. The peak of the plastic work is located at the upper right corner of the structure. In Fig. 2b, the optimal design is plotted and a comparison to simulations using the assumption of small strains reveals that the optimal design will be highly influenced by the load level.

References

[1] Maute, K., Schwarz, S., Ramm, E.: Adaptive topology optimization of elastoplastic structures. Structural Optimization **15**(2), 81–91 (1998)
[2] Simo, J.C., Miehe, C.: Associative coupled thermoplasticity at finite strains: Formulation, numerical analysis and implementation. Comput. Methods Appl. Mech. Engng. **98**, 41–104 (1992)
[3] Michaleris, P., Tortorelli, D.A., Vidal, C.A.: Tangent operators and design sensitivity formulations for transient non-linear coupled problems with applications to elastoplasticity. International Journal for Numerical Methods in Engineering **37**(14), 2471–2499 (1994)
[4] Svanberg, K.: The method of moving asymptotes- a new method for structural optimization. Int. J. Numer. Meth. Engng. **24**, 359–373 (1987)

STRUCTURAL TOPOLOGY OPTIMIZATION OF WIND TURBINE BLADES FABRICATED BY ADDITIVE MANUFACTURING

Miguel Fernandez-Perez[1a)], José Pedro Blasques[2]
[1]Vestas Wind Systems A/S, Aarhus, Denmark
[2]Department of Wind Energy, Technical University of Denmark, Roskilde, Denmark

Summary This article proposes a method to identify optimal wind turbine blade structures fabricated by additive manufacturing based on topology optimization techniques. The structural model is based on the beam cross-sections through a 2D finite element representation. The optimization problems are formulated through the blade properties and response at the cross-section level. The numerical experiments performed challenge the topology optimization method proposed against several problem formulations, geometries and candidate materials.

INTRODUCTION

Large scale wind turbine blade designs are heavily influenced by the manufacturing constraints currently inherent in their production using fiber-reinforced composites. The emergence of industrial-scale additive manufacturing techniques has the potential to release most manufacturing constraints from design, thus enable novel blade structures which are more efficient in the use of material in order to withstand loads and capture wind power. Topology optimization techniques allow the highest degree of design freedom for the optimal allocation of structural mass inside an available design space. Therefore, it is considered here as the methodology for conceptual design of wind turbine blades built by additive manufacturing.

METHODOLOGY

The optimization problems are based on the structural model of a blade by Timoshenko beam finite elements. These are defined from the stiffness and mass matrices at the beam cross-section level. Through a 2D solid finite element discretization of a beam slice, its cross-section stiffness matrix is obtained using the cross-section analysis tool BECAS [1]. The formulated problems use the 2D FE discretization of the beam cross-sections as design variables through the SIMP parameterization extended for multiple materials. The objective is to minimize the overall structural mass of the blade with constraints formulated in terms of the cross section deformations described by the in- and out-of-plane strains and curvatures, due to the forces and moments along the blade. The restrictions on the deformations along the blade are set attending to structural and aero-elastic criteria. The loads and deformations are pre-processed from the DTU-10MW-RWT [2] benchmark blade, from nonlinear time-domain wind turbine simulations using the aero-elastic code Hawc2 [3]. The optimization is solved by the interior point solver IPOPT [4], using the analytical solutions of the objective and constraint functions and their sensitivities.

RESULTS AND DISCUSSION

The results presented demonstrate the ability of the proposed methodology to generate optimal topologies of a set of cross-sections along a wind turbine blade, by achieving the lowest mass possible while ensuring that it withstands multiple extreme load cases. The topologies for each cross-section are obtained from a very fine discretization of the design space available inside a predefined aero-foil surface. The computational expense of these problems is orders of magnitude lower than the full blade discretization with solid 3D finite elements. This level of refinement can reflect the low volume fraction that characterizes modern wind turbine blade structures. The solutions for multiple material topology optimization problems reflect the influence of combining orthotropic materials in the topology to optimally carry loads inside a blade. The topologies obtained are reproduced as small-scale prototypes through additive manufacturing.
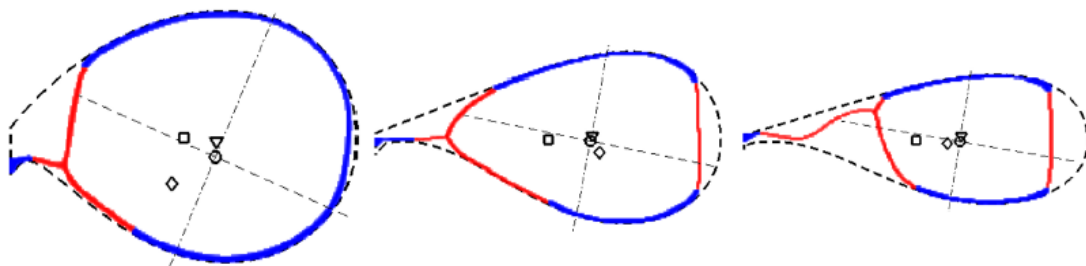

Figure 1 Topologies with minimum mass that comply with deformation restrictions on the cross-sections of the 10MW-RWT blade at 15m, 21m and 28m, respectively. Each topology is composed of unidirectional (blue) and bidirectional (red) glass fiber composite laminates. The design space is the area enclosed by the dashed line.

---

a) Corresponding author. Email: mifpe@vestas.com.
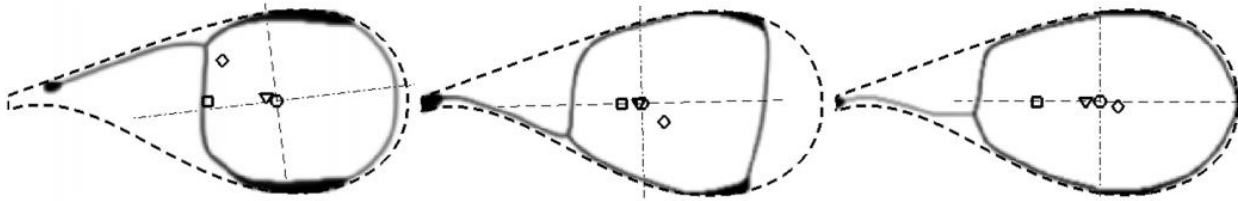
Figure 2 Topologies with minimum isotropic material that comply with deformation restrictions on each strain and curvature component set by the benchmark 10MW-RWT blade at 21m. The topology on the left fulfills a more restrictive constraint for the curvature around the in-plane horizontal axis (higher flapwise stiffness). The central topology allows a lower curvature around the in-plane vertical axis (higher edgewise stiffness). The topology on the right is restricted to a lower twist (higher torsional stiffness).

References

[1] Blasques, J. P.; Stolpe, M.: Multi-material topology optimization of laminated composite beam cross sections. *Composite Structures*, 2012, vol. 94, no 11, p. 3278-3289.

[2] Bak, C. et al.: "Light Rotor: The 10-MW reference wind turbine." *EWEA 2012-European Wind Energy Conference & Exhibition*. 2012.

[3] Larsen, T. J.; Hansen, A. M.: *How 2 HAWC2, the user's manual*. Risø National Laboratory, 2007.

[4] Wächter, A.; Biegler, L. T.: On the implementation of an interior-point filter line-search algorithm for large-scale nonlinear programming.*Mathematical programming*, 2006, vol. 106, no 1, p. 25-57.

STRUCTURAL DESIGN UNDER DAMAGE CONSTRAINTS WITH XFEM AND LEVEL SETS.

Lise Noël [*1], Pierre Duysinx[2], and Kurt Maute[3]

[1,2]*Department of Aerospace and Mechanics, University of Liège, Liège, Belgium*
[3]*Center for Aerospace Structures, University of Colorado, Boulder, Colorado, USA*

Summary This work aims at developing tools to design structures that can sustain a certain level of degradation, i.e. structures that present a low sensitivity to damage. To achieve this goal, an optimization approach is chosen. The analysis of the structures is performed resorting to an XFEM-level set framework. The damage propagation is represented through a non-local model and solved resorting to a non-linear analysis controlled by prescribed displacement. To optimize structures considering a potential degradation, a sensitivity analysis of the damage process is required. The latter is carried out through a fully analytical approach and considering both the direct and the adjoint formulations. Finally, the developed methodology is applied to design 2D structures undergoing damage constraints. The influence of the degradation of the materials constituting the structures can be observed on the optimized designs.

INTRODUCTION

Composite materials exhibits extremely interesting properties as they combine a high stiffness and a very light weight. However, their integration in structures is made difficult because of their high damage sensibility. The latter is scarcely taken into account while designing structures. Therefore, this work aims at developing a systematic methodology to design structures exhibiting a certain resistance to degradation. An optimization approach is chosen. To represent complex geometries and deal with large shape modifications, a level set representation of the geometry advantageously combined with the extended finite element method (XFEM) is used. The degradation of the material is represented using a non-local damage model, which reduces the material stiffness by a scalar damage value D. To solve optimization problem with damage constraints, a sensitivity analysis of the damage process is required. As damage growth is an irreversible process, the history of the structural response has to be taken into account. A fully analytical approach is developed to perform the sensitivity analysis accurately and efficiently. Finally, ongoing work aims at applying the developed tools to design structures with damage constraints.

FRAMEWORK

The structural response is obtained combining the XFEM and a level set representation of the geometries. The XFEM allows representing discontinuities, such as material interfaces, within finite elements. A fixed mesh can be used through the optimization process and costly remeshing operations are avoided. The level set description of the geometries enables to represent discontinuities, interfaces . . . implicitly. It allows an easy handling of moving boundaries.

DAMAGE MODEL

The degradation of the materials is represented using a non-local damage model. The damage is given by a scalar value D evaluated at each Gauss point of the structure. The stiffness of the materials are directly reduced by these damage values. The damage growth is characterized by an evolution law depending on the displacement $\mathbf{u}$: $\mathbf{D} = g(\mathbf{u})$. The obtained damage variables $\mathbf{D}$ are then smoothed using a smoothing function f^S to avoid abrupt change from zero to non-trivial values. Finally, a damage filter is applied to the smoothed damage values $\mathbf{D}^S$ to prevent the localization of the degradation in a thin strip of elements.

DAMAGE PROCESS ANALYSIS

The damage process is non-linear and presents a limit point in its force-displacement curve. Classical iterative solvers, as Newton-Raphson, can no longer be used except if dealing with low damage values. A displacement controlled solver, based on imposed incremental displacements at each iteration, is then implemented to be able to reach high degradation in the materials. The problem is solved simultaneously on the displacement $\mathbf{u}$ and the damage $\mathbf{D}$ state variables, collected in a global one $\mathbf{y}$. The damage propagation is an irreversible process and the damage growth history has to be taken into account. This path dependence shows through the residuals, given as functions of the current (k) and the previous $(k-1)$ iterations and the design parameters $\mathbf{s}$:

$$\mathbf{R}^{(k)} = \mathbf{R}(\mathbf{y}^{(k)}, \mathbf{y}^{(k-1)}, \mathbf{s}). \tag{1}$$

*Lise.Noel@ulg.ac.be

DAMAGE PROCESS SENSITIVITY ANALYSIS

To perform the sensitivity analysis, a fully analytical approach, inspired from Michaleris et al. [3] is developed. The evaluation of the derivatives is following and extending the basic methodology explained in Noël et al. [2]. The derivatives of an objective/constraint function $\mathcal{F}$ with respect to a particular design parameter s_i is given as:

$$\mathcal{F}^{(k)} = \mathcal{F}(\mathbf{y}^{(k)}, \mathbf{s}), \qquad \frac{d\mathcal{F}^{(k)}}{ds_i} = \frac{\partial \mathcal{F}^{(k)}}{\partial s_i} + \frac{\partial \mathcal{F}^{(k)}}{\partial \mathbf{y}^{(k)}} \frac{d\mathbf{y}^{(k)}}{ds_i}. \tag{2}$$

To evaluate this expression, the derivatives of the state variables $\mathbf{y}$ with respect to the considered design parameter s_i are required. They can be obtained through the computation of the derivatives of the residuals $\mathbf{R}$:

$$\frac{d\mathbf{R}^{(k)}}{ds_i} = \frac{\partial \mathbf{R}^{(k)}}{\partial s_i} + \frac{\partial \mathbf{R}^{(k)}}{\partial \mathbf{y}^{(k)}} \frac{d\mathbf{y}^{(k)}}{ds_i} + \frac{\partial \mathbf{R}^{(k)}}{\partial \mathbf{y}^{(k-1)}} \frac{d\mathbf{y}^{(k-1)}}{ds_i}. \tag{3}$$

Using the direct (resp. adjoint) approach and proceeding from the first (resp. last) to the last (resp. first) iterations, the derivatives of the objective/constraint function can be recovered provided that $\frac{\partial \mathbf{R}^{(k)}}{\partial s_i}$, $\frac{\partial \mathbf{R}^{(k)}}{\partial \mathbf{y}^{(k)}}$ and $\frac{\partial \mathbf{R}^{(k)}}{\partial \mathbf{y}^{(k-1)}}$ are known.

VALIDATION

The accuracy of the developed sensitivity analysis is illustrated on a simple benchmark example: a plate with a hole. The considered problem is illustrated in Figure 1 and all the used parameters are given in Table 1. The derivative of the compliance with respect to the four design parameters a, b, ξ, η is shown in Figure 2. One can see that the sensitivity results using finite difference (FD) are in very good agreement with the analytical ones either resorting to the direct (A Direct) or the adjoint (A adjoint) formulations.

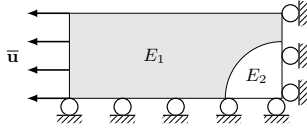Figure 1: Plate with a hole: description.

Table 1: Plate with a hole: parameters.

Dimensions	[m]	$L = 7.5,\ l = 3$
Elastic moduli	[N/m²]	$E_1 = 3 * 10^{10},\ E_2 = 3 * 10^4$
Displacement	[m]	$\bar{u} = 10^{-4}$
Level set function		$\phi(x,s) = (\frac{x}{a})^\xi + (\frac{y}{b})^\eta - 1$
Gauss points per subelement		$n_{gp} = 7$
Strain threshold		$\varepsilon_{th} = 10^{-4}$
Smoothing parameter		$\eta_S = 7$
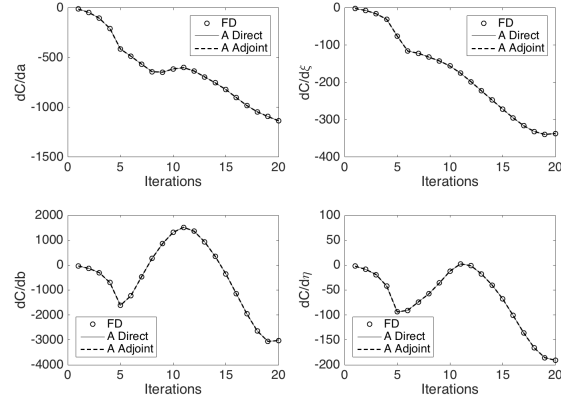
Figure 2: Plate with a hole: sensitivity analysis.

CONCLUSIONS

An optimization approach to design structures resistant to degradation is developed. The analysis is performed within an XFEM-level set framework and resorting to a displacement controlled iterative solver. The sensitivity analysis of the damage process is carried out through a fully analytical approach. Finally, the optimization procedure will be applied to design structures under damage constraints.

References

[1] James K. A., Waisman H.: Failure mitigation in optimal topology design using a coupled nonlinear continuum damage model. Comp. Methods Appl. Mech. Engrg 268:614-631, 2013.

[2] Noël L., Van Miegroet L., Duysinx P.: Analytical sensitivity analysis using the extended finite element method in shape optimization of bimaterial structures. Int. J. Numer. Meth. Engng DOI: 10.1002/nme.5181, 2015.

[3] Michaleris P., Tortorelli D., Vidal C. A.: Tangent operators and design sensitivity formulations for transient non-linear coupled problems with applications to elastoplasticity. Int. J. Numer. Meth. Engng 37:2471-2499, 1994.

A SECOND-ORDER METHOD FOR STRUCTURAL SHAPE OPTIMIZATION WITH THE LEVEL-SET METHOD.

Jean-Léopold Vié [*1,2], Éric Cancès[1], and Grégoire Allaire[2]

[1]*CERMICS, École des Ponts Paristech, Champs-sur-Marne, France*
[2]*CMAP, École Polytechnique, Palaiseau, France*

Summary In topology optimization, there are two formalisms for computing derivatives : one where the variations of the shape are given by a transformation by a diffeomorphism, and another one where they are described by the flow of a regular vector field. In the level-set approach, a shape is represented by the negative domain of a scalar function, and its variations are performed trough a transport equation, namely the Hamilton-Jacobi equation. The present work focuses on computing derivatives in that context. The knowledge of the second order shape derivatives gives also different indications on numerical aspects, that we illustrate with a few examples at the end.

SHAPE DERIVATIVES

The derivation with respect to a shape - a variable subset of $\mathbb{R}^d$ - is a crucial tool in shape optimization. It was widely developed by many authors [5], [6], [12] (and references therein). Here we follow the approach and notations of Murat and Simon [6, 11]. Given a bounded open set Ω_0 of $\mathbb{R}^d$, a variation of the domain is a perturbation by a regular mapping : any domain Ω "close" to Ω_0 can be seen as $\Omega = (\text{Id} + \theta)(\Omega_0)$, where θ is a small displacement field and Id the identity operator on $\mathbb{R}^d$. Following this idea, one can define Fréchet derivatives of functions depending on Ω. Zolésio and co-workers [3, 12], proposed another point of view which consits in considering a moving domain

$$[0, \tau[\ni t \mapsto \Omega_t,$$

with $\Omega_t = X_V(t, \Omega_0)$, where $X_V : [0, \tau[\times\mathbb{R}^d \to \mathbb{R}^d$ is the maximal flow of a regular vector field $V \in C^k(\mathbb{R}_+ \times \mathbb{R}^d; \mathbb{R}^d)$: $\partial_t X_V(t, x) = V(t, X_V(t, x))$ with $X_V(0, x) = x$. This allows one to derive a function of the shape with respect to the time parameter t. The structure of the second order shape derivatives is also known in this context.

DERIVATION WITH RESPECT TO NORMAL EVOLUTION

The goal of this work is to derive along time trajectories, in the framework of the level-set method [1], when the vector field is aligned with the outer normal to the shape at every point of its boundary. Let ϕ_0 be a level-set function representing Ω_0 :

$$\begin{cases} x \in \Omega_0 & \text{if } \phi_0(x) < 0, \\ x \in \partial\Omega_0 & \text{if } \phi_0(x) = 0, \\ x \in \mathbb{R}^d\backslash\overline{\Omega}_0 & \text{if } \phi_0(x) > 0. \end{cases} \tag{1}$$

The boundary of Ω_0 is given by the level set $\{x \in \mathbb{R}^d \mid \phi_0(x) = 0\}$. Given a regular vector field $v \in C^k(\mathbb{R}_+ \times \mathbb{R}^d; \mathbb{R})$, let $\phi_v \in C^k([0, \tau[\times\mathbb{R}^d)$ be a classical solution of the following Hamilton-Jacobi equation (with t small enough) :

$$\begin{cases} \partial_t \phi_v(t, x) + v(t, x) |\nabla_x \phi_v(t, x)| = 0, \\ \phi_v(0, x) = \phi_0(x). \end{cases} \tag{2}$$

For $0 \leq t < \tau$ we define Ω_t as being the set of negative values of $\phi_v(t, \cdot)$: $\Omega_t = \{x \in \mathbb{R}^d \mid \phi_v(t, x) < 0\}$. The perturbation by the Hamiltlon-Jacobi equation corresponds to a normal evolution of the shape. Thanks to the bicharacteristics method for solving the Hamilton-Jacobi equation [10], we can compute shape derivatives in this framework. It appears that the first derivatives are all the same, and that the second derivatives are all different.

EXTENSION OF A SCALAR FIELD - APPROXIMATION OF THE SHAPE HESSIAN.

The first shape derivatives only depends on the trace of the field v on $\partial\Omega$. It is then necessary to extend v to $\mathbb{R}^d$. This question has already been studied in [2, 4]. As a result, v being a descent direction we may choose any extension method from $\partial\Omega$ to $\mathbb{R}^d$. On the first hand, the structure of the second order shape derivatives allows to find an extension method that may be efficient. On the other hand, it helps to approximate the shape Hessian, which is the basic idea of a quasi-Newton method [7].

---

*Corresponding author. Email: viej@cermics.enpc.fr

NUMERICAL EXPERIMENTS

At the end we show some numerical comparison between the presented quasi-Newton, the Newton method and the gradient method. For example, we consider the case of a bridge, and try to minimize the compliance with a fixed penalization on the volume. We consider three algorithms : the gradient method (`GExt0,GExt1` in Figure 2), the Newton method (`NExt0,NExt1`) and a Quasi-Newton method (`QExt0,QExt1`). We also try on each algorithm two extension method. Below we plot the evolution of the objective L, where $L(\Omega_\infty)$ is the minimum of each method.
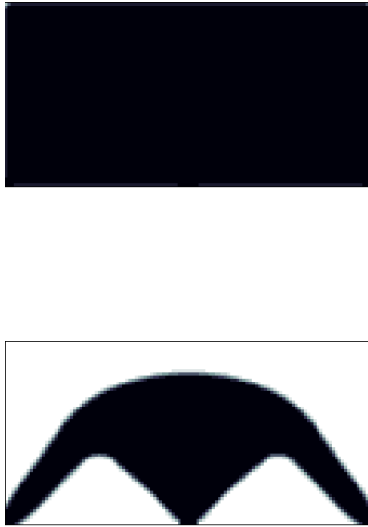

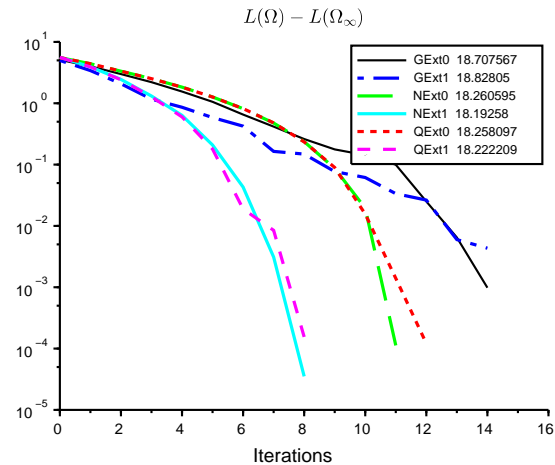Figure 1: Initial and Optimal domains.

Figure 2: Evolution of the error with each optimal value $L(\Omega_\infty)$. The value of $L(\Omega_\infty)$ is different for each method; it is given in the legend.

CONCLUSION

The computation of the second order shape derivatives in the level-set framework and the knowledge of their structures allowed us to propose some extension method coupled to a gradient, a Newton and a Quasi-Newton algorithms. This combination seems at first to be efficient in some basics numerical examples.

References

[1] G. ALLAIRE, F. JOUVE, A-M. TOADER, *Structural optimization using sensitivity analysis and a level-set method*, J. Comp. Phys., Vol 194/1, pp.363-393, 2004.

[2] M. BURGER, *A Framework for the Construction of Level Set Methods for Shape Optimization and Reconstruction*, Interfaces and Free Boundaries, 2002, 5, 301-329

[3] M-C. DELFOUR AND J-P. ZOLÉSIO, *Velocity method and lagrangian formulation for the computation of the shape Hessian*, SIAM Journal on Control and Optimization, 29(6):14141442, 1991.

[4] F. DE GOURNAY, *Velocity Extension for the Level-set Method and Multiple Eigenvalues*, Shape Optimization SIAM Journal on Control and Optimization, 2006, 45, 343-367

[5] A. HENROT, M. PIERRE, *Variation et optimisation de formes*, Springer, 2005.

[6] F. MURAT AND J. SIMON, *Sur le contrôle par un domaine géométrique.* Rapport du l.a., Université Paris VI, 1976.

[7] J. NOCEDAL, S-J. WRIGHT, *Numerical Optimization*, Springer, 1999.

[8] A. NOVRUZI, J-R. ROCHE, *Second order derivatives, Newton method, application to shape optimization*, INRIA, 1995.

[9] S. OSHER, J-A. SETHIAN, *Fronts propagating with curvature-dependent speed : Algorithms based on Hamilton-Jacobi formulations*, Journal of Computational Physics , 1988, Vol 79, pp 12-49.

[10] J. RAUCH, *Hyperbolic partial differential equations and geometrics optics*, volume 133 of Graduate Studies in Mathematics. American Mathematical Society, 2012.

[11] J. SIMON, *Differentiation with respect to the domain in boundary value problems*, Numer. Funct. Anal. Optim., 2:649687, 1980.

[12] J. SOKOLOWSKI AND J-P. ZOLESIO, *Introduction to Shape Optimization*, volume 16 of Springer Series in Computational Mathematics. Springer Berlin Heidelberg, 1992.

ON NONLINEAR FILTERS IN TOPOLOGY OPTIMIZATION

Eddie Wadbro[*1] and Linus Hägg[1]

[1]*Department of Computing Science, Umeå University, SE–901 87 Umeå, Sweden.*

Summary It is well known that material distribution topology optimization problems often are ill-posed if no restriction or regularization method is used. A drawback with the standard linear density filter is that the resulting designs have large areas of intermediate densities, so-called gray areas, especially when large filter radii are used. To produce final designs with less gray areas, several different methods have been proposed; for example, projecting the densities after the filtering or using a nonlinear filtering procedure. In a recent paper, we presented a framework that encompasses a vast majority of currently available density filters. In this talk, we present that these nonlinear filters ensure existence of solutions to a continuous version of the minimal compliance problem. Moreover, we show numerical experiments that illustrates that cascades of these nonlinear filters can be used to efficiently solve large-scale topology optimization problems.

INTRODUCTION—THE fW-MEAN FILTERED CONTINUOUS MINIMAL COMPLIANCE PROBLEM

Since the seminal paper by Bendsøe and Kikuchi [2] regarding topology optimization of linearly elastic continuum structures, the field of topology optimization has been subject to intense research. It is well known that material distribution topology optimization problems often are ill-posed if no restriction or regularization method is used. Amongst the most popular techniques to achieve mesh-independent designs is to use a filtering procedure. In a classic paper, Bourdin [4] established existence of solutions to a continuous version of the linearly filtered minimal compliance problem. Since the introduction of the linear density filter by Bruns and Tororelli [5], a whole range of *nonlinear* filters developed to produce final designs with less gray areas has been presented [6, 8, 9]. We have recently introduced the class of generalized fW-mean filters that include the vast majority of filters used in topology optimization [10] and provide a common framework for analyzing and evaluating various filters.

Here, we consider a standard test problem, namely the problem of designing a linearly elastic structure with minimal compliance given a certain load-case and an upper bound V on the availiable volume. Let $\Omega \subset \mathbb{R}^d$ be a bounded and connected domain in which we want to place our structure. We describe the design by using the material distribution approach to topology optimization and define the spatially varying forth order elasticity tensor $E(\rho) = (\underline{\rho} + (1 - \underline{\rho})P(F(\rho)))E_0$, where $\underline{\rho} > 0$, $F(\rho)$ is a continuous version of the fW-mean filter, $P : [0,1] \to [0,1]$ is a smooth and invertible penalty function, and E_0 is a constant forth order elasticity tensor. The above formulation includes the case when the problem is penalized using SIMP [3], that is the case when $P(x) = x^p$ for some $p > 1$. The continuous fW-mean filtered density is, for $x \in \Omega$, given by

$$\big(F(\rho)\big)(x) = f^{-1}\left(\int_\Omega w(x,y)(f \circ \rho)(y)\,\mathrm{d}y\right), \tag{1}$$

where $f : [0,1] \to [f_{\min}, f_{\max}] \subset \mathbb{R}$ is a smooth and invertible function and $w(x, \cdot)$ is a non-negative normalized weight function. We let $\mathcal{A} = \big\{\rho \mid 0 \le \rho \le 1 \text{ a.e. on } \Omega, \|F(\rho)\|_{L^1(\Omega)} \le V\big\} \subset L^\infty(\Omega)$ denote the set of admissible designs and assume that the boundary $\partial\Omega$ is Lipschitz and that the structure is fixed at a non-empty open boundary portion $\Gamma_D \subset \partial\Omega$. The displacement of the structure u solves the problem, find $u \in \mathcal{U}$ such that $a(\rho; u, v) = \ell(v) \; \forall v \in \mathcal{U}$, where $\mathcal{U} = \big\{u \in H^1(\Omega)^d \mid u|_{\Gamma_D} \equiv 0\big\}$ is the set of kinematically admissible displacements, a is the energy bilinear form, and ℓ denotes the load linear form. In this setting, the minimal compliance problem admits solutions, that is, we can formulate and prove the following theorem.

Theorem 1. *There exists a solution to the following variation of the minimal compliance problem. Find $u^* \in \mathcal{U}^*$ such that $\ell(u^*) = \inf\limits_{u \in \mathcal{U}^*} \ell(u)$, where $\mathcal{U}^* = \big\{u \in \mathcal{U} \mid \exists \rho \in \mathcal{A} \text{ such that } a(\rho; u, v) = \ell(v) \; \forall v \in \mathcal{U}\big\}$.*

Remark 1. *Theorem 1 also holds true for a cascade of fW-mean filters of the form* (1) *with different filter functions f.*

NUMERICAL EXPERIMENTS

Figure 1 shows the final physical designs (not post processed nor sharpened!) of cantilever beams optimized with aim of minimizing their compliance when a load is uniformly distributed over the middle 10 % of the beam's right side; a standard test problem in topology optimization. Here, we use an open–close filtering strategy (comprising a cascade of four fW-mean filters) over octagonal shaped neighborhoods as suggested by Sigmund [8]. However, instead of using exponential averaging, we use harmonic averaging as introduced in topology optimization by Svanberg and Svärd [9]. Remark that even though the open–close filtering strategy in general does not guarantee minimal size control for both structure and void [7], our

---

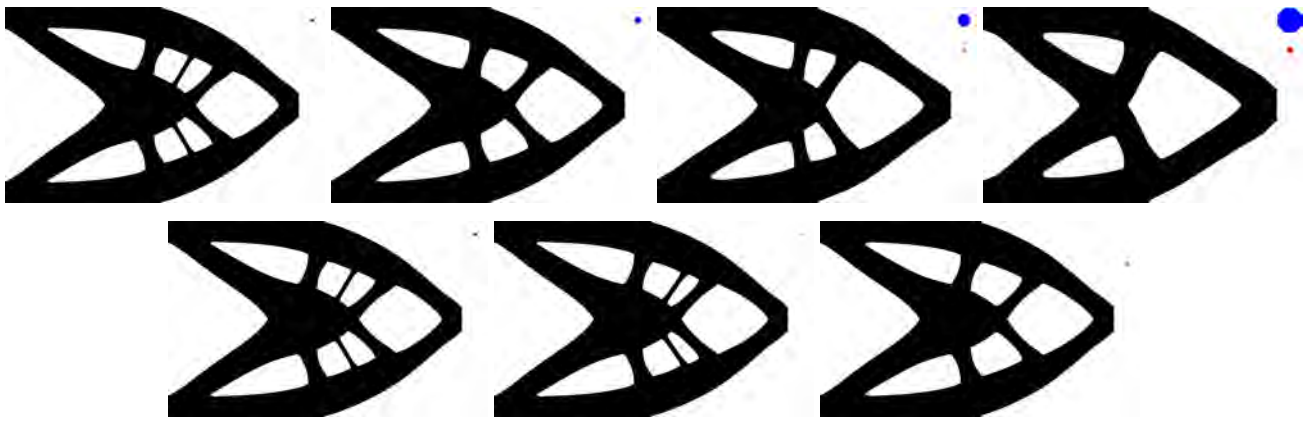[*]Corresponding author. Email: eddiew@cs.umu.se

Figure 1: Optimized cantilever beams using 1536×1024 elements, and different harmonic open–close filters. The filter neighborhoods are indicated in the upper-right corner of each sub-figure, and the upper neighborhood corresponds to the open step while the lower corresponds to the close step. Top row, the relative ratio between the filter radius used in the open and closed step is 4 for all experiments, filter radii increases toward the right. Bottom row, the relative ratio between the filter radius used in the open and close step is from left to right, 4, 1, and 1/4, respectively.

numerical experiments for the minimal compliance problems suggest that this strategy in combination with a gradient based optimization method guides the design into a desirable configuration. The volume fraction used was 0.5 and the final measure of non discreteness (of the physical design) is at most 0.3 %. To the best of our knowledge, previously no contribution has used an open–close or close–open filtering strategy to solve problems with more than a few tens of thousands degrees of freedom. Here, we capitalize on our fast filtering strategy [10] and use a modified version of the 2D multigrid-CG topology optimization code by Amir et al. [1] to solve design problem with approximately 1.5 million degrees of freedom. In each sub-figure in Figure 1, the upper neighborhood corresponds to the open step that should impose a minimum size on the material regions while the lower neighborhood corresponds to the close step that should impose a minimum size on the void regions. The beams in the top row are optimized with increasing filter radii from left to right while the beams in the bottom row are optimized by using a different ratio between the filter radii in the open and close step. As reference, the leftmost figures on both rows shows the same design.

For the cantilever beam in the third subfigure from the left in the top row in Figure 1, the size of the filter neighborhoods are $3,465$ elements for the *open step* and 249 elements for the *close step*. The solution process required 182 iterations and took 3 hours, the filtering and modification of sensitivities accounted for around 20 % of this time, on a desktop equipped with an Intel Xeon E5-1650 v3 CPU and 32 GB RAM. It should be noted that the fast summation algorithm was executed almost $40,000$ times and that the elementwise evaluation of the nonlinear functions, corresponding to f in equation (1), dominated the time required for the filtering and evaluation of the sensitivities.

References

[1] O. Amir, N. Aage, and B. S. Lazarov. On multigrid-CG for efficient topology optimization. *Struct. Multidiscip. Optim.*, 49(5):815–829, 2014.

[2] M. P. Bendsøe and N. Kikuchi. Generating optimal topologies in structural design using a homogenization method. *Comput. Methods Appl. Mech. Engrg.*, 71:197–224, 1988.

[3] M. P. Bendsøe and O. Sigmund. *Topology Optimization. Theory, Methods, and Applications*. Springer, 2003.

[4] B. Bourdin. Filters in topology optimization. *Internat. J. Numer. Methods Engrg.*, 50:2143–2158, 2001.

[5] T. E. Bruns and D. A. Tortorelli. Topology optimization of non-linear elastic structures and compliant mechanisms. *Comput. Methods Appl. Mech. Engrg.*, 190:3443–3459, 2001.

[6] J. K. Guest, J. H. Provost, and T. Belytschko. Achieving minimum length scale in topology optimization using nodal design variables and projection functions. *Internat. J. Numer. Methods Engrg.*, 61(2):238–254, 2004.

[7] M. Schevenels and O. Sigmund. On the implementation and effectiveness of morphological close-open and open-close filters for topology optimization. *Struct. Multidiscip. Optim.*, In press:1–7, 2016.

[8] O. Sigmund. Morphology-based black and white filters for topology optimization. *Struct. Multidiscip. Optim.*, 33(4–5):401–424, 2007.

[9] K. Svanberg and H. Svärd. Density filters for topology optimization based on the pythagorean means. *Struct. Multidiscip. Optim.*, 48(5):859–875, 2013.

[10] E. Wadbro and L. Hägg. On quasi-arithmetic mean based filters and their fast evaluation for large-scale topology optimization. *Struct. Multidiscip. Optim.*, 52(5):879–888, 2015.

ON SLOWLY MOVING BOUNDARIES IN DENSITY BASED STRUCTURAL TOPOLOGY OPTIMIZATION

Susana Rojas-Labanda[1] and Mathias Stolpe [*][1]

[1]*Technical University of Denmark, DTU Wind Energy Department, Roskilde, Denmark*

Summary Structural topology optimization problems are commonly defined using material interpolation schemes. One of the challenges observed in the review article [3] for this density based topology optimization is the slow convergence of the solvers when an almost solid-and-void design is found. In this work, we numerically investigate the reasons for slowly moving boundaries, which are often encountered in practice, and attempt to indicate how this problem can be remedied.

INTRODUCTION

The recent review article [3] studies, among many other topics, the way optimization algorithms generate the designs in structural topology optimization. The design parametrization is based on density based topology optimization combined with the SIMP approach [2]. The review article [3] reports that "the optimization rapidly finds a fairly good design but requires a very large number of iterations for just slight improvements in objective function but rather large changes in geometry". Thus, the final geometry is found by slowly moving the boundaries. This behaviour is illustrated in [3] by two different examples, namely the inverter mechanism design and a minimum compliance problem resulting in a two-bar truss like structure.

The authors of [3] suggest that the underlying reasons for the slowly moving boundaries is the use of the SIMP approach. However, other reasons could be the choice of problem formulation, the choice of optimization algorithms, the choice of regularization technique, a combination of several of these issues, or even something completely different.

The problems presented in [3] are only formulated in the nested approach. In contrast, this note shows the results using also the Simultaneous Analysis and Design (SAND) formulation of the problem. Furthermore, only two numerical optimization algorithms were tested in [3], the Method of Moving Asymptotes (MMA) method [5] and the Optimality Criteria (OC) method [6]. These two algorithms are first-order methods developed for structural optimization. However, none of the general purpose state-of-the-art nonlinear methods have been tested. The benchmarking study in [1] suggests that interior point methods, such as IPOPT [4], work particularly well for structural topology optimization problems. In fact, since they are second-order methods, the number of iterations is considerably reduced. Furthermore, special purpose second-order optimization methods have been successfully implemented in [1] for the minimum compliance problem, such as TopSQP (Sequential Quadratic Programming solver) and TopIP (interior point method).

We expect that the issue of slowly moving boundaries in topology optimization problems can be avoided, or at least decreased, by using different optimization solvers. The numerical results in this work support our hypothesis and suggest that this issue can potentially be reduced or even remedied by changing optimization methods.

PROBLEM FORMULATION

The structural topology optimization problem which is considered throughout is the classical single load minimum compliance problem

$$
\begin{aligned}
\underset{\mathbf{t}}{\text{minimize}} \quad & \mathbf{u}^T(\mathbf{t})\mathbf{K}(\mathbf{t})\mathbf{u}(\mathbf{t}) \\
\text{subject to} \quad & v(\mathbf{t}) \leq V \\
& \mathbf{0} \leq \mathbf{t} \leq \mathbf{1},
\end{aligned}
\tag{1}
$$

where $v(\mathbf{t})$ is the volume of the structure described by the design variables $\mathbf{t}$ and $V > 0$ is the volume limit. The nodal displacements $\mathbf{u}(\mathbf{t})$ are obtained from the equilibrium equations $\mathbf{K}(\mathbf{t})\mathbf{u} = \mathbf{f}$. The stiffness matrix is described with $\mathbf{K}(\mathbf{t})$. More details about the formulation of the problem (in both nested and SAND formulation) can be found in e.g. [2] and [1].

NUMERICAL EXPERIMENTS

In [3] a simple minimum compliance problem, namely 2-bar (see Figure 1), is used to illustrate the slowly moving boundaries issue. The design domain is discretized using 50 by 20 elements, with a volume fraction equal to 0.2. A density filter is used to avoid checkerboards and mesh-dependency problems. The SIMP penalization parameter is set to $p = 3$. Finally, the contrast gap between the Young's modulus of the void and solid material is set to $E_0/E_{\min} = 10^3$ as in [1].

Two different initial designs are considered to compare and study the slowly moving boundaries behaviour as in [3]; an uniform density (of 0.2) and a solid bar in the middle of the domain satisfying the volume constraint, see Figure 1.

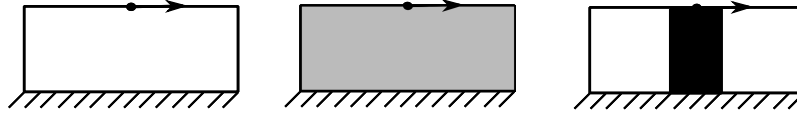[*]Corresponding author. Email: srla@dtu.dk

Figure 1: Design domain of the studied minimum compliance benchmarked problem (left), uniform density starting point (middle) and solid bar starting point (right).

Table 1: The table contains the objective function value and the number of iterations when the benchmarked problem is solved with MMA, TopSQP, TopIP, IPOPT-N and IPOPT-S. The table shows the results using two different starting points; the uniform design (U) and the solid band (S B).

Solver	MMA		TopSQP		TopIP		IPOPT-N		IPOPT-N*		IPOPT-S	
Initial point	U	S B	U	S B	U	S B	U	S B	U	S B	U	S B
Compliance	11.18	11.47	11.23	11.47	11.19	11.22	11.72	11.37	11.81	11.80	11.18	11.22
Iterations	40	173	34	108	58	48	60	266	74	111	50	85

Different optimization algorithms, such as MMA, TopSQP, TopIP (monotone approach), and IPOPT, are used to conduct the numerical experiments. In particular, the interior point solver in IPOPT is used to solve both the nested (IPOPT-N) and the SAND (IPOPT-S) formulation. All details of the parameter selection and implementation can be found in [1].

Table 1 shows the number of iterations and the objective function value at the local minima obtained by the solvers for the two different starting points. All the executions are run until some first-order necessary optimality conditions are numerically satisfied (norm of the KKT conditions is less than or equal to 10^{-4} for MMA and 10^{-6} for the rest).

For this particular problem, the slowly moving boundaries cannot be visually observed in most of the interior point methods presented, such as TopIP, IPOPT-S, and IPOPT-N* (monotone barrier parameter strategy selected with an initial barrier parameter value equal to 10). IPOPT-N uses a BFGS approximation while TopIP and IPOPT-S use the exact Hessian of the Lagrangian. Thus, the two latter solvers requires fewer iterations. In contrast, TopSQP behaves similar to MMA even if second-order information is used.

The reason of this performance is the ability of the interior point method to take advantage of the barrier function. Within few iterations, interior point methods modify the starting point to a "grey" design.

Nevertheless, further investigations are needed to avoid the slow moving boundaries when it is produced close to the optimal design, as in the inverter example. Since this effect occurs at the end of the optimization process, the barrier penalty parameter is very small and it will have very little effect in the solver.

CONCLUSIONS

The numerical results presented in Table 1 suggest (but by no means prove) that the choice of the optimization method might affect the slowly moving boundaries behaviour observed in the review article [3]. The remedy to this issue is thus to switch to second-order interior point solvers. However, this suggestion is only supported by a small and specific numerical experiment and must therefore be confirmed (or refuted) by additional and extensive numerical and theoretical surveys.

References

[1] Rojas-Labanda, S., Stolpe, M.: Mathematical programming methods for large-scale topology optimization problems. PhD Thesis, Technical University of Denmark, DTU Wind Energy PhD-0057, 2015.

[2] Bendsøe, M. P. and Sigmund, O.: Topology optimization: Theory, methods and applications. Springer, 2003.

[3] Sigmund, O. and Maute, K.: Topology optimization approaches. Structural and Multidisciplinary Optimization, 48(6):1031–1055, 2013.

[4] Wächter, A. and Biegler, L. T.: On the implementation of an interior point filter line-search algorithm for large-scale nonlinear programming. Mathematical Programming, 1(106):25–57. 2006.

[5] Svanberg, K.: The method of moving asymptotes - A new method for structural optimization. International Journal for Numerical Methods in Engineering, 24(2):359–373, 1987.

[6] Andreassen, E., Clausen, A., Schevenels, M., Lazarov, B.S. and Sigmund, O.: Efficient topology optimization in MATLAB using 88 lines of code. Structural and Multidisciplinary Optimization, 43(1):1–16, 2011.

TOPOLOGY OPTIMIZATION FOR ADDITIVE MANUFACTURING: CONSIDERING SUPPORT STRUCTURES THROUGH PROJECTED UNDERCUT PERIMETER

Xiaoping Qian [*1]

[1]*Department of Mechanical Engineering, University of Wisconsin-Madison, Madison, WI, USA*

Summary Additive manufacturing can build parts of complex shape through support structures. The fabrication of such support structures leads to the waste of the materials, build time and energy. This paper presents an approach for incorporating support structure consideration into topology optimization for additive manufacturing. A new measure based on the perimeter length of boundary with undercut, projected along the build direction, is developed to characterize the support volume. By constraining this projected undercut perimeter in topology optimization, the amount of support structures in the resulting designs can be effectively controlled. Our study has also revealed one interesting finding, that is, accounting for support structures in topology optimization can, in some cases, lead to designs with better performance, in addition to the reduction of support volume.

INTRODUCTION

Additive manufacturing builds part by depositing materials layer-by-layer under computer control. For part shapes with undercuts, sacrificial support structures are usually used to hold the subsequent layers. The fabrication of such support structures leads to the waste of the materials, build time and energy. Topology optimization [1] is a computational design tool that can generate optimal topology and shape under physical constraints. As a design tool, it has been become the method of choice for exploiting shape freedom of additive manufacturing. However, thus far, limited research [2] has been done in reducing support structures during the part design stage.

In order to consider support structures in topology optimization, a new measure based on the perimeter length of boundary with undercut, projected along the build direction, is developed in this paper to characterize the support volume. By constraining this projected undercut perimeter (PUP) in topology optimization, the amount of support structures in the resulting designs can be effectively controlled.

CONSIDERING PROJECTED UNDERCUT PERIMETER IN TOPOLOGY OPTIMIZATION

Our topology optimization formulation for considering support structures via PUP is as follows

$$\min_{\mathbf{u} \in U, \gamma} \quad C(\mathbf{u}) \qquad \text{Compliance} \qquad (1a)$$

$$\text{s.t.} \quad a_E(\mathbf{u}, \mathbf{v}) = l(\mathbf{v}), \forall \mathbf{v} \in U_0 \qquad \text{Equilibrium} \qquad (1b)$$

$$\frac{\int_\Omega \gamma \, \mathrm{d}\Omega}{V_0} \le \theta_0, \gamma[0,1] \qquad \text{Volume fraction constraint} \qquad (1c)$$

$$\int_\Omega H(\mathbf{b} \cdot \nabla\gamma)\mathbf{b} \cdot \nabla\gamma \, \mathrm{d}\Omega \le P_0 \quad \text{Projected undercut perimeter constraint} \qquad (1d)$$

$$\frac{\int_\Omega 4\gamma(1-\gamma) \, \mathrm{d}\Omega}{V_0} \le \varepsilon_0 \qquad \text{Density grayness constraint,} \qquad (1e)$$

where V_0 represents the volume of the design domain, θ_0 represents the allowed volume fraction of the material, P_0 represents the allowed projected undercut perimeter, and ε_0 the specified grayness measure [3]. In this formulation, equations (1a), (1b), (1c) form the standard formulation of density based topology optimization of a minimal compliance problem under an equilibrium equation and the volume constraint. In order to take into account the support structures, we here add two additional constraints with (1d) constraining the projected undercut perimeter and (1e) constraining the grayness in the resulting design.

For a density field γ, its spatial gradient $\nabla\gamma$ and directional gradient $\mathbf{b} \cdot \nabla\gamma$ along build direction $\mathbf{b}$, the LHS of (1d) represents the integration of the directional gradient multiplied with the Heaviside function $H(\mathbf{b} \cdot \nabla\gamma)$ over the design domain to obtain. Therefore, when the directional gradient $\mathbf{b} \cdot \nabla\gamma$ is negative, i.e. there is no undercut, this term does nothing. When it has undercut, i.e. the directional gradient is positive, it has contribution to the term in (1d). By constraining this term within a pre-specified value, we constraint the amount of support needed in a design.
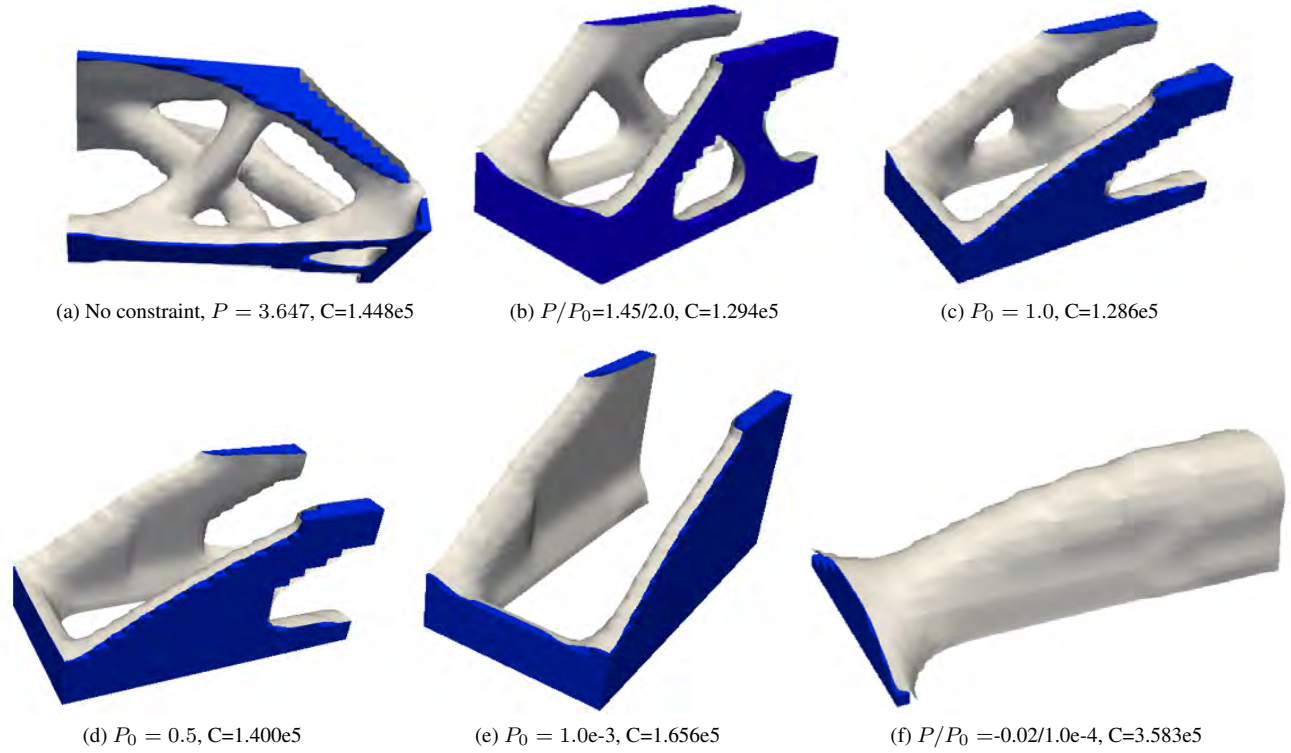
[*]Email: xiaoping.qian@wisc.edu

(a) No constraint, $P = 3.647$, C=1.448e5   (b) P/P_0=1.45/2.0, C=1.294e5   (c) $P_0 = 1.0$, C=1.286e5

(d) $P_0 = 0.5$, C=1.400e5   (e) $P_0 = 1.0e\text{-}3$, C=1.656e5   (f) P/P_0 =-0.02/1.0e-4, C=3.583e5

Figure 1: 3D minimal compliance optimization under different undercut perimeter constraint.

NUMERICAL RESULTS

Figure 1 shows optimized 3D designs under different projected undercut perimeter area. The domain is of size $4 \times 2 \times 2$ and is divided into 9,600 linear tetrahedral elements, consisting of 18,081 nodes. The volume fraction θ_0 is 15% of the design domain. The Young's modulus is 1 for solid and 10^{-9} for the void. The r in the PDE filter is 0.087. All designs are obtained with $\varepsilon_0 = 0.2$, except the last two designs. The last two designs are obtained with $\varepsilon_0 = 0.15$. Figure 1(a) shows two views of the optimized design without the PUP constraint and the compliance is 1.448e5. Optimized design under various PUP constraints and the corresponding compliance are shown in the figure. It can be seen that, as the PUP becomes smaller, the resulting designs have less support volume. In the end, when the PUP becomes close to zero, the resulting designs, Fig. 1(e) and (f), have no undercut. This suggests that the proposed PUP is an effective measure for controlling the support structures. Also, an optimized 3D design with PUP constraint does not necessarily lead to worse compliance since the design in Fig. 1(b), (c), and (d) are all have smaller compliance than the design in Fig. 1(a). This can be ascribed to the fact that multiple local minimums exist for the non-convex optimization problem.

CONCLUSIONS

This paper presents a formulation in topology optimization to take into account support structures via PUP and grayness constraints. Our numerical results demonstrate that PUP is an effective in controlling the amount of support in the optimized design. Accounting for support structures in 3D topology optimization for additive manufacturing may lead to designs with better performance, in additive to the reduction of support structures. This PUP formulation is also computationally efficient and involves just one extra constraint, without the need for solving any state equation.

References

[1] M.P. Bendsøe and O. Sigmund. *Topology Optimization: Theory, Methods, and Applications*. Springer Verlag, 2003.

[2] Andrew T Gaynor and James K Guest. Topology optimization for additive manufacturing: considering maximum overhang constraint. In *15th AIAA/ISSMO multidisciplinary analysis and optimization conference*, pages 16–20, 2014.

[3] Ole Sigmund. Morphology-based black and white filters for topology optimization. *Structural and Multidisciplinary Optimization*, 33(4-5):401–424, 2007.

OVERHANGING CONSTRAINTS IN ADDITIVE MANUFACTURING USING THREE DIFFERENT TOOLS

Simon Bauduin[*1], Maxime Collet[1], and Pierre Duysinx[1]

[1]*Aerospace and Mechanical engineering departement, University of Liege Liege, Belgium*

Summary As manufacturing methods undergo huge evolution thanks to the emergence of additive manufacturing techniques, the interest of a coupling with the topology optimization design tool is highly demanded by industries (such as automotive and aerospace). The challenges are still numerous around such coupling and this work focuses on the overhanging problem related to the metalic additive manufacturing technics (LBM and EBM). To tackle the problem, various research directions are investigated and compared to another.

INTRODUCTION

Topology optimization is widely used as a design tool for advanced application in mechanical, aerospace and automotive industries. This technique offers an optimal distribution of a predetermined amount of material in a given design space. In the last years, a lot of efforts has been invested into the development of high performance methods such as homogenization, SIMP or BESO. However as the state of the art in manufacturing experiences evolution, a coupling between topology optimization and additive manufacturing is needed.

Additive manufacturing has numerous advantages that fits the characteristics of topology optimized designs. It can manufacture highly complex design without high cost increase and furthermore continuous density material of the SIMP method could be manufactured by lattice structures. With all the opportunities given by the additive manufacturing the urge to bind the last one to topology optimization is heavily required.

Specific constraints related to manufacturing issues have to be taken into account [1] such as the need of supports structures to ensure a good heat evacuation during the manufacturing process, as well as to hold up overhanging section as shown in Figure 1. Some researches have been done to try to include this constraint in the optimization problem such as Leary and al [2] or Andrew T. Gaynor [3]. However this work focuses on 3 different methods (projection scheme, computer vision techniques and mechanical approach) to tackle the overhanging problem and compare them .
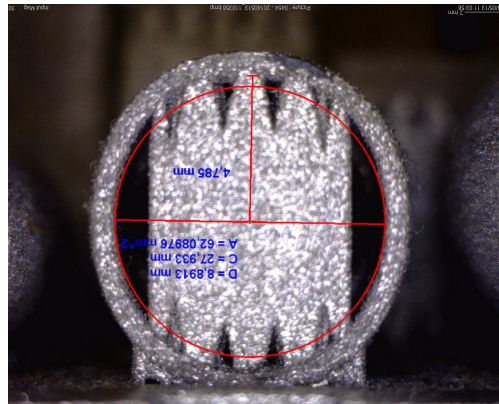

Figure 1: Overhanging problem

METHODS TO TACKLE THE OVEHANGING PROBLEM

Projection scheme Approach

The first approach to be investigated is similar to the idea proposed by Gaynor [3] in his work. A projection scheme [4] with particular shape has to ensure a self supported design. The choice of the shapes are guided by the need to have a big library of different shapes and the superformula of Geilis [5] offers us this diversity of the projective domain. The optimization problem can be expressed as fellows for the projection scheme:

[*]Corresponding author. Email: S.Bauduin@ulg.ac.be

$$\min_{\rho_n, u} \quad \mathbf{f^T u} \tag{1}$$

$$s.t. \quad \mathbf{K(\rho_n)u = f} \tag{2}$$

$$\sum_{e \in \Omega} \rho^e(\boldsymbol{\rho_n})v^e \leq V \tag{3}$$

$$\rho_n^{min} \leq \rho_n \leq 1 \quad \forall \mathbf{n} \in \boldsymbol{\Omega} \tag{4}$$

In the expression, the nodal densities n_i are linearly projected onto the element e if

$$dist_{n_i e} \leq r(\theta_{n_i e}) = \frac{1}{[(|\frac{1}{a}cos(\theta_{n_i e}\frac{m}{4})|)^{n_2} + (|\frac{1}{b}sin(\theta_{n_i e}\frac{m}{4})|)^{n_3}]^{\frac{1}{n1}}} \tag{5}$$

Computer Visison Approach

The second approach tends to use the work done in computer vision researchers to construct the skeleton of the design and check if the latest does not show overhanging problem. This view of using computer vision technics in topology optimization problem was initially introduce by Sigmund [6] and opens up lots of new possibilities.

Body load Approach

The last approach relies more on a mechanical approach by adding body load cases [7] during the manufacturing process. Hence the optimization problem is formulated by introducing multiple body load cases to simulate the printing process and thus tackling the overhanging problem.
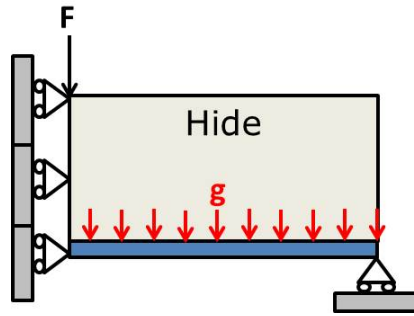

Figure 2: Body load approach

References

[1] B. Meunier : Perspectives de dveloppement pour le couplage optimisation topologique et fabrication additive de composants mecaniques. Master thesis, University of Liege, Liege, Belgium, 2014.

[2] M. Leary, L. Merli, F. Torti, M. Mazur, Milan Brandt : Optimal topology for additive manufacture: A method for enabling additive manufacture of support-free optimal structures. Materials & Design 63:678-690, 2014.

[3] Andrew T. Gaynor : TOPOLOGY OPTIMIZATION ALGORITHMS FOR ADDITIVE MANUFATURING. PhD Thesis, The Johns Hoptkins University, Baltimor, Maryland, USA, 2015.

[4] J. K. Guest, J. H. Prevost, T. Belytschko : Achieving minimum length scale in topology optimization using nodal design variables and projection functions. Int. J. Numer. Meth. Engng 61:238-254, 2004.

[5] J. Geilis : A GENERIC GEOMETRIC TRANSFORMATION THAT UNIFIES A WIDE RANGE OF NATURAL AND ABSTRACT SHAPES. Amercian Journal of Botany 90(3):333-338, 2003.

[6] O. Sigmund : Morphology-based black and white filters for topology optimization. Struct Multidisc Optim 33:401-424, 2007.

[7] M. Bruyneel, P. Duysinx : Note on topology optimization of continuum structure including self weight. Struct Multidisc Optim 29:245-256, 2005.

TOPOLOGY/SIZING OPTIMIZATION OF AICRAFT STRUCTURAL COMPONENTS

Vasily Chedrik[1a)], Sergey Tuktarov[1]
[1]Central Aerohydrodynamic Institute (TsAGI),
Zhukovsky, 140180, Russia

Summary The application of energy-based topology optimization methods together with two-level design method for determination of structural sizes is considered. Main stages of such evolutionary approach to synthesis structural layouts of aircraft components are described. The approach is demonstrated on the example of structural optimization of helicopter wing and tail boom. It is shown that sizing optimization with including strength/buckling/aeroelasticity constraints results in to the design with significantly less weight compared with the one obtained by conventional approach.

INTRODUCTION

Nowadays, leading aviation companies often use topology optimization methods as an efficient tool for obtaining new and lighter structural component designs. Most of such researches are related with design of small structural parts such as ribs, spars, door intercostals, etc. [1]. The application of topology optimization for determination of reasonable structural layout was proven to result in advanced designs. Significant weight reducing is achieved after the sizing optimization of the obtained structural layout. The purpose of this research is to develop novel approach which combines modern topology optimization methods with two-level sizing optimization technique for design of larger aircraft components such as wing, tail and fuselage. Some approaches to design of wing structures with using topology optimization were demonstrated in the papers [2, 3]. The proposed method is based on the integration of the global-local method for sizing optimization described in [4] together with topology optimization in the unified cycle of multidisciplinary design which includes aerodynamic and aeroelasticity analyses.

METHODOLOGY OF TOPOLOGY/SIZING OPTIMIZATION

The general flow-chart of the developed approach is presented in Figure 1 on example of wing design. The first step of the procedure is to build solid topology optimization model and aerodynamic model which are specified by geometric outlines from CAD system. The specified geometric outlines of mechanical body define the place of load-bearing structure or design domain. Some part of the domain is supposed to be fixed and another part is subjected by external loads. The design domain is subdivided in detail on 3D finite elements for analysis of displacements and stresses.
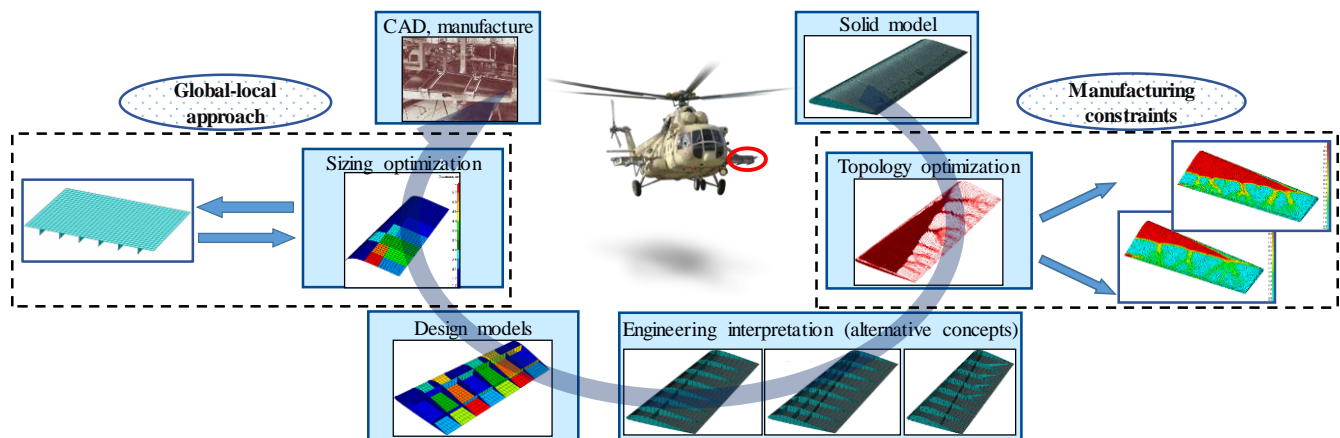

Fig. 1 – Flowchart of topology/sizing optimization

The second step is to perform a set of topology optimizations with different control parameters. The topology optimization results can be slightly different for these parameters. For example, manufacturing constraints with extrusion in vertical direction can give pattern with more explicit place for wing box. The obtained topology patterns allow us to reveal where load-bearing material should be located in global sense. Location of ribs is specified by intuition and then it can be determined by sizing optimization taking into account buckling constraints.

[a)] Corresponding author. Email: chedrik@yandex.ru.

The third step is most complicated and it implies engineering interpretation of the obtained topology results. It is difficult to determine one optimal structure. So we should imagine several alternative structural layouts to choose one of them as optimal. The forth step is generation of finite element models for the alternative structures. These structures we consider as shell/beam ones which usually include skins, ribs and spars. At generation of the models it is necessary to take into consideration various manufacturing constraints such location of control surfaces, fuel tanks and technology factors. The fifth step is accomplishment of design optimization for determination of sizes of structural elements with satisfying stress/buckling/aeroelasticity constraints. Stress and aeroelasticity constraints are involved into the optimization process on the global level model while the buckling constraints are engaged on the local level models of structural panels. The final step is ranking of obtained structural layouts based on comparison of optimal weights.

NUMERICAL RESULTS

The proposed method is demonstrated on the example of helicopter wing design. An aerodynamic model of the wing was developed to determine aerodynamic forces in extreme load cases and to perform aeroelasticity analyses. It was important for this problem to correctly transfer pressure loads from aerodynamic model to FE model. It was performed by interpolation of the obtained pressures with using polynomial function of nodal coordinates on outer surfaces of the FE model. Topology optimization was performed with the aim to minimize compliance at saving 50 percent of initial solid model weight in the final design. The obtained patterns where the load-bearing material should be distributed are shown in Figure 1 (right). Seven alternative structural layouts based on these results and engineering intuition were proposed. The structural optimization under strength/buckling/aeroelasticity requirements for the layouts leads to the final optimal design with different weight values. Comparison of the chosen alternative structural layouts with optimal distribution of material showed that the weight benefit was about 10 percent owing to the choice of location of the primary elements. The best structural layout is two-spar wing with additional sloped ribs at the wing end rear part. Note that this design is lighter by 60% than the design obtained by traditional methods used in design companies. The second example is a helicopter tail boom. The optimization procedure and topology and sizing results are presented in pictures in Figure 2.
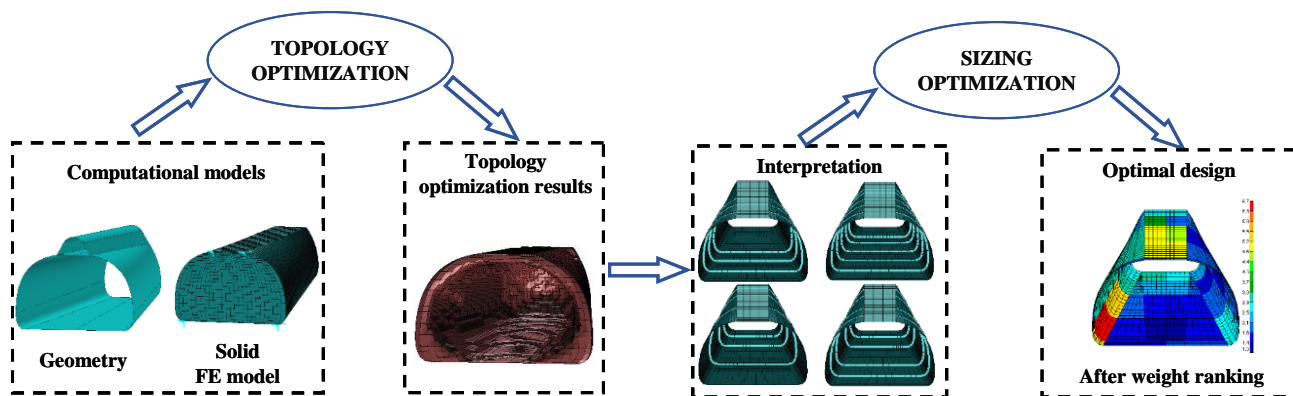

Fig. 2 – Optimization results for helicopter tail boom structure

The solid finite element model was generated based on CAD drawing and the nodes of its larger section were fixed. Forces which modelled vertical/horizontal bending and torsion were applied to the nodes on the opposite section. Two extreme load cases were considered. Topology optimization was performed at saving 30 percent of initial weight in the final design. It can be seen that the obtained design can be treated as a semi-monocoque, namely a structure including stiffened shell. Such structure is traditional for aircraft fuselages. In this example the topology optimization results show some regions which can be considered as design variables for sizing optimization. Four alternative structural layouts were proposed based on the topology pattern. Strength/buckling optimization identified optimal design which had three frames separating the regions of different panel thicknesses.

References

[1] Krog L., Tucker A., Kemp M. and Boyd R.: Topology optimization of aircraft wing box ribs. 10th AIAA/ISSMO Multidisciplinary Analysis and Optimization Conference, 2004, Albany, New York, USA.

[2] Eves J., Toropov V.V., Thompson H.M., Gaskell P.H., Doherty J.J., Harris J.C.: Topology Optimization of Aircraft with Non-Conventional Configurations. 8th World Congress on Structural and Multidisciplinary Optimization, 2009, Lisbon, Portugal, WCSMO-8.

[3] Chedrik V.V., Tuktarov S.A.: Structural design of aircraft wing based on topology and global-local optimization. 11th World Congress on Structural and Multidisciplinary Optimization, 2015, Sydney, Australia, WCSMO-11.

[4] Chedrik V.V., Tuktarov S.A.: Optimization of Composite Structures Based on Global-Local Approach. International Conference on Engineering and Applied Sciences Optimization, 2014, Kos, Greece, ISBN:978-960-99994-5-8, OPT-i.

DESIGN OF HOMOGENIZED MICROSTRUCTURES USING STRESS-BASED TOPOLOGY OPTIMIZATION

Maxime Collet [*1], Matteo Bruggi[2], Lise Noël[3], Simon Bauduin[4], and Pierre Duysinx[5]

[1,3,4,5]*Aerospace and Mechanical Engineering Department, University of Liège, Liège, Belgium*
[2]*Department of Civil and Environmental Engineering, Politecnico di Milano, Milan, Italy*

<u>*Summary*</u> This paper aims at designing microstructures using stress-based topology optimization. Most of the developments so far have been made for compliance design in various field of applications as reflected in the literature. The emergence of the new additive manufacturing techniques allows to consider porous material, such as lattice structures for instance, which ca be used for the design of structural components subject to various solicitations. Those components must account for the stress level to prevent failure everywhere in the microstructures and by extension the whole structure itself. This work proposes to design such microstructures using topology optimization with limitation on the stress level within the microstructures before printing the result. The homogenization technique is used to determine the equivalent material properties. The issues and perspectives are also discussed.

ABSTRACT

Topology optimization aims at giving the optimal distribution of the material within a design domain, enabling to place the material where it is the most efficient while staying with void in less effective regions. Problems based on the discrete valued approach (0-1) of the optimal distribution of material are difficult to solve numerically but they are also ill-posed exhibiting convergence issues. To overcome this difficulty, Bendsøe and Kikuchi [2] proposed to relax the problem by introducing porous material, made of an infinite number of holes, whose effective properties can be computed thanks to the homogenization techniques, see e.g. Hassani and Hinton [4, 5, 6]. Even if the numerical solution of the problems is tractable, the manufacturability of the optimized design based on classic machine tooling techniques is not straightforward. Thus clear designs, i.e. nearly black-and-white designs, can be enforced by introducing a penalization of intermediate densities. To this end, a successful approach is the famous SIMP approach as proposed in Bendsøe. [3]. However nowadays, thanks to the emergence and the effectiveness of the novel additive manufacturing techniques, structures including regions made of porous microstructures are now becoming possible to fabricate and topology optimization using homogenization methods receive a revived interest as attested by recent works of Andreassen et al [1] and Xia [8]. The practical applications of these designs including microstructures is motivated by the great performances that can be achieved compared to classical solutions of topology optimization.

In this work, a stress based–topology optimization procedure is considered along with the homogenization technique for the computation of the equivalent material properties of the porous material. Most of the contributions dealing with the design of porous material are indeed focused on compliance minimization in a wide variety of applications. The design using stress–based topology optimization is however gaining in interest, as pointed out by Le et al [7], and it has become critically important to account for the strength of the microstrucutres and not only their stiffness. To this end, we investigate here the problem of bounding the stress level within microstructures, problem that has not been much considered so far, to the author knowledge. The design problem is to find the optimal material distribution within the periodic base cell subject to prescribed macro strains and bounded stress criterion everywhere in the microstructure and *de facto* ensure the structural intregrity of the whole component.

The adopted approach continues along the work developed by the authors. The SIMP approach is adopted while a sequential convex programming approach using MMA is used to solve the optimization problems. The paper discusses the design problem formulation as well as the choice of the considered failure criterion (von Mises, principal stresses, etc) while solving numerical applications. The numerical procedure is at first validated against some analytical results proposed by Vigdergauz [9, 10] for a single inclusion before investigating more complex loading conditions. Design obtained with pure stress–based topology optimization is compared to a formulation embedding both stress constraints and a global compliance constraint. The former method has proven to exhibit better numerical performances, i.e. reduced CPU time . The work focuses also on an efficient and accurate way to measure the stress field coming from the solution of the adopted finite element procedure. Numerical issues and perspectives for further works are also discussed.

Finally the optimized designs are fabricated using a multimaterial inkjet polymer printer (Connex by Stratasys) to assess the actual performance of the optimized designs compared to more conventional results such as compliance–based designs.

ACKNOWLEDGMENTS

---

*Corresponding author. Email: maxime.collet@ulg.ac.be

References

[1] Andreassen, E., Jensen, J. S., Sigmund, O., & Thomsen, J. J. (2015). Optimal Design of Porous Materials. DTU Mechanical Engineering. (DCAMM Special Report; No. S172).

[2] Bendse, M.P. and Kikuchi N. (1988). Generating Optimal Topologies in Structural Design Using a Homogenization Method. Comp. Meth. in Appl. Mech Engng. 71, 197-224

[3] Bendsoe M.P. (1989) Optimal shape design as a material distribution problem. Structural Optimization 1, 193-202.

[4] Hassani B., Hinton E. (1998) A review of homogenization and topology optimization I- homogenization theory for media with periodic structure. Computers and Structures 69:707-717

[5] Hassani B., Hinton E. (1998) A review of homogenization and topology optimization II -homogenization theory for media with periodic structure. Computers and Structures 69:719-738

[6]] Hassani B., Hinton E. (1998) A review of homogenization and topology optimization III- homogenization theory for media with periodic structure. Computers and Structures 69:739-756

[7] Le C., Norato J., Bruns T., Ha C., Tortorelli D.(2010) Stress-based topology optimization for continua. Struct Multidisc Optim 41:605-620.

[8] Xia L. (2015) Towards Optimal Design of Multiscale Nonlinear Structures. PhD Thesis, Universit de Technologie de Campigne. Novembre 2015.

[9] Vigdergauz S. (1994). Two dimensional grained composites of extreme rigidity J. of Applied Mechanics 61(2), 390-394.

[10] Grabovsky Y and Kohn R. (1995). Microstructures minimizing the energy of a two phase elastic composite in two space dimensions. II: The vigdergauz microstructure. Journal of the Mechanics and Physics of Solids. 43 (6), 949972

A NOVEL TOPOLOGY OPTIMIZATION METHOD FOR PERIODICAL CELLULAR MATERIALS

Jie Gao[1], Liang Gao[1a] & Mi Xiao[1] & Hao Li[1] & Zhen Luo[2]

[1]*The State Key Laboratory of Digital Manufacturing Equipment and Technology, School of Mechanical Science and Engineering, Huazhong University of Science and Technology, Wuhan, China*
[2]*School of Mechanical and Mechatronic Engineering, The University of Technology Sydney, Sydney, Australia*

Summary The design of periodic microstructural composite materials to attain specific properties has been carried out by a new combination method of the parametric level set method (PLSM) and the energy-based homogenization method (EBHM) in this article. The PLSM is utilized to determine microstructural architecture of the representative volume element (RVE) in composites. And its objective function is defined by the EBHM which is employed to predict specific material properties. The key characteristic of the PLSM is that the implicit level set function is interpolated by a series of compactly support radial basis functions (CSRBF). Besides, the EBHM eliminates the bound of macro structure and material microstructure design based on the energy principle and has an easier numerical implementation compared with the numerical homogenization method. Finally, some optimal microstructures are achieved by the proposed method, and which validate the design capability and favourable features compared with the other design method.

PARAMETRIC LEVEL SET METHOD

The level set method has become popular recently for tracking and modelling the motion of a dynamic interface. Because many favourable characteristics of the PLSM [1] are quite benefit to numerical implementation, it is chosen as the basis of the microstructural optimization formulation, and which is to determine the layout of materials with a specified volume fraction in the RVE. The mathematical formulation could be approximately divided into four key parts. The first part is that the structural design boundary is implicitly described by the zero level set of a higher dimension scalar function, the dynamic evolution of design boundary is equivalent to propagating the LSF. The second part is that the dynamic evolution process of structural boundary is formulated by the rigorous mathematical function. The structural design domain is modeled as the zero level set and updated with the merging and splitting of the design boundary. By introducing a pseudo-time t into zero level set function and then differentiating on both sides with respect to time, the motion of the structure boundary is modelled by a first-order H-J PDE. It is shown at Eq (1).

$$\frac{\partial \Phi(\mathbf{x},t)}{\partial t} + \mathbf{v} \cdot \nabla \Phi(\mathbf{x},t) = 0 \tag{1}$$

The intention of the third part is to eliminate these poor numerical features of the standard LSM based on above two parts. The LSF is interpolated by a series of compactly supported radial basis functions (CSRBF) and unknown expansion coefficients, so that the time and space have been decoupled in LSF. It is shown as follows:

$$\Phi(\mathbf{x},t) = \left(\boldsymbol{\varphi}(\mathbf{x})\right)^T \mathbf{a}(t) = \sum_{i=1}^{N} \phi_i(x)\alpha_i(t) \tag{2}$$

The Eq (2) has shown that the LSF have been completely transformed into a linear algebraic system equation based on the discretized design domain. The final part is that the velocity function is computed by the shape derivative analysis.

ENERGY-BASED HOMOGENIZATION METHOD

The homogenization theory [2] is built on the small asymptotic expansion theory, and which is utilized to evaluate the homogenized effective properties of the periodical composites from directly analysing its periodic RVE. The homogenized effective elasticity tensor and the subjected elasticity equilibrium function are reflected at Eq (3).

$$\begin{cases} E_{ijkl}^H = \dfrac{1}{|\mathbf{Y}|} \int_\Omega \left(\varepsilon_{pq}^{0(ij)} - \varepsilon_{pq}^{*(ij)}\right)^T E_{pqrs} \left(\varepsilon_{rs}^{0(kl)} - \varepsilon_{rs}^{*(kl)}\right) d\Omega \quad (i,j,k,l = 1,2,\cdots,d) \\[2mm] \displaystyle\int_\Omega E_{ijpq}\varepsilon_{rs}^{*(kl)} \dfrac{\partial v_i}{\partial y_j} d\Omega = \int_\Omega E_{ijpq}\varepsilon_{rs}^{0(kl)} \dfrac{\partial v_i}{\partial y_j} d\Omega \quad \forall v_i \in H_{per}\left(\Omega,\mathbf{R}^3\right) \end{cases} \tag{3}$$

The Eq (3) could be transformed into the sum of the integration of the finite-element based on the FEA.

$$E_{ijkl}^H = \sum_{e=1}^{NE} \left\{ \frac{1}{|\mathbf{Y}_e|} \left(\int_{\Omega_e} \left(\varepsilon_{pq}^{0e(ij)} - \varepsilon_{pq}^{*e(ij)}\right)^T E_{pqrs} \left(\varepsilon_{rs}^{0e(kl)} - \varepsilon_{rs}^{*e(kl)}\right) d\Omega_e \right) \right\} \tag{4}$$

Observing the marked Eq (4), the part surrounded by the dotted red line could be interpreted as the average strain energy of each finite-element, and which is named by the element mutual energy densities [3]. Hence, it is important to note that the elasticity tensor is calculated by the summation of the element mutual energy densities. It is necessary to build appropriate boundary conditions in order to evaluate element mutual energy based on the FEA.

---

[a] Corresponding author. Email: gaoliang@mail.hust.edu.cn.

MICROSTRUCTURAL DESIGN MODEL AND SENSITIVITY ANALYSIS

The intention of material design [4] is defined by seeking optimal configuration of the RVE in order to obtain the improved homogenized properties. In this article, a new systematic design method is constructed by integrating the PLSM with the EBHM. The material microstructural optimization formulation is defined as follows:
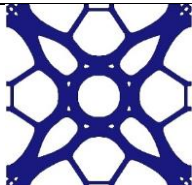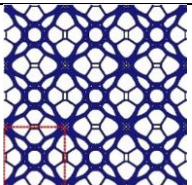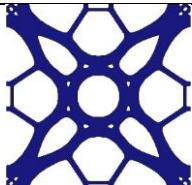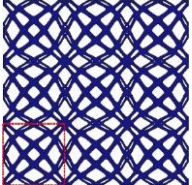
$$\underset{(\mathbf{u}^*,\Phi)}{Minimize}: J\left(\mathbf{u}^*,\Phi\right)= \sum_{i,j,k,l=1}^{d} \eta_{ijkl}E_{ijkl}^{H}$$

$$Subject\ to: \begin{cases} V\left(\Phi\right)= \int_{\Omega} H\left(\Phi\right)d\Omega - V_{max} \leq 0 \\ a\left(\mathbf{u}^*,\mathbf{v},\Phi\right)=l\left(\mathbf{v},\Phi\right) \quad \forall\ \mathbf{v} \in H_{per}\left(\Omega,\mathbf{R}^3\right) \\ \alpha^L \leq \alpha_i \leq \alpha^U \quad \left(i=1,2,\cdots,NE\right) \end{cases} \tag{5}$$

The OC method is employed to update design variables in the proposed method, and which requires first-order derivatives of the objective function and volume constraint function with respect to design variables. as follows:

$$\frac{\partial J}{\partial \boldsymbol{\alpha}} = \sum_{i,j,k,l=1}^{d}\left(\eta_{ijkl}\frac{\partial E_{ijkl}^{H}}{\partial \boldsymbol{\alpha}}\right) = \frac{1}{|\mathbf{Y}|}\left(\sum_{i,j,k,l=1}^{d}\left(\eta_{ijkl}\int_{D}\left(\varepsilon_{pq}^{0(ij)}-\varepsilon_{pq}^{*(ij)}\right)^{T}E_{pqrs}\left(\varepsilon_{rs}^{0(kl)}-\varepsilon_{rs}^{*(kl)}\right)\boldsymbol{\varphi}(\mathbf{x})^{T}\delta\left(\Phi\right)d\Omega\right)\right) \tag{6}$$

NUMERICAL EXAMPLES

In all examples, the Young's modulus are defined $E_0^s = 1$ of the solid phase, and $E_0^v = 0.001$ of the void phase. The Possion's ratio are equal 0.3. The lower and upper bounds of design variables $\boldsymbol{\alpha}$ are defined as $\alpha^L = 2 \times min\{\alpha_i\}$ and $\alpha^U = 2 \times max\{\alpha_i\}$ $(i = 1,2,\cdots,NE)$ in OC method. Finally, the optimization will be terminated when the difference of objective functions between two successive steps is less than 10-4.

Parameters	PLSM + EBHM	3*3 Repetitive RVE	PLSM + NHM	J
0.40 120×120 Bulk modulus $J = K = \sum_{i,j=1}^{2} E_{iijj}^{H}$				0.136
0.50 100×100 Shear modulus $J = G = E_{1212}^{H}$				0.130

Tab 1: the optimal configuration of the RVE in different parameters

CONCLUSIONS

In conclusion, a new systematic, scientific and efficient computation design method is proposed to design the cellular material microstructure, and which optimize the shape and topology of the RVE by the PLSM subjected to the objective function defined by the EBHM. Based on above results, it is summarized that the optimized results have the distinct and smooth structure boundary and the optimal microstructures derived by two different homogenization methods are mostly identical.

Acknowledgments

References

[1] Luo, Z., et al.: A level set-based parameterization method for structural shape and topology optimization. Int. J. Numer. Methods Eng. 76:1-26, 2008.

[2] Sigmund, O.: Materials with prescribed constitutive parameters: an inverse homogenization problem. Int. J. Solids Struct. 31:2313-2329, 1994.

[3] Xia L., et al.: Design of materials using topology optimization and energy-based homogenization approach in Matlab. Struct. Multidiscip. Optim. 52: 1229-1241. 2015.

[4] Cadman, J.E., et al.: On design of multi-functional microstructural materials. J. Mater. Sci. 48: 51-66. 2012.

TOPOLOGY OPTIMIZATION USING BERNSTEIN BASIS POLYNOMIALS

Andrew Lambe[*1] and Aleksander Czekanski[1]

[1]*Department of Mechanical Engineering, York University, Toronto, Ontario, Canada*

Summary A new method for density-based topology optimization is presented in which the density field is parametrized using Bernstein polynomial basis functions on a finite-element mesh. This parametrization permits a continuous variation of the density between mesh elements to suppress checkerboards without a filter. In addition, rather than refining the design variable mesh, the material boundary is more accurately captured by elevating the order of the basis functions. Standard meshing techniques may be used to define the design variable mesh, even with complex domain shapes, and different meshes may be used to define the design variables and the finite element analysis. Results are presented for two structural topology design problems.

DENSITY FIELD PARAMETRIZATION

In density-based topology optimization with element-based design variables, each finite element is assigned a design variable to indicate whether that element is solid material or void. Important issues with optimal solutions computed using element-based design variables include checkerboards of solid and void elements, ragged edges of features not aligned with the design mesh, and mesh-dependence of the optimal topology. Typically, these issues are mitigated using a filter. In a filter, the density value of a given element is computed using a weighted average of the density variables in a small neighborhood of that element. This approach leads to a "gray" transition between solid and void regions whose size depends on the filter size. Material boundaries are then identified using a projection method.

Several alternative density-field parametrizations also exist to mitigate the issues identified above without using filters. Matsui and Terada [1] assign design variables to linear shape functions to define a continuous distribution of the density field. Ngyuen et al. [2] define a multiresolution topology optimization scheme (MTOP) in which each element contains many constant-density regions with corresponding design variables. Kang and Wang [3] assign density design variables to points in the domain and use Shepard interpolation to compute the density at any other point in the domain. Qian [4] embeds the design domain in a tensor-product B-spline mesh and assigns design variables to the B-spline basis functions.

We propose a density field parametrization based on Bernstein polynomial basis functions. The degree-n basis functions are given by

$$b_{k,n}(x) = \binom{n}{k} x^k (1-x)^{n-k} \quad k = 0, ..., n. \tag{1}$$

Over the interval $x \in [0, 1]$, these $n + 1$ functions are nonnegative and sum to one regardless of the choice of n. These properties make the Bernstein polynomials ideal for parametrizing a density field whose values must stay between zero and one. Figure 1 shows the cubic Bernstein polynomials as basis functions for two adjacent one-dimensional elements, compared to the cubic Lagrange polynomials over the same interval. Figure 2 shows two example basis functions for adjacent square elements.

This particular parametrization has several attractive features. First, we are not restricted to using linear basis functions, so more detailed features of the density field may be revealed with fewer elements. Second, the support size of the basis
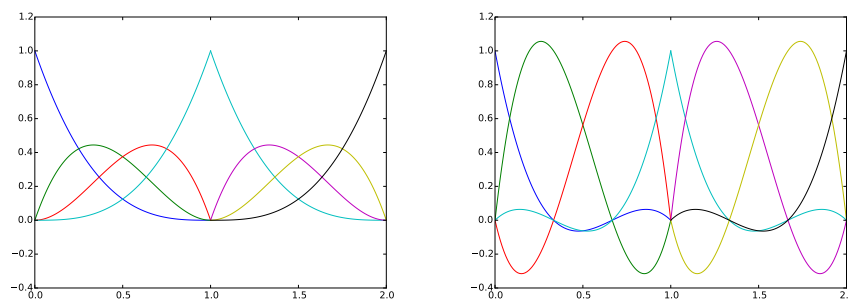

Figure 1: The cubic Bernstein polynomials (left), unlike the cubic Lagrange polynomials (right), never take values greater than one or less than zero.

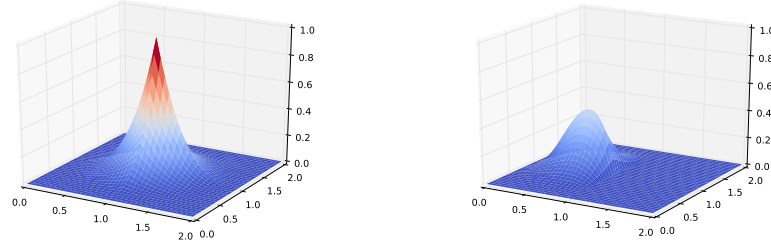*Corresponding author. Email: alambe@yorku.ca

Figure 2: Bicubic Bernstein basis functions for square Q16 elements. The left image shows a nodal basis function while the right shows a basis function on the edge between elements.
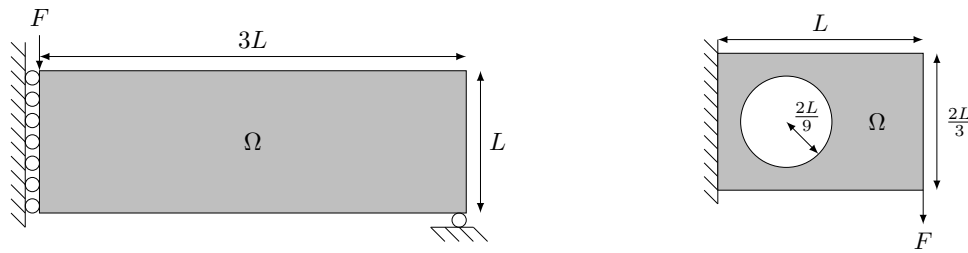

Figure 3: Design domains of (left) the MBB beam and (right) the cantilever beam with a circular hole.

functions is restricted to adjacent elements, so feature size control is naturally integrated into mesh generation and refinement. Third, the parametrization may be applied to domains with complex geometry and may use a different mesh than that used in the finite element analysis. Finally, analogous to an h-p finite element method, the design variable mesh may be refined using both element size reduction and order elevation.

TEST PROBLEMS

We study two example problems from the literature: the classical MBB beam problem and a cantilever beam with a circular hole. Figure 3 shows the geometry and boundary conditions for these problems. The objective of both optimization problems is to minimize the compliance of the loaded structure subject to a volume fraction constraint of 0.5. We use deal.ii [5] for the design variable parametrization and finite element analysis and IPOPT [6] for the optimization.

Our results demonstrate the absence of checkerboard patterns in our optimized designs and the recovery of well-known topologies. We also show the effect of using higher-order basis functions on the optimal designs, especially on the identification of the material boundary with a coarse design variable mesh. Finally, we conduct a preliminary study of refining the design variable mesh using both element size reduction and order elevation.

References

[1] Matsui, K., Terada, K.: Continuous approximation of material distribution for topology optimization. Int. J. Numer. Meth. Engng. 59:1925–1944, 2004.

[2] Ngyuen, T.H., Paulino, G.H., Song, J., Le C.H.: A computational paradigm for multiresolution topology optimization (MTOP). Struct. Multidisc. Opt. 41:525–539, 2010.

[3] Kang, Z., Wang, Y.: Structural topology optimization based on non-local Shepard interpolation of density field. Comput. Methods Appl. Mech. Engrg. 200:3515–3525, 2011.

[4] Qian, X.: Topology optimization in B-spline space. Comput. Methods Appl. Mech. Engrg. 265:15–35, 2013.

[5] Bangerth, W., Hartmann, R., Kanschat, G.: deal.II – a general purpose object oriented finite element library. ACM Trans. Math. Softw. 33:24/1–24/27, 2007.

[6] Wächter, A., Biegler, L.: On the implementation of a primal-dual interior point filter line search algorithm for large-scale nonlinear programming, Mathematical Programming 106:25–57, 2006.

STRENGTH-BASED EVOLUTIONARY STRUCTURAL OPTIMIZATION

Chih-Hung G. Li

Department of Mechanical Engineering, Ming-Hsin University of Science and Technology, Hsinchu, Taiwan, ROC

<u>Summary</u> Here the author reports a novel structural design optimization method that deals with the orthotropic strength properties of Fused Deposition Modelling (FDM) structures. The proposed Strength-Based Evolutionary Structural Optimization (SBESO) method inherits the concept of the traditional ESO with a new severeness index to evaluate the stresses in all directions based on the orthotropic strengths. Material rejection in the finite element analyses and the topology evolution is performed based on the proposed severeness index.

INTRODUCTION TO THE PROBLEM

Fused Deposition Modelling (FDM) is a popular type of 3D printing technology, where molten material is ejected through a nozzle and deposited layer by layer to form a 3D object. Various thermoplastic polymers such as acrylonitrile butadiene styrene (ABS), polycarbonate (PC), or the others in the form of a filament are used as the raw material. It has been discovered that the structures fabricated using the FDM method exhibit significant anisotropy in the ultimate strength [1]. In the preliminary testing performed by the author for the properties of the FDM structures, similar results were observed. The ultimate strengths were found to be 26.5MPa along the filament direction, 11.98MPa in the direction normal to the filament, and 18.67MPa for shear. When forming a design guide for the designer aiming at achieving mass optimized FDM structures, such anisotropy should be considered for better accuracy. In this research, the author adopted the concept of the Evolutionary Structural Optimization (ESO) method for its simplicity and ease of implementation [2], noting that other sophisticated methods for topology optimization exist [3]. A Strength-Based ESO (SBESO) was devised to reflect the orthotropic strength characteristics of the FDM structures. A severeness index was defined to evaluate the stresses, instead of the von Mises stress commonly used for isotropic materials. The ultimate strengths mentioned above were used as the reference for calculating the severeness index of each stress component of each finite element. In this study, the SBESO was demonstrated with a short cantilever problem. A strategy of direct incrementing and fixed material removal rate was also adopted [4].

OPTIMIZATION PROCESS

The optimization process is detailed in Figure 1. A finite element model of the design envelop was first created with boundary conditions applied. The calculated stress components of each finite element were used to compute the severeness indices by taking the ratio of the stress to the strength. For each finite element, the maximum severeness index among the six components would be taken as the representative index of that element. All the elements would then be ranked based on the representative index, and the lowest 1% of the elements would be rejected for the next finite element calculation until a desired percentage of total material removal has been achieved.

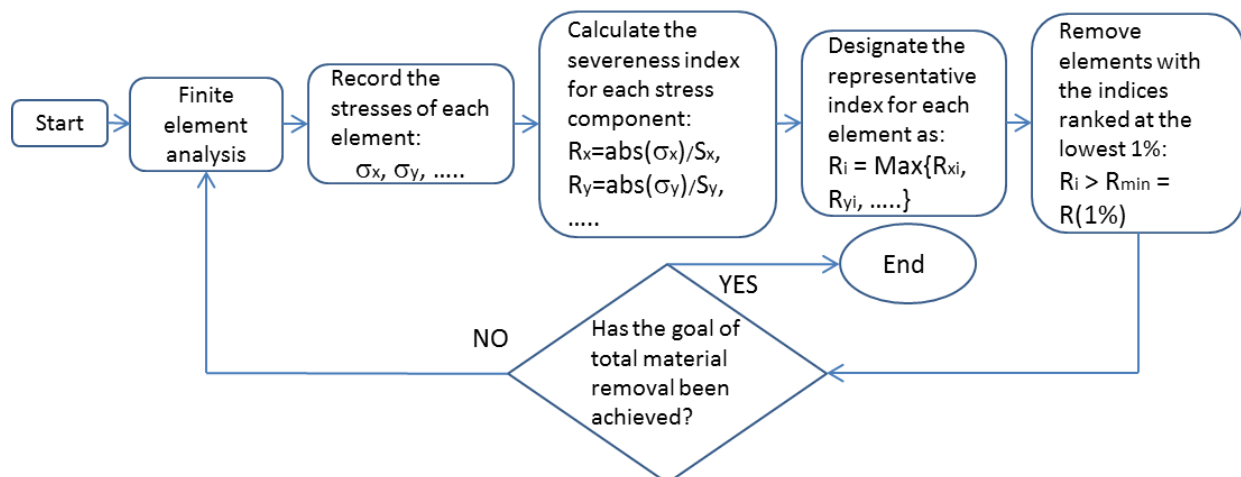**Figure 1.** The procedure of the Strength-Based Evolutionary Structural Optimization.

RESULTS AND DISCUSSIONS

A plane stress short cantilever problem was attempted using the proposed SBESO. The length of the beam is twice as much as the height; line constraints were applied at the right side of the beam, and a point load was applied at the bottom

---

[a] Corresponding author. Email: cL4e@must.edu.tw.

left corner (Figure 2 (a)). The optimized topology of the three cases calculated was shown in Figure 2. For the isotropic case, von Mises stress was used for evaluation. In the horizontal case, the filament direction was assumed to be horizontal; in the vertical case, the filament was vertical. The finite element model has 5000 elements in total. For each calculation increment, 1% of the total elements that have the lowest severeness indices were rejected. Thus, the volume fraction was controlled to be steadily decreasing until 20% as shown in Figure 3(a). The conventional rejection rate and evolutionary rate were not adopted [2]. However, for comparison reason, equivalent rejection rates were calculated by taking the ratio of the rejected severeness index to the maximum severeness index for every increment. The results were also shown in Figure 3(a). Note that although the evolutionary process of the topology was not driven by the rejection ratio, the history of the rejection ratio exhibits a similar increasing trend with progressing evolution. As a rough confirmation of the effectiveness in topology optimization, the collective representative severeness indices of the final models were compared with each other, along with some arbitrary topology (see Figures 2(e)&(f) and 3(b)&(c)). The optimized topology appears to have the lowest deviation from the average severeness index, indicating the highest efficiency in material usage in terms of stress distribution.
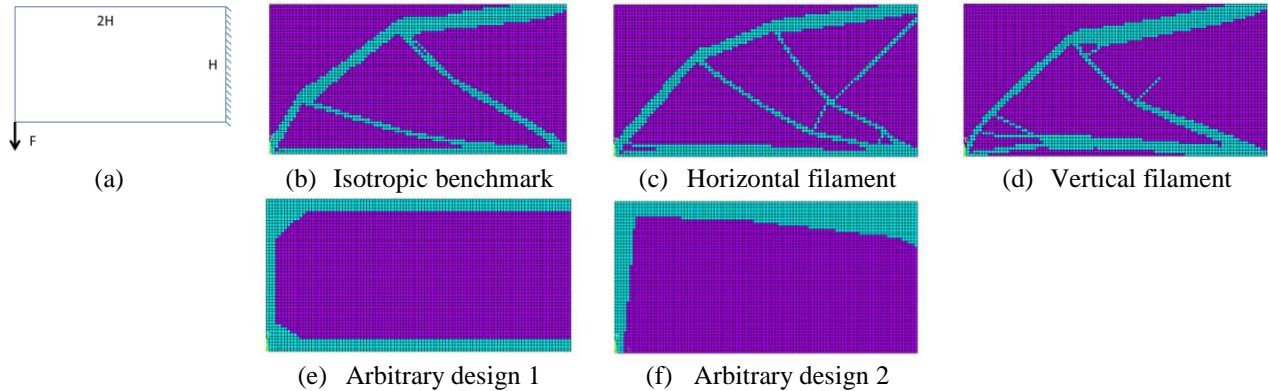

| (a) | (b) Isotropic benchmark | (c) Horizontal filament | (d) Vertical filament |

(e) Arbitrary design 1   (f) Arbitrary design 2

Figure 2. The problem of a short cantilever beam: (a), and the results of the optimized topology: (b), (c), & (d). Arbitrary designs for comparison: (e) & (f).
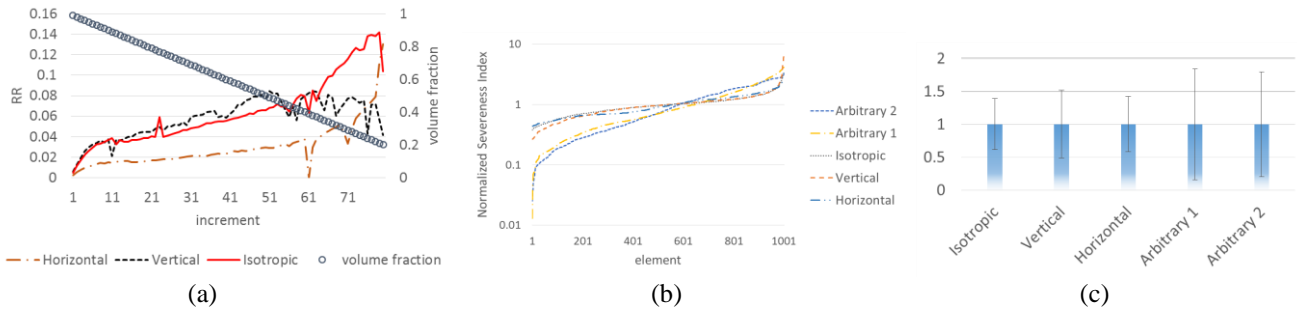

(a)   (b)   (c)

Figure 3. (a) Evolutionary histories of the equivalent rejection ratio and the volume fraction; (b) Distributions of the normalised severeness indices of the final models; (c) Averages and standard deviations of the normalized severeness indices.

CONCLUSIONS

A Strength-Based Evolutionary Structural Optimization method was proposed for the structures of the Fused Deposition Modelling, which exhibits significant orthotropy in the ultimate strength. Instead of using the von Mises stress as the rejection index, a severeness index for each stress component was defined, and the maximum value among the six components was taken as the representative index of every finite element. A strategy of direct incrementing and fixed material removal rate was also adopted. Results of a short cantilever problem showed that the optimized topology exhibited the highest efficiency in material usage in terms of stress distribution while compared with some arbitrary designs.

References

[1] Ahn S.H., Montero M., Odell D., Roundy S., Wright P.K.: Anisotropic Material Properties of Fused Deposition Modeling ABS. *Rapid Prototyping J.* 8(4):248-257, 2002.

[2] Xie Y.M., Steven G.P.: Evolutionary Structural Optimization. Springer, London 1997.

[3] Bendsøe M.P., Sigmund O.: Topology Optimization: Theory, Methods, and Applications. Springer, Berlin 2004.

[4] Li C. G.: Design of the Lower Chassis of a Monorail Personal Rapid Transit (MPRT) Car Using the Evolutionary Structural Optimization (ESO) Method. *Struct Multidisc Optim* (in press).

TOPOLOGY OPTIMIZATION of CONTACT PROBLEMS using CAHN-HILLIARD REGULARIZATION

Andrzej Myśliński[*1]

[1]*Systems Research Institute, Warsaw, Poland and Faculty of Manufacturing Engineering, Warsaw University of Technology, Warsaw, Poland*

Summary The paper is concerned with the topology optimization of elastic bodies in unilateral contact with a given friction. The aim of the optimization problem is to find such distribution of the material density function to minimize the normal contact stress. The phase field approach is used to analyze and solve numerically this optimization problem. The original cost functional is regularized using Ginzburg-Landau free energy functional including the surface and bulk energy terms. These terms allow to control global perimeter constraint and the occurrence of the intermediate solution values. The Lagrangian approach is used to calculate the derivative of the regularized cost functional and to formulate a necessary optimality condition. The optimal topology is obtained as the steady state of the phase transition governed by modified Cahn-Hilliard equation. The finite difference and finite element methods are used as the discretization methods. Numerical examples are provided and discussed.

TOPOLOGY OPTIMIZATION PROBLEM

Consider deformations of an elastic body occupying two–dimensional domain Ω with the smooth boundary Γ [6]. The body is subject to body forces $f(x) = (f_1(x), f_2(x))$, $x \in \Omega$. The boundary Γ of domain Ω is split into three mutually disjoint parts such that $\Gamma = \bar{\Gamma}_0 \cup \bar{\Gamma}_1 \cup \bar{\Gamma}_2$, $\Gamma_i \cap \Gamma_j = \emptyset$, $i \neq j$, $i, j = 0, 1, 2$. The body is clamped along the portion Γ_0 of the boundary Γ. The surface tractions $p(x) = (p_1(x), p_2(x))$, $x \in \Gamma$, are applied on a portion Γ_1 of the boundary Γ. The contact conditions with Tresca friction are prescribed on the portion Γ_2 of the boundary Γ. Let $\rho = \rho(x) : \Omega \to R$ denote the material density function at any generic point x in a design domain Ω. It is a phase field variable taking value close to 1 in the presence of material, while $\rho = 0$ corresponds to regions of Ω where the material is absent, i.e. there is a void or weak material. In the phase field approach the interface between material and void is described by a diffusive interfacial layer of a thickness proportional to a small lenght scale parameter $\epsilon > 0$ and at the interface the phase field ρ rapidly but smoothly changes its value [1, 2, 3, 5]. We require that $0 \leq \rho \leq 1$. The ρ values outside this range do not seem to correspond to admissible material distributions. The elastic tensor $\mathcal{A}$ of the material body is assumed to be a function depending on density function ρ:

$$\mathcal{A} = g(\rho)\mathcal{A}_0, \quad \mathcal{A}_0 = \{a_{ijkl}\}_{i,j,k,l=1}^2 \tag{1}$$

and $g(\rho) > 0$ is a suitable chosen function [5, 7]. It is assumed, that elements $a_{ijkl}(x)$, $i, j, k, l = 1, 2$, of the elasticity tensor $\mathcal{A}_0$ satisfy [1, 6] usual symmetry, boundedness and ellipticity conditions. We denote by $u = (u_1, u_2)$, $u = u(x)$, $x \in \Omega$, the displacement of the body and by $\sigma(x) = \{\sigma_{ij}(u(x))\}$, $i, j = 1, 2$, the stress field in the body. Consider elastic bodies obeying Hooke's law, i.e., for $x \in \Omega$ and $i, j, k, l = 1, 2$

$$\sigma_{ij}(u(x)) = g(\rho)a_{ijkl}(x)e_{kl}(u(x)) \text{ where } e_{kl}(u(x)) = \frac{1}{2}(u_{k,l}(x) + u_{l,k}(x)), \quad u_{k,l}(x) \stackrel{def}{=} \frac{\partial u_k(x)}{\partial x_l}. \tag{2}$$

We use here and throughout the paper the summation convention over repeated indices. The stress field σ satisfies the system of equations in the domain Ω [6]

$$-\sigma_{ij}(x)_{,j} = f_i(x) \quad x \in \Omega, i, j = 1, 2, \text{ where } \sigma_{ij}(x)_{,j} = \frac{\partial \sigma_{ij}(x)}{\partial x_j}. \tag{3}$$

The following boundary conditions are imposed on the boundary $\partial\Omega$

$$u_i(x) = 0 \text{ on } \Gamma_0, \quad i = 1, 2, \text{ and } \sigma_{ij}(x)n_j = p_i \text{ on } \Gamma_1, \quad i, j = 1, 2, \tag{4}$$

$$u_N \leq 0, \quad \sigma_N \leq 0, \quad u_N\sigma_N = 0 \text{ and } |\sigma_T| \leq 1, \quad u_T\sigma_T + |u_T| = 0 \text{ on } \Gamma_2, \tag{5}$$

where $n = (n_1, n_2)$ is the unit outward versor to the boundary Γ. Let us introduce the set U_{ad} of admissible domains. This set has the form: $U_{ad} = \{\Omega : \Omega \subset D \subset R^2 : \Omega$ is suitable regular, $Vol(\Omega) - Vol^{giv} \leq 0$, $P_D(\Omega) \leq const_1\}$ where $Vol(\Omega) = \int_\Omega dx$ and $P_D(\Omega) = \int_\Gamma dx$. The subset D as well as constants $Vol^{giv}, const_1 > 0$ are given. The set U_{ad} is assumed to be nonempty. Consider the following structural optimization problem: *for a given function $\eta \in M^{st}$, find a domain $\Omega^\star \in U_{ad}$ such that*

$$J_\eta(u(\Omega^\star)) = \min_{\Omega \in U_{ad}} J_\eta(u(\Omega)) \text{ where } J_\eta(u(\Omega)) = \int_{\Gamma_2} \sigma_N(u)\eta_N(x)ds. \tag{6}$$

The set $M^{st} = \{\eta = (\eta_1, \eta_2) \in [H^1(D)]^2 : \eta_i \leq 0 \text{ on } D, i = 1, 2, \quad \|\eta\|_{[H^1(D)]^2} \leq 1\}$ and the functional $J_\eta(\cdot)$ approximates the normal contact stress.

---

[*]Corresponding author. Email: myslinsk@ibspan.waw.pl

Phase field based topology optimization problem

We apply phase field approach to formulate a necessary optimality condition and to solve numerically the optimization problem (6). We shall consider domain Ω as a two phase domain. We use Ginzburg-Landau energy functional [3] as a regularization term rather than standard perimeter term. Material density function ρ describes the concentration of one of the phases in the domain Ω. The other phase is obtained as $(1 - \rho)$. This variable is used to describe the phase transition. In order to indicate the evolution of the material density function ρ let us assume this function depends not only on $x \in \Omega$ but also on the artificial time variable $t \in [0, T), T > 0$ given, i.e. $\rho = \rho(t, x)$. Let us introduce the regularized cost functional $J(\rho, u)$ in the form:

$$J(\rho, u) = J_\eta(u) + E(\rho), \;\; E(\rho) = \int_\Omega \psi(\rho) d\Omega, \;\; \psi(\rho) = \frac{\gamma\epsilon}{2} \mid \nabla\rho \mid^2 + \frac{\gamma}{\epsilon}\psi_B(\rho), \tag{7}$$

where the functional $J_\eta(u)$ is given by (6) and $\epsilon > 0$ is a constant, $\gamma > 0$ is a parameter related to the interfacial energy density, $\psi_B(\rho)$ is a double-well potential which characterizes the two phases [3] usually taken as an even-order polynomial of the form $\psi_B(\rho) = \rho^2(1 - \rho^2)$. The structural optimization problem (6) takes the form: *find $\rho^\star \in U_{ad}^\rho$ such that*

$$J(\rho^\star, u^\star) = \min_{\rho \in U_{ad}^\rho} J(\rho, u), \tag{8}$$

where $u^\star = u(\rho^\star)$ denotes a solution to the state system (3)-(5) depending on $\rho^\star$ and $U_{ad}^\rho = \{\rho : Vol(\Omega) = Vol^{giv}\}$ denotes the set of admissible material density functions.

NUMERICAL IMPLEMENTATION AND RESULTS

Necessary optimality condition for the optimization problem (8) in the form of the gradient flow generalized Cahn-Hilliard equation has been formulated. Finite difference and finite element methods have been used as approximation methods. Primal-dual active set method has been used to solve state and adjoint systems. Biconjugate gradient method has been used to solve generalized Cahn-Hilliard system. Fig. 1 presents the optimal domain obtained by solving structural optimization problem (8) in the computational domain D using the optimality condition. The areas with low values of density function appear in the central part of the body and near the fixed edges. The obtained normal contact stress is almost constant along the optimal shape boundary and has been significantly reduced comparing to the initial one (see Fig. 2).
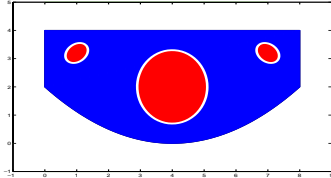

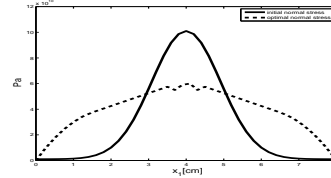Figure 1: Optimal material density distribution in domain $\Omega^\star$.

Figure 2: Initial and optimal normal contact stress.

CONCLUSION

The obtained numerical results indicate that the proposed numerical algorithm allows for significant improvements of the structure and reduction of the normal contact stress. Phase field approach based on the Cahn-Hilliard equation is flexible and can be easily combined with material density field. In this sense this approach follows SIMP method.

References

[1] Blank L., Garcke H., Sarbu L., Srisupattarawanit T., Styles V., Voigt A.: Phase-field approaches to structural topology optimization. *Constrained Optimization and Optimal Control for Partial Differential Equations*, G. Leugering, S. Engell, A. Griewank, M. Hinze, R. Rannacher, V. Schulz, M. Ulbrich, S. Ulbrich (Eds.), International Series of Numerical Mathematics, Birkhäuser, Basel, 160:245-256, 2012.

[2] Burger M., Stainko R.: Phase-field relaxation of topology optimization with local stress constraints. SIAM J. Control. Optim. 45:1447-1466, 2006.

[3] Dede L., Boroden M.J., Hughes T.J.R: Isogeometric analysis for topology optimization with a phase field model. Archives of Computational Methods in Engineering 19(3):427-465, 2012.

[4] van Dijk N.P., Maute K., Langlaar M., van Keulen F.: Level-set methods for structural topology optimization: a review. Struct. Multidisc Optim. 48: 437-472, 2013.

[5] Gain A.L., Paulino G.H.: Phase-field based topology optimization with polygonal elements: a finite volume approach for the evolution equation. Struct. Multidisc Optim. 46:327-342, 2012.

[6] Myśliński A.: Piecewise Constant Level Set Method for Topology Optimization of Unilateral Contact Problems. Advances in Engineering Software, 80:25-32, 2015.

[7] Wallin M., Ristinmaa M., Askfelt H.: Optimal topologies derived from a phase-field method. Struct. Multidisc Optim. 45:171-183, 2012.

ON OBJECTIVE FUNCTIONS IN TOPOLOGY OPTIMIZATION FOR VIBRATION AND WAVE PROPAGATION PROBLEMS

Bin Niu [1,a)], Xiaomeng He [1] & Rui Yang [1]

[1] *School of Mechanical Engineering, Dalian University of Technology, 116024 Dalian, China*

Summary This paper deals with the topological design of continuum structures for vibration and wave propagation problems. Different definitions of objective functions for minimizing vibration response and transmission are compared, and a new optimization model is proposed for minimizing the vibration response and the material used. The minimization of vibration transmission is also related with the bandgap design of wave propagation. Plane and plate structures are optimized using different optimization formulations in numerical examples. The influence of excitation frequencies, the eigenfrequencies of the structure, and damping are discussed in the numerical examples.

INTRODUCTION

Topology optimization on vibration and wave propagation problems has been widely studied. In comparison with well-known static compliance minimization, various objective functions are proposed in literature to minimize the response of vibrating structures, such as power flow, sound radiation, vibration transmission, and dynamic compliances, etc. Even for the dynamic compliance, different definitions are found in literature, which have quite different formulations and great influences on the optimization results. It has been found that the minimization of vibration transmission is also related with the bandgap design of wave propagation. The bandgap design may be realized by the maximization of the frequency gap of the free vibration of a structure, maximization of the frequency gap of wave propagation in a periodic microstructure, or maximization of the wave attenuation in a structure. The aim of this paper is to provide a comparison of these different objective functions for design optimization of vibrating and wave propagation problems. A more appropriate optimization model will be proposed based on the comparison results.

PROBLEM DEFINITION AND OPTIMIZATION FORMULATIONS FOR VIBRATING

An objective function termed as dynamic compliance is proposed to minimize the global response of vibrating structures by Olhoff and Du [1], where the objective function is calculated by the square of the product of force vector and displacement vector. By introducing damping, the optimization problem is reformulated as:

$$\min_{x_e, e=1,\ldots,N_E} \left(\mathbf{P}^{\mathrm{T}}\mathbf{U}\right)\overline{\left(\mathbf{P}^{\mathrm{T}}\mathbf{U}\right)}$$

$$s.t.: \quad (\mathbf{K}+i\omega_p\mathbf{C}-\omega_p{}^2\mathbf{M})\mathbf{U}=\mathbf{P},$$

$$\sum_{e=1}^{N_E} x_e V_e - V^* \leq 0 \quad, \quad \left(V^*=\alpha V_0\right), \tag{1}$$

$$0 < x_{\min} \leq x_e \leq 1 \quad, \quad \left(e=1,\ldots,N_E\right).$$

where $\mathbf{P}$ and ω_p are the prescribed amplitude and the frequency of the time-harmonic external mechanical loading $\mathbf{p}(t)=\mathbf{P}e^{i\omega_p t}$ respectively, and $\mathbf{U}$ is the amplitude of related displacement vector $\mathbf{a}(t)=\mathbf{U}e^{i\omega_p t}$. The problem will reduce to the well-known compliance minimization in static topology optimization when $\omega_p=0$. $\mathbf{K}$ and $\mathbf{M}$ are the stiffness matrix and mass matrix, $\mathbf{C}$ is the damping matrix, x_e denotes the design variable of the *e*-th element, and N_E is the total number of finite elements. $V^*=\alpha V_0$ is the given volume of material, and α is the volume fraction. Overbar denotes the conjugate of a complex quantity.

Jog [2] has introduced a new measure for the dynamic compliance, which is computed as the average input power over a cycle of the excitation. Minimization of the average input power $-1/2\,\omega_p\mathbf{P}^{\mathrm{T}}\mathbf{U_s}$ is chosen as the design objective, where $\mathbf{U_s}$ is the imaginary part of the displacement amplitude vector $\mathbf{U}$.

The minimizing the vibrating magnitude at a point, a line, or an area of a structure subjected to periodic loading was studied by Sigmund [3]. Olhoff and Niu [4] proposed an optimization formulation for vibration transmission in a lightweight building from vibrating machinery by simultaneous minimization of the power flow and the material used for the base plate design of the machinery. The minimization of vibration transmission is found to be related with the bandgap design of wave propagation. The optimization formulations for realizing bandgap structure are compared and discussed next.

PROBLEM DEFINITION AND OPTIMIZATION FORMULATIONS FOR WAVE PROPAGATION

---

a) Corresponding author. Email: **niubin@dlut.edu.cn**

By designing a periodic structure with band gap, it is effective to prevent the wave in the range of the band gap from propagating. The classical formulation for maximizing the bandgap is rewritten as, ref. Sigmund [3]:

$$\max_{x_e, \beta_1, \beta_2} \quad c(x) = \frac{\Delta \omega^2(x)}{\omega_0^2(x)} = 2\frac{\beta_2 - \beta_1}{\beta_2 + \beta_1}$$

$$s.t. \quad \beta_1 \geq \max_{\mathbf{k}} \omega_j^2(\mathbf{k}, x)$$

$$\beta_2 \leq \min_{\mathbf{k}} \omega_{j+1}^2(\mathbf{k}, x) \quad\quad\quad (2)$$

$$(\mathbf{K}(\mathbf{k}) - \omega^2 \mathbf{M})\mathbf{U} = \mathbf{0}$$

$$0 \leq x_e \leq 1, e = 1, \ldots, N_E$$

where ω_j is the jth order frequency, $\mathbf{K}$ and $\mathbf{M}$ are stiffness matrix and mass matrix of the unit cell, $\mathbf{k}$ is the wave vector, and β_1, β_2 are two scalar variables that denote the upper and lower bound parameters in the constraint equations, respectively.

The maximization of a frequency gap of the free vibration of a structure can result into a periodic structure, which has been demonstrated by Olhoff et al.[5] for a beam band gap design for travelling wave. The results demonstrate that there is almost perfect correlation between the bandgap size/location of the emerging band structure and the size/location of the corresponding natural frequencygap in the finite structure. The optimization formulation is written as:

$$\max_{\beta_2, \beta_1, x_e} \left\{ \beta_2 - \beta_1 \right\}$$

$$s.t. \quad \beta_2 - \omega_j^2 \leq 0, \quad\quad j = n, n+1, \ldots, J,$$

$$\omega_j^2 - \beta_1 \leq 0, \quad\quad j = 1, \ldots, n-1, \quad\quad\quad (3)$$

$$(\mathbf{K} - \omega^2 \mathbf{M})\mathbf{U} = \mathbf{0}$$

$$0 < x_{\min} \leq x_e, \quad e = 1, \ldots, N_E$$

Bandgap design can also be realized by maximizing the loss/attenuation of propagating waves as in Søe-Knudsen [6], Andreasen and Jensen [7]

$$\max_{c, x_e} \quad c$$

$$s.t. \quad (\mathbf{K} - k\mathbf{M})\mathbf{U} = \mathbf{0} \quad\quad\quad (4)$$

$$\eta = \frac{k''}{k'} \leq c$$

where the complex wave number $k = k' + ik''$, and c is a bound variable.

CONCLUSIONS

The topology optimization of continuum structures for vibrating and the wave propagation problems is studied in this paper. Different objective functions are presented and compared by numerical examples of plane and plate structures. The validity and efficiency of the objective functions are discussed for realizing the minimization of vibration response and transmission.

References

[1] Olhoff N., Du J.: Topological Design for Minimum Dynamic Compliance of Structures under Forced Vibration. G. Rozvany, T. Lewinski (Eds.), Topology Optimization in Structural and Continuum Mechanics, CISM International Centre for Mechanical Sciences, Springer, Vienna, 325-339, 2014.
[2] Jog CS.: Topology Design of Structures Subjected to Periodic Loading. *J Sound Vib* 253(3):687–709, 2002.
[3] Sigmund O., Jensen J.: Systematic Design Of Phononic Band–Gap Materials and Structures by Topology Optimization. *Philos T Roy Soc A* 361:1001-19, 2003.
[4] Olhoff N., Niu B.: Minimizing the vibrational response of a lightweight building by topology and volume optimization of a base plate for excitatory machinery. *Struct Multidiscip O* DOI 10.1007/s00158-015-1345-6, 2016.
[5] Olhoff N., Niu B., Cheng G.: Optimum Design of Band-Gap Beam Structures. *Int J Solids Struct* 49:3158-69, 2012.
[6] Søe-Knudsen A.: Design of stop-band filter by use of curved pipe segments and shape optimization. *Struct Multidiscip O* 44: 863-874, 2011
[7] Andreasen E., Jensen J.: Topology Optimization of Periodic Microstructures for Enhanced Dynamic Properties of Viscoelastic Composite Materials. *Struct Multidiscip O* 49:695-705, 2014.

# ADAPTIVE DESIGN PROCESS OF LATTICES PRODUCED BY ADDITIVE MANUFACTURING

Antonin Paquette-Rufiange[1], Serge Prudhomme *[1], Marc Laforest[1], and Augustin Schmidt[1]

[1]*Département de mathématiques et génie industriel, École Polytechnique Montréal, Montreal, Quebec, Canada*

Summary Recent developments in additive manufacturing now allow one to contemplate the fabrication of lightweight parts by the use of lattice structures. Most lattices to date are designed with a structured configuration (with repeated truss cells), while the freedom provided by additive manufacturing technologies does not impose this restriction on the design. We propose here a numerical methodology to design unstructured lattices such that material is only placed where it is needed. Lattices are described in terms of bar, beam and torsion models in order to handle the simulation of the lattice, even if they possess a large amount of trusses. For given operational constraints, we search for the truss configuration that minimizes the energy of deformation to weight ratio. The optimization is performed adaptively using a succession of increasingly complex models. This design process is finally tested on several numerical examples to demonstrate its performance.

INTRODUCTION

Additive manufacturing technologies, such as stereolithography and electron beam melting, now allow for the creation of complex structural parts using various materials like plastic and titanium alloy. In particular, one could replace solid parts by lattice structures with the main advantage of being lightweight while respecting geometrical and mechanical requirements. Lattices are therefore attractive to the aerospace and automobile industries because lighter parts lead to significant savings. Researches have been made in order to describe the mechanical strength of structured and/or conformal lattices. Also, published works have investigated the optimization of some parameters (e.g. the truss diameter) in order to obtain a homogeneous distribution of mechanical stresses within the lattice [1, 2].

Structural system   Structured lattice   Unstructured lattice
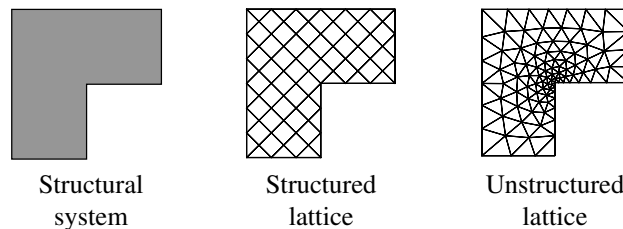
However, one faces several challenges when trying to optimize the design of an unstructured lattice. First, the entire lattice must be analyzed in a "discrete" way, meaning that each truss member must be represented. Hence, the number of degrees of freedom rapidly increases as the lattice becomes denser. Second, obtaining a somewhat optimized configuration of the truss with respect to loads applied to the system is computationally hard because the position and the size of each truss correspond to parameters of the optimization problem. We now briefly explain the novel strategies we employ to tackle some of these challenges.

DESCRIPTION OF THE LATTICE MODEL

We address the first challenge by modeling each truss member as unidimensional single bar, beam and torsion elements. This allows us to significantly reduce the number of degrees of freedom. For example, if one takes a cubic lattice of 15cm of length filled with truss members of minimal length of 5mm, one obtains approximatively 230 000 truss members connected by 30 000 nodes. Thus, using for example the bar model to describe each truss member, one would have about 90 000 degrees of freedom compared to millions of degrees of freedom if one was to discretize each bar solving for the 3D continuum linear elasticity equations by the finite element method. This approach can therefore considerably reduce the complexity and computational cost of simulating the mechanical behavior of the lattice.

*Corresponding author. Email: serge.prudhomme@polymtl.ca
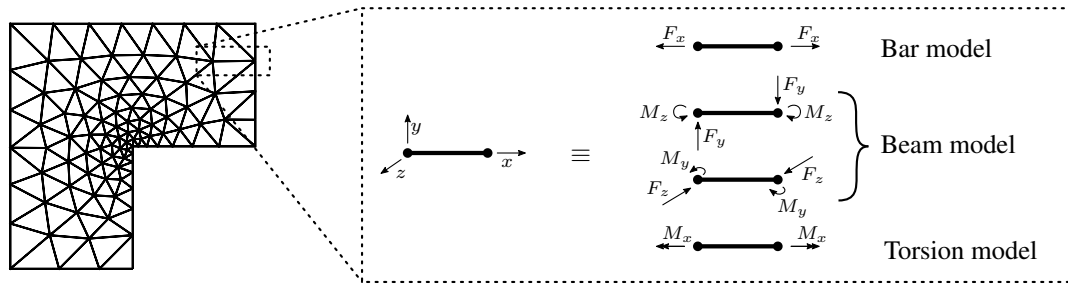
ADAPTIVE DESIGN PROCESS

The simple models presented in above section to simulate the mechanical response of a lattice can be used for design in such a way that the quantity of material involved be minimized while satisfying the specific operational requirements of the lattice. The design variables of the lattice are for example the number of truss members, their diameters, and their position within the computational domain. The following diagram describes the methodology of the adaptive design process.
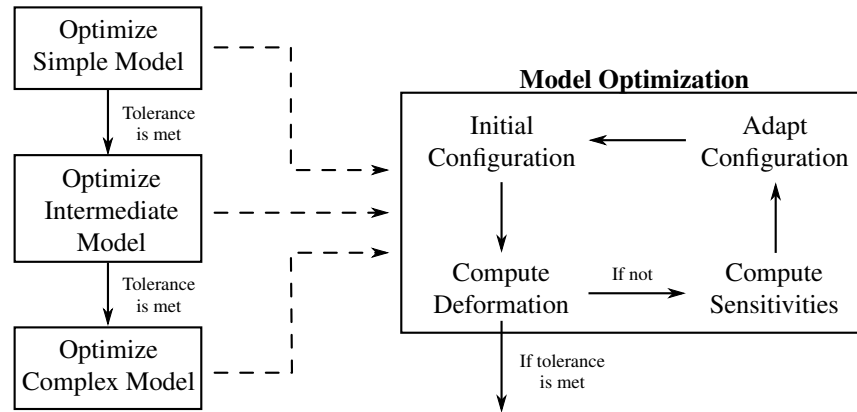
The adaptive process, with the objective of minimizing the computational cost, consists of two stages: 1) one is to start with a coarse lattice and refining it with truss members until mechanical tolerance is met, 2) the second is concerned with adaptive modeling in the sense that each lattice is first described with the simple bar model, which can be locally adapted with finer models, e.g. beam and torsion models, in order to reduce the modeling errors.

References

[1] Jason Nguyen, Sang-In Park, David W. Rosen, Luis Folgar, and James Williams. Conformal lattice structure design and fabrication. In *Solid Freeform Fabrication Symposium*, 2012

[2] S. Teufelhart and G. Reinhart. Optimization of strut diameters in lattice structures. In *Solid Freeform Fabrication Symposium*, 2012.

MULTIPLE DESIGNS APPROACH FOR CONTINUUM TOPOLOGY OPTIMIZATION

Bo Wang[1a)], Yan Zhou[2] & Yiming Zhou[3]

[1] State Key Laboratory of Structural Analysis for Industrial Equipment, Department of Engineering Mechanics, Dalian University of Technology, Dalian 116024, China

Summary Topology optimization can provide creative conceptual designs for industry design in the preliminary design stage. However, the traditional topology optimization approaches focus on searching for one optimal solution which may be invalid due to the refinements of models or the additional design requirements. This paper presents the Multiple Designs Approach (MDA) to get several diverse topology designs, which can reduce the risk of lacking full knowledge of the designs by providing multiple designs. Weighting function is used as the objective function to evaluate the performances of multiple solutions. Diversity function is used as constraint to measure the diversity between different topology solutions.

MOTIVATION

Many researchers are focused on finding an optimal topology design since Bendsøe and Kikuchi[1] first applied homogenization technique for generating optimal topology designs. In fact, topology optimization plays an important role in obtaining conceptual designs in the preliminary design stage[2]. These conceptual designs from topology optimization can give researchers the insights for shape and sizing optimization in detailed design stage. However, preliminary design stage lacks of full knowledge of all the constraints and objectives. In detailed design stage, more latent structural and multidisciplinary performances like strength, structural stability, thermal property, etc., need to be taken into consideration. Furthermore, it is a common practice to use coarse discretization and simpler models in simulations. This occasionally results in rendering the optimum design deficient or useless when checked with a refined model. Moreover, objectives and constraints may change in detailed design stage. If a tight constraint changes, the optimal solution may be out of the new feasible region. Hence designers would like to have multiple design alternatives to single optimal solution in the preliminary design stage.

In order to reduce design risks in detailed design stage, Villanueva[3] used k-means clustering algorithm in sub-regions surrogate-based optimization to find all global and local optimal solution. However, the local optima sometimes are not worth finding because they are not competitive. Also it is difficult to find all the optimal solutions for high-dimensional problems. Later, Zhou, Haftka[4] introduced several surrogate based algorithms to get two diverse competitive solutions in the design domain.

In topology optimization, it is usually a single objective problem to obtain material distribution under material volume constraint and other functional constraints. This paper presents a Multiple Designs Approach (MDA) for topology optimization with diversity constraint to get multiple designs. Thus it is not necessarily required to obtain global optimal solution in this paper.

MULTIPLE DESIGNS APPROACH

General topology optimization formula for MDA

$$\min_{\rho_1, \rho_2} : F = \sum_{i=1}^{n} \alpha_i F_i, \quad \sum_{i=1}^{n} \alpha_i = 1$$

$$s.t. : G_0^i(\rho_i) \le 0$$

$$G_j^i(\rho_i) \le 0 \tag{1}$$

$$\rho_i(\mathbf{x}) \in [0,1], \forall \mathbf{x} \in \Omega, i=1,2,...,n, j=1,2,...m$$

$$G(\rho_p, \rho_q) \le \eta, p,q = 1,2,...,n \text{ and } p \neq q$$

Where n represents the number of topology configurations, m represents the number of functional constraint. Topology optimization problem applied to find optimal material distribution $\rho_i(\mathbf{x})$ in design domain Ω to minimize the objective function F_i with material volume constraint G_0^i and other functional constraint G_j. In the formula, V is volume of design domain, V_f is material volume fraction.

Here, MDA uses a multi-objective problem to get multiple solutions simultaneously and tries to use the weighting function to solve this problem. $\alpha_i \in [0,1]$ is weighting coefficient. Furthermore, we add diversity constraint to obtain different topology configurations. G is the diversity constraint and η is the upper bound for diversity constraint.

Diversity constraint and similarity/difference functions

To obtain two topology configurations in MDA, we need to define a diversity constraint in equation (3). Diversity constraint is a function of ρ_1 and ρ_2 which can measure the difference between topology configurations. The function should be continuous, smooth and bounded for gradient algorithm.

[a)] Corresponding author. Email: wangbo@dlut.edu.cn**.**

In graphics, there are many approaches to measure difference or similarity between two images, including Cross-Correlation(CC), Sum of Squared Differences(SSD), Sum of Absolute Differences(SAD) and their derivative algorithm. Here, we give a simple Similarity Function as the diversity constraint.

$$G = SF(\rho_1, \rho_2) = \frac{\int_\Omega s(\rho_1(\mathbf{x}), \rho_2(\mathbf{x}))dv}{\int_\Omega dv} \tag{2}$$

$$s(\rho_1(\mathbf{x}), \rho_2(\mathbf{x})) = \rho_1(\mathbf{x})\rho_2(\mathbf{x}), \forall \mathbf{x} \in \Omega$$

For multiple design problems, all the objective and constraints as well as the material volume fraction for the designs are the same. In this case, the codomain of SF is related to V_f for binary configurations as follow:

$$SF \in [\max(0, 2V_f - 1), V_f] \tag{3}$$

It is worth noting that upper bound for diversity constraint must be larger than the low bound of SF.

As the codomains of SF are not uniform in different V_f, this paper presents a uniform metric for description of the diversity between topology configurations. Here, the difference function is defined by normalizing SF in the range of SF.

$$DF = 1 - \frac{SF - \max(0, 2V_f - 1)}{V_f - \max(0, 2V_f - 1)} \tag{4}$$

In this case, DF represents the relationship between non-overlap volume and material volume. DF is used as diversity measurement in the rest of the paper.

NUMERICAL EXAMPLE

In this paper, we give an example of L beam for minimization compliance topology problem. Design domain and dimensions of L beam are shown in figure 1 left. Its volume is 4800 and it is discretized into 4800 bi-linear elements. Design variables are element densities. Upper edge of model is clamped and unit load is applied on up-right vertex in figure 1 left. The upper bound of elastic modulus E_0 is 1, and the lower bound of elastic modulus E_{min} is 10^{-6}. Poisson's ratio of material ν is 0.3. Penalty of SIMP is 3, filter radius of sensitivity filtering is 1.5. Volume fraction of material V_f is 50%. Weighting factor $\alpha_1 = \alpha_2 = 0.5$. To get two configurations and ensure DF is equal to 0.2, η can be calculated by equation (5). Hence η are 0.4. The result is shown in figure 1 middle and right, which the middle one is Configuration I, and the right one is Configuration II. It is very different between the two configurations.

$$\eta = \max(0, 2V_f - 1) + (1 - DF)[V_f - \max(0, 2V_f - 1)] \tag{5}$$

Figure 1 Domain of L beam (Left) Configuration I (middle) Configuration II (right)
DF=0.2, F_1=83.08, F_2=82.82, F=82.95

CONCLUSIONS

This paper introduces multiple designs approach (MDA) for topology optimization to get diverse designs and presents the similarity and difference function as the diversity constraint. Compliance minimization examples based on SIMP method are tested in MDA algorithm framework to verify the validity of MDA.

References

[1] Bendsøe, M.P. and N. Kikuchi, Generating Optimal Topologies In Structural Design Using a Homogenization Method. Computer Methods In Applied Mechanics And Engineering, 1988. 71(2): p. 197-224.Icer D.F., Adams J.A.: Mathematical Elements for Computer Simulation. Montreal, Canada 1977.

[2] Olhoff, N., M.P. Bendsoe, and J. Rasmussen, On Cad-Integrated Structural Topology And Design Optimization. Computer Methods In Applied Mechanics And Engineering, 1991. 89(1-3): p. 259-279.

[3] Villanueva, D., R. Le Riche, G. Picard, et al. Dynamic design space partitioning for optimization of an integrated thermal protection system. in The 54th AIAA/ASME/ASCE/AHS/ASC Structures, Structural Dynamics, and Materials Conference, Boston, Massachusetts, USA. 2013.

[4] Zhou, Y., A. Chaudhuri, R.T. Haftka, et al., Global Search for Diverse Competitive Designs, in 15th AIAA Multidisciplinary Design Optimization Specialist Conference. 2014: Atlanta, Georgia, USA.

LATTICE HIP IMPLANT DESIGN
BY MULTI-SCALE MULTI-CONSTRAINT TOPOLOGY OPTIMIZATION

Yingjun Wang & Damiano Pasini[a)]
Department of Mechanical Engineering, McGill University, Montreal, Quebec, Canada

<u>*Summary*</u> Bone resorption is one of the main issues that lead to aseptic loosening and revision surgery after total hip arthroplasty. One of the reasons for bone resorption is stress shielding caused by the prosthesis stiffness usually much higher than that of the bone tissue. To address this problem, we present a mechanically biocompatible hip implant that consists of a graded-density lattice material obtained via multi-scale multi-constraint topology optimization (TO). Asymptotic homogenization is used to deal with the multi-scale mechanics of the implant and a modified proportional TO is used to obtain the relative density distribution of the implant. The result shows that bone resorption for the optimized implant is only 9% of that of a fully solid titanium implant that is commonly used in current total hip arthroplasty.

INTRODUCTION

Total hip arthroplasty (THA) is an effective treatment for osteoarthritis and has been successfully performed on over 1 million patients every year worldwide [1]. Current orthopedic prostheses are generally made of metals, such as 316L stainless steel, cobalt chromium alloys, titanium-based alloys and tantalum [2]. These materials, however, are much stiffer than the surrounding bone tissue, thereby yielding to stress shielding [3], one of the reasons for bone resorption. Currently, 13% of hip prostheses require revision surgeries as a result of bone resorption [4]. Khanoki and Pasini [2] introduced a hip replacement implant made of a lattice material with graded relative density capable to simultaneously reduce bone resorption and bone-implant interface stress. To solve the multi-objective optimization problem, they resorted to an evolutionary scheme, which was time consuming and applied to a planar domain only. In this paper, we focus on the minimization of bone resorption in a 3D lattice hip implant via a multi-scale multi-constraint topology optimization scheme, which is gradient free, more accurate and more efficient than the approach previously used [2].

METHODS

Figure 1 shows the scheme proposed in this paper to design a graded lattice implant with minimal bone resorption. The main steps are briefly described below.
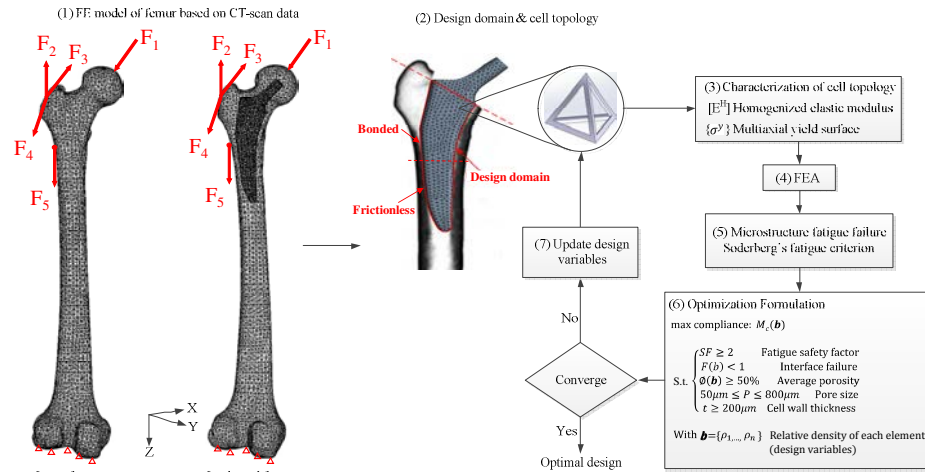

Figure 1. Design flow chart to obtain the optimal density distribution for the hip implant.

(1) A finite element (FE) model is created by processing the CT-scan data from the femur of a 38-year old patient. Two FE models are generated, one for the intact femur and the other for implanted femur; the difference in strain energy between them is used as proxy to quantify bone resorption [3]. The distal end and condyle are fixed and the loads, written in the (X, Y, Z) coordinate system, are F1 (-486, -295, 2063), F2 (75, 6, -111), F3 (9, 15, -111), F4 (-1, -1, 24) and F5 (-1, 19, 93).

(2) The macrogeometry of the implant is a minimally invasive design clinically relevant to current THA, whereas the microgeometry of the unit cell is a tetrahedron, which is used to aperiodically tessellate the implant domain. This unit cell is selected for its smooth mapping relationship to the tetrahedral solid element.

[a)] Corresponding authors: Email: damiano.pasini@mcgill.ca

(3) The properties of the unit cell are obtained via asymptotic homogenization (AH), e.g., the homogenized elastic modulus and the yield surfaces of the cell topology under multi-axial loading conditions. More details about the AH procedure can be found in [5].

(4, 5) The full strain and stress regimes for both the intact femur and the implanted femur are obtained via FEA. The mean and alternating stresses are used in the Soderberg's fatigue criterion to obtain the implant safety factor (SF).

(6, 7) A multi-constraint topology optimization (TO) scheme modified from the proportional TO [6] is used to optimize the relative density distribution of all elements associated to the 3D design domain. In particular, the maximal compliance problem is solved by using a density-continuous optimization approach modified from the proportional TO. In addition, the constraints of average porosity, pore size and cell wall thickness are directly taken into account during the optimization process by converting them into lower and upper bounds of relative density. Failure and fatigue analyses are performed at each iteration, and the design variables are updated to satisfy the failure and fatigue requirements. The optimal density distribution is obtained upon convergence of the modified TO.

RESULTS

Figure 2 (a), shows the optimal relative density distribution, and Figure 2 (b) the graded lattice obtained with an in-house code that can create the geometric model of the lattice ready for manufacturing. The performance of the optimized lattice implant is compared with a fully solid implant in Figure 2 (c), which shows that the former can greatly reduce bone resorption (1.4% vs 15.7%). Bone loss for the porous implant is only 9% of that for a benchmark implant with solid material. Comparing to our previous work [2], where the optimization time required to design a 2D implant was almost 3 days, the method presented in this paper for a more realistic 3D implant needs 10 minutes only, a factor that proves the superior efficiency of the scheme here proposed.
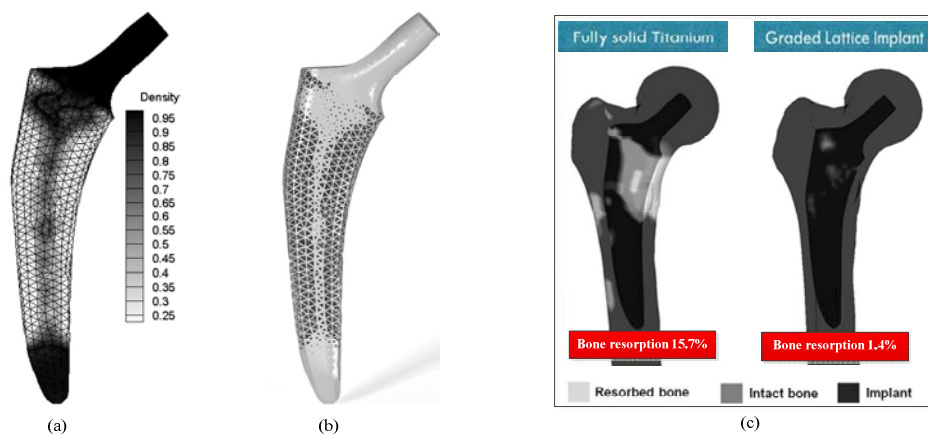

Figure 2. Results of optimized 3D lattice implant: (a) relative density distribution, (b) CAD model of the lattice implant and (c) bone resorption comparison with a fully solid implant.

CONCLUSIONS

In this paper, a multi-scale multi-constraint topology optimization method is proposed to optimize the relative density distribution of a 3D hip implant made of graded lattice material. Compared to a fully solid implant, the optimized implant here presented can reduce bone resorption of more than 90%.

References

[1] Pivec R., Johnson A.J., Mears S.C., Mont M.A.: Hip arthroplasty. *The Lancet* **380**:1768-1777, 2012.

[2] Khanoki S.A., Pasini D.: Multiscale design and multiobjective optimization of orthopedic hip implants with functionally graded cellular material. *Journal of biomechanical engineering* **134**:031004, 2012.

[3] Ridzwan M., Shuib S., Hassan A., Shokri A., Ibrahim M.M.: Problem of stress shielding and improvement to the hip implant designs: a review. *J Med Sci* **7**:460-467, 2007.

[4] Kurtz S., Ong K., Lau E., Mowat F., Halpern M.: Projections of primary and revision hip and knee arthroplasty in the United States from 2005 to 2030. *The Journal of Bone & Joint Surgery* **89**:780-785, 2007.

[5] Khanoki S.A., Pasini D.: Fatigue design of a mechanically biocompatible lattice for a proof-of-concept femoral stem. *Journal of the mechanical behavior of biomedical materials* **22**:65-83, 2013.

[6] Biyikli E., To A.C.: Proportional Topology Optimization: A New Non-Sensitivity Method for Solving Stress Constrained and Minimum Compliance Problems and Its Implementation in MATLAB. *PloS one* **10**, 2015.

ESTIMATES OF UPPER AND LOWER BOUNDS OF DISPERSIVE EFFECT IN THE HOMOGENIZED WAVE EQUATION

Takayuki Yamada[1 a] & Grégoire Allaire[2]

[1]*Department of Mechanical Engineering and Science, Kyoto University, Kyoto, Japan*
[2]*Centre de Mathématiques Appliquées, École Polytechnique, Palaiseau, France*

Summary Waves in periodic media undergo dispersion, namely the propagation velocity depends on the frequency. This effect can be modeled by an additional term in the homogenized wave equation. This paper presents the estimation of upper and lower bound of the dispersive effect in the two-dimensional wave equation in the case of an 8-fold symmetric periodic microstructure with constraints of volume, perimeter and homogenized properties.

INTRODUCTION

Dispersive effect is observed on wave propagation in inhomogeneous media. It is well known that the dispersive effect is modelled as a higher order terms (namely a fourth order term) in the homogenized wave equation. The fourth order term can be obtained by the method of two-scale asymptotic expansions or by the Bloch wave method. That is, wave propagation in periodic inhomogeneous media considering dispersive effect is modelled by the following equation.

$$
\begin{cases}
\dfrac{\partial^2 u_\epsilon}{\partial t^2} - \mathrm{div}(a^* \nabla u_\epsilon) + \epsilon^2 \mathbb{D}^* \nabla^4 u_\epsilon = f + \epsilon^2 \mathrm{div}(d^* \nabla f) \\
\qquad\qquad u_\epsilon(0, x) = u^{init}(x) \\
\qquad\qquad \dfrac{\partial u_\epsilon}{\partial t}(0, x) = v^{init}(x)
\end{cases}
\tag{1}
$$

where ϵ is the ratio between the period size and a characteristic length scale, a^* is homogenized material property $\mathbb{D}^*$ is a fourth-order tensor, called Burnnet tensor studied in [1,2,3], f is a source term and d^* is second-order tensor. The Burnnet tensor satisfies for any $\eta \in \mathbb{R}^d$ [2]

$$
\mathbb{D}^*(\eta \otimes \eta) : (\eta \otimes \eta) = -\int_Y a \nabla_y \left(\chi_\eta^{(1)} - \frac{1}{2} \left(\chi_\eta^{(1)} \right)^2 \right) \cdot \nabla_y \left(\chi_\eta^{(2)} - \frac{1}{2} \left(\chi_\eta^{(1)} \right)^2 \right) dy \le 0,
\tag{2}
$$

where $\chi_\eta^{(1)}$ and $\chi_\eta^{(2)}$ are defined as follows:

$$
-\mathrm{div}_y \left(a \nabla_y \chi_\eta^1 \right) = -\mathrm{div}_y(a\eta), \qquad \text{for } \eta \in \mathbb{R}^d
\tag{3}
$$

$$
-\mathrm{div}_y \left(a \nabla_y \chi_\eta^{(2)} \right) = b\eta \cdot \eta - a^* \eta \cdot \eta, \qquad \text{for } \eta \in \mathbb{R}^d
\tag{4}
$$
$$
\mathrm{b}_{ij} := a_{ij} - a\nabla_y \chi_i \cdot e_j - \mathrm{div}_y(\chi_i a e_j)
$$

The dispersive effect is very important in engineering standpoint, because the periodic size of microstructure is finite. This work presents numerical estimates of upper and lower bounds of the dispersive effect in the two-dimensional wave equation. We assume that the microstructure is imposed an 8-fold symmetric configuration and consist of two isotropic phases. Under this assumption, the Burnett tensor is characterized by two scalar parameters as follows:

$$
\mathbb{D}^*(\eta \otimes \eta) : (\eta \otimes \eta) = -\alpha \eta_1^4 - \beta \eta_1^2 \eta_2^2 - \alpha \eta_2^4
\tag{5}
$$

where is $\alpha, \beta \in \mathbb{R}_+^d$ defined as follows:

$$
\alpha := \int_Y a(\nabla \chi_{11} - \chi_1 \nabla \chi_1)^2 dy
\tag{6}
$$

---

[a] Corresponding author. Email: takayuki@me.kyoto-u.ac.jp

$$\beta := \int_Y a(\nabla\chi_{12} + \nabla\chi_{21} - \chi_1\nabla\chi_2 - \chi_2\nabla\chi_1)^2 dy \tag{7}$$

FORMULATION OF THE OPTIMIZATION PROBLEM

We introduce an additional assumption that the microstructure is made of two phases with boundary Γ and imposed constraints of phase proportions, interface perimeter and prescribed homogenized tensor. In order to estimate the upper and lower bound of the dispersive effect, we consider the multi-objective problems

$$\min_\Gamma \quad \text{or} \quad \max_\Gamma \qquad \alpha(\Gamma), \beta(\Gamma) \tag{8}$$

subject to: Volume constraint

                     Perimeter constraint   (9)

                     Prescribed homogenized tensor

That is, we compute the upper and lower curve in $\alpha - \beta$ coordinate system. In this work, the curve is estimated as a set of optimal solutions respect to a parameter θ_i utilizing level set-based shape optimization method [4]:.

$$\max_\Gamma \qquad J_i(\Gamma) = \alpha_{\theta_i} - c_p\beta_{\theta_i}^2 \tag{10}$$

where c_p is a parameter and

$$\begin{pmatrix} \alpha_{\theta_i} \\ \beta_{\theta_i} \end{pmatrix} := \begin{pmatrix} \cos\theta_i & \sin\theta_i \\ -\sin\theta_i & \cos\theta_i \end{pmatrix} \begin{pmatrix} \alpha_N \\ \beta_N \end{pmatrix}, \qquad \begin{pmatrix} \alpha_N \\ \beta_N \end{pmatrix} := \begin{pmatrix} \frac{\alpha(\Gamma)-\alpha_{\min}}{\alpha_{\max}-\alpha_{\min}} - c_\alpha \\ \frac{\beta(\Gamma)-\beta_{\min}}{\beta_{\max}-\beta_{\min}} - c_\beta \end{pmatrix}, \qquad 0 \le \theta_i \le 2\pi \tag{11}$$

where $\alpha_{\max}$, $\alpha_{\min}$, $\beta_{\max}$, $\beta_{\min}$ are maximum and minimum value of α, maximum and minimum value of β, respectively. That is, the Pareto optimal solutions are obtained by optimizing the interface Γ in the microstructure based on the optimization problem (10) and (11).

CONCLUSIONS

This works presents an optimization problem for the estimates of upper and lower bounds of the dispersive effect for wave propagation in two-phase periodic media.

References

[1] Santosa F., Symes, W.W.: A Dispersive Effective Medium for Wave Propagation in Periodic Composites, *SIAM Journal on Applied Mathmatics* **51**: 984-1005, 1991.

[2] Conca C. Orive R. Vanninatha, M.: On Burnett Coefficient in Periodic Media, *Journal of Mathematics Physics*, **47**: 032902, 2006.

[3] Lamacz A.: Dispersive Effective Models for Waves in Heterogeneous Media, *Math. Models Methods Appl. Sci.*, **21**:1871-1899, 2011.

[4] Allaire G., Jouve F., Toader A.M.: Structural Optimization Using Sensitivity Analysis and a Level Set Method, *Journal of Computational Physics*, **194**: 363-393, 2004.

GLOBAL MULTISCALE OPTIMIZATION DESIGN OF COMPOSITE LAMINATED FRAME STRUCTURE WITH MINIMUM STRUCTURAL COMPLIANCE

Zunyi Duan[1], Jun Yan[1, a)], Jingyuan Wang[1], Tao Yu[1], Erik Lund[2] & Guozhong Zhao[1]

[1]*State Key Laboratory of Structural Analysis for Industrial Equipment, Department of Engineering Mechanics, Dalian University of Technology, Liaoning, Dalian, 116024, China*

[2]*Department of Mechanical and Manufacturing Engineering, Aalborg University, Fibigerstraede 16, DK-9220 Aalborg East, Denmark*

<u>Summary</u> The concurrent multiscale optimization design of composite frames is investigated with gradient-based optimization algorithms. The winding angle in micro-material scale and the geometrical parameter of components of the frame in macro-structural scale are introduced as the independent variables on the two geometrical scales. The coupling effect of macro- and micro-scale design variables can be fully considered in the established multiscale optimization model to probe the potential of composite structures. The feasible domain is found to be non-convexity with the fiber winding angle as micro-material design variable. Then a new two-step optimization scheme is proposed to investigate the optimization design of the composite frame with minimum structural compliance, which increases the possibilities to find the global optimum with the gradient based algorithm.

INTRODUCTION

Fiber-reinforced composite frame structure is considered to be an ideal load carrying structure for aerospace structures. The composite frame can be considered as a geometrical multiscale structure, since the fiber-reinforced composite is characterized by its microstructure. With the point view of multiscale structure [1-3], the composite frame can be optimized concurrently at the macro-structural scale of geometrical parameters of components of the frame and at the micro-material scale of fiber winding angle. Significantly, filament winding parameters (filament winding angle, winding thickness and stacking sequence) can be considered as micro-material design variables which greatly influence the mechanical performance of the composite frame. However, one of the major difficulties using the filament winding angle as design variables is that the feasible domain of the optimization problem is non-convexity. This leads classical gradient-based optimization algorithms may be not effective, which is difficult to ensure the optimization converges to the global optimum [4]. The present paper presents a new two-step optimization scheme and investigates the optimization of composite frame with minimum structural compliance. It should be pointed out specially that the feasible domain is convex when the structural stiffness parameters (tension stiffness, bending stiffness, torsional stiffness) are considered as the design variables. The global optimum can be found in this case. Then adopting layer-wise constant shear beam theory, the equivalent structural stiffness parameters of composite beam can be explicitly integrally expressed as functions of filament winding angle. With ensuring the filament winding angle invariance of physical quantities, the sub-optimization problem between structural filament winding angle and equivalent structural stiffness parameter has been presented. Then implement the independent sub-optimization problems in the non-convex filament winding angle space and the convex structural stiffness parameter space iteratively. The objective sensitivity information with respect to design variables has been solved with the semi-analytical method [5] for the two kinds of design variables, i.e., the optimizations in the filament winding angle space and the equivalent structural stiffness parameter space. Numerical examples show that the proposed two-step optimization scheme can effectively improve the quality of optimization solution of the composite frame, which provides an effective method to approach a global optimum for the composite frame structure.

CONCURRENT OPTIMIZATION OF COMPOSITE FRAME

The schematic figure of concurrent multi-scale optimization of composite frame structure is shown in Fig. 1. For easy of deduction and no loss of generality, we assume the composite frame structure studied in this paper is composed with circular tubes. In macro-scale, the radius of cross-section (r_i) is recognized as macro design variable. As in classical topology optimization of frame structure, the tube's radius can be recognized as the size and topology variables at the same time. When the radius reaches its lower limit, the tube can be regarded to be deleted from the ground structure to realize the structural topology optimization. In micro-scale, the fiber winding angle (the continue fiber winding angles $\theta_{i,j}$) is recognized as the micro design variable.
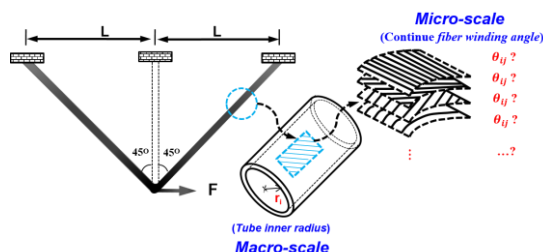
Fig. 1 Schematic of two-scale optimization of the composite frame structure

THE TWO-STEP OPTIMIZATION SCHEME FOR COMPOSITE FRAME

To cope with the non-convexity problem using the fiber winding angle as design variable, we propose a new two-step optimization scheme for composite frame optimization. The schematic diagram of the two-step optimization scheme is shown in Fig.2. Where x-axis represents the angle and the stiffness parameter space, y-axis is the value of optimized objective function. The solid black line represents the non-convex domain of fiber winding angle space. In the diagram, point A represents the local optimum, and point E is the global optimum. The black dashed line represents the convex domains of the stiffness parameter space.
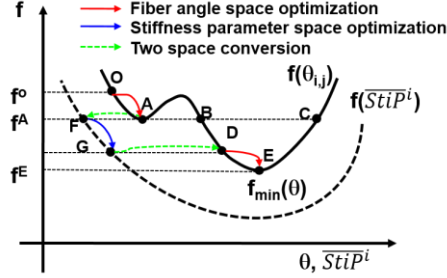

Fig. 2 Schematic diagram of the two space optimization

A two-step optimization scheme is established to lead the design domain to switch from a non-convex domain to a convex domain. Firstly, we generate a set of random or specified initial filament winding angle $^{SP}\theta_{i,j}$ as shown in Fig.2 with corresponding to the point O. Secondly, carry out the minimize optimization to obtain the local optimum point A with filament winding angle $^{OPT}\theta_{i,j}$ in fiber winding angle space. Thirdly, converse the filament winding angle $^{OPT}\theta_{i,j}$ to stiffness parameter space, then obtain the local optimum stiffness parameter $\left(^{OPT}\overline{StiP}^{k}\right)$ corresponding to point A. Finally, with the local optimum stiffness parameter $\left(^{OPT}\overline{StiP}^{k}\right)$ obtained by the previous step, we can obtain its corresponding objective function point F in the stiffness parameter space. Then set up the multi-objective minimized optimization problem in the parameter space $\min_{\theta_{i,j}} I$, where $I = \{4f_1 + f_2\}$, and following the constraints as $f\left\{\left(^{SP}\theta_{i,j}\right)^{k+1}\right\} \leq f\left\{\left(^{SP}\theta_{i,j}\right)^{k}\right\} \cap \left(^{SP}\theta_{i,j}\right)^{k+1} \neq \left(^{OPT}\theta_{i,j}\right)^{k}$. By this minimize optimization problem, we can get point G in stiffness space which is corresponding to point D in fiber winding angle space as the new starting point of design variables $\left(^{SP}\theta_{i,j}\right)^{k+1}$ in fiber winding angle space. Using the value of $\left(^{SP}\theta_{i,j}\right)^{k+1}$ as the new start point to optimize iteratively to approach point E. Repeat the third step and last step in this process until the $\min_{\theta_{i,j}} I$ can not determine a new start point for the optimization. Thus f^E will be regarded as the global optimum for the optimization of composite frame.

CONCLUSIONS

The present paper investigates the concurrent multiscale optimization design of composite frame with global optimization problem. With the layer-wise constant shear beam theory, we get the equivalent structural stiffness parameter by explicitly integrally expressed with respecting to the filament winding angle. To overcome the difficult of local optimum problem in case of the fiber winding angle as design variable, a new two-step optimization scheme is proposed. The multi-objective minimize optimization problem is established between the fiber winding angle space and stiffness parameter space, which can obtain a new optimized starting point in the fiber winding angle space and greatly increase the probability to approach the global optimal solution.

References

[1] Duan Z.Y., Yan J., Zhao G.Z.: Integrated optimization of the material and structure of composites based on the Heaviside penalization of discrete material model. Structural and Multidisciplinary Optimization, 2015 51, 721-732.
[2] Ferreira R.T.L, Rodrigues H.C., Guedes J.M., et al: Hierarchical optimization of laminated fiber reinforced composites. Composite Structures, 2014, 107: 246-259.
[3] Yan J, Duan Z.Y., Lund E., Zhao G.Z.: Concurrent multi-scale design optimization of composite frame structures using the heaviside panealization of discrete material model. Acta Mechanica Sinica, 2015, 1-12.
[4] Foldager J., Hansen J. S., Olhoff N.: A general approach forcing convexity of ply angle optimization in composite laminates. Structural Optimization, 1998. 16(2-3):201-211.
[5] Lund E: Buckling topology optimization of laminated multi-material composite shell structures. Composite Structures, 2009. 91(2):158-167